Part I
Introduction

Masamichi Fujihira
Tokyo Institute of Technology, Yokohama, Japan

Researches on *chemically modified electrodes* was initiated about three decades ago by Hubbard [1, 2], Murray [3], and Millar [4] and their coworkers. The field of the chemically modified electrodes diverged sharply from the traditional field of *adsorption on electrode surfaces* [5] in a sense that one *deliberately* seeks to immobilize a chemical on an electrode surface so that *the electrode displays the chemical, electrochemical, optical, and other properties of the immobilized molecule(s)*. After this first review, researches in the field in 1986 [6] is summarized and the concept of the chemically modified electrodes is extended from the viewpoint of the broadened definition of an electrode (system). In the broad sense, an ionically conductive phase being in contact with an electronically conductive phase can be regarded as the electrode (system). Then, a side view of an electrode (system) consists of (1) an electrode phase (the electronically conductive phase), (2) a transfer layer, (3) a diffused double layer, (4) a diffusion layer, and (5) a bulk solution. The region covering (2) and (3) is called an *electrical double layer*, and the region (2) ∼ (5) together corresponds to the ionically conductive phase. By broadening the definition of the electrode surface (or interface) including the region (2) ∼ (5) into the bulk of solution, variation of possible ways to deliberately design the functional electrode surfaces has been expanded. For example, electrochemistry in micelles, microemulsions, and related microheterogeneous fluids has been studied [7].

Not only the functional variations but also the chemical variations of the chemically modified electrodes have been broadened. Atomically modified electrode surfaces [7] have become popular with the developments in electrochemistry on surfaces of single crystals [8, 9] as well as the study of underpotential depositions (UPD) [10]. Introduction of functions into the region (2)–(4) has been attained by using polymers [11, 12]. After a pioneering electrochemical study by Taniguchi et al. [13], self-assembled monolayers (SAMs) of disulfides and thiols on gold electrodes [14, 15] have been studied extensively.

This Volume describes, how to prepare monolayer modified electrodes on metals, carbons, silicon, conducting metal oxides, and chalcogenides; how to prepare film modified electrodes including polymer

Encyclopedia of Electrochemistry. Edited by A.J. Bard and M. Stratmann
Vol. 10 *Modified Electrodes*. Edited by M.Fujihira, I.Rubinstein, and J.F.Rusling
Copyright © 2007 Wiley-VCH Verlag GmbH & Co. KGaA, Weinheim. ISBN: 978-3-527-30402-8

modified electrodes; how to characterize ex situ or in situ the modified electrodes, and, finally, functions and applications of modified electrodes.

References

1. R. F. Lane, A. T. Hubbard, *J. Phys. Chem.* **1973**, *77*, 1401–1410.
2. R. F. Lane, A. T. Hubbard, *J. Phys. Chem.* **1973**, *77*, 1411–1421.
3. P. R. Moses, L. Wier, R. W. Murry, *Anal. Chem.* **1975**, *47*, 1882–1886.
4. B. F. Watkins, J. R. Behling, E. Kariv et al., *J. Am. Chem. Soc.* **1975**, *97*, 3549–3550.
5. R. W. Murray, in *Electroanalytical Chemistry* (Ed.: A. J. Bard), Marcel Dekker, New York, 1984, pp. 191–368, Vol. 13.
6. M. Fujihira, in *Topics in Organic Electrochemistry* (Eds.: A. J. Fry, W. E. Britton), Plenum, New York, 1986, pp. 255–294.
7. J. F. Rusling, in *Electroanalytical Chemistry* (Ed.: A. J. Bard), Marcel Dekker, New York, 1994, pp. 1–88, Vol. 18.
8. J. Clavilier, *J. Electroanal. Chem.* **1980**, *107*, 205–209.
9. A. Hamelin, in *Modern Aspect of Electrochemistry* (Eds.: B. E. Conway, R. H. White, J. O. M. Bockris), Plenum, New York, 1985, pp. 1–101, Vol. 16.
10. D. M. Kolb, in *Advances in Electrochemistry and Electrochemical Engineering* (Eds.: H. Gerischer, C. W. Tobias), John Wiley & Sons, New York, 1978, pp. 125–271, Vol. 11.
11. R. Murray (Ed.), *Molecular Design of Electrode Surfaces*, in *Techniques of Chemistry* (Eds.: A. Weissberger, W. H. Saunders Jr.), John Wiley & Sons, New York, 1992, Vol. 22.
12. G. Inzelt, in *Electroanalytical Chemistry* (Ed.: A. J. Bard), Marcel Dekker, New York, 1994, pp. 89–241, Vol. 18.
13. I. Taniguchi, K. Toyosawa, H. Yamaguchi et al., *J. Chem. Soc., Chem. Commun.* **1982**, 1032–1033.
14. R. G. Nuzzo, D. L. Allara, *J. Am. Chem. Soc.* **1983**, *105*, 4481–4483.
15. L. H. Dubois, R. G. Nuzzo, *Annu. Rev. Phys. Chem.* **1992**, *43*, 437–463.

1.1 Modification of Transparent Conducting Oxide (TCO) Electrodes through Silanization and Chemisorption of Small Molecules

Michael Brumbach and Neal R. Armstrong
University of Arizona, Tucson, Arizona

1.1.1 Introduction

1.1.1.1 The Metal Oxide Electrode and Modification Schemes

Surface modification of transparent conducting oxide (TCO) thin film electrodes (indium–tin oxide (ITO), SnO_2, TiO_2, ZnO, etc.) has traditionally been directed toward enhancement of heterogeneous electron transfer rates of solution species for which the electron transfer process is thermodynamically favored but kinetically inhibited. The surface-confined molecule is intended to exhibit rapid and reversible electron transfer at the oxide surface to provide rapid mediation of electron transfer to a solution species [1]. Surface-confined molecules are typically not directly ''wired'' into the conduction or valence band of the oxide, but electron transfer rates are often reasonably fast for these species simply because they have been brought into close proximity to the electronically active sites of the metal oxide. Chemical modification of the TCO surface can be accomplished through covalent bond formation (silanization) or through chemisorption of molecules containing functional groups such as carboxylic acids, phosphonic acids, alkanethiols, and amines.

Initial modification strategies were employed for oxidation of biomolecules, such as ascorbic acid, neurotransmitters, heme proteins, and so forth using various surface-confined molecules or thin films of conducting polymers. Modification schemes have also been used to attach photoactive dye molecules, such as phthalocyanines, porphyrins, and a variety of organometallic complexes, to oxide surfaces to enhance redox processes between solution species and semiconducting electrodes [2–6]. Chemical modification of conducting oxide surfaces has also been used to enhance charge injection rates into condensed phase organic thin film devices (for example, in organic light emitting diodes (OLEDs) and organic photovoltaics (OPVs)). There is still some debate as to whether the enhancement in device performance is due to enhancements in wettability of the oxide surface toward the nonpolar molecules used in these devices, to changes in work function of the oxide surface, and/or to enhancements in

Encyclopedia of Electrochemistry. Edited by A.J. Bard and M. Stratmann
Vol. 10 *Modified Electrodes*. Edited by M.Fujihira, I.Rubinstein, and J.F.Rusling
Copyright © 2007 Wiley-VCH Verlag GmbH & Co. KGaA, Weinheim. ISBN: 978-3-527-30402-8

intrinsic rates of charge injection [7–13]. Many of the same strategies initially used to enhance solution electron transfer rates on these oxide surfaces appear to positively impact device efficiencies in simple OLEDs and OPVs [9, 14–18].

1.1.1.2 Commonly Encountered TCO Electrodes

The most commonly encountered TCO electrodes, typically studied as thin films, are antimony-doped tin oxide (ATO) or fluorine-doped tin oxide (FTO), ITO, titanium oxide (anatase or rutile, TiO_2), and zinc oxide (ZnO) [19]. There are also some recently reported trinary and ternary oxides based on modifications of ITO, zinc-indium tin oxide, ZITO or IZTO, for example, which may become more popular with time as electrodes for solution-based redox chemistry and as anodes in devices such as OLEDs and OPVs [7]. These new tailored composition oxides may exhibit higher stability, higher work functions, and/or a greater variety of surface sites with more possibilities for chemical modification.

An idealized metal oxide surface is shown in Fig. 1, where the metal atoms are in tetrahedral coordination with four oxygen atoms. This metal oxide, empirical formula MO_x, is stoichiometric, having no defects or surface hydrolysis products, and can be considered as a typical platform for understanding the modification of most TCO thin film materials of electrochemical interest. TCO films are typically deposited by sputtering, chemical vapor deposition, or pulsed laser deposition, and tend to be ''microcrystalline'' whose dominant exposed faces tend to be either ⟨111⟩ or ⟨100⟩ lattice terminations [19–23]. The structure and electronic properties of several TCO films can be summarized as follows:

Indium–Tin Oxide (ITO): ITO has the complex unit cell of indium oxide (bixbyite lattice) consisting of more than 80 atoms. Indium oxide has two distinct indium sites in the lattice and as many as four oxygen species, considering surface hydrolysis products and oxygen vacancies [24]. Oxygen vacancies and electron-rich interstitial tin dopant sites lie close in energy to the conduction band edge so that promotion of electrons into the conduction band, at room temperature, is facile [25]. Figure 2 shows the proposed band diagram for ITO exhibiting the common features that dictate the electrical properties of many TCO materials. The upper portion of the valence band arises from filled O(2p) orbitals, while the lower part of the conduction band arises from unfilled metal orbitals (In(5s) orbitals in the case of ITO). Oxygen defects are induced into the TCO material during its formation, usually by depositing or annealing the thin film in an oxygen-deficient atmosphere, thus creating electron-rich sites within a few kT of the conduction band edge. An interstitial dopant, tin, is often introduced into these In_2O_3 lattices at concentrations up to 10% (atomic), producing additional electron-rich sites within a few kT of the conduction band edge. In ITO, the donor density can be as high as 10^{20} cm^{-3} with a sheet resistance as low as 10 Ω sq^{-1}. The introduction of oxygen defect sites and other dopants, however, may also increase the chemical reactivity of these oxide surfaces toward hydrolysis

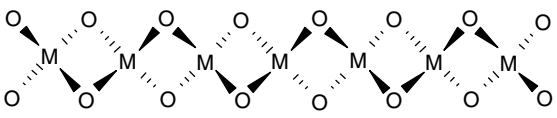


Fig. 1 Schematic view of an ideal metal oxide surface.

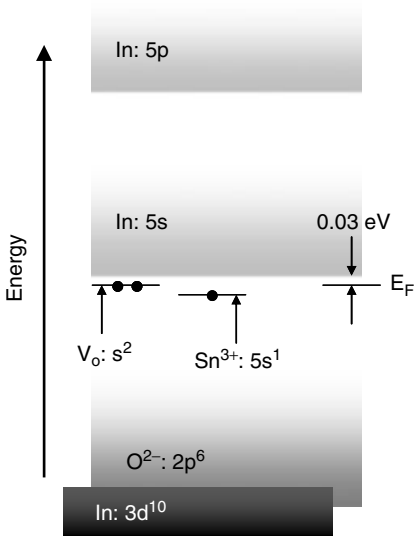


Fig. 2 Schematic view of the energy levels in ITO showing the components of the valence band and conduction band regions of the oxide, the presence of oxygen defect sites and interstitial tin dopant sites that contribute to electron density near the conduction band edge, rendering the oxide conductive at room temperature (after Ref. 25).

and other components of the vacuum deposition system. The reactivity of the oxide surface has important consequences for their further modification and enhancement of electron transfer rates, which have been extensively studied as functions of surface pretreatment [8, 24, 26, 27].

Tin Oxide (SnO_2): Tin oxide has a tetragonal rutile structure with a unit cell of six atoms. The electrical conductivity of n-doped SnO_2 is due to the presence of oxygen vacancies, interstitial tin (in excess), or added dopants such as fluorine, chlorine, or antimony. Carrier concentrations can be increased to approximately 10^{20} cm^{-3} through doping from the intrinsic concentration of approximately 10^{18} cm^{-3} for SnO_2 [19].

Titanium Oxide (TiO_2): Titanium oxide exists in three different crystallographic structures, rutile, anatase, and brookite. The most commonly studied material is rutile, being the most stable phase, although many studies have been conducted on the anatase phase as well [28]. Stoichiometric rutile contains Ti^{4+} in six-fold coordination with oxygen staggered by Ti^{4+} in five-fold coordination. Oxygen atoms at the surface are often bridging and only two-fold coordinated [23]. The band gap of rutile is 3.0 eV, and 3.2 eV for anatase, making titanium oxide a useful material for photocatalysis [29–31]. Photoelectrochemical cells based on sintered nanoparticulate arrays of anatase or thin film TiO_2 electrodes have been quite successful [32, 33]. Both anatase and rutile forms of TiO_2 are readily n-doped by creation of oxygen vacancies leaving electron-rich Ti^{3+} and Ti^{2+} states in the band gap, with electron energies sufficiently close to the conduction band edge so as to provide for reasonable room temperature conductivity.

1.1.1.3 Variability in TCO Electrodes

TCO thin films can exhibit tremendous variability in transparency, microstructure (and surface roughness), surface composition, conductivity, chemical stability at high current densities (in OLEDs, OPVs, and chemical sensors), and in their chemical compatibility with contacting organic layers. Variability is often noticeable from production batch to production batch and within batches of the same metal oxide material [34]. Surface pretreatment conditions have also been shown to dramatically impact the electrochemical, physical, and photophysical properties of metal oxide films [8, 9, 24, 26, 27, 35]. Modification

of these surfaces through silanization and chemisorption would appear to be a means for improving the stability of these oxide surfaces, enhancing their compatibility with nonpolar solvents and condensed phase materials, and optimizing rates of interfacial electron transfer.

1.1.2 Factors that Control the Surface Composition of the TCO Electrode

The structure shown in Fig. 1, representing an ideal metal oxide surface, provides a useful platform for understanding metal oxide surfaces. A further, and more realistic, modification to the model would account for the presence of surface hydrolysis products as shown in Fig. 3. Surface hydrolysis critically affects the chemical modification of the TCO surface. Moderate hydrolysis may only break bridging oxygen-metal bonds leaving surface hydroxyl groups. More extensive hydrolysis can lead to fully hydroxylated metal species that may remain physisorbed. The presence of dopants and/or oxygen vacancies, as shown in Fig. 4, can also affect the metal oxide surface by creating sites that can react with adventitious impurities present during, or after, deposition.

Varying degrees of hydroxylation and defect density, as well as the preferential migration of dopants to the near surface region, contribute to the high degree of heterogeneity in electron transfer rates and chemical compatibility commonly observed with oxide electrodes. Hydrolysis products on ITO remain strongly physisorbed (precipitated) to the electrode surface at greater than monolayer coverage, constituting a primary factor for the appearance of electrical ''dead spots'' on the oxide surface [24, 36, 37]. The so-called ''dead spots'' are regions exhibiting poor electroactivity or no electroactivity.

Surface hydrolysis of metal oxide surfaces can be examined by comparison to solution equilibrium constants for hydrolysis and solubility. Indium oxide has a favorable equilibrium constant for hydrolysis [38–40]:

$$In_2O_3 + 3H_2O \longleftrightarrow 2In(OH)_3 \qquad K = 4.3 \times 10^1 \quad (1)$$

Whereas, the fully hydrolyzed In moiety, $In(OH)_3$, has a very low solubility product.

$$In(OH)_3 \longleftrightarrow In^{3+} + 3OH^- \qquad K_{sp} = 1.3 \times 10^{-37} \quad (2)$$

There is also the possibility for incomplete hydrolysis of an indium surface oxide creating the intermediate hydroxylated species, InOOH:

$$In_2O_3 + H_2O \longleftrightarrow 2InOOH \quad (3)$$

This type of surface site may also arise by the nucleophilic attack of water on exposed oxide defects, which serve as sites for dissociative adsorption. In contrast, hydrolysis of tin oxide is significantly less

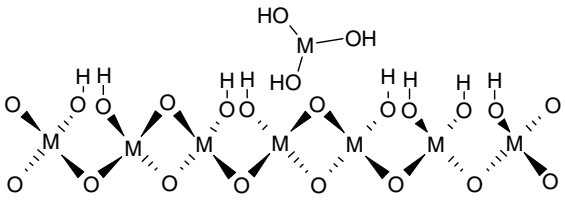


Fig. 3 Schematic view of an oxide surface that has undergone hydrolysis, producing hydroxylated sites, and even physisorbed metal hydroxide, monomers or polymers.

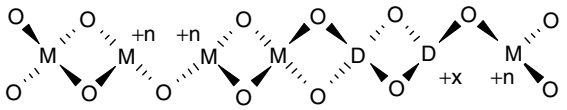


Fig. 4 Schematic view of the near surface region of the oxide thin film with oxygen vacancies, producing electron-rich metal sites and dopant sites of lower stoichiometry, and also creating electron-rich sites.

favored than for indium oxide, at any pH [38, 39]:

$$SnO_2 + 2H_2O \longleftrightarrow Sn(OH)_4 \qquad K = 5.6 \times 10^{-10} \quad (4)$$

While the solubility of tin hydroxide is higher than for indium hydroxide:

$$Sn(OH)_2 \longleftrightarrow Sn^{2+} + 2(OH^-) \qquad K = 1.4 \times 10^{-28} \quad (5)$$

$$Sn(OH)_4 \longleftrightarrow Sn^{4+} + 4(OH^-) \qquad K = 7.2 \times 10^{-14} \quad (6)$$

The typical doped SnO_2 thin film can therefore be expected to show monolayer (but not significantly higher) coverages of hydroxide species. Hydroxide species in excess of monolayer coverage would be expected to be more easily removed from the oxide surface through pretreatment steps.

For titanium oxides and zinc oxides, similar hydrolysis and dissolution processes must be considered [39, 41]:

$$Zn(OH)_2 \longleftrightarrow Zn^{2+} + 2OH^- \qquad K_{sp} = 3 \times 10^{-16} \quad (7)$$

$$Ti(OH)_4 \longleftrightarrow Ti^{4+} + 4OH^- \qquad K_{sp} = 7.94 \times 10^{-54} \quad (8)$$

Chemical modification of these oxides, therefore, needs to take into account the routes to formation and loss of surface hydroxide species playing a key role in determining the surface coverage of the modifier. Rates of electron transfer/charge injection at the modified oxide surface are subsequently affected. Despite the uncertainties in oxide surface composition, several modification protocols have been developed over the last thirty years, which yield improved electrochemical performance of the TCO thin film. Two strategies have continued to be successful at modifying metal oxide electrodes; silanization, covalent bond formation to metal hydroxides, and chemisorption, using functional groups known to either hydrogen bond to M–OH sites and/or to coordinate to metal cation sites.

1.1.3 Chemical Modification of TCO Surfaces Using Silane Chemistries

1.1.3.1 Introduction to Silane Modification

Surface modification of TCO thin films with monofunctional, difunctional, and trifunctional organosilanes arose initially from protocols developed in modifying silica surfaces [42]. The covalent attachment of functional groups to the oxide surface through silanization involves the coupling of the functionalized silane to the metal oxide at hydroxylated sites, through a metal–oxygen–silicon bonded network with the release of one or more ''leaving groups'' as shown in Fig. 5. ''Leaving groups'' are generally chlorides or alkoxides (methoxide or ethoxide) yielding HCl or the corresponding alcohol as by-products.

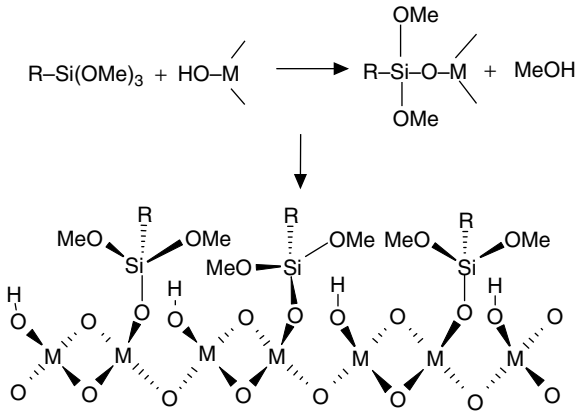


Fig. 5 Schematic view of silane modification of an oxide surface, using (as an example) a tri-methoxy silane. Reaction with only one surface hydroxide site is shown, releasing methanol as the product. Unreacted hydroxide sites remain, as do unreacted alkoxy groups on the silane, which can further cross-link under appropriate conditions.

In the absence of water, silane modifiers can form multiple bonds to the surface creating a clawlike multidentate attachment, Fig. 6(a) [43]. Silanes with multiple leaving groups, however, will generally cross-link during the surface attachment process, or afterward during storage in high humid environments, to form a polymeric, hydrolytically stable layer, as shown in Fig. 6(b). The functional group (R) can be an alkyl or aromatic group terminating with a redox active molecule (ferrocene, viologen, porphyrin, phthalocyanine, etc.) or can simply be tailored to control the wettability of the TCO surface.

It is desirable to start with a surface that has been mildly hydroxylated for surface modification, as opposed to the stoichiometric surface shown in Fig. 1, so that there are sufficient reactive sites for silanization. If the redox chemistry of an attached molecule is to be optimized, it is also desirable to work with monofunctional silanes. In this case, only one

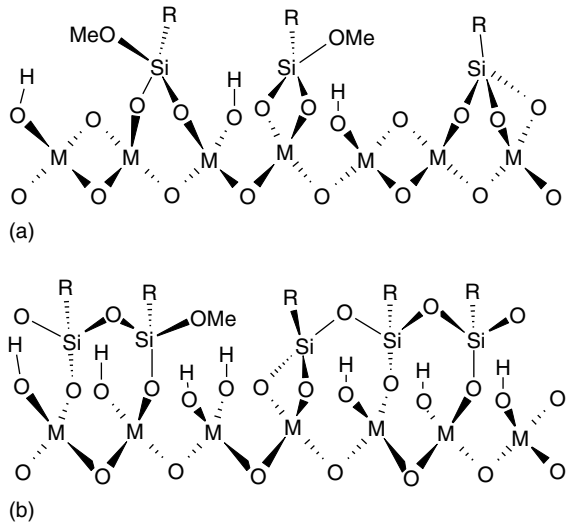


Fig. 6 Schematic view of cross-linking a silane surface modifier as it passes through the (a) multidentate/brush phase to the (b) fully cross-linked phase, with relatively few unreacted M−OH groups left on the oxide surface.

attachment site is created, thereby leaving the tethered redox group in close proximity to the electrode surface and promoting reasonable rates of electron transfer [1]. Control of surface hydroxylation, however, given the tendency of oxides to extensively hydrolyze, is problematic and affects the coverage of redox active groups that can be achieved through silanization reactions. Silane formation on SnO_2 surfaces, where hydrolysis can be more easily controlled appears to be a more advantageous strategy.

Silanization is generally performed in refluxing toluene or benzene with low concentrations of the desired silane. Silanes of the form $X(R2)_2SiR1$ have only one reactive bond and can therefore make only one bond with the metal oxide surface (see Fig. 5). X represents a chloride, methoxy, ethoxy, or other ''leaving group.'' R2 groups are typically small substitutents such as methyl groups, but can be changed to something larger such as phenyl groups to provide steric hindrance and blocking unsilanized surface sites. Large side chains would, however, also sterically reduce the number of silane molecules bound to the oxide. The energy barrier for the surface bonded silane to rehydroxylate, and the metal oxide to ''heal,'' with a bridging oxygen, is extremely low. Therefore, these brushlike phases are generally unstable and nearly all of the brushlike phases reported in the literature are produced with triply reactive silanes reacted under highly controlled dry conditions such that multiple bonds can be made with the surface, as shown in Fig. 6(a). According to Kirkov, there are 2.23×10^{15} Sn−O sites cm^2 on SnO_2 [44, 45], and similar site densities can be expected for ITO and TiO_2. Since not all sites will be uniformly reactive, a maximum surface coverage is approximately 10^{-10} moles cm^{-2} for a brushlike silanized layer with tridentate attachment.

1.1.3.2 Examples of Silane Modification

Trimethoxysilane molecules will covalently attach to ITO following a reflux of the electrode in a 10% (silane:toluene) solution for approximately 30 min [37]. Excess silane can be removed by sonication for 10 min in pure toluene. Water contact angle measurements on such modified surfaces immediately show increased contact angles, consistent with the addition of silane molecules with nonpolar functionality to the surface. On ITO, the contact angle can change from less than 30° before modification, to angles higher than 65° after modification, and even higher if cross-linking of the silane occurs [37, 46]. X-ray photoelectron spectroscopy (XPS) is also used to verify the presence of silicon on the surface. Shepard and Armstrong have measured the electrode interfacial capacitance at tin oxide electrodes modified with a series of silanes [47–50]. The capacitance studies showed the sensitivity of the electrical properties of modified surfaces to variations in reaction conditions during silanization, and to the types of functional groups attached to these surfaces.

Untereker et al. used several methods for creating clawlike brush phase silane layers on SnO_2, TiO_2, and glass [43]. SnO_2 was modified with γ-aminopropyl-triethoxysilane, 3-(2-(aminoethylamino)propyltrimethoxysilane), and β-trichlorosilyl-2-ethylpyridine by exposing the electrodes to 2–10% organosilane solutions in refluxing benzene or xylene under N_2 for up to 12 h. The electrodes were washed with dry benzene. A similar procedure was used for silanizing SnO_2 and TiO_2 at room temperature with lower silane concentrations.

Another brief exposure was performed with 1% organosilane in benzene at 6 °C under argon for 10 s. A more aggressive silanization procedure was used to modify glass with neat organosilane in a sealed tube at 90 °C for 12 h. The authors evaluated their films via XPS to determine thickness and approximate surface coverages.

Finklea and Murray accomplished the silanization of single crystal TiO_2 following a 5 min exposure of the electrodes to 10% silane solutions in either toluene or benzene. Excess silane was removed with fresh solvent, while methanol was found to reduce the silane coverage [51]. The silanes evaluated in these studies were 3-(2-aminoethylamino)-propyltrimethoxysilane, methyltrichlorosilane, and dimethyl-dichlorosilane. XPS surface analysis showed the presence of some cross-linking but could not conclusively characterize the homogeneity of the modified surface. Their photocurrent results indicated that the M−O−Si bond is oxidatively stable to photo-generated holes and, therefore, may provide a useful means of modifying TiO_2 particles for use in dye sensitized solar cells DSSCs. Redox active and photoelectrochemically active metal phthalocyanines were attached to γ-aminopropyltriethoxysilane-modified SnO_2. Tetrasulfonated cobalt and copper phthalocyanines (CoTSPc and CuTSPc) were modified with thionyl chloride, to provide for attachment to the silanized surface via formation of sulfonamide linkages [47, 50].

Phenyl and diphenyl silane-modified ITO surfaces have been used to improve the physical compatibility with Langmuir–Blodgett thin films of phthalocyanine assemblies, where the direct electron transfer of the assembly with the ITO surface was of concern [46].

C_{60} has been tethered to ITO in a self-assembled network by exposing the ITO to basic conditions followed by a reflux in high concentrations of $(MeO)_3Si(CH_2)_3NH_2$ in benzene for half a day [52]. The electrodes were then multiply rinsed before refluxing in a 1-mM solution of C_{60} in benzene for as long as 2 days. This scheme resulted in an ITO-silane-N-C_{60} tethered network and allowed for the formation of an organized C_{60} layer on the ITO surface. Quartz and glass were similarly modified for spectroscopic comparisons. Nearly, all monolayer coverage of C_{60} was determined electrochemically, 1.7×10^{-10} mols cm^{-2}. Reduction of C_{60} in these films is shifted more negatively, indicating a direct interaction between the underlying silyl-amine layer and C_{60}.

1.1.3.3 Silane Modification of Electrodes for Use in Devices

Perfect cross-linking of silane molecules is unlikely in most circumstances due to a mismatch in the lattice spacing between the cross-linked silane layer and the underlying metal oxide substrate. A more accurate picture of a silanized surface would consist of some silane molecules attached via multidentate binding interspersed with cross-linked neighboring silanes as shown in Fig. 6(b). Extensive cross-linking of surface silanes may provide a stable modified surface; however, it also appears to impede electron transfer and, for optimization of solution redox processes, may not be desirable [1, 46].

Marks and coworkers have shown how extensively cross-linked silane monolayers and multilayers can be used to stabilize an electrode and regulate charge injection in a condensed OLED phase [14, 53–55]. Their approach has been to start with silanes functionalized with various redox active

groups and to terminate by functional groups, which can subsequently be converted to new reactive silanes, to produce a layer-by-layer ''self-limiting'' chemistry. Multilayer formation can be well controlled, leading to desired film thicknesses and orientation of the charge transporting core molecules [14]. In general, these modified electrodes show significantly improved performance as anodes in OLEDs, apparently due to the fact that hole injection into the tri-arylamine hole transport layer (which is the core molecule being cross-linked by these silanes), is impeded after modification. This allows for a more balanced injection of both holes and electrons in the device and results in the emissive state forming in the middle of the thin film device [14].

Chlorosilanes are often used to aid in the extensive cross-linking that is desired for the modification of anodes for use in OLED devices. Chlorosilanes liberate HCl as a by-product of silane attachment, which can degrade the TCO surface if low concentrations of base are not added for neutralization. No significant etching of the TCO anode surface has been noted, and surface analysis of the modified electrode generally indicates no entrapped chlorine [14, 51–53].

Silane modification of ITO and SnO_2 electrodes has also been used to create nearly perfect ''blocking'' electrodes, such as thin films where rates of electron transfer are intentionally kept low, so as to provide for measurement in changes in interfacial potential of an additional overlayer, such as a bilayer lipid membrane, during ion transport, pH changes, and so forth. Hillebrandt and Tanaka have evaluated the effects of octyltrimethoxysilane (OTMS), octadecyltrimethoxysilane (ODTMS), and octadecyltrichlorosilane (OTS) on ITO for applications to lipid-membrane-based biological sensors [56–58]. The authors found that the ITO electrodes can be effectively blocked from electron transfer by silanization. Silanization results in more uniform films suitable for the biological sensor platform, with ionic diffusion occurring almost entirely from pinholes in the film. Silanization was accomplished by sonicating ITO substrates in 5 vol% solutions of the silane in dry toluene with 0.5 vol% n-butylamine, followed by 30 min of incubation. Temperatures were held below 293 K for ODTMS and below 280 K for OTMS. Sonication in dry toluene for 2 min removed excess silane. Markovich and Mandler also derivatized ITO with ODTMS but derivatization was performed over a seven-day period [59, 60].

The long alkyl chain length and stability of cross-linked silanized surfaces also allows for their use as masks for patterning and etching TCO substrates. ODTMS has been used as a mask for patterning ITO [61]. Luscombe et al. have used perfluorodecyltrichlorosilane as a mask for etch resists for lithographic processing of ITO surfaces [62].

1.1.4 Modification of TCO Surfaces through Chemisorption of Small Molecules

1.1.4.1 Modification using Small Molecules Containing Carboxylic Acid Functionality

Modification of electrode surfaces through chemisorption has been more in recent reports than silanization, and its discussion here is intended to contrast the strategies used for both types of surface modification. Chemisorption of small molecules to the TCO surface allows for robust modifications occurring over short distances and with relatively strong interactive forces (ΔH = ca. 200 kJ mol^{-1}) through

combinations of electrostatic, H-bonding, and metal ion coordination. Chemisorption processes generally have a high activation barrier for adsorption, may be irreversible, and can "self-limit" at monolayer coverage. Owing to the amphoteric nature of metal oxide surfaces, chemisorption of Lewis acids such as carboxylic acids, aliphatic and aromatic amines, and phosphonic acids are generally successful. Chemisorption typically anchors individual molecules in close proximity to metal cationic sites and may also compete for sites with surface hydrolysis products. Previous work has examined chemisorption to ITO, SnO_2, and TiO_2 surfaces, with most of the studies reporting adsorption of either carboxylic or phosphonic acids or salts.

Carboxylate functionalities have been used repeatedly and successfully as an anchoring group for molecular chemisorption to oxide electrodes proceeding through the formation of an ester linkage to the metal with the loss of water, or through hydrogen-bonding interactions to surface hydroxyl groups. Possible interactions for carboxylic groups are shown in Fig. 7. Binding constants for the carboxylic group for ITO and ATO have been determined to be as high as $8 \times 10^4\ M^{-1}$ [34].

Chemisorption is often as successful as silanization at obtaining monolayer coverages of small molecule modifiers. As an example, Davis and Murray attempted to couple iron porphyrins to amine-terminated silanized SnO_2 surfaces. The authors found that the surface coverage was independent of the apparent extent of surface silanization [63]. Silanized and unsilanized electrodes were soaked in 5 mM porphyrin dissolved in DMF, THF, or pyridine solutions overnight. Porphyrins with pendant carboxylic acid groups produced higher surface coverages (determined by coulometric analysis of the voltammetry of the surface-confined species) on bare, unmodified SnO_2 than seen on SnO_2 electrodes modified with 3-(2-aminoethylamino)propyltrimethoxysilane.

Zotti and coworkers adsorbed several carboxylated ferrocene derivatives on ITO: ferrocene-carboxylic acid (Fc(COOH)), ferrocene-dicarboxylic acid ($Fc(COOH)_2$), and ferrocenylheptanoic acid $Fc(CH_2)_6COOH$ [64]. Fc(COOH) was adsorbed from 1-mM solutions of the molecule in 5/95 ethanol/hexane for as

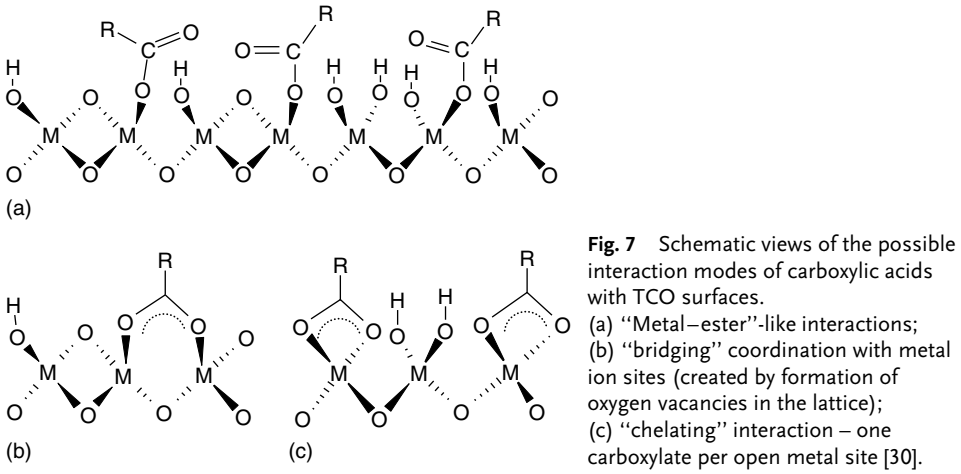


Fig. 7 Schematic views of the possible interaction modes of carboxylic acids with TCO surfaces.
(a) "Metal–ester"-like interactions;
(b) "bridging" coordination with metal ion sites (created by formation of oxygen vacancies in the lattice);
(c) "chelating" interaction – one carboxylate per open metal site [30].

long as 16 h, followed by a rinse with acetonitrile. Higher solution concentrations were found to yield higher surface coverage, following a Langmuir adsorption isotherm, with saturation coverage (ca. 1×10^{-10} mols cm^{-2}) occurring at approximately 10 mM solution concentration. The saturation coverage, however, was 25% of the expected monolayer coverage (4×10^{-10} mols cm^{-2}) based on the geometric area [65]. $Fc(COOH)_2$ was adsorbed from ethanol, while $Fc[(CH_2)_6COOH]$ was adsorbed from hexane. Adsorption of these molecules appears to be kinetically limited. Recent work has shown that time for adsorption is required to remove hydrolysis products (e.g. $In(OH)_3$) or other nonelectroactive species adsorbed to the ITO surface [66].

$Fc(COOH)_2$ has been used successfully to increase electron transfer rates and for enhancing the performance of organic light emitting devices and organic photovoltaics [24, 37]. In addition to modifications of electron transfer rates, carboxylic acid-modified small molecules have been used to introduce dipole fields at the surface of TCO substrates. For example, benzoic acid derivatives have been used to modify the interface dipole at ITO surfaces, attached to the oxide surface via formation of a Langmuir–Blodgett thin film. Changes in work function closely relate to changes in the dipole induced by the derivatized modifiers [67].

Dye molecules possessing carboxylate functionalities have been extensively explored as sensitizers of semiconducting oxide electrodes toward visible light in photoelectrochemical cells [4, 32, 68]. Dye sensitization was first explored as a means of enhancing the photocatalytic properties of TiO_2 [69–72]. Spitler and coworkers investigated dye sensitization of ZnO electrodes using carboxylic acid functionalized dyes [4–6]. The authors found that the photocurrent produced by dye sensitized TiO_2 and ZnO crystals closely resembled the absorption spectrum of the dye, indicating that the dye is in close proximity to the crystal and, upon excitation, injects charge into the semiconductor from energy levels that are relatively unperturbed.

The observation of photocurrent from dye sensitized planar semiconductors led to the evolution of the DSSC, on the basis of extremely high surface area nanoparticulate oxides, usually TiO_2. The most successful dye for sensitization, N3, *cis*-bis(isothiocyanato) bis(2,2′-bipyridyl-4,4′dicarboxylato) ruthenium (II), employs several carboxylic acid groups for adsorption to TiO_2, ZnO, SnO_2, and/or ITO from an ethanol or acetonitrile solution over a several-hour period [32]. Electron injection from the excited state of this dye to the conduction band

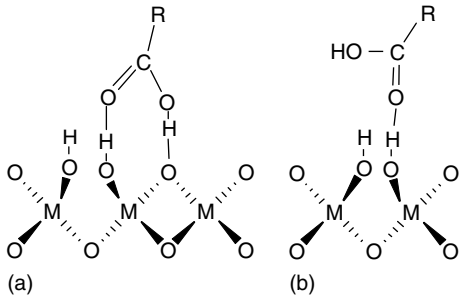


Fig. 8 Schematic views of possible hydrogen-bonding interactions of protonated carboxylic acids to an ideal TCO surface. (a) Interaction mode where the protonated carboxylic acid H-bonds to a bridging oxygen. A hydroxylated metal site also H-bonds to the second carboxylic oxygen. (b) A single hydrogen bond is also plausible.

of the oxide is believed to occur on a femtosecond timescale [73, 74]. Binding constants for the carboxylated dyes assuming an ester linkage are $8 \times 10^4\ M^{-1}$ on SnO_2 from chloroform [73]. A similar carboxylated ruthenium complex has been evaluated on ATO, ITO, TiO_2, and SiO_2 [34]. The authors argue for ester linkages on all substrates except silica. On silica, adsorption occurs through a chelating carboxylato link with a second carboxylate group hydrogen bonding to the surface. Hydrogen-bonding interactions for protonated carboxylic groups to TCO surfaces can also be envisioned as shown in Fig. 8. Notice that physisorption can occur to metal oxide surfaces, which are not hydroxylated, by formation of hydrogen bonds to bridging oxygens.

1.1.4.2 Modification Using Phosphonic Acids and Other Chemisorbing Functionalities

Phosphonic acids are known to chemisorb strongly to oxides such as ITO and have been used to help produce lithographically patterned ITO surfaces [75, 76]. The schematic view of the adsorption of such materials is shown in Fig. 9. Adsorption of hexylferrocene phosphonic acid ($Fc[(CH_2)_6PO(OH)_2]$) has been investigated by Vercelli et al. from ethanol to silanized and unsilanized ITO surfaces [77]. A maximum surface coverage was obtained at 4.2×10^{-10} mols cm^{-2}, approximately four times the surface coverage obtained with the analogous carboxylated ferrocene. Cyclic voltammetry (CV) of the adsorbed ($Fc[(CH_2)_6PO(OH)_2]$) exhibits a symmetric voltammogram about the x-axis (applied potential axis). The high degree of symmetry suggests fast, reversible electron transfer at the interface. Additionally, the modifying molecules were found to be very robust to CV cycling.

An amine derivatized ferrocene molecule, $Fc[CH_2N(CH_3)_2]$, was used to modify ITO, although less successfully than the carboxylic derivatives [64]. Modification with amines tends to create a less robust modification, where the molecules can be easily removed with solvents. CV cycling can also lead to the loss of amine modifiers. This phenomenon is clearly a result of the weaker Lewis base characteristics of the amine for the Lewis acid sites on the metal oxide surface. Han and coworkers, however, were able to design a dense self-assembled monolayer of 1,12-diaminododecane from methanol onto ITO after 60 h of immersion [78]. The terminating amine group allowed for the subsequent addition of a monolayer of phosphomolybdic acid to provide redox active centers. The diaminododecane, at

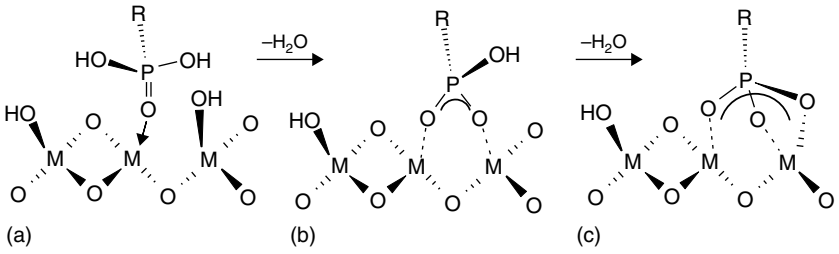


Fig. 9 Schematic views of the possible interaction modes of phosphonic acids with TCO surfaces; (a) monodentate attachment (b) unidentate attachment and (c) multidentate attachment.

6×10^{-10} mols cm^{-2}, provided a platform for one-third as much redox active acid. This protocol may allow for the modification of oxide surfaces through chemisorption to obtain surfaces similar to those obtained through silanization; however, the robustness of this platform was not evaluated.

Cyanuric chloride has been used to modify oxide and graphite electrodes [79]. The linkage, an ether bond through surface hydroxyls, is short and strong, allowing for a robust surface and enhanced electron transfer between the surface and the aromatic terminal group.

Another modification scheme of note is the selective addition of tin-phenoxides on an ITO surface, a process developed by Schwartz and coworkers for the modification of the effective work function of ITO surfaces [13, 80]. Because of the low concentration of tin sites on such surfaces, this modification scheme, which does not modify exposed indium sites, places the functional groups at some distance from each other, a type of modification not afforded by other modification schemes based on covalent bond formation, or chemisorption.

Heme proteins have also been adsorbed to TCO surfaces as ''modifiers'' of their electrochemical properties. These adsorption processes are undoubtedly a combination of electrostatic forces, H-bonding, and metal ion coordination in the TCO surface, and produce reasonably robust and active modifying layers. Cytochrome *C* (cyt *C*) has been the most extensively studied adsorbed heme protein. Hawkridge and coworkers have examined the electrochemical behavior at gold, platinum, and metal oxide electrodes [81]. Electron transfer rates as high as 10^{-2} cm s^{-1} were obtainable at ITO electrodes. Bowden and coworkers have determined that the electron transfer rates are associated with a conformational change of the molecule in the adsorbed state at the electrode surface [82, 83]. Above a certain scan rate, the conformational change can be overcome. More recently, Runge and Saavedra showed that cyt *C* forms a sufficiently stable adsorbed state such that it can be microcontact printed on ITO surfaces, while retaining high electron transfer rates [84].

1.1.5 Conclusions

The modification of TCO surfaces can clearly be used to enhance the electrochemical performance of oxide electrodes. There are, however, issues yet to be resolved regarding the initial surface composition of the oxide, especially for ITO, which prevent realization of the full electrochemical and electronic potential of these electrodes. In some cases, the modification chemistries produce a surface, which is sufficiently robust to be used in various sensor platforms or condensed phase devices. However, it is not yet clear whether long-term stability can be achieved in those cases where the oxide is exposed to solutions that also promote the hydrolysis of the oxide unless an extremely strong covalently bonded network, or chemisorption interaction can be produced. These modification strategies will continue to evolve with the increasing need for viable interfaces between electroactive materials and the metal oxide electrode.

Acknowledgments

Work cited in this review from our laboratories was supported in part by the National Science Foundation (Chemistry); the Office of Naval Research; the

Department of Energy, National Renewable Energy Laboratories Program, Photovoltaics Beyond the Horizon; the Department of Energy, Basic Energy Sciences, and the National Institutes of Health.

References

1. R. W. Murray, Molecular design of electrode surfaces in *Techniques of Chemistry* (Ed.: R. W. Murray), John Wiley & Sons, New York, 1992, pp. 1–48, Vol. 22.
2. F. Decker, J. Melsheimer, H. Gerischer, *Isr. J. Chem.* **1982**, *22*, 195–198.
3. K. Kalyanasundaram, M. Grätzel, *Photosensitization and Photocatalysis Using Inorganic and Organometallic Compounds*, Kluwer Academic Publishers, Boston, 1993.
4. M. A. Ryan, M. T. Spitler, *Langmuir* **1988**, *4*, 861–867.
5. M. T. Spitler, M. Calvin, *J. Chem. Phys.* **1977**, *66*, 4294–4305.
6. M. T. Spitler, M. Calvin, *J. Chem. Phys.* **1977**, *67*, 5193–5200.
7. J. Cui, A. Wang, N. L. Edleman et al., *Adv. Mater.* **2001**, *13*, 1476.
8. J. S. Kim, F. Cacialli, R. Friend, *Thin Solid Films* **2003**, *445*, 358–366.
9. J. S. Kim, R. H. Friend, F. Cacialli, *Synth. Met.* **2000**, *111–112*, 369–372.
10. R. W. Murray, *Acc. Chem. Res.* **1980**, *13*, 135–141.
11. J. J. Pesek, M. T. Matyska, *Interface Sci.* **1997**, *5*, 103–117.
12. K. D. Snell, A. G. Keenan, *Chem. Soc. Rev.* **1979**, *8*, 259–282.
13. A. R. Span, E. L. Bruner, S. L. Bernasek et al., *Langmuir* **2001**, *17*, 948–952.
14. J. E. Malinsky, G. E. Jabbour, S. E. Shaheen et al., *Adv. Mater.* **1999**, *11*, 227–231.
15. R. A. Hatton, S. R. Day, M. A. Chesters et al., *Thin Solid Films* **2001**, *394*, 292–297.
16. C. Ganzorig, K. J. Kwak, K. Yagi et al., *Appl. Phys. Lett.* **2001**, *79*, 272–274.
17. S. Besbes, A. Ltaief, K. Reybier et al., *Synth. Met.* **2003**, *138*, 197–200.
18. P. K. H. Ho, M. Granstrom, R. H. Friend et al., *Adv. Mater.* **1998**, *10*, 769–774.
19. H. L. Hartnagel, A. L. Dawar, A. K. Jain et al., *Semiconducting Transparent Thin Films*, Institute of Physics Publishing, Philadelphia, 1995.
20. R. Hengerer, B. Bolliger, M. Erbudak et al., *Surf. Sci.* **2000**, *460*, 162–169.
21. L.-Q. Wang, D. R. Baer, M. H. Engelhard et al., *Surf. Sci.* **1995**, *344*, 237–250.
22. L.-Q. Wang, K. F. Ferris, A. N. Shultz et al., *Surf. Sci.* **1997**, *380*, 352–364.
23. U. Diebold, *Appl. Phys. A.* **2003**, *76*, 681–687.
24. C. Donley, D. Dunphy, D. Paine et al., *Langmuir* **2002**, *18*, 450–457.
25. J. C. C. Fan, J. B. Goodenough, *J. Appl. Phys.* **1977**, *48*, 3524–3530.
26. N. D. Popovich, S. S. Wong, S. Ufer et al., *J. Electrochem. Soc.* **2003**, *150*, H255–H259.
27. N. D. Popovich, B. K. Yen, S. S. Wong, *Langmuir* **2003**, *19*, 1324–1329.
28. M. Lazzeri, A. Vittadini, A. Selloni, *Phys. Rev. B: Condens. Matter* **2001**, *63*, 155409.
29. M. R. Hoffmann, S. T. Martin, W. Choi et al., *Chem. Rev.* **1995**, *95*, 69–96.
30. K. Kalyanasundaram, M. Gratzel, *Coord. Chem. Rev.* **1998**, *177*, 347–414.
31. M. Fujihira, Y. Satoh, T. Osa, *J. Electroanal. Chem.* **1981**, *126*, 277–281.
32. M. K. Nazeeruddin, R. Humphry-Baker, P. Liska et al., *J. Phys. Chem., B* **2003**, *107*, 8981–8987.
33. M. K. Nazeeruddin, M. Grätzel, *J. Photochem. Photobiol., A* **2001**, *145*, 79–86.
34. T. J. Meyer, G. J. Meyer, B. W. Pfennig et al., *Inorg. Chem.* **1994**, *33*, 3952–3964.
35. J. S. Kim, F. Cacialli, M. Granstrom et al., *Synth. Met.* **1999**, *101*, 111–112.
36. Y. H. Liau, N. F. Scherer, K. Rhodes, *J. Phys. Chem., B.* **2001**, *105*, 3282–3288.
37. C. L. Donley, Interfaces in Organic Electronic Devices: Surface Characterization and Modification and Their Effect on Microstructure in Molecular Assemblies, PhD in Chemistry. 2003, University of Arizona, Tucson.
38. C. F. Baes Jr., R. E. Mesmer, *The Hydrolysis of Cations*, John Wiley & Sons, New York, 1976.
39. D. C. Harris, *Quantitative Chemical Analysis*, W. H. Freeman and Company, New York, 1999.
40. W. F. Linke, *Solubilities: Inorganic and Metal-Organic Compounds*, D. Van Nostrand Co., Inc., New York, 1958.
41. W. F. Linke, *Solubilities: Inorganic and Metal-Organic Compounds*, American Chemical Society, Washington D.C., 1965.

42. J. J. Kirkland, J. J. B. Adams, M. A. van Straten et al., *Anal. Chem.* **1998**, *70*, 4344–4352.
43. D. F. Untereker, J. C. Lennox, L. M. Wier et al., *J. Electroanal. Chem.* **1977**, *81*, 309–318.
44. P. Kirkov, *Electrochim. Acta* **1972**, *17*, 519–532.
45. P. Kirkov, *Electrochim. Acta* **1972**, *17*, 533–547.
46. C. Donley, D. Dunphy, W. J. Doherty et al., *Molecules as Components in Electronic Devices*, American Chemical Society, Washington, 2003.
47. N. R. Armstrong, V. R. Shepard, *J. Electroanal. Chem.* **1980**, *115*, 253–265.
48. N. R. Armstrong, A. W. C. Lin, M. Fujihira et al., *Anal. Chem.* **1976**, *48*, 741–750.
49. N. R. Armstrong, V. R. Shepard, *J. Phys. Chem.* **1981**, *85*, 2965–2970.
50. V. R. Shepard, N. R. Armstrong, *J. Phys. Chem.* **1979**, *83*, 1268–1276.
51. H. O. Finklea, R. W. Murray, *J. Phys. Chem.* **1979**, *83*, 353–358.
52. K. Chen, W. B. Caldwell, C. A. Mirkin, *J. Am. Chem. Soc.* **1993**, *115*, 1193–1194.
53. J. Cui, Q. L. Huang, J. C. G. Veinot et al., *Langmuir* **2002**, *18*, 9958–9970.
54. Q. Huang, G. Evmenenko, P. Dutta et al., *J. Am. Chem. Soc.* **2003**, *125*, 14704–14705.
55. W. Li, Q. Wang, J. Cui et al., *Adv. Mater.* **1999**, *11*, 730–734.
56. H. Hillebrandt, M. Tanaka, *J. Phys. Chem., B* **2001**, *105*, 4270–4276.
57. H. Hillebrandt, M. Tanaka, E. Sackmann, *J. Phys. Chem., B* **2002**, *106*, 477–486.
58. H. Hillebrandt, G. Wiegand, M. Tanaka et al., *Langmuir* **1999**, *15*, 8451–8459.
59. I. Markovich, D. Mandler, *J. Electroanal. Chem.* **2000**, *484*, 194–202.
60. I. Markovich, D. Mandler, *J. Electroanal. Chem.* **2001**, *500*, 453–460.
61. N. L. Jeon, K. Finnie, K. Branshaw et al., *Langmuir* **1997**, *13*, 3382–3391.
62. C. K. Luscombe, H. W. Li, W. T. S. Huck et al., *Langmuir* **2003**, *19*, 5273–5278.
63. D. G. Davis, R. W. Murray, *Anal. Chem.* **1977**, *49*, 194–198.
64. G. Zotti, G. Schiavon, S. Zecchin et al., *Langmuir* **1998**, *14*, 1728–1733.
65. J. Y. Gui, D. A. Stern, F. Lu et al., *J. Electroanal. Chem.* **1991**, *305*, 37–55.
66. C. Carter, M. T. Brumbach, C. Donley et al., manuscript in preparation.
67. M. Carrara, F. Nuesch, L. Zuppiroli, *Synth. Met.* **2001**, *121*, 1633–1634.
68. W.-P. Tai, *Sol. Energy Mater.* **2003**, *76*, 65–73.
69. T. Hoffmann, D. Wrobel, *J. Mol. Struct.* **1998**, *450*, 155–161.
70. P. R. Moses, R. W. Murray, *J. Am. Chem. Soc.* **1976**, *98*, 7435–7436.
71. P. Cuendet, M. Grätzel, M. L. Pelaprat, *J. Electroanal. Chem.* **1984**, *181*, 173–185.
72. P. Cuendet, M. Grätzel, *Bioelectrochem. Bioenerg.* **1986**, *16*, 125–133.
73. A. Hagfeldt, M. Gratzel, *Chem. Rev.* **1995**, *95*, 49–68.
74. A. Hagfeldt, S.-E. Lindquist, M. Gratzel, *Sol. Energy Mater.* **1994**, *32*, 245–257.
75. T. L. Breen, P. M. Fryer, R. W. Nunes et al., *Langmuir* **2002**, *18*, 194–197.
76. T. B. Carmichael, S. J. Vella, A. Afzali, *Langmuir* **2004**, *20*, 5593–5598.
77. B. Vercelli, G. Zotti, G. Schiavon et al., *Langmuir* **2003**, *19*, 9351–9356.
78. S.-Y. Oh, Y.-J. Yun, D.-Y. Kim et al., *Langmuir* **1999**, *15*, 4690–4692.
79. A. M. Yacynych, T. Kuwana, *Anal. Chem.* **1978**, *50*, 640–645.
80. E. L. Bruner, N. Koch, A. R. Span et al., *J. Am. Chem. Soc.* **2002**, *124*, 3192–3193.
81. E. F. Bowden, F. M. Hawkridge, H. N. Blount, *J. Electroanal. Chem.* **1984**, *161*, 355–376.
82. J. L. Willit, E. F. Bowden, *J. Electroanal. Chem.* **1987**, *221*, 265–274.
83. A. El Kasmi, M. C. Leopold, R. Galligan et al., *Electrochem. Commun.* **2002**, *4*, 177–181.
84. A. F. Runge, S. S. Saavedra, *Langmuir* **2003**, *19*, 9418–9424.

1.2 SAMs on Au and Ag Electrodes

1.2.1 Preparation of Self-assembled Monolayers (SAMs) on Au and Ag

Uichi Akiba and Masamichi Fujihira
Tokyo Institute of Technology, Yokohama, Japan

1.2.1.1 Introduction

1.2.1.1.1 Molecular Self-assembly at Surfaces Molecular self-assembly is a process in which an organized superstructure or pattern is spontaneously formed from an ensemble of the component molecules that are uncorrelated to each other in a liquid or gas phase [1–3]. The structure of molecular self-assembly can be divided into two types of organized systems: one is a system that organizes in a homogenous medium, and the other is a system that organizes at a heterogeneous interface. Self-assembled monolayers (SAMs) on substrates belong to the latter organized system because these monolayers need to be supported by the surfaces of solid, or liquid, that is, they are members of a kind of supported organic monolayers [4, 5]. Two different types of SAM adsorption processes on solid substrates are well characterized: all of the component molecules are chemically bonded one by one to the substrate, or they are themselves polymerized on the substrate [1]. A typical example of the former, is a thiol-based SAM on gold, which involves the specific interaction of sulfur–gold coordination as the principal driving force for assembling the organosulfur compound from the solution or gas phase onto a gold surface [6–10]. For the latter instance, a silane-based SAM is one of the most popular SAMs for modifying a silicon surface covered with a naturally grown oxide film [7, 11, 12]. The essence of these self-organization processes is that no external intervention is necessary to guide the processes once the assembling processes start [1, 2].

We can synthesize various component molecules in which predesigned structures are specifically coded with the rules necessary for the molecular assembly. This looks as if biomolecules in nature, such as DNAs or proteins, are coded by the structural specificity to express their functions. In the case of an alkanethiol-based SAM, the code is set in two structural parts, that is, a thiol substituent and an alkane chain. The thiol substituent is a soft binder effective to specific surfaces, such as gold, to which the component molecules can be chemically adsorbed from the solution or gas phase [5]. The alkane chain is a building block to form a monolayer and can serve as the structural unit that enables the spontaneous organization of the tightly packed monolayer through van der Waals interaction (or hydrophobic interaction in water) between the alkane chains. A schematic of alkanethiol-based SAM structure is shown in Fig. 1 [1].

1.2.1.1.2 Historical Background on SAMs Bringing together two concepts of supported organic monolayers and spontaneous organization (or self-assembling) was of crucial importance for the advent of SAMs [6, 12–19] and also for chemically modified electrodes [14, 20–29]. The idea of forming SAM on a substrate is not new; it was well known in the 1940s. Around that time, the self-assembling of supported organic monolayers had already been studied using acid/base interaction for the monolayer adsorption on substrates. In

Encyclopedia of Electrochemistry.Edited by A.J. Bard and M. Stratmann
Vol. 10 *Modified Electrodes*. Edited by M.Fujihira, I.Rubinstein, and J.F.Rusling
Copyright © 2007 Wiley-VCH Verlag GmbH & Co. KGaA, Weinheim.ISBN: 978-3-527-30402-8

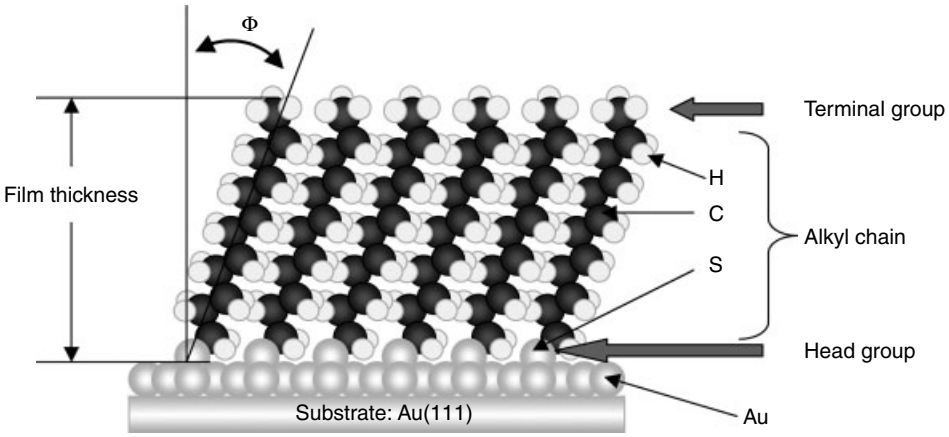


Fig. 1 A schematic of alkanethiol-based SAM structure depicted using a structural model of an *n*-dodecanethiolate SAM (C12-SAM) on a gold (111) substrate [1]. The definition of film thickness and tilt angle (ϕ).

1946 and 1947, Zisman and coworkers performed the first systematic studies of self-assembly of monolayers of long alkane chains of alkylalcohols, alkylamines, and alkylcarboxylic acids adsorbed to substrates of glass, metal, and metal oxide [5, 8, 30, 31]. They found that the systems were enabled to form spontaneously oriented monolayers, which have properties similar to the corresponding films formed by the Langmuir–Blodgett (L–B) techniques [9]. The driving force for the assembly, however, was not strong because physisorption or weak bonding between the functional groups and the substrate surfaces was used in this adsorption [6, 32]. Therefore, the supported monolayers created by them had low energies of adsorption (5–15 kcal mol^{-1}), which afforded only modest stability similar to those formed by the L–B method [5, 8, 31]. Their studies also suggested that the interfacial properties of SAMs, such as wetting and adhesion, could be controlled by changing the terminal functional groups. The difference was demonstrated using the change from methyl group to trifluoromethyl group [5, 8, 30, 33]. These SAMs have a potential necessary to self-assembly, nevertheless, the potentiality of interest was not recognized at that time [8]. However, the idea of self-assembling of supported organic monolayers was taken over by the following researchers [34–36]. Afterward, no rapid progress was made in the preparation technique of SAMs, and we have had to await the advent of a new methodology for SAM formation that enables us to generate a wide variety of stable SAMs.

On the other hand, we have long known that ordered, thermally stable organic overlayers can be formed on a metal surface in vacuum by exposing a clean surface to a small amount of volatile molecules [37–39]. Hubbard et al. studied the structure of a variety of molecules adsorbed on an electrode, from the standpoint of fundamental understanding of well-defined structural surfaces in vacuum and at the solid–liquid interface [15]. As a result, evidence for the spontaneous organization of supported organic monolayers on platinum surfaces has been obtained [16], although the molecules used

here were not surfactants. These systems, however, lack variations in the functionality of molecules for controlling the surface structures of the overlayers, because most functionalities react readily with the platinum surface used as the substrate [37]. Platinum surfaces were used widely in surface science, because a number of molecules can be strongly adsorbed on the surface. Thus, the self-organization of a variety of organic surfaces was difficult as long as platinum surface was used as a substrate for adsorbates.

In contrast to these systems of molecular adsorption on metal surfaces, the L–B techniques can be used to fabricate the supported monolayers [40–42]. Although the order of molecules in the L–B films can be quite good, this is potentially a nonequilibrium and difficult procedure, which is largely restricted to polyfunctional molecules bearing only one polar substituent [37]. Moreover, the L–B films on substrates usually have no good thermal stability. Thus, a stable monolayer with a high surface-free energy is difficult to form with this technique [8, 37, 41, 42].

In 1983, Nuzzo and Allara reported a useful technique for preparing supported organic monolayers of disulfide-based molecules with a variety of functional groups [6]. This technique extended the previous approach in a dramatic way. That is, they focused on chemisorption based on a strong and specific coordination bond between sulfur and gold, which has proved to provide a new methodology for spontaneous formation of supported organic monolayers with a variety of functional groups [6, 7, 43]. In contrast with the platinum surface commonly used as a substrate so far, a gold surface was recognized to be one of the least active metals in the chemisorption of many organic molecules [6, 7]. This character, in addition to the inertness of the gold surface against polar functional groups, is extremely convenient for the formation of SAMs with a wide variety of functional groups. The use of gold as a substrate is unique because, until that time, many studies had used gold only as a substrate in the experiments for reversible physisorption of organic molecules, but less for chemisorption [6, 7, 28, 29]. The specificity and stability of organosulfur compounds chemically adsorbed to a gold surface are of crucial significance for the study of the formation of a variety of model SAMs and the characterization of their structure and properties by various physical and chemical methods [37, 43–47]. These characteristic features of the sulfur–gold bond formation in the new type of SAMs also triggered extensive studies by surface scientists using a large number of physical surface-analytical methods [37, 48]. The characterization of the structure of simple SAMs on gold is also an important subject for our understanding of the SAMs at atomic level.

Since the first report by Nuzzo and Allara [6], early researches have been concerned with the physicochemical properties and structural characterization of basic alkanethiol-based SAMs on gold [37, 43–47]. Especially, Bain and Whitesides focused their interests on systematic studies of modeling organic surfaces made of a variety of SAMs based on ω-substituted long alkanethiols, $X(CH_2)_nSH$ with a wide variety of functional groups at the terminal, X [43, 44, 47]. The excellent feature of this system is that this model has the ease of preparation and the structural definition required to provide a firm understanding of interfacial phenomena [43, 44, 47]. The ω-substituted long alkanethiols adsorbed on gold, similar to the case of simple long alkanethiols, form densely packed, oriented monolayers. Consequently, they

could explore the relationships between the microscopic structure of the monolayers with the variety of functional groups, X, at the terminal of the SAMs and their macroscopic properties. They studied in detail the relation between wettability and the structure of the monolayers [43, 44, 47, 49–59]. Subsequently, similar model studies have been extended using the SAMs on silver [60–62] or copper [60, 63, 64], which are another variable structural factor of interest for understanding the influence on self-ordering of SAMs.

Many physical and chemical researchers have challenged the structural issues of SAMs formed from a gas phase in vacuum or a liquid phase, mainly focusing on alkanethiol-based SAMs on gold [48, 65–68]. Many kinds of surface-analytical techniques used in vacuum and at the solid–liquid interface have been applied to the studies of SAMs, which include ultrahigh vacuum scanning tunneling microscopy (UHV-STM) [48, 69–71] and grazing incidence X-ray diffraction (GIXD) [48, 72]. These instruments have provided complementary local and nonlocal probes for structural information on SAMs on gold. The most important consensus established by these measurements is that alkanethiol-based SAMs basically have enough characteristics to be considered structurally well-defined organic surfaces at the molecular level.

The excellent features of SAMs on gold may provide an invaluable opportunity for the understanding of self-assembly process at the molecular level. As described above, a progressive advance has been made to understand in depth the static structure formed on gold, whereas relatively little is known on the dynamics of the self-assembling process on gold at the molecular level [73]. Accordingly, the understanding of growth kinetics and dynamics in SAM formation processes on gold from the gas phase and solution phase is essentially significant for the fundamental perspective. The kinetic experiments of SAM formation on gold from the gas phase (under vacuum) have been carried out actively by Schreiber et al. using diffraction techniques [48, 73, 74]. The kinetics from the solution phase have been carried out by Bain et al. using ellipsometry [47]. Later, many research groups have studied the kinetics of SAM formation (more quantitatively) using various spectroscopic techniques [48, 75], such as second-harmonic generation (SHG) [76, 77], sum-frequency generation (SFG: see Ye & Uosaki) [78, 79], near edge X-ray absorption fine-structure spectroscopy (NEXAFS) [80], electrochemical quartz crystal microbalance (EQCM: see Shimazu) [81], surface plasmon resonance (SPR) [82], and Fourier transform infrared reflection absorption spectroscopy (FTIRRAS) [83].

Reaction chemistry is also one of the important aspects of SAMs from both fundamental and application issues. SAMs consist of three parts. The first is a SAM/substrate interface, in which we have a basic problem regarding the reaction sites between organosulfur compounds and a gold surface to generate a sulfur–gold chemical bonding. The second is a surrounding phase/SAM interface, in which a variety of reactions are possible because we can modify the surface of SAMs with a variety of functional groups at the terminal. The interface can be used alternatively to adsorb a variety of functional biomaterials. The third is an intermediate part between these two interfaces, which is a structural spacer at the interior of the monolayer. For example, if the spacer has a reactive structural unit of diacetylene at the interior part, photopolymerized SAMs can be prepared [84].

Regarding the application issue of SAMs, there are a large number of subjects in which SAMs have been used as materials for organic functional surfaces [9, 85, 86]. A wide variety of interdisciplinary researches with SAMs have been performed since early studies by electrochemists, Taniguchi [28, 29], Hill [87], and Weaver [88]. These impacts have extended the availability of SAMs into almost all surface sciences, including, materials chemistry [89–92], physical organic chemistry [93–97], physical chemistry [98–101], biochemistry and biology [102–104], and of course electrochemistry [105–109]. In recent years, the SAM formation techniques have played a critical role in the understanding and controlling of molecular electronics [110–115], biosensor devices [116–119], and biocompatible materials [9, 120–123], which are being developed rapidly at present.

The prominent features of the SAMs on gold as well-defined organic interfaces provide means to be amenable to fundamental sciences and a variety of interdisciplinary applications, especially in nanoscience and nanotechnology [9]. In such a sense, it is understandable that SAMs on gold are called *golden interfaces* [69].

1.2.1.2 Preparation Techniques of Substrates Used for Forming SAMs

1.2.1.2.1 Gold as a Substrate Material

There is a wide range of choice for substrate materials that can be used for SAM formation of organosulfur compounds, as summarized in Table 1 [86]. Among these materials, gold is the most frequently used substrate, for two reasons [9]. First, the melting point of gold is 1064 °C, which is not as high as that of platinum (1770 °C). This feature enables us to prepare easily a thin film of gold onto a flat base by physical vapor deposition (vacuum evaporation) [124–128], sputtering [127, 129, 130], electrodeposition [131], and electroless plating [132, 133]. Handmade preparation of a gold single-crystal electrode is widely used among electrochemists as described below. Further, the gold thin films prepared on a substrate are exceptionally useful to make patterns at micrometer scales by a combination of lithographic tools and chemical

Tab. 1 Chemical systems of organosulfur compounds and substrates that form SAMs

Surface materials	*Substrates*	*Organosulfur compounds*
Metal	Au	R–SH, R–SS–R, R–S–R
	Ag	R–SH
	Pt	R–SH
	Pd	R–SH
	Cu	R–SH
	Hg	R–SH
Semiconductor	GaAS (III–V)	R–SH
	InP	R–SH
	CdSe (II–VI)	R–SH
	ZnSe (II–VI)	R–SH
Oxide	Tl–Ba–Ca–Cu–O	R–SH
	ITO	R–SH

etchants [86, 89]. Thus, the gold thin films have been prepared as a substrate on which SAMs are deposited and characterized by a variety of surface-analytical instruments, including SPR spectroscopy [82, 134–137], electrochemical-surface plasmon resonance (EC-SPR) [138, 139], QCM [140, 141], EQCM [81, 142–145], IR-RAS [83, 146, 147], ellipsometry [47, 148], scanning tunneling microscopy (STM: see Itaya) [149, 150], atomic force microscopy (AFM: see Fujihira) [150–152], and various electroanalytical techniques [106, 153–155]. Second, unlike other metals, gold does not readily form an oxide surface and, in addition, is not contaminated readily even upon exposure to the atmosphere owing to its inertness for ionic (hard) interaction [5–7, 9, 10]. This feature is, in particular, of importance in biological applications of SAMs chemisorbed on gold, with its biocompatibility [102, 103, 120–123, 156] for cells and proteins. In fact, the cells adherent to the gold surface can effectively function without evidence of toxicity [9].

1.2.1.2.2 **Preparation Method of a Flat Gold Surface on Mica** One of the most popular techniques for preparing an atomically flat gold surface is the epitaxial growth of gold onto muscovite mica. The smoothness of the gold surface depends largely on the growth conditions [128]. The commonly used evaporation procedure of (111)-oriented gold surface on muscovite mica is as follows [124–127]: Freshly cleaved mica is set in a chamber of the high-vacuum evaporation instrument. The mica is baked for 12 or more hours at ~500 °C before gold evaporation [126]. The vacuum pressures are required to be 10^{-8} to 10^{-9} Torr. The gold for the evaporation usually requires at least 99.99% purity grade. The evaporation rate should be 0.1–0.5 nm s^{-1} or so, so that a size of (111)-oriented terraces of more than 100 nm^2 can be obtained. The evaporation with high speed tends to reduce the size of (111)-oriented terraces. Temperature control of the mica substrate during gold evaporation is another important parameter if one needs a preferable gold film surface with widely spreading (111)-oriented terraces [125, 126]. Chidsey et al. demonstrated that decreasing the evaporation temperature to 150 °C resulted in smaller plateaus surrounded by grooves of 5.0 to 7.5-nm depth [124]. Heating the mica at 300–350 °C is common during the evaporation. The thickness of the gold films is usually 100–250 nm. Thin gold films less than 100 nm in thickness have a lot of trenches of ~3-nm deep by which the individual domains are separated from each other [5]. After gold evaporation under these conditions, finally the deposited gold films are annealed for 12–24 hours at 300–350 °C in the chamber, so that the desired gold films with a large area of atomically flat faces on the surface can be obtained. Recently, an improved procedure for the vapor deposition of gold onto mica has been reported, where a two-step deposition process is performed for the formation of atomically flat gold thin films of 200-nm thickness on mica [157]. The first 150 nm of gold film is deposited at a high rate of 5 nm s^{-1}, followed by the second 50-nm gold film at a rather slow rate of 0.05 nm s^{-1}. Such a gold substrate prepared on mica has mechanical stability enough to be used in experiments in vacuum and in various liquids. It is recommended that such a flat gold substrate just prepared, or reannealed before use, should be used to modify the surface with SAMs as soon as possible. The deterioration of the widely

spreading area of (111)-oriented faces in the freshly prepared gold surface can be followed by STM. If the fresh gold films prepared are not used soon, these gold films on mica could be kept in absolute ethanol for preserving it from the oxidative atmosphere [158, 159] (see Schneeweiss and Rubinstein).

1.2.1.2.3 **Gold Substrate on Silicon Wafer** As an alternative to mica substrate for preparing a gold thin film, a silicon wafer covered with a native oxide film has been used widely as a base [5, 9, 127, 130, 131]. To improve adhesion between a silicon surface and a gold film, a titanium or chromium layer of 1–10-nm thick is used as a binder between the silicon surface and the gold film. However, it is believed that chromium tends to move more easily to the outer surface of the gold film, and thus it contaminates the gold surface. Moreover, this metal has a potential toxicity to cells adsorbed to the SAM in the application of biological interface [9]. As an alternative to the titanium or chromium layer, the application of (3-mercaptopropyl)trimethoxysilane as a molecular adhesive in the gold vapor deposition on silicon wafers or glass substrates was demonstrated by Majda [160] and Bard [161], and used by other researchers [162]. This technique was also applied to the nanotransfer printing method [163] (see also Sect. 1.2.1.7.7).

1.2.1.2.4 **Template-stripping Technique as Another Route for Preparation of Flat Gold Substrates** This technique, first reported by Hegner et al., has been developed as an improved method for preparing a widely flat gold surface on mica [164, 165]. The basic idea is to use the first deposited gold layer directly in contact with the mica surface rather than the top surface of the deposited gold film as described in Sect. 1.2.1.2.2. The method is based on three procedures (Fig. 2): (1) epitaxial growth of gold on mica (the same procedure as described in Sect. 1.2.1.2.2), (2) gluing the fresh gold surface to a piece of silicon wafer or glass substrate, and (3) chemical or consecutive mechanical stripping of the mica down to the freshly appearing gold surface [164]. Thus, this technique is termed *a template-stripping technique* and the obtained gold surface is termed *a template-stripped gold* (TSG) *surface*. This procedure generates large areas of the smoothest gold surfaces known to date [166]. It allows not only improvement of the flatness of the gold surface but also storage of the mica/gold/silicon multilayer for a long period after its preparation; that is, after the procedure (2) is performed, the substrate can be stored for several months without loss of quality, and later the procedure (3) is performed just before use for modifications with organic materials [167, 168]. Later, various further-improved procedures were proposed. These include the use of alternatives to the mica substrate in the procedure (1), gluing techniques in (2), and stripping techniques in (3). Instead of mica as a template of TSG, a silicon wafer has been used similarly [167]. In the gluing procedure (2), usually convenient adhesives, such as epoxy or ceramic glues have been used so far. These adhesives give rise to some problems during experiments using the TSG substrate. One of the problems is caused by the limited stability against a variety of solvents especially when epoxy is used as an adhesive. The other is caused by out-gassing problems under ultra high vacuum (UHV), where trapped air bubbles and solvent pockets in these adhesives are not compatible [169]. Rabe

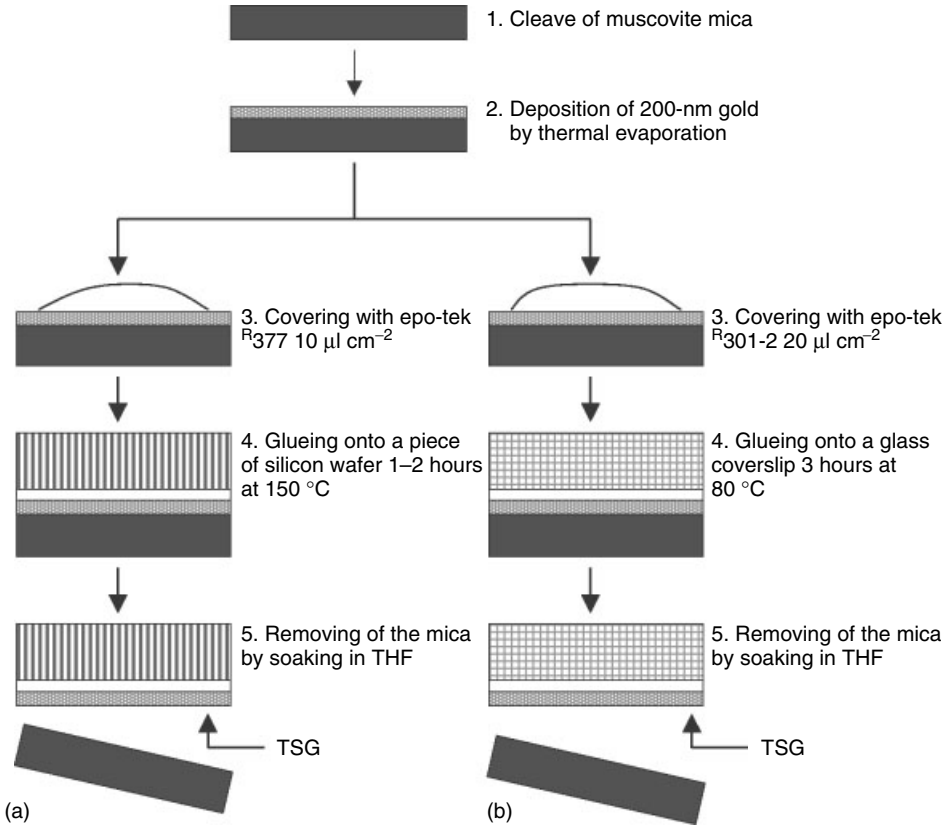


Fig. 2 Typical preparation procedures of template-stripped gold surfaces supported (a) by a piece of silicon wafer and (b) by a glass coverslip [165].

and coworkers developed an adhesive-free TSG supported on nickel. Nickel of 200-µm thickness was deposited on the gold surface on mica by electroplating in place of a piece of silicon wafer in procedure (2) described above [167, 170, 171]. Blackstock et al. recently demonstrated a new type of template-stripping technique without any adhesives in the procedure (2) [169]. This method is based on the gold cold-welding technique, which can also solve the conductivity problem of the TSG substrates produced by the conventional technique or Rabe's method. This character will be extremely important in the application of TSG substrates to sensors and electronics [169]. Improvements of the procedure (3), which involves the problem relating to mechanical stress in the stripping step, have been demonstrated by several researchers. Ulman et al. reported the utilization of organothiols as a stripping technique. Thiols can intercalate between the mica and gold layer of the TSG, thus lowering the adhesion between these two surfaces [166]. A more simple and reliable method for the stripping procedure (3) is demonstrated by Gooding and coworkers, in which mica can be removed by immersion of the

sample into liquid nitrogen [172]. This cryogenic stripping method is based on the difference in contraction between mica and gold, resulting in clean separation to leave large atomically flat planes, as well as patterned features without any change in substrate quality.

TSG substrates, as explained above, have been extensively used as a widely flat substrate for a variety of applications. The availability is, at present, being rapidly expanded to not only physical chemistry [173–176] but also biochemistry and biology [176–182]. In addition, the types of surfaces fabricated according to this TS technique have increased, including silver [171], platinum [183, 184], and titanium oxide [185].

1.2.1.2.5 **Single Crystal Bead of Gold** A handy, timesaving, and inexpensive method of preparation of a (111)-oriented gold surface is to use a single-crystal gold bead [10, 186–192]. Only a gold wire (99.99%) with ca 1 mm in diameter and a Bunsen hydrogen flame is necessary to make a single crystal bead by crystallizing the end of the gold wire. The crystallization needs skill, but it is very easy to try because expensive instruments such as physical vapor deposition are not required for making a single crystal bead. A number of atomically flat and wide terraces of a gold (111) face, more than 300 nm in size, are observed by STM after flame annealing by a hydrogen torch just before use. However, the area where we can use the (111)-oriented gold surface for experiments is limited to a small facet (usually less than 0.5 mm in diameter) with a (111) face, and we have to set up the experiment to directly use the small facet only. These single-crystal techniques are very familiar to electrochemists as the so-called Clavilier method or the flame annealing method. Clavilier and coworkers first demonstrated with platinum the effectiveness of a simple preparation of clean and well-defined low index surfaces by the flame annealing method, which was performed by heating the platinum wire in a Bunsen flame for minutes [186, 193, 194]. Later, this method was also applied to the preparation of gold and silver single-crystal electrodes by Hamelin et al. and Motoo et al. [189, 195–198].

1.2.1.2.6 **Single Crystal Cut of Gold** Such a single crystal bead itself is not amenable to various measurements that require a larger area of flat gold surface. If necessary, one can use a single crystal gold cut electrode [189, 190]. The cut electrode has an exposed (111)-surface prepared from the single crystal bead by mechanical polishing of a (111) face that is parallel to the facet of the bead [196, 198]. The cut bead is usually 3–5 mm in diameter, and can be repeatedly used after removing the adsorbates and doing flame annealing again.

1.2.1.2.7 **Other Substrates of Interest** As a new class of substrates for forming thiol-based SAMs, gallium arsenide (GaAs), the most prominent semiconductor alternative to silicon, is actively studied from the application viewpoint [199–203]. Allara et al. demonstrated that GaAs (100) could provide well-ordered organic surfaces of thiol-based SAMs, suggesting that the chemical bonds of RS−As (R = alkyl chain) form on the surface [199, 200, 202].

1.2.1.3 Preparation Techniques of Alkanethiol-based SAMs on Gold

1.2.1.3.1 **Preparation from Solution Phase** The most outstanding feature of SAMs is their ease of preparation. Namely, SAMs

are easily obtained by exposing a clean gold surface to a 0.01–1 mM solution of the organosulfur compound for an adequate period, usually for few minutes to 1 day, which depends on the compound structure and the purpose of the SAM formation. If a more ordered monolayer is required for the experiment, the immersion for a longer time will be recommended as described later. The process of SAM formation is determined from energetics and kinetics for adsorption of SAM [48]. Therefore, it may depend on the structure of the organosulfur compound, its concentration of the solution, and the polarity and structure of solvents used. The most frequently used solvent is ethanol [46, 47, 52], but SAMs can be prepared by using a variety of solvents, including hexadecane [46, 47, 49, 52], isooctane [52, 61], carbon tetrachloride [47], cyclooctane [47], toluene [47], tetrahydrofuran [47, 49, 61], acetonitrile [47, 52, 61], and dimethylformamide [47]. Nonetheless, the SAMs generated with these solvents show almost the same macroscopic behavior in their characteristics, such as wettability and thickness [44].

1.2.1.3.2 **Electrode Potential Control of SAM Deposition** Gold substrates for chemisorbing SAMs are a kind of electrode, so that it may be natural for us to assume that the electrode potentials could affect the formation process of SAMs. Studies on how an applied potential affects the SAM formation and its structures are of extreme importance for techniques of molecularly functional organization. These studies have been performed from two viewpoints: (1) the potential control of SAM formation process and (2) that of already-formed SAM structures. The studies [204, 205] focusing on the former will be described here and, as for the latter, the interested reader is referred to [206] (see also Kakiuchi).

Recently, it has been found that the control of SAM formation onto gold by electrode potentials is effectively available as a SAM deposition technique. First, Porter and coworkers demonstrated this possibility by taking into account reductive desorption and oxidative readsorption peaks observed in cyclic voltammograms of the SAM on gold [204, 205]. Stratmann et al. reported that octadecylthiol (C18)-based L (Langmuir) films formed on an aqueous subphase were transferred to gold substrates under the control of various electrode potentials, and compared it with the data on the basis of the corresponding SAM on gold [206]. When holding the electrode potential at slightly positive to the point of zero charge (pzc) of gold [192] in ethanol (varying between −0.3 and +0.1 V vs Ag/AgCl [207]), the thiol molecules were attracted to the gold surface through the chemical bond between the negatively charged sulfur and the substrate. Later they also reported that, at cathodic potentials, chemisorption of thiol molecules and the development of the highly ordered structure have slowed down significantly, demonstrating that the electrode potential affects the kinetics and mechanisms of SAM formation on gold [207]. Ron and Rubinstein [159], Ma and Lennox [208], and later Sumi and Uosaki [209] showed that the potential-assisted deposition of alkanethiols on gold could lead to a faster deposition and ultimately more complete SAM formation process than the common SAM deposition process. In particular, Ma and Lennox demonstrated that this potential control technique for SAM formation is critically effective to deposit two-component mixed SAMs with various compositions otherwise inaccessible using deposition under open-circuit potential

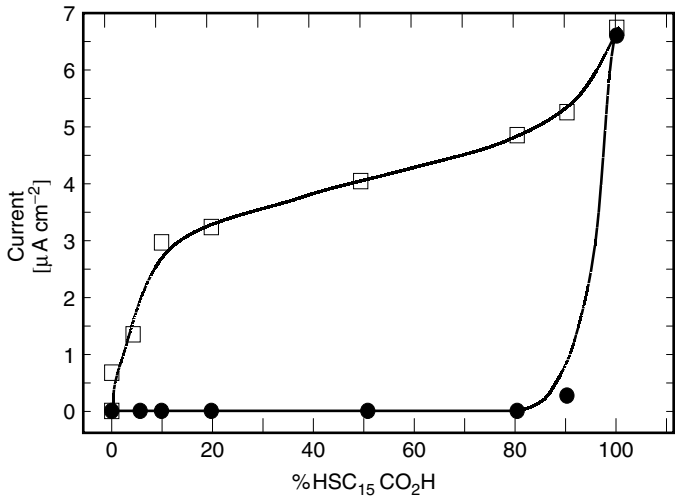


Fig. 3 Dependence of SAM composition on the solution composition, expressed as the percent $HSC_{15}COOH$ in mixed SAMs with $C_{16}SH$. Current was measured at −0.3 V versus Ag/AgCl in a 2 mM $Ru(NH_3)_6Cl_3$/1 M KBr solution for SAMs formed by potential deposition (at 0.6 V for 10 minutes; open squares) and passive incubation (24 hours; closed circles). Lines are drawn to assist data visualization [208].

conditions, that is, the common procedure with no applied voltages [210, 211] (Fig. 3). This acceleration effect in the kinetics of SAM formation has recently been applied to the SAM formation on gold with non-alkanethiols, such as thioacetyl-terminated oligo(phenyleneethynylene)s [212, 213], and ferrocenyl peptide disulfides [214]. These findings are also very important for further understanding of the property of gold–sulfur bonding indispensable for SAM formation [215].

Another electrochemical technique applicable for SAM formation has been studied in several groups. In this strategy, precursors of thiols must be designed in advance. When the precursors are used for SAM formation under an applied voltage, these are successfully transformed to the corresponding thiols in situ on the gold surface by an electrochemical reaction. Therefore, this method can be called *electrochemical self-assembly on gold*. First, Lukkari and coworkers demonstrated this strategy using alkyl thiosulfates (Bunte salts) as a precursor [216]. This technique was immediately applied to the microelectrode by Ferguson et al. They successfully demonstrated selective SAM formation in specific locations on the gold microelectrode using this electrochemical method [217]. This electrochemical mechanism was also discussed in detail. A proposed mechanism for the formation of SAMs on gold by electrochemical oxidation of alkanethiosulfates is shown in Fig. 4 [218].

1.2.1.3.3 **SAM Deposition from Aqueous Micellar Solution** Recently, an interesting idea for deposition techniques of SAM from solution phase has been

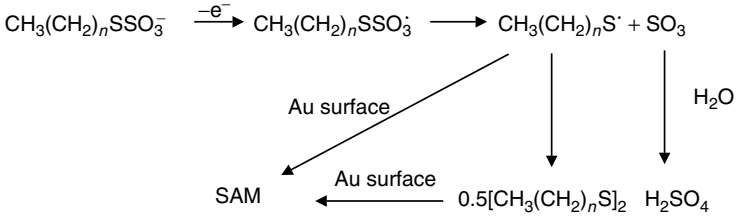


Fig. 4 A proposed mechanism for the formation of SAMs by oxidation of alkanethiosulfates at a gold [218].

demonstrated. It is a technique for SAM formation based on deposition from aqueous micellar solutions. The study of this micelle-assisted SAM formation technique has been reported first by Kaifer et al. [219]. Afterward, this technique has been examined in detail by Jennings et al. [220–223]. More recently, it has been demonstrated that this technique is versatile for the SAM formation of insoluble component, yielding dense, defect-free, and ordered SAMs [224].

1.2.1.3.4 **Preparation from Liquid and Supercritical Carbon Dioxide** A novel type of SAM preparation technique with liquid and supercritical carbon dioxide has been developed very recently by Weinstein et al. [225, 226]. They have demonstrated that environment-friendly mixed solvents such as supercritical carbon dioxide–ethanol can be used to control the properties of SAMs, such as the defect density by simply altering the composition of the mixed solvents [226].

1.2.1.3.5 **Preparation from the Gas Phase** Adsorption from the gas phase is another technique of critical importance for SAM formation, and is available for surface scientists, especially as a sophisticated deposition technique. Vapor deposition of adsorbates, such as alkanethiols and dialkyl disulfides with less than 10 in carbon number, has typically been performed under UHV conditions. The SAM in UHV can be kept all the time in the clean environment inherent to the UHV condition [10]. The vapor concentration of an adsorbate in the UHV chamber can be precisely controlled through the dosage valve at the submonolayer level. Temperature is also another controllable parameter, which is of crucial importance in the structural characterizations of model SAMs because thermal fluctuations of the adsorbate structure can be reduced by low temperature [48]. This situation is essentially different from the solution deposition in which the adsorbate molecules are always surrounded by solvent molecules. In addition to these features, one more indispensable advantage of the UHV technique is that various analytical tools, such as low-energy electron diffraction (LEED), STM, and X-ray photoelectron spectroscopy (XPS), directly connected to the UHV chamber, enable us to achieve in situ analyses of the structure of as-prepared SAM without exposing it to the atmosphere [10, 48].

1.2.1.4 Structural Characterization and Chemical Properties of SAMs

1.2.1.4.1 **Structure of Alkanethiol-based SAMs on Gold** Since Nuzzo and Allara demonstrated the idea of SAMs on

gold–organosulfur chemical bonding [6], the full-coverage structure of alkanethiol-based SAMs with a variety of long alkane chains have been thoroughly characterized chiefly by using spectroscopic [37, 67, 68], diffraction [72], and scanning probe microscopic [69–71, 150] methods. A comprehensive survey of these results was reviewed recently by Schreiber [48, 65, 66]. Here, we bring into focus the four parts that are of interest in the structure of simple alkanethiol-based SAMs (Fig. 5). The first is on the structure of the full coverage of SAMs formed on gold (111). The second is on the structure of the gold–sulfur bond that involves two structural issues: whether the bonding mode is alkanethiolate–gold, and which is the sulfur-binding site on a gold (111) surface, the top, bridge, or hollow sites. The third is on the structure of SAM surfaces that is organized with the terminal groups of the alkane chains. The order and orientation of the terminating groups are of particular importance as these can play a critical role in determining the macroscopic properties of organic surfaces, such as wetting, adhesion, lubrication, corrosion, and so on. The fourth

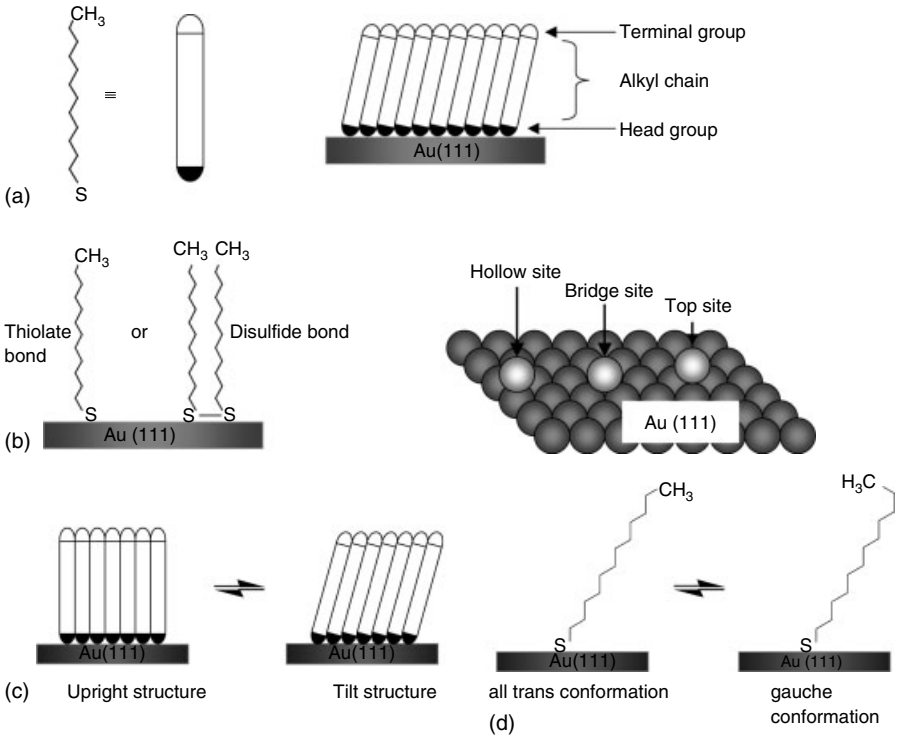


Fig. 5 Depiction of four parts of interest in the structure of simple alkanethiol-based SAMs. (a) The overall structure of the full coverage of SAMs formed on gold (111). (b) The structure of the gold–sulfur bond which includes two structural issues: the bonding mode, alkanethiolate–gold or dialkyldisulfide–gold, and which is the sulfur-binding site on a gold (111) surface, among the top, the bridge, or the hollow sites. (c) The conformational structure of assembled alkane chains. (d) The structure of SAM surfaces with the terminating groups of the alkane chains.

is on the effect of intermediate backbone spacer on the SAM structure. Here, these structural aspects of importance for characteristics of SAMs prepared on gold (111) will be summarized.

1.2.1.4.2 **Close-packed Structure of SAMs on Gold (111) Surface** Full-coverage structure of long-chain alkanethiol-based SAMs, such as octanethiol (C8)-SAM, decanethiol (C10)-SAM, and longer

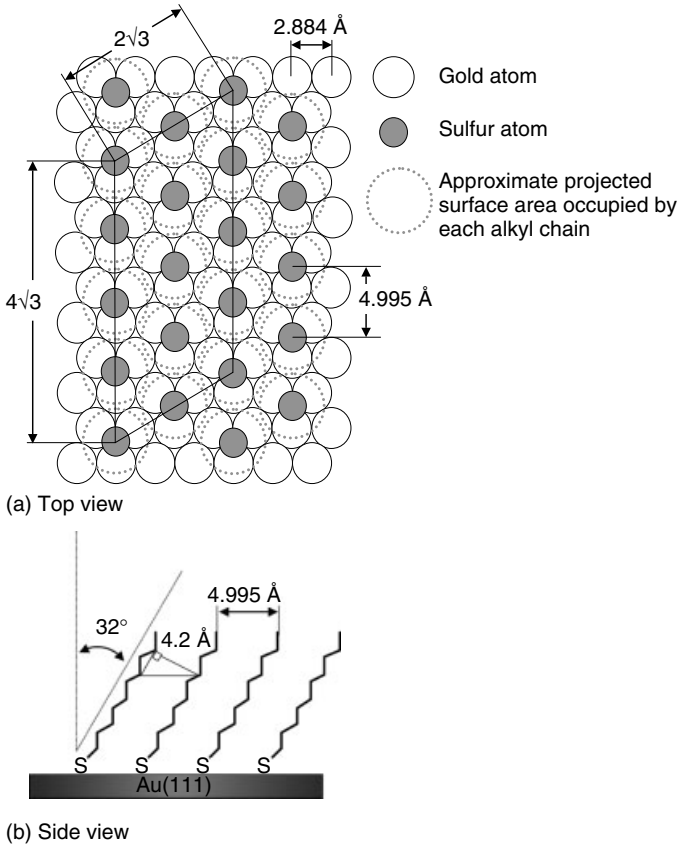


Fig. 6 Schematics depicting from two different perspectives for the structural models of the arrangement of a close-packed adlattice structure of decanethiol-based SAM on a gold (111) surface. (a) Top view, presenting a hexagonal close-packed gold (111) surface (open circles), and the SAM overlayer of a $(\sqrt{3} \times \sqrt{3})R30^\circ$ structure with respect to the underlying gold (111) surface where sulfur atoms (dark gray circles) are assumed to be positioned in the threefold hollow sites of the gold (111) surface. The light gray circles with dashed lines indicate the approximate projected surface area occupied by each alkane chain. The structure of a $c(4 \times 2)$ superlattice is not presented here, and the formal $c(4 \times 2)$ superlattice unit cell is marked. (b) Side view, where the decanethiolate molecules are arranged to be packed 5 Å apart with their alkyl chains tilted 32° from the surface normal in a trans-zigzag extended conformation [9, 10].

docosanethiol (C22)-SAM on gold (111), can be illustrated with two different perspectives (Fig. 6). The top view explains the structural characteristics of the full-coverage SAMs (Fig. 6a). The side view illustrates the tilted and twisted long-chain structures of alkanethiols, which are fully extended in a nearly *all-trans* conformation, and are commensurately ordered on a (111) oriented gold substrate (Fig. 6b). These structural views are generally accepted at present, except for an essentially difficult issue of sulfur–gold positioning. The thickness of these SAMs increasing linearly with chain lengths from 9 to 21 in carbon number has been measured using ellipsometry by Bain et al. [47]. The result provides a fairly good linearity between the measured SAM thickness and the alkanethiol chain lengths. Porter et al. have characterized the structure of a C22-SAM based on the average structural information obtained by infrared spectroscopy, optical ellipsometry, and electrochemistry [46]. Chidsey and Scoles performed a more sophisticated analytical experiment of the C22-SAM cooled to below 100 K by using low-energy helium diffraction (LEHD), and demonstrated the detection of crystalline order of the SAM surface [227, 228]. This crystalline order of SAM formed on gold (111) was previously suggested in electron diffraction studies by Strong and Whitesides [229]. The result arrived at by Chidsey and Scoles unambiguously revealed that the SAMs were closely packed in a hexagonal arrangement with an overlayer of a $(\sqrt{3} \times \sqrt{3})R30^\circ$ structure with respect to the underlying gold (111) surface, as illustrated in Fig. 6a. This structure corresponds to a neighboring alkane-chain spacing of 0.4995 nm, as determined by the spacing of the sulfur atoms chemisorbed on the gold (111) surface, which means an area per alkane-chain molecule of 0.216 nm^2/molecule. This surface density shows that there are 4.63×10^{14} chains cm^{-2}, which is roughly consistent with the results of tritium-labeling studies ($\sim 4.16 \times 10^{14}$ chains cm^{-2}) [37]. If the chains exhibit an upright structure, the molecular occupied area is expected to be 0.184 nm^2. The alkane chains, therefore, must be filled keeping the area per alkane–chain constant so that van der Walls chain–chain attractive interaction becomes maximum. Thus, the alkane chains in a SAM are forced to a structure tilted by arccos(0.184/0.216) $\sim 32^\circ$ with respect to the surface normal (Fig. 6b), together with the trans-zigzag segment of an alkane chain rotated by $\sim 55^\circ$ from the plane established by the chain axis and the surface normal vector [37, 43, 65]. These features were provided from IR data with C16-SAM studied by Nuzzo et al. [7, 43].

1.2.1.4.3 **Superlattice Structure of SAMs on Gold (111)** The IR spectra also provided the evidence for a superlattice structure from the hexagonal close-packed structure of the C22-based SAM, that is, there was an unambiguous splitting of the methylene scissors when measured at 80 K [37, 43, 230, 231]. Later, this superstructure was assigned to a $c(4 \times 2)$ superlattice structure, which is identified from several experimental results obtained using helium diffraction measurements for a C18-based SAM by Chidsey and Scoles and their coworkers [232] and a GIXD study by Fenter et al. [233]. Very low current detective STM was also used to observe the superlattice of C12-based SAMs by Anselmetti et al. [234] and by Delamarche et al. [235]. For a shorter chain of a C6-based SAM, it was performed by Bucher et al. [236], and also for a C8-based

SAM by Poirier et al. [237]. The reason for exhibiting the $(\sqrt{3} \times \sqrt{3})R30^\circ$ structure can be explained intuitively, while the reason why the superlattice is produced is thus far not obvious. However, it is believed that the features responsible for the formation of the superlattice structure are located in a very thin layer of the gold–sulfur interface [65].

There is an unsolved problem related to the gold–sulfur bond as described above. The reason is that it is difficult to measure only a very thin gold–sulfur interface. Moreover, as a candidate for the sulfur-binding site on gold (111), there are three types of binding sites, that is, the hollow, the bridge, and the top site. However, the energy difference between the hollow and bridge sites is not so large [66] that it makes it difficult to definitively prove the evidence for the binding mode even by using up-to-date powerful analytical tools [65]. Evidence that the sulfur atoms cannot be situated at such a single site but must be in a mixed arrangement is proposed spectroscopically using infrared-visible SFG by Yeganeh et al. [238].

1.2.1.4.4 **SAM Surface Structure** Model organic surfaces that SAMs can form are not limited to hydrophobic surfaces with methyl-terminating groups on alkanethiol-based SAMs, but can involve various functional-terminating groups. This feature is the most important consequence obtained by developing a methodology of SAM-modified electrodes. We can use this flexible capability for SAM preparation to understand the fundamentals of organic surface chemistry and to engineer new technological applications. Following Dubois et al. [239], Bain et al. [44] comprehensively demonstrated earlier experiments on model surfaces using a variety of SAMs with the functional-terminating groups, which were followed by many chemists who have made challenges to such issues [37, 65, 240–242] (see also Sect. 1.2.1.11). Accordingly, order and orientation of the functional-terminating groups situated on top of the SAMs are indispensable for their structural specifications. Until now, there have been numerous experiments for simple alkanethiol-based SAMs with methyl-terminating groups, indicating that these surfaces are highly ordered [37, 65, 228, 230, 231, 243–245]. In parallel with this characterization of the methyl-terminated SAMs, a number of studies have been performed on the structures of a variety of functional-terminating groups on the SAMs. These experiments are carried out using analytical tools, such as IR, NEXAFS, XPS, GIXD, low-energy atom diffraction (LEAD), ellipsometry, cyclic voltammetry, STM, Kelvin probe technique [246, 247], and so on. If a functional-terminating group has a similar size as a methyl-terminating group, the order and orientation of the functional-terminated SAMs strongly depend on the balance between the two structural parameters, that is, (1) polarity and hydrogen-bonding characters of the terminating groups and (2) the length of the alkyl chains connected to the terminal groups [37, 65, 71]. Recently, Schreiber [65] summarized these experimental results systematically.

1.2.1.4.5 **Characterization of Defects by STM** All thiol-based SAMs assembled spontaneously on gold have never exhibited perfect crystalline domains with single molecular lattice. STM is capable of observing the appearance of local disorder or molecular pinholes as a real-space imaging with atomic resolution. This method makes it possible to characterize such local

molecular and mesoscale defects on the SAMs, particularly providing additional details of domain shapes and domain size dispersion [71]. Poirier has presented an excellent account in which the characterization of defects of a C12-based SAM on gold (111) is introduced by exhibiting high-resolution images of domain boundaries, gold vacancy islands, and molecular vacancies observed by low current UHV-STM [71]. SAMs usually result in several types of domain boundaries on gold, the typical two of which are pure orientational domain boundary and translational domain boundary [71, 237], as well as domain boundary occurred because of difference in tilt direction (i.e. different azimuth angles) of alkanethiol-based SAMs on gold (111) [248]. On the other hand, gold vacancy are usually observed using STM as single gold atom deep pit defects with a variety of sizes and shapes in the domains of SAMs on gold [71]. The pit depth is 0.25 nm, which can be easily measured by STM, indicating that the pit area is also covered with the alkanethiol monolayer [249, 250]. In fact, the adlattice structure of the monolayer within a pit was confirmed by STM [251, 252]. The formation mechanism by which the gold vacancy is created at the domains of SAMs remains to be solved, but a possible mechanism is provided by Poirier [71].

1.2.1.4.6 **Structural Variation in the Backbone Unit of SAMs** Structural variations of alkane-chain backbone in SAMs have probably been examined first by Ulman and coworkers from fundamental viewpoints of the effect of the structural variations on molecular packing and orientation of the SAMs [8, 253, 254]. The investigation has been carried out from two viewpoints. One is a structure design to provide structural perfection of SAMs with few defects. The other is a structure design to have some advantage of the functional applications of SAMs. The flexibility in orientation of alkane chains tends to cause some defects, one of which is based on the boundary due to different azimuth angles of the tilted alkane chains on the gold surface [248]. Fujihira and coworkers succeeded in avoiding this type of defect by using cage molecules as a SAM component as shown in Fig. 7a [255]. When these cage structure-based disulfide compounds are chemisorbed onto gold (111) surfaces, STM images indicated that the SAM could be formed and each molecule was clearly discriminated at the molecular level. Formation of highly ordered close-packed structures was realized in this SAM with a thickness less than 1 nm (see also Sect. 1.2.1.9.1). In addition, in this SAM a domain boundary between two tilted alkane-chain domains with different azimuth angles cannot be seen (Fig. 7c). This result indicates that bicyclooctane(BCO)-based SAM exhibits no tilted structure, but a closely packed upright structure on gold (111) surface (Fig. 7b). Here, ordered 2D lattice is determined mainly by the size of BCO spherical backbone rather than the commensurability of the sulfur-binding site to the (111) oriented gold substrate.

The other typical example is a SAM formed of alkanethiols with an amide bond in the interior of a single alkane chain (Fig. 8) [256, 257]. Such a SAM has stability based on the lateral interaction not only due to van der Waals chain–chain interaction but also due to hydrogen-bonding interaction between neighboring amide moieties. A SAM formed from a mixed solution of this amide-containing long-chain alkanethiol with a commonly used alkanethiol results in the phase separation [258].

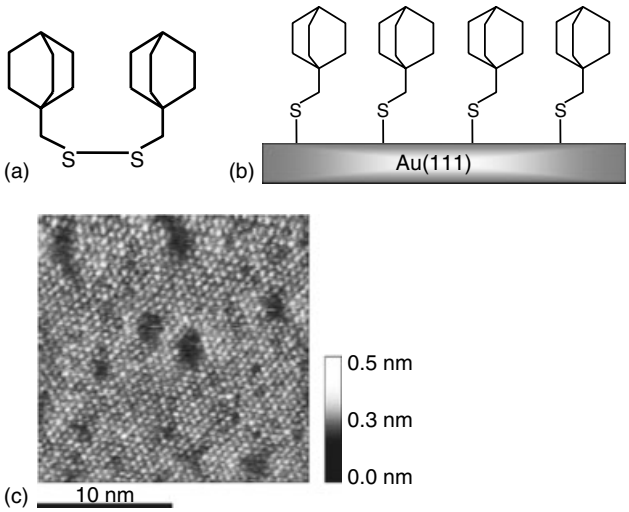


Fig. 7 (a) The structure of BCO disulfide compound synthesized, and (b) the schematic side view presenting the structure of the BCO-SAM on gold (111). (c) Constant-current STM image of a 20×20 nm^2 area of a BCO-SAM on gold (111) (tunneling current = 50 pA, sample bias voltage = +1 V) [255].

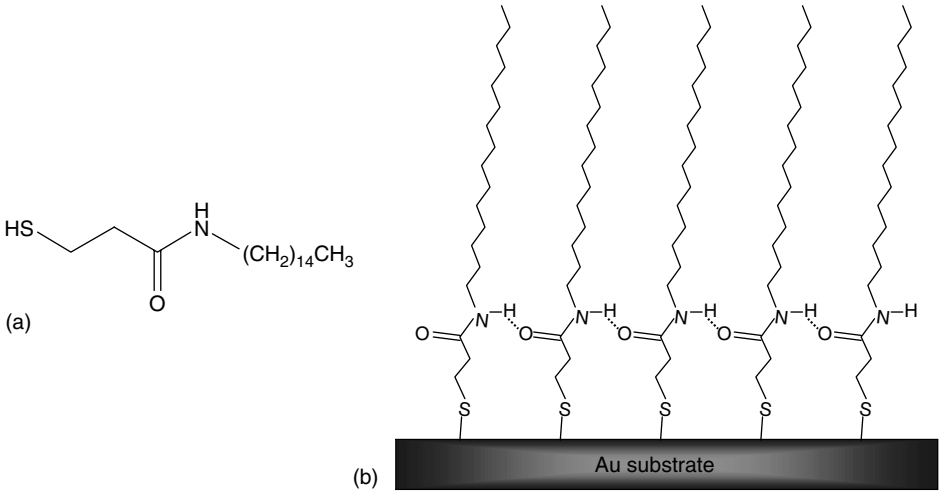


Fig. 8 The structural formula of an alkanethiol compound containing an amide bond in the interior (a), and the schematic side view presenting idealized SAM structure of the amide bond-containing alkanethiol-based SAM (b) [256].

Recently, a large number of structural variations have been designed for their potential applications. In particular, advanced studies on nonaliphatic SAMs have been done intensively. SAMs formed from thiols with the backbone structures of acetylenes, oligophenylenes, oligothiophenes, and so on can be used as an important component of molecular electronic devices. These examples are described in a separate section below (see also Sect. 1.2.1.10) to explain the trend of these SAMs briefly.

1.2.1.5 Chemistry and Energetics of the Formation of Alkanethiol-based SAMs on Gold

1.2.1.5.1 Overall Reaction and Energetics of Chemical Adsorption at the Gold/Thiol Interface When we prepare SAMs onto gold substrates by the solution deposition method, it is not easy for us to decide the most suitable preparation conditions in terms of solvent, solution concentration of the component, adsorption temperature, and immersion time. This is because different structures and properties of component organosulfur compounds themselves strongly influence the energetics and the mechanism of the SAM formation on the surface. Understanding the chemistry of SAM formation, even in the case of such simple models as alkanethiol-based SAMs, provides some clues actually helpful in choosing the better preparation conditions. Therefore, we describe here the fundamental issues relevant to the adsorption chemistry and energetics for the formation of alkanethiol-based SAMs on gold.

Organosulfur compounds interactive to the surface of gold to form SAMs are listed in Fig. 9 [8]. However, here we focus on two types of organosulfur compounds, that is, alkanethiol and dialkyl disulfide, because these have been most intensively investigated so far. In addition, these two organosulfur compounds give indistinguishable SAMs on gold when examined by ellipsometry and XPS, probably resulting in chemisorption through the alkanethiolate–gold bond [8, 10, 60, 76, 259, 260]. Whitesides and coworkers compared

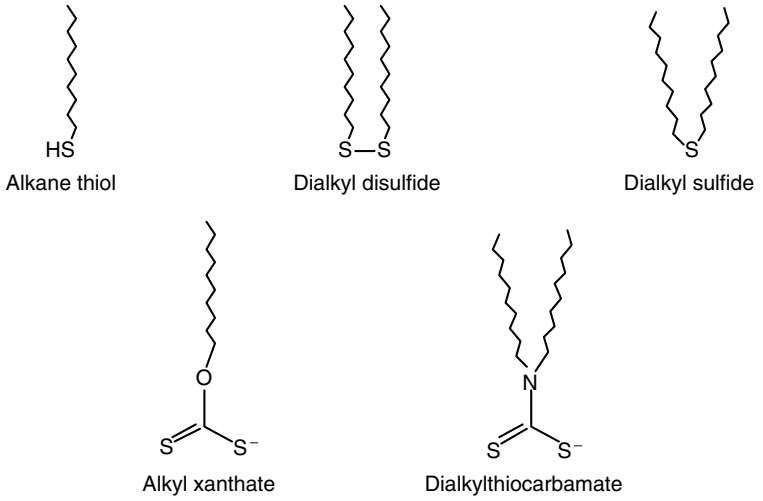


Fig. 9 Surface-active organosulfur compounds that form monolayers on gold [8].

SAMs formed from solution of disulfides with those of thiols. They also demonstrated that the rate of SAM formation from alkanethiols and dialkyl disulfides were indistinguishable, while the rate of replacement of molecules from SAMs by alkanethiols was much faster than that by dialkyl disulfides, by a factor of 50 [60, 261].

In the case of dialkyl disulfide, the reaction is probably a simple oxidative addition of the S−S bond to the gold surface [8]. In the case of alkanethiol, the adsorption reaction onto a clean gold surface may be considered formally as an oxidative addition of the S−H to the gold, probably through the hydrogen atom on the surface, finally followed by a reductive elimination of the hydrogen [8]. The fact that SAMs can be prepared from gas-phase deposition in an environment completely free of oxygen strongly supports this overall reaction mechanism [8, 262, 263].

The bond dissociation free energies for the chemisorption reaction process of RSH on gold are as follows: RS−H (87 kcal mol^{-1}), RS−Au (−40 kcal mol^{-1}), and 1/2H−H (−52 kcal mol^{-1}) [8, 10, 76, 264–266]. Consequently, free energy of this overall reaction can be calculated to be −5 kcal mol^{-1}, which means this chemisorption reaction is an exergonic process. In the discussions in the literature, there has been confusion between enthalpy (ΔH) and free energy (ΔG). This value is quite similar to that calculated by Schlenoff et al. (−5.5 kcal mol^{-1} for C18) [261]. They also estimated the free energy of adsorption for dioctadecyldisulfide to be −24 kcal mol^{-1}. By measuring the temperature dependence of the value, Blanchard and coworkers estimated the molar enthalpy of adsorption (−20 kcal mol^{-1}) and the entropy of adsorption (−48 cal mol^{-1} K^{-1}) [264, 266]. This relatively large amplitude and negative value of entropy apparently reflects the great degree of ordering that occurs as the alkanethiols change from randomly distributed orientations in solution to highly oriented SAM lattices on the surface [10].

1.2.1.5.2 **Chemisorption Energetics for Gold/Organosulfurs Interfaces** Gold–organosulfur interaction involves two adsorption regimes, physisorption and chemisorption. The former interaction is one between the gold surface and the adsorbate, and the latter interaction is derived from the chemical bond between the sulfur head group and the gold surface. Schreiber et al. discussed quantitatively the comparison of these interactions by taking account of a large variety of structures of alkanes and the corresponding alkanethiols [48, 267, 268]. The physisorption energy for decanethiol (C10) on gold (∼25 kcal mol^{-1} (∼104 kJ mol^{-1})) can be comparable to the corresponding chemisorption energy (∼30 kcal mol^{-1} (∼126 kJ mol^{-1})) due to the additive contributions of van der Waals interactions of the entire chain [48, 267, 268].

1.2.1.5.3 **Stabilization of SAM Structure due to Alkane Chain–Chain Interaction within the Densely Packed Monolayers** For densely packed monolayers of alkanethiol-based SAMs, the chain–chain interaction will become more and more important [48]. For decanethiol (C10) in the bulk one would expect ∼16 kcal mol^{-1} (66 kJ mol^{-1}) based on the heat of vaporization [48].

1.2.1.5.4 **Structural Effects on SAM Formation and Stability** The structures of the SAM forming components, of course, may have a strong effect on the

formation and stability of SAMs. For instance, the energy cost for a gauch defect in an isolated hydrocarbon chain is ~0.022 eV (~0.5 kcal mol^{-1}), which can be thermally activated at room temperature (RT = ~0.6 kcal mol^{-1}) [48]. Therefore, less closely packed SAMs result in gauch defects of the alkyl chains, and inevitably influence the formation and stability of SAMs. This is exemplified by Shon and Lee using uniquely designed chelating alkanedithiols [269]. Another unique system related to this issue is reported by Fujihira and coworkers using a single alkane chain inserted in a rigid BCO-based SAM matrix [270].

1.2.1.6 Growth Mechanisms of SAMs

1.2.1.6.1 General Profiles for SAM Formation Process Understanding the growth process of SAMs as well as the energetics of SAM formation is of fundamental importance for the advance in physical chemistry of molecular self-assembly and also for preparation of various structured SAMs on gold. The energetics of SAM formation, as discussed above for alkanethiol-based SAMs as a model case, have a direct impact on the growth of SAMs.

Bain et al. first studied the kinetics of alkanethiol-based SAMs onto gold in the solution phase of ethanol by measuring the wettability and thickness using ex situ macroscopic analytical methods, that is, contact angle goniometry and ellipsometry [8, 10, 47]. The results revealed that at least two distinct kinetic regimes could be characterized in the SAM formation process at the macroscopic resolution of such methods [8, 10, 47, 76]. The first regime, a very fast step that proceeds within a few minutes and strongly depends on solution concentrations used in the measurements, can be described approximately by the Langmuir growth curve for adsorption. The second regime, a slow step in which final macroscopic properties of SAM were reached only after several hours [76], was described as a surface crystallization process. In this regime, it was presumed that alkyl chains get out of the disordered state and into ordered unit cells [8, 48]. Later, it was analyzed in detail that this slow step can be further divided into two processes [10].

Comprehensive understanding at molecular levels on the detailed growth processes of SAMs has been revealed using several in situ analytical tools [10]. The first regime corresponds to the adsorption process onto gold, in which alkyl chains possess a high number of gauche defects on the surface [10, 80, 271]. In the second regime, the growth of an ordered monolayer film follows the first regime, which was first identified quantitatively ex situ using NEXAFS [80]. Difference in the timescale of these two regimes is at least ~2 orders of magnitude [81, 82]. During the second process, alkyl chains are highly ordered to assemble together. These chains straighten from the highly kinked conformations to the trans-extended zigzag conformations predominantly [80]. A subsequent process occurs at a rate of 35 times slower than the chain-straightening process [10]. When further continuous self-assembly in solution proceeds, films thicker than just monolayer are always formed, indicating that the physisorption process proceeds continuously onto the monolayer films [272]. Hence, the physisorbed adlayer produced by a procedure of a long time immersion into an ethanol solution has to be removed by rinsing with ethanol solvent after the solution deposition procedure. Such a rinsing procedure with a solvent is indispensable for a procedure for preparing complete

SAMs on gold surface. The fast and slow regimes of SAM growth onto gold in the solution deposition method first proposed by Bain et al., has now gained consensus, and a more detailed and comprehensive description on these issues is found in a review [10].

1.2.1.6.2 **Growth Studies from the Gas Phase** UHV technique allows precise control of the cleanliness of the substrate and the use of a wide range of surface-analytical techniques. These powerful techniques reveal information on the growth processes of SAMs as well as on their structural characterization. For details of these useful techniques, the interested readers are referred to the review by Schreiber [48]. In particular, UHV-STM seems to be extremely effective for understanding comprehensibly the growth process at the molecular levels. The self-assembly mechanism of alkanethiol-based SAM of C10 on a gold single crystal (111) surface was observed by Poirier et al. using UHV-STM [48, 71, 273]. They revealed unambiguously that the previously mentioned two-step process, that is, the fast step and subsequent slow step could be observed at the molecular levels. The fast step begins with the condensation of low-density crystalline islands with the alkanethiol molecular axes aligned parallel to the surface. The following phase transition results in a denser phase by realignment of the molecular axes parallel to the surface normal. These images are clearly obtained as a sequential molecular evolution of the SAM growth.

1.2.1.6.3 **Growth Studies from Solution Phase** The most convenient preparation method for SAMs is the solution deposition method. In this method, it is not necessary for us to use an expensive UHV equipment, and thus understanding of the SAM growth with this method is informative for the SAM preparation. However, in comparison with the gas phase, the solution method has a shortcoming regarding the substrate cleanliness. This situation is very different from the case of characterizing SAM structures, in which only the structure of the finally formed SAM requires the absence of contaminants. The substrate surface and solution themselves should be clean enough to secure no effect of contaminants during the timescale of the growth process, because strong effect of the contaminants on the process of the SAM growth is expected [48]. For a comprehensive understanding of the growth of SAMs from solution phase, comparisons between the solution and the gas-phase deposition of SAMs are very useful and are summarized in table 2 of Ref. 48. The major difference between the two phases is the solvent being present in solution phase. Solvent molecules, depending on their structural characters and polar properties, have a direct impact during the growth process of SAMs. Competitive physisorption between the sulfur compound and the solvent onto the gold surface may influence mainly the first step of the growth process, but the solvent effect may not be negligible in the succeeding steps toward the final structure of the SAM.

1.2.1.6.4 **Further Techniques for Investigating the Growth of SAMs on Gold** Until now, numerous studies on the growth processes of SAM formation have been conducted using several instrumental techniques. In addition to wettability, ellipsometry, and UHV-STM described above, various other techniques, such as SHG [76, 77], SFG [78, 79], NEXAFS [80], EQCM [81], SPR [82], and FTIRRAS [83],

have been applied to this issue. The results are reviewed in Refs 48, 75, 76. A unique technique using AFM cantilever as a substrate is recently introduced in Ref. 274.

1.2.1.7 Patterned SAMs

1.2.1.7.1 Two Approaches for Fabricating Patterned SAMs: the Top-down Method and the Bottom-up Method Patterned SAMs, in which specific self-assembling components have a deliberate spatial distribution on the surface, are generated to fabricate nanoscale architectures and to provide well-characterized supports for physicochemical and biochemical processes [86]. To confirm the origin of the friction contrast of the phase-separated domain between hydrocarbon (HC) and fluorocarbon (FC) in L–B films described below (Sect. 1.2.1.7.2), Fujihira and Morita [275] prepared deliberately patterned SAM samples having HC and FC domains by utilizing photolithographic and liftoff techniques. Therefore, development of techniques for tailoring such patterned SAMs and controlling their functions at the molecular level is of critical importance in a future technology. Toward such a goal, so-called nanotechnology is intensively being pursued [9, 276, 277]. If such a purpose could be accomplished, the fabrication techniques of molecular patterns would provide a direct impact on the preparation of chemically modified electrodes with such patterns. Generally, techniques for fabricating patterned structures onto a local surface of a substrate at the molecular scale are classified into two approaches.

One is a processing technique that is widely recognized as a traditional pattern formation method, since it has been successfully applied to patterning semiconductor surfaces using various lithographic and chemical etching techniques. A wide variety of investigations using such a technique have also been extensively undertaken from the viewpoint of fabrication of organized molecular interfaces, in particular, in nanobiotechnological interfaces [9, 86]. Such a set of techniques will be referred to as *the top-down method* for fabricating patterned SAMs.

The other is a kind of architectural technique that could be imagined from its analogy to our macroscopic world. That is, in our daily life, many elaborated devices have been made of a large number of small components and all buildings can be constructed step by step on the foundations. This type of technique in nanotechnology is referred to as *the bottom-up approach*, yet a premature one as compared to the top-down approach. We have to scale down the macroscopic architectural technique to the molecular scale. The realization of the techniques available to molecules can be inspired since it has been found that nature has already accomplished similar technology almost completely by using self-organization. Nature exquisitely architects many systems of predesigned nanostructures and effectively uses lots of molecular devices in the systems, such as genetic coding and decoding systems [278], photosynthetic reaction center systems [279], and so on. Therefore, this technique could be naturally combined with SAM materials that have a potential to make patterned nanostructures on various surfaces via molecular self-organization.

Such studies on the two approaches will be briefly described here. These include spontaneous phase separation of mixed SAMs as an example of the bottom-up method for fabricating patterned SAMs, and several techniques of lithography, printing, and nanohandling as examples of the top-down method. These techniques

are useful as methods for preparation of chemically modified electrodes, as described later. Whitesides and coworkers reported recent unconventional methods for fabricating and patterning nanostructures [280]. Their performance and intrinsic limits are summarized in tables in Ref. 280.

1.2.1.7.2 **Spontaneous Phase Separation** Multicomponent SAMs, so-called mixed SAMs, are usually formed by a solution deposition method. The simplest case is a mixed SAM of two components. When a substrate is exposed to a mixed solution with two different adsorbates, both species adsorb on the substrate surface [86]. The resultant SAM is presumed to have domains of the two adsorbates uniformly mixed at the molecular level if the molecular features of the components are quite similar. On the contrary, if the molecular features of the components are quite different phase segregates may result in mixed SAMs. In the latter case, the two components are separately adsorbed on the surface to form domains of different features depending on the component structure and properties.

The phase separation of SAMs has been characterized so far by various analytical techniques such as XPS, IR, ellipsometry, and scanning probe microscopes (SPMs). SPMs among them, in particular, have sufficient lateral resolution and therefore appear the most promising for direct imaging of nanometer scale patterned SAMs [281]. The analysis is required for characterizing the spatial distribution of molecules on the 1–100-nm scale [281]. STM is a powerful tool that meets the requirement [281–283]. Friction force microscopy (FFM) is also useful for the purpose [284–286]. Although studies were conducted using L–B films, Güntherodt and Fujihira and their coworkers demonstrated for the first time that FFM can be used to image the chemical contrast between the phase-separated domains with a resolution of ~5 Å [287, 288]. In FFM, both the normal and the lateral force were measured simultaneously during the scanning.

Many studies on spontaneous phase separation of alkanethiol-based SAMs have been conducted using different types of variation in the molecular composition [86]. Such systems include the coadsorption of short and long-chain alkanethiols (i.e. variation of the alkyl-chain length) [55, 56, 62, 282, 289, 290], molecules of similar alkane-chain length but with differing terminal groups (i.e. variation of the terminal functional group) [281], alkyl fluoroalkyldisulfides [284, 291], and variation of the buried functional group [258].

1.2.1.7.3 **Scanning Probe Lithography Using SAMs** Patterning of surfaces with SPMs, such as AFM and STM, has been explored, as the location of the probe tip can be placed on the surface at a specific set of coordinates and the resolution of the patterns can approach the molecular scale [86]. In addition to STM and AFM, scanning near-field optical microscopy (SNOM), which is also called *near-field scanning optical microscopy* (NSOM), was found to be useful for optical patterning of SAMs [292]. By controlling tip-sample separation of SNOM by AFM [293–295], optical patterning was readily achieved [292]. The readers interested in near-field optical microscopic manipulation and a local optical observation should be referred to a review article [296]. Such a SPM technique for lithography, which is referred to as *scanning probe lithography* (SPL), can be applied to a wide variety of functional

SAMs [297]. Alkanethiols can play a critical role in SPL on SAMs. Alkanethiols are often called *molecular inks*, the idea of which has been already recognized as reactive chemical "ink" of microcontact printing (μCP) [9].

The SPL on SAMs embodies several elementary procedures of molecular manipulation in molecular surface engineering. Gorman and his coworkers have classified these into three types of manipulation procedures by SPL, that is, elimination lithography, addition lithography, and substitution lithography (Fig. 10). Further, substitution lithography is subdivided into via in situ addition and via terminus modification (Fig. 10c-1,c-2) [297].

An early demonstration of SPL was reported by Kim and Bard [298]. They studied an alkanethiol-based SAM of *n*-octadecanethiol (ODT) on gold using STM in air, and observed that the tip mechanical force induced etching of the SAM resulted in defect sites (pits) with diameters of 5–10 nm under a low bias and high tunneling current. Crooks and coworkers established some of the early considerations in STM-based elimination lithography of SAMs under ambient conditions [297, 299]. Later, they proposed that the patterning mechanism for the SPL induced removal (or deposition) of ink from SAMs in air was faradaic electrochemical in nature [297, 300, 301].

For the experiment under a vacuum, Mizutani et al. conducted a study on nanoscale reversible molecular extraction and healing of *n*-nonanethiol (C9)-based SAM on gold (111) using UHV-STM [297, 302]. From the observations based on the molecularly resolved images by UHV-STM, it was demonstrated that by applying a bias voltage of 2.3–3 V to the sample, SAM component molecules could be extracted, which resulted in holes with diameters of 2–5 nm in the SAM [302].

Many investigations of elimination lithography, that is, localized removal of a SAM, have also been conducted by AFM [86, 297]. For instance, Liu and Salmeron observed that molecules could be displaced with an AFM tip under a high applied load (up to 100 nN) [86, 297, 303]. Zhou and Uosaki employed a current sensitive atomic force microscopy (CS-AFM) for localized removal of a SAM [86, 297, 304, 305]. With CS-AFM, they could compare the topography and current images of the resulting pattern of an ODT (C18)-based SAM simultaneously [297, 304, 305].

Substitution lithography is of extreme importance because this process can provide a direct means applicable to in situ nanoscale surface modification on SAMs to create a variety of specific patterned SAMs. An in situ replacement of one organic component by another in a SAM was reported by Chen et al. who used STM to replace conjugated molecules into a dodecanethiol (C12)-based SAM on a gold surface [297, 306]. Gorman et al. reported an in situ localized removal of a decanethiol (C10)-based SAM and subsequent replacement by dodecanethiol molecules using substitution lithography under an applied voltage in a nonpolar dodecane solution of 10 mM of dodecanethiol [297, 307]. The use of a low dielectric, nonpolar solvent (dodecane, mistylene) is due to the fact that we can avoid the use of coated tips that would normally have to be employed to avoid a high leak current (greater than 1 pA) from the tip into the surrounding solution [297, 307]. The mechanism of this removal was argued to be similar to that reported by Crooks et al. [297, 299].

Xu and Liu developed an alternating technique of the substitution lithography

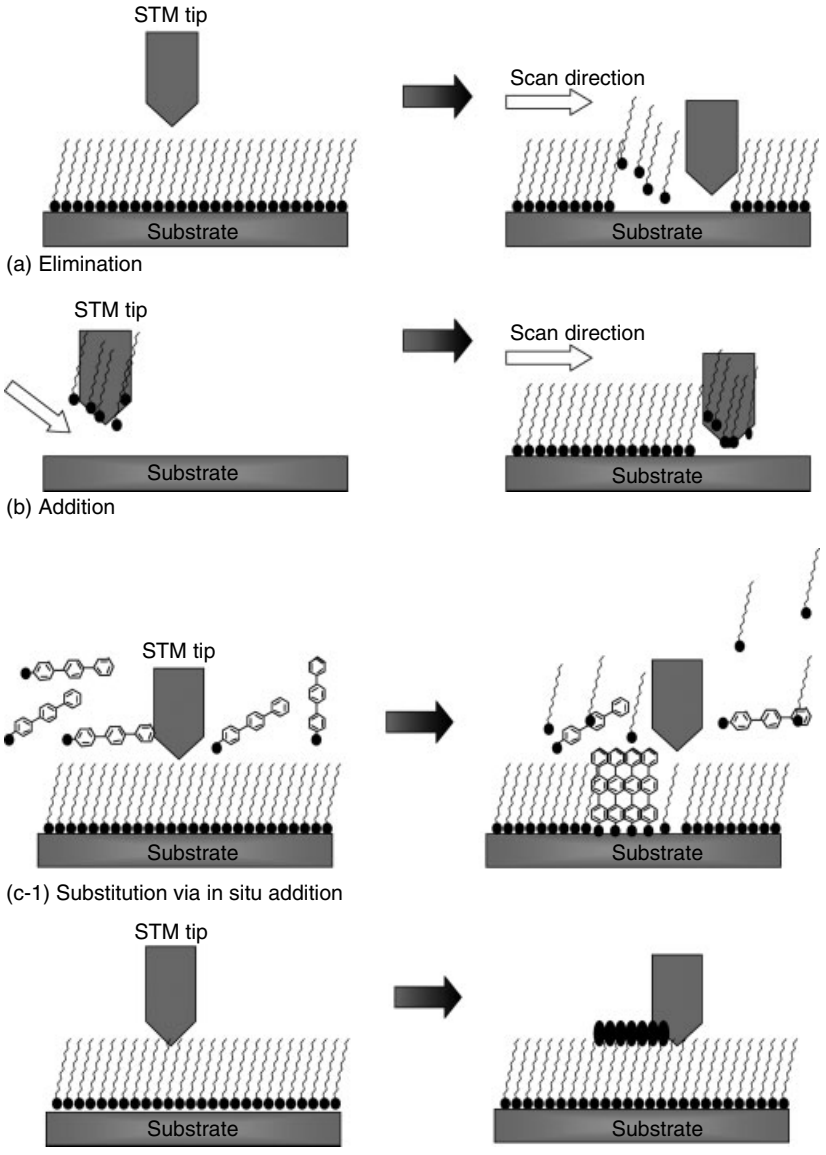


Fig. 10 Schematic diagrams illustrating three types of the manipulation procedures by SPL [297]: (a) elimination lithography, (b) addition lithography, (c) substitution lithography; the substitution lithography is subdivided into via in situ addition (c-1) and via terminus modification (c-2).

using an AFM tip in a solution containing another thiol [297, 308]. In this method, SAMs can be removed by mechanical means using an AFM tip followed by in situ replacement with a second component. They referred to this technique as nanografting. Their results are reviewed in [309]. Further intensive investigations related to the application of this technique to the fabrication of nanometer-sized protein and DNA patterned SAMs have been reported by Liu and coworkers [310–313]. Similarly, Porter et al. reported the investigation of approaches for the fabrication of protein patterns by SPL [314].

Addition lithography using SPMs on SAMs for fabrication of nanoscale patterned SAMs is extremely important as a technique of SPL methodologies. The most typical application of addition lithography with organothiols as ink on gold is well-known as *dip-pen nanolithography* (DPN) [86, 297]. We will describe this technique in the next section.

1.2.1.7.4 **Dip-pen Nanolithography** DPN was developed by Mirkin and coworkers as a kind of SPL (''direct write'') [86, 297, 315, 316]. Dip-pen technology, in which ink on a sharp object is transported to a paper substrate through capillary forces, is approximately 4000-years old and has been used extensively throughout history to transport molecules on macroscale dimensions [315]. The traditional dip-pen technology and DPN are analogous in style, but are different in scale and transport mechanism. DPN uses an AFM tip as a ''nib (penpoint)'', a solid-state substrate as a ''paper'', and molecules with a chemical affinity for the solid-state substrate as ''ink'' [315]. The fundamentals of DPN are intensively discussed, together with charming demonstrations of its application [297, 315–318]. The mechanism governing DPN is, however, still not fully understood [297, 319, 320]. Several improvements of the DPN technique are also discussed, such as parallel and serial writing [321], and a multiple-pen nanoplotter [322]. Other researchers have demonstrated several optional techniques: the use of the tapping mode AFM rather than the commonly used contact mode [323], and the application of electrochemical potential to the AFM tip in the DPN process [324].

In particular, when the methodology of DPN is combined with that of organothiol-based self-assembly on a gold surface, as depicted in the schematic representation of DPN (Fig. 11), it is naturally expected that DPN can become an extremely powerful technique as a SPL tool of nanotechnology [315, 316]. This expectation is based on a conspicuous advantage of the methodology of organothiol-based self-assembly on gold, that is, the flexible chemistry in respect to the terminal groups.

DPN is used to direct ''write'' patterns consisting of a relatively small collection of molecules in submicrometer dimensions [315]. Mirkin and coworkers have pursued their investigations for fabricating a wide variety of patterned SAMs. Some of them can be used for biochemical and diagnostic purposes [324–329].

1.2.1.7.5 **Microcontact Printing by Use of Organosulfur Inks** Whitesides and coworkers have developed a set of techniques called *soft lithography* that offers tools for micropatterning that complement and extend the conventional fabrication methods [89, 330]. They emphasize that the ability to control surface properties using SAMs is most useful when combined with spatially defined patterns. Soft lithography allows the creation of useful

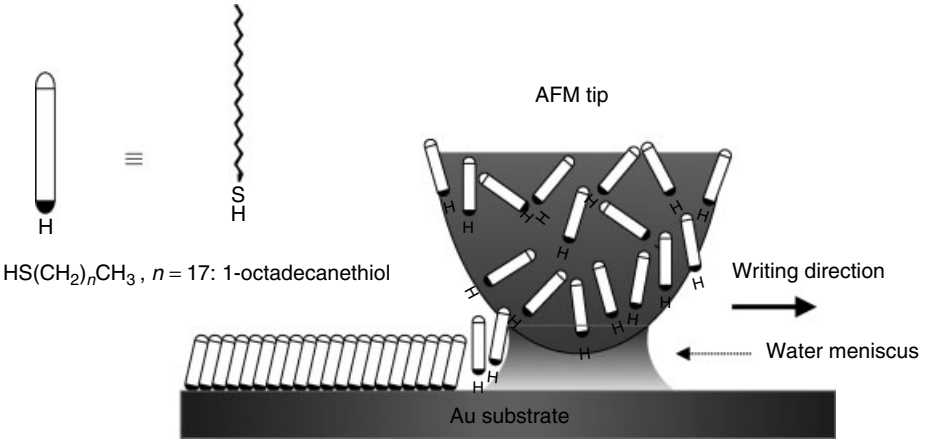


Fig. 11 Schematic presentation of DPN. A water meniscus forms between the AFM tip coated with 1-octadecanethiols (ODTs) and the gold substrate. The size of the meniscus, which is controlled by relative humidity, affects the ODT transport rate, the effective tip-substrate contact, and DPN resolution [315].

patterned surfaces using a combination of SAMs and μCP [330].

μCP is a method for patterning SAMs on surfaces which is operationally analogous to printing ink with a rubber stamp on paper [9, 86, 89, 330–333]. SAMs are formed naturally in the regions of contact between a topographically patterned elastomeric stamp and a bare surface of metal, metal oxide, or semiconductor [9, 89]. The stamp was wetted with (or containing dissolved) reactive chemical 'ink', such as *n*-alkanethiols, and other compounds forming SAMs. The details of the techniques can be found in the several papers and reviews described by the pioneers [9, 89, 330–334]. Here, we will briefly describe some important points of μCP for fabrication of patterned SAMs as well as the comparison between μCP and SPL.

The technique of μCP is generally cost-effective because no expensive instrument is needed to conduct the experiment. μCP can be applied to many substrates, such as gold [331], silver [335], and copper [336]. μCP can also be used in the form of nonplanar surfaces, such as, curved substrates [337]. This character is, in particular, unique [89]. The reproducibility of the μCP process is dependent on the stamp's resistance to degradation, the replication accuracy of the contact pressure that is applied to the substrate, and registration with other surface features [86]. Michel and coworkers describe a strategy for μCP that uses planar, elastomeric stamps to print chemical patterns onto gold substrate [338]. Using STM and wettability measurements, they also compared dodecanethiol (C12)-based SAMs on gold (111) prepared by μCP and by the solution deposition method, and found that both the characteristics of these SAMs were indistinguishable [339]. Using μCP, SAMs consisting of patterns having dimensions less than 0.5 μm can be routinely generated on gold [331, 332]. Whitesides and coworkers described the use of SAMs as ultrathin resists [331–334]. Xia and Whitesides described a number of approaches that have been employed to reduce the size of features of SAMs generated using

μCP [340]. Michel and coworkers reported a high-resolution printing technique based on transferring a pattern from an elastomeric stamp to a solid substrate by conformal contact, and described the potential for emerging micro- and nanoscale patterning technologies [91, 341].

Several new approaches using μCP have been reported. Patterned SAMs on gold can be prepared by the combination of μCP and the subsequent solution deposition methods [342]. μCP can be applied to the top surface of a SAM, which leads to a new type of lithographic approach to prepare patterned SAMs using a locally selective catalytic reaction [341, 343]. Patterning of proteins and cells using μCP is reported by Whitesides and coworkers [117, 330, 344, 345].

Electrostatic interaction on patterned SAMs fabricated using μCP are investigated. Using μCP with two types of ink, that is, alkanethiols substituted with anionic and cationic end groups, Aizenberg et al. fabricated a chemically patterned SAM with anionic and cationic regions [346]. On the patterned surface, they directly observe the process of patterned colloidal deposition and assembly, which are controlled by electrostatic and lateral capillary interaction. Whitesides and coworkers have demonstrated the microfabrication of chemically charged patterned SAMs using μCP [347]. They expanded this idea to directed self-assembly of two oppositely charged particles on patterned electrode controlled by an applied electric field [348].

As an analytical tool for such a chemically patterned SAM surface, pulsed-force-mode atomic force microscopy (PFM-AFM) designed by Marti and coworkers [349] is useful as scanning force microscopy with chemical recognition capability [350, 351] (see chemical force microscopy, CFM: Fujihira). Frisbie et al. coined a word for such an SPM, that is, CFM [352]. CFM was originally based on FFM due to its chemical recognition ability [287] as already described in Sect. 1.2.1.7.2. Using the force mapping with PFM-AFM, which maps the force between an AFM tip and a patterned sample surface just before contact (in noncontact) in air or in liquid, Fujihira and coworkers demonstrated imaging of a patterned surface with electrostatic charges with opposite signs in aqueous buffer solutions [350]. Before this study, they investigated the change of the surface charge on various oxide surfaces as a function of the pH of the solution, in which the oxides were dipped [353, 354]. They also measured the forces between a gold-coated tip and a gold plate in aqueous solutions, where electrode potentials of the tip and the plate were the same [355].

Fujihira and coworkers extended PFM-AFM to adhesive force mapping on a patterned SAM [356–358]. In this mode of PFM-AFM, difference in the adhesive force between the $-CH_3$ and $-COOH$ terminated regions on the μCP patterned SAM was mapped simultaneously with its topographic image. To achieve the quantitative analyses of the adhesive forces for chemical differentiation on the patterned surface by PFM-AFM, accurate information about the tip and substrate geometries [359, 360] and chemical modification of the tip surfaces [361] as well as the precise environmental control, such as electrolyte concentrations [292, 362, 363], and humidity [364] are indispensable. Recently, Bohn and coworkers used PFM-AFM to map the adhesion force between an AFM tip and samples of ω-substituted alkanethiol monolayer terminated with $-CH_3$ and $-COOH$ prepared by μCP

and to study electrochemically generated gradients [365].

The SPL described above is applicable to a variety of patterning techniques using a small STM or AFM tip end, in which the placement of the tip is three dimensionally controlled at the nanometer scale to fabricate patterned SAMs. The scanning tip, here, plays a central role for the nanoscale fabrication. In the case of μCP, a prepatterned stamp displaces the scanning tip, and plays a central role in the nanofabrication of patterned SAMs [9, 86, 89, 330–333]. A key difference between SPL and μCP is as follows. μCP can generate many features simultaneously on the surface in a single step, whereas SPL is a serial technique that writes only one feature at a time [9]. This contrast is the same as that between the photomask and the SNOM tip in the near-field irradiation [292]. SPL has a patterning feature that can be determined in situ and easily changed, whereas μCP requires a prepatterned stamp that has to be made in advance. However, once the stamp is available, multiple copies of the pattern can be produced using straightforward experimental techniques [89, 330–333]. Therefore, the two techniques are complementary to each other. Recently, Orden and coworkers demonstrated an alternative patterning technique, which they refer to as *Single Feature INKing and Stamping* (SFINKS) [366]. SFINKS combines elements of DPN and μCP to generate patterns. Namely, in SFINKS multiple tips with different inks deposit inks to individual stamp features and then the different inks are transferred to the different locations on the substrate by μCP. Notably, SFINKS can pattern multiple components with complex structures without cross-contamination.

1.2.1.7.6 **Photolithography for Fabricating Patterned SAMs** Lithography has long been developed as a common technique for fabricating microelectronic devices, using UV, electron-beam (e-beam), and X ray. Correspondingly, they are well known as UV photolithography, e-beam lithography, and X-ray lithography respectively [9, 275]. The development of photosensitive resists capable of replicating patterns written by photons or electrons with resolution below 10 nm remains a challenge for chemistry and materials science [9, 275]. Patterned SAMs are candidates alternative to the polymer resist used in the techniques. Whitesides and coworkers [9] describe that two characteristics make SAMs potentially useful as resists for lithography: (1) they consist of individual molecules that occupy areas smaller than $\sim 0.25\ nm^2$ and (2) they are very thin (<3 nm). Here we will discuss UV photolithography for fabricating patterned SAMs. For modification of SAMs by e-beam lithography and X-ray lithography, the readers can refer to a recent review by Zarnikov and Grunze [367].

UV-photolithography can be classified into two methods. One is a straightforward method for photopatterning alkanethiol-based SAMs on gold and silver surfaces with micron-scale resolution [368–372]. The process underlying photopatterning of SAMs on gold and silver is well known at the phenomenological level [368, 369, 371, 372]. Alkanethiolate formed by the adsorption of alkanethiols are oxidized on exposure to UV light in the presence of air to alkylsulfonates:

$$\text{Au-SR}(CH_2)_n\text{X} + 3/2\text{O}_2 \xrightarrow[h\nu]{} \text{Au}^+ + \text{X}(CH_2)_n\text{SO}_3^- \qquad (1)$$

The mechanism of this reaction has been the subject of some debate, but Leggett and coworkers showed that oxidation can

occur in the absence of ozone with use of a UV source emitting principally at 254 nm [373].

The other is the fabrication of SAMs by using photochemical reaction of photoactive pendant groups, as demonstrated in 1993 by Fujihira and coworkers [292], and by Wrighton and coworkers [374, 375], and recently by Turro group [376].

1.2.1.7.7 **Nanotransfer Printing of Patterned Gold Thin Films** While μCP offers fast and low-cost approaches for patterning flat or curved surfaces over large areas in a single processing step, it is generally subtractive in operation, that is, it typically requires the use of sacrificial resists, etching procedures, or postpatterning deposition steps. *Nanotransfer printing* (nTP) is a purely additive printing technique that has nanometer resolution, which has been developed by Rogers and coworkers [377]. The method allows us to transfer metal films from the raised regions of a stamp onto various oxide surfaces. Using nTP, we are able to transfer the metal pattern from a stamp with the relief feature, which defines the geometry of the pattern, onto both conformal (thin poly(dimethylsiloxane) film supported on plastic) and rigid (e.g. silicon wafer) substrates. They describe that using nTP, a wide range of patterns can be printed in parallel with nanometer length scale resolution over large areas. This technique, in particular, is expected to be useful in the fabrication of the electrical components of functional organic transistors and complementary inverter circuits [377–382].

1.2.1.7.8 **Other Methods** The bottom-up approaches intrinsically have numerous possibilities by means of the hybridization of techniques compatible with each other for fabrication of patterned SAMs. Such approaches will be combined with other methods, such as micromachining [383, 384], orthogonal self-assembly of electroactive monolayers [57, 385–387], enzymatic nanolithography [388–390], and nanofabrication using a nanopipet addressing [391].

1.2.1.8 Advanced Modification Technique of SAMs

1.2.1.8.1 **Protecting Groups for Unstable Organic Thiols** When we prepare a SAM of chemically unstable organic thiols that are easily oxidized to the disulfide molecules in the air, protecting the thiol group is important during preparation. Acetyl-protected thiols are most commonly used for organothiols, especially for aromatic and π-conjugated thiols. Tour et al. have found that acetyl-protected thiols provide an excellent method to alleviate the problem of isolating and using the oxidatively unstable thiols [392]. They noted that the use of disulfides (Ar−SS−Ar) as precursors, is impractical for the α, ω-dithiols, since successive oxidative oligomerization would generate insoluble poly(disulfides). The in situ deprotection immediately followed by the deposition of the deprotected sulfur compound onto gold surfaces under acid or alkaline condition of the solution would be better than the stepwise reactions of deprotection and deposition as the preparation method of SAMs from chemically unstable thiols. Moreover, they found that the acetyl-protected thiols can adsorb directly on the gold surface without the use of an exogenous base, although higher concentrations of the thioacetyl compounds are required than those of thiols [392].

Tour and coworkers have also found a thiocyanate to be an excellent precursor for

thiolate assemblies [393]. They described that these easily synthesized molecules can be assembled on gold surfaces directly in a variety of solvents and are an excellent complement to free thiol and protected assembly procedures. This technique is ideal for aromatic systems and α, ω-dithiol-derived molecules. Hutchison and coworkers have reported that in situ deprotection and assembly of *S*-tritylalkanethiols on gold yield monolayers, which are comparable to those prepared directly from alkanethiols [394].

1.2.1.8.2 **Modification Technique of SAMs of Dithiols** The generation of organic surfaces terminated by specific functional groups is significantly important for the application of SAMs. The most straightforward approach for obtaining such a SAM surface terminated by free thiol groups would be the use of alkanedithiols, $HS-(CH_2)_n-SH$. However, it has been shown that this straightforward approach leads to the formation of disordered, ill-defined alkanethiolate adlayers, with only a small number of free $-SH$ groups at the surface of the SAM.

Wöll and coworkers demonstrated that high-quality organothiolate adlayers exhibiting a SH-terminated surface could be prepared using dithiols where one of the thiol groups was protected by a thioester group [395]. After formation of the organothiolate adlayers, the protecting groups can be removed by immersion into a NaOH solution.

1.2.1.9 **Rigid SAMs**

1.2.1.9.1 **BCO and Adamantane SAMs** Chemical structures are among the trademarks of our profession, as surely as chemical flasks, beakers, and distillation columns [396]. Therefore, it is useful to see the chemical structures in terms of flexibility or rigidity, in particular, for molecular design of the backbone of the component molecules of SAMs. Analogously, we are able to divide SAMs into two classes of flexible SAMs and rigid SAMs. Cage molecules, such as BCO and adamantane, are two typical examples of rigid hydrocarbon molecules [397–401]. We can adopt their structures into the backbone units of component molecules of SAMs, just like alkane chains in alkanethiol-based SAMs. This strategy was already described in Sect. 1.2.1.4.6 using BCO-based SAMs [255]. Fujihira and coworkers also demonstrated that a stable adamantane-based SAM was formed successfully on a gold (111) surface [402]. Recently, Weiss and coworkers have also examined the property of a SAM using an adamantanethiol derivative [403]. The structural difference between the two adamantane-based components of the SAMs is the presence or the absence of a methylene spacer connecting between a rigid adamantane unit and a thiol head group. Schreiber described that such an extra methylene spacer plays a critical role for removing the steric hindrance in the SAMs [48]. Therefore, such a spacer is called *a geometrical buffer* [403].

The most important characteristics of these cage hydrocarbons are their higher boiling points than those of single alkane chains with similar molecular lengths. The difference can be interpreted by higher van der Waals molecule–molecule interactions of the cage hydrocarbons than those of the linear single alkane chains [402, 403]. In other words, stable SAMs could be formed from disulfides with these cage hydrocarbon units in spite of their short molecular lengths. In addition, when these spherical cage components formed

SAMs on a gold (111) surface, the grain boundaries observed in the linear alkane-based SAMs were not observed. The result was rationalized by the spherical shape of the cage backbones, which do not require the molecular axes to be tilted in the SAMs [402]. In consequence of the absence of the tilt, only single molecular defects instead of the defects due to the grain boundaries were seen in the SAMs [404]. The short heights allow us to use these organosulfur compounds for formation of SAM matrices, in which other thiol molecules can be inserted into the single molecular defects as upright single molecules. The single molecular electronic and mechanical properties were measured by STM and noncontact-AFM, respectively, using such systems [270, 404–410].

As to early studies using cage compounds with thiol head groups, the readers are referred to Refs 411, 412.

1.2.1.9.2 **Cholesterol SAM** Cholesterol is another type of rigid molecule, which is present widely in biological membranes. The studies using cholesterol-based SAMs were reported by Yang et al. [5, 413, 414].

1.2.1.9.3 **Aromatic SAMs** A different type of rigid molecule is the aromatic molecule, which exhibits rich molecular chemistry. The most distinct attribute of this structure is its electrical properties due to π electrons. Many studies have been conducted using various aromatic SAMs, and thus, in this introductory account, it is impossible to take up all subjects of the aromatic SAMs studied by many researchers. Here we will describe only some aromatic SAMs of interest from the viewpoints of SAM preparation.

The most typical family of aromatic SAMs is composed of a series of oligophenylenethiols, that is, phenyl-, biphenyl-, and terpheny thiols, which were first prepared on gold as a new family of SAMs by Rubinstein and coworkers in 1993 [415]. After that, the structures of SAMs of aromatic-containing thiols on gold or silver were characterized by Tao and coworkers using IR [416] and STM [417]. The structure was also discussed using molecular dynamics simulation [418]. They revealed that such aromatic SAMs certainly exhibited a close-packed structure in a hexagonal arrangement with an overlayer of a $(\sqrt{3} \times \sqrt{3})R30^{\circ}$ with respect to the underlying gold (111) surface if the component molecule, that is aromatic thiol, has a methylene spacer connecting the thiol head group and the aromatic unit.

Early STM investigations by other groups using thiosalicylic acid as a component molecule forming a SAM were reported [419]. Studies on the kinetics and stability of aromatic SAMs have been undertaken [420, 421]. After the early successful investigations, the fabrication and characterization of structures and properties of various aromatic SAMs on gold and/or silver have been extensively investigated using a wide variety of instruments. The families of terphenyl-based SAMs have been studied by Wöll [422–425], Tokumoto and Fujihira [426–428], Zharnikov [429, 430], and Terfort [431, 432] and their coworkers.

Biphenyl-based SAMs were intensively investigated by Ulman and coworkers [433–439]. They first studied aromatic SAMs to investigate the influence of aromatic units incorporated in long alkane chains of alkanethiol-based SAMs on gold [8, 41]. These studies were followed by recent researches by Grunze and coworkers [440, 441]. Many other relevant studies have been performed

by Zharnikov and coworkers [442, 443], Wöll and coworkers [444, 445], and others [446–448]. Surface-enhanced Raman study of phenyl- and phenylmethyl-disulfides adsorbed on silver [449] were undertaken as early as 1982, and followed by the study on copper, silver, and gold [450], and the studies by Szafranski et al. [451, 452].

Nonphenyl types of aromatic SAMs are also the subjects of importance. The foresighted idea of fabricating bioaccessible interfaces of SAMs was first demonstrated in 1982 by Taniguchi and coworkers [29]. Recently, this field of bio-SAMs has been extremely well realized in biophysical chemistry and electrochemistry [101] (see also Sect. 1.2.1.12.3). Several groups have investigated pyridinethiol-based SAMs [453–455] and thiophene-based SAMs [456].

1.2.1.10 π-Conjugated SAMs

This category is defined as a structural expansion of the aromatic SAMs described above, in which some aromatics, such as phenyl and thiophenyl, are conjugated in a series, or alternately conjugated with ethynyl or acetylene units. These SAMs have been intensively investigated recently because of their potential applications in molecular electronic devices [457]. The π-conjugated SAMs have been intensively investigated by Tour [392], Sita [458–461], Otsubo [462], and Bao [463] and their coworkers.

1.2.1.11 Chemistry on SAMs

1.2.1.11.1 Click Reaction on SAMs SAMs provide ideal molecularly defined bases to study reactions in two dimensions [464]. SAMs formed from alkanethiols and aromatic thiols have well-ordered structures, and allow a wide range of functionalities to be incorporated into the monolayers [465], although the substrates for SAMs are limited to a few metals such as gold and silver. Therefore, we can perform a rich chemistry on the exposed surface of SAMs. Love et al. described that there are three general strategies for engineering the composition of the exposed surfaces [9]: (1) Synthesis of functionalized thiols for forming single-component or mixed SAMs by (co-) adsorption, (2) insertion of synthesized thiols into defect sites of preformed SAMs, and (3) modification of the structure composition of a preformed SAM.

Methods for modifying SAMs after their formation are critical for the development of surfaces that present the large, complex ligands, and molecules needed for biology and biochemistry [9]. We can see that there are a number of studies on the reactivity of SAM surfaces, for example, early intensive studies by Crooks and coworkers [466–471], and later by others [472–474]. Through these studies, we can realize that both covalent and noncovalent interactions (i.e. van der Waals interaction, hydrogen-bonding, and metal-ligand bonding) can generate new interfaces of SAMs [9]. Here we will describe the recent new modification strategy, clicking functionality onto exposed surfaces of SAMs [97].

This new strategy is the application of Sharpless "click" chemistry [475]. Collman, Devaraj, and Chidsey first applied this chemistry to the exposed surface of SAMs (Fig. 12). They demonstrated that this reaction proceeds completely at room temperature in aqueous solvent. The reaction is extremely specific with high yield, indicating that this offers a convenient method to modify well-defined electrode surfaces [97]. This reaction uses the formation of triazoles through the classic

Huisgen 1,3-dipolar cycloaddition [9, 475]. Almost simultaneously, Choi and coworkers reported the reactivity of acetylenyl-terminated SAMs on gold toward ''click'' chemistry, leading to the formation of a similar modification as described above [476]. Functionalization of SAMs on gold through cycloadditions has already been demonstrated with Diels–Alder chemistry [477]. Direct interfacial reactions of exposed functional groups are listed in [9]. Further, Devaraj et al. demonstrated this method to apply to the fabricating oligonucleotide functional SAMs [478].

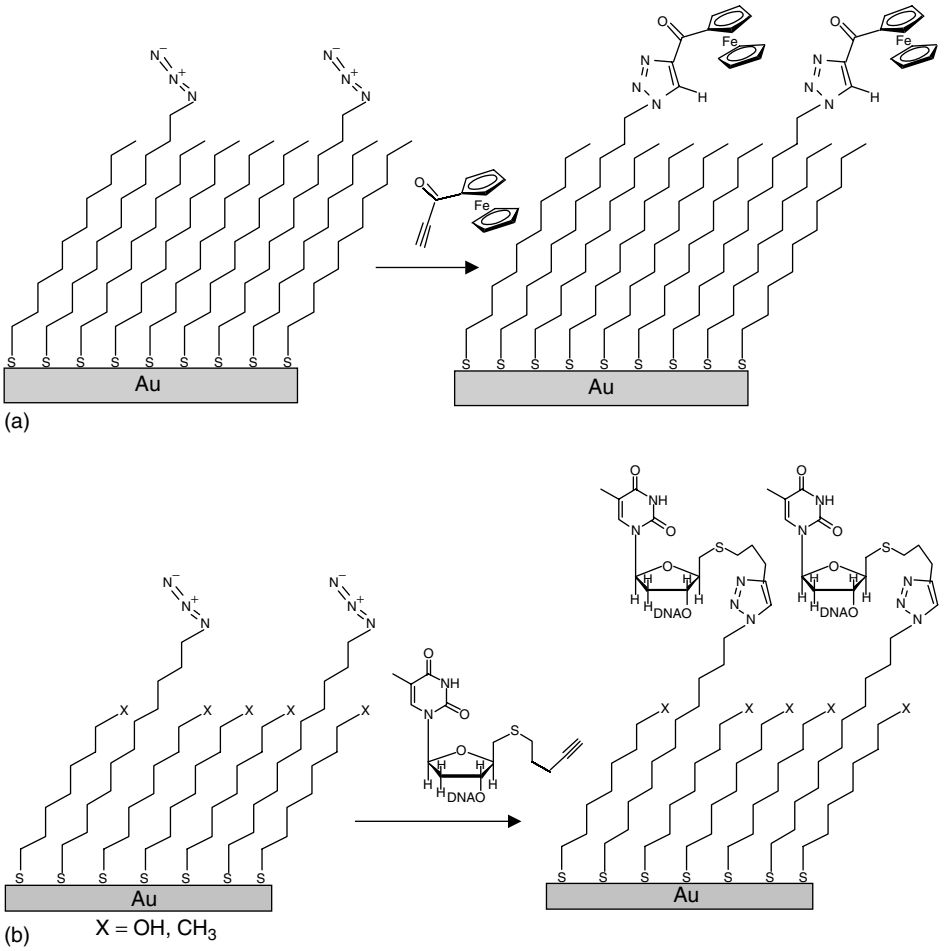


Fig. 12 (a) Depiction of a mixed SAM-modified gold electrode surface before and after ''click'' chemistry between azidoundecanethiol (inserting into the SAM) and ferrocene propynone (dissolving in aqueous ethanol solution) [97]. (b) Depiction of a similar ''click'' reaction to (a) except for the coupling of an oligonucleotide probe in aqueous dimethyl sulfoxide solution [478]. (c) Depiction of a acetylenyl-terminated SAM on gold surface before and after ''click'' chemistry between the SAM terminated with acetylenyl groups and 3'-azide-3'-deoxythymidine dissolving in aqueous ethanol solution [476].

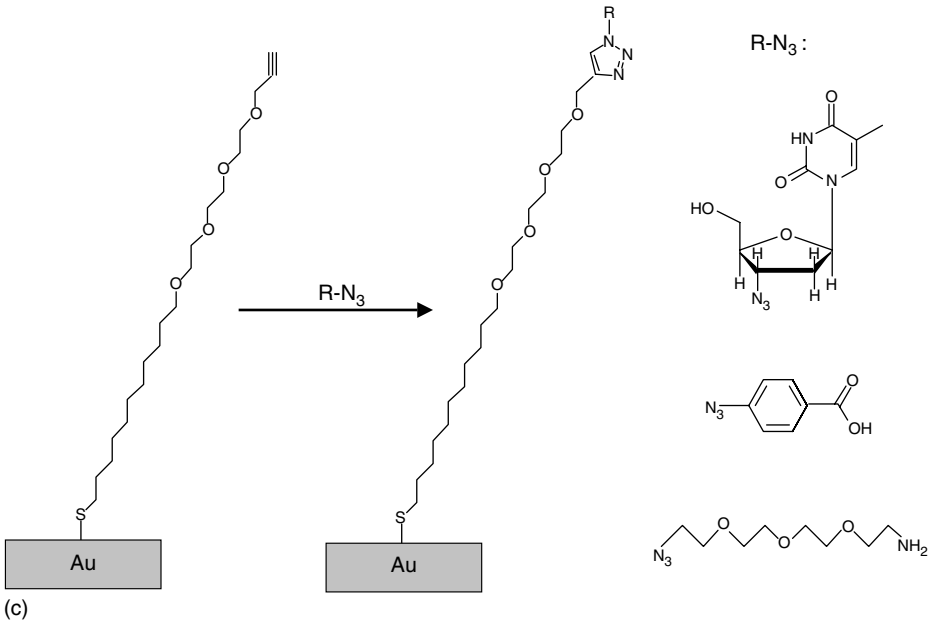


Fig. 12 (*continued*).

1.2.1.11.2 **Electrochemistry on Thiol-based SAMs Modified at Electrodes** Electrode reactions consist of the combination of elementary processes, that is, electron-transfer reaction processes between redox-active species and electrodes coupled to the preceding and/or succeeding chemical processes [479]. If these chemical processes are fast relative to the electron-transfer reactions, the chemical processes are thermodynamically reflected in the overall electrode reaction. If these chemical processes are slow, the overall electrode reactions are kinetically characterized. Therefore, the electrode reaction can express the specificity depending on the characteristics of the chemical processes spatially and temporally coupled to the electron-transfer reaction. We can take advantage of this fundamental principle of electrochemical reactions to provide a wide variety of specificity into the nanoscale electrochemistry on the exposed surface of SAMs. As a nanoscale foundation, SAMs themselves are also able to couple to electrochemical reaction processes aggressively depending on their structure [480].

The field of electrochemistry on SAMs modified at electrodes have an emergent possibility for accessing chemical and biological molecules at the nanoscale through the exposed surfaces of SAMs. In such a system, SAMs play a vital role in mediating between electrodes and abundant chemical and biological interactions or reactions generated at the surfaces. Thus, this system involves various issues of electrochemical reactions coupled to chemical and biological reaction processes [108]. Many experiments relevant to electrochemistry on SAMs ranging from the fundamentals to the applications have been reported so far. The experiments on the fundamental issues include electron-transfer model systems [88, 98, 99, 105–107, 153,

481–492], scanning electrochemical microscopy [155, 493], electrochemical STM [493–496], ionic recognition [497], and biomolecular recognition [498–506].

The experiments for the applications include electrochemical polymerization of electrically conducting polymers on the surfaces of SAMs [507–509], the expression of porphyrin functions in supramolecular systems [510–518], and structural control of electroactive molecules on SAMs [519].

Electrochemical techniques offer attractive approaches to the detection and identification of nucleic acids, a central activity of modern chemical biology [520]. High sensitivity, low costs of instrumentation, a ready capacity for miniaturization, and direct electronic readout offer strong motivations for the development of this field [520]. Recently, there has been a growing tendency toward the development of this technology.

Liu and Barton have demonstrated DNA electrochemistry by developing methodology to assemble DNA duplexes onto gold surfaces with SAM techniques and to use daunomycin as a redox reporter intercalating to DNA through covalent cross-link to guanine residues [521]. Kelley and coworkers have reported a nanoscale approach to DNA biosensing that uses oligonucleotide-functionalized gold nanoelectrode ensembles coupled to electrocatalytic system, that is, a redox cycle of $Ru(NH_3)_6^{3+}/Fe(CN)_6^{3-}$, demonstrating that this method using the redox cycle amplification is extremely useful in an ultrasensitive DNA detection system [522].

Electrochemical control is another important technique in this field [102, 103, 109]. Mrksich [102, 103, 523–526], Whitesides [527], and Yang and Kwak [528] and their coworkers have intensively demonstrated the importance of electrochemistry on SAMs through a series of interesting experimental challenges to the issue on electrochemically induced coupling reactions and releases of the attached molecules and cells.

1.2.1.11.3 **Bio-SAMs** Biomaterials are of great importance for many medical and bioanalytical applications [529]. Two families characterizing biointerfaces by using SAMs can be referred to as bio-SAMs. One is biofunctional SAMs, which may be defined as SAMs that make it possible to interact actively with biomolecules and systems, such as proteins, enzymes, oligosaacharides, oligonucleotides, receptors biomembranes, cells, tissues, and so on. Early leading studies of the biofunctional SAMs were reported by several research groups, such as Ringsdorf and Knoll and their coworkers [136, 530–532], Plant [533], and Whitesides and coworkers [534, 535]. Until now, numerous experiments have been reported for the functional SAMs, for instance, biofunctional proteins [524, 525, 528, 536–538], enzymes [116, 539], antibody [540, 541], oligonucleotides [520–522, 542–549], biomembrane [550, 551], receptors [552], and cells [526, 527, 553].

The other is the so-called biocompatible materials [104, 123] in a sense that these materials do no mischief to life and biosphere. Biocompatible SAMs are defined as SAMs that make it possible to inhibit the adsorption of nonspecific biomolecules and cells onto the surface.

Oligo(ethyleneglycol) terminated alkanethiol-based SAMs (OEG-SAMs) on gold is a well known typical example and is the prototype of the biocompatible SAMs. This type of SAMs is intriguing because we can realize that structural disorder and flexibility of organized surfaces at the molecular

level are also of extreme importance as a variety of functionalized surfaces. Therefore, we will briefly describe the course of development in the following text.

Whitesides and coworkers first prepared OEG terminated alkanethiol-based SAMs on gold and the formation was characterized by XPS, contact angles, and ellipsometry [121]. They revealed that these SAMs have substantial disorder in the OEG-containing segment. Subsequently, the studies of the adsorption of proteins at the model surfaces formed using mixed SAMs containing hydrophobic (methyl-terminated) and hydrophilic [hydroxyl-, maltose-, and hexa(ethylene glycol)-terminated] alkanethiols on gold have been performed [120, 156]. The kinetics of the adsorption of proteins on a variety of functional-terminated SAMs, containing a hexa(ethylene glycol)-terminated SAMs, were scrutinized using SPR spectroscopy, demonstrating no protein was adsorbed on the surface of hexa(ethylene glycol)-terminated alkanethiol SAM [554].

OEG-SAMs are not unique in their ability to resist the adsorption of proteins. SAMs presenting other functional groups are also protein resistant, the data of which are shown for adsorption of fibrinogen and lysozyme onto single-component SAMs [122]. Whitesides [122] and Grunze [555] and their coworkers have focused on the mechanism of protein resistance by OEG-SAMs. Whitesides and coworkers have discussed this issue by examining it on the basis of a survey of ~50 organic functional groups (X-) terminating in X-$(CH_2)_n$SH for the components of protein-resistant SAMs. They noted that several different types of X- can form the basis of surfaces that resist protein adsorption, and conformational flexibility (such as OEG groups) is also not a prerequisite for protein resistance of a surface [122]. Grunze and coworkers have systematically investigated protein resistance of oligoether-terminated SAMs on gold and silver surfaces to elucidate structural factors that determine whether a SAM will be able to resist protein adsorption [555]. They concluded that both internal and terminal hydrophilicity favor the protein resistance of an oligoether monolayer [555]. It is also suggested that the penetration of water molecules in the interior of the SAM is a necessary prerequisite for protein resistance [555].

Whitesides and other groups have adopted the feature of OEG units into the architecture of a wide variety of structured surfaces relevant to biocompatible SAMs as well as biofunctional SAMs for various targets. This strategy has been used for numerous experiments and the availability has been exemplified [102–104, 116, 117, 123, 524–527, 556–558].

Finally, carbohydrate modified SAMs can be added as a new family of bio-SAMs. Cell-surface carbohydrates play a fundamental role in important biological processes such as cell–cell recognition for adhesion or communication; the interactions of bacteria, viruses, and cancer cells with hosts; the working of the immune system; and the tissue growth and repair [559]. It is now realized that carbohydrate–protein interactions provide the key to an understanding of such biological recognition phenomena [559]. Therefore, some carbohydrate-terminated SAMs have been prepared to use a model system for studies of carbohydrate–protein interactions by several researchers [560–564]. The structure of such carbohydrate-SAMs was studied by high-resolution AFM [565].

1.2.1.12 Concluding Remarks

The idea of supported SAMs on gold and the concept of chemically modified electrodes have naturally fused to produce a new field of interdisciplinary researches as described here, which are based on chemical, physical, electrochemical, and biological fundamentals and techniques. In this section, we can realize that such new researches stem from unique characteristics of SAMs on gold. These include the convenient techniques for preparation, not simple but relatively precise identification of structures like that of molecules themselves, relatively stable forms presenting functionalized organic surfaces, and the capability of variations in the backbone structures.

The well-ordered structural feature of SAMs is available to the numerous experiments conducted so far for demonstrating various intriguing applications. We have described here only three topics, organic, electrochemical, and biological new approaches, from the aspect of chemistry on SAMs. We have omitted another important topic of the preparation and applications in SAMs useful to studies on molecular electronics (molectronics-SAM), in which the techniques of SAM preparation are prerequisite to the arrangement of the experiments.

The structural order of SAMs that we can certainly control at the molecular level, through the simple preparation principle of self-organization on substrates, is only for height direction with respect to the substrate surface and not for lateral directions over the two-dimensional surface. Several techniques described here for fabricating patterned SAMs are effective approaches to have access to the issue on the technique for the lateral control at the nanoscale. Advanced organic chemical approaches are also intriguing as a solution, in which structurally unique molecular components themselves would serve an essential role in the controllable lateral order of molecules.

Another order of SAMs, which is of a higher level, is the molecular order being present in the well-defined adlattice structures of SAMs. This order depends on the underlying surface structure of the supporting substrates as well as the bulkiness and shape of the molecular components. The availability of such a molecularly ordered arrangement remains the subject of future preparation techniques.

On the other hand, we realized that SAM surfaces presenting disordered hydrophilic property are extremely effective for fabricating practicable bio-SAMs, such as OEG-SAMs. This finding is also of importance in the fundamentals and applications of SAMs.

Finally, it is no exaggeration to say that supported SAMs can play a central role as a "mediator" connecting our experimental tools and nanoscopic phenomena. It is because the SAMs and their preparation techniques have already been providing fruitful opportunities to allow us to challenge future technology, in particular, electrochemical and biological nanotechnology.

References

1. D. L. Allara, *Biosens. Bioelectron.* **1995**, *10*, 771–783.
2. G. M. Whitesides, J. P. Mathias, C. T. Seto, *Science* **1991**, *254*, 1312–1319.
3. G. M. Whitesides, B. Grzybowski, *Science* **2002**, *295*, 2418–2421.
4. G. M. Whitesides, P. E. Laibinis, *Langmuir* **1990**, *6*, 87–96.
5. P. E. Laibinis, B. J. Palmer, S.-W. Lee et al., in *Thin Films* (Ed.: A. Ulman), Academic Press, San Diego, 1998, pp. 1–41, Vol. 24.
6. R. G. Nuzzo, D. L. Allara, *J. Am. Chem. Soc.* **1983**, *105*, 4481–4483.
7. R. G. Nuzzo, F. A. Fusco, D. L. Allara, *J. Am. Chem. Soc.* **1987**, *109*, 2358–2368.

8. A. Ulman, *Chem. Rev.* **1996**, *96*, 1533–1554.
9. J. C. Love, L. A. Estroff, J. K. Kriebel et al., *Chem. Rev.* **2005**, *105*, 1103–1169.
10. R. Colorado Jr, T. R. Lee, in *Encyclopedia of Materials: Science and Technology* (Ed.: A. Ulman), Elsevier, Oxford, 2001, 9332–9344, Vol. 10.
11. I. Haller, *J. Am. Chem. Soc.* **1978**, *100*, 8050–8055.
12. E. E. Polymeropoulos, J. Sagiv, *J. Chem. Phys.* **1978**, *69*, 1836–1847.
13. J. Sagiv, *J. Am. Chem. Soc.* **1980**, *102*, 92–98.
14. R. F. Lane, A. T. Hubbard, *J. Phys. Chem.* **1973**, *77*, 1401–1410.
15. A. T. Hubbard, *Acc. Chem. Res.* **1980**, *13*, 177–184.
16. M. P. Soriaga, A. T. Hubbard, *J. Am. Chem. Soc.* **1982**, *104*, 3937–3945.
17. F. J. Boerio, S. L. Chen, *J. Colloid Interface Sci.* **1980**, *73*, 176–185.
18. D. L. Allara, R. G. Nuzzo, *Langmuir* **1985**, *1*, 45–52.
19. D. L. Allara, R. G. Nuzzo, *Langmuir* **1985**, *1*, 52–66.
20. P. R. Moses, L. Wier, R. W. Murray, *Anal. Chem.* **1975**, *47*, 1882–1886.
21. B. F. Watkins, J. R. Behling, E. Kariv et al., *J. Am. Chem. Soc.* **1975**, *97*, 3549–3550.
22. N. R. Armstrong, A. W. C. Lin, M. Fujihira et al., *Anal. Chem.* **1976**, *48*, 741–750.
23. M. Fujihira, T. Matsue, T. Osa, *Chem. Lett.* **1976**, *5*, 875–880.
24. (a) T. Osa, M. Fujihira, *Nature* **1976**, *264*, 349–350. (b) M. Fujihira, N. Ohishi, T. Osa, *Nature* **1977**, *268*, 226–228.
25. R. W. Murray, *Acc. Chem. Res.* **1980**, *13*, 135–141.
26. J. L. Stickney, M. P. Soriaga, A. T. Hubbard, *J. Electroanal. Chem.* **1981**, *125*, 73–88.
27. M. J. Eddowes, H. A. O. Hill, *J. Chem. Soc., Chem. Commun.* **1977**, 771–772.
28. I. Taniguchi, K. Toyosawa, H. Yamaguchi et al., *J. Chem. Soc., Chem. Commun.* **1982**, 1032–1033.
29. I. Taniguchi, K. Toyosawa, H. Yamaguchi et al., *J. Electroanal. Chem.* **1982**, *140*, 187–193.
30. W. C. Bigelow, D. L. Pickett, W. A. Zisman, *J. Colloid Sci.* **1946**, *1*, 513–538.
31. W. C. Bigelow, E. Glass, W. A. Zisman, *J. Colloid Sci.* **1947**, *2*, 563–591.
32. E. G. Schafrin, W. A. Zisman, *J. Colloid Sci.* **1949**, *4*, 571–590.
33. F. Schulman, W. A. Zisman, *J. Colloid Sci.* **1952**, *7*, 465–481.
34. W. C. Bigelow, L. O. Brockway, *J. Colloid Sci.* **1956**, *11*, 60–68.
35. L. S. Bartell, R. J. Ruch, *J. Phys. Chem.* **1956**, *60*, 1231–1234.
36. W. A. Zisman, *Adv. Chem. Ser.* **1964**, *43*, 1–51.
37. L. H. Dubois, R. G. Nuzzo, *Annu. Rev. Phys. Chem.* **1992**, *43*, 437–463.
38. G. A. Somorjai, *Chemistry in Two Dimensions: Surface*, Cornell University Press, Ithaca, 1981.
39. G. A. Somorjai, *Introduction to Surface Chemistry and Catalysis*, John Wiley & Sons, New York, 1994.
40. M. A. Richard, J. Deutch, G. M. Whitesides, *J. Am. Chem. Soc.* **1978**, *100*, 6613–6625.
41. A. Ulman, *An Introduction to Ultrathin Organic Films*, Academic Press, New York, 1991.
42. G. L. Gains, *Insoluble Monolayer at Liquid-Gas Interfaces*, Interscience, New York, 1966.
43. R. Nuzzo, L. H. Dubois, D. L. Allara, *J. Am. Chem. Soc.* **1990**, *112*, 558–569.
44. C. D. Bain, G. M. Whitesides, *Angew. Chem., Int. Ed. Engl.* **1989**, *28*, 506–512.
45. C. D. Bain, G. M. Whitesides, *Science* **1988**, *240*, 62–63.
46. M. D. Porter, T. B. Bright, D. L. Allara et al., *J. Am. Chem. Soc.* **1987**, *109*, 3559–3568.
47. C. D. Bain, E. B. Troughton, Y.-T. Tao et al., *J. Am. Chem. Soc.* **1989**, *111*, 321–335.
48. F. Schreiber, *Prog. Surf. Sci.* **2000**, *65*, 151–256.
49. E. B. Troughton, C. D. Bain, G. M. Whitesides et al., *Langmuir* **1988**, *4*, 365–385.
50. C. D. Bain, G. M. Whitesides, *J. Am. Chem. Soc.* **1988**, *110*, 3665–3666.
51. C. D. Bain, G. M. Whitesides, *J. Am. Chem. Soc.* **1988**, *110*, 5897–5898.
52. C. D. Bain, J. Evall, G. M. Whitesides, *J. Am. Chem. Soc.* **1989**, *111*, 7155–7164.
53. C. D. Bain, G. M. Whitesides, *J. Am. Chem. Soc.* **1989**, *111*, 7164–7175.
54. C. D. Bain, G. M. Whitesides, *J. Am. Chem. Soc.* **1988**, *110*, 6560–6561.
55. J. P. Folkers, P. E. Laibinis, G. M. Whitesides, *Langmuir* **1992**, *8*, 1330–1341.
56. J. P. Folkers, P. E. Laibinis, G. M. Whitesides et al., *J. Phys. Chem.* **1994**, *98*, 563–571.

57. P. E. Laibinis, J. J. Hickman, M. S. Wrighton et al., *Science* **1989**, *245*, 845–847.
58. C. D. Bain, H. A. Biebuyck, G. M. Whitesides, *Langmuir* **1989**, *5*, 723–727.
59. H. A. Biebuyck, G. M. Whitesides, *Langmuir* **1993**, *9*, 1766–1770.
60. H. A. Biebuyck, C. D. Bain, G. M. Whitesides, *Langmuir* **1994**, *10*, 1825–1831.
61. P. E. Laibinis, G. M. Whitesides, D. L. Allara et al., *J. Am. Chem. Soc.* **1991**, *113*, 7152–7167.
62. P. E. Laibinis, M. A. Fox, J. P. Folkers et al., *Langmuir* **1991**, *7*, 3167–3173.
63. P. E. Laibinis, C. D. Bain, R. G. Nuzzo et al., *J. Phys. Chem.* **1995**, *99*, 7663–7676.
64. P. E. Laibinis, G. M. Whitesides, *J. Am. Chem. Soc.* **1992**, *114*, 9022–9028.
65. F. Schreiber, in *Encyclopedia of Materials: Science and Technology* (Ed.: A. Ulman), Elsevier, Oxford, 2001, pp. 9323–9332, Vol. 10.
66. F. Schreiber, *J. Phys.: Condens. Matter* **2004**, *16*, R881–R900.
67. M. Zharnikov, M. Grunze, *J. Phys.: Condens. Matter* **2001**, *13*, 11333–11365.
68. N. Sandhyarani, T. Pradeep, *Int. Rev. Phys. Chem.* **2003**, *22*, 221–262.
69. E. Delamarche, B. Michel, H. A. Biebuyck et al., *Adv. Mater.* **1996**, *8*, 719–729.
70. E. Delamarche, B. Michel, *Thin Solid Films* **1996**, *273*, 54–60.
71. G. E. Poirier, *Chem. Rev.* **1997**, *97*, 1117–1127.
72. P. Fenter, in *Thin Films* (Ed.: A. Ulman), Academic Press, San Diego, 1998, pp. 111–147, Vol. 24.
73. F. Schreiber, A. Eberhardt, T. Y. B. Leung et al., *Phys. Rev., B* **1998**, *57*, 12476–12481.
74. P. Schwartz, F. Schreiber, P. Eisenberger et al., *Surf. Sci.* **1999**, *423*, 208–224.
75. D. K. Schwartz, *Annu. Rev. Phys. Chem* **2001**, *52*, 107–137.
76. O. Dannenberger, M. Buck, M. Grunze, *J. Phys. Chem. B* **1999**, *103*, 2202–2213.
77. M. Buck, F. Eisert, J. Fisher et al., *Appl. Phys. A* **1991**, *53*, 552–556.
78. T. H. Ong, P. B. Davies, C. D. Bain, *Langmuir* **1993**, *9*, 1836–1845.
79. C. D. Bain, P. R. Greene, *Curr. Opin. Colloid Interface Sci.* **2001**, *6*, 313–320.
80. G. Hähner, Ch. Wöll, M. Buck et al., *Langmuir* **1993**, *9*, 1955–1958.
81. K. Shimazu, I. Yagi, Y. Sato et al., *Langmuir* **1992**, *8*, 1385–1387.
82. R. F. DeBono, G. D. Loucks, D. D. Manna et al., *Can. J. Chem.* **1996**, *74*, 677–688.
83. K. D. Truong, P. A. Rowntree, *Prog. Surf. Sci.* **1995**, *50*, 207–216.
84. D. N. Batchelder, S. D. Evans, T. L. Freeman et al., *J. Am. Chem. Soc.* **1994**, *116*, 1050–1053.
85. J. D. Swalen, D. L. Allara, J. D. Andrade et al., *Langmuir* **1987**, *3*, 932–950.
86. R. K. Smith, P. A. Lewis, P. S. Weiss, *Prog. Surf. Sci.* **2004**, *75*, 1–68.
87. P. M. Allen, H. A. O. Hill, N. J. Walton, *J. Electroanal. Chem.* **1984**, *178*, 69–86.
88. T. T.-T. Li, M. J. Weaver, *J. Am. Chem. Soc.* **1984**, *106*, 6107–6108.
89. Y. Xia, G. M. Whitesides, *Angew. Chem., Int. Ed. Engl.* **1998**, *37*, 550–575.
90. Y. Xia, G. M. Whitesides, in *Encyclopedia of Materials: Science and Technology* (Ed.: A. Ulman), Elsevier, Oxford, 2001, pp. 8309–8315.
91. B. Michel, A. Bernard, A. Bietsch et al., *IBM J. Res. Dev.* **2001**, *45*, 697–719.
92. L. Yan, W. T. S. Huck, G. M. Whitesides, *J. Macromol. Sci. Part C Polym. Rev.* **2004**, *44*, 175–206.
93. R. M. Crooks, A. J. Ricco, *Acc. Chem. Res.* **1998**, *31*, 219–227.
94. L. M. Goldenberg, M. R. Bryce, M. C. Petty, *J. Mater. Chem.* **1999**, *9*, 1957–1974.
95. V. Chechik, R. M. Crooks, C. J. M. Stirling, *Adv. Mater.* **2000**, *12*, 1161–1171.
96. S. Flink, F. C. J. M. van Veggel, D. N. Reinhoudt, *Adv. Mater.* **2000**, *12*, 1315–1328.
97. J. P. Collman, N. K. Devaraj, C. E. D. Chidsey, *Langmuir* **2004**, *20*, 1051–1053.
98. D. M. Adams, L. Brus, C. E. D. Chidsey et al., *J. Phys. Chem. B* **2003**, *107*, 6668–6697.
99. C. E. D. Chidsey, *Science* **1991**, *251*, 919–922.
100. L. J. C. Jeuken, *Biochim. Biophys. Acta* **2003**, *1604*, 67–76.
101. M. Fedurco, *Coord. Chem. Rev.* **2000**, *209*, 263–331.
102. M. Mrksich, *Cell. Mol. Life Sci.* **1998**, *54*, 653–662.
103. M. Mrksich, *Chem. Soc. Rev.* **2000**, *29*, 267–273.
104. D. G. Castner, B. D. Ratner, *Surf. Sci.* **2002**, *500*, 28–60.
105. A. J. Bard, H. D. Abruña, C. E. Chidsey et al., *J. Phys. Chem.* **1993**, *97*, 7147–7173.

106. H. O. Finklea, in *Electroanalytical Chemistry* (Eds.: A. J. Bard, I. Rubinstein), Marcel Dekker, New. York, 1996, pp. 109–335, Vol. 19.
107. H. O. Finklea, in *Encyclopedia of Analytical Chemistry: Applications, Theory and Instrumentation* (Ed.: R. A. Meyers), John Wiley, Chichester, 2000, pp. 10090–10115, Vol. 15.
108. S. Creager, in *Encyclopedia of Materials: Science and Technology* (Ed.: A. Ulman), Elsevier, Oxford, 2001, pp. 8299–8304, Vol. 9.
109. V. M. Mirsky, *Trends Anal. Chem.* **2002**, *21*, 439–450.
110. I. Lee, J. W. Lee, E. Greenbaum, *Phys. Rev. Lett.* **1997**, *79*, 3294–3297.
111. D. L. Allara, T. D. Dunbar, P. S. Weiss et al., *Ann. N.Y. Acad. Sci.* **1998**, *852*, 349–370.
112. B. A. Parviz, D. Ryan, G. M. Whitesides, *IEEE Trans. Adv. Package.* **2003**, *26*, 233–241.
113. B. A. Mantooth, P. S. Weiss, *Proc. IEEE* **2003**, *91*, 1785–1802.
114. J. J. Davis, *Philos. Trans. R. Soc. London, Ser. A* **2003**, *361*, 2807–2825.
115. J. G. Kushmerick, D. L. Allara, T. E. Mallouk et al., *MRS Bull.* **2004**, *29*, 396–402.
116. I. Willner, E. Katz, *Angew. Chem., Int. Ed. Engl.* **2000**, *39*, 1180–1218.
117. M. Mrksich, G. M. Whitesides, *TIBTECH* **1995**, *13*, 228–235.
118. Th. Wink, S. J. van Zuilen, A. Bult et al., *Analyst* **1997**, *122*, 43R–50R.
119. N. K. Chaki, K. Vijayamohanan, *Biosens. Bioelectron.* **2002**, *17*, 1–12.
120. K. L. Prime, G. M. Whitesides, *Science* **1991**, *252*, 1164–1167.
121. C. P. Grosdemange, E. S. Simon, K. L. Prime et al., *J. Am. Chem. Soc.* **1991**, *113*, 12–20.
122. R. S. Kane, P. Deschatelets, G. M. Whitesides, *Langmuir* **2003**, *19*, 2388–2391.
123. M. Schaeferling, S. Schiller, H. Paul et al., *Electrophoresis* **2002**, *23*, 3097–3105.
124. C. E. D. Chidsey, D. N. Loiacono, T. Sleator et al., *Surf. Sci.* **1988**, *200*, 45–66.
125. A. Putnam, B. L. Blackford, M. H. Jericho et al., *Surf. Sci.* **1989**, *217*, 276–288.
126. J. A. DeRose, T. Thundat, L. A. Nagahara et al., *Surf. Sci.* **1991**, *256*, 102–108.
127. Y. Golan, L. Margulis, I. Rubinstein, *Surf. Sci.* **1992**, *264*, 312–326.
128. J. A. DeRose, R. M. Leblanc, *Surf. Sci. Rep.* **1995**, *22*, 73–126.
129. M. Kawasaki, H. Uchiki, *Surf. Sci.* **1997**, *388*, L1121–L1125.
130. C. O'Dwyer, G. Gay, B. Viaris de Lesegno et al., *Langmuir* **2004**, *20*, 8172–8182.
131. L. E. Erickson, P. Schmuki, G. Champion, *J. Vac. Sci. Technol., B* **2000**, *18*, 3198–3201.
132. Z. Hou, N. L. Abbott, P. Stroeve, *Langmuir* **1998**, *14*, 3287–3297.
133. Z. Hou, S. Dante, N. L. Abbott et al., *Langmuir* **1999**, *15*, 3011–3014.
134. S. Löfås, B. Johonson, *J. Chem. Soc., Chem. Commun.* **1990**, 1526–1528.
135. M. Malmqvist, *Nature* **1993**, *361*, 186–187.
136. J. Spinke, M. Liley, F.-J. Schmitt et al., *J. Chem. Phys.* **1993**, *99*, 7012–7019.
137. J. Lahiri, L. Isaacs, J. Tien et al., *Anal. Chem.* **1999**, *71*, 777–790.
138. N. J. Tao, S. Boussaad, W. L. Huang et al., **1999**, *70*, 4656–4660.
139. X. Yao, F. Zhou, J. Wang et al., *J. Phys. Chem. B* **2004**, *108*, 7206–7212.
140. M. D. Ward, D. A. Buttry, *Science* **1990**, *249*, 1000–1007.
141. J. Wang, L. M. Frostman, M. D. Ward, *J. Phys. Chem.* **1992**, *96*, 5224–5228.
142. M. R. Deakin, D. A. Buttry, *Anal. Chem.* **1989**, *61*, 1147A–1154A.
143. J. J. Donohue, D. A. Buttry, *Langmuir* **1989**, *5*, 671–678.
144. H. C. De Long, D. A. Buttry, *Langmuir* **1990**, *6*, 1319–1322.
145. K. Shimazu, I. Yagi, Y. Sato et al., *J. Electroanal. Chem.* **1994**, *372*, 117–124.
146. M. D. Porter, *Anal. Chem.* **1988**, *60*, 1143A–1155A.
147. C.-J. Zhong, M. D. Porter, *J. Am. Chem. Soc.* **1994**, *116*, 11616–11617.
148. J. Shi, B. Hong, A. N. Parikh et al., *Chem. Phys. Lett.* **1995**, *246*, 90–94.
149. C. A. Widrig, C. A. Alves, M. D. Porter, *J. Am. Chem. Soc.* **1991**, *113*, 2805–2810.
150. J.-B. D. Green, C. A. McDermott, M. T. McDermott et al., in *Frontiers of Electrochemistry* (Eds.: J. Lipkoeski, P. N. Ross), Wiley-VCH, New York, 1999, pp. 249–303, Vol. 5.
151. C. A. Alves, E. L. Smith, M. D. Porter, *J. Am. Chem. Soc.* **1992**, *114*, 1222–1227.
152. C.-J. Zhong, M. D. Porter, *Anal. Chem.* **1995**, *67*, 709A–715A.
153. H. O. Finklea, S. Avery, M. Lynch et al., *Langmuir* **1987**, *3*, 409–413.
154. A. B. Steel, T. M. Herne, M. J. Tarlov, *Anal. Chem.* **1998**, *70*, 4670–4677.

155. I. Rubinstein, (Ed.), *Physical Electrochemistry*, Marcel Dekker, New York, 1995.
156. K. Prime, G. M. Whitesides, *J. Am. Chem. Soc.* **1993**, *115*, 10714–10721.
157. B. Lüssen, S. Karthäuser, H. Haselier et al., *Appl. Surf. Sci.* **2005**, *249*, 197–202.
158. H. Ron, S. Matlis, I. Rubinstein, *Langmuir* **1998**, *14*, 1116–1121.
159. H. Ron, I. Rubinstein, *J. Am. Chem. Soc.* **1998**, *120*, 13444–13452.
160. C. A. Goss, D. H. Charych, M. Majda, *Anal. Chem.* **1991**, *63*, 85–88.
161. Y. S. Obeng, A. J. Bard, *Langmuir* **1991**, *7*, 195–201.
162. S. E. Creager, L. A. Hockett, G. K. Rowe, *Langmuir* **1992**, *8*, 854–861.
163. Y.-L. Loo, R. L. Willett, K. W. Baldwin et al., *J. Am. Chem. Soc.* **2002**, *124*, 7654–7655.
164. M. Henger, P. Wagner, G. Semenza, *Surf. Sci.* **1993**, *291*, 39–46.
165. P. Wagner, M. Henger, H.-J. Güntherodt et al., *Langmuir* **1995**, *11*, 3867–3875.
166. P. Gupta, K. Loos, A. Korniakov et al., *Angew. Chem., Int. Ed. Engl.* **2004**, *43*, 520–523.
167. P. Samorì, J. P. Rabe, *J. Phys.: Condens. Matter* **2002**, *14*, 9955–9973.
168. D. Losic, J. G. Schapter, J. J. Gooding, *Langmuir* **2001**, *17*, 3307–3316.
169. J. J. Blackstock, Z. Li, G.-Y. Jung, *J. Vac. Sci. Technol., A* **2004**, *22*, 602–605.
170. P. Samorì, J. Diebel, H. Löwe et al., *Langmuir* **1999**, *15*, 2592–2594.
171. J. Diebel, H. Löwe, P. Samorì et al., *Appl. Phys. A: Mater. Sci. Process.* **2001**, *73*, 273–279.
172. J. Mazurkiewicz, F. J. Mearns, D. Losic et al., *J. Vac. Sci. Technol., B* **2002**, *20*, 2265–2270.
173. S.-S. Wong, M. D. Porter, *J. Electroanal. Chem.* **2000**, *485*, 135–143.
174. M. J. Loiacono, E. L. Granstrom, C. D. Frisbie, *J. Phys. Chem. B* **1998**, *102*, 1679–1688.
175. I. Touzov, C. B. Gorman, *J. Phys. Chem. B* **1997**, *101*, 5263–5276.
176. J. J. Gooding, F. Mearns, W. Yang et al., *Electroanalysis* **2003**, *15*, 81–96.
177. M. Hegner, P. Wagner, G. Semenza et al., *FEBS Lett.* **1993**, *336*, 452–456.
178. P. Wagner, F. Zaugg, P. Kernen et al., *J. Vac. Sci. Technol., B* **1996**, *14*, 1466–1471.
179. M. Hegner, M. Dreier, P. Wagner et al., *J. Vac. Sci. Technol., B* **1996**, *14*, 1418–1421.
180. U. Dammer, M. Hegner, D. Anselmetti et al., *Biophys. J.* **1996**, *70*, 2437–2441.
181. P. Wagner, *FEBS Lett.* **1998**, *430*, 112–115.
182. J. J. Gooding, P. Erokhin, D. Losic et al., *Anal. Sci.* **2001**, *17*, 3–9.
183. J. J. Blackstock, Z. Li, M. R. Freeman et al., *Surf. Sci.* **2003**, *546*, 87–96.
184. R. Ragan, D. Ohlberg, J. J. Blackstock et al., *J. Phys. Chem. B* **2004**, *108*, 20187–20192.
185. P. Cacciafesta, A. D. L. Humphris, K. D. Jandt et al., *Langmuir* **2000**, *16*, 8167–8175.
186. K. Itaya, S. Sugawara, K. Sashikata et al., *J. Vac. Sci. Technol., A* **1990**, *8*, 515–519.
187. H. Honbo, S. Sugawara, K. Itaya, *Anal. Chem.* **1990**, *62*, 2424–2429.
188. T. Sawaguchi, T. Yamada, Y. Okinaka et al., *J. Phys. Chem.* **1995**, *99*, 14149–14155.
189. A. Hamelin, in *Modern Aspect of Electrochemistry* (Eds.: B. E. Conway, R. H. White, J. O. M. Bockris), Plenum, New York, 1985, pp. 1–101, Vol. 16.
190. A. Hamelin, *J. Electroanal. Chem.* **1996**, *407*, 1–11.
191. D. M. Kolb, *Prog. Surf. Sci.* **1996**, *51*, 109–173.
192. D. M. Kolb, *Angew. Chem., Int. Ed. Engl.* **2001**, *40*, 1162–1181.
193. J. Clavilier, *J. Electroanal. Chem.* **1980**, *107*, 205–209.
194. J. Clavilier, *J. Electroanal. Chem.* **1980**, *107*, 211–216.
195. A. Hamelin, A. Katayama, *J. Electroanal. Chem.* **1981**, *117*, 221–232.
196. S. Motoo, N. Furuya, *J. Electroanal. Chem.* **1984**, *172*, 339–358.
197. A. Hamelin, L. Doubova, *J. Electroanal. Chem.* **1987**, *220*, 155–160.
198. A. Hamelin, S. Morin, J. Richer et al., *J. Electroanal. Chem.* **1990**, *285*, 249–262.
199. O. S. Nakagawa, S. Ashok, C. W. Sheen et al., *Jpn. J. Appl. Phys.* **1991**, *30*, 3759–3762.
200. C. W. Sheen, J.-X. Shi, J. Märtensson et al., *J. Am. Chem. Soc.* **1992**, *114*, 1514–1515.
201. R. C. Tiberio, H. G. Craighead, M. Lercel et al., *Appl. Phys. Lett.* **1993**, *62*, 476–478.
202. K. Adlkofer, W. Eck, M. Grunze et al., *J. Phys. Chem. B* **2003**, *107*, 587–591.
203. K. Adlkofer, M. Tanaka, *Langmuir* **2001**, *17*, 4267–4273.
204. D. E. Weisshaar, B. D. Lamp, M. D. Porter, *J. Am. Chem. Soc.* **1992**, *114*, 5860–5862.
205. C. A. Widrig, C. Chung, M. D. Porter, *J. Electroanal. Chem.* **1991**, *310*, 335–359.

206. R. Lösch, M. Stratmann, H. Viefhaus, *Electrochim. Acta* **1994**, *39*, 1215–1221.
207. M. Rohwerder, K. de Weldige, M. Stratmann, *J. Solid State Electrochem.* **1998**, *2*, 88–93.
208. F. Ma, R. B. Lennox, *Langmuir* **2000**, *16*, 6188–6190.
209. T. Sumi, K. Uosaki, *J. Phys. Chem. B* **2004**, *108*, 6422–6428.
210. C.-J. Zhong, N. T. Woods, G. B. Dawson et al., *Electrochem. Commun.* **1999**, *1*, 17–21.
211. M. C. Atiya, D. Mandler, *J. Electroanal. Chem.* **2003**, *550–551*, 267–276.
212. L. Cai, Y. Yao, J. Yang et al., *Chem. Mater.* **2002**, *14*, 2905–2909.
213. L. Cheng, J. Yang, Y. Yao et al., *Langmuir* **2004**, *20*, 1335–1341.
214. G. A. Orlowski, S. Chowdhury, Y.-T. Long et al., *Chem. Commun.* **2005**, 1330–1332.
215. P. Krysinski, R. V. Chamberlain II, M. Majda, *Langmuir* **1994**, *10*, 4286–4294.
216. J. Lukkari, M. Meretoja, I. Kartio et al., *Langmuir* **1999**, *15*, 3529–3537.
217. C.-C. Hsueh, M.-T. Lee, M. S. Freund et al., *Angew. Chem., Int. Ed. Engl.* **2000**, *39*, 1228–1230.
218. M.-T. Lee, C.-C. Hsueh, M. S. Freund et al., *Langmuir* **2003**, *19*, 5246–5253.
219. J. Liu, A. E. Kaifer, *Isr. J. Chem.* **1997**, *37*, 235–239.
220. D. Yan, J. A. Saunders, G. K. Jennings, *Langmuir* **2000**, *16*, 7562–7565.
221. D. Yan, J. A. Saunders, G. K. Jennings, *Langmuir* **2002**, *18*, 10202–10212.
222. D. Yan, J. L. Jordan, V. Burapatana et al., *Langmuir* **2003**, *19*, 3357–3364.
223. D. Yan, J. A. Saunders, G. K. Jennings, *Langmuir* **2003**, *19*, 9290–9296.
224. L. Patrone, S. Palacin, J.-P. Bourgoin et al., *Langmuir* **2004**, *20*, 11577–11582.
225. R. D. Weinstein, D. Yan, G. K. Jennings, *Ind. Eng. Chem. Res.* **2001**, *40*, 2046–2053.
226. D. Yan, G. K. Jennings, R. D. Weinstein, *Ind. Eng. Chem. Res.* **2002**, *41*, 4528–4533.
227. C. E. D. Chidsey, G.-Y. Liu, P. Rowntree et al., *J. Chem. Phys.* **1989**, *91*, 4421–4423.
228. N. Camillone III, C. E. D. Chidsey, G.-y. Liu et al., *J. Chem. Phys.* **1991**, *94*, 8493–8502.
229. L. Strong, G. M. Whitesides, *Langmuir* **1988**, *4*, 546–558.
230. L. H. Dubois, B. R. Zegarski, R. G. Nuzzo, *J. Electron Spectrosc. Relat. Phenom.* **1990**, *54–55*, 1143–1152.
231. R. G. Nuzzo, E. M. Korenic, L. H. Dubois, *J. Chem. Phys.* **1990**, *93*, 767–773.
232. N. Camillone III, C. E. D. Chidsey, G.-y. Liu et al., *J. Chem. Phys.* **1993**, *98*, 3503–3511.
233. P. Fenter, P. Eisenberger, K. S. Liang, *Phys. Rev. Lett.* **1993**, *70*, 2447–2450.
234. D. Anselmetti, A. Baratoff, H.-J. Güntherodt et al., *Europhys. Lett.* **1994**, *27*, 365–370.
235. E. Delamarche, B. Michel, Ch. Gerber et al., *Langmuir* **1994**, *10*, 2869–2871.
236. J. P. Bucher, L. Santesson, K. Kern, *Appl. Phys. A* **1994**, *59*, 135–138.
237. G. E. Poirier, M. J. Tarlov, *Langmuir* **1994**, *10*, 2853–2856.
238. M. S. Yeganeh, S. M. Dougal, R. S. Polizzotti et al., *Phys. Rev. Lett.* **1995**, *74*, 1811–1814.
239. L. H. Dubois, B. R. Zegarski, R. G. Nuzzo, *Proc. Natl. Acad. Sci. U.S.A.* **1987**, *84*, 4739–4742.
240. L. H. Dubois, B. R. Zegarski, R. G. Nuzzo, *J. Am. Chem. Soc.* **1990**, *112*, 570–579.
241. C. E. D. Chidsey, D. N. Loiacono, *Langmuir* **1990**, *6*, 682–691.
242. O. Dannenberger, K. Weiss, H.-J. Himmel et al., *Thin Solid Films* **1997**, *307*, 183–191.
243. L. H. Dubois, B. R. Zegarski, R. G. Nuzzo, *J. Chem. Phys.* **1993**, *98*, 678–688.
244. N. Camillone III, C. E. D. Chidsey, P. Eisenberger et al., *J. Chem. Phys.* **1993**, *99*, 744–747.
245. F. Bensebaa, T. H. Ellis, A. Badia et al., *J. Vac. Sci. Technol., A* **1995**, *13*, 1331–1336.
246. S. D. Evans, A. Ulman, *Chem. Phys. Lett.* **1990**, *170*, 462–466.
247. M. Fujihira, *Annu. Rev. Mater. Sci.* **1999**, *29*, 353–380.
248. H. Sellers, A. Ulman, Y. Shnidman et al., *J. Am. Chem. Soc.* **1993**, *115*, 9389–9401.
249. K. Edinger, A. Gölzhäuser, K. Demota et al., *Langmuir* **1993**, *9*, 4–8.
250. L. Häussling, B. Michel, H. Ringsdorf et al., *Angew. Chem., Int. Ed. Engl.* **1991**, *30*, 569–572.
251. C. Schönenberger, J. Jorritsma, L. A. M. S. Huethorest et al., *J. Phys. Chem.* **1995**, *99*, 3259–3271.
252. C. A. McDermott, M. T. McDermott, J.-B. Green et al., *J. Phys. Chem.* **1995**, *99*, 13257–13267.
253. S. D. Evans, E. Urankar, A. Ulman et al., *J. Am. Chem. Soc.* **1991**, *113*, 4121–4131.

254. S. D. Evans, K. E. Goppert-Berarducci, E. Urankar et al., *Langmuir* **1991**, *7*, 2700–2709.
255. S. Fujii, U. Akiba, M. Fujihira, *Chem. Commun.* **2001**, 1688–1689.
256. R. S. Clegg, J. E. Hutchison, *Langmuir* **1996**, *12*, 5239–5243.
257. R. S. Clegg, J. E. Hutchison, *J. Am. Chem. Soc.* **1999**, *121*, 5319–5327.
258. R. K. Smith, S. M. Reed, P. A. Lewis et al., *J. Phys. Chem. B* **2001**, *105*, 1119–1122.
259. T. Pradeep, N. Sandhyarani, *Pure Appl. Chem.* **2002**, *74*, 1593–1607.
260. A. Badia, L. Demers, L. Dickinson et al., *J. Am. Chem. Soc.* **1997**, *119*, 11104–11105.
261. J. B. Schlenoff, M. Li, H. Ly, *J. Am. Chem. Soc.* **1995**, *117*, 12528–12536.
262. R. C. Thomas, L. Sun, R. M. Crooks, *Langmuir* **1991**, *7*, 620–622.
263. O. Chailapakul, L. Sun, C. Xu et al., *J. Am. Chem. Soc.* **1993**, *115*, 12459–12467.
264. D. S. Karpovich, H. M. Schessler, G. J. Blanchard, in *Thin Films* (Ed.: A. Ulman), Academic Press, San Diego, 1998, pp. 43–80, Vol. 24.
265. D. S. Karpovich, G. J. Blanchard, *Langmuir* **1994**, *10*, 3315–3322.
266. H. M. Schessler, D. S. Karpovich, G. J. Blanchard, *J. Am. Chem. Soc.* **1996**, *118*, 9645–9651.
267. D. J. Lavrich, S. M. Wetterer, S. L. Bernasek et al., *J. Phys. Chem. B* **1998**, *102*, 3456–3465.
268. S. M. Wetterer, D. J. Lavrich, T. Cummings et al., *J. Phys. Chem. B* **1998**, *102*, 9266–9275.
269. Y.-S. Shon, T. R. Lee, *J. Phys. Chem. B* **2000**, *104*, 8192–8200.
270. M. Suzuki, S. Fujii, S. Wakamatsu et al., *Nanotechnology* **2004**, *15*, S150–S153.
271. M. Himmelhaus, F. Eisert, M. Buck et al., *J. Phys. Chem. B* **2000**, *104*, 576–584.
272. K. A. Peterlinz, R. Georgiadis, *Langmuir* **1996**, *12*, 4731–4740.
273. G. E. Poirier, E. D. Pylant, *Science* **1996**, *272*, 1145–1148.
274. M. Godin, P. J. Williams, V. Tabard-Cossa et al., *Langmuir* **2004**, *20*, 7090–7096.
275. M. Fujihira, Y. Morita, *J. Vac. Sci. Technol., B* **1994**, *12*, 1609–1613.
276. K. E. Drexler, *Engines of Creation: The Coming Era of Nanotechnology*, John Brockman Associates, New York, 1986.
277. G. M. Whitesides, J. C. Love, *Sci. Am.* **2001**, *285*, 38–47.
278. J. D. Watson, A. Berry, *DNA: The Secret of Life*, Alfred A. Knopf, a division of Random House, New York, 2003.
279. A. M. Lesk, *Introduction to Protein Science*, Oxford University Press, Oxford, 2004.
280. Y. Xia, J. A. Rogers, K. E. Paul et al., *Chem. Rev.* **1999**, *99*, 1823–1848.
281. S. J. Stranick, A. N. Parikh, Y.-T. Tao et al., *J. Phys. Chem.* **1994**, *98*, 7636–7646.
282. S. J. Stranick, S. V. Atre, A. N. Parikh et al., *Nanotechnology* **1996**, *7*, 438–442.
283. T. Ishida, W. Mizutani, H. Tokumoto et al., *Appl. Surf. Sci.* **1998**, *130–132*, 786–791.
284. T. Ishida, S.-I. Yamamoto, W. Mizutani et al., *Langmuir* **1997**, *13*, 3261–3265.
285. W. Mizutani, T. Ishida, S.-I. Yamamoto et al., *Appl. Phys. A* **1998**, *66*, S1257–S1260.
286. W. A. Hayes, H. Kim, X. Yue et al., *Langmuir* **1997**, *13*, 2511–2518.
287. R. M. Overney, E. Meyer, J. Frommer et al., *Nature* **1992**, *359*, 133–135.
288. H. Takano, J. R. Kenseth, S.-S. Wong et al., *Chem. Rev.* **1999**, *99*, 2845–2890.
289. P. E. Laibinis, R. G. Nuzzo, G. M. Whitesides, *J. Phys. Chem.* **1992**, *96*, 5097–5105.
290. S. V. Atre, B. Liedberg, D. L. Allara, *Langmuir* **1995**, *11*, 3882–3893.
291. H. Schönherr, H. Ringsdorf, M. Jaschke et al., *Langmuir* **1996**, *12*, 3898–3904.
292. M. Fujihira, H. Monobe, H. Muramatsu et al., *Ultramicroscopy* **1995**, *57*, 176–179.
293. M. Fujihira, H. Monobe, H. Muramatsu et al., *Chem. Lett.* **1994**, *23*, 657–660.
294. H. Muramatsu, N. Chiba, T. Ataka et al., *Ultramicroscopy* **1995**, *57*, 141–146.
295. H. Muramatsu, N. Chiba, K. Homma et al., *Appl. Phys. Lett.* **1995**, *66*, 3245–3247.
296. R. C. Dunn, *Chem. Rev.* **1999**, *99*, 2891–2927.
297. S. Krämer, R. R. Fuierer, C. B. Gorman, *Chem. Rev.* **2003**, *103*, 4367–4418.
298. Y.-T. Kim, A. J. Bard, *Langmuir* **1992**, *8*, 1096–1102.
299. C. B. Ross, L. Sun, R. M. Crooks, *Langmuir* **1993**, *9*, 632–636.
300. J. K. Schoer, F. P. Zamborini, R. M. Crooks, *J. Phys. Chem.* **1996**, *100*, 11086–11091.
301. J. K. Schoer, R. M. Crooks, *Langmuir* **1997**, *13*, 2323–2332.
302. W. Mizutani, T. Ishida, H. Tokumoto, *Langmuir* **1998**, *14*, 7197–7202.

303. G.-Y. Liu, M. B. Salmeron, *Langmuir* **1994**, *10*, 367–370.
304. J. W. Zhao, K. Uosaki, *Langmuir* **2001**, *17*, 7784–7788.
305. J. W. Zhao, K. Uosaki, *Nano Lett.* **2002**, *2*, 137–140.
306. J. Chen, M. A. Reed, C. L. Asplund et al., *Appl. Phys. Lett.* **1999**, *75*, 624–626.
307. C. B. Gorman, R. L. Carroll, Y. He et al., *Langmuir* **2000**, *16*, 6312–6316.
308. S. Xu, S. Miller, P. E. Laibinis et al., *Langmuir* **1999**, *15*, 7244–7251.
309. G.-Y. Liu, S. Xu, Y. Qian, *Acc. Chem. Res.* **2000**, *33*, 457–466.
310. K. W. Mesthrige, N. A. Amro, J. C. Garno et al., *Biophys. J.* **2001**, *80*, 1891–1899.
311. G.-Y. Liu, N. A. Amro, *Proc. Natl. Acad. Sci. U.S.A.* **2002**, *99*, 5165–5170.
312. M. Liu, N. A. Amro, C. S. Chow et al., *Nano Lett.* **2002**, *2*, 863–867.
313. M. Liu, G.-Y. Liu, *Langmuir* **2005**, *21*, 1972–1978.
314. J. R. Kenseth, J. A. Harnisch, V. W. Jones et al., *Langmuir* **2001**, *17*, 4105–4112.
315. R. D. Piner, J. Zhu, F. Xu et al., *Science* **1999**, *283*, 661–663.
316. D. S. Ginger, H. Zhang, C. A. Mirkin, *Angew. Chem., Int. Ed. Engl.* **2004**, *43*, 30–45.
317. D. A. Weinberger, S. Hong, C. A. Mirkin et al., *Adv. Mater* **2000**, *12*, 1600–1603.
318. L. M. Demers, C. A. Mirkin, *Angew. Chem., Int. Ed. Engl.* **2001**, *40*, 3069–3071.
319. P. E. Sheehan, L. J. Whitman, *Phys. Rev. Lett.* **2002**, *88*, 1561041–1561044.
320. S. Rozhok, R. Piner, C. A. Mirkin, *J. Phys. Chem. B* **2003**, *107*, 751–757.
321. S. Hong, J. Zhu, C. A. Mirkin, *Science* **1999**, *286*, 523–525.
322. S. Hong, C. A. Mirkin, *Science* **2000**, *288*, 1808–1811.
323. G. Agarwal, L. A. Sowards, R. R. Naik et al., *J. Am. Chem. Soc.* **2003**, *125*, 580–583.
324. G. Agarwal, R. R. Naik, M. O. Stone, *J. Am. Chem. Soc.* **2003**, *125*, 7408–7412.
325. D. L. Wilson, R. Martin, S. Hong et al., *Proc. Natl. Acad. Sci. U.S.A.* **2001**, *98*, 13660–13664.
326. J. Hyun, S. J. Ahn, W. K. Lee et al., *Nano Lett.* **2002**, *2*, 1203–1207.
327. K.-B. Lee, S.-J. Park, C. A. Mirkin et al., *Science* **2002**, *295*, 1702–1705.
328. K.-B. Lee, J.-H. Lim, C. A. Mirkin, *J. Am. Chem. Soc.* **2003**, *125*, 5588–5589.
329. L. M. Demers, D. S. Ginger, S.-J. Park et al., *Science* **2002**, *296*, 1836–1838.
330. G. M. Whitesides, E. Ostuni, S. Takayama et al., *Annu. Rev. Biomed. Eng.* **2001**, *3*, 335–373.
331. A. Kumar, G. M. Whitesides, *Appl. Phys. Lett.* **1993**, *63*, 2002–2004.
332. A. Kumar, H. A. Biebuyck, G. M. Whitesides, *Langmuir* **1994**, *10*, 1498–1511.
333. A. Kumar, N. L. Abbott, E. Kim et al., *Acc. Chem. Res.* **1995**, *28*, 219–226.
334. Y. Xia, X.-M. Zhao, G. M. Whitesides, *Microelectron. Eng.* **1996**, *32*, 255–268.
335. Y. Xia, E. Kim, G. M. Whitesides, *J. Electrochem. Soc.* **1996**, *143*, 1070–1079.
336. Y. Xia, E. Kim, M. Mrksich et al., *Chem. Mater.* **1996**, *8*, 601–603.
337. R. J. Jackman, J. L. Wibur, G. M. Whitesides, *Science* **1995**, *269*, 664–666.
338. M. Geissler, A. Bernard, A. Bietsch et al., *J. Am. Chem. Soc.* **2000**, *122*, 6303–6304.
339. N. B. Larson, H. Biebuyck, E. Delamarche et al., *J. Am. Chem. Soc.* **1997**, *119*, 3017–3026.
340. Y. Xia, G. M. Whitesides, *Langmuir* **1997**, *13*, 2059–2067.
341. B. Michel, A. Bernard, A. Bietsch et al., *Chimia* **2002**, *56*, 527–542.
342. G. Bar, S. Rubin, A. N. Parikh et al., *Langmuir* **1997**, *13*, 373–377.
343. X.-M. Li, V. Paraschiv, J. Huskens et al., *J. Am. Chem. Soc.* **2003**, *125*, 4279–4284.
344. R. Singhvi, A. Kumar, G. P. Lopez et al., *Science* **1994**, *264*, 696–698.
345. R. S. Kane, S. Takayama, E. Ostuni et al., *Biomaterials* **1999**, *20*, 2363–2376.
346. J. Aizenberg, P. V. Braun, P. Wiltzius, *Phys. Rev. Lett.* **2000**, *84*, 2997–3000.
347. J. Tien, A. Terfort, G. M. Whitesides, *Langmuir* **1997**, *13*, 5349–5355.
348. A. Winkleman, B. D. Gates, L. S. McCarty et al., *Adv. Mater.* **2005**, *17*, 1507–1511.
349. A. Rosa-Zeiser, E. Weilandt, S. Hild et al., *Meas. Sci. Technol.* **1997**, *8*, 1333–1338.
350. T. Miyatani, M. Horii, A. Rosa, M. Fujihira, O. Marti, *Appl. Phys. Lett.* **1997**, *71*, 2632–2634.
351. T. Miyatani, S. Okamoto, A. Rosa et al., *Appl. Phys. A* **1998**, *66*, S349–S352.
352. C. D. Frisbie, L. F. Rozsnyai, A. Noy et al., *Science* **1994**, *265*, 2071–2074.
353. T. Arai, M. Fujihira, *J. Electroanal. Chem.* **1994**, *374*, 269–273.

354. T. Arai, D. Aoki, Y. Okabe et al., *Thin Solid Films* **1996**, *273*, 322–326.
355. T. Arai, M. Fujihira, *J. Vac. Sci. Technol., B* **1996**, *14*, 1378–1382.
356. Y. Oabe, U. Akiba, M. Fujihira, *Appl. Surf. Sci.* **2000**, *157*, 398–404.
357. Y. Okabe, M. Furugori, Y. Tani et al., *Ultramicroscopy* **2000**, *82*, 203–212.
358. M. Fujihira, M. Furugori, U. Akiba et al., *Ultramicroscopy* **2001**, *86*, 75–83.
359. K. Akimoto, F. Sato, T. Morikawa et al., *Jpn. J. Appl. Phys.* **2004**, *43*, 4492–4498.
360. F. Sato, H. Okui, U. Akiba et al., *Ultramicroscopy* **2003**, *97*, 303–314.
361. M. Fujihira, Y. Okabe, Y. Tani et al., *Ultramicroscopy* **2000**, *82*, 181–191.
362. S. P. Han, S. Yoda, K. J. Kwak et al., *Ultramicroscopy* **2005**, *105*, 148–154.
363. W. A. Ducker, T. J. Senden, R. M. Pashley, *Nature* **1991**, *353*, 239–241.
364. M. Fujihira, D. Aoki, Y. Okabe et al., *Chem. Lett.* **1996**, *25*, 499–500.
365. K. M. Balss, G. A. Fried, P. W. Bohn, *J. Electrochem. Soc.* **2002**, *149*, C450–C455.
366. J. D. Gerding, D. M. Willard, A. V. Orden, *J. Am. Chem. Soc.* **2005**, *127*, 1106–1107.
367. M. Zharnikov, M. Grunze, *J. Vac. Sci. Technol., B* **2002**, *20*, 1793–1807.
368. J. Huang, J. C. Hemminger, *J. Am. Chem. Soc.* **1993**, *115*, 3342–3343.
369. M. J. Tarlov, D. R. F. Burgess Jr, G. Gillen, *J. Am. Chem. Soc.* **1993**, *115*, 5305–5306.
370. J. Huang, D. A. Dahlgren, J. C. Hemminger, *Langmuir* **1994**, *10*, 626–628.
371. M. Lewis, M. Tarlov, K. Carron, *J. Am. Chem. Soc.* **1995**, *117*, 9574–9575.
372. S. Sun, K. S. L. Chong, G. J. Leggett, *J. Am. Chem. Soc.* **2002**, *124*, 2414–2415.
373. N. J. Brewer, R. E. Rawsterne, S. Kothari et al., *J. Am. Chem. Soc.* **2001**, *123*, 4089–4090.
374. E. W. Wollman, D. Kang, C. D. Frisbie et al., *J. Am. Chem. Soc.* **1994**, *116*, 4395–4404.
375. L. F. Rozsnyai, M. S. Wrighton, *Langmuir* **1995**, *11*, 3913–3920.
376. K. Lee, F. Pan, G. T. Caroll et al., *Langmuir* **2004**, *20*, 1812–1818.
377. Y.-L. Loo, R. L. Willett, K. W. Baldwin et al., *Appl. Phys. Lett.* **2002**, *81*, 562–564.
378. C. Kim, M. Shtein, S. R. Forrest, *Appl. Phys. Lett.* **2002**, *80*, 4051–4053.
379. Y.-L. Loo, J. W. P. Hsu, R. L. Willett et al., *J. Vac. Sci. Technol., B* **2002**, *20*, 2853–2856.
380. Y.-L. Loo, R. D. V. Lang, J. A. Rogers et al., *Nano Lett.* **2003**, *3*, 913–917.
381. J. Zaumseil, M. A. Meitl, J. W. P. Hsu et al., *Nano Lett.* **2003**, *3*, 1223–1227.
382. E. Menard, L. Bilhaut, J. Zaumseil et al., *Langmuir* **2004**, *20*, 6871–6878.
383. N. L. Abbott, J. P. Folkers, G. M. Whitesides, *Science* **1992**, *257*, 1380–1382.
384. N. L. Abbott, A. Kumar, G. M. Whitesides, *Chem. Mater.* **1994**, *6*, 596–602.
385. J. J. Hickman, D. Ofer, C. Zou et al., *J. Am. Chem. Soc.* **1991**, *113*, 1128–1132.
386. J. J. Hickman, P. E. Laibinis, D. I. Auerbach et al., *Langmuir* **1992**, *8*, 357–359.
387. T. J. Gardner, C. D. Frisbie, M. S. Wrighton, *J. Am. Chem. Soc.* **1995**, *117*, 6927–6933.
388. C.-H. Jang, B. D. Stevens, P. R. Carlier et al., *J. Am. Chem. Soc.* **2002**, *124*, 12114–12115.
389. C.-H. Jang, B. D. Stevens, R. Phillips et al., *Nano Lett.* **2003**, *3*, 691–694.
390. J. Hyun, J. Kim, S. L. Craig et al., *J. Am. Chem. Soc.* **2004**, *126*, 4770–4771.
391. A. Bruckbauer, D. Zhou, D.-J. Kang et al., *J. Am. Chem. Soc.* **2004**, *126*, 6508–6509.
392. J. M. Tour, L. Jones II, D. L. Pearson et al., *J. Am. Chem. Soc.* **1995**, *117*, 9529–9534.
393. J. W. Ciszek, M. P. Stewart, J. M. Tour, *J. Am. Chem. Soc.* **2004**, *126*, 13172–13173.
394. C. E. Inman, S. M. Reed, J. E. Hutchison, *Langmuir* **2004**, *20*, 9144–9150.
395. A. Niklewski, W. Azzam, T. Strunskus et al., *Langmuir* **2004**, *20*, 8620–8624.
396. R. Hoffman, P. Laszlo, *Angew. Chem., Int. Ed. Engl.* **1991**, *30*, 1–16.
397. G. Olah, in *Cage Hydrocarbons* (Eds.: G. Olah, P. von Schleyer), Wiley, New York, 1990, pp. 1–45.
398. J. S. Moor, *Nature* **1993**, *361*, 118–119.
399. P. F. Schwab, M. D. Levin, J. Michl, *Chem. Rev.* **1999**, *99*, 1863–1933.
400. R. C. Merkle, *Nanotechnology* **2000**, *11*, 89–99.
401. J. E. Dahl, S. G. Liu, R. M. K. Carlson, *Science* **2003**, *299*, 96–99.
402. S. Fujii, U. Akiba, M. Fujihira, *J. Am. Chem. Soc.* **2002**, *124*, 13629–13635.
403. A. A. Dameron, L. F. Charles, P. S. Weiss, *J. Am. Chem. Soc.* **2005**, *127*, 8697–8704.
404. S. Wakamatsu, S. Fujii, U. Akiba et al., *Ultramicroscopy* **2003**, *97*, 19–26.
405. S. Wakamatsu, S. Fujii, U. Akiba et al., *Nanotechnology* **2003**, *14*, 258–263.
406. S. Fujii, U. Akiba, M. Fujihira, *Appl. Surf. Sci.* **2003**, *210*, 79–83.

407. S. Wakamatsu, S. Fujii, U. Akiba et al., *Nanotechnology* **2004**, *15*, S137–S141.
408. S. Fujii, U. Akiba, M. Fujihira, *Nanotechnology* **2004**, *15*, S19–S23.
409. B. Bat-Uul, S. Fujii, T. Shiokawa et al., *Nanotechnology* **2004**, *15*, 710–715.
410. K. Ishizuka, M. Suzuki, S. Fujii et al., *Jpn. J. Appl. Phys.* **2005**, *44*, 5382–5385.
411. Y.-T. Kim, R. L. McCarley, A. J. Bard, *J. Phys. Chem.* **1992**, *96*, 7416–7421.
412. Y. S. Obeng, M. E. Laing, A. C. Friedli et al., *J. Am. Chem. Soc.* **1992**, *114*, 9943–9952.
413. Z. P. Yang, I. Engquist, J.-M. Kauffmann et al., *Langmuir* **1996**, *12*, 1704–1707.
414. Z. Yang, I. Engquist, M. Wirde et al., *Langmuir* **1997**, *13*, 3210–3218.
415. E. Sabatani, J. Cohen-Boulakia, M. Bruening et al., *Langmuir* **1993**, *9*, 2974–2981.
416. S.-C. Chang, I. Chao, Y.-T. Tao, *J. Am. Chem. Soc.* **1994**, *116*, 6792–6805.
417. Y.-T. Tao, C.-C. Wu, J.-Y. Eu et al., *Langmuir* **1997**, *13*, 4018–4023.
418. T.-W. Li, I. Chao, Y.-T. Tao, *J. Phys. Chem. B* **1998**, *102*, 2935–2946.
419. A. H. Schäfer, C. Seidel, L. Chi et al., *Adv. Mater.* **1998**, *10*, 839–842.
420. K. Bandyopadhyay, M. Sastry, V. Paul et al., *Langmuir* **1997**, *13*, 866–869.
421. R. R. Kolega, J. B. Schlenoff, *Langmuir* **1998**, *14*, 5469–5478.
422. H.-J. Himmel, A. Terfort, C. Wöll, *J. Am. Chem. Soc.* **1998**, *120*, 12069–12074.
423. C. Fuxen, W. Azzam, R. Arnold et al., *Langmuir* **2001**, *17*, 3689–3695.
424. R. Arnold, W. Azzam, A. Terfort et al., *Langmuir* **2002**, *18*, 3980–3992.
425. W. Azzam, B. I. Wehner, R. A. Fischer et al., *Langmuir* **2002**, *18*, 7766–7769.
426. T. Ishida, W. Mizutani, U. Akiba et al., *J. Phys. Chem. B* **1999**, *103*, 1686–1690.
427. T. Ishida, N. Choi, W. Mizutani et al., *Langmuir* **1999**, *15*, 6799–6806.
428. T. Ishida, W. Mizutani, N. Choi et al., *J. Phys. Chem. B* **2000**, *104*, 11680–11688.
429. S. Frey, V. Stadler, K. Heister et al., *Langmuir* **2001**, *17*, 2408–2415.
430. Y. Tai, A. Shaporenko, W. Eck et al., *Langmuir* **2004**, *20*, 7166–7170.
431. A. Shaporenko, M. Brunnbauer, A. Terfort et al., *J. Phys. Chem. B* **2004**, *108*, 14462–14469.
432. J. Müller, M. Brunnbauer, M. Schmidt et al., *Synthesis* **2005**, 998–1004.
433. J. F. Kang, S. Liao, R. Jordan et al., *J. Am. Chem. Soc.* **1998**, *120*, 9662–9667.
434. J. F. Kang, A. Ulman, S. Liao et al., *Langmuir* **1999**, *15*, 2095–2098.
435. S. Liao, Y. Shnidman, A. Ulman, *J. Am. Chem. Soc.* **2000**, *122*, 3688–3694.
436. T. Y. B. Leung, P. Schwartz, G. Scole et al., *Surf. Sci.* **2000**, *458*, 34–52.
437. J. F. Kang, A. Ulman, S. Liao et al., *Langmuir* **2001**, *17*, 95–106.
438. A. Ulman, *Acc. Chem. Res.* **2001**, *34*, 855–863.
439. T. L. Brower, M. Cook, A. Ulman, *J. Phys. Chem. B* **2003**, *107*, 11721–11725.
440. F. Buckel, F. Effenberger, C. Yan et al., *Adv. Mater.* **2000**, *12*, 901–905.
441. K. Heister, S. Frey, A. Ulman et al., *Langmuir* **2004**, *20*, 1222–1227.
442. K. Heister, M. Zharnikov, M. Grunze et al., *J. Phys. Chem. B* **2001**, *105*, 4058–4061.
443. K. Heister, H.-T. Rong, M. Buck et al., *J. Phys. Chem. B* **2001**, *105*, 6888–6894.
444. H.-T. Rong, S. Frey, Y.-J. Yang et al., *Langmuir* **2001**, *17*, 1582–1593.
445. W. Azzam, P. Cyganik, G. Witte et al., *Langmuir* **2003**, *19*, 8262–8270.
446. A. Nakasa, U. Akiba, M. Fujihira, *Appl. Surf. Sci.* **2000**, *157*, 326–331.
447. P. Cyganik, M. Buck, *J. Am. Chem. Soc.* **2004**, *126*, 5960–5961.
448. G. Yang, G.-y. Liu, *J. Phys. Chem. B* **2003**, *107*, 8746–8759.
449. C. J. Sandroff, D. R. Herschbach, *J. Phys. Chem.* **1982**, *86*, 3277–3279.
450. K. T. Carron, L. G. Hurley, *J. Phys. Chem.* **1991**, *95*, 9979–9984.
451. C. A. Szafranski, W. Tanner, P. E. Laibinis et al., *Langmuir* **1998**, *14*, 3570–3579.
452. C. A. Szafranski, W. Tanner, P. E. Laibinis et al., *Langmuir* **1998**, *14*, 3580–3589.
453. T. Sawaguchi, F. Mizutani, I. Taniguchi, *Langmuir* **1998**, *14*, 3565–3569.
454. L.-J. Wan, Y. Hara, H. Noda et al., *J. Phys. Chem. B* **1998**, *102*, 5943–5946.
455. L.-J. Wan, M. Terashima, H. Noda et al., *J. Phys. Chem. B* **2000**, *104*, 3563–3569.
456. J. Noh, E. Ito, K. Nakajima et al., *J. Phys. Chem. B* **2002**, *106*, 7139–7141.
457. J. M. Tour, *Acc. Chem. Res.* **2000**, *33*, 791–804.
458. A.-A. Dhirani, R. W. Zehner, R. P. Hsung et al., *J. Am. Chem. Soc.* **1996**, *118*, 3319–3320.

459. A.-A. Dhirani, P.-H. Lin, P. Guyot-Sionnest et al., *J. Chem. Phys.* **1997**, *106*, 5249–5253.
460. R. W. Zehner, B. F. Parsons, R. P. Hsung et al., *Langmuir* **1999**, *15*, 1121–1127.
461. G. Yang, Y. Qian, C. Engtrakul et al., *J. Phys. Chem. B* **2000**, *104*, 9059–9062.
462. T. Otsubo, Y. Aso, K. Takimiya, *J. Mater. Chem.* **2002**, *12*, 2565–2575.
463. B. de Boer, H. Meng, D. F. Perepichka et al., *Langmuir* **2003**, *19*, 4272–4284.
464. T. P. Sullivan, W. T. S. Huck, *Eur. J. Org. Chem.* **2003**, 17–29.
465. C. D. Bain, S. D. Evans, *Chem. Br.* **1995**, *31*, 46–48.
466. L. Sun, B. Johnson, T. Wade et al., *J. Phys. Chem.* **1990**, *94*, 8869–8871.
467. L. Sun, R. C. Thomas, R. M. Crooks, *J. Am. Chem. Soc.* **1991**, *113*, 8550–8552.
468. L. Sun, L. J. Kepley, R. M. Crooks, *Langmuir* **1992**, *8*, 2101–2103.
469. L. Sun, R. M. Crooks, A. J. Ricco, *Langmuir* **1993**, *9*, 1775–1780.
470. M. Wells, D. L. Dermody, H. C. Yang et al., *Langmuir* **1996**, *12*, 1989–1996.
471. H. C. Yang, D. L. Dermody, C. Xu et al., *Langmuir* **1996**, *12*, 726–735.
472. H.-J. Himmel, K. Weiss, B. Jäger et al., *Langmuir* **1997**, *13*, 4943–4947.
473. L. Yan, C. Marzolin, A. Terfort et al., *Langmuir* **1997**, *13*, 6704–6712.
474. H. H. J. Persson, W. R. Caseri, U. W. Suter, *Langmuir* **2001**, *17*, 3643–3650.
475. H. C. Kolb, M. G. Finn, K. B. Sharpless, *Angew. Chem., Int. Ed. Engl.* **2001**, *40*, 2004–2021.
476. J. K. Lee, Y. S. Chi, I. S. Choi, *Langmuir* **2004**, *20*, 3844–3847.
477. Y. Kwon, M. Mrksich, *J. Am. Chem. Soc.* **2002**, *124*, 806–812.
478. N. K. Dervaraj, G. P. Miller, W. Ebina et al., *J. Am. Chem. Soc.* **2005**, *127*, 8600–8601.
479. A. J. Bard, L. R. Faulkner, *Electrochemical Methods: Fundamentals and Applications*, Johon Wiley & Sons, New York, 1980.
480. Y.-T. Long, H.-T. Rong, M. Buck et al., *J. Electroanal. Chem.* **2002**, *524–525*, 62–67.
481. H. O. Finklea, D. D. Hanshew, *J. Electroanal. Chem.* **1993**, *347*, 327–340.
482. C. E. D. Chidsey, C. R. Bertozzi, T. M. Putvinski et al., *J. Am. Chem. Soc.* **1990**, *112*, 4301–4306.
483. C. Miller, P. Cuendet, M. Grätzel, *J. Phys. Chem.* **1991**, *95*, 877–886.
484. C. Miller, M. Grätzel, *J. Phys. Chem.* **1991**, *95*, 5225–5233.
485. T. T.-T. Li, H. Y. Liu, M. J. Weaver, *J. Am. Chem. Soc.* **1984**, *106*, 1233–1239.
486. J. F. Smalley, S. W. Feldberg, C. E. D. Chidsey et al., *J. Phys. Chem.* **1995**, *99*, 13141–13149.
487. M. T. Carter, G. K. Rowe, J. N. Richardson et al., *J. Am. Chem. Soc.* **1995**, *117*, 2896–2899.
488. H. O. Finklea, L. Liu, M. S. Ravenscroft et al., *J. Phys. Chem.* **1996**, *100*, 18852–18858.
489. S. B. Sachs, S. P. Dudek, R. P. Hsung et al., *J. Am. Chem. Soc.* **1997**, *119*, 10563–10564.
490. J. J. Sumner, S. E. Creager, *J. Am. Chem. Soc.* **2000**, *122*, 11914–11920.
491. T. Morita, S. Kimura, *J. Am. Chem. Soc.* **2003**, *125*, 8732–8733.
492. J. Zhang, Q. Chi, T. Albrecht et al., *Electrochim. Acta* **2005**, *50*, 3143–3159.
493. A. J. Bard, F.-R. F. Fan, M. V. Mirkin, in *Electroanalytical Chemistry* (Ed.: A. J. Bard), Marcel Dekker, New York, 1994, pp. 243–373, Vol. 18.
494. A. J. Bard, F.-R. F. Fan, M. Mirkin, in *Physical Electrochemistry* (Ed.: I. Rubinstein), Marcel Dekker, New York, 1995, pp. 209–242.
495. Y.-Q. Li, O. Chailapakul, R. M. Crooks, *J. Vac. Sci. Technol., B* **1995**, *13*, 1300–1306.
496. F. P. Zamborini, R. M. Crooks, *Langmuir* **1997**, *13*, 122–126.
497. I. Rubinstein, S. Steinberg, Y. Tor et al., *Nature* **1988**, *332*, 426–429.
498. J. Haladjian, P. Bianco, R. Pilard, *Electrochim. Acta* **1983**, *28*, 1823–1828.
499. T. Sagara, K. Niwa, A. Sone et al., *Langmuir* **1990**, *6*, 254–262.
500. T. M. Nahir, E. F. Bowden, *J. Electroanal. Chem.* **1996**, *410*, 9–13.
501. I. Taniguchi, S. Yoshimoto, K. Nishiyama, *Chem. Lett.* **1997**, *26*, 353–354.
502. R. A. Clark, E. F. Bowden, *Langmuir* **1997**, *13*, 559–565.
503. Q. Chi, J. Zhang, J. U. Nielsen et al., *J. Am. Chem. Soc.* **2000**, *122*, 4047–4055.
504. K. Niki, W. R. Hardy, M. G. Hill et al., *J. Phys. Chem. B* **2003**, *107*, 9947–9949.
505. D. A. Di Giusto, W. A. Wlassoff, S. Giesebrecht et al., *J. Am. Chem. Soc.* **2004**, *126*, 4120–4121.
506. K. Ataka, F. Giess, W. Knoll et al., *J. Am. Chem. Soc.* **2004**, *126*, 16199–16206.

507. R. J. Willicut, R. L. McCarley, *J. Am. Chem. Soc.* **1994**, *116*, 10823–10824.
508. R. J. Willicut, R. L. McCarley, *Langmuir* **1995**, *11*, 296–301.
509. I. Turyan, D. Mandler, *J. Am. Chem. Soc.* **1998**, *120*, 10733–10742.
510. J. E. Hutchison, T. A. Postlethwaite, R. W. Murray, *Langmuir* **1993**, *9*, 3277–3283.
511. J. Zak, H. Yuan, M. Ho et al., *Langmuir* **1993**, *9*, 2772–2774.
512. D. A. Offord, S. B. Sachs, M. S. Ennis et al., *J. Am. Chem. Soc.* **1998**, *120*, 4478–4487.
513. G. Ashkenasy, G. Kalyuzhny, J. Libman et al., *Angew. Chem., Int. Ed. Engl.* **1999**, *38*, 1257–1261.
514. C. V. K. Sharma, G. A. Broker, G. J. Szulczewski et al., *Chem. Commun.* **2000**, 1023–1024.
515. M. S. Boeckl, A. L. Bramblett, K. D. Hauch et al., *Langmuir* **2000**, *16*, 5644–5653.
516. N. Kanayama, T. Kanbara, H. Kitano, *J. Phys. Chem. B* **2000**, *104*, 271–278.
517. T. A. Eberspacher, J. P. Collman, C. E. D. Chidsey et al., *Langmuir* **2003**, *19*, 3814–3821.
518. B. J. Vesper, K. Salaita, H. Zong et al., *J. Am. Chem. Soc.* **2004**, *126*, 16653–16658.
519. A. S. Viana, A. H. Jones, L. M. Abrantes et al., *J. Electroanal. Chem.* **2001**, *500*, 290–298.
520. D. A. Di Giusto, W. A. Wlassoff, S. Giesebrecht et al., *Angew. Chem., Int. Ed. Engl.* **2004**, *43*, 2809–2812.
521. T. Liu, J. K. Barton, *J. Am. Chem. Soc.* **2005**, *127*, 10160–10161.
522. R. Gasparac, B. J. Taft, M. A. Lapierre-Devlin et al., *J. Am. Chem. Soc.* **2004**, *126*, 12270–12271.
523. C. D. Hodneland, M. Mrksich, *Langmuir* **1997**, *13*, 6001–6003.
524. M. N. Yousaf, M. Mrksich, *J. Am. Chem. Soc.* **1999**, *121*, 4286–4287.
525. C. D. Hodneland, M. Mrksich, *J. Am. Chem. Soc.* **2000**, *122*, 4235–4236.
526. W.-S. Yeo, M. N. Yousaf, M. Mrksich, *J. Am. Chem. Soc.* **2003**, *125*, 14994–14995.
527. X. Jiang, R. Ferrigno, M. Mrksich et al., *J. Am. Chem. Soc.* **2003**, *125*, 2366–2367.
528. K. Kim, M. Jang, H. Yang et al., *Langmuir* **2004**, *20*, 3821–3823.
529. L. Tiefenauer, R. Ros, *Colloids Surf. B Biointerfaces* **2002**, *23*, 95–114.
530. L. Häussling, H. Ringsdorf, F.-J. Schmitt et al., *Langmuir* **1991**, *7*, 1837–1840.
531. J. Spinke, M. Liley, H.-J. Guder et al., *Langmuir* **1993**, *9*, 1821–1825.
532. C. Erdelen, L. Häussling, R. Naumann et al., *Langmuir* **1994**, *10*, 1246–1250.
533. A. L. Plant, *Langmuir* **1993**, *9*, 2764–2767.
534. G. P. Lòpez, H. A. Biebuyck, R. Härter et al., *J. Am. Chem. Soc.* **1993**, *115*, 10774–10781.
535. G. P. Lòpez, M. W. Albers, S. L. Schreiber et al., *J. Am. Chem. Soc.* **1993**, *115*, 5877–5878.
536. J. Brask, H. Wackerbarth, K. J. Jensen et al., *J. Am. Chem. Soc.* **2003**, *125*, 94–104.
537. J. Zhang, Q. Chi, A. M. Kuznetsov et al., *J. Phys. Chem. B* **2002**, *106*, 1131–1152.
538. L. Li, S. Chen, S. Jiang, *Langmuir* **2003**, *19*, 2974–2982.
539. J. J. Gooding, V. G. Praig, E. A. H. Hall, *Anal. Chem.* **1998**, *70*, 2396–2402.
540. Y. M. Bae, B.-K. Oh, W. Lee et al., *Biosens. Bioelectron.* **2005**, *21*, 103–110.
541. S. J. Metallo, R. S. Kane, R. E. Holmlin et al., *J. Am. Chem. Soc.* **2003**, *125*, 4534–4540.
542. M. Boncheva, L. Scheibler, P. Lincoln et al., *Langmuir* **1999**, *15*, 4317–4320.
543. E. A. Smith, M. J. Wanat, Y. Cheng et al., *Langmuir* **2001**, *17*, 2502–2507.
544. (a) P. A. Johnson, M. A. Gaspar, R. Levicky, *J. Am. Chem. Soc.* **2004**, *126*, 9910–9911. (b) P. A. Johnson, R. Levicky, *Langmuir* **2003**, *19*, 10288–10294.
545. H. Wackerbarth, R. Marie, M. Grubb et al., *J. Solid State Electrochem.* **2004**, *8*, 474–481.
546. H. Wackerbarth, M. Grubb, J. Zhang et al., *Angew. Chem., Int. Ed. Engl.* **2004**, *43*, 198–203.
547. D. Peelen, L. M. Smith, *Langmuir* **2005**, *21*, 266–271.
548. E. L. S. Wong, E. Chow, J. J. Gooding, *Langmuir* **2005**, *21*, 6957–6965.
549. A. K. Boal, E. Yavin, O. A. Lukianova et al., *Biochemistry* **2005**, *44*, 8394–8407.
550. I. Lee, J. W. Lee, A. Stubna et al., *J. Phys. Chem. B* **2000**, *104*, 2439–2443.
551. B. S. Ko, B. Babcock, G. K. Jennings et al., *Langmuir* **2004**, *20*, 4033–4038.
552. J. Madoz, B. A. Kuznetzov, F. J. Medrano et al., *J. Am. Chem. Soc.* **1997**, *119*, 1043–1051.
553. M. Mrksich, *MRS Bull.* **2005**, *30*, 180–184.
554. G. B. Sigal, M. Mrksich, G. M. Whitesides, *J. Am. Chem. Soc.* **1998**, *120*, 3464–3473.

555. S. Herrwerth, W. Eck, S. Reinhardt et al., *J. Am. Chem. Soc.* **2003**, *125*, 9359–9366.
556. J. Lahiri, E. Ostuni, G. M. Whitesides, *Langmuir* **1999**, *15*, 2055–2060.
557. S. Herrwerth, T. Rosendahl, C. Feng et al., *Langmuir* **2003**, *19*, 1880–1887.
558. W. S. Dillmore, M. N. Yousaf, M. Mirksich, *Langmuir* **2004**, *20*, 7223–7231.
559. A. Varki, *Glycobiology* **1993**, *3*, 97–130.
560. D. J. Revell, J. R. Knight, D. J. Blyth et al., *Langmuir* **1998**, *14*, 4517–4524.
561. S. Svedhem, L. Öhberg, S. Borrelli et al., *Langmuir* **2002**, *18*, 2848–2858.
562. N. Horan, L. Yan, H. Isobe et al., *Proc. Natl. Acad. Sci. U.S.A.* **1999**, *96*, 11782–11786.
563. Y. Zhang, V. Telyatnikov, M. Sathe et al., *J. Am. Chem. Soc.* **2003**, *125*, 9292–9293.
564. M. J. Hernàiz, J. M. de la Fuente, A. G. Barrientos et al., *Angew. Chem., Int. Ed. Engl.* **2002**, *41*, 1554–1557.
565. C. Tromas, P. Eaton, J. Mimault et al., *Langmuir* **2005**, *21*, 6142–6144.

1.2.2

Photoelectrochemical Properties of Electrodes Modified with Self-assembled Monolayers (SAMs) of Various Alkylthiol Derivatives

Toshihiro Kondo
Ochanomizu University, Tokyo, Japan

Kohei Uosaki
Hokkaido University, Sapporo, Japan

1.2.2.1 Introduction

In order to achieve modern nanotechnology, we must arrange molecules in order on a solid on a nanometer level. Previously, the Langmuir–Blodgett (LB) method [1, 2] was generally used to construct the ordered molecular layers on a solid surface. Because the molecules are physorbed onto the solid surface in LB films, their structures easily change and soon become random. On the other hand, the self-assembly (SA) technique has become one of the most popular methods of constructing ordered molecular layers during the last two decades, because the self-assembled monolayers (SAMs) are chemisorbed onto the solid surface and therefore their molecularly ordered structure must be more stable. The SAMs of alkylthiols on metals, especially on gold, have been extensively studied because of their potential applications in many fields, such as sensors, corrosion inhibition, wetting control, and biomolecular, and molecular electronic devices [3–5]. The SAM-modified electrodes play very important roles in these fields because we have to arrange the molecules in order onto the solid surface for these applications. Although there is another SAM constructed by the silane coupling reaction of alkoxysilane on an oxide surface [3, 4], here we concentrate only on the alkylthiol SAM.

The preparation of alkylthiol SAM on a solid surface, especially gold, is very simple. Just dipping the solid substrate (Au, Ag, Cu, Pt, ITO (indium tin oxide), etc.) in a solution containing the appropriate alkylthiol derivatives allows us to prepare the molecular layers on the substrate surface. To arrange the molecules in order, however, we have to clean the substrate and flatten its surface on a molecular level before the preparation. For example, with gold as the substrate, the Au(111) surface is generally used as a substrate and it should be annealed by a flame and be quenched both for cleaning and flattening before dipping it in the solution. In this case, we can easily observe a molecular image by scanning probe microscope (SPM), such as a scanning tunneling microscope (STM) and atomic force microscope (AFM) [6–8] even in solution.

Functionalization of the SAM-modified electrodes is also simple. We can easily introduce functional groups into the SAM. There are two methods to introduce the functional group into the SAM. One is the synthesis of the alkylthiol derivatives, whose terminal group synthetically changes to the functional group, before the preparation. This method has the advantage that a surface with several functionalities is easily prepared just by dipping the substrate into the solution as described above, although this has the disadvantage that the synthesis of the alkylthiol derivatives with the functional group is rather difficult. The other method is a sequential multilayer formation. First, an alkylthiol SAM with a terminal group, that can easily form a bond with a terminal group of other functional molecule is formed

Encyclopedia of Electrochemistry.Edited by A.J. Bard and M. Stratmann
Vol. 10 *Modified Electrodes*. Edited by M.Fujihira, I.Rubinstein, and J.F.Rusling
Copyright © 2007 Wiley-VCH Verlag GmbH & Co. KGaA, Weinheim.ISBN: 978-3-527-30402-8

on a substrate and then the functional molecule, which has the terminal group for the bond formation with the terminal group of the SAM, is synthetically attached to this SAM-modified surface. This method has the advantage that multilayer formation is easy, although this has the disadvantage that the synthetic yield of such a surface reaction is usually not high enough to form a perfect monolayer, and then the thicker the multilayer, the lower the surface density.

For future nanotechnology, we should arrange the molecules on a solid surface at a molecular level. For this purpose, as described above, the alkylthiol SAM with a wide variety of functionalities is a good candidate for constructing the elaborate molecular machinery. Thus, the SAMs with many functionalities have been extensively employed, and many research groups, including our group, have extensively investigated the electrochemical properties of the alkylthiol SAMs in detail since 1990 [2, 3, 6–46]. The application in photoelectric devices, especially for the SAM-modified electrodes, is one of the most important fields in this research area. In this section, we focus on photo-induced electron transfer, control of electron transfer by photoisomerization, and application of luminescence, especially to sensors, regarding the photochemical properties and review the photochemical characteristics of the alkylthiol SAM-modified electrodes.

1.2.2.2 **Photo-induced Electron Transfer at SAM-modified Electrodes**

Construction of a very efficient artificial photoelectric conversion device mimicking a natural photosynthetic system is one of the dreams of scientists. In natural systems, molecules of various functionalities, such as a photon absorber like chlorophylls and electron donors and acceptors like pheophytins and quinones, are well organized with molecular dimensions so that very efficient photo-induced charge separation and photo-induced electron transfer are achieved with a minimum reverse electron transfer [47, 48]. Thus, it is of great interest to mimic the elaborate molecular machinery of natural systems for the realization of a highly efficient artificial photosynthetic system. This concept was first employed by Moore et al. and Fujihira et al., who used lipid bilayer membranes [49, 50] and the LB films [4, 51–55], respectively, to arrange molecules in order. Unfortunately, the quantum efficiencies of these systems were quite low (0.4–1.5%) [49, 50] compared with that of the natural systems because the molecular arrangements of these systems were not enough to achieve a highly efficient photo-induced electron transfer.

We have achieved for the first time the construction of an alkylthiol SAM for an artificial photosynthetic system using a porphyrin–quinone–thiol coupling molecule (PQSH) as shown in Fig. 1(a) [56, 57]. PQSH with porphyrin as the photon-absorber, quinone as the electron relay, and thiol as the surface-active group was synthesized and its SAM was constructed on a gold surface. In an electrolyte solution containing methylviologen (MV^{2+}) and ethylenediaminetetraacetic acid (EDTA) as the electron acceptor and donor, respectively, anodic and cathodic photocurrents were observed at potentials more positive and more negative, respectively, than the redox potential of the quinone moiety (curve (a) in Fig. 2), indicating that the photo-induced electron transfer direction can be controlled by the electrode potential [56].

When the pH of the solution increased, the redox potential of the quinone moiety shifted in the more negative direction and, accordingly, the potential dependence of the photocurrents also shifted in the negative direction (curves (b) and (c) in Fig. 2), indicating that the photoinduced electron transfer direction can be controlled by the pH of the electrolyte solution [57].

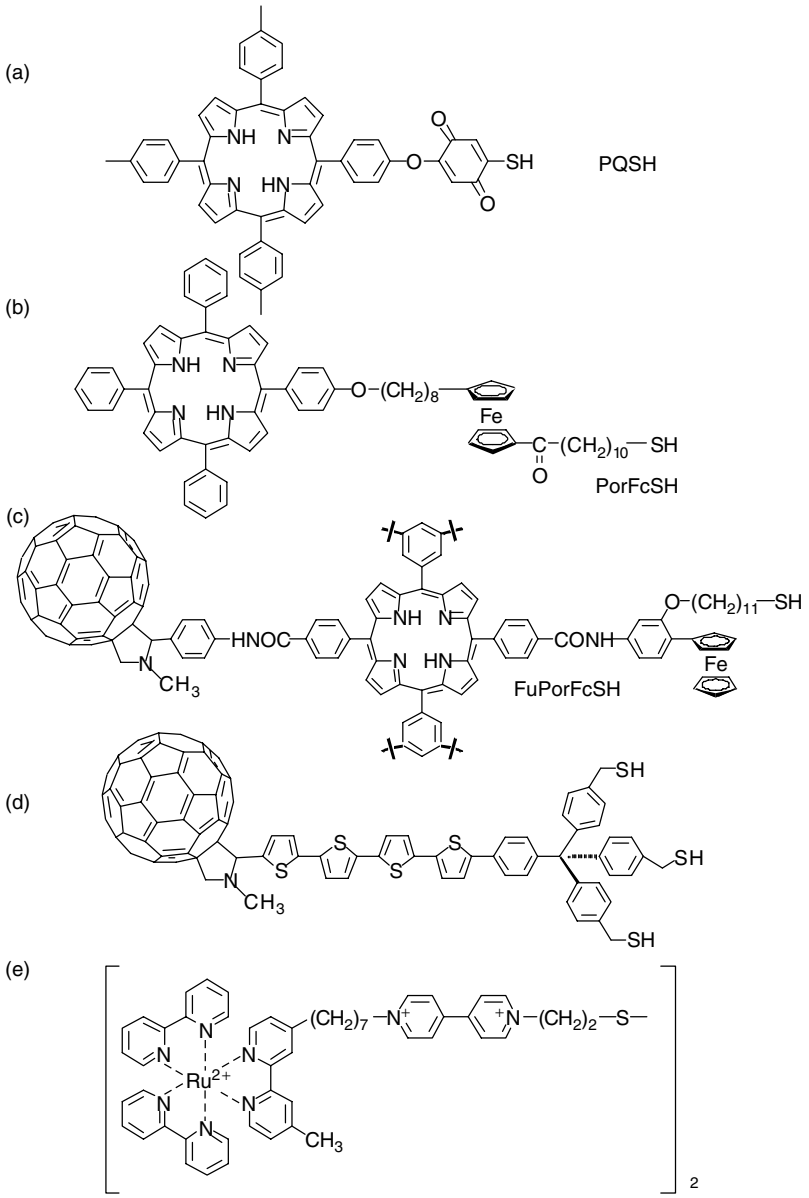


Fig. 1 Alkylthiol and disulfide molecules with functional groups used in this section.

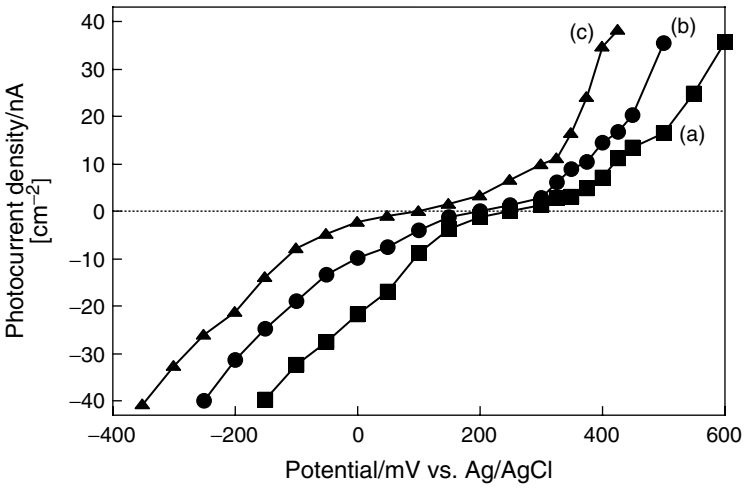


Fig. 2 Potential dependence of photocurrents of the PQSH SAM-modified gold electrode measured in a phosphate buffer solution containing 0.1 M Na_2SO_4 + 50 mM EDTA + 5 mM MV^{2+} at a pH of 3.5 (a), 4.5 (b), and 5.5 (c) [56, 57].

Although we could achieve the construction of the photo-induced electron transfer system using the SA technique as described above, the quantum efficiency of this system is relatively low (ca. 0.3–3%), because PQSH has no alkyl chains and/or the adsorbed amount of the molecules is low, and therefore, the orders of the molecular layer was low. A novel molecule (Fig. 1b), which has porphyrin, ferrocene, and thiol groups as the photoactive, electron transport or relay, and surface binding groups, respectively, separated from each other by alkyl chains (PorFcSH) was then synthesized and its SAM was constructed on gold [58]. Ferrocene was chosen as the electron relay group because the electron transfer of this group is known to be very fast [38] and the alkyl chains were introduced to form a well-ordered SAM so that the reverse electron transfer and energy transfer from the excited porphyrin to the gold electrode can be reduced. When the gold electrode modified with the SAM of PorFcSH was illuminated by monochromated light (430 nm) in the solution containing MV^{2+} as an electron acceptor, a stable photocurrent flowed if the potential was more negative than +650 mV (vs. Ag/AgCl), which coincides with the redox potential of the ferrocene moiety in the PorFcSH SAM (Fig. 3). This stable photocurrent flowed for more than 3 h without any signs of deterioration. After prolonged illumination of this SAM-modified electrode, the color of the solution in front of the electrode changed to blue, showing that MV^{2+} was reduced to the methylviologen cation radical ($MV^{+\cdot}$). Since the redox potential of $MV^{2+}/MV^{+\cdot}$ is −630 mV, we have achieved the up-hill transport of electrons of more than 1.2 eV by visible light illumination. The photocurrent action spectrum of the PorFcSH SAM-modified gold electrode matched well with the absorption spectrum of the PorFcSH SAM, confirming that the porphyrin group in the SAM

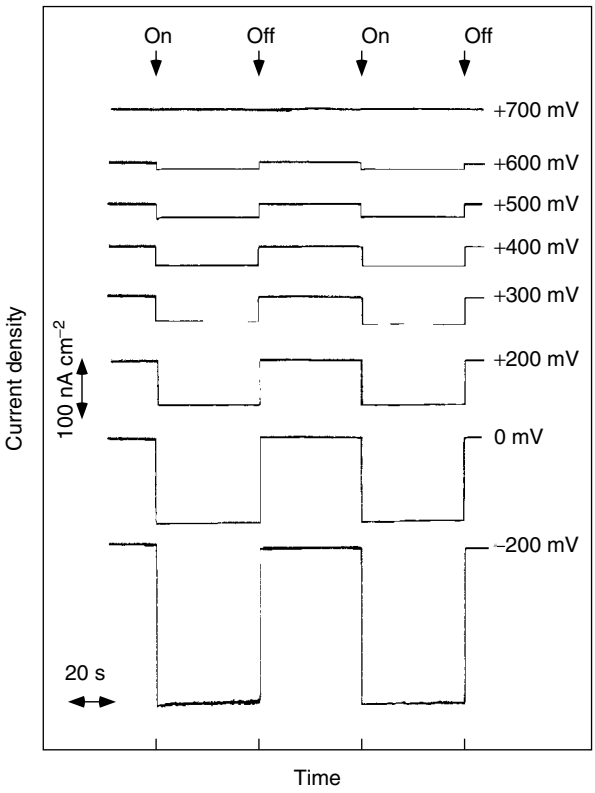


Fig. 3 Time course of the current at the PorFcSH SAM-modified gold electrode held at various potentials when the electrode was illuminated with 430 nm pulsed light (40 μW cm^{-2}; 8.7 × 10^{13} photon s^{-1} cm^{-2}) [58].

really acted as a photoactive site. The quantum efficiency of this system was more than 10%. It is demonstrated by the results of the alkyl chain length dependence, a structural study by angle-resolved X-ray photoelectron spectroscopy (ARXPS), and the electrode surface flatness dependence that the reason for the achievement of this very high efficiency is the relatively high orientation of this SAM and then the reverse electron and energy transfer are minimized [59–61].

After our reports, there were a large number of photo-induced electron transfer studies using alkylthiol SAMs [62–79]. Imahori et al. synthesized a fullerene–porphyrin–ferrocene–thiol coupling molecule (FuPorFcSH, in Fig. 1c), which has two electron relay groups, such as ferrocene and fullerene, and porphyrin as a photon-absorber between them, and many derivatives similar to it, then constructed their SAMs on gold and indium tin oxide (ITO) [62–71]. As a result of a comparison of their photocurrent generation efficiencies, the highest efficiency among them was achieved at 20 to 25% by the gold electrode modified with the SAM of FuPorFcSH. They concluded that utilization of the fullerene group with the small

reorganization energy satisfies the severe requirement for the photocurrent generation, leading to a high efficiency even at the metal electrode. They constructed the mixed SAM with FuPorFcSH and a pyrene-thiol linked molecule as an antenna group to mimic the natural systems and achieved light harvesting with a photocurrent generation efficiency of 0.6 to 1.5% [72]. They also constructed the SAM of a fullerene-olligothiophenes linked molecule (Fig. 1d) and observed a relatively large photocurrent [73, 74]. Ishida and Majima observed a much more intense photocurrent by the surface plasmon excitation than that provided by conventional direct photoexcitation at the SAM of a porphyrin-thiol linked molecule [75]. A ruthenium complex was also used as a photon-absorber [76–78]. Yamada et al. constructed the SAM of a ruthenium (II) tris(2,2′-bipyridine) ($Ru(bpy)_3^{2+}$) -viologen-thiol derivative (Fig. 1e) on gold and ITO, and photocurrent generation was observed. A report that fullerene was used as a photon-absorber is also available [79].

There are examples of photocurrent observations at the multilayer-modified electrodes using the SAM as an underlayer. Reese and Fox constructed the SAM of a thiol-terminated oligonucleotide on gold and then an oligonucleotide duplex with a pyrene end-labeled oligonucleotide was constructed on its SAM-modified electrode (Fig. 4) [80]. They observed a photocurrent at this SAM-modified gold electrode in a solution containing MV^{2+} as the electron acceptor. Thompson et al. also observed photocurrent generation at the photoactive multilayers constructed on the porphyrin SAM-modified gold electrode using the electrostatic interaction between a zirconium cation and a phosphate anion (Fig. 5) [81]. Shinkai et al. also constructed the multilayer of fullerene-cationic homooxacalix[3]arene inclusion complex and anionic porphyrin polymer on an ITO electrode modified with the SAM of a sulfonate-terminated thiol molecule (Fig. 6), and a relatively large photocurrent was observed [82].

The alkylthiol SAM can also form on a semiconductor surface [83–88]. However, it is not easy to prepare it at room temperature as compared with the case

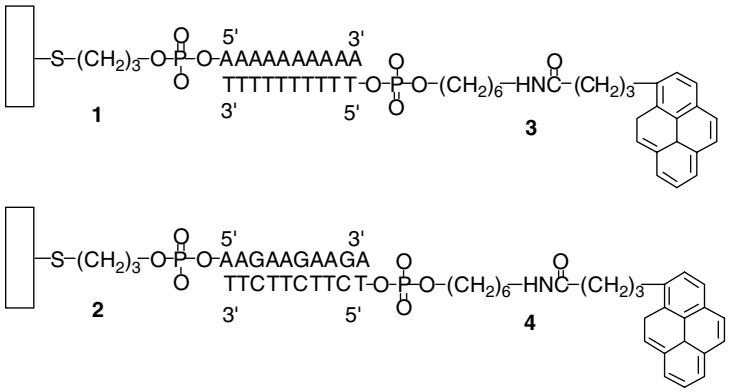


Fig. 4 Constructed photoactive SAMs using surface-confined oligonucleotides **1** and **2** associated with their pyrene end-labeled complements **3** and **4** by Reese and Fox [80].

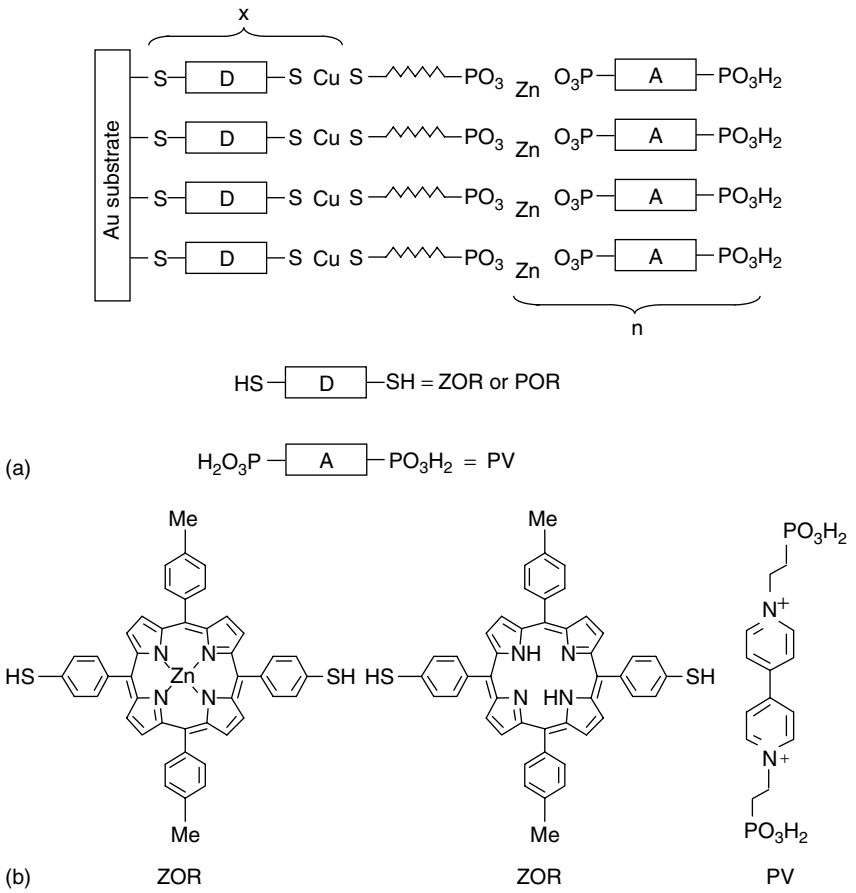
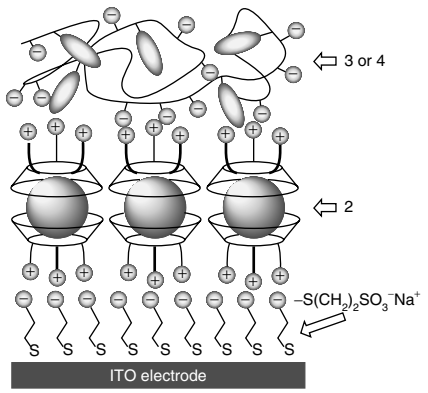


Fig. 5 (a) Schematic side view of the photoactive multilayers developed by Thompson et al. using the molecules shown below. (b) Structures of the porphyrins and the viologen derivative used to construct the above multilayers [81].

Fig. 6 Schematic view of the photoactive multilayers of sodium 3-mercaptoethane-sulfonate (first layer), fullerene-cationic homooxa-calix[3]arene inclusion complex **2** (second layer), anionic porphyrin polymer **3** or **4** (third layer) on an ITO electrode [82].



of the alkylthiol SAM on a metal surface. A relatively ordered monolayer of the alkylthiol can be prepared by heating the solution containing the appropriate alkylthiol and simultaneously by dipping the semiconductor substrate in it for several hours. Gu and Waldeck constructed the *n*-InP semiconductor electrode modified with the SAMs of *n*-alkylthiols having several different alkyl chain lengths and observed the photocurrent [84–88]. They investigated the alkyl chain length dependence on the photocurrent and demonstrated that the studies of the photocurrent versus chain length of the alkylthiols can be used to examine how the electron transfer rate constant depends on the thickness of the insulating layer. They suggested that of particular interest is the ability of the alkylthiol SAM-modified electrodes to probe the distance dependence of the electronic coupling. The principles of the photocurrent generation at the semiconductor electrodes were well studied and summarized in the literature [89–92].

1.2.2.3 **Photo-induced Electron Transfer at Electrodes Modified with SAM-covered Nanocluster Layers**

Since Brust et al. reported that the gold nanoclusters, whose surfaces were covered with the alkylthiol SAMs, are stable and easy to introduce to functional groups by a place-exchange method [93–95], many studies on photo-induced electron transfer using alkylthiol SAM-modified metal or semiconductor nanoclusters were reported [96–111]. Yamada et al. observed the photocurrent at the ITO electrodes modified with the multilayer of gold nanoclusters and porphyrin-tetraalkylthiol molecules (Fig. 7) [96]. Imahori et al. investigated the photophysical properties of gold nanoclusters modified with the SAM of a porphyrin-thiol coupling molecule [97, 98] and observed a photocurrent at the SnO_2 electrode modified with electrophoretically deposited layers of gold nanoclusters, whose surface is covered with the mixed SAMs of porphyrin-thiol and fullerene-thiol coupling molecules [99]. Li et al. also observed a photocurrent at the gold electrode modified with electrostatically deposited layers of gold nanoclusters, whose surface is covered with the SAM of a porphyrin-viologen coupling molecule [100].

For the gold electrode modified with the semiconductor nanocluster layers, a unique preparation procedure is employed. First, semiconductor nanoclusters, which are covered with the surfactant sodium bis(2-ethylhexyl) sulfosuccinate (Aerosol OT, AOT), were prepared in reverse micelles [101]. After this the dithiol SAMs were prepared on the gold surface, and then the layers of the semiconductor nanoclusters were prepared by dipping the dithiol SAM-modified gold in a nanocluster dispersion (Fig. 8) [102–108]. It was confirmed by XPS that the terminated thiol group, which is not connected with the gold, in the dithiol SAMs on gold is covalently bonded to the surface atoms of the semiconductor nanoclusters [102] and, as a result, the SAM forms on the semiconductor nanocluster surface. Relatively large photocurrents were observed at the gold electrodes modified with many kinds of semiconductor nanoclusters, such as CdS [103–106], ZnS [105], PbS [107], and CdSe [108], which were prepared by the above procedures shown in Fig. 8. There is an interesting preparation method by which the tellurium nanoclusters were electrochemically deposited on the gold electrodes modified with the SAMs of molecular templates, whose terminal group is β-cyclodextrin [109]. Woo

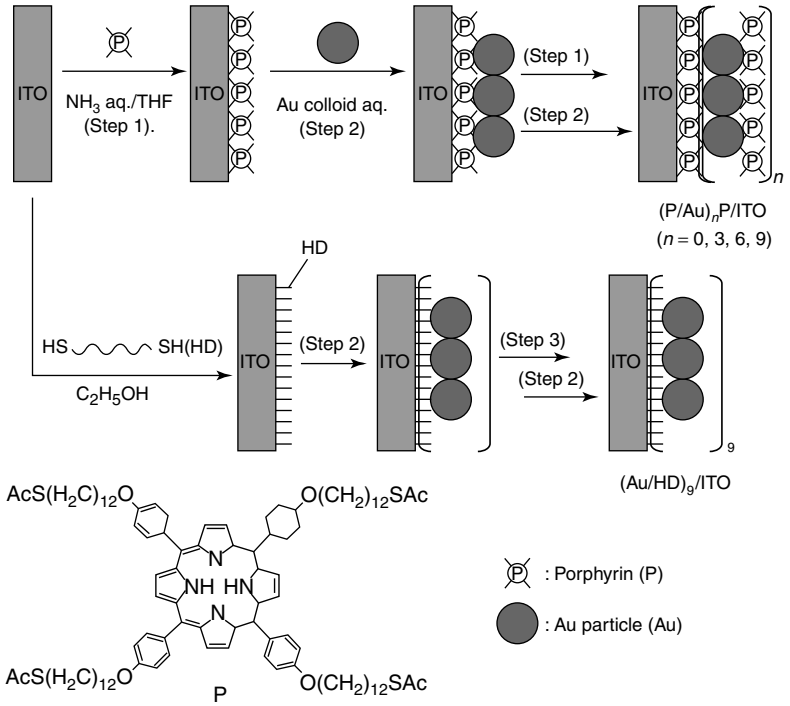


Fig. 7 Schematic illustration for the fabrication of multilayer assemblies; (**P**/**Au**)$_n$P/ITO (n = 0,3,6 9) and (**Au**/**HD**)$_9$/ITO [96].

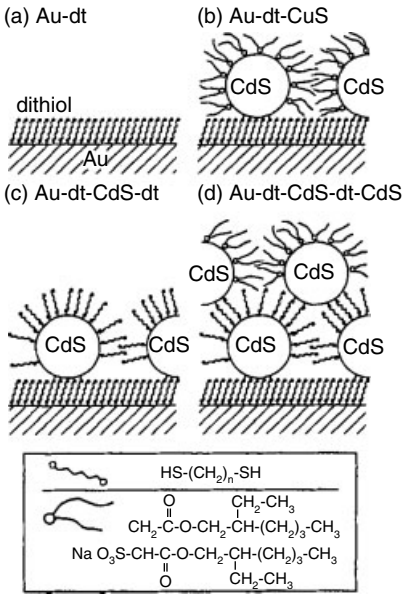


Fig. 8 Schematic illustration of binding of the CdS nanoclusters from reverse micelles onto gold via dithiol and the formation of alternating layer-by-layer structure: (a) dithiol SAM on a gold substrate (Au-dt); (b) CdS nanoclusters attached on the SAM (Au-dt-CdS); (c) adsorption of dithiol layers on CdS nanoclusters (Au-dt-CdS-dt); (d) formation of a second CdS-nanocluster layer (Au-dt-CdS-dt-CdS). Each component is drawn in size according to the estimation from experimental results [102].

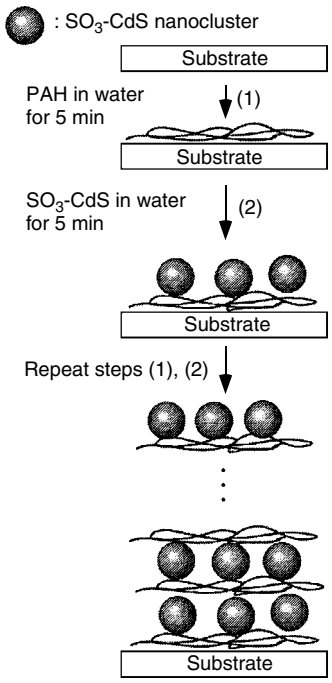


Fig. 9 Preparation procedures of CdS nanoclusters/PAH multilayers by the alternate two-step dip of the substrate into aqueous solutions containing CdS nanoclusters and PAH [111].

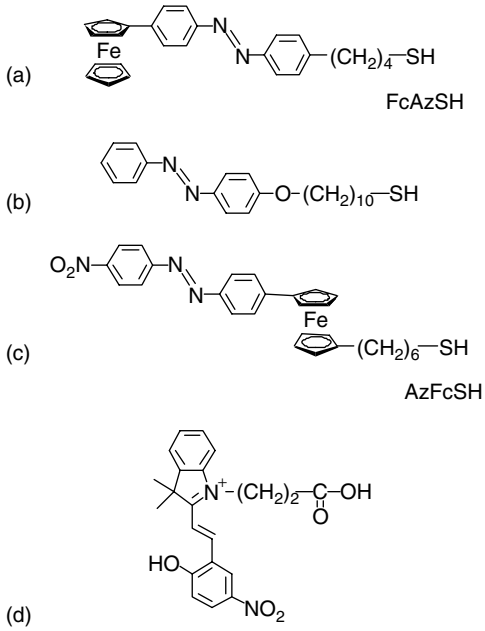
et al. observed a photocurrent at this modified gold electrode.

Another method was also employed to construct the multilayers of the alkylthiol SAMs-covered nanoclusters on the electrode surface [27–30, 110, 111]. Multilayers of the semiconductor nanoclusters covered with the alkylthiol SAMs, whose terminated groups are the charged groups, can be constructed on the basis of an electrostatic interaction (Fig. 9). Relatively large and stable photocurrents were observed at this electrode and photoelectrochemical properties of the semiconductor nanoclusters were discussed on the basis of quantum size effect [109, 110].

1.2.2.4 Electron Transfer Controlled by Photoisomerization at SAM-modified Electrodes

Azobenzene is one of the most popular groups to photoisomerize with a structural change and was often used even for the alkylthiol SAM-modified electrodes [112–124]. Introducing this group into the SAM-modified electrodes allows us to construct a photo-switching system. Mirkin et al. synthesized the ferrocene-azobenzene-thiol linked molecule (FcAzSH) shown in Fig. 10(a) and achieved a photon-gated electron transfer at the gold electrode modified with the mixed SAMs of FcAzSH and an azobenzene-thiol linked molecule (Fig. 11) [112]. The electron source of this photon-gated electron transfer is ferrocyanide in the electrolyte solution. Figure 12(a) shows the cyclic voltammogram (CV) of the gold electrode modified with the SAM of a *cis*-azobenzene-thiol molecule (*cis*-AzSH). For the *cis*-form of the SAM-modified gold electrode, no peaks due to the redox of ferrocyanide in the solution were observed. After doping of FcAzSH in the *cis*-form SAM, only the redox peaks due to ferrocene fixed in the mixed SAM were observed (Fig. 12b). It is noted that no redox species such as ferrocyanide were contained in this case. After the addition of ferrocyanide to the solution, however, a catalytic current due to the oxidation of ferrocyanide was observed (Fig. 12c) around the redox potential of ferrocene, showing that ferrocene fixed in this mixed SAM plays the role of a catalyst. After photo-irradiation, reversible peaks due to the redox of both ferrocene fixed in this mixed SAM and ferrocyanide in the solution were observed (Fig. 12d). These electrochemical and photoelectrochemical behaviors showed that they achieved a photon-gated electron transfer.

Fig. 10 Alkylthiol molecules with functional groups used in this section.



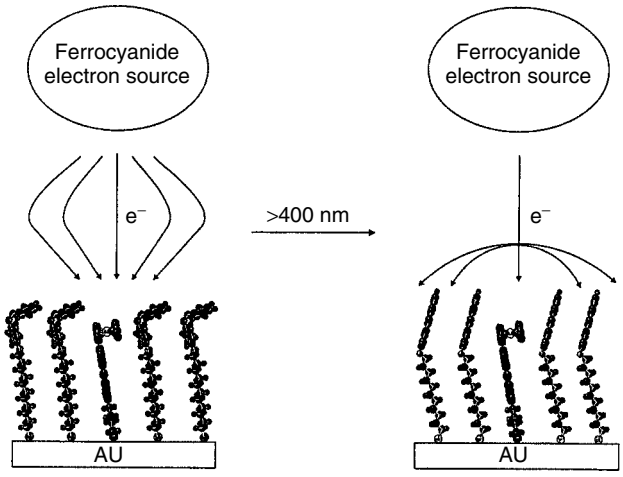


Fig. 11 Schematic illustration of control of electron transfer by photo-irradiation at the FcAzSH SAM-modified gold electrodes [112].

Fujishima et al. found interesting electrochemical properties at the gold electrode modified with the SAM of the azobenzene-thiol linked molecule shown in Fig. 10(b) [115–117] and with the LB films of the azobenzene derivatives [125–129]. The reduction potential of *cis*-azobenzene to hydrazobenzene is much more positive than that of the *trans*-form. They also showed that reduced

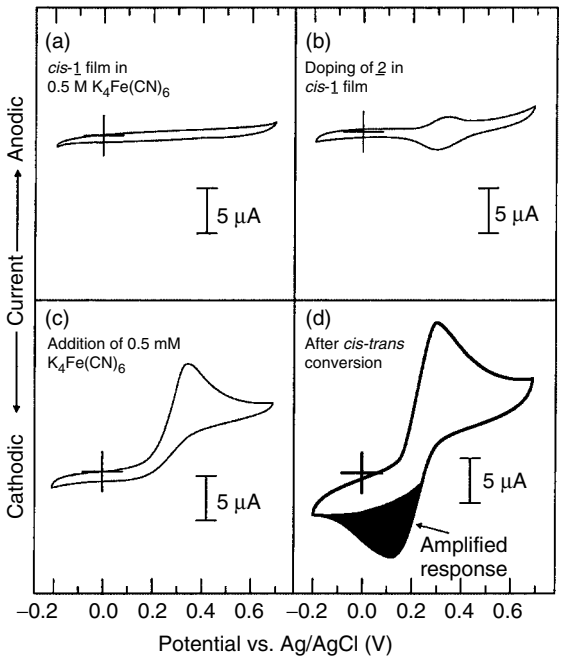


Fig. 12 CVs for (a) a pure *cis*-AzSH SAM in the absence of light and in the presence of 0.5 mM $K_4Fe(CN)_6$; (b) the *cis*-AzSH SAM after doping it with 1% FcAzSH (no $K_4Fe(CN)_6$); (c) the two-component SAM (1 : 99 = FcAzSH: *cis*-AzSH) after addition of 0.5 mM $K_4Fe(CN)_6$ to the cell; (d) the two-component SAM, in the presence of 0.5 mM $K_4Fe(CN)_6$, after irradiation with >400 nm light for 1 h. The geometric area of the working electrode was 0.21 cm^2. The electrolyte used in all of the above experiments was 0.2 M $NaClO_4$. Scan rate = 100 mV s^{-1} [112].

hydrazobenzene is electrochemically oxidized only to *trans*-azobenzene around +200 mV (vs. Ag/AgCl), even if the original form is the *cis*-form. Using this phenomenon, we can control the charge transfer rate at the gold electrode modified with the SAM of the azobenzene–ferrocene–thiol linked molecule (AzFcSH) shown in Fig. 10(c) [118]. In a CV of the gold electrode modified with the SAM of 100% *trans*-form AzFcSH (Fig. 13a), only a pair of waves due to the redox of ferrocene in the potential range between 0 and +750 mV appeared and did not change shape after the potential scan or UV irradiation. The CV of gold modified with the SAM of 20% *cis*- and 80% *trans*-forms AzFcSH (Fig. 13b), which was prepared from the solution containing AzFcSH after UV irradiation, also showed that only the redox peaks due to ferrocene were observed in the potential range between +200 and +750 mV. When the potential was scanned to 0 mV, a pair of waves due to the redox of the azobenzene moiety appeared, in addition to that of ferrocene in the first potential scan (solid line in Fig. 13c). The wave due to the redox of azobenzene, however, disappeared, and the redox potential and the peak separation of the redox wave due to ferrocene became more negative and smaller, respectively, in the second scan (dotted line in Fig. 13c). The redox potential and the peak separation returned to the original values after UV irradiation. These changes in the electrochemical characteristics of the latter electrode were reversible. On the basis of the structural analysis results by in situ Fourier-transform infrared reflection absorption spectroscopy (FT-IRRAS), we concluded that the electrochemical properties, that is, the redox potential and the charge transfer rate, of the ferrocene group in the SAM-modified gold electrode can be reversibly controlled

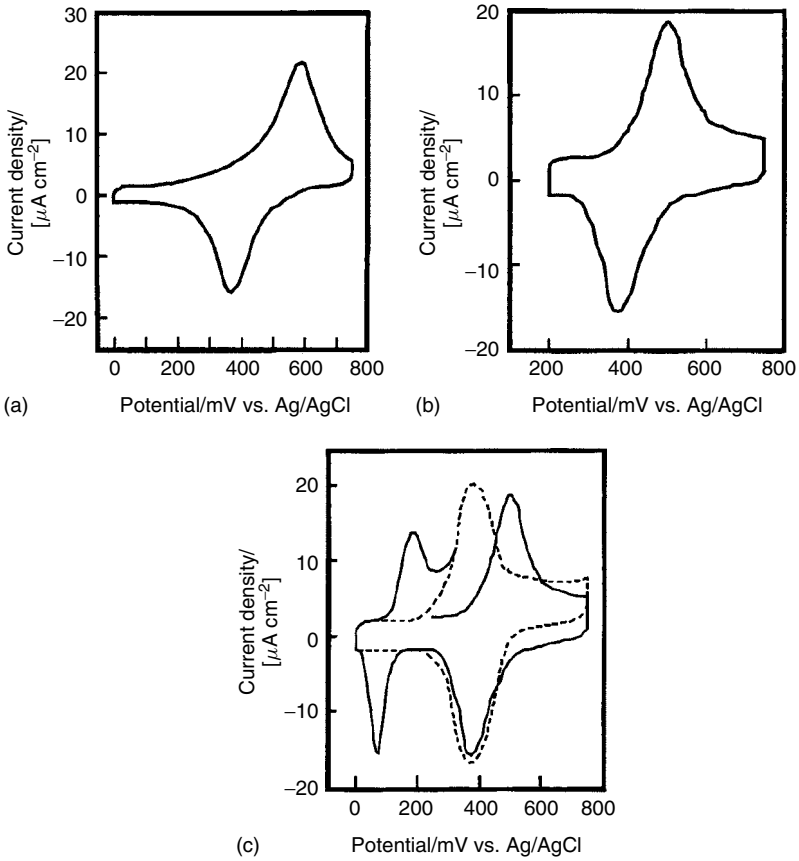


Fig. 13 CVs of (a) the 100% *trans*-AzFcSH SAM-modified gold electrode measured in the potential range between 0 and +750 mV; (b) the 20% *cis*- and 80% *trans*-AzFcSH SAM-modified gold electrode measured in the potential range between +200 and +750 mV. (c) The first scan (solid line) and second scan (dotted line) of the CVs of the 20% *cis*- and 80% *trans*-AzFcSH SAM-modified gold electrode measured in the potential region between 0 and +750 mV. Note that the potential scan was started from +200 mV in the positive direction. The electrolyte and scan rate in all of the above experiments were 0.1 M $HClO_4$ and 50 mV s^{-1}, respectively [118].

by electro- and photochemical structural conversions between the *cis*- and *trans*-forms of the azobenzene moiety in the SAM (Fig. 14).

Spiropyran/merocyanine photoisomerization was also used at the alkylthiol SAM-modified gold electrodes to gate/ungate electron transfer [130–133]. Willner et al. constructed a spiropyran/merocyanine-terminated SAM-modified gold electrode using the synthesized β-1-[3,3-dimethyl-6′-nitrospiro-(indoline-2,2′-2H-benzopyran)] propionic acid (Fig. 10d) and the amine-terminated alkylthiol SAM (Fig. 15). Using this SAM, they achieved photo-switchable on/off bioactivities. Figure 16 shows an example of their photo-switchable on/off bioactivity systems (redox of cytochrome *c*)

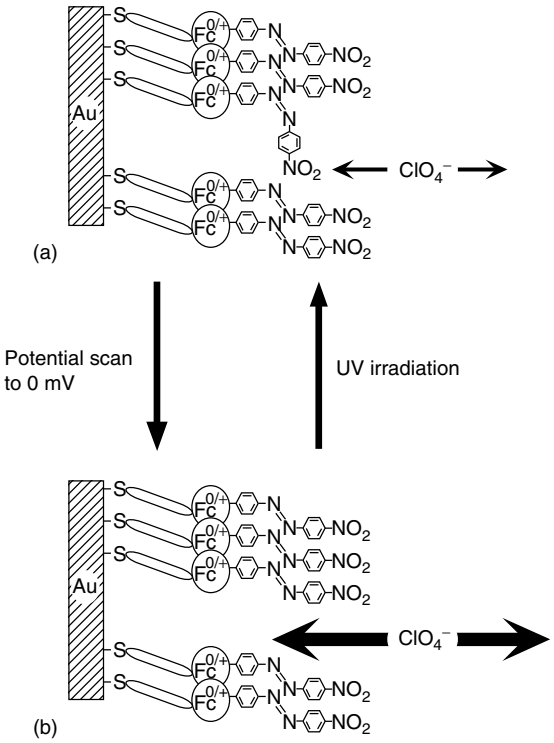


Fig. 14 Schematic illustration at the interface (a) between the 100% *trans*-AzFcSH SAM-modified gold electrode and the electrolyte solution containing perchlorate anions and (b) between the 20% *cis*- and 80% *trans*-AzFcSH SAM-modified gold electrode and the electrolyte solution containing perchlorate anions before the potential scan to 0 mV [118].

using this SAM-modified electrode [131]. In this case, they used the mixed SAM of spiropyran/merocyanine-terminated and 4-pyridine thiol.

In addition to the photoisomerization of the azobenzene and spiropyran/merocyanine system, (pyridylazo)benzene [134], stilbene [135], and diarylethene [136] were used as the photoisomerization group in the alkylthiol SAM-modified electrodes.

1.2.2.5 **Application of Luminescence from SAM-modified Electrodes**

Luminescence from the SAM-modified electrodes has been extensively studied. Fox and Wooten constructed the SAM of an anthracene-thiol linked molecule (Fig. 17a), measured the luminescent intensity and FT-IR spectrum of the SAMs, and investigated dimer formation of the anthracene moiety in this SAM [137]. Guo et al. constructed the photoactive and electrochemical active myoglobin protein layer on gold electrodes modified with the SAMs of metalloporphyrin-thiol linked molecules (Fig. 17b) by reconstitution of apomyoglobin in solution with the corresponding metalloporphyrin and investigated their fluorescence spectra [138]. Fluorescence from the mixed SAMs of the ferrocene-thiol derivative and Zn tetraarylporphyrin-thiol derivative were measured under open circuit conditions and the amounts of the photo-storaged charge in the SAM were quantitatively examined by Roth et al. [139] Bohn et al. constructed the protein-connected SAMs by using the procedures shown in Fig. 18, measured the fluorescence intensity from the polystyrene nanosphere doped as a

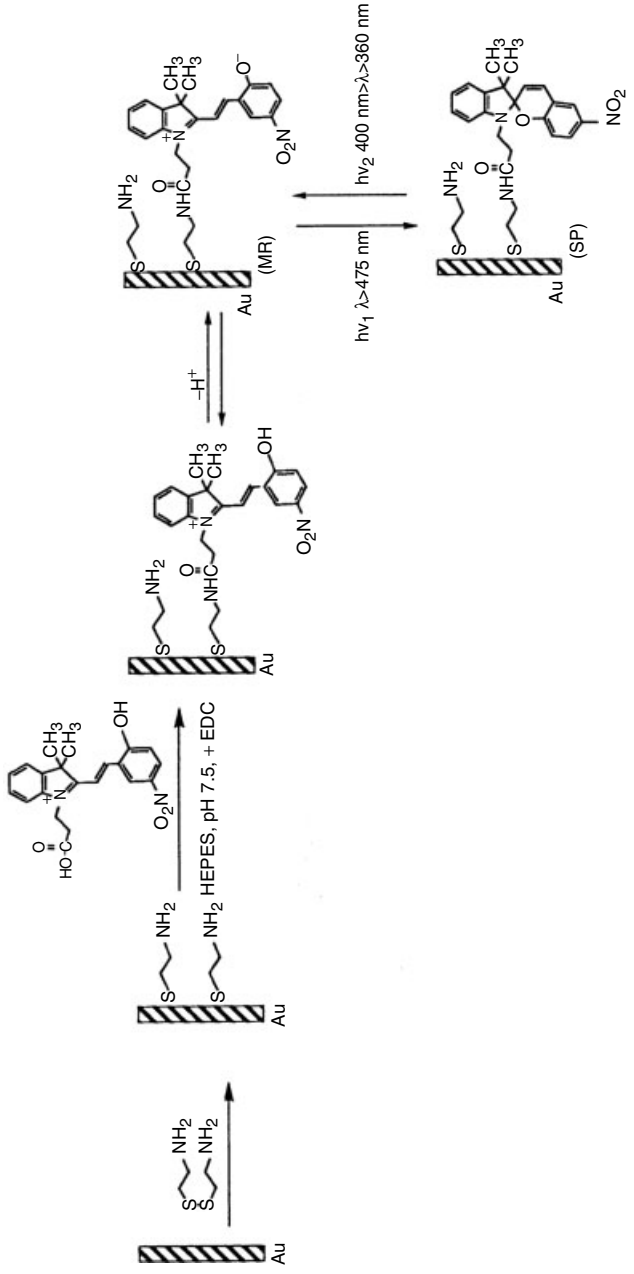


Fig. 15 Schematic modification procedure of a gold electrode by a photoisomerizable spyropyran SAM [130–133].

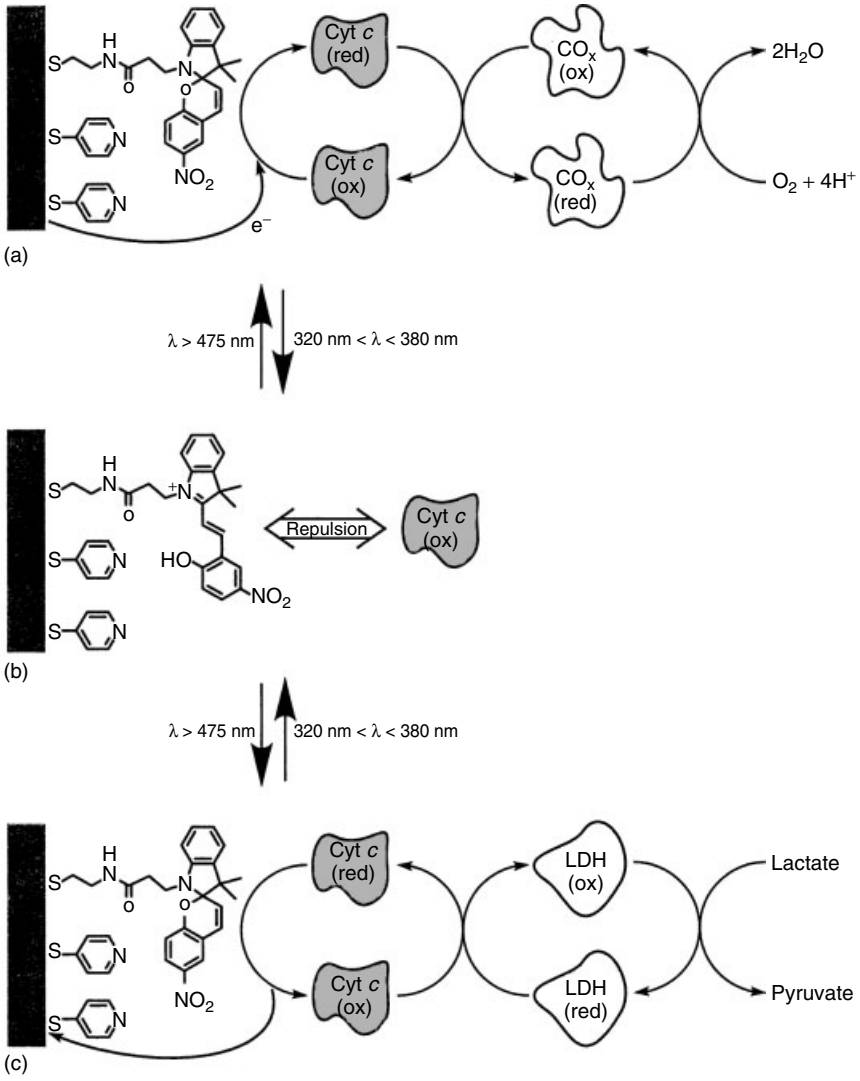


Fig. 16 Schematic coupling model of the photo-switchable interactions between cytochrome *c* and the mixed SAM of spiropyran/merocyanine-terminated and 4-pyridine thiol with (a) the reduction of O_2 by CO_x and (c) the oxidation of lactate by lactate dehydrogenase (LDH). (b) When the electrode is in the cationic merocyanine state, repulsive interactions disallow the functioning of the bioelectrocatalytic processes [130].

fluorescent label in the SAMs, and investigated cellular adhesion and motility by measuring the surface composition gradients of extracellular matrix proteins such as fibronection [140, 141].

The electrochemical and electrogenerated chemiluminescence (ECL) from the gold and ITO electrodes modified with the SAM of tris(2,2′-bipyridine) ruthenium(II) ($Ru(bpy)_3^{2+}$) -thiol linked molecules

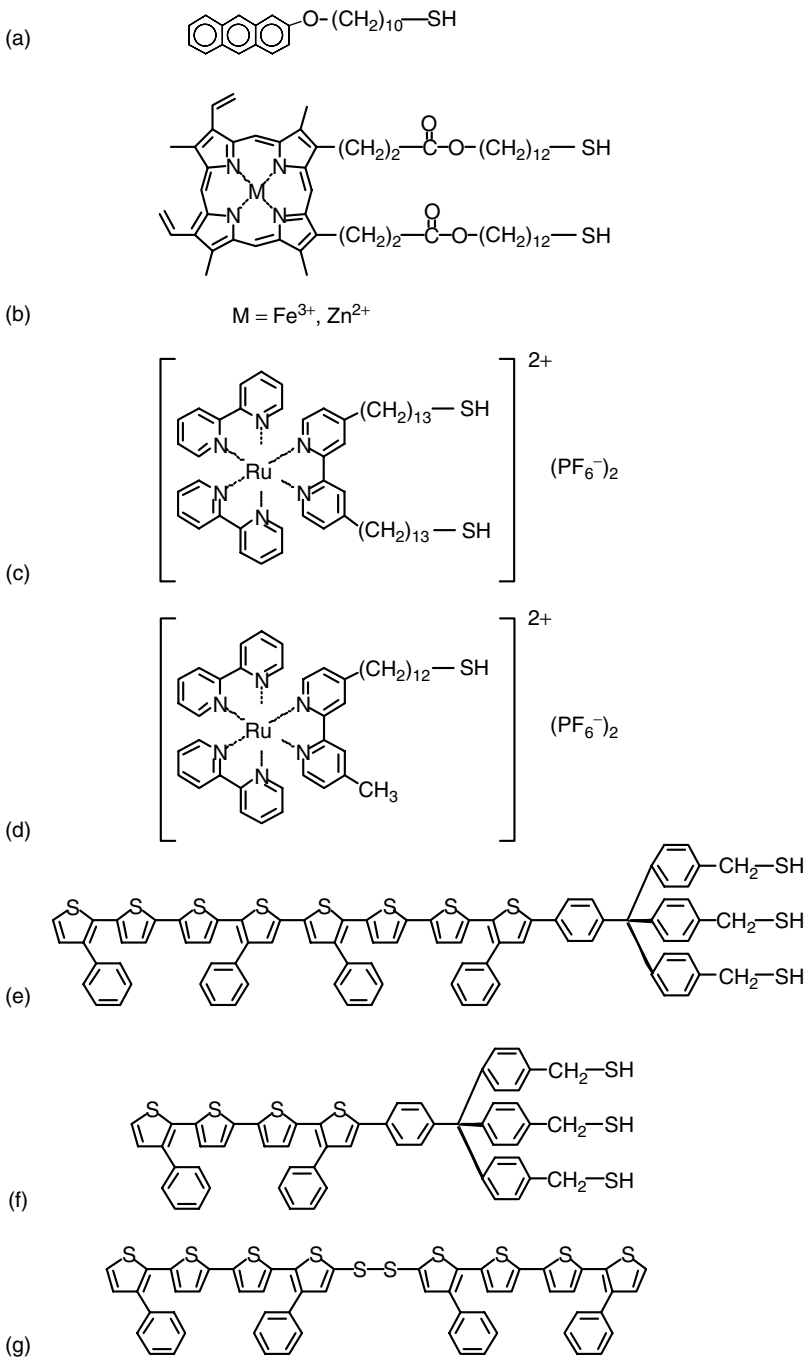


Fig. 17 Alkylthiol and disulfide molecules with functional groups used in this section.

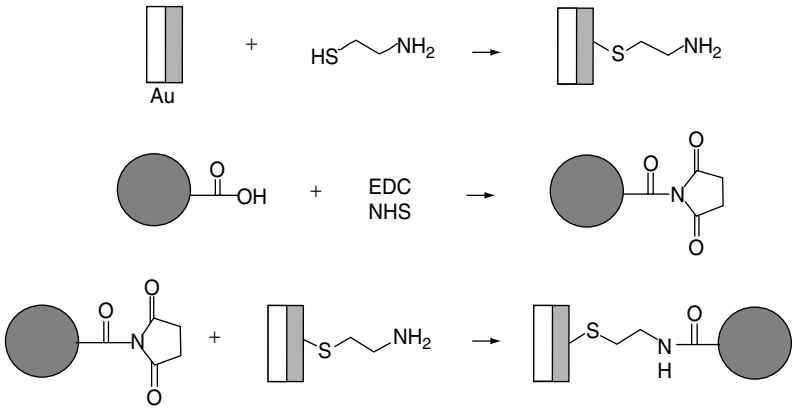


Fig. 18 Schematic modification process of the fluorescent nanospheres containing a large number ($\sim 10^6$ per sphere) of pendant carboxylic acid moieties, which were exploited to couple the nanospheres to amine-terminated thiol SAMs through amide bond formation [140].

(Fig. 17c [142] and Fig. 17d [143, 144]) were reported. The potential dependence of the emission intensity (Fig. 19) and luminescent spectrum (Fig. 20) were observed at the $Ru(bpy)_3^{2+}$ SAM-modified electrode in a solution containing $C_2O_4^{2-}$ and the following reactions were considered to take place within the positive potential region where emission was observed [142]:

$$Ru(bpy)_3^{2+} \longrightarrow Ru(bpy)_3^{3+} + e^- \quad (1)$$

$$Ru(bpy)_3^{3+} + C_2O_4^{2-} \longrightarrow Ru(bpy)_3^{2+} + CO_2 + CO_2^{\bullet -} \quad (2)$$

$$Ru(bpy)_3^{3+} + CO_2^{\bullet -} \longrightarrow Ru(bpy)_3^{2+*} + CO_2 \quad (3)$$

$$Ru(bpy)_3^{2+*} \longrightarrow Ru(bpy)_3^{2+} + h\nu \quad (4)$$

$$Ru(bpy)_3^{2+*} \longrightarrow Ru(bpy)_3^{3+} + e^- \quad (5)$$

In these processes, electrochemically generated $Ru(bpy)_3^{3+}$ oxidizes $C_2O_4^{2-}$, forming CO_2 and $CO_2^{\bullet -}$, and becomes $Ru(bpy)_3^{2+}$ which again donates an electron to the electrode (reaction (1)). Thus, the $Ru(bpy)_3^{2+/3+}$ head group in the SAM acts as a mediator for the oxidation of oxalate, and therefore, a monotonic increase in the anodic current was observed as the potential becomes more positive (Fig. 19). $CO_2^{\bullet -}$ reduces $Ru(bpy)_3^{3+}$ to $Ru(bpy)_3^{2+*}$ which has excess energy. $Ru(bpy)_3^{2+*}$ may directly donate an electron to the electrode (reaction (5)) or relax to $Ru(bpy)_3^{2+}$ with a light emission efficiency controlled by the electron transfer rate of the reaction (5) which should be dependent on the distance between the electrode and the $Ru(bpy)_3^{2+/3+}$ head group in the SAM. Bard et al. also used the following oxidation reaction of tripropylamine (TPrA) and the above reactions (1) and (4), and observed ECL from the generated $Ru(bpy)_3^{2+*}$ at the SAM-modified gold and platinum electrodes [145, 146].

$$TPrA \longrightarrow TPrA^{\bullet +} + e^- \quad (6)$$

$$Ru(bpy)_3^{3+} + TPrA \longrightarrow Ru(bpy)_3^{2+} + TPrA^{\bullet +} \quad (7)$$

$$TPrA^{\bullet +} \longrightarrow TPrA^{\bullet} + H^+ \quad (8)$$

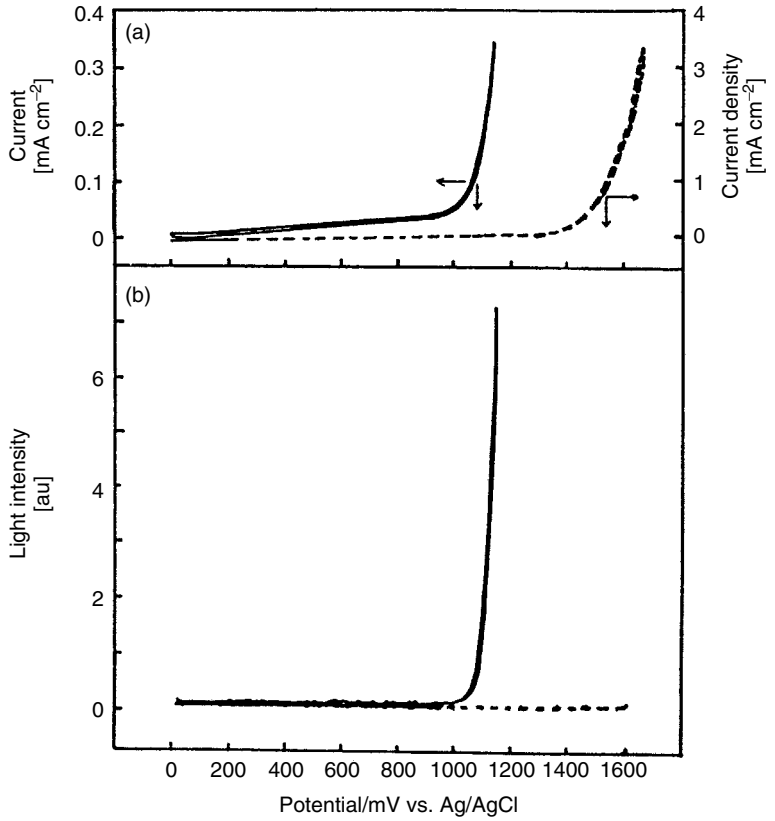
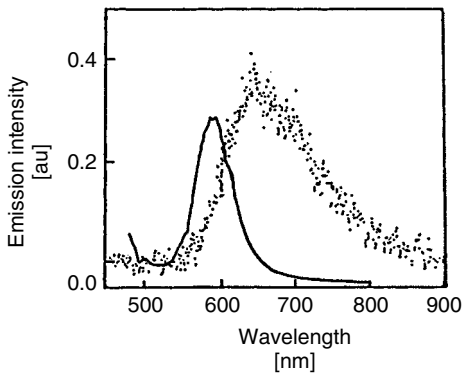


Fig. 19 Potential dependence of (a) the currents of the unmodified (broken curve) and SAM-modified (solid curve) ITO electrodes, and (b) the ECL intensity of the unmodified (broken curve) and SAM-modified (solid curve) ITO electrodes in a solution containing 0.4 M Na_2SO_4 + 0.1 M $Na_2C_2O_4$ [142].

Fig. 20 ECL spectrum of the $Ru(bpy)_3^{2+}$-thiol SAM-modified ITO electrode in a solution containing 0.4 M Na_2SO_4 + 0.1 M $Na_2C_2O_4$ at 1.15 V (dots) and the emission spectrum of $Ru(bpy)_3^{2+}$-thiol in CH_2Cl_2 solution (solid curve) [142].



$$Ru(bpy)_3^{3+} + TPrA^{\cdot} \longrightarrow Ru(bpy)_3^{2+*} + \text{products} \quad (9)$$

Using this ECL behavior of the $Ru(bpy)_3^{2+}$/TPrA system, the surface hydrophobicity [145] and immobilization of DNA and protein [146] were investigated. Except for the above reports, the ECL behaviors at the $Ru(bpy)_3^{2+}$ SAM-modified electrodes were used to fabricate an optoelectrochemical microring array [147].

There is a report that describes the application of a SAM-modified electrode in an electroluminescence (EL) device. Yamashita et al. used gold electrodes modified with the SAMs of the tripod-shaped π-conjugated thiols and disulfide (Figs 17(e)–(g)) and investigated enhanced hole injection from the EL of these SAM-modified electrodes [148]. They constructed layers of 4,4″-bis(3-methylphenylphenylamino)biphenyl (TPD), tris(8-hydroxyquinolinato)aluminum(III) (Alq_3), and Mg–Ag alloy, as a hole transport, emission, and electron transport layers, respectively, on these SAMs by vacuum evaporation. As a reference, these layers deposited both on the bare gold and bare ITO substrates were also used. Figure 21 shows the EL characteristics of these devices. Both the current-voltage (I-V) and luminescence-voltage (L-V) curves of these devices shifted to higher voltages in the order of SAM(f), which means the SAM of the molecule (f) shown in Fig. 16, <

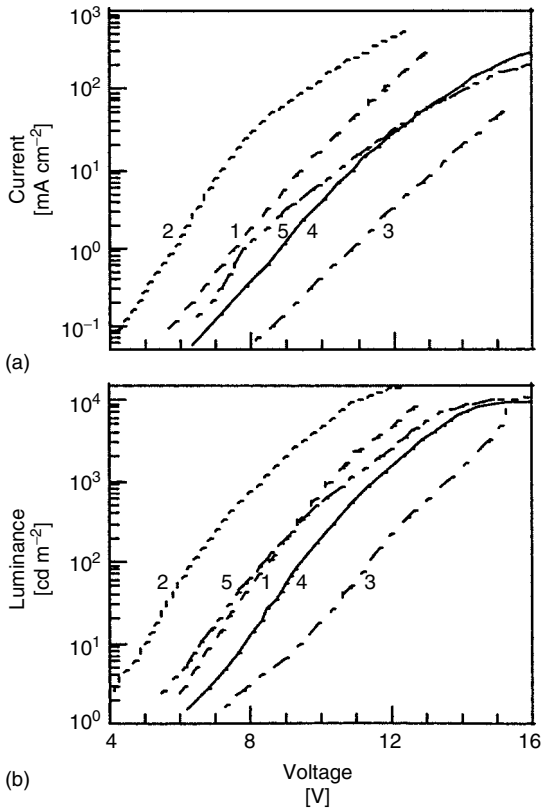


Fig. 21 (a) I-V and (b) L-V characteristics of (1) SAM(e), (2) SAM(f), (3) SAM(g), (4) bare gold, and (5) bare ITO devices [148].

SAM(e) ≈ bare ITO < bare gold < SAM(g). Compared to the bare gold device, the SAM(f) device exhibited a significantly improved EL performance, for example, greatly reduced operating potential, yielding much greater maximum brightness, permitting much higher current, and better stability. In contrast, the SAM(g) device showed EL characteristics poorer than the bare gold device. The different effects of the SAMs on the EL properties of the devices were concluded to be due to the modification density of the SAMs, leading to the vacuum level shift at the Au/TPD interface by the SAMs. The results of the CVs at the gold electrodes modified with these SAMs showed that the packing of the tripod-shaped thiol SAM(f) was compact, of the thiol SAM(e) less, and of the disulfide SAM(g) very poor. These modifications influence the hole injection barrier height at the Au/TPD interface and then affect the EL characteristics of the devices.

It is quite important to apply the SAM-modified electrode to a biosensor using the fluorescence from it [149, 150]. Sato et al. investigated the electrooxidative chemiluminescence from a luminol/hydrogen peroxide system catalyzed by the ferrocene-thiol SAM-modified gold electrode (Fig. 22). When luminol and hydrogen peroxide were contained in the electrolyte solution, in addition to the oxidation peak due to the redox of ferrocene, the catalytic oxidation current of luminol was observed (solid line in Fig. 22a) and light emission was simultaneously observed (open circle in Fig. 22b). The ECL intensity depended on the pH of the solution. They applied this system to detect glucose in the presence of glucose oxidase [150].

There is an interesting report about fluorescence from a porphyrin, which is incorporated in a SAM, although it is not on an electrode. Reich et al. constructed Au and Au/Ni nanowires whose surface was modified with the SAMs of a porphyrin-thiol coupling molecule [151]. Fluorescence microscopy was used to optimize the functionalization of two-segment gold-nickel nanowires for selectivity and

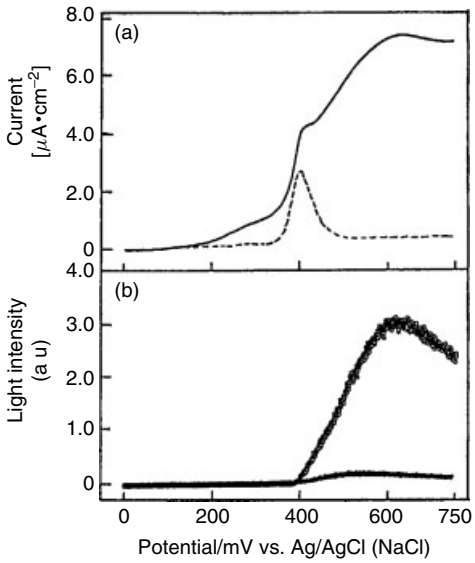


Fig. 22 (a) Linear sweep voltammograms of ferrocene-thiol SAM-modified gold electrode measured in electrolyte solution (0.1 M $NaClO_4$/0.1 M buffer solution, pH 8.2) with 100 μM luminol and 10 mM H_2O_2 (solid line) and without luminol and H_2O_2 (dotted line). Sweep rate: 2 mV s^{-1}. (b) ECL intensities of ferrocene-thiol SAM-modified gold electrode (open circle) simultaneously measured with the linear sweep voltammograms. ECL intensity of unmodified gold electrode (closed diamond) [149].

stability of the nanowire-molecule linkages. Magnetic trapping was employed as a technique where single nanowires are captured from a fluid suspension using lithographically patterned micromagnets. They investigated the influence of an external magnetic field on this process and suggested a model based on the interplay of dipolar forces and viscous drag from the results of the dynamics of the magnetic trapping.

1.2.2.6 Concluding Remarks

We have described thiol derivatives with photo-functionalities and presented schematic illustrations of the photoelectrochemically active SAMs and multilayers constructed on the electrode surfaces as many as possible in this section. However, since there are a large number of studies on wide range of photoactive alkylthiol SAM-modified electrodes, we cannot review all the important subjects in this section such as photopatterning [152–156] and nonlinear optical properties [157,158]. Instead we have listed many references for the interested readers.

References

1. G. Roberts, *Langmuir-Blodgett Films*, Plenum Press, New York, 1990.
2. M. Fujihira, *New Funct. Mater.* **1993**, *C*, 473–480.
3. J. Sagiv, *J. Am. Chem. Soc.* **1980**, *102*, 92–98.
4. A. Ulman, *An Introduction to Ultrathin Organic Films from Langmuir-Blodgett to Self-Assembly*, Academic Press, New York, 1991.
5. H. O. Finklea in *Electroanalytical Chemistry* (Eds.: A. J. Bard, I. Rubinstein), Marcel Dekker, New York, 1996, pp. 109–335, Vol. 19.
6. R. Yamada, K. Uosaki, *Langmuir* **1997**, *13*, 5218–5221.
7. R. Yamada, K. Uosaki, *Langmuir* **1998**, *14*, 855–861.
8. S. Xu, S. J. N. Cruchon-Dupeyrat, J. C. Garno et al., *J. Chem. Phys.* **1998**, *108*, 5002–5012.
9. K. Uosaki, Y. Sato, H. Kita, *Langmuir* **1991**, *7*, 1510–1514.
10. K. Uosaki, Y. Sato, H. Kita, *Electrochim. Acta* **1991**, *36*, 1799–1801.
11. K. Shimazu, I. Yagi, Y. Sato et al., *Langmuir* **1992**, *8*, 1385–1387.
12. Y. Sato, H. Itoigawa, K. Uosaki, *Bull. Chem. Soc. Jpn.* **1993**, *66*, 1032–1037.
13. K. Shimazu, I. Yagi, Y. Sato et al., *J. Electroanal. Chem.* **1994**, *372*, 117–124.
14. Y. Sato, B. L. Frey, R. M. Corn et al., *Bull. Chem. Soc. Jpn.* **1994**, *67*, 21–25.
15. K. Shimazu, S. Ye, Y. Sato et al., *J. Electroanal. Chem.* **1994**, *375*, 409–413.
16. T. Otsuka, Y. Sato, K. Uosaki, *Langmuir* **1994**, *10*, 3658–3662.
17. T. Kondo, M. Takechi, Y. Sato et al., *J. Electroanal. Chem.* **1995**, *381*, 203–209.
18. S. Ye, Y. Sato, K. Uosaki, *Langmuir* **1997**, *13*, 3157–3161.
19. Y. Sato, M. Fujita, F. Mizutani et al., *J. Electroanal. Chem.* **1996**, *409*, 145–154.
20. S. Ye, A. Yashiro, Y. Sato et al., *J. Chem. Soc., Faraday Trans.* **1996**, *92*, 3813–3821.
21. Y. Sato, S. Ye, T. Haba et al., *Langmuir* **1996**, *12*, 2726–2736.
22. M. Abe, T. Kondo, K. Uosaki et al., *J. Electroanal. Chem.* **1999**, *473*, 93–98.
23. M. Abe, A. Sato, T. Inomata et al., *J. Chem. Soc., Dalton Trans.* **2000**, *16*, 2693–2702.
24. A. Sato, M. Abe, T. Inomata et al., *Phys. Chem. Chem. Phys.* **2001**, *3*, 3420–3426.
25. T. Kondo, M. Okamura, K. Uosaki, *J. Organomet. Chem.* **2001**, *637–639*, 841–844.
26. T. Kondo, T. Sumi, K. Uosaki, *J. Electroanal. Chem.* **2002**, *538/539*, 59–63.
27. T. Kondo, M. Okamura, K. Uosaki, *Chem. Lett.* **2001**, *30*, 930–931.
28. K. Uosaki, T. Kondo, M. Okamura et al., *Faraday Discuss.* **2002**, *121*, 373–389.
29. W. Song, M. Okamura, T. Kondo et al., *J. Electroanal. Chem.* **2003**, *554/555*, 385–393.
30. S. Wenbo, M. Okamura, T. Kondo et al., *Phys. Chem. Chem. Phys.* **2003**, *5*, 5279–5284.
31. T. Sumi, H. Wano, K. Uosaki, *J. Electroanal. Chem.* **2003**, *550–551*, 321–325.
32. H. Wano, K. Uosaki, *Langmuir* **2001**, *17*, 8224–8228.
33. C. E. D. Chidsey, D. N. Loiacono, *Langmuir* **1990**, *6*, 682–691.

34. C. E. D. Chidsey, C. R. Bertozzi, T. M. Putvinski et al., *J. Am. Chem. Soc.* **1990**, *112*, 4301–4306.
35. L. De, C. Hugh, D. A. Buttry, *Langmuir* **1990**, *6*, 1319–1322.
36. C. Miller, P. Cuendet, M. Grätzel, *J. Phys. Chem.* **1991**, *95*, 877–886.
37. J. J. Hickman, D. Ofer, C. Zou et al., *J. Am. Chem. Soc.* **1991**, *113*, 1128–1132.
38. C. E. D. Chidsey, *Science* **1991**, *251*, 919–922.
39. D. M. Collard, M. A. Fox, *Langmuir* **1991**, *7*, 1192–1197.
40. S. L. Miehelhaugh, C. Bhardwaj, G. J. Cali et al., *Corrosion* **1991**, *47*, 322–328.
41. S. E. Creager, G. K. Rowe, *Anal. Chim. Acta* **1991**, *246*, 233–239.
42. D. Mandler, A. J. Bard, *J. Electroanal. Chem.* **1991**, *307*, 217–228.
43. C. A. Widrig, C. Chung, M. D. Porter, *J. Electroanal. Chem.* **1991**, *310*, 335–359.
44. L. Sun, R. M. Crooks, *J. Electrochem. Soc.* **1991**, *138*, L23–L25.
45. M. A. Bryant, J. E. Pemberton, *J. Am. Chem. Soc.* **1991**, *113*, 8284–8293.
46. H. O. Finklea, D. D. Hanshew, *J. Am. Chem. Soc.* **1992**, *114*, 3173–3181.
47. L. Stryer, *Biochemistry*, 3rd ed., Freeman, New York, 1988.
48. J. Deisenhofer, O. Epp, K. Miki et al., *J. Mol. Biol.* **1984**, *180*, 385–398.
49. P. Seta, E. Bienvenue, A. L. Moore et al., *Nature* **1985**, *316*, 653–655.
50. Y. Sakata, H. Tatemitsu, E. Bienvenue et al., *Chem. Lett.* **1988**, *17*, 1625–1628.
51. M. Fujihira, *Mol. Cryst. Liq. Cryst.* **1990**, *183*, 59–69.
52. M. Fujihira, K. Nishiyama, H. Yamada, *Thin Solid Films* **1985**, *132*, 77–82.
53. M. Fujihira, H. Yamada, *Thin Solid Films* **1988**, *160*, 125–132.
54. M. Sakomura, M. Fujihira, *Thin Solid Films* **1994**, *243*, 616–619.
55. M. Fujihira, *Adv. Chem. Ser., Mol. Biomol. Electron.* **1994**, *240*, 373–394.
56. T. Kondo, T. Ito, S. Nomura et al., *Thin Solid Films* **1996**, *284/285*, 652–655.
57. T. Kondo, M. Yanagida, S. Nomura et al., *J. Electroanal. Chem.* **1997**, *438*, 121–126.
58. K. Uosaki, T. Kondo, X.-Q. Zhang et al., *J. Am. Chem. Soc.* **1997**, *119*, 8367–8368.
59. M. Yanagida, T. Kanai, X.-Q. Zhang et al., *Bull. Chem. Soc. Jpn.* **1998**, *71*, 2555–2559.
60. T. Kondo, T. Kanai, K. Iso-o et al., *Z. Phys. Chem.* **1991**, *212*, 23–30.
61. T. Kondo, M. Yanagida, X.-Q. Zhang et al., *Chem. Lett.* **2000**, *29*, 964–965.
62. H. Imahori, H. Yamada, Y. Nishimura et al., *J. Phys. Chem.* **2000**, *104*, 2009–2108.
63. H. Imahori, H. Norieda, S. Ozawa et al., *Langmuir* **1998**, *14*, 5335–5338.
64. H. Imahori, H. Yamada, S. Ozawa et al., *Chem. Commun.* **1999**, *13*, 1165–1166.
65. H. Imahori, T. Azuma, A. Ajavakom et al., *J. Phys. Chem. B* **1999**, *103*, 7233–7237.
66. H. Imahori, S. Ozawa, K. Ushida et al., *Bull. Chem. Soc. Jpn.* **1999**, *72*, 485–502.
67. H. Imahori, H. Norieda, Y. Nishimura et al., *J. Phys. Chem. B* **2000**, *104*, 1253–1260.
68. H. Imahori, T. Hasobe, H. Yamada et al., *Langmuir* **2001**, *17*, 4925–4931.
69. H. Yamada, H. Imahori, S. Fukuzumi, *J. Mater. Chem.* **2002**, *12*, 2034–2040.
70. H. Yamada, H. Imahori, Y. Nishimura et al., *J. Am. Chem. Soc.* **2003**, *125*, 9129–9139.
71. T. Hasobe, H. Imahori, K. Ohkubo et al., *J. Porphyr. Phthalocya.* **2003**, *7*, 296–312.
72. H. Imahori, H. Norieda, H. Yamada et al., *J. Am. Chem. Soc.* **2001**, *123*, 100–110.
73. D. Hirayama, K. Takimiya, Y. Aso et al., *J. Am. Chem. Soc.* **2002**, *124*, 532–533.
74. D. Hirayama, T. Yamashiro, K. Takimiya et al., *Chem. Lett.* **2000**, *29*, 570–571.
75. A. Ishida, T. Majima, *Nanotechnology* **1999**, *10*, 308–314.
76. N. Terasaki, T. Akiyama, S. Yamada, *Langmuir* **2002**, *18*, 8666–8671.
77. T. Akiyama, M. Inoue, Y. Kuwahara et al., *Jpn. J. Appl. Phys.* **2002**, *41*, 4737–4738.
78. N. Terasaki, T. Akiyama, S. Yamada, *Chem. Lett.* **2000**, *29*, 668–669.
79. O. Enger, F. Nuesch, M. Fibbioli et al., *J. Mater. Chem.* **2000**, *10*, 2231–2233.
80. R. S. Reese, M. A. Fox, *Can. J. Chem.* **1999**, *77*, 1077–1084.
81. F. B. Abdelrazzaq, R. C. Kwong, M. E. Thompson, *J. Am. Chem. Soc.* **2002**, *124*, 4796–4803.
82. A. Ikeda, T. Hatano, S. Shinkai et al., *J. Am. Chem. Soc.* **2001**, *123*, 4855–4856.
83. C. W. Sheen, J.-X. Shi, J. Mårtensson et al., *J. Am. Chem. Soc.* **1992**, *114*, 1514–1515.
84. T. Baum, S. Ye, K. Uosaki, *Langmuir* **1999**, *15*, 8577–8579.

85. K. Adlkofer, M. Tanaka, H. Hillebrandt et al., *Appl. Phys. Lett.* **2000**, *76*, 3313–3315.
86. Y. Gu, D. H. Waldeck, *J. Phys. Chem. B* **1998**, *102*, 9015–9028.
87. Y. Gu, K. Kumar, A. Lin et al., *J. Photochem. Photobiol. A* **1997**, *105*, 189–196.
88. Y. Gu, D. H. Waldeck, *J. Phys. Chem.* **1996**, *100*, 9573–9576.
89. A. J. Bard, M. Stratmann, S. Licht, (Eds.), *Encyclopedia of Electrochemistry, Vol. 6, Semiconductor Electrodes and Photoelectrochemistry*, Wiley-VCH, Weinheim, 2002.
90. H. Gerischer, *NATO Adv. Study Inst. Ser., Ser. B: Phys.* **1981**, *B69* (Photovoltaic Photoelectrochem. Sol. Energy Convers.), 199–261.
91. J. O. M. Bockris, K. Uosaki, *J. Electrochem. Soc.* **1978**, *125*, 223–227.
92. A. Fujishima, K. Honda, *Nature* **1972**, *238*, 27–28.
93. M. Brust, M. Walker, D. Bethell et al., *J. Chem. Soc., Chem. Commun.* **1994**, *7*, 801–802.
94. M. Brust, J. Fink, D. Bethell et al., *J. Chem. Soc., Chem. Commun.* **1995**, *16*, 1655–1656.
95. M. J. Hostetler, A. C. Templeton, R. W. Murray, *Langmuir* **1999**, *15*, 3782–3789.
96. S. Yamada, T. Tasaki, T. Akiyama et al., *Thin Solid Films* **2003**, *438-439*, 70–74.
97. H. Imahori, Y. Kashiwagi, Y. Endo et al., *Langmuir* **2004**, *20*, 73–81.
98. H. Imahori, S. Fukuzumi, *Adv. Mater.* **2001**, *13*, 1197–1199.
99. T. Hasobe, H. Imahori, P. V. Kamat et al., *J. Am. Chem. Soc.* **2003**, *125*, 14962–14963.
100. G. Li, W. Fudickar, M. Skupin et al., *Angew. Chem., Int. Ed. Engl.* **2002**, *41*, 1828–1852.
101. M. L. Steigerwald, A. P. Alivasatos, J. M. Gibson et al., *J. Am. Chem. Soc.* **1988**, *110*, 3046–3050.
102. T. Nakanishi, B. Ohtani, K. Uosaki, *J. Phys. Chem. B* **1998**, *102*, 1571–1577.
103. S. Ogawa, F.-R. F. Fan, A. J. Bard, *J. Phys. Chem.* **1995**, *99*, 11182–11189.
104. T. Nakanishi, B. Ohtani, K. Uosaki, *J. Electroanal. Chem.* **1998**, *455*, 229–234.
105. T. Nakanishi, B. Ohtani, K. Uosaki, *Jpn. J. Appl. Phys.* **1999**, *38*, 518–521.
106. M. Miyake, T. Torimoto, M. Nishizawa et al., *Langmuir* **1999**, *15*, 2714–2718.
107. S. Ogawa, K. Hu, F.-R. F. Fan et al., *J. Phys. Chem. B* **1997**, *101*, 5705–5711.
108. E. P. A. M. Bakkers, A. L. Roest, A. W. Marsman et al., *J. Phys. Chem. B* **2000**, *104*, 7266–7272.
109. D.-H. Woo, S.-J. Choi, D.-H. Han et al., *Phys. Chem. Chem. Phys.* **2001**, *3*, 3382–3386.
110. M. Miyake, T. Torimoto, T. Sakata et al., *Langmuir* **1999**, *15*, 1503–1507.
111. K. Uosaki, M. Okamura, K. Ebina, *Faraday Discuss.* **2003**, *125*, 39–53.
112. D. G. Walter, D. J. Campbell, C. A. Mirkin, *J. Phys. Chem. B* **1999**, *102*, 402–405.
113. D. J. Campbell, B. R. Herr, J. C. Hulteen et al., *J. Am. Chem. Soc.* **1996**, *118*, 10211–10219.
114. W. B. Caldwell, D. J. Campbell, K. Chen et al., *J. Am. Chem. Soc.* **1995**, *117*, 6071–6082.
115. R. Wang, T. Iyoda, D. A. Tryk et al., *Langmuir* **1997**, *13*, 4644–4651.
116. R. Wang, T. Iyoda, L. Jiang et al., *J. Electroanal. Chem.* **1997**, *438*, 213–219.
117. H.-Z. Yu, Y.-Q. Wang, J.-Z. Cheng et al., *Langmuir* **1996**, *12*, 2843–2848.
118. T. Kondo, T. Kanai, K. Uosaki, *Langmuir* **2001**, *17*, 6317–6324.
119. M. Jaschke, H. Schönherr, H. Wolf et al., *J. Phys. Chem.* **1996**, *100*, 2290–2301.
120. Z. Liu, C. Zhao, M. Tang et al., *J. Phys. Chem.* **1996**, *100*, 17337–17344.
121. H.-Z. Yu, Y.-Q. Wang, S.-M. Cai et al., *Chem. Lett.* **1996**, *25*, 903–904.
122. W.-W. Zhang, X.-M. Ren, H.-F. Li et al., *J. Coll. Interface Sci.* **2002**, *255*, 150–157.
123. K. Tamada, J. Nagasawa, F. Nakanishi et al., *Langmuir* **1998**, *14*, 3264–3271.
124. S. W. Han, C. H. Kim, S. H. Hong et al., *Langmuir* **1999**, *15*, 1579–1583.
125. R. Wang, L. Jiang, T. Iyoda et al., *Langmuir* **1996**, *12*, 2052–2057.
126. K. Morigaki, A.-F. Liu, K. Hashimoto et al., *J. Phys. Chem.* **1995**, *99*, 14771–14777.
127. R. Wang, T. Iyoda, K. Hashimoto et al., *J. Phys. Chem.* **1995**, *99*, 3352–3356.
128. K. Morigaki, T. Enomoto, K. Hashimoto et al., *Mol. Cryst. Liq. Cryst.* **1994**, *246*, 409–412.
129. Z. F. Liu, B. H. Loo, R. Baba et al., *Chem. Lett.* **1990**, *19*, 1023–1026.
130. A. N. Shipway, I. Willner, *Acc. Chem. Res.* **2001**, *34*, 421–432.
131. E. Katz, M. Lion-Dagan, I. Willner, *J. Electroanal. Chem.* **1995**, *382*, 25–31.

132. M. Lion-Dagan, E. Katz, I. Willner, *J. Am. Chem. Soc.* **1994**, *116*, 7931–7914.
133. I. Willner, S. Rubin, Y. Cohen, *J. Am. Chem. Soc.* **1993**, *115*, 4937–4938.
134. Z. Wang, M. J. Cook, A.-M. NygÅrd et al., *Langmuir* **2003**, *19*, 3779–3784.
135. M. A. Fox, M. O. Wolf, R. S. Reese, *NATO ASI Ser., Ser. C: Math. Phys. Sci.* **1996**, *485* (Physical Supramolecular Chemistry), 143–162.
136. N. Nakashima, T. Nakanishi, A. Nakatani et al., *Chem. Lett.* **1997**, *26*, 591–592.
137. M. A. Fox, M. D. Wooten, *Langmuir* **1997**, *13*, 7099–7105.
138. L.-H. Guo, G. McLendon, H. Razafitrimo et al., *J. Mater. Chem.* **1996**, *6*, 369–374.
139. K. M. Roth, J. S. Lindsey, D. F. Bocian et al., *Langmuir* **2002**, *18*, 4030–4040.
140. S. T. Plummer, P. W. Bohn, *Langmuir* **2002**, *18*, 4142–4149.
141. S. T. Plummer, Q. Wang, P. W. Bohn et al., *Langmuir* **2003**, *19*, 7528–7536.
142. Y. Sato, K. Uosaki, *J. Electroanal. Chem.* **1995**, *384*, 57–66.
143. Y. S. Obeng, A. J. Bard, *Langmuir* **1991**, *7*, 195–201.
144. W. A. Jackson, D. R. Bobbitt, *Microchem. J.* **1994**, *49*, 99–109.
145. Y. Zu, A. J. Bard, *Anal. Chem.* **2001**, *73*, 3960–3964.
146. W. Miao, A. J. Bard, *Anal. Chem.* **2003**, *75*, 5825–5834.
147. S. Szunerits, D. R. Walt, *Anal. Chem.* **2002**, *74*, 1718–1723.
148. L. Zhu, H. Tang, Y. Harima et al., *J. Mater. Chem.* **2002**, *12*, 2250–2254.
149. Y. Sato, S. Yabuki, F. Mizutani, *Chem. Lett.* **2000**, *29*, 1330–1331.
150. Y. Sato, T. Sawaguchi, F. Mizutani, *Electrochem. Commun.* **2001**, *3*, 131–135.
151. D. H. Reich, M. Tanase, A. Hultgren et al., *J. Appl. Phys.* **2003**, *93*, 7275–7280.
152. N. Matsuda, T. Sawaguchi, M. Osawa et al., *Chem. Lett.* **1995**, *24*, 145–146.
153. K. C. Chan, T. Kim, J. K. Schoer et al., *J. Am. Chem. Soc.* **1995**, *117*, 5875–5876.
154. L. F. Rozsnyai, M. S. Wrighton, *J. Am. Chem. Soc.* **1994**, *116*, 5993–5994.
155. R. Vaidya, L. M. Tender, G. Bradley et al., *Biotechnol. Prog.* **1998**, *14*, 371–377.
156. S. Y. Oh, J. K. Park, C. M. Chung et al., *Opt. Mater.* **2002**, *21*, 265–269.
157. T. Kondo, S. Horiuchi, I. Yagi et al., *J. Am. Chem. Soc.* **1999**, *121*, 391–398.
158. R. Baba, A. Fujishima, K. Hashimoto et al., *Nonlin. Opt.* **1999**, *22*, 497–500.

1.3
SAMs on Hg Electrodes and Si

1.3.1
SAMs on Hg Electrodes

Rolando Guidelli
Florence University, Firenze, Italy

1.3.1.1 Introduction and Scope

Mercury has a homogeneous, featureless, defect-free surface that lends itself to the formation of well-behaved self-assembled monolayers (SAMs). One of the first applications of Hg as a support for a monolayer dates back to the early 1970s, when Miller and coworkers [1, 2] described the self-assembly of phospholipid monolayers on a dropping mercury electrode with a long drop time. From then on, phospholipid SAMs on mercury electrodes have been extensively investigated not only for their intrinsic properties but also, and mainly, for their applications as models of biological membranes. To this end, molecules of biological importance, lipophilic ions, peptides, and proteins have been incorporated in Hg-supported phospholipid SAMs with the aim of investigating their behavior in an environment mimicking that of biological membranes. Much before the first applications of phospholipid SAMs on Hg, in 1940 Kolthoff and Barnum [3] described a dc polarographic adsorption prewave for cysteine electrooxidation, which prefigured the formation of a monolayer of this amino acid provided with a sulfhydryl group. This finding started a series of electroanalytical investigations on the deposition of water-soluble thiol films on Hg, usually at a submonolayer level. Only recently, after the investigations on the interesting properties of alkanethiol SAMs on gold electrodes, attention has been focused on analogous investigations on Hg, aiming at exploiting the unique properties of this liquid metal. While on a solid substrate such as Au it is the lattice structure that governs the organization of the SAM molecules, on Hg this is mainly governed by intermolecular interactions.

Without having the pretension of being comprehensive, this review covers the main aspects of the preparation, characterization, and properties of the above SAMs on Hg.

1.3.1.2 Phospholipid SAMs on Hg

Phospholipid monolayers consist of a hydrocarbon tail region with a dielectric constant comparable with that of alkanes (≈ 2) and a polar head region containing ionizable groups (phosphate, amino, carboxyl groups) whose polarizability imparts to this region a higher dielectric constant (from 10 to 30). The interface between an aqueous phase and the polar head region of lipid monolayers is equivalent to that between the same aqueous phase and lipid bilayers, which represent the main constituents of biological membranes. Thus, as long as interactions with foreign molecules are only confined to the polar head region, no appreciable differences are expected. This is why phospholipid monolayers supported by mercury have been extensively employed as experimental models of biological membranes.

1.3.1.2.1 Preparation Methodology and Procedures The first attempt to deposit a lipid monolayer on mercury was carried out by Miller and Bach [1] by causing an aqueous dispersion of dipalmitoylphosphatidylcholine (DPPC) to be adsorbed on

Encyclopedia of Electrochemistry. Edited by A.J. Bard and M. Stratmann
Vol. 10 *Modified Electrodes*. Edited by M.Fujihira, I.Rubinstein, and J.F.Rusling
Copyright © 2007 Wiley-VCH Verlag GmbH & Co. KGaA, Weinheim. ISBN: 978-3-527-30402-8

the surface of a dropping mercury electrode with a long drop time. Because of the very low solubility of DPPC and its gel state at room temperature, the film was less than monomolecular, exhibiting a high differential capacity C of about $8\,\mu F\,cm^{-2}$ over the potential range from -0.2 to -0.6 V/SCE. Subsequently, Pagano and Miller [2] transferred Langmuir–Blodgett (LB) films of different amphiphilic molecules at their equilibrium spreading pressure from a deaerated Langmuir trough onto a dropping mercury electrode; this was adjusted above the film in such a position as to start growing in the nitrogen atmosphere, to touch the nitrogen/water interface after 1–2 seconds, and to continue growing for other 10–15 seconds before falling off the capillary. A film of ^{3}H-labeled oleic acid on mercury obtained by this procedure had a surface concentration of about (1/19) molecules/Å^2 over the potential range from -0.1 to -1.2 V, in agreement with a close-packed monolayer of fully extended molecules in a vertical orientation. Subsequently, Miller and coworkers found that well-organized phospholipid monolayers with a differential capacity of about $1.7\,\mu F\,cm^{-2}$, namely, twice that of solvent-free black lipid membranes [4], could be obtained by a similar procedure not only at the equilibrium spreading pressure of the lipid film on the aqueous subphase but also with lipid surface concentrations at the nitrogen/water interface corresponding to two [5] or three [6] lipid monolayers. The lipid film is obtained by spreading a solution of the lipid in an alkane (usually pentane or hexane) on the surface of an aqueous electrolyte and by allowing the alkane to evaporate. This lipid film can be regarded as a monolayer at its equilibrium spreading pressure plus a lipid excess in equilibrium with the monolayer. At any rate, as this film comes into contact with the mercury electrode, a well-organized monolayer is formed on its surface, by ''self-assembly''. This procedure, which should be distinguished from the ''LB transfer'' of a preconstituted, organized monolayer from a Langmuir trough onto an electrode, exploits the fact that mercury is the most hydrophobic metal. This by no means implies that mercury has no affinity for the oxygen of water; in fact, at the potential of zero charge (pzc), the water molecules adsorbed on mercury are slightly oriented with the oxygen turned toward mercury, although less than on other metals [7, 8]. However, as the adsorbing lipid molecules have to decide where to turn their hydrophilic polar head to attain a minimum in their adsorption free energy, they choose to turn it toward the aqueous phase, where it can form hydrogen bonds with the adjacent water molecules.

The technique was further improved by using a hanging mercury drop electrode (HMDE) in place of a dropping mercury electrode, thereby creating more favorable conditions for the attainment of adsorption equilibrium. In fact, the lipid monolayer may not adjust readily to an expanding mercury drop, especially if it incorporates a lipophilic substance capable of decreasing its fluidity. The drop is formed after positioning the HMDE about 0.2 mm above the lipid film previously spread on the aqueous electrolyte [5]. As the drop touches the film following its growth, it is covered almost completely by a self-assembled lipid monolayer, while its neck remains in contact with the lipid reservoir previously spread on the surface of the aqueous electrolyte. A variant of this procedure was later adopted by

Nelson and coworkers [9, 10]: a commercial HMDE was used to form a mercury drop in a nitrogen atmosphere above a lipid film spread on an aqueous electrolyte in an amount $>0.3\ \mu g\ cm^{-2}$, corresponding to about three monolayers; the drop was then slowly immersed in the electrolyte across the lipid film. This procedure gives rise to a self-assembled phospholipid monolayer supported by mercury. A special home-made HMDE that uses an oleodynamic system for moving the electrode vertically inside a water-jacketed box and extrudes stationary drops maintaining a constant area for periods of up to 90 minutes, with a reproducibility better than 1%, was described by Moncelli and Becucci [11]. The transfer of a lipid monolayer on this electrode provides differential capacity values with an accuracy better than $0.02\ \mu F\ cm^{-2}$. A simple procedure for measuring the charge density σ_M on the surface of a lipid-coated mercury electrode consists in contracting the lipid-coated drop while keeping its neck in contact with the lipid reservoir spread at the water/argon interface [12]. This procedure, which exploits the free exchange of lipid material between the lipid monolayer that coats the mercury drop and the lipid film spread on the solution, ensures that the monolayer maintains its properties, including its thickness, as the drop is contracted. The charge following the contraction divided by the decrease in drop area yields directly the charge density σ_M on the mercury surface. A further, more lengthy procedure to self-assemble a dioleoylphosphatidylcholine (DOPC) monolayer on an HMDE consists in keeping it immersed in an aqueous dispersion of DOPC liposomes for about 15 minutes, while scanning the potential repeatedly from -0.4 to -0.7 V/SCE until a constant value of $1.85\ \mu F\ cm^{-2}$ is attained [13].

1.3.1.2.2 **Structure and Physical Properties of Phospholipid SAMs on Hg**

1.3.1.2.2.1 **Differential Capacity of Phospholipid SAMs on Hg** The differential capacity of a self-assembled DOPC monolayer attains a constant minimum value over a potential range from -0.15 to -0.7 V/SCE (Fig. 1); this value, which amounts to $\sim 1.8\ \mu F\ cm^{-2}$, is not affected by changes in pH, temperature, ionic strength, and nature of the electrolyte. The value of the minimum capacity and its potential range vary slightly with the nature of the phospholipid. Thus, with dioleoylphosphatidylethanolamine (DOPE) the minimum capacity amounts to $\sim 1.7\ \mu F\ cm^{-2}$ and ranges from -0.15 to -0.9 V/SCE, whereas with dioleoylphosphatidylserine (DOPS) it decreases from 1.9 to $1.6\ \mu F\ cm^{-2}$ as the pH passes from 8 to 2.3 [14]. At positive potentials the region of minimum capacity is delimited by a capacity increase that precedes mercury oxidation; at negative potentials this region is delimited by two sharp peaks that lie at about -0.9 and -1.0 V (peaks 1 and 2 in Fig. 1) and by a third peak at about -1.35 V in the case of DOPC. With dimyristoyl phosphatidylcholine (PC) and bovine phosphatidylserine (PS), peaks 1 and 2 are replaced by a single peak [14]. Lipids that are not in the liquid-crystalline state cannot be transferred satisfactorily to the mercury drop because of lack of fluidity. Thus, dipalmitoyl PS, whose transition temperature from the gel to the liquid-crystalline state is about $42\,^{\circ}C$, can be transferred to mercury only at higher temperatures [9]. If the area of a lipid-coated HMDE is expanded while keeping it immersed in the aqueous electrolyte, the minimum capacity varies proportionally to the drop area A [9, 15]. Since under these conditions the film expansion maintains the amount of lipid material on the

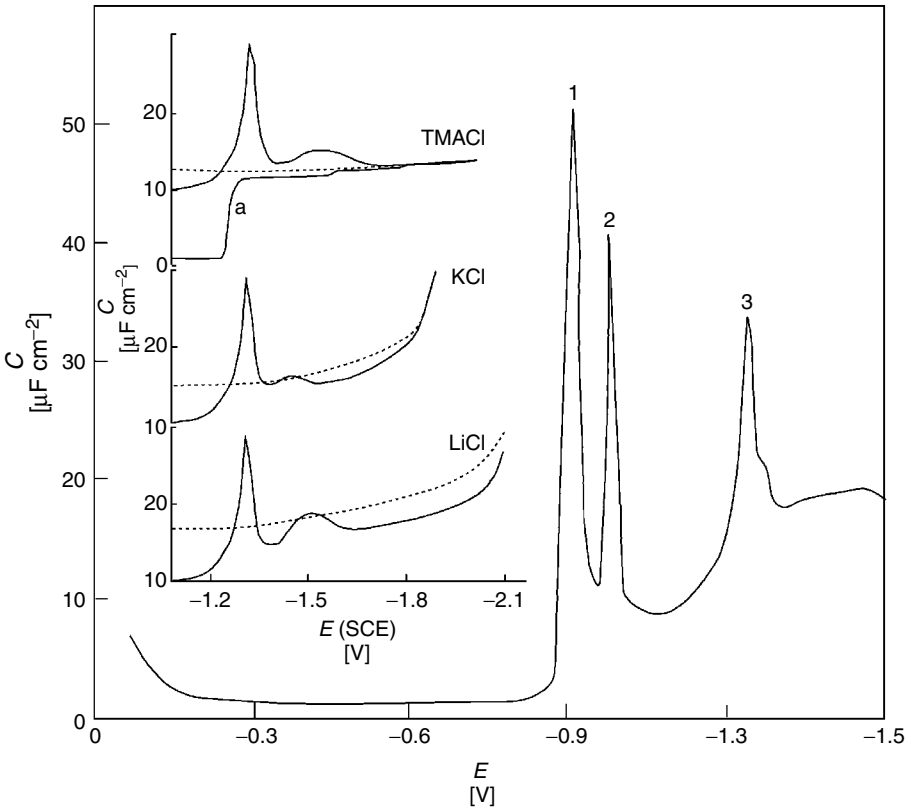


Fig. 1 Curve of the differential capacity C versus potential E for DOPC-coated mercury in 0.1 M KCl. The inset shows C versus E curves for bare (dashed line) and DOPC-coated (solid line) mercury in 0.1 M solutions of TMACl, KCl, and LiCl [16].

drop surface constant, this behavior can be explained by assuming that the drop expansion causes a progressive tilt of the lipid molecules, without incorporation of water into the lipid monolayer, and hence without altering the dielectric constant ε of the film. The capacity C of the film can be approximately expressed by the Helmholtz formula, $\varepsilon_0\varepsilon/d$, for a parallel-plate capacitor, where d is the film thickness and ε_0 is the permittivity of the free space; noting that, for a constant volume $V = Ad$ of the lipid material, A is inversely proportional to d, the direct proportionality between C and A requires the constancy of ε.

Peaks 1 and 2 of DOPC are capacitive in nature and are due to field-induced, two-dimensional phase transitions. A decrease in pH from 8 to 1 causes a positive shift in peak 1 and a negative shift in peak 2, whereas an increase in temperature from 5 to 60 °C shifts peaks 1 and 2 negatively and peak 3 positively [17]. A decrease in ionic strength broadens the potential range of the capacity minimum by shifting peaks 1 and 2 negatively and the capacity rise at the more positive potentials positively. At constant ionic strength, the latter capacity rise is shifted negatively by those anions that are more strongly adsorbed on Hg, such as

bromide and iodide ions, probably because of a competition with the lipid for the metal surface. On the other hand, peak 1 shifts positively in response to the electrolyte cation in the order: $Ca^{2+} = Mg^{2+} > Li^{+} > Na^{+} > K^{+} > Cs^{+}$, namely, in the order of the increasing binding of these cations to the phosphate group of the polar heads of the lipid.

The third peak in Fig. 1 exhibits hysteresis in the reverse potential scan [9] and is due to partial desorption of the lipid. Complete desorption takes place at potentials negative enough to cause a merging of the curve of the differential capacity C versus the applied potential E recorded on lipid-coated mercury with that obtained on bare mercury, under otherwise identical conditions. The inset of Fig. 1 shows C versus E plots in 0.1 M solutions of KCl, LiCl, and tetramethylammonium chloride (TMACl) both on bare and on DOPC-coated mercury [16]; the behavior in 0.1 M NaCl and CsCl is similar to that in 0.1 M KCl. The best overlap is attained in 0.1 M TMACl. The charge at a DOPC-coated mercury electrode which follows a chronocoulometric step from the pzc, −0.450 V/SCE, for bare Hg in 0.1 M TMACl, to a potential, −1.850 V/SCE, of total desorption in this electrolyte amounts to $Q = -22.4 \pm 0.1\ \mu C\ cm^{-2}$. By knowing the charge density, $-23.2 \pm 0.1\ \mu C\ cm^{-2}$, at −1.850 V/SCE on bare Hg from electrocapillary measurements [18], the charge density, $-23.2\ \mu C\ cm^{-2} - Q = -0.8 \pm 0.1\ \mu C\ cm^{-2}$, on DOPC-coated mercury at −0.450 V/SCE is obtained [16]. Therefore, coating Hg with a DOPC monolayer shifts the pzc toward positive values. This is due to the positive shift, $\Delta\chi$, in the surface dipole potential χ that accompanies such a coating, and that must be compensated for by a negative charge density on the metal to keep the applied potential on lipid-coated mercury at the same value as the pzc on bare mercury. In fact, the coating involves the removal of adsorbed water molecules, whose surface dipole potential amounts to ∼−100 mV [19] (negative toward the mercury), and their replacement by a PC monolayer, whose polar heads have a surface dipole potential of ∼+200 mV [20].

If a DOPC SAM obtained by the spreading procedure is subjected to a potential scan from the region of the flat capacity minimum to a potential just negative of peak 2 and the potential is then scanned back, peaks 1 and 2 and the capacity minimum are fully recovered [13]. On the other hand, if the potential is scanned beyond peak 3 (say, up to the desorption potential of −1.85 V/SCE) and is then scanned back, peak 3 is shifted positively and, most importantly, the capacity minimum is higher, revealing some defects upon readsorption. A different behavior is observed with SAMs obtained from DOPC vesicles. In this case, scanning the potential for the first time from the region of the capacity minimum to a potential just negative of peak 2 yields a capacity curve practically identical with that recorded with SAMs obtained by the spreading procedure; however, the subsequent backward scan exhibits smaller peaks 2 and 1 and a capacity minimum lower than the pristine one. If the potential is scanned from the capacity minimum beyond peak 3 and is then scanned back, no peaks are observed in the reverse scan and the pristine capacity minimum is substantially recovered. This difference in behavior is due to the constant presence of liposomes, which tend to heal the defects in the SAM, as they are formed at sufficiently negative potentials, and may also fuse with the SAM.

At potentials of complete lipid desorption, the lipid molecules remain in close proximity to the mercury surface for hours as positively charged micellar aggregates, and spread back readily on the electrode surface with a positive shift in potential [16, 21]. This desorption/readsorption process was imaged using epi-fluorescence microscopy and including a small amount of an amphiphilic fluorescent dye molecule in the lipid SAM [22]. On a Hg electrode, as distinct from a Au electrode, fluorescence can be detected even if the fluorophore is at a small distance from the electrode. In fact, the fluorescence quenching efficiency, due to nonradiative energy transfer to the electrode, is 2 to 3 orders of magnitude lower on Hg than on Au. Upon scanning the potential progressively in the negative direction up to film desorption, the fluorescence intensity maintains a constant low level along the flat capacity minimum; a large increase in fluorescence is observed at the far negative potentials, indicating a separation of the DOPC monolayer from the electrode surface. By scanning back the potential, the fluorescence decreases slowly down to the positive potential limit; neither the fluorescence nor the capacity recover the pristine value, denoting a defectively re-formed SAM. In contrast to a similar gold system [23], the fluorescent particles or aggregates on Hg are freely mobile, preventing an image analysis yielding their number density and size.

The inset in Fig. 1 shows that in 0.1 M LiCl the capacity remains constantly lower than that of bare mercury, even at far negative potentials at which complete desorption is observed with the other alkaline chlorides. A similar behavior is observed in the presence of Ca^{2+} [24], which is known to interact strongly with the phosphate groups of phospholipids. This indicates that, in the presence of Li^{+} or Ca^{2+}, the lipid aggregates are not completely detached from the negatively charged mercury surface even at the most negative potentials; this is probably to be ascribed to their high positive charge density, owing to the particularly strong interaction of the highly hydrated Li^{+} ion or of Ca^{2+} with the lipid film [25], which prevents the merging of the C versus E curve on PC-coated mercury with that on bare mercury. In particular, the presence of Ca^{2+} imparts a high stability to the SAM [24]; thus, upon scanning the potential back from −1.85 V/SCE, the pristine capacity minimum is recovered, in contrast to experiments in the absence of Ca^{2+}.

Impedance spectroscopy measurements
Electrochemical impedance spectroscopy is extensively employed for the investigation of SAMs because the broad range of frequencies covered by this technique (usually from 10^{-3} to 10^{5} Hz) may allow processes with different relaxation times taking place within the electrified interphase to be detected and sorted out. Unfortunately, the various relaxation times often differ by less than 2 orders of magnitude, thus requiring a certain amount of arbitrariness and of physical intuition for their separation. In fact, it is well known that the same impedance spectrum can often be equally well fitted to different equivalent circuits, which are consequently ascribed to different relaxation processes. Impedance spectra are frequently reported on a Y'/ω versus Y''/ω plot, where Y' and Y'' are the in-phase and quadrature components of the electrochemical admittance and ω is the angular frequency. This plot is particularly suitable for representing a series RC network. Thus, a series connection of R and C yields

a semicircle of radius $C/2$ in this plot, with center of coordinates ($Y''/\omega = C/2$; $Y'/\omega = 0$) and a maximum characterized by an ω value equal to $1/RC$.

Nelson and coworkers used a series RC network to fit the impedance spectra of a DOPC SAM on mercury in 0.1 M KCl over the potential range from the flat capacity minimum to peak 2 [26]. However, to account for all features of the spectra, they modified the expression of the admittance for a simple RC series circuit, $Y = [R + (1/i\omega C)]^{-1}$, by introducing two constant phase elements (CPEs) in place of $i\omega C$:

$$Y = \left\{ R + 1 \Big/ \left[A(i\omega)^{\beta} \left(\frac{C_s - C_{inf}}{1 + B(i\omega)^{\alpha}} + C_{inf} \right) \right] \right\}^{-1} \quad (1)$$

Here, C_s and C_{inf} are capacities in the low- and high-frequency limits, respectively. Incidentally, a CPE is an empirical admittance function of the type $A(i\omega)^{\alpha}$, which reduces to a pure conductance, $A = 1/R$, when $\alpha = 0$ and to a pure capacity when $\alpha = 1$; its use is justified if the relaxation time of the process under study is not single valued, but is distributed continuously around a mean [27]. In Eq. (1), a β value <1 was ascribed to a certain "roughness" at the interphase, while an α value <1 was ascribed to a continuous distribution of low-frequency relaxation phenomena. The physical significance of these two CPEs is not entirely clear. At any rate, over the potential range of the capacity minimum (i.e. between -0.4 and -0.7 V/SCE) both α and β were found to be very close to unity, thus denoting that the behavior of the SAM approaches that of a simple series RC network closely. Nelson and coworkers also analyzed the impedance spectra of DOPC-coated mercury in contact with different alkali metal chlorides with principal component analysis and regression [28].

To investigate the behavior of a DOPC SAM on mercury at its desorption potential of -1.85 V/SCE, Bizzotto et al. [24] compared the impedance spectrum of this SAM with that of a bare mercury electrode at the same potential using a less involved equivalent circuit; this consisted of the resistance, R_{sol}, of the solution adjacent to the film, with in series, the parallel arrangement of a capacity C_{dl} and of a CPE Q, namely, a $C_{dl}Q$ "mesh", simulating the film. At the desorption potential, the C_{dl} and Q elements are practically identical for the bare and the DOPC-coated mercury electrode, but the solution resistance R_{sol} is about 20% higher on the latter electrode. This apparently anomalous behavior was tentatively explained by the presence of a lipid layer at some separation from the water-coated electrode surface, at this negative desorption potential. This organic material, also revealed by epi-fluorescence measurements, is assumed to be sufficiently close to the electrode surface to slow down the migration of ions in response to the ac signal.

Setting a CPE in parallel with the film capacity C_{dl} has the effect of accounting for a depressed semicircular arc (namely, an arc whose center lies below the horizontal axis), a feature often encountered in the spectra of SAMs plotted in a Y'/ω versus Y''/ω diagram. Depressed arcs are also reported in spectra plotted in a Z'' versus Z' diagram (sometimes called a *Nyquist diagram*), where Z' and Z'' are the in-phase and quadrature components of the impedance $Z = 1/Y$. A depressed semicircular arc may be simulated by a

CPE in parallel with a capacity C, under the assumption that it is generated by a continuous distribution of relaxation processes around a mean [27]. However, a depressed semicircular arc may also be ascribed to a discrete number of relaxation processes whose time constants differ by 2 orders of magnitude or less. These relaxation processes may be attributed to the movement of ions across slabs with different dielectric properties composing the SAM. Roughly speaking, the movement of ions to and fro across each slab is accounted for by its resistance, while the accumulation of charges at its boundaries is accounted for by its capacity. In other words, each slab may be represented by an RC mesh (namely, a resistance R and a capacity C in parallel), and the whole SAM by an equivalent circuit consisting of a series of RC meshes. Such an equivalent circuit was adopted to interpret the impedance spectrum of a bilayer lipid membrane (BLM) [29], revealing the presence of three dielectric slabs, which were ascribed to the polar heads, the glycerol backbone, and the hydrocarbon tails.

A single RC mesh yields a semicircle with radius $R/2$ and center of coordinates ($Z' = R/2$, $Z'' = 0$) in a Z'' versus Z' diagram, while it yields a semicircle with radius $C/2$ and center of coordinates ($\omega Z'' = C/2$, $\omega Z' = 0$) in a $\omega Z'$ versus $\omega Z''$ diagram [30]. In both cases, the maximum of the semicircle corresponds to an angular frequency $\omega = 1/RC$. If we force an RC mesh to satisfy the equation for a semicircle in a Y'/ω versus Y''/ω diagram, we obtain a frequency-dependent radius equal to $C/2[1 + (\omega RC)^{-2}]$. Consequently, at frequencies that are not too low, an RC mesh yields a semicircle even in the Y'/ω versus Y''/ω plot. In practice, plotting the impedance spectrum in a $\omega Z'$ versus $\omega Z''$ diagram often allows a better separation of the different relaxation processes than plotting it in a Z'' versus Z' diagram. Figure 2 shows such a plot for a DOPC SAM on Hg in 0.1 M KCl at −0.55 V/SCE, in the

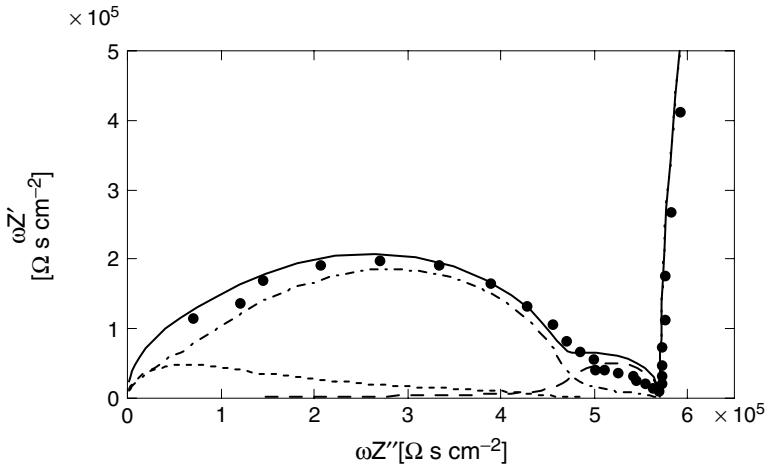


Fig. 2 Plot of $\omega Z'$ versus $\omega Z''$ for a DOPC SAM on Hg in 0.1 M KCl at −0.55 V/SCE [31]. The solid curve is the best fit of the experimental points to an equivalent circuit consisting of four RC meshes in series. The dashed curves represent the contributions of the four different RC meshes to the solid curve.

middle of the flat capacity minimum [31]. The plot is fitted to a series of four RC meshes, whose contributions are represented by the four dashed curves in the figure. Starting from the origin, the contributions follow each other in the order of decreasing relaxation times. In view of their R and C values, they can be ascribed, in the order, to the glycerol backbone, the hydrocarbon tails, the polar heads, and the aqueous solution adjacent to the film.

1.3.1.2.2.2 **Inhibitive Properties of Phospholipid SAMs on Hg** The electroreduction of the Cd(II), Cu(II), and Pb(II) ions to metal amalgam and that of the Eu(III) and V(III) ions to the divalent form, which on bare mercury occur over the potential range of the capacity minimum of the DOPC-coated mercury, are inhibited by the lipid monolayer and initiate at potentials somewhat positive of peak 1 [32]. This indicates that the phase transition responsible for peak 1 increases the permeability of the monolayer. The inhibition of the E(III)/Eu(II) and V(III)/V(II) electrode reaction indicates that no electron tunneling can occur across the lipid film, at least over the potential range of its stability. The hydrated Cd(II) ion permeates the monolayer more easily than the chloro and sulfate complexes. On the other hand, polarizable anions such as bromide and iodide facilitate Cd(II) reduction and Cd(Hg) oxidation to the extent with which they penetrate the monolayer at more positive potentials. The current for Cu(II) reduction along the foot of the wave inhibited by the lipid monolayer is independent of time, denoting exclusive control by the penetration of the ion across the film [32]. At potentials approaching peak 1 the current decreases in time, and its decay is interpreted on the basis of a model in which the permeable areas in the defective lipid film are regarded as forming an array of regularly distributed microelectrodes [21]. Phospholipid films inhibit the two-electron reduction of O_2 to H_2O_2 [10], even though O_2 can penetrate these films. However, in the presence of substances such as furosemide, whose incorporation makes the lipid film permeable to hydrogen ions, such an electroreduction can take place [33].

1.3.1.2.2.3 **Modeling of Phospholipid SAMs on Hg** The experimental behavior of phospholipid monolayers on a metal substrate can be analyzed on the basis of a model of the membrane–solution interphase that accounts for the presence of any charged ionizable groups buried well inside the polar head region and is schematically depicted in Fig. 3 [34]. In this model the potential difference $\Delta\phi$ across the metal–solution interface consists of the sum of the potential differences across the hydrocarbon tail region, the polar head region, and the diffuse-layer region. It can be written as:

$$\Delta\phi = \frac{\beta}{\varepsilon_0\varepsilon_\beta}\sigma_M + \frac{\gamma}{\varepsilon_0\varepsilon_\gamma}(\sigma_M + \sigma_{in}) - \frac{N\mu_{dip}}{\varepsilon_0\varepsilon_\gamma} + \phi_d(c, \sigma_{tot})$$
$$\text{with : } \sigma_{tot} \equiv \sigma_M + \sigma_{in} + \sigma_{ex} \qquad (2)$$

Here the first term is the potential difference across the hydrocarbon tail region, of thickness β and dielectric constant $\varepsilon_\beta \sim 2$, which depends on the charge density σ_M on the metal. The second term is the potential difference across the polar head region, of thickness γ and dielectric constant ε_γ, which depends upon the sum of σ_M and of the charge density σ_{in} of any charged

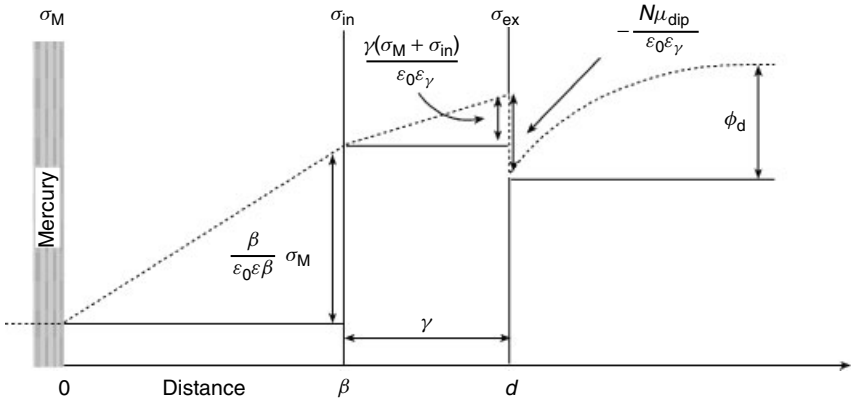


Fig. 3 Schematic diagram of the model for a lipid monolayer deposited on mercury. The dashed curve represents the profile of the average potential against the distance from the mercury surface. The diffuse-layer thickness has been compressed with respect to the monolayer thickness, for ease of representation [34].

groups buried well inside the polar head region. The third term is the dipole potential due to the polar heads, where μ_{dip} is the dipole-moment normal component of the polar heads and N is their number per unit surface; this term also includes any contribution to the dipole potential from the orientation of the water molecules in direct contact with the polar heads. Finally, ϕ_d is the potential difference across the diffuse layer, which according to the Gouy–Chapman (GC) theory is a function of the electrolyte concentration c and of the whole charge density σ_{tot} experienced by the diffuse-layer ions, namely, the sum of σ_M, σ_{in} and the charge density σ_{ex} of any ionized groups directly exposed to the aqueous phase. Differentiation of Eq. (2) with respect to σ_M yields the following expression for the reciprocal of the differential capacity:

$$\frac{1}{C} = \frac{d\Delta\phi}{d\sigma_M} = \left(\frac{\beta}{\varepsilon_0 \varepsilon_\beta} + \frac{\gamma}{\varepsilon_0 \varepsilon_\gamma}\right) + \frac{\gamma}{\varepsilon_0 \varepsilon_\gamma}\frac{d\sigma_{in}}{d\sigma_M} + \frac{d\phi_d}{d\sigma_{tot}}\left(1 + \frac{d\sigma_{in}}{d\sigma_M} + \frac{d\sigma_{ex}}{d\sigma_M}\right) \quad (3)$$

under the reasonable assumption that μ_{dip} is practically insensitive to the small changes in σ_M. In fact, σ_M assumes values from -0.2 to $-0.5\ \mu C\ cm^{-2}$ under usual experimental conditions, with the major changes in σ_{tot} being due to σ_{in} end σ_{ex} as a consequence of a change in pH. $d\phi_d/d\sigma_{tot}$ is expressed by the GC theory. The charges σ_{in} and σ_{ex} of the ionizable groups are considered to depend on the corresponding protonation constants K_{in} and K_{ex} according to Langmuir isotherms:

$$\sigma_j = \sigma_j^{max}\frac{K_j[H^+]}{1 + K_j[H^+]};$$

$$\sigma_j = \sigma_j^{max}\frac{1}{1 + K_j[H^+]};$$

$$[H^+] = e^{-F\phi_j/(RT)}$$

$$\text{for } j = \text{in}\ ;\ \phi_j = \phi_{x=\beta}$$

$$\text{for } j = \text{ex}\ ;\ \phi_j = \phi_d \quad (4)$$

Here σ_j^{max} is the charge density corresponding to the fully ionized jth group, which is positive in the first expression of Eq. (4) and negative in the second.

For lipids with no ionizable groups buried inside the hydrocarbon tail region ($\sigma_{in} = 0$), the differential capacity takes the simple form:

$$\frac{1}{C} = \frac{1}{C_m} + \frac{d\phi_d}{d\sigma_{tot}}\left(1 + \frac{d\sigma_{ex}}{d\sigma_M}\right)$$

$$\text{with : } C_m = \left[\left(\frac{\beta}{\varepsilon_0\varepsilon_\beta} + \frac{\gamma}{\varepsilon_0\varepsilon_\gamma}\right)\right]^{-1} \quad (5)$$

Here C_m is the capacity of the lipid monolayer, which for dioleoylphospholipids can be accurately estimated at 1.7 μF cm^{-2}; σ_{ex} depends upon σ_M only through the diffuse-layer potential difference ϕ_d. Fitting the small changes in C with varying the concentration of the 1,1-valent electrolyte KCl at different pH values to Eq. (5), with σ_{ex} expressed by Eq. (4), yields a pK_a value of 0.5 for the phosphate group of DOPE and of 0.8 for that of DOPC [35].

The behavior of DOPS is more involved, since its phosphate group is buried somewhere inside the polar head region, while the carboxyl and ammonium groups are more exposed to the aqueous phase. The more general expression of Eq. (3) was therefore adopted, with σ_{in} equated to the charge density of the phosphate group. The fitting to Eq. (3), with σ_{in} and σ_{ex} expressed by Eq. (4), requires not only the measurement of C as a function of the KCl concentration and of pH but also that of σ_M as a function of pH; the latter measurement was carried out by the procedure based on the contraction of the lipid-coated mercury drop [12]. It was concluded that the overall charge density, $\sigma_{in} + \sigma_{ex}$, of a DOPS monolayer varies from slightly negative to slightly positive values as the bulk pH of the bathing solution is varied from 7 to 4 [34]. Analogously, the overall charge density of a dioleoylphosphatidic acid (DOPA) monolayer passes from negative to positive values as the pH is varied from 4 to 1.5. Once the charge densities σ_M, σ_{in}, σ_{ex} of DOPS and DOPA are determined at different pH values and at a constant applied potential E, Eq. (2) allows the surface dipole potential $\chi \equiv -N\mu_{dip}/\varepsilon_0\varepsilon_\gamma$ to be estimated as a function of σ_{tot}, apart from an additive constant. In fact, $\phi_d(c, \sigma_{tot})$ can be calculated from the GC theory, while $\Delta\phi$ differs from E by an unknown constant that depends exclusively on the choice of the reference electrode. The plot of (χ + constant) versus ($\sigma_{in} + \sigma_{ex}$) for DOPS and DOPA, shown in Fig. 4, exhibits a sigmoidal shape, with the maximum slope lying at $(\sigma_{in} + \sigma_{ex}) = 0$. This plot is reminiscent of the surface dipole potential χ_w because of the gradual alignment of the water molecules adjacent to the surface of a bare metal along the direction of the electric field created by the charge density on the metal [36]; this strongly suggests that the change in χ with varying the overall charge density of the DOPS and DOPA monolayers is mainly to be ascribed to the reorientation of the water molecules in contact with the polar heads.

To estimate the whole surface dipole potential χ, a property of phospholipid monolayers in the liquid-crystalline state at room temperature was exploited, namely, the possibility of increasing their initial area A by over 3 times by expanding the supporting mercury drop completely immersed in the aqueous electrolyte, without incorporation of water into the monolayer [15]. During the gradual drop expansion, the lipid molecules must progressively increase their tilt and decrease their number N per unit surface, so as to continue covering the whole drop surface. Denoting by θ the angle formed by the axis of the tilted lipid molecules with the normal

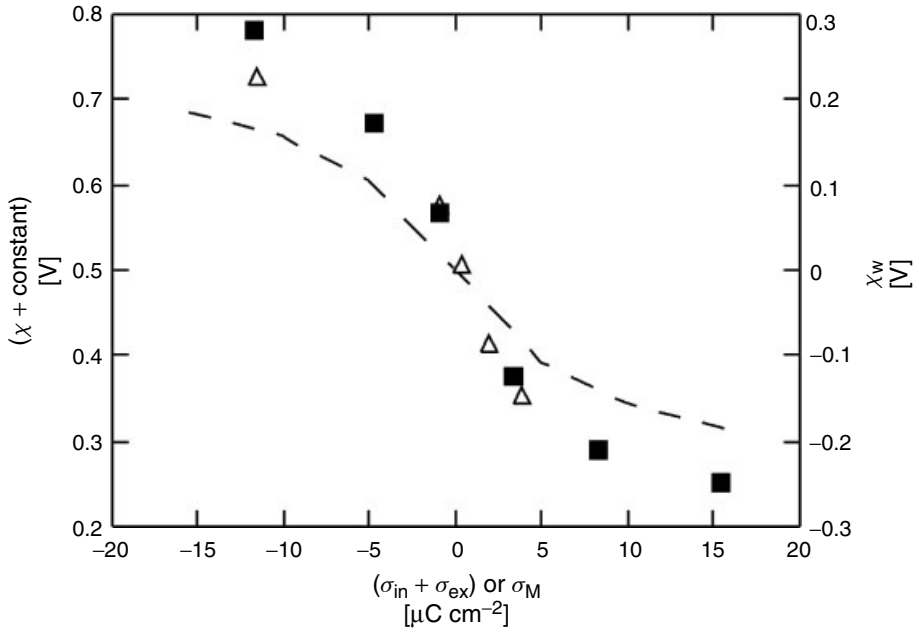


Fig. 4 Plots of (χ + constant) versus ($\sigma_{in} + \sigma_{ex}$) for DOPS (■) and DOPA (△) self-assembled monolayers at −0.50 V/SCE in buffered solutions of 0.1 M KCl [24]. For comparison, the dashed line is a curve of χ_w against the charge density σ_M calculated by Damaskin and Frumkin [36] for a metal–water interface.

to the plane of the lipid monolayer, its cosine is just equal to the ratio, $A/A(\theta)$, of the initial unexpanded area A of the film to the final expanded one, $A(\theta)$. Moreover, the number N of lipid molecules per unit surface, the dipole-moment normal component μ_{dip} of their polar heads, the charge densities σ_{in} and σ_{ex} due to the ionized groups of the polar heads, and the thickness β and γ of the hydrocarbon tail and polar head regions, after drop expansion will all be equal to their initial values times cos θ. Recalling that the potential difference $\Delta\phi$ across the whole interface before the expansion has the form of Eq. (2) and considering how the various parameters in this equation change following the expansion, the potential difference after the expansion will take the form:

$$\Delta\phi = \frac{\sigma_M(\theta)}{C_m}\cos\,\theta + \frac{\gamma}{\varepsilon_0\varepsilon_\gamma}\sigma_{in}\cos^2\theta - \frac{N\mu_{dip}}{\varepsilon_0\varepsilon_\gamma}\cos^2\theta + \phi_d(c,\ \sigma_{tot}\cos\theta)$$

or, after rearrangement:

$$\frac{\sigma_M(\theta)\cos\theta}{C_m} + \phi_d(c,\ \sigma_{tot}\cos\theta) = \left(\frac{N\mu_{dip}}{\varepsilon_0\varepsilon_\gamma} - \frac{\gamma}{\varepsilon_0\varepsilon_\gamma}\sigma_{in}\right)\cos^2\theta - \Delta\phi \qquad (6)$$

The charge density $\sigma_M(\theta)$ on the metal as a function of θ in Eq. (6) can be estimated by noting that the charge $Q(\theta)$ following

the drop expansion is clearly equal to:

$$Q(\theta) = \sigma_M(\theta)A(\theta) - \sigma_M A \qquad (7)$$

$Q(\theta)$ is obtained by measuring the charge that follows the expansion of a lipid-coated mercury drop with the drop completely immersed in the aqueous electrolyte, whereas the charge density σ_M on the unexpanded film is obtained as already described, by measuring the charge following the contraction of a lipid-coated mercury drop while keeping its neck in contact with the lipid film spread on the surface of the aqueous electrolyte [12]. By estimating the potential difference ϕ_d across the diffuse layer as a function of θ by the use of the GC theory, the whole left-hand side of Eq. (6) can be measured as a function of θ. By plotting this quantity against $\cos^2\theta$ at a constant applied potential $\Delta\phi$, a straight line is obtained, whose slope is equal to the surface dipole potential minus the potential difference across the polar head region created by any charged groups buried in this region.

The slopes of the plots for DOPC and DOPS at those pH values at which these monolayers are neutral are similar, and yield a dipole potential of +140−+150 mV, positive toward the interior of the film. Conversely, the dipole potential for DOPA is much smaller, +30 mV [15]. The DOPS and DOPC monolayers having very similar surface dipole potentials indicate that this potential is not to be ascribed to the serine or choline group of their polar heads, but rather to a group common to these two lipids and buried deeper inside the polar head region. This can be reasonably identified with the glycerol backbone. This also explains the low value of the dipole potential of DOPA, whose polar head consists of the sole phosphate group and whose glycerol backbone is, therefore, exposed to the aqueous phase and effectively screened by the water molecules. At the higher pH values at which the polar heads of DOPS and DOPA become progressively more negative, their surface dipole potential values estimated from Eq. (6) become progressively more positive. If we subtract from these values the contribution from water reorientation, as estimated from Fig. 4 by setting $\chi = 0$ for $(\sigma_{in} + \sigma_{ex}) = 0$, we obtain values close to those directly calculated from the neutral DOPS and DOPA monolayers. This indicates that the dipole potential in phospholipids consists of two main contributions: a contribution from the glycerol backbone, which amounts to about +150 mV and is positive toward the interior, and a further contribution from the orientation of the adsorbed water molecules, which is small on a neutral lipid monolayer and becomes progressively more positive with an increase in the negative charge on the polar heads of the lipid.

Application of Eq. (2) to a DOPC SAM, which does not contain ionizable groups inside the hydrocarbon tail region ($\sigma_{in} = 0$), allows an extrathermodynamic estimation of the absolute potential difference, $\Delta\phi$, across the whole mercury−aqueous solution interphase [37]. Upon ignoring the small potential difference, ϕ_d, across the diffuse layer, Eq. (2) can be written as follows:

$$\Delta\phi = \frac{\sigma_M}{C_m} + \chi_m \text{ with } : \chi_m = -\frac{N\mu_{dip}}{\varepsilon_0\varepsilon_\gamma} \qquad (8)$$

where χ_m is the surface dipole potential of the polar heads and the capacity C_m of the lipid SAM is given by Eq. (5). $\Delta\phi$ includes the dipole potential due to the electron spillover, which, however, can be regarded as constant in view of its small rate of change with a change in the charge

density σ_M on the metal. Both σ_M and C_m in Eq. (8) are experimentally accessible and thermodynamically significant. Thus, C_m on DOPC-mercury equals $1.8\,\mu F\,cm^{-2}$, while σ_M equals $-0.8 \pm 0.1\,\mu C\,cm^{-2}$ at -0.450 V/SCE (see Sect. 1.1.3.2.2.1 and Ref. 16). Moreover, the dipole potential χ_m due to the oriented polar heads of a DOPC monolayer, as estimated by different procedures both on BLMs and on a mercury electrode [15, 20], has been reported to assume values ranging from $+150$ and $+250$ mV, positive toward the hydrocarbon tails. Upon ascribing to χ_m an average value of $+200$ mV, Eq. (8) can be written:

$$\begin{aligned}\Delta\phi(-0.450\ \text{V/SCE}) &= \frac{\sigma_M}{C_m} + \chi_m \\ &= \frac{-0.80\ \mu C\,cm^{-2}}{1.8\ \mu F\,cm^{-2}} + (0.200 \pm 0.050)\text{V} \\ &\cong -(250 \pm 50)\text{mV} \qquad (9)\end{aligned}$$

It follows that the absolute potential difference $\Delta\phi$ between mercury and the aqueous phase can be obtained by increasing the applied potential E measured versus the SCE by about 250 mV.

The adsorption isotherm of lipids monolayers and the reorientation peaks Leermakers and Nelson [38] determined the adsorption isotherm of lipid monolayers on a metal substrate by an approximate statistical treatment of a lattice model in which apolar water monomers and segments of heads and tails of the lipid molecules interact with each other and with the substrate; the interactions of the water monomers and of the lipid head segments with the substrate are considered to become progressively more attractive with an increase in the absolute value of the interfacial electric field, in view of their polarizability. The model predicts the tails in contact with the metal and the heads exposed to the aqueous phase along the flat capacity minimum. A negative shift in the applied potential causes an increasing attraction of the heads for the substrate. Competition of the heads (and, to a minor extent, of the water monomers) with the tails for the substrate causes a displacement of tail segments by head segments at potentials at which the tail segments still have a higher affinity for the substrate compared to water. This gives rise to a inhomogeneous layer of two phases consisting of a thin lipid bilayer and of a thin lipid monolayer, both incorporating some water molecules: in the thin bilayer the tails of the lipid molecules are directed toward each other. This transition is regarded as responsible for peak 1. At still more negative potentials the affinity of the tails for the substrate is overtaken by that of the water molecules. In view of the constant amount of lipid molecules on the surface of the mercury drop, this leads to one-half of the drop surface almost exclusively covered by water and the other half covered by a lipid bilayer. This further transition is regarded as responsible for peak 2. If the affinity of the tail segments for the substrate is not particularly high, at sufficiently negative potentials head segments and water monomers displace the tail segments from the surface in a single transition, giving rise to a single peak due to a direct passage from a lipid monolayer to patches of lipid bilayer and of water covered areas. According to the authors [38], this may explain the merging of peaks 1 and 2 into a single peak and a decrease in the potential range of the flat capacity minimum in passing from dioleoyl phosphatidylcholine to dipalmitoyl phosphatidylcholine and to dimyristoyl phosphatidylcholine, under the reasonable assumption that an increase in the hydrocarbon chain length and the presence of

C=C double bonds enhance the hydrophobicity of the tails, and hence their affinity for mercury. At any rate, even assuming that the lipid molecules tend to form a lipid bilayer along peak 2, such a bilayer must be somewhat disorganized and permeable to water. In fact, by keeping the neck of the lipid-coated mercury drop in contact with a lipid film spread on the surface of an aqueous electrolyte at potentials slightly negative of peak 2, the differential capacity remains much higher than the value, 0.7–0.8 μF cm^{-2}, expected for a compact lipid bilayer, even though the lipid material required for the formation of a lipid bilayer covering the whole drop surface is now available [12].

The current transients obtained by stepping the potential across the potential range of peak 2 show a minimum followed by a maximum and by an exponential decay to zero [21]; the time dependence of the current satisfies the expression for an instantaneous nucleation and growth process, and was ascribed to the growth and coalescence of the preexisting defects formed along peak 1.

1.3.1.2.3 Incorporation of Lipophilic Molecules in Phospholipid SAMs on Hg

1.3.1.2.3.1 Electroinactive Compounds

Electroinactive neutral compounds As a rule, incorporation of neutral hydrophobic organic compounds, such as polynuclear aromatic hydrocarbons [39], polychlorinated biphenyls, and phenothiazine [40] into DOPC monolayers on Hg causes a negative shift and a depression of peaks 1 and 2, which is often accompanied by a slight decrease in the differential capacity minimum. This effect becomes more pronounced with an increase in the aromaticity and hydrophobicity of the compound. Thus, while the effect of benzene and naphthalene is negligible, it becomes appreciable with hydrocarbons with three, four or five aromatic rings [41]. Hydrophobicity alone, as measured, say, by the octanol/water partition coefficient, is not sufficient to explain this effect; thus, undecane and dodecane have a high partition coefficient but no observable effect on lipid monolayers. The hydrophobic compounds may be adsorbed in the film from very dilute aqueous solutions or else by spreading a mixed solution of the compound and of the lipid in pentane on the surface of the electrolyte and by transferring the mixture to an HMDE. In the latter case the mole fraction of the compound in the film is known, and by comparing the response of the film so obtained with that obtained by slow equilibration of a lipid-coated electrode with an aqueous solution of the compound, the adsorption isotherm of the given compound can be obtained.

The negative shift in the capacity peaks increases with the bulk concentration of the compound first linearly, but then tends to attain a limiting value. Planar polyaromatic molecules intercalate more easily between the lipid tails than the nonplanar, twisted ones, and hence are more effective in shifting the peak potentials in the negative direction. Thus, 4-monochlorobiphenyl is more effective than 2-monochlorobiphenyl, whose structure is distorted by the steric hindrance of the ortho-chloro substituent [40]. Both the above chlorinated biphenyls are more effective than biphenyl because of their greater molecular polarizability.

The slight decrease in the flat capacity minimum, which is often observed with an increase in the bulk concentration of these compounds, is probably to be ascribed to a thickening of the film following their incorporation in the lipid monolayer; this should more than compensate for the expected increase in capacity stemming

from the higher dielectric constant of aromatic compounds compared to that, ≈2, of the lipid tails. The concomitant decrease in the height of the reorientation peaks 1 and 2 and their broadening are due to a decrease in the cooperativity of the reorientation of the lipid molecules, caused by the intercalation of the foreign molecules.

Adsorption of neutral molecules in the polar head region may appreciably alter its surface dipole potential. The resulting change $\Delta\chi$ in χ can be determined from Eqs (2) and (5) by measuring the change $\Delta\sigma_M$ in σ_M that accompanies this adsorption at constant applied potential $E = \Delta\phi + \text{constant}$. With DOPC monolayers, σ_{in} equals zero, and the changes in $\phi_d(c, \sigma_{tot})$ that accompany the small changes in σ_M are negligibly small. Hence $\Delta\chi = -\Delta(N\mu_{dip}/\varepsilon_0\varepsilon_\gamma)$ is practically equal to $-\Delta\sigma_M/C_m$, where $C_m = 1.7\ \mu F\ cm^{-2}$ is the capacity of the DOPC monolayer (see Eq. 8). It was thus shown that the so-called hybrid polar compounds produce a positive shift in the surface dipole potential of phospholipid monolayers [42], an effect that can explain why compounds with such different structures may act as powerful inducers of terminal differentiation of various types of tumors.

6-Ketocholestanol (KC), a steroid that differs from cholesterol mainly by the presence of a carbonyl group, was reported to form pores inside a mercury-supported DOPC SAM by a mechanism of nucleation and growth similar to that of a number of channel-forming peptides [43]. The potential steps responsible for pore formation by KC molecules give rise to the potentiostatic charge versus time curves shown in Fig. 5, whose sigmoidal shape reveals two consecutive two-dimensional phase transitions. These transitions are characterized by an increased flow of negative capacitive charge and by a concomitant increased separation between consecutive charge versus time curves in Fig. 5. At potentials positive of −0.250 V/SCE, the differential capacity of a DOPC SAM containing 33 mol% KC is as low as 1.2 μF cm^{-2}. Under these conditions, the DOPC and KC molecules are expected to be randomly distributed within the monolayer, and KC has the same effect as cholesterol in increasing the rigidity of the film and decreasing its differential

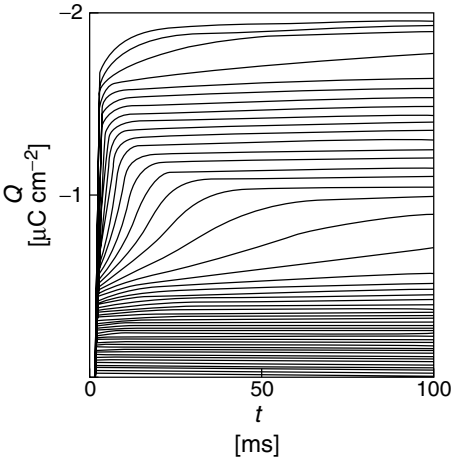


Fig. 5 Charge versus time curves following a series of potential steps from a fixed initial potential $E_i = -0.250$ V to final potentials E varying by −10 mV increments from −0.250 to −0.750 V on a mercury electrode coated with a lipid monolayer consisting of 67 mol% DOPC + 33 mol% KC and immersed in aqueous 0.1 M KCl [43].

capacity. The first phase transition is ascribed to an increase in the alignment of the KC dipoles along the direction of the interfacial electric field, with the oxygen of the carbonyl group more fully turned toward the aqueous solution. This charge movement causes a positive shift in the potential difference across the lipid monolayer, as measured from the metal toward the solution. At constant applied potential, this shift is compensated for by a flow of electrons to the mercury surface along the external circuit. This causes the increase in negative charge that characterizes the first two-dimensional phase transition. The increase in differential capacity from 1.2 to 6.5 $\mu F\ cm^{-2}$ observed over the potential range between the two phase transitions is ascribed to the first phase transition giving rise to bundles of KC molecules, with the oxygens turned toward the interior of the bundles. In these hydrophilic pores the inorganic ions can move back and forth following the ac signal, causing an increase in differential capacity. The decrease in differential capacity from 6.5 to 1.8 $\mu F\ cm^{-2}$ after the second phase transition suggests that this transition involves the disruption of the pores and a return to a random distribution of DOPC and KC molecules within the mixed monolayer. The permeability of the lipid film to Tl^+ ions induced by the first phase transition, and its abrupt decrease induced by the second phase transition, support the formation and subsequent disruption of pores across the lipid monolayer.

Lipophilic ions As a rule, lipophilic ions tend to permeate the lipid monolayer on the negative side of the region of the capacity minimum if cationic, and on the positive side if anionic. Such a permeation, which is due to electrostatic attraction for the charged electrode surface, causes a progressive increase in the differential capacity and a resulting narrowing of the region of the flat capacity minimum. The increase in capacity is ascribable to the charge displacement resulting from ion translocation from the polar heads to the mercury surface and backward across the hydrocarbon tail region, following the a.c. signal superimposed on the bias potential; it may also be partly due to a certain destabilization of the lipid film and to a resulting increase in its permeability. The effect of lipophilic ions on the capacity minimum is analogous to that of other lipophilic compounds and may be summarized as follows. If the compound is simply ''adsorbed'' on top of the lipid film or intercalated between the polar heads, it will not affect the tail region, whose capacity C_t is much lower than that of the head region and close to that, C_m, of the whole lipid monolayer. In this case the capacity, C_c, of the film of the compound will be in series with C_t, causing a decrease in the overall capacity $C \sim (C_t^{-1} + C_c^{-1})^{-1}$. In general, this decrease will be low, because the polarizability of the compound (and hence its C_c value) is higher than that of the lipid tails. While remaining merely adsorbed in the polar head region, the compound may also determine a condensation and an increase in the alignment of the lipid monolayer, resulting in its thickening and in a decrease in capacity. On the other hand, if the compound ''penetrates'' the tail region, the fraction θ of the electrode surface covered by the compound will have a capacity C_c higher than that, C_m, of the pure lipid domains. As a rough approximation and disregarding any edge effects at the boundary between the two different domains, the overall capacity is given by $C = \theta C_c + (1 - \theta) C_m$ and is, therefore, higher than that of the pure lipid film. The cationic phenothiazine

derivatives cause a moderate increase in the capacity minimum [40, 44]. The anionic diuretic furosemide causes an initial slight decrease in the capacity minimum at low bulk concentrations [33] and then an increase at higher concentrations [33, 44]. This may indicate that these anions start interacting with the polar heads at low concentrations, before penetrating the tail region at higher concentrations. All these ions depress and broaden peaks 1 and 2, just as neutral compounds.

Small lipophilic ions such as tetraphenylphosphonium ($TPhP^+$) and tetraphenylborate ($TPhB^-$) prefer to be located in the polar head region ($x \approx \beta$ in Fig. 3) and in direct contact with the electrode surface ($x \approx 0$) rather than in the much less polarizable intermediate hydrocarbon tail region. We can therefore envisage two potential energy wells for these ions at $x = 0$ and $x = \beta$, with a potential energy barrier in between [45]. The charge involved in a potential step from a potential negative (positive) enough for the anion (the cation) to be entirely located at $x = \beta$ to a potential positive (negative) enough to induce a complete translocation of the ion to $x = 0$, once decreased by the charge involved in the same potential step in the absence of the incorporated ion, yields directly the opposite of the charge density of the ion in the lipid film. This procedure allowed the determination of the adsorption isotherms of the $TPhP^+$ and $TPhB^-$ ions in DOPC and DOPS monolayers [45]. In interpreting these isotherms, discreteness-of-charge effects were considered.

Peptides and proteins The cationic antibiotic polymyxin narrows the minimum capacity region on the negative side and decreases the capacity minimum by $\sim 0.35\ \mu F\ cm^{-2}$ [46]. This indicates that this peptide does not penetrate the hydrocarbon tail region. Thrombin, which stimulates blood coagulation, results from the cleavage of the plasma protein prothrombin under the catalytic action of the prothrombinase complex in the presence of Ca^{2+} ions. This cleavage also yields two other molecular fractions of prothrombin, namely, fragment I and fragment II. It is generally assumed that prothrombin adheres to negatively charged membrane surfaces by Ca^{2+} bridges between the negative charges of PS and the γ-carboxyglutamic acid residues of fragment I of prothrombin. By adsorbing prothrombin on PS monolayers supported by mercury, Lecompte and Miller [6, 47] found, however, that appreciable adsorption is also obtained in the absence of Ca^{2+}. This indicates that hydrophobic interactions are also operative, in addition to electrostatic interactions. Thus, for instance, by complexing Ca^{2+} with EDTA, not all the prothrombin incorporated in a PS monolayer is displaced from the surface [5]. In the presence of prothrombin, the quadrature component of the electrode admittance shows a flat capacitive minimum at about -0.5 V versus Ag/AgCl. At more negative potentials this is followed by a rounded pseudocapacity peak due to the reduction of the charge-transfer complex, $(RS)_2Hg$ or $(RS)_2Hg_2$, which the cystine residues form with the mercury surface atoms at the most positive potentials. The cysteine resulting from such a reduction tends to desorb (see Sect. 1.1.3.3.2.2). Both the capacity minimum and the pseudocapacity peak increase with the prothrombin concentration until about $3\ \mu g\ cm^{-3}$, when the capacity minimum, C, attains the limiting value of $7\ \mu F\ cm^{-2}$. This value is attained at higher prothrombin bulk concentrations if Ca^{2+} is absent or if the pure PS

monolayer is replaced by a mixed monolayer of 75% PC and 25% PS. Expressing C by the equation $C = \theta C_p + (1 - \theta)C_m$, where C_m is the capacity of the pure lipid monolayer and $C_p \sim 14\ \mu F\ cm^{-2}$ is that of a pure protein monolayer, a limiting value of 0.4 is obtained for the surface coverage θ by the protein domain. The charge under the voltammetric peak for the reduction of $(RS)_2Hg$ at a PS monolayer points to a maximum value of 4 out of the 12 cysteine residues present in a prothrombin molecule, indicating that not all its electroactive groups have access to the electrode surface. While the separate fragment I exhibits a behavior similar to that of prothrombin, fragment II, and thrombin, which do not contain γ-carboxyglutamic acid residues and cannot attach to the negatively charged monolayers by Ca^{2+} bridges, are insensitive to the presence of Ca^{2+} and determine an increase in the capacity minimum only at higher bulk concentrations. The adsorption of prothrombin on PC monolayers is negligible, but it is appreciably increased in the presence of Ca^{2+} [5]; in this case the effect of Ca^{2+} may be due to a decrease in the charge and in the resulting electrostatic repulsion between adsorbed prothrombin molecules.

Lipoproteins are molecular aggregates that transport water-insoluble lipids in the blood plasma: they contain a core of neutral lipids, coated with a monolayer of phospholipids in which special proteins (apolipoproteins) and cholesterol are embedded. The interaction of apolipoprotein A-I with PC-coated mercury proceeds in steps when increasing progressively its bulk concentration, c_{A-I} [48]. For $c_{A-I} \leq 4\ \mu g\ cm^{-3}$ the differential capacity minimum C is not affected, but the concomitant decrease in the orientation peaks of PC points to an interaction of apoA-I with the polar heads of the lipid, possibly electrostatic, through its hydrophilic amino acids. With a further increase in c_{A-I} the plot of C versus c_{A-I} shows a first sigmoidal step, with a plateau at $\sim 4\ \mu F\ cm^{-2}$, which is then followed by a further sigmoidal step, with a plateau at $\sim 7.5\ \mu F\ cm^{-2}$. These C versus c_{A-I} steps correspond to two consecutive penetration steps into the hydrocarbon tail region, probably associated with two different conformational changes of apoA-I. Ten mole percent cholesterol in the PC monolayer suppresses the second penetration step, while 25 mol% suppresses both steps. This may be explained by the cholesterol molecules rigidifying the lipid monolayer, thereby preventing it from associating with some penetrating domains of apoA-I.

Ion channels are responsible for the flow of hydrophilic ions across biomembranes along their electrochemical potential gradient, namely, from the membrane side where the electrochemical potential of the ion is higher to that where it is lower (passive transport). A widely investigated ion channel is gramicidin, a linear pentadecapeptide with helical structure that turns its hydrophobic groups toward the exterior of the helix and its hydrophilic carboxyl groups toward the interior. The length of a gramicidin channel is of 13 Å, about one-half the thickness of a biomembrane. To span a biomembrane, two helical monomers of gramicidin form a helical dimer, with the N-terminals of the dimer interacting in the center of the membrane. The resulting hydrophilic pore allows the transport of monovalent cations, such as alkali metal ions, across the membrane.

The monomer of gramicidin incorporated in a mercury-supported phospholipid monolayer has been reported by Nelson to act as an ion channel toward Tl^+

ion, thus allowing its penetration across the monolayer and its electroreduction to thallium amalgam [49–54]. From a cyclic voltammetric and a chronoamperometric investigation of Tl^+ ion electroreduction through the gramicidin channel, Nelson proposed a CE mechanism, in which the rate-determining step is a preceding homogeneous chemical step associated with Tl^+ entry into the channel prior to Tl^+ electroreduction [51, 52]. This electrode process at a mercury-supported phospholipid monolayer incorporating gramicidin was employed by Nelson as a model system to probe the effect of lipid charge, solution composition, and incorporation of biologically active compounds on ion channel transport. Thus, it was shown that a negatively charged DOPS monolayer increases the rate of Tl^+ transport with respect to a neutral DOPC monolayer, while polyvalent cations, such as Mg^{2+} and Dy^{3+}, have an opposite effect [52]. This is ascribed to the electrostatic interaction of this charge with Tl^+ ions in the immediate vicinity of the lipid film, with a resulting influence on their local concentration. Incorporation of retinol in a gramicidin-modified DOPC monolayer accelerates Tl^+ transport, while incorporation of the aromatic pesticide dichlorodiphenyl trichloroethane (DDT) slows it down [51]. This is ascribed to the effect of these neutral compounds within the monolayer on the energy barrier to the translocation of the ion within the channel. Rueda and Nelson et al. [53] investigated Tl^+ electroreduction in gramicidin-modified DOPC monolayers on mercury by electrochemical impedance spectroscopy. The potential, E_{min}, of the minimum in the curve of the Warburg coefficient against potential was found to shift by 13 mV toward positive values with respect to the reversible half-wave potential for Tl^+ electroreduction at a bare mercury electrode. Since the CE mechanism previously proposed by Nelson [51, 52] predicts a negative shift in E_{min}, a CEC mechanism was postulated, which provides a satisfactory fit to the impedance spectroscopic data. The chemical step preceding the electrochemical step was again treated as homogeneous, while no interpretation was provided for the following chemical step. The same system was investigated by Becucci et al. [55] by the potential-step chronocoulometric technique. On a bare mercury electrode, the thallous ion is electroreduced to a thallium amalgam, giving rise to a sigmoidal curve of the chronocoulometric charge $Q(t, E)$ at constant $t = 100$ ms versus the final potential E, as shown in Fig. 6, curve a. Its rising section exhibits a Nernstian behavior and its plateau is exclusively controlled by diffusion. If the mercury electrode is coated with a phospholipid monolayer, the thallous ion cannot permeate the film and hence no reduction current is observed. If gramicidin is incorporated in the lipid monolayer, the sigmoidal charge versus potential curve for thallous reduction reappears (solid curve b in Fig. 6). The rising section still exhibits a Nernstian behavior, but the plateau is lower because it is controlled not only by diffusion but also by the rate of penetration of the thallous ions into the ion channel. This behavior can be explained quantitatively by a mechanism that includes the diffusion of the thallous ions toward the lipid film and a potential-independent ''heterogeneous'' step consisting in the dehydration of the ion and its binding to a site located at the mouth of the ion channel. The further step involving the surmounting of a potential energy barrier located somewhere in the middle of the channel is considered to be in quasiequilibrium, and hence its potential dependence is of the Nernstian type.

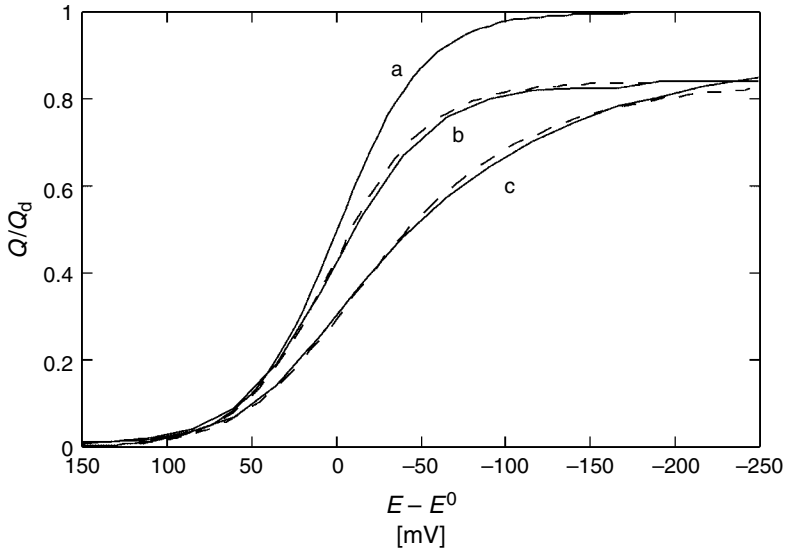


Fig. 6 Plots of the ratio of the chronocoulometric charge Q ($t = 100$ ms) to its diffusion limiting value Q_d against ($E - E^0$), obtained from a 0.1 M KCl aqueous solution containing 4×10^{-4} M $Tl^+ + 1.5 \times 10^{-7}$ M gramicidin by stepping from a fixed initial potential $E_i = -0.250$ V/SCE to progressively more negative potentials: (a) on bare mercury, (b) on mercury coated with a DOPC monolayer upon stirring to allow gramicidin incorporation, (c) on mercury coated with a DOPC monolayer containing 23 mol% 6-ketocholestanol upon stirring. The dashed curves were calculated on the basis of the mechanism outlined in the text [55].

Since the transfer of the thallous ion in direct contact with the metal surface to the mercury with amalgam formation is expected to be Nernstian, the dependence of the faradaic charge upon the overall applied potential E is also Nernstian. The mechanism predicts a plateau that is controlled partially by diffusion toward the film and partially by the binding step at the mouth of the channel; it also predicts a positive shift in the half-wave potential with respect to the formal potential, E^0, of the thallous ion/thallium amalgam couple by an amount equal to $(RT/F)\ln(Q_d/Q_l)$, where Q_d is the diffusion limiting charge and Q_l is the limiting charge in the presence of the gramicidin-modified DOPC film. This prediction agrees with experiment, as shown by the dashed curve b in Fig. 6, which was calculated on the basis of the above mechanism. More recently, Rueda and coworkers [56], by investigating this system by electrochemical impedance spectroscopy, postulated an additional homogeneous chemical step mimicking the deactivation and release of a Tl^+-gramicidin intermediate from the electrode surface, in competition with the surmounting of the potential energy barrier located within the channel.

Two lipophilic neutral molecules are commonly incorporated into membranes with the aim of altering their dipole potential, namely, phloretin, which creates a dipole potential negative toward the interior of the lipid film, and KC, which creates a dipole potential positive toward the interior, because of the presence of a carbonyl

group [57, 58]. As expected, incorporation of phloretin in the lipid monolayer containing gramicidin has no effect on the charge versus potential curve for thallous ion reduction [55]. In fact, the favorable dipole potential created by phloretin, negative toward the interior of the film, cannot accelerate the overcoming of the potential energy barrier more than predicted by a Nernstian-type behavior. Conversely, the unfavorable dipole potential, positive toward the interior of the film, created by incorporating 23 mol% KC in the DOPC monolayer, slows down this intermediate step by increasing the height of the potential energy barrier within the ion channel. This leads to a decrease in the rate constant for the surmounting of the barrier, which has the typical Butler–Volmer dependence upon the applied potential. This causes a drawing out of the charge versus potential curve for Tl^+ reduction. The solid curve c in Fig. 6 is the experimental $Q(t = 100\ \text{ms})$ versus $(E - E^0)$ curve, whereas the corresponding dashed curve was calculated on the basis of the pertinent mechanism.

1.3.1.2.3.2 **Electroactive Compounds** Retinal, the aldehydic form of vitamin A, is the light-absorbing molecule of the visual system of all organisms that possess image-producing eyes. A cyclic voltammetric investigation of retinal incorporated in mercury-supported phospholipid monolayers was carried out by Nelson [59]. Incorporation in a DOPC monolayer yields a single irreversible voltammetric peak that shifts by 62 mV toward more negative potentials per each unitary increment in pH and is tentatively ascribed to reduction to the corresponding alcohol, retinol. Incorporation of retinal in DOPS or DOPE monolayers causes the reduction peak to split into two. The more positive peak depends weakly on pH at pH values < 8 and is tentatively ascribed to the reduction of a Schiff base formed between retinal and the amino group of DOPS or DOPE. In fact, the Schiff base is known to be reduced at potentials more positive than the corresponding aldehyde and is expected to be mainly in the protonated form at pH values < 8, in view of its pK_a value of about 8.

Ubiquinone-10 (UQ) is an important, ubiquitous biomolecule that is present in many membranes and acts as a proton and electron carrier in the respiratory chain of the mitochondrial membrane. The mechanism of its reduction inside a phospholipid monolayer supported by mercury was investigated by carrying out a series of consecutive potential steps from a fixed initial value E_i, where UQ is still electroinactive, to progressively more negative potentials [60]. The charge $Q(t)$ following each potential step was recorded versus the time t elapsed from the instant of the step for 50 ms, after which the potential was stepped back to the initial value, where ubiquinol is completely reoxidized to UQ. Figure 7 shows a series of curves of the charge $Q(t)$ as a function of time for progressively more negative final potentials, as provided by a DOPC monolayer containing 1 mol% UQ. At the less negative potentials at which UQ is still electroinactive, the charge $Q(t)$ increases abruptly in less than 1 ms, owing to the flow of the capacitive current that is required to charge the interphase, and then remains constant in time. At more negative final potentials $Q(t)$ increases in time first abruptly, owing to the capacitive contribution, and then more slowly, because of the gradual electroreduction of UQ in time. With a further negative shift of the final potential, the rate

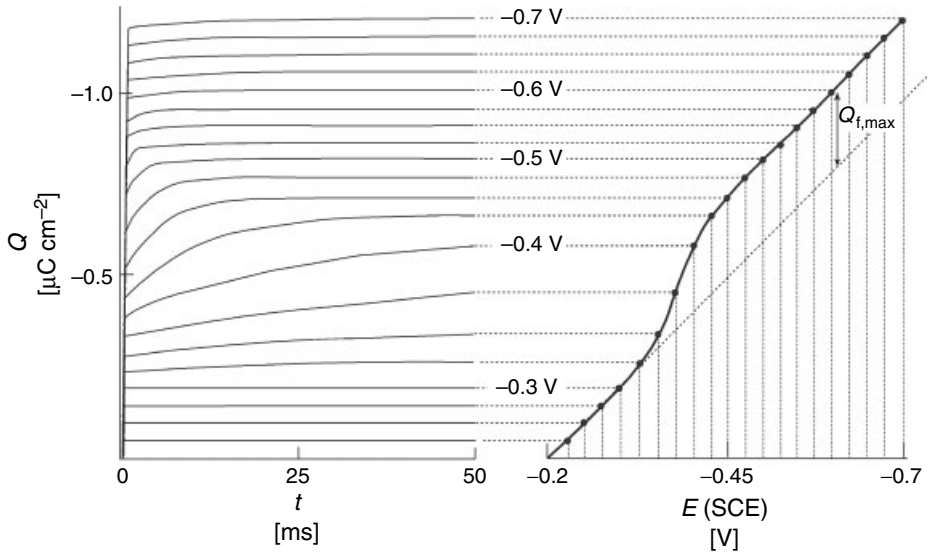


Fig. 7 The left-hand side of the figure shows $Q(t)$ versus t curves for 1 mol% UQ reduction in a 0.075 M borate buffer of pH 9.4, as obtained by stepping the potential from a fixed initial value $E_i = -0.200$ V/SCE to final values E varying from -0.225 to -0.700 V in 25 mV increments. The right-hand side shows the corresponding $Q(t = 50\ \text{mV})$ versus E curves [60].

of UQ electroreduction increases progressively, until ultimately the UQ incorporated in the lipid monolayer is completely reduced in less than 1 ms, after which $Q(t)$ becomes again independent of time. Plotting the charge $Q(t)$ at a constant electrolysis time, say 50 ms, against the applied potential yields a sigmoidal curve, with a rising portion preceded by a sloping foot and followed by a sloping plateau, as shown in Fig. 7. The foot and the plateau run practically parallel, and their common slope is a measure of the differential capacity of the lipid monolayer. The faradaic contribution, $Q_f(t)$, to $Q(t)$ due to the reduction of UQ is readily estimated by measuring the charge from the straight line obtained by extrapolation of the foot of the charge versus potential curve. The maximum limiting value $Q_{f,max}$ attained by $Q_f(t)$ measures the charge involved in the complete reduction of the UQ incorporated in the film and agrees with a two-electron reduction of UQ to UQH_2, for UQ concentrations in the lipid film < 1 mol%.

The charge versus time curves at different potentials and pH values allow the mechanism of UQ reduction to be clarified on the basis of a general approach. UQ reduction takes place via the reversible uptake of one electron yielding the UQ radical anion, $UQ^{-\bullet}$, followed by the rate-determining protonation of this radical anion yielding the corresponding neutral radical, $UQH^{\bullet}$:

$$UQ + e \xleftrightarrow{\text{Equilibrium}} UQ^{-\bullet}$$

$$[UQ]/[UQ^{-\bullet}] = \exp\left[\frac{F}{RT}(E - E^0)\right]$$

$$UQ^{-\bullet} + H^+ \xrightarrow{\text{r.d.s.}} UQH^{\bullet}$$

$$\text{Rate} = k[H^+][UQ^{-\bullet}] \qquad (10)$$

This rate-determining step is followed by the rapid uptake of a further electron and a further proton yielding the final product, ubiquinol. The rate of consumption of UQ is therefore proportional to the hydrogen ion concentration of the buffer solution adjacent to the lipid monolayer times the concentration of the $UQ^{-\bullet}$ radical anion; this can be expressed as a function of the UQ concentration, [UQ], via the Nernst equation as applied to the first electron-transfer step in quasiequilibrium. The resulting differential equation can be integrated by separation of variables between time $t = 0$, when $[UQ] = [UQ]_{in}$, and a given time t:

$$\frac{d[UQ]}{dt} = -k[H^+][UQ]e^{-\frac{F}{RT}(E-E^0)};$$

$$\int_{[UQ]_{in}}^{[UQ](t)} \frac{d[UQ]}{[UQ]} = -kt[H^+]\, e^{-\frac{F}{RT}(E-E^0)} \tag{11}$$

If the UQ concentration at the given time t, $[UQ](t)$, is kept constant, then the integral in Eq. (11) is also constant, and the same is true for the corresponding right-hand side. Keeping the right-hand side constant allows one to write it in such a way as to express the applied potential E as a function of electrolysis time t at constant pH, or else as a function of pH at constant t:

$$\frac{F}{2.3\ RT}E = \log t + \text{constant}$$

for constant $[H^+]$ and [UQ]

$$\frac{F}{2.3\ RT}E = -\text{pH} + \text{constant}$$

for constant t and [UQ] (12)

The UQ concentration at a given time t is kept constant if the faradaic charge $Q_f(t)$ that consumes the initial UQ concentration, $[UQ]_{in}$, is kept constant. Plotting $FE/(2.3\ RT)$ versus $\log t$ at constant pH and Q_f yields a roughly straight line of unit slope, and the same result is obtained by plotting $FE/(2.3\ RT)$ versus – pH at constant t and Q_f, in agreement with Eq. (12) and, therefore, with the mechanism of Eq. (10).

The oxidation of ubiquinol-10, UQH_2, incorporated in a DOPC monolayer was investigated by cyclic voltammetry using an approach perfectly analogous to that adopted for the above chronocoulometric measurements [61]. Thus, upon noting that the potential E_p of the voltammetric peak for UQH_2 oxidation practically corresponds to a constant faradaic charge Q_f, the quantity $FE_p/(2.3\ RT)$ was plotted against the logarithm of the scan rate, $\log v$, at constant pH as well as against – pH at constant v. The unit slope of both these plots points to the mechanism:

$$UQH_2 - e^- \longleftrightarrow UQH_2^{+\bullet};\ UQH_2^{+\bullet} + OH^- \xrightarrow{\text{rds}} UQH^\bullet + H_2O;$$

$$UQH^\bullet + OH^- - e^- \longleftrightarrow UQ + H_2O \tag{13}$$

A reversible uptake of the first transferring electron followed by a rate-determining protonation step, as in the case of UQ reduction (see Eq. 10), was also reported for the reduction of oxidized glutathione [62] and of diphenyl disulfide [63] incorporated in DOPC-coated mercury, on the basis of cyclic voltammograms yielding a unit slope for the plot of $FE_p/(2.3\ RT)$ versus – pH at constant v.

The chronocoulometric procedure employed for UQ was also adopted to study

the electrochemical behavior of vitamin K_1, an essential constituent for blood coagulation, upon incorporating this physiological quinone in a self-assembled DOPC monolayer supported by mercury [64]. The mechanism of K_1 reduction and that of oxidation of the corresponding quinol, K_1H_2, are analogous to those for the UQ/UQH_2 couple. The only difference is represented by the fact that, in K_1H_2 oxidation, the main proton acceptor involved in the rate-determining deprotonation of the $K_1H_2^{+\bullet}$ cation radical is H_2O, rather than OH^-. Consequently, the kinetics of K_1H_2 oxidation is independent of pH. The chronocoulometric procedure was also employed to study the electroreduction of the polyaromatic cation safranine [65] and that of the azocrown ether L16 to the corresponding hydrazo form [66], both incorporated in a Hg-supported DOPC monolayer. The data analysis, carried out on the basis of Eq. (12), points to a reversible electron-transfer step followed by a rate-determining protonation step, as in the case of UQ reduction.

Viologens are electroreduced in two pH-independent electron-transfer steps, $V^{2+} \rightarrow V^+$ and $V^+ \rightarrow V^0$. Chronocoulometric measurements on the lipophilic dioctadecylviologen $(C_{18})_2V^{2+}$ (henceforth briefly denoted by V^{2+}) incorporated in a DOPC monolayer, carried out by the same potential-step procedure adopted for UQ (see, e.g. Fig. 7), yield two sigmoidal waves in the plot of the charge $Q(t, E)$ against the applied potential E at constant electrolysis time $t = 100$ ms: the first chronocoulometric wave is three times higher than the second [67]. At V^{2+} concentrations less than 1 mol% the overall height of the two waves corresponds to the uptake of two electrons per V^{2+} molecule in the lipid monolayer. The plot of $\ln t$ versus $FE/(RT)$, as obtained from the $Q(t, E)$ versus t curves at different potentials E by keeping the faradaic charge constant at a value corresponding to the first Q versus E wave, is linear and exhibits a slope of 3. This slope can be rationalized on the basis of the mechanism:

$$V^{2+} + e \overset{E_1^0}{\longleftrightarrow} V^+;\ V^+ + e \overset{E_2^0}{\longleftrightarrow} V^0;$$

$$V^+ + V^0 \overset{\text{rds, } k}{\longrightarrow} V_2^+ \qquad (14)$$

where the first two elementary charge-transfer steps are in quasiequilibrium and the third one is a chemical rate-determining step. In this case the rate v of the process is given by:

$$\begin{aligned} v &= \frac{d[V_2^+]}{dt} = -\frac{1}{2}\frac{d[V^{2+}]}{dt} = k[V^+][V^0] \\ &= k \exp[f(2E_1^0 + E_2^0)][V^{2+}]^2 \\ &\exp(-3fE) \quad \text{with} : f \equiv \frac{F}{RT} \end{aligned} \qquad (15)$$

where the concentrations $[V^+]$ and $[V^0]$ are expressed as a function of $[V^{2+}]$ through the corresponding Nernst equations: $[V^{2+}]/[V^+] = \exp[f(E - E_1^0)]$ and $[V^+]/[V^0] = \exp[f(E - E_2^0)]$. By integrating this equation after separation of variables we obtain:

$$\int_{[V^{2+}](t)}^{[V^{2+}]*} d[V^{2+}]/[V^{2+}]^2 = 2k \exp[f(2E_1^0 + E_2^0)] \exp[-3fE]t \qquad (16)$$

where $[V^{2+}]^*$ is the initial viologen concentration. This equation shows that, if we extract from the $Q(t, E)$ versus t curves the pairs of values of t and E corresponding to a constant value of Q (and, hence, to a constant value of the concentration $[V^{2+}](t)$ of the still unreduced V^{2+} species), the left-hand side of Eq. (16) is kept constant and,

therefore, the same is true for the right-hand side. This explains the slope of 3 for the $\ln t$ versus $FE/(RT)$ plot. The mechanism of Eq. (14) is consistent with the presence of two $Q(t = 100\,\text{ms}, E)$ versus E waves, the first of which is three times higher than the second. Since the overall height of the two waves corresponds to the uptake of 2 F mol^{-1} of V^{2+}, the two consecutive waves involve the uptake of 3/2 and 1/2 of 1 F, respectively. The processes responsible for the two waves are therefore:

$$2V^{2+} + 3e \longrightarrow V_2^+;\ V_2^+ + e \longrightarrow 2V^0 \tag{17}$$

the first of which agrees with the mechanism of Eq. (14). All the main features of the dependence of $Q(E, t)$ upon t and E are quantitatively accounted for on the basis of the above mechanism [67]. Thus, for instance, the increasing separation between the two waves with an increase in $[V^{2+}]^*$ is explained by the increasing stability of the V_2^+ dimer with respect to the two V^{2+} and V^0 monomers. V^{2+} acts as an electron-transfer mediator from $Fe(CN)_6^{3-}$ dissolved in the aqueous solution to the mercury surface across the DOPC monolayer, which is impermeable to $Fe(CN)_6^{3-}$ in the absence of V^{2+}.

An analogous mechanism is operative in the reduction of the diheptylviologen dication $(C_7)_2V^{2+}$ incorporated in a DOPC monolayer [68]. The main difference is represented by the fact that $(C_7)_2V^{2+}$ is incorporated in the lipid monolayer from its aqueous solution, where it is sparingly soluble. The incorporation step is diffusion controlled. Consequently, the chronocoulometric $Q(E, t)$ versus t curves along the plateau of the two waves consist of a capacitive contribution Q_c, a faradaic contribution Q_f due to the amount of viologen incorporated under equilibrium conditions at the initial potential E_i where it is still electroinactive, plus a further faradaic contribution Q_d due to $(C_7)_2V^{2+}$ diffusion from the bulk solution during the electrolysis time t at the final potential E. While the first two contributions flow almost instantaneously, Q_d increases progressively in time and its time dependence is expressed by the Cottrell equation, $Q_d(t) = 2nF(Dt/\pi)^{1/2}[(C_7)_2V^{2+}]^*$, where n is the number of Faradays exchanged per mole of the reactant and D is the diffusion coefficient of the latter. The slope of the linear $Q(E, t)$ versus $t^{1/2}$ plots is indeed proportional to the viologen bulk concentration and yields an n value of 1.5 along the plateau of the first wave and of 2 along the second one, in agreement with the mechanism of Eqs (15) and (17).

1.3.1.3 Thiol SAMs on Hg

The formation of thiol monolayers on Hg was first reported by Kolthoff and coworkers [3, 69] in studies of the cysteine/cystine system by dc polarography. These authors demonstrated that thiol films form spontaneously on Hg in solutions containing cysteine. These initial findings started a series of investigations on the formation of films of water-soluble thiols on Hg from their aqueous solutions. However, many of these investigations were focused on electroanalytical detection of thiols by stripping [70–72] or square-wave voltammetry [73–75] under conditions in which the amount of the thiol deposit on Hg is proportional to its bulk concentration, that is, at submonolayer levels. The mechanism of formation of these SAMs on mercury was barely investigated [76–79]. Only after the extensive studies of self-assembled alkanethiols and their derivatives on gold, which have provided a route to well-ordered, oriented monolayer films [80, 81],

the use of liquid mercury in place of gold [16, 82–87] has attracted much interest because of the unique properties of this liquid metal. Like Au, Hg has a high affinity for thiols. However, Hg has a homogeneous, featureless, defect-free surface, while Au exhibits surface steps and kinks that play a significant role in establishing defects in the deposited films. Moreover, mercury electrodes are readily renewable and there is no need to condition them prior to use.

1.3.1.3.1 **Preparation Methodology and Procedures** Water-soluble thiols, such as cysteine, self-assemble spontaneously on mercury from their aqueous solutions. As distinct from phospholipids, the self-assembly is accompanied by partial or total electron transfer from the sulfhydryl group to the metal and by concomitant sulfhydryl deprotonation, according to the general reaction:

$$\mathrm{Hg} + \mathrm{RSH} \Longleftrightarrow \mathrm{Hg} - \mathrm{SH}_{1-\alpha}\mathrm{R}^{+\lambda-\alpha} + \lambda e + \alpha \mathrm{H}^{+} \qquad (18)$$

Here λ is the partial charge-transfer coefficient, namely, the fraction of electron charge transferred from a sulfur atom to the mercury upon adsorption, and α is the degree of dissociation of the sulfhydryl group. Since partial electron transfer from the sulfhydryl groups and their deprotonation are strictly correlated events, α and λ are expected to assume close values. The Hg notation is merely used to denote chemisorption of the RSH thiol on Hg, and has no stoichiometric implications. As a matter of fact, under conditions of total charge transfer ($\alpha = \lambda = 1$), formation of mercurous [3, 69] or both mercurous and mercuric [77, 79] thiolate monolayers has been postulated. However, no definite evidence for the formation of these monolayers can be gained, because the passage from mercurous to mercuric thiolate does not involve a flow of electrons along the external circuit. Moreover, referring to mercurous or mercuric thiolate monolayers becomes meaningless in the case of partial charge transfer.

Self-assembly of thiols on Hg also takes place under open-circuit conditions, with hydrogen evolution in the absence of oxygen or, much more easily, with oxygen reduction to water in its presence. Thus, full SAMs of 6-thioguanine and 6-thioguanosine were reported to form on an HMDE under open-circuit conditions only in the presence of oxygen [88]. In this case, the reaction of Eq. (18), with $\lambda = 1$, proceeds to full electrode coverage because it occurs simultaneously with oxygen reduction, which removes electrons from the Hg electrode. In the absence of oxygen, these electrons can only be removed through the flow of an oxidation current along a closed electric circuit, at an appropriate applied potential. As a rule, transfer of SAMs of rather soluble thiols from the thiol solution in which they have been formed to a thiol-free solution in the same solvent causes a partial dissolution of the SAM. Thus, a SAM of mercaptopropionic acid in a thiol-free solution is disrupted on a Hg support, but not on a Au support. This may be due to the lower Hg−S binding energy (~200 kJ mol^{-1}) with respect to the Au−S binding energy (~400 kJ mol^{-1}), or also to a slight, but detectable, tendency of Hg-thiol adducts such as $\mathrm{Hg(SR)_2}$ to dissolve [73]. No such dissolution of gold by thiols has ever been reported.

SAMs of water-insoluble thiols, such as long-chain alkanethiols, at the Hg–water interface are usually obtained by immersing a mercury drop in a 20% (by volume)

solution of the thiol in ethanol or hexadecane from 10 seconds to 2 minutes [82, 86]. The thiol-coated mercury drop obtained by this ''soaking procedure'' is then rinsed with the solvent to remove unadsorbed alkanethiol and immersed into the aqueous solution. Another procedure (spreading procedure) consists in spreading an amount of thiol corresponding to six to nine monolayers, dissolved in a suitable solvent (e.g. pentane or hexane), on the surface of an aqueous solution, allowing the solvent to evaporate and immersing the mercury electrode into the solution through the thiol film at a well-defined velocity [86]. After one or two immersions and subsequent emersions, an alkanethiol monolayer is formed, with the sulfur atoms firmly bound to the surface of the mercury drop and the alkyl chains exposed to the solution. These SAMs are stable for a long time in thiol-free aqueous solutions. Normal handling of an HMDE coated with these SAMs, such as rinsing, mounting in a cell, or stirring the solution with a stir bar, does not affect the SAM properties. Naturally, long-chain alkanethiols insoluble in water are soluble in organic polar solvents such as ethanol [16, 85] and acetonitrile [84]: in electrolytic solutions of these solvents they can self-assemble on Hg and be investigated by electrochemical techniques. Same considerations apply to alkanethiols with up to eight carbon atoms in 0.2–0.5 M NaOH aqueous solutions, where they are soluble under the form of alkanethiolates [74, 87].

1.3.1.3.2 Structure and Physical Properties of Thiol SAMs on Mercury

1.3.1.3.2.1 Surface-sensitive Techniques

Owing to the difficulty of applying surface-sensitive techniques to a liquid surface such as mercury, only very few structural investigations by these techniques are available in the literature. The structure of SAMs of *n*-alkanethiols with a number n_C of carbon atoms from 8 to 30 on mercury was investigated by grazing-incidence X-ray diffraction (GIXD), which is sensitive to the molecular structure within the surface plane [89]. The main result was the observation that these SAMs have no in-plane long-range order, as opposed to analogous SAMs on solid supports such as Au, or to Langmuir monolayers on aqueous or organic subphases. This difference in behavior is explained by a competition between interchain van der Waals interactions within the monolayer and interactions of the monolayer with its support. On a solid support such as Au(111), the strong Au−S bonds prevail over interchain interactions, imposing a well-defined long-range order; the small mismatch between this support and alkane spacings is compensated by a molecular tilt of $\sim 30^\circ$. In Langmuir monolayers the order is induced by interchain interactions, which exceed the strength of the hydrogen bonds between the monolayer and the subphase, at least for alkanethiols with $n_C > 10–15$. On liquid mercury the strong Hg−S interactions prevail over interchain interactions, but since the liquid mercury surface has no intrinsic long-range order, there is no underlying corrugation potential to order the thiol SAM. Alkanethiol SAMs on Hg were also investigated by X-ray reflectivity [89], which probes the electronic density profile along the surface normal. Figure 8 shows this normalized profile for bare Hg (dashed line) and for *n*-octadecanethiol and *n*-dodecanethiol monolayers. This was obtained by fitting the reflectivity data to a density-dependent model reflectivity calculated from the Born approximation. The atomic surface layering of bare mercury persists in the thiol-covered surface, indicating that the

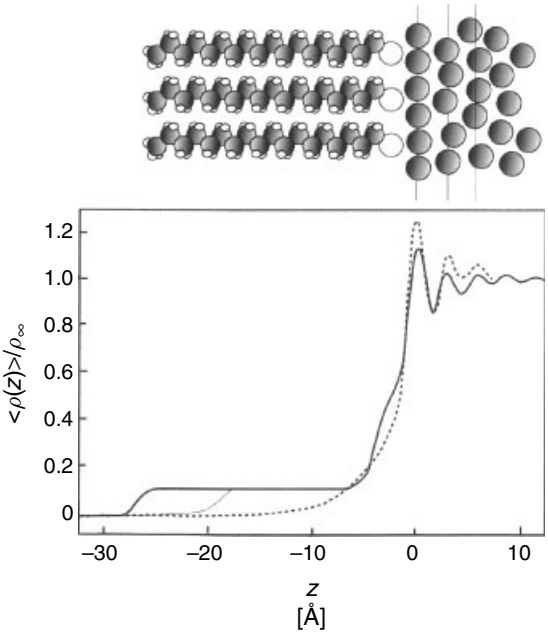


Fig. 8 Schematic real-space model and normalized electron density profiles $< \rho(z) > / \rho_\infty$ (where ρ_∞ is the bulk electron density of mercury) obtained from the fits of reflectivity data to a density-dependent model for *n*-octadecanethiol (bold line) and *n*-dodecanethiol (thin line). The upper and lower figures are aligned with each other. Vertical lines in the model mark the position of the three outermost surface layers of mercury, with the origin of *z* coinciding with the first mercury layer [89].

thiol monolayer induces no major changes in the liquid/(metal surface) structure. In both cases, the surface roughness, estimated from the width of the density profile of the outermost mercury layer, is about 1 Å. The only differences with respect to bare mercury are a shoulder in the density profile at the position of the sulfur atoms, a slight decrease in the amplitude of the first mercury layers, and a step at the position of the alkyl chain. The length of this step matches that of the fully extended alkanethiol molecules, pointing to a vertical orientation of these molecules within the SAM. The high SAM electron density (0.34 ± 0.02 e Å^{-3}), which is close to that in crystalline alkanes, points to a densely packed monolayer. This agrees with a cross-sectional area per molecule of 19.23 Å^2, estimated from the in-plane peaks of the GIXD patterns of thiol multilayers on Hg, where an in-plane order is observed [90]. A vertical orientation appears only when strong headgroup–mercury interactions exist. For alkanes, lacking such headgroups, only lying-down phases on mercury are found [91], while fatty acids, which interact with Hg more weakly than thiols, exhibit standing-up phases at high coverage and lying-down phases at low coverage [92].

An attempt to obtain scanning tunneling microscopy (STM) images of alkanethiol SAMs on mercury was made by Bruckner-Lea et al. [93]. A mercury sessile drop, whose volume was regulated by a syringe, was partially coated with *n*-octanethiol by exposing it to the thiol vapor for less than 2 minutes. Using the constant height mode, the STM images of bare mercury show broad oscillations along the slow-scan (y) axis, but not along the fast-scan (x) one. These y-directed oscillations, due to slow waving of the mercury surface, were avoided by resetting the height baseline at every x scan. In this way, STM images of bare mercury appear smooth,

while those of thiol-coated mercury show large surface features. In particular, by decreasing the drop volume slightly, the sessile drop maintains its spherical shape, thus suggesting that the thiol film is in the liquid-like region of the surface pressure–area curve. Under these conditions, the STM image shows reproducible islands of similar tunneling current on a background of lower tunneling current. As the volume of the sessile drop is decreased further, the drop assumes a flattened shape owing to an increase in the surface area-to-volume ratio. This suggests that the thiol film is now in an ordered two-dimensional solid state. The resulting STM images show small parallel *n*-octanethiol ridges of higher current density (1–10 nA high). Unfortunately, no STM images of single thiol molecules have been obtained so far on Hg.

1.3.1.3.2.2 Electrochemical Properties

Soluble thiols The electrochemical behavior of water-soluble thiols is exemplified by cysteine, which is one of the most extensively investigated. At an HMDE cysteine yields a dc adsorption polarographic prewave over a pH range from 2 to 9 [3, 69]. This is due to cysteine adsorption with partial charge transfer, according to Eq. (18). At very low cysteine concentration the limiting current of this prewave is diffusion controlled. At concentrations $>\sim 2 \times 10^{-4}$ M the growing area, $A(t)$, of the drop is instantaneously covered by a compact thiol monolayer as soon as it protrudes from the capillary orifice, and the mean limiting current attains a maximum value that does not increase with a further increase in the thiol bulk concentration. Under these conditions the charge $Q(t)$ transferred to the mercury upon adsorption is equal to $\Gamma_m A(t)$, where Γ_m is the maximum surface concentration of the thiol. Hence, noting that $A(t)$ equals $0.85\, m^{2/3} t^{2/3}$ in view of the volume of the spherical drop being proportional to the time t elapsed from drop birth, the maximum mean limiting current is given by $i_m(t) = Q(t)/t = 0.85 \lambda F \Gamma_m m^{2/3} t^{-1/3}$, where m is the mercury flow rate. This equation allows $\lambda F \Gamma_m$ to be estimated at $\sim$70 μC cm^{-2}. This value corresponds to a compact cysteine SAM for $\lambda = 1$. This indicates that in the present case charge transfer is total; in practice, total charge transfer can be safely assumed for all soluble thiols. Any arguments in favor of the formation of a mercurous or mercuric cysteine thiolate monolayer are purely hypothetical [3, 69, 77, 79]. Similar dc oxidation prewaves are observed with many thiols, such as benzyl mercaptan, 1-butanethiol and 1-decanethiol in 0.2 M NaOH [74], and 2-mercaptopyridine N-oxide [78]. At more positive potentials, cysteine and other water-soluble thiols [74] yield a dc polarographic wave (the so-called main wave) that starts developing as soon as the prewave has attained its maximum limiting height and whose limiting current is diffusion controlled. There is no general consensus on the nature of the resulting oxidation product. For 2-mercaptopyridine N-oxide the formation of the corresponding disulfide was postulated [78]. In the case of cysteine, it is usually assumed that the product is a Hg(I) thiolate [69, 74, 77] which, being insoluble in water, disproportionates into the corresponding Hg(II) thiolate and Hg [74]. Since Hg(II) thiolate is also sparingly soluble in water, it is expected to ultimately deposit and form a multilayer on the mercury surface [74, 75]. Linear sweep voltammograms of cysteine at an HMDE yield an oxidation peak that

levels off when the charge under the peak attains a maximum limiting value of about 80 μF cm^{-2} [76], in fairly good agreement with the charge estimated from the corresponding dc adsorption prewave.

The dc polarographic main wave has often been ascribed to a faradaic process inhibited by the film formed during the prewave and which may proceed only after a breakdown of this film [69, 74]. As a matter of fact, it is quite probable that the prewave is due to a process facilitated by adsorption of the product of the electrode reaction of Eq. (18), with $\lambda = \alpha = 1$, with respect to the case in which the mercury thiolate is not adsorbed. Differently stated, the free energy involved in the formation of the prewave is decreased by an amount corresponding to the free energy of adsorption of the mercury thiolate, and therefore the prewave is developed at a less positive potential than in the absence of mercury thiolate adsorption [94]. The main wave starts to develop at bulk thiol concentrations at which there is no longer room for adsorbed product molecules on the drop surface, and the product must diffuse away from the electrode. If the product is sparingly soluble, as in the case of mercury cysteine thiolate, it may also deposit on the drop surface, at least partially. This seems to be the case with cysteine. Thus, if a stationary mercury electrode is pretreated in a cysteine solution at a potential positive of the rising portion of the dc polarographic main wave, and is then subjected to a negative linear potential scan, a voltammetric reduction peak is observed. This is ascribed to the release of electrons from the mercury to the sulfur atoms of adsorbed cysteine according to the backward reaction of Eq. (18), with release of cysteine molecules to the aqueous solution. However, the charge under this reductive desorption peak has often been found to be greater than that of the corresponding oxidative adsorption peak or, equivalently, of the oxidative adsorption dc prewave [69]. This excess charge may be ascribed to reduction of a mercury thiolate multilayer formed on top of the thiol chemisorbed monolayer in direct contact with mercury, during the pretreatment [74, 75].

Quite often, the reductive desorption peak of cysteine and of other thiols [74, 75, 78] has been reported to split into two, usually at relatively high concentrations. Different tentative explanations have been provided for this splitting. Thus, it was attributed to the presence of both mercuric and mercurous cysteine thiolates in the film, with the less negative peak being due to the Hg(I) compound [79], or to the result of ''compacting'' of the mercuric cysteine thiolate film [76]. The fact that the additional peak appears at a less negative potential than the single peak present before the splitting as soon as the bulk concentration becomes higher than that required for the formation of a compact monolayer under diffusion control strongly suggests that it is due to dissolution of a mercury thiolate multilayer on top of the monolayer in direct contact with the mercury surface [75]. The latter monolayer is expected to be more difficult to reduce than the overhanging multilayer if the Hg−S bond is stronger than the interaction forces within the multilayer.

Cystine, the disulfide resulting from the chemical oxidation of cysteine, chemisorbes on Hg with cleavage of the −S−S−bond and formation of two Hg−S bonds [3, 77, 79, 95]. The resulting film is, therefore, analogous to that resulting from cysteine chemisorption. The first dc polarographic reduction wave [77] (or the first voltammetric reduction peak [76]) of a cystine solution has the character of a desorption wave resulting from the

transfer of negative charge from the mercury to the sulfur atom of the adsorbed monolayer and release of cysteine to the solution. As distinct from a cysteine solution, this desorption wave is followed by an irreversible diffusion-controlled wave [77], because of the electroreduction to cysteine of bulk cystine diffusing toward the electrode. The irreversible character of the latter wave may possibly be due to a slow cleavage of the −S−S−bond [79]. Aqueous solutions of cystine also yield a dc polarographic oxidative adsorption wave, which is ascribed to an irreversible electron transfer from the S atoms to mercury [77]. The foot of this adsorption wave is characterized by a positive pseudocapacitive current, as distinct from the negative purely capacitive current exhibited by the supporting electrolyte alone. This is ascribed to a reversible partial electron transfer from S to mercury [77].

n-Alkanethiolates with a number n_c of carbon atoms from two to eight yield two voltammetric oxidation peaks in aqueous 0.5 M NaOH, as shown in Fig. 9 [87].

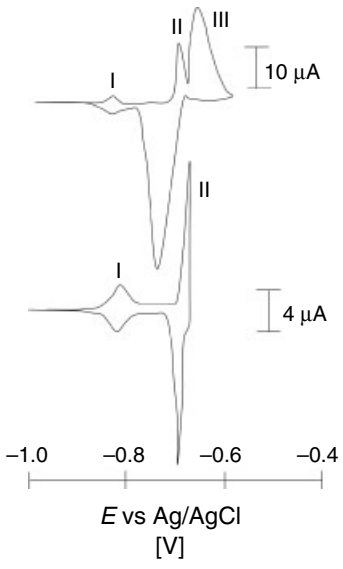


Fig. 9 Top: cyclic voltammogram of Hg in aqueous 0.5 M NaOH solution containing 5 mM $C_5H_{11}S^-$; scan rate = 100 mV s^{-1}. Bottom: cyclic voltammogram recorded at a higher current sensitivity over a narrower potential range, so as to avoid recording peak III [87].

The more negative (peak I) is ascribed to a rapid and reversible oxidative adsorption of a submonolayer quantity of $C_{nc}H_{2nc+1}S^-$, while the second, considerably sharper peak (peak II) results from further deposition of $C_{nc}H_{2nc+1}S^-$ to yield an essentially compact monolayer. The charge under the two peaks increases from 80 to 95 μC cm^{-2} with an increase in chain length; the latter value corresponds to a practically close-packed monolayer in the case of total charge transfer ($\lambda = 1$). *n*-Alkanethiolates with $n_c < 6$ also show a further more positive oxidation peak (peak III), owing to the deposition of a bulk film of mercurous or mercuric thiolate. For $n_c \geq 6$ no peak III is observed, probably because of an increased compactness of the SAM, which becomes impermeable to the thiolate molecules. Reversal of the voltage scan yields two cyclic voltammetric reduction peaks corresponding to the oxidation peaks I and II (see Fig. 9, bottom). The midpoint between the reduction peak potential and the corresponding oxidation one, $E_{1/2} = (E_{pa} + E_{pc})/2$, yields the Gibbs adsorption free enthalpy for the oxidative/reductive adsorption process via the relation $\Delta G_{ads} = -FE_{1/2}$; this decreases linearly with n_c according to the relation $\Delta G_{ads} = A - Bn_c$ [87]. The n_c-dependent term is considered to measure the energetic contribution resulting from the transfer of the amphiphilic *n*-alkanethiolate from bulk water onto the

metal surface, while the A term is regarded as the constant contribution associated with the Hg−S interaction.

Cyclic voltammograms of soluble thiols are often characterized by an oxidative adsorption peak, due to the forward electrode reaction of Eq. (18) with $\lambda = \alpha = 1$, during the positive potential scan, and by a reductive desorption peak, due to the corresponding backward reaction, during the negative potential scan (see Fig. 10a). At higher bulk thiol concentrations, the reductive desorption peak may undergo splitting [96, 97]. The nature of the functional group affects the sharpness and potential of the reduction peak. Thus, this peak sharpens and shifts to more negative potentials with an increase in thiol length and a decrease in the size of its headgroup. At potentials negative of the adsorption–desorption peaks, thiols are generally not desorbed, but remain physisorbed on the mercury surface. Clear evidence for such a physisorption was provided in the case of ω-mercaptoalkanoic acids [98] by ex situ measurements; these consisted in adsorbing the thiol on an HMDE from a thiol solution at a potential negative of the adsorption–desorption peaks, removing the electrode from the solution under the same applied potential, rinsing it with water, immersing it in a thiol-free solution under a potential positive of the adsorption–desorption peaks, and scanning the potential in the negative direction. The charge under the resulting reductive desorption peak increases with an increase in the thiol concentration used for the adsorption, attaining a maximum limiting value corresponding to a full monolayer coverage (83 μC cm^{-2}). This procedure was also used to measure the adsorption isotherms of two ω-mercaptoalkanoic acids, which were found to satisfy the Frumkin model with attractive lateral interactions. If the ex situ procedure is modified by immersing the thiol-coated mercury drop in a thiol-free solution at a potential negative of

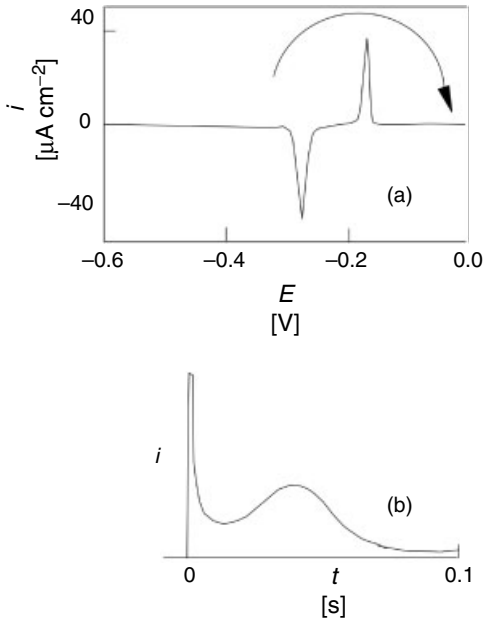


Fig. 10 (a) Cyclic voltammogram of mercury in a pH 4 aqueous solution of 0.l M acetic acid containing 1×10^{-4} M 6-thioguanine. (b) Current versus time curve obtained by stepping the potential from −0.35 to −0.025 V/SCE across the oxidative adsorption peak of Fig. 10a [100b].

the desorption peak, keeping the drop at this potential for a given rest time and then recording the adsorption and desorption peaks, the charge under the peaks decreases with an increase in the rest time. This behavior denotes a gradual dissolution of the physisorbed thiol in the thiol-free solution. On the other hand, if the ex situ procedure is modified by adsorbing the thiol from the thiol solution for a given rest time at a potential positive of the adsorption peak, and then by recording the desorption peak in the thiol-free solution, the charge under the peak increases progressively with the rest time. This is due to the formation of a progressively thicker film of the thiol during the rest time, because films of ω-mercaptoalkanoic acids with eight or less carbon atoms do not sufficiently block the electron transfer. A somewhat different behavior was reported for mercaptohexanol [96]. Keeping an HMDE in a 20 μM mercaptohexanol solution in 0.5 M NaOH at a potential positive of the adsorption–desorption peaks for progressively increasing times, a single reductive desorption peak is first observed; at longer times this is accompanied by a less negative reductive desorption peak, which becomes progressively sharper. The charge under both desorption peaks attains a limiting value of 73 μC cm^{-2}, which is close to that corresponding to a full thiol monolayer, and no multilayers are formed. When a single desorption peak is observed, at potentials positive of the peak, the film is not blocking toward $Ru(NH_3)_6^{3-}$ electroreduction, while it becomes blocking when the further less negative desorption peak develops at longer times. A similar evolution of the reductive desorption peak in time is observed with a pH 4 solution of 30 μM 4-mercaptophenol [97]. In this case, the appearance of a second sharper and less negative reductive desorption peak is ascribed to a passage of the thiol molecules from a flat to a vertical orientation. At potentials positive of the final compact SAM of vertically oriented molecules, only a modest decrease in the rate of $Ru(NH_3)_6^{3-}$ electroreduction is observed.

Mercapto derivatives of nucleobases such as 6-thiopurine [99, 100a] and 6-thioguanine [100b, c, 101] form particularly compact SAMs on Hg, thanks to strong attractive intermolecular interactions, specifically ring–ring stacking interactions. Scanning the potential in the positive direction gives rise to an oxidative adsorption peak that marks the passage from a physisorbed, well-organized phase to a two-dimensional condensed SAM; the latter inhibits multilayer formation and oxygen electroreduction, while it has no effect on the rate of outer-sphere electron-transfer processes, such as $Ru(NH_3)_6^{3-}$ reduction [99]. The adsorption peak, which is sharp and symmetrically shaped, shifts by 60 mV toward more negative potentials per each unitary increment in pH, in agreement with the general reaction of Eq. (18), for $\lambda = \alpha = 1$. Ex situ experiments indicate that the condensed SAM is stable in thiol-free solutions, while the physisorbed phase gradually dissolves. The condensed SAM is formed by a mechanism of nucleation and growth, as clearly demonstrated by the shape of the current–time curves obtained by stepping the potential from the region of the physisorbed phase to that of the two-dimensional condensed one, across the oxidative adsorption peak (see Fig. 10b). These curves show a minimum followed by a maximum, which is typical of a two-dimensional phase transition [100b]. The current maximum increases and becomes narrower with an increase in the width of the potential jump, while the charge under the current–time curve remains constant, being practically equal to

that involved in the voltammetric adsorption peak. In the case of 6-thioguanine, the current transients are close to those predicted for a two-dimensional instantaneous nucleation, and can be interpreted quantitatively by including an additional contribution from double-layer charging and one from slow adsorption of disordered thiol molecules [100c].

Insoluble thiols Water-insoluble thiols, such as long-chain *n*-alkanethiols, are characterized by a broad potential range over which they form stable SAMs with a low and practically constant differential capacity. This range extends in both directions with an increase in chain length. Thus, while oxidation of bare mercury in 0.1 M NaF takes place at about 0.4 V/SCE, a mercury electrode coated with a SAM of *n*-hexadecanethiol is not oxidized until about 1.4 V [82]. This is due to the highly impermeable and defect-free SAM, which protects Hg against oxidation. A negative linear voltage scan yields a desorption peak due to the backward electrode reaction of Eq. (18). The peak may also split into two at high pH values [16]. The charge under the peak depends to some extent on the nature of the solvent. It is usually higher in organic solvents, where *n*-alkanethiols are moderately soluble and are directly adsorbed from the solvent. Thus, under saturating conditions, it amounts to $\sim$115 μC cm^{-2} for *n*-octadecanethiol from ethanol [16] and $\sim$80 μC cm^{-2} for *n*-hexadecanethiol from acetonitrile [84]. Henceforth, *n*-alkanethiols with a number n_c of carbon atoms will be briefly denoted by C_n. If, after reductive desorption of the thiol, the mercury electrode is kept for 2–4 minutes at a potential corresponding to the flat capacity minimum, a close-packed SAM with exactly the same properties is often restored [16, 86]. This occurs more frequently by using the ''spreading'' procedure (see Sect. 1.3.1.3.3.1), in which the aqueous solution is saturated with the thiol that is spread on its surface. This restoration can be explained by postulating that the desorption gives rise to thiol micelles or similar organizations, which remain in the proximity of the electrode and can spread back onto the electrode surface without any loss of material. Reverting the potential scan, just after the negative-going scan that causes reductive desorption, yields an oxidation readsorption peak, whose peak potential shifts in the negative direction by about 60 mV per each unitary increment in pH [16]. This indicates that charge transfer from the sulfhydryl group to the metal is accompanied or preceded by deprotonation. In aqueous solution, the charge under the reduction peak of C_{18} decreases with an increase in scan rate, attaining a constant minimum value of $\sim$70 μC cm^{-2} for scan rates $\geq$ 100 mV s^{-1} [16]. This phenomenon is ascribed to a slow hydrogen evolution resulting from the penetration of water molecules into the partially disordered C_{18} SAM and their electroreduction by the catalytic action of the sulfur atoms; this is prevented by a sufficiently high scan rate. For *n*-alkanethiols with a number of carbon atoms higher than about five, the charge under the reduction peak attains an almost constant maximum value [84, 85]. The flat capacity minimum of *n*-alkanethiols extends over a broader potential region in water than in organic solvents such as ethanol, owing to the increased hydrophobic interactions resulting from the lower solubility of thiols in water. Moreover, it is usually higher in organic solvents than in water. Thus, the flat capacity minimum in acetonitrile varies from 3 to 6 μF cm^{-2} on passing from C_{18} to C_6 [84], while in water it varies

from 0.70 to 0.95 $\mu F\,cm^{-2}$ on passing from C_{18} to C_{14} [86]. The values in water are in fairly good agreement with the differential capacities calculated from the Helmholtz formula for a parallel-plate capacitor, $C = \varepsilon_0\varepsilon/d$, by setting the dielectric constant ε equal to the value, 2.1, of decane and the thickness d of the thiol film equal to the length of a space-filling model of the thiols in the most extended configuration. C values of n-alkanethiol SAMs with n_c from 8 to 18 also satisfy the Helmholtz formula with $\varepsilon = 2.0$ [85].

A closer insight into the electrical properties of thiol-coated mercury can be gained by using electrochemical impedance spectroscopy. The mercury–thiol solution interface can be satisfactorily simulated with an equivalent circuit in which the thiol monolayer is represented as a capacitor C_t with a parallel resistor R_t, due to the presence of any traces of impurities capable of penetrating the film; the aqueous electrolyte is represented as a resistor R_Ω is series with the thiol monolayer (see inset 1 of Fig. 11). While the impedance of the capacitor C_t is given by $-j/(2\pi f C_t)$, where f is the frequency of the ac signal, the impedance of the resistors R_t and R_Ω is equal to their resistance, and is therefore frequency independent. Over a broad frequency range, the modulus, $|Z|$, of the impedance is controlled by the capacitor C_t. Therefore, the plot of log $|Z|$ versus log f (Bode plot) has a slope of -1 (Fig. 11). At very high frequencies the impedance of the capacitor becomes so low that the control of the impedance passes to the series resistor R_Ω, and the Bode plot tends to become horizontal. This occurs at higher frequencies the lower is R_Ω, and hence the higher is the electrolyte concentration. On the other hand, at very low frequencies, $-j/(2\pi f C_t)$ tends to become comparable to, and ultimately greater than R_t. Hence, the control of the impedance tends to pass to R_t, and the Bode plot tends again to become horizontal. With well-behaved n-alkanethiol SAMs, R_t is of the order of 20 $M\Omega\,cm^2$, and starts controlling Z for $f < 10^{-1}$ Hz. Strictly speaking, the equivalent circuit should also include the capacity C_d of the diffuse layer adjacent to the thiol SAM, in series with the R_tC_t mesh (inset 2 of Fig. 11). In practice, the capacity C_t of n-alkanethiols is so low that the contribution of C_d is entirely negligible. A different situation is encountered with thiolpeptides, namely, oligopeptide molecules that terminate with a sulfhydryl group for anchoring to the metal [102]. These relatively hydrophilic molecules form SAMs that exhibit a high resistance comparable with that of n-alkanethiols, but a capacity of the order of 10 $\mu F\,cm^{-2}$, because of the high polarizability of the peptide bonds. In this case the diffuse-layer capacity C_d can be estimated by making it comparable with C_t by the use of KCl concentrations c as low as 5×10^{-3} M. By covering a KCl concentration range from 5×10^{-3} to 0.1 M and regarding C_t as independent of the electrolyte concentration, the use of the equivalent circuit in inset 2 of Fig. 11 allows C_d to be measured as a function of c. Fitting this dependence to the GC theory, as shown in inset 3 of Figure 11, allows the charge density, q, experienced by the diffuse-layer ions to be estimated at $-3\,\mu C\,cm^{-2}$.

1.3.1.3.2.3 **Total and Free Charge Density on Mercury Coated with Thiol SAMs** One important parameter of alkanethiol monolayers is the charge involved in their self-assembly on electrodes; this has often been identified with the charge under the reductive desorption peak, with [103] or without [87, 104] correction for the

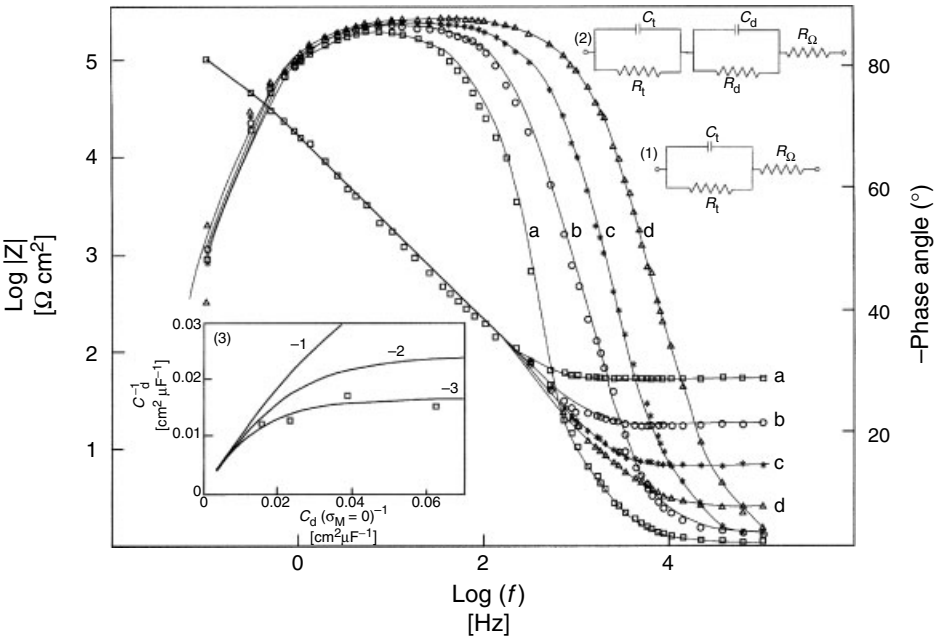


Fig. 11 Plots of log $|Z|$ and of the phase angle versus log f for a thiolpeptide-coated mercury drop immersed in 5×10^{-3} M (a), 1.3×10^{-2} M (b), 3.6×10^{-2} M (c), and 0.1 M (d) KCl, as obtained at −1.000 V/SCE over the frequency range from 0.1 to 10^5 Hz. At frequencies $< 10^2$ Hz all Bode plots coincide; hence, only the experimental points for the lower KCl concentration were reported. The solid curves are least-squares fits to the simple equivalent circuit of inset 2, which consists of the electrolyte resistance R_Ω, in series with an R_tC_t mesh representing the self-assembled thiol and a further R_dC_d mesh representing the diffuse layer. $R_t = 0.14$ MΩcm^2; $C_t = 11$ μF cm^{-2}; $R_d = 4.53$ (a), 4.17 (b), 1.27 (c), and 0.87 KΩ cm^2 (d). $C_d = 68$ (a), 61 (b), 80 (c) and 84 μF cm^{-2} (d). Inset 3 shows the reciprocal, $1/C_d$, of the experimental diffuse-layer capacitance versus the $1/C_d(\sigma_M = 0)$ value corresponding to the same KCl concentration, as calculated on the basis of the Gouy–Chapman (GC) theory. The solid curves are $1/C_d(\sigma_M)$ versus $1/C_d(\sigma_M = 0)$ plots calculated from the GC theory for different charge densities σ_M on the metal, whose values are reported on each curve [102].

capacitive contribution. In this connection it should be pointed out that the only thermodynamically significant charge in adsorption processes involving partial or total charge transfer between the adsorbate and the electrode is the charge to be supplied to the electrode to keep the applied potential E constant when the electrode surface is increased by unity and the composition of the bulk phases is kept constant. This quantity is called "total charge" by Frumkin [105] and will be denoted here by $\sigma_M(E)$. It should be distinguished from the "free charge" $q(E)$, namely, the charge density on the metal side of the interphase, due to the surface excess of free electrons, which is actually experienced by the diffuse-layer ions; in the presence of adsorption with charge transfer, the latter quantity can only be estimated on the basis of extrathermodynamic assumptions.

The method of choice to measure σ_M both on solid and liquid electrodes consists in starting with an uncoated electrode

immersed in a solution of the supporting electrolyte alone and in stepping the applied potential from the pzc to a final potential E_f negative enough to exclude the adsorption of the adsorbate under investigation, provided such a potential is experimentally accessible: the charge Q accompanying the potential step pzc $\rightarrow E_f$ is then just the common value, $\sigma_M(E_f)$, of the total charge density both in the presence and in the absence of the adsorbate. The charge accompanying a further potential step from any given initial potential E to E_f at an adsorbate-coated electrode in the same supporting electrolyte will be equal to $\sigma_M(E_f) - \sigma_M(E)$, thus allowing the estimation of the total charge density $\sigma_M(E)$ at E. Application of this procedure to a C_{18} SAM on a mercury electrode immersed in aqueous 0.1 M tetramethylammonium chloride, where this SAM is completely desorbed at $E_f = -1.85$ V/SCE, yields a σ_M value of $\sim +56\ \mu C\ cm^{-2}$ over the whole broad potential range of stability of the monolayer [16]. In fact, because of the very low differential capacity of the C_{18} monolayer, the changes in σ_M over this potential range lie within the limits of experimental accuracy.

An alternative procedure applicable to liquid electrodes consists in recording the charge accompanying the expansion of an HMDE immersed in a solution of the adsorbing surfactant at constant applied potential E. It can be applied only in the presence of surfactant concentrations high enough to ensure an almost instantaneous adsorption equilibrium during drop expansion. This procedure was adopted to measure σ_M for monolayers of n-alkanethiols with $8 \leq n_c \leq 18$ [85]. These thiols were self-assembled on mercury from methanolic $NaClO_4$ solutions, where they are sufficiently soluble. The resulting σ_M values range from 70 ± 10 to $80 \pm 10\ \mu C\ cm^{-2}$. This procedure is substantially identical with that based on the measurement of the maximum limiting height of dc polarographic adsorption waves, such as the oxidation adsorption prewave of cysteine (see Sect. 1.1.3.3.2.2), which yields a σ_M value of $\sim 70\ \mu C\ cm^{-2}$. From a thermodynamic point of view, it is impossible to separate σ_M into a capacitive and a faradaic contribution [106]. This is possible only on the basis of extrathermodynamic assumptions. In the following, it will be shown that the capacitive contribution can be approximately identified with the free charge density $q(E)$, which is very small over the potential range of stability of n-alkanethiol SAMs.

The charge under the reductive desorption peak of n-alkanethiols is not a precise measure of σ_M, since it includes the difference between the capacitive charge at a potential E_2 just negative of the desorption peak and that at a potential E_1 just positive of it. While the latter capacitive charge is very small, the former is not negligible. As a first approximation, it can be identified with the charge density σ_M at E_2 on a bare mercury electrode, even though, at potentials just negative of the desorption peak, thiol desorption is not complete. In the case of a C_{18} SAM on a mercury electrode immersed in aqueous 0.1 M tetramethylammonium chloride, the charge under the desorption peak amounts to $-70\ \mu C\ cm^{-2}$, while the σ_M value on bare mercury at a potential just negative of the peak equals $-16\ \mu C\ cm^{-2}$ [16]. This yields a total charge density of $+54\ \mu C\ cm^{-2}$ over the range of stability of the C_{18} SAM, in excellent agreement with the value obtained by the more accurate potential-step chronocoulometric procedure (vide supra).

The charge under the oxidation adsorption peaks of long-chain alkanethiolates from aqueous 0.5 M NaOH was reported to amount to $\sim +95\ \mu C\ cm^{-2}$ [87], and that under the reductive desorption peak of C_{10} from acetonitrile was found to be equal to $\sim -98\ \mu C\ cm^{-2}$ [84]. Both charge values were not corrected for the capacitive contribution. If this can be reasonably considered to be of the order of $15-20\ \mu C\ cm^{-2}$, in both cases σ_M is close to $80\ \mu C\ cm^{-2}$.

The cross-sectional area of a linear hydrocarbon chain in close-packed monolayers of aliphatic compounds is estimated at $\sim 0.20\ nm^2$ [85]; for the transfer of one electron per *n*-alkanethiol molecule in the monolayer, a total charge density of $\sim +80\ \mu C\ cm^{-2}$ is obtained. This value agrees with that estimated from GIXD and X-ray reflectivity measurements on *n*-alkanethiol SAMs on Hg [89] (see Sect. 1.1.3.3.2.1). Therefore, experimental σ_M values close to $\sim +80\ \mu C\ cm^{-2}$ point to a close-packed monolayer of perpendicularly oriented *n*-alkanethiol molecules resulting from total charge transfer from the sulfhydryl group to mercury. These values are normally reported for monolayers that are directly self-assembled from thiol solutions in organic solvents, such as methanol [85] and acetonitrile [84], or for thiolates dissolved in strongly alkaline aqueous solutions [87]. In these solutions the solubility of mercury adducts is not entirely negligible. Thus, the dissolution of mercury in organic solutions of thiols is significant, and can be reduced only in acidic media [73, 84]. Strongly alkaline aqueous solutions may also favor a modest solubility of mercury adducts, as indicated by the formation of a massive deposit of mercury alkanethiolates from aqueous 0.5 M NaOH at potentials as negative as -0.6 V versus a Ag/AgCl reference electrode [87]. Since such dissolution involves total charge transfer, σ_M values close to $+80\ \mu C\ cm^{-2}$ are not surprising.

A more significant estimate of the partial charge-transfer coefficient λ requires the absence of equilibrium between the surface compound due to charge transfer from the adsorbate to the metal, and the corresponding compound in the bulk solution. This requirement is fulfilled, for example, by C_{18} SAMs in aqueous solutions of pH less than the $pK_a = 12$ of this thiol, where the C_{18} coating shifts the onset of mercury oxidation to potentials positive of those observed on bare mercury in the same electrolyte, instead of favoring such an oxidation. In this case, taking into account both the partial charge-transfer coefficient λ and the degree of dissociation α of the sulfhydryl groups as expressed by Eq. (18), the potential difference across the interphase can be approximately expressed as follows [16]:

$$\Delta\phi = \frac{d}{\varepsilon_0\varepsilon_\infty}(\sigma_M + \lambda\sigma_i) + \frac{d-\beta}{\varepsilon_0\varepsilon_\infty}[(1-\lambda)\sigma_i - (1-\alpha)\sigma_i] + \chi_t = \frac{d}{\varepsilon_0\varepsilon_\infty}(\sigma_M + \alpha\sigma_i) - \frac{\beta}{\varepsilon_0\varepsilon_\infty}(\alpha - \lambda)\sigma_i + \chi_t \qquad (19)$$

Here, β is the distance of the center of charge of the sulfur atoms from the metal surface, d is the whole length of the thiol molecule, ε_∞ is a dielectric constant accounting for distortional polarization, σ_i is the charge density of the $-S^-$ groups of a hypothetical close-packed monolayer of thiolate ions, and χ_t is the surface dipole potential of the thiol. The $(d/\varepsilon_0\varepsilon_\infty)(\sigma_M + \lambda\sigma_i)$ term is the potential difference across the whole length of the thiol molecule created by the "free charge" on the metal, which is given

by the negative charge $\lambda\sigma_i$ transferred from the sulfur atoms to the metal, plus the thermodynamically significant and experimentally accessible charge density σ_M. The $[(d-\beta)/\varepsilon_0\varepsilon_\infty][(\alpha-\lambda)\sigma_i]$ term is the potential difference across the chain of the thiol, of length $(d-\beta)$, created by the charge density on the sulfhydryl groups. In the limiting case of a zero degree of dissociation α, the transfer of a negative charge density $\lambda\sigma_i$ to the metal leaves an equal and opposite positive charge density $-\lambda\sigma_i$ on the sulfur atoms. In the opposite limiting case of a unitary degree of dissociation, this charge density is negative and equal to $(1-\lambda)\sigma_i$. After rearranging terms, we can neglect the $(\beta/\varepsilon_0\varepsilon_\infty)\ (\alpha-\lambda)\sigma_i$ term with respect to the other, $(d/\varepsilon_0\varepsilon_\infty)\ (\sigma_M+\alpha\sigma_i)$, both because β is$\ll d$ and because α and λ are expected to assume close values, since partial charge transfer and deprotonation of the sulfhydryl group are strictly correlated events.

Differentiating Eq. (19) with respect to σ_M under the assumption that the dipole potential χ_t and the partial charge-transfer coefficient $\lambda \approx \alpha$ are not appreciably affected by a change in σ_M, yields the following expression for the reciprocal of the differential capacity of the thiol monolayer:

$$\frac{d\Delta\phi}{d\sigma_M} = \frac{1}{C} = \frac{d}{\varepsilon_0\varepsilon_\infty} \qquad (20)$$

Combining Eqs (19) and (20) yields:

$$\Delta\phi = \frac{\sigma_M + \alpha\sigma_i}{C} + \chi_t \qquad (21)$$

If we apply this equation to the C_{18} alkanethiol, the dipole potential χ_t of the *n*-alkyl chain can be regarded as negligible to a good approximation. Moreover, σ_M equals $+56\ \mu C\ cm^{-2}$ (vide supra) and the charge density, σ_i, on the $-S^-$ groups of a hypothetical close-packed monolayer of C_{18} anions is about $-80\ \mu C\ cm^{-2}$. In practice, the charge density $(\sigma_M + \alpha\sigma_i)$ is small, since the absolute values of σ_M and $\alpha\sigma_i$ are much greater than their algebraic sum. Thus, from the approximate extrathermodynamic estimate of the absolute potential difference across the mercury–aqueous solution interphase, $\Delta\phi$, (see Eq. (9)) and from the differential capacity, $C_t = 0.7\ \mu F cm^{-2}$, of the C_{18} SAM, $|\sigma_M + \alpha\sigma_i|$ turns out to be about 2 orders of magnitude smaller than $|\sigma_i|$ [16]. Taking into account that σ_M and $|\sigma_i|$ are both much greater than $|\sigma_M + \alpha\sigma_i|$, we can set $\alpha \approx -\sigma_M/\sigma_i = 0.7$ to a good approximation; this is also an approximate estimate of the partial charge-transfer coefficient λ for C_{18}.

In the case of the water-soluble thiolpeptide of Fig. 11, its dipole potential χ_t cannot be regarded as negligible. However, as distinct from the C_{18} alkanethiol, the capacity C of thiolpeptide-coated Hg is high enough not to obliterate diffuse-layer effects, thus allowing the free charge density $q = \sigma_M + \lambda\sigma_i$ experienced by the diffuse-layer ions to be estimated at $-3\ \mu C\ cm^{-2}$ from the GC theory [102] (see Sect. 1.1.3.3.2.2). Moreover, the charge density σ_i estimated on the assumption of a close-packed hexagonal array of thiolpeptide molecules is approximately equal to $-20\ \mu C\ cm^{-2}$, while the total charge density σ_M measured at -1.000 V/SCE by the potential-step procedure equals $+17\ \mu C\ cm^{-2}$. In this case the partial charge-transfer coefficient $\lambda \approx (q - \sigma_M)/\sigma_i$ is, therefore, approximately equal to unity. The knowledge of q also allows an estimation of the dipole potential χ_t of the thiolpeptide through Eq.(21). In view of the considerations made in connection with Eq. (9), $\Delta\phi$ is more positive than the applied potential E measured versus the SCE by ~ 250 mV. At -1.000

V/SCE, where C equals 11 μF cm^{-2} [102], $\Delta\phi$ is therefore equal to −0.750 V. Substituting these numbers in Eq. (21), a χ_t value of about −470 mV is obtained. Using the same approach for an SAM of triethyleneoxythiol, another relatively hydrophilic thiol, values of σ_M, C and q equal to +13 μC cm^{-2}, 11 μF cm^{-2} and −3.5 μC cm^{-2}, respectively, were measured at −0.785 V/SCE [107]. From Eq. (21) it follows that χ_t amounts to ∼ −200 mV [37]. Upon estimating σ_i at −70 μC cm^{-2} from a space-filling model of this thiol, a partial charge-transfer coefficient λ of 0.24 was determined.

1.3.1.3.2.4 **Electron Transfer across Thiol SAMs on Mercury** While short-chain *n*-alkanethiol and ω-thiocarboxylic acid monolayers, say with $n_c = 2$, affect the rate of electron transfer of redox couples such as $Ru(NH_3)_6^{3+/2+}$ only slightly, long-chain thiols inhibit electron transfer the more the longer is their chain [82, 84, 86]. Thus, *n*-alkanethiols whose transition temperature to the liquid-crystalline state is higher than room temperature block almost completely not only inorganic redox couples such as $Ru(NH_3)_6^{3+/2+}$ and $Fe(CN)_6^{3-/4-}$ but also lipophilic couples such as UQ/ubiquinol-10 or viologens. Even the electroinactive lipophilic ions $TPhB^-$ and $TPhP^+$ are prevented from translocating across a C_{18} monolayer on Hg [86]. However, Pb^{2+}, a typical example of a metal ion/metal amalgam couple, shows a reduction current across a C_{16} SAM, which may reach up to 4% of that on bare mercury [82].

The reduction current density i of $Ru(NH_3)_6^{3+}$ across SAMs of *n*-alkanethiols with $8 \le n_c \le 18$ from aqueous 0.5 M KCl was thoroughly investigated by Majda and coworkers [85, 108, 109]. This current density is much lower than its diffusion limiting value. Thus, it is exclusively controlled by slow electron tunneling kinetics and depends upon the overpotential η according to the well-known relation $i = Fk_{ap}c*$, with $k_{ap} = k_{ap}^o \exp(-\alpha\eta F/RT)$, where $c*$ is the bulk reactant concentration and α is the charge-transfer coefficient. The current density measured at constant applied potential decreases exponentially with the length of the hydrocarbon chain, according to the relation $i = i_0 \exp(-\beta n_c)$; here β is the decay constant per methylene group and i_0 is regarded as the current density in the absence of the thiol monolayer. The β value amounts to 1.14 ± 0.09 [85].

Monolayers of *n*-alkanethiols with n_c from 9 to 14 maintain their impermeability and dielectric properties upon slow stepwise expansion of the HMDE up to 30%, thanks to their liquid-crystalline state at room temperature. Conversely, *n*-alkanethiols with $n_c > 14$ fracture easily upon mercury drop expansion in excess of ∼5% [85, 110]. Thus, by keeping the drop expansion within the above limits, the $Ru(NH_3)_6^{3+}$ reduction current continues to be limited by slow electron tunneling kinetics. Moreover, the differential capacity C per unit surface increases proportionally to the drop area during drop expansion, as in the case of phospholipid-coated mercury (see Sect. 1.1.3.2.2.1). This denotes a constancy in the dielectric constant of the SAM, which maintains its volume, density, and dielectric properties through a gradual tilting of the thiol chains. Figure 12 shows plots of $\ln i$ versus the film thickness at constant E both for different *n*-alkanethiols on an unexpanded drop and for C_{12} on a progressively expanded drop. It is apparent that the current upon drop expansion increases with a decrease in film thickness much less than

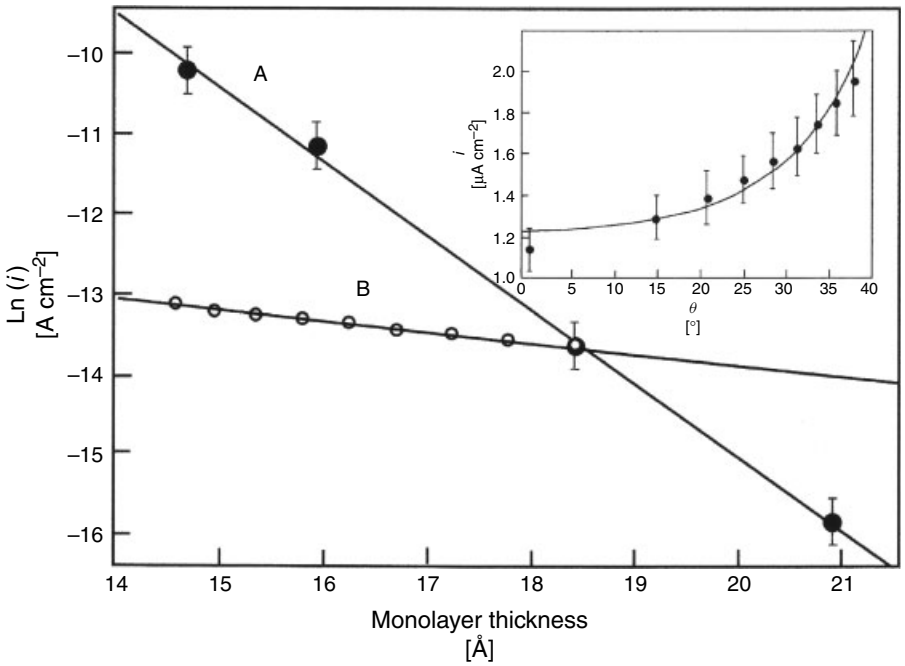


Fig. 12 Plots of the logarithm of the tunneling current density i versus the geometric monolayer thickness. Data recorded at −0.65 V/SCE on an unexpanded HMDE coated with *n*-alkanethiol monolayers of different chain length (A) and on a progressively expanded HMDE coated with a C_{12} monolayer (B). The inset refers to the data of curve B and shows a plot of i versus the tilt angle θ of the C_{12} chains. The solid curve is a least-squares fit of Eq. (22) to the data [85].

predicted under the assumption that the monolayer behaves as an isotropic dielectric barrier in which electron tunneling efficiency is independent of its molecular structure [85]. This provides the first direct evidence that electron tunneling proceeds primarily through the alkyl chains, a pathway that does not change in length during monolayer expansion. The modest current increase observed as the film thickness decreases following drop expansion is ascribed to lateral ''hops'' between adjacent alkyl chains. For simplicity, the tunneling current i is regarded as consisting of a main contribution due to a whole ''through σ-bonds'' pathway along a single alkyl chain of length d, $i_0 \exp(-\beta_{tb} d)$, plus a minor contribution in which this pathway is modified by the inclusion of a single lateral ''chain-to-chain'' hop. From Figure 13(a) it is apparent that this lateral ''through-space'' hop decreases the length of the whole ''through σ-bonds'' pathway by an amount $x = d_{cc} \tan\theta$, where d_{cc} is the contact distance between adjacent alkyl chains modeled as cylinders, and θ is the tilt angle. By ascribing to the latter pathway a probability equal to the number n_c of carbon atoms in the *n*-alkanethiol chain, the current i is therefore given by:

$$i = i_0 \exp(-\beta_{tb} d) + i_0 n_c \exp[-\beta_{tb}(d - d_{cc} \tan\theta)] \exp(-\beta_{ts} d_{cc}) \qquad (22)$$

where β_{tb} and β_{ts} are the through-bond and through-space decay constants.

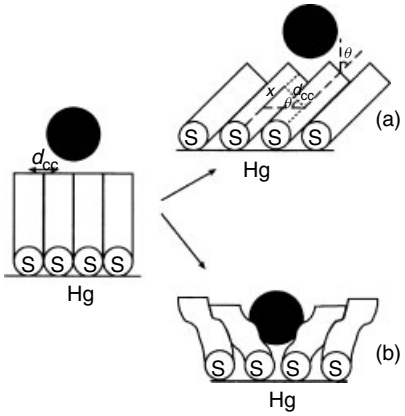


Fig. 13 Schematic representation of two possible different structures adopted by an alkanethiol monolayer upon expansion of an HMDE. (a) The monolayer is essentially pinhole free. A redox probe is located outside the monolayer/solution interface. The chains exhibit a tilt adopted in response to monolayer expansion. In addition to the through-bonds pathway, which dominates in perpendicularly oriented monolayers, an additional pathway (marked by the densely dashed line) involves a chain-to-chain coupling. (b) Hg drop expansion results in the formation of pinhole defects. A redox probe can partially permeate the alkane region of the monolayer [85, 109].

Fitting this equation to the experimental i versus θ plot for the C_{12} SAM (inset of Fig. 12) yields $\beta_{tb} = 0.91 \pm 0.01$ Å^{-1} and $\beta_{ts} = 1.31 \pm 0.05$ Å^{-1}. The latter value is in excellent agreement with an estimate obtained by ab initio calculations [85]. As expected, the chain-to-chain coupling is significantly weaker than the through-bonds coupling.

To exclude the possibility that the small increase in the tunneling current following drop expansion might be ascribed to partial penetration of the redox probe into the *n*-alkanethiol monolayer, as shown schematically in Fig. 13(b), the reorganization energies λ of the $IrCl_6^{2-/3-}$ redox probe and of the more hydrophobic ferrocene derivative, $FeCH_2N{-}(CH_3)_3^{2+/+}$, were determined on both unexpanded and expanded mercury drops [109]. In fact, if partial penetration of a redox probe into an expanded monolayer causes a certain increase in tunneling current as a result of a shorter tunneling distance, it should also cause a decrease in λ. On an unexpanded C_{16}-coated HMDE the reduction current i for both probes, recorded at a scan rate high enough (>5 V s^{-1}) to exclude partial diffusion control, increases with a negative shift in the overpotential η first exponentially, but then tends to a plateau. Thus, the i versus $-\eta$ plots show an inflection point, while the plots of $dk_{ap}/d\eta$, where $k_{ap} = i(\eta)/Fc^*$ is the apparent rate constant, are bell-shaped (see Fig. 14 for the case of $IrCl_6^{2-}$). The attainment of a plateau in the i versus $-\eta$ plots requires extremely negative overpotentials ($-e\eta > 2\lambda$) and corresponds to Marcus' inverted region for homogeneous electron-transfer reactions. When the role of electron donor is played by a metal, no decrease in the electron-transfer rate can be observed with an increase in driving force, because tunneling from the continuum of electronic states below the Fermi level ε_F is still possible for $-e\eta > \lambda$. An expression for k_{ap} is obtained by integrating the expression $\rho(\text{metal}) H_d{}^2(\varepsilon) \rho(\text{ox})$ over the electron energy levels ε, where $\rho(\text{metal}) = \{\exp[(\varepsilon - \varepsilon_F)/kT] + 1\}^{-1}$ is the Fermi distribution density of electronic states in the metal, $\rho(\text{ox}) = (4\pi\lambda kT)^{-1/2} \exp[-(\lambda - e\eta)^2/4\lambda kT]$ is the distribution density in the redox probe according to Marcus, and $H_d{}^2(\varepsilon)$ is the electronic coupling.

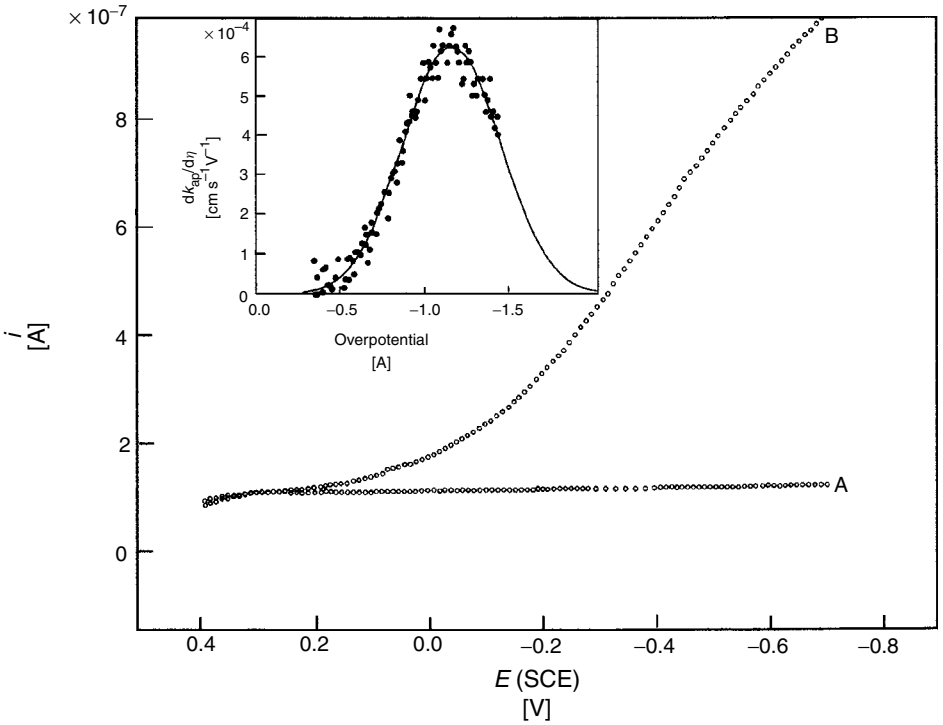


Fig. 14 Current versus potential curve of C_{16}-coated mercury in aqueous 0.5 M KCl in the absence (A) and in the presence (B) of 1.0×10^{-3} M $IrCl_6^{2-}$; scan rate = 5.12 V s^{-1}; electrode surface area = 0.0246 cm^2. The inset shows a plot of $dk_{ap}/d\eta$ versus η for the reduction of $IrCl_6^{2-}$ under the same experimental conditions. The solid curve corresponds to the Gaussian fit through the data [109].

Assuming that the Fermi distribution is a step function and that $H_d^2(\varepsilon)$ is independent of η, $dk_{ap}/d\eta$ takes the form $(4\pi^2/h)\rho(\text{metal})H_d^2\rho(\text{ox})$, which depends upon η only via the Gaussian function $\rho(\text{ox})$. Fitting this expression to the experimental $dk_{ap}/d\eta$ versus η plots (inset of Fig. 14) yields λ values close to 1 eV for both redox probes [109], in good agreement with the predictions of the Marcus dielectric continuum model for an aqueous environment. Therefore, the access of $IrCl_6^{2-}$ and $FeCH_2N-(CH_3)_3^{2+}$ to the electrode surface is restricted to a plane outside the C_{16} unexpanded monolayer. When carrying out analogous measurements on differently expanded C_{16} SAMs, the maxima of the Gaussian $dk_{ap}/d\eta$ versus η plots for the $IrCl_6^{2-}$ probe lie at the same overpotential up to a maximum tilt of the alkyl chains of ~20°. This indicates that the λ value is invariant with the monolayer expansion and that no penetration of $IrCl_6^{2-}$ into the alkyl chains of the SAM takes place. Conversely, in the case of the hydrophobic ferrocene probe, even a small expansion (2%) of the C_{16} SAM results in a very large increase in current and a destruction of the monolayer, due to mercury oxidation.

A film of chlorophyllide (Chlide), a chlorophyll molecule lacking the phytyl

chain, was adsorbed on top of mercury-supported SAMs of *n*-alkanethiols of chain length from C_{12} to C_{18} [111]. Illumination of Chlide causes the photoexcited molecule to take one electron from the metal, with formation of the $Chlide^-$ radical anion. The reduction photocurrents following illumination of the Chlide film were measured over the potential range in which this photoexcitable molecule is electroinactive in the dark, and their action spectra were determined. Differentiating these photocurrents with respect to the applied potential and plotting the resulting derivatives against potential yields bell-shaped curves that can be fitted to a Gaussian. The potential of the Gaussian maximum was used to determine the reorganization energy λ for the Chlide electroreduction process; λ was found to decrease regularly with an increase in the thiol chain length. This trend is opposite to that observed with chlorophyll molecules adsorbed on mercury-supported thiol SAMs [112], where λ is greater for C_{14} than for C_{12} [112]. The decrease in the reorganization energy λ for Chlide electroreduction with an increase in the thiol chain length is tentatively explained by a concomitant decrease in the amount of water molecules incorporated in the thiol SAM [111]. Increasing the thickness of the alkanethiol SAM by increasing its chain length causes the photocurrent, corrected for the reorganization energy, to decay exponentially with a decay constant β as low as 0.17 $Å^{-1}$. This low β value is explained by a concomitant energy transfer. If the thickness of an alkanethiol monolayer is decreased by expanding the drop surface, the photocurrent increases much less than observed by decreasing the alkanethiol chain length on a nonexpanded drop, thus confirming that electron transfer takes place primarily along a ''through σ-bonds'' pathway.

When two volumes of mercury are separated by an alkanethiol film, they do not coalesce; rather, they form a Hg−Hg junction consisting of two alkanethiol monolayers anchored to the surface of the two contacting mercury phases, with no chain intercalation at the resulting bilayer midplane [113, 114]. Thus, the plot of the reciprocal of the differential capacity C of the film against its thickness d, equated to the sum of the lengths of two fully extended alkanethiol molecules in a perpendicular orientation with respect to the mercury surfaces, satisfies the Helmholtz formula, $C = \varepsilon_0\varepsilon/d$ [113, 114]. When using two volumes of mercury in a glass tube, the dielectric constant ε of the junction was found to be 2.7 ± 0.3 [113], while the use of two contacting thiol-coated HMDEs, positioned vertically and coaxially one above the other, yielded an ε value of 2.0 ± 0.3 [114]. The latter device allows the formation of both symmetric and asymmetric $Hg-C_n//C_m-Hg$ bilayer junctions, with n and $m \geq 9$; here and in the following, the double dash denotes van der Waals interactions at the interface between terminal groups of the two SAMs. Thanks to the liquid nature of mercury, which has no macroscopic surface roughness, as distinct from solid electrodes, the junction area can be estimated with sufficient accuracy. As in the case of thiol-coated Hg electrodes, the tunneling current density measured at a voltage bias $V = -1.5$ V decreases exponentially with the length of the hydrocarbon chain, according to the relation $i = i_0 \exp(-\beta n_c)$, with the decay constant β per methylene group equal to 0.89 ± 0.1 [114]. Insertion of an amide group −CONH−, in place of a methylene group, in the bilayer junction results in an increase in the tunneling current, and hence in the electronic coupling. Junction experiments

can be carried out over a wide range of voltages; thus, Hg−C_{16}//C_{16}−Hg junctions are stable under voltages as large as ±2.5 V. However, the tunneling decay constant β decreases only slightly with an increase in voltage V, much less than predicted by the theory of electron tunneling between two metal plates across a square potential energy barrier. Apparently, the through σ-bonds mode of electron tunneling is only scarcely affected by the external electric field. The lifetime of these Hg−SAM(1)//SAM(2)−Hg junctions is of the order of 100 s, or greater, only with alkanethiols longer than C_8, and increases with their chain length [115]. Owing to the van der Waals and coulombic forces squeezing the junctions, their structure evolves with time, as shown by impedance spectroscopy measurements. This time evolution involves chain disorder and chain–chain intercalation, ultimately leading to junction breakdown; intercalation seems to proceed more rapidly for thicker junctions.

Hg−SAM(1)//SAM(2)−Ag junctions have also been prepared by forming a SAM on the surface of an evaporated film of silver, covering it with a solution of hexadecane containing C_{16}, immersing an HMDE into this solution so as to form a Hg−C_{16} SAM, and bringing it into contact with the silver electrode with a micromanipulator [116]. SAM(2) was formed with alkanethiols from C_8 to C_{16}, oligophenylene thiols, $HS(Ph)_kH$ ($k = 1, 2, 3$), and their benzylic homologs, $HSCH_2(Ph)_kH$. The decrease in current density with increasing length of the molecules forming SAM(2), and therefore with the distance, $d_{Ag,Hg}$, separating the electrodes, follows the relation $i = i_0 \exp(-\beta d_{Ag,Hg})$, with β approximately independent of the bias voltage V over the range from 0.1 to 1 V. The current increases linearly with V at low V values, and exponentially at high V values. This behavior is typical of electron transport by ''superexchange tunneling'', namely, tunneling mediated by interactions between donor and acceptor (in the present case, the two metal electrodes) and unoccupied orbitals of the organic material separating them. This situation is encountered when the Fermi level of the metal electrodes and the lowest unoccupied molecular orbital (LUMO) of the ''molecular bridge'' interposed between them are separated by a large energy gap. When the SAM(2) tethered to the silver electrode is formed from a dialkyl disulfide with a covalently linked tetracyanoquinodimethane (TCNQ) group, the Hg−C_{16}//SAM(2)−Ag rectifies current, in that the current flowing from Hg to Ag is about nine times higher than that flowing in the opposite direction, at 1 V magnitude bias [117]. This behavior is explained by the single TCNQ functional group having an energy different from the rest of the sites of the molecular bridge and a different site-coupling energy to its neighbors; thus, it is covalently linked to the rest of SAM(2), while it is only in van der Waals contact with SAM(1). This determines a potential drop through the TCNQ site, which is asymmetric with respect to bias.

An ''electrochemical inclusion junction'' has also been described [118, 119]. It consists of two HMDEs, both of which support a SAM of the ruthenium pentamine pyridine-terminated thiol, $HS(CH_2)_{10}CONHCH_2pyRu(NH_3)_5$, and are brought into contact in an aqueous solution. The potentials of the two electrodes are controlled independently with respect to a common reference electrode immersed in the solution, by using a bipotentiostat. Under certain

conditions, the more negative electrode (the cathode) transfers an electron to Ru^{III} of its own SAM; the resulting Ru^{II} releases its electron to Ru^{III} of the adjacent SAM, which transfers it to the corresponding, more positive electrode (the anode). This electron transfer takes place only when the electronic states of the Ru^{II}/Ru^{III} couple fall between the Fermi energies of the two mercury electrodes. In one experiment, the potential difference between the two electrodes was kept constant at 0.1 V, and both potentials were shifted upwards, so as to move both Fermi energies from above to below the electronic states of the Ru^{II}/Ru^{III} couple; the plot of the resulting current against the potential of the anode is bell-shaped, with the maximum lying in the proximity of the Ru^{II}/Ru^{III} redox potential. The mechanism responsible for this current is considered to be resonant tunneling, with electrons actually populating the molecular bridge, or a two-step hopping mechanism, with electrons localized somewhere in the molecular bridge for an appreciable time during electron transport.

1.3.1.4 Tethered Bilayer Lipid Membranes on Hg

The possibility of self-assembling bilayers covalently on metals with the formation of rugged functionalized electrodes has stimulated research aiming at exploiting self-assembly for the realization of biomembrane models capable of incorporating integral proteins in a functionally active state. This has potential not only for fundamental research on protein functions but also for biosensor applications. To achieve this goal, biomembrane models consisting of lipid bilayers (often referred to as *tethered bilayer lipid membranes*, tBLMs) should meet a number of requirements: (1) they should be robust enough for long-term stability, and be easily and reproducibly prepared; (2) they should be as flexible and fluid as lipid films in the liquid-crystalline state; (3) they should have water on both sides of the lipid bilayer; and (4) they should be sufficiently free from pinholes and other defects that might provide preferential pathways for electron and ion transport across the lipid bilayer [120]. Requirements (2) and (3) are necessary for the incorporation of integral proteins into the lipid bilayer in a functionally active state. In fact, integral proteins have a hydrophobic section buried inside the lipid leaflet of the biomembrane, which must therefore be sufficiently flexible to accommodate this section. Often, they also have hydrophilic sections protruding by over 60 Å outside the lipid bilayer. To avoid their denaturation and to promote their function, the incorporation of integral proteins into biomembranes must ensure that their protruding hydrophilic sections are accommodated in a hydrophilic medium on both sides of the lipid bilayer. Moreover, the transport of hydrophilic ions across the lipid bilayer, via ion channels or ionophores, is possible only if an aqueous layer is interposed between the bilayer and the electrode surface. Requirement (4) is needed to make the biomembrane model sufficiently blocking as to characterize ion channel activity by electrochemical means, without the disturbing presence of stray currents due to defects.

Mixed alkanethiol–phospholipid bilayers on an HMDE are readily prepared by exploiting the hydrophobic interactions between the hydrocarbon tails of the alkanethiol and those of the phospholipid [64]. Thanks to the high affinity of mercury for sulfur, an alkanethiol monolayer is first obtained by immersing the mercury drop for 1 or 2 minutes in a thiol solution in ethanol. The phospholipid monolayer on

top of the alkanethiol monolayer is then obtained by immersing the thiol-coated mercury drop in an aqueous solution on whose surface a phospholipid monolayer has been previously spread. The differential capacity of the mixed bilayer so obtained agrees with the value calculated from the equation $C = C_t C_p/(C_t + C_p)$, where C_t and C_p are the experimental values of the capacities of the thiol and phospholipid SAMs on mercury. The flexibility and fluidity of the chemisorbed alkanethiol monolayer in direct contact with the electrode is much less than that of BLMs; this makes these Hg-supported mixed bilayers unsuitable for ion transport mediated by ionophores and practically impermeable to lipophilic molecules of biological importance, such as UQ and vitamin K_1 [64]. Moreover, no hydrophilic layer is interposed between the bilayer and the electrode surface, thus excluding the space and water required for the proper folding of the extramembrane parts of integral proteins.

In a first attempt to overcome these limitations, the alkanethiol monolayer was replaced by a SAM of a hydrophilic ''thiolspacer'' consisting of a polyethyleneoxy [107] or an oligopeptide [102] chain terminated with a sulfhydryl group for anchoring to the mercury surface. The thiolspacer is self-assembled on an HMDE by keeping the mercury drop immersed in its ethanol solution for 30 minutes. The thiolspacer-coated mercury drop is then extracted from the solution, allowing the ethanol to evaporate. Subsequently, the drop is brought into contact with a lipid film that has been previously spread on the surface of an aqueous electrolyte, taking care to keep the drop neck in contact with the lipid reservoir. This disposition allows a free exchange of material between the thiolspacer-coated drop and the lipid reservoir on the surface of the aqueous electrolyte, with formation of a floating lipid bilayer on top of the hydrophilic thiolspacer. Thanks to the defect-free surface of liquid mercury, this mercury-supported thiolspacer/(lipid bilayer) system exhibits a differential capacity close to that of solvent-free black lipid membranes, thus denoting a very low number of pinholes and other surface defects. Complete immersion of the drop into the solution is to be avoided, because the relative solubility of the thiolspacer in water causes the gradual dissolution of the film. In these tBLMs, incorporation of ionophores such as the ion carrier valinomycin [102, 107] and the channel-forming peptide melittin [107] decreases the resistance of the film. Thus, it determines a typical minimum in the plot of the phase angle of the electrochemical impedance against the frequency over the frequency range that would be exclusively controlled by the capacity of the biomimetic membrane if the ionophore were absent.

The potential difference across the floating lipid bilayer on top of the thiolspacer SAM (i.e. the transmembrane potential) can be estimated by noting that its zero value is practically attained at the applied potential E at which the absolute potential difference across the whole interphase, $\Delta\phi \approx (E/\mathrm{SCE} + 0.250\ \mathrm{V})$ (see Eq. 9), is equal to the calculated value of χ_t. In fact, from Eq. (21) it is apparent that, under these conditions the charge density $q = \sigma_M + \alpha\sigma_i$ experienced by the diffuse-layer ions is zero, just as the electric field across the floating lipid bilayer. The applied potential at which the transmembrane potential equals zero can also be approximately estimated by incorporating valinomycin in the lipid bilayer [37, 121]. Valinomycin is a K^+-selective ion carrier that may shuttle K^+ ions across

the bilayer, thus increasing its conductivity. When q is positive, the K^+ ions are electrostatically repelled from the thiolspacer. Shifting the applied potential to more negative values, K^+ ions start penetrating into the thiolspacer, and the conductance of the tBLM increases up to a limiting value; ultimately, at still more negative potentials, the conductance decreases owing to saturation of the thiolspacer. Under the simplifying assumption that the short-range interactions of K^+ with the thiolspacer medium are comparable with those with the aqueous phase, it can be demonstrated that the inflection point of the curve of the conductance against the applied potential E corresponds to a zero value of the transmembrane potential [37]. The voltage-gated channel of melittin, incorporated in a tBLM prepared with a triethyleneoxythiol thiolspacer [107], was found to open at a calculated transmembrane potential practically equal to that reported on a BLM.

In spite of some satisfactory results obtained with lipid bilayers self-assembled on top of mercury-supported hydrophilic thiolspacers, their use is rather uncomfortable, since the drop neck must be kept in contact with the lipid reservoir on the surface of the aqueous electrolyte during measurements. More convenient tBLMs are obtained if the HMDE is coated with a monolayer of a ''thiolipid'' [30, 37, 121–123]. This consists of a hydrophylic spacer terminated with a sulfhydryl or disulfide group at one end, for anchoring to the mercury surface, and covalently linked to the polar head of a phospholipid at the other end. Tethering the thiolipid to the metal surface yields half a lipid bilayer, with the hydrocarbon tails turned toward the aqueous solution. Immersing the thiolipid-coated mercury drop into an aqueous electrolyte, on whose surface a lipid film has been previously spread, causes a lipid monolayer to self-assemble on top of the thiolipid monolayer, with the hydrocarbon tails of the two monolayers turned toward each other. This procedure yields a lipid bilayer anchored to the mercury surface through the hydrophilic portion of the thiolipid, which mimics the aqueous phase on the metal side of the bilayer.

A particularly convenient thiolipid named *DPTL* consists of a tetraethyleneoxy chain covalently linked to a lipoic acid residue for anchoring to the metal at one end, and bound via ether linkages to two phytanyl chains at the other end (see its structure in Fig. 15); it has been used by Naumann et al. [124] for the preparation and characterization of tBLMs on gold. A tBLM obtained by self-assembling a diphytanoylphosphatidylcholine monolayer on top of a DPTL-coated mercury electrode was investigated by impedance spectroscopy over a frequency range from 1×10^{-2} to 1×10^{5} Hz and over a potential range of 0.8 V, both in the absence and in the presence of the ion carrier valinomycin [30]. The impedance spectra obtained upon incorporating valinomycin in this tBLM from its 1.5×10^{-7} M solution in aqueous 0.1 M KCl are particularly rich in characteristic features, especially when reported in a $\omega Z'$ versus $\omega Z''$ plot (see Sect. 1.3.2.2.1). This plot shows four partially fused semicircles (see Fig. 15), which can be straightforwardly fitted to an equivalent circuit consisting of four RC meshes in series. Each semicircle corresponds to a RC mesh; the diameter of the semicircle measures the reciprocal, $1/C$, of the capacity of the RC mesh, while the ω value at the maximum of the semicircle measures the reciprocal of its time constant, $\tau = RC$. The frequency increases in the direction of increasing $\omega Z''$.

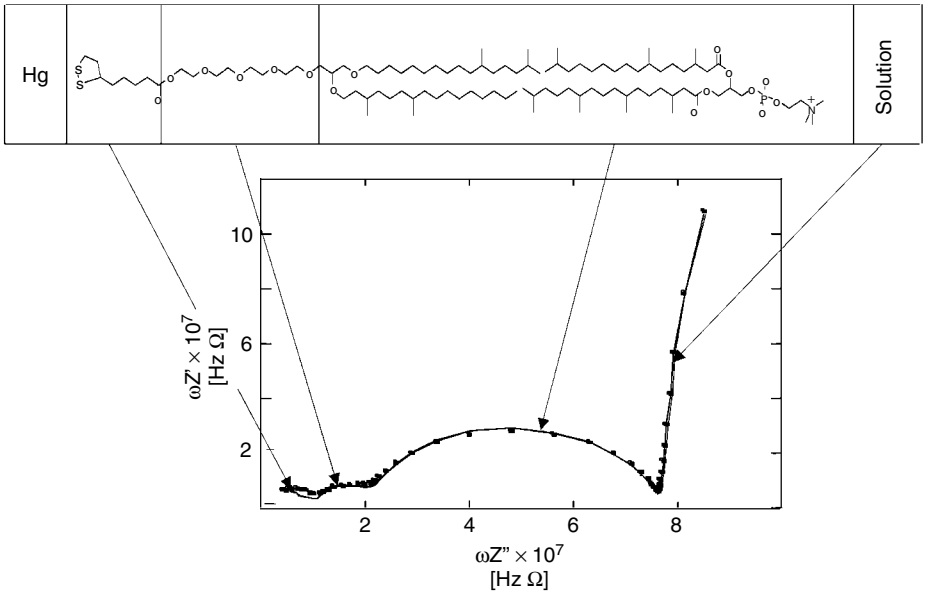


Fig. 15 Top: structure of the DPTL thiolipid in contact with a diphytanoylphosphatidylcholine molecule. Bottom: plot of $\omega Z'$ versus $\omega Z''$ for a tBLM in aqueous solution of 0.1 M KCl and 1.5×10^{-7} M valinomycin, recorded at −0.41 V/SCE. The arrows relate the semicircles of the $\omega Z'$ versus $\omega Z''$ plot to the different substructural elements of the tBLM [30].

The four RC meshes are ascribed to different portions of the tBLM, on the basis of the potential dependence of their R and C values, which is interpreted by a model of the electrified interface [30]. In fact, the tBLM is a heterogeneous system with a substructure in which the dielectric and conductance properties of the substructural elements are different; this gives rise to a dispersion of the impedance with frequency, due to interfacial polarization at the substructural-element interfaces, which provides a means of detecting and characterizing these dielectric slabs. When proceeding in the direction of increasing $\omega Z''$, the RC meshes in Fig. 15 are ascribed to the lipoic acid residue, the tetraethyleneoxy moiety, the lipid bilayer, and the aqueous solution adjacent to the tBLM. This tBLM was also used to incorporate the channel-forming protein OmpF porin from its aqueous dispersion in detergent [123]. The analysis of the impedance spectra indicates that OmpF porin increases the conductivity of the tBLM over a narrow potential range straddling the zero value of the potential difference across the lipid bilayer moiety.

References

1. I. R. Miller, D. Bach, *J. Colloid Interface Sci.* **1969**, *29*, 250–260.
2. R. E. Pagano, I. R. Miller, *J. Colloid Interface Sci.* **1973**, *45*, 126–137.
3. I. M. Kolthoff, C. Barnum, *J. Am. Chem. Soc.* **1940**, *62*, 3061–3065.
4. M. Montal, *Annu. Rev. Biophys. Bioeng.* **1976**, *5*, 119–175.
5. M. F. Lecompte, I. R. Miller, *J. Colloid Interface Sci.* **1988**, *123*, 259–266.
6. M. F. Lecompte, I. R. Miller, *Biochemistry* **1980**, *19*, 3439–3446.

7. S. Trasatti, in *Modern Aspects of Electrochemistry* (Eds.: B. E. Conway, J. O. M. Bockris), Plenum, New York, 1979, pp. 81–206. Vol. 13.
8. S. Trasatti, in *Electrified Interfaces in Physics, Chemistry and Biology* (Eds.: R. Guidelli), Kluwer, Dordrecht, 1992, pp. 245–273.
9. A. Nelson, A. Benton, *J. Electroanal. Chem.* **1986**, *202*, 253–270.
10. A. Nelson, N. Auffret, *J. Electroanal. Chem.* **1988**, *248*, 167–180.
11. M. R. Moncelli, L. Becucci, *J. Electroanal. Chem.* **1997**, *433*, 91–96.
12. L. Becucci, M. R. Moncelli, R. Guidelli, *J. Electroanal. Chem.* **1996**, *413*, 187–193.
13. V. Stauffer, R. Stoodley, J. O. Agak et al., *J. Electroanal. Chem.* **2001**, *516*, 73–82.
14. A. Nelson, F. A. M. Leermakers, *J. Electroanal. Chem.* **1990**, *278*, 73–83.
15. L. Becucci, M. R. Moncelli, R. Herrero et al., *Langmuir* **2000**, *16*, 7694–7700.
16. F. Tadini Buoninsegni, L. Becucci, M. R. Moncelli et al., *J. Electroanal. Chem.* **2001**, *500*, 395–407.
17. A. Nelson, N. Auffret, *J. Electroanal. Chem.* **1988**, *244*, 99–133.
18. F. M. Kimmerle, H. Ménard, *J. Electroanal. Chem.* **1974**, *54*, 101–121.
19. S. Trasatti, *J. Electroanal. Chem.* **1977**, *82*, 391–402.
20. (a) R. J. Clarke, *Biochim. Biophys. Acta* **1997**, *1327*, 269–278; (b) A. D. Pickar, R. Benz, *J. Membr. Biol.* **1978**, *44*, 353–376; (c) K. Gawrisch, D. Ruston, J. Zimmerberg et al., *Biophys. J.* **1992**, *61*, 1213–1223; (d) R. F. Flewelling, W. L. Hubbell, *Biophys. J.* **1986**, *49*, 541–552.
21. D. Bizzotto, A. Nelson, *Langmuir* **1998**, *14*, 6269–6273.
22. D. Bizzotto, Y. Yang, J. L. Shepherd et al., *J. Electroanal. Chem.* **2004**, *574*, 167–184.
23. J. Shepherd, Y. Yang, D. Bizzotto, *J. Electroanal. Chem.* **2002**, *524–525*, 54–61.
24. J. O. Agak, R. Stoodley, U. Retter et al., *J. Electroanal. Chem.* **2004**, *562*, 135–144.
25. (a) H. Akutsu, J. Seelig, *Biochemistry* **1981**, *20*, 7366–7373; (b) J. Seelig, P. M. Macdonald, P. G. Scherer, *Biochemistry* **1987**, *26*, 7535–7541; (c) R. J. Clarke, C. Lüpfert, *Biophys. J.* **1999**, *76*, 2614–2624.
26. C. Whitehouse, R. O'Flanagan, B. Lindholm-Sethson et al., *Langmuir* **2004**, *20*, 136–144.
27. J. Ross Macdonald, W. B. Johnson, in *Impedance Spectroscopy* (Ed.: J. Ross Mcdonald), John Wiley & Sons, New York, 1987, pp. 1–26. i
28. B. Lindholm-Sethson, P. Geladi, A. Nelson, *Anal. Chim. Acta* **2001**, *446*, 121–131.
29. R. G. Ashcroft, H. G. L. Coster, J. R. Smith, *Biochim. Biophys. Acta – Biomembr.* **1981**, *643*, 191–204.
30. L. Becucci, M. R. Moncelli, R. Guidelli, *J. Am. Chem. Soc.* **2005**, *127*, 13316–13323.
31. E. Falletta, M. R. Moncelli, L. Becucci et al., unpublished.
32. A. Nelson, H. P. van Leewen, *J. Electroanal. Chem.* **1989**, *273*, 183–199.
33. I. R. Miller, *J. Membr. Biol.* **1988**, *101*, 113–118.
34. M. R. Moncelli, L. Becucci, F. Tadini Buoninsegni et al., *Biophys. J.* **1998**, *74*, 2388–2397.
35. M. R. Moncelli, L. Becucci, R. Guidelli, *Biophys. J.* **1994**, *66*, 1969–1980.
36. B. B. Damaskin, A. N. Frumkin, *Electrochim. Acta* **1974**, *19*, 173–176.
37. L. Becucci, M. R. Moncelli, R. Guidelli, *Langmuir* **2003**, *19*, 3386–3392.
38. F. A. Leermarkers, A. Nelson, *J. Electroanal. Chem.* **1990**, *278*, 53–72.
39. A. Nelson, *Anal. Chim. Acta* **1987**, *194*, 139–149.
40. A. Nelson, N. Auffret, J. Borlakoglu, *Biochim. Biophys. Acta* **1990**, *1021*, 205–216.
41. A. Nelson, N. Auffret, J. Readman, *Anal. Chim. Acta* **1988**, *207*, 47–57.
42. R. Herrero, M. R. Moncelli, R. Guidelli et al., *Biochim. Biophys. Acta* **2000**, *1466*, 278–288.
43. L. Becucci, M. R. Moncelli, R. Guidelli, *J. Am. Chem. Soc.* **2003**, *125*, 3785–3792.
44. M. R. Moncelli, L. Becucci, *Bioelectrochem. Bioenerg.* **1996**, *39*, 227–234.
45. M. R. Moncelli, R. Herrero, L. Becucci et al., *J. Phys. Chem.* **1995**, *99*, 9940–9951.
46. I. R. Miller, D. Bach, M. Teuber, *J. Membr. Biol.* **1978**, *39*, 49–56.
47. M. F. Lecompte, I. R. Miller, J. Elion et al., *Biochemistry* **1980**, *19*, 3434–3438.
48. M.-F. Lecompte, A.-C. Bras, N. Dousset et al., *Biochemistry* **1998**, *37*, 16165–16171.
49. A. Nelson, *J. Electroanal. Chem.* **1991**, *303*, 221–236.
50. A. Nelson, *J. Chem. Soc., Faraday Trans.* **1993**, *89*, 2799–2805.
51. A. Nelson, *Langmuir* **1996**, *12*, 2058–2067.

52. A. Nelson, *Langmuir* **1997**, *13*, 5644–5651.
53. M. Rueda, I. Navarro, G. Ramirez et al., *Langmuir* **1999**, *15*, 3672–3678.
54. A. Nelson, D. Bizzotto, *Langmuir* **1999**, *15*, 7031–7039.
55. L. Becucci, M. R. Moncelli, R. Guidelli, *Biophys. J.* **2002**, *82*, 852–864.
56. F. Prieto, I. Navarro, M. Rueda, *J. Electroanal. Chem.* **2003**, *550–551*, 253–265.
57. J. C. Franklin, D. S. Cafiso, *Biophys. J.* **1993**, *65*, 289–299.
58. E. Gross, R. S. Bedlack, L. M. Loew, Jr. *Biophys. J.* **1994**, *67*, 208–216.
59. A. Nelson, *J. Electroanal. Chem.* **1992**, *335*, 327–343.
60. M. R. Moncelli, L. Becucci, A. Nelson et al., *Biophys. J.* **1996**, *70*, 2716–2726.
61. M. R. Moncelli, R. Herrero, L. Becucci et al., *Biochim. Biophys. Acta* **1998**, *1364*, 373–384.
62. R. Herrero, J. L. Barriada, J. M. López-Fonseca et al., *Langmuir* **2000**, *16*, 5148–5153.
63. P. Lodeiro, R. Herrero, M. E. Sastre de Vicente, *Langmuir* **2002**, *18*, 9377–9382.
64. R. Herrero, F. Tadini Buoninsegni, L. Becucci et al., *J. Electroanal. Chem.* **1998**, *445*, 71–80.
65. R. Herrero, M. R. Moncelli, L. Becucci et al., *J. Electroanal. Chem.* **1997**, *425*, 87–95.
66. I. Zawisza, R. Bilewicz, M. R. Moncelli et al., *J. Electroanal. Chem.* **2001**, *509*, 31–41.
67. R. Herrero, M. R. Moncelli, L. Becucci et al., *J. Phys. Chem. B* **1997**, *101*, 2815–2823.
68. M. R. Moncelli, R. Herrero, L. Becucci et al., *Isr. J. Chem.* **1997**, *37*, 247–257.
69. I. M. Kolthoff, W. Stricks, N. Tanaka, *J. Am. Chem. Soc.* **1955**, *77*, 5211–5215.
70. W. M. Moore, V. F. Gaylor, *Anal. Chem.* **1977**, *49*, 1386–1390.
71. T. M. Florence, *J. Electroanal. Chem.* **1979**, *97*, 219–236.
72. J. T. Stock, R. E. Larson, *Anal. Chim. Acta* **1982**, *138*, 371–374.
73. I. Turyan, D. Mandler, *Anal. Chem.* **1994**, *66*, 58–63.
74. R. L. Birke, M. Mazorra, *Anal. Chim. Acta* **1980**, *118*, 257–269.
75. M. Youssefi, R. L. Birke, *Anal. Chem.* **1977**, *49*, 1380–1385.
76. M. Stankovich, A. J. Bard, *J. Electroanal. Chem.* **1977**, *75*, 487–505.
77. M. Heyrovsky, P. Mader, V. Veselá et al., *J. Electroanal. Chem.* **1994**, *369*, 53–70.
78. I. Pardo, M. Angulo, R. Marin Galvin et al., *Electrochim. Acta* **1996**, *41*, 133–139.
79. I. R. Miller, J. Teva, *J. Electroanal. Chem.* **1972**, *36*, 157–166.
80. M. D. Porter, T. B. Bright, D. L. Allara et al., *J. Am. Chem. Soc.* **1987**, *109*, 3559–3568.
81. E. B. Troughton, C. D. Bain, G. M. Whitesides et al., *Langmuir* **1988**, *4*, 365–385.
82. A. Demoz, D. J. Harrison, *Langmuir* **1993**, *9*, 1046–1050.
83. N. Muskal, I. Turyan, A. Shurky et al., *J. Am. Chem. Soc.* **1995**, *117*, 1147–1148.
84. N. Muskal, I. Turyan, D. Mandler, *J. Electroanal. Chem.* **1996**, *409*, 131–136.
85. K. Slowinski, R. V. Chamberlain, C. J. Miller et al., *J. Am. Chem. Soc.* **1997**, *119*, 11910–11919.
86. F. T. Buoninsegni, R. Herrero, M. R. Moncelli, *J. Electroanal. Chem.* **1998**, *452*, 33–42.
87. K. J. Stevenson, M. Mitchell, H. S. White, *J. Phys. Chem. B* **1998**, *102*, 1235–1240.
88. Z. González Arias, J. L. Muñiz Álvarez, J. M. López Fonseca, *J. Electroanal. Chem.* **2005**, *575*, 243–248.
89. O. M. Magnussen, B. M. Ocko, M. Deutsch et al., *Nature* **1996**, *384*, 250–252.
90. M. Deutsch, O. M. Magnussen, B. M. Ocko et al., *Thin Films* **1998**, *24*, 179–203.
91. H. Kraack, B. M. Ocko, P. S. Pershan et al., *J. Chem. Phys.* **2003**, *119*, 10339–10349.
92. H. Kraack, B. M. Ocko, P. S. Pershan et al., *Langmuir* **2004**, *20*, 5375–5385.
93. C. Bruckner-Lea, J. Janata, J. F. T. Conroy, *Langmuir* **1993**, *9*, 3612–3617.
94. R. Guidelli, F. Pergola, *J. Electroanal. Chem.* **1977**, *84*, 255–270.
95. I. M. Kolthoff, C. Barnum, *J. Am. Chem. Soc.* **1941**, *63*, 520–526.
96. J. J. Calvente, R. Andreu, L. González et al., *J. Phys. Chem. B* **2001**, *105*, 5477–5488.
97. P. Ramírez, R. Andreu, J. J. Calvente et al., *J. Electroanal. Chem.* **2005**, *582*, 179–190.
98. (a) N. Muskal, D. Mandler, *Electrochim. Acta* **1999**, *45*, 537–548; (b) N. Muskal, D. Mandler, *Curr. Separations* **2000**, *19:2*, 49–54.
99. J. M. Sevilla, T. Pineda, R. Madueño et al., *J. Electroanal. Chem.* **1998**, *442*, 107–112.
100. (a) R. Madueño, T. Pineda, J. M. Sevilla, M. Blázquez, *Langmuir* **2002**, *18*, 3903–3909; (b) *J. Electroanal. Chem.* **2004**, *565*, 301–310; (c) *J. Phys. Chem. B* **2005**, *109*, 1491–1498.

101. (a) Z. González Arias, J. L. Muñiz Álvarez, J. M. López Fonseca, *J. Colloid Interface Sci.* **2002**, *250*, 295–302; (b) **2004**, *276*, 132–137.
102. C. Peggion, F. Formaggio, C. Toniolo et al., *Langmuir* **2001**, *17*, 6585–6585
103. (a) D. F. Yang, C. P. Wilde, M. Morin, *Langmuir* **1996**, *12*, 6570–6577; (b) **1997**, *13*, 243–249.
104. C. A. Widrig, C. Chung, M. D. Porter, *J. Electroanal. Chem.* **1991**, *310*, 335–359.
105. A. Frumkin, O. Petrii, B. Damaskin, *J. Electroanal. Chem.* **1970**, *27*, 81–100.
106. P. Delahay, *J. Phys. Chem.* **1966**, *70*, 2373–2379.
107. L. Becucci, R. Guidelli, Q. Liu et al., *J. Phys. Chem. B* **2002**, *106*, 10410–10416.
108. K. Slowinski, R. V. Chamberlain, R. Bilewicz et al., *J. Am. Chem. Soc.* **1997**, *118*, 4709–4710.
109. K. Slowinski, K. U. Slowinska, M. Majda, *J. Phys. Chem. B* **1999**, *103*, 8544–8551.
110. C. Bruckner-Lea, R. J. Kimmel, J. Janata et al., *Electrochim. Acta* **1995**, *40*, 2897–2904.
111. F. Tadini Buoninsegni, M. R. Moncelli, G. Aloisi et al., *J. Am. Chem. Soc.* **2005**, *127*, 2231–2237.
112. F. Tadini Buoninsegni, A. Dolfi, R. Guidelli, *Collect. Czech. Chem. Commun.* **2004**, *69*, 292–308.
113. M. A. Rampi, O. J. A. Schueller, G. M. Whitesides, *Appl. Phys. Lett.* **1998**, *72*, 1781–1783.
114. K. Slowinski, H. K. J. Fong, M. Majda, *J. Am. Chem. Soc.* **1999**, *121*, 7257–7261.
115. K. Slowinski, M. Majda, *J. Electroanal. Chem.* **2000**, *491*, 139–147.
116. R. E. Holmlin, R. Haag, M. L. Chabinyc et al., *J. Am. Chem. Soc.* **2001**, *123*, 5075–5085.
117. M. L. Chabinyc, X. Chen, R. E. Holmlin et al., *J. Am. Chem Soc.* **2002**, *124*, 11730–11736.
118. C. Grave, E. Tran, P. Samorì et al., *Synth. Met.* **2004**, *147*, 11–18.
119. E. Tran, C. Grave, G. M. Whitesides et al., *Electrochim. Acta* **2005**, *50*, 4850–4856.
120. R. Guidelli, G. Aloisi, L. Becucci et al., *J. Electroanal. Chem.* **2001**, *504*, 1–28.
121. M. R. Moncelli, L. Becucci, S. M. Schiller, *Bioelectrochemistry* **2004**, *63*, 161–167.
122. L. Becucci, R. Guidelli, C. Peggion et al., *J. Electroanal. Chem.* **2005**, *576*, 121–128.
123. L. Becucci, M. R. Moncelli, R. Guidelli, *Langmuir* **2006**, *22*, 1341–1346.
124. (a) R. Naumann, S. M. Schiller, F. Gieβ et al., *Langmuir* **2003**, *19*, 5435–5443; (b) R. Naumann, D. Walz, S. M. Schiller et al., *J. Electroanal. Chem.* **2003**, *550–551*, 241–247; (c) S. M. Schiller, R. Naumann, K. Lovejoy et al., *Angew. Chem., Int. Ed. Engl.* **2003**, *42*, 208–211.

1.3.2 Modification of Silicon Wafer Surfaces with Small Organic Moieties

Taro Yamada
RIKEN, 2-1 Hirosawa, Wako-shi, Saitama 351-0198, Japan

1.3.2.1 Introduction

Monolayers of organic adsorbates bonded on silicon wafer surfaces have properties for prospective applications in nanometer-scale physical science, chemistry, biology, and industrial technology [1–3]. The covalent linkage in organic adsorbates can mediate the connection of a variety of molecular groups with surface Si atoms. The diversity of organic species can guarantee almost limitless possibilities for molecules and moieties attached to Si surface.

This article deals with a category of organic adsorbates that is attached to the outermost surface Si by the C−Si covalent bond. Figure 1 illustrates two typical examples of hydrocarbon moieties attached directly to surface Si. One is a linear alkyl chain terminating one surface Si atom. The other is a hydrocarbon moiety fixed by two C−Si bonds. The existence of the C−Si

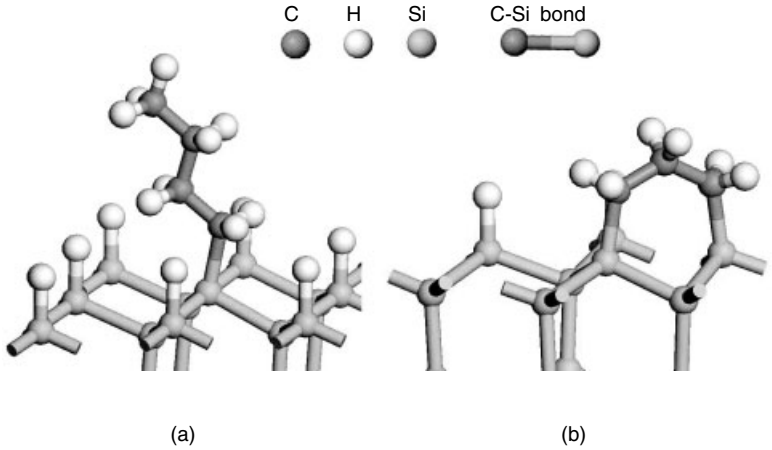


Fig. 1 Schematic view of hydrocarbon adsorbates covalently bonded on Si(111) surface. (a) Single-chain alkyl fixed by one C−Si bond. (b) Bridging hydrocarbon fixed by two C−Si bonds.

bond on the surface is important because it brings about advantageous properties such as thermal stability, low mobility along the surface, and chemical stability. The dissociation energy of C−Si bond has been estimated to be $>300\ kJ\ mol^{-1}$ [4], notably larger than the adsorption heat of molecules on noble metals. Actually CH_3 species on Si(111) remains undecomposed at 600 K in vacuum [5]. Related to this, the covalently bonded species are anticipated to be immovable along the surface, as the C−Si bonds on the single-crystalline planes are electronically localized. More practically, Si surfaces covered with grafted organic moieties have been frequently reported to be robust against the practical environment and even in powerful reagents [6–9]. It is certainly amazing that just one monolayer of organic fragments can nullify the harsh reactivity of the clean Si surface, such as Si(111)-(7 × 7) reserved in vacuum, into inertness in the atmosphere.

The robustness of organic-modified Si(111) frequently attracts interest application. The passivation and modification of electronic properties were conducted by Buriak on porous Si surfaces, on which the organic adsorbate was utilized for photolithography and photoluminescence [10]. Modification of electronic properties was frequently attempted [10–14]. Application for biochemical analysis has also been extensively pursued. Hamers et al. reported fixation of single strand DNA by covalent linkage on Si and other semiconductors, and performed electrochemical detection of DNA hybridization [15, 16]. This attempt is probably the leading edge in the development of intelligent biochips with integrated electronics for signal detection and processing. Another category of prospective application is electronics by molecular chains. Lopinski et al. first found a chain reaction of styrene adsorption on a (2 × 1)-hydrogen-terminated Si(100) wafer [17]. The single line composed of adsorbed molecules can be easily imagined as a material of molecular wires [11, 18], and the electronic properties of this ''nanowire'' were examined [19]. Figure 2 shows scanning tunneling spectroscopy (STM) images of a

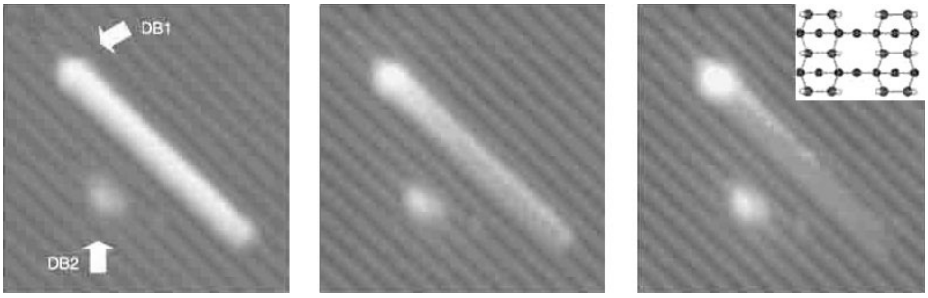


Fig. 2 Visualization of the electrostatic potential emanating from a point source for a styrene chain on H:Si(100). (a) With negatively charged dangling bonds labeled DB1 and DB2. The prominent white bar is a line of surface-bound molecules. At increased sample bias of −2.4 V, molecular p-states are ''turned on'', causing molecules to appear bright (topographically elevated) and of nearly constant height across the line. (b) At an intermediate bias of −1.8 V, molecules appear darker, increasingly so at greater distances from DB1. (c) In the absence of a negative dangling bond all molecules would appear dark at −1.6 V, but the molecules nearest to the dangling bond remain prominent. (Figure 1 of P. G. Piva, G. A. DiLabio, J. L. Pitters et al., *Nature* **2005**, *435*, 658 [19]).

styrene chain formed on H:Si(100)-(2 × 1), in which the electronic orbitals in each styrene adsorbate are modified by the existence of a dangling bond located at one end of the chain. This phenomenon was explained on the basis of molecular-orbital calculation.

Despite those prospects of practical applications, the details of structure and composition of the organic adlayer, which directly influence the quality of surface, have not been always well recognized. The practical criterion that characterizes covalent adsorbates on semiconductor surfaces is that every dangling bond generated by the truncation of a single crystal should be terminated by an adsorbate. The dangling bonds on surfaces of Si and Ge are reactive with O_2 and other components of air and would result in the deterioration of the whole surface. If the surface is supposed to be handled in air or in liquid, complete rejection of dangling bonds should be achieved by appropriate reaction and handling conditions. The discovery of H:Si(111)-(1 × 1), on which every surface Si is monohydride terminated [20], was an epoch-making event to open up the field of organic chemistry on semiconductors handled out of ultrahigh vacuum (UHV).

There are some typical cases in which every surface Si atom is actually terminated by one C−Si bond, namely, that in which the stoichiometric full coverage is attained. On clean Si(100), (2 × 1) adlattices can be formed by cycloaddition of cyclic olefins onto surface Si−Si dimers [21]. Hamers et al. presented a highly ordered adlayer terminating all Si atoms just by exposing clean Si(100)-(2 × 1) to gaseous cyclopentene (C_5H_8) in UHV environment [22]. Figure 3 shows STM images of cyclopentene molecules bonded in parallel to the dimer rows of Si(100)-(2 × 1) terraces. This sort of full-coverage adlayer can be expected only when the adsorbate is small enough to be contained within one (2 × 1) supercell.

On Si(111), it was demonstrated that even CH_3–, the smallest alkyl moiety, fills

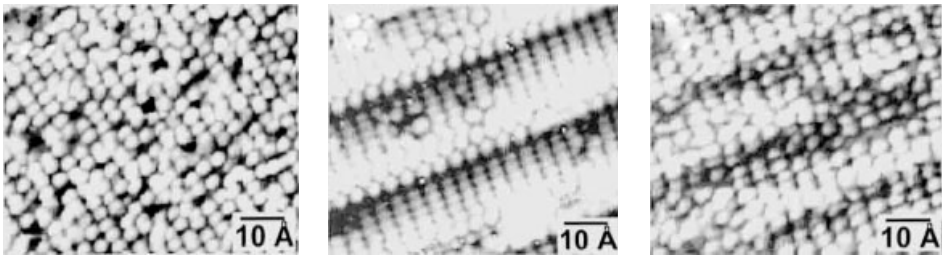


Fig. 3 High-resolution STM images of cyclopentene. (a) Cyclopentene adsorbed on "on-axis" Si(001). (b) Clean surface of 4°-miscut Si(001) showing double-height steps. (c) Cyclopentene adsorbed on 4°-miscut Si(001), showing retention of molecular orientation across step edges. (Figure 3 of J. S. Hovis, H. Liu, R. J. Hamers, *Appl. Phys. A* **1998**, *66*, S553 [23]).

most of the space over a single-crystalline Si(111) surface when every surface Si is terminated by one CH_3 group [24]. Even a C_2H_5– group is slightly too bulky to be accommodated within Si(111)-(1 × 1) unit cell. Because steric hindrance is anticipated between adsorbates, most of the organic moieties cannot make one-by-one termination of Si(111) in a macroscopic area [12].

Attempts to make an adlayer with species bulkier than those typical adsorbates inevitably lead to formation of a mixed adlayer with small adsorbates that fill the spacing areas, such as terminating H, OH, or silicon oxide. Long-chain alkyls and aromatics cannot be accommodated without such spacing species [25]. This sort of monolayer usually exhibits a good robustness and is as useful as fully terminated surfaces. On the basis of fundamental surface science on single crystals, it is preferable to arrange organic adsorbates and spacing adsorbates in a well-ordered manner, such as designated ($m \times n$) periodicity (m, n: integer). On real adlayers, the adsorbates are arranged randomly [26]. This is a difficulty in obtaining ordered adlayers due to the lack of mobility along the surface, compared with the cases of small admolecules on noble-metal surfaces, which can be put in order by thermalization. One exceptional case, reported by Allongue et al. [7, 27], is a series of para-substituted phenyl groups grafted by electrolysis of precursor diazonium cations on hydrogen-terminated Si(111). Their STM images were explained to represent a (2 × 1) adlattice composed of phenyls and terminating hydrogen atoms arranged alternately.

Another microscopic structural issue to be tackled is the detailed bonding arrangement near the anchoring part. The structure of the anchoring part depends on the method of forming the C−Si bond. The most frequently used method of organic deposition is called *hydrosilylation*, in which hydrogen-terminated Si surfaces are treated in terminally double-bonded olefins with a proper source of excitation (radical initiator, heat, light) or by catalysis. In such treatment, one should consider not only the formation of isomeric adsorbates but also the reactions at unexpected portions in the reactant molecule. Attachment of olefins modified with functional groups is more complicated as the functional groups may be more reactive with hydrogen-terminated Si

than terminal C=C. Photoadsorption of 1-amino-3-cyclopentene in liquid phase onto H:Si(100) seemed to deposit molecules linked to Si by C=C and those by NH_2 [28]. The technique of protected derivatives commonly used in organic synthesis was applied on Si(100) surface to deposit amino-terminated hydrocarbons [29].

In general, we should assess the by-products and contamination during the process of deposition as well as during the procedure of surface analysis. Oxidation of Si substrate cannot be avoided completely in treating H:Si(111) in aqueous/nonaqueous solvents in conventional sealed glassware. Oxidative reagents should be avoided in solutions. We also have to be careful of the hydrocarbon contaminants in atmosphere, which often obscure the target adsorbates and bother surface analysis. Most surface-sensitive analytical tools can usually present adequate information on contaminants with high fidelity. The signs of impurities should be carefully watched and quantified by proper methods of calibration under cross-checking with different techniques. In this article, the procedures to handle Si wafer surfaces are briefly discussed in terms of deposition reaction and surface analysis. Then, some topics on hydrogen-terminated Si(111) and chlorine-terminated Si(111) that emerged in the last few years are introduced. To learn more about the development of this field, the review articles by Yates et al. [30], Wayner et al. [31], Wolkow [32], Bent et al. [33, 34], and Buriak [35] are excellent.

1.3.2.2 Handling of Si Specimens for Adsorbate Preparation and Surface Analysis

Surface treatment of Si wafers as purchased usually starts with degreasing by sonication or rinsing in organic solvents. It is a good idea to use two kinds of solvents, such as trichloroethylene and acetone, which dissolve different kinds of organic debris. Then the wafers are subjected to extensive oxidation in reagent mixtures such as $H_2SO_4 + H_2O_2$ (3:1, 100 °C, Sulfuric acid-Peroxide Mixture, SPM or ''piranha'' solution), $NH_4OH + H_2O_2$ (Ammonium-Peroxide Mixture, APM), $HCl + H_2O_2$ (90 °C, Hydrochloric acid-Peroxide Mixture, HPM), diluted $HNO_3 + H_2O$ (1:1, 90 °C), and so on. The sacrifice oxide layer after treatment in such solutions is approximately 10-nm thick. To obtain a homogeneous thickness of the oxide layer, the wafers are sometimes pretreated in HF (a few percent) to remove irregular precovering oxide layer.

For Si(111), etching in dilute HF or 40% aqueous solution of NH_4F at room temperature effectively removes the oxide layer to form ideal H:Si(111)-(1 × 1) [20]. The produced surface can be kept clean in air for at least a few minutes. The surface is strongly hydrophobic, and microscopic perfection of H:Si(111)-(1 × 1) was well studied by various methods [36, 37]. Spectroscopically useful D:Si(111)-(1 × 1) can be prepared by fluoride solution in D_2O [38, 39]. For hydrogen-terminated Si(100), H:Si(100)-(2 × 1) and H:Si(100)-(3 × 1) are well known [40]. H:Si(100)-(2 × 1) is composed of surface Si−Si dimers with each Si terminated by one hydrogen atom. The H:Si(100) (3 × 1) surface is composed of alternate rows of monohydride dimers and dihydride silicon atoms [41]. These surfaces can be prepared by atomic H treatment of clean Si(100)-(2 × 1) or heating in high-pressure hydrogen gas [42]. The surface usually contains unterminated dangling bonds (neutral Si surface monoradicals), which can hardly be eliminated by extensive hydrogen treatment [43]. Due

to such dangling bonds, the surface cannot survive in the atmosphere [44]. Etching of Si(100) in fluoride solutions results in an inhomogeneous surface composed of partially (100)-(2 × 1) and (111) facets [45] and the surface is much less defined than H:Si(111)(1 × 1).

The process of adsorbate deposition should be carried out in a well-controlled environment. UHV is ideal in storing the surfaces and is indispensable for handling clean Si surfaces of Si. UHV chambers and tubings are convenient for most heating and gas exposure treatments. H:Si(111) and organic-modified Si surfaces are resistive to air and can be passed between vacuum or purged containers through air. Immersion of H:Si(111) in water without deaeration promotes oxidation of the surface [9]. It is difficult to perform liquid-phase reactions on H:Si(111) for an extended period of time in aqueous solutions unless some reducing reagents are added. Reactions in organic solvents are successfully performed in airtight glassware or glove boxes purged with inert gas, such as N_2 or Ar. The specimens should be rinsed and dried under a dry atmosphere after the reaction. However, just a short period of exposure to the atmosphere does not usually oxidize the surface to any detectable extent and the laboratory procedures can be done conveniently.

Introduction of the Si specimens into a vacuum chamber should be done carefully. When the specimen is in the atmosphere, H:Si(111) and organic-modified Si are not positively contaminated within a short period. The largest chance of contamination is when the surface is in the stage of initial vacuum pumping. The residual gas in the vacuum generated by oil rotary pump is water and oil, and the latter causes severe hydrocarbon contamination. It is necessary to use an oil-free pump, such as liquid-nitrogen cooled sorption pump or helium cooled cryopump, for evacuation from atmospheric pressure. After quick, clean evacuation from the atmospheric pressure to $\sim 10^{-4}$ Torr, the vacuum container can be switched to a turbomolecular pump running at top speed. By this procedure, contamination by hydrocarbons and oxidation can be reduced below the limit of spectroscopic detection. In UHV, electron sources sometimes deliver hydrocarbon contamination on Si. Operation of a B–A gauge placed on a line of sight from the specimen should be avoided.

1.3.2.3 Summary of the Latest Researches

1.3.2.3.1 Adsorption of Terminal Olefins on H:Si(111) Since 1995 when Linford et al. first reported the fabrication methods of long alkyl chains (>10 carbons) [6], the reaction between H:Si(111) and terminally double-bonded olefins (1-alkenes) has been accepted as a practical method of organic deposition. The adlayer of long alkyl chains is robust and convenient to stabilize Si surfaces and to make modifications over the adsorbates. The deposition reaction was activated by the coexistence of a radical initiator in liquid phase [6], by heating [6], by light irradiation [46–48], or by using Lewis-acid catalysis. Use of diluted olefins in an inert solvent (such as saturated alkanes) improves the quality of the alkyl adlayer [49].

Linford et al. first hypothesized that the spacing species to accommodate alkyl chains on Si(111) is OH species according to X-ray photoelectron spectroscopy (XPS) observation [6]. The origin of OH might be the peroxide radical initiator or O_2 dissolved in the reaction fluid. Most

of the succeeding researches using long-chain alkenes lack in assessment of oxygen directly bonded on the Si surface. The long-chain alkyls may screen the adsorbates nearest the surface Si atoms, and the wetting and chemical properties of the whole adlayer usually seem not to be affected by the existence of oxygen adsorbate. Small portions of SiO_2 deposited during the adsorption process are considered to be the nuclei of SiO_2 island enlargement [7]. Adsorption of O can be due to accidental oxidation from the environment, and the residual amount of surface oxygen is an index of the reproducible, well-defined adlayer. Oxygen not incorporated in SiO_2 at Si surface is often detected by XPS [25] or Auger electron spectroscopy (AES) [9], which is supposed to be oxygen attached to the adsorbates, or just H_2O molecules entangled in the adlayer. Webb et al. summarized the extent of substrate oxidation depending on the method of reaction activation [13], in which the best quality was attained by Grignard reaction on chlorinated Si substrate discussed in the next chapter.

This category of methods has been most utilized to form adsorbates including functional groups. Sieval reported amino-terminated alkyl grafted on hydrogen-terminated Si(100) by a rather sophisticated amine protection/deprotection process to avoid direct reaction of NH_2 and Si surface [50]. A small extent of substrate oxidation was not inevitable, probably due to the treatment in aqueous solution for hydrolysis. Strother et al. [15] deposited amino-terminated decyl by a similar protection/deprotection method, and furthermore grafted DNA on the amino group. The adsorbates are bulky and the substrate–adsorbate interface did not perhaps affect the function of DNA. In some cases the attachment of functional groups to Si surface can be avoided by the difference of reaction rates between the terminating double bond and the functional group [39, 51].

The mechanism of hydrosilylation has been elucidated as the ejection of a terminating hydrogen atom to form a Si dangling bond followed by an attack of the terminal double bond in olefin to form C−Si bond [6]. The C radical, generated in the preadsorbate as a result of C−Si bond formation, immediately picks up a neighborhood surface-terminating H, leaving one Si dangling bond. A complete alkyl adsorbate is then formed. The leftover dangling bond again captures olefin. The dangling bond (·Si) plays the role of chain carrier for the whole process, which is formulated as:

$$\text{H:Si(111)(surface)} \xrightarrow{\text{radical initiator, } \Delta, \text{ or } h\nu} \cdot\text{Si(surface)} + \cdot\text{H(This} \cdot \text{H dissipates away.)} \quad (1)$$

$$\text{R}-\text{CH}=\text{CH}_2 + \cdot\text{Si(surface)} \longrightarrow \text{R}-(\text{CH}\cdot)-\text{CH}_2-\text{Si(surface)} \quad (2)$$

$$\text{R}-(\text{CH}\cdot)-\text{CH}_2-\text{Si(surface)} + \text{H:Si(111)(surface)} \longrightarrow \text{R}-\text{CH}_2-\text{CH}_2-\text{Si(surface)} + \cdot\text{Si(surface)} \quad (3)$$

This process is actually visualized by Lopinski et al. [17], who revealed the chain growth of styrene along the dimer row of H:Si(100)-(2 × 1) by STM. They could discern isolated dangling bonds (vacancies of hydrogen termination) and styrene

admolecules in UHV. Adsorption of styrene takes place on a site nearest to a dangling bond, and one end of the styrene chain is always accompanied by a dangling bond. Lopinski et al. proposed a similar reaction mechanism on H:Si(111)-(1 × 1). [52] Recently, the photoadsorption of allylamine ($CH_2{=}CH{-}CH_2NH_2$) on D:Si(111)-(1 × 1) was performed, and incorporation of surface-terminating D into alkyl adsorbate was evidenced by vibrational analysis [39].

The activation by Lewis-acid catalyst, such as $C_2H_5AlCl_2$, was explained to proceed by the generation of surface Si cationic radical [13, 53], which seems to be taken over immediately by adsorbate bonding.

Strictly speaking, the anchoring C−Si part of olefin-originated alkyls can be either of primary carbon or of secondary carbon. Figure 4 shows these two types of adsorbates for allylamine precursor. The primary type (*n*-type) is simple and usually accepted, while there had been no reason presented to reject the secondary type (sec-type). Recently, Yamada et al. presented a vibrational evidence that sec-type and *n*-type adsorbates from gaseous allylamine appear sequentially according to the increase of total coverage [39]. The adsorbates of sec-type were characterized by the vibrational modes of $-CH_3$ group, which the sec-type adsorbates nominally contain. The photoreaction was performed in an UHV setup, which is ideal for impurity rejection and the succeeding surface analysis.

Another possibility for future in-depth consideration is whether the alkyl chains, which are considered to be indifferent of H-terminated Si surface, may be excited and subjected to bond formation with Si besides the reaction of double-bond end. This causes the formation of bridge type adsorbates, such as shown in Fig. 1b. The

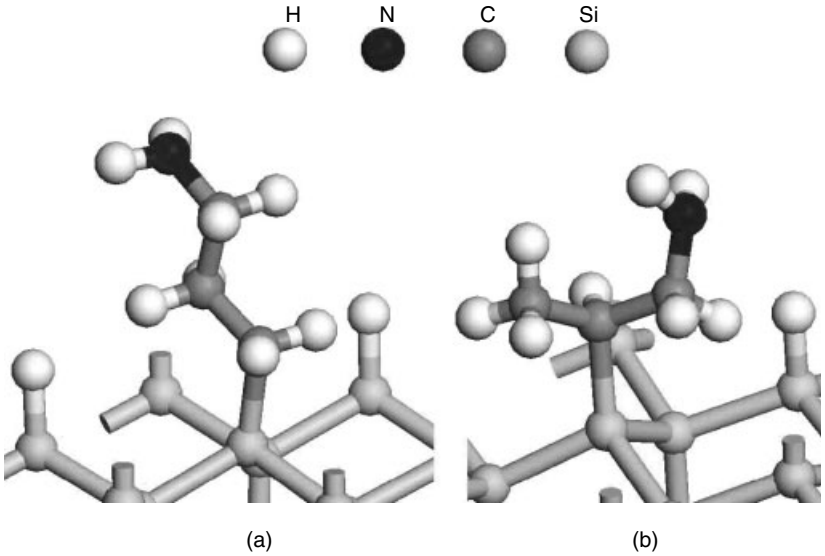


Fig. 4 Schematic view of allylamine adsorbates anticipated on Si(111) surface. (a) Primary (*n*-type) adsorbate, (b) secondary (sec-type) adsorbate.

photoadsorption of 1-butene on H:Si(111) did not yield CH_3 vibrational signals, indicating that the original methyl end in 1-butene was destroyed [39]. The existence of a bridge type adsorbate on Si(111) has not been recognized widely so far but it will be interesting to find a concrete method of preparation and to exploit its characteristic macroscopic properties.

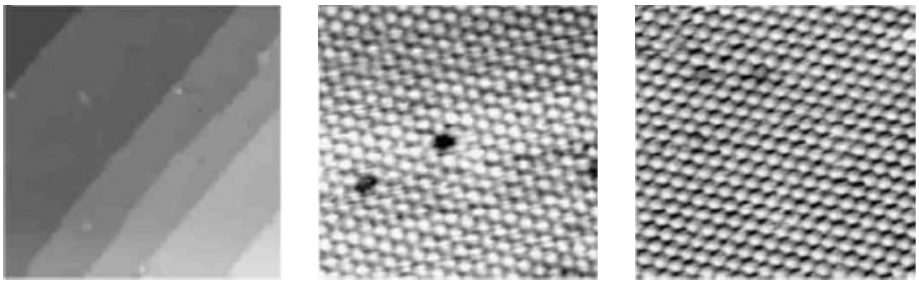
1.3.2.3.2 **Grignard Reaction on Halogenated Si(111)** The formation of C−Si bond by Grignard reagents (C_mH_nMgX, X=Cl, Br, I) has been widely used in organosilicon synthesis, and Si(111) was also subjected to Grignard reaction in the early stage. Bansal et al. [54, 55] chlorinated H:Si(111) in a benzene solution of PCl_5 under coexistence of radical initiator and then immersed the chlorinated surface in alkyl−Li solution or alkyl−MgX solution. Despite imperfect impurity rejection and surface analysis, this work was pioneering in the use of alkylating reagents on Si surfaces. The mechanism is simply formulated as:

$$\mathrm{RMgX} + \mathrm{Cl{:}Si(111)} \longrightarrow \mathrm{R{:}Si(111)} + \mathrm{MgXCl} \quad (4)$$

Grignard reagents are delivered as solutions in diethylether or tetrahydrofuran (THF), which are commercially available.

The precursor halogenated Si surfaces had not been put into detailed investigation until recently. Lopinski et al. [56, 57] reported well-ordered monolayers of Cl:Si(111)-(1 × 1) and Br:Si(111)-(1 × 1) examined by STM and high-resolution electron energy loss spectroscopy (HREELS) formed by (photo-)reaction in gaseous Cl_2 or Br_2 on H:Si(111). The surface was composed almost solely of monohalide Si atoms. The halogenated surfaces were atomically flat with low defect density, even better than hydrogen-terminated Si(111) (Fig. 5). Removal of surface Si atoms as gaseous Si halides is considered to be involved in flattening the modified surfaces. Cl:Si(111) and Br:Si(111) slowly react with components of air and should be handled in vacuum or in inert gas. Recently Rivillon et al. [58, 59] applied an outstanding method of surface infrared spectroscopy and detected Cl−Si vibration signals.

As one of the most attractive topics in the field of Si surface science, the formation



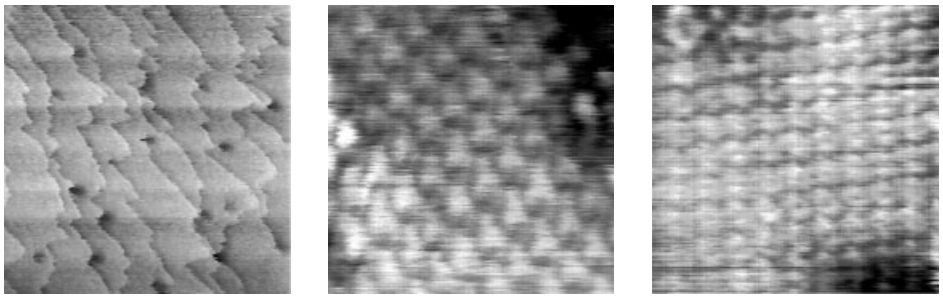
(a) (b) (c)

Fig. 5 STM constant current images of halogenated Si(111) prepared by gas phase reactions at room temperature; (a) Cl/Si(111)-50 × 50 nm, −1 V (sample bias), 40 pA, (b) Cl/Si(111)-6.5 × 6.5 nm, −0.5 V, 50 pA, (c) Br/Si(111)-6.5 × 6.5 nm, −0.4 V, 400 pA. (Figure 2 of B. J. Eves, G. P. Lopinski, *Surf. Sci.* **2005**, *579*, L89 [57]).

and structure of methyl-terminated Si(111) by Grignard reaction has been studied in detail. The CH_3– group is probably the only hydrocarbon species that can terminate Si(111) in (1 × 1) periodicity with practical stability. Terry et al. examined a methyl-terminated Si(111) from Cl:Si(111) and CH_3Li by X-ray photoelectron diffraction and spectroscopy aided by synchrotron radiation [60]. They concluded that the length of C−Si bond vertical to the surface is 0.186 nm. Bansal et al. [55] listed the results for CH_3 and longer alkyls and assumed that CH_3 can terminate every surface Si atom on Si(111) on the basis of geometrical consideration. Webb et al. [13] also extensively compared the perfection of alkyl adlayers prepared by various methods.

A concrete evidence for methyl (1 × 1) termination was presented by Yamada et al. [24, 61] as high-resolution STM images. Figure 6 shows the flatness of the methylated surface viewed in a wide zone, as well as the lattice of methyl moieties arranged in (1 × 1) periodicity. The features representing methyl groups changed according to the STM gap voltage. The features actually represent the electron orbitals, and it is difficult to extrude the geometric arrangement of H atoms in CH_3 just by viewing the images. HREELS of CH_3:Si(111)-(1 × 1) was also presented (Fig. 7), indicating all the characteristic vibration modes including the C−Si stretching motion. The amount of SiO_2 impurity, sensitively detected by HREELS, was controlled below 0.1%.

In terms of the movement of adsorbed CH_3 group, the rotation about the C−Si axis vertical to the surface is attractive. However, so far no methods have been found to observe this rotation collectively. The energy barrier of rotation excitation may be analogous to that of torsion of C−Si bond in an isolated CH_3-SiH_3 molecule, which corresponds to a frequency of 590.5 cm^{-1}. Yu et al. performed STM imaging of CH_3:Si(111)-(1 × 1) at the low temperature of 4.7 K [62]. They claimed that the rotation of every CH_3 group was locked at a position of C−H bonds rotated by $(7 \pm 3)^\circ$ away from the center of the neighboring $-CH_3$ group.



(a) (b) (c)

Fig. 6 (a) A wide-range STM image of methylated Si(111). Scan size = 500 nm × 500 nm, gap voltage = −1.21 V (sample negative), preset tunneling current = 2.58 nA. (b) A high-resolution STM image, 10 nm × 10 nm, −1.48 V, 2.38 nA. (c) 4 nm × 4 nm, −1.51 V, 19.65 nA. (Figures 3 and 4 of T. Yamada, M. Kawai, A. Wawro et al., *J. Chem. Phys.* **2004**, *121*, 10660 [24]).

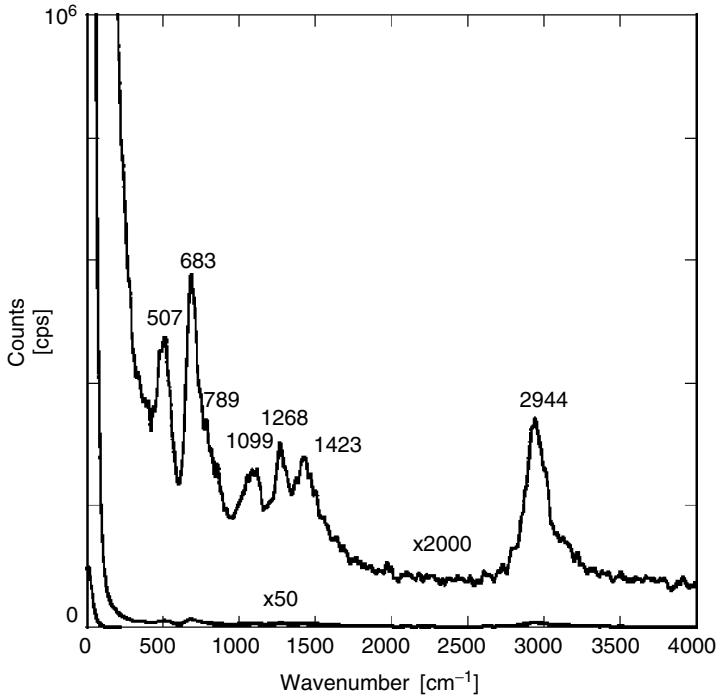


Fig. 7 HREELS of the methylated Si(111). HREELS incident electron energy 2.84 eV, incident angle = exit angle = 60° from the surface normal. The full width at half maximum of inelastic peak = 7.6 meV. 2944 cm^{-1}: C−H stretching, 1423 cm^{-1}: CH_3 umbrella motion, 1268 cm^{-1}: CH_3 asymmetric bending, 1099 cm^{-1}: Si−O stretching in SiO_2, 789 cm^{-1}: CH_3 rocking, 683 cm^{-1}: C−Si stretching, 507 cm^{-1}: C−Si bending. (Figure 2 of T. Yamada, M. Kawai, A. Wawro et al., *J. Chem. Phys.* **2004**, *121*, 10660 [24]).

It is interesting to address the electronic property of CH_3:Si(111)-(1 × 1) not only for the purpose of application as the lithography resist layer but also as the basis of nanoelectronic devices. The I–V characteristic curve of STM reached a peak at −1.5 eV in the occupied levels additionally to the I–V curve of H:Si(111). This peak corresponds to the electronic state that contributes to electronic conduction through the surface. This conducting property is also materialized in an electrolytic phenomenon. Niwa et al. [61] demonstrated that CH_3:Si(111)-(1 × 1) as an electrode in an aqueous redox solution exclusively lowers the peak potential of redox reaction. CH_3:Si(111)-(1 × 1) was also applied as the ultrathin channel medium of field-effect transistor [14].

As for Grignard reagents containing alkyl groups larger than methyl, the space filling of adsorbates does not geometrically allow every Si atom to be terminated, and a certain part of terminating Cl atoms must be left over in the space between alkyl adsorbates. Such Cl atoms are considered to be replaced by oxygen-containing species during rinsing or by exposure

to air. Webb et al. reported that high-resolution XPS did not detect Cl after deposition of C_2H_5– or C_6H_5–CH_2– on Cl:Si(111) rinsed in methanol [25]. The possible terminating species was anticipated to be hydrogen. The replacement of residual Cl species is probably uncontrollable and introduces more chances of contamination. It is certainly easier to replace a part of the terminating hydrogen atoms on H:Si(111) by alkyl groups. This issue is discussed in the next chapter.

1.3.2.3.3 **Grignard Reagents and H:Si(111)**
H:Si(111) is less likely than Cl:Si(111) to react with alkylmagnesium reagents according to the classic formulation of Grignard reaction. However, so far, many cases of adsorbate formation on hydrogen-terminated Si surfaces have been reported. Kim et al. [63] first reported derivatization of hydrogen-terminated porous silicon by Grignard reagents. They included a quenching procedure with acetic acid after the Grignard reaction. By using CH_3COOD, incorporation of Si-terminating D species was detected. Kim et al. explained this process by dissociative insertion of R−MgX into Si−Si bonds just below the surface (called *backbonds*). The formation of Si−R and Si−MgX was assumed, and the Si−MgX species was considered to be quenched in Si−D by the presence of deutrated acetic acid. This interpretation fitted with a rather rough surface of porous Si, which was advantageous in the detection of surface products.

Formation of decyl ($C_{10}H_{21}$–) adsorbates by decyl Grignard reagent on H:Si(111) was first performed by Boukherroub et al. [64] The atomic force microscope (AFM) images of alkyl-terminated Si(111) show a flat Si surface without any sign of pit formation related to the backbond breakage. Replacement of terminating H with decyl groups was recognized. The robust properties of this surface were found to be the same as those formed by alkene photoadsorption or by Lewis-acid catalysis. Boukherroub et al. concluded that a new mechanism of Grignard reagent should be proposed to replace terminating H [64]. On flat H:Si(111), rinsing in a THF solution of CF_3COOD did not introduce D−Si [65].

The formation of C−Si bond in methyl Grignard reaction on H:Si(111) was first evidenced by Yamada et al. [5]. The STM images of CH_3MgBr-treated H:Si(111) showed that methyl groups just formed small lattice patches and adsorbates were randomly placed with a significant open area [66]. Careful use of D:Si(111) and HREEL showed C−Si stretching signal at 678 cm^{-1} [5]. The HREEL spectra always contain H(D)−Si stretching signal, indicating that Grignard reaction cannot completely remove original terminating hydrogen atoms.

At the same time, a limitation was recognized in detecting organic adsorbates and terminating hydrogen by infrared spectroscopy. The H−Si stretching signal at 2090 cm^{-1} became invisible to IR as the coverage of organic increased [26]. However with HREELS, the H−Si signal was apparently detected on surfaces prepared under the same condition. Infrared spectroscopy seems to be more affected by adsorbate screening effects than HREELS.[5] This fact influences the interpretation of spectra of CH_3:Si(111) formed by electrochemical anodization in a Grignard reagent solution, that 100% methylated surfaces were obtained [67, 68].

The Grignard reaction on H:Si(111) is probably the most useful method to obtain robust Si surfaces for practical purposes. The adlayers formed are constantly a mixture of alkyl and H regardless of the chain length. The C signals of AES [26] and XPS [55] indicating the saturation coverages are proportional to the chain length, indicating that the adsorbate-wise areal density is constant, regardless of the chain length. The chance of unwanted substrate oxidation during the fabrication process can be minimized, compared to the case for Cl:Si(111). More varieties of hydrocarbons, such as branched or unsaturated hydrocarbon moieties [26, 39, 65], can be deposited with adequate stability. In nearly all the cases, the hydrocarbon groups are transferred to the Si surfaces within the precursor Grignard reagents without isomerization and component detachment. The alkyl-hydrogen mixed adlayers are strongly hydrophobic and resistive toward dissolved oxygen in water [9], alkali solutions [64], or even in a Cu-plating solution containing F^- for a short period [9].

The mechanism of H:Si(111) replacement by Grignard reagent has not been elucidated on the basis of concrete experimental evidences. Recently Fellah et al. proposed a mechanism involving a trace amount of alkyl halide residue contained in the Grignard reagent solution [69]. Decyl bromide intentionally added in a diethylether solution of decyl magnesium bromide significantly accelerated deposition of decyl groups. Treatment of H:Si(111) in pure tetradecyl bromide yielded a finite amount of alkyl adsorbate and a significant amount of SiO_2. It was difficult to compare the reaction kinetics with the Grignard reagent. The effects of alkyl halide were scrutinized by voltammetric electrolysis of Grignard reagent, by using *n*-type and *p*-type silicon, and by considering the electronic and thermodynamic energy levels of RX, RMgX, and Si. Although this analysis was not completed, we can expect the application of alkyl halides as the alkylation reagent to open a new route to organic deposition on Si.

References

1. C. S. Whelan, M. J. Lercel, H. G. Craighead et al., *J. Vac. Sci. Technol.* **1996**, *B14*, 4085.
2. H. Sugimura, K. Okiguchi, N. Nakagiri et al., *J. Vac. Sci. Technol.* **1996**, *B14*, 4140.
3. D. Niwa, Y. Yamada, T. Homma et al., *J. Phys. Chem. B* **2004**, *108*, 3240.
4. W. Lie, D. G. Fedorov, K. Hirao, *J. Phys. Chem. A* **2002**, *106*, 7057.
5. T. Yamada, T. Inoue, K. Yamada et al., *J. Am. Chem. Soc.* **2003**, *125*, 8039.
6. M. R. Linford, P. Fenter, P. M. Eisenberger et al., *J. Am. Chem. Soc.* **1995**, *117*, 3145.
7. C. H. de Villeneuve, J. Pinson, M. C. Bernard et al., *J. Phys. Chem.* **1997**, *B101*, 2415.
8. A. B. Sieval, A. L. Demirel, J. W. M. Nissink et al., *Langmuir* **1998**, *14*, 1759.
9. T. Yamada, N. Takano, K. Yamada et al., *J. Electroanal. Chem.* **2002**, *532*, 247.
10. M. P. Stewart, J. M. Buriak, *J. Am. Chem. Soc.* **2001**, *123*, 7821.
11. W. A. Hofer, A. J. Fisher, G. P. Lopinski et al., *Chem. Phys. Lett.* **2002**, *365*, 129.
12. A. B. Sieval, C. L. Huisman, A. Schö1necker et al., *J. Phys. Chem. B* **2003**, *107*, 6846.
13. L. J. Webb, N. S. Lewis, *J. Phys. Chem. B* **2003**, *107*, 5404.
14. D. Niwa, H. Fukunaga, T. Homma et al., *Chem. Lett.* **2005**, *34*, 520.
15. T. Strother, R. J. Hamers, L. M. Smith, *Nucl. Acid Res.* **2000**, *28*, 3535.
16. W. Cai, J. R. Peck, D. W. van der Weide et al., *Biosens. Bioelectron.* **2004**, *19*, 1013.
17. G. P. Lopinski, D. D. M. Wayner, R. Wolkow, *Nature* **2000**, *406*, 48.
18. Z. Hossain, H. S. Kato, M. Kawai, *J. Am. Chem. Soc.* **2005**, *127*, 15030.
19. P. G. Piva, G. A. DiLabio, J. L. Pitters et al., *Nature* **2005**, *435*, 658.
20. G. S. Higashi, Y. J. Chabal G. W. Trucks et al., *Appl. Phys. Lett.* **1990**, *56*, 656.

21. R. J. Hamers, S. K. Coulter, M. D. Ellison et al., *Acc. Chem. Res.* **2000**, *33*, 617.
22. R. J. Hamers, J. S. Hovis, S. Lee et al., *J. Phys. Chem. B* **1997**, *101*, 1489.
23. J. S. Hovis, H. Liu, R. J. Hamers, *Appl. Phys. A* **1998**, *66*, S553.
24. T. Yamada, M. Kawai, A. Wawro et al., *J. Chem. Phys.* **2004**, *121*, 10660.
25. L. J. Webb, E. J. Nemanick, J. S. Biteen et al., *J. Phys. Chem. B* **2005**, *109*, 3930.
26. T. Yamada, N. Takano, K. Yamada et al., *Jpn. J. Appl. Phys.* **2001**, *40*, 4845.
27. P. Allongue, C. H. de Villeneuve, J. Pinson, *Electrochim. Acta* **2000**, *45*, 3241. and
28. Z. Lin, T. Strother, W. Cai et al., *Langmuir* **2002**, *18*, 788.
29. A. B. Sieval, R. Linke, G. Heij et al., *Langmuir* **2001**, *17*, 7554.
30. H. N. Waltenburg, J. T. Yates Jr., *Chem. Rev.* **1995**, *95*, 1589.
31. D. D. M. Wayner, R. A. Wolkow, *J. Chem. Soc., Perkin Trans.* **2002**, *2*, 23.
32. R. A. Wolkow, *Annu. Rev. Phys. Chem.* **1999**, *50*, 413.
33. S. F. Bent, *Surf. Sci.* **2002**, *500*, 879.
34. M. A. Filler, S. F. Bent, *Prog. Surf. Sci.* **2003**, *73*, 1.
35. J. M. Buriak, *Chem. Rev.* **2002**, *102*, 1271.
36. G. S. Higashi, R. S. Becker, Y. J. Chabal et al., *J. Appl. Phys. Lett.* **1991**, *58*, 1656.
37. R. B. Doak, Y. J. Chabal, G. S. Higashi et al., *J. Electron Spectrosc. Relat. Phenom.* **1990**, *54*, 291.
38. H.-H. Luo, C. E. D. Chidsey, *Appl. Phys. Lett.* **1997**, *72*, 477.
39. T. Yamada, M. Noto, K. Shirasaka et al., *J. Phys. Chem. B* **2006**, *110*, 6740.
40. C. Thirstrup, M. Sakurai, T. Nakayama et al., *Surf. Sci.* **1998**, *411*, 203.
41. R.-P. Chen, D.-S. Lin, *Surf. Sci.* **2000**, *454–456*, 196.
42. T. Hitosugi, T. Hashizume, S. Heike et al., *Jpn. J. Appl. Phys.* **1997**, *36*, L361.
43. H. Kajiyama, S. Heike, T. Hitosugi et al., *Jpn. J. Appl. Phys.* **1998**, *37*, L1350.
44. A. S. Baluch, N. P. Guisinger, R. Basu et al., *J. Vac. Sci. Technol. A* **2004**, *22*, L1.
45. U. Neuwald, H. E. Hessel, A. Feltz et al., *Surf. Sci.* **1993**, *296*, L8.
46. R. L. Cicero, M. R. Linford, C. E. D. Chidsey, *Langmuir* **2000**, *16*, 5688.
47. Q.-Y. Sun, L. C. P. M. de Smet, B. van Lagen et al., *Angew. Chem., Int. Ed.* **2004**, *43*, 1352.
48. Q.-Y. Sun, L. C. P. M. de Smet, B. van Lagen et al., *J. Am. Chem. Soc.* **2005**, *127*, 2514.
49. A. B. Sieval, V. Vleeming, H. Zuilhof et al., *Langmuir* **1999**, *15*, 8288.
50. A. B. Sieval, R. Linke, G. Heij et al., *Langmuir* **2001**, *17*, 7554–7559.
51. H. Asanuma, G. P. Lopinski, H.-Z. Yu, *Langmuir* **2005**, *21*, 5013.
52. R. L. Cicero, C. E. D. Chidsey, G. P. Lopinski et al., *Langmuir* **2002**, *18*, 305.
53. J. M. Buriak, M. J. Allen, *J. Am. Chem. Soc.* **1998**, *120*, 1339.
54. A. Bansal, X. Li, I. Lauermann et al., *J. Am. Chem. Soc.* **1996**, *118*, 7225.
55. A. Bansal, X. Li, S. I. Yi et al., *J. Phys. Chem. B 105*, **2001**, 10266.
56. G. P. Lopinski, B. J. Eves, O. Hul'ko et al., *Phys. Rev. B 71*, 125308, **2005**.
57. B. J. Eves, G. P. Lopinski, *Surf. Sci.* **2005**, *579*, L89.
58. S. Rivillon, F. Amy, Y. J. Chabal, *Appl. Phys. Lett.* **2004**, *85*, 2583.
59. S. Rivillon Y. J. Chabal, L. J. Webb et al., *J. Vac. Sci. Technol. A 23*, **2005**, 1100.
60. J. Terry, M. R. Linford, C. Wigren et al., *Appl. Phys. Lett.* **1997**, *71*, 1056.
61. D. Niwa, T. Inoue, H. Fukunaga et al., *Chem. Lett.* **2004**, *33*, 284.
62. H. Yu, L. J. Webb, R. S. Ries et al., *J. Phys. Chem. B* **2005**, *109*, 671.
63. N. Y. Kim, P. E. Laibinis, *J. Am. Chem. Soc.* **1998**, *120*, 4516.
64. R. Boukherroub, S. Morin, F. Bensebaa et al., *Langmuir* **1999**, *15*, 3831.
65. T. Yamada, K. Shirasaka, M. Noto et al., *J. Phys. Chem. B* **2006**, *110*, 7357.
66. T. Yamada, N. Takano, K. Yamada et al., *Electrochem. Commun.* **2001**, *3*, 67.
67. A. Fidélis, F. Ozanam, J.-N. Chazalviel, *Surf. Sci.* **2000**, *444*, L7.
68. T. Miyadera, A. Koma, T. Shimada, *Surf. Sci.* **2003**, *526*, 177.
69. S. Fellah, R. Boukherroub, F. Ozanam et al., *Langmuir* **2004**, *20*, 6359.

1.3.2

Modification of Silicon Wafer Surfaces with Small Organic Moieties

Taro Yamada
RIKEN, 2-1 Hirosawa, Wako-shi, Saitama 351-0198, Japan

1.3.2.1 Introduction

Monolayers of organic adsorbates bonded on silicon wafer surfaces have properties for prospective applications in nanometer-scale physical science, chemistry, biology, and industrial technology [1–3]. The covalent linkage in organic adsorbates can mediate the connection of a variety of molecular groups with surface Si atoms. The diversity of organic species can guarantee almost limitless possibilities for molecules and moieties attached to Si surface.

This article deals with a category of organic adsorbates that is attached to the outermost surface Si by the C−Si covalent bond. Figure 1 illustrates two typical examples of hydrocarbon moieties attached directly to surface Si. One is a linear alkyl chain terminating one surface Si atom. The other is a hydrocarbon moiety fixed by two C−Si bonds. The existence of the C−Si bond on the surface is important because it brings about advantageous properties such as thermal stability, low mobility along the surface, and chemical stability. The dissociation energy of C−Si bond has been estimated to be >300 kJ mol^{-1} [4], notably larger than the adsorption heat of molecules on noble metals. Actually CH_3 species on Si(111) remains undecomposed at 600 K in vacuum [5]. Related to this, the covalently bonded species are anticipated to be immovable along the surface, as the C−Si bonds on the single-crystalline planes are electronically localized. More practically, Si surfaces covered with grafted organic moieties have been frequently reported to be robust against the practical environment and even in powerful reagents [6–9]. It is certainly amazing that just one monolayer of organic fragments can nullify the harsh reactivity of the clean Si surface, such as Si(111)-(7 × 7) reserved in vacuum, into inertness in the atmosphere.

The robustness of organic-modified Si(111) frequently attracts interest application. The passivation and modification of electronic properties were conducted by Buriak on porous Si surfaces, on which the organic adsorbate was utilized for photolithography and photoluminescence [10]. Modification of electronic properties was frequently attempted [10–14]. Application for biochemical analysis has also been extensively pursued. Hamers et al. reported fixation of single strand DNA by covalent linkage on Si and other semiconductors, and performed electrochemical detection of DNA hybridization [15, 16]. This attempt is probably the leading edge in the development of intelligent biochips with integrated electronics for signal detection and processing. Another category of prospective application is electronics by molecular chains. Lopinski et al. first found a chain reaction of styrene adsorption on a (2 × 1)-hydrogen-terminated Si(100) wafer [17]. The single line composed of adsorbed molecules can be easily imagined as a material of molecular wires [11, 18], and the electronic properties of this ''nanowire'' were examined [19]. Figure 2 shows scanning tunneling spectroscopy (STM) images of a styrene chain formed on H:Si(100)-(2 × 1), in which the electronic orbitals in each styrene adsorbate are modified by the existence of a dangling bond located at one end of the chain. This phenomenon was

Encyclopedia of Electrochemistry.Edited by A.J. Bard and M. Stratmann
Vol. 10 *Modified Electrodes*. Edited by M.Fujihira, I.Rubinstein, and J.F.Rusling
Copyright © 2007 Wiley-VCH Verlag GmbH & Co. KGaA, Weinheim.ISBN: 978-3-527-30402-8

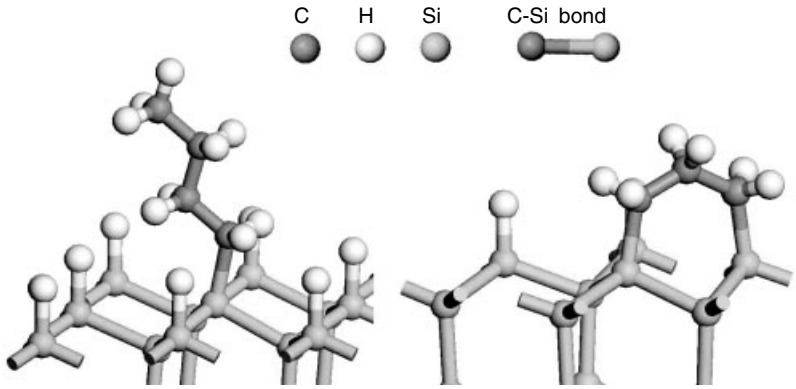


Fig. 1 Schematic view of hydrocarbon adsorbates covalently bonded on Si(111) surface. (a) Single-chain alkyl fixed by one C—Si bond. (b) Bridging hydrocarbon fixed by two C—Si bonds.

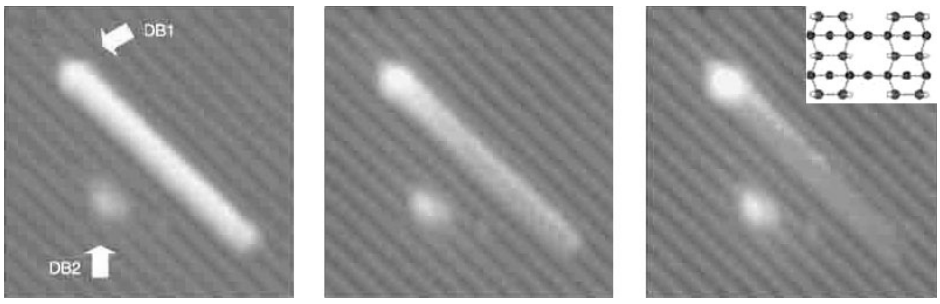


Fig. 2 Visualization of the electrostatic potential emanating from a point source for a styrene chain on H:Si(100). (a) With negatively charged dangling bonds labeled DB1 and DB2. The prominent white bar is a line of surface-bound molecules. At increased sample bias of −2.4 V, molecular p-states are ''turned on'', causing molecules to appear bright (topographically elevated) and of nearly constant height across the line. (b) At an intermediate bias of −1.8 V, molecules appear darker, increasingly so at greater distances from DB1. (c) In the absence of a negative dangling bond all molecules would appear dark at −1.6 V, but the molecules nearest to the dangling bond remain prominent. (Figure 1 of P. G. Piva, G. A. DiLabio, J. L. Pitters et al., *Nature* **2005**, *435*, 658 [19]).

explained on the basis of molecular-orbital calculation.

Despite those prospects of practical applications, the details of structure and composition of the organic adlayer, which directly influence the quality of surface, have not been always well recognized. The practical criterion that characterizes covalent adsorbates on semiconductor surfaces is that every dangling bond generated by the truncation of a single crystal should be terminated by an adsorbate. The

dangling bonds on surfaces of Si and Ge are reactive with O_2 and other components of air and would result in the deterioration of the whole surface. If the surface is supposed to be handled in air or in liquid, complete rejection of dangling bonds should be achieved by appropriate reaction and handling conditions. The discovery of H:Si(111)-(1 × 1), on which every surface Si is monohydride terminated [20], was an epoch-making event to open up the field of organic chemistry on semiconductors handled out of ultrahigh vacuum (UHV).

There are some typical cases in which every surface Si atom is actually terminated by one C−Si bond, namely, that in which the stoichiometric full coverage is attained. On clean Si(100), (2 × 1) adlattices can be formed by cycloaddition of cyclic olefins onto surface Si−Si dimers [21]. Hamers et al. presented a highly ordered adlayer terminating all Si atoms just by exposing clean Si(100)-(2 × 1) to gaseous cyclopentene (C_5H_8) in UHV environment [22]. Figure 3 shows STM images of cyclopentene molecules bonded in parallel to the dimer rows of Si(100)-(2 × 1) terraces. This sort of full-coverage adlayer can be expected only when the adsorbate is small enough to be contained within one (2 × 1) supercell.

On Si(111), it was demonstrated that even CH_3–, the smallest alkyl moiety, fills most of the space over a single-crystalline Si(111) surface when every surface Si is terminated by one CH_3 group [24]. Even a C_2H_5– group is slightly too bulky to be accommodated within Si(111)-(1 × 1) unit cell. Because steric hindrance is anticipated between adsorbates, most of the organic moieties cannot make one-by-one termination of Si(111) in a macroscopic area [12].

Attempts to make an adlayer with species bulkier than those typical adsorbates inevitably lead to formation of a mixed adlayer with small adsorbates that fill the spacing areas, such as terminating H, OH, or silicon oxide. Long-chain alkyls and aromatics cannot be accommodated without such spacing species [25]. This sort of monolayer usually exhibits a good robustness and is as useful as fully terminated surfaces. On the basis of fundamental surface science on single crystals, it is preferable to arrange organic adsorbates and spacing adsorbates in a well-ordered manner, such as designated ($m \times n$) periodicity (m, n: integer). On real adlayers, the adsorbates are arranged randomly [26]. This is a difficulty in obtaining ordered adlayers due to the lack

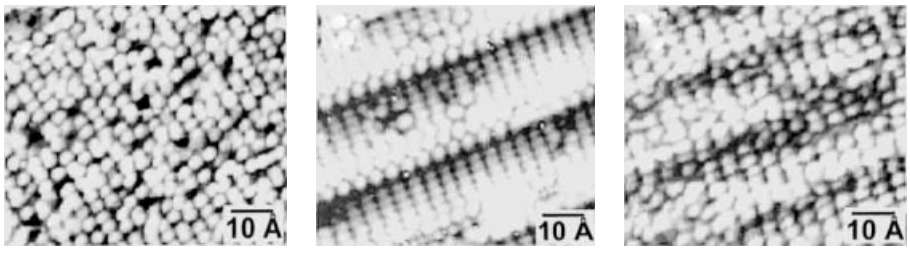


Fig. 3 High-resolution STM images of cyclopentene. (a) Cyclopentene adsorbed on ''on-axis'' Si(001). (b) Clean surface of 4°-miscut Si(001) showing double-height steps. (c) Cyclopentene adsorbed on 4°-miscut Si(001), showing retention of molecular orientation across step edges. (Figure 3 of J. S. Hovis, H. Liu, R. J. Hamers, *Appl. Phys. A* **1998**, *66*, S553 [23]).

of mobility along the surface, compared with the cases of small admolecules on noble-metal surfaces, which can be put in order by thermalization. One exceptional case, reported by Allongue et al. [7, 27], is a series of para-substituted phenyl groups grafted by electrolysis of precursor diazonium cations on hydrogen-terminated Si(111). Their STM images were explained to represent a (2×1) adlattice composed of phenyls and terminating hydrogen atoms arranged alternately.

Another microscopic structural issue to be tackled is the detailed bonding arrangement near the anchoring part. The structure of the anchoring part depends on the method of forming the C−Si bond. The most frequently used method of organic deposition is called *hydrosilylation*, in which hydrogen-terminated Si surfaces are treated in terminally double-bonded olefins with a proper source of excitation (radical initiator, heat, light) or by catalysis. In such treatment, one should consider not only the formation of isomeric adsorbates but also the reactions at unexpected portions in the reactant molecule. Attachment of olefins modified with functional groups is more complicated as the functional groups may be more reactive with hydrogen-terminated Si than terminal C=C. Photoadsorption of 1-amino-3-cyclopentene in liquid phase onto H:Si(100) seemed to deposit molecules linked to Si by C=C and those by NH_2 [28]. The technique of protected derivatives commonly used in organic synthesis was applied on Si(100) surface to deposit amino-terminated hydrocarbons [29].

In general, we should assess the by-products and contamination during the process of deposition as well as during the procedure of surface analysis. Oxidation of Si substrate cannot be avoided completely in treating H:Si(111) in aqueous/nonaqueous solvents in conventional sealed glassware. Oxidative reagents should be avoided in solutions. We also have to be careful of the hydrocarbon contaminants in atmosphere, which often obscure the target adsorbates and bother surface analysis. Most surface-sensitive analytical tools can usually present adequate information on contaminants with high fidelity. The signs of impurities should be carefully watched and quantified by proper methods of calibration under cross-checking with different techniques. In this article, the procedures to handle Si wafer surfaces are briefly discussed in terms of deposition reaction and surface analysis. Then, some topics on hydrogen-terminated Si(111) and chlorine-terminated Si(111) that emerged in the last few years are introduced. To learn more about the development of this field, the review articles by Yates et al. [30], Wayner et al. [31], Wolkow [32], Bent et al. [33, 34], and Buriak [35] are excellent.

1.3.2.2 Handling of Si Specimens for Adsorbate Preparation and Surface Analysis

Surface treatment of Si wafers as purchased usually starts with degreasing by sonication or rinsing in organic solvents. It is a good idea to use two kinds of solvents, such as trichloroethylene and acetone, which dissolve different kinds of organic debris. Then the wafers are subjected to extensive oxidation in reagent mixtures such as $H_2SO_4 + H_2O_2$ (3:1, 100 °C, Sulfuric acid-Peroxide Mixture, SPM or ''piranha'' solution), $NH_4OH + H_2O_2$ (Ammonium-Peroxide Mixture, APM), $HCl + H_2O_2$ (90 °C, Hydrochloric acid-Peroxide Mixture, HPM), diluted $HNO_3 + H_2O$ (1:1, 90 °C), and so on. The sacrifice oxide layer after treatment in such solutions is approximately 10-nm thick. To obtain a homogeneous thickness of

the oxide layer, the wafers are sometimes pretreated in HF (a few percent) to remove irregular precovering oxide layer.

For Si(111), etching in dilute HF or 40% aqueous solution of NH_4F at room temperature effectively removes the oxide layer to form ideal H:Si(111)-(1 × 1) [20]. The produced surface can be kept clean in air for at least a few minutes. The surface is strongly hydrophobic, and microscopic perfection of H:Si(111)-(1 × 1) was well studied by various methods [36, 37]. Spectroscopically useful D:Si(111)-(1 × 1) can be prepared by fluoride solution in D_2O [38, 39]. For hydrogen-terminated Si(100), H:Si(100)-(2 × 1) and H:Si(100)-(3 × 1) are well known [40]. H:Si(100)-(2 × 1) is composed of surface Si−Si dimers with each Si terminated by one hydrogen atom. The H:Si(100) (3 × 1) surface is composed of alternate rows of monohydride dimers and dihydride silicon atoms [41]. These surfaces can be prepared by atomic H treatment of clean Si(100)-(2 × 1) or heating in high-pressure hydrogen gas [42]. The surface usually contains unterminated dangling bonds (neutral Si surface monoradicals), which can hardly be eliminated by extensive hydrogen treatment [43]. Due to such dangling bonds, the surface cannot survive in the atmosphere [44]. Etching of Si(100) in fluoride solutions results in an inhomogeneous surface composed of partially (100)-(2 × 1) and (111) facets [45] and the surface is much less defined than H:Si(111)(1 × 1).

The process of adsorbate deposition should be carried out in a well-controlled environment. UHV is ideal in storing the surfaces and is indispensable for handling clean Si surfaces of Si. UHV chambers and tubings are convenient for most heating and gas exposure treatments. H:Si(111) and organic-modified Si surfaces are resistive to air and can be passed between vacuum or purged containers through air. Immersion of H:Si(111) in water without deaeration promotes oxidation of the surface [9]. It is difficult to perform liquid-phase reactions on H:Si(111) for an extended period of time in aqueous solutions unless some reducing reagents are added. Reactions in organic solvents are successfully performed in airtight glassware or glove boxes purged with inert gas, such as N_2 or Ar. The specimens should be rinsed and dried under a dry atmosphere after the reaction. However, just a short period of exposure to the atmosphere does not usually oxidize the surface to any detectable extent and the laboratory procedures can be done conveniently.

Introduction of the Si specimens into a vacuum chamber should be done carefully. When the specimen is in the atmosphere, H:Si(111) and organic-modified Si are not positively contaminated within a short period. The largest chance of contamination is when the surface is in the stage of initial vacuum pumping. The residual gas in the vacuum generated by oil rotary pump is water and oil, and the latter causes severe hydrocarbon contamination. It is necessary to use an oil-free pump, such as liquid-nitrogen cooled sorption pump or helium cooled cryopump, for evacuation from atmospheric pressure. After quick, clean evacuation from the atmospheric pressure to $\sim 10^{-4}$ Torr, the vacuum container can be switched to a turbomolecular pump running at top speed. By this procedure, contamination by hydrocarbons and oxidation can be reduced below the limit of spectroscopic detection. In UHV, electron sources sometimes deliver hydrocarbon contamination on Si. Operation of a B–A gauge placed on a

line of sight from the specimen should be avoided.

1.3.2.3 Summary of the Latest Researches

1.3.2.3.1 Adsorption of Terminal Olefins on H:Si(111) Since 1995 when Linford et al. first reported the fabrication methods of long alkyl chains (>10 carbons) [6], the reaction between H:Si(111) and terminally double-bonded olefins (1-alkenes) has been accepted as a practical method of organic deposition. The adlayer of long alkyl chains is robust and convenient to stabilize Si surfaces and to make modifications over the adsorbates. The deposition reaction was activated by the coexistence of a radical initiator in liquid phase [6], by heating [6], by light irradiation [46–48], or by using Lewis-acid catalysis. Use of diluted olefins in an inert solvent (such as saturated alkanes) improves the quality of the alkyl adlayer [49].

Linford et al. first hypothesized that the spacing species to accommodate alkyl chains on Si(111) is OH species according to X-ray photoelectron spectroscopy (XPS) observation [6]. The origin of OH might be the peroxide radical initiator or O_2 dissolved in the reaction fluid. Most of the succeeding researches using long-chain alkenes lack in assessment of oxygen directly bonded on the Si surface. The long-chain alkyls may screen the adsorbates nearest the surface Si atoms, and the wetting and chemical properties of the whole adlayer usually seem not to be affected by the existence of oxygen adsorbate. Small portions of SiO_2 deposited during the adsorption process are considered to be the nuclei of SiO_2 island enlargement [7]. Adsorption of O can be due to accidental oxidation from the environment, and the residual amount of surface oxygen is an index of the reproducible, well-defined adlayer. Oxygen not incorporated in SiO_2 at Si surface is often detected by XPS [25] or Auger electron spectroscopy (AES) [9], which is supposed to be oxygen attached to the adsorbates, or just H_2O molecules entangled in the adlayer. Webb et al. summarized the extent of substrate oxidation depending on the method of reaction activation [13], in which the best quality was attained by Grignard reaction on chlorinated Si substrate discussed in the next chapter.

This category of methods has been most utilized to form adsorbates including functional groups. Sieval reported amino-terminated alkyl grafted on hydrogen-terminated Si(100) by a rather sophisticated amine protection/deprotection process to avoid direct reaction of NH_2 and Si surface [50]. A small extent of substrate oxidation was not inevitable, probably due to the treatment in aqueous solution for hydrolysis. Strother et al. [15] deposited amino-terminated decyl by a similar protection/deprotection method, and furthermore grafted DNA on the amino group. The adsorbates are bulky and the substrate–adsorbate interface did not perhaps affect the function of DNA. In some cases the attachment of functional groups to Si surface can be avoided by the difference of reaction rates between the terminating double bond and the functional group [39, 51].

The mechanism of hydrosilylation has been elucidated as the ejection of a terminating hydrogen atom to form a Si dangling bond followed by an attack of the terminal double bond in olefin to form C−Si bond [6]. The C radical, generated in the preadsorbate as a result of C−Si bond formation, immediately picks up a neighborhood surface-terminating H, leaving one Si dangling bond. A complete alkyl adsorbate is then formed. The leftover

dangling bond again captures olefin. The dangling bond (·Si) plays the role of chain carrier for the whole process, which is formulated as:

$$\text{H:Si(111)(surface)} \xrightarrow{\text{radical initiator, } \Delta, \text{ or } h\nu} \cdot\text{Si(surface)} + \cdot\text{H(This} \cdot \text{H dissipates away.)} \quad (1)$$

$$\text{R}-\text{CH}=\text{CH}_2 + \cdot\text{Si(surface)} \longrightarrow \text{R}-(\text{CH}\cdot)-\text{CH}_2-\text{Si(surface)} \quad (2)$$

$$\text{R}-(\text{CH}\cdot)-\text{CH}_2-\text{Si(surface)} + \text{H:Si(111)(surface)} \longrightarrow \text{R}-\text{CH}_2-\text{CH}_2-\text{Si(surface)} + \cdot\text{Si(surface)} \quad (3)$$

This process is actually visualized by Lopinski et al. [17], who revealed the chain growth of styrene along the dimer row of H:Si(100)-(2 × 1) by STM. They could discern isolated dangling bonds (vacancies of hydrogen termination) and styrene admolecules in UHV. Adsorption of styrene takes place on a site nearest to a dangling bond, and one end of the styrene chain is always accompanied by a dangling bond. Lopinski et al. proposed a similar reaction mechanism on H:Si(111)-(1 × 1). [52] Recently, the photoadsorption of allylamine (CH_2=CH−CH_2NH_2) on D:Si(111)-(1 × 1) was performed, and incorporation of surface-terminating D into alkyl adsorbate was evidenced by vibrational analysis [39].

The activation by Lewis-acid catalyst, such as $C_2H_5AlCl_2$, was explained to proceed by the generation of surface Si cationic radical [13, 53], which seems to be taken over immediately by adsorbate bonding.

Strictly speaking, the anchoring C−Si part of olefin-originated alkyls can be either of primary carbon or of secondary carbon. Figure 4 shows these two types of adsorbates for allylamine precursor. The primary type (*n*-type) is simple and usually accepted, while there had been no reason presented to reject the secondary type (sec-type). Recently, Yamada et al. presented a vibrational evidence that sec-type and *n*-type adsorbates from gaseous allylamine appear sequentially according to the increase of total coverage [39]. The adsorbates of sec-type were characterized by the vibrational modes of $-CH_3$ group, which the sec-type adsorbates nominally contain. The photoreaction was performed in an UHV setup, which is ideal for impurity rejection and the succeeding surface analysis.

Another possibility for future in-depth consideration is whether the alkyl chains, which are considered to be indifferent of H-terminated Si surface, may be excited and subjected to bond formation with Si besides the reaction of double-bond end. This causes the formation of bridge type adsorbates, such as shown in Fig. 1b. The photoadsorption of 1-butene on H:Si(111) did not yield CH_3 vibrational signals, indicating that the original methyl end in 1-butene was destroyed [39]. The existence of a bridge type adsorbate on Si(111) has not been recognized widely so far but it will be interesting to find a concrete method of preparation and to exploit its characteristic macroscopic properties.

1.3.2.3.2 **Grignard Reaction on Halogenated Si(111)** The formation of C−Si bond by Grignard reagents (C_mH_nMgX, X=Cl, Br, I) has been widely used in

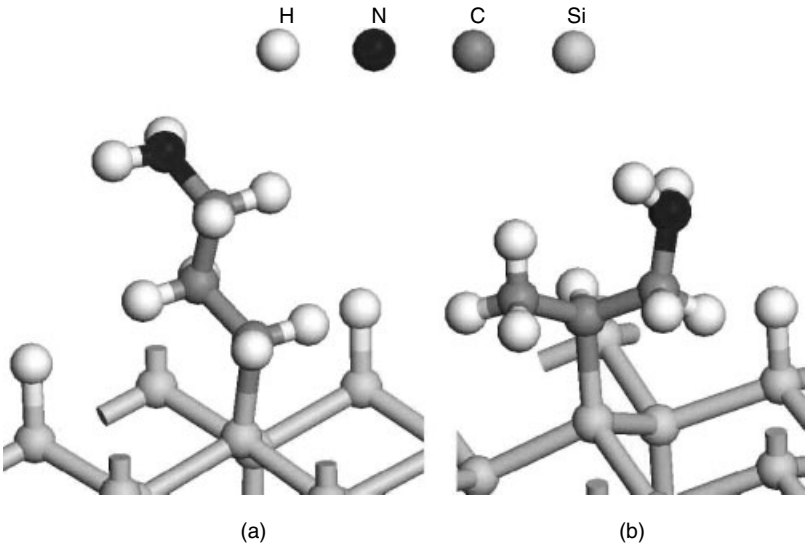


Fig. 4 Schematic view of allylamine adsorbates anticipated on Si(111) surface. (a) Primary (*n*-type) adsorbate, (b) secondary (sec-type) adsorbate.

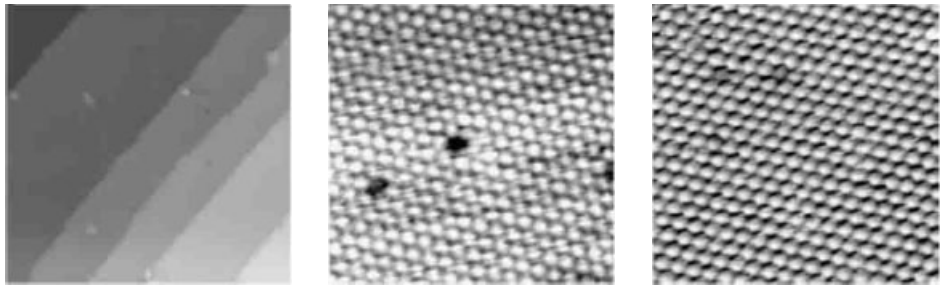
organosilicon synthesis, and Si(111) was also subjected to Grignard reaction in the early stage. Bansal et al. [54, 55] chlorinated H:Si(111) in a benzene solution of PCl_5 under coexistence of radical initiator and then immersed the chlorinated surface in alkyl–Li solution or alkyl–MgX solution. Despite imperfect impurity rejection and surface analysis, this work was pioneering in the use of alkylating reagents on Si surfaces. The mechanism is simply formulated as:

$$\mathrm{RMgX} + \mathrm{Cl{:}Si(111)} \longrightarrow \mathrm{R{:}Si(111)} + \mathrm{MgXCl} \quad (4)$$

Grignard reagents are delivered as solutions in diethylether or tetrahydrofuran (THF), which are commercially available.

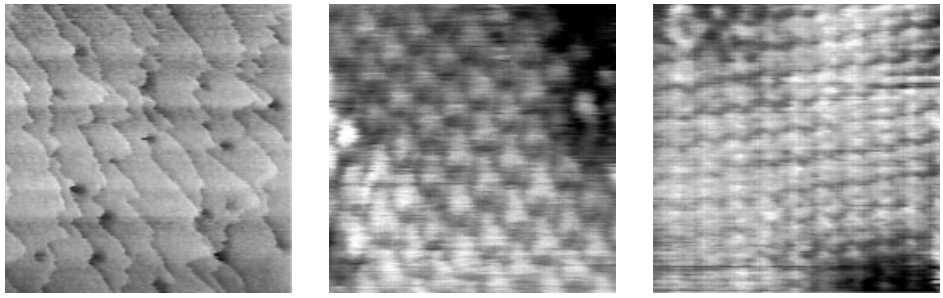
The precursor halogenated Si surfaces had not been put into detailed investigation until recently. Lopinski et al. [56, 57] reported well-ordered monolayers of Cl:Si(111)-(1 × 1) and Br:Si(111)-(1 × 1) examined by STM and high-resolution electron energy loss spectroscopy (HREELS) formed by (photo-)reaction in gaseous Cl_2 or Br_2 on H:Si(111). The surface was composed almost solely of monohalide Si atoms. The halogenated surfaces were atomically flat with low defect density, even better than hydrogen-terminated Si(111) (Fig. 5). Removal of surface Si atoms as gaseous Si halides is considered to be involved in flattening the modified surfaces. Cl:Si(111) and Br:Si(111) slowly react with components of air and should be handled in vacuum or in inert gas. Recently Rivillon et al. [58, 59] applied an outstanding method of surface infrared spectroscopy and detected Cl–Si vibration signals.

As one of the most attractive topics in the field of Si surface science, the formation and structure of methyl-terminated Si(111) by Grignard reaction has been



(a) (b) (c)

Fig. 5 STM constant current images of halogenated Si(111) prepared by gas phase reactions at room temperature; (a) Cl/Si(111)-50 × 50 nm, −1 V (sample bias), 40 pA, (b) Cl/Si(111)-6.5 × 6.5 nm, −0.5 V, 50 pA, (c) Br/Si(111)-6.5 × 6.5 nm, −0.4 V, 400 pA. (Figure 2 of B. J. Eves, G. P. Lopinski, *Surf. Sci.* **2005**, *579*, L89 [57]).



(a) (b) (c)

Fig. 6 (a) A wide-range STM image of methylated Si(111). Scan size = 500 nm × 500 nm, gap voltage = −1.21 V (sample negative), preset tunneling current = 2.58 nA. (b) A high-resolution STM image, 10 nm × 10 nm, −1.48 V, 2.38 nA. (c) 4 nm × 4 nm, −1.51 V, 19.65 nA. (Figures 3 and 4 of T. Yamada, M. Kawai, A. Wawro et al., *J. Chem. Phys.* **2004**, *121*, 10660 [24]).

studied in detail. The CH_3– group is probably the only hydrocarbon species that can terminate Si(111) in (1 × 1) periodicity with practical stability. Terry et al. examined a methyl-terminated Si(111) from Cl:Si(111) and CH_3Li by X-ray photoelectron diffraction and spectroscopy aided by synchrotron radiation [60]. They concluded that the length of C−Si bond vertical to the surface is 0.186 nm. Bansal et al. [55] listed the results for CH_3 and longer alkyls and assumed that CH_3 can terminate every surface Si atom on Si(111) on the basis of geometrical consideration. Webb et al. [13] also extensively compared the perfection of alkyl adlayers prepared by various methods.

A concrete evidence for methyl (1 × 1) termination was presented by Yamada et al. [24, 61] as high-resolution STM images. Figure 6 shows the flatness of the methylated surface viewed in a wide zone, as well as the lattice of methyl moieties arranged in (1 × 1) periodicity. The features representing methyl groups changed according to the STM gap voltage. The

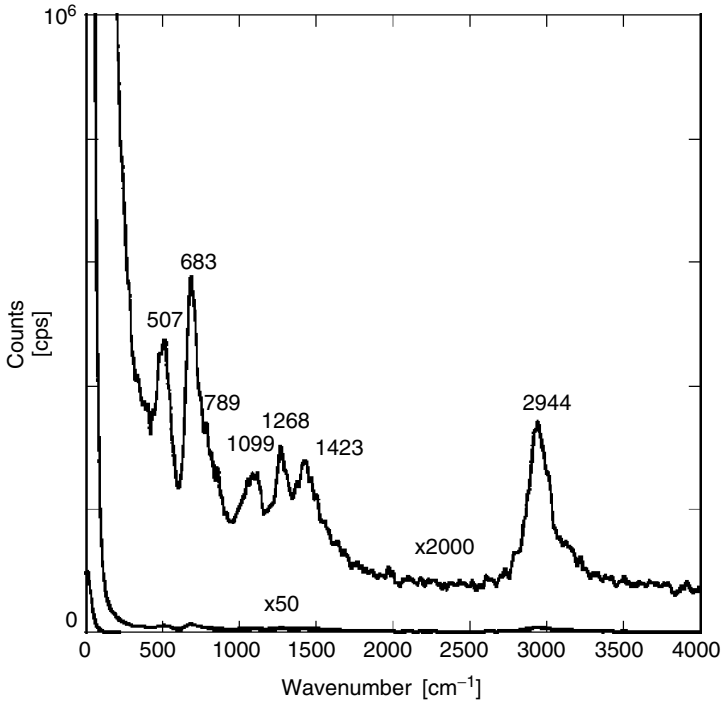


Fig. 7 HREELS of the methylated Si(111). HREELS incident electron energy 2.84 eV, incident angle = exit angle = 60° from the surface normal. The full width at half maximum of inelastic peak = 7.6 meV. 2944 cm^{-1}: C−H stretching, 1423 cm^{-1}: CH_3 umbrella motion, 1268 cm^{-1}: CH_3 asymmetric bending, 1099 cm^{-1}: Si−O stretching in SiO_2, 789 cm^{-1}: CH_3 rocking, 683 cm^{-1}: C−Si stretching, 507 cm^{-1}: C−Si bending. (Figure 2 of T. Yamada, M. Kawai, A. Wawro et al., *J. Chem. Phys.* **2004**, *121*, 10660 [24]).

features actually represent the electron orbitals, and it is difficult to extrude the geometric arrangement of H atoms in CH_3 just by viewing the images. HREELS of CH_3:Si(111)-(1 × 1) was also presented (Fig. 7), indicating all the characteristic vibration modes including the C−Si stretching motion. The amount of SiO_2 impurity, sensitively detected by HREELS, was controlled below 0.1%.

In terms of the movement of adsorbed CH_3 group, the rotation about the C−Si axis vertical to the surface is attractive. However, so far no methods have been found to observe this rotation collectively. The energy barrier of rotation excitation may be analogous to that of torsion of C−Si bond in an isolated CH_3-SiH_3 molecule, which corresponds to a frequency of 590.5 cm^{-1}. Yu et al. performed STM imaging of CH_3:Si(111)-(1 × 1) at the low temperature of 4.7 K [62]. They claimed that the rotation of every CH_3 group was locked at a position of C−H bonds rotated by $(7 \pm 3)^\circ$ away from the center of the neighboring $-CH_3$ group.

It is interesting to address the electronic property of CH_3:Si(111)-(1 × 1) not only for the purpose of application as

the lithography resist layer but also as the basis of nanoelectronic devices. The I–V characteristic curve of STM reached a peak at −1.5 eV in the occupied levels additionally to the I–V curve of H:Si(111). This peak corresponds to the electronic state that contributes to electronic conduction through the surface. This conducting property is also materialized in an electrolytic phenomenon. Niwa et al. [61] demonstrated that CH_3:Si(111)-(1 × 1) as an electrode in an aqueous redox solution exclusively lowers the peak potential of redox reaction. CH_3:Si(111)-(1 × 1) was also applied as the ultrathin channel medium of field-effect transistor [14].

As for Grignard reagents containing alkyl groups larger than methyl, the space filling of adsorbates does not geometrically allow every Si atom to be terminated, and a certain part of terminating Cl atoms must be left over in the space between alkyl adsorbates. Such Cl atoms are considered to be replaced by oxygen-containing species during rinsing or by exposure to air. Webb et al. reported that high-resolution XPS did not detect Cl after deposition of C_2H_5- or C_6H_5-CH_2- on Cl:Si(111) rinsed in methanol [25]. The possible terminating species was anticipated to be hydrogen. The replacement of residual Cl species is probably uncontrollable and introduces more chances of contamination. It is certainly easier to replace a part of the terminating hydrogen atoms on H:Si(111) by alkyl groups. This issue is discussed in the next chapter.

1.3.2.3.3 **Grignard Reagents and H:Si(111)**
H:Si(111) is less likely than Cl:Si(111) to react with alkylmagnesium reagents according to the classic formulation of Grignard reaction. However, so far, many cases of adsorbate formation on hydrogen-terminated Si surfaces have been reported. Kim et al. [63] first reported derivatization of hydrogen-terminated porous silicon by Grignard reagents. They included a quenching procedure with acetic acid after the Grignard reaction. By using CH_3COOD, incorporation of Si-terminating D species was detected. Kim et al. explained this process by dissociative insertion of R−MgX into Si−Si bonds just below the surface (called *backbonds*). The formation of Si−R and Si−MgX was assumed, and the Si−MgX species was considered to be quenched in Si−D by the presence of deutrated acetic acid. This interpretation fitted with a rather rough surface of porous Si, which was advantageous in the detection of surface products.

Formation of decyl ($C_{10}H_{21}$-) adsorbates by decyl Grignard reagent on H:Si(111) was first performed by Boukherroub et al. [64] The atomic force microscope (AFM) images of alkyl-terminated Si(111) show a flat Si surface without any sign of pit formation related to the backbond breakage. Replacement of terminating H with decyl groups was recognized. The robust properties of this surface were found to be the same as those formed by alkene photoadsorption or by Lewis-acid catalysis. Boukherroub et al. concluded that a new mechanism of Grignard reagent should be proposed to replace terminating H [64]. On flat H:Si(111), rinsing in a THF solution of CF_3COOD did not introduce D−Si [65].

The formation of C−Si bond in methyl Grignard reaction on H:Si(111) was first evidenced by Yamada et al. [5]. The STM images of CH_3MgBr-treated H:Si(111) showed that methyl groups just formed small lattice patches and adsorbates were randomly placed with

a significant open area [66]. Careful use of D:Si(111) and HREEL showed C−Si stretching signal at 678 cm^{-1} [5]. The HREEL spectra always contain H(D)−Si stretching signal, indicating that Grignard reaction cannot completely remove original terminating hydrogen atoms.

At the same time, a limitation was recognized in detecting organic adsorbates and terminating hydrogen by infrared spectroscopy. The H−Si stretching signal at 2090 cm^{-1} became invisible to IR as the coverage of organic increased [26]. However with HREELS, the H−Si signal was apparently detected on surfaces prepared under the same condition. Infrared spectroscopy seems to be more affected by adsorbate screening effects than HREELS.[5] This fact influences the interpretation of spectra of CH_3:Si(111) formed by electrochemical anodization in a Grignard reagent solution, that 100% methylated surfaces were obtained [67, 68].

The Grignard reaction on H:Si(111) is probably the most useful method to obtain robust Si surfaces for practical purposes. The adlayers formed are constantly a mixture of alkyl and H regardless of the chain length. The C signals of AES [26] and XPS [55] indicating the saturation coverages are proportional to the chain length, indicating that the adsorbate-wise areal density is constant, regardless of the chain length. The chance of unwanted substrate oxidation during the fabrication process can be minimized, compared to the case for Cl:Si(111). More varieties of hydrocarbons, such as branched or unsaturated hydrocarbon moieties [26, 39, 65], can be deposited with adequate stability. In nearly all the cases, the hydrocarbon groups are transferred to the Si surfaces within the precursor Grignard reagents without isomerization and component detachment. The alkyl-hydrogen mixed adlayers are strongly hydrophobic and resistive toward dissolved oxygen in water [9], alkali solutions [64], or even in a Cu-plating solution containing F^- for a short period [9].

The mechanism of H:Si(111) replacement by Grignard reagent has not been elucidated on the basis of concrete experimental evidences. Recently Fellah et al. proposed a mechanism involving a trace amount of alkyl halide residue contained in the Grignard reagent solution [69]. Decyl bromide intentionally added in a diethylether solution of decyl magnesium bromide significantly accelerated deposition of decyl groups. Treatment of H:Si(111) in pure tetradecyl bromide yielded a finite amount of alkyl adsorbate and a significant amount of SiO_2. It was difficult to compare the reaction kinetics with the Grignard reagent. The effects of alkyl halide were scrutinized by voltammetric electrolysis of Grignard reagent, by using *n*-type and *p*-type silicon, and by considering the electronic and thermodynamic energy levels of RX, RMgX, and Si. Although this analysis was not completed, we can expect the application of alkyl halides as the alkylation reagent to open a new route to organic deposition on Si.

References

1. C. S. Whelan, M. J. Lercel, H. G. Craighead et al., *J. Vac. Sci. Technol.* **1996**, *B14*, 4085.
2. H. Sugimura, K. Okiguchi, N. Nakagiri et al., *J. Vac. Sci. Technol.* **1996**, *B14*, 4140.
3. D. Niwa, Y. Yamada, T. Homma et al., *J. Phys. Chem. B* **2004**, *108*, 3240.
4. W. Lie, D. G. Fedorov, K. Hirao, *J. Phys. Chem. A* **2002**, *106*, 7057.

5. T. Yamada, T. Inoue, K. Yamada et al., *J. Am. Chem. Soc.* **2003**, *125*, 8039.
6. M. R. Linford, P. Fenter, P. M. Eisenberger et al., *J. Am. Chem. Soc.* **1995**, *117*, 3145.
7. C. H. de Villeneuve, J. Pinson, M. C. Bernard et al., *J. Phys. Chem.* **1997**, *B101*, 2415.
8. A. B. Sieval, A. L. Demirel, J. W. M. Nissink et al., *Langmuir* **1998**, *14*, 1759.
9. T. Yamada, N. Takano, K. Yamada et al., *J. Electroanal. Chem.* **2002**, *532*, 247.
10. M. P. Stewart, J. M. Buriak, *J. Am. Chem. Soc.* **2001**, *123*, 7821.
11. W. A. Hofer, A. J. Fisher, G. P. Lopinski et al., *Chem. Phys. Lett.* **2002**, *365*, 129.
12. A. B. Sieval, C. L. Huisman, A. Schö1necker et al., *J. Phys. Chem. B* **2003**, *107*, 6846.
13. L. J. Webb, N. S. Lewis, *J. Phys. Chem. B* **2003**, *107*, 5404.
14. D. Niwa, H. Fukunaga, T. Homma et al., *Chem. Lett.* **2005**, *34*, 520.
15. T. Strother, R. J. Hamers, L. M. Smith, *Nucl. Acid Res.* **2000**, *28*, 3535.
16. W. Cai, J. R. Peck, D. W. van der Weide et al., *Biosens. Bioelectron.* **2004**, *19*, 1013.
17. G. P. Lopinski, D. D. M. Wayner, R. Wolkow, *Nature* **2000**, *406*, 48.
18. Z. Hossain, H. S. Kato, M. Kawai, *J. Am. Chem. Soc.* **2005**, *127*, 15030.
19. P. G. Piva, G. A. DiLabio, J. L. Pitters et al., *Nature* **2005**, *435*, 658.
20. G. S. Higashi, Y. J. Chabal G. W. Trucks et al., *Appl. Phys. Lett.* **1990**, *56*, 656.
21. R. J. Hamers, S. K. Coulter, M. D. Ellison et al., *Acc. Chem. Res.* **2000**, *33*, 617.
22. R. J. Hamers, J. S. Hovis, S. Lee et al., *J. Phys. Chem. B* **1997**, *101*, 1489.
23. J. S. Hovis, H. Liu, R. J. Hamers, *Appl. Phys. A* **1998**, *66*, S553.
24. T. Yamada, M. Kawai, A. Wawro et al., *J. Chem. Phys.* **2004**, *121*, 10660.
25. L. J. Webb, E. J. Nemanick, J. S. Biteen et al., *J. Phys. Chem. B* **2005**, *109*, 3930.
26. T. Yamada, N. Takano, K. Yamada et al., *Jpn. J. Appl. Phys.* **2001**, *40*, 4845.
27. P. Allongue, C. H. de Villeneuve, J. Pinson, *Electrochim. Acta* **2000**, *45*, 3241. and
28. Z. Lin, T. Strother, W. Cai et al., *Langmuir* **2002**, *18*, 788.
29. A. B. Sieval, R. Linke, G. Heij et al., *Langmuir* **2001**, *17*, 7554.
30. H. N. Waltenburg, J. T. Yates Jr., *Chem. Rev.* **1995**, *95*, 1589.
31. D. D. M. Wayner, R. A. Wolkow, *J. Chem. Soc., Perkin Trans.* **2002**, *2*, 23.
32. R. A. Wolkow, *Annu. Rev. Phys. Chem.* **1999**, *50*, 413.
33. S. F. Bent, *Surf. Sci.* **2002**, *500*, 879.
34. M. A. Filler, S. F. Bent, *Prog. Surf. Sci.* **2003**, *73*, 1.
35. J. M. Buriak, *Chem. Rev.* **2002**, *102*, 1271.
36. G. S. Higashi, R. S. Becker, Y. J. Chabal et al., *J. Appl. Phys. Lett.* **1991**, *58*, 1656.
37. R. B. Doak, Y. J. Chabal, G. S. Higashi et al., *J. Electron Spectrosc. Relat. Phenom.* **1990**, *54*, 291.
38. H.-H. Luo, C. E. D. Chidsey, *Appl. Phys. Lett.* **1997**, *72*, 477.
39. T. Yamada, M. Noto, K. Shirasaka et al., *J. Phys. Chem. B* **2006**, *110*, 6740.
40. C. Thirstrup, M. Sakurai, T. Nakayama et al., *Surf. Sci.* **1998**, *411*, 203.
41. R.-P. Chen, D.-S. Lin, *Surf. Sci.* **2000**, *454–456*, 196.
42. T. Hitosugi, T. Hashizume, S. Heike et al., *Jpn. J. Appl. Phys.* **1997**, *36*, L361.
43. H. Kajiyama, S. Heike, T. Hitosugi et al., *Jpn. J. Appl. Phys.* **1998**, *37*, L1350.
44. A. S. Baluch, N. P. Guisinger, R. Basu et al., *J. Vac. Sci. Technol. A* **2004**, *22*, L1.
45. U. Neuwald, H. E. Hessel, A. Feltz et al., *Surf. Sci.* **1993**, *296*, L8.
46. R. L. Cicero, M. R. Linford, C. E. D. Chidsey, *Langmuir* **2000**, *16*, 5688.
47. Q.-Y. Sun, L. C. P. M. de Smet, B. van Lagen et al., *Angew. Chem., Int. Ed.* **2004**, *43*, 1352.
48. Q.-Y. Sun, L. C. P. M. de Smet, B. van Lagen et al., *J. Am. Chem. Soc.* **2005**, *127*, 2514.
49. A. B. Sieval, V. Vleeming, H. Zuilhof et al., *Langmuir* **1999**, *15*, 8288.
50. A. B. Sieval, R. Linke, G. Heij et al., *Langmuir* **2001**, *17*, 7554–7559.
51. H. Asanuma, G. P. Lopinski, H.-Z. Yu, *Langmuir* **2005**, *21*, 5013.
52. R. L. Cicero, C. E. D. Chidsey, G. P. Lopinski et al., *Langmuir* **2002**, *18*, 305.
53. J. M. Buriak, M. J. Allen, *J. Am. Chem. Soc.* **1998**, *120*, 1339.
54. A. Bansal, X. Li, I. Lauermann et al., *J. Am. Chem. Soc.* **1996**, *118*, 7225.
55. A. Bansal, X. Li, S. I. Yi et al., *J. Phys. Chem. B 105*, **2001**, 10266.
56. G. P. Lopinski, B. J. Eves, O. Hul'ko et al., *Phys. Rev. B 71*, 125308, **2005**.
57. B. J. Eves, G. P. Lopinski, *Surf. Sci.* **2005**, *579*, L89.
58. S. Rivillon, F. Amy, Y. J. Chabal, *Appl. Phys. Lett.* **2004**, *85*, 2583.

59. S. Rivillon Y. J. Chabal, L. J. Webb et al., *J. Vac. Sci. Technol. A 23*, **2005**, 1100.
60. J. Terry, M. R. Linford, C. Wigren et al., *Appl. Phys. Lett.* **1997**, *71*, 1056.
61. D. Niwa, T. Inoue, H. Fukunaga et al., *Chem. Lett.* **2004**, *33*, 284.
62. H. Yu, L. J. Webb, R. S. Ries et al., *J. Phys. Chem. B* **2005**, *109*, 671.
63. N. Y. Kim, P. E. Laibinis, *J. Am. Chem. Soc.* **1998**, *120*, 4516.
64. R. Boukherroub, S. Morin, F. Bensebaa et al., *Langmuir* **1999**, *15*, 3831.
65. T. Yamada, K. Shirasaka, M. Noto et al., *J. Phys. Chem. B* **2006**, *110*, 7357.
66. T. Yamada, N. Takano, K. Yamada et al., *Electrochem. Commun.* **2001**, *3*, 67.
67. A. Fidélis, F. Ozanam, J.-N. Chazalviel, *Surf. Sci.* **2000**, *444*, L7.
68. T. Miyadera, A. Koma, T. Shimada, *Surf. Sci.* **2003**, *526*, 177.
69. S. Fellah, R. Boukherroub, F. Ozanam et al., *Langmuir* **2004**, *20*, 6359.

1.4 Langmuir–Blodgett (LB) Films on Electrodes

1.4.1 Photoelectrochemistry

Masaru Sakomura
Yokohama National University, Yokohama, Japan

Masamichi Fujihira
Tokyo Institute of Technology, Yokohama, Japan

1.4.1.1 History of the Langmuir–Blodgett (LB) Film

Surface films of materials that have very poor solubility in the supporting liquid phase but exhibit interesting and useful properties, have been recognized for centuries. The materials forming the so-called insoluble monolayers, such as fatty acids, are essentially insoluble in water but are still surface active.

By 1919, under Langmuir's guidance, Miss Katharine Blodgett had succeeded in transferring fatty acid monolayers from water surfaces to solid supports. Such built-up monolayer assemblies are now referred to as *Langmuir–Blodgett* (LB) films, while floating monolayers at the air–water interface are called *Langmuir films*. The first formal report describing the preparation of built-up films did not appear until 1935 [1]. A series of their pioneering works are introduced in the book by Gaines [2] together with the contributions of other early investigators, including the earliest scientific paper on the effect of oily films on water by Benjamin Franklin in 1774 [3], and the preparation of the first monolayers at the air–water interface by Agnes Pockels in 1891 [4]. The LB method was the first technique to provide a chemist with the practical (and still the most extensively used) capability to construct ordered molecular assemblies.

In the mid-1960s, Hans Kuhn et al. began their stimulating experiments on monolayer organization [5]. A self-assembled monolayer (SAM) was introduced as a possible alternative to the LB films. The LB and SAM films have attracted much attention recently, because optoelectronics and molecular electronics have become areas at the frontier of materials science [6]. For more details of the historical aspects, the reader is referred to a relevant textbook [7] as well as to the Gaines' book mentioned earlier.

1.4.1.2 Basic Principles of Surface and Film

Surface Tension A molecule in a liquid bulk phase is bound to the neighboring molecules surrounding it. But a molecule at the surface misses the contact with the neighbors on top (Fig. 1). Such a molecule, therefore, has higher energy than the molecule in the bulk phase. When increasing the surface of a liquid, the number of molecules in energy-rich interfacial positions increases. The free energy change with increasing the surface area by a small amount dA in a reversible way is proportional to dA:

$$dG = \gamma dA \tag{1}$$

The proportionality constant γ is called *surface energy* or *surface tension*. In surface science, γ is the most fundamental quantity. Considering such a situation as illustrated in Fig. 2, we can empirically define γ by the following equation:

$$\gamma = \frac{f}{2L} \tag{2}$$

Encyclopedia of Electrochemistry. Edited by A.J. Bard and M. Stratmann
Vol. 10 *Modified Electrodes*. Edited by M.Fujihira, I.Rubinstein, and J.F.Rusling
Copyright © 2007 Wiley-VCH Verlag GmbH & Co. KGaA, Weinheim. ISBN: 978-3-527-30402-8

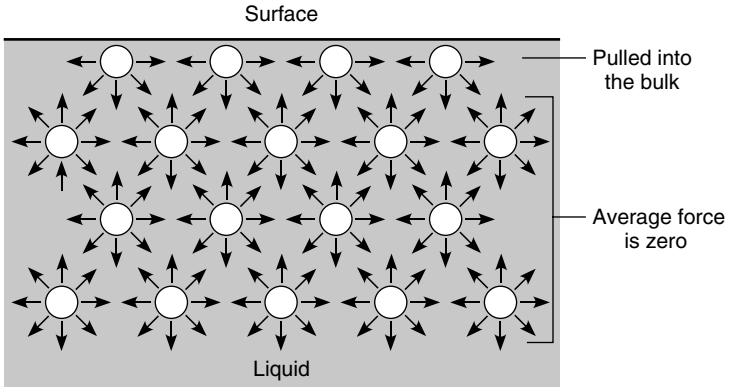


Fig. 1 Higher energy of a molecule at the surface than in the bulk.

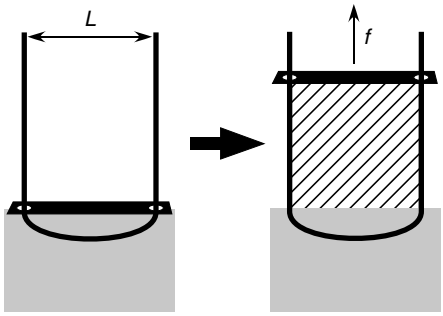


Fig. 2 Withdrawing a soap film.

where f is the force required to withdraw a soap film from a surfactant solution by lifting a movable frame and L is the length of the movable frame. Because the film has a front and back side, twice $L\gamma$ should be balanced with f. From the viewpoint of this empirical law, we call the proportionality constant *surface tension*, the dimension of which is (N m^{-1}).

There have been various methods for measuring the surface tension [2]. The Wilhelmy plate is commonly employed in the usual LB apparatuses to monitor the change in the surface pressure. In the Wilhelmy method [8], the force balanced with the surface tension is determined by a plate vertically suspended and partially immersed in the water phase. Figure 3 illustrates the experimental configuration. The liquid surface near the three-phase contact line is oriented almost vertically. Thus, the surface tension drags the plate downward. For a rectangular plate of dimensions l, w, and t, immersed to a depth h in a liquid (as shown in Fig. 3), the net downward force, F, is given by

$$F = 2\gamma(t + w)\cos\theta + \rho_P\, glwt - \rho_L\, gtwh \tag{3}$$

where θ is the contact angle, ρ_P is the material density of the plate, g is the gravitational acceleration, and ρ_L is the density of the liquid. The second and third terms on the right-hand side of Eq. (3) represent the downward gravity force and the upward buoyancy force, respectively. The usual procedure is to choose appropriate materials for the plate (quartz, glass, mica, platinum, and filter paper) that should

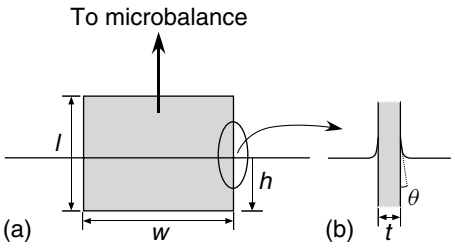


Fig. 3 A Wilhelmy plate: (a) front view; (b) side view.

be completely wettable by the liquid (i.e. $\theta = 0$) and measure the change in F for a stationary plate ($h = \text{const.}$). The change in force ΔF is then related to the change in surface tension $\Delta\gamma$ by

$$\Delta\gamma = \frac{\Delta F}{2(t + w)} \tag{4}$$

If the plate is thin, so that $t \ll w$, then

$$\Delta\gamma = \frac{\Delta F}{2w} \tag{5}$$

Thus, Wilhelmy method can be used without any correction factors.

Surface Activity The chemical species given the general name of surface-active agents or surfactants have a special tendency to adsorb at interfaces, or to form colloidal aggregates in solution at very low molar concentrations. A surface-active material possesses ''lyophobic'' part, which has little attraction for the solvent, and ''lyophilic'' part, which has a strong attraction for the solvent, in its chemical structure. In water-based systems, the terms *hydrophobic* and *hydrophilic* are quite frequently employed in place of ''lyophobic'' and ''lyophilic,'' respectively.

Figure 4 illustrates the basic molecular structure of surface-active materials. Such materials are also referred to as being *amphiphilic*. If the hydrophobic tail group is present in an aqueous phase, the water structure will be unfavorably distorted. Such a distortion (in this case ordering) of the water structure surrounding the hydrophobic group decreases the overall entropy of the system. This entropy, however, is regained when surfactant molecules are transported to the water surface and the associated water molecules are released. Since less energy is required to bring surfactant molecules to the air–water interface relative to water molecules, the presence of the surfactant decreases the energy required to expand the interfacial area. If the water molecules on the surface are replaced by adsorbed surfactant molecules with lower specific excess surface energy, the surface tension of the solution is decreased.

The fundamental principle of the surface activity is expressed by the Gibbs adsorption equation:

$$\Gamma = -\frac{c}{\mathrm{RT}} \cdot \frac{\mathrm{d}\gamma}{\mathrm{d}c} \tag{6}$$

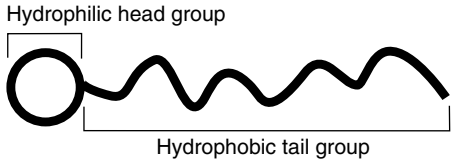


Fig. 4 Typical structure of surface-active molecules.

This equation relates the surface tension γ to the surface excess Γ (i.e. the amount of surfactant per unit area of surface). When the surfactant is enriched at the surface, Γ increases with the concentration of the surfactant, c, and with the tendency of the solute to decrease the surface tension, $-\mathrm{d}\gamma/\mathrm{d}c$.

As for correlations between surface activity and the chemical structures of surfactants, a large body of literature has appeared. Although most of the studies are semiquantitative at best, they can provide good guidance for choice and development of the best surfactant for a given situation. The reader will find discussions about such structure–property relationships in a relevant textbook [9].

Gibbs and Insoluble Monolayers The adsorption of surfactant molecules at the surface of a liquid can be so strong that a monomolecular film (Gibbs monolayer) of unidirectionally ordered surfactants is formed (Fig. 5). Since the decrease in surface tension is directly related to the surface excess adsorption of the surfactant by the Gibbs adsorption equation (Eq. 6), the formation of the Gibbs monolayer can be monitored by decrease of the surface tension. The maximum number of molecules filling a given area depends upon the area occupied by each molecule. The cross-sectional area of the hydrophobic chain or of the hydrophilic head group, whichever is greater, determines the molecular occupied area. Since the adsorbing species forming the Gibbs monolayer has a sufficiently large solubility in the solvent, when the area of the saturated surface is more expanded, the surface-active molecules dissolved in the solution will fill in the created area.

In contrast, there are practically insoluble amphiphiles, for example, a fatty acid molecule that consists of a hydrophilic part (carboxyl group) and a hydrophobic part (a long hydrocarbon chain), which prevents the molecule from dissolving in the aqueous phase. Such a molecule forms an insoluble monolayer on a water surface. Drops of the solution of the fatty acid in a volatile organic solvent are placed on an aqueous surface and after evaporation of the solvent a fatty acid's monolayer remains. This process is called *spreading*. The adsorbed molecules forming the insoluble monolayer are essentially isolated on the surface; therefore, the surface excess Γ is equal to the added amount of material divided by the surface area.

Surface Pressure In a traditional way, a film balance composed of a shallow rectangular container (called *trough*) and a movable barrier has been used to study

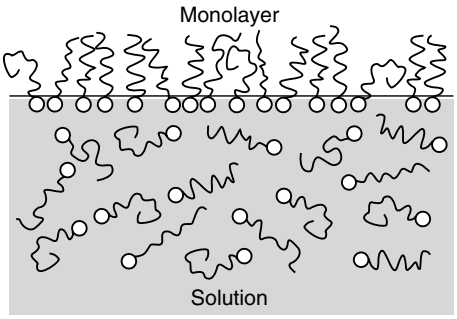


Fig. 5 Formation of a Gibbs monolayer.

floating monolayers. A liquid phase (called *subphase*) is added in the trough until a meniscus appears above the rim and the area of the surface is controlled with the movable barrier that rests across the edge of the trough. There are numerous modifications of the early film balances as reviewed in Gaines' book [2]. The design of the conventional type of a Langmuir or a Langmuir–Blodgett trough system (*vide infra*) is based on the composition of the traditional film balance.

A schematic comparison of the two situations of the film balance is illustrated in Fig. 6. The trough is filled with pure water and the left and right side of the surface is separated. At the beginning, the surface of the subphase is completely clean and the surface tension of each side is that of pure water (γ_0). In case (a), a soluble surfactant is placed on one side of the trough. A Gibbs monolayer will be immediately formed by adsorption of the surfactant molecules to the surface on this side, while the residual molecules will be dissolved in the subphase. The surfactant molecule in the aqueous phase can diffuse to the opposite side of the barrier; therefore, after the system reaches equilibrium, the formation of the saturated film accompanying the same decrease of the surface tension will be achieved on both the sides.

On the other hand, in case (b), an insoluble amphiphile is spread on one side of the trough. An insoluble monolayer will be formed on this side, while the aqueous surface of the opposite side will be kept clean even after any practical period of time. In this case, the surface tension of the side to which the amphiphile is added has been lowered, while the other side remains that of the pure water (γ_0).

If the barrier could move freely, it would drift in the direction of the side with higher surface tension. Under the beginning condition of the film balance and the situation in case (a), the barrier is balanced by the same surface tensions on both the sides, whereas in case (b), the barrier moves in the direction to decrease the clean water surface. The barrier movement looks as if a lateral pressure due to the film is acting on the barrier. From the viewpoint of this, the surface pressure π is defined as the difference between the surface tension of the clean subphase γ_0 and the surface tension of the subphase covered by amphiphiles γ:

$$\pi = \gamma_0 - \gamma \tag{7}$$

The surface pressure can be determined by direct measurement of the force acting on the barrier in the differential way. However, in the usual Langmuir–Blodgett trough systems, the surface pressure is mostly measured with the Wilhelmy plate by monitoring the change in the surface tension from that of pure water as mentioned above.

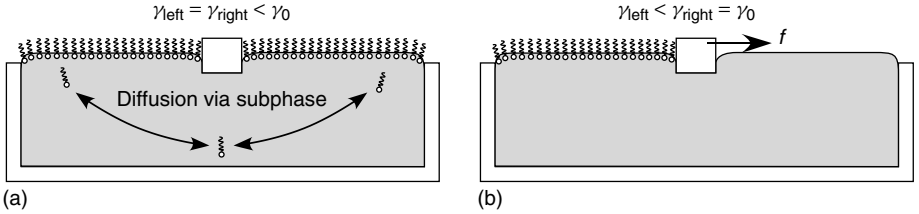


Fig. 6 A comparison of (a) Gibbs and (b) insoluble monolayers.

Surface Pressure – area ($\pi - A$) Isotherm
Experimentally, one can spread a known amount of material (too small to saturate the starting area) on a subphase in a trough at constant temperature and move a barrier to compress an insoluble monolayer formed on the surface by slowly decreasing the available area. When the surface excess Γ increases by compression of the film, the lowering of the surface tension is expected from the Gibbs equation (Eq. 6). A pressure-area ($\pi - A$) isotherm measured by the above procedures gives us very important information about physical nature of the film and molecular characteristics of the adsorbed materials.

As for Gibbs monolayers, the compression of the film cannot be performed by using a Langmuir trough because amphiphiles would diffuse via the subphase to both sides of the barrier. The Gibbs monolayers can be compressed by using the PLAWM (named by the combination of the first letter of Pockels, Langmuir, Adam, Wilson, and McBain) trough, which is a two-compartment type trough with a flexible membrane fixed to the movable barrier [10, 11].

Analogous to three-dimensional bulk materials, monolayer films exhibit characteristics that can be almost equated to the solid, liquid, and gaseous states of matter. As the monolayer is compressed on the water surface, phase transitions between these analogous states should occur and the changes could be detected by the measurement of the $\pi - A$ isotherms. Figure 7 shows an example of the $\pi - A$ isotherm. It shows the following phases:

Gaseous (G): The molecules are relatively far apart and have significant surface mobility. The molecules act essentially independently and the surface pressure is almost zero ($\gamma \approx \gamma_0$).

Liquid (L): When compressing a gaseous film, there can be a first-order phase transition to the liquid state. We can consider at least two types of liquid phase. A liquid-expanded (LE) phase appears first. In this phase, the molecules are touching each other but there is no lateral order.

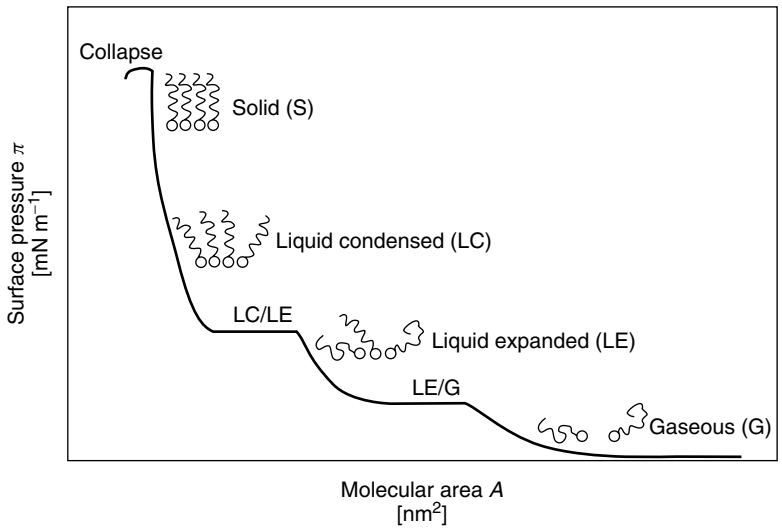


Fig. 7 Schematic $\pi - A$ isotherm of a monolayer.

After passing a plateau of the first-order phase transition, a liquid-condensed (LC) phase is reached. Here, the amphiphiles exhibit a tilted phase with a decreasing tilt angle. The film is relatively stiff but still more compressible.

Solid (S): The films are rigid and densely packed with high surface viscosity. The molecules are oriented almost perpendicular to the surface. The $\pi - A$ isotherms are linear and its extrapolation to zero surface pressure gives an area per molecule that corresponds to the molecular cross-sectional area.

1.4.1.3 Preparation Methods for LB Films

Molecules and Subphase We confine our discussion here to the most popular supporting liquid for monolayer studies, that is, water. The quality of water is of prime importance to the LB studies. Many researchers choose an ultrapure water system, which includes mixed anion and cation exchange resins, a reverse osmosis unit, ultraviolet sterilizer, and photooxidation unit, supplying water of high specific resistance (1.8×10^5 Ωm) and total organic contamination (TOC) in the ppb (parts per 10^9) level.

A classical example of an amphiphile, which can form an insoluble monolayer on a water subphase, is stearic acid, where the long hydrocarbon tail group ($CH_3(CH_2)_{16}-$) is hydrophobic, and the carboxylic acid head group ($-COOH$) is hydrophilic. The ionization of the carboxylic group will be suppressed at low pH. At pH 4, stearic acid behaves like a neutral molecule. At higher pH, the carboxylic group dissociates to form carboxylate ion ($-COO^-$). The presence of doubly charged cations (e.g. Ca^{2+}, Ba^{2+}, and Cd^{2+}), acting as counterions, can stabilize the monolayer of the anionic amphiphile, and then, facilitate monolayer transfer on solid surfaces. The effect of the ion binding to reduce the extent of electrostatic repulsion between charged head groups allows for close packing of the monolayer. In order to secure the reproducibility of the $\pi - A$ isotherms, it is crucial to keep temperature, pH, and composition of the subphase at the constant conditions.

The reader can find a discussion of the properties of monolayer films of a variety of amphiphiles in Gaines' book [2]. Today, many scientists use organic synthesis to construct amphiphiles for different purposes. Such molecular engineering is very important, especially in the design of amphiphiles with functional groups such as chromophores, donors, acceptors, and so on. For more details, see the relevant textbooks [5–7].

LB Deposition Although many different techniques for transferring a floating monolayer to a solid plate have appeared (e.g. ''touching'' [12] and ''lifting'' [13, 14] techniques), we will concentrate on the LB method, first introduced by Langmuir [15] and applied extensively by Blodgett [1, 16]. This technique involves the vertical movement of a solid substrate through the monolayer/air interface. In the most commonly used method, the substrate (e.g. a glass slide) is first lowered through the monolayer so that it dips into the subphase and then withdrawn under a constant surface pressure. The value of surface pressure that gives the best results depends on the nature of the monolayer, and is established empirically.

If the slide is used as a hydrophilic surface, deposition follows the sequence of events described in Fig. 8. The water

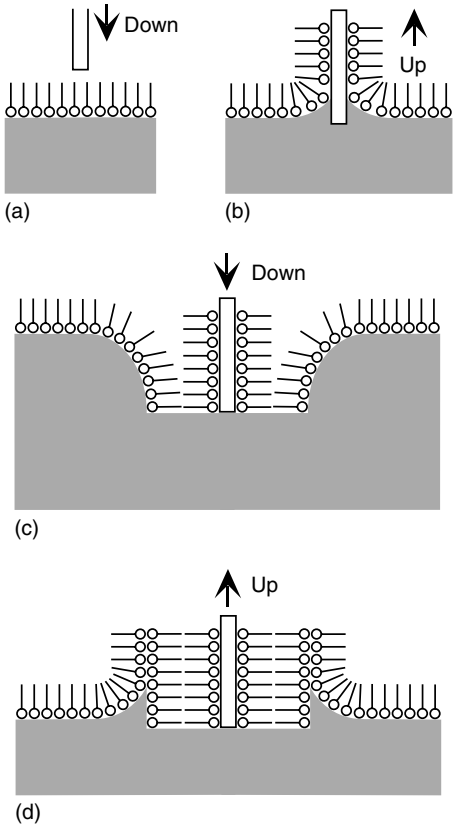


Fig. 8 Y-type Langmuir–Blodgett film deposition.

wets the slide's surface and the meniscus turns up; there is no mechanism for deposition at the first dipping. The first monolayer is transferred as the slide is raised through the water. The substrate may, therefore, be placed in the subphase before the monolayer is spread. As the slide is withdrawn, the meniscus is wiped over the slide's surface and it leaves behind a monolayer in which the hydrophilic groups are turned toward the hydrophilic surface of the slide. To avoid disordering of the film structure on the withdrawing process, the deposition speed must be limited by the rate at which the ascending substrate sheds water. The bonding of the monolayer to the slide will only be complete after the intervening layer of water has drained away or evaporated. It is important not to raise the substrate faster than the rate at which water drains from the solid. This drainage is not due to gravity but is a result of the adhesion between the monolayer being transferred and the material on the substrate, which acts along the line of contact and so drives out the water film. The second dipping into the subphase differs from the first in that the slide is now hydrophobic; the meniscus turns down and a second monolayer is deposited with its tail groups in contact with the exposed tail groups on the slide. In contrast to the withdrawing process, the dipping substrate can be moved quite rapidly without affecting the monolayer transfer. The second withdrawal exactly resembles the first except that the new monolayer is now being deposited onto the hydrophilic head groups of the monolayer already present. This type of deposition, in which layers are laid down each time the substrate moves across the phase boundary, with a head-to-head and tail-to-tail configuration is referred to as *Y-type* deposition.

Although this is the most frequently encountered situation, it is also possible for monolayer deposition to occur only when the substrate enters the subphase, depending on the nature of the monolayer, substrate, subphase, and the surface pressure. These deposition modes are called X-type (monolayer transfer on the downstroke only) and Z-type (transfer on the upstroke only). The ideal structures resulted from the deposition modes are illustrated in Fig. 9.

The deposition ratio, τ (also called the *transfer ratio*), is often used as a measure of

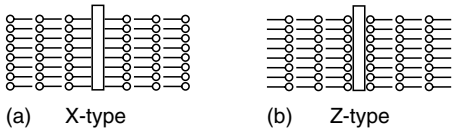


Fig. 9 The multilayer structures formed by (a) X-type deposition and (b) Z-type deposition.

the quality of deposition. It is defined as the ratio of the decrease in the area occupied by the monolayer (held at constant surface pressure) on the water surface, A_L, to the coated area of the substrate, A_S, that is,

$$\tau = \frac{A_L}{A_S} \tag{8}$$

The area removed from the water surface is easily measured by the mechanism used to maintain a constant surface pressure, and there is then a direct electrical readout of surface area. Under most circumstances a transfer ratio of unity is taken as a criterion for good deposition, and one would then expect the orientation of molecules on the slide to be very similar to their orientation on the water. Occasionally, there is a large but consistent deviation from a value of unity; this points to a situation in which the molecular orientation is changing during transfer. Variable transfer ratios are almost always a sign of unsatisfactory film deposition. If asymmetric substrates are used (e.g. a glass slide metalized on just one surface), then some care must be exercised in interpreting the measured deposition ratio; it is unlikely that τ will be identical for different surfaces.

Equipment for LB Deposition By now, many kinds of the LB deposition protocols have been achieved by developing a variety of Langmuir–Blodgett troughs. Many types of trough systems are produced by employing the basic design of the traditional film balance, as mentioned in the earlier section.

The most conventional type of trough is like that shown in Fig. 10. As shown in the figure, the trough with the single movable barrier can compress a monolayer on the left side of the barrier. The ''well'' at the left end of the trough offers the depth allowing for the up and down stroke of relatively large substrates on the LB depositions. As shown in the former section, the successive deposition of a monolayer can be easily achieved with this trough.

If one intends to construct alternate-layered structures of two different types of molecules by using the conventional trough, the two different materials would have to be alternately spread onto and removed from the subphase surface [17]. Such procedures are very time consuming and wasteful. To achieve the deposition of such alternate-layered structures more conveniently, some kinds of troughs for

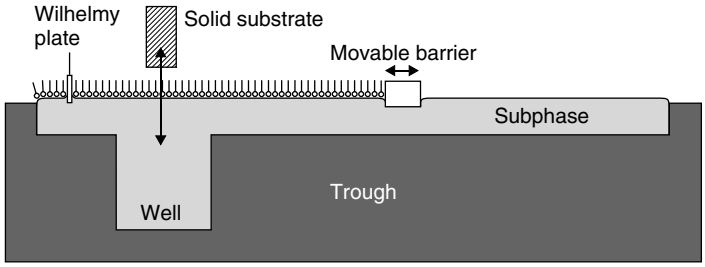


Fig. 10 Cross-sectional view of a Langmuir–Blodgett trough.

alternate deposition have been designed [18–20]. The trough with the double movable barriers shown in Fig. 11 is one of the alternate types. The two fixed barriers placed on the center part of the trough separate the water surface into three compartments (A, B, and C). Two different monolayers can be formed in the two compartments (A and B) between the movable and fixed barriers on each side. Another compartment C sandwiched by the two fixed barriers at the center of the trough is usually a clean water surface. The lifter clutching the substrate consists of an upper arm and a lower arm. These arms can move up and down independently and rotate. The underarm can transport a substrate dipped thoroughly into the subphase to any compartment without taking it out from the water.

In addition to the above-mentioned troughs of the single- and the triple-compartment type, the multicompartment type trough will be briefly taken up here. The multicompartment circular trough with two independent drive barriers (Fig. 12) was described by Fromherz [21]. The compartments (eight in Fromherz's design) are separated by walls, which are slightly lower than the edges of the trough. A Wilhelmy plate is suspended from the

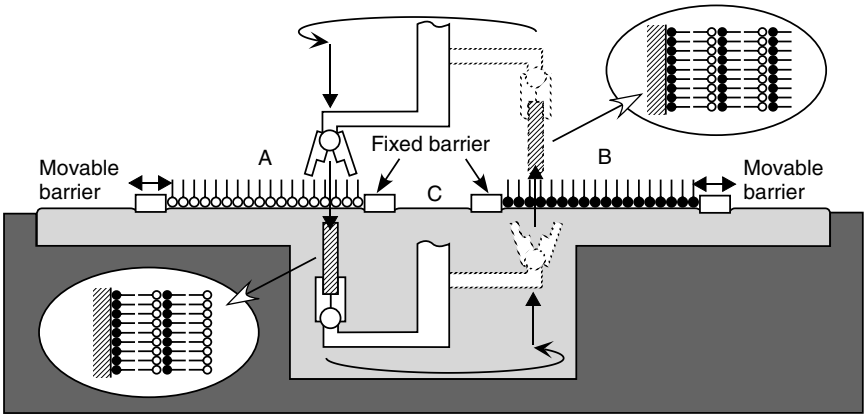


Fig. 11 Cross-sectional view of an alternate type Langmuir–Blodgett trough.

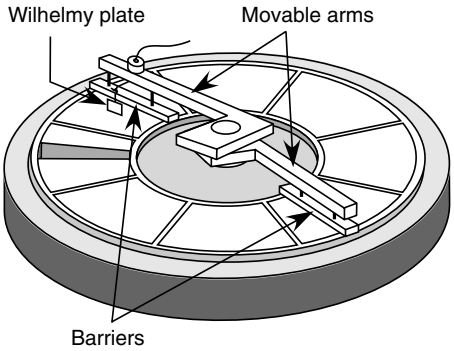


Fig. 12 Fromherz multicompartment circular trough.

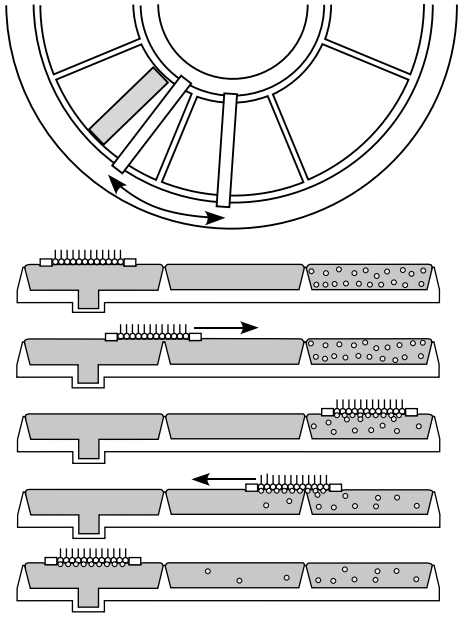


Fig. 13 Monolayer manipulation using the multicompartment trough.

upper part of one of the movable arms; therefore, the surface pressure is measurable at any compartment. The film transfer onto a substrate has to be carried out only on a compartment in which a well for the LB deposition is provided. When the film compression would be performed, the barrier held by the arm with the Wilhelmy plate must be fixed and the other barrier would be moved to decrease the available area. After the compression, the monolayer formed between the two barriers can be transported to other compartments with different subphases by the synchronized motion of the two barriers (Fig. 13). Such monolayer manipulation by the multicompartment trough may be applied, for example, for studies on the adsorption between a back surface of a floating monolayer and a soluble material in a subphase [22, 23], or in chemical reactions.

1.4.1.4 LB Assemblies Designed for Photoelectric Devices

Energy Transfer in Monolayer Organization
The Langmuir trough technique enables us to construct simple artificial membrane systems consisting of cooperative molecular components. Much of the pioneering work in this field has been carried out by Kuhn and his colleagues. They organized a large variety of monolayer assemblies to investigate intermolecular interactions, and photophysical and photochemical processes [24–26].

As good examples of their research, the investigations of the energy transfer from a sensitizing molecule to an acceptor molecule within the complex monolayer organization will be given here. A system harvesting light energy and channeling the energy should be of interest as a component in any proposed photoelectrical device for solar energy conversion.

In a monolayer of dye I (Fig. 14, host) with traces of dye II (Fig. 14, guest) the host is harvesting light energy and the guest, which absorbs at longer wavelength, is trapping the energy. The energy migration in the layer of the host depends strongly on the interaction of the molecules. As proposed by Kuhn et al. J aggregates in monolayers prepared by spreading the dyes and the long chain hydrocarbon octadecane in a 1:1 mixture can be regarded as two-dimensional crystals with a brickstone arrangement of the chromophores [5, 27]. In these films, octadecane acts as a spacer and contributes to the arrangement of the aliphatic region. It can be demonstrated by a quantum mechanical calculation that the exciton hopping time in this very compact arrangement of chromophores is $\Delta t = 10^{-13}$ s. Since the

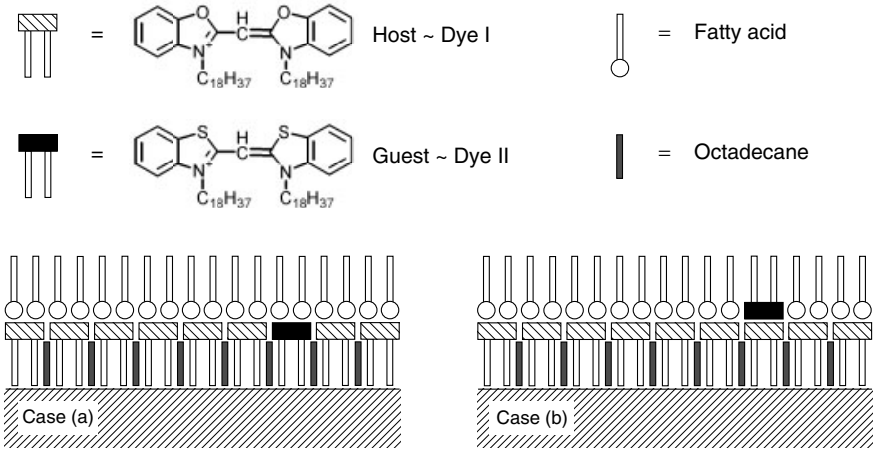


Fig. 14 Monolayer assemblies for energy channeling system consisting of dye I and dye II as light harvesting and trapping molecules, respectively.

fluorescence time of the single molecule is 10^4 times longer than Δt, an unusual long exciton diffusion path can be expected. If an exciton trap is exactly interlocking in this structure, the coupling should be sufficiently strong to get a trapping of the energy absorbed by the host even if there is one molecule of the guest among 10^4 molecules of the host. This condition should be fulfilled in the present case where dye II differs from I only by two sulfur atoms instead of two oxygen atoms. The molecule can substitute a molecule of the host in the lattice.

They fabricated two LB assemblies as shown in Fig. 14. In the film of case (a), the guest molecule is incorporated in the lattice of the host, whereas in case (b), it exists in the fatty acid monolayer deposited on a layer of the host. The monolayer assemblies are fabricated on a glass plate and illuminated with UV light, which can excite the host only. A plate where the guest is absent shows the violet fluorescence of the host. On the other hand, the host's fluorescence is quenched but the blue fluorescence of the guest is observed with a plate where the guest is present. The fluorescence change is due to light harvesting via energy transfer from the excited host to the guest. The changes of the relative fluorescence intensity of the host are plotted in Fig. 15. In case (a), a considerable quenching of the fluorescence of I and a sensitized fluorescence II was seen even if only one among 50 000 molecules of I is exchanged by a molecule of II (Fig. 14). It should be noted that this artificial device for channeling energy is far more efficient than the device used in plant photosynthesis where there is one energy trap among 300 chlorophyll molecules for harvesting energy.

If I and I_0 are the intensity of the fluorescence of the host in the presence and in the absence of the guest, respectively, we can write

$$I = \frac{I_0 r_d}{r_d + r_{en}} \tag{9}$$

where r_d is the rate of deactivation by fluorescence and thermal collisions and

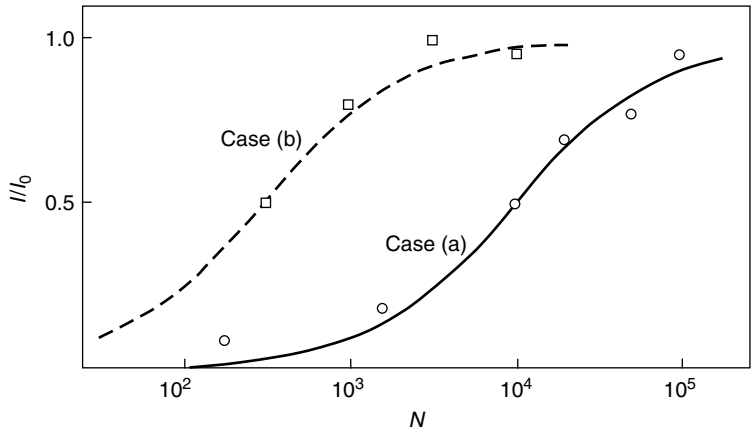
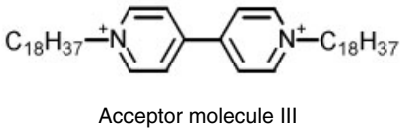
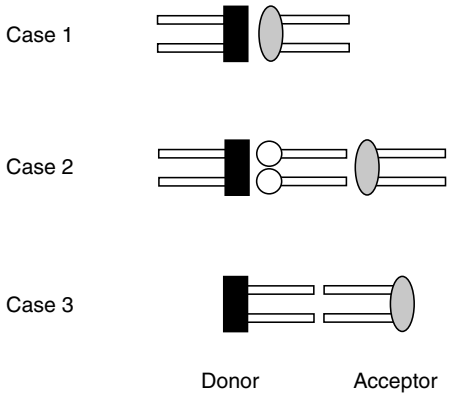


Fig. 15 A plot of I/I_0 (relative fluorescence intensity of dye I) against N (number of molecules of dye I per molecule of dye II) for case (a) (circles) and (b) (squares).

Fig. 16 Assembly of monolayers of donor (dye II) and electron acceptor III.



Acceptor molecule III



r_{en} is the rate of energy transfer. Since r_{en} is proportional to the surface density of the guest (inversely proportional to N, where N is the number of molecules of host per molecule of guest) then

$$\frac{I}{I_0} = \frac{1}{1 + \dfrac{\text{const.}}{N}} \qquad (10)$$

Using the values const. $= 10^4$ and const. $= 300$ for cases (a) and (b) respectively, we obtain the full and broken curves in Fig. 15. This example shows the importance of a well-defined architecture of the monolayer assembly.

Layer-by-layer Assemblies of Electron Acceptor and Dye Molecules With appropriate components and film structures, quenching of fluorescence due to electron transfer from an excited dye to an electron acceptor can also be observed in monolayer assemblies. For this purpose, Kuhn designed LB assemblies in which dye II in monomeric form and the electron acceptor molecule III (viologen) are incorporated separately in two monolayers (Fig. 16). In case (1), the dye and electron acceptor are in direct contact. In case (2), they are separated by inserting a fatty acid spacer-layer between

dye and acceptor layers. In case (3), dye chromophore and acceptor are separated by the hydrocarbon substituents of both layers. In each dye layer, dye II is diluted by fatty acid (not shown symbolically). In cases (1) and (3), the heterogeneous LB films are formed by Y-type depositions; therefore, these monolayer assemblies are easily fabricated with a conventional LB trough (Fig. 10) by spreading and removing the different films on a water surface repeatedly in the course of the film depositions. If an LB trough of an alternate type (Fig. 11) is available, the heterogeneous depositions can be achieved more conveniently. On the other hand, the film of case (2) includes also a Z-type structure. To realize case (2), the substrate is covered by the dye and then by a fatty acid layer of desired length in the usual manner (Y-type deposition). Now the layer is dipped in water without a surface layer, the water is then covered by an acceptor layer, and the plate is taken out. This is a somewhat tricky step since rearrangements must be avoided. The substrate is taken out by slowly lifting the sample in a horizontal position. The hydrophilic side of the film must be moderately hydrophilic and well adjusted in its composition to make the intended contact.

The fluorescence of each sample was compared with that of the reference sample where the acceptor is absent. This fluorescence is totally quenched in case (1), half quenched in case (2) if the C_{16} fatty acid is used as the spacer-layer, and totally unquenched in case (3) [28].

The dependence of the fluorescence intensity I in case (2) on the thickness of the spacer layer was also investigated. On the basis of a similar relation as Eq. (9), the ratio $(I_0 - I)/I$, where I_0 is the fluorescence intensity without acceptor, measures the rate of the electron transfer. This ratio is given by the ratio of the rate of electron transfer (k_{et}) and rate of deactivation of the excited dye in the absence of the electron acceptor (k_d). For nonadiabatic electron transfer, k_{et} is described by the following equations [29]:

$$k_{et} = k(r) \exp\left(\frac{-\Delta G^*}{RT}\right) \qquad (11)$$

$$k(r) = k_0 \exp\{-\beta(r - r_0)\} \qquad (12)$$

where $k(r)$ is the preexponential factor of the rate constant; r is the distance between electron donor and acceptor; ΔG^* is the free-energy barrier of reaction; r_0 is the value of distance r at which $k(r)$ equals some preassigned value of k_0, that is, 1×10^{13} s^{-1}; and β is the parameter of the distance dependence of the rate. If the electron transfer is purely tunneling, the rate of electron transfer should be practically independent of temperature and decrease exponentially with increasing r corresponding to the thickness of the spacer layer, d. Therefore, the logarithm of $(I_0 - I)/I$ plotted against d should form a straight line. Figure 17 shows that this is in fact the case for spacer layers with 14–22 C atoms [24].

In the case of pyrene as the dye and again viologen as the electron acceptor, the linear relation of log $\{(I_0 - I)/I\}$ against d could also be demonstrated by Möbius [28]. In this case, the standard technique of producing monolayer assemblies could be applied since the pyrene was bound to the methyl group at the end of a fatty acid chain while the cationic viologen III is at the hydrophilic head of the molecule. It is therefore easy in this case to separate chromophore and electron acceptor by a single monolayer of hydrocarbon chains.

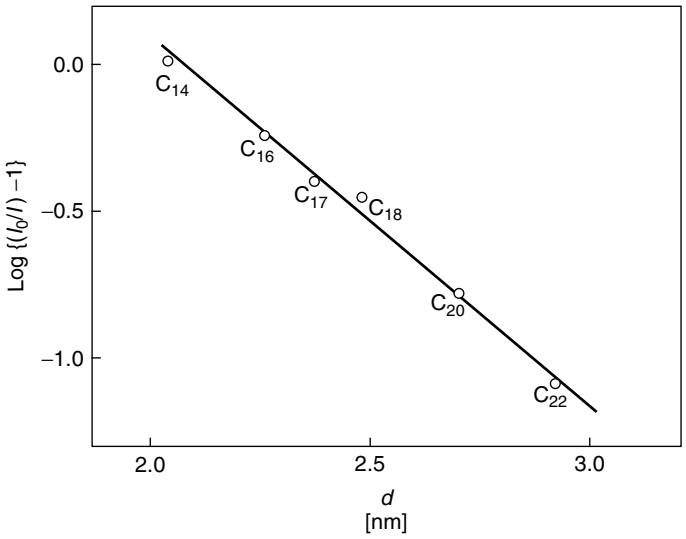


Fig. 17 Quenching of fluorescence of dye II (D) by electron acceptor III (A) in the arrangement of Fig. 16, case (b). Log{$(I_0/I) - 1$} is plotted against the spacer layer thickness d for fatty acids with 14-22 C atoms.

Acceptor/Sensitizer/Donor Multilayer Systems A variety of electronic components with molecular dimensions have been investigated since the introduction of the foresighted concept of molecular diode by Aviram and Ratner [30]. For example, Mezger and Panetta [31] have made an effort to realize the molecular diode proposed by them.

Fujihira et al. fabricated the acceptor/sensitizer/donor (A/S/D) type LB multilayer system as a molecular photodiode based on Kuhn's idea of the light-driven electron pump [32] on a gold optically transparent electrode (AuOTE) [33]. The structure and function of the molecular photodiode of A/S/D are shown in Fig. 18(a), where hydrophilic parts and hydrophobic units are indicated by circles and squares, respectively. Three functional compounds tend to orient regularly in the heterogeneous LB films due to their amphiphilic properties.

Kuhn [24, 26, 34], Möbius [28, 35], and others [36, 37] have studied the distance dependence of the rate of photoinduced electron transfer in LB films. Their observed dependence agrees in a qualitative sense with the other experimental [38–48] and theoretical [29] results described by Eq. (11) and Eq. (12). As they did, the distances between the three functional moieties, that is, A, S, and D, within LB monolayers can be closely controlled at known values.

In addition to the distance dependence, the effect of the standard free energy difference ΔG° for the electron transfer, that is, the difference between the energy levels of the excited (or ground state) donor and the ground state (or excited) acceptor [29, 49, 50], is another important factor in determining the rate of electron transfer. Relationship (13) was first introduced by Marcus where the free-energy barrier for the reaction, that is, ΔG^* in Eq. (11), is

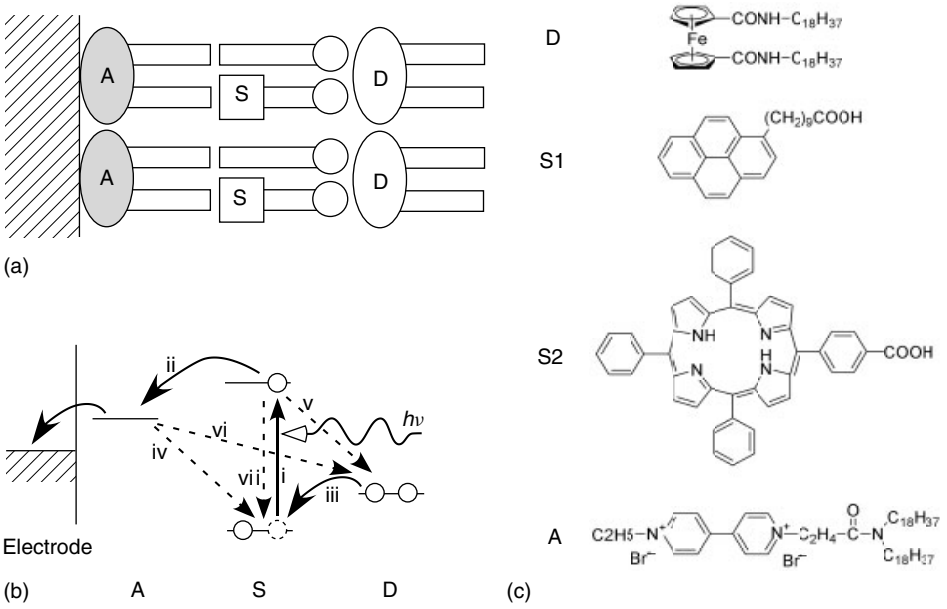


Fig. 18 Molecular photodiode with heterogeneous A/S/D LB film on an electrode: (a) structure, (b) energy diagram, and (c) structural formulae of A, S, and D amphiphiles.

given [29] in terms of the reorganization energy λ:

$$\Delta G^* = \frac{\lambda}{4}\left(1 + \frac{\Delta G^\circ}{\lambda}\right)^2 \qquad (13)$$

The changes in bond lengths of the reactants and the changes in solvent orientation coordinates in the electron transfer are related [29] to λ. In Marcus's original theory, the motion of the nuclei was treated classically. There have been several attempts [29, 50] to treat the nuclear coordinates quantum mechanically and to modify the equation for the energy gap ΔG°. In connection with the design of the proper energy diagram for the molecular photodiode, the inverted region, where the rate decreases with an increase in large excess of $-\Delta G^\circ$, predicted by Eq. (13) is most important. The presence of the inverted region has been confirmed experimentally by the use of internal electron transfer systems with rigid spacers and the electron transfer in solutions [51–60].

Therefore, to design a better molecular photodiode the distance and ΔG° dependence should be kept in mind. In Fig. 18(b), the energy diagram of the A/S/D molecular photodiode is depicted as a function of distance across the LB film. If the forward processes indicated by arrows with solid lines are accelerated, and the backward processes with dashed lines are retarded by setting the distances and the energy levels appropriately, the photoinduced vectorial flow of electrons can be achieved, that is, the acceleration by setting ΔG° equal to λ is assumed for the forward electron transfer processes (ii) and (iii), while the retardation, as a consequence of the inverted region, is assumed for the back-electron transfer processes (iv) and (v). Once an electron-hole pair is separated successfully, the recombination of

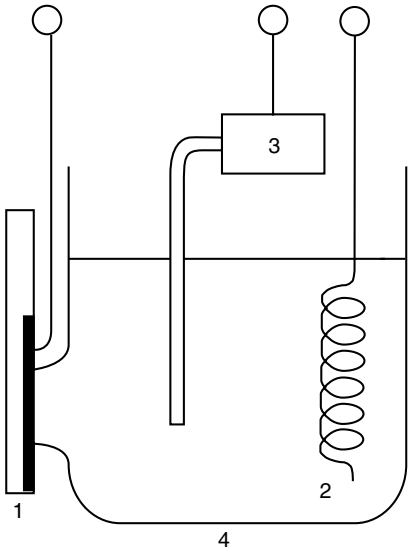


Fig. 19 A cell for photoelectrochemical measurements: (1) an LB modified AuOTE; (2) a Au wire counterelectrode; (3) a saturated calomel electrode (SCE) with a salt bridge; (4) a cell container.

the pair across the large separation by LB film (process (vi)) is hindered by the distance dependence.

The three kinds of functional amphiphilic derivatives used for the first A/S/D-type molecular photodiode [33] are shown in Fig. 18(c) together with porphyrin sensitizer S2 used later. By depositing these three amphiphiles on AuOTE, as shown in Fig. 18(a), and by the use of the resulting electrode as a working electrode in a photoelectrochemical cell (Fig. 19) [38–41], the photoinitiated vectorial flow of electron is achieved and detected as photocurrents. The AuOTE is a metal electrode and hence does not by itself possess a rectifying ability as does a semiconductor electrode [38–41]. Yet, in spite of the inability of the substrate electrode to rectify, the photocurrent in opposing directions depending on the spatial arrangement of A/S/D or D/S/A is detected [61]. The direction is in accordance with the energy profile across LB films in Fig. 18(b).

Much higher photocurrents can be observed [33, 61] for stacks of multilayers of each component, for example, in the form of A,A,A/S,S,S/D,D,D and D,D,D/S,S,S/A,A,A. The directions of the photocurrents also agree with those expected for the multilayered systems.

In such heterogeneous LB films, the long alkyl chains are intervened between the A and S and between the S and D moieties. As a result, parts of the excited sensitizers were deactivated by the emission of photons (Fig. 18b, vii) without quenching by electron transfer. To cope with this problem, Kakimoto, Imai, and their coworkers used polyimide LB films consisting of A, S, and D units (Fig. 20) for constructing more efficient molecular photodiodes [62, 63]. They have reported the preparation and properties of polyimide LB films [64–66]. Since polyimide LB films have no long alkyl spacer between the layers (monolayer thickness, 0.4–0.6 nm), electrons should be more readily transferred. For example, the photoelectrical conversion efficiencies of AuOTEs coated with 6 layers of aromatic polyimide itself as A, 2 layers of a porphyrin derivative with aliphatic polyimide as S, and 6 layers of a ferrocene derivative with aliphatic polyimide as D is enhanced about 10 times larger than those for photodiodes with conventional LB films [62]. Later, the hole-carrier property of the D layer was further improved by the use of triphenylamine in place of ferrocene as the D moiety [63].

LB Assemblies of Synthetic Molecular Photodiodes Another approach to shortening the distances between the functional moieties is the use of synthetic molecular

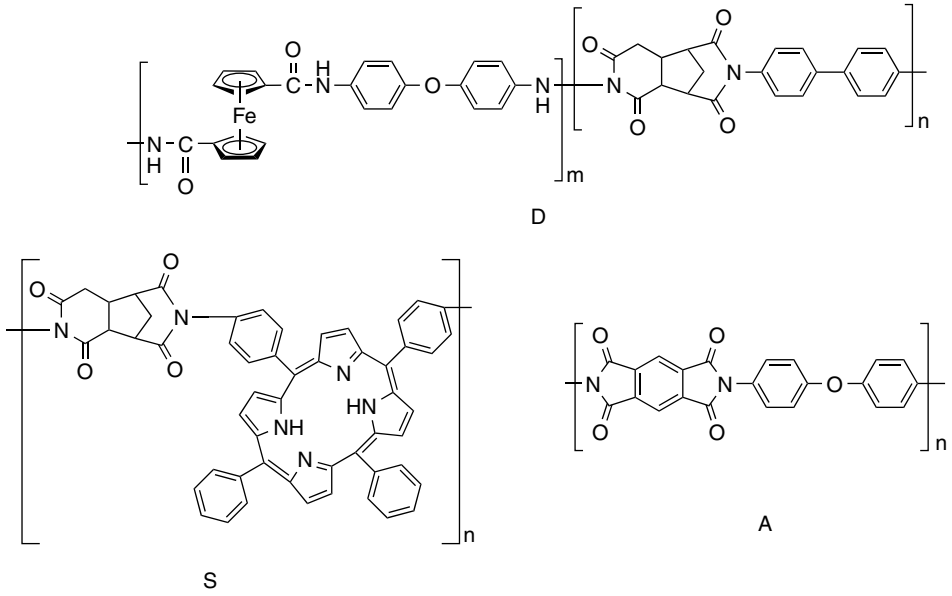


Fig. 20 Structural formulae of D, S, and A components of polyimide heterogeneous LB film molecular photodiode.

photodiodes, where chromophores and redox moieties are linked covalently. Such intramolecular charge separation systems are also studied as model compounds for a natural photosynthetic reaction center (RC), in particular, since the structural determination of bacteria's photosynthetic reaction center to atomic resolution using X-ray crystal analysis by Deisenhofer et al. [67–69]

In biosystems, the molecules organize themselves into complex functional entities with cooperating components of molecular dimensions. Higher plants use two different reaction centers, called *photosystems I and II* (PSI and PSII), whereas bacteria make do with a single reaction center. All reaction centers in plants and bacteria are complexes containing protein subunits and donor–acceptor molecules. Following light activation of antenna pigments, photon energies are harvested and funneled to the special pair acting as the initial donor in a series of short range, fast, and efficient electron transfer steps. The multistep electron transfer reaction through the array of the redox species with appropriate energetics and spatial coordination arranged by transmembranal span of the complexes in the plant or bacterial cell culminates in a long-lived charge-separated state. The well-organized and asymmetric molecular arrangement across the membrane plays an important role in charge separation in photosynthesis. For design of artificial photosynthetic molecular devices, it is of great interest to mimic the elaborate molecular machinery.

So far, a variety of synthetic polychromophoric model systems, that is, triads, tetrads, pentads, and so on, have been studied in connection with photosynthesis and reported by several groups [70–88]. The electron-transport components, porphyrins, quinones, aromatic imides, and fullerenes are commonly employed by

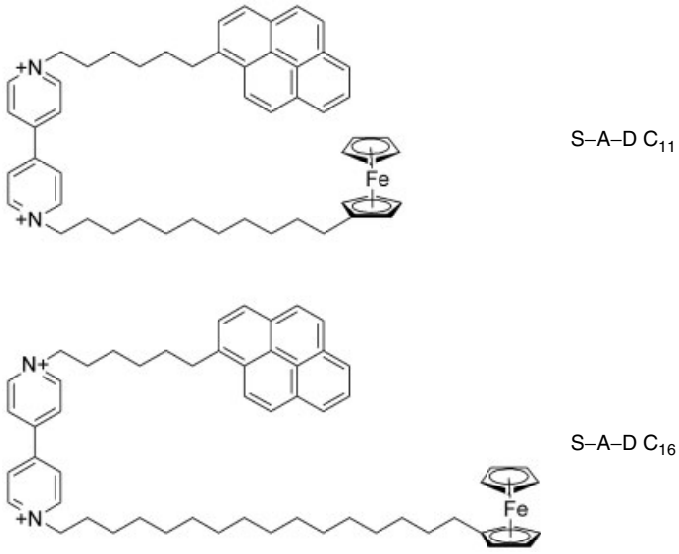


Fig. 21 Structural formulae of the folded-type triads.

many of the reaction center models. The primary event of photosynthetic solar energy conversion including absorption of visible light, singlet energy transfer between pigments, and photoinduced electron transfer from excited singlet states to give long-lived charge-separated states in high yield have been realized with some of these artificial systems. However, mimicry of the farther aspects of photosynthesis including chemical processes driven by the chemical potential in the form of the long-lived charge separation is still difficult and has only been reported in a few works [89, 90].

A–S–D Triad Monolayer Systems Since 1985 [33], Fujihira's group has been studying amphiphilic triad molecules that can spread and form monolayers on water surfaces. The early amphiphilic triads [33, 91] are shown in Fig. 21. In these amphiphilic triads, three functional moieties, a dicationic electron acceptor (A, viologen (V^{2+})), a neutral sensitizer (S, pyrene (Py)), and a neutral electron donor (D, ferrocene (Fc)), were combined in the order of S−A−D (Py–V^{2+}–Fc), in which the active components were linked by sigma-bonded tunneling bridges. At an air–water interface, the triad forms stable mixed monolayer with arachidic acid, in which the dicationic hydrophilic A moiety of the triad is oriented toward water and two hydrophobic alkyl chains terminated by S and D subunits extend into the air. In such monolayers, the spatial arrangement of the three moieties in the order of acceptor–sensitizer–donor was expected (Fig. 22a) under high surface pressure, owing to the difference in the length of the two alkyl chains (C_6 and C_{11} or C_{16}) linking A to S and D, respectively. Because of the folded form of the oriented molecules on a water surface, the S–A–D triads were called the *folded-type* triad. In this highly ordered folded-type S–A–D triad, two steps of intramolecular electron transfer would be initiated through light absorption of

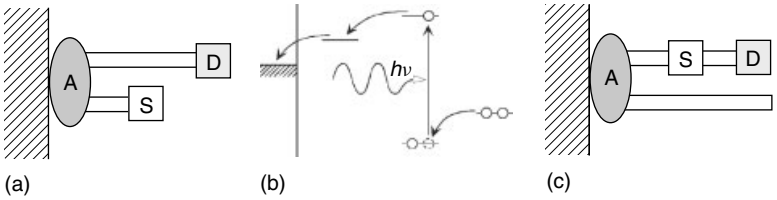


Fig. 22 Schematic representation of (a) oriented folded-type S−A−D triad and (c) oriented linear-type A−S−D triad, and (b) corresponding energy diagram.

the sensitizer moiety. If the oriented triad molecules were transferred onto a AuOTE as they are on the air–water interface using the LB technique, the photodiode function of this molecular device would be expected from the energy diagram shown in Fig. 22(b). And then electron transfer from the resultant long-lived charge-separated state, $Py–V^{+\bullet}–Fc^{\bullet}$, to the AuOTE under controlled potential may occur. Such photoelectric conversion devices are readily fabricated, and the photodiode function played by the highly oriented triad molecules of the folded type is successfully observed.

It was found in the early studies that the appropriate spatial arrangements for the charge separation of the folded-type triads were attained only under high surface pressures [91]. In order to achieve the spatial arrangement of the A, S, and D moieties more readily and completely, *linear-type* A–S–D triad molecules I−V (Fig. 23) [71, 92–94] were synthesized. In these triads, the three moieties are combined linearly in the order of A, S, and D; therefore, asymmetric spatial arrangements of them in monomolecular layers should be in the same order (Fig. 22c). The mixed monolayers of the

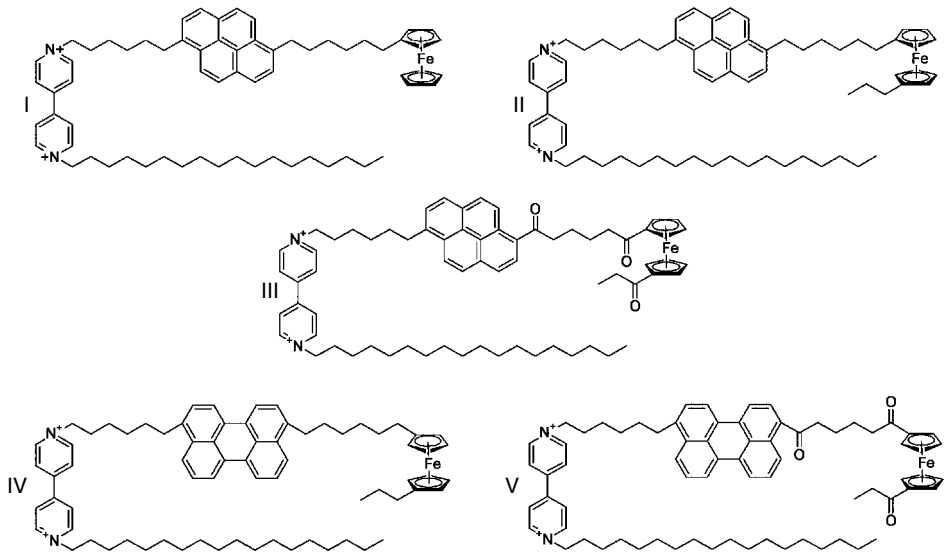


Fig. 23 Structural formulae of linear-type triads.

linear-type triads with behenic acid exhibit much higher photocurrents than those of the folded-type triads. This indicates that more ideal spatial arrangements of the A, S, and D moieties are attained in the linear triad molecules ordered in the mixed monolayers. A favorable orientation for the photoelectric conversion of the linear-type triad was also accomplished at a relatively low surface pressure of 15 mN m^{-1} in contrast with the inactive orientation of the folded-type triad molecule deposited at the same surface pressure.

To confirm that the triad absolutely acts as a molecular photodiode in the monolayer, the photocurrent of the AuOTE modified with the triad monolayer with opposite directional orientation (Fig. 24) should be examined. For the purpose of the study, a new type of photoelectrochemical cell (Fig. 24 c) equipping such an LB modified AuOTE are developed [94]. The fabrication of the new type of photoelectrochemical cell is performed by the following procedures. A Au mirror electrode is first treated with a thiol compound with a short alkyl chain (C_3). By this treatment, a hydrophilic Au surface was changed to a hydrophobic thiol-modified surface. The cell container is first put into the Langmuir trough. An aqueous subphase is poured into the trough, and then the triad monolayer is formed on the aqueous surface. The hydrophobic Au electrode set just above the cell container is dipped into water. At the end of film deposition, the electrode is released to fall inside the cell. The cell container is then taken out of the trough together with the subphase solution and the Au electrode in it. More of the supporting electrolyte is added, and a counter (Au wire) and reference (saturated

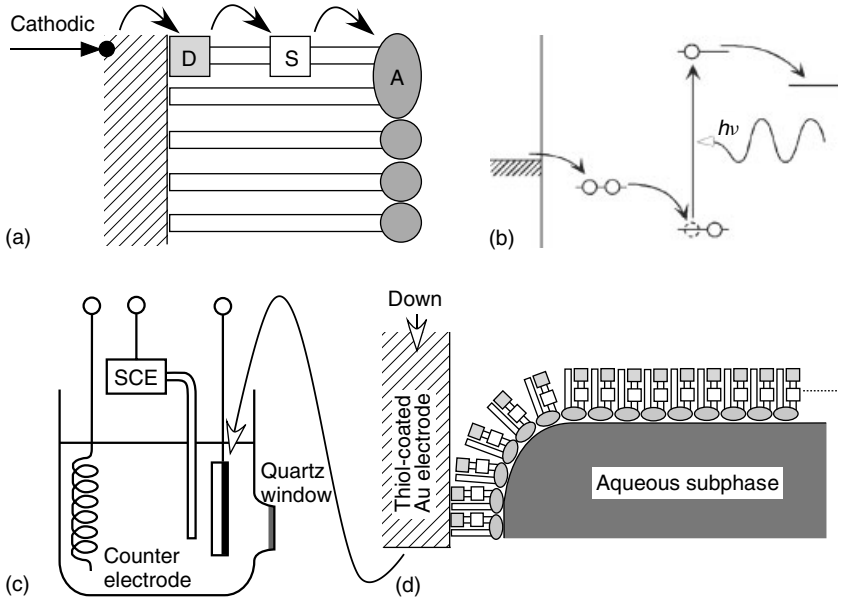


Fig. 24 Schematic representations of: (a) molecular orientation of A–S–D triad on a Au electrode, (b) the corresponding energy diagram, (c) the new type of photoelectrochemical cell, (d) the deposition of a triad monolayer on a hydrophobic surface of a Au electrode by the LB method.

calomel electrode, SCE) electrodes are set into it. With this new type of cell, cathodic photocurrent consistent with the energy diagram for the opposite direction can be observed. The controllability of the direction of the photocurrent clearly indicates that the oriented triad rectifies the photocurrent and acts as a molecular photodiode.

Alternate Multilayered Systems for Scanning Maxwell Stress Microscopy As already described, the LB technique is suitable for making highly oriented molecular assemblies. But detailed structures of LB films had not been clarified until these films were studied by scanning probe microscopies (SPMs) [95–101]. The SPMs, such as scanning tunneling microscopy (STM) [102] and atomic force microscopy (AFM) [103], have been used to analyze surfaces of many levels, from molecular arrangements at interfaces to electronic structures in semiconductors [99]. These SPMs, however, provided only limited information about the chemical nature of systems studied.

For the studies of LB monolayer assemblies, information about the orientation of amphiphilic molecules in the monolayers is important, as well as determination of the chemical functionalities. The Kelvin method [104] is a well-established technique for determining the contact potential differences (CPDs) between reference electrode and a metal sample. The CPD for clean metal surfaces is given by the difference in the work functions of the two materials. The work functions can be changed by adsorption of molecules with different dipole moments. Therefore, the photoinduced dipole change of the triad molecules unidirectionally oriented in LB monolayers on electrode surface can be easily detected as a change of CPD by Kelvin method. The Kelvin method of measuring the CPD makes use of the vibrating capacitor.

A modified version of the AC scanning force microscope with a Kelvin probe

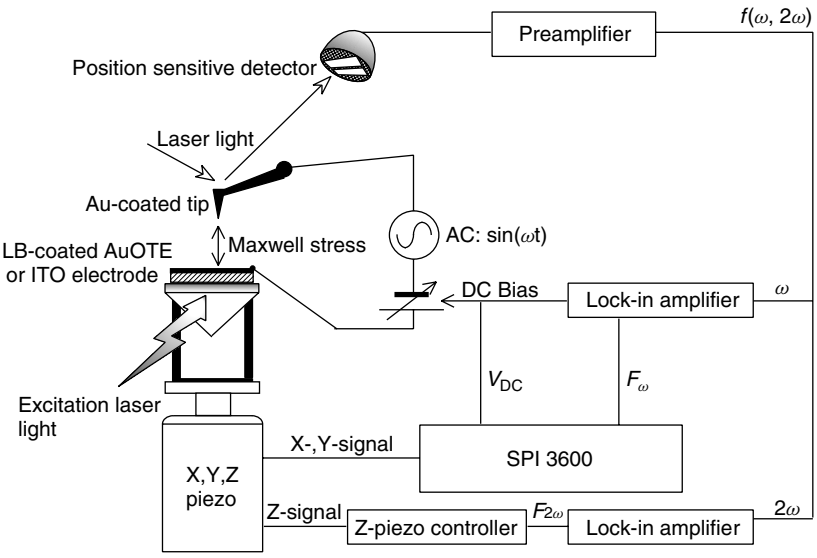


Fig. 25 Schematic diagram of SMM.

tip is called a *Kelvin probe force microscope* (KFM) [105, 106]. The method was further simplified and named the *scanning Maxwell stress microscopy* (SMM) (Fig. 25) [107–113]. With these methods, a lateral image of the variation in CPD on the surface on a submicron scale can be observed.

For the SMM studies of LB films containing unidirectionally oriented A–S–D triads, the alternate LB multilayer systems shown in Fig. 26 are constructed [95]. In the LB assemblies, linear-type A–S–D triads are arranged unidirectionally in two ways with the D tail of the triad toward the air (a) or toward the substrate plate (b), respectively. For the fabrication of these LB assemblies, a fatty acid is used as a spacer and a diluent. By photoexcitation of the S moiety, the electron and hole can be separated unidirectionally, but with opposite directions in the LB films as in the same way as the primary process in photosynthesis [70, 96, 114]. The resulting photoinduced changes in dipole moments of the highly oriented triad molecules are detected as the surface potential changes of gold electrodes covered with the LB films by SMM under illumination as shown in Fig. 27. The change in surface potentials of the LB films of cases (a) and (b) with a pulse illumination of the excited light of 125 ms are shown in Fig. 28. The polarities of the surface potential changes are again consistent with the molecular orientations.

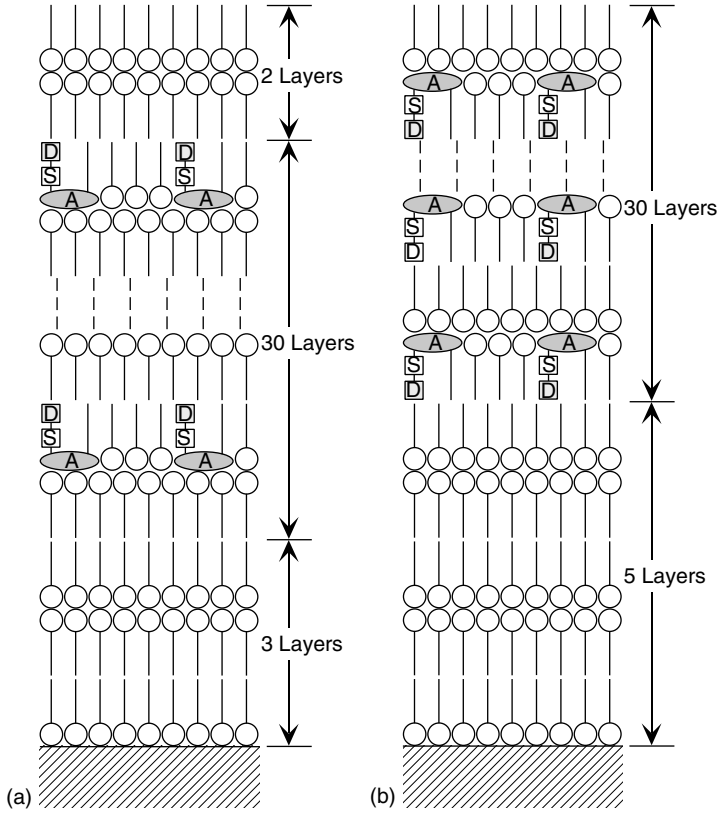


Fig. 26 Unidirectionally oriented A–S–D triad in LB assemblies.

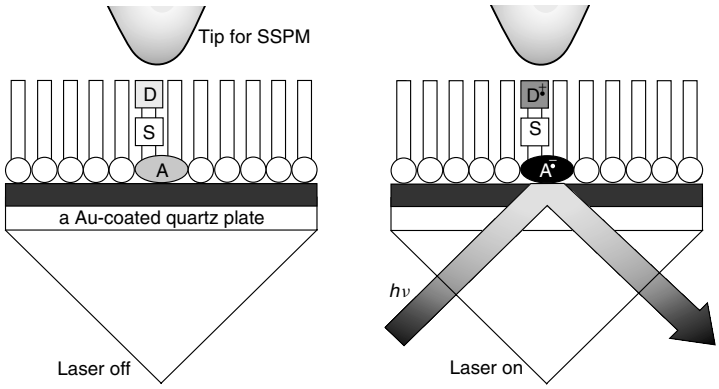


Fig. 27 Detection by SMM of the change in photoinduced surface dipole moments in highly oriented A–S–D triads in artificial photosynthetic reaction centers as the local surface potential changes.

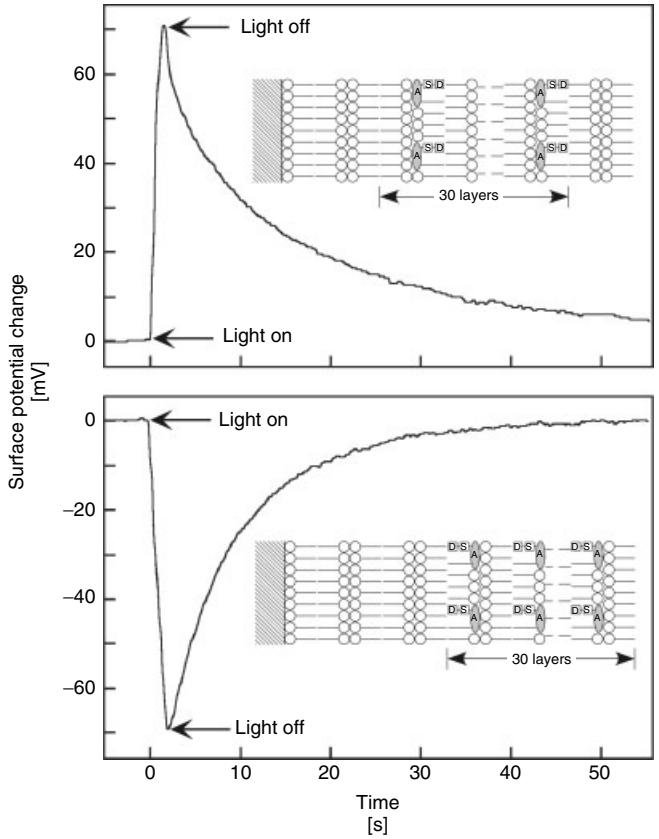


Fig. 28 The change in the surface potential by step illumination for ca. 2-3 s with a He—Cd laser light in a total reflection mode.

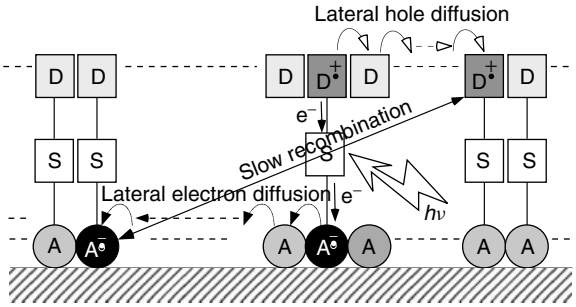


Fig. 29 Schematic illustration of slow charge recombination via lateral diffusion of electrons and holes in the A and the D layer, respectively, in the A–S–D triad monolayer. Anion and cation radicals on the A and the D moieties were created by photoexcitation of the S moieties followed by charge separation.

The exponential-like decays after shutting the illumination down reflect the decrease in the number of the separated charges by recombination. If the charge separation and recombination proceed only within the triads, that is, via intramolecular processes, it seems that the observed recombination rates are too slow in comparison with the intramolecular recombination rates for folded-type triads (ca. 25 ps) [115] and a linear-type triad (ca. 50 ns) [71, 116]. The much slower recombination can be interpreted as arising from further charge separation via a lateral diffusion mechanism of photocreated anion and cation radicals [117–119], as illustrated in Fig. 29.

A–S–D Triad Monolayer and Second Donor Bilayer Alternate Systems To increase the charge separation efficiency, the increase in the lifetime of the charge separation perpendicular to the film by adding a second door D' or an acceptor A′ to form A–S–D–D′ or A′–A–S–D quadruplet should be examined. In fact, in the reaction center of natural photosynthesis, A′–A–S–D structure is used for its efficient charge separation [68]. Because of laboriousness of quadruplet syntheses, the quadruplet structure by depositing a D′ (16-ferrocenylhexadecanoic acid) monolayer on a D end of an A–S–D monolayer is constructed [120]. The ionization potential of the donor moiety in D′ molecule is smaller than that of the D moiety of the A–S–D triad; therefore, the layer can act as a second donor layer with a sufficient driving free energy.

Figures 30(a) and (b) show the surface potential changes of the LB assemblies without and with a pure bilayer of D′, respectively, under step illumination for 125 ms with a laser light and the schematic representations of the corresponding film structures. It is remarkable that the photoinduced surface potential change increased about 1 order of magnitude by addition of the D′ layer. The drastic increase in the surface potential is attributable to the efficient lateral diffusion because of prolonged lifetime of the perpendicular charge separation by the A–S–D/D′ quadruplet system.

LB Assemblies for Simulations of Key Aspects in Natural Photosynthesis The development of an artificial photosynthesis system is one of the most fascinating

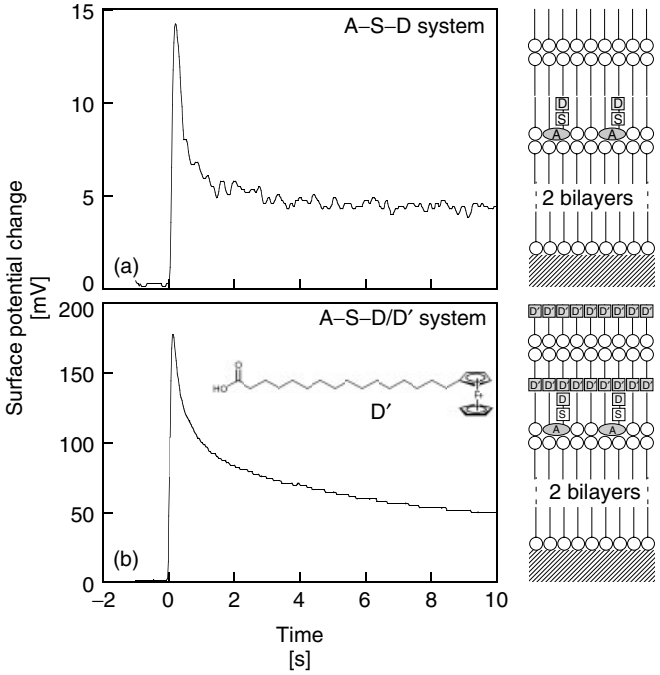


Fig. 30 Photoinduced surface potential change under step illumination by He–Cd laser (441.6 nm) for the LB assemblies (a) without and (b) with a pure D′ bilayer. The A–S–D mixed monolayer consists of A–S–D (V) and 22-tricosenoic acid (1:5).

challenges. As illustrated in Fig. 31, the monomolecular layer assembly including a triad and a synthetic antenna molecule is designed to mimic the two successive aspects of a primary process in natural photosynthesis: antenna and reaction center [93]. For the light-harvesting (H) antenna pigments, an amphiphilic pyrene derivative [121] is used. For the amphiphilic linear triad molecule, an acylated perylene moiety, as the S unit, and viologen and diacylated ferrocene moieties, as the A and the D units, respectively, are used. Because of the good overlap of the emission spectrum of the antenna pyrene moiety (Py) and the absorption spectrum of the sensitizer perylene moiety (Pe) of the triad (Fig. 32), light energies harvested by the antenna molecules are efficiently transferred to the sensitizer moiety of the triad. Thus, the excitation energy of the perylene moiety should be converted to electrical energies via multistep electron transfer across the monolayer as described above. Figure 33 shows the photocurrent spectrum of the mixed monolayer of the triad and the antenna with a molar ratio of 1:4. Maxima of anodic photocurrents at ca. 350 and 470 nm are found. These correspond to the adsorption maxima of pyrene and acylated perylene (solid curves in Fig. 32). The result indicates that charge separation in the triad molecules was initiated by light absorption both with perylene sensitizer itself and with the pyrene antennas followed by the energy transfer.

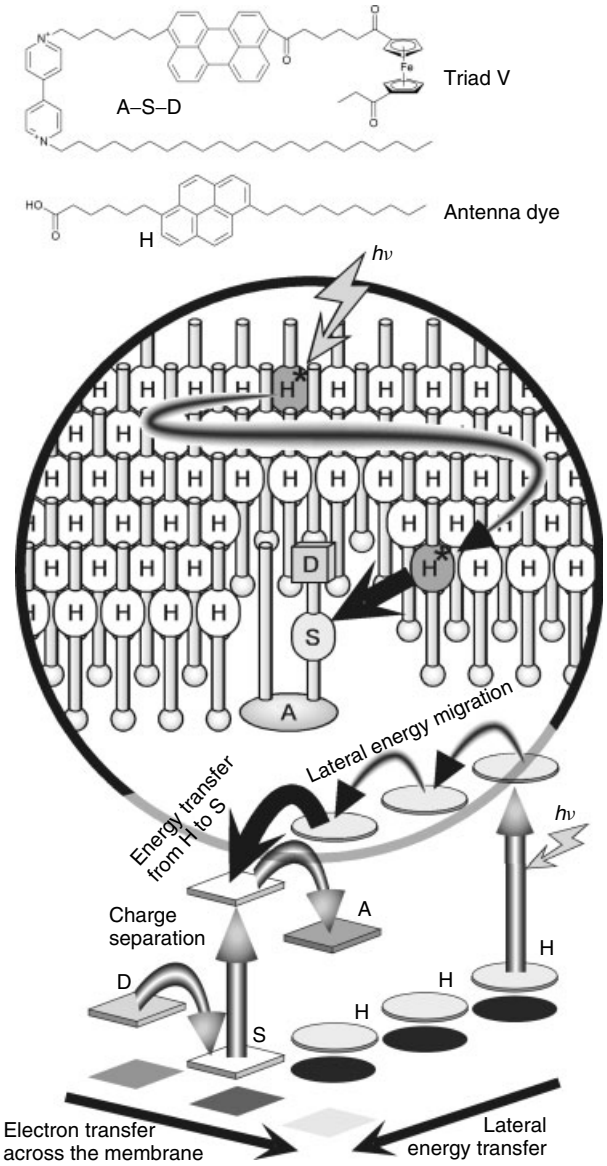


Fig. 31 Schematic representation of the artificial photosynthetic reaction center by a monolayer assembly of antenna (H) and A–S–D triad molecules for light harvesting, energy migration and transfer, and charge separation via multistep electron transfer.

To focus only on the energy transfer process from Py to Pe, the dependence of sensitized emission intensity on the ratio of H with an energy acceptor molecule is also examined [122]. The result indicates that the most efficient energy transfer

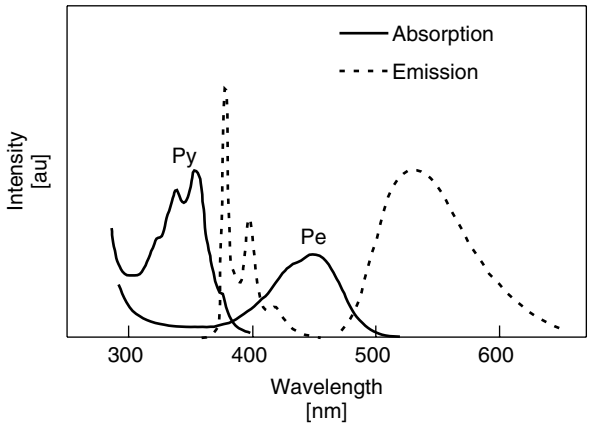


Fig. 32 UV and visible absorption (solid line) and fluorescence (dashed line) spectra of antenna H pyrene (Py) and monoacylated perylene (Pe) derivative in ethanol.

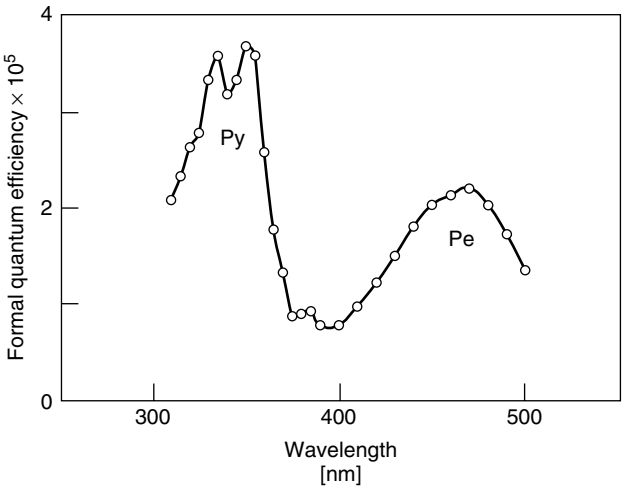


Fig. 33 Photocurrent spectrum of the mixed monolayer of antenna H and triad V with a molar ratio of 4:1 (solid line).

from Py* to Pe is attained with the molar ratio Py:Pe = 30 : 1. While in the mixed monolayers of the cyanine (dye I in Fig. 14) and the pyrene amphiphiles, a much more efficient light harvesting can be attained by the combination of the energy donor, dye I, and the energy acceptor, Pe [123]. The antenna effect of dye I in this system is such that ca. 250 molecules of cyanine can harvest light for excitation of one Pe.

Next, a further advanced LB assembly as a biomimetic model system to seek to mimic the three successive aspects of photosynthesis, antenna pigment, reaction center, and quinone pool, is examined [124, 125]. In natural photosynthesis

systems of higher plants, a lipid soluble and diffusible quinone called *plastoquinone* (PQ) acts as a mobile component of the electron transport between two different photosynthetic reaction centers, PSI and PSII. Not only the electron link but also an electron buffer in the form of a pool is a unique function of PQ. The electrons from PSII can be accumulated within the plastoquinone pool in the reduced form of plastoquinone, that is, plastoquinol (PQH_2).

The film structure and the expected photophysical processes are schematically illustrated in Fig. 34. After the light

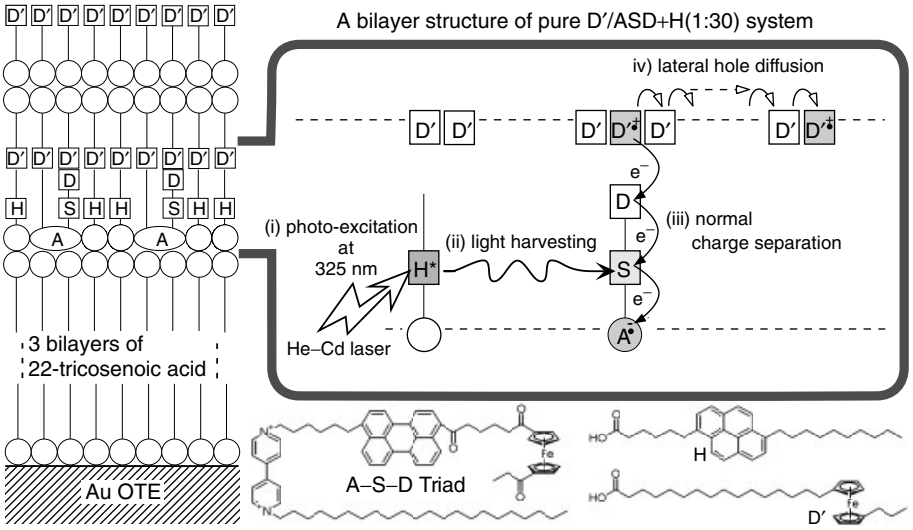


Fig. 34 Schematic illustration of the LB assembly for simulation of the primary process in natural photosynthetic reaction center. The photoelectric conversion with the LB assemblies is attained by the processes (i)–(iv).

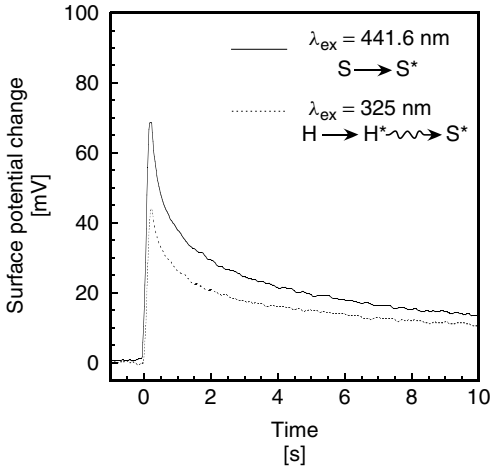


Fig. 35 Photoinduced surface potential change under step illumination at 441.6 nm (solid curve) or 325 nm (dotted curve). The S moiety of the triad is directly excited by the 441.6 nm irradiation, whereas at 325 nm, the excited state S* is induced via energy transfer from H*.

harvesting (ii) and successive charge separations (iii) proceed similarly as in the former monolayer of A–S–D and H, hole diffusion (iv) via hole migration in the second donor layer and hole and electron accumulations in the D′ and A plane are expected to occur in this system.

On the basis of the energy transfer study of the Py—Pe system mentioned above, the mixed A–S–D monolayer with H with the molar mixing ratio 1:30 is added by a D′ bilayer. Figure 35 shows the change in surface potential measured with the (A–S–D + H)/D′ system under the step illumination of 441.6 nm (a solid curve) and 325 nm (a dotted curve) [124]. With the light illumination at 441.6 nm, the perylene sensitizer in A–S–D is directly excited and H contributes as a diluent similar to fatty acids, whereas excited perylene sensitizer is induced by energy transfer from excited pyrene of H to the perylene in the grand state under illumination at 325 nm. Normally, the change in surface potential would not be detectable with such diluted A–S–D layer alone because prolonged intermolecular distances suppress lateral charge migrations. But the film added by D′ bilayer, which acts as charge diffusion layer, gave large surface potential change at both wavelengths. The pyrene absorbance of the film at 325 nm is estimated to be ca. 25 times larger than that of perylene at 441.6 nm [95, 121]. The number of the photons of the incident light at 325 nm is ca. 1/35 against that at 441.6 nm of the He—Cd laser used. Considering the difference between the resulted signals at 325 and 441.6 nm, it can be concluded that the light energy harvested by the antenna molecules is mostly funneled to the sensitizer moiety of the A–S–D triad molecule.

References

1. K. B. Blodgett, *J. Am. Chem. Soc.* **1935**, *57*, 1007.
2. G. L. J. Gaines, *Insoluble Monolayers at Liquid Gas Interfaces*, Wiley, New York, 1966.
3. B. Franklin, *Philos. Trans. R. Soc. London* **1774**, *64*, 445.
4. A. Pockels, *Nature* **1891**, *43*, 437.
5. H. Kuhn, D. Möbius, H. Bücher, in *Techniques of Chemistry*, Vol. 1 (Eds.: A. Weissberger, B. W. Rossiter), Wiley, New York, 1972, pp. 577–702.
6. A. Ulman, *An Introduction to Ultra Thin Films from Langmuir-Blodgett to Self Assembly*, Academic Press, New York, 1991.
7. G. Roberts, *Langmuir-Blodgett Films*, Plenum Publishing, New York, 1990.
8. L. Wilhelmy, *Ann. Phys. Chem.* **1863**, *119*, 177–217.
9. D. Myers, *Surfaces, Interfaces and Colloids*, VCH Publishers, New York, 1991.
10. J. W. McBain, T. F. Ford, D. A. Wilson, *Kolloid-Z.* **1937**, *78*, 1–9.
11. J. W. McBain, J. R. Vinograd, D. A. Wilson, *J. Am. Chem. Soc.* **1940**, *62*, 244–249.
12. J. H. Schulman, R. B. Waterhouse, J. A. Spink, *Kolloid-Z.* **1956**, *146*, 77–95.
13. I. Langmuir, V. J. Schaefer, *J. Am. Chem. Soc.* **1938**, *60*, 1351–1360.
14. K. Fukuda, H. Nakahara, T. Kato, *J. Colloid Interface Sci.* **1976**, *54*, 430.
15. I. Langmuir, *Trans. Faraday Soc.* **1920**, *356*, 62–74.
16. K. B. Blodgett, *J. Am. Chem. Soc.* **1934**, *56*, 495.
17. A. K. Kapil, V. K. Srivastava, *J. Colloid Interface Sci.* **1979**, *72*, 342–343.
18. B. Holcroft, M. C. Petty, G. G. Roberts, *Thin Solid Films* **1985**, *134*, 83–88.
19. A. Barraud, J. Leloup, S. Palacin, *Thin Solid Films* **1985**, *133*, 117–123.
20. T. Kato, *Jpn. J. Appl. Phys.* **1987**, *26*, L1377–L1380.
21. P. Fromherz, *Rev. Sci. Instrum.* **1975**, *46*, 1380–1385.
22. P. Fromherz, *Biochim. Biophys. Acta* **1971**, *225*, 382–387.
23. P. Fromherz, D. Marcheva, *FEBS Lett.* **1975**, *49*, 329–333.
24. H. Kuhn, *J. Photochem.* **1979**, *10*, 111.
25. H. Kuhn, *Pure Appl. Chem.* **1981**, *53*, 2105.

26. H. Kuhn, *Thin Solid Films* **1983**, *99*, 1.
27. H. Bücher, H. Kuhn, *Chem. Phys. Lett.* **1970**, *6*, 183.
28. D. Möbius, *Ber. Bunsen-Ges. Phys. Chem.* **1978**, *82*, 848.
29. R. A. Marcus, N. Sutin, *Biochim. Biophys. Acta* **1985**, *811*, 265–322.
30. A. Aviram, M. A. Ratner, *Chem. Phys. Lett.* **1974**, *29*, 277–282.
31. R. M. Metzger, C. A. Panetta, in *Molecular Electronic Devices II* (Ed.: F. L. Carter), Marcel Dekker, New York, 1987, p. 5.
32. H. Kuhn, *Chem. Phys. Lipids* **1972**, *8*, 401.
33. M. Fujihira, K. Nishiyama, H. Yamada, *Thin Solid Films* **1985**, *132*, 77.
34. H. Kuhn, *Proc. Robert A. Welch Found.* **1986**, *30*, 339.
35. D. Möbius, *J. Am. Chem. Soc.* **1981**, *14*, 63–68.
36. W. F. Mooney, D. G. Whitten, *J. Am. Chem. Soc.* **1986**, *108*, 5712.
37. Y. Hsu, T. L. Penner, D. G. Whitten, *J. Phys. Chem.* **1992**, *96*, 2790–2795.
38. T. Osa, M. Fujihira, *Nature* **1976**, *264*, 349.
39. M. Fujihira, N. Ohishi, T. Osa, *Nature* **1977**, *268*, 226.
40. M. Fujihira, T. Kubota, T. Osa, *J. Electroanal. Chem.* **1981**, *119*, 379.
41. M. Fujihira, in *Topics in Organic Electrochemistry* (Eds.: A. J. Fry, W. E. Britton), Plenum Publishing, New York, 1986, p. 255.
42. L. T. Calcaterra, G. L. Closs, J. R. Miller, *J. Am. Chem. Soc.* **1983**, *105*, 670.
43. G. L. Closs, L. T. Calcaterra, N. J. Green et al., *J. Chem. Phys.* **1986**, *90*, 3673.
44. J. R. Miller, *New J. Chem.* **1987**, *11*, 83.
45. J. M. Warman, M. P. De Hass, M. N. Paddon-Row et al., *Nature* **1986**, *320*, 615.
46. J. W. Verhoeven, *Pure Appl. Chem.* **1986**, *58*, 1285.
47. K. I. Zamaraev, R. F. Khairutdinov, in *Topics in Current Chemistry, Vol. 163, Photoinduced Electron Transfer IV* (Ed.: J. Mattay), Springer-Verlag, Berlin, 1992, p. 1.
48. B. A. Leland, A. D. Joran, P. M. Felker et al., *J. Phys. Chem.* **1985**, *89*, 5571.
49. R. A. Marcus, *J. Chem. Phys.* **1965**, *43*, 2654.
50. J. Ulstrup, J. Jortner, *J. Chem. Phys.* **1975**, *63*, 4358.
51. J. R. Miller, L. T. Calcaterra, G. L. Closs, *J. Am. Chem. Soc.* **1984**, *106*, 3047.
52. J. R. Miller, J. V. Beitz, R. K. Huddleston, *J. Am. Chem. Soc.* **1984**, *106*, 5057.
53. M. R. Wasielewski, M. P. Niemczyk, W. A. Svec et al., *J. Am. Chem. Soc.* **1985**, *107*, 5562–5563.
54. N. Mataga, in *Dynamics and Mechanisms of Photoinduced Electron Transfer and Related Phenomena* (Eds.: N. Mataga, T. Okada, H. Masuhara), Elsevier, Amsterdam, 1992, p. 3.
55. T. Asahi, N. Mataga, *J. Phys. Chem.* **1991**, *95*, 1956.
56. T. Ohno, A. Yoshimura, N. Mataga et al., *J. Phys. Chem.* **1989**, *93*, 7635.
57. N. Mataga, Y. Kanda, T. Asahi et al., *J. Chem. Phys.* **1988**, *127*, 239.
58. I. R. Gould, S. Farid, *J. Phys. Chem.* **1992**, *96*, 7635.
59. I. R. Gould, D. Ege, J. E. Moser et al., *J. Am. Chem. Soc.* **1990**, *112*, 4290.
60. I. R. Gould, D. Ege, S. L. Mattes et al., *J. Am. Chem. Soc.* **1987**, *109*, 3794.
61. M. Fujihira, K. Nishiyama, H. Yoneyama, *J. Chem. Soc. Jpn.* **1987**, 2119.
62. Y. Nishikata, A. Morikawa, M. Kakimoto et al., *J. Chem. Soc., Chem. Commun.* **1989**, 1772.
63. Y. Nishikata, A. Morikawa, M. Kakimoto et al., *Thin Solid Films* **1992**, *210–211*, 296.
64. M. Suzuki, M. Kakimoto, T. Konishi et al., *Chem. Lett.* **1986**, 395.
65. M. Kakimoto, M. Suzuki, T. Konishi et al., *Chem. Lett.* **1986**, 823.
66. Y. Nishikata, M. Kakimoto, A. Morikawa et al., *Chem. Lett.* **1989**, 861.
67. J. Deisenhofer, O. Epp, K. Miki et al., *J. Mol. Biol.* **1984**, *180*, 385.
68. J. Deisenhofer, K. Miki, R. Huber et al., *Nature* **1985**, *318*, 618.
69. C. H. Chang, M. Schiffer, D. Tiede et al., *J. Mol. Biol.* **1985**, *186*, 201.
70. M. Fujihira, in *Thin Films* (Eds.: A. Ulman), Academic Press, Boston, 1995, pp. 239–277.
71. M. Sakomura, S. Lin, T. A. Moore et al., *J. Phys. Chem. A* **2002**, *106*, 2218.
72. D. Gust, T. A. Moore, *Adv. Photochem.* **1991**, *16*, 1.
73. D. Gust, T. A. Moore, A. L. Moore, *Acc. Chem. Res.* **1993**, *26*, 198–205.
74. J. L. Bahr, D. Kuciauskas, P. A. Liddell et al., *Photochem. Photobiol.* **2000**, *72*, 528.
75. D. Kuciauskas, P. A. Liddell, S. Lin et al., *J. Phys. Chem. B* **2000**, *104*, 4307–4321.
76. D. Kuciauskas, P. A. Liddell, S. Lin et al., *J. Am. Chem. Soc.* **1999**, *121*, 8604.

77. P. A. Liddell, J. P. Sumida, A. N. Macpherson et al., *Photochem. Photobiol.* **1994**, *60*, 537.
78. P. A. Liddell, D. Kuciauskas, J. P. Sumida et al., *J. Am. Chem. Soc.* **1997**, *119*, 1400–1405.
79. M. R. Wasielewski, *Chem. Rev.* **1992**, *92*, 435–461.
80. M. Bixon, J. Fajer, G. Feher et al., *Isr. J. Chem.* **1992**, *32*, 449.
81. A. Osuka, G. Noya, S. Taniguchi et al., *Chem. Eur. J.* **2000**, *6*, 33.
82. T. Asahi, M. Ohkohchi, R. Matsusaka et al., *J. Am. Chem. Soc.* **1993**, *115*, 5665.
83. H. Imahori, K. Tamaki, D. M. Guldi et al., *J. Am. Chem. Soc.* **2001**, *123*, 2607.
84. H. Imahori, H. Norieda, H. Yamada et al., *J. Am. Chem. Soc.* **2001**, *123*, 100.
85. H. Imahori, S. Ozawa, K. Ushida et al., *Bull. Chem. Soc. Jpn.* **1999**, *72*, 485.
86. S. Komamine, M. Fujitsuka, O. Ito et al., *J. Phys. Chem. A* **2000**, *104*, 11497.
87. K. A. Jolliffe, S. J. Langford, M. G. Ranasinghe et al., *J. Org. Chem.* **1999**, *64*, 1238.
88. N. J. Head, J. Thomas, M. J. Shephard et al., *J. Photochem. Photobiol.* **2000**, *133*, 105.
89. G. Steinberg-Yfrach, J.-L. Rigaud, E. N. Durantini et al., *Nature* **1998**, *392*, 479–482.
90. P. Yeh, T. J. Kuwana, *J. Electrochem. Soc.* **1976**, *123*, 1334.
91. M. Fujihira, H. Yamada, *Thin Solid Films* **1988**, *160*, 125.
92. M. Fujihira, M. Sakomura, *Thin Solid Films* **1989**, *179*, 471.
93. M. Fujihira, M. Sakomura, T. Kamei, *Thin Solid Films* **1989**, *180*, 43–50.
94. M. Sakomura, M. Fujihira, *Thin Solid Films* **1994**, *243*, 616.
95. M. Fujihira, M. Sakomura, D. Aoki et al., *Thin Solid Films* **1996**, *273*, 168–176.
96. M. Fujihira, *NATO ASI Ser. E: Appl. Sci.* **1995**, *286*, 567–591.
97. M. Fujihira, *NATO ASI Ser. E: Appl. Sci.* **1996**, *319*, 205–221.
98. M. Fujihira, *NATO ASI Ser. E: Appl. Sci.* **1997**, *330*, 239–260.
99. J. Frommer, *Angew. Chem., Int. Ed. Engl.* **1992**, *31*, 1298–1328.
100. R. M. Overney, E. Meyer, J. Frommer et al., *Nature* **1992**, *359*, 133.
101. E. Meyer, R. M. Overney, R. Luthi et al., *Thin Solid Films* **1992**, *220*, 132.
102. G. Binnig, H. Rohrer, C. Gerber et al., *Phys. Rev. Lett.* **1982**, *42*, 57–61.
103. G. Binnig, C. F. Quate, C. Gerber, *Phys. Rev. Lett.* **1986**, *56*, 930–933.
104. L. Kelvin, *Philos. Mag.* **1898**, *46*, 91–120.
105. M. Nonnenmacher, M. O'Boyle, H. K. Wickramsinghe, *Appl. Phys. Lett.* **1991**, *58*, 2921–2923.
106. M. Nonnenmacher, M. O'Boyle, H. K. Wickramsinghe, *Ultramicroscopy* **1992**, *42*, 268–273.
107. H. Yokoyama, K. Saito, T. Inoue, *Mol. Electron. Bioelectron.* **1992**, *3*, 79–88.
108. H. Yokoyama, T. Inoue, M. Hattori et al., *Proceedings of the 11th Symposium on Future Electron Devices*, Chiba, 1992, pp. 29–34.
109. H. Yokoyama, T. Inoue, *Thin Solid Films* **1994**, *242*, 33–39.
110. T. Inoue, H. Yokoyama, *Thin Solid Films* **1994**, *243*, 399–402.
111. T. Inoue, H. Yokoyama, *J. Vac. Sci. Technol.* **1994**, *B12*, 1569–1571.
112. M. Fujihira, H. Kawate, M. Yasutake, *Chem. Lett.* **1992**, 2223–2226.
113. M. Fujihira, H. Kawate, *J. Vac. Sci. Technol.* **1994**, *B12*, 1604–1608.
114. M. Fujihira, *Annu. Rev. Mater. Sci.* **1999**, *29*, 353–380.
115. E. G. Wilson, *Thin Solid Films* **1996**, *273*, 1–7.
116. R. Sawada, M. Sakomura, K. Hirukawa et al., *Colloids Surf., A*, Submitted.
117. M. Sakomura, M. Fujihira, *Thin Solid Films* **1998**, *327*, 718.
118. M. Sakomura, M. Fujihira, *Chem. Lett.* **1998**, 701.
119. M. Sakomura, T. Oono, R. Sakon et al., *Ultramicroscopy* **2002**, *91*, 215.
120. M. Sakomura, M. Fujihira, *Thin Solid Films* **1998**, *327*, 708.
121. M. Fujihira, T. Kamei, M. Sakomura et al., *Thin Solid Films* **1989**, *179*, 485–492.
122. M. Fujihira, M. Sakomura, R. Sawada, *Mol. Cryst. Liq. Cryst.* **1998**, *322*, 313–318.
123. M. Sakomura, T. Takagi, H. Nakayama et al., *Colloids Surf., A* **2002**, *198*, 769–775.
124. M. Sakomura, M. Fujihira, *J. Photochem. Photobiol. A: Chem.* **2004**, *166*, 45–56.
125. M. Sakomura, K. Ueda, M. Fujihira, *Chem. Commun.* **2004**, 2392–2393.

1.4.2
Langmuir–Blodgett (LB) Films on Electrodes (B) Electrochemistry

Takashi Nakanishi
National Institute for Materials Science (NIMS), Tsukuba, Japan

Naotoshi Nakashima
Kyushu University, Fukuoka, Japan

1.4.2.1 Introduction

In this chapter, the electrochemistry of Langmuir–Blodgett (LB) films of functionalized molecules including ''molecular wire'' compounds, phthalocyanines, artificial lipids, proteins and fullerene derivatives, and carbon nanotubes (CNTs) is described.

The use of electrodes modified with immobilized redox-active molecules provides a simple methodology by which to study the ultrathin film electrochemistry of water-insoluble redox-active molecules, encouraging the application of such techniques to biomimetic membranes in aqueous media. It is of interest to use monolayer and LB films of enzymes, proteins, and antibodies as biosensors or biomolecular switches because of their high sensitivity for their substrates and antigens, respectively. The formation of thin fullerene films including fullerene-lipid hybrid and fullerene-lipid composite bilayer membranes is of interest both from a fundamental and practical application point of view. Multiwalled carbon nanotubes (MWNTs) and single-walled carbon nanotubes (SWNTs) are novel nanomaterials that have remarkable electronic, mechanical, and thermal properties, and specific functions. Soluble carbon nanotubes in aqueous and organic systems are of interest since their study allows the chemical and biochemical design of functional carbon nanotubes. We describe here how to make ultrathin films of nanotubes on substrates.

1.4.2.2 Electrochemistry of LB Films of ''Molecular Wires'' and Phthalocyanines

It is known that LB techniques can be applied for the construction of thin film electronic devices and molecular rectifiers [1–5]. Conjugated redox-active compounds are candidates for ''molecular wires'' and are expected to be a convenient tool for the construction of molecular electronic devices. We have reported that LB films of π-conjugated electrochemically active quinolinium complexes transferred on to gold electrodes show rectified transmembrane electron transfer, through the LB monolayer, to hexacyanoferrate(II) ($[Fe(CN)_6]^{4-}$) in solution [6, 7]. Potential-step chronocoulometric responses revealed that the LB monolayer acts as an organic ultramicroelectrode array. Metzger et al. constructed electrical rectification systems using LB monolayers of substituted quinolinium tricyanoquinodimethanides (Fig. 1) on electrodes by scanning tunneling spectroscopy (STS) [1, 3]. The unimolecular electrical rectifiers prepared by using LB techniques are useful for the construction of molecular electrode devices [1–5].

Ultrathin films of electrochromic molecules such as multireducible double-decker phthalocyanines are one important possible component of color display devices. The double-decker lutetium(III) phthalocyanine molecules having long alkyl chains (Fig. 2) were mixed with amphiphilic matrices and cast on electrodes as thin films [8–10]. These phthalocyanines undergo up to five reductions at the modified electrode. The fifth reduction had been theoretically

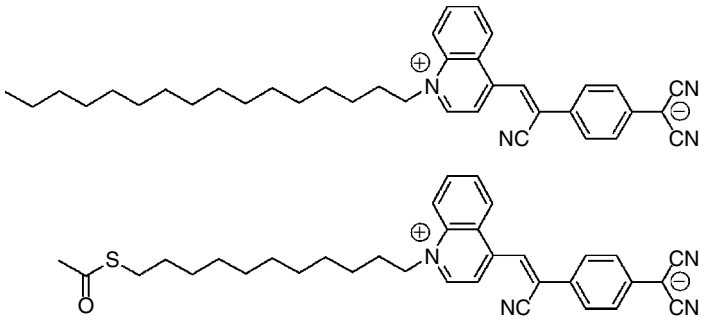


Fig. 1 Chemical structures of the quinolinium tricyanoquinodimethanides.

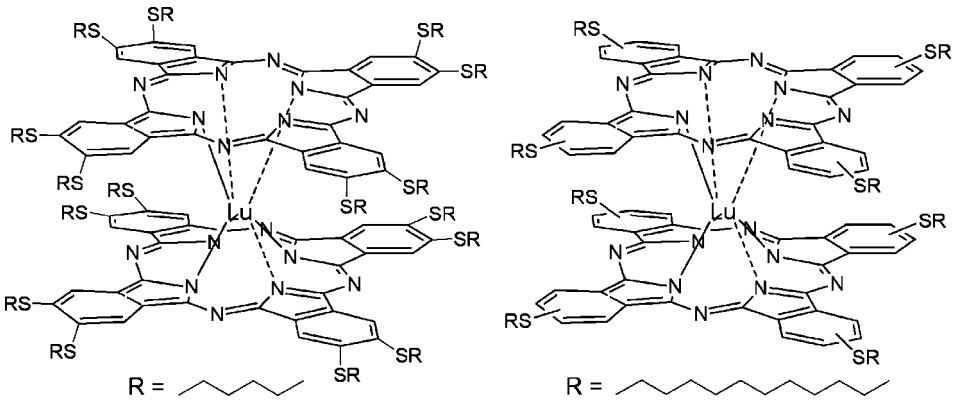


Fig. 2 Chemical structures of the alkylthio substituted double-decker lutetium(III) phthalocyanines.

predicted but had not been previously observed for any double-decker lutetium phthalocyanines. Moreover, use of cationic matrices is important because reduced anions of the phthalocyanines can be stabilized in these matrices. Multicolor electrochromism, that is, green, brown-red, blue, and purple, are observed at LB films of octakis-substituted heavy rare-earth metal double-decker phthalocyanines in contact with an aqueous electrolyte [11]. Saja et al. reported that LB films of rare-earth metal double-decker phthalocyanines deposited onto indium tin oxide (ITO) microelectrodes have sensing properties for NO gas and vapors of volatile organic compounds such as alcohols, aldehydes, and esters, which are contained in aromas of foods and beverages [12, 13].

LB films of artificial lipids transferred onto electrode substrates could be used as glucose [14] and calcium ion [15] sensors and for hydrogen evolution [16]. Okahata et al. coated a SnO_2 electrode with LB films of synthetic phospholipids [15]. Oxidation peak currents of a maker ion ($[Fe(CN)_6]^{3/4-}$) in the aqueous phase through the lipid films increased with the addition of Ca^{2+} ions only when the LB films were in the fluid liquid crystalline phase above the phase transition

temperature since Ca^{2+} ion can only bind and penetrate into the fluid liquid crystalline phase of the films and disturb or expand the LB membrane structures. The LB films of glucose oxidase (GOD)-artificial lipid monolayers deposited onto Pt electrodes act as glucose-sensing ultrathin membranes with a short response time [14]. Miyake et al. reported electrochemical hydrogen evolution using LB films of hydrogenase protein complexed with poly-L-lysine, in which methyl viologen was used as a mediator [16]. Ariga et al. developed a novel type of vitamin B_{12}-functionalized electrode [17], in which the monolayer properties of the vitamin B_{12} mimics were investigated as a mixed monolayer with an organosilane lipid (Fig. 3). The obtained electrodes have the potential to transform environmentally toxic chemicals into nonhazardous ones through an electrochemical process. The lipid LB film modified electrodes provide a suitable interface for the electrochemistry of cytochrome *c* [18] and myoglobin [19]. Thus, the synthetic artificial lipids provide suitable environments for the electrochemistry of redox-active biomolecules.

1.4.2.3 Langmuir Monolayer of Fullerenes at the Air–Water Interface

The construction of fullerene ultrathin films with an ordered structure is of interest from both a fundamental and practical point of view [20–22]. C_{60} alone and amphiphilic fullerene derivatives form monolayers at the air–water interface and these monolayers can be transferred onto solid substrates [23–27]. The authors [28–38] and others [39–43] have been interested in combining fullerene chemistry and the

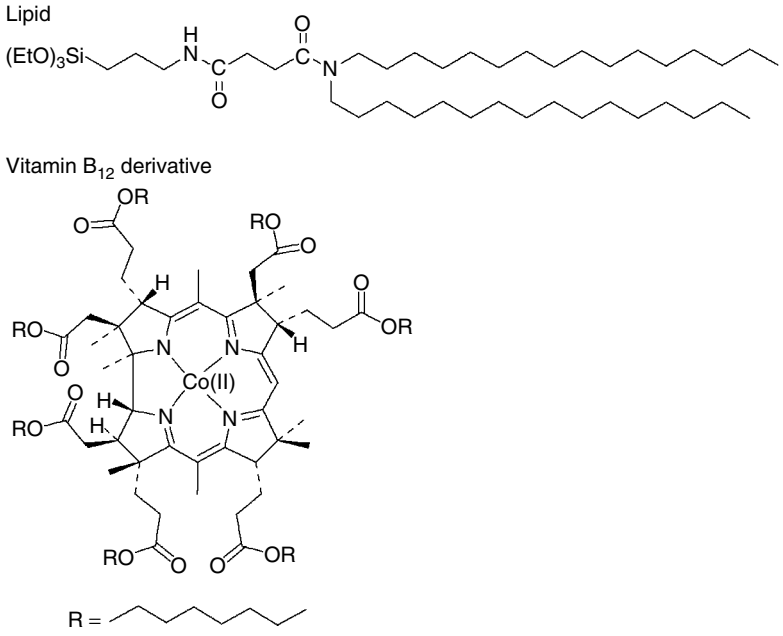


Fig. 3 Chemical structures of the organosilane amphiphile and vitamin B_{12} derivative.

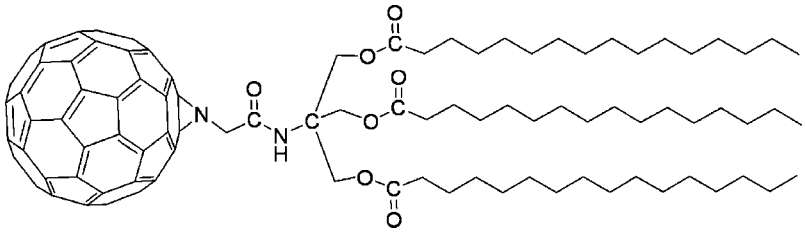


Fig. 4 Chemical structure of the fullerene lipid.

chemistry of lipid bilayer membranes, which may create a novel field in the chemistry and biochemistry of fullerenes. We have reported the design, synthesis, and characterization of a C_{60}-bearing triple-chain lipid [28, 32, 33, 36, 37] (Fig. 4). This lipid forms stable Langmuir monolayers at the air–water interface [32, 37]. The surface-pressure–area isotherm of the fullerene lipid gives limiting areas of 0.78 and 0.98 nm^2/molecule, suggesting the formation of monolayers with hexagonal and simple square packing, respectively [32]. In situ X-ray reflectometry (XR) techniques revealed the nanostructure of the fullerene-lipid monolayer on water, that is, the fullerene moiety was in contact with the water surface and the lipid tail extended to the air [37] (Fig. 5).

The LB film prepared in the dark shows temperature dependent UV–vis absorption spectra. At lower temperatures, there is an electronic interaction between the fullerene moieties in the LB film. Upon heating over 47 °C, which is the subphase transition temperature of the cast films of the fullerene lipid [28, 36], the electronic interaction of the fullerene moieties is loosened. The electronic interaction between the fullerene moieties can be controlled by the phase change of the film. The fundamental property of the self-assembled bilayer membrane film is maintained in the LB film prepared in the dark, indicating that the molecular orientations of the

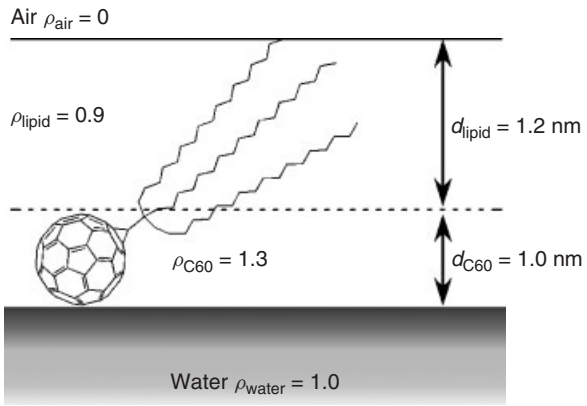


Fig. 5 Schematic illustration of the nanostructure of the monolayer of the fullerene lipid on water revealed by in situ X-ray reflectometry measurements.

fullerene moieties of the LB film and cast film of the fullerene lipid are not significantly different. This is important from the viewpoint of the introduction of lipid bilayer properties of the fullerene lipids to the LB system. This information is useful for the design and construction of functional supramolecular ultrathin fullerene films at the air–water interface and on solid surfaces.

1.4.2.4 Electrochemistry of LB Films of Fullerenes on Electrodes

Electrochemistry of LB films of fullerenes has been widely studied and remains the subject of much research effort from both theoretical and experimental approaches. Bard et al. have studied basic electrochemistry of C_{60} fullerene LB films on an electrode in acetonitrile solutions [23]. The study indicated that reduction of the fullerene films could form insoluble films with incorporated electrolyte cations or lead to dissolution. The study on C_{60} LB films has become a focus of considerable interest; however, it is difficult to fabricate high-quality LB films of pure C_{60} due to its intrinsic hydrophobicity. Kajiyama et al. applied a multistep creep method as an LB technique for constructing a fairly homogeneous C_{60} monolayer, which is regularly packed in a hexagonal array [44]. Kunitake et al. developed the electrochemical replacement method to form epitaxial adlayers of fullerenes on Au(111) surfaces [45]. The ''wet process'' method consists of the transfer of Langmuir films of fullerene onto iodine-modified Au(111) surfaces at an air–water interface followed by the electrochemical removal and replacement of iodine adlayers with fullerene adlayers in solution. The fullerene adlayers prepared by this method showed excellent quality and uniformity. A visualizing technique by in situ scanning tunneling microscopy (STM) for the surface morphology of fullerene LB films on iodine-modified Pt(111) surfaces was also developed [46].

As an alternative way to avoid the formation of low-quality aggregated structures of fullerenes, several functionalized fullerene derivatives with nonpolar or polar groups were synthesized. Subsequently, electrochemical characterization of the higher-quality LB films was performed. The electrochemistry of LB films of fullerene derivatives in organic solvents showed well-defined reversible multi-electroreductions [47], but this was not observed in all of the cases. LB films of fullerenes have several intrinsic properties such as nonlinear optical features and gas sensing. The LB films of a crowned C_{60}-pyrrolidine [48] and of a 4-acetylphenyl-substituted C_{60}-pyrrolidine [49] exhibit optical second-harmonic responses. The second-harmonic intensity is strongly dependent on the number of layers of the LB films. Spatial control of arachidic acid LB films by introduction of C_{60} molecules as the spacers to a polymer backbone, poly(allylaminehydrochloride) (PAH), is reported to be a novel sensor for α-pinene, citral, β-caryophyllene, Nerilidol, and *n*-octadecane in the gas phase [50, 51]. Models of natural photoreaction centers can be constructed using LB films of fullerene derivatives. Tkachenko et al. described the preparation of LB films of a phytochlorin-fullerene [52] and of a porphyrin-fullerene [53] that show vectorial photoinduced electron transfer reactions (Fig. 6). These donor–acceptor dyad LB film systems are an attractive example for the development of molecular optoelectronic devices.

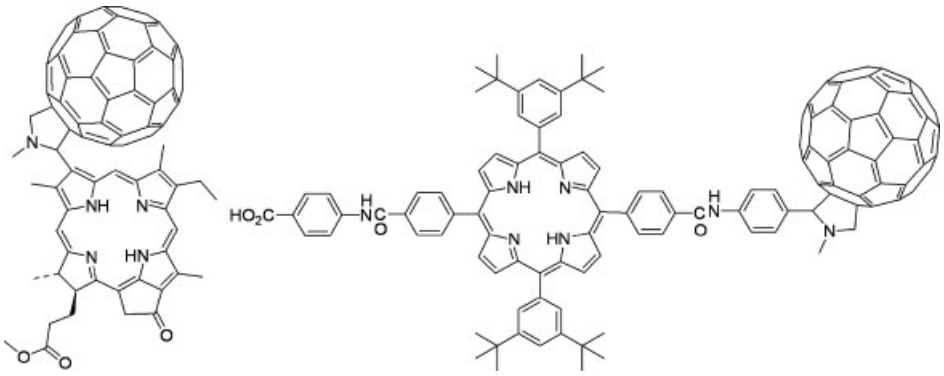


Fig. 6 Chemical structures of the phytochlorin-fullerene (left) and porphyrin-fullerene (right) dyads.

1.4.2.5 **Carbon Nanotube LB Films**

Iijima discovered MWNTs [54] and SWNTs [55] in 1991 and 1993, respectively. Since the first findings, carbon nanotubes have been at the forefront of nanoscience and nanotechnology because of their remarkable electronic, mechanical, and thermal properties, and specific functions [56–59]. Soluble carbon nanotubes in aqueous and organic systems are of interest since their study can lead to the chemical and biochemical design of functional carbon nanotubes.

The preparation of carbon nanotube sheets, called *carbon nanotube papers* [60] and carbon nanotube films by physical adsorption [61] is already known. However, reports describing the preparation of thin films with high homogeneity from purified-carbon nanotubes dissolved or dispersed in solution are very limited. By utilizing soluble nanotubes, carbon nanotube ultrathin films can be formed. Ultrathin composite films of carbon nanotubes and amphiphiles are formed by means of the LB technique [62]. Krstic et al. described the formation of monolayers of SWNTs and a surfactant on substrates with lithographically defined electrode arrays [63]. They measured the electrical transport of the electrodes. The current/voltage characteristics showed a nonlinear dependence with steplike features. Minami et al. [64] prepared optically homogeneous and structurally controlled (oriented) LB films from soluble SWNTs. LB film formation of crown ether-modified soluble MWNTs and SWNTs have been reported by Guo et al. [65] Luccio et al. [66] described the formation of LB films of SWNTs and behenic acid with densely packed and uniform coverage on hydrophobic Si(100) substrates. Preparation of carbon nanotube/polyelectrolyte thin films by the layer-by-layer technique has been reported [67]. We have reported the dissolution of shortened SWNTs in aqueous micelle of an electroactive surfactant, 11-ferrocenylundecy poly(ethylene glycol), and then the formation of SWNT films from the solution by electrodeposition, whose process was monitored by an electrochemical quartz crystal microbalance (EQCM) [68]. Barisci and coworkers [69] reported EQCM studies of SWNTs dispersed in water or in acetonitrile. Carbon nanotube ultrathin films described earlier are considered to possess ordered and oriented structures and therefore these films may be useful for the construction of optical and optoelectronic devices.

1.4.2.6 Conclusions

We have reviewed a recent progress on the electrochemistry of LB films and related films of functionalized molecules including ''molecular wire'' compounds, phthalocyanines, artificial lipids, proteins and fullerene derivatives, and carbon nanotubes. Ultrathin films with ordered structures on substrates should be promising nanomaterials for future nanoelectronic and molecular-information transducers with controllable and fine structures at the molecular level. The construction of such artificial nanomolecular devices is a great challenge in the near future.

References

1. R. M. Metzger, T. Xu, I. R. Peterson, *J. Phys. Chem. B* **2001**, *105*, 7280.
2. S. Zhou, Y. Liu, W. Qiu et al., *Adv. Funct. Mater.* **2002**, *12*, 65.
3. A. Jaiswal, R. R. Amaresh, M. V. Lakshmikantham et al., *Langmuir* **2003**, *19*, 9043.
4. J. Matsui, M. Mitsuishi, A. Aoki et al., *Angew. Chem., Int. Ed. Engl.* **2003**, *42*, 2272.
5. R. M. Metzger, *Chem. Rev.* **2003**, *103*, 3803.
6. M. Kunitake, K. Nasu, O. Manabe et al., *Bull. Chem. Soc. Jpn.* **1994**, *67*, 375.
7. M. Kunitake, K. Nasu, Y. Narikiyo et al., *Bull. Chem. Soc. Jpn.* **1995**, *68*, 2497.
8. K. M. Kadish, T. Nakanishi, A. Gürek et al., *J. Phys. Chem. B* **2001**, *105*, 9817.
9. I. Yilmaz, T. Nakanishi, A. Gürek et al., *J. Porphyr. Phthalocya.* **2003**, *7*, 227.
10. T. Nakanishi, I. Yilmaz, N. Nakashima et al., *J. Phys. Chem. B* **2003**, *107*, 12789.
11. Y. Liu, K. Shigehara, M. Hara et al., *J. Am. Chem. Soc.* **1991**, *113*, 440.
12. Y. Gorbunova, M. L. Rodríguez-Méndez, I. P. Kalashnikova et al., *Langmuir* **2001**, *17*, 5004.
13. M. L. Rodríguez-Méndez, Y. Gorbunova, J. A. de Saja, *Langmuir* **2001**, *18*, 9560.
14. Y. Okahata, T. Tsuruta, K. Ijiro et al., *Langmuir* **1988**, *4*, 1373.
15. Y. Ebara, H. Ebato, K. Ariga et al., *Langmuir* **1994**, *10*, 2267.
16. K. Noda, N. A. Zorin, C. Nakamura et al., *Thin Solid Films* **1998**, *327–329*, 639.
17. K. Ariga, K. Tanaka, K. Katagiri et al., *Phys. Chem. Chem. Phys.* **2001**, *3*, 3442.
18. N. Nakashima, K. Abe, T. Hirohashi et al., *Chem. Lett.* **1993**, 1021.
19. A.-E. F. Nassar, Y. Narikiyo, T. Sagara et al., *J. Chem. Soc., Faraday Trans.* **1995**, *91*, 1775.
20. W. E. Billups, M. A. Ciufolini, (Eds.), *Buckminsterfullerenes*, VCH, New York, 1993.
21. H. W. Kroto, *The Fullerenes; New Horizons for the Chemistry, Physics and Astrophysics of Carbon*, Cambridge University Press, Cambridge, 1997.
22. D. M. Guldi, N. Martin, (Eds.), *Fullerenes; From Synthesis to Optoelectronic Properties*, Kluwer Academic Publishers, The Netherlands, 2002.
23. J. Chlistunoff, D. Cliffel, A. J. Bard, *Thin Solid Films* **1995**, *257*, 166.
24. M. Matsumoto, H. Tachibana, R. Azumi et al., *Langmuir* **1995**, *11*, 660.
25. S. E. Campbell, G. Luengo, V. I. Srdanov et al., *Nature* **1996**, *382*, 520.
26. M. I. Sluch, I. D. W. Samuel, A. Beeby et al., *Langmuir* **1998**, *14*, 3343.
27. F. Cardullo, F. Diederich, L. Echyegoyen et al., *Langmuir* **1998**, *14*, 1955.
28. H. Murakami, Y. Watanabe, N. Nakashima, *J. Am. Chem. Soc.* **1996**, *118*, 4484.
29. N. Nakashima, T. Kuriyama, T. Tokunaga et al., *Chem. Lett.* **1998**, 633.
30. N. Nakashima, T. Tokunaga, Y. Nonaka et al., *Angew. Chem., Int. Ed. Engl.* **1998**, *37*, 2671.
31. N. Nakashima, Y. Nonaka, T. Nakanishi et al., *J. Phys. Chem. B* **1998**, *102*, 7328.
32. T. Nakanishi, H. Murakami, N. Nakashima, *Chem. Lett.* **1998**, 1219.
33. T. Nakanishi, H. Murakami, T. Sagara et al., *J. Phys. Chem. B* **1999**, *103*, 304.
34. T. Nakanishi, H. Murakami, T. Sagara et al., *Chem. Lett.* **2000**, 340.
35. N. Nakashima, T. Ishii, M. Shirakusa et al., *Chem. Eur. J.* **2001**, *7*, 1766.
36. T. Nakanishi, M. Morita, H. Murakami et al., *Chem. Eur. J.* **2002**, *8*, 1641.
37. E. Mouri, T. Nakanishi, N. Nakashima et al., *Langmuir* **2002**, *18*, 10042.
38. T. Nakanishi, H. Ohwaki, H. Tanaka et al., *J. Phys. Chem. B* **2004**, *108*, 7754.
39. H. Hungerbühler, D. M. Guldi, K.-D. Asmus, *J. Am. Chem. Soc.* **1993**, *115*, 3386.

40. S. Niu, D. Mauzerall, *J. Am. Chem. Soc.* **1996**, *118*, 5791.
41. M. Cassell, C. L. Asplund, J. M. Tour, *Angew. Chem., Int. Ed. Engl.* **1999**, *38*, 2403.
42. M. Sano, K. Oishi, T. Ishii et al., *Langmuir* **2000**, *16*, 3773.
43. S. Zhou, C. Burger, B. Chu et al., *Science* **2001**, *291*, 1944.
44. M. Yanagida, A. Takahara, T. Kajiyama, *Bull. Chem. Soc. Jpn.* **2000**, *73*, 1429.
45. S. Uemura, M. Sakata, I. Taniguchi et al., *Langmuir* **2001**, *17*, 5.
46. S. Uemura, M. Sakata, C. Hirayama et al., *Langmuir* **2004**, *20*, 9198.
47. L. M. Goldenberg, G. Williams, M. R. Bryce et al., *J. Chem. Soc., Chem. Commun.* **1993**, 1310.
48. D. Zhou, L. Gan, C. Luo et al., *Sold State Commun.* **1997**, *102*, 891.
49. D. Zhou, G. J. Ashwell, R. Rajan et al., *J. Chem. Soc., Faraday Trans.* **1997**, *93*, 2077.
50. S. S. Shiratori, M. Shimizu, K. Ikezaki, *Thin Solid Films* **1998**, *327–329*, 655.
51. S. S. Shiratori, K. Kohno, M. Yamada, *Sens. Actuators, A* **2000**, *64*, 70.
52. N. V. Tkachenko, E. Vuorimaa, T. Kesti et al., *J. Phys. Chem. B* **2000**, *104*, 6371.
53. N. V. Tkachenko, V. Vehmanen, J.-P. Nikkanen et al., *Chem. Phys. Lett.* **2002**, *366*, 245.
54. S. Iijima, *Nature* **1991**, *354*, 56.
55. S. Iijima, T. Ichihashi, *Nature* **1993**, *363*, 603.
56. P. J. F. Harris, *Carbon Nanotubes and Related Structures*, Cambridge University Press, Cambridge, 1999.
57. K. Tanaka, T. Yamabe, K. Fukui, (Eds.), *The Science and Technology of Carbon Nanotubes*, Elsevier, Oxford, 1999.
58. P. Avouris, G. Dresselhaus, M. S. Dresselhaus, (Eds.), *Carbon Nanotubes: Synthesis, Structure, Properties and Applications*, Springer-Verlag, Berlin, 2000.
59. S. Reich, C. Thomsen, J. Maultzsch, *Carbon Nanotubes: Basic Concepts and Physical Properties*, Wiley, Berlin, 2004.
60. R. H. Baughman, C. Cui, A. A. Zakhidov et al., *Science* **1999**, *284*, 1340.
61. Q. Chen, L. Dai, *Appl. Phys. Lett.* **2000**, *76*, 2719.
62. M. Burghard, V. Krstic, G. S. Duesberg et al., *Synth. Met.* **1999**, *103*, 2540.
63. V. Krstic, J. Muster, G. S. Duesberg et al., *Synth. Met.* **2000**, *110*, 245.
64. Y. Kim, N. Mimami, W. Zhu et al., *Synth. Met.* **2003**, *135–136*, 747.
65. Y. Guo, N. Minami, K. Nobutsugu et al., *Physica. B. Condens. Matter* **2002**, *323*, 235.
66. T. Di Luccio, F. Antolini, P. Aversa et al., *Carbon* **2004**, *42*, 1119.
67. A. A. Mamedov, N. A. Kotov, M. Prato et al., *Nat. Mater.* **2002**, *1*, 190.
68. N. Nakashima, H. Kobae, H. Murakami, *Chem. Phys. Chem.* **2002**, *3*, 456.
69. J. N. Barisci, G. G. Wallace, R. H. Baughman, *Electrochim. Acta* **2000**, *46*, 509.

1.4.2
Langmuir–Blodgett (LB) Films on Electrodes (B) Electrochemistry

Takashi Nakanishi
National Institute for Materials Science (NIMS), Tsukuba, Japan

Naotoshi Nakashima
Kyushu University, Fukuoka, Japan

1.4.2.1 Introduction

In this chapter, the electrochemistry of Langmuir–Blodgett (LB) films of functionalized molecules including "molecular wire" compounds, phthalocyanines, artificial lipids, proteins and fullerene derivatives, and carbon nanotubes (CNTs) is described.

The use of electrodes modified with immobilized redox-active molecules provides a simple methodology by which to study the ultrathin film electrochemistry of water-insoluble redox-active molecules, encouraging the application of such techniques to biomimetic membranes in aqueous media. It is of interest to use monolayer and LB films of enzymes, proteins, and antibodies as biosensors or biomolecular switches because of their high sensitivity for their substrates and antigens, respectively. The formation of thin fullerene films including fullerene-lipid hybrid and fullerene-lipid composite bilayer membranes is of interest both from a fundamental and practical application point of view. Multiwalled carbon nanotubes (MWNTs) and single-walled carbon nanotubes (SWNTs) are novel nanomaterials that have remarkable electronic, mechanical, and thermal properties, and specific functions. Soluble carbon nanotubes in aqueous and organic systems are of interest since their study allows the chemical and biochemical design of functional carbon nanotubes. We describe here how to make ultrathin films of nanotubes on substrates.

1.4.2.2 Electrochemistry of LB Films of "Molecular Wires" and Phthalocyanines

It is known that LB techniques can be applied for the construction of thin film electronic devices and molecular rectifiers [1–5]. Conjugated redox-active compounds are candidates for "molecular wires" and are expected to be a convenient tool for the construction of molecular electronic devices. We have reported that LB films of π-conjugated electrochemically active quinolinium complexes transferred on to gold electrodes show rectified transmembrane electron transfer, through the LB monolayer, to hexacyanoferrate(II) ($[Fe(CN)_6]^{4-}$) in solution [6, 7]. Potential-step chronocoulometric responses revealed that the LB monolayer acts as an organic ultramicroelectrode array. Metzger et al. constructed electrical rectification systems using LB monolayers of substituted quinolinium tricyanoquinodimethanides (Fig. 1) on electrodes by scanning tunneling spectroscopy (STS) [1, 3]. The unimolecular electrical rectifiers prepared by using LB techniques are useful for the construction of molecular electrode devices [1–5].

Ultrathin films of electrochromic molecules such as multireducible double-decker phthalocyanines are one important possible component of color display devices. The double-decker lutetium(III) phthalocyanine molecules having long alkyl chains (Fig. 2) were mixed with amphiphilic matrices and cast on electrodes as thin films [8–10]. These phthalocyanines undergo up to five reductions at the modified electrode. The fifth reduction had been theoretically

Encyclopedia of Electrochemistry.Edited by A.J. Bard and M. Stratmann
Vol. 10 *Modified Electrodes*. Edited by M.Fujihira, I.Rubinstein, and J.F.Rusling
Copyright © 2007 Wiley-VCH Verlag GmbH & Co. KGaA, Weinheim.ISBN: 978-3-527-30402-8

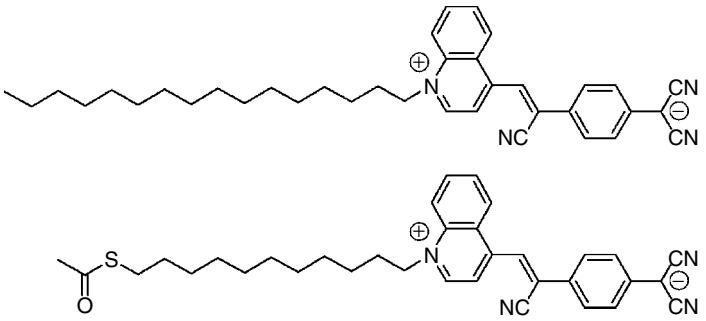


Fig. 1 Chemical structures of the quinolinium tricyanoquinodimethanides.

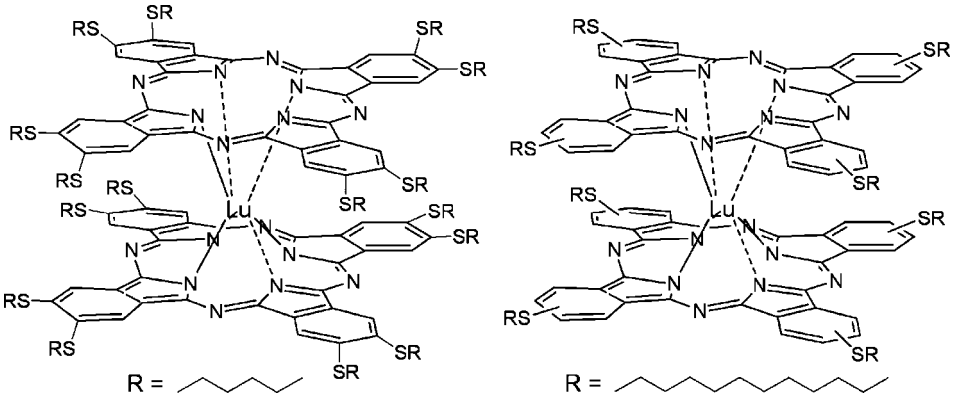


Fig. 2 Chemical structures of the alkylthio substituted double-decker lutetium(III) phthalocyanines.

predicted but had not been previously observed for any double-decker lutetium phthalocyanines. Moreover, use of cationic matrices is important because reduced anions of the phthalocyanines can be stabilized in these matrices. Multicolor electrochromism, that is, green, brown-red, blue, and purple, are observed at LB films of octakis-substituted heavy rare-earth metal double-decker phthalocyanines in contact with an aqueous electrolyte [11]. Saja et al. reported that LB films of rare-earth metal double-decker phthalocyanines deposited onto indium tin oxide (ITO) microelectrodes have sensing properties for NO gas and vapors of volatile organic compounds such as alcohols, aldehydes, and esters, which are contained in aromas of foods and beverages [12, 13].

LB films of artificial lipids transferred onto electrode substrates could be used as glucose [14] and calcium ion [15] sensors and for hydrogen evolution [16]. Okahata et al. coated a SnO_2 electrode with LB films of synthetic phospholipids [15]. Oxidation peak currents of a maker ion ($[Fe(CN)_6]^{3/4-}$) in the aqueous phase through the lipid films increased with the addition of Ca^{2+} ions only when the LB films were in the fluid liquid crystalline phase above the phase transition

temperature since Ca^{2+} ion can only bind and penetrate into the fluid liquid crystalline phase of the films and disturb or expand the LB membrane structures. The LB films of glucose oxidase (GOD)-artificial lipid monolayers deposited onto Pt electrodes act as glucose-sensing ultrathin membranes with a short response time [14]. Miyake et al. reported electrochemical hydrogen evolution using LB films of hydrogenase protein complexed with poly-L-lysine, in which methyl viologen was used as a mediator [16]. Ariga et al. developed a novel type of vitamin B_{12}-functionalized electrode [17], in which the monolayer properties of the vitamin B_{12} mimics were investigated as a mixed monolayer with an organosilane lipid (Fig. 3). The obtained electrodes have the potential to transform environmentally toxic chemicals into nonhazardous ones through an electrochemical process. The lipid LB film modified electrodes provide a suitable interface for the electrochemistry of cytochrome *c* [18] and myoglobin [19]. Thus, the synthetic artificial lipids provide suitable environments for the electrochemistry of redox-active biomolecules.

1.4.2.3 Langmuir Monolayer of Fullerenes at the Air–Water Interface

The construction of fullerene ultrathin films with an ordered structure is of interest from both a fundamental and practical point of view [20–22]. C_{60} alone and amphiphilic fullerene derivatives form monolayers at the air–water interface and these monolayers can be transferred onto solid substrates [23–27]. The authors [28–38] and others [39–43] have been interested in combining fullerene chemistry and the

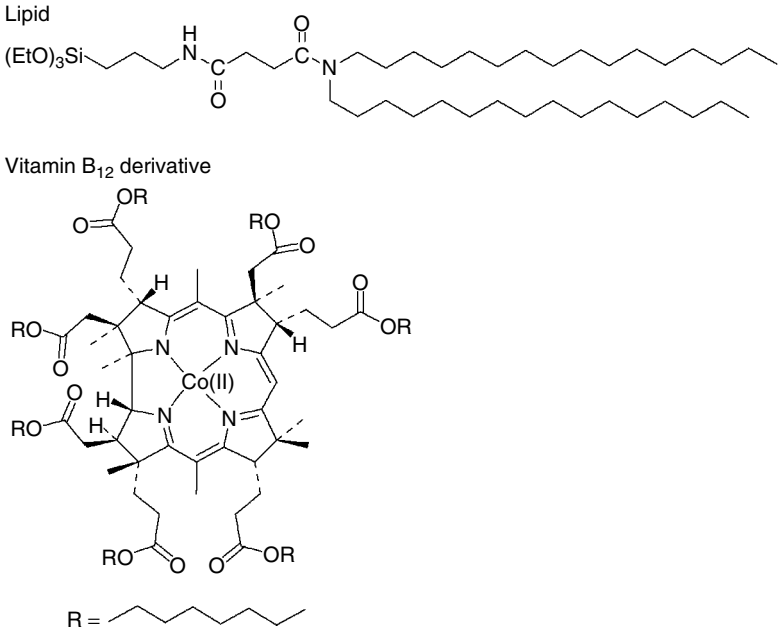


Fig. 3 Chemical structures of the organosilane amphiphile and vitamin B_{12} derivative.

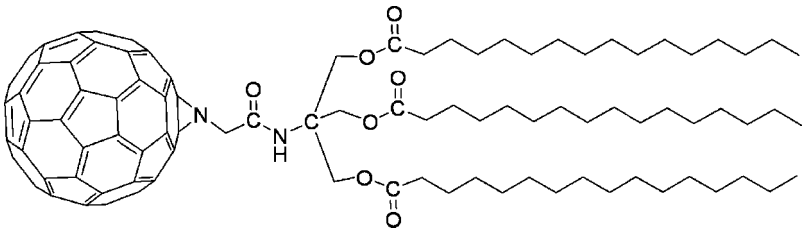


Fig. 4 Chemical structure of the fullerene lipid.

chemistry of lipid bilayer membranes, which may create a novel field in the chemistry and biochemistry of fullerenes. We have reported the design, synthesis, and characterization of a C_{60}-bearing triple-chain lipid [28, 32, 33, 36, 37] (Fig. 4). This lipid forms stable Langmuir monolayers at the air–water interface [32, 37]. The surface-pressure–area isotherm of the fullerene lipid gives limiting areas of 0.78 and 0.98 nm^2/molecule, suggesting the formation of monolayers with hexagonal and simple square packing, respectively [32]. In situ X-ray reflectometry (XR) techniques revealed the nanostructure of the fullerene-lipid monolayer on water, that is, the fullerene moiety was in contact with the water surface and the lipid tail extended to the air [37] (Fig. 5).

The LB film prepared in the dark shows temperature dependent UV–vis absorption spectra. At lower temperatures, there is an electronic interaction between the fullerene moieties in the LB film. Upon heating over 47 °C, which is the subphase transition temperature of the cast films of the fullerene lipid [28, 36], the electronic interaction of the fullerene moieties is loosened. The electronic interaction between the fullerene moieties can be controlled by the phase change of the film. The fundamental property of the self-assembled bilayer membrane film is maintained in the LB film prepared in the dark, indicating that the molecular orientations of the

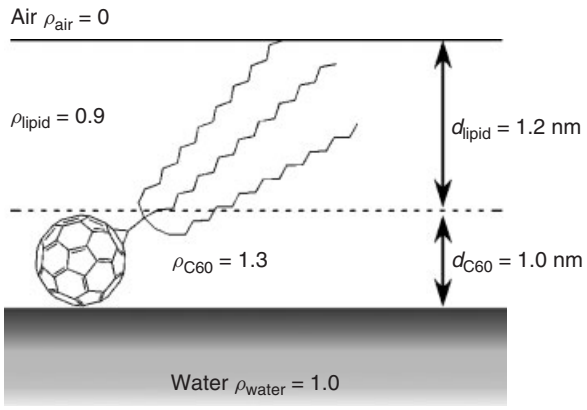


Fig. 5 Schematic illustration of the nanostructure of the monolayer of the fullerene lipid on water revealed by in situ X-ray reflectometry measurements.

fullerene moieties of the LB film and cast film of the fullerene lipid are not significantly different. This is important from the viewpoint of the introduction of lipid bilayer properties of the fullerene lipids to the LB system. This information is useful for the design and construction of functional supramolecular ultrathin fullerene films at the air–water interface and on solid surfaces.

1.4.2.4 Electrochemistry of LB Films of Fullerenes on Electrodes

Electrochemistry of LB films of fullerenes has been widely studied and remains the subject of much research effort from both theoretical and experimental approaches. Bard et al. have studied basic electrochemistry of C_{60} fullerene LB films on an electrode in acetonitrile solutions [23]. The study indicated that reduction of the fullerene films could form insoluble films with incorporated electrolyte cations or lead to dissolution. The study on C_{60} LB films has become a focus of considerable interest; however, it is difficult to fabricate high-quality LB films of pure C_{60} due to its intrinsic hydrophobicity. Kajiyama et al. applied a multistep creep method as an LB technique for constructing a fairly homogeneous C_{60} monolayer, which is regularly packed in a hexagonal array [44]. Kunitake et al. developed the electrochemical replacement method to form epitaxial adlayers of fullerenes on Au(111) surfaces [45]. The ''wet process'' method consists of the transfer of Langmuir films of fullerene onto iodine-modified Au(111) surfaces at an air–water interface followed by the electrochemical removal and replacement of iodine adlayers with fullerene adlayers in solution. The fullerene adlayers prepared by this method showed excellent quality and uniformity. A visualizing technique by in situ scanning tunneling microscopy (STM) for the surface morphology of fullerene LB films on iodine-modified Pt(111) surfaces was also developed [46].

As an alternative way to avoid the formation of low-quality aggregated structures of fullerenes, several functionalized fullerene derivatives with nonpolar or polar groups were synthesized. Subsequently, electrochemical characterization of the higher-quality LB films was performed. The electrochemistry of LB films of fullerene derivatives in organic solvents showed well-defined reversible multi-electroreductions [47], but this was not observed in all of the cases. LB films of fullerenes have several intrinsic properties such as nonlinear optical features and gas sensing. The LB films of a crowned C_{60}-pyrrolidine [48] and of a 4-acetylphenyl-substituted C_{60}-pyrrolidine [49] exhibit optical second-harmonic responses. The second-harmonic intensity is strongly dependent on the number of layers of the LB films. Spatial control of arachidic acid LB films by introduction of C_{60} molecules as the spacers to a polymer backbone, poly(allylaminehydrochloride) (PAH), is reported to be a novel sensor for α-pinene, citral, β-caryophyllene, Nerilidol, and n-octadecane in the gas phase [50, 51]. Models of natural photoreaction centers can be constructed using LB films of fullerene derivatives. Tkachenko et al. described the preparation of LB films of a phytochlorin-fullerene [52] and of a porphyrin-fullerene [53] that show vectorial photoinduced electron transfer reactions (Fig. 6). These donor–acceptor dyad LB film systems are an attractive example for the development of molecular optoelectronic devices.

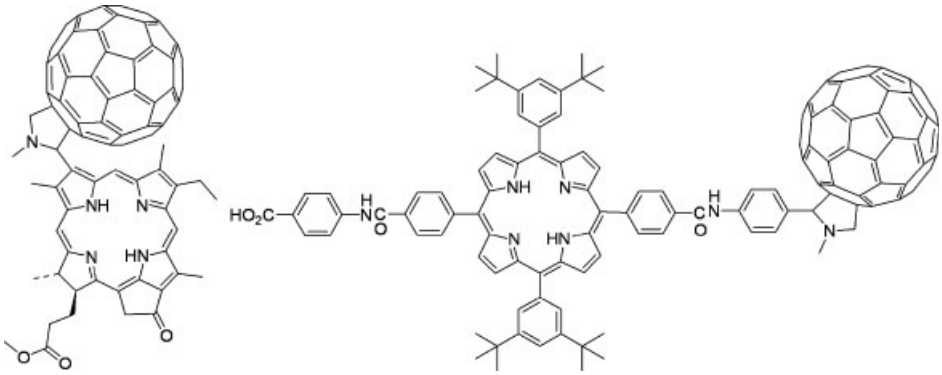


Fig. 6 Chemical structures of the phytochlorin-fullerene (left) and porphyrin-fullerene (right) dyads.

1.4.2.5 Carbon Nanotube LB Films

Iijima discovered MWNTs [54] and SWNTs [55] in 1991 and 1993, respectively. Since the first findings, carbon nanotubes have been at the forefront of nanoscience and nanotechnology because of their remarkable electronic, mechanical, and thermal properties, and specific functions [56–59]. Soluble carbon nanotubes in aqueous and organic systems are of interest since their study can lead to the chemical and biochemical design of functional carbon nanotubes.

The preparation of carbon nanotube sheets, called *carbon nanotube papers* [60] and carbon nanotube films by physical adsorption [61] is already known. However, reports describing the preparation of thin films with high homogeneity from purified-carbon nanotubes dissolved or dispersed in solution are very limited. By utilizing soluble nanotubes, carbon nanotube ultrathin films can be formed. Ultrathin composite films of carbon nanotubes and amphiphiles are formed by means of the LB technique [62]. Krstic et al. described the formation of monolayers of SWNTs and a surfactant on substrates with lithographically defined electrode arrays [63]. They measured the electrical transport of the electrodes. The current/voltage characteristics showed a nonlinear dependence with steplike features. Minami et al. [64] prepared optically homogeneous and structurally controlled (oriented) LB films from soluble SWNTs. LB film formation of crown ether-modified soluble MWNTs and SWNTs have been reported by Guo et al. [65] Luccio et al. [66] described the formation of LB films of SWNTs and behenic acid with densely packed and uniform coverage on hydrophobic Si(100) substrates. Preparation of carbon nanotube/polyelectrolyte thin films by the layer-by-layer technique has been reported [67]. We have reported the dissolution of shortened SWNTs in aqueous micelle of an electroactive surfactant, 11-ferrocenylundecy poly(ethylene glycol), and then the formation of SWNT films from the solution by electrodeposition, whose process was monitored by an electrochemical quartz crystal microbalance (EQCM) [68]. Barisci and coworkers [69] reported EQCM studies of SWNTs dispersed in water or in acetonitrile. Carbon nanotube ultrathin films described earlier are considered to possess ordered and oriented structures and therefore these films may be useful for the construction of optical and optoelectronic devices.

1.4.2.6 Conclusions

We have reviewed a recent progress on the electrochemistry of LB films and related films of functionalized molecules including ''molecular wire'' compounds, phthalocyanines, artificial lipids, proteins and fullerene derivatives, and carbon nanotubes. Ultrathin films with ordered structures on substrates should be promising nanomaterials for future nanoelectronic and molecular-information transducers with controllable and fine structures at the molecular level. The construction of such artificial nanomolecular devices is a great challenge in the near future.

References

1. R. M. Metzger, T. Xu, I. R. Peterson, *J. Phys. Chem. B* **2001**, *105*, 7280.
2. S. Zhou, Y. Liu, W. Qiu et al., *Adv. Funct. Mater.* **2002**, *12*, 65.
3. A. Jaiswal, R. R. Amaresh, M. V. Lakshmikantham et al., *Langmuir* **2003**, *19*, 9043.
4. J. Matsui, M. Mitsuishi, A. Aoki et al., *Angew. Chem., Int. Ed. Engl.* **2003**, *42*, 2272.
5. R. M. Metzger, *Chem. Rev.* **2003**, *103*, 3803.
6. M. Kunitake, K. Nasu, O. Manabe et al., *Bull. Chem. Soc. Jpn.* **1994**, *67*, 375.
7. M. Kunitake, K. Nasu, Y. Narikiyo et al., *Bull. Chem. Soc. Jpn.* **1995**, *68*, 2497.
8. K. M. Kadish, T. Nakanishi, A. Gürek et al., *J. Phys. Chem. B* **2001**, *105*, 9817.
9. I. Yilmaz, T. Nakanishi, A. Gürek et al., *J. Porphyr. Phthalocya.* **2003**, *7*, 227.
10. T. Nakanishi, I. Yilmaz, N. Nakashima et al., *J. Phys. Chem. B* **2003**, *107*, 12789.
11. Y. Liu, K. Shigehara, M. Hara et al., *J. Am. Chem. Soc.* **1991**, *113*, 440.
12. Y. Gorbunova, M. L. Rodríguez-Méndez, I. P. Kalashnikova et al., *Langmuir* **2001**, *17*, 5004.
13. M. L. Rodríguez-Méndez, Y. Gorbunova, J. A. de Saja, *Langmuir* **2001**, *18*, 9560.
14. Y. Okahata, T. Tsuruta, K. Ijiro et al., *Langmuir* **1988**, *4*, 1373.
15. Y. Ebara, H. Ebato, K. Ariga et al., *Langmuir* **1994**, *10*, 2267.
16. K. Noda, N. A. Zorin, C. Nakamura et al., *Thin Solid Films* **1998**, *327–329*, 639.
17. K. Ariga, K. Tanaka, K. Katagiri et al., *Phys. Chem. Chem. Phys.* **2001**, *3*, 3442.
18. N. Nakashima, K. Abe, T. Hirohashi et al., *Chem. Lett.* **1993**, 1021.
19. A.-E. F. Nassar, Y. Narikiyo, T. Sagara et al., *J. Chem. Soc., Faraday Trans.* **1995**, *91*, 1775.
20. W. E. Billups, M. A. Ciufolini, (Eds.), *Buckminsterfullerenes*, VCH, New York, 1993.
21. H. W. Kroto, *The Fullerenes; New Horizons for the Chemistry, Physics and Astrophysics of Carbon*, Cambridge University Press, Cambridge, 1997.
22. D. M. Guldi, N. Martin, (Eds.), *Fullerenes; From Synthesis to Optoelectronic Properties*, Kluwer Academic Publishers, The Netherlands, 2002.
23. J. Chlistunoff, D. Cliffel, A. J. Bard, *Thin Solid Films* **1995**, *257*, 166.
24. M. Matsumoto, H. Tachibana, R. Azumi et al., *Langmuir* **1995**, *11*, 660.
25. S. E. Campbell, G. Luengo, V. I. Srdanov et al., *Nature* **1996**, *382*, 520.
26. M. I. Sluch, I. D. W. Samuel, A. Beeby et al., *Langmuir* **1998**, *14*, 3343.
27. F. Cardullo, F. Diederich, L. Echyegoyen et al., *Langmuir* **1998**, *14*, 1955.
28. H. Murakami, Y. Watanabe, N. Nakashima, *J. Am. Chem. Soc.* **1996**, *118*, 4484.
29. N. Nakashima, T. Kuriyama, T. Tokunaga et al., *Chem. Lett.* **1998**, 633.
30. N. Nakashima, T. Tokunaga, Y. Nonaka et al., *Angew. Chem., Int. Ed. Engl.* **1998**, *37*, 2671.
31. N. Nakashima, Y. Nonaka, T. Nakanishi et al., *J. Phys. Chem. B* **1998**, *102*, 7328.
32. T. Nakanishi, H. Murakami, N. Nakashima, *Chem. Lett.* **1998**, 1219.
33. T. Nakanishi, H. Murakami, T. Sagara et al., *J. Phys. Chem. B* **1999**, *103*, 304.
34. T. Nakanishi, H. Murakami, T. Sagara et al., *Chem. Lett.* **2000**, 340.
35. N. Nakashima, T. Ishii, M. Shirakusa et al., *Chem. Eur. J.* **2001**, *7*, 1766.
36. T. Nakanishi, M. Morita, H. Murakami et al., *Chem. Eur. J.* **2002**, *8*, 1641.
37. E. Mouri, T. Nakanishi, N. Nakashima et al., *Langmuir* **2002**, *18*, 10042.
38. T. Nakanishi, H. Ohwaki, H. Tanaka et al., *J. Phys. Chem. B* **2004**, *108*, 7754.
39. H. Hungerbühler, D. M. Guldi, K.-D. Asmus, *J. Am. Chem. Soc.* **1993**, *115*, 3386.

40. S. Niu, D. Mauzerall, *J. Am. Chem. Soc.* **1996**, *118*, 5791.
41. M. Cassell, C. L. Asplund, J. M. Tour, *Angew. Chem., Int. Ed. Engl.* **1999**, *38*, 2403.
42. M. Sano, K. Oishi, T. Ishii et al., *Langmuir* **2000**, *16*, 3773.
43. S. Zhou, C. Burger, B. Chu et al., *Science* **2001**, *291*, 1944.
44. M. Yanagida, A. Takahara, T. Kajiyama, *Bull. Chem. Soc. Jpn.* **2000**, *73*, 1429.
45. S. Uemura, M. Sakata, I. Taniguchi et al., *Langmuir* **2001**, *17*, 5.
46. S. Uemura, M. Sakata, C. Hirayama et al., *Langmuir* **2004**, *20*, 9198.
47. L. M. Goldenberg, G. Williams, M. R. Bryce et al., *J. Chem. Soc., Chem. Commun.* **1993**, 1310.
48. D. Zhou, L. Gan, C. Luo et al., *Sold State Commun.* **1997**, *102*, 891.
49. D. Zhou, G. J. Ashwell, R. Rajan et al., *J. Chem. Soc., Faraday Trans.* **1997**, *93*, 2077.
50. S. S. Shiratori, M. Shimizu, K. Ikezaki, *Thin Solid Films* **1998**, *327–329*, 655.
51. S. S. Shiratori, K. Kohno, M. Yamada, *Sens. Actuators, A* **2000**, *64*, 70.
52. N. V. Tkachenko, E. Vuorimaa, T. Kesti et al., *J. Phys. Chem. B* **2000**, *104*, 6371.
53. N. V. Tkachenko, V. Vehmanen, J.-P. Nikkanen et al., *Chem. Phys. Lett.* **2002**, *366*, 245.
54. S. Iijima, *Nature* **1991**, *354*, 56.
55. S. Iijima, T. Ichihashi, *Nature* **1993**, *363*, 603.
56. P. J. F. Harris, *Carbon Nanotubes and Related Structures*, Cambridge University Press, Cambridge, 1999.
57. K. Tanaka, T. Yamabe, K. Fukui, (Eds.), *The Science and Technology of Carbon Nanotubes*, Elsevier, Oxford, 1999.
58. P. Avouris, G. Dresselhaus, M. S. Dresselhaus, (Eds.), *Carbon Nanotubes: Synthesis, Structure, Properties and Applications*, Springer-Verlag, Berlin, 2000.
59. S. Reich, C. Thomsen, J. Maultzsch, *Carbon Nanotubes: Basic Concepts and Physical Properties*, Wiley, Berlin, 2004.
60. R. H. Baughman, C. Cui, A. A. Zakhidov et al., *Science* **1999**, *284*, 1340.
61. Q. Chen, L. Dai, *Appl. Phys. Lett.* **2000**, *76*, 2719.
62. M. Burghard, V. Krstic, G. S. Duesberg et al., *Synth. Met.* **1999**, *103*, 2540.
63. V. Krstic, J. Muster, G. S. Duesberg et al., *Synth. Met.* **2000**, *110*, 245.
64. Y. Kim, N. Mimami, W. Zhu et al., *Synth. Met.* **2003**, *135–136*, 747.
65. Y. Guo, N. Minami, K. Nobutsugu et al., *Physica. B. Condens. Matter* **2002**, *323*, 235.
66. T. Di Luccio, F. Antolini, P. Aversa et al., *Carbon* **2004**, *42*, 1119.
67. A. A. Mamedov, N. A. Kotov, M. Prato et al., *Nat. Mater.* **2002**, *1*, 190.
68. N. Nakashima, H. Kobae, H. Murakami, *Chem. Phys. Chem.* **2002**, *3*, 456.
69. J. N. Barisci, G. G. Wallace, R. H. Baughman, *Electrochim. Acta* **2000**, *46*, 509.

1.5 Electrochemistry of Monolayer Assemblies at the Air/Water Interface

Marcin Majda
University of California, Berkeley, California

1.5.1 Langmuir and Gibbs Monolayers at the Air/Water Interface

The air/water interface is a unique platform for the formation of monolayer assemblies. As in the case of all liquids, the water surface is nearly molecularly smooth [1]. Water has the highest surface tension of all molecular liquids. Water is also a liquid of exceedingly high polarity, which renders a large fraction of nonionic molecules and some ionic amphiphiles water insoluble. A moderately high boiling temperature and partial pressure of water allow one to investigate monolayer films at the air/water interface in the temperature range of roughly 0–50 °C. High surface tension and high polarity of water allow spreading of Langmuir monolayers, films of insoluble, typically amphiphilic compounds deposited on the water surface as solutions in volatile solvents such as chloroform. Following spreading and solvent evaporation, the surface concentration of a compound can be controlled mechanically by sweeping the water surface with a Teflon barrier that confines the known quantity of the spread compound to a specific surface area of a Langmuir trough [2–7]. Another class of structurally similar monolayer films involves water-soluble surfactants. These types of monolayers, termed *Gibbs monolayers*, form spontaneously at the air/water interface as a result of surface partitioning equilibria [8].

Just as there exist numerous types of amphiphiles such as single alkane chain alcohols, amines, fatty acids and esters, various phospholipids and polymeric amphiphiles, it is also possible to talk about a range of physical phenomena and practical applications that drive research in this area of science. Fundamentally, Langmuir monolayers constitute a relatively easy to control class of systems where physical phenomena such as ordering, phase transitions, critical phenomena, and dynamics of lateral transport can be investigated in 2D. Biophysicists regard Langmuir films as model systems of biological membranes and investigate the relationship between their composition, structure, and monolayer dynamics [9]. Surface adsorption and the resulting Gibbs monolayers have long been of interest to scientists interested in surface rheology, wetting, formation of foams and emulsions, and other related phenomena. Finally, it is important to mention that Langmuir films can be sequentially transferred onto solid surfaces to form the so-called Langmuir–Blodgett films (see Sect. 1.5.2.1.5). The L—B films have been of long standing interest in the chemical, physical, and materials sciences as a general, molecular level methodology of forming ordered multilayer assemblies of controlled structure and composition [10].

A schematic diagram of a *Langmuir trough*, a shallow Teflon dish filled with ultrapure water commonly used to study Langmuir and Gibbs monolayer films is shown in Fig. 1. Such instruments are typically equipped with a precision driven Teflon *barrier* enabling the control of the area of the water surface, a *surface balance* – allowing one to record surface pressure versus mean molecular area (π vs. MMA) isotherms [2, 5, 7], a *Kelvin probe* – an instrument measuring surface

Encyclopedia of Electrochemistry. Edited by A.J. Bard and M. Stratmann
Vol. 10 *Modified Electrodes*. Edited by M.Fujihira, I.Rubinstein, and J.F.Rusling
Copyright © 2007 Wiley-VCH Verlag GmbH & Co. KGaA, Weinheim. ISBN: 978-3-527-30402-8

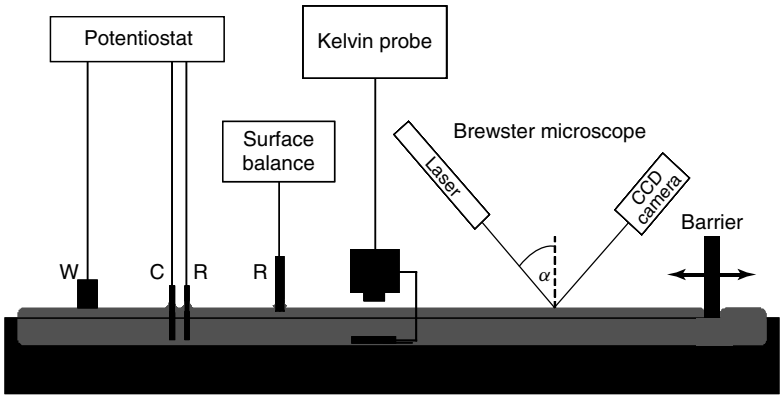


Fig. 1 A schematic drawing of a Langmuir trough instrument. The working electrode resides at the air/water interface. Its type and design reflect a particular type of electrochemical experiment to be carried out to characterize monolayers on the air/water interface.

potential that can reveal the dependence of the surface normal component of an average dipole moment of the molecules spread on the water surface as a function of their MMA [11], and a *Brewster angle microscope* (BAM) [12, 13]. The latter technique allows one to image morphology of surface films during compression. The potentiostatic setup shown in Fig. 1 and a working electrode touching the water surface are used to electrochemically characterize the surface monolayer film. Application of the electrochemical methods in the studies of Langmuir films is, indeed, the main subject of this review.

The use of electrochemistry to characterize Langmuir films directly at the air/water interface was introduced in the mid-eighties. Since then two classes of experiments have been developed: (1) horizontal touch (HT) experiments involving a planar working electrode held directly above the air/water interface and contacting a monolayer film spread on the water surface; and (2) two-dimensional (2D) electrochemical measurements involving line microelectrodes positioned in the plain of the air/water interface. In the following sections, we discuss these approaches and present key experimental results. For the sake of completeness, it is worth adding that scanning electrochemical microscopy (SECM) has also been applied to investigate Langmuir films. This indirect method of probing charge transport in Langmuir films involves a disk microelectrode held in the subphase, directly underneath the water surface. Current versus distance dependence is recorded and analyzed as the disk microelectrode is slowly brought into a close proximity of a Langmuir monolayer film. Several examples of this approach to the studies of Langmuir films were reported by Unwin and coworkers [14–17]. Scanning Electrochemical Microscopy (SECM) is the subject of Sect. 3.2.8, in Volume 3.

1.5.2 Horizontal Touch Electrochemical Characterization of Monolayer Films at the Air/Water Interface

Horizontal touch is a term that can be attributed to Langmuir and Schaefer who

described a transfer technique of a monolayer from the air/water interface to a flat surface of a solid substrate [18]. This involved lowering a plate onto the water surface "in a nearly horizontal position." Early on, Miller and coworkers used a similar methodology to transfer monolayer films on mercury electrodes and carry out electrochemical experiments with the resulting Langmuir–Blodgett (LB) type films in the subphase [19, 20]. The electrochemistry of LB and self-assembled films on mercury has been reviewed by Guidelli (see Sect. 1.5.2.1.3) Horizontal touch electrochemistry carried out with a working electrode just touching the interface was first demonstrated by Fujihira and Araki [21]. They showed that by contacting a Langmuir film of a surfactant derivative of anthraquinone with a flat glassy carbon electrode, they were able to electrochemically address the molecules forming the Langmuir film. This technique was further developed by Miller, Bard and coworkers [22–24]. Their experiments involved indium-doped tin oxide (ITO) and pyrolitic graphite electrodes. Their work proceeded in three directions. On the one hand, they showed that HT voltammetry can offer sensitive means of detecting the presence of solid domains in Langmuir films [22]. Compounds such as $Ru(bpy)_2(bpy\text{-}C_{19})$ (bpy is 2,2′-bipyridine and bpy-C_{19} is a bpy ligand with a single stearamido moiety attached to one pyridine ring in 4-position) aggregate upon spreading forming large, 2D, solid domains within which each $Ru(bpy)_2(bpy\text{-}C_{19})$ occupies an area of ca. 120 $Å^2$/molecule. Repetitive HT voltammetric experiments were carried out each with a freshly cleaned 0.5 cm^2 ITO electrode touching $Ru(bpy)_2(bpy\text{-}C_{19})$ film of submonolayer coverage (240 and 600 $Å^2$/molecule). The authors observed stochastic behavior in these experiments. Not every act of placing an electrode on the monolayer covered water surface resulted in making contact with the monolayer material. The probability of recording a voltammetric signal due to $Ru(bpy)_2(bpy\text{-}C_{19})$ oxidation depended inversely on the MMA of the ruthenium surfactant, and clearly reflected the fact that only a fraction of the water surface was covered with the solid aggregates of the compound. The authors proposed that experiments of this type, if done with electrodes of different surface areas, could be interpreted in terms of the average size of the 2D aggregates.

In the second related direction of their research, Miller and coworkers developed a Langmuir monolayer imaging technique involving the electrogenerated chemiluminescence (ECL) phenomenon [23]. HT voltammetry of Langmuir monolayers of $Ru(bpy)_2(bpy\text{-}C_{19})$ (and of other ruthenium complexes) was used to generate Ru(III+) species. These reacted with oxalate ions purposefully added to the subphase in a Langmuir trough. The well-known sequence of reactions generated an excited state of the ruthenium complex. The ECL emission was collected with a CCD camera to generate photographs of a section of the Langmuir monolayer contacted by the electrode surface. These experiments offered confirmation of the heterogeneous structure of the Langmuir monolayers of the ruthenium complexes.

In the third direction of their research, Miller and Bard also relied on HT voltammetry of Langmuir monolayer films to develop a trace analytic method of determination of water insoluble redox-active species [24]. They demonstrated that μL volumes of such compounds can be deposited on the water surface in a miniature Langmuir trough, and then assayed electrochemically by HT voltammetry yielding detection limits of

ca. 1 pmol. Lower detection limits were anticipated if much smaller electrodes and Langmuir apparatus were to be used.

The HT voltammetry with gold electrodes was also recently used to measure the surface partitioning constant of a soluble, redox-active surfactant at the air/water interface [25]. Malec and coworkers modified the surface of gold electrodes by self-assembly of short alkane chain thiols in order to mimic the thermodynamic properties of the air/water interface. They relied on the fact that the surface tensions of the air/water interface and of the liquid alkane/water interface are similar [8]. Indeed, the HT measurements of the Gibbs monolayer formation constant were in agreement with their surface tensiometry and Brewster angle microscopic measurements [25].

Lipkowski and coworkers used the HT electrochemistry to study electrochemically inactive compounds such as octadecanoic acid in Langmuir monolayers under controlled surface pressure conditions [26–32]. These experiments involved single crystal gold (111) electrodes flamed prior to each HT experiment and then suspended slightly above the water surface (the hanging meniscus method) trapping a Langmuir monolayer at the metal solution interface. The subsequent electrochemical experiments involved measurements of the interfacial capacitance and chronocoulometry. The latter technique allowed the authors to precisely measure the charge density at the metal solution interface as a function of potential. Integration of the charge versus potential data yields plots of the surface pressure versus the electrode potential. Surface pressure is defined as the difference between interfacial tension in the absence and in the presence of the surfactant. The results of these experiments can be summarized in the following two conclusions of fundamental importance. The first one concerns the effect of the electrode potential. The authors conclusively demonstrated a direct relationship between the electrode potential and the surface pressure of the surfactant monolayer on the metal/solution interface. The surface pressure is at a maximum at a potential of zero charge, and corresponds therefore to the highest monolayer packing density. It then decreases with an increasing negative potential and thus increasing negative charge at the metal/solution interface. At a sufficiently negative potential, the surface pressure becomes zero, indicating a complete desorption of the monolayer film. The summary of these results is shown in Fig. 2. Overall, Lipkowski's measurements demonstrated that in the HT experiments the electrode potential is the parameter controlling the surface pressure of a monolayer film at the metal/solution interface just as the surface pressure of a Langmuir monolayer is controlled mechanically by adjusting the surface area of a Langmuir trough [30]. The surface pressure of a monolayer at the water/air interface and at the metal/solution interface is the same only at the potential of zero charge. The second conclusion of Lipkowski's research is a discovery that the application of a negative potential results in the formation of small micelle-like aggregates of the surfactant desorbed from the metal/solution interface, and that the process is reversible resulting in monolayer respreading at the metal/solution interface at less negative potentials [30]. The existence and the structure of the surfactant aggregates near the metal surface were investigated by reflectance spectroscopy and light scattering measurements [29]. Additional electrochemical and spectroscopic work probing the questions of monolayer

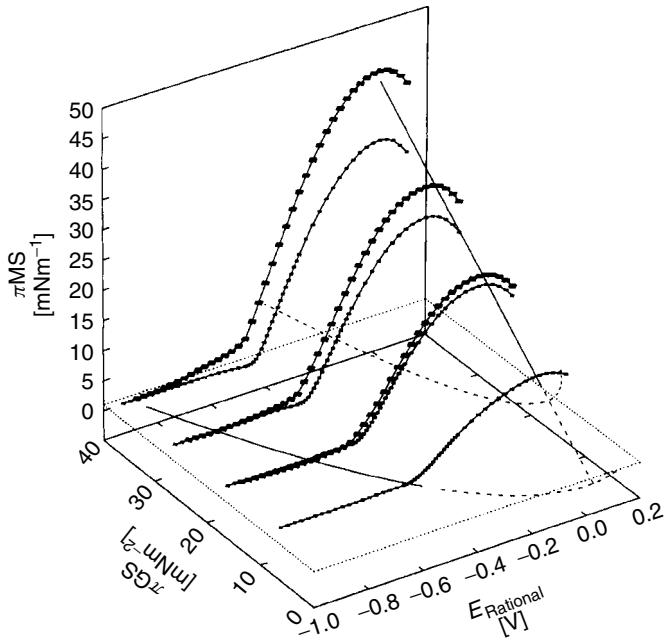


Fig. 2 Thermodynamics of the octadecanol ($C_{18}OH$) monolayer films at the air/water (GS), and metal/solution (MS) interfaces investigated by the HT electrochemical methods. Three-dimensional representation of the film pressure at the MS interface as a function of the film pressure at the GS interface (at the time of an HT experiment in which a freshly flamed Au (111) electrode is placed at the GS interface), and the electrode potential. The straight line, drawn at $E = E_{pzc}$, represents conditions under which the surface pressure of the $C_{18}OH$ film is the same at both interfaces (from Ref. 28).

desorption and aggregation was reported by Bizzotto and coworkers [33–36].

The HT investigations of redox inactive Langmuir monolayers raised the question of whether monolayers at the metal/solution interface could respond to surface pressure changes at the adjacent air/water interface. The answer was offered independently first by Miller [37] and coworkers and then by Lipkowski [38]. It appears that a lateral monolayer flow from the air/water interface to the metal/solution interface is possible in cases of liquid films. As discussed next, the rate of this transport depends on the surface pressure gradient as well as on the structure dependent monolayer fluidity.

An entirely different application of electrochemical methods involving a horizontal touch approach was developed recently by Miller and coworkers [37, 39–41]. Unlike the previous authors, Miller used a gold electrode coated with a monolayer of long alkyl chain molecules, typically octadecane thiols. The HT step led to the formation of a lipid bilayer structure at the metal/solution interface in which the bottom half of the bilayer constituted a Langmuir film on the water surface. Several different variations of this general

scheme were developed and used for different purposes. In their first paper, Steel and Miller used a rotating cylinder gold electrode with its cylindrical surface modified with an octadecane thiol monolayer [39]. The radius and the length of the cylinder were 3.63 and 0.10 cm, respectively. The electrode was positioned with the cylinder's axis oriented parallel to the water surface, and with a constant segment of the cylindrical surface contacting the Langmuir monolayer coated water surface. The cylinder was rotated 0.7 rev/min. In this position, at the electrode/air/solution triple line associated with the instroke, the rotation of the cylinder resulted in the monolayer transfer onto the section of the cylindrical surface contacting the subphase. At the triple line associated with the outstroke, the bilayer assembly formed at the metal/solution interface delaminated releasing the Langmuir monolayer. This intricate arrangement of the modified cylindrical surface rotating against a Langmuir monolayer allowed the authors to continually measure the AC admittance of the metal/bilayer/solution interface as a function of the surface pressure of the Langmuir film. Admittance data were collected for 18 different compounds forming Langmuir films. The admittance – MMA isotherms correctly reflected the phase behavior, packing density, and subphase composition effects such as ion-inclusion and interactions with the monolayer films investigated by this new technique.

In a different application of HT electrochemistry involving an alkanethiol-coated working electrode, Miller and coworkers devised a way to measure the flow rate of a Langmuir monolayer along the metal–alkanethiol/solution interface [37, 40, 41]. In this experiment, an alkanethiol-coated gold electrode is initially touching a clean water surface. The experiment begins when an amphiphilic compound of interest is spread on the water surface to form a Langmuir film at a given surface pressure (see Fig. 3). AC admittance is used to follow the time-dependent interfacial capacitance of the metal–alkanethiol/solution interface as the Langmuir monolayer flows into, or penetrates that interface to form a new interface featuring a bilayer assembly, metal-alkanethiol-monolayer/solution with a different interfacial capacitance. The plots of the capacitance versus time obtained for the oleic and stearic acid monolayers are shown in Fig. 4. Fluorescence microscopy imaging was also used to follow the progress of the lateral monolayer flow into the metal/solution interface. To interpret the capacitance versus time transients, the author defined a *flow parameter*, FP [cm $s^{-1/2}$]:

$$FP = m\left(\frac{w}{C_{Bi} - C_{SAM}}\right) \qquad (1)$$

where, m is the measured slope of the capacitance versus $t^{1/2}$ plots, w is the length of the monolayer flow path into the metal/solution interface and C_{Bi} and C_{SAM} are the values of the capacitance of the bilayer assembly and of the alkanethiol monolayer, respectively [37]. The FP was shown to be a quantity characterizing the structure and dynamic properties of the two monolayer films involved in the flow experiments, as well as their dynamic interactions. It can be clearly seen in Fig. 4, that only liquid Langmuir films, such as oleic acid, are capable of laterally flowing into the gold-alkanethiol/water interface and exhibit measurable FP values. The FPs of different monolayer forming compounds were measured and shown to linearly depend on the square root of the surface pressure of a Langmuir film (see inset in Fig. 4A). Numerous lipids with different

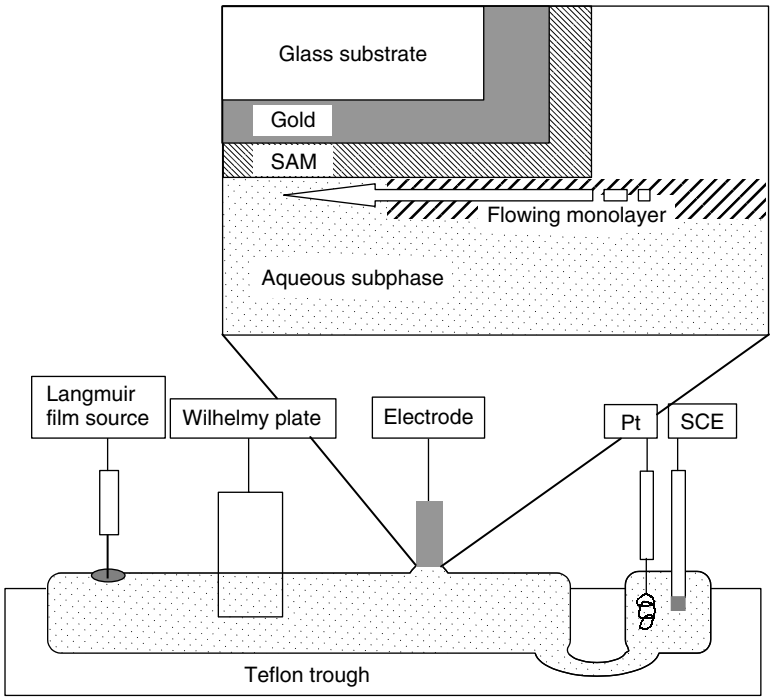


Fig. 3 Schematic depiction of the Langmuir trough apparatus and the positioning of the electrodes used in the lateral monolayer flow experiments. The inset shows the Au-coated glass slide working electrode modified with a self-assembled monolayer (SAM) of dodecanethiol. The working electrode is touching the air/water interface. A compound that forms a Langmuir monolayer is deposited on the water surface. It immediately spreads to cover the entire interface. Subsequently, the Langmuir film flows across the triple phase boundary into the SAM/water interface forming a bilayer. The lateral flow is completed when the entire electrode/solution interface is coated with a bilayer (from Ref. 37).

structural features were investigated to develop correlations between *FP* and lipid molecular structure [37, 41]. The effect of molecules and ions partitioning into the bilayer assembly was also discovered and investigated. This led the authors to develop a chemical sensor in which measurements of the *FP* were related to the concentration of H^+, Ca^{2+}, and Cd^{2+} ions [40].

In the independent investigations, a slow, surface pressure driven flow of 4-pentadecylpyridine ($C_{15}-Py$) monolayer from the air/water interface to the gold (111)/solution interface was also documented by Lipkowski and coworkers [38]. Using in situ neutron reflectivity measurements, these authors showed that in the limit of long time equilibration (10–19 h), first a monolayer and then a bilayer of $C_{15}-Py$ is formed on the gold/solution interface. The former involved a change of orientation of the $C_{15}-Py$ molecules as it crossed the triple phase line of gas/liquid/metal to allow the pyridine head group to be oriented toward the gold surface. The tail-to-tail type bilayer is then formed. We also point out that electrochemically induced surface

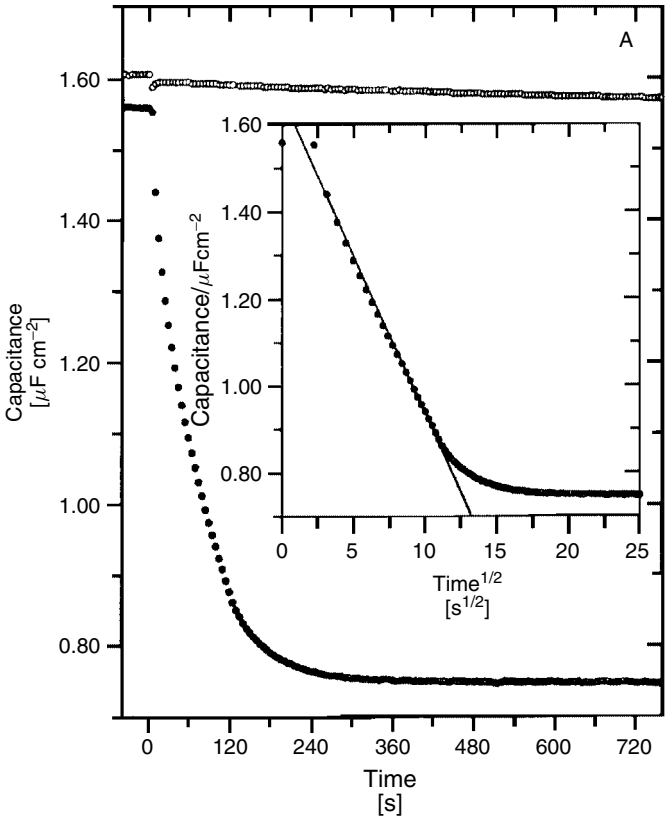


Fig. 4 Lateral flow measurements of oleic and stearic acids at a 1-dodecanethiol modified gold electrode. Plots of the electrode capacitance versus time for a $C_{12}SH$ modified gold electrode prior to and after the application of excess oleic acid (filled circles) and stearic acid (open circles) to the air/water interface. Inset: the capacitance data for oleic acid are plotted versus the square root of time. The solid line is the best fit through the linear portion of the capacitance drop used to calculate the flow parameter (from Ref. 37).

pressure gradients in Gibbs monolayers and the resulting monolayer flow phenomena (referred to as *Marangoni effect*) were investigated by Abbott and coworkers using different methods [42–44].

1.5.3 Two-dimensional Electrochemistry

Unlike in the case of HT electrochemistry, where a planar electrode touches a large section of a Langmuir film on the water surface, two-dimensional, or 2D electrochemistry refers to the methodology in which a "line" microelectrode is placed in the plane of the air/water interface to probe the dynamics of lateral processes that are evolving in a Langmuir monolayer near the line microelectrode [45]. Thus, there is a direct analogy between 2D electrochemistry and classical electrochemical measurements. Just as

a generic planar electrode immersed in a solution of redox species has been used to electrochemically investigate 3D systems, the development of the line microelectrode created the opportunity to study lateral processes in Langmuir and Gibbs monolayer films at the air/water interface.

While the range of problems that can be addressed using 2D electrochemistry is different from those investigated by the classical (3D) electrochemical methods, the 2D electrochemical techniques, cyclic voltammetry, chronoamperometry, and so on, are identical to those known and used to study 3D systems – *except for the reduction of dimensionality*. The latter is a direct result of the ''confinement'' of a chemical system to a quasi-2D Langmuir film [45]. Reduction of dimensionality can be accomplished by substituting the product of the bulk concentration of the electroactive reagent and the electrode surface area (C^*A) appearing in many 3D electrochemical equations, by the product of the surface concentration of the electroactive species and the electrode length ($\Gamma^* l$) to obtain the 2D versions of those equations. Note that the units of C^*A and $\Gamma^* l$ are the same, and thus this substitution does not change the units of the equation where this product appears. For example, the 2D version of the equation expressing the diffusion controlled peak current in cyclic voltammetry (the Randles-Ševčik equation) is:

$$i_p = 2.69x10^5 n^{3/2} D^{1/2} v^{1/2} \Gamma^* l \qquad (2)$$

where D is the diffusion constant and v is the scan rate. When the length of a line microelectrode becomes short relative to the diffusion layer thickness, radial diffusion in 2D sets in. As demonstrated quantitatively by Charych and coworkers, in such cases, one must use cylindrical diffusion equations [46]. As shown in Fig. 5, the reduction of dimensionality eliminates the length dimension of the cylinder. It is also important to note that the diffusion constant defined by the Fick's first law has the same units in 2D as in 3D.

1.5.3.1 Fabrication and Characterization of Line Microelectrodes

The exact positioning of the line electrode in the plane of the air/water interface is of critical importance. It is accomplished by a self-positioning phenomenon involving a sharply defined gradient of wettability at the edge of a gold microband electrode. The drawings shown in Fig. 6 illustrate the fabrication procedure and the positioning of a microelectrode at the air/water interface. Figure 6(a) shows the pattern of the vapor-deposited gold film. It consists

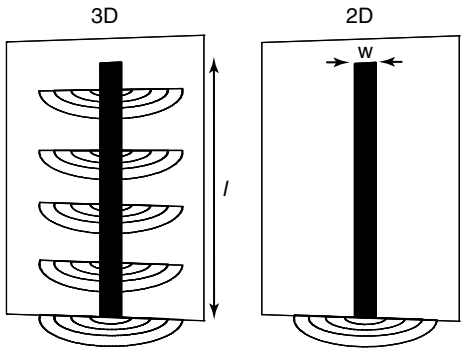


Fig. 5 A cartoon illustrating development of a hemi-cylindrical diffusion profile near a band microelectrode in 3D, and a hemi-circular diffusion profile near a line electrode in 2D experiments. The two types of diffusion processes are analogous. Reduction of dimensionality converts the product of the electrode length (l) and a reagent bulk concentration (C^*) appearing in the cylindrical diffusion equations into the surface concentration (Γ^*): $C^* l \Leftrightarrow \Gamma^*$ (see text and Ref. 46).

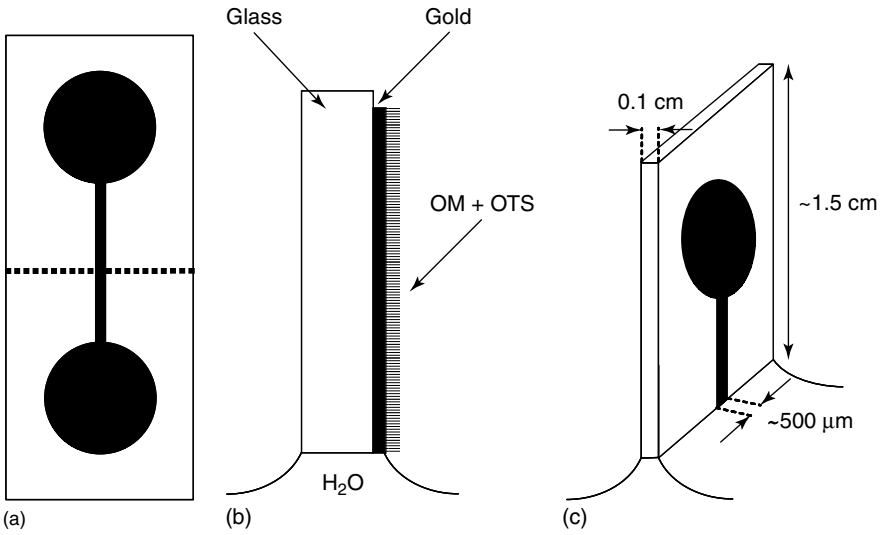


Fig. 6 Design of a line microelectrode and its positioning at the air/water interface. (a) The pattern of vapor-deposited gold on a glass substrate. The dotted line shows the fracture line of the glass slide creating two line electrodes. (b) A side view of one half of the original gold-coated glass slide and its positioning on the water surface. Prior to fracturing, the gold and glass surfaces were coated with monolayers of OM and OTS, respectively. For clarity, only the OM monolayer on the gold surface is shown. (c) A line electrode at the air/water interface.

of two circular areas, later used as electrical contact pads, and a strip of gold (typically 500 μm in width) running between them. The width of the gold strip can be varied from ~1μm to a few millimeters. It determines the length of the line microelectrode. Thoroughly cleaned, standard microscope glass slides (ca. $10 \times 30\ mm^2$) can be used. The detailed fabrication procedure of line electrodes can be found in the literature [46–49]. The major steps include the following: The glass slides are first chemically treated with 3-mercaptopropyltrimethoxysilane (MPS) to form a thin film that assures adhesion of the vapor-deposited gold layer via Au-thiol chemical bonding [50], and results in a substantially lower background current relative to a more commonly used thin Cr under layers. Following vapor deposition of ~100-nm thick gold film, a monolayer of octadecane mercaptan (OM) is self-assembled onto the gold surface. Subsequently, a monolayer of octadecyltrichlorosilane (OTS) is formed on the glass surfaces of the gold-coated electrode substrates. These steps render all the surfaces of the gold-coated substrate hydrophobic (see Fig. 6b). The water contact angles on the treated gold and glass surfaces should be 110–115°. The next step creates two line electrodes: the gold-coated glass slide is fractured in half along a line perpendicular to the gold strip drawn with a diamond pencil on the side of the glass substrate not coated with gold. This exposes clean and therefore hydrophilic edge surfaces of the two halves of the slide. Each of the two halves can be positioned at the air/water interface by touching the water surface with the clean, hydrophilic edge of the electrode substrate as shown in Fig. 6(c). The line of wettability formed spontaneously along the edge of the gold

microband, between the hydrophilic gold cross-sectional area and the hydrophobic (OM-coated) front face of the gold strip, functions as the line electrode. Thus, simple wetting of the gold microband results in self-positioning of the line electrode in the plane of the water surface. The placement of the line electrode at the air/water interface should follow a monolayer spreading and solvent evaporation. Depending on the purity of the water, of the spreading solvent and monolayer samples, as well as on the cleanliness of the entire Langmuir apparatus, stable performance of each line electrode at the air/water interface is reproducible for as long as 30–60 min. Inevitably, however, their performance begins to deteriorate due to adsorption of impurities. This process tends to be irreversible and the electrode must be discarded. Well-behaved line microelectrodes exhibit characteristics consistent with their nominal dimensions. Thus, charging current recorded with a 500-μm long electrode on a 50-mM HNO_3 subphase in a 100 mV s^{-1} voltammetric scan is typically 10 pA [49]. The charge due to the underpotential deposited Pb ad-layer is also commensurate with the geometric cross-sectional area of the Au microband [48].

1.5.3.2 2D Electrochemical Investigations of Langmuir Monolayer Films

The ability to place a line microelectrode in the plane of a monomolecular film at the air/water interface opened the possibility of investigating phenomena intrinsic to this class of chemical systems. While the list given in the following is perhaps not complete as the development of the 2D electrochemical methods continues, it outlines the main areas of research and suggests some future directions.

1.5.3.2.1 Dynamics of the Lateral Diffusion of Surfactants on the Water Surface

The lateral diffusion coefficients (D) of the electrochemically active amphiphiles can be readily measured using 2D chronoamperometry or voltammetry (see Eq. 2 given earlier and the related discussion). To this end, the Langmuir monolayer technique offers accurate and precise means of controlling the surface concentration of the surfactant [2, 7], the necessary parameters to interpret voltammetric current in terms of D. We point out that by generating a gradient of redox species in a Langmuir monolayer, and monitoring current limited by the resulting lateral diffusion, the 2D electrochemical measurements are analogous to the fluorescence photorecovery after photo-bleaching (FRAP) [4, 5, 51]. The latter has been used to probe lateral diffusion of the fluorescently labeled phospholipids in Langmuir monolayers [52] and in supported lipid bilayers and biological membranes [53].

Several amphiphilic derivatives of ferrocene (Fc) [48, 54] and 2,2,6,6-tetramethyl-1-piperidinyloxy free radical [25] were investigated as a function of their surface concentration, the polarity of the group linking the redox moiety to the alkane chain, and the chain length. In all cases, the lateral diffusion constant was found to decrease with the increasing surface concentration suggesting that the monolayer viscosity is an important parameter. This behavior results in linear plots of D versus MMA, as shown in Fig. 7 featuring data for several Fc-dodecane amphiphiles with different polar groups [54]. We also learned from these results that the head group polarity is the second important parameter. Those Fc derivatives with more polar groups such as amide diffuse slower than Fc ester derivatives carrying the least polar head group moiety in this group

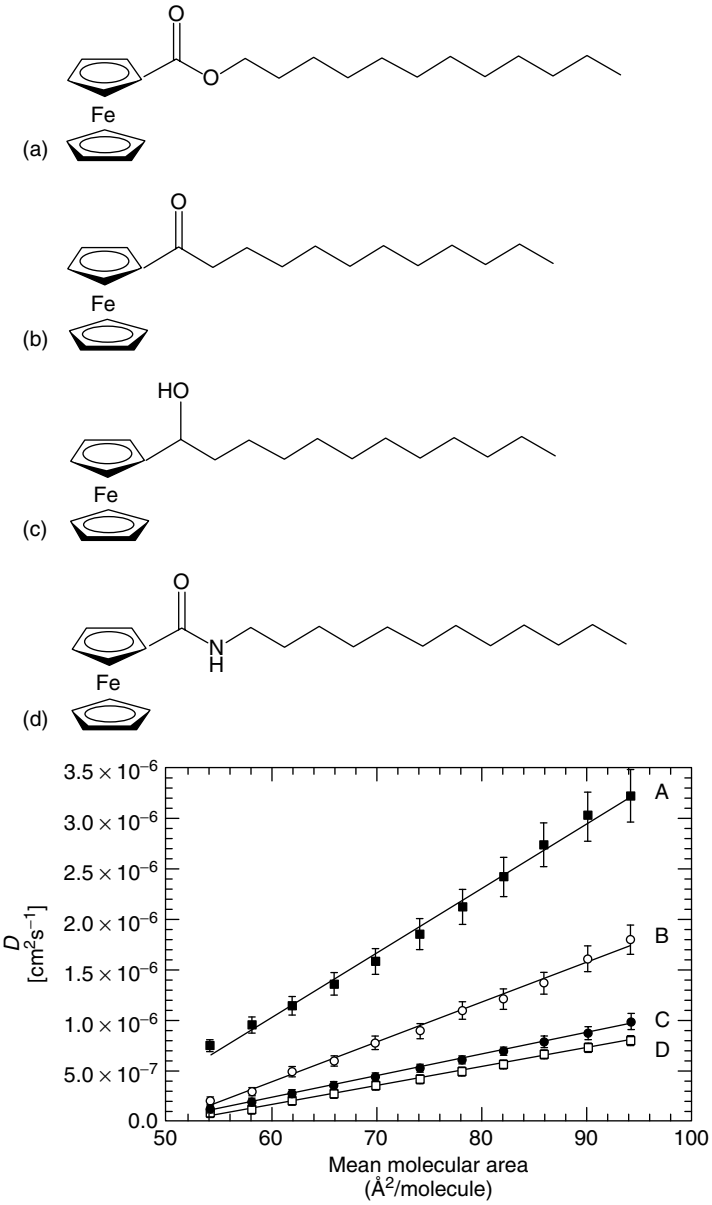


Fig. 7 Structures of four ferrocene amphiphiles with different head group polarities and the corresponding plots of their lateral diffusion constants versus MMA obtained using 2D electrochemistry on the water surface (1 M $HClO_4$) at 26 °C (from Ref. 54).

of compounds. The latter observation also suggests that surfactant's polar group is at least partially immersed in the subphase, and that the immersion depth is yet another parameter influencing lateral mobility. The notion that the polar groups of surfactants are immersed in water was proven by observing a linear correlation of D values with the inverse of the subphase viscosity [54]. The latter was varied by adding glycerol, a surface inactive compound, to the subphase solutions.

The surface concentration dependence of the lateral mobility of Fig. 7 was analyzed in terms of the free-volume theory of hard sphere liquids of Cohen and Turnbull [55, 56], as well as in view of the Enskog theory of dense gases [57] extended by Alder's molecular dynamics calculations to liquid densities [58]. The latter approach was particularly successful. It revealed that the lateral diffusion constant of the Fc amphiphiles does follow the expected linear dependence on the relative free area, A_f/A_0, where $A_f = A - A_0$, $A =$ MMA, and A_0 is the molecular area of a surfactant molecule. It also revealed that the slope of this dependence which is expected to inversely depend on the molecular mass of a diffusing particle, was more than 3 orders of magnitude smaller [54]. Clearly, this discrepancy is due to the effect of the viscous drag of the polar head groups in water, a factor not included in the Enskog theory.

Finally, the effect of the alkane chain length was also investigated in the Fc-amide series covering the range of 12 to 16 carbon atoms (see Fig. 8) [54]. Counter intuitively, those Fc-amide derivatives with longer chain length exhibited slightly larger diffusivities. Similar observation was reported recently in the case of viologen surfactants [59]. To account for these results, we invoked the Saffman and Delbrück theory [60–62]. It concerns quasi 2D diffusion of a cylinder-like particle of height, h, in a slab of the same height and a certain viscosity bounded by a medium of a different viscosity. The theory was developed to treat protein diffusion in lipid bilayers [60], but it was also used to analyze lipid diffusion in membranes [63]. Using this theoretical model, the anomalous chain length dependence of Fig. 8 was related to the modulation of the amide group immersion depth by chain–chain interactions. Specifically, our data analysis yielded the immersion depths of the C_{16}–Fc-amide and C_{12}–Fc-amide to be 4.0 Å and 6.4 Å, respectively. These values depended neither on the surface concentration of the Fc surfactants nor on the viscosity of subphase. This treatment of the experimental data also showed that over 90% of the viscous drag experienced by a surfactant molecule diffusing in a Langmuir monolayer is due to its immersion in the aqueous subphase, and only a small fraction originates in the monolayer's hydrocarbon region. As expected, the former does decrease slightly with increasing MMA.

The data discussed earlier concerned the lateral mobility in the liquid region of the Langmuir films spanning a range of MMAs of ca. 50–100 Å^2/molecule. Our inability to probe surfactants' mobilities at lower surface concentration was related to the liquid/gas (L/G) phase transition, as discussed in Sect. 1.5.3.2.2. A far more complete picture regarding surfactants lateral mobility was obtained for the 2,2,6,6-tetramethyl-1-piperidinyloxy free radical (Tempo) derivatives, which are supercritical fluids at room temperature and thus do not undergo a L/G phase transition [49, 64, 65]. (See the structure of **C $_{16}$ Tempo**.)

The discovery of the supercritical nature of the Tempo surfactants (see

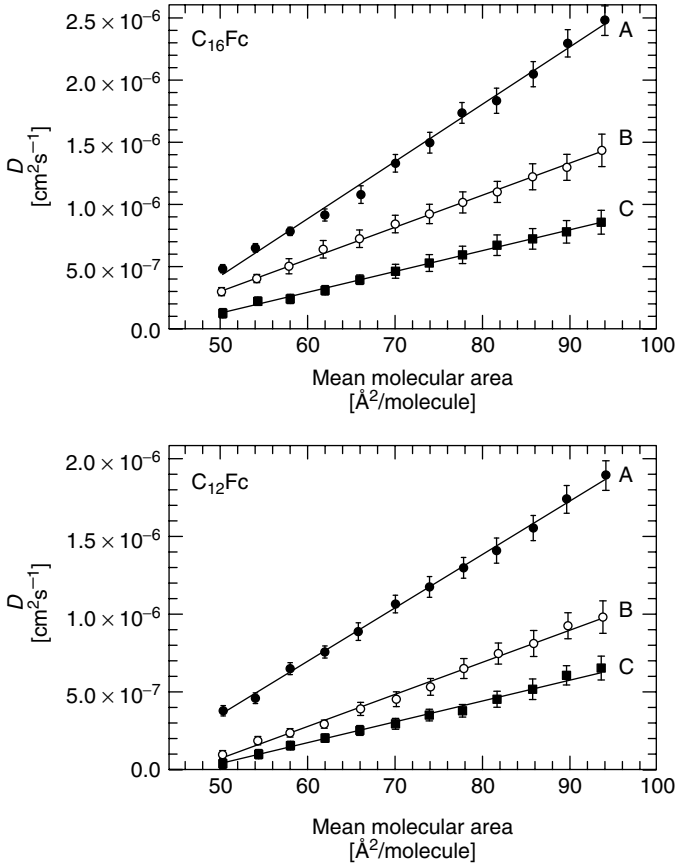
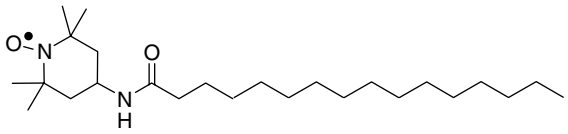


Fig. 8 Plots of the lateral *D* values of the ferrocene-amide derivatives (see structure **D** in Figure 7), $C_{16}Fc$ and $C_{12}Fc$ vs. MMA measured on the 0.05 M $HClO_4$ subphase containing (A) 0, (B) 20, and (C) 40 wt% glycerol. The viscosities of these solutions were 1.1, 1.9, and 3.7 cP, respectively (from Ref. 54).



Sect. 1.5.3.2.2) allowed us to measure their lateral mobility in a far broader range of surface concentrations, as shown in Fig. 9. This range is extended to MMAs as high as 800 $Å^2$/molecule [25, 65].

Comparison of the data obtained for three different Tempo derivatives with the chain length ranging from C_8 to C_{18} shows essentially no differences in the lateral mobility [25]. We concluded that

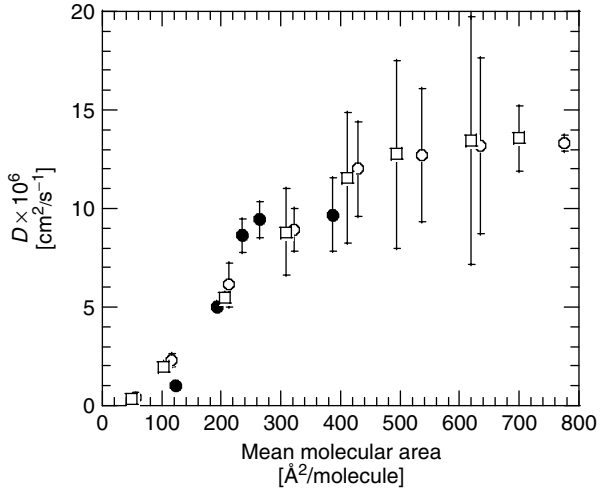


Fig. 9 Plot of the lateral diffusion constants versus MMA of C_8Tempo (closed circles), C_{14}Tempo (open circles), and C_{18}Tempo (open squares) (adapted from Ref. 25).

their mobility is limited primarily by the viscous coupling of their polar fragments to water, and their surface concentration, but not by the chain–chain interactions. The increase of the D values with mean molecular area of the surfactants in Fig. 9 reflects the decreasing effective viscosity of the monolayer in the head group region as the concentration of the diffusing particles decreases. This effect was observed in the Fc studies [54] and is consistent with the behavior of particle–fluid suspensions [66, 67]. We also point out that this result is not inconsistent with the ferrocene-amide surfactant data of Fig. 8, since in that case, a significantly higher concentration range was investigated, and the effect was related to the dependence of the surfactant's immersion depth on the chain length and not directly to the chain–chain interactions. Finally, it is interesting to point out the change of the slope of the D versus MMA plot in Fig. 9 at higher MMAs. This phenomenon is perhaps related to the change in the dynamics of intermolecular collisions. In the limit of very low surface concentrations, the surfactant mobility appears to be limited solely by the viscous coupling of the polar head group to the subphase. This suggests that the analysis of the lateral diffusivities of surfactants with known and shallow immersion depths can reveal the dynamic properties of the water liquid/gas interfacial region.

To this end, we have recently examined the orientation of C_{18}Tempo on the water surface using X-ray reflectivity [65]. As shown earlier, this water insoluble surfactant features two polar fragments located on the opposite ends of the hydrophobic piperidine ring, the nitroxide (>N−O), and the amide that serves as a linking group between Tempo and the alkane chain. Analysis of the various conformations of this head group suggested that it is not possible for both the nitroxide and amide groups to be immersed in water without also immersing a large fragment of the piperidine ring. The latter

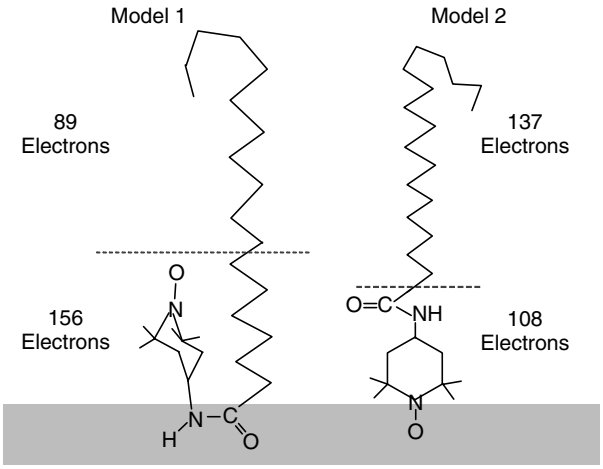


Fig. 10 Schematic representation of two different conformations of C_{18}Tempo at the air/water interface at 52 Å^2/molecule. These were proposed assuming that either the amide group (Model 1) or the nitroxy group (Model 2) is hydrated. Within each model, the dotted line separates the molecule into two ''boxes'' with different numbers of electrons shown in the figure (see text; from Ref. 65).

is likely energetically too costly. Thus, we postulated that only one of the two polar fragments is immersed. The detailed account of these measurements is beyond the scope of this review, and are presented elsewhere [65]. Briefly, we report here on the X-ray reflectivity measurements at a single pressure of 21 mN m^{-1} (corresponding to an MMA of 52 Å^2/molecule), and present the key result that allowed us to distinguish between two opposing confirmations of C_{18}Tempo on the water surface. These are shown schematically in Fig. 10 where Model 1 assumes the dominance of the amide group and Model 2 assumes the dominance of the nitroxide group as the polar fragment immersed in the aqueous subphase. X-ray reflectivity is a technique sensitive to the gradient of the electron density in a molecular film at an interface [68, 69]. Consequently, we deconstruct the two C_{18}Tempo conformations of Fig. 10 into a stack of two boxes containing a different number of electrons (also shown in the figure). This allowed us to simulate the X-ray reflectivity response and to compare the two models with the experimental results. The comparison is shown in Fig. 11. It is clear that Model 1, assuming immersion of the amide group, offers a significantly better agreement with the measurements as quantitatively reflected in a much smaller χ^2 value (6.2 vs. 26.1).

Recently, we have also examined 2,2,6,6-tetramethyl-1-piperidinyloxy, Tempo itself, a weak, water-soluble surfactant [70]. Our investigations suggested that, as it diffuses along the air/water interface, Tempo is coupled to the interfacial region via a single water molecule hydrogen-bonded to its oxygen atom. A large lateral diffusion constant of Tempo (1.5×10^{-4} cm^2 s^{-1}) indicated that the air/water interfacial region is as much as four times less viscous than the bulk water [70]. While this result

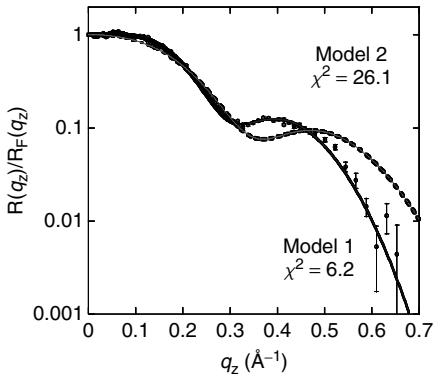


Fig. 11 X-ray reflectivity data for C_{18}TEMPO at 21 mN m^{-1} at 21 °C (points with error bars). The solid and the dashed lines are fits to the data using the box models discussed in the text and shown in Figure 10 (from Ref. 65).

is still somewhat preliminary, it gives the first direct experimental assessment of the dynamic nature of the aqueous interfacial region. Furthermore, these results illustrate how 2D voltammetry of shallowly immersed surfactants can contribute to the investigations of this important interfacial system.

1.5.3.2.2 Measurements of the LE/G Phase Transitions and their Critical Temperature

Characterization of the phase behavior of Langmuir monolayers, and particularly its relationship to the lipid's molecular structure, is of fundamental importance to the understanding of their behavior. Recent work involving monolayer X-ray diffraction methods [71] and BAM [12, 13] led to a rapid progress in the structural characterization of ordered condensed phases of Langmuir films of numerous types of lipids. In comparison, the issues concerned with liquid, specifically liquid expanded (LE), and gaseous monolayer states and the related phase transitions and critical phenomena have not been systematically studied. Johnson and coworkers reported recently that a line electrode residing in the plane of the air/water interface is a sensitive sensor of the onset of an LE/G phase transition [64]. This sensing behavior is illustrated in Fig. 12, where sudden disappearance of cyclic voltammetric signal due to oxidation of a tetradecane ferroceneketone (C_{14}Fc) was observed during its monolayer expansion over just 3 Å^2/molecule near LE/G phase transition. The phenomenon is reversible upon monolayer recompression. This and later experiments carried out with the Tempo surfactants [49] showed that a line electrode functions as the monolayer gas phase nucleating site. This property, not unlike the well-known "boiling chip" phenomenon, apparently involves preferential wetting of the line electrode with the freshly nucleated bubble of the 2D gas phase and results in loss of electrochemical signal. The latter is due to the fact that the amphiphile's concentration in the gas phase is much smaller than that in the corresponding LE phase. Line electrodes were found to be very sensitive and reproducible sensors capable of indicating the position of the LE/G phase transition. Using this new 2D electrochemical capability, Johnson and coworkers determined the position of the C_{22}Tempo LE/G phase transition to be 98.5 ± 0.5 Å^2/molecule at 23.5 °C [49]. Brewster angle microscopy was employed to verify this measurement. A set of BAM micrographs recorded near the LE/G transition of C_{22}Tempo is shown

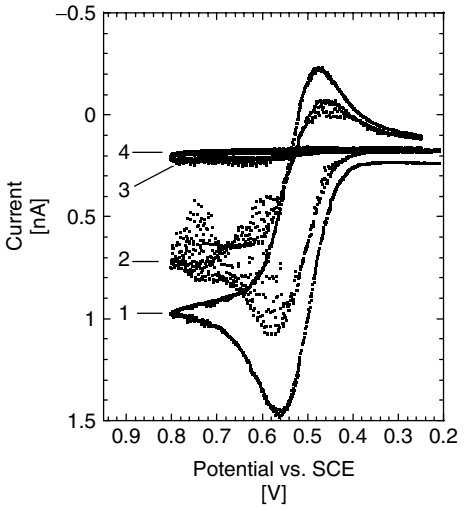


Fig. 12 A set of four consecutive 2-D voltammograms recorded during a slow expansion of a C_{14}Fc keton monolayer on a 50-mM $HClO_4$ subphase. The mean molecular areas corresponding to the voltammogram 1–4 are: 65, 66, 67, and 68 Å^2/molecule, respectively. The *i-E* curves were recorded with a 500-µm line microelectrode at 0.2 V s^{-1}. The disappearance of the voltammetric signal at 66–67 Å^2/molecule is due to the onset of the LE/G phase transition (adapted from Ref. 64).

in Fig. 13. Indeed, careful observation of the texture of a Langmuir monolayer at each stage of its gradual expansion allows one to determine the position of the phase transition. However, in comparison with BAM, 2D electrochemistry was proven to be not only equally accurate but more precise, reliable, and convenient. It is also free of false negative type measurements intrinsic to the BAM observations. Johnson and coworkers also measured the critical temperature of C_{20}Tempo to be 28 °C [49]. All shorter chain Tempo derivatives were found to be supercritical at temperatures down to 0 °C. The molecular origin of this rather unusual phenomenon was postulated to involve rotation of the Tempo head group leading to an increase of its cross-sectional area, and the resulting decrease of the chain–chain interactions [49]. In other words, the ability of Tempo to change its orientation at the air/water interface during monolayer expansion results in the shortening of the effective length of its hydrocarbon chain and thus in a decrease of the cohesive van der Waals interactions normally associated with a LE/G phase transition. This hypothesis was supported by the surface potential measurements [49] and by recent X-ray reflectivity data [72].

1.5.3.2.3 **Kinetics of Electron Hopping in Langmuir Monolayers** Rapid electron exchange between adjacent molecules of different oxidation states in a Langmuir film is an alternative mechanism of the lateral, diffusive charge transport. Electron hopping may proceed in parallel and compete with translational diffusion. For example, in the case of Fc surfactants, we showed that the ferrocene rate constant of self exchange is not high enough for the electron hopping process to compete with the observed surfactants lateral diffusion (see Sect. 1.5.3.2.1) even under the conditions of high surface concentrations, where the rate of the Fc translational diffusion is at a minimum, and where the electron hopping transport is most effective. Consequently, no increase of the voltammetric current due to translational diffusion was observed rendering

characterization of the hopping process impossible [48].

Electron hopping was unambiguously observed in solid monolayer films of osmium tris-4,7-diphenyl-1,10-phenanthroline perchlorate ($Os(DPP)_3$) [73–77]. Upon spreading of this large, nonamphiphilic osmium complex on the water surface, $Os(DPP)_3$ forms 2D solid aggregates that can be imaged by BAM (see Fig. 14). The onset of 2D voltammetric activity coincides with the rise of the surface pressure during compression of the $Os(DPP)_3$ monolayer. Unlike in the cases of Fc [54] and Tempo surfactants [25], where 2D voltammetric current decreased with increasing surface concentration in response to the increasing monolayer viscosity, the opposite effect of the monolayer compressing was observed in this case, as can be seen in Fig. 15 [75]. This effect was conclusively related to the electron hopping percolation [78, 79]. Upon compression of the solid aggregates of $Os(DPP)_3$, their mutual connectivity increases resulting in an increase of the extent of the electroactivity of the entire film. A quantitative agreement with 2D percolation theory was demonstrated by plotting the normalized apparent diffusion constant due to electron hopping obtained from the electrochemical measurements of Fig. 15 versus the fractional surface concentration of $Os(DPP)_3$ on the water surface. Three such plots, corresponding to the 2D experiments carried out with the line electrodes of increasing length, are shown in Fig. 16. It is interesting to note that when line electrodes with a length comparable to the aggregate size are used, on–off type behavior that deviates from the percolation theory is observed. However, when the hopping dynamics is averaged over sufficiently large areas of this 2D system, by using line electrodes with lengths

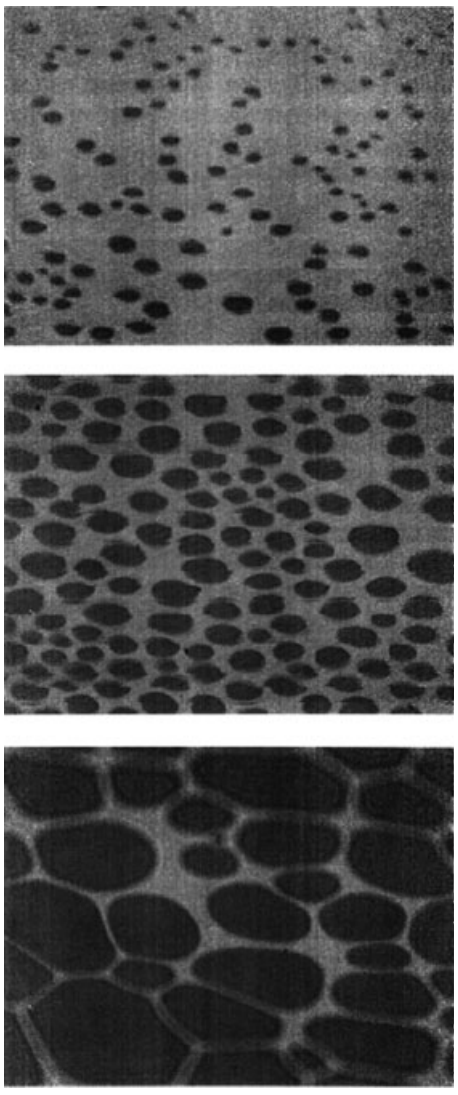


Fig. 13 Brewster angle micrographs of C_{22}TEMPO monolayer recorded at (from top to bottom) 99, 105, and 130 $Å^2$/molecule, on a 50-mM HNO_3 subphase at 23.5 °C. The length of the horizontal edges of these images corresponds to 430 µm (from Ref. 49).

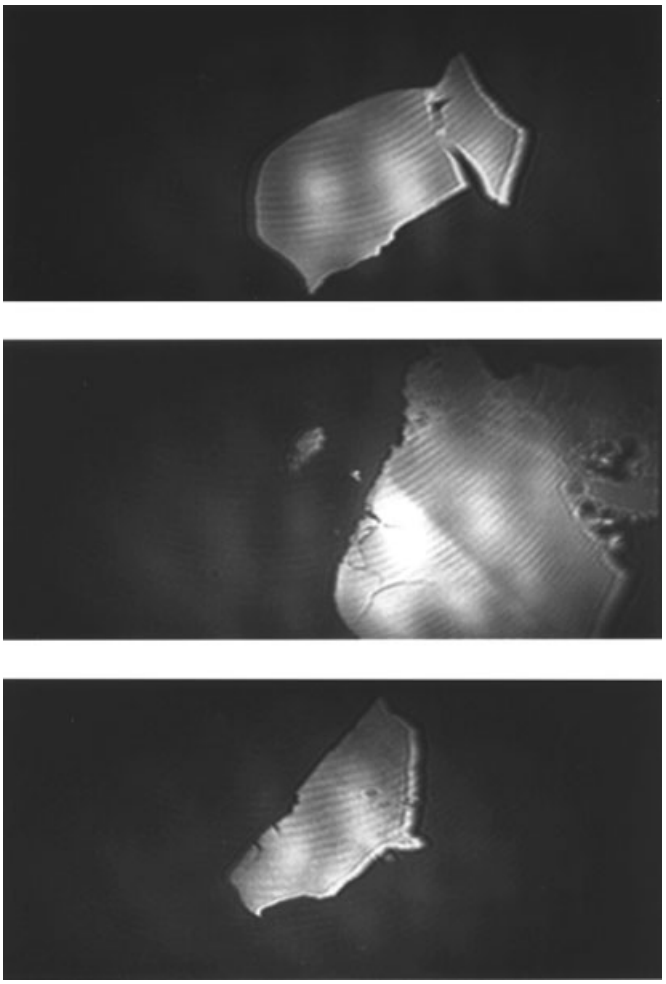


Fig. 14 Three Brewster angle microscopic images of $Os(DPP)_3$ monolayer on a 50-mM $HClO_4$ subphase recorded at 360 $Å^2$/molecule showing typical shapes and sizes of 2D aggregates formed on the water surface upon spreading. The length of the vertical edges of these images corresponds to 730 mm (from Ref. 75).

that are large compared to the average aggregate size, the system's behavior reflects predictions of the 2D percolation theory [75].

In order to interpret the maximum value of the lateral diffusion constant in terms of the electron transfer–rate constant, we first carried out structural characterization of the $Os(DPP)_3$ films by grazing incidence angle X-ray diffraction [71]. These measurements showed that the $Os(DPP)_3$ forms a hexagonal lattice in the plane of the air/water interface. The lattice spacing of 10.89 Å gave the Os—Os distance of 12.57 Å [75]. It is interesting to compare the 2D crystal structure of

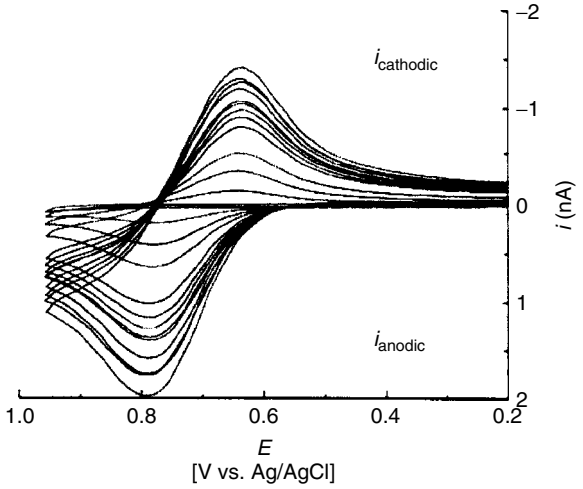


Fig. 15 A set of 2D cyclic voltammograms of $Os(DPP)_3$ monolayer at the air/water interface recorded concurrently with the monolayer compression. The CVs were recorded with a single 400-μm line microelectrode at a scan rate of 0.2 V s^{-1}. Increasing current corresponds to decreasing mean molecular area of $Os(DPP)_3$ from ca. 120 to 90 $Å^2$/molecule (from Ref. 75).

$Os(DPP)_3$ with the isostructural $Ru(DPP)_3$ complex described in the literature [80]. In 3D, $Ru(DPP)_3$ chloride crystallizes in a monoclinic space group $P2_{1/c}$ with the distances between nearest Ru−Ru neighbors range from 13.085 to 16.576 Å. Thus, the 2D crystal structure features a higher symmetry unit cell and shorter (12.57 Å) metal–metal spacing.

With these data in hand, the maximum value of the electron hopping diffusion constant, $D = 1.8 \times 10^{-6}$ cm^2 s^{-1}, can be interpreted to yield the unimolecular rate constant (k_1) of electron transfer between adjacent $Os(DPP)_3$ sites according to the following equation:

$$D = \tfrac{1}{4} k_1 r^2 \qquad (3)$$

This gives $k_1 = 4.7 \times 10^8$ s^{-1} [75]. The latter corresponds to the bimolecular rate constant of electron exchange k_{ex} of 2.8×10^8 $M^{-1}s^{-1}$. It was obtained relying on the precursor complex model in which k_{ex} is expressed as a product of k_1 and K_p, a precursor complex "equilibrium constant" [48, 81]. This assessment of the electron hopping kinetics involved an assumption of complete electroactivity of all $Os(DPP)_3$ sites in the Langmuir monolayer. However, compression of the 2D aggregates imaged in Fig. 14 likely results in defects at the domain boundaries, which may make that assumption uncertain.

A more accurate measurement of the electron hopping diffusion constant, and of the related k_{ex}, that did not require the assumption of 100% electroactivity of the $Os(DPP)_3$ film, was obtained with a novel 2D electrochemical technique relying on a tandem of two collinear 40 μm long line microelectrodes spaced by 10 μm and acting as a generator probe and a collector probe. In this method, referred

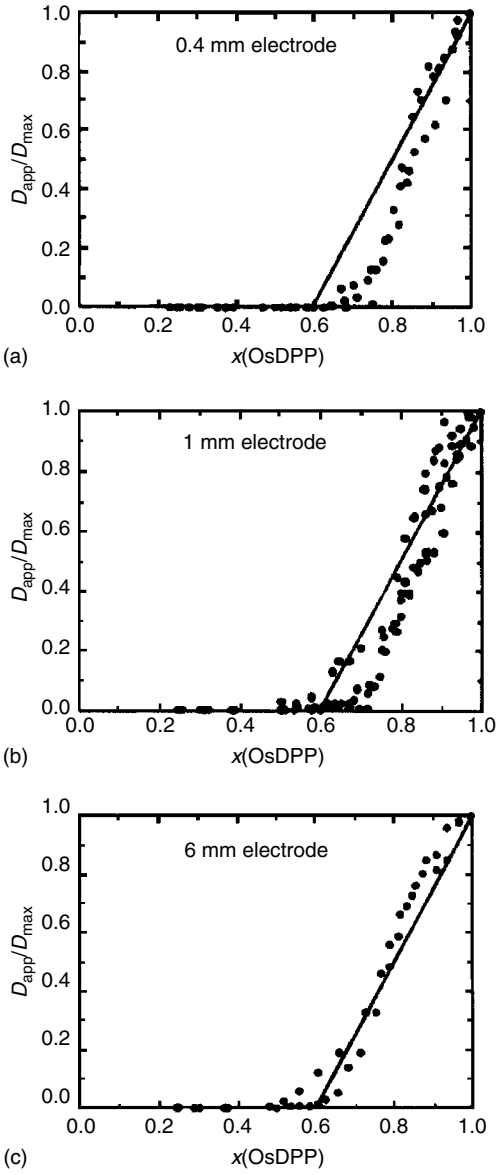


Fig. 16 The plots of D_{app}/D_{max} vs. $X(Os(DPP)_3)$ obtained on the basis of several series of cyclic voltammetric experiments as those in Figure 13 carried out with 0.4, 1.0, and 6.0 mm long line microelectrodes (from Ref. 75).

to as 2D electrochemical time-of-flight (2D ETOF), one line electrode generated $Os(DPP)_3$ (III+) species and the other, held at the reducing potential, monitored their diffusive arrival rate [77]. Naturally, the diffusion of $Os(DPP)_3$ (III+) species physically involved electron hopping process. While the experimental details of 2D ETOF are beyond the scope of this review, one important advantage of this method worth mentioning here is that it does not require surface concentration of

redox species as an input parameter to interpret the experimental $i-t$ transients. These experiments carried out by Wittek and coworkers showed that only 73% of all the $Os(DPP)_3$ species are electrochemically active and participate in the electron hopping process [77]. We argued that the remaining, nonactive sites are in the regions near grain boundaries of the 2D aggregates. This measurement allowed us then to recalculate the rate constant of electron hopping. We obtained $k_{ex} = 1.0 \times 10^9\ M^{-1}\ s^{-1}$ which is more than 1 order of magnitude higher than a literature value obtained for $Os(DPP)_3$ (III+/II+) couple in an acetonitrile solution [82]. This rather substantial enhancement of the electron-transfer kinetics in a solid $Os(DPP)_3$ monolayer could be due to one or both of the following factors. (1) The distances between the osmium centers and a particular alignment of the DPP ligands could result in a higher electronic coupling between Os(II) and Os(III) relative to those prevailing when these ions collide and exchange an electron in a homogeneous solution. (2) The reorganization energy of the $Os(DPP)_3$ molecules in a monolayer at the water surface could be smaller due to a partial solvation.

Solvation of the $Os(DPP)_3$ molecules in its Langmuir monolayer and the dynamic solvent effects on electron hopping kinetics were investigated by Charych and coworkers in a set of solvent exchange experiments [74]. These involved incremental addition of aliquots of a polar, organic solvent to the aqueous subphase supporting a compressed $Os(DPP)_3$ monolayer on its surface. Following each addition and equilibration, a 2D voltammogram was recorded to measure the rate constant of electron transfer (see Eq. 3). This sequence of solvent additions and 2D voltammogram recordings was continued until the rate constant achieved a new constant value forecasting a complete resolvation of the $Os(DPP)_3$ molecules. The effect of five solvents on electron-transfer kinetics was investigated. Addition of some solvents such as acetonitrile resulted in an increase of the electron hopping kinetics. Other solvents such as benzonitrile had the opposite effect. Charych and coworkers analyzed these measurements in terms of Marcus theory. This revealed a good correlation between the nuclear frequency factor, extracted from the measured values of the electron-transfer rate constant and the inverse longitudinal relaxation time of the solvents used in the solvent exchange experiments [74]. This correlation is consistent with a highly adiabatic character, or in other words, a strong electronic coupling existing between the $Os(DPP)_3$ molecules in their 2D solid aggregates discussed by Wittek et al. [77].

Acknowledgments

The author gratefully acknowledges donors of the Petroleum Research Fund, administered by the ACS for partial support of his research. Additional support has been provided by the National Science Foundation.

References

1. A. Braslau, M. Deutsch, P. S. Pershan et al., *Phys. Rev. Lett.* **1985**, *54*, 114–117.
2. G. L. J. Gaines, *Insoluble Monolayers at Liquid-Gas Interfaces*, Wiley-Interscience, New York, 1966.
3. A. W. Adamson, *Physical Chemistry of Surfaces*, 4th edition, John Wiley & Sons, New York, 1982.
4. C. M. Knobler, C. D. Rashmi, *Annu. Rev. Phys. Chem.* **1992**, *43*, 207–236.
5. C. M. Knobler, *Science* **1990**, *249*, 870–874.
6. H. Möhwald, *Annu. Rev. Phys. Chem.* **1990**, *41*, 441–476.

7. M. C. Petty, *Langmuir-Blodgett Films: An Introduction*, Cambridge University Press, Cambridge, UK, 1996.
8. S. S. Dukhin, G. Kretzschmar, R. Miller, *Dynamics of Adsorption at Liquid Interfaces. Theory, Experiment, Application*, Elsevier, Amsterdam, 1995.
9. D. A. Cadenhead, Monomolecular films as biomembrane models in *Structure and Properties of Cell Membranes. Methodology and Properties of Membranes* (Ed.: G. Benga), CRC Press, Boca Raton, 1985, pp. 21–62, Vol. 3.
10. G. Roberts, *Langmuir-Blodgett Films*, Plenum Publishing Corporation, New York, 1990.
11. V. Vogel, D. Möbius, *J. Colloid Interface Sci.* **1988**, *126*, 408–420.
12. S. Henon, J. Meunier, *Rev. Sci. Instrum.* **1991**, *62*, 936–939.
13. D. Hönig, D. Mobius, *J. Phys. Chem.* **1991**, *95*, 4590–4592.
14. S. Cannan, J. Zhang, F. Grunfeld et al., *Langmuir* **2004**, *20*, 701–707.
15. J. Zhang, A. L. Barker, D. Mandler et al., *J. Am. Chem. Soc.* **2003**, *125*, 9312–9313.
16. J. Zhang, P. R. Unwin, *J. Am. Chem. Soc.* **2002**, *124*, 2379–2383.
17. J. Zhang, C. J. Slevin, C. Morton et al., *J. Phys. Chem. B* **2001**, *105*, 11120–11130.
18. I. Langmuir, V. J. Schaefer, *J. Am. Chem. Soc.* **1938**, *60*, 1351–1360.
19. R. E. Pagano, I. R. Miller, *J. Colloid Interface Sci.* **1973**, *45*, 126–137.
20. I. R. Miller, J. Rishpon, A. Tenenbaum, *Bioelectrochem. Bioenerg.* **1976**, *3*, 528–542.
21. M. Fujihira, T. Araki, *Chem. Lett.* **1986**, *15*, 921.
22. X. Zhang, A. J. Bard, *J. Am. Chem. Soc.* **1989**, *111*, 8098–8105.
23. C. J. Miller, P. McCord, A. J. Bard, *Langmuir* **1991**, *7*, 2781–2787.
24. C. J. Miller, A. J. Bard, *Anal. Chem.* **1991**, *63*, 1714–1719.
25. A. D. Malec, D. G. Wu, M. Louie et al., *Langmuir* **2004**, *20*, 1305–1310.
26. J. J. Noöl, D. Bizzotto, J. Lipkowski, *J. Electroanal. Chem.* **1993**, *344*, 343–354.
27. D. Bizzotto, J. J. Noöl, J. Lipkowski, *Thin Solid Films* **1994**, *248*, 69–77.
28. D. Bizzotto, J. J. Noöl, J. Lipkowski, *J. Electroanal. Chem.* **1994**, *369*, 259–265.
29. D. Bizzotto, J. Lipkowski, *J. Electroanal. Chem.* **1996**, *409*, 33–43.
30. D. Bizzotto, J. Lipkowski, *Prog. Surf. Sci.* **1996**, *50*, 237–246.
31. D. Bizzotto, J. Lipkowski, *Prog. Colloid Polym. Sci.* **1997**, *103*, 201–215.
32. I. Zawisza, I. Burgess, G. Szymanski et al., *Electrochim. Acta* **2004**, *49*, 3651–3664.
33. T. Sagara, V. Zamlynny, D. Bizzotto et al., *Isr. J. Chem.* **1997**, *37*, 197–211.
34. D. Bizzotto, B. Pettinger, *Langmuir* **1999**, *15*, 8309–8314.
35. D. Bizzotto, E. Wong, Y. Yang, *J. Electroanal. Chem.* **2000**, *480*, 233–240.
36. J. Shepherd, Y. Yang, D. Bizzotto, *J. Electroanal. Chem.* **2002**, *524–525*, 54–61.
37. A. B. Steel, B. J. Cheek, C. J. Miller, *Langmuir* **1998**, *14*, 5479–5486.
38. V. Zamlynny, I. Burgess, G. Szymanski et al., *Langmuir* **2000**, *16*, 9861–9870.
39. A. B. Steel, C. J. Miller, *Langmuir* **1996**, *12*, 4243–4248.
40. B. J. Cheek, A. B. Steel, C. J. Miller, *Langmuir* **2000**, *16*, 10334–10339.
41. A. B. Steel, B. J. Cheek, C. J. Miller, *Langmuir* **2001**, *17*, 7851–7856.
42. B. S. Gallardo, V. K. Gupta, F. D. Eagerton et al., *Science* **1999**, *283*, 57–60.
43. B. S. Gallardo, K. L. Metcalfe, N. L. Abbott, *Langmuir* **1996**, *12*, 4116–4124.
44. D. E. Bennett, B. S. Gallardo, N. L. Abbott, *J. Am. Chem. Soc.* **1996**, *118*, 6499–6505.
45. M. Majda in *Thin Films, Organic Thin Films and Surfaces. Directions for the Nineties* (Ed.: A. Ulman), Academic Press, San Diego, 1995, pp. 331–347, Vol. 20.
46. D. H. Charych, C. A. Goss, M. Majda, *J. Electroanal. Chem.* **1992**, *323*, 339–345.
47. C. A. Widrig, C. J. Miller, M. Majda, *J. Am. Chem. Soc.* **1988**, *110*, 2009–2011.
48. D. H. Charych, E. M. Landau, M. Majda, *J. Am. Chem. Soc.* **1991**, *113*, 3340–3346.
49. M. J. Johnson, C. Majmudar, J. J. Skolimowski et al., *J. Phys. Chem. B* **2001**, *105*, 9002–9010.
50. C. A. Goss, D. H. Charych, M. Majda, *Anal. Chem.* **1991**, *63*, 85–88.
51. H. M. McConnell, *Annu. Rev. Phys. Chem.* **1991**, *42*, 171–195.
52. R. Peters, K. Beck, *Proc. Natl. Acad. Sci. U. S. A.* **1983**, *80*, 7183–7187.
53. R. Lipowsky, E. Sackmann, *Structure and Dynamics of Membranes*, Elsevier, Amsterdam, 1995, Vol. 1A and 1B.
54. Y.-S. Kang, M. Majda, *J. Phys. Chem. B* **2000**, *104*, 2082–2089.
55. M. H. Cohen, D. Turnbull, *J. Chem. Phys.* **1959**, *31*, 1164–1169.

56. D. Turnbull, M. H. Cohen, *J. Chem. Phys.* **1970**, *52*, 3038–3041.
57. H. J. V. Tyrrell, K. R. Harris, *Diffusion in Liquids, A Theoretical and Experimental Study*, Butterworth, London, 1984, p. 266, Vol. 5.
58. B. J. Alder, D. M. Gass, T. E. Wainwright, *J. Chem. Phys.* **1970**, *53*, 3813–3826.
59. D. K. Lee, Y. S. Kang, *J. Phys. Chem. B* **2004**, *108*, 4063–4070.
60. P. G. Saffman, M. Delbrück, *Proc. Natl. Acad. Sci. U.S.A.* **1975**, *72*, 3111–3113.
61. P. G. Saffman, *J. Fluid Mech.* **1976**, *73*, 593–602.
62. B. D. Hughes, B. A. Pailthorpe, L. R. White, *J. Fluid Mech.* **1981**, *110*, 349–372.
63. B. D. Hughes, B. A. Pailthorpe, L. R. White et al., *Biophys. J.* **1982**, *37*, 673–676.
64. M. J. Johnson, D. J. Anvar, J. J. Skolimowski et al., *J. Phys. Chem. B* **2001**, *105*, 514–519.
65. D. G. Wu, A. Malec, J. Majewski et al., *Electrochim. Acta* **2005**, in press.
66. A. J. C. Ladd, *J. Chem. Phys.* **1990**, *93*, 3484–3494.
67. R. A. Lionberger, W. B. Russel in *Advances in Chemical Physics* (Eds.: I. Prigogine, S. A. Rice), John Wiley & Sons, New York, 2000, pp. 399–474, Vol. 111.
68. J. Als-Nielsen, K. Kjaer, *Proceedings of the NATO Advanced Study Institute, Phase Transitions in Soft Condensed Matter, Geilo, Norway, April 4–14, 1989*, Plenum Publishing Corporation, New York, 1989.
69. K. Kjaer, *Physica B* **1994**, *198*, 100–109.
70. D. G. Wu, A. Malec, M. Head-Gordon et al., *J. Am. Chem. Soc.* **2005**, *127*, 4490–4496.
71. J. Als-Nielsen, D. Jackuemain, K. Kjaer et al., *Phys. Rep.* **1994**, *246*, 251–313.
72. D. G. Wu, A. Malec, J. Majewski et al., *Electrochim. Acta* **2005**, in press.
73. D. H. Charych, M. Majda, *Thin Solid Films* **1992**, *210–211*, 348–351.
74. D. H. Charych, D. J. Anvar, M. Majda, *Thin Solid Films* **1994**, *242*, 1–6.
75. W.-Y. Lee, M. Wittek, G. Brezesinski et al., *J. Phys. Chem. B* **1999**, *103*, 6950–6956.
76. R. J. Forster, T. E. Keyes, M. Majda, *J. Phys. Chem. B* **2000**, *104*, 4425–4432.
77. M. Wittek, G. Müller, M. J. Johnson et al., *Anal. Chem.* **2001**, *73*, 870–877.
78. D. N. Blauch, J.-M. Savéant, *J. Am. Chem. Soc.* **1992**, *114*, 3323–3332.
79. D. N. Blauch, J.-M. Savéant, *J. Phys. Chem.* **1993**, *97*, 6444–6448.
80. B. M. Goldstein, J. K. Barton, H. M. Berman, *Inorg. Chem.* **1986**, *25*, 842–847.
81. J. T. Hupp, M. J. Weaver, *J. Electroanal. Chem.* **1983**, *152*, 1–14.
82. M.-S. Chan, A. C. Wahl, *J. Phys. Chem.* **1978**, *82*, 2542–2549.

1.6 Recent Trends in Chemically Modified sp^2 and sp^3 Bonded Carbon Electrodes

Doug Knigge, Pushwinder Kaur, and Greg M. Swain
Michigan State University, East Lansing, Michigan

1.6.1 Introduction

Electrochemical technologies make use of carbon electrode materials with different microstructures and properties. sp^2 bonded carbon materials, like highly oriented pyrolytic graphite (HOPG), glassy carbon (GC), carbon fibers, activated carbon powders, and carbon nanotubes, have been used for several decades in electroanalysis, energy storage and conversion devices, and chemical sensors [1]. More recently, electrically conducting sp^3 bonded carbon materials, such as diamond and tetrahedral amorphous carbon (Ta−C), have begun to be studied and employed as electrochemical electrodes [2–5]. Faradaic electrochemical processes involve electron transfer across an electrified interface (electrode–electrolyte), and the redox reaction kinetics and mechanisms are often strongly influenced by the physical structure and chemical properties of the electrode surface. The rich surface chemistry of most carbon materials affords the possibility for chemical modification using a number of well-established strategies. Attention is often paid to an electrode's surface chemistry for catalytic and mechanistic purposes, and sensor applications [6–9]. Nowadays, carbon is also finding use in the emerging field of molecular electronics [10]. The carbon electrode surface chemistry can be quite variable from material to material and depends on the past history [11–16]. The surface chemistry plays a key role with carbon electrode function, exerting a strong influence on the electric double-layer structure, molecular adsorption, and electrode reaction kinetics. The concept of chemically modified electrodes was, in part, born out of the electrochemist's desire to control the chemical nature of the electrode surface so as to influence the electrode reaction kinetics and mechanisms.

sp^2 carbon electrodes have been extensively studied over the past four decades [1, 11–16]. It has long been known that electrochemical reactions at carbon electrodes are dependent on the type of carbon, and how the material was handled and prepared for use. The relationship between the surface microstructure and chemistry, and the electrochemical properties of these materials has been thoroughly reviewed elsewhere [1, 11–16]. More recently, sp^3 bonded carbon materials have begun to be investigated as electrodes because of their interesting and, in some cases, unique properties [2–5, 17–39]. Carbon electrodes, in general, offer a wide working potential window, good chemical stability in a variety of solvent systems, and renewable properties via surface pretreatment.

The relationship between the electrochemical behavior of a carbon electrode and the material's physical, chemical, and electronic properties is often difficult to unravel for at least three reasons. First, the electronic properties, surface microstructure, and surface chemistry differ from carbon material to material. For instance, the properties of GC are vastly different from those of HOPG or boron-doped diamond, even though all are carbon. Also, the properties of a particular type of carbon

Encyclopedia of Electrochemistry. Edited by A.J. Bard and M. Stratmann
Vol. 10 *Modified Electrodes*. Edited by M.Fujihira, I.Rubinstein, and J.F.Rusling
Copyright © 2007 Wiley-VCH Verlag GmbH & Co. KGaA, Weinheim. ISBN: 978-3-527-30402-8

from two different sources or sometimes even from the same source can be quite variable.

Second, the surface chemistry, microstructure, and electronic properties can influence the electrode reaction kinetics and mechanisms for redox systems to differing extents [1–5, 12–15]. Good electrical conductivity is essential for all electrodes, so the electronic properties affect the electrode reaction kinetics of all redox systems. The surface chemistry, on the other hand, can influence the kinetics and mechanisms for some redox systems more than others. For example, surface carbon–oxygen functionalities on sp^2 carbon electrodes increase the heterogeneous electron-transfer rate constant for aquo $Fe^{+3/+2}$ but exert little influence on the rate constant for $Ru(NH_3)_6^{+3/+2}$ [40]. It is important to note that if the goal is to understand structure–function relationships at carbon electrodes, then there needs to be a judicious choice of redox systems to probe this relationship with.

Third, many pretreatment methods have been developed for ''activating'' carbon electrodes for electron transfer. Pretreatments often affect more than one electrode property (e.g. surface chemistry and microstructure) making it difficult to elucidate structure–function relationships. As a consequence of the variable nature of pretreatments, carbon electrode surfaces tend to vary greatly from laboratory to laboratory and from day to day, complicating one's ability to relate the electrode surface structure to the electrochemical response [1, 5, 12–16].

The factor that probably most complicates the study of structure–function relationships at carbon electrodes is the surface chemistry, specifically, the variety of surface oxygen functional groups that can exist, particularly on sp^2 bonded materials [1–5, 12–15, 40]. The oxygen functional group type and coverage depend on the exposed carbon microstructure, the nature of any pretreatment applied, and the electrode's past history, and are difficult to control. The oxygen functional groups influence the electrode polarity, wettability, molecular adsorption, and the electric double-layer structure. These functional groups exist mainly as a consequence of the electrode being used and ''activated'' in air. There are also a large number of chemical and electrochemical treatments that introduce the functionality. Carbon–oxygen functionalities can be both friend and foe. On one hand, specific functional groups can be influential both kinetically and mechanistically for certain redox reactions. For instance, surface carbonyl functional groups on GC and HOPG are known to catalyze the $Fe^{+3/+2}$ redox reaction in 0.1 M $HClO_4$ [41]. On the other hand, surface oxides are one of the main reasons carbon electrodes can be rapidly deactivated by impurity adsorption, as these polar and sometimes charged functional groups promote the strong adsorption of polar molecules (e.g. contaminants). Surface oxides, and the increased electrode area that accompanies their formation on sp^2 bonded carbon electrodes, generally lead to increased voltammetric and amperometric background currents, increased noise, and reduced signal-to-background ratios because some types are redox-active (quinones/hydroquinones) and some types are acidic and ionizable (e.g. carboxylic acids). The redox activity depends on the potential range and the ionization depends on the solution pH. Of the different sp^2 and sp^3 carbon electrode types, diamond is the most chemically inert, most structurally stable, and the only one that is inherently low in surface oxygen because of the hydrogen-rich environments in which

the material is usually synthesized. As a consequence, the surface carbon atoms are terminated by strong covalent bonds with hydrogen prior to use. There are also some sp^2 carbon electrodes that are inherently low in surface oxygen, such as low defect HOPG, carbon nanotubes, and hydrogenated glassy carbon (HGC) [42, 43].

Chemical modification is an approach for reducing the complexity of the carbon electrode surface chemistry. Modifying carbon electrode surfaces can make them more monofunctionalized, more reproducible in terms of their electrochemical properties, less susceptible to degradation because of surface oxidation reactions, and less prone to fouling by impurity adsorption. In general, modification enables the systematic investigation of how the surface chemistry influences electrode reaction kinetics and mechanisms. Monofunctionalizing a surface through covalent attachment of atoms and molecules affords a means to control the surface chemistry. New chemical modification strategies and improved spectroscopic probes of modified surfaces have rejuvenated this field of research in recent years, which had its origins back in the 1970s ([6–9] and references therein). Some of the approaches employed over the years for modifying carbon electrodes include organosilane chemistry [6, 9]; the covalent attachment of quinone molecules [8]; the introduction of surface carbon–oxygen functional groups via plasma, chemical, and electrochemical treatment [44]; and the deposition of various polymers [7]. One more recent modification strategy involves the covalent attachment of aryl groups during the electrochemical reduction of phenyl diazonium salts [45].

Some of the research trends with chemically modified sp^2 and sp^3 bonded carbon electrodes are reviewed in this chapter. This monograph is not a comprehensive review of the entire field of modified electrodes as it has existed for the past four decades, but rather summarizes some of the more recent progress. While the chemical modification of sp^2 carbon electrodes has been the subject of much study over the years, the modification of sp^3 carbon electrodes (diamond) is a new field of research that has emerged only during the past couple of years. Several strategies for altering the surface chemistry (i.e. removing surface oxides) and covalently bonding molecules to both sp^2 and sp^3 bonded electrodes are discussed herein. One strategy that is extensively discussed herein is the electrochemically-assisted modification of carbon surfaces via the reduction of diazonium salts [45–55]. It should be noted that other chemical modification strategies, such as polymer deposition and the chemisorption of molecules, are important but not covered herein, nor are the vast number of modification methods for producing oxygen functionalities on the carbon surface.

1.6.2 Chemically Modified sp^2 Bonded Carbon Electrodes

1.6.2.1 Hydrogen-terminated Surfaces

Glassy carbon or GC is one of the most widely used electrode materials in all of electrochemistry, particularly for electroanalytical measurements. GC surfaces prepared in air and/or used in aqueous environments have edge plane and defect sites that will be terminated with surface oxides of varying type and coverage [1]. As stated earlier, the heterogeneous distribution of surface carbon–oxygen functional groups can be a cause for significant variability in the electrochemical response and can lead to poor response stability.

Some of these oxides are redox-active (e.g. quinone/hydroquinone couple) and some are ionizable (e.g. carboxylic acid), both of which lead to pH-dependent changes in the voltammetric and amperometric background current over a wide potential range. Several approaches have been employed for removing surface oxides from sp^2 carbon electrodes including high vacuum heat treatment [56–58] and mechanical polishing in an anaerobic environment [13]. Hydrogen plasma treatment is another effective method for removing carbon–oxygen functional groups from HOPG, carbon fiber, and GC surfaces [42, 43]. HGC is prepared, for example, by exposing GC to a hydrogen microwave plasma or to hydrogen gas activated by passage over a heated metal (e.g. tungsten) filament. Atomic hydrogen, not molecular hydrogen, is the principal reactant that chemisorbs at the exposed edge plane sites and leads to the replacement of terminal oxygen functional groups [42]. This treatment is fundamentally different from vacuum heat treatment or mechanical polishing in an anaerobic environment because it not only removes the surface oxides but also stabilizes the surface carbon atoms by forming strong covalent C–H bonds. The hydrogenated surfaces are low in oxygen content (atomic O/C <0.02), as determined by X-ray photoelectron spectroscopy (XPS), and quite hydrophobic with an initial water contact angle that is greater than 65°. In fact, the oxygen content remains low even during air exposure for weeks due to the stability of the C–H bonds [43]. On the basis of static secondary ion mass spectrometry (SIMS) results, it was proposed that the hydrogenated surface is actually composed of aliphatic hydrocarbon moieties (e.g. CH_3, C_3H_3, C_2H_5, C_3H_5, etc.) rather than simply hydrogen, as the chemisorption of atomic hydrogen not only replaces terminal oxygen groups but causes ring opening reactions that lead to the formation of surface hydrocarbon moieties [42]. Figure 1 shows a proposed surface structure for HGC.

HGC exhibits lower voltammetric background current, comparable electrochemical activity for several redox systems, enhanced S/B ratios, and improved response stability compared with freshly polished (i.e. oxygenated) GC. Relatively rapid electrochemical reaction kinetics were observed for $Fe(CN)_6^{-3/-4}$ and $Ru(NH_3)_6^{+3/+2}$, while slightly slower kinetics were seen for dopamine and 4-methylcatechol. Very sluggish kinetics were found for $Fe^{+3/+2}$. For example, apparent heterogeneous electron-transfer

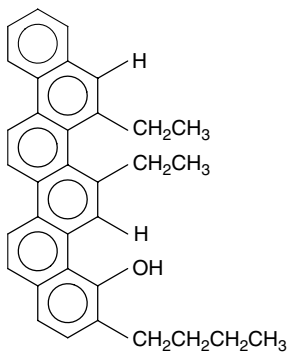


Fig. 1 Proposed surface chemistry of hydrogenated glassy carbon [42].

rate constants, k^{o}_{app}, of 0.01 to 0.03 cm s^{-1} were reported for $Fe(CN)_6^{-3/-4}$ and $Ru(NH_3)_6^{+3/+2}$ while slightly lower values of $\sim 5 \times 10^{-3}$ cm s^{-1} were observed for dopamine and 4-methylcatechol [42]. Significantly lower rate constants of $\sim 3 \times 10^{-5}$ cm s^{-1} were seen for $Fe^{+3/+2}$ [42]. The low k^{o}_{app} for $Fe^{+3/+2}$ was attributed to the absence of mediating carbonyl functional groups on the HGC surface [40, 41]. The voltammetric responses for all five redox analytes were extremely stable even after a 3-month period of air exposure. This reflects how resistive this hydrophobic surface is to deactivation (fouling) via contaminant adsorption. Further evidence for the lack of molecular adsorption (polar molecules) was revealed from chronocoulometric measurements performed with anthraquinone-2,6-disulfonate (2,6-AQDS) [39]. AQDS strongly physisorbs at high coverages on the polar, oxygenated GC [39, 59]. However, negligible adsorption was detected on HGC. The results demonstrate that hydrogenation is a suitable modification method for producing stable, low-oxide GC surfaces.

1.6.2.2 Surfaces Modified by Chemisorbed Molecules

One strategy that has become popular in recent years for controlling the chemistry of sp^2 carbon electrodes involves electrochemically-assisted derivatization. This field was recently reviewed by Downard [45], so only a brief synopsis is given herein. This relatively versatile chemical modification strategy involves either the oxidation or reduction of a precursor molecule to form a solution radical species at the electrode–electrolyte interface. This radical species then rapidly reacts at the surface to form a covalently attached admolecule. A wide range of molecules have been covalently attached to sp^2 carbon surfaces in this manner including primary and secondary amines, alcohols, and a variety of substituted phenyl diazonium salts (e.g. nitrophenyl, carboxyphenyl, alkylphenyl groups/molecules, etc.) [45]. For example, Barbier et al. described the modification of carbon fibers by the electrochemical oxidation of aliphatic polyamines (e.g. ethylene diamine) in nonaqueous medium [60]. The oxidation of the diamine leads to the generation of a cation radical species in the vicinity of the electrode surface, which then covalently attaches to surface atoms. The grafting occurred during polarization at 1.5 V vs. SCE in dry acetonitrile containing 0.1 M NBu_4BF_4. In another example, Deinhammer et al. modified GC surfaces using a variety of organic amines [61]. The method utilized the electrooxidation of amines to their analogous cation radicals in a nonaqueous medium. The radicals formed covalently attach to the electrode surface through the amine nitrogen. Finally, in another example, Buttry and coworkers demonstrated that both thermal reactions and the electrochemical oxidation of amines at carbon fibers in a non-aqueous medium lead to the covalent attachment of these molecules to the fiber surface, presumably via the nucleophilic attack of the amine at electrophilic C=C sites and subsequent formation of C−N bonds between the surface and the amine [62]. One reaction described in their manuscript was the attachment of 2-aminoanthraquinone during the polarization of the carbon fiber at 0.9 V vs. SCE in dry acetonitrile containing 0.1 M $NaClO_4$. The general reaction scheme for this modification is shown in Fig. 2.

Another type of electrochemically-assisted modification reaction that has become popular in recent years for controlling the surface chemistry of sp^2

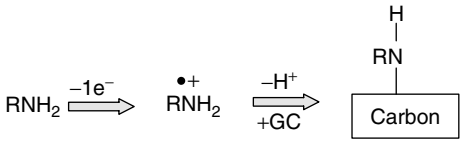


Fig. 2 Covalent attachment of amine functional groups to the surface of carbon electrodes by the electrooxidation of amine precursor molecules in nonaqueous medium.

carbon electrodes (GC, carbon fiber, the edge and basal plane of HOPG and HGC) involves the reduction of substituted phenyldiazonium derivatives ($R-N_2^+$). Some 20-plus molecules having been investigated so far [45–55]. The one-electron reduction of these derivatives in nonaqueous solvent/electrolyte produces a reactive substituted phenyl radical in the vicinity of the electrode that then binds to the surface. The reaction sequence is shown in Fig. 3.

It has been shown that the binding is nonselective for the basal of edge plane sites of the sp^2 carbon electrode. The structure and thickness of the aryl adlayer depend on the electrolysis (modification) time, the applied potential, the type of carbon electrode material, the particular diazonium derivative, and the solution concentration of the derivative [48, 49]. Mono or multilayer films can form depending on the deposition time [46, 52]. The coupling reactions tend to be favored by both the adsorption of the diazonium prior to electrolysis and by the relatively positive reduction potential that prevents simultaneous reduction of the aryl radical [48, 49]. Most often, the derivatization reaction is performed in a nonaqueous medium (e.g. CH_3CN) but there have also been a few reports of the successful derivatization of sp^2 carbon surfaces in acidic aqueous media [50, 63]. The derivatization reactions proceed on both the basal and edge plane sites of HOPG, for example, but the reaction kinetics are much faster at the edge plane sites [48, 50, 52, 55]. As mentioned earlier, a multitude of substituted aryl groups have been attached to various carbon electrodes including phenyl, 4-nitrophenyl, 4-carboxyphenyl, 4-alkylphenyl, biphenyl, and so on. A comprehensive list is given in the review by Downard [45]. These derivatized surfaces tend to be quite stable during storage in air, exposure to different solvents, ultrasonication, and exposure to moderate temperatures.

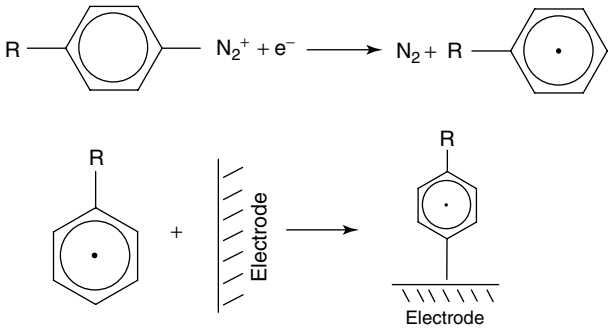


Fig. 3 Covalent attachment of functionalized aryl molecules to the surface of carbon electrodes by the electroreduction of phenyl diazonium salts in nonaqueous medium.

In the first report of this reaction chemistry, Delamar et al. showed that the electrochemical reduction of a 4-nitrophenyl diazonium salt in nonaqueous medium results in the covalent attachment of nitrophenyl groups on GC and HOPG electrode surfaces [46]. The authors estimated the adlayer surface coverage through the integration of the reduction current for the nitro functional group and found that a closed packed monolayer was nearly achieved, $\Gamma = 14 \times 10^{-10}$ mol cm^{-2}. It was observed that the surface coverage can be controlled by adjusting the concentration of the diazonium derivative in solution and the electrolysis (deposition) time. It was proposed that two factors favored the grafting reaction: (1) adsorption of the diazonium salt prior to its electroreduction and (2) the fact that the aryl radical is not reduced at the relatively low reduction potential of the diazonium salt. A detailed study of a number of diazonium derivatives was carried out with GC and HOPG by Allongue et al. [49]. The above two works spawned the more recent efforts to use this versatile method to chemically modify a variety of carbon and noncarbon surfaces [45, 47, 48, 50–55]. Notable work has been performed by the McCreery [10, 48, 51, 55], McDermott [52], Downard [45, 63], and Belanger groups [50]. Important components of these works have been the characterization of the orientation of aryl adlayers by Raman spectroscopy [48, 51, 55], the morphology of mono and multilayer films by electrochemical atomic force microscopy (ECAFM) [52], and the role of the aryl adlayer on the electron-transfer kinetics for several solution-based redox systems [50, 55].

Harnisch et al. described a new strategy for chemically modifying sp^2 carbon stationary phases for use in electrochemically modulated liquid chromatography [53]. They showed that GC and porous graphitic carbon (PGC) stationary phases can be modified with either 4-nitrophenyl diazonium or 4-hexylphenyl diazonium. The presence of the covalently attached admolecule was determined by XPS and by comparing the reversed-phase separation of a series of solutes. The main purposes for modifying the stationary phases were (1) to impart some degree of selectivity for the separation of different solute classes and (2) to improve the stability of the carbon support during extended exposure to aggressive mobile phases. The utility of the modified stationary phases was assessed by the separation of substituted phenols and various pharmaceutical agents.

As mentioned earlier, the grafting reaction tends to be nonselective for the oxygen-terminated edge plane and basal plane sites of the sp^2 carbon materials. The reaction also proceeds facilely on hydrogen-terminated edge plane sites as McCreery and coworkers have shown HGC surfaces can also be derivatized by the reduction of phenyl diazonium salts [43]. The reduction of nitrophenyl and (trifluoromethyl)phenyl diazonium ion in acetonitrile were carried out with the former and studied in greatest detail. On GC or graphite electrodes, the reduction of nitrophenyl diazonium leads to the formation of a compact nitrophenyl monolayer, as confirmed by XPS, Raman spectroscopy, and cyclic voltammetry. The cyclic voltammetric features during the derivatization reaction resembled those for polished GC. Raman spectra for the covalently attached admolecule were also similar at both surfaces exhibiting prominent peaks at 849, 1108, and 1177 cm^{-1}, which correspond to the NO_2 and phenyl C−H bending motions.

1.6.2.3 Effect of Surface Modification on the Electrochemical Properties

There are a number of reasons for controlling the surface chemistry of carbon materials including promoting the interfiber bonding in carbon fiber composites, inhibiting corrosion, controlling molecular adsorption, developing platforms for chemical and biological sensing, and improving the electrode reaction kinetics for a particular redox system (as examples [62, 64, 65]). Of particular importance to the electrochemist is an understanding what effect surface chemistry has on the electrode reaction kinetics. sp^2 bonded carbon electrodes have a rich chemistry with a variety of carbon–oxygen functionalities being present [64–66]. Characterization of the chemical identity and local environment of the surface oxides has been undertaken by the McCreery group using several creative synthetic approaches. For example, the group probed the presence of carbonyl functional groups on HOPG and GC surfaces by the selective derivatization with dinitrophenylhydrazine (DNPH) [67]. DNPH is a specific reagent for ketone and aldehyde groups, which leads to a resonance Raman-active product with a large scattering cross section. The derivatization permits detection of carbonyl groups down to about 1% of a monolayer. The surface carbonyl functional group density, as probed by this chemistry, was found to increase during electrochemical polarization. The effect of these functional groups on the GC electrode reaction kinetics for a number of aqueous-based redox systems ($Fe(CN)_6^{-3/-4}$, $Ru(NH_3)_6^{+3/+2}$, $IrCl_6^{-2/-3}$, $Fe_{aq}^{+3/+2}$, and $V_{aq}^{+3/+2}$) was also investigated [67]. The kinetics of the aquated ions were found to be quite sensitive to the presence of these functional groups, while other redox systems were not nearly as affected. Specifically, chemical derivatization of the carbonyl groups (blocking these) decreased the electron-transfer rate for $Fe^{+3/+2}$, for example, by 2–3 orders of magnitude, but had little effect on the rate constants for $Ru(NH_3)_6^{+3/+2}$ or $IrCl_6^{-2/-3}$.

In other words, the group studied the electron-transfer kinetics for nine aqueous-based redox systems at GC surfaces modified with reagents that react specifically with different oxygen functional groups [68]. The DNPH reaction was used to selectively derivatize carbonyl groups while dinitrobenzoyl chloride (DNBC) was used to selectively derivatize hydroxyl groups. Raman spectroscopy, XPS, and electrochemical methods were used to confirm the presence of the derivatizing agent, to determine the surface coverage and to assess the effect of functional group blockage on the kinetics. The authors categorized the different redox systems according to their relative sensitivity to the GC electrode surface structure and chemistry. The specific adsorbers, DNBC and particularly DNPH, caused a significant decrease in the electron-transfer kinetics for $Fe_{aq}^{+3/+2}$, $V_{aq}^{+3/+2}$, and $Eu_{aq}^{+3/+2}$, but had less effect on the other redox systems. In a related work, the group used Raman spectroscopy to study how the surface coverage of carbonyl and hydroxyl functional groups on GC changes with pretreatment [68]. The DNPH (carbonyls) and DNBC (hydroxyls) reactants were used along with a new fluoroscein mixed anhydride (FMA) reagent for selective binding with hydroxyl groups. The results revealed that FMA reacts selectively with the hydroxyl groups and the FMA-surface adduct is a Raman-sensitive probe of the hydroxyl group coverage. The point that the surface oxide coverage on GC is sensitive

to both the initial conditions and subsequent chemical treatment procedures was emphasized.

Several groups have investigated how the electrochemical properties of GC are altered after being modified by the reduction of diazonium salts [50, 54, 55]. For example, Belanger and coworkers investigated the effect of 4-carboxyphenyl and 4-nitrophenyl adlayers on the electrochemical response of GC for $Fe(CN)_6^{-3/-4}$, $Ru(NH_3)_6^{+3/+2}$, hydroquinone, and ferrocene [50]. Blocking properties were seen for the adlayers, the extent to which depended on electrostatic and electrolyte/solvent effects. Bath and coworkers studied the role of surface modification on the carbon fiber response for the catecholamine and dopamine [54]. The purpose for the work was to use chemical modification to reduce the electrode response time and increase the sensitivity for dopamine. Under physiological conditions, the sensitivity of a carbon fiber electrode for dopamine is strongly influenced by the extent of molecular adsorption with the response time being controlled by the adsorption and desorption kinetics. Through surface modification, the authors sought to gain better control of the surface chemistry and to make it more homogeneous as compared to a native carbon fiber. The electrode surface was modified by (1) physisorbed anthraquinone disulfonate and (2) chemisorbed 4-carboxyphenyl or catechols via diazonium salt reduction. Different behaviors were seen for the modified carbon fibers depending on the surface chemistry and the fiber microstructure. The strength of the interaction between the cationic dopamine (pH 7.4) and the anionic surface sites was found to dominate the electrochemical behavior.

1.6.3 Chemically Modified sp^3 Bonded Carbon Electrodes

1.6.3.1 CVD Diamond Thin-film Growth

Electrically conducting diamond is a new type of carbon electrode material that is finding more and more use in electrochemistry. A brief discussion is given below of how the material is synthesized. Most often diamond is grown as a thin film on a conducting substrate like doped Si, Mo, W, or Ti. Diamond can be grown by one of several methods: microwave plasma, hot-filament, or combustion flame-assisted chemical vapor deposition (CVD). The most common method is microwave plasma CVD. One reason for this is the commercial availability of such reactor systems. While the mechanism of film growth differs slightly from method to method, all serve to activate a carbonaceous source gas, producing a growth precursor in close proximity to the substrate surface [2]. A typical CVD reactor consists of the growth chamber and equipment associated with the particular activation method (e.g. microwave power source), as well as various accessories, such as mass flow controllers for regulating the source gas flows, a throttle exhaust value and controller for regulating the system pressure, a pumping system, temperature measurement capability, and the gas handling system for supplying the source gases. A block diagram of a typical CVD system is shown in Fig. 4.

In the case of microwave-assisted CVD, the microwave energy from the generator is directed to and focused within a quartz cavity, producing a spherically shaped, glow-discharge plasma directly above the substrate. The substrate can either be positioned outside of (few mm) or immersed within the intense discharge

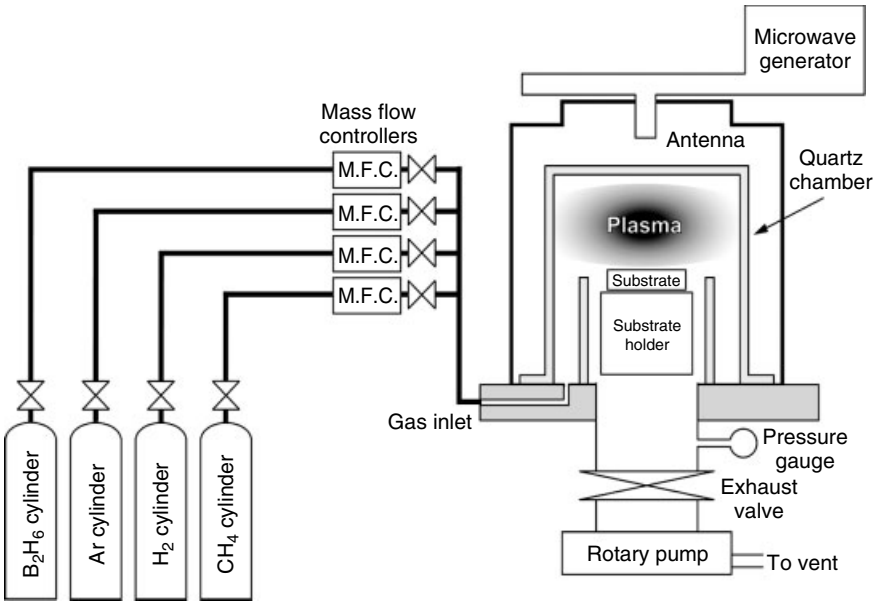


Fig. 4 Typical layout of a microwave plasma chemical vapor deposition system.

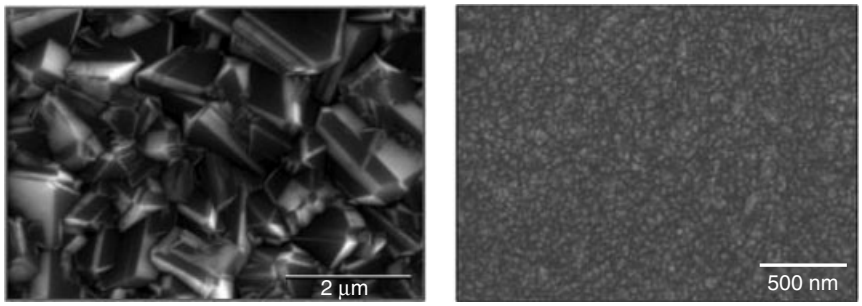


Fig. 5 SEM images of (a) a boron-doped microcrystalline and (b) a boron-doped nanocrystalline diamond thin film grown on Si.

region. The plasma is where the reactive species involved in the diamond growth are formed. The key deposition parameters to control are the source gas composition, microwave power, system pressure, and substrate temperature.

There are two types of synthetic diamond thin film routinely produced: microcrystalline and nanocrystalline [2]. The names for these two film types arise from their nominal crystallite size and morphology. Figure 5 shows scanning electron microscopy (SEM) images of the two types of boron-doped diamond thin film deposited on Si. High quality microcrystalline diamond films are deposited from CH_4/H_2 source gas mixtures with volumetric ratios of 0.3 to 1.0%,

microwave powers of 0.8–1 kW, pressures of 35–65 torr, and substrate temperatures of 700–850 °C. Under these conditions, CH_3. is the primary growth precursor. The added hydrogen serves several key functions: (1) abstraction of hydrogen from chemisorbed methyl substituents on the growing film surface to produce active sites for carbon addition, (2) passivation of dangling bonds on the surface to minimize reconstruction from sp^3 to sp^2 bonding, and (3) rapid gasification of any sp^2 bonded, nondiamond carbon impurity that forms on the growing surface. As can be seen from the image, microcrystalline films are well faceted, polycrystalline diamond with crystallite sizes on the order of a few micrometers, or greater, in lateral dimension. The individual crystallites are randomly oriented and there is significant twinning. A grain boundary is present at the junction between two or more crystallites, which has structural, chemical, and electronic properties that are different from the grains.

High quality nanocrystalline diamond films are deposited from CH_4/Ar source gas mixtures using a volumetric ratio of 0.5 to 1.0% with little or no added hydrogen, microwave powers of 0.8–1 kW, pressures of 130–160 torr, and substrate temperatures of 700–850 °C. Gruen and coworkers discovered that phase-pure nanocrystalline diamond can be grown from CH_4/Ar gas mixtures with very little or no added hydrogen [69, 77, 78]. The most remarkable difference in films grown using hydrogen-poor Ar gas mixtures, compared with those grown from conventional hydrogen-rich mixtures, is the nanocrystallinity and smoothness (rms roughness ~10–30 nm over large areas) of the former, as can be seen in the SEM image. Noble or inert gas addition to hydrogen-rich plasmas (e.g. 0.5% CH_4/H_2) enhances the growth rate of films by increasing the CH_3• and atomic hydrogen concentrations in the plasma. The low excitation energy of inert gases, like Ar or Xe, results in a plasma discharge with a higher electron density, and this leads to the higher levels of CH_3. and H.. There is a fundamental change in the plasma chemistry, growth mechanism, growth rate, and film properties as one transitions from a hydrogen-rich to a hydrogen-poor plasma. In particular, hydrogen-poor plasmas have a high concentration of carbon dimer, C_2, which serves as both the primary growth and nucleation species [79, 80]. The nanocrystallinity is the result of a growth and nucleation mechanism involving the insertion of C_2 into surface C−H bonds. Apparently, during growth, there is sufficient hydrogen from the CH_4 to minimize surface reconstruction to an sp^2 bonded phase. The C_2 addition is believed to occur by a two-step growth mechanism [69–79]. A C_2 molecule approaches the unreconstructed monohydride surface and inserts into a C−H bond. The C_2 molecule then rotates to insert its other carbon into a neighboring C−H bond on the surface. A C_2 molecule then inserts into an adjacent C−H bond, parallel to the newly inserted C_2 dimer. The original state of the surface is recovered by the formation of a bond between carbon atoms in the adjacent surface dimers. Very high rates of heterogeneous renucleation are observed on the order of 10^{10} cm^{-2}, and the resulting films consist of randomly oriented, phase-pure grains of diamond with well-delineated grain boundaries [69–79]. Nanocrystalline films produced in Ar-rich plasma possess a very fine, uniform grain size (3–5 nm is typical for high quality ultrananocrystalline diamond) and a small but nonnegligible amount of sp^2 bonded carbon at the abrupt grain boundaries [69, 78, 79].

The instantaneous rate of nucleation during diamond growth on untreated, smooth nondiamond substrates is generally low. Therefore, substrate pretreatment is a prerequisite for deposition. A common substrate preparation involves either mechanical polishing with small diameter diamond powder (0.01–1 μm diameter), or ultrasonication in a diamond powder/solvent suspension. For example, with the latter, the diamond powder can be suspended in ethanol and the sonication is performed in this medium. Either pretreatment results in the formation of scratches and other defects, as well as the dispersion of some diamond particles over the surface. Most pretreatments also involve subsequent substrate washing to remove polishing debris and clusters of diamond particles. Ultrasonic cleaning in organic solvents (isopropanol, acetone, and methanol) is common practice. Enhancement of the instantaneous heterogeneous nucleation density results from both the physical defects introduced and the highly dispersed diamond seed particles.

1.6.3.2 **Surface Termination**

Electrically conductive diamond electrodes possess several properties that clearly distinguish them from conventional sp^2 carbon electrodes, like GC, and make them attractive for electrochemical use [2–5, 21]: (1) background current densities approximately 5–10 times lower than freshly polished GC leading to enhanced S/B ratios, (2) a working potential window of 3–4 V in aqueous media, which is over 1 V wider than GC, (3) superb response precision and stability due to the stable surface morphology and microstructure, even during high current density (0.5 A cm^{-2}) electrolysis, (4) relatively rapid electrode reaction kinetics (k^o_{app} 0.02–0.2 cm s^{-1}) for several aqueous-based redox analytes without any conventional pretreatment (e.g. $Fe(CN)_6^{-3/-4}$), and (5) weak adsorption of polar molecules, like 2,6-anthraquinonedisulfonate, rendering the material resistant to fouling and passivation [25, 29, 39]. Electrical conductivity (typically 100–1000 Ω^{-1} cm^{-1}) is introduced by doping with impurities, such as boron. Boron-doping levels for highly conductive films are normally in the range of 10^{19} to 10^{20} B cm^{-3}. Typical carrier concentrations (holes) in the more highly doped films range from 10^{18} to 10^{20} cm^{-3} with carrier mobilities varying from 0.1 to 100 cm^2 V s^{-1}, depending on the film microstructure and morphology.

Most of the work, so far, with diamond electrodes, has involved electroanalytical measurements using films with a hydrogen surface termination. The heterogeneous electron-transfer rate constants for several aqueous redox systems have been measured at good quality, boron-doped, polycrystalline, hydrogen-terminated electrodes [2–5, 21]. In general, the lowest level of absorption, the largest heterogeneous electron-transfer rate constant for several aqueous redox analytes, and the most reproducible electrochemical response is observed for the hydrogen-terminated surface [2–5, 21]. Figure 6 shows the structure of the hydrogen-terminated surface. The carbon atoms are covalently bonded to

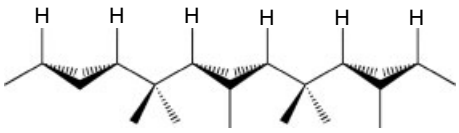


Fig. 6 A schematic representation of the hydrogen-terminated diamond surface.

one another through sp^3 hybridized bonds. The figure shows that each surface carbon atom is monofunctionalized with hydrogen. In fact, some of the surface atoms maybe terminated with methyl groups.

In addition to electroanalysis, diamond has recently attracted attention as a semiconductor for chemical sensing due to its large potential window for water stability, chemical inertness, and absence of in-diffusion of ions [80–85]. Of special interest is the hydrogen-terminated diamond surface, which occurs after CVD growth or special postgrowth hydrogen plasma treatment. It has been found that there is a hydrogen-induced surface conductivity that can be controlled by adsorption of a number of reducing or oxidizing gases [80–83]. As a consequence of this somewhat unique electrical property, several device concepts based on a H-terminated diamond surface have been developed for gas sensors and ion-selective field-effect transistors (FET's) [84, 85]. Seminal work has been performed by Ristein, Kohn, and their coworkers on understanding the conduction mechanism [80–83], and by Kawarada and his coworkers on the FET sensors [84, 85].

The hydrogen surface termination of diamond can easily be altered with two common functional groups, namely, fluorine and oxygen. There are a couple of reasons for the interest in changing the surface termination: (1) understanding the manner in which the terminal atom affects adsorption, corrosion (oxidation) and electrochemical kinetics, and (2) designing ''slippery,'' low friction surfaces that can be exposed to a wide range of temperatures and conditions. Something that is unique about diamond as compared to sp^2 carbon electrodes is the fact that the chemical changes are confined to the surface. There is usually no degradation of the microstructure during treatment, something that often happens with sp^2 carbon materials and leads to the progressive formation of new reaction sites for chemisorption.

Exposure of hydrogen-terminated diamond surfaces to activated fluorine-containing gases, like HF, F_2, or CF_4, leads to fluorine substitution [86]. Figure 7 shows a schematic representation of a fluorine-terminated surface.

Activation of these gases, for example, by microwave-assisted plasma CVD, produces reactive atomic fluorine. Freedman exposed diamond (111) and (100) surfaces to beams of atomic fluorine and chlorine in the UHV. The fluorinated surfaces were characterized by XPS, temperature programmed desorption, and low-energy electron diffraction [86]. Fluorine adds to both surfaces to form carbon monofluoride species, reaching a saturation coverage of ca. 0.75 monolayer at 300 K. The rate of chemisorption was found to depend on the diamond crystallographic orientation with the difference in behavior being ascribed to variations in bonding geometry, which leads to steric hindrance on the (100) surface. Atomic fluorine appears to function much like atomic hydrogen in terms of its ability to abstract surface hydrogen producing reactive sites for diamond growth [86]. The larger chlorine atoms were found to weakly chemisorb on the diamond (100)

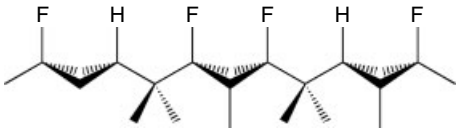


Fig. 7 Schematic representation of a fluorine-terminated diamond surface.

surface at a saturation surface coverage of ca. 0.5 monolayer at 300 K. Unlike the fluorinated surface, the chlorinated surface is unstable when exposed to aqueous environments; therefore, it has no practical use as an electrode modification method.

Several other approaches have been used to fluorinate undoped polycrystalline diamond thin films, single crystals, and powders [87, 88]. These highly resistive materials are not practical for use as electrodes; nevertheless, the surface treatments are worth mentioning because they could be applied to conductive diamond materials. For example, Yates and coworkers used **X**-ray irradiation to modify undoped diamond single crystal surfaces with perfluoroalkyl iodide (C_4F_9-I) radicals [87]. The modified surfaces were thoroughly characterized by XPS. In their approach, which is shown in Fig. 8, C_4F_9-I molecules were first dosed onto a clean diamond (100) surface in the UHV at 120 K. The surface was initially cleaned by UHV heat treatment at 1450 K, a process that removes impurities as well as the chemisorbed hydrogen atoms terminating the surface. The coated surface was then irradiated with **X**-ray radiation to produce fluoroalkyl radical species that covalently bind to the diamond surface. The **X**-ray radiation dissociates the C–I bond producing perfluorinated alkyl radicals for attachment. The irradiation was performed at 120 K and this was followed by gentle heating to 300 K in order to desorb the unreacted C_4F_9-I molecules. The modified surface was then heated up to 900 K to decompose the surface C_4F_9 groups producing a surface largely terminated by fluorine atoms. The XPS F/C atomic ratio was 0.6 after decomposition of the attached C_4F_9 species. The fluorinated surface was stable up to 1500 K at which point the chemisorbed fluorine atoms begin to desorb. This fluorination was shown to occur on both bare (desorbed surface hydrogen) and deuterium-terminated surfaces.

From an electrochemical point of view, one might speculate that a fluorine surface termination would render the diamond electrode surface more resistant to oxidation and perhaps even less susceptible to adsorption (e.g. Teflon-like surface). Angus and coworkers fluorinated boron-doped, polycrystalline diamond electrodes by exposure to a CF_4 radio frequency plasma [88]. This is the only example, to the best of our knowledge, of an electrochemical study of an F-terminated diamond electrode. The XPS F/C atomic ratio was in the range of 0.16 to 0.18 after plasma treatment. The first voltammetric scan out to 2.5 V vs. SHE in 0.5 M H_2SO_4 produced

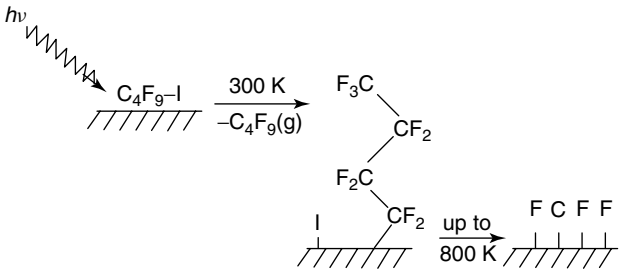


Fig. 8 Reaction sequence for modifying diamond surfaces with fluorine atoms using perfluoroalkyl iodide and **X**-ray radiation.

two anodic peaks at approximately +1.6 and +2.2 V. The onset potential for oxygen evolution was also shifted in a slightly more positive direction from the value observed for the hydrogen-terminated surface. However, after the first scan, the onset potential for oxygen evolution shifted back negatively to its original value and the charge associated with the oxidation processes disappeared. Oxygen was incorporated into the surface during cycling as the F/C atomic ratio decreased to approximately 0.03 while the O/C ratio increased to approximately 0.11. This indicates that C−F surface bonds are broken and new C−O bonds are formed in this potential range. Most interesting is the fact that the redox charge (ca. +1.83 V vs. SHE) associated with electroactive sp^2 carbon impurities, presumably located at the intercrystalline grain boundaries, was eliminated after plasma treatment in CF_4. The authors proposed that the two anodic peaks observed during the initial voltammetric scan toward positive potentials are due to the oxidation of an adsorbed fluorocarbon polymeric layer that forms during plasma treatment. The fluorination treatment appears to be effective at removing sp^2 carbon impurities from the surface and/or inhibiting the oxidation of grain boundary carbon. However, the C−F bonds formed are susceptible to oxidation in this medium at potentials of approximately +2.0 V or greater.

1.6.3.3 Oxygen-terminated Surfaces

Oxygen surface functionalities can be introduced by chemical and or electrochemical oxidation of diamond electrodes. The XPS atomic O/C ratio increases from approximately 0.01 to 0.15 after extensive electrochemical oxidation in $HClO_4$ or H_2SO_4 [40, 89, 90]. The types of oxygen functional groups formed have not been identified yet, but in related work, diffuse reflectance FTIR investigations of gas phase oxidized diamond powders revealed the formation of C−O−C and C=O bonds after exposure to oxygen above 300 °C [91]. Martin and Morrison used IR difference spectroscopy to identify C−OH and C−O−C functional groups on the diamond film surface after electrochemical oxidation [92]. A systematic study of how the anodic charge passed correlates with the surface oxygen coverage and, in turn, how the surface oxygen affects the electrochemical reaction kinetics for different aqueous redox systems has been performed [40, 89, 90]. There is a progressive increase in the cyclic voltammetric ΔE_p for $Fe(CN)_6^{-3/-4}$ and a positive shift in E_p^{ox} for ascorbic acid with increasing surface oxygen coverage [40, 90]. Contrarily, the ΔE_p for $Ru(NH_3)_6^{+3/+2}$ is relatively unaffected by the surface oxygen at least for the surfaces polarized as they were in this work. The results demonstrate, in a quantitative way, that the electrochemical kinetics for $Fe(CN)_6^{-3/-4}$ and ascorbic acid are strongly inhibited by the presence of surface oxygen. The inhibitory effects of the oxygen can be removed by rehydrogenating the surface in a hydrogen microwave plasma. After plasma treatment, ΔE_p and E_p^{ox} for $Fe(CN)_6^{-3/-4}$ and ascorbic acid, respectively, return to their original values. This trend indicates that adventitious sp^2 carbon impurity phases, which are gasified during the plasma treatment, do not play a significant role in the electrochemical response of these materials, and that the most active response, at least for these three systems, is observed for the hydrogen surface termination. Work is still needed to identify the types of oxygen functional groups formed and to understand why they inhibit these two redox reactions.

1.6.3.4 Surfaces Modified by Chemisorbed Molecules

Diamond surfaces can also be chemically modified by covalently attaching various molecules. In one of the first examples of a modified diamond electrode, Ohtani and coworkers attached pyridine to polycrystalline, boron-doped diamond using a multistep procedure [93]. The first step involved treating the hydrogen-terminated diamond surface with Cl_2 under UV irradiation (>200 nm). This photolysis produced Cl radicals that attack the surface and replace some of the surface hydrogen. The chlorinated surface was then exposed to boiling pyridine to produce a quarternary pyridinium salt modified surface with the linkage through the ring nitrogen. XPS revealed O/C and Cl/C atomic ratios for the chlorine-treated surface to be 0.10 and 0.01, respectively. The low chlorine and high oxygen incorporation results from the reaction of the chlorinated surface with atmospheric oxygen, presumably during sample transfer. The N 1s peak at ca. 400 eV increased after exposure to boiling pyridine. Limited electrochemical data were reported; however, the authors did indicate that the atomic chlorine-treated surface exhibited very sluggish electrochemical reaction kinetics for $Fe(CN)_6^{-3/-4}$ as evidenced by a poorly defined waveform with a large peak separation. This was probably due to the presence of surface oxygen, which formed during the exposure of the chlorinated surface to the atmospheric as discussed earlier.

Kim et al. investigated the low temperature photochemical attachment of perfluorobutyl (C_4F_9I) moieties on undoped, hydrogen-free, and hydrogen-terminated, single crystal (110) diamond surfaces [94]. This is somewhat similar to the strategy developed by Yates and coworkers that was described earlier. The adlayer was studied using multiple internal reflection infrared spectroscopy (MIRIRS). C_4F_9I physisorbed to form multilayers at 90 K on both surface terminations. The physisorbed C_4F_9I desorbed when heated above 200 K regenerating the starting surface. The electronic structure and vibrational spectra of the perfluorobutyl group were calculated for perfluorobutyl chloride and bromide, and the MIRIRS of the physisorbed multilayer agreed well with calculated IR spectra. After exposing the multilayer at 90 K to UV radiation (200 W Hg lamp) for 30 min and subsequent heating above 200 K, perfluorobutyl groups were covalently attached to the surface. The characteristic vibrational features of the attached perfluorobutyl group were observed between 1138 and 1355 cm^{-1}. A series of annealing experiments revealed that these modes persist even up to 600 K, but they completely disappear by 700 K. Similar results were found for both the hydrogen-terminated and hydrogen-free surfaces.

Hamers and coworkers showed that undoped diamond (001) surfaces undergo [2 + 2] cycloaddition reactions with a prototypical alkene, cyclopentene [95]. The (001) surfaces of diamond, silicon, and germanium share a similar bonding motif in which pairs of atoms can bond to each other via a strong σ bond and a weaker π bond forming a dimer. Normally, the formation of dimers on the diamond surface is prevented by hydrogen chemisorption; however, the diamond (001) surface was made reactive for the addition reaction by heat treatment in the UHV at 1375 K. At these temperatures, the surface is cleaned of impurities and surface hydrogen desorbs. This leads to the formation of carbon atoms paired into C=C dimers with a partial π bond [95]. This surface is essentially an extended array of alkene-like C=C

bonds, but with a distorted surface geometry [95]. The reactive diamond surface was then exposed to cyclopentene vapor at 300 K in the UHV. A [2 + 2] cycloaddition reaction occurred as the π bond of an alkene adsorbate and the weak π bond of a surface dimer were broken and two new σ bonds were formed linking the alkene to the surface through a four-member ring. UHV−FTIR (internal reflection mode) was used to study the sp^3 C−C and C−H bonding. The C−H absorption bands at 2953 and 2880 cm^{-1} were used to confirm the presence of the chemisorbed cyclopentane groups. The admolecule was stable during UHV heat treatment up to 573 K.

The Hamers's group also reported on the attachment of functionalized organic molecules to polycrystalline diamond film surfaces via irradiation of hydrogen-terminated diamond covered with liquid films of an appropriately functionalized alkene [96]. The hydrogen-free surfaces react with unsaturated C=C bonds of organic alkenes. The authors modified the diamond surface with (1) perfluorodecane (3,3,4,4,5,5,6,6,7,7,8,8,9,9,10,10,10-heptadecafluoro-1-decene), (2) 1-fluorononane, and (3) the trifluoroethyl ester of ω-undecenoic acid, the trifluoroacetamide-protected 10-aminodec-1-ene and the t-BOC-protected 10-aminodec-1-ene. All modified surfaces were characterized using XPS, in particular, the F 1s line at 689 eV and the C1s region near 284 eV. The chemical functionalization was accomplished by placing a small volume of the long-chain organic compound on the diamond film surface to form a thin liquid film, sealing the coated film in a reaction vessel with a quartz window, and irradiating the film/liquid with UV light (254 nm) over a 2-h period. The results showed that the H-terminated diamond surface could be chemically modified through a UV-mediated reaction with functionalized alkenes. Some of these organic molecules contained amine and carboxylic acid functional groups that are good starting points for attachment of more complex molecules (e.g. DNA).

Krysiński et al. reported on the covalent attachment of admolecules on diamond surfaces using a simple displacement reaction that begins with a hydrous oxide surface [97]. An optically transparent diamond thin film deposited on quartz was used as the substrate [26]. Figure 9 shows the multistep reaction scheme devised by the authors. The first step involved introducing surface oxides on the hydrogen-terminated surface by exposure to Piranha solution (10 min, 40 °C). This oxidation treatment introduced carbon–oxygen functionalities, in particular, hydroxyl and carbonyl functional groups. The most important of these are the hydroxyl groups. The oxidized surface was then reacted with adipoyl chloride in dry acetonitrile under nitrogen with 4-methylmorpholine acting as the Lewis base to produce an acid chloride surface. After rinsing with ethyl acetate and drying under a stream of nitrogen, the terminal acid chloride functionalized surface was then reacted with 1-aminopyrene. The covalent attachment of the pyrene through the amine group was observed to be relatively fast with a coverage limited by the steric constraints imposed by the diamond surface structure or possibly by the bridging across two electrode surface sites by two COCl terminal groups of the same adipoyl chloride molecule. The pyrene-modified surfaces were characterized by electrochemical methods, IR reflection–absorption spectroscopy, and time-resolved fluorescence measurements. The adlayer was stable to washing and immersion in organic solvents. The covalently bound adlayer was not as ordered as

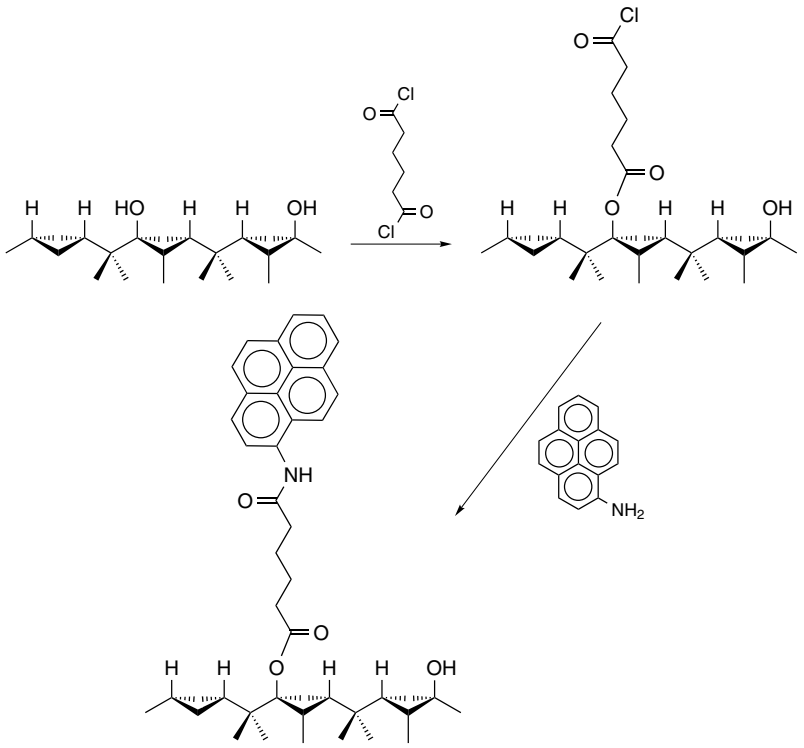


Fig. 9 Reaction sequence for the covalent attachment of 1-aminopyrene to the surface of a diamond optically transparent electrode [97].

an alkanethiol self-assembled monolayer (SAM) on Au, but exhibited more organization than amorphous physisorbed adlayers. The surface coverage was determined to be $\sim 4 \times 10^{-12}$ mol cm^{-2}, which corresponds to ca. 0.5% of full monolayer coverage.

Ida and coworkers reported on a new method for introducing carboxylic acid groups onto a diamond powder surface [98]. Hydrogenated diamond surfaces were treated in a solvent containing benzoyl peroxide and an alkane dicarboxylic acid. Surface characterization was performed by diffuse reflectance FTIR. The reaction sequence follows a free radical substitution as listed below. Benzoyl peroxide decomposes via the following reaction.

$$C_6H_5{-}COO{-}OOC{-}C_6H_5 \longrightarrow C_6H_5{-}COO\cdot + \cdot OOC{-}C_6H_5$$

The covalent attachment of phenyl groups to the H-terminated diamond surface probably involves the following reaction steps.

$$(\text{diamond}){-}H + C_6H_5COO\cdot \longrightarrow (\text{diamond})\cdot + C_6H_5COOH$$

$$HOOC{-}(CH_2)_n{-}COOH + C_6H_5COO\cdot \longrightarrow HOOC{-}(CH_2)_n{-}COO\cdot + C_6H_5COOH$$

$$(\text{diamond})\cdot + HOOC{-}(CH_2)_n{-}COO\cdot \longrightarrow (\text{diamond}){-}OOC{-}(CH_2)_n{-}COOH$$

$$(\text{diamond})\cdot + C_6H_5COO\cdot \longrightarrow \text{diamond}-OOC-C_6H_5$$

IR modes at 3072 cm^{-1} for the aromatic C−H stretch, 1735 cm^{-1} for the C=O groups of the carboxylic acid and aliphatic C−H stretches between 2750 and 2950 cm^{-1} were monitored to confirm the presence of the attached molecules. The chemical state of the diamond surface is determined by the relative proportion of $[-OOC-(CH_2)_n-COOH]$ versus $[-OOC-C_6H_5]$ sites.

Chemical modification of diamond electrode surfaces has also been accomplished by the reduction of diazonium salts, as discussed previously. Kuo et al. showed that substituted phenyl groups can be covalently attached to hydrogen-terminated, boron-doped diamond electrodes during the electrochemical reduction of substituted phenyl diazonium salts in acetonitrile (see Fig. 3) [51]. Diamond electrodes were modified with nitrophenyl, nitroazobenzene and trifluoromethyl phenyl admolecules, and all showed strong XPS signals for surface nitrogen (N 1s, ~402 eV) and/or fluorine (F 1s, ~686 eV). All adlayers were stable during exposure to air and different organic solvents. Raman spectroscopy was employed to interrogate the structure of chemisorbed nitroazobenzene on diamond and the spectral features were found to be similar to those observed for derivatized GC. Estimated surface coverages of 50–70% of a compact monolayer were achieved, on the basis of the XPS data. This coverage is too high to be attributed solely to modification of any adventitious sp^2 carbon impurity phase. The high coverage of covalently bound molecules, achievable by diazonium reduction, indicates that a variety of surface functionalities can be introduced on the normally unreactive diamond surface.

More recently, our group has been conducting detailed studies of the diazonium modification of diamond electrode surfaces with two types of diamond being investigated: microcrystalline and nanocrystalline thin films. Figure 10 shows typical first-scan cyclic voltammograms for the reduction of 4-nitrophenyl diazonium in 0.1 M $TBAClO_4/CH_3CN$. Curves for both

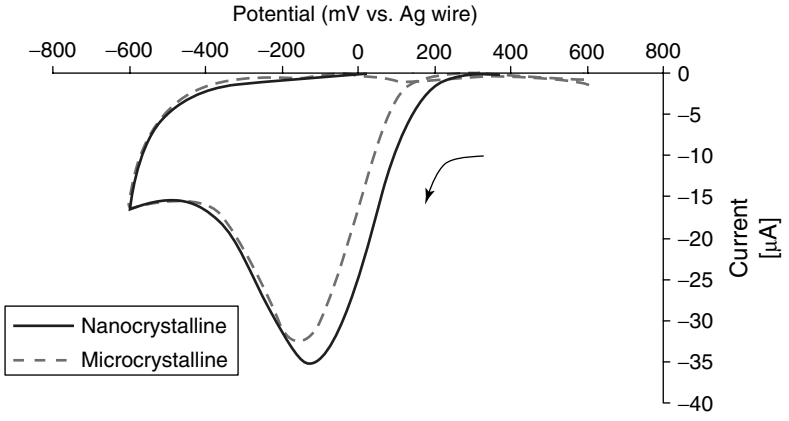


Fig. 10 First scan–cyclic voltammetric i−E curves for the reduction of 4-nitrophenyl diazonium tetrafluoroborate at microcrystalline and nanocrystalline diamond thin-film electrodes. Scan rate = 100 mV s^{-1}.

diamond film types are shown. The potential was swept initially in the negative direction from 600 to −600 mV at 0.1 V s^{-1}. The cathodic current increases for both electrodes at 200 mV, reaching a maximum near −150 mV. The peak current for both electrodes is ca. 35 μA as the geometric area is the same for both. The cathodic current is associated with the $1e^-$ reduction of the diazonium to form a nitrophenyl radical, as shown in the following. There is no anodic current during the reverse sweep as the reaction is chemically irreversible.

$$^{+}N_2-C_6H_4-NO_2 + e^- \longrightarrow \cdot C_6H_4-NO_2$$

Integration of the reduction peak current gives a charge density of $5.64(\pm 0.25) \times 10^{-2}$ and $6.81(\pm 0.06) \times 10^{-2}$ C cm^{-2} for microcrystalline and nanocrystalline diamond, respectively. The results indicate that the response of both diamond types is similar and that the response for multiple electrodes is quite reproducible. These charge values correspond to $3.55(\pm 0.16) \times 10^{17}$ and $4.28(\pm 0.04) \times 10^{17}$ radicals/cm^2 produced. A radical formed at the electrode–solution interface can then react as a surface site to form a covalently attached admolecule according to the reactions below. At least two radicals are needed for the surface modification. One is required to abstract hydrogen from the diamond surface creating an active site for radical coupling. The second radical then forms a covalent bond with the surface.

$$\text{(diamond)}-H + \cdot C_6H_4-NO_2 \longrightarrow \text{(diamond)}\cdot + C_6H_5-NO_2\{\text{abstraction}\}$$

$$\text{(diamond)}\cdot + \cdot C_6H_4-NO_2 \longrightarrow \text{(diamond)}-C_6H_4-NO_2\{\text{grafting}\}$$

For both electrodes, the number of radicals produced is at least 2 orders of magnitude greater than what is needed to form a compact monolayer. Liu and McCreery reported the theoretical coverage for the case of close packing on a flat surface with the nitrophenyl molecule upright, 12×10^{-10} mol cm^{-2} or 7×10^{14} molecules/cm^2 [48]. XPS (N 1s signal) was used to confirm the presence of the nitrophenyl adlayer.

The surface coverage of electrochemically active nitrophenyl groups was also determined on the basis of the charge passed during the reduction of the nitro functional group. In nonaqueous medium, the reduction of the attached nitro group involves the $1e^-$ reversible reduction to the anion radical. The reaction is shown below in Fig. 11.

The voltammetric reduction or oxidation charge can be used to calculate the number of electroactive molecules that are attached to the surface. Figure 12 shows cyclic voltammetric i−E curves for the reduction of the bound nitrophenyl groups at both types of modified diamond electrodes. The curves were recorded in 0.1 M TBATFB in CH_3CN

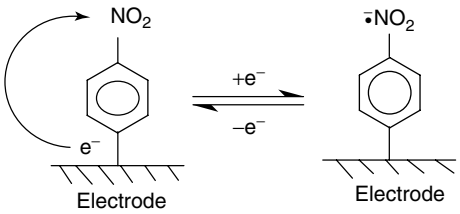


Fig. 11 Reaction mechanism for the electroreduction of the attached nitrophenyl admolecules.

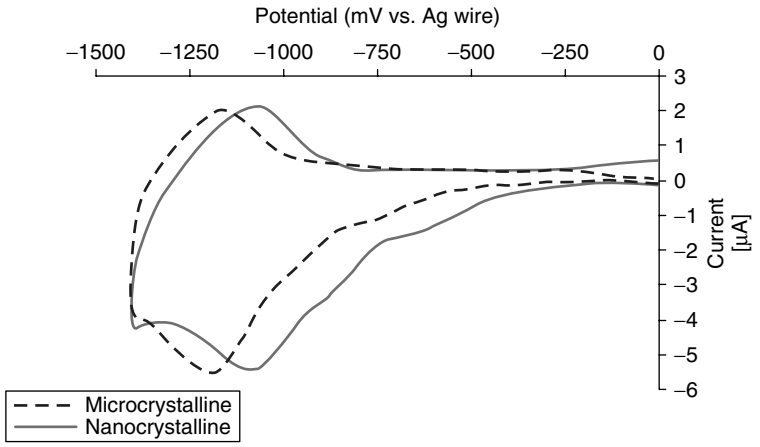


Fig. 12 Cyclic voltammetric i−E curves for the reduction of the nitrophenyl admolecules on the surface of microcrystalline and nanocrystalline diamond thin-film electrodes. Scan rate = 0.025 V s^{-1}.

at 0.025 V s^{-}. The cathodic current for the reduction begins at approximately −600 mV for both modified electrodes, reaching a maximum between −1100 and −1200 mV. The peak current for both electrodes is in the range of 5–6 μA or ca. 27 μA cm^{-2}. The curve shapes were quite stable with cycle number and were recorded after extensive electrode washing to remove unattached physisorbed molecules. On the basis of the oxidation peak charge, the surface coverage of electroactive molecules on both electrode types was calculated to be 1.1×10^{-9} mol cm^{-2} or 6.5×10^{14} molecules/cm^2. This value is very close to the theoretical monolayer coverage of 7×10^{14} mol/cm^2 [48], and is in good agreement with the value reported by Wang and coworkers for ultrananocrystalline diamond thin-film electrodes [99]. The results demonstrate that the diazonium chemistry is a viable method for chemically modifying diamond electrode surfaces and that the admolecules are in good electronic communication with the conducting electrode.

The Hamers' group has been particularly active and innovative in recent years with the chemical modification of diamond surfaces for biological applications [100]. Diamond appears to be a suitable material for integrated sensing and signal processing because of its chemical and electrical properties. The authors showed that nanocrystalline diamond thin films can be covalently modified with DNA oligonucleotides and that diamond surfaces provide a stable and selective platform for subsequent hybridization processes. A photochemical modification scheme was used to first modify a clean and hydrogen-terminated diamond surface. This step produced a homogeneous layer of amine groups that serve as sites for DNA attachment. After linking DNA to the amine groups, hybridization reactions with fluorescently tagged complementary and noncomplementary oligonucleotides showed no detectable nonspecific adsorption with extremely good selectivity between the matched and mismatched sequences. Comparison of DNA-modified

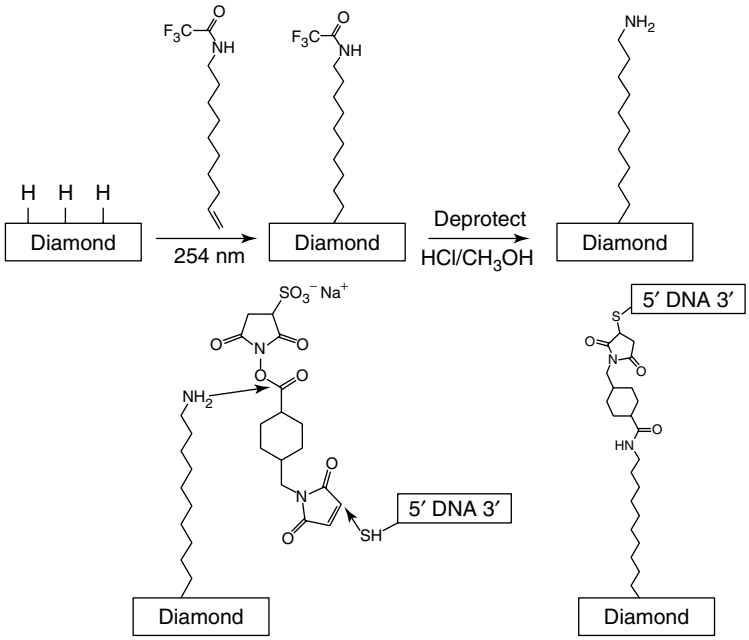


Fig. 13 Reaction steps in the DNA attachment to diamond thin-film surfaces [100].

ultrananocrystalline diamond (produced from CH_4/Ar mixtures) with other commonly used surfaces for biological modification, such as Au, GC, Si, and glass, showed that diamond is unique in its ability to achieve very high stability and sensitivity while also being compatible with microelectronics processing technologies. The authors concluded that diamond might be the ideal substrate for integration of microelectronics with biological modification and sensing. Figure 13 shows the reaction sequence.

1.6.3.5 Effect of Surface Modification on the Electrochemical Properties

So far, there has been minimal work reported on how the surface modification of diamond affects the electron-transfer and adsorption properties. The exception to this is some work on the effect of adding surface oxygen [40, 89, 90]. Our group has investigated the effect of modifying the surface of diamond electrodes with nitrophenyl admolecules via the aryldiazonium reduction reaction. Using cyclic voltammetry and redox systems such as $Fe(CN)_6^{-3/-4}$, $Ru(NH_3)_6^{+3/+2}$, catechol, methylcatechol, and *tert*-butylcatechol, the preliminary work indicates that the nitrophenyl admolecules act as a blocking layer for some systems ($Fe(CN)_6^{-3/-4}$ and $Ru(NH_3)_6^{+3/+2}$). Similar blocking layer effects have been reported by Wang and coworkers for nitrophenyl adlayers on ultrananocrystalline diamond [99]. This may be due to the formation of multilayers [52]. On the other hand, the adlayer seems to exhibit little influence on the voltammetric response for other redox systems (catechols). Much remains to be done in this area.

1.6.4 Conclusions

This chapter gives a brief overview of some of the recent trends in the area of chemically modified sp^2 and sp^3 bonded carbon electrodes. Electrochemically-assisted modification of carbon electrode surfaces, both sp^2 and sp^3 types, is fairly well developed. A variety of tools are available for characterizing modified electrode surfaces. For example, SEM and AFM are used to probe the modified electrode surface topography, XPS is used to determine the surface chemical composition, and Raman spectroscopy is employed to examine the orientation and coverage of admolecules. The chemical modification of sp^2 carbon materials is quite a mature field; on the other hand, the chemical modification of sp^3 carbon materials is in its infancy. Electrically conducting diamond is an advanced carbon electrode that meets the requirements for a wide range of applications. Research has already shown that this material is superior to commonly used sp^2 carbon electrodes (e.g. GC) in terms of several properties and in some of its functioning in electrochemical applications. Much remains to be learned, however, about structure–function relationships at electrically conducting diamond electrodes. Research directed toward the development of chemistries useful for modifying the surface of sp^2 and sp^3 carbon materials will ultimately provide molecular of interactions at electrified interfaces. The fundamental knowledge gained from this research will enable a better understanding of structure–function relationships with these electrode materials. Clearly, one area of research with sp^3 bonded carbon (e.g. diamond) that will continue to evolve is the use of this material as a platform for chemical and biological sensing.

Acknowledgments

The financial support provided by the National Science Foundation (NIRT Program, CTS-0210366) and the Department of Energy Office of Basic Science (DE-FG02-01ER15120) is gratefully acknowledged.

References

1. R. L. McCreery, in *Electroanalytical Chemistry* (Ed.: A. J. Bard), Marcel Dekker, New York, 1991, pp. 221–374, Vol. 17.
2. G. M. Swain, Electrically conducting diamond thin-films: advanced electrode materials for electrochemical technologies in *Electroanalytical Chemistry* (Eds.: A. J. Bard, I. Rubinstein), Marcel Dekker, New York, 2004, pp. 182–277, Vol. 22.
3. G. M. Swain, Electroanalytical applications of diamond electrodes in *Thin-Film Diamond II*, (Semiconductors and Semimetals) (Eds.: C. E. Nebel, J. Ristein), Elsevier, Amsterdam, The Netherlands, 2004, pp. 121–148, Vol. 77.
4. M. Hupert, A. Muck, J. Wang et al., *Diamond Relat. Mater.* **2003**, *12*, 1940.
5. A. Fischer, Y. Show, G. M. Swain, *Anal. Chem.* **2004**, *76*, 2553.
6. C. M. Elliot, R. W. Murray, *Anal. Chem.* **1976**, *48*, 1247.
7. R. W. Murray, *Philos. Trans. R. Soc. London, Ser. A* **1981**, *302*, 253.
8. D. H. Karweik, C. W. Miller, M. D. Porter et al., *Prospects in the Analysis of Chemically Modified Electrodes, ACS Symposium Series, #199 Industrial Applications of Surface Analysis* (Eds.: L. A. Casper, C. J. Powell), Copyright 1982 by the American Chemical Society, 1982, pp. 89–119.
9. R. W. Murray, A. G. Ewing, R. A. Durst, *Anal. Chem.* **1987**, *59*, 379A.
10. R. L. McCreery, *Interface* **2004**, *13*, 46.
11. I. F. Hu, D. H. Karweik, T. Kuwana, *J. Electroanal. Chem.* **1985**, *188*, 59–72.
12. P. Chen, M. A. Fryling, R. L. McCreery, *Anal. Chem.* **1995**, *67*, 3115.
13. P. Chen, R. L. McCreery, *Anal. Chem.* **1996**, *68*, 3958.
14. S. Ranganathan, T.-C. Kuo, R. L. McCreery, *Anal. Chem.* **1995**, *71*, 3574.

15. S. Hunt-DuVall, R. L. McCreery, *Anal. Chem.* **1999**, *71*, 4594.
16. G. K. Kiema, M. Aktay, M. T. McDermott, *J. Electroanal. Chem.* **2003**, *540*, 7.
17. K. B. Holt, A. J. Bard, Y. Show et al., *J. Phys. Chem. B* **2004**, *108*, 15117.
18. J. A. Bennett, J. Wang, Y. Show et al., *J. Electrochem. Soc.* **2004**, *151*, E306.
19. P. Sonthalia, E. McGaw, Y. Show et al., *Anal. Chim. Acta* **2004**, *522*, 35.
20. Y. Show, M. A. Witek, P. Sonthalia et al., *Chem. Mater.* **2003**, *15*, 879.
21. M. C. Granger, M. Witek, J. Xu et al., *Anal. Chem.* **2000**, *72*, 3793.
22. J. Xu, G. M. Swain, *Anal. Chem.* **1998**, *70*, 1502.
23. M. D. Koppang, M. Witek, J. Blau et al., *Anal. Chem.* **1999**, *71*, 1188; M. A. Witek, G. M. Swain, *Anal. Chim. Acta* **2001**, *440*, 119.
24. G. W. Muna, N. Tasheva, G. M. Swain, *Environ. Sci. Technol.* **2004**, *38*, 3674.
25. G. W. Muna, V. Quaiserova, G. M. Swain, *Electroanal.* in press.
26. J. Stotter, J. K. Zak, Y. Show et al., *Anal. Chem.* **2002**, *73*, 908.
27. S. Haymond, J. K. Zak, Y. Show et al., *Anal. Chim. Acta* **2003**, *500*, 137.
28. J. Stotter, S. Haymond, J. K. Zak et al., *Interface* **2003**, *12*, 33.
29. C. Terashima, T. N. Rao, B. V. Sarada et al., *Anal. Chem.* **2002**, *74*, 895.
30. J. Wang, G. Chen, M. P. Chatrathi et al., *Anal. Chem.* **2003**, *75*, 935.
31. D. Shin, B. V. Sarada, D. A. Tryk et al., *Anal. Chem.* **2003**, *75*, 530.
32. David. Sopchak, Barry. Miller, Rafi. Kalish et al., *Electroanal.* **2002**, *14*, 473.
33. T. N. Rao, B. H. Loo, B. V. Sarada et al., *Anal. Chem.* **2002**, *74*, 1578.
34. E. Popa, Y. Kubota, D. A. Tryk et al., *Anal. Chem.* **2000**, *72*, 1724.
35. S. Sarada, T. N. Rao, D. A. Tryk et al., *Anal. Chem.* **2000**, *72*, 1632.
36. H. B. Martin, A. Argoitia, U. Landau et al., *J. Electrochem. Soc.* **1996**, *143*, L133.
37. C. Prado, G. Flechsig, P. Gruendler et al., *Analyst* **2002**, *127*, 329.
38. J. Cvacka, V. Quaiserova, J. Park et al., *Anal. Chem.* **2003**, *75*, 2678.
39. J. Xu, Q. Chen, G. M. Swain, *Anal. Chem.* **1998**, *70*, 3146.
40. M. C. Granger, G. M. Swain, *J. Electrochem. Soc.* **1999**, *146*, 4551.
41. C. A. McDermott, K. R. Kneten, R. L. McCreery, *J. Electrochem. Soc.* **1993**, *140*, 2593.
42. Q. Chen, G. M. Swain, *Langmuir* **1998**, *14*, 7017.
43. T.-C. Kuo, R. L. McCreery, *Anal. Chem.* **1999**, *71*, 1553–1560.
44. C. Ueda, D. C.-S. Tse, T. Kuwana, *Anal. Chem.* **1982**, *54*, 850–856.
45. A. J. Downard, *Electroanal.* **2000**, *12*, 1085–1096.
46. M. Delamar, R. Hitmi, J. Pinson et al., *J. Am. Chem. Soc.* **1992**, *114*, 5883–5884.
47. C. Bourdillon, M. Delamar, C. Demaille et al., *J. Electroanal. Chem.* **1992**, *336*, 113–123.
48. Y.-C. Liu, R. L. McCreery, *J. Am. Chem. Soc.* **1995**, *117*, 11254–11259.
49. P. Allongue, M. Delamar, B. Desbat et al., *J. Am. Chem. Soc.* **1997**, *119*, 201–207.
50. B. Ortiz, C. Saby, G. Y. Champagne et al., *J. Electroanal. Chem.* **1998**, *455*, 75–81.
51. T.-C. Kuo, R. L. McCreery, G. M. Swain, *Electrochem. Solid-State Lett.* **1999**, *2*, 288–290.
52. J. K. Kariuki, M. T. McDermott, *Langmuir* **2001**, *17*, 5947–5951.
53. J. A. Harnisch, D. B. Gazda, J. W. Anderegg et al., *Anal. Chem.* **2001**, *73*, 3954–3959.
54. B. D. Bath, H. B. Martin, R. M. Wightman et al., *Langmuir* **2001**, *17*, 7032–7039.
55. A. O. Solak, L. R. Eichorst, W. J. Clark et al., *Anal. Chem.* **2003**, *75*, 296–305.
56. D. T. Fagan, I.-F. Hu, T. Kuwana, *Anal. Chem.* **1985**, *57*, 2759.
57. K. J. Stutts, P. M. Kovach, W. G. Kuhr et al., *Anal. Chem.* **1983**, *54*, 1632–1634.
58. G. M. Swain, T. Kuwana, *Anal. Chem.* **1992**, *64*, 565–568.
59. M. T. McDermott, K. Kneten, R. L. McCreery, *J. Phys. Chem.* **1992**, *96*, 3124–3130.
60. B. Barbier, J. Pinson, G. Desarmot et al., *J. Electrochem. Soc.* **1990**, *137*, 1757–1764.
61. R. S. Deinhammer, M. Ho, J. W. Anderegg et al., *Langmuir* **1994**, *10*, 1306–1313.
62. D. A. Buttry, J. C. M. Peng, J.-B. Donnet et al., *Carbon* **1999**, *37*, 1929–1940.
63. P. A. Brooksby, A. J. Downard, *Langmuir* **2004**, *20*, 5038.
64. S. Kwon, R. Vidic, E. Borguet, *Carbon* **2002**, *40*, 2351–2358.
65. S. Kwon, R. Vidic, E. Borguet, *Surf. Sci.* **2003**, *522*, 17–26.

66. R. L. McCreery, Carbon electrode surface chemistry in *Neuromethods, Vol. 27: Voltammetric Methods in Brain Systems* (Eds.: A. Boulton, G. Baker, R. N. Adams), Humana Press, Totowa, NJ, USA, 1995
67. M. A. Fryling, J. Zhao, R. L. McCreery, *Anal. Chem.* **1995**, *67*, 967.
68. K. G. Ray III, R. L. McCreery, *J. Electroanal. Chem.* **1999**, *469*, 150.
69. D. M. Gruen, *Annu. Rev. Mater. Sci.* **1999**, *29*, 211.
70. D. M. Gruen, S. Liu, A. K. Krauss et al., *Appl. Phys. Lett.* **1994**, *64*, 1502.
71. C. D. Zuiker, A. R. Krauss, D. M. Gruen et al., Characterization of diamond thin films by core-level photoabsorption and UV excitation raman spectroscopy in *Applications of Synchrotron Radiation Techniques to Material Sciences III* (Eds.: L. J. Terminello, S. M. Mini, H. Ade et al.), Proceedings of the Materials Research Society, San Francisco, April 8–12, 1996, p. 211, Vol. 437.
72. T. G. McCauley, D. M. Gruen, A. R. Krauss, *Appl. Phys. Lett.* **1998**, *73*, 1646.
73. P. C. Redfern, D. A. Horner, L. A. Curtiss et al., *J. Phys. Chem.* **1996**, *100*, 11654.
74. D. M. Gruen, *R&D Mag.* **1997**, *4*, 57.
75. D. Zhou, D. M. Gruen, L. C. Qin et al., *J. Appl. Phys.* **1998**, *84*, 1981.
76. L. C. Qin, D. Zhou, A. R. Krauss et al., *Appl. Phys. Lett.* **1998**, *72*, 3437.
77. D. Zhou, T. G. McCauley, L. C. Qin et al., *J. Appl. Phys.* **1998**, *83*, 540.
78. J. Birrell, J. A. Carlisle, O. Auciello et al., *Appl. Phys. Lett.* **2002**, *81*, 2235.
79. J. Birrell, J. E. Gerbi, O. Auciello et al., *Diam. Rel. Mater.* **2005**, *14*, 86.
80. F. Maier, M. Riedel, B. Mantel et al., *Phys. Rev. Lett.* **2000**, *85*, 3472; J. Chevallier, Hydrogen diffusion and acceptor passivation in diamond in *Thin-Film Diamond II*, Semiconductors and Semimetals (Eds.: C. E. Nebel, J. Ristein), Elsevier, Amsterdam, The Netherlands, 2004, pp. 1–35, Vol. 77.
81. F. Maier, J. Ristein, L. Ley, *Phys. Rev. B* **2001**, *64*, 165411.
82. A. Denisenko, A. Aleksov, A. Pribil et al., *Diamond Relat. Mater.* **2000**, *9*, 1138.
83. R. Muller, A. Denisenko, E. Kohn, *Diamond Relat. Mater.* **2003**, *12*, 554.
84. H. Umezawa, H. Taniuchi, T. Arima et al., *Diamond Relat. Mater.* **2001**, *10*, 1743–1748.
85. S. Miyamoto, H. Matsudaira, H. Ishizaka et al., *Diamond Relat. Mater.* **2003**, *12*, 399.
86. A. Freedman, *J. Appl. Phys.* **1994**, *75*, 3112.
87. V. S. Smentkowski, J. T. Yates Jr., *Science* **1996**, *271*, 193.
88. H. B. Martin, A. Argoitia, J. C. Angus et al., *J. Electrochem. Soc.* **1999**, *146*, 2959.
89. I. Duo, C. Levy-Clement, A. Fujishima et al., *J. Appl. Electrochem.* **2004**, *34*, 935.
90. A. Hanks, G. M. Swain, unpublished work.
91. T. Ando, K. Yamamoto, M. Ishii et al., *J. Chem. Soc. Faraday Trans.* **1993**, *89*, 3635.
92. H. B. Martin, P. W. Morrison Jr., *Electrochem. Solid-State Lett.* **2001**, *4*, E17.
93. B. Ohtani, Y.-H. Kim, T. Yano et al., *Chem. Lett.* **1998**, 953.
94. C. S. Kim, R. C. Mowrey, J. E. Butler et al., *J. Phys. Chem. B* **1998**, *102*, 9290.
95. J. S. Hovis, S. K. Coulter, R. J. Hamers et al., *J. Am. Chem. Soc.* **2000**, *122*, 732.
96. T. Stother, T. Knickerbocker, J. N. Russell Jr. et al., *Langmuir* **2002**, *18*, 968.
97. P. Krysinski, Y. Show, J. Stotter et al., *J. Am. Chem. Soc.* **2003**, *125*, 12726.
98. S. Ida, T. Tsubota, S. Tanii et al., *Langmuir* **2003**, *19*, 9693.
99. J. Wang, M. A. Firestone, O. Auciello et al., *Langmuir* **2004**, *20*, 11450.
100. W. Yang, O. Auciello, J. E. Butler et al., *Nature Mater.* **2002**, *1*, 253.

1.7 Chemically Modified Oxide Electrodes

Chimed Ganzorig and Masamichi Fujihira
Tokyo Institute of Technology, Yokohama, Japan

1.7.1 Introduction

This chapter describes the chemical modification of various *n*-type transparent conducting oxide (TCO) electrode surfaces with different organic molecules, in which one end is a binding group, the other end is a terminal group with a different functionality (e.g. permanent dipole moment), and these two ends are linked by groups of alkyl chain and π-system. Studies for the formation of various organic monolayers with carboxylic and phosphonic acids as well as organosilanes on these oxide electrodes are reviewed and discussed comprehensively in this chapter. Several examples of organic chemical treatments used for surface modifications of *n*-type TCO electrodes are presented. In addition, useful descriptions of the most widely used preparative deposition techniques for thin films of TCO electrodes are presented (see Sect. 1.7.2).

1.7.2 Electrode Preparation

1.7.2.1 General: Transparent Conducting Oxide Films

The first report of a transparent conducting oxide (TCO) was published in 1907, when Bädeker [1] reported that thin films of Cd metal deposited on glass in a glow-discharge chamber could be oxidized to become transparent while remaining conducting. Since then, most researches have focused on *n*-type semiconductors consisting of metal (Sn^{4+}, Ti^{2+}, In^{3+}, Zn^{2+}, and Cd^{2+}) oxides and their corresponding alloys to develop highly transparent and electrically conductive thin films. The early published material in this field up to about 1955 has been reviewed by Holland [2]. Major developments in this field as regards the deposition techniques of preparation, properties of TCO films and some applications until the mid-1980s have been summarized in several comprehensive reviews [3–10]. More recent reviews of TCO films are available [11–16].

The principle constituents of *n*-type TCOs have been simple or binary oxides of SnO_2, In_2O_3, ZnO, and CdO. Sb-doped SnO_2, F-doped SnO_2, Sn-doped In_2O_3, and F- or Al-doped ZnO have been the principle commercial TCO films in practical use [13–15]. The most widely used TCO film is Sn-doped In_2O_3 (indium–tin oxide or ITO) due to its high conductivity, work function, and transparency in the visible spectral range. Conductive ZnO films doped with an impurity have recently attracted much attention as an alternative candidate to ITO. Although ZnO films are nontoxicity, material abundance, low cost, and easily etchable, they are more chemically unstable than ITO films [17].

CdO is not often used as a TCO semiconductor because of its relatively low bandgap of about 2 eV resulting in excessive light absorption from about 0.5 μm down into the ultraviolet [7]. Much better is cadmium stannate (Cd_2SnO_4) film [18], which has better transmission and lower resistivity than CdO. Ternary compounds such as Cd_2SnO_4, $CdSnO_4$, and $CdIn_2O_4$ were developed prior to 1980 [8, 9, 18], but their TCO films have not yet been used widely. To obtain new *n*-type multicomponent TCO films using ternary

Encyclopedia of Electrochemistry. Edited by A.J. Bard and M. Stratmann
Vol. 10 *Modified Electrodes*. Edited by M.Fujihira, I.Rubinstein, and J.F.Rusling
Copyright © 2007 Wiley-VCH Verlag GmbH & Co. KGaA, Weinheim. ISBN: 978-3-527-30402-8

compounds, several approaches have been studied in recent years [15]. In addition to *n*-type TCO films, new *p*-type TCO materials such as $CuAlO_2$ and $SrCu_2O_2$ have been reported recently [19–22].

Titanium dioxide, TiO_2, is known to exist in the amorphous form and in three crystalline modifications, rutile, anatase, and brookite. Thin films of TiO_2 have been shown to possess either a rutile or anatase structure depending upon their mode of deposition. Brookite is not a stable modification and anatase is converted to rutile at high temperatures, 800–900 °C [2]. TiO_2 is the most investigated system in the surface science of metal oxides. Recent progress in understanding the surface science of TiO_2 was reviewed extensively by Diebold [23].

Original works and their useful descriptions of the most widely used deposition methods of preparation for TCO films have been discussed comprehensively in reviews [3–16, 23] and books [2, 24–30]. Several different techniques have been tried out to fabricate films of TCO electrodes. Thin-film deposition techniques are generally classified in two main groups: *chemical methods* (spray pyrolysis, chemical vapor deposition, sol-gel, chemical bath deposition, electroplating) and *physical methods* (evaporation, sputtering, reactive ion plating, pulsed laser deposition). Some of the innovations [1, 31–63] in these deposition techniques for TCO thin films are listed in Table 1. After the cleaning methods of the substrate surfaces are discussed in briefly in Sect. 1.7.2.2, a brief account of numerous methods used for film deposition, particularly during the past years, in Sects. 1.7.2.3 and 1.7.2.4. Some early references are also cited wherever necessary. In addition, the characterization of TCO thin films is described in Sect. 1.7.2.5.

1.7.2.2 Cleaning of Substrate Surfaces

A number of techniques have been advocated for preparing highly clean substrate before depositing thin films on its surface by various deposition techniques. Depending on the deposition technique, the substrate can have a significant influence on the properties of thin films. Glass substrates are most commonly used. The low temperature processes such as magnetron sputtering, ion beam sputtering, and reactive ion plating allow the deposition of oxide films also onto polymer substrates such as plastic, Mylar, and poly(ethylene-terephthalate) [9].

Surfaces exposed to the atmosphere are generally contaminated. Any unwanted material and/or energy on a surface are regarded as a contaminant. Surface contamination can be gaseous, liquid, or solid in its physical state and may be present as a film or in particulate form. Furthermore, it can be ionic or covalent and inorganic or organic in its chemical character. Most scientific and technical investigations and applications, however, require clean surfaces.

The cleaning of surfaces is a very important and also a very difficult and delicate operation. There are number of diverse cleaning techniques used in various scientific and industrial cleaning problems [64]. Cleaned surfaces can be classified into two categories: atomically clean surfaces and technologically clean surfaces. Surfaces of the first category are required for special scientific purposes and these can be only realized in ultrahigh vacuum.

A further distinction must be made between cleaning methods that are applicable in the atmosphere and those that are applicable only in vacuum. In all cases where handling of the parts and the use of solvents is required, cleaning cannot

Tab. 1 History of processes for making *n*-type TCO thin films [1, 31–63]

Material	*Deposition technique*	*References*
CdO	Sputtered Cd films	1
SnO_2	Postoxidation of Sn	31
TiO_2	Fuming of $TiCl_4$	32
SnO_2:Cl	Spray pyrolysis	33
TiO_2	Postoxidation of Ti	34
ZnO	Postoxidation of Zn	35
SnO_2:Sb	Spray pyrolysis	36
In_2O_3:Cl	Spray pyrolysis	37
SnO_2	Reactive sputtering	38
SnO_2:F	Spray pyrolysis	39
In_2O_3:Sn	Spray pyrolysis	40
ZnO	Reactive sputtering	41
In_2O_3	Reactive sputtering	42
In_2O_3:Sn	Reactive sputtering	43
ZnO	Direct sputtering	44
SnO_2:Sb	CVD	45
ZnO:Al	Magnetron sputtering	46
Cd_2SnO_4	Direct sputtering	47
Cd_2SnO_4	Spray pyrolysis	48
ZnO:Cl	Spray pyrolysis	49
SnO_2:F	CVD	50
ZnO:In	Spray pyrolysis	51
ZnO:B, Ga, In	Magnetron sputtering	52
TiN	CVD	53
ZnO:B	CVD	54
ZnO:Ga	Sputtering	55
ZnO:F	CVD	56
ZnO:Al	CVD	57
ZnO:Ga	CVD	58
ZnO:In	CVD	59
Zn_2SnO_4	Magnetron sputtering	60
$ZnSnO_3$	Magnetron sputtering	61
Cd_2SnO_4	Pulsed laser deposition	62
ZnO:Al	Pulsed laser deposition	63

be performed in a vacuum. If cleaning in vacuum, for example, by heating operations and particle bombardment is used, then this is generally conducted inside the deposition system [27].

1.7.2.2.1 **Cleaning with Solvents** In this process, various cleaning fluids are used. A distinction must be made between demineralized water or aqueous systems such as water with detergents, diluted acids or bases and nonaqueous solvents such as alcohols, ketones, petroleum fractions, and chlorinated or fluorinated hydrocarbons. Emulsions and solvent vapors are also used. The type of solvent used depends on the nature of the contaminants [64]. There are many reports on cleaning of glass by solvents; some examples are given in Refs. 2, 27, 64–67.

Rubbing and Immersion Cleaning Perhaps the simplest method of removing superficial dirt from glass is to rub the surface with cotton wool dipped in the mixture of precipitated chalk and alcohol or ammonia. There is evidence, however, that traces of chalk can be left behind on such surfaces so that after that treatment the parts must carefully be washed off in pure water or alcohol. This method is best suited as a precleaned operation, that is, as the first step in a cleaning sequence.

A simple and often used cleaning technique is that of immersion or dip cleaning. The basic equipment employed in dip cleaning is easy to construct and inexpensive. An open tank of glass, plastic, or stainless steel is filled with a cleaning fluid and the glass parts, which are clamped with a pair of tweezers or are inserted in a special holder, are then dipped in the fluid. If the degree of cleaning is not sufficient, the operation can be repeated by further dipping in the same fluid or other cleaning fluids.

In addition to physical cleaning, chemical reactions can be also exploited for cleaning purposes. Various acids with strengths ranging from weak to strong, as well as mixtures such as chromic and sulfuric acid are used. All acids, with the exception of hydrofluoric acid, must be used hot, that is, between 60 and 85 °C, to produce a clean glass surface. Acid cleaning cannot be used for all types of glasses. This is especially true for glasses having a high barium or lead oxide content, such as some optical glasses. According to a report in [67], a cold diluted mixture of 5% HF, 33% HNO_3, 2% Teepol®, and 60% H_2O should be an excellent universal fluid for cleaning glass and silica.

Caustic solutions exhibit a detergency and the ability to remove oils and greases. The lipids and fatty materials are saponified by the bases to soaps. These water-soluble reaction products can readily be rinsed off the clean surface. It is desirable to limit the removal process to the contaminant layer, but a mild attack of the substrate material itself is often tolerable and ensures that the cleaning process is complete. Attention must be paid to unwanted, stronger etching, and leaching effects. Such processes may destroy the surface quality and should therefore be avoided.

Vapor Degreasing Vapor degreasing is a process that is primarily useful for removing grease and oil films from surfaces. In glass cleaning, it is often used as the last step in a sequence of various cleaning operations. A vapor-degreasing apparatus consists essentially of an open tank with heating elements in the bottom and water-cooled condensing coils running around the top perimeter. The cleaning fluid may be isopropyl alcohol or one of the chlorinated and fluorinated hydrocarbons. The solvent is vaporized and forms a hot, high-density vapor, which remains in the equipment because the condenser coils prevent vapor loss. The precleaned cold glass pieces, in special holders, are immersed in the dense vapor for periods ranging from 15 s to several minutes. Pure cleaning fluid vapor has a high solvency for fatty substrates, and when it condenses on cold glass a solution is formed with the contaminant, which drips off and is replaced by more pure condensing solvent. The process runs until the glass is so hot that condensation ceases [66, 67].

Vapor degreasing is an excellent way to obtain highly clean surfaces. The efficiency of cleaning can be checked by determining the coefficient of friction, in addition to dark-field-inspection, contact-angle, and

thin-film-adhesion measurements. High values are typical for clean surfaces [67].

Ultrasonic Cleaning Ultrasonic cleaning provides a valuable method of removing stronger adherent contaminants. This process produces an intense physical cleaning action and is therefore a very effective technique for breaking loose contaminants that are strongly bonded to a surface. Inorganic acidic, basic, and neutral cleaning fluids, as well as organic liquids, are used. The cleaning is performed in a stainless steel tank containing the cleaning fluid and equipped with transducers on the bottom or at the sidewalls. These transducers convert an oscillating electrical input into a vibratory mechanical output [66]. Glass is chiefly cleaned at frequencies between 20 and 40 kHz. The action of these sound waves gives rise to cavitation at the glass surface/cleaning liquid interface. Ultrasonic cleaning is also used to remove pitch and polishing-agent residues from glass surface.

Spray Cleaning The spray-cleaning process uses the shearing forces exerted by a moving fluid on small particles to break the adhesion forces holding the particles to the surface [27]. The particles will be suspended in the turbulent fluid and carried away from the surface. In general, the same types of liquids that are used for immersion cleaning can also be used for spray cleaning. Increasing the pressure and the corresponding liquid velocity results in an increase in cleaning efficiency. Pressures of about 350 kPa are used. High-pressure spraying of organic liquids causes problems with surface cooling followed by unwanted water-vapor condensation, which can leave surface spots. This can be prevented either by using a surrounding nitrogen atmosphere or using a water spray, which shows no spotting, instead of an organic liquid. High-pressure liquid spraying is a very powerful and effective method to remove particles as small as 5 μm. In some cases also, high-pressure air or gas jets are very powerful.

1.7.2.2.2 **Cleaning by Heating and Irradiation** Placing substrates in a vacuum causes evaporation of volatile impurities. The effectiveness of this process also depends on how long the substrates remain in the vacuum and on the temperature as well as on the type of contaminant and on the substrate material. Under high-vacuum conditions at ambient temperature, the influence of partial pressure on desorption is negligible. Therefore, desorption is produced here by heating. Heating the glass surfaces causes a more or less strong desorption of adsorbed water and various hydrocarbon molecules, depending on the temperature. The applied temperatures are in the range between 100 and 350 °C and the required heating time is between 10 and about 60 min. Only in case of ultrahigh vacuum applications is it necessary to use heating temperatures higher than 450 °C in order to obtain atomically clean surfaces.

Cleaning by heating is particularly advantageous in all those cases where, because of desired special film properties, film deposition is performed at higher substrate temperatures. But, as a consequence of heating, polymerization of some hydrocarbons to larger aggregates and decomposition to carbonaceous residues may also occur. This sometimes makes such heat treatments problematical. However, treatment with high-temperature flames, for instance, a hydrogen-air flame, shows good results, although the surface temperature

in such a process reaches only about 100 °C. In a flame, various kinds of ions as well as impurities and molecules of high thermal energy [68, 69] are present. It is assumed [67] that the cleaning action of a flame is similar to that of a glow discharge in which highly energetic, ionized particles strike the surface of the parts to be cleaned. According to this model, removal of material from a glass surface in a flame may occur because of the high-energy particles, which impart their energy to the adsorbed contaminants. Particle bombardment and surface recombination of ions will liberate heat and may in this way also help to desorb contaminant molecules.

Another technique for cleaning surfaces is the use of ultraviolet (UV) radiation to decompose hydrocarbons. Exposure times of about 15 h in air produced clean glass surfaces [70]. If properly precleaned surfaces are placed within a few millimeters of an ozone-producing UV source, clean surfaces are produced in even less than one minute [71]. This clearly demonstrates that the presence of ozone increases the cleaning speed. As for the cleaning mechanism, it is known that the contaminant molecules are excited and/or dissociated under the influence of UV. Furthermore, it is also known that the production and the presence of ozone produce highly reactive atomic oxygen. It is assumed that the excited contaminant molecules and the free radicals, produced by the dissociation of the contaminant, react with atomic oxygen and form simpler and volatile molecules like H_2O, CO_2, and N_2.

1.7.2.2.3 **Cleaning by Stripping Lacquer Coatings** The use of strippable adhesive or lacquer coatings to remove dust particles from a surface is a very special and somewhat unconventional cleaning technique. The basic cleaning procedure is quite simple. The thick lacquer coating is applied to the precleaned surface with a brush or by dipping. The parts are then allowed to dry completely. In a subsequent operation, performed in a laminar flow box to prevent recontamination, the lacquer film is stripped off. Attempts to strip off the film in vacuum prior to thin-film deposition were only partly successful because of the difficulty in detecting surface residues inside the evacuated system [27].

1.7.2.2.4 **Cleaning in an Electrical Discharge** Undoubtedly, one of the most efficient methods of cleaning a glass surface is to immerse it in a glow discharge, and much of work on this subject has been reviewed by Holland [2, 67]. Generally, the discharge burns between two, only negligibly sputtered, aluminum electrodes, which are positioned near the substrates. Oxygen and sometimes argon are normally used to form the necessary gas atmosphere. It seems, however, that mild cleaning is effective only when oxygen is present. Typical discharge voltages are in the range between 500 and 5000 V. The substrates are immersed into the plasma, without being a part of the glow-discharge circuit. Only precleaned substrates are treated. A glass surface immersed in the plasma of a glow discharge is bombarded by electrons, mainly positive ions and activated atoms and molecules. Therefore, the cleaning action of a glow discharge is very complex.

The most important parameters in glow-discharge cleaning are the type of applied voltage (AC or DC), the value of discharge voltage, the current density, type of gas and gas pressure, duration of treatment, type of material to be cleaned, shape and arrangement of electrodes,

and position of the parts to be cleaned. Substrate cleaning in high vacuum by bombardment with ions generated in special ion guns is seldom used for industrial coating processes. Ion-beam technologies, however, offer interesting possibilities not only in cleaning but also in polishing and machining of optical surfaces, as well as for modifying the optical constants of subsurface layers [27].

1.7.2.2.5 **Cleaning Cycles** Surface cleaning is performed by various methods, such as washing with solvents, heating, stripping, and plasma treatment. Each has its range of applicability. Solvent cleaning has the greatest range of utility but is inadequate in many cases, particularly where the solvents themselves are contaminants. Heating is useful up to the temperature limits of the surfaces to be cleaned. Plasma treatment provides a cleaning method where contaminant bond strengths exceed the temperature limits of the system. The plasma energy can be much higher than that achieved thermally and still not damage surfaces because of the low thermal flux.

No one method, however, has all the desired features of simplicity, low cost, and effectiveness. To achieve optimum cleanliness of substrate surfaces, combinations of the various cleaning methods must be used. There is no universal approach to cleaning cycles. There are, however, some general guidelines to follow when establishing cleaning sequences.

Precleaning of glass parts usually starts with immersion cleaning in detergent solutions, assisted by rubbing, wiping, or ultrasonic agitation, followed by rinsing in demineralized water and/or alcohol. It is important to get the parts dry without allowing solution sediment to remain on the surface because it is often hard to remove later [27].

In a cleaning operation, the sequence of cleaning liquids must be chemically compatible and mixable without precipitation at all stages. A change from acidic solutions to caustic solutions requires rinsing with plain water in between. The change from aqueous solutions to organic fluids always requires an intermediate treatment with a mixable co-solvent such as alcohol or special dewatering fluids. The last steps in a cleaning cycle must be performed extremely carefully. In a wet operation, the final rinsing fluid used must be as pure as possible and, generally, it should be as volatile as is practical. Finally, it is important that cleaned surfaces are not left unprotected. Proper storage and handing before further treatment by film deposition are stringent requirements. Mattox [72] discussed the types and origins of various contaminants and reviewed the cleaning processes for oxide, metal, and organic surfaces and the mechanisms of adhesion to these surfaces.

1.7.2.2.6 **Cleaning of Organic Glass** Cleaning of organic glass and plastic materials requires special techniques and handling because of their low thermal and mechanical stability. Organic glass surfaces may be covered with low molecular weight fractions, surface oils, antistatic films, fingerprints, and so on. Most of the contaminants can be removed by an aqueous detergent wash or by other solvent cleaning possibly associated with mild liquid etching. However, care must be taken with cleaning fluids because they may be adsorbed into the polymer structure causing it to swell and possibly to craze on drying.

With organic polymers, cleaning means that the surface must be modified in

such a way that it does not represent an area of insufficient adhesion at the interface substrate surface/film formed after film deposition. Therefore, frequent cleaning of plastics may simply mean the modification of the surface so that the contaminant initially present is afterward no longer considered as a contaminant. The proper treatment in glow discharge plasma is very effective for that purpose since, in addition to micro roughening, it also causes chemical activation and cross-linking [72]. Proper cleaning fluids and short cleaning time as well as carefully established energy limits and proper doses in particle bombardment or in radiation treatment are important for optimum results.

There are many cheaper cleanliness tests such as inspection of the breath figure, the atomizer test and the water-break test [27]. All of these qualitative tests are based on the wettability, which is generally high on clean glass surfaces. The contact angle of water droplets and droplets of other materials on a surface can even be a quantitative measure of wettability [73]. Surface cleaning and recontamination of glass was monitored by contact angle measurements using distilled water [67].

The best precaution for preventing recontamination, beside cleanliness of operator and environment, is to avoid long intervals between cleaning and film deposition. The cleaned parts should be mounted into the substrate holders immediately after cleaning and the whole device should be placed carefully and quickly in the coating systems.

1.7.2.3 **Chemical Methods of Film Deposition**

1.7.2.3.1 **Spraying Pyrolysis** Many studies have been done over about five decades on spray pyrolysis (thermal decomposition) for preparation of TCO films. Many variants have been tried to grow the films but the basic technique used by all the workers is similar to that described in Ref. 8. For example, a solution of $SnCl_4$ or $InCl_3$ in a mixture of alcohol and water is sprayed onto heated substrates. The hydrolysis of chlorides [4] is normally involved. The thermal decomposition takes place on the hot substrate surface giving rise to a continuous film. The prime requisite for obtaining good quality thin films is the optimization of preparative conditions, namely substrate temperature, spray rate, concentration of solution, and so on [9].

Some review articles pertaining to spray pyrolysis processing and the range of thin films deposited by this technique for various applications have appeared in the literature. Viguié and Spitz [74] have classified chemical spray deposition process according to the type of reaction. A most recent survey on thin-film materials prepared by spray pyrolysis and advances in the field, especially different atomization techniques, was presented [12]. The critical operations for the spray pyrolysis technique are (1) preparation of uniform and fine droplets and (2) the controlled thermal decomposition of these droplets in terms of environment, location, and time.

Since the production of the first thin films of SnO_2 by oxidation of a metallic Sn film in air [31], such films have been prepared by blowing fumes of $SnCl_2$ onto heated glass [75], dip-coating heated hot vitreous substrate in the solution containing $SnCl_4$ [33], and pyrolytic decomposition of $SnCl_4$ [36, 39]. There are also some patents in the literature, based on spraying the hot glass with a solution of $InCl_3$ [37] or introducing it into an airstream containing $SnCl_4$ [76]. Thin films of SnO_2

are most commonly produced by thermal decomposition of aqueous acidified $SnCl_4$ sprayed onto a hot glass substrate [36, 39]. Their techniques consisted of spraying a solution of stannic chloride and water onto a glass surface heated to 550–650 °C so that a layer of SnO_2 was formed [33, 36, 37, 39]. Earlier reviews were written by Bauer [31] and Fischer [77].

TCO thin films of SnO_2 [31, 78–85], SnO_2:Sb [85–89], and SnO_2:F [89–92] have been deposited by spraying alcoholic solution usually of $SnCl_4$ and sometimes of $SnCl_2$ [88, 89], $SnBr_4$ [82], or tetrabutyltin [82]. Antimony doping is achieved by adding $SbCl_3$ to the spray solution. $SbCl_5$ has also been tried as the dopant of Sn. Fluorine doping is achieved by adding NH_4F and sometimes trifluoroacetic acid [90] or HF [91]. Similarly, $InCl_3$ is used as a source of indium in In_2O_3 [93, 94], ITO [90, 94–96], or In_2O_3:F [97] films. Tin doping is achieved by adding $SnCl_4$.

The solutions are made usually by dissolving $SnCl_4$ or $InCl_3$ in some solvents such as ethanol [83, 90], methanol [92], propanol [85], butyl acetate [93], HCl [92], and H_2O [84]. Alcoholic solvents were the most preferred because of their low surface tension and viscosity facilitates the formation of small spray droplets while its low boiling point enables it to be efficiently removed from the deposition chamber in the vapor phase. The solvent is made slightly acidic with HCl (or HF for fluoride doping) [91, 92].

Films of ZnO [49, 98–101], ZnO:In [51], ZnO:Al [102–104], ZnO:Li [105], and ZnO:Tb [106] have been deposited by the pyrolytic decomposition using alcoholic solutions of $ZnCl_2$ or $Zn(CH_3COO)_2$. Various dopants were added to above precursor solutions in the form of chlorides, sulfates, nitrates as well as acetates and acetylacetonates [11]. TCO films using undoped ZnO by spray pyrolysis were reported by Aranovich and coworkers [49] in 1979.

A simple and effective method for preparing of TiO_2 films by decomposing $TiCl_4$ with atmospheric water vapor was first proposed by Cartwright and Turner in 1939 [32] and further developed by Tanner and Lockhart [107], Banning [108], and Hass [109]. Banning [108] found that the hardness and refractive index of TiO_2 films were increased by raising the glass temperature to 200 °C and maintaining the liquid tetrachloride at 60 °C.

Hass [109] reported that TiO_2 films formed by the vapor reaction process on substrates at temperatures below 280 °C are amorphous, and above this temperature have a structure of anatase. The anatase thin films of TiO_2 with good crystallinity and large area were obtained from the spray pyrolysis technique [110–113]. The porosity of the films increased with increasing substrate temperature. Films made near 325 °C substrate temperature contained only the anatase phase with 75% optical transmittance, and at higher temperatures (above 450 °C), the films were cloudy and contained both rutile and anatase phase [114].

CdO was the first material reported to be semitransparent to visible light and at the same time electrically conducting. It can be prepared by means of oxidative pyrolysis of various Cd-alkyls [115]. Cd_2SnO_4 is another transparent conductor having desirable properties, namely good durability and chemical resistance. Cd_2SnO_4 [116] films have been deposited by spraying appropriate combinations of $SnCl_4-CdCl_2$. Cd_2SnO_4 films have been used as electrodes in photogalvanic cells [26].

1.7.2.3.2 **Chemical Vapor Deposition**

Films with high demands for purity, stoichiometry, and structural perfection

could be obtained by chemical vapor deposition (CVD) methods [3], which allow deposition near thermodynamic equilibrium conditions. This technique could offer also economic advances of relatively low equipment cost and simple processing. CVD is based on the use of volatile organometallic compounds of tin, indium, zinc, titanium, and so on. CVD consists of a surface reaction on a solid surface, involving one or more gaseous reacting species. The principle of CVD preparation of oxide films was described in detail [26].

Since the 1980s, chemical vapor deposition has been widely adopted in the continuous production of with F-doped SnO_2 (SnO_2:F) [13]. By far, the majority of TCO films are currently produced in this way. Although ITO was first made by spray pyrolysis, sputtering has become the preferred mode for its production. Significant achievements have also been made to obtain low-resistivity and textured ZnO films using CVD [50, 53, 54, 56–59].

Thin films of SnO_2 [74, 117–122], SnO_2:Sb [123], In_2O_3 [74, 124], ITO [125, 126], ZnO [124, 127–129], and TiO_2 [130, 131] have been deposited by CVD. The oxidizing agents used are usually O_2, H_2O, or H_2O_2 [117, 120]. O_2, N_2, or argon are generally used as carrier gases. The tin or indium compounds may be evaporated at relatively low temperature (~100 °C) when organometallic compounds [123] are used or at higher temperatures when chlorides are used [120].

Kane and coworkers [119] have grown SnO_2 films using dibutyl tin diacetate as the organometallic compound, nitrogen as the carrier gas, and oxygen as the reagent gas. The substrate was kept at a temperature of about 420 °C. SnO_2:Sb films were also fabricated [123] under similar conditions. Ghandhi and coworkers [121] have extended their work to grow SnO_2 films by adopting the CVD technique to use radio frequency (RF) plasma-activated oxygen as the reagent. The main advantage of this technique is that it allows the growth of high-quality films at room temperature.

1.7.2.3.3 **Sol-gel Process** The first appearance of sol-gel reactions was observed by Ebelmen [132], who was the first to prepare a metal alkoxide from $SiCl_4$ and alcohol, and he found that the compound gelled on exposure to the atmosphere. This was for a while only a matter for chemists. The material aspect appeared in the 1930s in the work of Geffcken and Berger [133]. They suggested using alkoxides for the preparation of optical oxide films. Pioneering work was done in the Schott Glass Company in Germany, which led to the first products in the 1960s. The process development and the resulting film properties were reviewed in Refs. 134–137.

In general, the sol-gel process is used as a phenomenological term to describe the conversion of colloid suspensions from a liquid (sols) into a solid (gel). The gel consists then of two phases: a solid network penetrated by a second phase, either a liquid (wet gel) or a gas (xerogel). The most important technologies used to deposit sol-gel films technically are dip and spin coating [28].

Transition metal sol-gel chemistry has successfully been applied since more than 30 years in the form of titania coating on architectural glass, produced by the Schott Company in Germany [138]. A smooth and dense TiO_2 anatase film was prepared, using the sol-gel techniques and subsequent heat-treatment at a temperature of 450–500 °C [139–145].

1.7.2.4 Physical Methods of Film Deposition

Physical vapor deposition encompasses sputtering and evaporation. They are applied, dependent on particular requirements of the production technology. Obviously, they have their specific advantages and simultaneously introduce given limitations. In Refs. 2–16, 24–30, these techniques will be classified and described in detail.

1.7.2.4.1 **Evaporation** Vacuum and also reactive evaporation using metallic or oxide sources have been employed to deposit various TCO films. The important control parameters are the evaporation rate, substrate temperature, source-to-substrate distance, and oxygen partial pressure.

Postoxidation of Metal Films Thin films of SnO_2 [31, 146], In_2O_3 [147], ZnO [35, 147–149], and TiO_2 [34, 109, 150] have been prepared by the oxidation of the respective metal films. A technique for preparing TiO_2 film is to deposit a layer of Ti, which is then oxidized by baking at 400 °C in air. This method has been used by Hammer [34] and was developed in Germany. Ohnishi and coworkers [151] found that ZnO films can be made successfully at a low temperature by the oxidation of vacuum deposited ZnSe films without the direct sublimation of ZnO powder or crystals.

Reactive Evaporation Reactive evaporation of SnO_2 [152], In_2O_3 [153], ITO [154], and TiO_2 [155] thin films has been achieved by the vacuum evaporation of the corresponding metal or alloy in an oxygen atmosphere onto substrates heated to about 400 °C at rates of about 100–300 Å min^{-1}.

Activated Reactive Evaporation In the activated reactive evaporation method, the reaction between the evaporated species and the gas is activated by establishing thermionically assisted plasma in the reactive zone. Dense plasma is generated in the reaction zone by employing a thoriated tungsten emitter and a low-voltage anode assembly. The technique has been used to deposit excellent quality TCO films of ITO [154, 156] and SnO_2:Sb [157].

Direct Evaporation Thin films of SnO_2 [158], In_2O_3 [159–161], ITO [161–163], ZnO [164, 165], and TiO_2 [2, 166] have been deposited by thermal [158–161], electron beam [162–164], or arc plasma [165] evaporated of oxide sources. Owing to its high melting point, SnO_2 has been deposited by electron beam [167] and flash [168] evaporation methods. When pure or mixed oxides are evaporated, they reduce and form opaque films of lower oxides. TCOs are hence obtained either by the postoxidation of lower oxide films [167] or by the introduction of oxygen [158–162] during evaporation. The reduced TiO_x films can be converted to TiO_2 by anodic oxidation [2, 109]. Hamberg and Granqvist [10] reviewed work on ITO films prepared by reactive evaporation of In_2O_3 with up to 9 mol % SnO_2 onto heated glass.

1.7.2.4.2 **Sputtering** Every sputtering process involves the creation of gas plasma (usually in argon) in a low pressure chamber (from 5×10^{-1} to 10^{-4} mbar) between a cathode, the target holder, and the anode that is conveniently

used as the substrate holder [6]. The sputtering by ions generated in the glow discharge (plasma sputtering) is the mainly used method of thin-film deposition for industrial and laboratory purposes. There are two basics: DC and radio frequency (RF) diode sputtering systems and their numerous modifications in use. Both reactive and nonreactive forms of DC and RF sputtering and magnetron and ion beam sputtering have been used. Reactive sputtering process was extensively studied experimentally as well as theoretically [26].

Reactive Sputtering of Metallic Targets Subsequent to McMaster's work with chemically prepared SnO_2 films, it was found by Preston [38] that partially oxidized Sn or Cd films deposited by cathodic sputtering in an oxygen-containing atmosphere (this technique being termed *reactive sputtering*) also formed TCO layers when heated in air.

The general technique and ideas involved in reactive sputtering have been well described by Holland [2]. Thin films of CdO [38, 42, 169–171], SnO_2 [38, 42, 172–175], SnO_2:Sb [175, 176], In_2O_3 [42, 177, 178], ITO [43, 176, 179–182], TiO_2 [2], and Cd_2SnO_4 [183] have been reactively sputtered. $Ar-O_2$, N_2-O_2, or O_2 are generally used as the sputtering gas. This sputtering technique was investigated by Holland and Siddall in details [42, 184].

Giani and Kelly [173] have also prepared SnO_2 thin films by a high-voltage anodizing method. The anode was a Sn sheet and the cathode was either an Al sheet or a Pt cylinder. The electrolyte used was an ammonium pentaborate in ethylene glycol, which was varied by adding water. The anodizing voltage was 50 V d.c. producing a current density of 10 mA cm^{-2}.

Sputtering of Oxide Targets (Direct Sputtering) Sputtering from oxide targets to form TCO films is significantly different from reactive sputtering of metal targets. The control of film stoichiometry has been found to be easier with oxide targets, thus obviating the need for high temperature, postdeposition annealing. Furthermore, there are no problems with diffusion in mixed oxide targets of $SnO_2-Sb_2O_3$ or $In_2O_3-SnO_2$. However, a new set of problems are encountered with oxide targets. Target fabrication is quite difficult [4].

Highly transparent and conducting films of SnO_2 [185, 186], SnO_2:Sb [187–189], In_2O_3 [190], ITO [187, 191–195], ZnO [44, 196, 197], ZnO:Ga [55], and Cd_2SnO_4 [18, 47] have been deposited by this technique. Yamanaka and Oohashi [185] have prepared sputtered SnO_2 films using the cathode in the form of a tin oxide disk sintered from SnO_2 powder at 1770 K in air. The distance between the cathode and substrate was 6 cm and the sputtering voltage was 4.5 kV. Vossen and coworkers [187, 191] have sputtered targets of $In_2O_3 + 20$ mole% SnO_2 in pure Ar. Under the optimum sputtering conditions, the films were anion deficient and very highly conducting as deposited. Excellent ITO films were obtained using argon [192, 193] or oxygen [194] as working gas with pressures of about 0.66 Pa [192, 194] or 1.3 Pa [193].

Ion Beam Sputtering Ion beam sputtering differs from conventional plasma sputtering in that the projectiles bombarding the target are generated in external ion sources that are separated from the deposition chamber by pressure stages [198]. Since ion beam sputtering unlike RF sputtering, involves minimal intrinsic heating and electron bombardment, so the effect

on the substrate is minimized. Applying this technique Dubow and coworkers [199, 200] prepared excellent ITO films from cold-pressed $In_2O_3-SnO_2$ powder target in an oxygen partial pressure of 1.3×10^{-3} Pa.

High-quality films of TCOs have been fabricated by ion beam sputtering from oxide targets [173, 201] at deposition temperatures less than 100 °C. Fan [201] has used an argon-ion beam source with a typical value of current of 50 mA.

In addition to these sputtering techniques, a few workers have used other techniques, for example, glow discharge [202], and the Pyrosol process [203]. But these processes have not been widely used.

Magnetron Sputtering Conventional sputtering sources suffer mainly from two disadvantages: (1) the deposition rate is very low and (2) there is a substantial heating due to target secondary electron bombardment of the substrate [8]. By employing a magnetic field to confine these electrons to a region close to the target surface, the heating effect is substantially reduced and the plasma is intensified, leading to greatly increased deposition rates. Reactive magnetron sputtering process of thin films was reviewed by Safi [204] and references cited in it.

Film preparation of TCO films have been tried by magnetron sputtering [195, 205, 206]. Buchanan and coworkers [195] have grown films of indium–tin oxide of resistivity as low as 5×10^{-4} ohm cm and transmittance of ~85%. The substrate temperature was kept ~730 °C and the rate of deposition was ~16 nm min^{-1}. They were able to deposit these films onto a variety of substrates including Pyrex, quartz, and Mylar.

TCO films using ZnO:Al prepared by RF-magnetron sputtering were reported by Wasa and coworkers [46] in 1971. Although undoped ZnO films with a resistivity of $4.5 \times 10^{-4}\Omega$ cm were prepared by RF-magnetron sputtering in 1982 [207], they were found to be unstable in temperatures above about 150 °C [208]. Impurity-doped ZnO films such as ZnO:In prepared by spray pyrolysis were reported by Chopra and coworkers [51] in 1984. For the purpose of improving stability at high temperatures, Minami and coworkers [209] reported in 1984 that ZnO:Al films prepared by RF-magnetron sputtering were stable in use at temperatures as high as 400 °C. ZnO films [210] were prepared by impurity doping with a Group III element [15, 52, 211] such as Al, Ga, In, and B, or a Group IV element [212] such as Si substituted to a Zn atom site. ZnO [209, 213] and zinc–tin oxide [214] films were also prepared by RF-magnetron sputtering on glass substrates.

In_2O_3 [215], ITO [216], and indium–zinc oxide [217] films have been prepared by DC- and RF-magnetron sputtering.

1.7.2.4.3 **Reactive Ion Plating** The production of low resistivity coatings normally requires elevated temperatures of the order of 400–500 °C. An alternative to the supply of energy to the condensing molecules by heating the substrates is to provide it by the simultaneous bombardment of the surface with high-energy active molecules, and then reactive processes can be encouraged on the substrate surface [8]. The process where these particles are provided from a discharge running in the residual gas in the vacuum chamber has become to be known as *ion-plating*. Since the substrate temperatures involved are very low, this process can be used to coat in plastic materials, and it can be introduced into almost all the sputtering processes.

Reactive ion plating technique has been employed to deposit films of SnO_2 [218], In_2O_3 [218–220], ITO [220–222], In_2O_3:F [223], and TiN [219] at temperatures as low as room temperature. Howson and coworkers [218, 220] have used a reactive ion plating process to grow coatings of the oxides of indium and indium–tin alloys staring from the metal sources.

1.7.2.4.4 **Pulsed Laser Deposition** Recently, ZnO:Al and ZnO:Ga films with resistivities of the order $1 \times 10^{-4}\Omega$ cm were prepared by pulsed laser deposition (PLD) [224, 225]. Crystalline erbium (Er)-doped ZnO thin films have been grown by PLD [226]. $SrTiO_3$ thin films were grown using PLD from a single-crystal $SrTiO_3$ target [227]. This deposition technique is well suited for these studies, because it is one of the most kinetic methods for deposition. ITO thin films were grown on glass substrates by PLD without postdeposition annealing [228].

1.7.2.4.5 **Other Techniques** Several other processes have been described for the deposition of TCO films. None of these appear to be in wide use, so they will not be described in detail. Some of these processes are borrowed from ceramic fabrication and metallization. There have been reports of screen-printed [229] or doctor-bladed [230, 231] techniques of In_2O_3 and In_2O_3:Sn. The major problem with these processes is the roughness of the surface produced. Thin films were also prepared by anodization for SnO_2 [173], coprecipitation from appropriate mixture solutions for SnO_2:Sb [232] and liquid phase deposition method for $SrTiO_3$ [233]. Recently, soft solution electrochemical processes for the fabrication of oxide materials such as ZnO, TiO_2, and $SrTiO_3$ as well as the fundamental electrodeposition mechanisms were reviewed [234].

The chemical solution growth technique, well known for chalcogenide films, has been extended to the deposition of oxide films (Mn_2O_3, Fe_2O_3, ZnO, and SnO_2) [9]. Metal ions in aqueous solution, under certain conditions, form solid phases of hydroxides $M(OH)_n$ or hydrous oxides ($M_2O_n \cdot xH_2O$), which on heating yield the corresponding metal oxides. The major parameters that control the deposition process are the composition of the deposition bath, its pH, and its temperature.

1.7.2.5 The Properties of Transparent Conducting Oxide Electrode Surfaces

The methods of preparation of TCO thin films have been described in previous sections of this chapter. The structural, electrical, and optical properties of TCO thin films in pure and doped forms have been reviewed [3–16]. The mechanisms of electrical conduction and optical transmission are very much interdependent [4].

A new optical approach was demonstrated by Kuwana and coworkers [235] in 1964, that is, the use of TCO electrode in which the product of an electrochemical reaction is monitored spectroscopically. There has been considerable interest in the fundamental electrochemical properties of SnO_2 semiconducting electrodes deposited on glass or quartz substrate [236–241]. In this form, electrodes have been prepared that can be used to observe electroactive species near the electrode-solution interface by internal reflectance spectroscopy in the visible region of the spectrum [237–239]. The electrochemical and surface characteristics of doped SnO_2 and In_2O_3 film electrodes [242] were discussed and compared to those of Pt and Au film electrodes [242, 243].

Developments in spectroelectrochemistry based on TCO electrodes under semi-infinite diffusion conditions were reviewed by Kuwana and Winograd in 1974 [244]. Since 1974, significant developments in absorption spectroelectrochemistry have occurred under semi-infinite diffusion conditions and in optically transparent thin-layer electrochemistry, several new TCO electrodes have been characterized, and the indirect coulometric titration technique has been developed and applied to biological systems [245].

Kuwana [246] has reviewed some earlier studies of the effect of light irradiation on electrochemical cells and also others in which light emission is a consequence of an electrochemical process. Gerischer [247–250] has discussed the photoeffects in electrochemical systems under illumination associated with semiconductor electrodes. Spectral photosensitization was also discussed from an electrochemical point of view, as it was caused by electron transfer from or to excited molecules [248]. Since Gerischer [247] started using ZnO, the electrochemical spectral sensitization works for various electrode materials, including TiO_2 [251] and SnO_2 [252], have been mainly studied to elucidate the mechanism of spectral sensitization. Little attention, however, had been paid until the early 1970s to an application of these effects for energy conversion.

Fujishima and Honda [251] have discussed an electrochemical photocell based on an *n*-type TiO_2 electrode in contact with an aqueous electrolyte and with platinum as counter electrode. The photoreaction in their system is the decomposition of water due to an oxygen evolution at the irradiated TiO_2 electrode and a hydrogen evolution at the Pt electrode. Unfortunately, TiO_2 has a low quantum yield for the photochemical conversion of solar energy. High-surface-area TiO_2 films deposited on a conducting glass sheet from colloidal suspensions was reported by O'Regan and Grätzel [253]. The use of these films with the addition of dye molecules has been shown to improve solar cells [253]. The preparation and characterization of nanoporous nanocrystalline TiO_2 films have been described in detail [253–255]. Another photoelectrochemical cell for energy conversion has been discussed by Tributsch [256] and by Calvin [257] using the sensitization of photocurrents by dyes that are adsorbed on semiconductor electrodes.

Most of the useful TCOs with a wide bandgap ($\geq$ 3 eV) studied up to now have been chemically inert conductive oxides, such as TiO_2 [258], SnO_2 [259], In_2O_3 [177, 260], and ZnO [247]. The bandgaps of these *n*-type semiconductors correspond to the energy photons in the UV region. Schematic band diagram of these oxides [254, 261–264] is shown in Fig. 1. Solar energy reaching the Earth's surface has, however, a spectrum distribution in the longer wavelength range and cannot, therefore, be used effectively by these electrodes [249]. Spectral sensitization would solve this problem. Osa and Fujihira [265] have developed a new type of electrochemical photocell, using a TCO electrode whose surface was modified by the chemical binding of sensitizing dyes. The solar cells developed by Grätzel and his coworker [253] described earlier are in this category.

The material properties of In_2O_3 are generally described by a high optical transparency for visible light and a high electrical conductivity [10]. To increase the conductivity of In_2O_3, it is generally doped with Sn, which is known as ITO (or In_2O_3:Sn). The conductivity of ITO films can be as high as $0.5–1.0 \times 10^4$ S cm^{-1} [10, 14]. In ITO

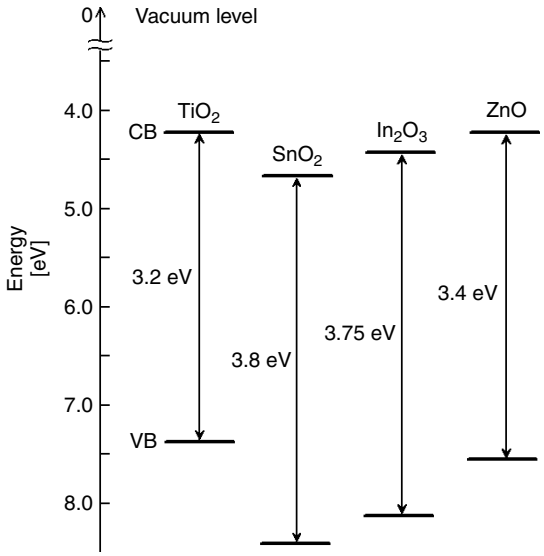


Fig. 1 Schematic diagram illustrating the energy levels of conduction band (CB) and valence band (VB) of some *n*-type undoped semiconductor oxides such as TiO_2 [261], SnO_2 [254, 262], In_2O_3 [177, 263], and ZnO [264].

Tab. 2 Bandgap energy and work function for some *n*-type transparent conductive pure or doped semiconductor oxides

Material	*Bandgap [eV]*	*Work function [eV]*	*References*
SnO_2	3.8	4.7	254, 266
SnO_2:F	–	4.4	267
In_2O_3	3.75	4.4 ± 0.1	263, 268
In_2O_3:Sn	3.8–4.5	4.4–4.8	263, 269
ZnO	3.4	4.3	264, 270
ZnO:F	–	4.2	14
ZnO:Al	3.9	4.4	271
TiO_2	3.0–3.2	4.2–4.3	261, 272
$SrTiO_3$	3.4	4.0	273, 274

films, the electron concentration of ITO is $\sim 10^{21}$ cm^{-3} [10, 241, 242], with optical transparency still surviving. Their unique characteristics as transparent electrodes have led to the exclusive utilization of ITO films in flat-panel displays and solar cells. The conductivity increases with the product of concentration of free electrons and mobility. For wide-bandgap *n*-type semiconductors, the maximum number of electronically active dopant atoms that can be placed in the lattice determines the free-electron concentration. The maximum electron concentration and the maximum conductivity in TCOs generally are found to increase in the following order: ZnO:F<SnO_2:F<ZnO:Al<In_2O_3:Sn< Ag or Cu [14].

The electrical, optical, and chemical properties as well as physical properties of TCO materials can be controlled by altering their chemical compositions [15].

The physical properties shown in Table 2 are the bandgap energy and work function for various types of pure and doped TCO semiconductors [14, 254, 261–274]. Bandgap widening associated with doping has been observed in earlier work on doped In_2O_3 films [10, 263]. The optical data [10] indicated that a gradual shift of the bandgap was toward higher energy as the electron density was increased. This is actually a well-known effect, which has been reported for heavily doped *n*-type semiconductors based on In_2O_3 [9, 10, 263]. Values for the work function (ϕ_0) are defined, as the minimum energy required for an electron to escape into vacuum from the Fermi level. The presence of dipoles or electrical charges on the surface determines the effective work function (ϕ_{eff}) [275, 276]. The work function of TCO electrodes can be controlled after chemical modification [277]. The work function [267, 269] of TCO electrode surfaces also depend upon cleaning method.

Friend and coworkers [278] have reported a detailed study of the characterization of different surface treatments on TCO electrodes such as ITO in terms of morphology, carrier concentration and mobility, sheet resistance, work function, surface energy and polarity, and chemical composition. The studies of various surface treatments for ITO were summarized in Ref. 277. The most commonly used, treatments are oxygen plasma and UV-ozone [269, 279–281]. Nüesch and coworkers [282] have studied acid and base treatments of the surface (the surface was cleaned with oxygen plasma prior to acid treatment).

1.7.3 Electrode Modification

1.7.3.1 General

Formation of monolayers by self-assembly at electrode surfaces has been widely used in recent years. How to bind molecules on electrode surfaces has been studied extensively among electrochemists since mid-1970s, and is called *chemical modification of electrode surfaces* [283–285]. More recently, chemisorbed ordered organic monolayers on gold, silver, and oxides have been studied extensively and are called *self-assembled monolayers* (SAMs) [286–289]. SAMs are

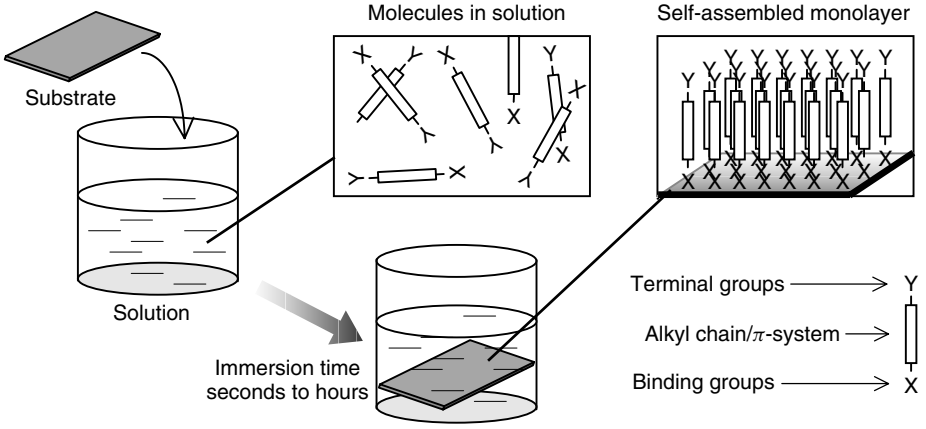


Fig. 2 Schematic drawing of self-assembled monolayers formed by simply immersing a solid substrate into a solution containing surface-active organic molecules.

ordered molecular assemblies formed by the adsorption of molecules with a surface-active binding group on a solid surface (see Fig. 2). This simple process makes SAMs inherently manufacturable and thus technologically attractive for building superlattices and for surface engineering.

Organosilanes have been used for chemical modification and as coupling agents since the first reports by Murray and coworkers [290] in the mid-1970s. Kuwana and coworkers discussed the silanization of SnO_2 in detail [242]. Since the first reports, the silanization has been used more widely for chemical modification of electrode surfaces [283–285]. Fujihira and coworkers [291, 292] carried out pioneering work on covalently attaching organic molecules with functional groups such as −COOH and −COCl onto SnO_2 surface.

This chapter describes chemical modification of various *n*-type TCO electrode surfaces with various organic molecules in which one end is a binding group (X−), the other end is a terminal group with a different functionality (e.g. permanent dipole moment) (−Y), and these two ends are linked by groups of alkyl chain and π-system as shown schematically in Fig. 2. Studies for formation of various organic monolayers with carboxylic and phosphonic acids as well as organosilanes on these oxide electrodes are reviewed and discussed comprehensively in this chapter. Several examples of organic chemical treatments used for surface modifications of various TCO wide bandgap *n*-type electrodes are summarized.

1.7.3.2 SnO_2

In our previous studies [291, 292], we found that a SnO_2 surface could be modified with functional groups such as −COOH and −COCl. The latter was more reactive [292]. As shown in Fig. 3, dehydrative coupling of a carboxyl group of rhodamine B (RhB−COOH) with a surface hydroxyl group of untreated SnO_2 electrodes was tried using dicyclohexylcarbodiimide (DCC) as a dehydrating agent [291]. Chemical modification of SnO_2 electrode with tetra-(*p*-chlorocarbonylphenyl) porphyrin ($TPP(COCl)_4$) was carried out by dipping the untreated SnO_2 in $TPP(COCl)_4$-methylene chloride solution for ca. one week at room temperature, in the presence and absence of pyridine (Py) as a catalyst for the condensation reaction [292]. It was found later that −COOH is selectively chemisorbed on various oxides and −SH on Au and Ag [289, 293–295].

SAMs can be built from a variety of molecules having surface-specific functional groups. Among the best

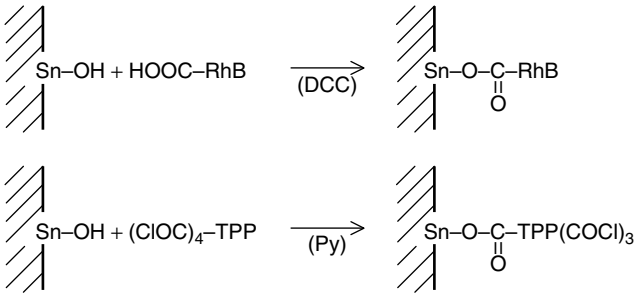


Fig. 3 Scheme for chemical modification of SnO_2 electrodes with RhB−COOH and $TPP(COCl)_4$ [291, 292].

Tab. 3 Examples of organic chemical treatments used for surface modifications of *n*-type semiconductors of SnO_2 and ITO

Semiconductor	*Chemical modification*	*References*
SnO_2	RhB-COOH and $TPP(COCl)_4$	291, 292
SnO_2 or TiO_2	4-(2-Pyridin-4-yl-vinyl)-benzylphosphonic acid	299
	$Ru(bpy)_2$(bpy-4,4′-dicarboxylic acid)$^{2+}$	300–303
	$Ru(bpy)_2$(bpy-4-CH_3-4'-carboxylic acid)$^{2+}$	303
SnO_2:Sb	Ru(terpy)(bpy-4,4′-dicarboxylic acid)$^{2+}$	303
SnO_2:Sb or ITO	(PTZ-COOH) and [MV-COOH]$(PF_6)_2$	303
SnO_2:Sb or TiO_2	Ru(4-(1′-ethyl-(bpy))(bpy-4,4′-dimethylphosphonic acid)$_2^{2+}$	304
SnO_2:F or TiO_2	Eicosylcarboxylic acid and eicosylphosphonic acid	305
ITO	12-Ferrocenyldodecanoic and perfluorodecanoic acids	298
	6-Ferrocenylhexylphosphonic acid	298
	Oligo(*para*-phenylene)-functionalized carboxylic acid	306
	p-(H-, Br-, CN-, NO_2-, CH_3O-)benzoic acids	307, 308
	Bicarbazyl-*N*, *N*′-dialkanoic acids ($n = 2$, 5, or 10)	308, 309
	N, *N*′-Dioctyl-3,3′-bicarbazyl-6,6′-dicarboxylic acid	308
	8-Hydroxyquinoline-5-carboxylic acid	309
	2-Chloroethyl-, trichloromethyl-, and aminomethyl-phosphonic acids	310, 311
	(4-Nitrophenyl)phosphonic acid	311
	p-(H-, Cl-, NO_2-, CF_3-)benzenesulfonyl and benzoyl chlorides	312, 313
	p-(H-, Cl-)phenylphosphoryl dichlorides	312
	n-Nonanoyl chloride and *n*-palmitoyl chloride	313
	Ferrocene dicarboxylic acid and 3-thiophene acetic acid	314–316
	$Ru(bpy)_2$(bpy-4,4′-dicarboxylic acid)$^{2+}$	307, 308
	Ru(terpy)(H_2O)(bpy-4,4′-diphosphonic acid)$^{2+}$	317
	Alkanecarboxylic acids CH_3-$(CH_2)_n$COOH ($n = 16$, 18) and bifunctional SH-$(CH_2)_{15}$COOH	318
	1,12-dodecanedicarboxylic acid	319
ITO or SnO_2:F	12-Phosphonododecanoic acid	320, 321
ITO or ZnO:In	Alkanephosphonic acids CH_3-$(CH_2)_n PO_3H_2$ ($n = 15$, 17)	322

characterized systems are alkanethiolates on Au [289, 293–295]. Another class of self-assembling systems takes advantage of strong chemisorption of carboxylates and phosphonates on various oxide surfaces [289, 296–298].

Stilbazole derivatives and π-conjugated compounds with a pyridine unit have been extensively studied for a wide range of applications. The grafting of phosphonic acid–derived stilbazole (4-(2-pyridin-4-yl-vinyl)-benzylphosphonic acid) on SnO_2 or TiO_2 was examined as listed in Table 3 [299]. The surface was modified for 3 days, with the phosphonic acid derivative dissolved in H_2O at 100 °C. Solid state ^{31}P NMR spectroscopic data indicated that the phosphonic group has reacted at the surface of SnO_2 with formation of P–O–Sn bonds [299].

Transparent porous SnO_2 films have been prepared from 30 to 50 Å diameter colloids. These types of films strongly adsorb organic dye-sensitizer

molecules. SnO_2 electrodes modified with bis(2,2′-bipyridine)$_2$(2,2′-bipyridine-4,4′-dicarboxylic acid)ruthenium(II) perchlorate ($Ru(bpy)_2(dcbpy)^{2+}$) exhibit excellent photoelectrochemical response in the visible spectral region with a power conversion efficiency of ∼1% at 470 nm [300]. Preparation of the complex $Ru(bpy)_2(dcbpy)^{2+}$ was reported in the literature [301]. In addition, porous films consisting of SnO_2 and ZnO colloids were also modified with similar $Ru(bpy)_2(dcbpy)^{2+}$ derivative by boiling the plate in the solution (2×10^{-4} M in ethanol) for 3 min [302].

Meyer and coworkers [303] described the surface attachment and photophysical properties of $Ru(bpy)_2(dcbpy)^{2+}$ and carboxylic acid derivatives of phenothiazine (PTZ-COOH) or methyl viologen [MV-COOH]$(PF_6)_2$ on metal oxides (SnO_2, TiO_2, In_2O_3, SnO_2:Sb, ITO, or SiO_2) and the application of resonance Raman spectroscopy to the elucidation of surface binding. In addition, the mixed surfaces were prepared by either sequential or competitive binding. For most experiments, metal oxide electrodes were etched in 10% HNO_3/H_2O (v/v) and rinsed thoroughly in nanopure H_2O before attachment. The cleaned electrodes were then soaked in solutions that were 10^{-4} M in Ru complex or carboxylic acid derivative in CH_3CN or CH_2Cl_2 with an equal amount of DCC overnight in a dry box. The mono(carboxylic acid) salt ($Ru(bpy)_2(bpy\text{-}4\text{-}CH_3\text{-}4'\text{-carboxylic acid})^{2+}$) was also attached to SnO_2 with a maximum surface coverage of $\sim 1 \times 10^{-10}$ mol cm^{-2} [303].

Fujihira and Osa [323] were the first to demonstrate that resonance Raman spectroscopy has bright prospects in the studies of adsorbed dye (methylene blue) layers at SnO_2 electrode–aqueous solution interface. The change in the Raman intensity as a function of electrode potential was also studied. This method can be applied widely for the study of a variety of interfaces in situ, involving electrode-solution interfaces with TCOs.

Resonance Raman measurements [303] on surfaces containing the Ru complexes implied that attachment to SnO_2, In_2O_3, and TiO_2 was via an ester link or H-bonding to the surface [303]. For SiO_2, two modes of binding were suggested, a majority by chelating carboxylate modes and a minority by ester-like linkage. The smaller organic compounds, PTZ-COOH, and MV-COOH]$(PF_6)_2$ displayed similar surface coverages. For $MV^{2+/+}$-COOH couple was observed the worst surface stability [303].

A transparent nanostructured SnO_2:Sb, TiO_2, or Al_2O_3 films was immersed in an ethanol solution (typically 2×10^{-4} mol dm^{-3}, pH 3.0) of ruthenium complexes such as Ru(4-(1′-ethyl-(bpy))(bpy-4,4′-dimethylphosphonic acid)$_2^{2+}$ (R^PV^{C4}) for 2 h [304]. The resulting heterosupramolecular assemblies were washed thoroughly with ethanol and stored in a darkened vacuum desiccator until required for use. Covalent organization of these hetersupermolecules yields the heterosupramolecular assembly $TiO_2-R^PV^{C4}$ for which the associated hetersupramolecular function, long-lived light-induced charge separation, has been demonstrated [304]. These findings and associated insights may find practical applications in the area of optical information storage.

The structures of monolayers of long-chain aliphatic acids deposited on SnO_2:F and TiO_2 using Langmuir–Blodgett (LB) techniques have been studied [305]. Briefly, solutions of eicosylcarboxylic acid ($CH_3(CH_2)_{19}CO_2H$, 1 mM) and eicosylphosphonic acid ($CH_3(CH_2)_{19}PO_3H_2$, 0.5 mM) were prepared in chloroform. The

substrates were mounted in the dipped position in the LB trough. The effects of pH, dissolved ions, different conditions, and different substrate materials on the structures of deposited monolayers have been examined. The findings will be used to optimize nanocrystalline solar cells and electrochromic windows based on metal oxide films modified by molecules adsorbed at the surface using phosphonic acid linker groups [305].

1.7.3.3 ITO

Table 3 presents several examples of organic chemical treatments used to modify ITO surface electronic properties. Chemical structures of these organic materials used to modifiy ITO electrode surfaces are also shown in Fig. 4. Chemical structures of carboxylated and phosphonated ruthenium complexes and their derivatives are not shown in Fig. 4.

Wrighton and coworkers [298] took advantage of the selective surface attachment of carboxylic or phosphonic acid to ITO electrode and thiol to Au electrode. This selective surface-attachment chemistry is termed *orthogonal self-assembly* (OSA) and can be used to direct the spontaneous assembly of molecular reagents onto ITO and Au microstructures. The OSA has been achieved for ITO and Au substrates simultaneously exposed for 30 min to solutions (1×10^{-4} M in each molecule with 5% ethanol in isooctane) of (1) carboxylic acid and thiol or (2) phosphonic acid and thiol. They found that phosphonic acids bind to ITO more aggressively than carboxylic acids, based on the observed coverage ratios (1 or 2) on ITO [298].

Zuppiroli and coworkers [306–309] observed improved performance in the organic light-emitting diodes (OLEDs) using poly(*para*-phenylene)-functionalized carboxylic acid (PPP-func) [306], *p*-substituted benzoic acids [307, 308], bicarbazyl-*N*, *N*′-dialkanoic acids [308], and 8-hydroxyquinoline-5-carboxylic acid [309] monolayers grafted to ITO electrode. Using a similar approach, Willis and coworkers demonstrated that ITO electrode modification with 2-chloroethyl- [310], trichloromethyl-, aminomethyl-, and 4-nitrophenylphosphonic acids [311] greatly enhanced the OLED device performance, most notably by reduction of turn-on voltages.

Before grafting, ITO substrates were cleaned by sonication and subsequent Ar^+ ion bombardment (plasma cleaning) at low power [306–309]. Without leaving the glove box, they were transferred into a 10^{-3} M PPP-func and *p*-substituted benzoic acid solutions in tetrahydrofurane (THF). After several hours of grafting, the substrates were briefly rinsed in pure THF and dried [306–308]. ITO was also immersed in ethanol solution containing 10^{-4} M of carboxylated $Ru(bpy)_2(dcbpy)^{2+}$ complex [307, 308]. After the grafting process, the ITO was again briefly rinsed in pure ethanol and dried. The Langmuir isotherms were measured in solution and yielded a maximum surface density of 1.3×10^{18} and 3.0×10^{17} molecules m^{-2} for *p*-nitrobenzoic acid and $Ru(bpy)_2(dcbpy)^{2+}$, respectively [307]. Bicarbazyl-*N*, *N*′-dialkanoic acids and *p*-substituted benzoic acids [308, 309] are all in the order of 10^{18} molecules m^{-2}.

Solutions of each 2-chloroethyl-, trichloromethyl-, or 4-nitrophenylphosphonic acid (1×10^{-4} M) [310, 311] were prepared in 30% methanol in chloroform, with the exception of aminomethylphosphonic acid for which an aqueous solution was used. For device fabrication, ITO substrates were derivatized with a SAM by immersion in a solution of the appropriate phosphonic acid, typically for a period of

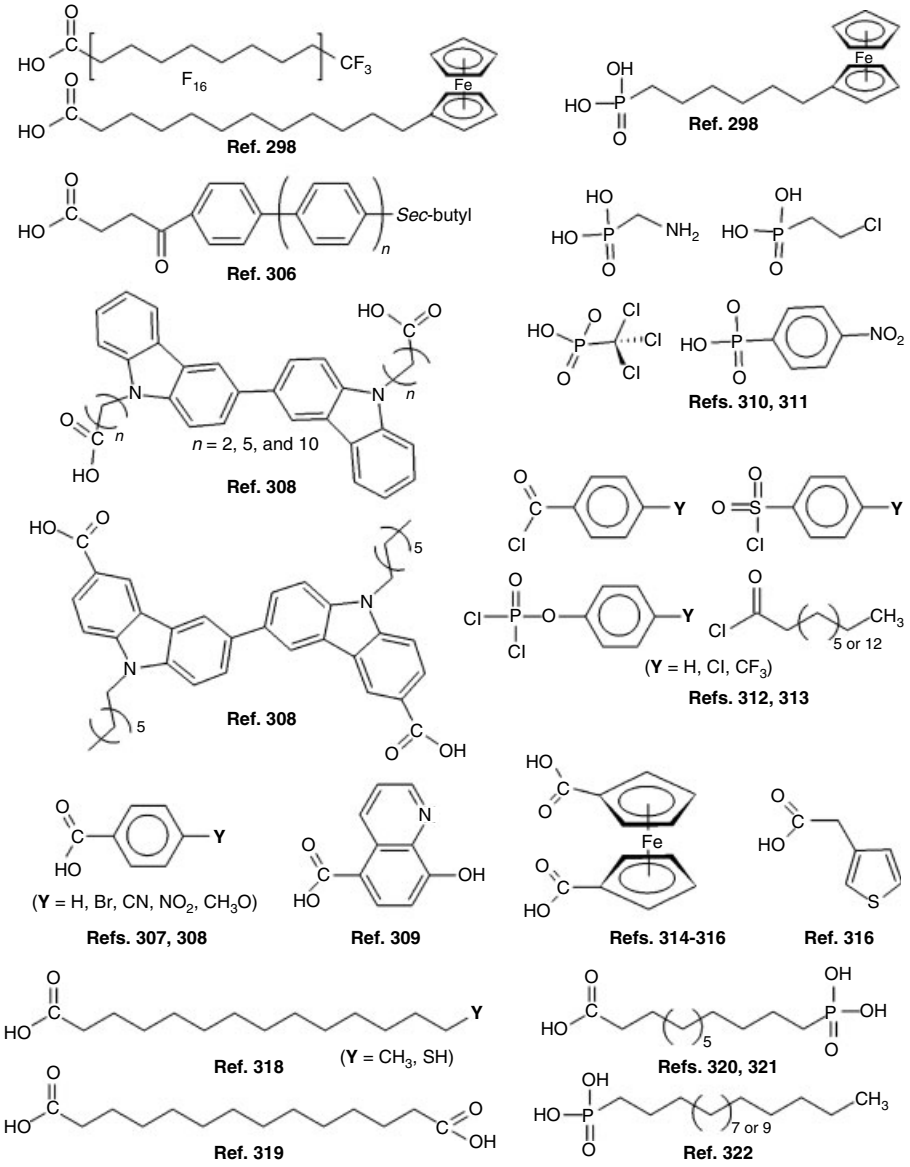


Fig. 4 Chemical structures of carboxylic acid and phosphonic acid derivatives used for the surface modification of ITO.

16 h. After derivatization, ITO electrodes were removed from solution and rinsed thoroughly with fresh solvent [311]. The presence of each phosphonic acid on ITO surface was confirmed by measuring the advanced contact angle relative to bare ITO of triply distilled water on the surface.

By the use of acid chlorides [312, 313], ITO surfaces were modified quickly and the fine and wide change in ITO

work function was realized. After cleaning with acetone and isopropanol, the ITO substrates were immersed for 5 min in dichloromethane solutions containing 1 mM of *p*-substituted benzenesulfonyl chloride, benzoylchloride, or phenylphosphoryl dichloride [312]. *n*-Nonanoyl chloride and *n*-palmitoyl chloride were also used [313]. These modified substrates were rinsed in pure dichloromethane to remove excess unbound molecules and then vacuum dried for 1 h. SAM modification of ITO substrates [324, 325] closely followed the procedure described in Ref. 312.

Adsorption of small redox-active molecules (e.g. ferrocene [326]) on ITO can be used to probe changes in electrochemical activity of ITO surface as a function of surface pretreatment [314]. Adsorption of ferrocene dicarboxylic acid ($Fc(COOH)_2$) and 3-thiophene acetic acid (3-TAA) onto ITO was achieved by soaking ITO in a 1 mM solution of these small molecules in pure ethanol for 10 min and then rinsing briefly with acetonitrile [314–316]. To ensure reproducibility, the adsorption of $Fc(COOH)_2$ on pretreated ITO was repeated a minimum of three times on three separate ITO samples, for each pretreatment condition [314]. Chemisorbed small molecules on ITO will provide for better direct contact of added conducting polymer layers and/or hole transport layers (HTLs) in the devices [316].

Meyer and coworkers [317] reported the preparation of surface structures based on $Ru(tpy)(H_2O)$(bpy-4,4′-diphosphonic acid)$^{2+}$ (tpy is 2,2′, 2″-terpyridine) and kinetic evidence that surface oxidation of $Ru^{III}-OH^{2+}$ to $Ru^{IV}-O^{2+}$ involves proton-coupled electron transfer. Stable surface coatings of the Ru complex on ITO were prepared by exposing electrodes to various (0.1×10^{-5} to 2×10^{-4} M) concentrations of metal complex in water at pH 3. The monolayers were relatively stable for several hours at pH 1, with ~10% of the electroactive coverage lost in the first hour of exposure. At pH 7, the complex desorbs from the surface with a half-time of ~30 min. At pH >10, it desorbs within 10 min.

A few studies investigate the coating ITO with organic monolayers of amphiphilic molecules [318–322]. Stearic and archidic acid [318] solutions were made by dissolution in hexadecane at 40 °C. The solutions were kept for 24 h at 30 °C during ITO sample immersion. After the solutions cooled to ambient temperature, the samples were rinsed with hexane and blown dry with N_2. Bifunctional $HS(CH_2)_{15}COOH$ was adsorbed from 0.5 mM ethanol solution at room temperature. These molecules were found to form stable and ordered monolayers on ITO. $HS(CH_2)_{15}COOH$ molecules can be utilized to generate a thiol-terminated SAM on ITO [318].

Napier and Thorp [319] developed a nucleic acid detection system based on the catalytic oxidation of guanine residues by a $Ru(bpy)_3^{2+}$ mediator. Monolayers were self-assembled by immersion of ITO in 5 mM 1,12-dodecanedicarboxylic acid in hexadecane for 36–48 h. The electrodes were thoroughly rinsed with hexane to remove any physically adsorbed molecules. The activation of surface carboxylates was performed by placing 40 mL of a freshly prepared 10 mM water-soluble carbodiimide in 20 mM sodium phosphate buffer (pH 7.0) onto ITO. The carbodiimide was allowed to dry on ITO surface. Nucleic acids were then coupled to the activated ITO surface [319].

Close-packed and ordered monolayers of 12-phosphonododecanoic acid (12-PDA) were recently observed to form on ITO

and SnO_2:F through phosphonate-indium bonding interaction [320]. Phosphonic acid functional groups were found to preferentially interact with ITO surface relative to carboxylic acid groups. ITO and SnO_2:F were cleaned via 20 min of UV-ozone to yield a clean hydrophilic surface. The cleaned electrodes were immersed for 16 h in deposition solution of 10 mM 12-PDA in 50% dimethyl sulfoxide (DMSO)/50% H_2O. Then the electrodes were rinsed with H_2O followed by drying the electrodes with N_2.

In addition, electrocatalytic detection of surface-immobilized nucleic acid probes using the $Ru(bpy)_3^{2+}$ mediator is highly dependent upon the preparation of ITO surface [321]. To maximize electron-transfer between $Ru(bpy)_3^{2+}$ and ITO, the charge at ITO needs to be negative. Phosphonated SAM was allowed to form on ITO by immersing the electrode in solution of 1 mM 12-phosphonododecanoic acid in 50% DMSO/50% H_2O for 16.5 h. ITO electrodes were removed from solution and washed with successive 10 min rinses of H_2O, 1 M NaCl, and H_2O [321].

Recently, Breen and coworkers [322] described patterning of ITO and ZnO:In films using microcontact printing (μCP) of either hexadecylphosphonic acid (HDPA) or octadecylphosphonic acid (ODPA) and wet etching, in which etch resistance depends on thickness and uniformity of printed alkanephosphonic multilayers. Prior to μCP, ITO or ZnO:In films were cleaned by UV-ozone for 30 min. A 5 mM solution of ODPA or HDPA in 2-propanol was filtered through a 0.2-μm PTFE Acrodisc syringe filter. PDMS stamps were inked in either flooding method or spraying method [322]. 2-Propanol evaporated from the stamp surface as the ink was sprayed, leaving a film of neat alkanephosphonic acid. Inked stamps were placed on ITO or ZnO:In surface using tweezers, left for 1 min, and then removed. The printed samples were etched in an aqueous oxalic acid solution (0.05 M), with mild agitation. Typical etching times were ~5 min for 500 Å films [322]. Other useful alkanediphosphonic acids were possibly synthesized by Michaelis–Arbuzov reaction [327, 328].

Elastomeric stamp patterning of ITO using tetrabutyl-ammonium hydroxide (TBOH) was demonstrated [329]. The stamp is immersed for 2 min in a 3×10^{-3} M solution of TBOH in ethanol or water. After drying under N_2 flow, the stamp was pressed onto cleaned ITO and removed after a few seconds. TBOH reacts with the surface of ITO to form a double ionic layer that drastically inhibits the ability to inject holes in the device [329].

There are many other studies of ITO surface modification [277] for the purpose of enhanced hole injection. ITO work function can be changed by treatment with UV-ozone [269, 312, 330, 331], plasma [332–334], acids or bases [335–337], and charge transfer [338] as well as by binding dipolar molecules [339, 340] using organotin (or zirconium) alkoxides [341–343]. The work function of ITO may be changed by electrostatically controlled self-assembled polymer layers [344–349]. The hole injection was also enhanced by electrochemically prepared thin films [350], *p*-type doped thin films [351–354] and plasma polymerized fluorocarbon films [355].

Schwartz and coworkers reported that bonding of carboxylic acids [341, 342] or phenols [343] to surface hydroxyl (−OH) groups of ITO could be stabilized using zirconium alkoxide complex-derived interface. In this process, a surface-bound alkoxyzirconium species is first formed, and subsequent ligand exchange

or metathesis with carboxylic acid generates a covalently bound alkanecarboxyzirconium surface complex species [341]. Such surface modification does not constitute an insulating barrier between ITO and a third material near the interface [339, 340, 343]. In a typical procedure, a substrate was treated tetra(*tert*-butoxy)zirconium vapor at ca. 10^{-2} Torr for 45 min, followed by evacuation for 60 min at ca. 10^{-2} Torr to remove any physisorbed molecules [341]. Treated ITO substrates were then dipped in a saturated ethereal solution of acrylic acid for 30 min, removed, rinsed with copious amounts of diethyl ether, and dried in vacuo to give surface-bound zirconium carboxycopolymer. Treated ITO substrates [341] were also dipped in a 10^{-3} M solution of ferrocenecarboxylic acid (FcCOOH) in dry diethyl ether under an inert atmosphere for 30 min and then rinsed [342]. Alternatively, a 1 mM solution of FcCOOH in diethyl ether was sprayed onto treated ITO using N_2. The solvent was then removed by evacuation.

1.7.3.4 ZnO

Dye-sensitized TiO_2 electrodes have been investigated due to their potential use in solar cells [253, 254]. Systems based on dye sensitizer such as $Ru(NCS)_2(dcbpy)_2^{2+}$ adsorbed on TiO_2 are the most extensively studied and, at present, the most efficient for dye-sensitized solar cells [356]. Besides TiO_2, some oxides such as SnO_2 [300], ZnO [357], and $SrTiO_3$ [261] have also been studied for photoelectric conversion. $SrTiO_3$ offers the possibility of higher open-circuit voltages through closer alignment of sensitizer excited state levels with conduction band edge [261]. For ZnO, it is similar in bandgap and band edge position to TiO_2 (shown in Table 2) with similar (10–20 nm in diameter) or smaller (5 nm) crystallite sizes than those for typical TiO_2 films [357].

Table 4 summarizes examples of surface treatments used for chemical modifications of wide bandgap semiconductors such as ZnO and TiO_2. Several attempts [358–362] have been made to use ZnO in photoelectrochemical solar cells. In 1994 Grätzel and coworkers [358] obtained overall solar-to-energy conversion efficiency of 0.4% when using $Ru(NCS)_2(dcbpy)_2^{2+}$ on nanocrystalline ZnO films. By improving the interfacial contact between dyes and ZnO particles in the film, Hagfeldt and coworkers [359–362] recently obtained a high overall efficiency from 2% up to 5% of $Ru(NCS)_2(dcbpy)_2^{2+}$ adsorbed on ZnO. Therefore, one may find ZnO to be a candidate as a nanostructured material in efficient solar cells [362]. However, cells based on ZnO have shown lower efficiencies compared to cells based on TiO_2.

Nanocrystalline ZnO electrodes were prepared by deposition of a colloidal ZnO solution on TCO substrates (usually SnO_2:F or ITO). The electrodes were sintered at 450 °C for 30 min in airflow to form nanostructured film electrodes [360]. Prior to sensitization freshly prepared ZnO films were heated at their firing temperature for 20 min to activate the film surface by removing adsorbed water. The still warm electrode (about 80 °C) was immersed into a 0.5 mM ethanol dye solution of $Ru(NCS)_2(dcbpy)_2^{2+}$. Carboxyl groups are the commonly used anchoring groups for chemisorption of dye molecules onto TCO electrode surfaces [291]. The film remained in the above solution for up to 7 days. The sensitized film was stored in ethanol until required for use [358–362].

Several groups have shown that ZnO can be electrodeposited from aqueous solutions in both nonporous [445, 446]

Tab. 4 Examples of organic chemical treatments used for surface modifications of *n*-type semiconductors of ZnO and TiO_2 as well as ZrO_2

Semiconductor	*Chemical modification*	*Reference*
ZnO	$Ru(NCS)_2$(bpy-4,4′-dicarboxylic acid)$_2^{2+}$	358–363
	Metal complexes of 2,9,16,23-tetrasulfophthalocyanines	364–366
	Riboflavin 5′-phosphate	367
	N, *N*′-Bis(ethylenesulfate)-3,4,9,10-perylene tetracarboxylic acid diimide	368
	$Ru(NCS)(Me_2bpy)$(2,2′:6′,2″-terpy-4-phosphonic acid)$^{2+}$	369
	Fullerence (C_{60}) carboxylic acid derivatives	370
	Succinic acid derivatives (*p*-CN−, CF_3−, OCH_3−, CH_3−, H-terminated in the benzene ring)	371
TiO_2	$[Ru(bpy)_2(CN)_2]_2Ru$(bpy-4,4′-dicarboxylic acid)$_2^{2+}$	253, 372
	Ru(bpy-4,4′-dicarboxylic acid)$_3^{2+}$	373–375
TiO_2 or ZrO_2	$Ru(bpy)_2$(bpy-4,4′-dicarboxylic acid)$^{2+}$; $Ru(bpy)_2(ina)_2^{2+}$	303, 376–378
TiO_2 or ZrO_2	$Ru(Me_2bpy)_2$(bpy-4-CH_3-4′-(3-propyl)carboxylic acid)$^{2+}$	379
	$Ru(X)_2$(bpy-4,4′-dicarboxylic acid)$_2^{2+}$ (X=Cl−, CN−, CNS−)	356, 380–385
	$Ru(CNS)_3$(2,2′:6′,2″-terpy-4,4′,4″-tricarboxylic acid)$^{2+}$	386, 387
	$Ru(bpy)_2$(bpy-4,4′-diphosphonic acid)$^{2+}$	377
	$Ru(CNS)(Me_2bpy)$(H2,2′ : 6′, 2″-terpy-4-phosphonic acid)$^{2+}$	388–390
	Ru(4-(1′-ethyl-(bpy))(bpy-4,4′-dimethylphosphonic acid)$_2^{2+}$	304, 391
	Ru(bpy-4,4′-$CH_2PO(OCH_2CH_3)_2)_3^{2+}$	392
	$Ru(Me_2bpy)_2$-Rh(bpy-4,4′-dicarboxylic acid)$_3$	393
TiO_2 or $SrTiO_3$	RhB-COOH, $TPP(COCl)_4$ and $ZnTPP(COOH)_4$	291, 292, 374
	Benzene derivatives benzoic, phthalic or salicylic acid	394, 395
	Carboxylate-terminated dimeric viologen	396
TiO_2 or ZrO_2	Mc2 merocyanine acid	397
TiO_2 or ITO	3,5-Bis(phosphonomethyl)benzoic acid derivatives	377, 398
TiO_2 or ZnO	HCOOH, CH_3COOH, and C_2H_5COOH	399–422
	Benzoic acid (C_6H_5COOH)	408, 423
	Bi-isonicotinic acid (bpy-4,4′-dicarboxylic acid)	424–426
	Oxalic acid (HOOC−COOH)	427
	Glycine (NH_2CH_2COOH)	428
	Maleic anhydride ($C_4H_2O_3$)	429
	p-(H−, Br−, CN−, NO_2−, CH_3O−) benzoic acids	430
ZrO_2	$CH_3(CH_2)_nCO_2H$ ($n = 9, 13–18, 20$) and $HO(CH_2)_{11or15}CO_2H$	431
TiO_2 or ZrO_2	$HOOC(CH_2)_nPO_3H_2$ ($n = 2, 3, 11, 15$)	432
TiO_2	11-Aminoundecanoic acid, $NH_2(CH_2)_{11}COOH$	433
TiO_2 or ZrO_2	Alkane(R)−PO_3H_2 (R = CH_3−, C_2H_5−, *n*-C_4H_9−, C_6H_5−)	434
TiO_2 or ZrO_2	Stearic (octadecanoic) acid, $CH_3(CH_2)_{16}COOH$	435
TiO_2 or ZrO_2	Octadecanephosphonic acid, $CH_3(CH_2)_{17}PO_3H_2$	435–440
TiO_2	Octadecanephosphoric acid, $CH_3(CH_2)_{17}OPO(OH)_2$	441
TiO_2 or ZrO_2	Dodecanephosphoric acid, OH−or $CH_3(CH_2)_{11}OPO(OH)_2$	442–444

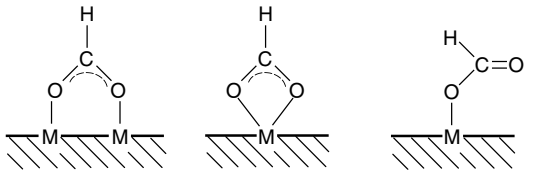
and porous [363–368] forms. Grätzel and coworkers [369] have recently developed a nonaqueous electrodeposition route to very high surface area ZnO films with a wide range of morphologies. Nanoporous ZnO thin films have been applied to dye sensitization with metal complexes of 2,9,16,23-tetrasulfophthalocyanines (TSPcMs, Ms=Zn^{2+}, Al^{3+} or $Si^{4+}[OH]_2$) [364–366], riboflavin 5′-phosphate (R5-P) [367], *N*, *N*′-bis(ethylenesulfate)-3,4,9,10-perylenetetra carboxylic acid diimide (SO_3EtPTCDI) [368], $Ru(NCS)_2(dcbpy)_2^{2+}$ [363], and $Ru(NCS)(Me_2bpy)(2,2':6',2''$-terpy-4-phosphonic acid$)^{2+}$ [369]. Deposited dye-modified ZnO films have been found to perform as sensitized photoelectrodes, thus opening up a new synthetic route to photoactive materials in dye-sensitized solar cells [363, 366].

The electrodeposition of ZnO was carried out potentiostatically at −0.7 or −0.9 V (vs. SCE) for 60 min in a 0.1 M $Zn(NO_3)_2$ aqueous solution maintained at 70 °C [445]. The deposition of ZnO/dye films was achieved simply by adding typically 50 μM TSPcMs [364, 365], R5-P [367] and SO_3EtPTCDI [368] into the zinc nitrate bath. In the case of SO_3EtPTCDI [368], electrolysis was carried out under the same conditions as described in Ref. 445. The deposited films were rinsed by water, dried in air at room temperature and subjected to further analysis. The anchoring of TSPcMs to ZnO is expected to occur through the coordination of sulfonic acid group to the surface Zn^{2+} of ZnO. Formation of the $Ti-OSO_2-Pc$ bond was found by FTIR analysis of TiO_2/TSPcCo composite [447].

Phosphonated dyes have recently been found effective especially for solid-state dye-sensitized solar cells using electrodeposited nanoporous nanocrystalline ZnO [367]. A monolayer of $Ru(NCS)(Me_2bpy)(2,2':6',2''$-terpy-4-phosphonic acid$)^{2+}$ complex was adsorbed onto the ZnO from ethanol/DMSO (70%/30%) [369]. The electrodes were placed into 5 mL of $\sim 10^{-4}$ M dye solution when they reacted at 120 °C, while cooling from a second 30 min heating to 380 °C. Adsorption was 90% complete within 12 h. Phosphonic acid groups bind strongly to ZnO. Other phosphonated Ru polypyridyl dyes gave similar results [369].

Carboxylic acid groups are by far the most popular binding groups in dye-sensitized solar cells, and a deeper understanding of the binding kinetics and bonding nature is therefore important [291, 292]. Photoelectron spectroscopic measurements of carboxylated Ru complexes adsorbed onto ZnO and TiO_2 indicate a bridge bonding (the carboxyl group is deprotonated and each oxygen atom interacts with a separate surface metal atom) in the case of TiO_2, whereas the carboxyl group was found to be protonated when binding to ZnO [361, 448]. Adsorption on oxide surfaces has also been addressed by computational methods [448].

Quantum chemical calculations have mostly been limited to small adsorbates such as formic acid (HCOOH) on different ZnO surfaces [449, 450]. Three structures have been suggested for the formate anion adsorbed on metal oxide surfaces: bridging, bidentate, and unidentate structures as shown in Fig. 5. The energy difference between bridging structure and unidentate structure in interactions with the surface OH species was calculated to be very small [449]. Thus, theoretical studies of the adsorption of HCOOH on ZnO surface energetically favor a bridging structure, which is also found to be the most stable adsorption mode [449]. However, the results also indicate that the bonding mode of HCOOH on ZnO is sensitive to the



(a) Bridging type (b) Bidentate type (c) Unidentate type

Fig. 5 Three possible geometries for formate anions adsorbed on metal oxide surfaces.

surface coverage [361, 450]. In addition, the adsorption is a dynamic process allowing translational mobility of adsorbate on the surface. It is therefore likely that several bonding modes may be involved in the adsorbate interaction with ZnO surface.

Cahen and coworkers showed that current density-voltage (I−V) characteristics of Au−GaAs and Au−SiO_x/Si diodes could be modified by adsorbing a monolayer of dipolar molecules onto the semiconductor or metal surface [451, 452]. They used the same system but with, as semiconductor, ZnO, a much more ionic solid than GaAs [370, 371]. Fullerene (C_{60}) carboxylic acid derivatives were easily adsorbed from solution as monolayers on ZnO and modify the semiconductor work function [370]. Moreover, succinic acid derivatives with *p*-substituents (CN−, CF_3−, CH_3O−, CH_3−, and H−) in the benzene ring were adsorbed onto ZnO into roughly one monolayer by overnight immersion in a 2.5 mM acetonitrile solution [371]. With ZnO, the interface index found to be 0.55, five times that was of GaAs. Molecular control over the effective barrier height was more effective with ZnO than with GaAs. Thus, molecularly modified ZnO-based diodes open up possibilities for using light-sensitive molecules to study molecule-semiconductor charge transfer in a solid-state device structure [371].

1.7.3.5 TiO_2 and ZrO_2

The adsorption of a wide variety of inorganic and organic molecules on TiO_2 surfaces was reviewed in Ref. 23. Transition metal complexes or organic dyes as sensitizers are grafted on semiconductors through anchoring groups such as carboxylate or phosphonate, which bind strongly to TiO_2 by coordination of surface Ti ions [453–455]. In addition, the adsorption of small organic molecules is briefly described in this section. Several examples of chemical modifications of TiO_2 with various organic molecules are listed in Table 4.

1.7.3.5.1 Polypyridyl Ru Complexes and Organic Dyes as Sensitizers

The preparation and characterization of *n*-type nanocrystalline TiO_2 for dye-sensitization studies of Ru complexes containing carboxylate and phosphonate polypyridyl ligands [253–255, 356, 372–393, 453–455] have been discussed in detail [456]. The carboxylate and phosphonate functionality as an anchoring group to immobilize the complex on nanocrystalline TiO_2 films have also been discussed in Ref. 456.

Since the first systematic study of complexes of the $RuX_2(dcbpy)_2^{2+}$ (X=Cl−, Br−, I−, CN−, SCN−) [356], many other complexes have been synthesized and tested [372–393]. The best photovoltaic performance in terms of both conversion yield and long-term stability has so far been achieved with Ru complexes [356, 372, 386]. However, in 2001, ''black dye'' complex achieved a record 10.4% solar to power conversion efficiency in full sunlight [387]. Charge transport in

nanocrystalline TiO_2 films has been under intense investigation [453] and has been best described by a random walk model [457]. Charge separation, charge injection, and charge transfer from molecular excited states to the empty states [378, 381] in TiO_2 have been discussed [254, 255, 384, 389–392]. The charge injection from the dye $Ru(SCN)_2(dcbpy)_2^{2+}$ into transparent hole (CuSCN, CuI, $CuAlO_2$) [19–22] and electron (SnO_2:F, porous TiO_2) [14, 253] conductors has recently been investigated by transient and spectral photovoltaic techniques [458].

The nature of linkage between a sensitizer and a semiconductor surface can influence excited state and interfacial electron-transfer behavior as well as the redox potentials. Earlier studies based on $Ru(dcbpy)_3^{2+}$, $Ru(bpy)_2(dcbpy)^{2+}$, $Ru(NCS)_2(dcbpy)_2^{2+}$, and $[Ru(bpy)_2(CN)_2]_2Ru(dcbpy)_2^{2+}$ have unambiguously shown the utility of carboxylate as an efficient anchoring group [253, 303, 356, 372–374, 376]. Fujihira and coworkers [291, 292] were the first to report on organic dyes containing functional groups such as $-CO_2H$ and $-COCl$ bind to SnO_2 or TiO_2 electrode surface using ester-like linkage.

Several studies have addressed how carboxylated Ru complexes interact with TiO_2 surface [303, 378, 380–382, 385]. In most vibrational studies, an asymmetric C–O stretch consistent with carboxylate binding modes (bidentate or bridging) has been reported [378, 380, 385]. Evidence for ester linkages and H-bonded network have also been reported [303, 376, 382]. Qu and Meyer [378] demonstrated that high surface proton concentrations favor ''carboxylic acid'' type linkage where low proton concentrations favor ''carboxylate'' type binding modes for complexes. Possible modes of coordination of the carboxylate are shown in Fig. 6. Fillinger and Parkinson [383] found that the initial binding involves one carboxylate, with subsequent binding of two or more carboxylate groups on the surface. Finnie and coworkers [385] suggested a bidentate or bridging coordination to TiO_2 surface via carboxylate groups per dye molecule.

Nanocrystalline TiO_2 films were prepared by spreading a viscous dispersion of colloidal TiO_2 particles on conducting glass support with heating under air for 30 min at 450 °C [253, 356, 387]. Coating of the TiO_2 surface with dye was carried out by soaking the film for at least 3 h in a 3×10^{-4} M solution of the Ru complex in dry ethanol. The dye coating was done immediately after the high-temperature annealing. The electrode was dipped into the dye solution while it was still hot, that is, its temperature was ca. 80 °C. After completion of the dye adsorption, the electrode was withdrawn from the solution under a stream of dry air or argon. It was stored in dry ethanol or immediately wetted with redox electrolyte solution for testing [303, 375, 378–387, 393].

A disadvantage of carboxylate group binding to TiO_2 is the fragility of the resulting surface link toward hydrolysis. Recent reports [377, 388–392] suggested that much higher surface stabilities could be achieved by the utilization of phosphonated derivatives and phosphonate surface binding. Grätzel and coworkers [388, 389] reported the results of their studies involving Ru complexes with one or more of phosphonated terpyridine (P-terpy) as a key ligand. Studies on dye adsorption showed that the adsorption is much better for P-terpy complex as compared to the analogous dcbpy complex [388]. Therefore, a more efficient electron injection was obtained in the cells. Incorporation of phosphonic acid groups creates a basis

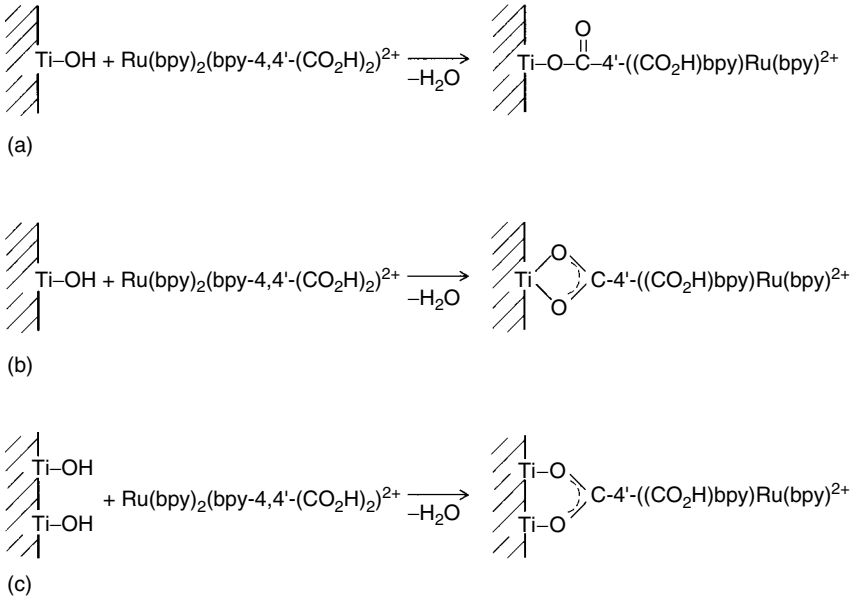


Fig. 6 Three possible carboxylate coordination modes to TiO_2 surfaces: (a) unidentate, (b) bidentate chelating, and (c) bridging.

for stable surface adsorption, and then the surface linkage strategy is a success [377]. Grätzel and coworkers [456] also described the difference in binding properties of complexes containing carboxylate, and phosphonate binding groups might stem from the differences in the pK_a values of the ligands.

Nanocrystalline TiO_2 (or ZrO_2) films on ITO substrates and TiO_2 (or ZrO_2) colloids were prepared by a method described in Refs. 379, 388. The films were heated to 400 °C for 30 min, cooled and immersed in solutions ca. 10^{-4} M in phosphonated complexes in ethanol solution for 16 h. After derivatization, the electrodes were rinsed with ethanol and stored in a fresh ethanol until use [377, 388–392]. Surface coverages were determined by spectroscopic measurement of the amount of complex in $\sim 10^{-4}$ M ethanol solution before and after the attachment, or by desorbing the complexes with 2 M NaOH solution.

Surface complexation of colloidal TiO_2 by benzene derivatives, that is, benzoic acid, phthalic acid, and salicylic acid was investigated and was found to obey the Langmuir isotherm [394]. The complexation of these acids by TiO_2 surface dramatically accelerates the rates of interfacial electron transfer to acceptors in the solution. These acids chemisorbed at TiO_2 by chelation to surface Ti^{4+} atoms are used as a spacer. Attachment of a methylviologen to the above spacers has been studied. The second acceptor of the heterotriad, antraquinone, is linked to methylviologen [394, 395]. The dramatic rate enhancement of interfacial electron transfer by bidentate benzene derivatives on TiO_2 was observed. Viologens form a group of redox indicators that undergo drastic changes upon oxidation/reduction. The reduced form

of methylviologen, for example, is deep blue, while the oxidized form is colorless. Efficient reduction of anchored viologen compounds by conduction band electrons of TiO_2 can be used for the amplification of an optical signal [396].

The best candidate for organic solar cells have been derivatives of merocyanine 3-acetyl-5-(2-(3-ethyl-2-benzothiazolidinylidene)ethylidene)-rhodanine (Mc2), which is the dye studied [397]. The polar group (carboxylic group) of Mc2 points toward the salt solution and pairs with a hydrated metal cation. Thereby, the dye molecules are oriented, which assists the formation of the appropriate aggregate geometry. Intercalated solvent molecules stabilize the structure. Grätzel and coworkers [397] successfully applied this method to induce J- and H-aggregation of carboxylated merocyanine dyes by impregnating highly porous metal oxide (TiO_2, Al_2O_3, and ZrO_2) substrates with a hydroxide salt.

Organic phosphonates and phosphates bind to metal oxide surfaces much more tightly than carboxylic acid [392, 459]. In addition, two phosphonate groups on the same molecular anchor should bind much tighter to a metal oxide surface than one phosphonate group. Meyer and coworkers [377, 398] described the synthesis of a protected diphosphonate anchor of 3,5-bis(phosphonomethyl)benzoic acid, its coupling of its carboxylate group to an amino group of a proline-chromophore, its deprotection, and finally its demonstration as an anchor on nanocrystalline TiO_2, ZrO_2, and ITO. Surface coverages of 1.5×10^{-10} mol cm^{-2} and 4.9×10^{-11} mol cm^{-2} are at TiO_2 and ITO electrodes, respectively. Moreover, 3,5-bis(dimethoxyphosphinylmethyl)benzoic acid was converted to an amino derivative by attaching a diamino butane linker [398].

1.7.3.5.2 **Short-chain Alkanoic and Benzoic Acids** Formic acid is one of the best investigated organic systems on TiO_2 and ZnO surfaces. Because many of other carboxylic acids follow the behavior of formic acid, the adsorption and reaction of HCOOH was recently discussed in some detail in Ref. 23. A large number of the adsorption and reaction processes of carboxylic acids (formic acid, acetic acid, propanic acid, acrylic acid, benzoic acid, bi-isonicotinic acid, oxalic acid, and glycine) were investigated by several groups [399–423].

In early adsorption studies, a single-crystalline ZnO [399–402], TiO_2 [401–408], SnO_2 [409], and ZrO_2 [410] surfaces were used for adsorption of formic acid and acetic acid. Formic and acetic acid adsorption and reaction on rutile TiO_2 surfaces were investigated by different groups [401–408]. The adsorption occurs via reaction (1) with no further details on the adsorption geometry given. Generally, HCOOH dissociates at TiO_2 to give formate:

$$HCOOH_{gas} + O_{lattice} = HCOO_{ads}{}^{-} + O_{lattice}H_{ads} \quad (1)$$

Here the H atom forms a hydroxyl with a surface atom $O_{lattice}$. Quantitative information about the adsorption sites, geometry, and lateral interaction between formats and hydroxyls were obtained (see below).

The majority of $HCOO^-$ are adsorbed in a bidentate fashion, with the oxygen atoms bridge-bonded between two fivefold coordinated Ti atoms and molecular plane oriented in (001) direction [411]. The absorption spectroscopic studies [407–413] concluded that that there is a minority species present, with the molecular plane oriented parallel to the (110) direction.

This species is probably adsorbed at the vacancies in the bridging oxygen rows. In addition, the separation of ν(C=O)–ν(CO) was observed at 282 cm^{-1}, which is closer to the value expected for monodentate bonding [413]. The vertical Ti—O distance was determined as 2.1 Å and the O—C—O bond angle was estimated $126 \pm 4^{\circ}$ [414]. This agrees well with theoretical calculations [415, 449, 450]. Atom-resolved images of TiO_2 surfaces with single formate ions [416–418] are also consistent with the adsorption site at Ti atoms reported in Refs. 411–413.

Dehydrogenation ($HCOOH \rightarrow CO_2 + H_2$) and dehydration ($HCOOH \rightarrow CO + H_2O$) are two main reaction mechanisms of HCOOH on TiO_2. Both reactions were observed upon formic acid exposure on TiO_2 (110) [406]. The decomposition of formic acid has been studied on rutile TiO_2 (001) [403, 404], TiO_2 (110) [405, 406], and TiO_2 (100) [419]. It is now clear that the substrate plays a very active role in formic acid decomposition and reaction processes; surface atoms are incorporated in reaction products, and the substrate itself is reoxidized upon formate decomposition [23]. Scanning probe techniques have also contributed to the understanding of this adsorption reaction.

Formic acid was dosed on TiO_2 through a translatable directional dozer. Accurate and reproducible gas exposures were obtained by means of a micron-sized pinhole [417]. A neat format monolayer was made by exposing the substrate to formic acid vapor at room temperature for 3 Langmuirs ($1\ L = 1 \times 10^{-6}$ Torr s) [416]. To prepare mixed monolayer, the formate-covered surface was then exposed to acetic acid vapor. An exchange reaction occurred between adsorbed and gas-phase molecules. The amount of adsorbed acetate could be controlled by the exposure amount to acetic acid, while the total (formate + acetate) coverage was maintained at the saturation [415, 416].

The adsorption of acetic acid and propanoic acid generally follows the same trends found for formic acid [400–404, 407, 412, 417]. Formate, acetate, and propanate are formed on TiO_2 (110) by dissociative adsorption of the corresponding acid, with hydroxyl species also being formed [404–407, 418]. Thornton and coworkers [412] examined the orientation of formate, acetate, and propanate in their 2×1 overlayers on TiO_2 (110) at 300 K. In all cases the carboxylate plane is almost perpendicular to the surface and apparently twisted out of the principle azimuths. The twist angles probably arise from averaging of majority and minority species. These angles out of the azimuths vary from $26 \pm 5^{\circ}$ to $39 \pm 10^{\circ}$, indicating a bond geometry essentially independent of alkyl chain length [412].

Iwasawa and coworkers [420] directly observed the decomposition of acetic acid with scanning tunneling microscopy (STM). STM images after a temperature jump to 580 K were analyzed. The number of bright spots on the surface decreased exponentially with time. This was assigned as a unimolecular decomposition of acetate to release ketene. This agreed well with a rate law deduced from a thermal desorption study [404]. Two main decomposition products such as methyl ketene ($CH_3HC{=}CO$) and diethyl ketone ($CH_3CH_2COCH_2CH_3$) as well as divinyl ketone ($CH_2{=}CHCOCH{=}CH_2$) were formed at elevated temperatures [404]. Iwasawa and coworkers reported the first example of noncontact atomic force microscopy (NC-AFM) images of oxide surfaces with oxygen point defects on TiO_2 (110) [421]. It is possible to distinguish

between coadsorbed formate and acetate molecules with NC-AFM [417, 418].

The reactions of acrylic acid (CH_2=CHCOOH) over TiO_2 provide a clear example of the complexity of the chemistry of conjugated molecules [422]. There was little evidence that CH_2=CH− (olefin) side chain affected binding of acrylic acid to the surface. However, once a decarboxylation has occurred, a range of products due to the olefin fragment is seen. These products included ethene, ethyne, butene, and butadiene. These pathways are undoubtedly related to the conjugated nature of the adsorbate because they are absent in the case of propanoic acid decomposition [404].

Williams and coworkers [408, 423] demonstrated the adsorption of benzoic acid on TiO_2 (110) using STM, electron-stimulated desorption ion angular distribution (ESDIAD) and low energy electron diffraction (LEED) at room temperature. The adsorption is dissociative, forming benzoate and surface hydroxyl. Benzoate dimerizes along the (001) direction through the interaction between hydrogen of aromatic ring and π orbital [423]. It was proposed that rotation of the phenyl ring takes place, allowing the formation of dimers of benzoate at the surface [408].

The adsorption of large organic molecules on TiO_2 is rapidly gaining in technological importance, for example, in dye-sensitization of solar cells [253]. Understanding the molecule-surface linkages in these systems is an important step in developing such molecular devices [379]. The adsorption of more complex acids was extended to bi-isonicotinic acid (2,2′-bipyridine-4,4′-dicarboxylic acid) on TiO_2 (110) in X-ray photoelectron spectroscopy (XPS) and near edge X-ray absorption fine structure (NEXAFS) studies [424, 425], combined with quantum chemical calculations [424–426]. The molecules bind to two neighboring Ti rows in a bidentate mode through the dehydroxylated O atoms, and is connected via the rings along the (110) direction. In addition, the molecules stand up with a 25° tilt angle and have a preferred azimuthally orientation of 44° with respect to the (001) direction in excellent agreement with calculated values [425, 426]. N1s NEXAFS spectra were modeled successfully using this adsorption geometry in a cluster model [424, 425].

Minot and coworkers [427] performed theoretical investigation of oxalic acid (HOOC−COOH) on rutile and anatase TiO_2. The calculations suggested that oxalic acid undergoes dissociative adsorption leading to the oxalate ($C_2O_4^{2-}$) bonded to two adjacent Ti atoms, which seems to be the most stable form of oxalic acid on TiO_2 surfaces. The adsorption is stronger on the anatase than on the rutile and thus crystal growth of TiO_2, in the presence of oxalic acid, leads to the rutile structure.

Multilayers of glycine, adsorbed on TiO_2 (110), were studied with synchrotron radiation-based UV light [428]. Ultraviolet photoemission spectroscopy (UPS) and XPS data showed the multilayers as formed by glycine molecules in polar zwitterionic form (NH_3^+ CH_2COO^-). Photon induced damage of multilayers occurs fast (produces a first order desorption of zwitterionic molecules with total cross section). The remaining layer is formed by C, NH_x ($x = 1, 2$) and OH hydroxyl species. Small coverages on TiO_2 surface indicated dissociative adsorption where most of the amino group is released into the gas phase.

Although maleic anhydride ($C_4H_2O_3$) is not a carboxylic acid, it may behave similarly. The reactions of $C_4H_2O_3$ have been investigated on TiO_2 (001) by

temperature programed desorption (TPD) [429]. Moreover, semiempirical calculations of $C_4H_2O_3$ over a relaxed $Ti_{13}O_{45}H_{38}$ rutile clusters were conducted. Two modes of adsorption were considered. The dissociated mode of adsorption is more favored than the nondissociated mode by 0.5 eV. The model was suggested where one C−O−C bond was broken and bonded to one Ti. TPD results indicated breaking of C=C bond and formation of ketene with an H atom that could either come from more complete dissociation of $C_4H_2O_3$ or as an impurity from the bulk.

Grätzel and coworkers [430] demonstrated that modification of para-functionalized benzoic acids on TiO_2 can be used to systematically improve the I−V characteristics of solid-state dye-sensitized solar cells. The results have been shown to be consistent with the variation in the work function of modified TiO_2, measured on the free surface. They attributed this effect to a change in band bending at TiO_2/HTL interface induced by the dipole moment of adsorbed benzoic acid. Nanocrystalline TiO_2 layers were treated a 1 mM solution of benzoic acid in CH_3CN at room temperature. Sample preparations as well as the measurements were carried out under an atmosphere of argon.

1.7.3.5.3 **Long-chain Organic Acids** Organic monolayers of amphiphilic alkanoic acids [431, 433, 435] and alkanephosphonic [432, 434–440] or alkanephosphoric acids [441–444] onto TiO_2 and ZrO_2 surfaces by adsorption from solution have been studied in the past few years (see Table 4). Amphiphilic organic acids on metal oxides are a class of SAMs, which have been studied to a much lesser extent than thiols on gold. Although the adsorption of long-chain carboxylic acids on metal oxides produced the first SAMs [296, 297, 460], relatively few studies have been carried out compared to others systems.

The chain length is an important variable in regard to whether extended versus looping structures will form. Looping structures were reported for $HO(CH_2)_{15}CO_2H$ adsorbed on Al_2O_3 [295], but the same surfactant forms densely packed, all-trans chains on ZrO_2 due to the formation of zirconium carboxylate bonds [431]. In the case of carboxyalkylphosphonic acids, both acid groups can interact with metal oxide surface, and particle–particle interactions may include bridging structures in which a surfactant molecule binds to two particles. The likelihood of such bridging structures increases with increasing chain length and decreasing particle size.

To investigate the influence of chain length and particle size, a series of diacids, $HO_2C(CH_2)_nPO_3H_2$ ($n = 2$, 3, 11, and 15), were deposited on nonporous TiO_2 and ZrO_2 powders and nanocrystalline ZrO_2 with average particle diameters of 21, 30, and 5 nm, respectively [432]. The surface bonding, chain conformation, and mobility were characterized by ^{13}C and ^{31}P solid-state NMR and IR. These indicated that $-PO_3H_2$ binds selectively to the surface producing a monolayer of HOOC-terminated chains. The average chain conformation depends on the substrate in addition to the chain length. A longer chain length to promote extended chain structures may be required when the additional polar functionality also has a strong affinity for a particular metal oxide as in the case of carboxylic acids and ZrO_2.

Composite multilayers made of 11-aminoundecanoic acid ($NH_2(CH_2)_{10}CO_2H$) capped-TiO_2 nanoparticles (63 ± 2 Å total diameter and 20–24 Å core diameter) and charged polyelectrolytes were prepared by layer-by-layer self-assembly

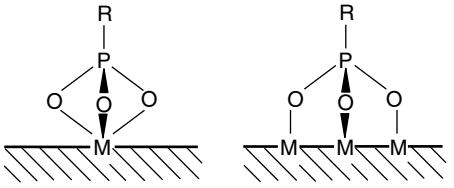
[433]. It should be emphasized that this method of layering can be potentially extended to any oxide particles capable of interacting with carboxyl group of any amino acid. The composite film coated by a layer of gold has been shown to function as a Schottky diode.

Modifications of TiO_2 and ZrO_2 membranes and powders with phosphoric acid and short-chain alkanephosphonic acids for separations in biotechnology have been studied [434]. The membranes and powders were dried at 70 °C before immersion in the acid solutions. These were left for 4 h in 0.1 M acid solution, and then lightly rinsed with appropriate solvent. The adsorption modes were characterized by direct analysis using infrared spectroscopy (IR). IR data suggested that phosphate and alkanephosphonates are bounded to metal oxide surfaces in the same C_{3v} symmetry. This symmetry can be achieved with a tridentate chelating bonding mode (a) or a tridentate bridging mode (b), as illustrated in Fig. 7. The alkyl chain (R) is perpendicular to the surface.

Whitesides and coworkers [435] have examined the preparation and properties of SAMs obtained by adsorption of long-chain alkanoic acids and alkanephosphonic acids as well as alkanehydroxamic acids onto metal oxide surfaces such as TiO_2 and ZrO_2. Monolayers of octadecanoic acid and octadecanephosphonic acid were formed from solutions in either isooctane or ethanol with concentrations of 1 mM in adsorbate. The use of octodecanoic [435], octadecanephosphonic [435–440], and octadecanephosphoric acids [441] for surface modification of TiO_2 and ZrO_2 has also been reported. In addition, TiO_2 and ZrO_2 surfaces were coated with dodecanephosphoric acid monolayers by immersion of the substrates into aqueous solutions [442–444].

Reven and coworkers [436–438] have employed solid-state NMR technique for characterizing the surface bond and chain dynamics in SAMs of octadecanephosphonic acid on both planar and particle surfaces of TiO_2 and ZrO_2 as well as Al_2O_3. In a typical preparation, a fivefold excess of the acid relative to the moles for a full surface coverage on the oxide was dissolved in 1000 mL of 3 : 1 methanol-water mixed solvent. A suspension of 2 g of metal oxide in 200 mL of deionized water was added dropwise to the acid solution. The resulting suspension was held at 100 °C for 3 days with stirring. The solid was washed and centrifuged with 200 mL of methanol seven times to remove any physisorbed acid and then dried under vacuum at room temperature [436]. For long-chain phosphonic acids, ZrO_2 appeared to be the best substrate for the formation of ordered monolayers [436, 437].

Fadeev and coworkers [439] have reported the comparative study of the reactions of octadecanesilanes with different headgroups and of octadecanephosphonic acid for the surface modification of TiO_2



(a) Tridentate chelating (b) Tridentate bridging

Fig. 7 Alkanephosphonic (or alkanephosphoric) acid bonding modes on metal oxide surfaces such as TiO_2 and ZrO_2: (a) thridentate chelating and (b) tridentate bridging.

(anatase). The work was focused on the structure, kinetics, and mechanism of the growth of the monolayers derived from different surface coupling agents on TiO_2. On the basis of the kinetics measurements, the following range of reactivity was established: $C_{18}H_{37}SiCl_3$ >> $C_{18}H_{37}PO(OH)_2$ > $C_{18}H_{37}Si(CH_3)_2Cl$ > $C_{18}H_{37}Si(OCH_3)_3$ > $C_{18}H_{37}SiH_3$.

Fadeev and coworkers [440] have also reported the results on hydrolytic stability of different C_{18}-monolayers supported on TiO_2 and ZrO_2 surfaces. The monolayers of $C_{18}H_{37}PO(OH)_2$ demonstrated the best hydrolytic stability among the studied surfaces. 10 mL of solution of $C_{18}H_{37}PO(OH)_2$ in toluene was injected into the vials using a syringe. The solutions contained 25 μmol of modifier per each square meter of TiO_2, which corresponded approximately to a threefold excess in respect to the complete monolayer coverage of the surface with alkyl groups (~5 group/nm^2). Upon addition of solution, the reaction vessels were left at room temperature. After a given time (1–240 h), the reactions were quenched by filtering on a Büchner funnel with a fritted disk. The samples were subsequently washed with toluene, acetone, water-acetone (1 : 1), and acetone, then dried on the filter to a dry state, and then dried in an oven at 60 °C overnight [439, 440]. The extent of hydrolysis ($\theta_{HYDROLYZED}$) at 25 °C for TiO_2 and ZrO_2 supported surfaces was ~0.02–0.05. At 65 °C, the values of $\theta_{HYDROLYZED}$ were ~0.05–0.15 for ZrO_2 and ~0.15–0.2 for TiO_2-supported surfaces [440]. High stability of these monolayers is explained because of strong specific interactions of phosphonic acid group with the surfaces of metal oxides. The surface of ZrO_2 is more basic (isoelectric points (IEP) ~7–11) than that of TiO_2 (IEP ~4–7), which results in a stronger bonding of phosphonic acids [440].

Hähner and coworkers [441] have described the preparation and characterization of SAMs of long-chain alkanephosphoric acid esters on oxide surfaces of Ti, Al, and Nb from an organic solvent. They have focused on a direct determination of the orientation and order of acid monolayers on the surface. Octadecanephosphoric acid was dissolved in *n*-heptane/propan-2-ol (100 : 0.4 (v/v)) solvent mixture at 0.5 mM concentration. SAMs were formed by immersion of the substrates in the solution for up to 48 h. Following immersion, the substrates were removed from the solution and rinsed with propan-2-ol, blow-dried with N_2, and stored in air until analysis. The preparation of well-ordered SAMs from heptane/propan-2-ol is applicable to various oxide substrates covered by alkanephosphates. This might open up the possibility of chemically tailoring many technologically important oxide surfaces via self-assembly.

Spencer and coworkers [442, 443] have described results on both pure and mixed SAMs of CH_3–and OH-terminated dodecanephosphoric acids deposited on TiO_2 and ZrO_2 as well as other oxides (Al_2O_3, Ta_2O_5, and Nb_2O_5) from aqueous solution. However, the presence of a functional group has been showed to influence the order of the adsorbed monolayer [444]. The substrates were immersed for 48 h in the acid solution and removed, each being rinsed with 10 mL of high-purity water and finally blown dry with N_2. SAM formation did not occur on SiO_2 surface under the same conditions [442]. SAMs were characterized by water contact-angle (wettability), microdroplet density measurements (condensation figures to judge homogeneity), and XPS (coverage and orientation of molecules) [443]. The

synchrotron-based technique gave direct information on the average orientation of molecules and the amount of defects, parameters that played a pivotal role for the preparation of organic surfaces with tailored properties [444].

1.7.3.6 Other Oxides

Much research has been focused on the self-assembly of various organic molecules on wide bandgap *n*-type TCO substrates as described earlier. The metal oxides with a large bandgap such as ZrO_2 ($E_g = 5.8$ eV) [461], for example, are ruled out by a low electron affinity, which places the conduction band edge above the excited state potential of most dyes (Fig. 8). The adsorption of organic monolayers on ZrO_2 is described in the previous section and also summarized in Table 4. Other large bandgap oxides are discussed in this section. The chemical surface modification of large bandgap oxides with organic monolayers [295–297, 460, 462–490] is listed in Table 5 as described in the following.

Most studies of the adsorption of carboxylic acids on metals have involved surfaces exposed to air prior to adsorption and thus largely refer to adsorption on native oxide overlayers. Allara and Nuzzo [296, 297] studied the adsorption of *n*-alkanoic (C_6–C_{24}) acids and CH≡C- or CH_2=CH-terminated alkanoic (C_{19}) acids

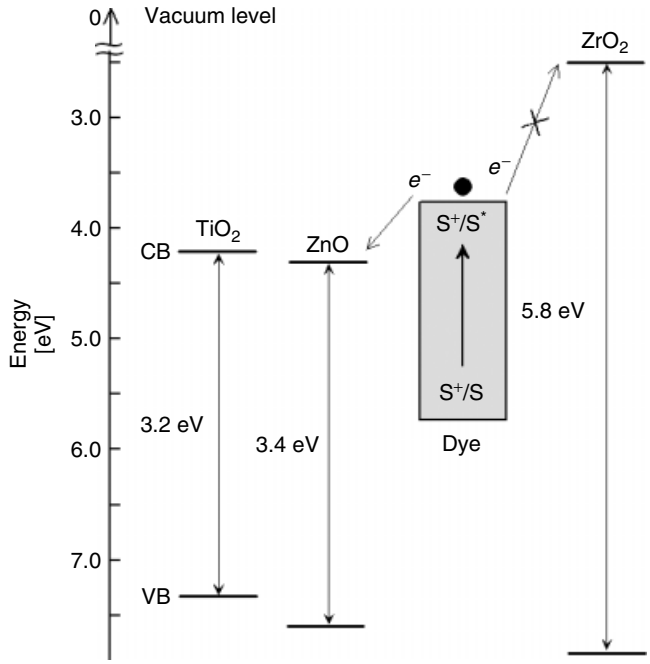


Fig. 8 Schematic energy band diagram of suitable and unsuitable metal oxides for organic dyes as sensitizers. Election injection from the dye-excited state to the energy level of conduction band (CB) is energetically favorable for wide bandgap oxides such as TiO_2 and ZnO [261, 264], but forbidden for large bandgap oxides such as ZrO_2 [461].

Tab. 5 Examples of organic chemical treatments used for surface modifications of large bandgap Al_2O_3 and various other oxide substrates

Substrate	*Chemical modification*	*References*
Al_2O_3	*n*-Alkanoic acids and CH≡C− or CH_2=CH$(CH_2)_{19}$COOH	296, 297
	Tere-, isophthalic, 1,4-cyclohexanedicarboxylic, benzoic, aliphatic dicarboxylic (HOOC$(CH_2)_{3-8,10}$COOH) acids	460
	Cl-, F-, OH-, $CH_3(CH_2)_{15-17}$COOH and $CF_3(CF_2)_8$COOH	295
	n-Alkanoic acids, $CH_3(CH_2)_{2-18,22}$COOH	435, 462–466
	4-Acetoxybenzoic acid, 4-CH_3(C=O)OC_6H_4COOH	467
	Zr (or Sn) alkoxide-mediated bonding carboxylic acids	468–470
	Octadecanephosphonic acid, $CH_3(CH_2)_{17}PO_3H_2$	435, 436, 471
Al_2O_3 or CuO	Alkanephosphonic and alkanebisphosphonic acids	472, 473
	Alkanephosphoric acids, OH− or $CH_3(CH_2)_{11,17}$OPO$(OH)_2$	441, 442
	Polypyridyl Ru complexes and organic dyes	304, 397, 474
AgO or CuO	*n*-Alkanoic acids, $CH_3(CH_2)_n$COOH ($n = 2–20, 22$)	462, 464, 475, 476
	4-alkoxybiphenyl-4′-carboxylic and 6-alkoxy-2-naphthoic acid derivatives with aliphatic long-chains ($n = 15–19$)	464
Steel or Brass	Alkanephosphonic and alkanebisphosphonic acids	473
Steel	Thienyl- or bithienylhexanphosphonic acids	477
Nb_2O_5 or Ta_2O_5	Octadecanephosphoric acid, $CH_3(CH_2)_{17}$OPO$(OH)_2$	441, 478–480
	Dodecanephosphoric acid, OH− or $CH_3(CH_2)_{11}$OPO$(OH)_2$	442
SiO_2	Ru$(bpy)_2$(bpy-4,4′-dicarboxylic acid)$^{2+}$	303
	Stearic acid, $CH_3(CH_2)_{16}$COOH	481
	Phosphorus oxychloride, ($POCl_3$)	482
Zirconated SiO_2	Octadecanephosphonic acid, $CH_3(CH_2)_{17}PO_3H_2$	436
SiO_2 or Mica	Octadecanephosphonic acid, $CH_3(CH_2)_{17}PO_3H_2$	483–489
CaHAP	R−PO_3H_2 (R = *n*-C_8H_{17}, *n*-$C_{18}H_{37}$, *n*-$C_8F_{17}F$−$(CH_2)_2$)	490

on oxidized Al_2O_3. Al substrates were prepared by the evaporation of Al from resistively heated W boats onto Si wafer. Ogawa and coworkers [460] studied the adsorption of tere- and isophthalic acids, *cis*- and *trans*-1,4-cyclohexanedicarboxylic acids, and aliphatic ($C_{3-8,10}$) dicarboxylic acids on γ-Al_2O_3 powders. In addition, the

adsorption of alkanoic acids on natively oxidized Al_2O_3 [435, 462–466] and AgO or CuO [435, 464, 475] surfaces has also been investigated.

A stable monolayer assembly can be formed on Ag by the spontaneous adsorption of arachidic acid ($CH_3(CH_2)_{18}COOH$) from hexadecane [475]. Surface X-ray diffraction of docosanoic acid ($CH_3(CH_2)_{20}COOH$) monolayers on Ag(111) surface showed that the carboxylate anion adsorbs in a $p(2 \times 2)$ overlayer structure, with interchain spacing of 5.78 Å. The area per chain within the SAMs is 28.8 $Å^2$ [476]. The alkyl chains are in *all-trans* extended configuration, and are tilted at 26.7° from the surface normal toward the nearest neighbor. The plane that bisects the methylene groups is twisted with respect to the plane of the carboxylate group. Polarized IR external reflection spectroscopy studies confirm this structure [462, 475].

Tao [462] has showed that the chemisorption of alkanoic acids on amorphous metal oxide surfaces is not unique. It was found that on AgO surfaces, the carboxylate two oxygen atoms bind to the surface nearly symmetrically, while on surfaces Al_2O_3 and CuO, the carboxylate binds asymmetrically to the surface displaying tilt angles close to zero. Observations made by Allara and Nuzzo [296, 297], Thompson and Pemberton [463], and Sondag and coworkers [467] indicated that stearic acid adsorbs to AgO and Al_2O_3 in slightly different orientations. However, IR studies by Tao suggested that monolayers on AgO are more ordered than their counterparts on Al_2O_3. Tao and coworkers [464] also reported the self-assembly of biphenyl- or naphthyl-containing alkanoic acids on the surfaces of Ag and Cu. Different behavior observed on Ag and Cu has been attributed to site specificity, binding geometry, and binding strength, among other factors.

Whitesides and coworkers [295] demonstrated the formation of orthogonal SAMs obtained by adsorption of alkanethiol on Au and alkanoic acids on Al_2O_3. SAMs were formed by exposing the clean grid to a mixture of $CF_3(CF_2)_8CO_2H$ and $Cl(CH_2)_8SH$, each $\sim$ 1 μm, in isooctane for 24 h, which was then removed from solution and washed with hexanes. This technique provides control over the scale of the dimensions reached by the microlithograpically generated features.

Aluminum is commonly used as a metallization layer in the microelectronics industry. Whitesides and coworkers [471] showed that octadecanephosphonic acid can be patterned on Al_2O_3/Al by μCP and that patterned structures are electrically similar to samples prepared by conventional photolithography and lift-off. The patterned structures resulting from etching are continuous and electrically conductive within each pattern, and separated patterns are electrically isolated. Using μCP, Schottky diodes of aluminum have been prepared on *p*-type Si(100). Octadecanephosphonic acids are air stable compounds that are known to form stable, ordered monolayers on metal oxide surfaces [298, 435]. SAMs on the native oxides of aluminum [435, 472, 473] and copper or iron [435, 473] have been formed from alkanephosphonic acids.

Alkanecarboxylic acids adsorb on Al_2O_3/Al as the carboxylate anion, but this interaction results in a weakly bound, easily displaced adsorbate [296, 297]. Schwartz and Bernasek [468–470] developed a method to increase the binding of SAMs of carboxylic acids on a hydroxide terminated Al_2O_3/Al surface by first priming the metal hydroxide surface with Zr alkoxide. This study

was, however, performed in ultrahigh vacuum, and the reactivity of Zr alkoxides may limit its application to monolayers formed in solution.

Dense, highly ordered monolayers can be prepared by the adsorption of octadecanephosphonic acid onto nonporous ZrO_2, TiO_2, Al_2O_3, and zirconated silica [436]. The surface bonding and conformational order of octadecanephosphonic acids adsorbed onto Al_2O_3, ZrO_2, TiO_2, and zirconated silica were characterized by solid-state NMR and IR spectroscopy. The results show that octadecanephosphonic acid reacts strongly with Al_2O_3 to form a bulk (aluminoalkyl)phosphonate [436]. Self-assembled octadecanephosphonic acid layers were also prepared on a Si substrate by a solution spreading method and studied using AFM [483]. Octadecanephosphonic acid molecules were found to be highly mobile, as evidenced by the experimental observation of a reorganization of layers and a formation of rodlike structures on bilayer surfaces at room temperature.

Transparent nanoporous nanocrystalline Al_2O_3 films (4-μm thick, 14-nm diameter nanocrystals) supported on a microscope glass slide were prepared as described by Grätzel and coworkers [397]. The absorption spectra of Al_2O_3-RVs (R = phosphonated Ru complexes, V = viologen) are not significantly different from those of Al_2O_3-RVs in solution [304]. Furthermore, no visible emission is detected from Al_2O_3-RVs. Equally clearly, irradiation with the blue output of an Ar-ion laser (200 mW cm^{-2}) for 15 s does not lead to a measurable change in the optical absorption spectrum of Al_2O_3-RVs. These findings, however, are not unexpected, since the bandgap of Al_2O_3 is so large (about 9 eV) that are no conduction band states isoenergetic with the electronically excited state of the Ru component of Al_2O_3-RVs [304, 397].

First attempts to apply SAMs for corrosion protection were made with the use of alkanethiols on iron and copper [491]. Alkane mono- and diphosphonates were applied successfully to form well-oriented SAMs on aluminum [435, 472, 473], copper or brass [473], and iron or steel [473, 477]. Immobilized molecules are able to act as adhesion promoters and corrosion inhibitors. These investigations have shown that the phosphonic acid group is one of the best anchor groups for building stable SAMs on passivated iron [477].

Octadecanephosphoric acid ($CH_3(CH_2)_{17}OPO(OH)_2$) and dodecanephosphoric acid ($OH-$or $CH_3(CH_2)_{11}OPO(OH)_2$) have been shown to form SAMs on Ta_2O_5 and Nb_2O_5 [441, 442, 478–480]. Using a combination of dedicated surface characterization techniques, the molecular structure of these adlayers has been demonstrated to be similar to thiols on gold with an intermolecular spacing of 5 Å (corresponding to 21 $Å^2$ per molecule) and a tilt angle of the molecular axis of 30–35° relative to the surface normal [479]. The binding of the phosphate head group to the surface is believed to be through direct coordination between phosphate and metal cation and arguments have been given for the presence of both mono- and bidentate binding of the phosphate group thus enabling the formation of a close-packed layer.

The monolayer films of metal phosphate have been fabricated with divalent (Ca^{2+}) and tetravalent (Zr^{4+}) metal ions on the phosphoric acid (PA) modified substrates [482]. While Zr^{4+} ions combined with PA monolayer maintain the positive charge as Zr^{2+}, Ca^{2+} combined with PA monolayers forms a neutral surface. *p*-Type Si(100) wafers were used as a substrate

for the SAMs. The cleaned Si substrates were immersed for 12 h at 70 °C in a fresh 1 : 1 mixed solution of 10 mM phosphorus oxychloride ($POCl_3$) and 10 mM 2,4,6-collidine in acetonitrile. These substrates were dipped into a 0.5 mM aqueous solution of Zr^{4+} or Ca^{2+} ions for 20 min to bind metal ions. Nanometer-scale patterning on the self-assembled metal phosphate films has been achieved using AFM.

Recently, there have been reports of the use of octadecanephosphonic acid ($CH_3(CH_2)_{17}PO_3H_2$) molecules to form monolayers on Si [483], mica [484–488], sapphire [489], and Ca hydroxyapatite [490] surfaces. An Si wafer and a cleaved mica substrate were used as the support for preparing $CH_3(CH_2)_{17}PO_3H_2$ samples. A concentration of 5 mM $CH_3(CH_2)_{17}PO_3H_2$ solution in ethanol was used for preparing $CH_3(CH_2)_{17}PO_3H_2$ samples on the Si surface, while a 2-mM solution was used for formation on the mica surface [483]. When a diluted solution of $CH_3(CH_2)_{17}PO_3H_2$ was used to wet the mica substrate, a monolayer of $CH_3(CH_2)_{17}PO_3H_2$ was observed using AFM. The headgroup of $CH_3(CH_2)_{17}PO_3H_2$ molecules is found to be bonded to the mica surface, resulting in a monolayer having a great potential for application as an ordered surface providing hydrophobic chemistry [484–487]. The monolayers on a mica substrate is very stable upon heating at temperatures up to 80 °C [488], indicating that the interaction between the hydrophilic headgroup and the mica surface is quite strong.

Schwartz and coworkers [486] studied the growth kinetics of $CH_3(CH_2)_{17}PO_3H_2$ on mica by examining films removed from solution before completion. Surface coverage of submonolayer islands was extracted from AFM images as a function of immersion time for solution concentrations from 0.02 to 2 mM. These data were compared to two models for diffusion-limited and adsorption-limited (Langmuir) kinetics. Russell and coworkers [487] studied the dynamics of self-healing of scratches made on $CH_3(CH_2)_{17}PO_3H_2$ monolayers employing AFM as the experimental tool. Scratch morphological evolution was followed as a function of time, at room temperature, for samples prepared by the drip coating and crystal melting methods. Self-healing, ranging from partial to complete was observed on drip-coated samples.

Schwartz and coworkers [489] also extended their $CH_3(CH_2)_{17}PO_3H_2$ SAM studies to a new substrate as sapphire (corundum). Sapphire, undoped single crystal of α-Al_2O_3, is widely used as a substrate for thin-film deposition of metals, semiconductors, or insulators. Several crystallographic faces of sapphire are available, two of which have been studied, namely, C-face (1000) and R-face (1102). Different growth kinetics were observed for the two crystal orientations, which could be related to the surface energetics [489].

Very little is known about surface modification of nonoxide surfaces, such as that of inorganic phosphates, for example, calcium hydroxyapatite ($Ca_{10}(PO_4)_6(OH)_2$ or CaHAP), the major mineral component of hard tissues (teeth and bones). Fadeev and coworkers [490] studied the surface modification of CaHAP with organophosphonic acids ($R-PO_3H_2$). The solution-phase reactions of $R-PO_3H_2$ ($R = n$-C_8H_{17}, n-$C_{18}H_{37}$, and n-C_8F_{17}F-$(CH_2)_2$) were studied with two types of CaHAP substrates: high surface area powder and thin films supported on Ti/Si wafers. Solutions of low concentration (~5–10 mM or less) yielded covalently attached monolayers supported on CaHAP. According to FTIR spectroscopy, the major products

of the reaction were organophosphonic groups bound to the surface via P_S-O-P bonds. Modified surfaces showed good hydrolytic and thermal stability [490].

1.7.4 Organosilanization

1.7.4.1 General

Silanes with the general formula, $X_{4-n}-Si-R_n$ (where X represents a halide, alkoxide, or alkyl group; and R an organofunctionality), have been used for chemical modification and as coupling agents since the first reports by Murray and coworkers [290] and others [242, 265]. Organosilanes can act as a bridge between organic and inorganic layers. X is a hydrolyzable, a reactive leaving group that attaches the Si to the surface, the functional groups R are chosen to form protective layers, modified electrodes, or immobilize large functional groups such as biomolecules on surfaces [23, 283–289]. SAMs of organosilane derivatives require hydroxylated substrate surfaces for their monolayer formation. Substrates on which these monolayers have been prepared include SnO_2 [242, 265, 290, 492–494], TiO_2 [439, 440, 495–503], ZnO [503–505], ITO [347, 506–529], Al_2O_3 [498, 530–532], and SiO_2 [533–575] as well as other oxide surfaces [440, 493, 501–503, 573–575] (see Table 6).

Tab. 6 Examples of chemical modification of organosilane derivatives on various oxide surfaces

Substrate	*Organosilanemolecule, $X_{4-n}-Si-R_n$*	*References*
SnO_2	X_3-Si-R; X = C_2H_5O, CH_3O, Cl; R = $(CH_2)_3NH_2$, $(CH_2)_3NHC_2H_5NH_2$, $(CH_2)_2CHCl_2$, $C_2H_5C_5H_4N$	290
	$(C_2H_5O)_3-Si-(CH_2)_3-R$; R = 4-arylazo-1-naphtol NH_2, aryl amine	242, 265, 291
	$Ru(bpy)_2(\beta$-(4-trichlorosilylethyl-4′-CH_3-bpy$)^{2+}$	492
SnO_2 or Fe_2O_3	Cl_3-Si-R; R = tridecafluoro-1,1,2,2-tetrahydrooctyl	493
	Octadecyltrimethoxysilane, $(CH_3O)_3-Si-(CH_2)_{17}CH_3$	494
TiO_2	$(C_2H_5O)_2-Si(C_2H_5)_2$, $(CH_3O)_3-Si-(CH_2)_2CF_3$, $(C_2H_5O)_3-Si-CH=CH$, and $(C_2H_5O)_4-Si$	495–497
TiO_2 or ZrO_2	$X_3-Si-C_{18}H_{37}$; X = H, Cl, CH_3O, $(CH_3)_2Cl$	439, 440, 498
	Benzyltrimethylsilanes, $(CH_3)_3-Si-CH_2Ph$-R; where R = 3-CH_3O, 4-CH_3, 3-CH_3, 3-Cl, 4-Cl, 4-F, or 3-CF_3)	499
	$(CH_3O)_3-Si-(CH_2)_3NHC_6H_5$	500
TiO_2, ZrO_2, HfO_2, ZnO, NiO, Al_2O_3	H_3-Si-R; R = SiH_3, $C_{18}H_{37}$, C_8H_{17}, $(CH_2)_6CH=CH_2$, $(CH_2)_2C_6F_{13}$	501–503
ZnO	$(CH_3O)_3-Si-(CH_2)_2(CF_2)_7CF_3$	504
	$(HO)_3-Si-R$; R = $(CH_2)_{3,7}CH_3$, $(CH_2)_3NH_2$, $(CH_2)_3SH$	505
ITO	$(CH_3O)_3-Si-(CH_2)_3NH_2$	506–508
	$(CH_3O)_3-Si-R$; R = $(CH_2)_3NH_2$, $(CH_2)_3N(CH_3)_3^+$	347
ITO or SiO_2	Octachlorotrisiloxane, $Si_3O_2Cl_8$	509–511
	$N(p$-$C_6H_4(CH_2)_3SiCl_3)_3$ and TPD-$((CH_2)_3SiCl_3)_2$	512–516

Tab. 6 (*continued*)

Substrate	*Organosilanemolecule, $X_{4-n}-Si-R_n$*	*References*
ITO or SiO_2	$(C_2H_5O)_3-Si-(CH_2)_3NHCO_2$-TPA (triphenylamine)	517
	3-[*N*-CH_3-*N*-4-(4-nitrophenylazo)phenyl-amino]-propylmethyldiethoxysilane	518, 519
	(Dichloromethyl)dimethylchlorosilane	520
	$(CH_3O)_3-Si-R$; R = ethyl, allyl, 1-propanthiol	521
	Octyltrimethoxysilane, $(CH_3O)_3-Si-(CH_2)_7CH_3$	522
	$Cl_3-Si-(CH_2)_2(CF_2)_7CF_3$	523
	Octadecyltrimethoxysilane, $(CH_3O)_3-Si-(CH_2)_{17}CH_3$	524–526
ITO or SiO_2	Docosyltrichlorosilane, $Cl_3-Si-CH_2(CH_2)_{20}CH_3$	527, 528
	$Cl_3-Si-(CH_2)_{7,17,21}CH_3$	529
Al_2O_3	10-undecenyl- or 18-nonadecenyltrichlorosilanes	530
Al_2O_3, SiO_2, TiO_2	Octadecyltrichlorosilane, $Cl_3-Si-(CH_2)_{17}CH_3$	498, 531, 532
SiO_2	Octadecyltrichlorosilane, $Cl_3-Si-(CH_2)_{17}CH_3$	527, 533–541
SiO_2, Al_2O_3, Si_3N_4	Octadecyltrichlorosilane, $Cl_3-Si-(CH_2)_{17}CH_3$	463, 542, 543
	X_3-Si-R; X = CH_3O, Cl; R = $(CH_2)_2(CF_2)_{5,7}CF_3$, $(CH_2)_{17}CH_3$, $(CH_2)_3OCF(CF_3)_2$, $(CH_2)_3NH(CH_2)_6NH_2$	544–548
	$(C_2H_5O)_3-Si-(CH_2)_3NH_2$	549–551
	4-Aminobutyl-dimethyl-monomethoxysilane	552
	(3-Bromopropyl)trichlorosilane	553–555
	Mono-, di-, and trichloroalkylsilanes, Cl-$SiMe_2R$, $Cl_2-SiMeR$, Cl_3-SiR; R = C_1-C_4, C_6-C_8, $C_{10,12,or18}$	556–558
SiO_2 or Al_2O_3	$Cl_3-Si-(CH_2)_3$-3-(pyridine-4-methyl)-urea	559, 560
	$Cl_3-Si-(CH_2)_{12}-R$; R = carbazole, CO_2CH_2-R′; R′ = phenyl, retinal, pyrene), and $CH=CH_2$	561, 562
	$(CH_3O$ or $Cl)_3-Si-(CH_2)_{3,6,8,or10}SH$	563–566
	p-Aminophenyltrimethoxysilane	567
	Phenyltrichlorosilane, $Cl_3-Si-C_6H_5$	568
	$Cl_3-Si-(CH_2)_{11}-O-C_6H_5$	569
	$(CH_3O)_3-Si-R$; R = $(CH_2)_{5,7}CH_3$, $(CH_2)_6CH=CH_2$, 3-(2-aminoethyl)-aminopropyl	570, 571
	$Cl_3-Si-(CH_2)_2(CF_3)_5CF_3$; $Cl_3-Si-(CH_2)_{3,17}CH_3$; $Cl_3-Si-(CH_2)_2C_6H_5R$ (R = 4-H, 4-Cl, 4-SO_2Cl); $Cl_3-Si-(CH_2)_3R$ (R=CH_2Cl, CH_2Br, CF_3);	572
CaHAP	$[(CH_3)_3-Si]_2-NH_2$; $(CH_3O)_3-Si(CH_2)_3O_2CCH_3=CH_2$	573–575

1.7.4.2 **Wide Bandgap Transparent Conducting Oxide Electrodes**

1.7.4.2.1 **SnO_2** It is known from chromatographic [576] and other studies that the order of reactivity of halosilanes with silica is $X_3SiR > X_2SiR_2 > XSiR_3$. This relationship was also observed with SnO_2 surfaces in a series of reactions where X = Cl and R = methyl. The Si 2p band was most intense for SnO_2 treated with Cl_3SiCH_3, and least for $ClSi(CH_3)_3$ [290].

Silanization reactions were carried out in dry deaerated benzene or xylene. Electrode specimens were reacted under 50 ml of a ca. 10% solution of refluxing silane, under nitrogen, for several hours with trichlorsilanes to several days with triethoxysilanes. After reaction, the solution was decanted and the specimens were washed under nitrogen with several portions of fresh solvent [290]. Surface bonding depends on reactions of organosilane reagents with hydroxyl groups on SnO_2.

For the amide-linked electrode, the cleaned SnO_2 or TiO_2 electrodes were treated with γ-aminopropyltrichloroethoxysilane, $(C_2H_5O)_3Si(CH_2)_3\ NH_2$, in toluene to form the aminopropyl-modified SnO_2 electrodes [292] by the method developed by Murray and coworkers [290]. As shown in Fig. 9, Fujihira and coworkers [265, 291, 292] have tried to increase the surface coverage of the amide-linked organic dyes such as RhB−COOH or $TPP(COOH)_4$ and ultimately to increase the sensitized photocurrent by improving yields of the silanization reaction. On the average, two of the four −COOH groups of $TPP(COOH)_4$ might be bound to SnO_2 [292]. If the chemical modification of electrode surfaces are applied to the solar cells, the sensitizers should be bound as close to the electrode surfaces as possible in order to increase the efficiency of spectral sensitization [291].

Since the mid-1970s, the surface attachment of electroactive molecules to modify electrode properties has been studied very extensively and chemicals with various properties have been immobilized [284]. Ghosh and Spiro [492] have used this approach to covalently attach $Ru(bpy)_3^{2+}$ to *n*-type SnO_2 via condensation of surface hydroxyl groups with $Ru(bpy)_2(\beta$-(4-trichlorosilylethyl-4′-CH_3-bpy$)^{2+}$ and have studied electrochemistry and photochemistry of the coated electrodes. Organosilanes spontaneously react with hydroxylated surfaces to form films of specific chemical functionality for a variety of applications. For example, the utility of the thermally generated organosilane masks was demonstrated through selected area deposition of sol-gel derived materials such as SnO_2 [493]. Such thermal lithographic method is a new approach to patterning surfaces [494].

1.7.4.2.2 **TiO_2 and ZrO_2** A series of silanes on clean and water-dosed TiO_2 (110) surfaces were investigated by Campbell and coworkers [495–497]. The simplest molecule, tetraethoxysilane (TEOS), consists of a central Si atom bound to four ethoxy (EtO) groups. At low coverages, it readily dissociates, splitting off one or several EtO groups. Multilayers form at high dosages at low temperatures

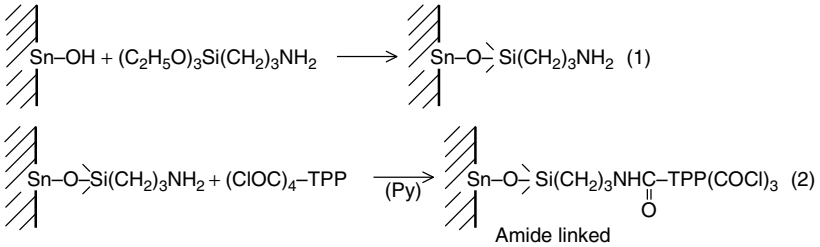


Fig. 9 Schematic presentation for formation of aminopropyl-modified SnO_2 electrodes with organic dyes such as $TPP(COCl)_4$ [292].

[495]. Vinyl- and diethyldiethoxysilanes also dissociate on TiO_2 surface in the absence of water by splitting off two EtO groups [496]. $(C_2H_5O)_3Si(CH_2)_3\ NH_2$ (with a $(CH_2)_3-NH_2$ group substituting one EtO in TEOS) does not dissociate on TiO_2 in any measurable quantity [496]. $(CH_3O)_3-Si-(CH_2)_2CF_3$ turned out to be more reactive than ethoxysilanes considered. This molecule also adsorbs dissociatively by splitting off $-OCH_3$ groups. Spectroscopic data showed that these bind to exposed Ti sites, and that the Si in the remaining $(CH_3O-Si-(CH_2)_2CF_3)$ complex binds to two lattice oxygens (two bridging oxygen atoms in the proposed model) [497]. Methoxysilanes are more reactive with TiO_2 (110) than ethoxysilanes [497].

Fadeev and coworkers [439, 440] have studied the reactions of octadecylsilanes with different head groups ($X_3SiC_{18}H_{37}$, X = H, Cl, CH_3O) with surfaces of TiO_2 and ZrO_2. According to the rate constants [439], the following range of reactivity was established: $C_{18}H_{37}SiCl_3 >> C_{18}H_{37}PO(OH)_2 > C_{18}H_{37}Si(CH_3)_2Cl > C_{18}H_{37}Si(OCH_3)_3 > C_{18}H_{37}SiH_3$. They also studied the reactions of different end-functional organosilicon hydrides (H_3SiR, R = (SiH_3, $(CH_2)_2C_6F_{13}$, $(CH_2)_6CH=CH_2$, C_8H_{17}, $C_{18}H_{37}$) with TiO_2, ZrO_2, and HfO_2 as well as other metal oxides (groups II–VIII) [501, 503]. According to the rate constants, the following range of reactivity was established: $H_3Si(CH_2)_8SiH_3 > H_3Si(CH_2)_2C_6F_{13} \approx H_3SiC_8H_{17} > H_3SiC_{18}H_{37}$ [501]. All the SAMs good thermal stability and no mass loss were observed below ~200 °C in air [439, 501]. The structure of the monolayers and the reaction mechanisms were discussed in detail [501, 503].

An organic solvent free heterojunction of *n*-TiO_2/*p*-polyaniline (PANI) with enhanced photovoltaic properties could be constructed by chemical polymerization of aniline followed by covalent grafting via $(CH_3O)_3-Si-(CH_2)_3NHC_6H_5$ compound [500]. PANI was able to sensitize TiO_2 efficiently in the presence of SAM. In recent years, many mechanistic details have been collected about this TiO_2-sensitized photooxidative process starting with benzylic derivatives such as alcohols and silanes) in CH_3CN [499]. Benzyltrimethylsilanes, $(CH_3)_3SiCH_2Ph$-R; where R = 3-CH_3O, 4-CH_3, 3-CH_3, 3-Cl, 4-Cl, 4-F, 3-CF_3) were used.

1.7.4.2.3 **ZnO** A simple method of electrochemical deposition was adopted to prepare conductive hydrophobic ZnO thin films [504]. These ZnO films were fabricated by overpotential electrochemical deposition at room temperature, and the surface modified by a (fluoroalkyl)silane showed superhydrophobic properties. The prepared thin films were treated with a methanol solution of hydrolyzed (heptadecafluorodecyl)trimethoxysilane $(CH_3O)_3Si(CH_2)_2(CF_2)_7CF_3$, 1.0 wt %) for 3 h and subsequently heated at 100 °C for 1 h. Wettability studies revealed that the surface of the as-prepared thin films showed a contact angle (CA) for water of $128.3 \pm 1.7°$, whereas the superhydrophobic surface with a water CA of $152.0 \pm 2.0°$ was obtained by (fluoroalkyl)silane modification [504].

In addition, molecular dynamics simulations at 298 K were used to study the interaction of adsorbed silane molecules (octyltrihydroxysilane, butyltrihydroxysilane, aminopropyltrihydroxysilane, and thiolpropyltrihydroxysilane) with the polar ZnO(0001) surface [505]. Kornherr and coworkers [505] have compared a model of a reconstructed surface with a model of ideal bulk terminated surface. Surface morphology is shown to have little effect

on the orientation of silane adsorbates (except thiolpropyltrihydroxysilane), with adsorption energy being correlated with the surface polarity.

1.7.4.2.4 **ITO** Mirkin and coworkers [506] have reported the first SAMs of C_{60} attached onto 3-aminopropyltrimethoxysilane ($(CH_3O)_3Si(CH_2)_3NH_2$)-modified ITO electrode. The ITO surface was first derivatized to form a positively charged layer of pH-insensitive and redox-inactive $-CH_2CH_2CH_2N(CH_3)_3^+$ groups by silylation [347]. These substrates were then alternatively immersed in a polyanion and then a polycation solution. Fukuzumi and coworkers [507, 508] have recently reported the first photogeneration by ITO modified chemically with SAMs of porphyrin-C_{60} linked molecules (H_2P-C_{60}/ITO) and its zinc complex (ZnP-C_{60}/ITO). In addition, only a small number of studies have been reported that aim at attaching alkyl chains onto ITO surfaces via silane chemistry [522–529]. The general conclusion of these studies is that the formation of densely packed defect-free SAMs on ITO is difficult due to the high surface roughness and low hydroxyl coverage.

Patterning ITO electrode is conventionally achieved via photolithography. Other methods of patterning ITO have been explored as cost-efficient alternatives. Marks and coworkers [528, 529] have described "hot microcontact printing" to form patterned $Cl_3-Si-(CH_2)_{7,17,20,21}CH_3$ and $Cl_3-Si-(CF_2)_5CF_3$-based SAMs on ITO that modulate the luminescence of OLEDs [528, 529]. The ease of preparation of these monolayers, combined with the ease of patterning and their high etch resistance, will open the way to their use as commercially important etch resists [523].

Armstrong and coworkers [510, 511] have reported the use of layer-by-layer, self-limiting chemisorptive octachlorotrisiloxane ($Si_3O_2Cl_8$) self-assembly techniques to introduce robust, conformal, microstructurally/electronically well-defined charge injection dielectric layers at ITO/HTL interface of OLEDs. Preparation and deposition of self-assembled siloxane dielectric layers were described [509].

Marks and coworkers [512–515] have demonstrated that a spin-coated, $N(p\text{-}C_6H_4(CH_2)_3SiCl_3)_3$ and TPD-$((CH_2)_3SiCl_3)_2$ derived adhesion/injection interlayers at ITO/HTL interface of the devices. They have also reported that chemically tuning the interface structure represents an effective approach to studying nanoscale injection layers and yields with high efficiency ($\sim$70 000 cd m^{-2}), low turn-on voltages ($\sim$4 V), and high current efficiencies ($\sim$8 cd/A) [516].

Functionalized alkylsilanes, such as $(CH_3O)_3Si(CH_2)_3NH_2$, have been used mainly for attaching dye molecules such as triphenylamine [517] and azobenzene derivatives [518, 519]. The grafting of molecular dipoles at the surface of ITO anode has been found to lead to a significant lowering of the injection barrier [518]. However, this lowering is not as large as expected from a naive estimate, which is due to the fact that the dipoles are not densely packed and do not stand perfectly perpendicular to the electrode surface. Silanization of ITO using short-chain alkylsilanes [520, 521] was reported and shown to be anchor with a good stability on ITO.

1.7.4.3 Large Bandgap Oxide Electrodes

Octadecyltrichlorosilane, $Cl_3Si(CH_2)_{17}CH_3$, have been patterned on Al_2O_3 and TiO_2 as well as SiO_2 surfaces by μCP [498,

530–532, 535–539, 541, 557, 567]. SAMs have also been patterned on a number of substrates: Al/Al_2O_3, Si/SiO_2, TiN/TiO_2, glasses (for example, glass microscope slides), ITO, and plasma-modified polyimide [531]. The patterns were transferred into the substrates using both dry and wet etching. The Al and Ti were etched using electron cyclotron resonance plasma source and Si was etched in HF to remove the native oxide, followed by KOH [498]. μCP using octadecyltrichlorosilane ink is a convenient and easy way to pattern both metal and nonmetal (Al_2O_3, SiO_2) surfaces without the extended use of photolithography.

One of the most useful classes of SAMs is that formed by alkanesilanes such as $Cl_3Si(CH_2)_{17}CH_3$ on hydroxyl-terminated surfaces with a native oxide, such as Al/Al_2O_3 [463, 530–532, 542] and Si/SiO_2 [288, 527, 533–538, 543]. Al easily passivates in the presence of air forming a thin Al_2O_3 overlayer ca. 40–60 Å thick, which protects the underlying metal [463]. The oxide overlayer completely covers and is firmly adherent to the underlying metal surface. The Al_2O_3 layer formed either by air oxidation or by electrochemical anodization is amorphous and is referred to as α-Al_2O_3, but upon heating, this form of oxide changes to a harder crystalline form known as γ-Al_2O_3 [463]. Cleaned Si(100) wafers are oxidized in a freshly prepared 4 : 1 mixture of 96% sulfuric acid and 30% hydrogen peroxide (piranha solution) at 100 °C [534]. After the substrates have been allowed to cool to room temperature, the samples were rinsed with deionized water and dried in vacuum. The oxidized Si samples were immersed into a freshly prepared solution of $Cl_3Si(CH_2)_{17}CH_3$ in dried toluene at room temperature [534].

Trichlorosilane ($Cl_3Si(CH_2)_{17}CH_3$) SAM films having $-CH_3$ and $-CH_2Br$ terminal functionalities were grown on oxidized Si surfaces, HF-treated silicon nitride surfaces, and HF-treated Si_3N_4 probe tips [537]. Experimental data suggested that the monolayers formed on oxygen-depleted Si_3N_4 surfaces are similar to those formed on oxidized Si [537]. While S–Au bond is mostly charge transfer in nature, the "headgroup-substrate" interaction of the silane and SiO_2 surface is quite different; here, the silane molecules condense with native hydroxyl groups adorning the SiO_2 surface, forming a thin layer of covalently linked polysiloxane at the interface [577]. This small polymer interface is much more thermally stable than its RS–Au counterpart, thus affording greater stability and an extremely robust system.

Films made from fluorinated alkylsilanes have been studied and they were found to yield well-ordered monolayers on Si substrates with the native oxide [544–548]. Sugimura and coworkers [545, 548] have studied the relations between the fluoroalkyl chain lengths of the fluoroalkylsilane molecules and properties of the films produced, including thickness, water repellency, chemical properties, and morphology. They [546] have also demonstrated nanostructuring of insulator based on current-injecting AFM lithography. In addition, microstructures composed of two types of organosilane SAMs terminated with different functional groups have been constructed on Si substrates covered with native oxide [547]. Surface potential images of these microstructures were acquired by Kelvin-probe force microscopy.

Lieber and coworkers [549] have reported systematic force microscopy studies of the interactions between different chemical functional groups covalently

linked to a probe tip and sample substrate. In order to study the interactions, they have utilized monolayers of 11-mercaptoundecanoic acid on the probe tip and $(C_2H_5O)_3-Si-(CH_2)_3R$ ($R = NH_2$, COOH, and CH_3) on the Si(100) substrate [549–551]. Adhesion studies between SAMs which terminate with COOH and CH_3 functional groups have shown that the interaction between COOH/COOH > CH_3/CH_3 > $COOH/CH_3$ [549].

Surface modification can be achieved by binding of different substituted alkylsilanes at the surface. SAMs have been reported from alkyltrichlorosilanes with terminal groups of amine [552, 570], halogen [553–555, 572], alkyl ($C_{1-4,6-8,10,12,18}$) [556–558, 570–572], 3-(pyridine-4-methyl)-urea [559, 560], carbazole [561], vinyl [561, 570], CO_2CH_2-R′ (R′ = phenyl, retinol, pyrene) [561, 562], thiol [563–566], *p*-aminophenyl [567], 4-chlorosulfonylphenyl [572], and phenyl [568, 569, 572]. SAMs with low surface free energy have been prepared using partially fluorinated alkylsilanes [544, 545, 572]. When alkyltrichlorosilane is used, Si–Cl bonds react with the OH groups present on the surface of the substrate to form a siloxane network. The structure of alkylsilane SAMs on Si have also been studied [463, 527, 533, 547, 549, 556, 563].

Surface modification reactions are important not only for engineering of surface energy and interfacial properties such as wetting, adhesion, and friction, but also for providing active surfaces for the attachment of molecules with different properties such as polymers [552], ruthenium phthalocyanine (RuPc) [560], π-electron moieties [561], and deoxyribonucleic acid (DNA) [566, 570]. Organosilanes with more than one reactive group have the potential of binding to more than one surface site [556]. In addition, the use of organosilanes, mostly trialkoxysilanes, for surface modification of nonoxide surfaces such as CaHAP and Ca phosphate ceramics has been described [573–575].

Cahen and coworkers [553, 554] have reported that self-assemblies of organosilanes can be used to tune the electronic properties of Si surfaces. Batlogg and coworkers [572] have more recently reported controllable shift of the threshold voltage and the turn-on voltage in pentacene thin-film transistors and rubrene single crystal field effect transistors (FETs) incorporating nine organosilanes with different functional groups (see Table 6). Prior to the depositing the organic semiconductors, organosilanes were applied to the SiO_2 gate insulator from solution and form a SAM. Si wafers were immersed for 3 h in a 3 mM solution of the organosilane in anhydrous toluene and then cleaned in fresh toluene for 2 min. The observed shifts of the transfer characteristics range from −2 to 50 V and can be related to the surface potential of the layer next to the transistor channel. This shift is governed by the build-in electric field of the SAM and can be explained using a simple energy level diagram [572].

1.7.5 Potential Applications

Starting from the pioneering works of chemical modification of TCO electrodes [242, 265, 290, 291], a lot of application possibilities have been developed. These electrodes are widely applied in electrochemistry and electrocatalysis. Electrochemical studies on chemically modified oxide electrodes have been discussed in details in Refs. 283–285. Recent developments in optoelectronic and photovoltaic device systems require control of the chemical and

physical as well as photophysical properties of TCO thin films used as electrodes [254, 255, 275–277]. The following section gives some examples of the applications of chemically modified oxide electrodes for controlling the performance of optoelectronic and photovoltaic devices based on organic materials.

1.7.5.1 Tuning the Work Function of Electrodes

Contact potential difference (CPD) for clean metal surfaces is given by the difference in the work functions of the two materials. The work functions can be changed by adsorption of molecules with different dipole moments [276]. In a simple model, the contact potential between the two materials is $V_{CPD} = -(\phi_1 - \phi_2)/e$, where ϕ_1 and ϕ_2 are the work functions of the conductors including changes due to the adsorbed layers.

Large surface potential difference was observed between fluorocarbon (FC) and hydrocarbon (HC) covered water surfaces by Vogel and Möbius [578]. Similarly, the CPD due to large work function difference was observed between FC and HC covered gold, SiO_2, and ITO surfaces with scanning surface potential microscopy (SSPM) [276, 579–584]. These experiments were carried out to determine the phase-separated structure of a mixed monolayer of FC and HC amphiphiles ion-complexed with a cationic polymer deposited on Si(100) observed by friction force microscopy [582]. Artificial photosynthetic molecular systems were also studied with various scanning probe microscopes including SSPM [584]. Later, Campbell and coworkers [585, 586] applied the large work function difference between FC and HC on silver to control Schottky energy barriers in organic electronic devices. The work function of ITO was increased more than 0.5 eV by changing a surface covering pure monolayer from HC to FC with a terminal group CF_3- [276, 580]. Two dipole layers with large electric dipole moments have been introduced at the surfaces [578–586] via a binding group (X–) and a terminal group (–Y). The molecular control of work functions of other semiconductors, such as CdTe, CdSe, GaAs, and InP, than ITO were also reported using benzoic acid [587] and dicarboxylic acid derivatives [451].

The work function control by alloy formation [588–592] and by the surface modification has been applied to enhanced charge injection at electrodes for OLEDs [306–313, 324, 325], electrochemical [314] and photovoltaic (PV) cell studies [308, 316]. In this molecular design, we prefer π-conjugated systems to alkyl chains as the π-conjugated linkage can reduce the barrier heights for charge injection [291, 292, 584, 593]. Selection of bonding modes of molecules with high permanent dipole moments is also important because additional dipole is created through the bonding [277, 312] in the same way as in chemical adsorption of acids and bases [311, 335–337, 594].

Recently, we reported that the chemical modification of ITO with different binding groups ($-SO_2Cl$, $-COCl$, and $-PO_2Cl_2$) of *p*-substituted (H–, Cl–, and CF_3-) benzene derivatives leads to enormous increase in ITO work function [312]. Binding site and terminal group are linked by *n*-alkylene or *p*-phenylene group as shown in Fig. 10(b) and (c). In Fig. 10(a), expected energy diagrams are also shown. Directions of two dipole layers are preferable for enhanced hole injection. The increases in work function due to dipoles of binding and terminal groups are Δ_1 and Δ_2, respectively. The vector addition of the component dipole moments holds

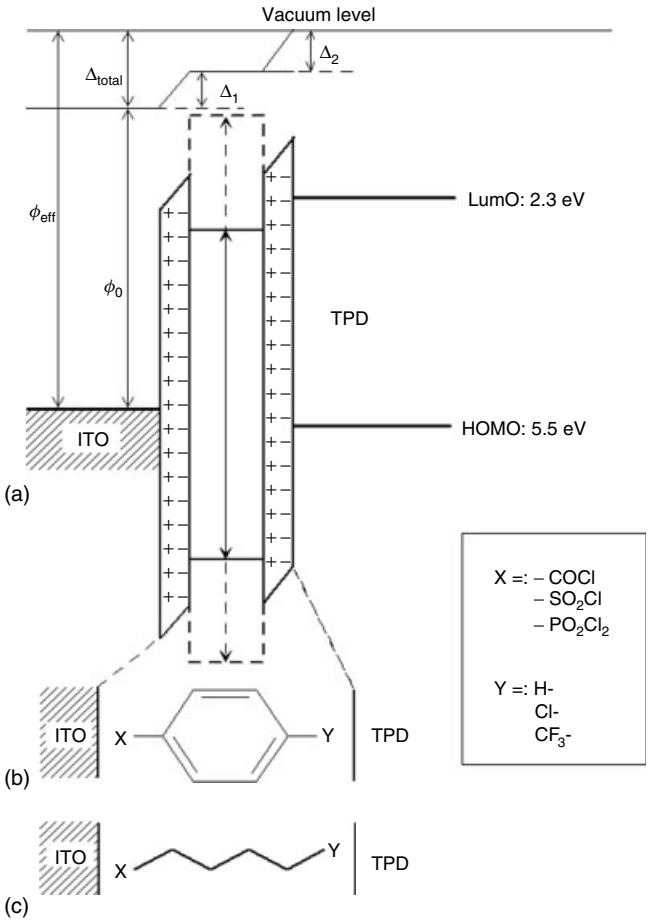


Fig. 10 Schematic illustration of (a) the energy diagram near the interface between a *N*, *N*′-diphenyl-*N*, *N*′-bis(3-methylphenyl)-1, 1′-biphenyl-4,4′-diamine (TPD) film and an ITO anode chemically modified with various compounds with a binding site (X—) and a terminal group (—Y) linked with (b) *p*-phenylene or (c) *n*-butylene. Δ_{total}: a shift of a vacuum level at the ITO/TPD interface due to two dipole sheets (Δ_1 and Δ_2) formed by chemical modification of ITO. ϕ_0: work function of ITO without dipole layers. ϕ_{eff}: effective work function of ITO after chemical modification [312].

in general [595]. The barrier heights of *n*-alkylene (dashed) and *p*-phenylene (solid) were estimated from our previous photoelectron spectroscopic data [596, 597]. In contrast, the barrier heights for binding sites and terminal groups are more arbitrarily and schematically drawn because of the variety of these groups studied [292]. It is obvious from the energy diagram that *p*-phenylene is better than *n*-butylene because of the lower barrier height for hole injection.

The change in work function due to chemical modification of ITO was

observed by SSPM [579–581] using gold-coated atomic force microscopy tips derivatized with 1-decanethiol. The modified tips gave reproducible results. In Fig. 11(a), CPD values observed on ITO modified with benzoyl chlorides with H−, Cl−, and CF_3–terminal groups in para position are shown. For comparison, the CPDs of as-cleaned, heat-treated, and UV-ozone treated ITO measured with the same modified tip are also plotted. The CPD decreases with the increase in the work function of ITO [276]. As we would expect, the work function of ITO increased as the permanent dipole in the para position increased.

In order to tune the work function of ITO fine, the effect of binding groups on the work function was also studied. In Fig. 11(b), CPD values observed on ITO chemically modified with $-SO_2Cl$, −COCl, and $-PO_2Cl_2$ binding groups of *p*-chlorobenzene derivatives. The large decrease in CPD down to ∼ −770 mV, that is,

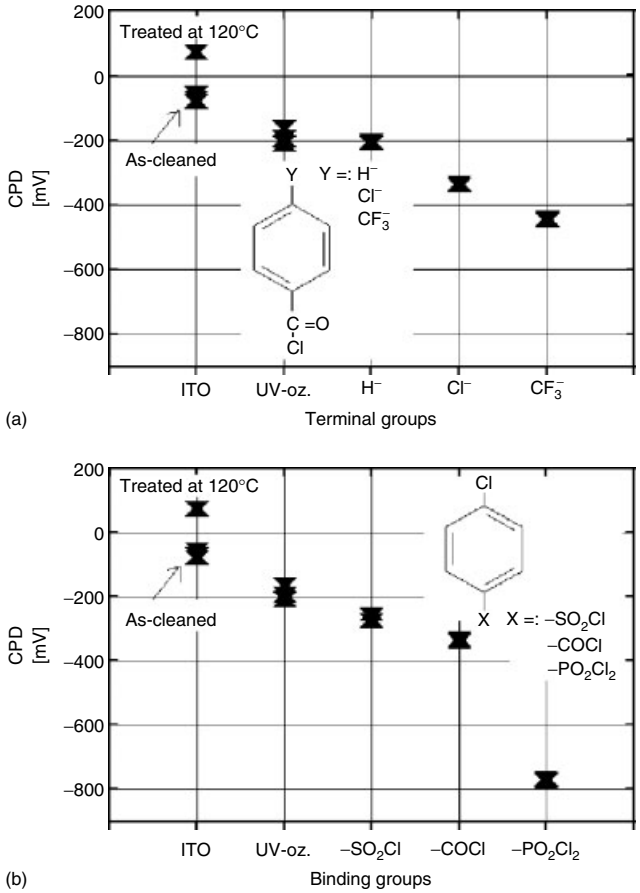


Fig. 11 The change in contact potential difference of modified ITO as a function of (a) benzoyl chlorides with various terminal groups and (b) $-SO_2Cl$, −COCl, and $-PO_2Cl_2$ binding groups of *p*-chlorobenzene derivatives [312].

the increase in the work function of ITO, was observed with $-PO_2Cl_2$, while the moderate decreased values of CPD, that is, ~ -350 and ~ -270 mV, were observed with $-COCl$ and $-SO_2Cl$, respectively. Even on the latter modified ITO anodes, the work function increase was greater than that on the UV-ozone treated ITO. The effect of the binding group on work function has not been studied systematically so far except the study described in Ref. 312. However, the results shown in Fig. 11(b) can be compared with the work function change of ITO treated with various acids [335], where the electrical double layer was created by formation of a double ionic surface layer. The work function shifts with respect to nontreated ITO were reported to be 0.7, 0.4, and 0.1 eV for H_3PO_4, HPF_6, and HNO_3, respectively. In the double ionic surface layer model [335–337], large counter anions should increase the surface dipoles, since their charge will be sterically separated further away from the protonated positive surface. This picture was applied to the difference between HPF_6 and HNO_3, while the enormous shift for H_3PO_4 was rationalized by specificity of this acid whose two protons at least were considered to bind to the surface thus increasing the adsorbed dipole [335].

The molecular approach allows for fine-tuning the work function using organic molecules on ITO depending upon magnitude and direction of the dipole moment [312]. The work function can be changed when surface dipole is oriented as shown in Fig. 12. An interface dipole with its negative end pointing toward the organic layer and its positive site toward the electrode surface increases ITO work function (i.e. the Fermi energy is down) and HOMO energy level in the organic layer is up by adding an electrostatic energy. As a result, the hole injection barrier ϕ_h is reduced (Fig. 12b). Reversing the direction of the dipole, we can reduce the work function, and thus the electron injection barrier, ϕ_e, as shown in Fig. 12(c). Thus, the work function increase (or decrease) is associated with enhanced hole (or electron) injection [312, 331, 338]. Various possible origins for interface dipoles formed at the interfaces have been proposed [275, 598].

Although various inorganic treatments have been shown to change the work function of ITO [330–337], these procedures do not easily lend themselves to adjustable modification of ITO surface. With molecules carrying a high dipole moment oriented perpendicular to the surface, it has been observed that total interface dipole can be rather easily tuned by changing chemically the magnitude of the molecular dipole moment [598]. Impressive tests of the dipole layer on electrode surfaces have been conducted with use of SAMs of *p*-substituted arylthiols on Au [599] or Cu [585], *p*-substituted benzoic acids on CdTe, CdSe, GaAs [451, 587], TiO_2 [430], and ITO [308, 594] as well as both *p*- and *o*-substituted phenols on modified ITO with tetra(*tert*-butoxy)tin [339].

1.7.5.2 Correlation of Device Performance with Changes in the Work Function

The increasing level of research and device development activity involving a variety of organic, often molecular, interfaces, and their modification using organic- and inorganic-induced surface dipoles [275, 276, 600] has tested the fundamental understanding of basic surface energetics, which was developed primarily for well-defined, clean, mostly nonmolecular inorganic surfaces and interfaces [601]. In addition, the nature of developments in what are often called *organic electronics* [602–604], molecular electronics [593,

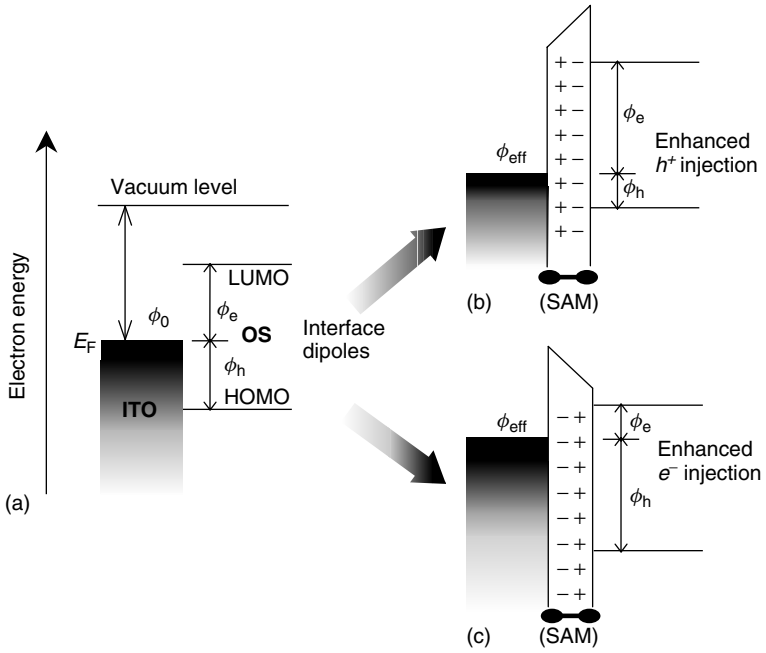


Fig. 12 Schematic energy level diagram of the impact of the formation of an interface dipole at an ITO/organic semiconductor (OS) interface: (a) the barrier in the absence of the dipole layer; (b) and (c) reduction of the hole injection and the electron injection barrier, respectively, in the presence of the interface dipole layer on the surfaces of ITO. Here, the interface dipoles with opposite sign are directed toward the ITO surfaces (b) increasing and (c) decreasing the work function of ITO.

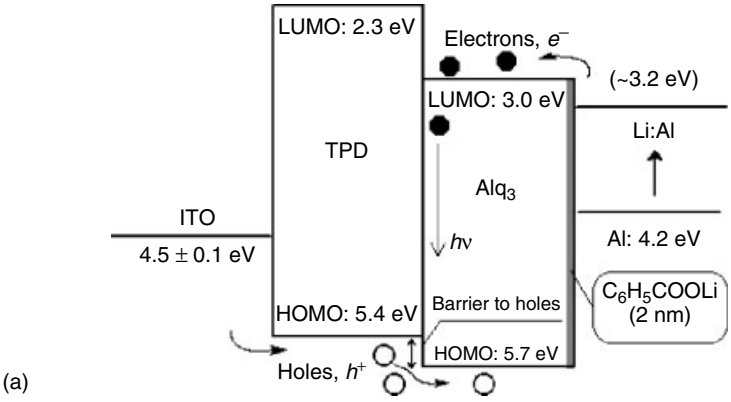
605–607] and dye-sensitized solar cells [253, 265, 291, 608–610], including organic molecules on more traditional surfaces [611], has tested the ability to make the ''classical'' understanding available to specialists from areas other than that of surface science.

To achieve enhanced hole injection from ITO anode, its Fermi level must be aligned with the highest occupied molecular orbital (HOMO) of the adjacent organic film. However, the work function of ITO is generally not sufficiently large for the contact to be Ohmic and so there is a barrier to carrier injection. The work function of ITO measured by UPS has a consistent value of 4.5 ± 0.1 eV, even though originating from different providers [269, 612, 613]. In Table 7, we summarize the experimental values of CPDs for ITO modified with various binding groups of *p*-substituted benzene derivatives [312]. The values of CPD were reported to be ~ -60 mV and ~ -190 mV for as-cleaned and UV-ozone treated ITO, respectively. Schematic energy diagram used for a two-layer organic electroluminescent (EL) device [590] and the range of ITO work functions estimated by CPD values [312] are shown in Fig. 13. As-received a bare ITO work function is considered to be in the range 4.4–4.6 eV [612, 613].

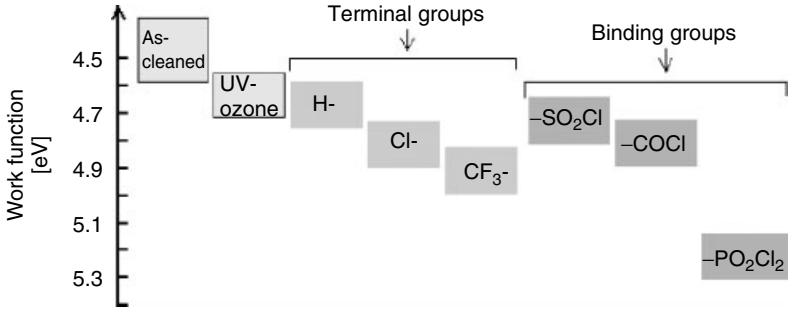
We have demonstrated that ITO surface modification, by SAM formation, with H−,

Tab. 7 Work function ϕ of SAM modified ITO with $-SO_2Cl$, $-COCl$, and $-PO_2Cl_2$ binding groups of *p*-chlorobenzene derivatives estimated from V_{CPD} and the work function of 4.5 ± 0.1 eV for cleaned ITO [312]

Terminal groups			*Binding groups*		
$Y-C_6H_5COCl$	$V_{CPD}(V)$	$\phi_{ITO-SAM}(eV)$	$p\text{-}ClC_6H_5-X$	$V_{CPD}(V)$	$\phi_{ITO-SAM}(eV)$
H−	0.21 ± 0.01	4.71 ± 0.1	$-SO_2Cl$	0.27 ± 0.01	4.77 ± 0.1
Cl−	0.35 ± 0.01	4.85 ± 0.1	−COCl	0.35 ± 0.01	4.85 ± 0.1
CF_3-	0.45 ± 0.01	4.95 ± 0.1	$-PO_2Cl_2$	0.77 ± 0.01	5.27 ± 0.1



(a)



(b)

Fig. 13 (a) Schematic energy level diagram used for a two-layer organic EL device [590] (ITO/TPD/Alq_3/C_6H_5COOLi(2 nm)/Al, where Alq_3 is a tris(8-hydroxyquinoline) aluminum) and (b) values of estimated work function for chemically modified ITO from the results of CPD measurements [312].

Cl−, and CF_3−terminated benzoyl chlorides increases its work function by ca. 0.21, 035, and 0.45 eV, respectively [312]. Dipole-induced work function change of ITO is related to dipole moment of the assembled molecules, μ [311]. The

order of the magnitude of the permanent dipole moments is expected to be $\mu_{CF3-} > \mu_{Cl-} > \mu_{H-}$ [312, 451, 578, 599, 614]. Substitution of benzoic acid in para position with moieties of varying electron-withdrawing or -donating capability is well known to alter both intramolecular dipole moment and acidity of carboxylic acid group [337, 615, 616]. The para substitution can be varied to such an extent that the dipole moment of substituted benzene (part of the carboxylic acid) is directionally reversed, that is, for $-OCH_3$ functionalization $\mu = -1.2$ D vs. $\mu = +2.82$ D for $-CF_3$. [451, 617]. Thus, in general, electron-withdrawing substituents lead to increased work function in comparison to benzoic acid treatment and electron-donating substituents, which yield decreased the work function.

In our improved EL devices [277, 312, 331, 354, 590, 591], holes injected from ITO anode into TPD HTL first reach to the TPD/Alq_3 interface and then injected further into Alq_3 layer, while electrons injected into the Alq_3 layer move toward the TPD/Alq_3 interface and are blocked at the interface, as shown in Fig. 13(a). If the electron and hole injections are well balanced, almost all these charges with opposite signs are recombined inside the emission zone near the TPD/Alq_3 interface inside the Alq_3 layer [331, 618]. The optimization of thickness of Li benzoate was examined and when the thickness of Li benzoate was *ca.* 2.0 nm the lowest turn-on voltage was observed (Fig. 13a).

We have studied the effect of two dipole layers, that is, those of binding site and terminal group, on work function of ITO and EL characteristics using *p*-phenylene linkage [312]. The EL characteristics, in particular the drive voltages, which were well correlated with the change in work function, were dramatically improved by the chemical modification [277, 312, 313].

I–V and luminance–current density (L–I) characteristics of the ITO/TPD(75 nm)/Alq_3(75 nm)/C_6H_5COOLi (2 nm)/Al devices with ITO modified with benzoyl chlorides with various terminal groups in the para position are shown in Fig. 14. In Fig. 14(a), the turn-on voltages shift to less bias voltage with the increase in the permanent dipole moment of the terminal group, which directs toward the ITO electrode. The drive voltage was most effectively reduced when CF_3-terminated benzoyl chloride was used. With ITO modified with Cl-terminated benzoyl chloride having the intermediate dipole moment, the characteristics became better than those with UV-ozone treated ITO. Even on the modified ITO with H-terminated benzoyl chloride without any appreciable dipole moment in the para position, the characteristics were better than those on cleaned ITO. In terms of EL efficiency shown in Fig. 14(b), however, the intermediate Cl-terminal group gave the highest performance suggesting that the best balance between electron and hole injection [331] was attained on this modified electrode. In addition to *p*-terminated benzoyl chlorides, *n*-nonanoyl- and *n*-palmitoyl chlorides were also used for chemical modification of ITO [313].

In Fig. 15, I–V and L–I characteristics of the EL devices with ITO chemically modified with *p*-chlorobenzene derivatives with $-COCl$, $-SO_2Cl$, and $-PO_2Cl_2$ binding groups are compared with those of the devices with as-cleaned and UV-ozone treated ITO. All binding groups lowered the drive voltages. Among them, $-PO_2Cl_2$ exhibited the best I–V characteristics and gave an extremely low operating voltage of 4.3 V for 100 cd m^{-2}. The binding $-COCl$ group gave slightly better I–V

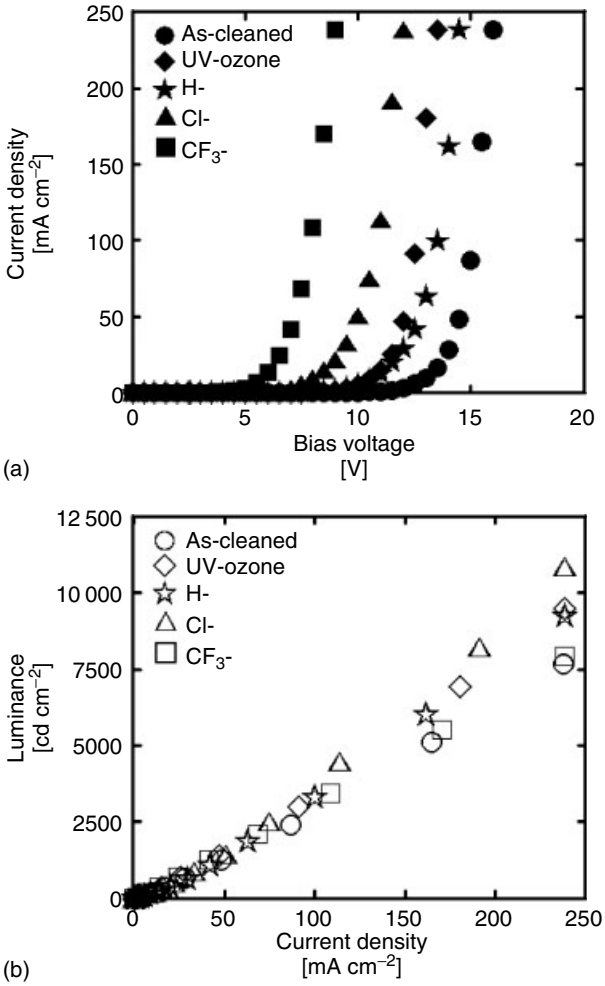


Fig. 14 (a) I−V and (b) L−I characteristics of EL devices with ITO chemically modified with benzoyl chlorides with −H, −Cl, and – CF_3 terminal groups in the para position having different permanent dipoles.

characteristics than $-SO_2Cl$. These results suggest that the efficient hole injection into TPD was due to the increase in work function of ITO covered with the two dipole layers introduced by the chemical modification. In particular, the results show that the selection of the binding sites is also important to tune the total work function change Δ_{total} in Fig. 10. As shown in Fig. 15(b), the devices with ITO modified with −COCl and $-SO_2Cl$ exhibited the best EL efficiency (~5 cd A^{-1} observed at 250 mA cm^{-2}). This can be interpreted again by the best balance between the hole and the electron injection. Too much higher hole injection with $-PO_2Cl_2$ results in the lower EL efficiencies. Our decision which EL device

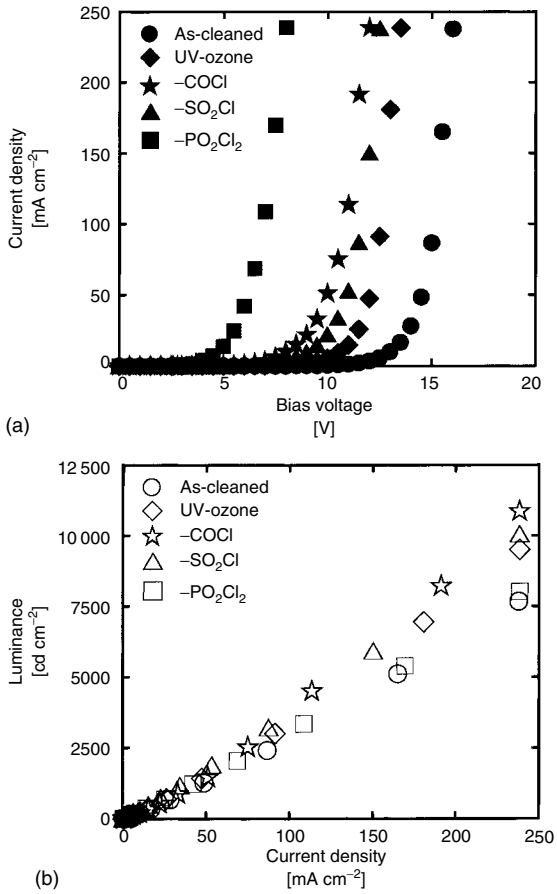


Fig. 15 (a) I–V and (b) L–I characteristics of EL devices with ITO chemically modified with $-SO_2Cl$, $-COCl$, and $-PO_2Cl_2$ binding groups of *p*-chlorobenzene derivatives. The device structure is ITO(various treated)/TPD(75 nm)/Alq_3(75 nm)/C_6H_5COOLi (2 nm)/Al.

we should use depends on our choice between the EL efficiency and the power efficiency. Therefore, EL characteristics were strongly correlated with the changes in observed work functions of various treated ITO [312, 331].

1.7.5.3 Other Possible Applications

1.7.5.3.1 **SnO_2** The work function of SnO_2 [619] or F-doped SnO_2 (SnO_2:F) [267] is about 4.4 ± 0.1 eV, independent of surface cleaning methods including UV-ozone treatment [619] or hydrogen peroxide/ammonia [267]. This value is the same as those obtained for as-received ITO and cleaned ITO with acetone/isopropanol, but lower than the value of 4.7–4.9 eV obtained for ITO cleaned with hydrogen peroxide/ammonia or UV-ozone treatment [267]. The fact that neither work function nor chemical composition depends upon the cleaning methods indicates that SnO_2 or SnO_2:F is more stable to oxidation than ITO, especially when the outermost surface lacks fluorine [267]. One important characteristic of SnO_2:F is that the surface is very flat [267]. Furthermore, SnO_2:F is less expensive to produce than ITO, and there is no indium present

to possibly diffuse into organic layers in OLEDs [267]. SnO_2 was also used as a transparent anode electrode to improve charge balance and device efficiency [620]. In addition, SnO_2 or SnO_2:F is presently used as a transparent back contact where charge extraction is the primary application [621–624], in PV devices such as TiO_2 dye-sensitized solar cells [253].

SnO_2 is a stable wide-bandgap semiconductor and has been widely used in a variety of electrochemical and electrooptical devices. Compared to TiO_2 or ZnO, SnO_2 is a better electron acceptor since its conduction band ($E_{CB} = +0.45$ V vs. NHE at pH 1) lies ~0.5 V more positive than that of TiO_2 [254]. Many organic dyes and organometallic complexes such as $Ru(bpy)_3^{2+}$ (bpy = 2,2′-bipyridyl) dissolved in solution have been employed to sensitize SnO_2 electrodes. Some examples include chlorophyll [625], croconate violet [626], rhodamine [627, 628], and $Ru(bpy)_3^{2+}$ [262, 492, 629]. However, the power efficiency in these examples has remained very low ($\eta \ll 0.1\%$).

1.7.5.3.2 **ITO** Chemisorption of small redox-active molecules on ITO can be used to probe changes in electrochemically activity of ITO surface as a function of surface pretreatment [314–316, 326]. The modification of ITO surface with electroactive small molecules such as $Fc(COOH)_2$ and 3-TAA provides for better wettability of organic layers to the polar ITO surface and enhanced electrical contact between ITO and copper phthalocyanine (CuPc) layers in multilayer excitonic organic EL and PV technologies [316]. Ferrocene terminated SAMs (Fc-SAMs) [326] are one of the most studied redox-active two dimensional aggregates on metal surfaces [630].

Over the past few years, functionalized siloxanes [509] or alkylsilanes [347, 512, 518] and amines [631] have also been used mainly for attaching organic molecules onto ITO.

μCP is a soft lithographic technique useful in patterning SAMs [632, 633]. Whitesides and coworkers [632] used low concentrations of thiols in ethanol as the ink to stamp patterns onto Au. Printed organosilane SAMs have been used as etch resists to pattern Si/SiO_2, Al/Al_2O_3, Ti/TiO_2, and ITO [498, 523, 527, 528], and alkanephosphonic acids have been used similarly to pattern Al/Al_2O_3 [471].

1.7.5.3.3 **ZnO** Zinc oxide is a wide bandgap semiconductor material with a large exciton binding energy [9, 264]. Its fundamental optical properties near the band edge have been extensively studied over the past few years [634, 635]. Recently, doped ZnO, especially Al-doped ZnO (ZnO:Al) films have been used as a transparent electrode in optoelectronic device applications [636, 637]. These films can be also used in other applications such as electrochemical cells [357], thin-film transistors [638], sensors [639], and photonic crystals [640]. However, potential applications in optoelectronic devices necessitate better understanding of the factors controlling the structural and electrical properties of ZnO thin films [641–643].

1.7.5.3.4 **TiO_2** To date, almost all applications of molecular excited states in sol-gel processed semiconductors such as TiO_2 have been for solar energy conversion. Wide bandgap TCO semiconductors, $E_g > 3$ eV, do not appreciably absorb visible light, and the incorporation of molecular chromophores allows efficient solar harvesting [253–255, 644,

645]. Most robust and efficient sensitizers are based on the metal-to-ligand charge transfer (MLCT) excited states of polypyridyl Ru compounds, which have been well reviewed [254, 255]. Dye-sensitized nanocrystalline electrochemical photovoltaic system has recently become a validated and credible competitor to solid-state junction devices for the conversion of solar energy into electricity [453–455]. More details of some applications can be found in the Sect. 1.7.3.5 and Vol. 6 [456].

1.7.5.3.5 **Other Oxides** In addition to large bandgap oxides such as ZrO_2 [646], the very large bandgap (~9 eV) gate oxides such as Al_2O_3 and SiO_2 and potential barriers for electrons of ~3 eV at Al/Al_2O_3 and Si/SiO_2 interfaces have been studied [647]. For example, metal Al is easily oxidized to form Al_2O_3 layer with ~20 Å or more thick under typical conditions [648]. One of the most challenging problems is that of controlling the oxide interfacial layers ranging from ~0.5 nm to several nanometers thick, which form during the deposition of the material on Si. Therefore, interfacing the oxide layers with Si is a major challenge [649]. A key requirement for the large bandgap gate oxide is that it acts as an insulator–it has a low leakage current. While the thicker layer prevents direct tunneling across the oxide, conduction can still occur by excitation of electrons and holes by Schottky emission into the oxide conduction or valence bands (Fig. 16).

The charge neutrality level (CNL) of Si is low in its gap, only 0.2 V above the valence band, but the CNL of most oxides can be high in their gaps [647]. Hence, the alignment of Si and the oxides tends to give small conduction-band offsets. Indeed, it gives zero offset for $SrTiO_3$. The band offsets for various oxides in contact with metal or silicon were found by calculating their Schottky barrier slopes S, and their CNLs [650]. The CNLs for the oxides are given in Table 8 and shown schematically in Fig. 17 together with the experimental values of their bandgaps and electron affinities. Kahn and coworkers [651] extended the concepts of CNL and induced density of interface states and proposed that the energy-level alignment is driven by the alignment of the CNLs.

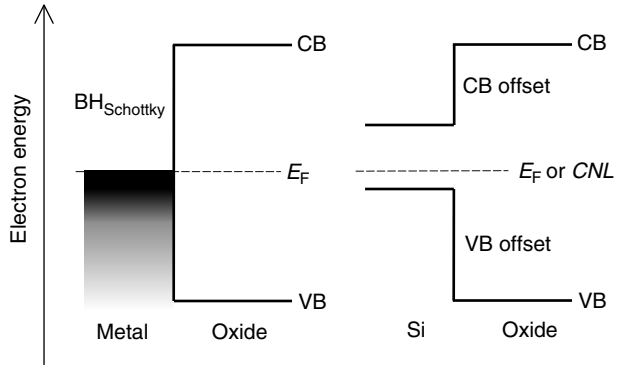


Fig. 16 Schematic illustration of band offsets at a semiconductor heterojunction and metal/semiconductor interface. $BH_{Schottky}$ is Schottky barrier height and CNL is the charge neutrality level of Si.

Tab. 8 Experimental bandgaps, dielectric constants ε_∞, and electron affinity (EA), and calculated CNLs and CB offsets on Si for each oxide [647, 650]

Oxide	*Gap (eV)*	ε_∞	*EA (eV)*	*CNL (eV)*	*CB offset (eV)*
Si	1.1	12	4.0	0.2	–
SiO_2	9	2.25	0.9	–	3.5 (exp.)
Al_2O_3	8.8	3.4	1.0[a]	5.5	2.8
ZrO_2	5.8	4.8	2.5[a]	3.6	1.4
Ta_2O_5	4.4	4.84	3.2	3.3	0.36
Si_3N_4	5.3	3.8	2.1	–	2.4 (exp.)
$SrTiO_3$	3.3	6.1	3.9	2.6	−0.1
TiO_2	3.05	7.8	3.9[a]	2.2	0

[a] Estimated values.

To ensure higher gate oxide capacitance, SiO_2 layer thickness has been decreased to less than 2 nm, and future generations a further reduction below 1.5 nm will be demanded. At that moment, SiO_2 can no longer be considered as an insulator because the direct tunneling current rises over $1\,A\,cm^{-2}$ [652]. Only a thicker insulator with a dielectric constant higher than that of SiO_2 could reduce the leakage current while still keeping the capacitance high. For several candidates, such as Al_2O_3, ZrO_2, and Ta_2O_5, operating devices have been fabricated. However, until now, no one has demonstrated that all of the extraordinary electrical properties of the Si/SiO_2 system can be reproduced.

High-quality gate insulator surfaces such as Al_2O_3 can be prepared by anodization (electrochemical oxidation) of the gate metals [542]. These surfaces possess surface hydroxyl groups, which

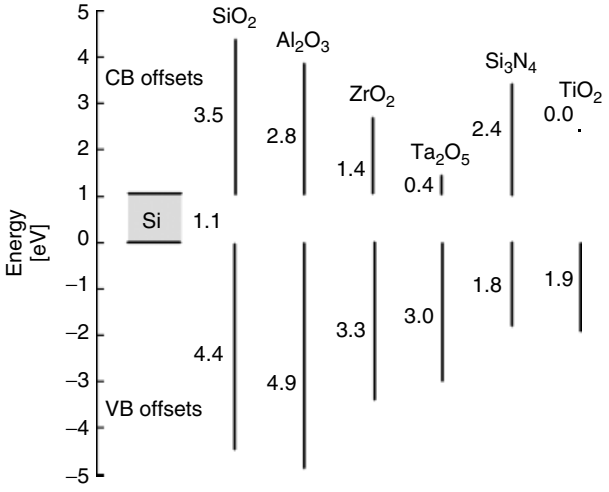


Fig. 17 Calculated conduction band (CB) and valence band (VB) offsets of various oxides in Si [647, 650].

are highly detrimental to carrier mobility. To improve the device performance of organic FETs, the oxide surfaces can be treated either by silanization [542, 543, 653], which change the surface wetting properties of the oxides [542]. However, the precise mechanism of the mobility enhancement due to surface modification is somewhat controversial.

Organosilane on SiO_2 have been of great utility in the photoresist industry, in which their patterning by energetic beams affords structures that can direct the substrates' topographical etching [577]. Recently, AFM induced formation of SiO_2 structures in the electrochemical nanocell was demonstrated [654, 655].

Regarding applications, long-chain phosphoric (and also phosphonic) acid esters are expected to have potential for applications in areas where the specific surface functionalization of oxides by extremely thin films is essential to the quality of a product [479]. One area where application of octadecylphosphate on tantalum oxide has already proven to be successful is optical biosensor technology, where the use of well-controlled octadecylphosphate SAMs on optical waveguide chips has been demonstrated to increase both the specificity and selectivity when sensing extremely low quantities of biomolecules using evanescent field and fluorescence techniques.

1.7.6 Summary

This chapter has highlighted various approaches in which organic monolayers play an important role in chemically modifying the properties of the surface of TCO electrodes. We have described the chemical modification of various *n*-type TCO electrode surfaces with various organic molecules in which one end is a binding group (X−), the other end is a terminal group with a different permanent dipole moment (−Y), and these two ends are linked by groups of alkyl chains and π-systems (see Fig. 2). We have also presented several examples of organic chemical treatments used for the surface modifications of various wide- and large-bandgap oxide electrodes. Studies for the formation of various organic monolayers with carboxylic acids and phosphonic acids as well as organosilane derivatives on these oxide electrodes were summarized comprehensively in this chapter. Further studies on the preparation and characterization of chemically modified electrodes will be expanding our understanding and advancement of the science and applications of inorganic and organic electronic materials and devices. The information in this chapter may help in choosing the most appropriate TCO electrode materials for a new use.

Acknowledgement

We would like to gratefully acknowledge and thank financial support of this work provided by the Grant-in-Aid for Creative Scientific Research on ''Devices on molecular and DNA levels'' (No. 13GS0017) from the Ministry of Education, Science, Sports, and Culture of Japan.

References

1. K. Bädeker, *Ann. D. Physik* **1907**, *22*, 749.
2. L. Holland, *Vacuum Deposition of Thin Films*, John Wiley & Sons, New York, 1958, pp. 464–509.
3. Z. M. Jarzebski, J. P. Marton, *J. Electrochem. Soc.* **1976**, *123*, 199C, 299C, 333C.
4. J. L. Vossen, *Phys. Thin Films* **1977**, *9*, 1.

5. G. Haacke, *Ann. Rev. Mater. Sci.* **1977**, *7*, 73.
6. J. C. Manifacier, *Thin Solid Films* **1982**, *90*, 297.
7. Z. M. Jarzebski, *Phys. Status Solidi A* **1982**, *71*, 13.
8. A. L. Dawar, J. C. Joshi, *J. Mater. Sci.* **1984**, *19*, 1.
9. K. L. Chopra, S. Major, D. K. Pandya, *Thin Solid Films* **1983**, *102*, 1.
10. I. Hamberg, C. G. Granqvist, *J. Appl. Phys.* **1986**, *60*, R123.
11. R. B. H. Tahar, T. Ban, Y. Ohya et al., *J. Appl. Phys.* **1998**, *83*, 2631.
12. P. S. Patil, *Mater. Chem. Phys.* **1999**, *59*, 185.
13. D. S. Ginley, C. Bright, *MRS Bull.* **2000**, *25*((8)), 15.
14. R. G. Gordon, *MRS Bull.* **2000**, *25*((8)), 52.
15. T. Minami, *MRS Bull.* **2000**, *25*((8)), 38.
16. K. Ellmer, *J. Phys. D: Appl. Phys.* **2001**, *34*, 3097.
17. T. Minami, S. Suzuki, T. Miyata, *Thin Solid Films* **2001**, *398–399*, 53.
18. G. Haacke, *Appl. Phys. Lett.* **1976**, *28*, 622.
19. H. Kawazoe, M. Yasukawa, H. Hyodo et al., *Nature (London)* **1997**, *389*, 939.
20. A. Kudo, H. Yanagi, H. Hosono et al., *Appl. Phys. Lett.* **1998**, *73*, 220.
21. H. Kawazoe, H. Yanagi, K. Ueda et al., *MRS Bull.* **2000**, *25*((8)), 28.
22. D. Ginley, B. Roy, A. Ode et al., *Thin Solid Films* **2003**, *445*, 193.
23. U. Diebold, *Surf. Sci. Rep.* **2003**, *48*, 53.
24. K. L. Chopra, *Thin Film Phenomena*, McGraw-Hill, New York, 1969.
25. Z. M. Jarzebski, *Oxide Semiconductors*, Pergamon Press, Oxford, 1973.
26. J. L. Vossen, W. Kern, *Thin Film Processes*, Academic Press, New York, 1978.
27. H. K. Pulker, *Coatings on Glass*, Thin Films Science and Technology, Elsevier, Amsterdam, 1984, Vol. 6.
28. C. E. Morosanu, *Thin Films by Chemical Vapour Deposition*, Thin Films Science and Technology, Elsevier, Amsterdam, 1990, Vol. 7.
29. H. L. Hartnagel, A. L. Dawar, A. K. Jain et al., *Semiconducting Transparent Thin Films*, Institute of Physics Publishing, Philadelphia, 1995.
30. Y. Pauleau, *Chemical Physics of Thin Film Deposition Processes for Micro- and Nano-Technologies*, NATO Science Series II: Mathematics, Physics and Chemistry, Kluwer Academic Publishers, Dordrecht, 2002, Vol. 55.
31. G. Bauer, *Ann. Phys. (Leipzig)* **1937**, *30*, 433.
32. C. H. Cartwright, A. F. Turner, *Phys. Rev.* **1939**, *55*, 1128.
33. H. A. McMaster, Br. Pat. No. 632,256 1942, U.S. Pat. No. 2,429,420 1947; *Chem. Abstr.* **1948**, *41*, 3925d.
34. K. Hammer, *Optik* **1948**, *3*, 495.
35. E. Mollwo, F. Stöckmann, *Ann. Phys.* **1948**, *3*((6)), 223; E. Mollwo, *Ann. Phys.* **1948**, *3*((6)), 230.
36. J. M. Mochel, U.S. Pat. No. 2,522,531 1950; *Chem. Abstr.* **1951**, *45*, 1318e.
37. M. J. Zunick, U.S. Pat. No. 2,516,663 1950; *Chem. Abstr.* **1950**, *44*, 11054e.
38. J. S. Preston, *Proc. R. Soc. Lond. A* **1950**, *202*, 449.
39. W. O. Lytle, A. E. Junge, U.S. Pat. No. 2,566,346 1951; *Chem. Abstr.* **1952**, *46*, 1373i.
40. J. K. Davis, U.S. Pat. No. 2,564,677; *Chem. Abstr.* **1951**, *46*, 228a; J. M. Mochel, U.S. Pat. No. 2,564,707 1951; *Chem. Abstr.* **1952**, *46*, 228b.
41. H. Fritzsche, *Z. Phys.* **1952**, *133*, 422.
42. L. Holland, G. Siddall, *Vacuum* **1953**, *3*, 375.
43. Y. T. Sihvonen, D. R. Boyd, *Rev. Sci. Instrum.* **1960**, *31*, 992.
44. G. A. Rozgonyi, W. J. Polito, *Appl. Phys. Lett.* **1966**, *8*, 220.
45. H. F. Dates, J. K. Davis, U.S. Pat. No. 3,331,702 1967; *Chem. Abstr.* **1967**, *67*, 93683w.
46. K. Wasa, S. Hayakawa, T. Hada, *Jpn. J. Appl. Phys.* **1971**, *10*, 1732.
47. A. J. Nozik, *Phys. Rev. B* **1972**, *6*, 453.
48. A. J. Nozik, H. Haacke, U.S. Pat. No. 3,957,029 1976.
49. J. Aranovich, A. Ortíz, R. H. Bube, *J. Vac. Sci. Technol.* **1979**, *16*, 994.
50. R. G. Gordon, U.S. Pat. No. 4,146,657 1979.
51. S. Major, A. Banerjee, K. L. Chopra, *Thin Solid Films* **1984**, *122*, 31.
52. T. Minami, H. Sato, H. Nanto et al., *Jpn. J. Appl. Phys.* **1985**, *24*, L781.
53. S. R. Kurtz, R. G. Gordon, *Thin Solid Films* **1986**, *140*, 277.
54. P. S. Vijayakumar, K. A. Blaker, R. D. Weiting et al., U. S. Patent No. 4,751,149 1988.
55. B. H. Choi, H. B. Im, J. S. Song et al., *Thin Solid Films* **1990**, *193*, 712.

56. J. Hu, R. G. Gordon, *Solar Cells* **1991**, *30*, 437.
57. J. Hu, R. G. Gordon, *J. Appl. Phys.* **1992**, *71*, 880.
58. J. Hu, R. G. Gordon, *J. Appl. Phys.* **1992**, *72*, 5381.
59. J. Hu, R. G. Gordon, *Mater. Res. Soc. Symp. Proc.* **1993**, *283*, 891.
60. H. Enoki, T. Nakayama, J. Echigoya, *Phys. Status Solidi A* **1992**, *129*, 181.
61. T. Minami, H. Sonohara, S. Takata et al., *Jpn. J. Appl. Phys.* **1994**, *33*, L1693.
62. J. M. McGraw, P. A. Parilla, D. L. Schulz et al., *Mater. Res. Soc. Symp. Proc.* **1995**, *388*, 51.
63. A. Suzuki, T. Matsushita, N. Wada et al., *Jpn. J. Appl. Phys.* **1996**, *35*, L56.
64. P. B. Adams, *J. Test. Eval.* **1977**, *5*, 53.
65. C. G. Patano, L. L. Hench, *J. Test. Eval.* **1977**, *5*, 66.
66. T. Putner, *Br. J. Appl. Phys.* **1959**, *10*, 332.
67. L. Holland, *Properties of Glass Surfaces*, Chapman and Hall, London, 1964, pp. 290–347.
68. P. F. Knewstubb, T. M. Sugden, *Nature (London)* **1958**, *181*, 474; **1958**, *181*, 1261.
69. J. Deckers, A. V. Tiggelen, *Nature (London)* **1958**, *181*, 1460; **1958**, *182*, 863.
70. R. R. Sowell, R. E. Cuthrell, D. M. Mattox et al., *J. Vac. Sci. Technol.* **1974**, *11*, 474.
71. J. R. Vig, J. W. LeBus, *IEEE Trans. PHP* **1976**, *12*, 365.
72. D. M. Mattox, *Thin Solid Films* **1978**, *53*, 81.
73. G. W. Longman, R. P. Palmer, *J. Colloid Interface Sci.* **1972**, *24*, 185.
74. J. C. Viguié, J. Spitz, *J. Electrochem. Soc.* **1975**, *122*, 585.
75. R. Gomer, *Rev. Sci. Instrum.* **1953**, *24*, 993.
76. W. O. Lytle, A. E. Junge, U.S. Pat. No. 2,651,585 1953; *Chem. Abstr.* **1954**, *48*, 976.
77. A. Fischer, *Z. Naturforsch. A* **1954**, *9*, 508.
78. K. Ishiguro, T. Sasaki, T. Arai et al., *J. Phys. Soc. Jpn.* **1958**, *13*, 296, 755.
79. V. K. Miloslavskii, *Opt. Spektrosk.* **1959**, *7*, 154.
80. A. Y. Kuznetsov, *Sov. Phys. Solid State* **1960**, *2*, 30.
81. H. Koch, *Phys. Status Solidi* **1963**, *3*, 1059; *3*, 1619.
82. H. Kim, H. A. Laitinen, *J. Am. Ceram. Soc.* **1975**, *58*, 23.
83. J. S. Maudes, T. Rodríquez, *Thin Solid Films* **1980**, *69*, 183.
84. M. Fujimoto, T. Urano, S. Murai et al., *Jpn. J. Appl. Phys.* **1989**, *28*, 2587.
85. E. Shanthi, A. Banerjee, V. Dutta et al., *Thin Solid Films* **1980**, *71*, 237.
86. R. E. Aitchison, *Aust. J. Appl. Sci.* **1954**, *5*, 10.
87. H. Kaneko, K. Miyake, *J. Appl. Phys.* **1982**, *53*, 3629.
88. E. Elangovan, K. Ramamurthi, *Cryst. Res. Technol.* **2003**, *38*, 779.
89. B. Thangaraju, *Thin Solid Films* **2002**, *402*, 71.
90. J. C. Manifacier, L. Szepessy, J. F. Bresse et al., *Mater. Res. Bull.* **1979**, *14*, 109.
91. P. Grosse, F. J. Schmitte, G. Frank et al., *Thin Solid Films* **1982**, *90*, 309.
92. G. C. Morris, A. E. McElnea, *Appl. Surf. Sci.* **1996**, *92*, 167.
93. A. Raza, O. P. Agnihotri, B. K. Gupta, *J. Phys. D: Appl. Phys.* **1977**, *10*, 1871.
94. R. Groth, *Phys. Status Solidi* **1966**, *14*, 69.
95. H. Köstlin, R. Jost, W. Lems, *Phys. Status Solidi A* **1975**, *29*, 87.
96. S. M. Rozati, T. Ganj, *Renewable Energy* **2004**, *29*, 1671.
97. S. M. Rozati, T. Ganj, *Renewable Energy* **2004**, *29*, 1665.
98. C. Eberspacher, A. L. Fahrenbruch, R. H. Bube, *Thin Solid Films* **1986**, *136*, 1.
99. M. Krunks, E. Mellikov, *Thin Solid Films* **1995**, *270*, 33.
100. C. H. Lee, L. Y. Lin, *Appl. Surf. Sci.* **1996**, *92*, 163.
101. P. M. R. Kumar, C. S. Kartha, K. P. Vijayakumar et al., *J. Appl. Phys.* **2005**, *97*, 013509.
102. A. F. Aktaruzzaman, G. L. Sharma, L. K. Malhotra, *Thin Solid Films* **1991**, *198*, 67.
103. M. Gabás, S. Gota, J. R. R. Barrado et al., *Appl. Phys. Lett.* **2005**, *86*, 042104.
104. H. M. Suárez, A. Maldonado, M. de la Olvera et al., *Appl. Surf. Sci.* **2002**, *193*, 52.
105. A. Ortíz, C. Falcony, J. Hernández et al., *Thin Solid Films* **1997**, *293*, 103.
106. C. Falcony, A. Ortíz, M. Garcia et al., *J. Appl. Phys.* **1988**, *63*, 2378.
107. H. A. Tanner, L. B. Lockhart, *J. Opt. Soc. Am.* **1946**, *36*, 701.
108. M. Banning, *J. Opt. Soc. Am.* **1947**, *37*, 688.
109. G. Hass, *Vacuum* **1952**, *2*, 331.
110. A. Aoki, G. Nogami, *J. Electrochem. Soc.* **1996**, *143*, L191.
111. N. Vlachopoulos, P. Liska, J. Augustynski et al., *J. Am. Chem. Soc.* **1988**, *110*, 1216.

112. L. Kavan, B. O'Regan, A. Kay et al., *J. Electroanal. Chem.* **1993**, *346*, 291.
113. L. Kavan, M. Grätzel, *Electrochim. Acta* **1993**, *40*, 643.
114. S. Zhang, Y. F. Zhu, D. E. Brodie, *Thin Solid Films* **1992**, *213*, 265.
115. R. F. Raymond, B. J. Dennison, U.S. Pat. No. 2,592,601 1952; *Chem. Abstr.* **1952**, *46*, 6804d.
116. O. P. Agnihotri, B. K. Gupta, A. K. Sharma, *J. Appl. Phys.* **1978**, *49*, 4540.
117. R. F. Bartholomew, H. M. Garfinkel, *J. Electrochem. Soc.* **1969**, *116*, 1205.
118. C. G. Fonstad, A. Linz, R. H. Rediker, *J. Electrochem. Soc.* **1969**, *116*, 1269.
119. J. Kane, H. P. Schweizer, W. Kern, *J. Electrochem. Soc.* **1975**, *122*, 1144.
120. T. Muranoi, M. Furukoshi, *Thin Solid Films* **1978**, *48*, 309.
121. S. K. Ghandhi, R. Siviy, J. M. Borrego, *Appl. Phys. Lett.* **1979**, *34*, 833.
122. R. J. Holdsworth, P. A. Martin, D. Raisbeck et al., *J. Phys. IV France* **1999**, *9*, Pr8–109.
123. J. Kane, H. P. Schweizer, W. Kern, *J. Electrochem. Soc.* **1976**, *123*, 270.
124. L. A. Ryabova, Y. S. Savitskaya, *Thin Solid Films* **1968**, *2*, 141.
125. J. Kane, H. P. Schweizer, W. Kern, *Thin Solid Films* **1975**, *29*, 155.
126. S. Seki, Y. Sawada, T. Nishide, *Thin Solid Films* **2001**, *388*, 22.
127. G. Galli, J. E. Coker, *Appl. Phys. Lett.* **1970**, *16*, 439.
128. S. K. Ghandhi, R. J. Field, J. R. Shealy, *Appl. Phys. Lett.* **1980**, *37*, 449.
129. A. P. Roth, D. F. Williams, *J. Appl. Phys.* **1981**, *52*, 6685.
130. A. Turković, M. Ivanda, A. Dranšner et al., *Thin Solid Films* **1991**, *198*, 199.
131. M. Thelakkat, C. Schmitz, H. W. Schmidt, *Adv. Mater.* **2002**, *14*, 577.
132. J. J. Ebelmen, *Ann. Chim. Phys., Ser. 3* **1846**, *57*, 319.
133. W. Geffcken, E. Berger, Ger. Pat. No. 736,411; U.S. Pat. No. 2,366,516 1939; *Chem. Abstr.* **1945**, *39*, 2231.
134. H. Schroeder, *Phys. Thin Films* **1969**, *5*, 87.
135. J. Livage, M. Henry, C. Sanchez, *Prog. Solid State Chem.* **1988**, *18*, 259.
136. L. L. Hench, J. K. West, *Chem. Rev.* **1990**, *90*, 33.
137. D. R. Uhlmann, T. Suratwala, K. Davidson et al., *J. Non-Cryst. Solids* **1997**, *218*, 113.
138. H. Dislich, E. Hussmann, *Thin Solid Films* **1981**, *77*, 129.
139. M. K. Nazeeruddin, P. Liska, J. Moser et al., *Helv. Chim. Acta.* **1990**, *73*, 1788.
140. S. M. Tracey, S. N. B. Hodgson, A. K. Ray, *J. Sol.-Gel Sci. Technol.* **1998**, *13*, 219.
141. A. C. Arango, L. R. Johnson, V. N. Bliznyuk et al., *Adv. Mater.* **2000**, *12*, 1689.
142. K. Miyairi, E. Itoh, Y. Hashimoto, *Thin Solid Films* **2003**, *438–439*, 147.
143. E. Itoh, Y. Ohmori, K. Miyairi, *Jpn. J. Appl. Phys.* **2004**, *43*, 817.
144. W. Chen, J. Zhang, Q. Fang et al., *Sens. Actuators B* **2004**, *100*, 195.
145. W. Feng, T. Umeda, A. Fujii et al., *Jpn. J. Appl. Phys.* **2004**, *43*, 3473.
146. T. Nishino, Y. Hamakawa, *Jpn. J. Appl. Phys.* **1970**, *9*, 1085.
147. G. Rupprecht, *Z. Phys.* **1954**, *139*, 504.
148. I. Niikura, H. Watanabe, M. Wada, *Jpn. J. Appl. Phys.* **1969**, *8*, 755.
149. H. Watanabe, *Jpn. J. Appl. Phys.* **1970**, *9*, 418.
150. A. P. Bradford, G. Hass, *J. Opt. Soc. Am.* **1953**, *43*, 326.
151. M. Ohnishi, M. Yoshizawa, S. Ibuki, *Jpn. J. Appl. Phys.* **1970**, *9*, 412.
152. W. Spence, *J. Appl. Phys.* **1967**, *38*, 3767.
153. S. Noguchi, H. Sakata, *J. Phys. D: Appl. Phys.* **1980**, *13*, 1129.
154. H. U. Habermeier, *Thin Solid Films* **1981**, *80*, 157.
155. H. K. Pulker, G. Paesold, E. Ritter, *Appl. Opt.* **1976**, *15*, 2986.
156. P. Nath, R. F. Bunshah, B. M. Basol et al., *Thin Solid Films* **1980**, *72*, 463.
157. H. S. Randhawa, M. D. Matthews, R. F. Bunshah, *Thin Solid Films* **1981**, *83*, 267.
158. T. Arai, *J. Phys. Soc. Jpn* **1960**, *15*, 916.
159. T. Nagatomo, O. Omoto, *Jpn. J. Appl. Phys.* **1977**, *16*, 2279.
160. C. A. Pan, T. P. Ma, *Appl. Phys. Lett.* **1980**, *37*, 163.
161. M. Mizuhashi, *Thin Solid Films* **1980**, *70*, 91.
162. A. Hjortsberg, I. Hamberg, C. G. Granqvist, *Thin Solid Films* **1982**, *90*, 323.
163. R. X. Wang, C. D. Beling, S. Fung et al., *J. Appl. Phys.* **2005**, *97*, 033504.
164. N. L. Kenigsberg, A. N. Chernets, *Sov. Phys. Solid State* **1963**, *10*, 2235.
165. T. Minami, S. Ida, T. Miyata et al., *Thin Solid Films* **2003**, *445*, 268.

166. H. Barrell, J. S. Preston, *Proc. Phys. Soc. London B* **1951**, *64*, 97.
167. T. Feng, A. K. Ghosh, C. Fishman, *J. Appl. Phys.* **1979**, *50*, 8070.
168. J. C. Manifacier, M. de Murcia, J. P. Fillard et al., *Thin Solid Films* **1977**, *41*, 127.
169. G. Helwig, *Z. Phys.* **1952**, *132*, 621.
170. J. Stuke, *Z. Phys.* **1954**, *137*, 401.
171. K. Tanaka, A. Kunioka, Y. Sakai, *Jpn. J. Appl. Phys.* **1969**, *8*, 681.
172. W. R. Sinclair, F. G. Peters, *J. Am. Ceram. Soc.* **1963**, *46*, 20.
173. E. Giani, R. Kelly, *J. Electrochem. Soc.* **1974**, *121*, 394.
174. E. Leja, J. Korecki, K. Krop et al., *Thin Solid Films* **1979**, *59*, 147.
175. W. R. Sinclair, F. G. Peters, D. W. Stillinger et al., *J. Electrochem. Soc.* **1965**, *112*, 1096.
176. H. W. Lehmann, R. Widmer, *Thin Solid Films* **1975**, *27*, 359.
177. R. L. Weiher, R. P. Ley, *J. Appl. Phys.* **1966**, *37*, 299.
178. H. K. Müller, *Phys. Status Solidi* **1968**, *27*, 723.
179. V. A. Williams, *J. Electrochem. Soc.* **1966**, *113*, 234.
180. W. W. Molzen, *J. Vac. Sci. Technol.* **1975**, *12*, 99.
181. F. H. Gillery, *J. Vac. Sci. Technol.* **1978**, *15*, 306.
182. A. J. Steckl, G. Mohammed, *J. Appl. Phys.* **1980**, *51*, 3890.
183. N. Miyata, K. Miyake, *Jpn. J. Appl. Phys.* **1978**, *17*, 1673.
184. L. Holland, G. Siddall, *Vacuum* **1953**, *3*, 245.
185. S. Yamanaka, T. Oohashi, *Jpn. J. Appl. Phys.* **1969**, *8*, 1058.
186. R. H. Deitch, E. J. West, T. G. Giallorenzi et al., *Appl. Opt.* **1974**, *13*, 712.
187. J. L. Vossen, E. S. Poliniak, *Thin Solid Films* **1972**, *13*, 281.
188. A. G. Sabnis, L. D. Feisel, *J. Vac. Sci. Technol.* **1977**, *14*, 685.
189. A. G. Sabnis, *J. Vac. Sci. Technol.* **1978**, *15*, 1565.
190. C. E. Wickersham, J. Greene, *Phys. Status Solidi A* **1978**, *47*, 329.
191. J. L. Vossen, *RCA Rev.* **1971**, *32*, 289.
192. D. B. Fraser, H. D. Cook, *J. Electrochem. Soc.* **1972**, *119*, 1368.
193. J. C. C. Fan, F. J. Bachner, *J. Electrochem. Soc.* **1975**, *122*, 1719.
194. Y. Ohhata, F. Shinoki, S. Yoshida, *Thin Solid Films* **1979**, *59*, 255.
195. M. Buchanan, J. B. Webb, D. F. Williams, *Appl. Phys. Lett.* **1980**, *37*, 213.
196. H. W. Lehmann, R. Widmer, *J. Appl. Phys.* **1973**, *44*, 3868.
197. J. B. Webb, D. F. Williams, M. Buchanan, *Appl. Phys. Lett.* **1981**, *39*, 640.
198. G. Gautherin, C. Weissmantel, *Thin Solid Films* **1978**, *50*, 135.
199. J. B. Dubow, D. E. Burk, J. R. Sites, *Appl. Phys. Lett.* **1974**, *29*, 494.
200. J. Shewchun, J. Dubow, C. W. Wilmsen et al., *J. Appl. Phys.* **1979**, *50*, 2832.
201. J. C. C. Fan, *Appl. Phys. Lett.* **1979**, *34*, 515.
202. D. E. Carlson, *J. Electrochem. Soc.* **1975**, *122*, 1334.
203. G. Blandenet, M. Court, Y. Lagarde, *Thin Solid Films* **1981**, *77*, 81.
204. I. Safi, *Surf. Coat. Technol.* **2000**, *127*, 203.
205. J. F. Smith, A. J. Aronson, D. Chen et al., *Thin Solid Films* **1980**, *72*, 469.
206. R. P. Howson, M. I. Ridge, *Thin Solid Films* **1981**, *77*, 119.
207. T. Minami, H. Nanto, S. Takata, *Appl. Phys. Lett.* **1982**, *41*, 958.
208. T. Minami, H. Nanto, S. Shooji et al., *Thin Solid Films* **1984**, *111*, 167.
209. T. Minami, H. Nanto, S. Takata, *Jpn. J. Appl. Phys.* **1984**, *23*, L280.
210. N. Mehan, V. Gupta, K. Sreenivas et al., *J. Appl. Phys.* **2004**, *96*, 3134.
211. H. T. Cao, Z. L. Pei, J. Gong et al., *Surf. Coat. Technol.* **2004**, *184*, 84.
212. T. Minami, H. Sato, H. Nanto et al., *Jpn. J. Appl. Phys.* **1986**, *25*, L776.
213. S. H. Jeong, S. B. Lee, J. H. Boo, *Curr. Appl. Phys.* **2004**, *4*, 655.
214. H. Q. Chiang, J. F. Wager, R. L. Hoffman et al., *Appl. Phys. Lett.* **2005**, *86*, 013503.
215. G. Kiriakidis, M. Bender, N. Katsarakis et al., *Phys. Status Solidi A* **2001**, *185*, 27.
216. B. H. Lee, I. G. Kim, S. W. Cho et al., *Thin Solid Films* **1997**, *302*, 25.
217. J. J. Ho, C. Y. Chen, *J. Electrochem. Soc.* **2005**, *152*, G57.
218. R. P. Howson, J. N. Avaritsiotis, M. I. Ridge et al., *Thin Solid Films* **1979**, *58*, 379.
219. Y. Murayama, *J. Vac. Sci. Technol.* **1975**, *12*, 818.
220. R. P. Howson, J. N. Avaritsiotis, M. I. Ridge et al., *Appl. Phys. Lett.* **1979**, *35*, 161.
221. J. E. Morris, M. I. Ridge, C. A. Bishop et al., *J. Appl. Phys.* **1980**, *51*, 1847.
222. S. Takaki, K. Matsumoto, K. Suzuki, *Appl. Surf. Sci.* **1988**, *33–34*, 919.

223. J. N. Avaritsiotis, R. P. Howson, *Thin Solid Films* **1981**, *77*, 351.
224. A. Suzuki, T. Matsushita, Y. Sakamoto et al., *Jpn. J. Appl. Phys.* **1996**, *35*, 5457.
225. M. Hiramatsu, K. Imaeda, N. Horio et al., *J. Vac. Sci. Technol. A* **1998**, *16*, 669.
226. R. P. Casero, A. G. Llorente, O. P. Y. Moll et al., *J. Appl. Phys.* **2005**, *97*, 054905.
227. D. A. Muller, N. Nakagawa, A. Ohtomo et al., *Nature (London)* **2004**, *430*, 657.
228. H. Kim, A. Piqué, J. S. Horwitz et al., *Appl. Phys. Lett.* **1999**, *74*, 3444.
229. R. L. Amans, U.S. Pat. No. 3,295,002 1966; *Chem. Abstr.* **1967**, *66*, 109516m.
230. M. S. Jaffe, E. G. Fridrich, U.S. Pat. No. 3,315,111 1967; *Chem. Abstr.* **1968**, *68*, 25102b.
231. D. Menzies, Q. Dai, Y. Bing et al., *J. Mater. Sci.* **2004**, *39*, 6361.
232. C. A. Vincent, D. G. C. Weston, *J. Electrochem. Soc.* **1972**, *119*, 518.
233. Y. Gao, Y. Masuda, K. Koumoto, *J. Korean Chem. Soc.* **2003**, *40*, 213.
234. Y. Matsumoto, *MRS Bull.* **2000**, *25*((9)), 47.
235. T. Kuwana, R. K. Darlington, D. W. Leedy, *Anal. Chem.* **1964**, *36*, 2023.
236. J. W. Strojek, T. Kuwana, *J. Electroanal. Chem.* **1968**, *16*, 471.
237. V. S. Srinivasan, T. Kuwana, *J. Phys. Chem.* **1968**, *72*, 1144.
238. T. Osa, T. Kuwana, *J. Electroanal. Chem.* **1969**, *22*, 389.
239. N. Winograd, T. Kuwana, *J. Electroanal. Chem.* **1969**, *23*, 333.
240. H. A. Laitinen, C. A. Vincent, T. M. Bednarski, *J. Electrochem. Soc.* **1968**, *115*, 1024.
241. D. Elliott, D. L. Zellmer, H. A. Laitinen, *J. Electrochem. Soc.* **1970**, *117*, 1343.
242. N. R. Armstrong, A. W. C. Lin, M. Fujihira et al., *Anal. Chem.* **1976**, *48*, 741.
243. M. Fujihira, T. Kuwana, *Electrochim. Acta* **1975**, *20*, 565.
244. T. Kuwana, N. Winograd, in *Electroanalytical Chemistry* (Ed.: A. J. Bard), Marcel Dekker, New York, 1974, pp. 1–78, Vol. 7.
245. W. R. Heineman, F. M. Hawkridge, H. N. Blount, in *Electroanalytical Chemistry* (Ed.: A. J. Bard), Marcel Dekker, New York, 1984, pp. 1–113, Vol. 13.
246. T. Kuwana, in *Electroanalytical Chemistry* (Ed.: A. J. Bard), Marcel Dekker, New York, 1966, pp. 197–240, Vol. 1.
247. H. Gerischer, *J. Electrochem. Soc.* **1966**, *113*, 1174.
248. H. Gerischer, *Photochem. Photobiol.* **1972**, *16*, 243.
249. H. Gerischer, *J. Electroanal. Chem.* **1975**, *58*, 263.
250. H. Gerischer, C. W. Tobias, *Advances in Electrochemistry and Electrochemical Engineering*, John Wiley & Sons, New York, 1978, Vol. 11.
251. A. Fujishima, K. Honda, *Nature (London)* **1972**, *238*, 37.
252. R. Memming, *Photochem. Photobiol.* **1972**, *16*, 325.
253. B. O'Regan, M. Grätzel, *Nature (London)* **1991**, *353*, 737.
254. A. Hagfeldt, M. Grätzel, *Chem. Rev.* **1995**, *95*, 49.
255. J. M. Stipkala, F. N. Castellano, T. A. Heimer et al., *Chem. Mater.* **1997**, *9*, 2341.
256. H. Tributsch, *Photochem. Photobiol.* **1972**, *16*, 261.
257. M. Calvin, *Science* **1974**, *184*, 375.
258. D. C. Cronemeyer, *Phys. Rev.* **1952**, *87*, 876.
259. M. Nagasawa, S. Shionoya, *J. Phys. Soc. Jpn* **1971**, *30*, 1118.
260. O. Lang, C. Pettenkofer, J. F. Sánchez-Royo et al., *J. Appl. Phys.* **1999**, *86*, 5687.
261. S. Burnside, J. E. Moser, K. Brooks et al., *J. Phys. Chem. B* **1999**, *103*, 9328.
262. R. W. Fessenden, P. V. Kamat, *J. Phys. Chem.* **1995**, *99*, 12902.
263. I. Hamberg, C. G. Granqvist, K. F. Berggren et al., *Phys. Rev. B* **1984**, *30*, 3240.
264. D. C. Look, *Mater. Sci. Eng. B* **2001**, *80*, 383.
265. T. Osa, M. Fujihira, *Nature (London)* **1976**, *264*, 349.
266. W. N. Hansen, D. M. Kolb, *J. Electroanal. Chem.* **1979**, *100*, 493.
267. A. Andersson, N. Johansson, P. Bröms et al., *Adv. Mater.* **1998**, *10*, 859.
268. A. Klein, *Appl. Phys. Lett.* **2000**, *77*, 2009.
269. K. Sugiyama, H. Ishii, Y. Ouchi et al., *J. Appl. Phys.* **2000**, *87*, 295.
270. J. A. Aranovich, D. Golmayo, A. L. Fahrenbruch et al., *J. Appl. Phys.* **1980**, *51*, 4260.
271. X. Jiang, F. L. Wong, M. K. Fung et al., *Appl. Phys. Lett.* **2003**, *83*, 1875.
272. A. J. Breeze, Z. Schlesinger, S. A. Carter, *Phys. Rev. B* **2001**, *64*, 125205.
273. M. N. Kamalasanan, N. D. Kumar, S. Chandra, *J. Appl. Phys.* **1993**, *74*, 679.
274. W. J. Lo, G. A. Somorjai, *Phys. Rev. B* **1978**, *17*, 4942.

275. H. Ishii, K. Sugiyama, F. Ito et al., *Adv. Mater.* **1999**, *11*, 605.
276. M. Fujihira, *Annu. Rev. Mater. Sci.* **1999**, *29*, 353.
277. M. Fujihira, C. Ganzorig, in *Conjugated Polymer and Molecular Interfaces* (Eds.: A. Kahn, J. J. Pireaux, W. R. Salaneck et al.), Marcel Dekker, New York, 2002, pp. 817–858.
278. J. S. Kim, F. Cacialli, R. H. Friend, *Thin Solid Films* **2003**, *445*, 358.
279. C. C. Wu, C. I. Wu, J. C. Sturm et al., *Appl. Phys. Lett.* **1997**, *70*, 1348.
280. Y. H. Liau, N. F. Scherer, K. Rhodes, *J. Phys. Chem. B* **2001**, *105*, 3282.
281. C. N. Li, A. B. Djurišić, C. Y. Kwong et al., *Appl. Phys. A* **2005**, *80*, 301.
282. F. Nüesch, E. W. Forsythe, Q. T. Le et al., *J. Appl. Phys.* **2000**, *87*, 7973.
283. R. W. Murray, in *Electroanalytical Chemistry* (Ed.: A. J. Bard), Marcel Dekker, New York, 1984, pp. 191–368, Vol. 13.
284. M. Fujihira, in *Topics in Organic Electrochemistry* (Eds.: A. J. Fry, W. E. Britton), Plenum, New York, 1986, pp. 255–294.
285. R. Murray, *Molecular Design of Electrode Surfaces*, Techniques of Chemistry, John Wiley & Sons, New York, 1992, pp. 1–48, Vol. 22.
286. A. Ulman, *An Introduction to Ultrathin Organic Films: From Langmuir-Blodgett to Self-Assembly*, Academic Press, Boston, 1991
287. A. Ulman, *Chem. Rev.* **1996**, *96*, 1533.
288. A. Ulman, *Organic Thin Films and Surfaces: Directions for the Nineties*, Thin Films, Academic Press, San Diego, 1995, Vol. 20.
289. A. Ulman, *Self-Assembled Monolayers of Thiols*, Thin Films, Academic Press, San Diego, 1998, Vol. 24.
290. P. R. Moses, L. Wier, R. W. Murray, *Anal. Chem.* **1975**, *47*, 1882.
291. M. Fujihira, N. Ohishi, T. Osa, *Nature (London)* **1977**, *268*, 226.
292. M. Fujihira, T. Kubota, T. Osa, *J. Electroanal. Chem.* **1981**, *119*, 379.
293. R. J. Nuzzo, D. L. Allara, *J. Am. Chem. Soc.* **1983**, *105*, 4481.
294. R. J. Nuzzo, F. A. Fusco, D. L. Allara, *J. Am. Chem. Soc.* **1987**, *109*, 2358.
295. P. E. Laibinis, J. J. Hickman, M. S. Wrighton et al., *Science* **1989**, *245*, 845.
296. D. L. Allara, R. G. Nuzzo, *Langmuir* **1985**, *1*, 45.
297. D. L. Allara, R. G. Nuzzo, *Langmuir* **1985**, *1*, 52.
298. T. J. Gardner, C. D. Frisbie, M. S. Wrighton, *J. Am. Chem. Soc.* **1995**, *117*, 6927.
299. R. Frantz, M. Granier, J. O. Durand et al., *Tetrahedron Lett.* **2002**, *43*, 9115.
300. I. Bedja, S. Hotchandani, P. V. Kamat, *J. Phys. Chem.* **1994**, *98*, 4133.
301. P. J. Giordano, C. R. Bock, M. S. Wrighton et al., *J. Am. Chem. Soc.* **1977**, *99*, 3187.
302. K. Tennakone, G. R. R. A. Kumara, I. R. M. Kottegoda et al., *Chem. Commun.* **1999**, 15.
303. T. J. Meyer, G. J. Meyer, B. W. Pfennig et al., *Inorg. Chem.* **1994**, *33*, 3952.
304. G. Will, G. Boschloo, S. N. Rao et al., *J. Phys. Chem. B* **1999**, *103*, 8067.
305. X. Marguerettaz, D. Fitzmaurice, *Langmuir* **1997**, *13*, 6769.
306. F. Nüesch, L. Si-Ahmed, B. Francois et al., *Adv. Mater.* **1997**, *9*, 222.
307. F. Nüesch, F. Rotzinger, L. Si-Ahmed et al., *Chem. Phys. Lett.* **1998**, *288*, 861.
308. L. Zuppiroli, L. Si-Ahmed, K. Kamaras et al., *Eur. Phys. J. B* **1999**, *11*, 505.
309. S. G. Conto, M. Carrard, L. Si-Ahmed et al., *Adv. Mater.* **1999**, *11*, 112.
310. S. F. J. Appleyard, M. R. Willis, *Opt. Mater.* **1998**, *9*, 120.
311. S. E. J. Appleyard, S. R. Day, R. D. Pickford et al., *J. Mater. Chem.* **2000**, *10*, 169.
312. C. Ganzorig, K. J. Kwak, K. Yagi et al., *Appl. Phys. Lett.* **2001**, *79*, 272.
313. Y. Enatsu, C. Ganzorig, M. Fujihira, *Mater. Res. Soc. Symp. Proc.* **2003**, *771*, 111.
314. C. Donley, D. Dunphy, D. Paine et al., *Langmuir* **2002**, *18*, 450.
315. G. Zotti, G. Schiavon, S. Zecchin et al., *Langmuir* **1998**, *14*, 1728.
316. N. R. Armstrong, C. Carter, C. Donley et al., *Thin Solid Films* **2003**, *445*, 342.
317. S. A. Trammell, J. C. Wimbish, F. Odobel et al., *J. Am. Chem. Soc.* **1998**, *120*, 13248.
318. C. Yan, M. Zharnikov, A. Gölzhäuser et al., *Langmuir* **2000**, *16*, 6208.
319. M. E. Napier, H. H. Thorp, *Langmuir* **1997**, *13*, 6342.
320. S. H. Brewer, D. A. Brown, S. Franzen, *Langmuir* **2002**, *18*, 6857.
321. N. D. Popovich, B. K. Yen, S. S. Wong, *Langmuir* **2003**, *19*, 1324.
322. T. L. Breen, P. M. Fryer, R. W. Nunes et al., *Langmuir* **2002**, *18*, 194.
323. M. Fujihira, T. Osa, *J. Am. Chem. Soc.* **1976**, *98*, 7850.

324. J. Morgado, A. Charas, N. Barbagallo, *Appl. Phys. Lett.* **2002**, *81*, 933; J. Morgado, N. Barbagallo, A. Charas et al., *J. Phys. D: Appl. Phys.* **2003**, *36*, 434.
325. S. Khodabakhsh, D. Poplavskyy, S. Heutz et al., *Adv. Funct. Mater.* **2004**, *14*, 1205.
326. C. E. D. Chidsey, C. R. Bertozzi, T. M. Putvinski et al., *J. Am. Chem. Soc.* **1990**, *112*, 4301; C. E. D. Chidsey, *Science* **1991**, *251*, 919.
327. H. C. Yang, K. Aoki, H. G. Hong et al., *J. Am. Chem. Soc.* **1993**, *115*, 11855.
328. H. E. Katz, *Chem. Mater.* **1994**, *6*, 2227.
329. F. Nüesch, Y. Li, L. J. Rothberg, *Appl. Phys. Lett.* **1999**, *75*, 1799.
330. M. G. Mason, L. S. Hung, C. W. Tang et al., *J. Appl. Phys.* **1999**, *86*, 1688.
331. C. Ganzorig, M. Fujihira, *Appl. Phys. Lett.* **2002**, *81*, 3137.
332. J. S. Kim, F. Cacialli, A. Cola et al., *Appl. Phys. Lett.* **1999**, *75*, 19.
333. D. J. Milliron, I. G. Hill, C. Shen et al., *J. Appl. Phys.* **2000**, *87*, 572.
334. V. Christou, M. Etchells, O. Renault et al., *J. Appl. Phys.* **2000**, *88*, 5180.
335. F. Nüesch, L. J. Rothberg, E. W. Forsythe et al., *Appl. Phys. Lett.* **1999**, *74*, 880.
336. A. L. Swint, P. W. Bohn, *Appl. Phys. Lett.* **2004**, *84*, 61.
337. A. L. Swint, P. W. Bohn, *Langmuir* **2004**, *20*, 4076.
338. W. Osikowicz, X. Crispin, C. Tengstedt et al., *Appl. Phys. Lett.* **2004**, *85*, 1616.
339. E. L. Bruner, N. Koch, A. R. Span et al., *J. Am. Chem. Soc.* **2002**, *124*, 3192.
340. J. Schwartz, E. L. Bruner, N. Koch et al., *Synth. Met.* **2003**, *138*, 223.
341. S. K. VanderKam, A. B. Bocarsly, J. Schwartz, *Chem. Mater.* **1998**, *10*, 685.
342. S. K. VanderKam, E. S. Gawalt, J. Schwartz et al., *Langmuir* **1999**, *15*, 6598.
343. J. Schwartz, E. S. Gawalt, G. Lu et al., *Polyhedron* **2000**, *19*, 505.
344. F. Ghebremichael, *Appl. Phys. Lett.* **2002**, *81*, 2971.
345. F. Zhang, A. Petr, L. Dunsch, *Appl. Phys. Lett.* **2003**, *82*, 4587.
346. A. C. Fou, O. Onitsuka, M. Ferreira et al., *J. Appl. Phys.* **1996**, *79*, 7501.
347. P. K. H. Ho, M. Granström, R. H. Friend et al., *Adv. Mater.* **1998**, *10*, 769.
348. P. K. H. Ho, J. S. Kim, J. H. Burroughes et al., *Nature (London)* **2000**, *404*, 481.
349. S. Kato, C. Pac, *J. Phys. Chem. B* **2004**, *108*, 19932.
350. F. Zhang, A. Petr, U. Kirbach et al., *J. Mater. Chem.* **2003**, *13*, 265.
351. S. A. Carter, M. Angelopoulos, S. Karg et al., *Appl. Phys. Lett.* **1997**, *70*, 2067.
352. M. Pfeiffer, A. Beyer, T. Fritz et al., *Appl. Phys. Lett.* **1998**, *73*, 3202.
353. C. Ganzorig, K. Suga, M. Fujihira, *Chem. Lett.* **2000**, *29*, 1032.
354. C. Ganzorig, M. Fujihira, *Appl. Phys. Lett.* **2000**, *77*, 4211.
355. L. S. Hung, L. R. Zheng, M. G. Mason, *Appl. Phys. Lett.* **2001**, *78*, 673.
356. M. K. Nazeeruddin, A. Kay, I. Rodicio et al., *J. Am. Chem. Soc.* **1993**, *115*, 6382.
357. P. Hoyer, H. Weller, *J. Phys. Chem.* **1995**, *99*, 14096.
358. G. Redmond, D. Fitzmaurice, M. Grätzel, *Chem. Mater.* **1994**, *6*, 686.
359. H. Rensmo, K. Keis, H. Lindström et al., *J. Phys. Chem. B* **1997**, *101*, 2598.
360. K. Westermark, H. Rensmo, H. Siegbahn et al., *J. Phys. Chem. B* **2002**, *106*, 10102.
361. K. Keis, C. Bauer, G. Boschloo et al., *J. Photochem. Photobiol., A* **2002**, *148*, 57.
362. K. Keis, E. Magnusson, H. Lindström et al., *Sol. Energy Mater. Sol. Cells* **2002**, *73*, 51.
363. S. Karuppuchamy, K. Nonomura, T. Yoshida et al., *Solid State Ionics* **2002**, *151*, 19.
364. T. Yoshida, K. Miyamoto, N. Hibi et al., *Chem. Lett.* **1998**, *27*, 599.
365. T. Yoshida, M. Tochimoto, D. Schlettwein et al., *Chem. Mater.* **1999**, *11*, 2657.
366. T. Yoshida, H. Minoura, *Adv. Mater.* **2000**, *12*, 1219.
367. S. Karuppuchamy, T. Yoshida, T. Sugiura et al., *Thin Solid Films* **2001**, *397*, 63.
368. T. Oekermann, S. Karuppuchamy, T. Yoshida et al., *J. Electrochem. Soc.* **2004**, *151*, C62.
369. B. O'Regan, D. T. Schwartz, S. M. Zakeeruddin et al., *Adv. Mater.* **2000**, *12*, 1263.
370. D. Bonifazi, A. Salomon, O. Enger et al., *Adv. Mater.* **2002**, *14*, 802.
371. A. Salomon, D. Berkovich, D. Cahen, *Appl. Phys. Lett.* **2003**, *82*, 1051.
372. R. Amadelli, R. Argazzi, C. A. Bignozzi et al., *J. Am. Chem. Soc.* **1990**, *112*, 7099.
373. J. Desilvestro, M. Grätzel, L. Kavan et al., *J. Am. Chem. Soc.* **1985**, *107*, 2988.
374. R. Dabestani, A. J. Bard, A. Campion et al., *J. Phys. Chem.* **1988**, *92*, 1872.

375. B. I. Lemon, J. T. Hupp, *J. Phys. Chem. B* **1999**, *103*, 3797.
376. S. Anderson, E. C. Constable, M. P. Dare-Edwards et al., *Nature (London)* **1979**, *280*, 571.
377. S. A. Trammell, J. A. Moss, J. C. Yang et al., *Inorg. Chem.* **1999**, *38*, 3665.
378. P. Qu, G. J. Meyer, *Langmuir* **2001**, *17*, 6720.
379. T. A. Heimer, S. T. D'Arcangelis, F. Farzad et al., *Inorg. Chem.* **1996**, *35*, 5319.
380. R. Argazzi, C. A. Bignozzi, T. A. Heimer et al., *Inorg. Chem.* **1994**, *33*, 5741.
381. T. Hannappel, B. Burnfeindt, B. Storck et al., *J. Phys. Chem. B* **1997**, *101*, 6799.
382. K. Murakoshi, G. Kano, Y. Wada et al., *J. Electroanal. Chem.* **1995**, *396*, 27.
383. A. Fillinger, B. A. Parkinson, *J. Electrochem. Soc.* **1999**, *146*, 4559.
384. G. Benkö, J. Kallioinen, J. E. I. K. Tommola et al., *J. Am. Chem. Soc.* **2001**, *124*, 489.
385. K. S. Finnie, J. R. Bartlett, J. L. Woolfrey, *Langmuir* **1998**, *14*, 2744.
386. M. K. Nazeeruddin, P. Péchy, M. Grätzel, *Chem. Commun.* **1997**, 1705.
387. M. K. Nazeeruddin, P. Péchy, T. Renouard et al., *J. Am. Chem. Soc.* **2001**, *123*, 1613.
388. S. M. Zakeeruddin, M. K. Nazeeruddin, P. Péchy et al., *Inorg. Chem.* **1997**, *36*, 5937.
389. P. Bonhôte, J. E. Moser, R. H. Baker et al., *J. Am. Chem. Soc.* **1999**, *121*, 1324.
390. B. Jing, H. Zhang, M. Zhang et al., *J. Mater. Chem.* **1998**, *8*, 2055.
391. J. Sotomayor, G. Will, D. Fitzmaurice, *J. Mater. Chem.* **2000**, *10*, 685.
392. S. G. Yan, J. T. Hupp, *J. Phys. Chem.* **1996**, *100*, 6867.
393. C. A. Bignozzi, R. Argazzi, C. J. Kleverlaan, *Chem. Soc. Rev.* **2000**, *29*, 87.
394. J. Moser, S. Punchihewa, P. P. Infelta et al., *Langmuir* **1991**, *7*, 3012.
395. X. Marguerettaz, D. Fitzmaurice, *J. Am. Chem. Soc.* **1994**, *116*, 5017.
396. G. E. Brown, V. E. Henrich, W. E. Casey et al. *Chem. Rev.* **1999**, *99*, 77.
397. F. Nüesch, J. Moser, V. Shklover et al., *J. Am. Chem. Soc.* **1996**, *118*, 5420.
398. B. M. Nakhle, S. A. Trammell, K. M. Sigel et al., *Tetrahedron* **1999**, *55*, 2835.
399. J. M. Vohs, M. A. Barteau, *Surf. Sci.* **1986**, *176*, 91.
400. J. M. Vohs, M. A. Barteau, *Surf. Sci.* **1988**, *201*, 481.
401. M. A. Barteau, *J. Vac. Sci. Technol., A* **1993**, *11*, 2162.
402. M. A. Barteau, *Chem. Rev.* **1996**, *96*, 1413.
403. K. S. Kim, M. A. Barteau, *Langmuir* **1990**, *6*, 1485.
404. K. S. Kim, M. A. Barteau, *J. Catal.* **1990**, *125*, 353.
405. H. Onishi, T. Aruga, C. Egawa et al., *Surf. Sci.* **1988**, *193*, 33.
406. H. Onishi, T. Aruga, Y. Iwasawa, *J. Am. Chem. Soc.* **1993**, *115*, 10460.
407. Q. Guo, I. Cocks, E. M. Williams, *J. Chem. Phys.* **1997**, *106*, 2924.
408. Q. Guo, E. M. Williams, *Surf. Sci.* **1999**, *433–435*, 322.
409. V. A. Gercher, D. F. Cox, *Surf. Sci.* **1994**, *312*, 106.
410. P. A. Dilara, J. M. Vohs, *J. Phys. Chem.* **1993**, *97*, 12919.
411. B. E. Hayden, A. King, M. A. Newton, *J. Phys. Chem. B* **1999**, *103*, 203.
412. A. G. Sosa, P. M. Escolano, H. Raza et al., *Surf. Sci.* **2001**, *471*, 163.
413. Z. Chang, G. Thornton, *Surf. Sci.* **2000**, *462*, 68.
414. S. Thevuthasan, G. S. Herman, Y. J. Kim et al., *Surf. Sci.* **1998**, *401*, 261.
415. P. Käckell, K. Terakura, *Appl. Surf. Sci.* **2000**, *166*, 370.
416. H. Onishi, K. Fukui, Y. Iwasawa, *Colloids. Surf. A* **1996**, *109*, 335.
417. K. Fukui, Y. Iwasawa, *Surf. Sci.* **2000**, *464*, L719.
418. A. Sasahara, H. Uetsuka, H. Onishi, *J. Phys. Chem. B* **2001**, *105*, 1.
419. M. A. Henderson, *J. Phys. Chem.* **1995**, *99*, 15253.
420. H. Onishi, Y. Yamaguchi, K. Fukui et al., *J. Phys. Chem.* **1996**, *100*, 9582.
421. K. Fukui, H. Onishi, Y. Iwasawa, *Phys. Rev. Lett.* **1997**, *79*, 4202.
422. D. J. Titheridge, M. A. Barteau, H. Idriss, *Langmuir* **2001**, *17*, 2120.
423. Q. Guo, I. Cocks, E. M. Williams, *Surf. Sci.* **1997**, *393*, 1.
424. L. Patthey, H. Rensmo, P. Persson et al., *J. Chem. Phys.* **1999**, *110*, 5913.
425. P. Persson, S. Lunell, A. Brühwiler et al., *J. Chem. Phys.* **2000**, *112*, 3945.
426. P. Persson, A. Stashans, R. Bergström et al., *Int. J. Quantum Chem.* **1998**, *70*, 1055.
427. A. Fahmi, C. Minot, P. Fourré et al., *Surf. Sci.* **1995**, *343*, 261.
428. E. Soria, E. Román, E. M. Williams et al., *Surf. Sci.* **1999**, *433–435*, 543.

429. J. N. Wilson, D. J. Titheridge, L. Kieu et al., *J. Vac. Sci. Technol., A* **2000**, *18*, 1887.
430. J. Krüger, U. Bach, M. Grätzel, *Adv. Mater.* **2000**, *12*, 447.
431. S. Pawsey, K. Yach, J. Halla et al., *Langmuir* **2000**, *16*, 3294.
432. S. Pawsey, K. Yach, L. Reven, *Langmuir* **2002**, *18*, 5205.
433. T. Cassagneau, J. H. Fendler, T. E. Mallouk, *Langmuir* **2000**, *16*, 241.
434. J. Randon, P. Blanc, R. Paterson, *J. Membr. Sci.* **1995**, *98*, 119.
435. J. P. Folkers, C. B. Gorman, P. E. Laibinis et al., *Langmuir* **1995**, *11*, 813.
436. W. Gao, L. Dickinson, C. Grozinger et al., *Langmuir* **1996**, *12*, 6429.
437. W. Gao, L. Dickinson, C. Grozinger et al., *Langmuir* **1997**, *13*, 115.
438. A. Badia, R. B. Lennox, L. Reven, *Acc. Chem. Res.* **2000**, *33*, 475.
439. R. Helmy, A. Y. Fadeev, *Langmuir* **2002**, *18*, 8924.
440. S. Marcinko, A. Y. Fadeev, *Langmuir* **2004**, *20*, 2270.
441. G. Hähner, R. Hofer, I. Klingenfuss, *Langmuir* **2001**, *17*, 7047.
442. R. Hofer, M. Textor, N. D. Spencer, *Langmuir* **2001**, *17*, 4014.
443. S. Tosatti, R. Michel, M. Textor et al., *Langmuir* **2002**, *18*, 3537.
444. M. Zwahlen, S. Tosatti, M. Textor et al., *Langmuir* **2002**, *18*, 3957.
445. M. Izaki, T. Omi, *Appl. Phys. Lett.* **1996**, *68*, 2439.
446. S. Peulon, D. Lincot, *J. Electrochem. Soc.* **1998**, *145*, 864.
447. U. Schubert, A. Lorenz, N. Kundo et al., *Chem. Ber./Recueil* **1997**, *130*, 1585.
448. H. Rensmo, K. Westermark, S. Södergren et al., *J. Chem. Phys.* **1999**, *111*, 2744.
449. H. Nakatsuji, M. Yoshimoto, Y. Umemura et al., *J. Phys. Chem.* **1996**, *100*, 694.
450. P. Persson, L. Ojamäe, *Chem. Phys. Lett.* **2000**, *321*, 302.
451. A. Vilan, A. Shanzer, D. Cahen, *Nature (London)* **2000**, *404*, 166.
452. Y. Selzer, D. Cahen, *Adv. Mater.* **2001**, *13*, 508.
453. A. Hagfeldt, M. Grätzel, *Acc. Chem. Res.* **2000**, *33*, 269.
454. M. Grätzel, *Nature (London)* **2001**, *414*, 338.
455. M. Grätzel, *J. Photochem. Photobiol. A* **2004**, *164*, 3.
456. M. K. Nazeeruddin, M. Grätzel, in *Encyclopedia of Electrochemistry* (Eds.: A. J. Bard, M. Stratmann, S. Licht), Wiley-VCH, Weinheim, 2002, pp. 407–431, Vol. 6.
457. J. Nelson, *Phys. Rev. B* **1999**, *59*, 15374.
458. B. Mahrov, G. Boschloo, A. Hagfeldt et al., *Appl. Phys. Lett.* **2004**, *84*, 5455.
459. P. Péchy, F. P. Rotzinger, M. K. Nazeeruddin et al., *J. Chem. Soc., Chem. Commun.* **1995**, 65.
460. H. Ogawa, T. Chihara, K. Taya, *J. Am. Chem. Soc.* **1985**, *107*, 1365.
461. C. C. Fulton, T. E. Cook Jr., G. Lucovsky et al., *J. Appl. Phys.* **2004**, *96*, 2665.
462. Y. T. Tao, *J. Am. Chem. Soc.* **1993**, *115*, 4350.
463. W. R. Thompson, J. E. Pemberton, *Langmuir* **1995**, *11*, 1720.
464. Y. T. Tao, M. T. Lee, S. C. Chang, *J. Am. Chem. Soc.* **1993**, *115*, 9547.
465. J. Wang, S. Yang, M. Chen et al., *Surf. Coat. Technol.* **2004**, *176*, 229.
466. K. M. Pertays, G. E. Thompson, M. R. Alexander, *Surf. Interface Anal.* **2004**, *36*, 1361.
467. A. H. M. Sondag, A. J. W. Tol, F. J. Touwslager, *Langmuir* **1992**, *8*, 1127.
468. Y. G. Aronoff, B. Chen, G. Lu et al., *J. Am. Chem. Soc.* **1997**, *119*, 259.
469. K. L. Purvis, G. Lu, J. Schwartz et al., *Langmuir* **1998**, *14*, 3720.
470. J. Schwartz, S. L. Bernasek, *Catal. Today* **2000**, *66*, 3.
471. L. B. Goetting, T. Deng, G. M. Whitesides, *Langmuir* **1999**, *15*, 1182.
472. Ch. Bram, Ch. Jung, M. Stratmann, *Fresenius' J. Anal. Chem.* **1997**, *328*, 108.
473. J. G. V. Alsten, *Langmuir* **1999**, *15*, 7605.
474. E. Barrena, J. O. Ossó, F. Schreiber et al., *J. Mater. Res.* **2004**, *19*, 2061.
475. N. E. Schlotter, M. D. Porter, T. B. Bright et al., *Chem. Phys. Lett.* **1986**, *132*, 93.
476. M. G. Samant, C. A. Brown, J. G. Gordon, *Langmuir* **1993**, *9*, 1082.
477. U. Harm, R. Bürgler, W. Fürbeth et al., *Macromol. Symp.* **2002**, *187*, 65.
478. D. Brovelli, G. Hähner, L. Ruiz et al., *Langmuir* **1999**, *15*, 4324.
479. M. Textor, L. Ruiz, R. Hofer et al., *Langmuir* **2000**, *16*, 3257.
480. R. Hofer, M. Textor, N. D. Spencer, *Langmuir* **2001**, *17*, 4123.
481. S. L. Ren, S. R. Yang, J. Q. Wang et al., *Chem. Mater.* **2004**, *16*, 428.

482. S. M. Kim, S. J. Ahn, H. Lee et al., *Ultramicroscopy* **2002**, *91*, 165.
483. H. Y. Nie, M. J. Walzak, N. S. McIntyre, *Langmuir* **2002**, *18*, 2955.
484. J. T. Woodward, A. Ulman, D. K. Schwartz, *Langmuir* **1996**, *12*, 3626.
485. J. T. Woodward, D. K. Schwartz, *J. Am. Chem. Soc.* **1996**, *118*, 7861.
486. J. T. Woodward, I. Doudevski, H. D. Sikes et al., *J. Phys. Chem. B* **1997**, *101*, 7535.
487. B. R. A. Neves, M. E. Salmon, E. B. Troughton et al., *Nanotechnology* **2001**, *12*, 285.
488. B. R. A. Neves, M. E. Salmon, P. E. Russell et al., *Langmuir* **2000**, *16*, 2409.
489. C. Messerschmidt, D. K. Schwartz, *Langmuir* **2001**, *17*, 462.
490. S. C. D'Andrea, A. Y. Fadeev, *Langmuir* **2003**, *19*, 7904.
491. E. Kálmán, *Electrochim. Acta* **2001**, *46*, 3607.
492. P. K. Ghosh, T. G. Spiro, *J. Am. Chem. Soc.* **1980**, *102*, 5543.
493. N. O. Savage, S. Roberson, G. Gillen et al., *Anal. Chem.* **2003**, *75*, 4360.
494. N. Shirahata, W. Shin, N. Murayama et al., *Adv. Funct. Mater.* **2004**, *14*, 580.
495. L. Gamble, M. B. Hugenschmidt, C. T. Campbell et al., *J. Am. Chem. Soc.* **1993**, *115*, 12096.
496. L. Gamble, L. S. Jung, C. T. Campbell, *Langmuir* **1995**, *11*, 4505.
497. L. Gamble, M. A. Henderson, C. T. Campbell, *J. Phys. Chem. B* **1998**, *102*, 4536.
498. P. M. St. John, H. G. Craighead, *Appl. Phys. Lett.* **1996**, *68*, 1022.
499. M. Bettoni, T. Del Giacco, C. Rol et al., *J. Photochem. Photobiol. A* **2004**, *163*, 481.
500. G. K. R. Senadeera, T. Kitamura, Y. Wada et al., *J. Photochem. Photobiol. A* **2004**, *164*, 61.
501. A. Y. Fadeev, R. Helmy, S. Marcinko, *Langmuir* **2002**, *18*, 7521.
502. J. M. Kim, J. W. Lee, J. K. Kim et al., *Appl. Phys. Lett.* **2004**, *85*, 6368.
503. R. Helmy, R. W. Wenslow, A. Y. Fadeev, *J. Am. Chem. Soc.* **2004**, *126*, 7595.
504. M. Li, J. Zhai, H. Liu et al., *J. Phys. Chem. B* **2003**, *107*, 9954.
505. A. Kornherr, S. A. French, A. A. Sokol et al., *Chem. Phys. Lett.* **2004**, *393*, 107.
506. K. Chen, W. B. Caldwell, C. A. Mirkin, *J. Am. Chem. Soc.* **1993**, *115*, 1193.
507. H. Yamada, H. Imahori, Y. Nishimura et al., *Chem. Commun.* **2000**, 1921.
508. H. Yamada, H. Imahori, Y. Nishimura et al., *Adv. Mater.* **2002**, *14*, 892.
509. J. E. Malinsky, J. G. C. Veinot, G. E. Jabbour et al., *Chem. Mater.* **2002**, *14*, 3054.
510. J. E. Malinsky, G. E. Jabbour, S. E. Shaheen et al., *Adv. Mater.* **1999**, *11*, 227.
511. M. E. van der Boom., A. G. Richter, J. E. Malinsky et al., *Chem. Mater.* **2001**, *13*, 15.
512. J. Gui, Q. Huang, J. G. C. Veinot et al., *Langmuir* **2002**, *18*, 9958.
513. J. Cui, Q. Huang, J. G. C. Veinot et al., *Adv. Mater.* **2002**, *14*, 565.
514. Q. Huang, J. Cui, J. G. C. Veinot et al., *Appl. Phys. Lett.* **2003**, *82*, 331.
515. H. Yan, J. Cui, Q. Huang et al., *Adv. Mater.* **2003**, *15*, 835.
516. Q. Huang, G. Evmenenko, P. Dutta et al., *J. Am. Chem. Soc.* **2003**, *125*, 14704.
517. J. Lee, B. J. Jung, J. I. Lee et al., *J. Mater. Chem.* **2002**, *12*, 3494.
518. P. Sigaud, J. N. Chazalviel, F. Ozanam, *J. Appl. Phys.* **2002**, *92*, 992.
519. P. Sigaud, J.-N. Chazalviel, F. Ozanam et al., *Appl. Surf. Sci.* **2003**, *218*, 54.
520. R. A. Hatton, S. R. Day, M. A. Chesters et al., *Thin Solid Films* **2001**, *394*, 292.
521. K. W. Wong, H. L. Yip, Y. Luo et al., *Appl. Phys. Lett.* **2002**, *80*, 2788.
522. H. Hillebrandt, M. Tanaka, *J. Phys. Chem. B* **2001**, *105*, 4270.
523. C. K. Luscombe, H. W. Li, W. T. S. Huck et al., *Langmuir* **2003**, *19*, 5273.
524. I. Markovich, D. Mandler, *Analyst* **2001**, *126*, 1850.
525. I. Markovich, D. Mandler, *J. Electroanal. Chem.* **2001**, *500*, 453.
526. S. Asakura, A. Hozumi, T. Yamaguchi et al., *Thin Solid Films* **2004**, *467*, 127.
527. K. R. Finnie, R. Haasch, R. G. Nuzzo, *Langmuir* **2000**, *16*, 6968.
528. Y. Koide, M. W. Such, R. Basu et al., *Langmuir* **2003**, *19*, 86.
529. Y. Koide, Q. Wang, J. Cui et al., *J. Am. Chem. Soc.* **2000**, *122*, 11266.
530. N. G. Cave, A. J. Kinloch, *Polymer* **1992**, *33*, 1162.
531. N. L. Jeon, R. G. Nuzzo, *Langmuir* **1995**, *11*, 3024.
532. M. J. Lercel, H. G. Craighead, A. N. Parikh et al., *J. Vac. Sci. Technol. A* **1996**, *14*, 1844.
533. J. Sagiv, *J. Am. Chem. Soc.* **1980**, *102*, 92.
534. T. Balgar, R. Bautista, N. Hartmann et al., *Surf. Sci.* **2003**, *532–535*, 963.

535. T. Balgar, S. Franzka, N. Hartmann et al., *Langmuir* **2004**, *20*, 3525.
536. M. Heule, U. P. Schönholzer, L. J. Gauckler, *J. European Ceram. Soc.* **2004**, *24*, 2733.
537. J. E. Headrick, C. L. Berrie, *Langmuir* **2004**, *20*, 4124.
538. S. E. Kooi, L. A. Baker, P. E. Sheehan et al., *Adv. Mater.* **2004**, *16*, 1013.
539. M. Heule, L. Meier, L. J. Gauckler, *Mat. Res. Soc. Symp. Proc.* **2001**, *657*, EE9.4.
540. R. Tero, M. Takizawa, Y. J. Li et al., *Langmuir* **2004**, *20*, 7526.
541. K. S. Lee, G. B. Blanchet, F. Gao et al., *Appl. Phys. Lett.* **2005**, *86*, 074102.
542. L. A. Majewski, R. Schroeder, M. Grell et al., *J. Appl. Phys.* **2004**, *96*, 5781.
543. D. Knipp, R. A. Street, A. Völkel et al., *J. Appl. Phys.* **2003**, *93*, 347.
544. P. M. St. John, H. G. Craighead, *J. Vac. Sci. Technol. B* **1996**, *14*, 69.
545. A. Hozumi, K. Ushiyama, H. Sugimura et al., *Langmuir* **1999**, *15*, 7600.
546. H. Sugimura, O. Takai, N. Nakagiri, *J. Vac. Sci. Technol. B* **1999**, *17*, 1605.
547. K. Hayashi, N. Saito, H. Sugimura et al., *Langmuir* **2002**, *18*, 7469.
548. H. Sugimura, A. Hozumi, T. Kameyama et al., *Surf. Interface Anal.* **2002**, *34*, 550.
549. A. Noy, C. D. Frisbie, L. F. Rozsnyai et al., *J. Am. Chem. Soc.* **1995**, *117*, 7943.
550. Y. Cui, Q. Wei, H. Park et al., *Science* **2001**, *293*, 1289.
551. H. L. Li, N. Perkas, Q. L. Li et al., *Langmuir* **2003**, *19*, 10409.
552. D. Beyer, W. Knoll, H. Ringsdorf et al., *Thin Solid Films* **1996**, *284–285*, 825.
553. R. Cohen, N. Zenou, D. Cahen et al., *Chem. Phys. Lett.* **1997**, *279*, 270.
554. N. Zenou, A. Zelichenok, S. Yizchaik et al., *ACS Symp. Series* **1998**, *695*, 57.
555. P. Allongue, C. Henry de Villeneuve, J. Pinson et al., *Electrochim. Acta* **1998**, *43*, 2791.
556. A. Y. Fadeev, T. J. McCarthy, *Langmuir* **2000**, *16*, 7268.
557. C. R. Kagan, T. L. Breen, L. L. Kosbar, *Appl. Phys. Lett.* **2001**, *79*, 3536.
558. S. Iarlori, D. Ceresoli, M. Bernasconi et al., *J. Phys. Chem. B* **2001**, *105*, 8007.
559. F. Da Cruz, K. Driaf, C. Berthier et al., *Thin Solid Films* **1999**, *349*, 155.
560. V. Huc, F. Armand, J. P. Bourgoin et al., *Langmuir* **2001**, *17*, 1928.
561. J. Collet, S. Lenfant, D. Vuillaume et al., *Appl. Phys. Lett.* **2000**, *76*, 1339.
562. J. H. Schön, Z. Bao, *Appl. Phys. Lett.* **2002**, *80*, 332.
563. M. Hu, S. Noda, T. Okubo et al., *Appl. Surf. Sci.* **2001**, *181*, 307.
564. E. Pavlovic, A. P. Quist, U. Gelius et al., *J. Colloid Interface Sci.* **2002**, *254*, 200.
565. Y. Selzer, A. Salomon, D. Cahen, *J. Phys. Chem. B* **2002**, *106*, 10432.
566. D. Liu, R. K. Perdue, L. Sun et al., *Langmuir* **2004**, *20*, 5905.
567. N. Saito, N. Maeda, H. Sugimura et al., *Langmuir* **2004**, *20*, 5182.
568. N. Saito, H. Haneda, T. Sekiguchi et al., *Adv. Mater.* **2002**, *14*, 418.
569. R. Turgeman, O. Gershevitz, O. Palchik et al., *Cryst. Growth Design* **2004**, *4*, 169.
570. S. Yoda, S. P. Han, H. Kudo et al., *Jpn. J. Appl. Phys.* **2004**, *43*, 6297.
571. T. Arai, D. Aoki, Y. Okabe et al., *Thin Solid Films* **1996**, *273*, 322.
572. K. P. Pernstich, S. Haas, D. Oberhoff et al., *J. Appl. Phys.* **2004**, *96*, 6431.
573. R. Labella, M. Braden, S. Deb, *Biomaterials* **1994**, *15*, 1197.
574. H. Tanaka, T. Watanabe, M. Chikazawa et al., *J. Colloid Interface Sci.* **1998**, *206*, 205.
575. C. Santos, Z. B. Luklinska, R. L. Clarke et al., *J. Mater. Sci. Mater. Med.* **2001**, *12*, 565.
576. E. Grushka, *Bonded Stationary Phases in Chromatography*, Ann Arbor Science Pub., Ann Arbor, Michigan, 1974
577. R. K. Smith, P. A. Lewis, P. S. Weiss, *Prog. Surf. Sci.* **2004**, *75*, 1.
578. V. Vogel, D. Möbius, *J. Colloid Interface Sci.* **1988**, *126*, 408.
579. M. Fujihira, H. Kawate, M. Yasutake, *Chem. Lett.* **1992**, *21*, 2223.
580. H. Kawate, Scanning Surface Potential Microscopy for Local Surface Analysis, M. Eng. Thesis, Tokyo Institute of Technology, Yokohama, 1993
581. M. Fujihira, H. Kawate, *Thin Solid Films* **1994**, *242*, 163.
582. R. M. Overney, E. Meyer, J. Frommer et al., *Nature (London)* **1992**, *359*, 133.
583. E. Meyer, R. Overney, R. Lüthi et al., *Thin Solid Films* **1992**, *220*, 132.
584. M. Fujihira, in *Photochemical and Photoelectrochemical Conversion and Storage of Solar Energy: Proceedings of the 9th International Conference on Photochemical Conversion and*

Storage of Solar Energy, IPS 9, August 23–28, 1992, Beijing China, (Eds.: L. W. Tian, Y. Lao) International Academic Publishers, Beijing, 1993, pp. 193–216.
585. I. H. Campbell, S. Rubin, T. A. Zawodzinski et al., *Phys. Rev. B* **1996**, *54*, 14321.
586. I. H. Campbell, T. W. Hagler, D. L. Smith et al., *Phys. Rev. Lett.* **1996**, *76*, 1900.
587. M. Bruening, E. Moons, D. Y. Marcovich et al., *J. Am. Chem. Soc.* **1994**, *116*, 2972.
588. E. I. Haskal, A. Curioni, P. F. Seidler et al., *Appl. Phys. Lett.* **1997**, *71*, 1151.
589. S. E. Shaheen, G. E. Jabbour, M. M. Morrell et al., *J. Appl. Phys.* **1998**, *84*, 2324.
590. C. Ganzorig, M. Fujihira, *Jpn. J. Appl. Phys.* **1999**, *38*, L1348.
591. C. Ganzorig, K. Suga, M. Fujihira, *Mater. Sci. Eng. B* **2001**, *85*, 140.
592. C. Ganzorig, M. Fujihira, *Appl. Phys. Lett.* **2004**, *85*, 4774.
593. M. Fujihira, *Adv. Chem. Ser.* **1994**, *240*, 373; M. Fujihira, in *Forces in Scanning Prbe Methods* (Eds.: H.-J. Güntherodt, D. Anselmetti, E. Meyer), Klumer Academic Publishers, Dordrecht, 1995, pp. 567–591.
594. M. Carrara, F. Nüesch, L. Zuppiroli, *Synth. Met.* **2001**, *121*, 1633.
595. P. W. Atkins, *Physical Chemistry*, 5th ed., Oxford University Press, Oxford, 1995.
596. M. Fujihira, H. Inokuchi, *Chem. Phys. Lett.* **1972**, *17*, 554.
597. M. Fujihira, T. Hirooka, H. Inokuchi, *Chem. Phys. Lett.* **1973**, *19*, 584.
598. X. Crispin, V. Geskin, A. Crispin et al., *J. Am. Chem. Soc.* **2002**, *124*, 8131.
599. R. W. Zehner, B. F. Parsons, R. P. Hsung et al., *Langmuir* **1999**, *15*, 1121.
600. G. Ashkenasy, D. Cahen, R. Cohen et al., *Acc. Chem. Res.* **2002**, *35*, 121.
601. D. Cahen, A. Kahn, *Adv. Mater.* **2003**, *15*, 271.
602. C. W. Tang, S. A. VanSlyke, *Appl. Phys. Lett.* **1987**, *51*, 913.
603. M. G. Mason, C. W. Tang, L. S. Hung et al., *J. Appl. Phys.* **2001**, *89*, 2756.
604. R. H. Friend, R. W. Gymer, A. B. Holmes et al., *Nature (London)* **1999**, *397*, 121.
605. J. Jortner, M. Ratner, *Molecular Electronics*, Blackwell Science, Oxford, 1997.
606. D. Cahen, G. Hodes, *Adv. Mater.* **2002**, *14*, 789.
607. M. Batzill, K. Katsiev, U. Diebold, *Appl. Phys. Lett.* **2004**, *85*, 5766.
608. F. Pichot, B. A. Gregg, *J. Phys. Chem. B* **2000**, *104*, 6.
609. D. Cahen, G. Hodes, M. Grätzel et al., *J. Phys. Chem. B* **2000**, *104*, 2053.
610. S. Rüle, D. Cahen, *J. Appl. Phys.* **2004**, *96*, 1556.
611. S. Seker, K. Meeker, T. F. Kuech et al., *Chem. Rev.* **2000**, *100*, 2505.
612. Y. Park, V. Choong, Y. Gao et al., *Appl. Phys. Lett.* **1996**, *68*, 2699.
613. J. S. Kim, M. Granström, R. H. Friend et al., *J. Appl. Phys.* **1998**, *84*, 6859.
614. A. L. McClellan, *Tables of Experimental Dipole Moments*, W. H. Freeman and Company, San Francisco, 1963.
615. T. B. McMahon, P. Kebarle, *J. Am. Chem. Soc.* **1977**, *99*, 2222.
616. C. Hansch, A. Leo, R. W. Taft, *Chem. Rev.* **1991**, *91*, 165.
617. R. C. Weast, *Handbook of Chemistry and Physics*, 69th Ed., CRC Press, Inc., Boca Raton, Fluorida, 1988, p. E–58.
618. M. Fujihira, C. Ganzorig, *Mater. Sci. Eng. B* **2001**, *85*, 203.
619. A. C. Arias, L. S. Roman, T. Kugler et al., *Thin Solid Films* **2000**, *371*, 201.
620. W. Xie, L. Zhang, S. Liu, *Semicond. Sci. Technol.* **2004**, *19*, 380.
621. S. K. Das, *Thin Solid Films* **1993**, *226*, 259.
622. M. Turrión, J. Bisquert, P. Salvador, *J. Phys. Chem. B* **2003**, *107*, 9397.
623. J. Bandara, C. M. Divarathne, S. D. Nanayakkara, *Sol. Energy Mater. Soc. Cells* **2004**, *81*, 429.
624. L. M. Peter, N. W. Duffy, R. L. Wang et al., *J. Electroanal. Chem.* **2002**, *524–525*, 127.
625. T. Miyasaka, T. Watanabe, A. Fujishima et al., *J. Am. Chem. Soc.* **1978**, *100*, 6657.
626. P. V. Kamat, M. A. Fox, A. J. Fatiadi, *J. Am. Chem. Soc.* **1984**, *106*, 1191.
627. I. R. Harrison, T. I. Quickenden, *J. Phys. Chem.* **1987**, *91*, 1481.
628. A. Frippiat, A. K. de Mesmaeker, *J. Phys. Chem.* **1985**, *89*, 1285.
629. M. Krishnan, X. Zhang, A. J. Bard, *J. Am. Chem. Soc.* **1984**, *106*, 7371.
630. G. Valincius, G. Niaura, B. Kazakevičienė et al., *Langmuir* **2004**, *20*, 6631.
631. S. Y. Oh, Y. J. Yun, D. Y. Kim et al., *Langmuir* **1999**, *15*, 4690.
632. A. Kumar, G. M. Whitesides, *Appl. Phys. Lett.* **1993**, *63*, 2002.
633. B. Michel, A. Bernard, A. Bietsch et al., *IBM J. Res. & Dev.* **2001**, *45*, 697.

634. K. Hazu, T. Sota, S. Adachi et al., *J. Appl. Phys.* **2004**, *96*, 1270.
635. T. B. Hur, Y. H. Hwang, H. K. Kim, *J. Appl. Phys.* **2004**, *96*, 1507.
636. J. H. Schön, Ch. Kloc, B. Batlogg, *Synth. Met.* **2001**, *124*, 95.
637. A. Gupta, A. D. Compaan, *Appl. Phys. Lett.* **2004**, *85*, 684.
638. E. M. C. Fortunato, P. M. C. Barquinha, A. C. M. B. G. Pimentel et al., *Appl. Phys. Lett.* **2004**, *85*, 2541.
639. R. Martins, E. Fortunato, P. Nunes et al., *J. Appl. Phys.* **2004**, *96*, 1398.
640. D. Li, Y. H. Leung, A. B. Djurišić et al., *Appl. Phys. Lett.* **2004**, *85*, 1601.
641. F. Bertram, D. Forster, J. Christen et al., *Appl. Phys. Lett.* **2004**, *85*, 1976.
642. R. Ghosh, D. Basak, S. Fujihara, *J. Appl. Phys.* **2004**, *96*, 2689.
643. Y. W. Heo, L. C. Tien, D. P. Norton et al., *Appl. Phys. Lett.* **2004**, *85*, 2002.
644. M. Alebbi, C. A. Bignozzi, T. A. Heimer et al., *J. Phys. Chem. B* **1998**, *102*, 7577.
645. J. Miller, *Chemically Modified Surfaces in Catalysis and Electrocatalysis*, ACS Symposium Series 192, ACS, Washington, 1982
646. J. W. Schultze, M. M. Lohrengel, *Electrochim. Acta* **2000**, *45*, 2499.
647. J. Robertson, *MRS Bull.* **2002**, *27*((3)), 217.
648. D. A. Muller, G. D. Wilk, *Appl. Phys. Lett.* **2001**, *79*, 4195.
649. C. J. Först, C. R. Ashman, K. Schwarz et al., *Nature (London)* **2003**, *427*, 53.
650. J. Robertson, *J. Vac. Sci. Technol. B* **2000**, *18*, 1785.
651. H. Vázquez, W. Gao, F. Flores et al., *Phys. Rev. B* **2005**, *71*, 041306(R).
652. R. Degraeve, E. Cartier, T. Kauerauf et al., *MRS Bull.* **2002**, *27*((3)), 222.
653. H. Sirringhaus, N. Tessler, R. H. Friend, *Science* **1998**, *280*, 1741.
654. M. Yasutake, Y. Ejiri, T. Hattori, *Jpn. J. Appl. Phys.* **1993**, *32*, L1021.
655. H. Bloeβ, G. Staikov, J. W. Schulze, *Electrochim. Acta* **2001**, *47*, 335.

1.8 Surface Modification of Chalcogenide Electrodes

Chimed Ganzorig and Masamichi Fujihira
Tokyo Institute of Technology, Yokohama, Japan

1.8.1 Introduction

Metal chalcogenides of general formula, MX (M = Cd, Zn, etc.; X = S, Se, or Te) are important in a variety of applications ranging from solar cells to chemical/biological sensors. While thin films of these materials can be prepared by many methods (e.g. vacuum evaporation, chemical bath deposition), electrodeposition is an attractive alternative because of its simplicity, low cost, ambient temperature operation (and consequently the absence of interlayer diffusion), and its amenability to large and irregular area coatings [1].

Semiconductor nanocrystals exhibit a wide range of size-dependent properties. Variations in fundamental characteristics ranging from phase transitions to electrical conductivity can be induced by controlling the size of the crystals. Present status and new opportunities for research in this area of materials physical chemistry were reviewed in detail in Ref. 2. These nanocrystals are good candidates for electronic and optical devices [2, 3] due to their reduced dimensions, enabling one to reduce the size of electronic circuitry. Because of the increased oscillator strengths in these nanocrystals as a result of quantum confinement [4], these are expected to have higher quantum efficiencies in applications such as light emission.

Bawendi and coworkers [5] have reported a synthesis of highly luminescent (CdSe)ZnS composite quantum dots (QDs) with CdSe cores ranging in diameter from 2.3 to 5.5 nm. They have characterized these materials using a range of optical and structural techniques. The band gap of CdSe can be varied from 1.9 to 2.7 eV by changing the size of the particle from 5.5 to 2.3 nm [5]. Along with the band gap of the particle, the photoluminescence (PL) from these composite dots can also be varied through the red to blue region of the visible region [5].

Bawendi and coworkers [6] have also studied the band edge luminescence of surface-modified CdSe nanocrystallites with a variety of organic and inorganic ligands. There has been much speculation as to origin of the band edge emission in these quantum-confined structures [6]. Because of their large surface-to-volume ratios it has been suggested that the emission originates from surface-related states. They found good agreement between experiment and theory for surface-modified CdSe nanocrystallites. This agreement suggests that the band edge luminescence of CdSe QDs can be quantitatively understood using an intrinsic exciton model and that the role of the surface in the optical properties of the QDs lies in its defects which create deep red radiative and nonradiative pathways for recombination of the electron and hole upon photoexcitation of the nanocrystallite [6].

The band gaps and band edge positions for cadmium chalcogenides and other several semiconductors in the bulk state [7, 8] are shown in Fig. 1. For zinc chalcogenides, ZnSe (bulk band gap 2.7 eV) and ZnS (bulk band gap 3.6 eV) are wide band gap semiconductors [9]. Because of quantum confinement, their nanocrystals are interesting emitting materials in the blue to the ultraviolet range.

Encyclopedia of Electrochemistry. Edited by A.J. Bard and M. Stratmann
Vol. 10 *Modified Electrodes*. Edited by M.Fujihira, I.Rubinstein, and J.F.Rusling
Copyright © 2007 Wiley-VCH Verlag GmbH & Co. KGaA, Weinheim. ISBN: 978-3-527-30402-8

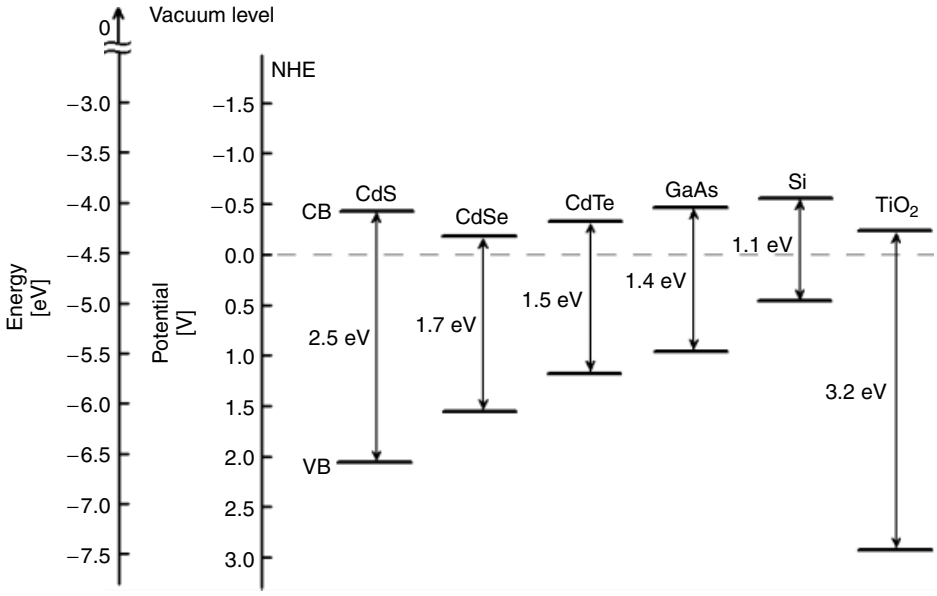


Fig. 1 Band gap and band edge position of cadmium chalcogenides and other several semiconductors in contact with an aqueous electrolyte at pH 1 [7, 8].

One of the principal methods for assessing adsorbate interactions with II–VI semiconductor surfaces has been to monitor steady-state PL intensities at low injection levels [10]. Under low injection conditions, recombination is considered a fast event and the rate-limiting step is the generation/transport of minority carriers that must move the surface. Under such conditions, a relatively small number of excess minority charge carriers are generated as compared to the majority carriers [11]. Under high injection conditions, recombination at the surface becomes the slow event, since there are more minority carriers generated and transported to the surface than can be easily recombined. This distinction between high and low injection levels is essentially qualitative, with high injection corresponding to situations where the concentration of injected excess carriers is larger or comparable to the concentration of donors or acceptors [10]. Many of these studies have been conducted with single-crystal samples of CdS and CdSe. The PL response to a broad range of analytes has been found to define a ''luminescent litmus test'': Lewis bases and acids cause PL enhancements and quenching, respectively, relative to reference ambient of either nitrogen or vacuum for gas-phase studies or pure solvent for solution studies [10]. In addition to steady-state PL measurements, there have been several time-resolved PL studies reported, generally for CdS and CdSe exposed to aqueous chalcogenide solutions used to stabilize these materials as photoelectrodes [10].

Recent density-functional-based studies on the structural, electronic, and optical properties of CdS, CdSe, and CdS/CdSe semiconductor nanoparticles over a wide range, from clusters containing just a few atoms to nanoparticles with up to about

1000 atoms were recently reviewed [12]. In particular, the effects of organization, embedding, and surfactants on the properties of these particles were discussed and illustrated by their own results and literature examples. The surface stabilization by ligands, core/shell embedding, or superstructure organization combined with electronic structure stabilization of these nanoparticles directly influences their properties: for stabilized nanoparticles a size-dependent decay of the lowest optical excitation energy toward the value of the bulk is found, as experimentally [12].

1.8.1.1 Surface Treatment of Substrate Chalcogenide Electrodes

Treatment of surfaces of II–VI (CdS, CdSe, and CdTe) and III–V (GaAs) semiconductors with alcoholic solutions of bromine is a common method for preparing fresh surfaces as described in more detail in Ref. 10. With the development of alternate etchants better suited for GaAs [13], the use of bromine treatments is generally found with II–VI semiconductor materials [10]. The bromine-induced etching behaviors of polycrystalline CdTe and single-crystal GaAs have been compared in a novel study by McGhee and coworkers [14], using radiolabeled bromine vapor, $^{82}BrBr$, to track the progress of the etching reactions.

1.8.1.2 Adsorption of Acids to Chalcogenides

A considerable number of adsorption studies have been conducted with carbonyl, phosphine oxide, and sulfide adsorbates on CdS and CdSe substrates [10]. For example, Cahen and Shanzer and their coworkers [15, 16] used families of benzoic acids and hydroxamic acids to demonstrate that the electron affinity of CdSe and CdTe substrates can be controlled independently of band bending. They observed that benzoic acids bind preferentially to Cd sites on CdTe, probably in a bridging binding mode, hydroxamic acids also bind to Cd, although their ligating mode was difficult to determine. Adsorption leads to changes in the work function of these materials that have been correlated to adsorbate dipole moments and to Hammett parameters.

As part of their studies, Bruening and coworkers [15] examined the effects of common etching procedures on the work function of CdSe. They observed that the bromine/methanol etch increases the work function while a subsequent hydrazine treatment then reduces it. Because the bromine/methanol etch leaves an elemental Se residue on the surface, the authors suggest that the higher work function of Se relative to CdSe may account for the increase in work function. They noted that such etching effects lead to irreproducible surfaces and can produce substantial variations in adsorption properties [15].

1.8.1.3 Adsorption of Organic Sulfur Compounds

In addition to the adsorption studies of carbonyl, phosphine oxide, and sulfide adsorbates noted in Ref. 10, the studies of interaction of anionic S donors such as dithiocarbamates [17], anionic S-containing species (MoS^{2-} and Et_2NCS^-) [18], thiolates [19], and polysulfides [20] with cadmium chalcogenides have been characterized by Wrighton and coworkers [17–20]. This chapter will focus on surface modification of cadmium chalcogenides with thiols, dithiols, sulfides, and disulfides.

1.8.2 Surface Modification

1.8.2.1 Dialkyl Chalcogenide Compounds

Adsorption of dialkyl chalcogenide compounds, which are candidate chemical vapor deposition precursor molecules, has been examined on CdSe substrates by Ellis and coworkers [21]. The compounds studied in these experiments include two families of dialkyl chalcogenides: $(CH_3)_2E$ (E = S, Se, Te) and R_2S (R = CH_3, C_2H_5, n-C_3H_7, i-C_3H_7, and t-C_4H_9. The electronic interaction between the adsorbate and the semiconductor surface has been modeled by assuming that a region near the surface whose thickness is on the order of the depletion width is nonemissive: electron-hole pairs photogenerated in this so-called dead layer are swept apart by the electric field [22–24]. The alkyl chalcogenides are expected to have Lewis basic character. By donating electron density to the solid, they can reduce the thickness of the dead layer and enhance the PL intensity, as observed in Ref. 21.

The dead-layer model was used to estimate adduct-induced reductions in depletion width thickness at saturation; values ranged from ~100 to 500 Å [21]. Reversible PL enhancements are seen, fitting the dead-layer model [22–24], with the magnitude increasing for R_2S in the order $CH_3 < C_2H_5 < n$-$C_3H_7 < i$-$C_3H_7 < t$-C_4H_9. Both electronic effects, correlated with ionization potentials, and steric effects appear to influence the PL response. Dimethyl selenide and dimethyl telluride gave responses similar to that of dimethyl sulfide [21].

It is worth mentioning that there is a substantial literature regarding the effects of sulfur-containing, redox-active molecules on II–VI semiconductor electrodes. These semiconductors have been used extensively in photoelectrochemical cells. Inorganic and organic sulfur-containing species have been observed to stabilize both polycrystalline and single-crystal CdS and CdSe electrodes [25].

1.8.2.2 Thiols

Tacconi and coworkers [1] have described two-step electrosynthesis approach for the preparation of CdS semiconductor layers on polycrystalline Au substrates. The sulfide ion precursor required for in situ CdS precipitation can be electrogenerated (via cathodic stripping) either from a preformed sulfur layer or a thiol-based self-assembled monolayer (SAM) on the Au surface [1]. The morphology of CdS formed in the two cases and the corresponding photoelectrochemical behavior were compared and contrasted. Clearly, further improvements are needed to make these films suitable for practical solar energy conversion applications [1].

The sulfide ion precursor for metal sulfide can also be generated from a thiol-based SAM. Indeed, chemical reaction of Cd^{2+} ions with Na_2S was used to precipitate ultrasmall CdS particles in different thiol-containing aqueous media [26–29]. Size of ultrasmall CdS particles was controlled by adding four kinds of thiols (mercaptoethylamine, mercaptopropionic acid, mercaptoethanol, and cysteine) to Cd^{2+} aqueous solution before mixing with Na_2S aqueous solution [26, 27]. The adsorption of thiols on the CdS surface was verified as the effect of surface charges by measuring the yield of photoinduced electron transfer from CdS to positively charged molecules in solution [27].

The chemical and physical properties of thiol-stabilized II–VI semiconductor nanocrystals were reviewed by Eychmüller and Rogach [30]. The materials prepared

include cadmium and mercury chalcogenides with sizes ranging between 1.4 and ~8 nm. In this size range, the optical properties of the particles are governed by the size-quantization effect. All nanocrystals synthesized belong to the cubic crystal structure. The general synthetic process follows a similar route for all nanocrystals: a metal salt is dissolved in water in the presence of the stabilizing thiol. The thiols used were 1-thioglycerol, 2-mercaptoethanol, 1-mercapto-2-propanol, 1,2-dimercapto-3-propanol, thioglycolic acid, thiolactic acid, and cysteamin. Some applications of this class of materials were outlined in the review article [30].

A method for immobilization of metal sulfide ultrafine particles such as CdS formed in reverse micellar systems in polythiourethane (PTU) via bonding of the thiol groups to the metal sulfide surface has been investigated [31, 32]. The resulting composite, CdS-PTU, improved its stability against photoirradiation and photocatalytic property for H_2 generation from aqueous solution of 2-propanol, when compared with the nano-CdS surface modified with thiophenol (CdS-Ph) [31]. In Ref. 32, the effects of thiols, used as the surface-modification agent for nano-CdS and the polymerizing monomer, on the photocatalytic properties of CdS-PTU were investigated.

Pietro and coworkers [33, 34] have demonstrated that a wide scope of interesting molecular moieties can be covalently tethered onto the surface of CdS nanocrystals, and that the properties of the resulting systems depend to a great extent on the nature of the surface groups. They [35] have also demonstrated that ~30 Å thiolate-capped CdS nanoclusters photodecompose to form bulk CdS and a single organic product, the symmetric disulfide corresponding to the thiolate cap, and further studied the effects of surface modification on the rate of photodecomposition. They found that the decomposition rate is enhanced by both electron donors and acceptors in the 4-position of the thiolate capping agent, and is strongly correlated with the fluorescent-quenching efficiency of the substituted cap [35].

1.8.2.3 Dithiols, Disulfides, and Other Sulfur Compounds

Mono- and multilayers of CdS nanoparticles were fabricated on a gold substrate covered with alkanedithiol SAMs by an alternative immersion of the substrate into ethanolic solutions of dithiol, that is, 1,6-hexanedithiol or 1,10-decanedithiol, and dispersion of CdS nanoparticles (ca 3 nm in diameter), the latter of which was prepared in sodium bis(2-ethylhexyl)sulfosuccinate in heptane [36]. The layer-by-layer structure of dithiol SAM and CdS monolayer was confirmed with X-ray photoelectron spectroscopy, Fourier transform infrared reflection–absorption spectroscopy, and inductively coupled plasma mass spectroscopy at each step of composite-film preparation. Photocurrent measurements revealed that the monolayers of CdS nanoparticles were immobilized without mutual aggregation of particles [36]. Cadmium selenide nanoparticles were prepared electrochemically on gold substrates modified with alkanethiolated β-cyclodextrin SAMs [37].

The formation of sulfur atomic layers on Au from alkaline solutions of sulfide and thiosulfate has been studied, and the relevance of these experiments to thiol-based SAMs was pointed out [38]. These studies are relevant to the formation of SAMs, as sulfide can be thought of as the simplest thiol and, thus, sulfur atomic layers as the shortest chain SAM. Sulfur atomic layers are also of interest

as precursors for the electrochemical formation of compound semiconductor thin films such as CdS, ZnS, and PbS [38]. The deposition of S was characterized using various analytical techniques. The same group had earlier used the oxidative underpotential deposition of sulfur for the preparation of CdS by electrochemical atomic layer epitaxy [38].

Wang and Tessier [39] have showed by solubility measurements that the solubility of CdS solids at various pH values (4.2–8.6) and sulfide concentrations ($10^{-4.3}$–$10^{-1.3}$ M) can be reproduced adequately by the following four bisulfide complexes: $CdHS^+$, $Cd(HS)_2$, $Cd(HS)_3^-$, and $Cd(HS)_4^{2-}$. The log K_n values for the general equation $Cd^{2+} + nHS = Cd(HS)_n^{2-n}$ are 7.38 ± 0.68, 14.43 ± 0.01, 16.26 ± 0.58, and 18.43 ± 0.05, respectively [39].

Bakkers and coworkers [40] have studied electron tunneling as a function of the distance between colloidal CdSe QDs and Au electrode. To vary this distance, they have used a variety of SAMs consisting of dithiols (1,3-propanedithiol, 1,6-hexanedithiol, and 1,9-nonanedithiol) and rigid disulfides (1,4-dithiane, 4, 4′-(tetrahydro-4*H*-thiopyran-ylidene), 4-(tetrahydro-4*H*-thiopyran-4-cyclohexylidene-4′-ylidene) tetrahydro-4*H*-thiopyran). QDs were chemisorbed on the Au electrode using these organic compounds. In addition, an ohmic contact was established by epitaxial electrodeposition of isolated QDs on Au [40]. CdSe suspension was prepared according to Ref. 41.

SAMs were prepared by immersing the Au film in a 5 mM dithiol/ethanol or saturated disulfide/ethanol solution for one week at 50 °C. The samples were subsequently rinsed with ethanol to remove the excess dithiol/disulfide from the surface and dried under a dry nitrogen flow. CdSe QDs were deposited on the SAM/Au electrode by immersion in the suspension for one week. The samples were rinsed with heptane to remove the excess particles [40]. After absorption of a photon with energy larger than the band gap, a long-lived excited state is formed in the QDs; this state can decay by electron tunneling to the gold substrate. The rate of photoinduced tunneling was measured directly by intensity-modulated photocurrent spectroscopy, and its distance dependence was studied using rigid SAMs separating the quantum CdSe and Au. The tunneling rate was found to depend exponentially on the distance, with a decay length of 2 Å [40].

The self-assembly of molecules such as thiols and dithiols on metal surfaces is well-established and has been used to attach cadmium chalcogenide nanocrystals, for example, to Au surfaces [42], and to measure their electrical properties [43, 44]. Attachment of CdS nanoparticle monolayer onto bifunctional 1,5-hexanedithiol or 1,10-decanedithiol SAM has been reported [36, 42, 45]. In addition, various authors have also demonstrated assembly of monolayers of alkanethiols and other molecules on GaAs surfaces [46–49]. The alkanethiols were presumed to bind selectively to arsenic atoms on GaAs (100) surface [48, 49].

A method has been described for attaching semiconductor CdS nanocrystals to metal (Au and Al) surfaces using difunctional SAMs as bridge compounds [42]. SAMs were prepared by immersing Au substrates in 5 mM ethanolic solutions of 1,3-propanedithiol, 1,6-hexanedithiol, and 1,8-octanedithiol for 8–12 hours. Al substrates were placed in solutions of 5 mM mercaptoacetic acid dissolved in ethanol and were allowed to sit for 12 hours. After immersion, the samples were removed

from solutions, rinsed with ethanol for 30 seconds, and then blown dry with argon. Samples could be stored in a desiccator prior to coating with nanocrystals. Both Al and Au substrates were prepared such that their surfaces contained free thiols. These SAMs were then exposed to solutions of CdS clusters in micelles. Typical immersion time was 12 hours, and afterward the samples were rinsed with heptane for 30 seconds and then blown dry with argon [42]. The nanocrystal films were characterized by resonance Raman scattering, Rutherford backscattering, contact angle measurements, and transmission electron microscopy. All techniques indicate the presence of quantum-confined clusters on the metal surfaces with a coverage of approximately 0.5 monolayers.

Recently, Greenham and coworkers [50] have reported the assembly and thorough characterization of CdSe nanocrystals attached to both *p*- and *n*-doped GaAs substrates. The self-assembly was performed using a 1,6-hexanedithiol to link CdSe nanocrystals to GaAs substrates. Cadmium chalcogenide nanocrystals were synthesized by the tri-*n*-octyl-phosphine-oxide (TOPO) method by Bawendi and coworkers [51] as modified by Alivisatos and coworkers [52]. Their diameter was determined by analysis of the absorption spectroscopy. Surface modification of the GaAs wafers was performed in a solution containing 88% 2-propanol, 12% aqueous ammonia solution, and 8×10^{-4}% 1,6-hexanedithiol (volume/volume) for 4 hours in darkness and at room temperature. The surface modification was followed by several thorough rinses with 2-propanol. The self-assembly of the CdSe nanocrystals was performed in a toluene solution containing 0.016 wt% CdSe nanocrystals for 12 hours in darkness and at room temperature. Two different sized CdSe nanocrystals were used [50].

The prepared films [50] have been characterized with attenuated total reflection Fourier infrared spectroscopy, PL, optical ellipsometry, and scanning tunneling microscopy, and the results are consistent with the formation of stable, disordered monolayers of CdSe nanocrystals with high packing density. This assembly technique may have applications for the production of molecular electronic devices on semiconductor substrates [50].

Zhang and Mu [53] reported a new approach to fabricate the CdS thin films by annealing the Cd^{2+}-dithiol multilayer films on both quartz and mica substrates and characterized the change of the composition, structure, and optical properties of the films before and after annealing. It opens up the possibility to fabricate the chalcogenide thin films by annealing the self-assembled multilayer films of metallic ion and organic dithiol [53].

Boilot and coworkers [54] have developed a scheme for the II–VI chalcogenide sol–gel synthesis, using CdS as a model system. They have reported the first extension of the sol–gel process on the preparation of transparent gels, thin films, and monoliths of CdS. They found that the use of the 4-fluorophenylthiol as a strong surface complexing agent, instead of the phenylthiol [41], greatly improves the dispersion of the particles in organic solvents. Dispersion can be achieved in acetone, tetrahydrofuran, or dimethylformamide at very high concentrations (at least 5 mol l^{-1}, i.e. a volume fraction of about 15%), and to a smaller extent in ethanol and chloroform [54]. This process should allow further developments of the sol–gel technique to other nonoxide materials.

1.8.3 Characterization and Applications

Semiconductor nanocrystals and nanoclusters are currently under intense investigation in various fields of science and technology. Quantum size effects result in unique physical and chemical properties that depend strongly on the size of the particles and clusters [2, 12, 26–28]. Significant progress has been made, particularly in the preparation of group II–VI semiconductors, by using capping ligands, such as thiolates, which cap the particle surface by direct coordination to surface atoms. Advanced materials built up from nanoscale particles give promise of a wide range of innovative applications in catalysis, sensors, nonlinear optics, and molecular electronics.

Bowmaker and coworkers [55] have recently demonstrated that electrospray mass spectrometry is a powerful technique for investigating the capping and functionalization of the surface of a CdS nanocluster, via ligand exchange reactions. The reactions of the thiophenolate-capped CdS cluster $[S_4Cd_{17}(SPh)_{28}]^{2-}$ with thiols (HSR), dithiols (HSRSH), thiol acids (HSRCOOH), thio acids (RCOSH), thiol alcohols (HORSH), diethyldithiocarbamate $[Et_2NCSS]^-$, isopropylxanthate $[(CH_3)_2CHOCSS]^-$, and 3-mercaptopropyltrimethoxysilane $[HS(CH_2)_3Si(OCH_3)_3]$ have been investigated [55].

Pseudo steady-state titration was found to be a valuable method for the determination of stability of colloidal nanocrystals upon change of the pH in the solutions [56]. CdSe nanocrystals coated with hydrophilic deprotonated thiol (thiolate) ligands were studied systematically. For comparison, CdTe and CdS nanocrystals coated with the same types of ligands were also examined. The results showed that the precipitation of the nanocrystals was caused by the dissociation of the nanocrystal-ligand-coordinating bonds from the nanocrystal surface. The ligands were removed from the surface due to protonation in a relatively low pH range, between 2 and 7 depending on the size, approximately within the quantum confinement size range, and chemical composition (band gap) of the nanocrystals [56].

The structure of the adsorbate systems formed by mercaptobenzothiazole and analogue molecules on CdS (1010) surface was studied quantum chemically using density functional theory [57]. Preliminary calculations of the free adsorptive molecules indicate an energetic preference of their thione form compared to the thiol form. For the anions of the adsorptive molecules, the role of the endocyclic nitrogen and the exocyclic sulfur as possible donor atoms was examined by means of known chelate complexes. Geometry optimizations showed that the structure of the adsorbate systems is dominated by the formation of two coordinative bonds from the donor atoms of the adsorptive anions to two adjacent Cd atoms of the surface. It showed that the molecular plane of the adsorptives is tilted with respect to the normal of the crystal face. They have shown that the tilt angle is mainly determined by the tendency of the surface Cd atoms to continue the tetrahedral coordination from the bulk [57].

Recent studies revealed that cadmium-based semiconductor nanocrystals did not affect the biological functions if they were completely coated with organic ligands [58, 59]. After the ligands were detached, the nanocrystals became extremely toxic [59]. The detachment of the ligands will not only destabilize the colloidal system but also cause possible cytotoxic problems [56].

The electroluminescence properties of CdSe nanoparticles embedded in organic semiconductor materials have been studied extensively and hybrid organic–inorganic light emitting diodes (LEDs) were realized [60–62]. Eychmüller and Rogach [30] fabricated CdTe nanocrystal/polyaniline composite films as well as films of closely packed CdTe nanocrystals to develop LED with low turn-on voltages. The emitted color of such device is tunable from green to red depending on the size of the nanocrystals.

1.8.4 Summary

In summary, while our understanding of II–VI semiconductor–molecular interfaces is still at a relatively young stage of development, it is advancing rapidly. There is reason to be optimistic that the experimental and theoretical methods and techniques have become available for characterizing these interfaces and structures. In this chapter, we have briefly described the surface modification of chalcogenide semiconductor electrodes with thiols, dithiols, and disulfides as well as other sulfur compounds.

Acknowledgments

We would like to gratefully acknowledge and thank financial support of this work provided by the Grant-in-Aid for Creative Scientific Research on ''Devices on molecular and DNA levels'' (No. 13GS0017) from the Ministry of Education, Science, Sports, and Culture of Japan.

References

1. N. Myung, S. Ham, B. Choi et al., *J. Electroanal. Chem.* **2005**, *574*, 367.
2. A. P. Alivisatos, *J. Phys. Chem.* **1996**, *100*, 13226.
3. S. V. Gapoenko, *Optical Properties of Semiconductor Nanocrystals*, Cambridge University Press, Cambridge, 1998.
4. L. E. Brus, *J. Phys. Chem.* **1986**, *90*, 2555.
5. B. O. Dabbousi, J. R. Viejo, F. V. Mikulec et al., *J. Phys. Chem. B* **1997**, *101*, 9463.
6. M. Kuno, J. K. Lee, B. O. Dabbousi et al., *J. Chem. Phys.* **1997**, *106*, 9869.
7. A. Hagfeldt, M. Grätzel, *Chem. Rev.* **1995**, *95*, 49.
8. K. Rajeshwar, in *Encyclopedia of Electrochemistry* (Eds.: A. J. Bard, M. Stratmann, S. Licht), Wiley-VCH, Weinheim, 2002, p. 13, Vol. 6.
9. L. S. Li, N. Pradhan, Y. Wang et al., *Nano Lett.* **2004**, *4*, 2261.
10. S. Seker, K. Meeker, T. F. Kuech et al., *Chem. Rev.* **2000**, *100*, 2505.
11. S. M. Sze, *Physics of Semiconductor Devices*, John Wiley & Sons, New York, 1969, pp. 46–50.
12. J. Frenzel, J. O. Joswig, P. Sarkar et al., *Eur. J. Inorg. Chem.* **2005**, *2005*, 3585.
13. D. J. Stirland, B. W. Straughan, *Thin Solid Films* **1976**, *31*, 139.
14. L. McGhee, I. Nicol, R. D. Peacock et al., *J. Mater. Chem.* **1997**, *4*, 2421.
15. M. Bruening, E. Moons, D. Cahen et al., *J. Phys. Chem.* **1995**, *99*, 8368.
16. M. Bruening, E. Moons, D. Y. Marcovich et al., *J. Am. Chem. Soc.* **1994**, *116*, 2972.
17. J. W. Thackeray, M. J. Natan, P. Ng et al., *J. Am. Chem. Soc.* **1986**, *108*, 3570.
18. J. J. Hickman, M. S. Wrighton, *J. Am. Chem. Soc.* **1991**, *113*, 4440.
19. M. J. Natan, J. W. Thackeray, M. S. Wrighton, *J. Phys. Chem.* **1986**, *90*, 4089.
20. A. B. Ellis, S. W. Kaiser, J. M. Bolts et al., *J. Am. Chem. Soc.* **1977**, *99*, 2839.
21. J. K. Lorenz, T. F. Kuech, A. B. Ellis, *Langmuir* **1998**, *14*, 1680.
22. R. E. Hollingsworth, J. R. Sites, *J. Appl. Phys.* **1982**, *53*, 5357.
23. A. A. Burk Jr., P. B. Johnson, W. S. Hobson et al., *J. Appl. Phys.* **1986**, *59*, 1621.
24. A. B. Ellis, R. J. Brainard, K. D. Kepler et al., *J. Chem. Educ.* **1997**, *74*, 680.
25. M. X. Tan, P. E. Laibinis, S. T. Nguyen et al., *Progress in Inorganic Chemistry*, John Wiley & Sons, New York, 1994, Vol. 41.
26. Y. Nosaka, K. Yamaguchi, H. Miyama et al., *Chem. Lett.* **1988**, *17*, 605.

27. Y. Nosaka, N. Ohta, T. Fukuyama et al., *J. Colloid Interface Sci.* **1993**, *155*, 23.
28. T. Vossmeyer, G. Reck, B. Schulz et al., *J. Am. Chem. Soc.* **1995**, *117*, 12881.
29. N. Gomez, J. O. Winter, F. Shieh et al., *Talanta* **2005**, *67*, 462.
30. A. Eychmüller, A. L. Rogach, *Pure Appl. Chem.* **2000**, *72*, 179.
31. S. Shiojiri, M. Miyamoto, T. Hirai et al., *J. Chem. Eng. Jpn.* **1998**, *31*, 425.
32. T. Hirai, M. Miyamoto, T. Watanabe et al., *J. Chem. Eng. Jpn.* **1998**, *31*, 1003.
33. H. Noglik, W. J. Pietro, *Chem. Mater.* **1994**, *6*, 1593.
34. J. G. C. Veinot, M. Ginzburg, W. J. Pietro, *Chem. Mater.* **1997**, *9*, 2117.
35. J. G. C. Veinot, J. Galloro, L. Pugliese et al., *Chem. Mater.* **1999**, *11*, 642.
36. T. Nakanishi, B. Ohtani, K. Uosaki, *J. Phys. Chem. B* **1998**, *102*, 1571.
37. S. J. Choi, D. H. Woo, N. Myung et al., *J. Electrochem. Soc.* **2001**, *148*, C569.
38. M. D. Lay, K. Varazo, J. Stickney, *Langmuir* **2003**, *19*, 8416.
39. F. Wang, A. Tessier, *Environ. Sci. Technol.* **1999**, *33*, 4270.
40. E. P. A. M. Bakkers, A. L. Roest, A. W. Marsman et al., *J. Phys. Chem. B* **2000**, *104*, 7266.
41. M. L. Steigerwald, A. P. Alivisatos, J. M. Gibson et al., *J. Am. Chem. Soc.* **1988**, *110*, 3046.
42. V. L. Colvin, A. N. Goldstein, A. P. Alivisatos, *J. Am. Chem. Soc.* **1992**, *114*, 5221.
43. D. L. Klein, P. L. McEuen, J. E. B. Katari et al., *Appl. Phys. Lett.* **1996**, *68*, 2574.
44. D. L. Klein, R. Roth, A. K. L. Lim et al., *Nature (London)* **1997**, *389*, 699.
45. S. Ogawa, F. R. F. Fan, A. J. Bard, *J. Phys. Chem.* **1995**, *99*, 11182.
46. S. R. Lunt, G. N. Ryba, P. G. Santangelo et al., *J. Appl. Phys.* **1991**, *70*, 7449.
47. T. Baum, S. Ye, K. Uosaki, *Langmuir* **1999**, *15*, 8577.
48. C. W. Sheen, J. X. Shi, J. Märtensson et al., *J. Am. Chem. Soc.* **1992**, *114*, 1514.
49. O. S. Nakagawa, S. Ashok, C. W. Sheen et al., *Jpn. J. Appl. Phys.* **1991**, *30*, 3759.
50. E. Marx, D. S. Ginger, K. Walzer et al., *Nano Lett.* **2002**, *2*, 911.
51. C. B. Murray, D. J. Norris, M. G. Bawendi, *J. Am. Chem. Soc.* **1993**, *115*, 8706.
52. J. E. B. Katari, V. L. Colvin, A. P. Alivisatos, *J. Phys. Chem.* **1994**, *98*, 4109.
53. Y. Zhang, J. Mu, *Colloids Surf. A* **2005**, *262*, 238.
54. T. Gacoin, L. Malier, J. P. Boilot, *Chem. Mater.* **1997**, *9*, 1502.
55. T. Løver, W. Henderson, G. A. Bowmaker et al., *Chem. Mater.* **1997**, *9*, 1878.
56. J. Aldana, N. Lavelle, Y. Wang et al., *J. Am. Chem. Soc.* **2005**, *127*, 2496.
57. B. Flemmig, R. Szargan, J. Reinhold, *J. Phys. Chem. B* **2001**, *105*, 5440.
58. B. Dubertret, P. Skourides, D. J. Norris et al., *Science* **2002**, *298*, 1759.
59. A. M. Derfus, W. C. W. Chan, S. N. Bhatia, *Nano Lett.* **2004**, *4*, 11.
60. V. L. Colvin, M. C. Schlamp, A. P. Alivisatos, *Nature (London)* **1994**, *370*, 354.
61. M. Gao, B. Richter, S. Kirstein, *Adv. Mater.* **1997**, *9*, 802.
62. S. Coe, W. K. Woo, M. Bawendi et al., *Nature (London)* **2002**, *420*, 800.

1.9 Metal Substrates for Self-assembled Monolayers

Marie Anne Schneeweiss and Israel Rubinstein
Department of Materials and Interfaces, Weizmann Institute of Science, Rehorot, Israel

1.9.1 Introduction

Self-assembled monolayers (SAMs) on metal substrates have been the focus of unusual scientific and technological interest for two decades, as such systems provide the unique possibility to form two-dimensional structures that are organized on the molecular level in a generally perpendicular direction. SAMs are therefore considered as possible candidates for the construction of future optical, electronic, and magnetic devices of minute dimensions, as well as for various other chemical and biological applications. Electrochemical issues related to SAMs have been discussed previously [1].

Various aspects of SAM formation, structure, properties, and possible applications are discussed in other chapters. The properties of a SAM of a certain composition depend on a number of parameters, such as the solvent used for self-assembly, the concentration of the adsorbing molecules, the adsorption time and temperature, and to an appreciable degree, on the properties of the substrate. The latter include the substrate type, chemical composition, morphology, preparation, pretreatment, and cleanliness.

Two groups of molecules have been used most frequently for monolayer formation, that is, molecules bearing a silane binding group (e.g. trichlorosilanes, trimethoxysilanes), and molecules bearing a sulfur-based binding group (e.g. thiols, disulfides, dialkyl sulfides). The latter are more relevant to electrochemistry, as the presence of the sulfur enables stable binding to various metal surfaces, that is, to electrodes. In the overwhelming majority of cases, the substrate of choice for the formation of SAMs of thiols, disulfides, and so on, has been gold. This is because of the strong interaction between sulfur and gold, as well as the chemical inertness of gold, eliminating the need to consider surface oxides (present on many other metals under usual conditions). Therefore, gold substrates will be the main topic in this chapter, while other metals will be discussed more briefly.

In this chapter, we differentiate between *polycrystalline* substrates and *single-crystalline* substrates of a well-defined orientation. An additional distinction is made between *thin metal films* on a support material and *bulk substrates* such as disks or wires. The use of a thin metal film – as opposed to bulk material – gives rise to a number of additional parameters associated with the preparation process, which determine the properties of the resulting surface and the adsorbed SAM; these will be discussed in depth. The process of adsorption of molecules on a substrate is sensitive to the presence of impurities on the surface. Therefore, *cleaning pretreatment* of surfaces will be addressed, as it plays an important role in the preparation procedure, as will be *annealing procedures* that bring about healing of surface defects and are crucial in the preparation of (atomically) flat surfaces.

It should be pointed out that the number of publications on SAMs on conducting substrates (primarily gold) is overwhelming, and these include a large variety of substrate types and pretreatment

Encyclopedia of Electrochemistry. Edited by A.J. Bard and M. Stratmann
Vol. 10 *Modified Electrodes*. Edited by M.Fujihira, I.Rubinstein, and J.F.Rusling
Copyright © 2007 Wiley-VCH Verlag GmbH & Co. KGaA, Weinheim. ISBN: 978-3-527-30402-8

procedures. It is practically impossible to encompass, in a concise chapter, all the published varieties. We therefore describe below those substrates and preparation methods that are either widely used or of particular interest.

1.9.2 General Considerations Regarding Substrates

1.9.2.1 Specific Requirements Imposed by Analysis Techniques

In many cases, the analysis techniques of choice dictate the kind of substrate used, when a specific surface characteristic is required for the application of a chosen technique. This is the case, for example, in the use of surface-enhanced Raman spectroscopy to study monolayers on copper or silver, where special pretreatment including etching or deposition on a rough support is applied. Other techniques may require special sample properties or geometries, for example, transparency (for transmission spectroscopy) or atomic smoothness (for scanning probe analysis). If the technique requires intimate contact with a measuring device, this may be achieved by evaporating the metal directly onto the device surface. The latter is the case, for example, in quartz crystal microbalance (QCM) or in surface acoustic wave (SAW) analysis. This, in turn, will determine the morphology of the surface.

1.9.2.2 Polycrystalline, Textured, Single-crystalline Substrates

With gold, as with other metal substrates, the relevant surface can be either polycrystalline, that is, composed of crystallites of random orientation, or single crystalline, that is, comprising one crystal plane of a well-defined and uniform orientation. In certain cases, a metal surface can be defined as ''textured,'' generally meaning that, although rich in defects and exhibiting a polycrystalline nature, one specific orientation in the direction normal to the surface is predominant. Metal surfaces show varying properties depending on their crystallinity, affecting electrochemical processes on the bare electrode and at SAM-covered electrodes. Moreover, in many cases the structure of the monolayer depends on the crystallographic face of the underlying metal. Single-crystal surfaces are usually necessary to study intrinsic properties of the monolayer, as opposed to properties determined by grain boundaries and other defects of the substrates. This is especially important for macroscopic methods.

1.9.2.3 Major Aspects Regarding Substrate Preparation/ Pretreatment

A number of aspects have to be considered with respect to the preparation of a substrate for modification with a SAM.

The largest group of substrates found in the literature comprises thin metal films on various support materials. In such cases, a major factor governing the outcome of the metal deposition is the method used, that is, resistive or electron gun evaporation; sputtering; electroless plating; or template stripping. The specific parameters of the deposition process determine the resulting surface topography.

Thermal treatment (annealing) is frequently an important step in the generation of a well-defined substrate. Heating of the substrate, which may be performed in an oven or using direct flame, leads to healing of defects and promotes the formation of atomically flat terraces on the substrate surface.

A crucial step in the substrate preparation is cleaning of the substrate prior

to monolayer self-assembly. Pretreatment methods include a wide variety of chemical, electrochemical, and dry procedures, as well as combinations thereof.

In certain cases, additional aspects have to be considered. For example, in the case of metals that are covered with an oxide layer under ambient conditions, the preparation of SAMs may require specific pretreatments aimed at eliminating or reducing the amount of metal oxides on the surface.

1.9.3 Substrates Used for SAM Preparation

1.9.3.1 Gold

1.9.3.1.1 Gold Films on Various Supports

1.9.3.1.1.1 Evaporated Gold Films

Introduction Evaporation of gold onto various supports preceded SAMs by many years. Originally, the interest focused on the epitaxial growth of thin metal films on mica and other flat surfaces. This introduction, therefore, deals with general aspects of evaporated gold films, while the proceeding subchapters refer specifically to studies of SAMs on the various gold surfaces.

The influence of the support material and the deposition temperature on the crystallinity and orientation of an evaporated metal film was already studied in 1936 by Brück [2]. A dependence of the orientation on the deposition temperature was also found by Rüdiger [3]. Pashley [4] reviewed a number of studies on the epitaxial growth of fcc metals on mica. Investigations on the epitaxy of gold deposited at high temperatures were carried out by Poppa et al. [5].

It was the introduction of the scanning tunneling microscope (STM) that revived the interest in thin film deposition. On one hand, from a fundamental point of view, the STM provides a highly potent tool for studying film morphology; features like monatomic steps, dislocations, and grain boundaries were clearly resolved, and nucleation and growth of the films could be better understood. On the other hand, achieving atomic resolution with the STM requires a well-defined, atomically flat substrate, which spurred the search for single-crystalline conducting surfaces other than highly oriented pyrolytic graphite (HOPG), silicon, and certain other semiconductors.

These motivations triggered a number of STM studies on thin gold films. Chidsey et al. [6] used STM to investigate the growth of gold films evaporated on mica, studying the effect of film thickness, deposition temperature, annealing, and a silver underlayer on the resulting gold morphology. Gold deposited at room temperature resulted in a typical ''rolling-hill'' topography. The films showed weak epitaxy with the mica substrate, a (111) texture, and occasional atomically flat terraces, while the hilltops were often round. Deposition on mica at 225 °C produced larger gold crystallites with flatter tops; the surface was composed of flat plateaus with grooves and valleys at grain boundaries. Deposition at 300 °C resulted in an even flatter morphology. Postdeposition annealing in the vacuum chamber also served to smoothen the surface. A silver underlayer resulted in very good epitaxy, but a high silver content was found in the gold. Thiols were added in order to simulate a heavily contaminated surface, but did not change the appearance in the STM [6].

Deposition temperatures above ~570 °C were shown to yield discontinuous gold films on mica [7]. Vancea et al. carried out a thorough STM study aimed at determining the effect of the support material (rough

Corning glass, Si(100), mica, NaCl, and HOPG) on the topography of evaporated gold [8]. Rabe and coworkers [9], looking for appropriate substrates for imaging LB films, found grainy structures (ca. 25 nm grain size) for gold and silver films evaporated on glass slides, being too rough for reliable STM molecular imaging of adsorbed monolayers. In the same study, films evaporated onto mica exhibited flatter grains of the same size. Films grown at higher temperatures were (111) textured according to low-energy electron diffraction (LEED), and exhibited atomically flat terraces, ca. 100 nm wide.

Rubinstein and coworkers [10, 11] studied evaporated as well as sputtered gold films (see Sect. 1.9.3.1.1.2) on several support materials by transmission electron microscopy (TEM) and STM. Evaporation on microscope glass cover slides, cleaved mica, and Si(111) substrates yielded flat-looking films with rather large, plate-shaped gold grains, showing a {111} texture. Films on Si(100) consisted of much smaller grains with no crystallographic texture. Annealing led to an increase in grain size and flatness, and in the case of glass, mica, and Si(111), to enhanced texture. Gold samples evaporated at temperatures of ca. 350 °C exhibited larger grains but a higher density of imperfections and voids in the film.

Buchholz et al. [12] used scanning electron microscopy (SEM), STM, and LEED to study 100 nm films of Ag, Au, Pd, and Cr on mica. They saw increasing grain size and grain flattening as the substrate temperature during deposition increased from −150 to 400 °C. At 400 °C, terraces of more than 100 nm across were formed. Characteristic holes of a few tens of nanometers, as well as holes on the nanometer scale, were observed, which may be attributed to impurities segregating to the surface. LEED established the existence of a (111) orientation. These authors also checked the influence of the pressure during evaporation, and found no difference for samples evaporated at 10^{-5} and 10^{-9} mbar.

In the following sections, gold films will be discussed according to the support material, using information taken only from studies concerned with the use of these substrates for the preparation of SAMs.

Gold films evaporated on mica Freshly cleaved mica is probably the most popular support for evaporated gold films. The mica surface is exceptionally flat and requires no cleaning prior to evaporation. As a rule, gold films on mica exhibit larger portions of atomically flat crystallites than those on highly polished silicon (see section on Gold films evaporated on silicon).

Gold is evaporated by resistive or electron beam evaporation onto freshly cleaved mica (ruby muscovite or green mica). The thickness of evaporated films is usually 100–300 nm, with most films being 150–250 nm thick. Heating the sample before (“prebaking”), during or after (“annealing”) evaporation enhances the quality of the resulting gold surface in terms of the number and size of atomically flat terraces.

The prebaking (preheating) temperatures and times found in the literature vary somewhat, for example, 500 °C for 24 h [13], 250–300 °C for about 1 h [14, 15], 325 °C [16] or 550 °C for 3 h [17]. When evaluating the effect of temperature during prebaking of the mica, it should be realized that the temperature of the heater is not necessarily that of the mica, the latter depending on the geometry of the setup

and the distance from the heater. For example, a heater temperature of 580 °C was estimated to be 100–200 °C on mica in one report [18]. When mica slides are heated during gold deposition, the temperatures reported are usually in the range 240 to 350 °C. Prebaking removes adsorbed water and some other contaminations.

Heating in the vacuum chamber during deposition can improve the film quality. It was shown [19] that the gold surface roughness is controlled by the mica substrate temperature during gold evaporation. Mica substrates were prebaked at 450 °C for ca. 6 h, brought to the desired temperature and further annealed in vacuum for 2 h at the deposition temperature. Grain size increased and surface roughness decreased with increasing deposition temperature. Numerous shallow depressions were detected on terraces of the sample prepared at 450 °C. A study comparing films grown in high vacuum (10^{-6}–10^{-5} Pa) and ultrahigh vacuum (10^{-8} Pa) [20] showed that the latter are generally flatter. The deposition rate is typically 0.5–1 Å s^{-1} [18] or 10 Å s^{-1} [21]. No clear relationship between evaporation rate and surface quality has been shown.

Kawasaki et al. [22] demonstrated that ultraflat gold films can be prepared on mica by sputtering at elevated substrate temperatures. They obtained 1 μm flat terraces, which favorably compare to other evaporated gold films. Nogues and Wanunu [23] developed a facile (5 min) postevaporation annealing procedure that gives similar size terraces.

In general, gold films evaporated on mica consist of crystallites (grains), which are separated by grain boundaries and topped by atomically flat (111) terraces. The size of the grains is typically 50–100 nm while the terrace size is considerably smaller, typically 10–20 nm. Heating before, during, or after the evaporation serves to considerably increase the grain and terrace size. In terms of surface roughness factors, values of ca. 1.1 ± 0.1 [21, 24–27] (calculated as the electrochemically determined area divided by the geometric area) up to 1.35 [28] were reported.

Gold films evaporated on glass Preparation of evaporated gold films on glass – usually either float glass or glass microscope slides – varies from the same procedure on mica, in that the support (glass) has to be cleaned before introduction into the vacuum chamber. For example, one possible protocol is ultrasonication in successive baths of Piranha solution, distilled water, and 2-propanol [29], but various other chemical cleaning procedures can be used with satisfactory results. Gold evaporation rates are usually between 0.1 and 1.0 nm s^{-1}. The thickness of the gold film is similar to that of films on mica, that is, typically 100–200 nm.

An intermediate layer evaporated prior to gold deposition to improve the gold adhesion to the glass, is usually considered necessary. This adhesion layer may consist of TiO_2, Cr, Ti, or 3-mercaptopropyl trimethoxysilane (MPS) [30]. It was shown by XPS that Cr does not diffuse to the gold surface 30 days after deposition [31]; in another study, the authors concluded that the type of adhesion layer does not influence the stability of an SAM on the respective gold film [32]. The thickness of the adhesion metal layer is typically 5–10 nm, although higher (20 nm) or lower (<1 nm) values were reported. There are a few exceptions to the use of adhesion layers. In most of these cases, the glass support is roughened for better adhesion, for example, by treatment with Ar plasma [33–36]. Evaporation of gold directly on

glass with no adhesion layer or roughening was also reported [37].

In contrast to mica, prebaking or heating of the slides during evaporation is only infrequently reported; for example, in [38] the glass surface was held at 300 °C during evaporation. The roughness factor of the resulting gold surface was 1.6, which presents no improvement.

Rubinstein and coworkers [10] found that gold films evaporated on glass are comparable in grain size, roughness, and (111) texture to similar films evaporated on mica. Other authors reported that the films on glass are of a lower quality in terms of roughness and crystallinity. Porter and coworkers [21] showed that gold on glass surfaces exhibited smaller and rougher crystallites (~25 nm in size) than films on mica. The gold surface showed mostly (111) character but there was also evidence for (110) sites. Abbott and Whitesides reported gold surfaces that are polycrystalline with a (111) texture [39]. In all cases, obtaining large, atomically flat (111) terraces required an annealing step (see section on Annealing procedures for evaporated gold films).

Special optically transparent films were used by Whitesides and coworkers [40] to control the contact angle and shape of drops of hexadecanethiol by electrochemical desorption. Using the drops as lenses, an optical switch was obtained, which focuses/defocuses light. The slides consisted of 100 Å gold evaporated onto titanium-primed (5 Å) glass or indium tin oxide. Even a 100-Å gold coating was sufficiently conductive to enable electrochemical reactivity.

Particularly versatile substrates for the study of ultrathin overlayers were reported by Rubinstein and coworkers [41]. The substrates were prepared by evaporation of 15 nm gold on silanized glass and annealing, providing continuous, smooth, (111) textured, optically transparent gold films. Such surfaces enable application of a wide range of techniques, including transmission UV-vis spectroscopy, ellipsometry, scanning probe, and electrochemical measurements, performed on the same substrate.

Gold films evaporated on silicon When used as supports for gold evaporation, highly polished silicon wafers, like glass, are usually covered with a thin layer of Cr, Ti, or MPS to improve the gold adhesion on the native SiO_2. This can be avoided if the silicon oxide is removed prior to evaporation, as gold was reported to adhere well to oxide-free, hydrogen-passivated Si(111) [31, 42]. Hydrogen passivation can be achieved by chemical removal of the oxide followed by etching/passivation in concentrated HF and blow-drying (no water rinse). Following hydrogen passivation, the slides are transferred to the vacuum chamber for gold evaporation. Gold films on oxide-free Si cannot be annealed or stored for long periods of time, as the Si diffuses through the gold and reaches the surface (where it oxidizes) at moderate temperatures [43, 44]; the Si diffusion is effectively suppressed when the native SiO_2 layer is maintained. In Ref. 31, no Si was detected on the gold surface (150 nm) 11 months after deposition; this may be due to the water rinse after the HF treatment, probably causing some Si oxidation.

With Si surfaces that are not hydrogen passivated, a thorough cleaning pretreatment should be applied to the Si slides, such as cleaning in Piranha solution (at 90 °C) for 5 min, rinsing with Millipore water, and drying under nitrogen [45, 46].

When adhesion layers are deposited prior to gold evaporation, their thickness

is typically 1–10 nm (even 15 nm for Cr); thinner layers are generally favored. Most reports do not indicate Cr diffusion to the surface [45, 46]. Ulman and coworkers examined gold films (150–200 nm) on chromium-primed (75–100 Å) Si wafers by Auger electron spectroscopy (AES), and found no Cr on the outer surface after two weeks. On the other hand, cyclic voltammetry showed chromium on the gold surface when thicker Cr layers were used, while no Cr was seen on the surface when an intermediate layer of 7 Å was used [47]. In another case employing commercial slides [48], Cr was found to diffuse to the surface of the gold. The Cr was oxidized by sulfochromic acid and then dissolved in HF (this was suggested as a general cleaning procedure). Ti is less frequently used as an adhesion layer [49, 50], with layer thicknesses of ca. 5–10 nm. When MPS is used for adhesion, the oxidized silicon wafer is treated twice (10 min each) with a hot solution of MPS and water in hot propanol (1 : 1 : 40), followed by 10 min curing at 115 °C [47]. Si wafers (with a native SiO_2 layer) can also be used as substrates for gold evaporation without any adhesion layer [51].

Usually n-type silicon (111) or (100) wafers are used, although in many cases the orientation is not specified. Typical thicknesses of the gold films, as with similar films on mica or glass, are 100–200 nm, although thicker or thinner films were also reported. Annealing in the vacuum chamber is not generally employed for gold films on silicon, but postdeposition annealing in air was reported [51].

The topography of the resulting gold surface is, in many cases, described as a ''rolling hills'' morphology. The surface is not atomically smooth but shows subtle variations of the thickness [52]. The average grain size is of the order of ~50 nm and the surface appears to be very smooth. X-ray diffraction suggests that at least 80% of the grains exhibit a (111) texture. An average roughness of ca. 10 Å and a maximum gradient of ca. 10° from the horizontal was reported [53]. Films evaporated on either Si(100) or Si(111) are usually described as being predominantly (111) textured. This is in contrast with the results of Golan et al. [10, 11], who reported nontextured gold on Si(100) for thin Au films (35 nm) with no adhesion layer. A comparative study [21] showed that the surface of gold on Si (as that of gold on glass) exhibited a (111) texture with evidence of (110) sites. The roughness factor was estimated by iodine chemisorption to be 1.1 [54].

Gold films evaporated on miscellaneous supports As mentioned in the Introduction, with some techniques it is necessary to evaporate gold directly onto the analytic device. Examples include QCM [55–57] where the gold is evaporated directly onto the quartz crystal plates; prisms for surface plasmon resonance (SPR) [58]; and others. The roughness of the support and the fact that annealing may not be possible impose certain limitations on the resultant surface quality. Cleaning of the support, usually with Piranha or organic solvents and sonication, is important in these cases, and the use of an adhesion layer may be necessary. Initial polishing of the support may be needed with particularly rough surfaces.

Other examples include laser desorption Fourier transform mass spectrometry, where gold was evaporated onto precoated Macor tips [59]; infrared reflection spectroscopy (IRS), where gold was evaporated onto Cr coated stainless steel rods [25]; and SAW [60–62] experiments, where gold was evaporated onto precoated SAW devices (ST-cut quartz with Al transducers).

Annealing procedures for evaporated gold films Flame annealing [63, 64] (usually in the reducing part of a hydrogen flame) not only produces larger grains, more uniform surfaces and large atomically flat terraces, it also serves to remove impurities, thereby eliminating the need for complicated cleaning procedures. The width of gold grains was found to increase fivefold after flame annealing [65].

Several annealing procedures have been reported, for example, annealing in an oven or flame annealing. Flame annealing can be carried out either in a Bunsen burner flame or in a hydrogen flame. The temperature of the latter has been claimed to be too high by some authors, but the process is still widely used. Flame annealing is only recommended with gold on special heat-resistant glass, such as quartz or Tempax, while common microscope slides are not suitable supports. Annealing in the vacuum chamber (as seen earlier) is usually reported for Au on mica only, while flame annealing appears to be more popular with Au/glass and Au/silicon. Annealing in the oven at temperatures comparable to those of the flame leads to similar results but at the risk of increased contamination.

A detailed STM study of the annealing process in a wide temperature range (200–500 °C) was performed by Millo and coworkers [66], using 80-nm gold films evaporated onto glass cover slips. Annealing was carried out in a temperature-controlled oven at atmospheric pressure. The authors found a monotonic increase in the average lateral grain dimension with annealing temperature (annealing time: 18 h), and a more complex temperature dependence for the vertical roughness. A time-dependency experiment at 200 °C showed a monotonic decay of the surface roughness with time. They propose two different mechanisms, that is, surface diffusion, which is dominant at temperatures up to 300 °C, and grain boundary migration and bulk-defect diffusion, which causes grain coarsening at higher temperatures.

Figures 1(a) and (b), respectively, show an evaporated gold film before and after flame annealing in a Bunsen burner flame [67], while Fig. 1(c) shows an SAM on the annealed surface. The sample was heated to dark red glow (700 °C) for ca. 1 min and quickly cooled on a copper block or in ethanol [68]. Surfaces of a similar quality can be produced by annealing in a hydrogen flame [69] (atomically flat terraces of several μm^2 size) or in a butane–oxygen flame [70] (defect-free terraces, 100–200 nm wide).

Indirect flame annealing under nitrogen flow of Au films evaporated on mica was reported to produce high-quality gold surfaces with large, μm-size atomically flat terraces [23].

Cleaning procedures for evaporated gold samples Various elements may significantly influence the self-assembly process, and hence, the resultant monolayer structure. These include the solvent, the structure, and concentration of the adsorbing molecule, adsorption time and temperature, substrate annealing, and surface cleanliness. Hence, removal of impurities present on the bare substrate prior to self-assembly plays an important role in determining the monolayer quality. Inconsistency in the results reported by different groups can, in many cases, be traced to the use of different pretreatment procedures [71].

As a rule, the time between preparation of the substrate and its introduction into the adsorption solution, that is, the length of exposure to the ambient, should be kept

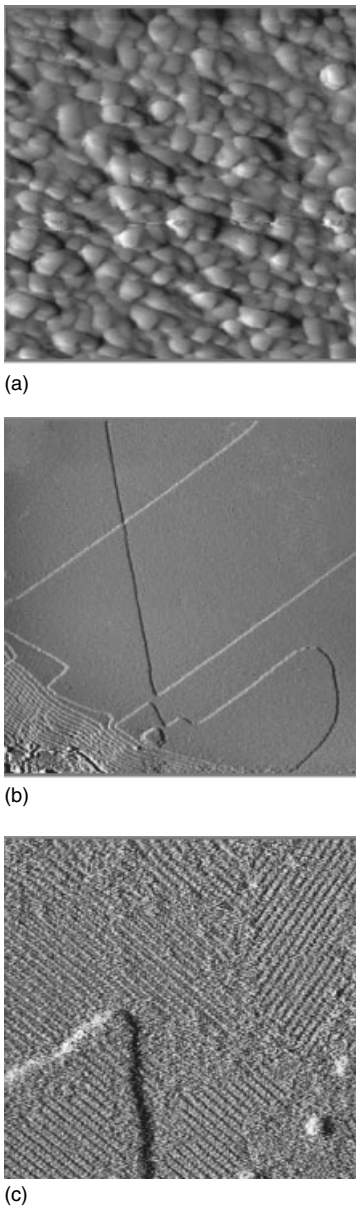


Fig. 1 (a) A 200-nm gold film on glass (with a 2-nm intermediate Cr layer) before annealing (500×500 nm^2). (b) A similar gold film after flame annealing (500×500 nm^2). (c) A SAM of thiosalicylic acid on a surface similar to that in (b) (53×53 nm^2). Adapted from [67, 68].

to a minimum in order to minimize surface contamination. With freshly prepared gold substrates, rinsing the surface with ultrapure water or with ethanol and drying under a stream of purified air or nitrogen may be sufficient. XPS showed that ethanol dip effectively removes surface contamination [72]. In addition, a large variety of cleaning procedures have been in use; these are required especially when gold substrates are prepared in batches and stored before use. In such cases, an aggressive pretreatment procedure may lead to an impurity-free substrate. It should be kept in mind that the pretreatment, in most cases, has little effect on the gold topography, crystallinity, and texture, which are determined primarily by the evaporation parameters and subsequent annealing (as seen earlier).

- **Chemical cleaning procedures**:

1. Immersion of substrates in Piranha solution (90 °C) for 5 min, followed by subsequent rinsing with Millipore water, and drying under a nitrogen stream [45]. Long exposures to hot Piranha may result in roughening of the gold surface [46].
2. Sonication in boiling 50 : 50 ethanol/chloroform for 5 min, drying under nitrogen, covering of the gold surface with Piranha for 1 min followed by thorough rinsing with deionized water, hydrogen peroxide, and ethanol. Storage in ethanol for no more than 24 h, exposure to air less than 30 s before self-assembly [71].
3. Ultrasonication in chlorobenzene, followed by immersion in a 5 : 1 : 1 $H_2O/NH_3/H_2O_2$ solution at 80 °C

for 3 min [73]. Rinsing with the solvent and immediate immersion in the amphiphile solution. XPS showed reduction of the sulfur and nitrogen peaks to insignificant levels after cleaning.

4. Rinsing with dilute hydrochloric acid, Millipore water and ethanol, drying under a stream of argon before self-assembly [54].
5. Cleaning in freshly prepared and cooled chromic acid, followed by thorough rinsing with deionized water [21, 74].
6. Repeated cycles of 30 s exposures to 50 °C sulfochromic acid, 3% aqueous HF and extensive rinsing. After three such cycles, transfer to the self-assembly solution [48]. This method also removes Cr, which may diffuse to the surface from the adhesion layer.

- **Electrochemical cleaning**: Electrochemical pretreatment of evaporated gold substrates, using a variety of potential windows, has been reported particularly in connection with electrochemical studies of monolayer modified electrodes. For example, alternating the potential between −1.86 and 0.65 V versus saturated calomel electrode (SCE) in 0.5 M sulfuric acid [75]. Electrochemical cleaning may be preceded by a chemical cleaning step, as in the following procedures: Brief dipping in hot Piranha [76] or sonication in chloroform and immersion in hot (>100 °C) concentrated sulfuric acid [77], followed by potential cycling between −0.4 and 1.4 V versus SCE in 0.5 M H_2SO_4 until a stable voltammogram is obtained.
- **UV/ozone – ethanol cleaning**: Exposure to UV/ozone, which results in oxidative removal of organic contamination as well as some oxidation of the gold surface itself, followed by immersion in ethanol, which reacts to reduce the gold oxide to metallic gold [34]. The UV irradiation serves to excite organic molecules on the surface, thereby facilitating their oxidation by the ozone. This procedure has the advantage of the major cleaning step being a ''dry'' process (same as plasma cleaning, see the following), thus minimizing the possibility of contamination originating from cleaning solutions. The procedure is effective, but causes formation of one-atom-deep pits on atomically flat terraces, as seen by STM [34]. On the other hand, on polycrystalline samples, a smoothening effect was reported, caused by removal of oxidized gold grains in the ethanol [78]. A general review of UV/ozone treatment can be found in [79].
- **Plasma cleaning**: Exposure to oxygen plasma, followed by removal of the gold oxide layer (generated by the reactive oxygen) by dipping in ethanol [35]. The effectiveness of the cleaning procedure is similar to that of the UV/ozone – ethanol treatment, but the more aggressive oxygen plasma induces considerable roughening of the gold surface. The oxide layer can also be removed by subsequent exposure of the sample to hydrogen plasma [80]. The use of air (rather than oxygen) plasma for cleaning evaporated gold films was also reported [81].

1.9.3.1.1.2 **Sputtered Gold Films** The sputtering process includes bombardment of a target (e.g. gold) surface by energetic ions, resulting in ejection of atoms from the target that can be condensed on the surface to be coated, forming a film on the latter.

Pretreatment of the support prior to gold coating and cleaning of the sputtered gold prior to monolayer adsorption (chemical, electrochemical, or a combination), are similar to those described earlier for evaporated gold films. Borosilicate glass (microscope slides), mica, or silicon have been used as support materials. Adhesion is usually improved by precoating with Ti or Cr, but, in the case of glass, roughening by argon plasma may also be used [82, 83].

A nontextured, pebble-like structure was found for sputtered gold films [10], attributed to surface damage induced by the energetic impact and the resulting large number of nucleation sites. Annealing of such films leads to enlargement of the grains, most significantly in films on glass or mica. X-ray diffraction patterns of sputtered gold films on silicon indicated that the films were polycrystalline and highly oriented in the (111) direction [84]. Other authors described sputtered films on glass as having irregularly shaped domains that are "relatively flat at the nanometer level," separated by nanometer-sized valleys [85], while others estimated a roughness of ~6 nm for similar substrates [86].

In general, sputtered films are not used when well-defined (111) surfaces are sought (as in structural investigations), but are used in studies concerned with chemical or electrochemical properties of the resulting SAMs.

It seems clear from the literature that gold sputtering carried out in different labs results in films of very different properties, while gold evaporation is a much more uniform process in terms of films prepared by different groups.

1.9.3.1.1.3 **Electroless Deposited Gold Films** Electroless metal deposition refers to reductive deposition from a solution of the metal ions, but, unlike in electrolytic processes, the reduction is chemical (catalyzed by the substrate) and no external electrical current is applied during the deposition. It was shown that gold, deposited electrolessly onto glass, shows significant (200), (220), and (311) reflections in X-ray diffraction, although (111) is the major crystallographic orientation [87]. The same authors showed that the difference in substrate orientation (evaporated vs electroless gold) resulted in the tilt angle of the SAM chains being markedly smaller on electroless gold compared to that on evaporated gold.

Gold can also be electrolessly deposited on a seed layer of evaporated gold [88], resulting in a (111) textured substrate. This can be used to thicken gold microstructures while maintaining the morphology of the evaporated layer. Gold was deposited (1) by electroless deposition onto high-index glass, followed by annealing (250 °C for 3h) and electrochemical cleaning; or (2) as a thin (5 nm) film evaporated onto a 1-nm Ti adhesive layer on a glass microscope slide, followed by immersion in a gold plating solution ($Na_3Au(SO_3)_2$ and formaldehyde) at room temperature. The electroless deposition is initially catalyzed by the evaporated gold film, and then autocatalyzed by the electrolessly deposited gold. X-ray diffraction showed only (111) (and very small (222)) reflections. Epitaxial growth of electroless Au (111) on a seed layer of evaporated gold may be useful in microfabrication applications.

1.9.3.1.1.4 **Template-stripped Gold** Template-stripped gold (TSG) refers to evaporation of gold onto a highly smooth support (cleaved mica or highly polished silicon), separating the gold from the support, and using the gold face that was previously in contact with the support (Fig. 2).

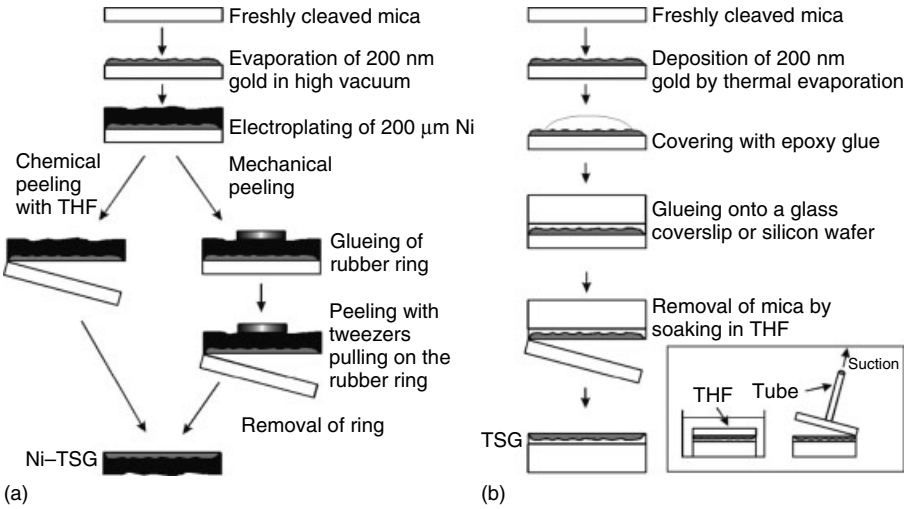


Fig. 2 (a) Schematic representation of Ni—TSG preparation. Adapted from [89]. (b) Schematic representation of the preparation of TSG surfaces using epoxy glue. Adapted from [90].

A common procedure consists of epitaxially growing gold on freshly cleaved mica, gluing the slide face down (i.e. the gold face) onto a silicon wafer, and stripping the mica off (Fig. 2b). The TSG surface is nearly as flat as that of the mica [91]. It has been described as an ultraflat polycrystalline Au (111) surface. The TSG thus produced cannot be used in solvents such as chloroform, which swell the epoxy glue and thus disrupt the gold layer. A number of alternative ways of preparing TSG have therefore been devised by Wagner et al. [90] (Fig. 3) using, for example, ceramic glues, which are inert in organic solvents. Hence, a 200-nm gold film was evaporated onto mica at 300 °C in either one or two steps. The latter procedure included interrupting the evaporation after 5-nm thickness, annealing for 6 h at 300 °C, and then concluding the deposition. The gold slides were glued face down onto Si (100) wafers or glass cover slips using epoxy glue and cured. Stripping was achieved by soaking in tetrahydrofuran (THF), which causes detachment of the mica layer from the gold. Optically transparent gold was similarly produced, by depositing only 20-nm gold. Gluing with Panavia required evaporation of an additional 200-nm layer of tin to facilitate the adhesion. Using Cerastil required a 10-nm titanium layer and a 150-nm silicon dioxide layer. In the two latter cases, the mica was stripped off using a Scotch tape. These surfaces were described as being particularly suitable for biological investigations. Epoxy- and ceramic-glued surfaces were shown by STM to have a (111) orientation and a mean roughness that was at least 10 times lower than that of evaporated gold surfaces. Characteristic triangular facets can often be seen (Fig. 3b). XPS analysis showed that only trace amounts of Si and Al were left on the surface.

A similar approach makes use of highly polished silicon wafers, claiming easier and more complete separation of the gold from the template [92]. Silicon wafers with thermally grown oxide layers were sonicated in double-deionized water, methanol, dichloromethane, and

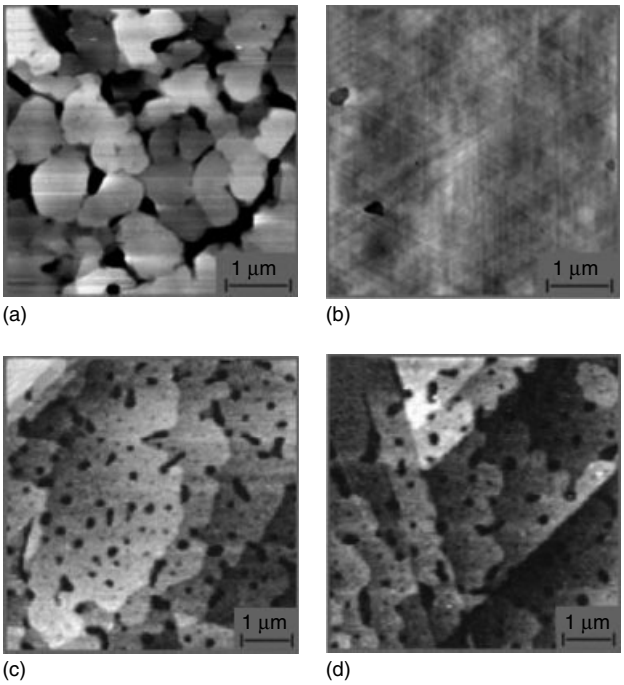


Fig. 3 (a) A gold (111) surface deposited on mica at 300 °C (mean roughness, 32.5 Å). (b) A TSG surface (mean roughness, 2.6 Å). (c) *N*-palmitoylcysteamine SAM prepared from disulfide precursor on the TSG substrate. (d) Same, formed by *in situ* acylation of a cysteamine SAM on TSG. All adapted from Ref. 90.

methanol. A 100–150 nm thick gold layer was evaporated at ambient temperatures. The samples were glued to glass slides with epoxy glue, and cured. The glass substrate was separated from the gold using tweezers. The average roughness of the gold surfaces thus obtained was ca. 2–3 Å, regardless of the size of the scanned area (in the micrometer range). Atomic force microscope (AFM) images did not reveal any structure on the surfaces; in only a few cases could grain boundaries be identified.

A different procedure for supporting the gold film was described by Rabe and coworkers [89], where TSG films were supported by a thick layer of electrodeposited Ni (Fig. 2a). These TSG films are completely solvent-resistant and can be readily used for monolayer self-assembly. Thus, 200-nm gold were evaporated onto freshly cleaved muscovite mica, followed by electroplating 200-μm Ni on the gold surface. The mica was stripped off mechanically using tweezers. The TSG substrates thereby obtained are flatter than those reported previously (due to minimal mechanical stress) and can be used in organic solvents. STM images showed atomically flat terraces extending up to several hundred nanometers and include triangular areas with 60° angles.

Of special interest is the TSG preparation procedure developed by Ulman and coworkers [93]. The new aspect in their scheme concerns the separation step, in which the mica is stripped from the

evaporated gold. In this procedure, the mica stripping is performed in the thiol solution, such that monolayer assembly is carried out *in situ* without any preexposure of the gold surface to the ambient. SAMs of exceptional quality were reported, showing essentially no contact-angle hysteresis.

1.9.3.1.2 **Bulk Gold**

1.9.3.1.2.1 **Polycrystalline Gold** Polycrystalline bulk gold substrates, usually in the form of wires, rods, disks or foils, are characterized by a surface that consists of randomly oriented crystallites. Although simple polycrystalline gold ''flags'' heated to incandescence in an air–gas flame may be used [77], the preparation of polycrystalline gold surfaces usually involves several steps. Pretreatment includes polishing, etching, and cleaning, and in some cases, encasement in epoxy or glass to provide a defined surface area. Polycrystalline surfaces may be used with macroscopic methods; when the primary intent of the study is concerned only with chemical or electrochemical properties of the monolayer; when a well-defined crystal plane is not needed for the implementation of a certain analytical method; and when the 2D lattice of the SAM is not of interest. The use of a polycrystalline substrate may be preferred for certain practical applications, such as, for example, electrodes for dispensable sensors.

Polishing is usually carried out with alumina slurry, while etching is done with hot nitric acid or with aqua regia for several minutes. On polycrystalline gold etched by either concentrated or dilute aqua regia ($3:1:6$ $HCl/HNO_3/H_2O$) at room temperature for 5 min, a ''splotchy'' surface was observed by optical microscopy, in which uniform regions were proposed to correspond to single grains of gold in the polycrystalline material [47]. SEM images showed rough ridges and deep etch pits.

Encasement to produce a well-defined substrate area was achieved, for example, in an electrochemical cell with a circular hole to which a gold electrode (consisting of a square of bulk polycrystalline gold) was pressed using an O-ring [94]. When applying gold wires, these are usually annealed and embedded in epoxy [95] or glass [96]. A gold disk (i.e. the wire cross-section) is then exposed, which is smoothed by sanding and polishing the end of the assembly. These substrates are easier to handle and eliminate the need for O-ring type cells [95]. Such wire substrates are usually pretreated by etching in dilute aqua regia or by cleaning in Piranha and rinsing with water or ethanol.

Another option is the use of a piece of bulk gold, which is coated with a thin layer of evaporated gold [97, 98]. Pieces of bulk polycrystalline gold were mechanically polished, rinsed with deionized water and hexane, and subjected to UV/ozone treatment. Then 200 nm gold were evaporated on both sides of the pieces. X-ray diffraction showed the surfaces to be polycrystalline with the predominant orientations (111), (220), and (311).

Specially roughened polycrystalline gold surfaces were used for surface-enhanced Raman scattering (SERS) experiments. Gao et al. [99] used a 4-mm gold disk sheathed in Teflon, which was mechanically polished with 0.3-μm alumina and rinsed with water. The gold surface was electrochemically roughened by repeated oxidation–reduction cycles in 0.1 M KCl, to yield SERS activity. In another study, roughened polycrystalline gold substrates were used for Raman spectroscopy, XPS, and electrochemistry [100]. Polycrystalline surfaces were cleaned

with Piranha, mechanically polished with successive grades of alumina down to 0.05 μm, rinsed in water and ethanol, and sonicated. The surfaces were electrochemically polished by scanning the potential at least 10 times between −0.2 and +1.2 V versus SCE in 1.0 M H_2SO_4. Milder roughening was achieved by applying three cycles in 0.1 M KCl (same potential range).

1.9.3.1.2.2 **Commercial Gold Single Crystals** As noted earlier, for certain applications, single-crystalline surfaces are essential. In some cases, gold films do not provide the necessary quality, or are difficult to prepare reproducibly, or are impractical to handle due to geometrical or instrumental reasons. Furthermore, if the study requires substrate orientations other than (111), there is almost no alternative to bulk single crystals. Depending on the initial quality of the crystal, all or some of the following preparative steps may be necessary: cutting, orienting, polishing, etching, cleaning, and annealing. The first two steps may be omitted if the commercial crystal is received in perfect condition. Orientation of the (111) plane to within 0.5° or better is advantageous, unless the study deals with the influence of a well-defined density of steps.

Polishing is usually done with alumina paste, while etching may be carried out by dipping in aqua regia or other solutions, for example, aqueous solution of KI (4M)/I_2 (6M) [28]. In cases where the crystal is not used in ultrahigh vacuum (UHV), flame annealing is widely applied, while the cleaning techniques are those described above for gold films. For crystals that are used in a vacuum chamber, the following procedures have been developed: The crystal is cleaned of trace carbon, sulfur, and calcium by neon ion bombardment at 300 K and 900 K [101] or argon ion bombardment [102]. Annealing is also performed in vacuum (a wide temperature range is found, for example, 900 K [101] or 800 °C [102]) while the cleanliness can be monitored with AES and LEED. This procedure produced large, impurity-free surfaces with atomically flat terraces, ∼500–1500 Å wide. The LEED patterns corresponded to the well-known gold $23 \times \sqrt{3}$ reconstruction [102]. Repeated cycles of argon sputtering and annealing led to perfect surfaces showing the herringbone structure of the reconstructed (111) surface [103–105].

1.9.3.1.3 **Gold Beads** The relatively simple procedure of preparing atomically flat gold surfaces in air using gold beads was originally developed by Hsu and Cowley for reflection electron microscopy [106]. Schneir et al. [107] followed that procedure in order to obtain highly ordered surfaces for STM. A 0.5-mm thick gold wire was melted in air by slowly pushing it into an oxygen–acetylene flame (set half-way between oxygen-rich and acetylene-rich). The wire forms a molten ball of gold at the end, which grows as more wire is fed into the flame. A wire of 4 cm produces a sphere ca. 2 mm across. As the gold ball crystallizes, atomically flat facets are formed on the sides. Most of these are perfect (111) crystal planes.

Gold beads were used, for example, by Crooks and coworkers [108, 109] to perform STM lithography on SAMs. The 0.25-mm diameter gold wire was first cleaned in Piranha solution, and then melted in a H_2/O_2 flame under nitrogen and annealed in a cooler region of the flame. This procedure yielded spheres 0.6–1 mm in diameter, which exhibited (111) facets, typically elliptical in shape with a long axis of ca. 100 μm, consisting

of atomically flat terraces of ca. 100-nm width. The beads were cleaned again in Piranha and rinsed with ethanol, and finally coated with silicone rubber leaving a single Au (111) facet exposed. This facet was polished electrochemically in 0.1 M $HClO_4/5 \times 10^{-5}$ M HCl solution.

1.9.3.1.4 **Oxidized Gold** Rubinstein and coworkers studied thiol monolayer assembly on preoxidized gold. The substrates were (111) textured gold films evaporated on glass; oxidation was achieved by either exposing the gold surface to oxygen plasma [35] or to UV/ozone [34]. The degree of oxidation was controlled by the length of exposure and monitored by ellipsometry and stripping voltammetry. The authors concluded that densely packed alkanethiol monolayers can be assembled on gold oxide surfaces, and that the (inherently unstable) gold oxide is stabilized for long periods of time under the blocking monolayer. In another study [36], monolayers were assembled in ethanol solutions onto gold surfaces held at positive potentials. It was shown that the net result of the simultaneous monolayer adsorption (enhanced by the applied potential), gold oxidation, and oxidative monolayer desorption, is considerably faster monolayer formation relative to the case of no applied potential. It was also shown that, unlike thiols, disulfides do not form monolayers on oxidized gold.

Woodward et al. [110] assembled a series of alkanethiols on thin (5 nm) gold films evaporated on Cr-primed Si wafers and preoxidized by UV/ozone treatment. AFM imaging after self-assembly showed surfaces covered with islands, whose height scales with the alkanethiol chain length and is about twice the molecule length. No oxygen was found (by XPS) on the surface. The authors suggested that the islands are gold-alkanethiolate bilayers, formed by reaction of the alkanethiols with gold oxide.

Grunze and coworkers [111] studied the formation of alkanethiol SAMs on gold (100 nm films on silicon + Ti intermediate layer), sputtered with Ar and oxidized by exposure to atomic oxygen in UHV. Gold oxide formation was monitored by XPS, up to 16 Å thick (after 20 min). The oxide layer was not affected by water rinse, but was gradually removed in ethanol (see section on Cleaning procedures for evaporated gold samples) or by exposure to air. The self-assembly process was strongly influenced by the presence of the oxide. Encapsulated gold oxide was found under the monolayer, which contained more thiol molecules than similar monolayers on regular gold.

1.9.3.1.5 **Other Gold Substrates for Special Applications** Several other types of gold substrates have been reported in connection with certain characterization methods or specific applications. A number of these are described below.

1.9.3.1.5.1 **Gold Powder** The adsorption of a thiol on gold powder was used to study the change in the chemical composition of the immersion solution during the modification process [112]. Gold powder (aggregates of spherical particles, 0.2–0.6 μm diameter) was passed through 100 mesh sieves and cleaned with ethanol. Self-assembly was carried out by shaking the powder in ethanolic solution of aminobenzenethiol while monitoring the UV spectrum of the supernatant solution.

1.9.3.1.5.2 **Gold Colloids (Nanoparticles)** Gold nanoparticles capped with thiol SAMs were synthesized by Brust, Schiffrin, and coworkers using a two-phase

procedure [113]. The monolayer-protected nanoparticles are hydrophobic and form stable colloids in organic solvents. Following this original work, the use of monolayer-capped metal nanoparticles has become widespread, as summarized in several review articles and books (see e.g. [114]).

1.9.3.1.5.3 **Transparent Gold Foil** Strong and Whitesides [115] used a variation of Pashley's method [116, 117] to produce single-crystal gold foils for TEM investigation. Gold was evaporated onto freshly cleaved NaCl (100) and BaF_2 (111) surfaces held at 300 °C. After evaporation of 60–80 nm gold, the temperature was raised to 450 °C and subsequently lowered slowly to room temperature. The supports were then dissolved in water to yield oriented crystalline foils, 40–80 nm thick, which were floated onto TEM grids and sandwiched between perforated covers to allow electrochemical pretreatment. The foils were rinsed with distilled water before immersing them in the adsorption solution, and used for TEM and electron diffraction studies of the structures of SAMs of various organosulfur compounds.

1.9.3.1.5.4 **Ultrathin Gold Island Films** Ultrathin (nominal thickness, ca. 10–100 Å) gold films evaporated on mica [118, 119] or quartz [120], possibly followed by annealing, were used by Rubinstein and coworkers as substrates for transmission of UV-vis spectroscopy of monolayers on gold (Fig. 4). Such films exhibit an array of (111) textured islands, increasing in size with increasing gold nominal thickness. The use of gold island films enabled to perform transmission UV-vis spectroscopy of chromophoric monolayers, with submonolayer sensitivity. Monitoring changes in the gold localized surface plasmon absorbance, resulting from adsorption of molecules on the gold island surface, was suggested as a general method for sensing molecular binding to gold [120, 121] as well as biosensing [122]. The morphology and optical properties of gold island films prepared by evaporation on silanized glass were studied [123].

A different approach to the preparation of gold and silver island films, termed *nanosphere lithography*, was developed by Schatz, Van Duyne and coworkers. The metal is evaporated through a mask comprising hexagonally close-packed polystyrene nanospheres, creating an array of triangularly shaped islands. Changes in the localized surface plasmon absorbance were measured during self-assembly of an organic multilayer [124].

1.9.3.1.5.5 **Electroplated Gold Films** Solid metal blocks were used to facilitate mounting of samples in spectrometers and cryostats in the study of semiconductor nanocrystals bound to metal surfaces [125]. The samples consisted of aluminum blocks on which gold films (1 μm) were electroplated. In this procedure, significant etching pretreatment of the aluminum produced a much smoother surface with a mirror finish. Such block samples, though ideal for low-temperature and photoemission applications, were rough and showed relatively low monolayer coverages

1.9.3.1.5.6 **Composite Substrates** A small number of studies have been published that deal with monolayer self-assembly on composite surfaces, where one of the surface components is gold. Whitesides and coworkers [126] produced gold–Al_2O_3 composite substrates by microlithography, on which they formed

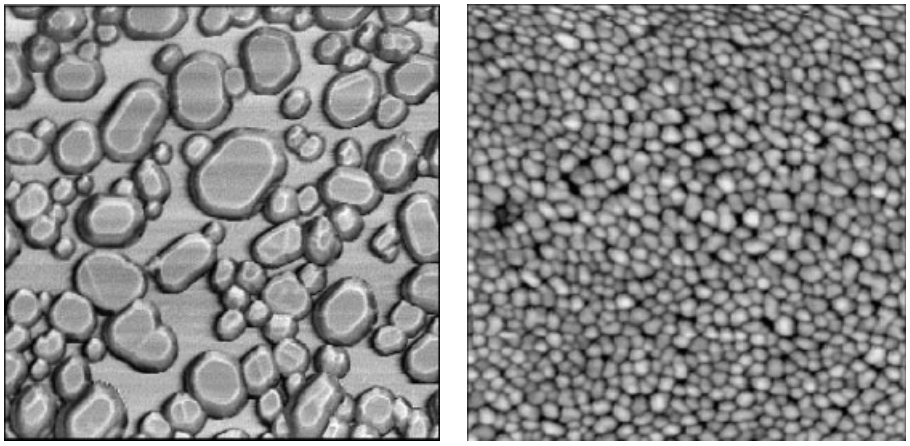


Fig. 4 (a) Noncontact AFM image (500×500 nm^2) of a gold island film (nominal thickness, 25 Å) evaporated on quartz at 0.05 Å s^{-1}. Adapted from [120]. (b) Tapping mode AFM phase-shift image of a gold island film (nominal thickness, 100 Å) evaporated on mica at 0.2–0.4 Å s^{-1} and annealed for 3 h at 250 °C (1.0×1.0 μm^2). Adapted from [119].

mixed monolayers comprising thiol and carboxylate components by self-assembly from a common solution. They demonstrated (using scanning Auger) "orthogonal self-assembly," that is, selective binding of the thiols to the gold and the carboxylates to the Al_2O_3.

A different approach was reported by Shabtai et al. [43, 44], who prepared gold–SiO_2 composite surfaces. The process included evaporation of gold onto oxide-free (hydrogen passivated) Si (111) wafers, followed by thermal diffusion of Si through the gold film to reach the gold surface, where it forms SiO_2 islands. The authors assembled mixed thiol–silane monolayers on the gold–SiO_2 surfaces, and, using a new XPS-based method (Controlled Surface Charging), they were able to establish selective binding of the thiols to the gold and the silanes to the SiO_2.

1.9.3.1.6 **Comparative Studies** A number of studies have been published where monolayer adsorption on different gold surfaces was compared. Some of these are summarized below.

Creager et al. [47] suggested that the gold topography (in terms of microscopic surface roughness) plays a role in alkanethiol adsorption. This was tested by comparing the blocking properties of alkanethiol monolayers on evaporated gold films versus etched polycrystalline gold electrodes. The defectiveness of the monolayers varied with the gold preparation method, that is, bulk gold substrates etched with aqua regia yielded monolayers with significantly fewer defects and superior blocking of electrochemical reactivity than those prepared on evaporated gold films. STM showed that the etched gold, while macroscopically rough, is microscopically flatter than the evaporated gold.

Guo et al.[19] showed that the blocking properties of SAMs change with the pinhole density, decreasing dramatically as the substrate is made smoother. For evaporated gold on mica, they showed that (1) the gold surface roughness was

controlled by the mica temperature during evaporation, influencing, in turn, the blocking characteristics of the SAM; and (2) the formation of dense blocking SAMs was inhibited as the gold became smoother. By comparing these substrates with gold on Si (which is macroscopically rougher), pretreated in acidic peroxide and by potential cycling, they suggested that Au surface pretreatment, rather than surface roughness, plays the more important role in molecular self-assembly.

Porter and coworkers [127] compared SAMs on gold films (300 nm) evaporated on Si (100), mica, and glass. Silicon and glass (but not mica) were precoated with a 15-nm Cr adhesion layer. Si and glass samples were not annealed, while mica samples were annealed. The authors used voltammetric reductive desorption and structural characterizations of thiol SAMs, as well as morphological assessment of the substrates. They concluded that differences in the voltammetry originate from difference in the microscopic roughness of the substrates, that is, the surface of the gold on mica is strongly (111) terraced, while the surface of gold on glass or Si has a higher step density. In other words, different types of monolayer binding sites produce differences in the reductive monolayer desorption.

1.9.3.2 **Silver**

As in the case of gold, the most common substrates are evaporated films and bulk metal, showing different degrees of crystallinity.

1.9.3.2.1 **Silver Films on Supports** Support materials for evaporated silver films include silicon (either (111) or (100) orientations), freshly cleaved mica, or glass slides. In most cases, the glass or silicon substrate is precoated with a thin (several nm) Cr adhesion layer. Film thicknesses usually range between 100 and 200 nm, using evaporation rates of 5–30 Å s^{-1} and a substrate temperature of ca. 300 °C (preferred). As silver oxidizes spontaneously in the ambient, postevaporation filling of the evaporator with argon or nitrogen is recommended. The presence of oxide on the silver surface appears to play only a minor role with respect to SAMs, but it has to be considered. Surface composition of evaporated Ag films, as studied by AES, showed sulfur, chlorine, carbon, and oxygen, reflecting the formation of ca. 2–5 monolayers of oxide [128]. This study showed that the oxygen content of freshly evaporated silver films almost doubled for 2 h in laboratory atmosphere, pointing to the need to avoid unnecessary delay in transferring the substrates to the adsorption solution. Transfer of evaporated Ag films under argon to the modification solution was reported, although there are indications that even under these conditions the surfaces are covered by a thin oxide film [129].

Surface characterization of silver films evaporated on mica or Si showed that the films consisted of small (ca. 25 nm) rough crystallites. The underpotential deposition (UPD) experiments indicated that the Ag films on all different supports were composed of Ag (100) and/or Ag (110) domains [21]; this differs from other reports on evaporated Ag films, which are usually described as heavily (111) textured (e.g. [130]), though less so than gold films prepared under similar conditions. Dhirani et al. [131] described silver films on mica as large grains, ca. 500 nm in diameter, with the tops showing atomically flat terraces containing monatomic steps. In another study, (111)-oriented surfaces (200 nm Ag on mica, evaporated at 250–300 °C) with

atomically flat terraces as large as several 1000 nm^2 [132] were reported. A comparative study of Ag, Au, Pd, and Cr films on mica showed increasing grain size and grain flattening as the substrate temperature is increased (−150 to 400 °C) [12].

Silver is the substrate of choice for SERS experiments, where bulk silver is usually used (see Sect. 1.9.3.2.2). However, if silver is evaporated on preroughened slides, the resulting substrates are rough enough for SERS purposes. In one such procedure [133], microscope slides were cleaned and then roughened by depositing a 600-nm thick layer of calcium fluoride, followed by evaporation of 50 nm of silver.

Jennings and Laibinis [134, 135] prepared atomic layers of silver on evaporated gold films by electrochemical UPD, to be used as substrates for self-assembly of alkanethiols. The UPD process was carried out in aqueous Ag_2SO_4 solution, and the Au/Ag(UPD) substrates were transferred in air to the adsorption solution.

Discontinuous, island-type silver films were prepared by Van Duyne and coworkers using nanosphere lithography (see Sect. 1.8.3.1.5.4) [136]. They were used primarily to study the properties of the localized surface plasmon absorbance of such films, including investigation of the dependence of the absorbance on the chain length of alkanethiol SAMs adsorbed on the island films [137].

1.9.3.2.2 **Bulk Silver** Polycrystalline bulk silver substrates are mainly used for SERS analysis of SAMs, and also with other analytical techniques. SERS requires roughening of the sample (usually a silver disk), carried out by polishing with alumina grid and/or sanding on silicon carbide sandpaper (the roughness in both cases depends on the grid size), usually followed by electrochemical cycling, for example, in 0.1 M KCl [138, 139]. Another procedure for electrochemical roughening of bulk Ag includes three cycles in 1 M $NaClO_4$, from −0.5 to 0.6 V versus Ag/AgCl, holding the potential for 30 s and 10 s at the negative and positive potential limits, respectively [140]. After roughening, the substrate is rinsed with water or ethanol and inserted into the adsorption solution. Silver substrates (including foils) may also be roughened by etching in HNO_3 (>3.5 M) [141, 142].

1.9.3.3 Copper

SAMs on copper have attracted relatively large attention, because of possible application in corrosion protection, interconnects in solid-state devices, and as a model system for self-assembly on nonnoble metals. In addition to this application-oriented interest, several basic studies have been conducted on the properties and structure of SAMs on copper.

1.9.3.3.1 **Copper Films on Supports** The supports of choice for evaporated copper films are mica, glass, and silicon, the latter two requiring an intermediate layer of Cr to facilitate the adhesion. Film thicknesses are similar to those of gold, that is, 5–20 nm of Cr and 100–200 nm of Cu. Surface oxidation in air is more severe than in the case of silver; hence, postdeposition filling of the evaporator has to be done with argon or nitrogen, and the samples have to be transferred under argon or nitrogen flow. If this procedure is carried out no later than 5 min after evaporation, no oxide is found on the copper surface [143].

Freshly evaporated copper samples left in air prior to self-assembly are quickly covered with an oxide layer. Better-defined evaporated copper surfaces were obtained by sputter cleaning and subsequent

annealing (320 °C for 3 h) under UHV conditions [144]. Oxide thicknesses of samples not deliberately oxidized were determined by XPS. The thickest oxide layer (>25 Å) was found on a sample left to age in air; freshly evaporated samples, or sputter-annealed samples exposed to air for 2 min, showed oxide thicknesses of ca. 10 Å; sputter-annealed samples freshly out of the UHV chamber yielded an average oxide thickness of less than 1 Å. Self-assembly from ethanol solutions produced inferior monolayers compared with toluene solutions, presumably due to strong adsorption of ethanol on Cu [144].

Other XPS studies on Cu films evaporated on mica showed that although untreated Cu surfaces have a relatively large amount of CuO and $Cu(OH)_2$ on the surface [145], after thiol self-assembly, no CuO or $Cu(OH)_2$ was detectable, the amount of oxygen being reduced by a factor of 20. The authors concluded that the copper oxide/hydroxide is transformed to copper thiolate.

Copper films evaporated on silicon were described as heavily {111} textured, but less so than gold prepared under similar conditions [130]. Unlike Au and Ag, Cu films are sensitive to the specific evaporator used. Copper deposition under poor vacuum conditions produced random polycrystalline surfaces.

A different approach to obtaining copper films was reported by Laibinis and coworkers, who prepared atomic layers of copper by electrochemical UPD on evaporated gold films. The Au/Cu(UPD) samples were used as substrates for self-assembly of alkanethiol [135] or alkanephosphonate [146] monolayers. The UPD process was carried out in aqueous $CuSO_4$ solution, and the Au/Cu(UPD) substrates were transferred in air to the adsorption solution.

1.9.3.3.2 **Bulk Copper** Preparation of bulk copper surfaces (samples may consist of rods, foils, or disks) includes polishing, rinsing, and in some cases degreasing. When samples are used for SERS, a roughening step is added. This was achieved by 4 min etching in 12% HNO_3 under vigorous stirring [133]. Copper foils, immersed in 3–5 M HNO_3 for several minutes, were described as having a red and sponge-type surface [147]. If no roughening is desired, initial preparation of the surface may consist of polishing with emery paper and alumina and ultrasonic cleaning in water and acetone [148]. Surface oxide removal for SAM adsorption may be achieved by galvanostatic reduction (1 mA cm^{-2} for 5 min) of a Cu electrode in 1 N $HClO_4$ under N_2 atmosphere, followed by rinsing in deaerated $EtOH/H_20$ (1 : 1) [148]. Another approach consists of controlled oxide growth and its chemical removal [149]. Polycrystalline Cu sheets were polished with alumina powder (0.3 μm), rinsed with deionized water and degreased ultrasonically in acetone. Oxide was grown by immersion in a hydrogen peroxide solution at 100 °C for 15 min. Removal of the oxide layer was carried out by etching in a 7 M HNO_3 solution for 1 min.

1.9.3.3.3 **Copper Oxide** It has been suggested that the oxide layers on copper surfaces may be instrumental in the formation of SAMs on copper. This was investigated by Sung et al. [149], who carried out a comparative study on SAMs on bare copper and on well-defined copper oxide layers. A polycrystalline copper sheet (polished, rinsed, and degreased ultrasonically) was superficially oxidized by 15 min immersion in hydrogen peroxide at 100 °C, generating an oxide layer of ca. 50 nm thickness. The authors found that alkanethiols do not adsorb directly

onto the oxidized copper, but rather reduce the oxide upon disulfide formation. The monolayer is thus formed on a reduced Cu surface. These findings are in agreement with the previous work of Ron et al. [144], who showed that high-quality alkanethiol monolayers can be formed on copper surfaces covered with a thin oxide layer, proposing the same mechanism.

1.9.3.4 **Iron**

Iron in air is covered with a thick and dense oxide layer, which is further blocked with contaminants such as water, CO, or hydrocarbons. Clean oxide-free iron surfaces can be prepared by Ar ion sputtering in UHV or by electrochemical reduction.

Stratmann and coworkers [150] described a procedure for thiol monolayer assembly on metallic iron, transferring the electrochemically reduced iron substrate to the modification solution under potential control. Vacuum melted Fe electrodes were polished and cleaned by dipping in a mixture of nitric and sulfuric acid, then etched slightly in dilute hydrochloric acid, and rinsed thoroughly with water. Metallic Fe surface was obtained by holding the electrode potential at −0.72 V versus standard hydrogen electrode (SHE) in aqueous 1 M $HClO_4$. The substrate is then slowly pulled under potential control through a layer of the thiol floating on the aqueous phase, allowing the thiol to form an SAM on an oxide-free Fe [151, 152]. This procedure does not ensure complete prevention of iron surface reoxidation during transfer through the thiol solution [153], resulting in a mixed thiol–oxide surface. The oxide defects may be healed by cycling the SAM-covered iron electrode several times in aqueous O_2-free solution, upon removing the oxide and rearranging the excess thiol on the surface.

1.9.3.5 **Aluminum**

Aluminum was evaporated onto glass slides, using an MPS adhesion layer [66]. The aluminum samples were plasma-etched prior to self-assembly of mercaptoacetic acid, to form monolayer bound to the Al surface through the acid groups. The free thiol groups were then used to bind semiconductor nanocrystals to the surface.

1.9.3.6 **Platinum**

Polycrystalline Pt disks or foils as well as single-crystalline samples have been used. Minor differences in thiol monolayer coverage are found when comparing single crystalline and polycrystalline Pt surfaces. Electrochemical cycling affects the coverage on the polycrystalline surface less than it does on the crystalline surface [154].

A polycrystalline Pt surface was polished with successive grades of alumina (down to 0.05 μm size), and then rinsed with ethanol and dipped in the thiol solution [155]. A Pt (111) surface was prepared by annealing a single crystal in a hydrogen flame for 10 min, slow cooling under Ar and submersion in deaerated water. The sample was then dipped in fuming sulfuric acid for 10 min, removed, and rinsed with deionized water, dried under Ar and immersed in the thiol solution [74]. The kind of sample used depends on the technique of choice. While a single crystal was used for sum frequency generation (SFG) measurements, Pt films on quartz were used for Fourier transform infrared (FTIR) spectroscopy. The latter were prepared by chemical vapor deposition (using platinum (II) acetylacetonate) onto quartz slides. FTIR showed that rinsing with ethanol left a hydrocarbon film on the Pt surface, while rinsing with chloroform did not. As previously reported for copper substrates [144], thiol monolayers prepared in ethanol solutions produced poor spectral

features, suggesting chemical interaction between alcohols and Pt [74].

Pt microelectrodes [156] were fabricated from 5- and 25-μm Pt wires by sealing into soft glass followed by polishing with emery paper and successive grades alumina slurry, followed by sonication in deionized water. The polished electrodes were electrochemically cleaned by cycling in 0.5 M H_2SO_4. The potential was then held in the double-layer region at a sufficiently negative value to ensure complete reduction of any surface oxide. The electrode was then cycled between −0.30 and 0.70 V (vs Ag/AgCl) in 0.1 M $LiClO_4$ until hydrogen desorption was complete. The surface roughness factor was between 1.5 and 2.0. The electrodes were used for the study of SAMs of Ru/Os dinuclear complexes on the Pt surface.

Ultrathin (10 nm) Pt films were obtained by argon sputtering on glass substrates. They were used for demonstrating redox switching [157] and photoswitching [158] of SAMs adsorbed on the Pt surface, using transmission UV-vis spectroscopy to monitor the switching. The ultrathin Pt substrates are particularly suitable for transmission spectroscopy of SAMs due to the transparency of Pt films in the visible region.

1.9.3.7 Nickel

As nickel is of substantial technological importance, studies of thiol monolayers on nickel are largely application oriented. One of the objectives is to develop protective treatments for Ni-based contact materials for separable connectors in electronic systems, and to find coatings that inhibit Ni corrosion without increasing contact resistance. Law et al. [159] studied protective treatments for Ni-based contact materials by cyclic voltammetry and contact resistance measurements, using brass coins coated with Ni deposits of ca. 2.54 μm thickness. Bright deposits were prepared in standard Ni sulfamate baths, while gray Ni alloys of low phosphor content were obtained in ammoniacal baths. The substrates were dipped into adsorption solutions immediately after plating.

Mekhalif et al. [160–162] studied the formation and structure of alkanethiol SAMs on nickel, comparing cleaned/polished substrates with others that underwent additional electrochemical pretreatment to remove surface oxide. Polycrystalline Ni disks were mechanically polished with diamond paste and rinsed with acetone and ethanol. The additional electrochemical pretreatment consisted of 20 min reduction in 1 M $HClO_4$ at 0.7 V versus SCE. Exposure time to the atmosphere prior to self-assembly was less than 3 s. Samples that were not electrochemically treated produced poor quality SAMs, with considerable part of the thiolates oxidized to sulfonates and sulfinates [160, 162]. The poor organization of the monolayers on such surfaces was reflected in their frictional, electrical, and wear properties [161]. Electrochemical pretreatment, on the other hand, led to monolayers with significantly enhanced properties, that is, improved molecular order, chemical stability, and resistance to electrochemical oxidation.

1.9.3.8 Titanium

Titanium offers a combination of low density, high mechanical stability, and a passivating oxide layer, making it technologically important for sophisticated materials and medical implants. In the latter case, the corroding action of the biological environment and rejection by the living tissues necessitate the modification of Ti surfaces with organic layers, such as

polymer films. Coating of titanium with conducting polymers, serving to prevent corrosion or for paint adhesion is also found. A possible approach to enhancing polymer adhesion to an oxidizable substrate such as Ti is coating of the surface with thiol SAMs. Mekhalif et al. [163] used thiol SAMs on Ti as primers for electrochemical polymerization. The substrates were polycrystalline Ti disks, mechanically polished with abrasive paper, rinsed, and sonicated with acetone and acetonitrile followed by transfer to the thiol solution.

1.9.3.9 **Stainless Steel**

SAMs on stainless steel are usually application oriented, due to the importance of thin films on stainless steel for corrosion protection and biocompatibility of medical implants. Two basic approaches have been presented, that is, SAM adsorption on reduced, oxide-free stainless steel and adsorption on the stainless steel native oxide.

Sukenik and coworkers [164] prepared alkylthiol and alkylamine SAMs on oxide-free stainless steel. The substrate was a stainless steel rod of 1 cm diameter, polished, rinsed, and sonicated. Electrochemically reduced (oxide-free) surfaces were obtained by application of −1.2 V (vs SCE) in deaerated $HClO_4$ solution. SAMs were assembled onto the reduced surface by exposure to 10 mM octadecylmercaptan or 50 mM octadecylamine. The procedure was optimized and further used to initiate formation of multilayers.

Mekhalif and coworkers [165] adopted the other approach, that is, assembly of organosilane molecules on oxide-covered stainless steel. The substrate was bulk stainless steel, polished, cleaned, and sonicated. Two organosilanes of similar chain length, a trichlorosilane, and a triethoxysilane, both terminated with hydrophobic perfluorinated tails, were assembled onto the stainless steel native oxide. The results indicate that the trichlorosilyl groups is more favorable for grafting of SAMs on stainless steel surfaces, forming denser monolayers in shorter times.

Formation of n-alkanoic acid monolayers on the native oxide of stainless steel under electrochemical conditions was described by Mandler and coworkers [166]. Stainless steel disks or plates were polished, washed, and sonicated. The clean electrodes were immersed into a deaerated solution containing 0.1-mM carboxylic acid in acetonitrile electrolyte solution. A potential sweep between −0.8 and 1.2 V (vs Ag/AgBr) was applied (10 cycles) to form a monolayer under oxidative conditions. The results show that long-chain acids form close-packed, highly ordered SAMs, while short chains result in disordered arrays.

A special case of SAM formation on oxidized stainless steel was reported by Sukenik and coworkers [167]. The stainless steel surface was polished, washed, and sonicated, followed by exposure to air plasma for 1 h. A thin layer (ca. 3 nm) of SiO_2 was formed on the oxidized stainless steel by treatment with tetraalkylorthosilicate. This layer served as an anchor for subsequent attachment of alkyltrialkoxysilane films.

1.9.3.10 **Mercury**

Mercury offers an ideal, atomically flat liquid metal surface with no preparation needed and with high affinity for thiol adsorption. SAMs on mercury surfaces are notable for the absence of defects, compact structure, and high reproducibility. One possibility is to use a homemade hanging mercury drop electrode (HMDE), which can be immersed in a thiol solution or passed through a layer of thiols floating on the electrolyte [168–171]. A static mercury

drop electrode (SMDE) [172] was also used, prepared by delivering ca. 3 mg of mercury onto the tip of a Pt wire held at a reducing potential in sulfuric acid to avoid oxide formation. The Pt wire is sealed in soft glass, mechanically polished, sonicated, and electrochemically cleaned prior to application of the Hg drop. The SMDE may be immersed in a solution or the neat thiol. Drops of Hg covered with SAMs were stacked to form capacitors in series [173].

STM measurements were carried out with a Hg sessile drop before and after thiol adsorption, which involve a complex drop flow system allowing control of the drop size and flattening of the drop surface [174]. Compression of the Hg drop to a flat shape allowed STM images to be obtained.

References

1. H. O. Finklea, in *Electroanalytical Chemistry* (Eds.: A. J. Bard, I. Rubinstein), Marcel Dekker, New York, 1996, Vol. 19.
2. L. Brück, *Ann. Phys. (Leipzig)* **1936**, *26*, 233.
3. O. Rüdiger, *Ann. Phys. (Leipzig)* **1937**, *30*, 505.
4. D. W. Pashley, *Adv. Phys.* **1965**, *14*, 327.
5. H. Poppa, K. Heinemann, A. G. Elliot, *J. Vac. Sci. Technol.* **1971**, *8*, 471.
6. C. E. D. Chidsey, D. N. Loiacono, T. Sleator et al., *Surf. Sci.* **1988**, *200*, 45.
7. X.-Y. Zheng, Y. Ding, L. A. Bottomley et al., *J. Vac. Sci. Technol., B* **1995**, *13*, 1320.
8. J. Vancea, G. Reiss, F. Schneider et al., *Surf. Sci.* **1989**, *218*, 108.
9. S. Buchholz, H. Fuchs, J. P. Rabe, *Adv. Mater.* **1991**, *3*, 51.
10. Y. Golan, L. Margulis, I. Rubinstein, *Surf. Sci.* **1992**, *264*, 312; **1992**, *273*, 460.
11. Y. Golan, L. Margulis, S. Matlis et al., *J. Electrochem. Soc.* **1995**, *142*, 1629.
12. S. Buchholz, H. Fuchs, J. P. Rabe, *J. Vac. Sci. Technol., B* **1991**, *9*, 857.
13. K. Kobayashi, H. Yamada, T. Horiuchi et al., *Appl. Surf. Sci.* **1999**, *144–145*, 435.
14. C. A. Alves, E. L. Smith, M. D. Porter, *J. Am. Chem. Soc.* **1992**, *114*, 1222.
15. E. L. Smith, C. A. Alves, J. W. Anderegg et al., *Langmuir* **1992**, *8*, 2707.
16. S. Xu, J. N. Cruchon-Dupeyrat, J. C. Garno et al., *J. Chem. Phys.* **1998**, *108*, 5002.
17. K. Tamada, J. Nagasawa, F. Nakanishi et al., *Langmuir* **1998**, *14*, 3264.
18. K. Tamada, M. Hara, H. Sasabe et al., *Langmuir* **1997**, *13*, 1558.
19. L.-H. Guo, J. S. Facci, G. McLendon et al., *Langmuir* **1994**, *10*, 4588.
20. C. Schönenberger, J. Jorritsma, J. A. M. Sondag-Huethorst et al., *J. Phys. Chem.* **1995**, *99*, 3259.
21. C. A. Widrig, C. Chung, M. D. Porter, *J. Electroanal. Chem.* **1991**, *310*, 335.
22. M. Kawasaki, T. Sato, T. Tanaka et al., *Langmuir* **2000**, *16*, 1719.
23. C. Nogues, M. Wanunu, *Surf. Sci.* **2004**, *573*, L383.
24. M. M. Walczak, D. D. Popenoe, R. S. Deinhammer et al., *Langmuir* **1991**, *7*, 2687.
25. D. E. Weishaar, M. M. Walczak, M. D. Porter, *Langmuir* **1993**, *9*, 323.
26. C. A. Alves, M. D. Porter, *Langmuir* **1993**, *9*, 3507.
27. C. A. Widrig, C. A. Alves, M. D. Porter, *J. Am. Chem. Soc.* **1991**, *113*, 2805.
28. W. B. Caldwell, D. J. Campbell, K. Chen et al., *J. Am. Chem. Soc.* **1995**, *117*, 6071.
29. C. A. Panetta, P. Wei-Fan, R. Fattah et al., *J. Org. Chem.* **1999**, *64*, 2919.
30. C. A. Goss, D. H. Charych, M. Majda, *Anal. Chem.* **1991**, *63*, 85.
31. R. H. Terrill, T. A. Tanzer, P. W. Bohn, *Langmuir* **1998**, *14*, 845.
32. W. R. Everett, I. Fritsch-Faules, *Anal. Chim. Acta* **1995**, *307*, 253.
33. E. Sabatani, J. Cohen-Boulakia, M. Bruening et al., *Langmuir* **1993**, *9*, 2974.
34. H. Ron, S. Matlis, I. Rubinstein, *Langmuir* **1998**, *14*, 1116.
35. H. Ron, I. Rubinstein, *Langmuir* **1994**, *10*, 4566.
36. H. Ron, I. Rubinstein, *J. Am. Chem. Soc.* **1998**, *120*, 13444.
37. K. Uosaki, Y. Sato, H. Kita, *Langmuir* **1991**, *7*, 1510.
38. K. Uosaki, Y. Sato, H. Kita, *Langmuir* **1991**, *7*, 1510.
39. N. L. Abbott, G. M. Whitesides, *Langmuir* **1994**, *10*, 1493.

40. C. B. Gorman, H. A. Biebuyck, G. M. Whitesides, *Langmuir* **1995**, *11*, 2242.
41. M. Wanunu, A. Vaskevich, I. Rubinstein, *J. Am. Chem. Soc.* **2004**, *126*, 5569.
42. M. V. Baker, J. Landau, *Aust. J. Chem.* **1995**, *48*, 1201.
43. K. Shabtai, I. Rubinstein, S. R. Cohen et al., *J. Am. Chem. Soc.* **2000**, *122*, 4959.
44. K. Shabtai, S. R. Cohen, H. Cohen et al., *J. Phys. Chem. B* **2003**, *107*, 5540.
45. S. D. Evans, K. E. Goppert-Berarducci, E. Urankar et al., *Langmuir* **1991**, *7*, 2700.
46. S. D. Evans, R. Sharma, A. Ulman, *Langmuir* **1991**, *7*, 156.
47. S. E. Creager, L. A. Hockett, G. K. Rowe, *Langmuir* **1992**, *8*, 854.
48. C. Miller, P. Cuendet, M. Grätzel, *J. Phys. Chem.* **1991**, *95*, 877.
49. G. P. López, H. A. Biebuyck, G. M. Whitesides, *Langmuir* **1993**, *9*, 1513.
50. L. Sun, L. J. Kepley, R. M. Crooks, *Langmuir* **1992**, *8*, 2101.
51. A. Hatzor, T. Moav, H. Cohen et al., *J. Am. Chem. Soc.* **1998**, *120*, 13469.
52. R. G. Nuzzo, F. A. Fusco, D. L. Allara, *J. Am. Chem. Soc.* **1987**, *109*, 2358.
53. T. H. Ong, P. B. Davies, C. D. Bain, *Langmuir* **1993**, *9*, 1836.
54. H. Imahori, T. Azuma, A. Ajavakom et al., *J. Phys. Chem. B* **1999**, *103*, 7233.
55. T. W. Schneider, D. A. Buttry, *J. Am. Chem. Soc.* **1993**, *115*, 12391.
56. D. S. Karpovich, G. J. Blanchard, *Langmuir* **1994**, *10*, 3315.
57. H. J. Kim, S. Kwak, Y. S. Kim et al., *Thin Solid Films* **1998**, *327*, 191.
58. S. Lingler, I. Rubinstein, W. Knoll et al., *Langmuir* **1997**, *13*, 7085.
59. Y. Li, R. T. McIver Jr., J. C. Hemminger, *J. Am. Chem. Soc.* **1992**, *114*, 2428.
60. C. T. Ross, L. Sun, R. M. Crooks et al., *Langmuir* **1991**, *7*, 620.
61. A. J. Ricco, G. C. Frye, S. J. Martin, *Langmuir* **1989**, *5*, 273.
62. L. Sun, R. M. Crooks, A. J. Ricco, *Langmuir* **1993**, *9*, 1775.
63. W. Haiss, D. Lackey, J. K. Sass et al., *J. Chem. Phys.* **1991**, *95*, 2193.
64. T. Will, M. Dietterle, D. M. Kolb, in *Nanoscale Probes of the Solid/Liquid Interface, NATO ASI Series E, Vol. 288* (Ed.: A. A. Gewirth, H. Siegenthaler), Kluwer Academic Publishers, Dordrecht, 1995, p. 137.
65. M. H. Dishner, M. M. Ivey, S. Gorer et al., *J. Vac. Sci. Technol., A* **1998**, *16*, 3295.
66. D. Porath, E. Bar-Sadeh, M. Wolovelsky et al., *J. Vac. Sci. Technol., A* **1995**, *13*, 1165.
67. A. H. Schäfer, C. Seidel, L. Chi et al., *Adv. Mater.* **1998**, *10*, 839.
68. A. H. Schäfer, Diploma Thesis, University of Münster, Münster, 1997
69. H. Schönherr, G. J. Vansco, B.-H. Huisman et al., *Langmuir* **1999**, *15*, 5541.
70. J.-P. Bucher, L. Santesson, K. Kern, *Langmuir* **1994**, *10*, 980.
71. F. Bensebaa, R. Voicu, L. Huron et al., *Langmuir* **1997**, *13*, 5335.
72. W. S. V. Kwan, L. Atanasoska, L. L. Miller, *Langmuir* **1991**, *7*, 1419.
73. M. Wirde, U. Gelius, L. Nyholm, *Langmuir* **1999**, *15*, 6370.
74. M. A. Hines, J. A. Todd, P. Guyot-Sionnest, *Langmuir* **1995**, *11*, 493.
75. K. A. Bunding Lee, *Langmuir* **1990**, *6*, 709.
76. H. O. Finklea, S. Avery, M. Lynch et al., *Langmuir* **1987**, *3*, 409.
77. H. O. Finklea, D. A. Snider, J. Fedyk, *Langmuir* **1990**, *6*, 371.
78. S. Tsuneda, T. Ishida, N. Nishida et al., *Thin Solid Films* **1999**, *339*, 142.
79. J. R. Vig, *J. Vac. Sci. Technol., A* **1985**, *3*, 1027.
80. C. D. Bain, E. B. Troughton, Y.-T. Tao et al., *J. Am. Chem. Soc.* **1989**, *111*, 321.
81. J. I. Henderson, S. Feng, T. Bein et al., *Langmuir* **2000**, *16*, 6183.
82. E. Sabatani, I. Rubinstein, R. Maoz et al., *J. Electroanal. Chem.* **1987**, *219*, 365.
83. E. Sabatani, I. Rubinstein, *J. Phys. Chem.* **1987**, *91*, 6663.
84. M. J. Tarlov, *Langmuir* **1992**, *8*, 80.
85. Y. S. Obeng, M. E. Laing, A. C. Friedli et al., *J. Am. Chem. Soc.* **1992**, *114*, 9943.
86. P. Tengwall, M. Lestelius, B. Liedberg et al., *Langmuir* **1992**, *8*, 1236.
87. Z. Hou, N. L. Abbott, P. Stroeve, *Langmuir* **1998**, *14*, 3287.
88. Z. Hou, S. Dante, N. L. Abbott et al., *Langmuir* **1999**, *15*, 3011.
89. P. Samorí, J. Diebel, H. Löwe et al., *Langmuir* **1999**, *15*, 2592.
90. P. Wagner, M. Hegner, H.-J. Güntherodt et al., *Langmuir* **1995**, *11*, 3867.
91. M. Hegner, P. Wagner, G. Semenza, *Surf. Sci.* **1993**, *291*, 39.
92. D. Stamou, D. Gourdon, M. Liley et al., *Langmuir* **1997**, *13*, 2425.

93. P. Gupta, K. Loos, A. Korniakov et al., *Angew. Chem., Int. Ed. Engl.* **2004**, *43*, 520.
94. S. E. Creager, G. K. Rowe, *Anal. Chim. Acta* **1991**, *246*, 233.
95. K. A. Groat, S. E. Creager, *Langmuir* **1993**, *9*, 3668.
96. G. Che, Z. Li, H. Zhang et al., *J. Electroanal. Chem.* **1998**, *453*, 9.
97. J. A. M. Sondag-Huethorst, L. G. J. Fokkink, *Langmuir* **1992**, *8*, 2560.
98. J. A. M. Sondag-Huethorst, L. G. J. Fokkink, *Langmuir* **1995**, *11*, 2237.
99. X. Gao, Y. Zhang, M. J. Weaver, *Langmuir* **1992**, *8*, 668.
100. M. H. Schoenfisch, J. E. Pemberton, *J. Am. Chem. Soc.* **1998**, *120*, 4502.
101. L. H. Dubois, B. R. Zegarski, R. G. Nuzzo, *J. Am. Chem. Soc.* **1990**, *112*, 570.
102. J. Li, K. S. Liang, G. Scoles et al., *Langmuir* **1995**, *11*, 4418.
103. G. E. Poirier, *Langmuir* **1997**, *13*, 2019.
104. G. E. Poirier, *Langmuir* **1999**, *15*, 1167.
105. T. Y. B. Leung, M. C. Gerstenberg, D. J. Lavrich et al., *Langmuir* **2000**, *16*, 549.
106. T. Hsu, J. M. Cowley, *Ultramicroscopy* **1983**, *11*, 239.
107. J. Schneir, R. Sonnenfeld, O. Marti et al., *J. Appl. Phys.* **1988**, *63*, 717.
108. C. B. Ross, L. Sun, R. M. Crooks, *Langmuir* **1993**, *9*, 632.
109. L. Sun, R. M. Crooks, *Langmuir* **1993**, *9*, 1951.
110. J. T. Woodward, M. L. Walker, C. W. Meuse et al., *Langmuir* **2000**, *16*, 5347.
111. C. Yan, A. Gölzhäuser, M. Grunze, *Langmuir* **1999**, *15*, 2414.
112. N. Mohri, M. Inoue, Y. Arai et al., *Langmuir* **1995**, *11*, 1612.
113. M. Brust, M. Walker, D. Bethell et al., *J. Chem. Soc., Chem Commun.* **1994**, 801.
114. D. L. Feldheim, C. A. Foss, (Eds.), *Metal Nanoparticles*, Marcel Dekker, New York, 2002
115. L. Strong, G. M. Whitesides, *Langmuir* **1988**, *4*, 546.
116. D. W. Pashley, *Philos. Mag.* **1959**, *4*, 316, 324.
117. D. W. Pashley, *Proc. R. Soc. London, Ser. A* **1960**, *255*, 218.
118. G. Kalyuzhny, A. Vaskevich, S. Matlis et al., *Rev. Anal. Chem.* **1999**, *18*, 237.
119. G. Kalyuzhny, A. Vaskevich, G. Ashkenasy et al., *J. Phys. Chem. B* **2000**, *104*, 8238.
120. G. Kalyuzhny, M. A. Schneeweiss, A. Shanzer et al., *J. Am. Chem. Soc.* **2001**, *123*, 3177.
121. G. Kalyuzhny, A. Vaskevich, M. A. Schneeweiss et al., *Chem. Eur. J.* **2002**, *8*, 3850.
122. M. Lahav, A. Vaskevich, I. Rubinstein, *Langmuir* **2004**, *20*, 7365.
123. I. Doron-Mor, Z. Barkay, N. Filip-Granit et al., *Chem. Mater.* **2004**, *16*, 3476.
124. A. J. Haes, S. Zou, G. C. Schatz et al., *J. Phys. Chem. B* **2004**, *108*, 109.
125. V. L. Colvin, A. N. Goldstein, A. P. Alivisatos, *J. Am. Chem. Soc.* **1992**, *114*, 5221.
126. P. E. Laibinis, J. J. Hickman, M. S. Wrighton et al., *Science* **1989**, *245*, 845.
127. M. M. Walczak, C. A. Alves, B. D. Lamp et al., *J. Electrochem. Chem.* **1995**, *396*, 103.
128. M. M. Walczak, C. Chung, S. M. Stole et al., *J. Am. Chem. Soc.* **1991**, *113*, 2370.
129. P. E. Laibinis, M. A. Fox, J. P. Folkers et al., *Langmuir* **1991**, *7*, 3167.
130. P. E. Laibinis, G. M. Whitesides, D. L. Allara et al., *J. Am. Chem. Soc.* **1991**, *113*, 7152.
131. A. Dhirani, M. A. Hines, A. J. Fisher et al., *Langmuir* **1995**, *11*, 2609.
132. R. Heinz, J. P. Rabe, *Langmuir* **1995**, *11*, 506.
133. K. T. Carron, L. G. Hurley, *J. Phys. Chem.* **1991**, *95*, 9979.
134. G. K. Jennings, P. E. Laibinis, *Langmuir* **1996**, *12*, 6173.
135. G. K. Jennings, P. E. Laibinis, *J. Am. Chem. Soc.* **1997**, *119*, 5208.
136. C. L. Haynes, R. P. Van Duyne, *J. Phys. Chem. B* **2001**, *105*, 5599.
137. M. Duval Malinsky, K. L. Kelly, G. C. Schatz et al., *J. Am. Chem. Soc.* **2001**, *123*, 1471.
138. M. A. Bryant, J. E. Pemberton, *J. Am. Chem. Soc.* **1991**, *113*, 546.
139. R. L. Sobocinski, M. A. Bryant, J. E. Pemberton, *J. Am. Chem. Soc.* **1990**, *112*, 6177.
140. M. Lewis, M. Tarlov, K. Carron, *J. Am. Chem. Soc.* **1995**, *117*, 9574.
141. Q. Dai, C. Xue, G. Xue et al., *J. Adhes. Sci. Technol.* **1995**, *9*, 1465.
142. G. Xue, M. Ma, J. Zhang et al., *J. Colloid Interface Sci.* **1992**, *150*, 1.
143. G. K. Jennings, J. C. Munro, T.-H. Yong et al., *Langmuir* **1998**, *14*, 6130.
144. H. Ron, H. Cohen, S. Matlis et al., *J. Phys. Chem. B* **1998**, *102*, 9861.

145. H. Keller, P. Simak, W. Schrepp et al., *Thin Solid Films* **1994**, *244*, 799.
146. M. V. Baker, G. K. Jennings, P. E. Laibinis, *Langmuir* **2000**, *16*, 3288.
147. F. Li, Y. Lu, G. Xue et al., *Chem. Phys. Lett.* **1997**, *264*, 376.
148. a) Y. Yakamoto, H. Nishihara, K. Aramaki, *J. Electrochem. Soc.* **1993**, *140*, 436; b) M. Itoh, H. Nishihara, K. Aramaki, *J. Electrochem. Soc.* **1994**, *141*, 2018; c) M. Itoh, H. Nishihara, K. Aramaki, *J. Electrochem. Soc.* **1995**, *142*, 1839, 3696; d) R. Haneda, K. Aramaki, *J. Electrochem. Soc.* **1998**, *145*, 2786.
149. M. M. Sung, K. Sung, C. G. Kim et al., *J. Phys. Chem. B* **2000**, *104*, 2273.
150. M. Volmer, M. Stratmann, H. Viefhaus, *Surf. Interf. Anal.* **1990**, *16*, 278.
151. M. Stratmann, *Adv. Mater.* **1990**, *2*, 191.
152. M. Volmer-Uebig, M. Stratmann, *Appl. Surf. Sci.* **1992**, *55*, 19.
153. M. Rohwerder, M. Stratmann, Surface Modification by Ordered Monolayers New Ways of Protecting Materials Against Corrosion, MRS Bulletin (July 1999) 43.
154. J. Y. Gui, B. E. Kahn, L. Laguren-Davidson et al., *Langmuir* **1989**, *5*, 819.
155. M. A. Bryant, S. L. Joa, J. E. Pemberton, *Langmuir* **1992**, *8*, 753.
156. E. Figgemeier, E. C. Constable, C. E. Housecroft et al., *Langmuir* **2004**, *20*, 9242.
157. S. Sortino, S. Petralia, S. Conoci et al., *J. Am. Chem. Soc.* **2003**, *125*, 1122.
158. S. Sortino, S. Petralia, S. Conoci et al., *J. Mater. Chem.* **2004**, *14*, 811.
159. H. H. Law, J. Sapjeta, C. E. D. Chidsey et al., *J. Electrochem. Soc.* **1994**, *141*, 1977.
160. Z. Mekhalif, J. Riga, J.-J. Pireaux et al., *Langmuir* **1997**, *13*, 2285.
161. Z. Mekhalif, J. Delhalle, J.-J. Pireaux et al., *Surf. Coat. Technol.* **1998**, *100–101*, 468.
162. Z. Mekhalif, A. Lazarescu, L. Hevesi et al., *J. Mater. Chem.* **1998**, *8*, 545.
163. Z. Mekhalif, J. Delhalle, P. Lang et al., *Synth. Met.* **1998**, *96*, 165.
164. C.-M. Ruan, T. Bayer, S. Meth et al., *Thin Solid Films* **2002**, *419*, 95.
165. F. Sinapi, A. Naji, J. Delhalle et al., *Surf. Interf. Anal.* **2004**, *36*, 1484.
166. G. Shustak, A. J. Domb, D. Mandler, *Langmuir* **2004**, *20*, 7499.
167. S. Meth, C. N. Sukenik, *Thin Solid Films* **2003**, *425*, 49.
168. F. T. Buoninsegni, R. Herrero, M. R. Moncelli, *J. Electroanal. Chem.* **1998**, *452*, 33.
169. N. Muskal, D. Mandler, *Electrochim. Acta* **1999**, *45*, 537.
170. K. Slowinski, K. U. Slowinska, M. Majda, *J. Phys. Chem. B* **1999**, *103*, 8544.
171. K. Slowinski, H. K. Y. Fong, M. Majda, *J. Am. Chem. Soc.* **1999**, *121*, 7257.
172. A. Demoz, D. J. Harrison, *Langmuir* **1993**, *9*, 1046.
173. M. A. Rampi, O. J. A. Schueller, G. M. Whitesides, *Appl. Phys. Lett.* **1998**, *72*, 1781.
174. C. Bruckner-Lea, J. Janata, J. Conroy et al., *Langmuir* **1993**, *9*, 3612.

2.1 Inorganic and Composite Films

Steven L. Suib
University of Connecticut, Storrs, CT, USA

Naifei Hu
Beijing Normal University, Beijing, China

James F. Rusling
University of Connecticut, Storrs, CT, USA
University of Connecticut Health Center, Farmington, WA, USA

2.1.1 Overview

This chapter concerns the synthesis, characterization, and applications of inorganic and composite films. The summary covers literature articles from 1995 until 2004. Several chapters cover developments before the mid-1990s [1, 2]. Specific applications in the present chapter include sensors, electrocatalysts, fuel cells, batteries, and others.

2.1.2 Inorganic and Composite Films

2.1.2.1 Synthesis

Gomez-Romero et al. [3, 4] have looked at electrochemical activity of hybrid inorganic electrodes of polypyrrole and phosphomolybdate anions. Films were prepared by multiple cyclic voltammetry experiments onto Pt electrodes. Such heterometallate systems are interesting because three reversible redox processes due to these anions were observed. These systems can be used for cation insertion reactions. Aurian-Blajeni et al. [5] have made similar composite electrodes of polyaniline and iridium oxide and studied electrochemical responses of such systems.

Guliants et al. [6] have published a review on synthesis, structure, and applications of ordered meso- and macroporous films and membranes. Solvent evaporation and *in situ* growth were used to synthesize these films. Functionalization of the inner pores was important for optimization of film properties and applications (*vide infra*). Such functionalization is often carried out by silanizing internal pore sites such as OH groups. The control of organic chains is important in such systems such as in use of alkoxides by Innocenzi et al. [7]

Zhitomirsky et al. [8] have shown that electrodeposition can also be used to prepare films of hybrid composites. Cathodic electrodeposition of iron oxide nanoparticles were deposited with a polyelectrolyte matrix. Inorganic proteins and fibroblasts have been deposited on single crystal Si and Si_3N_4, and doped Si substrates

Encyclopedia of Electrochemistry. Edited by A.J. Bard and M. Stratmann
Vol. 10 *Modified Electrodes*. Edited by M.Fujihira, I.Rubinstein, and J.F.Rusling
Copyright © 2007 Wiley-VCH Verlag GmbH & Co. KGaA, Weinheim. ISBN: 978-3-527-30402-8

by Giannoulis et al. [9] Protein adsorption was done from a solution for a period of 4 days. Differential adsorption of proteins was found in these studies. A review of uranyl compounds as thin films by Benavente et al. [10] primarily concerns self supported films. Electrochemical behavior is very different depending on the structure of the uranyl compound. Transport parameters such as cationic and anionic permeabilities were of interest in this study.

Considerable interest in preparation of oriented films such as in the review by Brinker is apparent [11]. Much of the work involves gas phase preparation from methods like chemical vapor deposition (CVD). However, solution phase sol–gel methods were also recently used in many studies. Heterogeneous nucleation and growth on preorganized modified substrates takes away the need to use single crystals. Hydrothermal alteration routes were also summarized [11].

Sol–gel films can be used to immobilize biomolecules. For example, Dong et al. developed thin sol–gel films on electrodes in which enzymes horseradish peroxidase (HRP) and glucose oxidase (GOD) were used to determine enzyme substrates [12]. A vapor-deposition sol–gel process [13] featuring a thin film of aqueous HRP solution into which titanium isopropoxide vapor was diffused to form a TiO_2 sol–gel film incorporating HRP prevented denaturation of the enzyme. Surfactants were used in preparation of sol–gel films incorporating redox proteins on electrodes to improve porosity and electrochemical and catalytic performance [14].

Besides biomolecule–nanoparticle films that will be discussed below, it is possible to produce transition metal oxide films by solvent extraction of supersaturated microemulsions on metal substrates as done by Walsh et al. [15] *In situ* mineralization of oxide films of iron (III), manganese (III/IV), and cobalt (II) were made with this method. Brass and copper substrates were used and the drops of emulsion were placed on these substrates with oxide films being formed after dip coating in hot hexane. There was constrained growth of inorganic oxide networks in such microemulsion films. The walls of such materials are mineralized and are made of nanoparticulates.

2.1.2.2 Characterization

A variety of characterization methods can be used to study inorganic films. Some of these methods are summarized in Table 1. Hybrid organic–inorganic films of alkoxysilanes of Innocenzi et al. [7] have been studied with Fourier transform infrared (FTIR) spectroscopy as well as multinuclear solid state nuclear magnetic resonance (NMR) techniques. Thermal treatment and condensation reactions have been monitored with FTIR and NMR methods. Siloxanes and TiO_2 composite materials have been made via sol–gel techniques for photonic applications by Que et al. [16] A variety of methods were used to characterize these systems such as FTIR, thermogravimetric analyses (TGA), Raman spectroscopy, and UV visible spectroscopy. A nanoindenter was used to study hardness and Young's modulus of these films. The C and Ti content was correlated with high hardness of these films.

Langmuir–Blodgett film transfer was used to prepare composites of CdS nanoparticles on Au substrates by Samokhvalov et al. [20]. Charge transfer was observed using laser photochemical techniques. X-ray photoelectron spectroscopy (XPS) methods were used to study oxidation states. Photochemical studies

Tab. 1 Summary of techniques used for characterizing films

Method	*Information obtained*	*References*
Fourier transform infrared (FTIR)	Functional groups	[3, 7, 16, 17]
Cyclic voltammetry	Redox properties, adsorption	[3–5, 8, 17–19]
Impedance spectroscopy	Electrical properties	[5, 10, 17]
Solid state NMR	Info on hybrid network formation	[7]
Thermogravimetric analysis (TGA)	Thermal stability	[16]
Raman spectroscopy	Functional groups	[16, 18, 19]
UV visible spectroscopy	Absorbance	[16]
X-ray photoelectron spectroscopy (XPS)	Oxidation states, charge transfer	[20]
Magnetic susceptibility	Magnetic properties, domains	[8]
Ellipsometry	Film thicknesses	[9]
Contact angle	Wettability, film thickness, adsorption properties	[9]
Capacity	Capacitance	[18, 19]
Scanning Auger microscopy	Surface imaging	[19]
Scanning tunneling and atomic force microscopy	Surface structures and morphologies	[21]

show that the films can either have a positive or negative charge depending on the intensity of the laser that excites the quantum confined CdS nanoparticles.

Zhitomirsky et al. [8] have shown that electrodeposited hybrid composites of iron oxides can be studied with magnetic and thermal (TGA) methods. The nanocomposites produced here are superparamagnetic. Such properties are dependent on the nanosizes of these systems.

Ellipsometry was used by Giannoulis et al. [9] to study film thicknesses of therapeutic silicon–based microdevices under development. *In situ* characterization of the growth of electroactive films of oxides and hydroxides of transition metals has been done with scanning tunneling microscopy (STM), atomic force microscopy (AFM), and intermittent contact atomic force microscopy (ICAFM). Shrinkage and enhanced thicknesses of films can be measured with these methods. Films of iridium oxide, nickel oxides, and polyaniline were studied here.

2.1.2.3 Applications of Inorganic Films

The review by Guliants et al. [6] shows that ordered meso- and macroporous films and membranes can be used for separations, sensors, heterogeneous catalysis, microelectronics, and photonics. Nanoparticles and their subsequent quantum confinement effects result from chemical functionalization of internal pores of these materials.

A current interest is the production of supercapacitors. Carbon electrodes have been modified by Leitner et al. [17] with naphthol derivatives, which utilize the electrical double layer of carbon and the redox capability of the naphthol. Similar strategies can be used with inorganic redox systems like indium tin oxide such as in the work of Miura et al. [22] The stability of charge in time is important in these systems. Electrochemical impedance measurements are needed to study the full capacity of these electrodes. Comparisons of increases in supercapacity are made to pristine carbon.

A unique recent application concerns the electrochemical switching of alkaline earth cation exchange as summarized by work of Reyes-Gomez et al. [23]. Composite electrodes of metal hexacyanoferrate are embedded in silica surfaces using sol–gel methods. Composite electrodes are 2 orders of magnitude higher activity as compared to bulk metal hexacyanoferrate electrodes. This switching of cation exchange is novel and may allow a variety of uses such as environmental cleanup, cleanup of mixtures of metals such as in sludges from electroplating plants, and in other areas such as radioactive waste separations.

Another continuing area of considerable interest involves preparation of secondary nonaqueous rechargeable batteries. Commercial lithium battery anodes are made of graphite. Graphite has a theoretical capacity of about 372 mAh g^{-1}. Silicon has a higher theoretical capacity of 4200 mAh g^{-1}. However there is poor reversibility of silicon powder due to volume changes during cycling. An approach that we have used is to coat silicon powder with carbon [16].

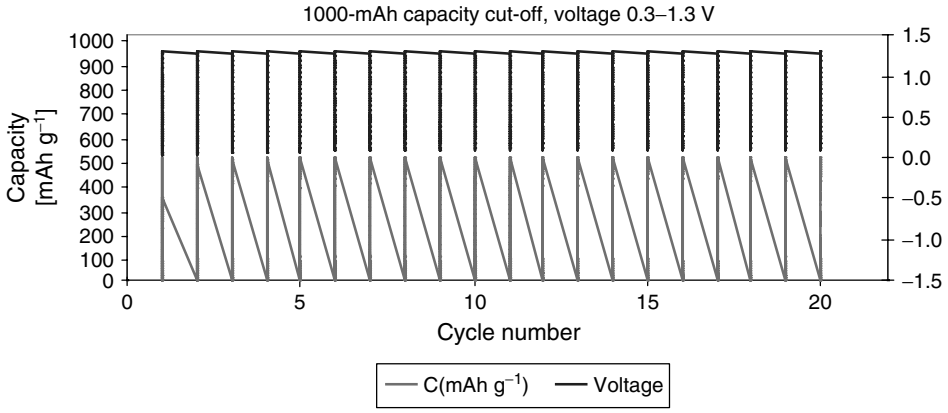


Fig. 1 Cycling studies of carbon-coated silicon anodes.

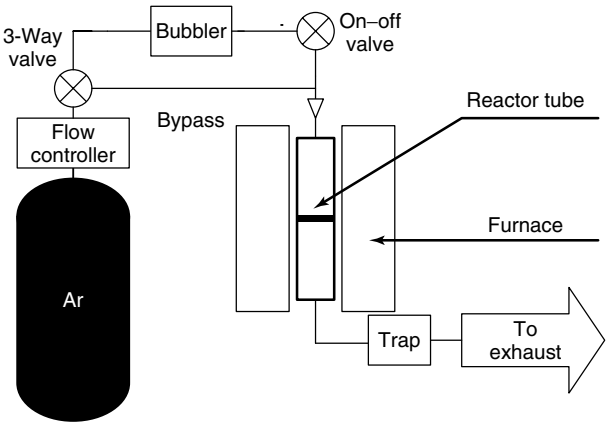


Fig. 2 CVD reactor.

Figure 1 shows the cycling of these carbon-coated anodes over 30 cycles. The capacity remains stable over these experiments.

The idea behind such experiments is to have lithium incorporate into silicon during cycling or charging and then deintercalate during discharge. The amount of lithium that can be incorporated into carbon is considerably greater than that which can be incorporated into carbon.

To obtain such results, chemical vapor–deposition methods were used in the setup shown in Fig.2.

In these experiments, Si powder was ground in an agate mortar and heated for 3 h in air (or H_2, or H_2 and NH_3). About 0.5 g sample of silicon was placed in a cold reactor for 1 h in flowing Ar gas. Temperature was then increased to 950 °C. Argon gas was then passed through a bubbler, which was filled with liquid toluene. After 30 min, the carrier flow was stopped and the reactor was allowed to cool down to room temperature. Besides cell cycling, thermogravimetric analyses, cyclic voltammetry, and Raman were used.

Similar studies have been done with SnO_2 mixed with high surface area carbon. The morphology of the carbon in such systems is important and is shown in Fig. 3. Figure 4 shows cycling studies of commercial tin oxide and the carbon (MCMB) tin oxide mixtures. The cycling data clearly show an advantage of the composite system.

The tin oxide was deposited using electroless plating methods by using $SnCl_2.2H_2O$, NaOH, and sodium or potassium citrate. Some of the parameters important in the synthesis include the nature of the tin oxide species, the particle size, the concentration of the reagents, the ratio of reagents used in the synthesis, the temperature, the mixing time, the aging time, and work-up procedures.

Both of the above systems show the enhanced cycling and enhanced capacity of composite anode materials. There are a variety of metals that might be used to intercalate lithium or incorporate lithium. Several studies are currently underway in these areas in our labs and in others. Some objectives include 35-Ah cells for aerospace applications, development of batteries for electric vehicles, and batteries for hybrid electric vehicles. Improved lithium ion technology, as regards improved performance, decreased cost, and more viable technology is mandatory for synthesis and use of such materials in novel secondary battery applications.

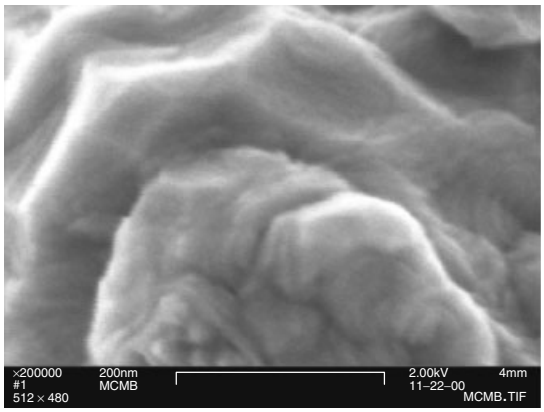


Fig. 3 SEM of carbon electrode.

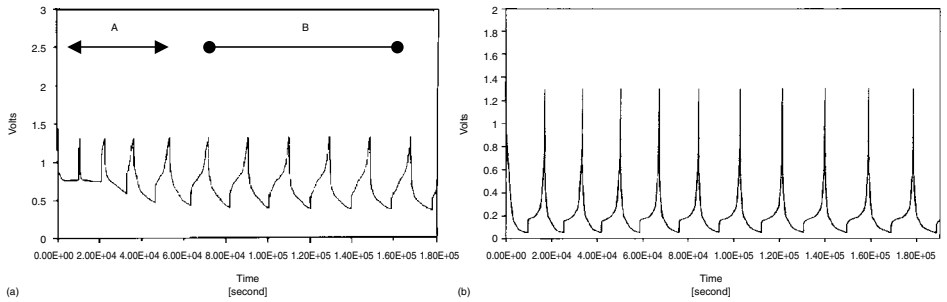


Fig. 4 Studies of commercial tin oxide and the carbon (MCMB) tin oxide mixtures. (a) Battery cycling of commercial tin oxide. (b) Cycling for MCMB/Sn oxide composites.

2.1.3 Electroactive Nanoparticle Films

Inorganic nanoparticles, with their unique structural stability, high surface area, low toxicity, good biocompatibility, and ease of preparation can also be used in electroactive films. Films of polyions and octahedral layered manganese oxide nanoparticles on carbon electrodes made by layer-by-layer alternate electrostatic adsorption were recently shown to be active for electrochemical catalysis of styrene epoxidation in solution in the presence of hydrogen peroxide and oxygen [24]. The pathway for styrene epoxidation at the highest yields required oxygen, hydrogen peroxide, and a reducing voltage, and may involve an activated oxygen species in the manganese oxide nanoparticles. ^{18}O isotope labeling studies suggested oxygen incorporation into the product from molecular oxygen, hydrogen peroxide and/or lattice oxygen from the catalytic nanoparticles.

Nanoparticle films provide a stable microenvironment for redox proteins and facilitate the direct electron transfer between those proteins and underlying electrodes. The simplest way to prepare such films is by composite deposition. Either a protein-nanoparticle or nanoparticle dispersion is deposited on electrodes. In the latter case, the protein is absorbed from solution. Clay [25–28], TiO_2 [29–31], SnO_2 [32], ZrO_2 [33], and Fe_3O_4 [34] were utilized to construct protein-nanoparticle films in this way, and direct electrochemistry of the proteins in these films was realized.

An example is protein-clay films cast on pyrolytic graphite (PG) electrodes [25]. Exfoliated clay particles have a platelet shape with nanoscale thickness, about 50–100 nm in these studies [35]. Protein-clay films were fabricated by casting an aqueous dispersion of protein and clay on PG electrodes and letting the water evaporate. Myoglobin (Mb), hemoglobin (Hb), and HRP in clay films gave well-defined,

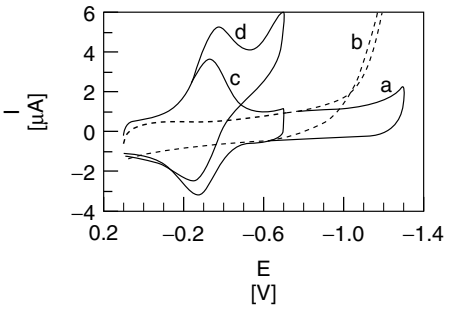


Fig. 5 Cyclic voltammograms at 0.2 V s^{-1} in pH 5.5 buffers for (a) clay film in buffers containing no TCA, (b) clay film in buffers containing 50 mM TCA, (c) Hb-clay film in buffers containing no TCA, (d) Hb-clay film in buffers containing 50 mM TCA (Adapted with permission from [25]. Copyright 2002 American Chemical Society).

quasi-reversible cyclic voltammetric peaks in buffer, characteristic of the protein heme Fe(III)/Fe(II) redox couples (e.g. Fig. 5c for Hb-clay films). X-ray diffraction showed that Mb-clay and Hb-clay films gave low-angle Bragg peaks suggesting ordered layered structures with Mb and Hb intercalated between clay layers. X-ray diffraction showed that HRP induced disorder in the clay films. Various substrates such as oxygen, trichloroacetic acid (TCA), nitrite, and hydrogen peroxide, were catalytically reduced at protein-clay film electrodes. For example, when TCA was added to the buffer, the HbFe(III) reduction peak of Hb-clay films at about −0.35 V increased in height (Fig. 5d), accompanied by a decrease of HbFe(II) oxidation peak. These results are consistent with the reduction of TCA by HbFe(II) in a catalytic cycle resulting in the reductive dechlorination of the acid [36]. Compared to direct reduction of TCA on clay films without protein (Fig. 5b), Hb-clay films lowered the overpotential for reduction of TCA by about 0.7 V. Proteins in these films were made to act like enzymes in these reactions.

Development of a layer-by-layer assembly method in the 1990s opened up new approaches to fabricate ultrathin films [37–39]. This method has been documented for other materials elsewhere in this volume, but also applies to biomolecules. Layer-by-layer assembly can be based on electrostatic interaction between oppositely charged polyions from their solutions in alternating adsorption steps. One advantage of the layer-by-layer approach is that film composition and thickness can be precisely controlled by varying the type of charged species and the number of adsorption cycles. Various $\{\text{nanoparticle/protein}\}_n$ layer-by-layer films, such as $\{\text{clay/protein}\}_n$ [35, 40], $\{SiO_2/\text{protein}\}_n$ [41–43], and $\{MnO_2/\text{protein}\}_n$ [43] films, were assembled on electrodes, and direct electrochemistry of the proteins in these films was observed.

Taking $\{SiO_2/Hb\}_n$ films as an example [41], the isoelectric point (pI) of SiO_2 nanoparticles is about 2 or 3, so they are negatively charged at pH 9.0, while Hb with pI 7.4 is positively charged at pH 5.0. Multilayer $\{SiO_2/Hb\}_n$ films were thus assembled on solid surfaces mainly by electrostatic attraction between SiO_2 and Hb. A quartz crystal microbalance (QCM) was used to monitor the assembly of these $\{SiO_2/Hb\}_n$ films. QCM results for dry films showed a roughly linear decrease of frequency with the adsorption step number (Fig. 6), indicating increasing film mass and regular and reproducible growth of SiO_2/Hb bilayers. Each SiO_2 layer caused a nearly constant frequency decrease of 490 Hz, corresponding to a

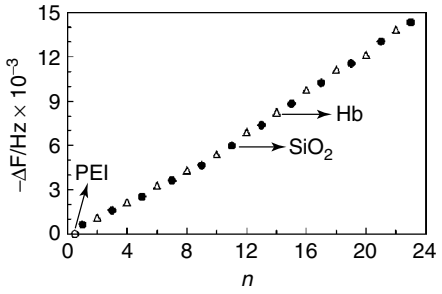


Fig. 6 Shift of QCM frequency with alternate adsorption steps of SiO_2 (pH 9.0) and Hb (pH 5.0) on Au/MPS/PEI electrodes: (•) SiO_2 adsorption steps; (Δ) Hb adsorption steps (Adapted with permission from [41]. Copyright 2004 American Chemical Society).

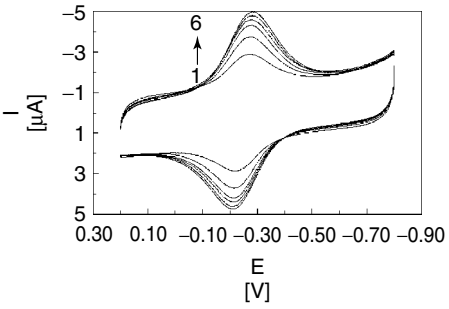


Fig. 7 Cyclic voltammograms for layer-by-layer $\{SiO_2/Hb\}_n$ films on PG/PEI electrodes at scan rate of 0.2 V s^{-1} in pH 5.5 buffer solutions with different numbers of bilayers. (Adapted with permission from [41]. Copyright 2004 American Chemical Society).

thickness of 7.6 nm, while each Hb adsorption layer resulted in a roughly constant frequency shift of 736 Hz, indicating a thickness of 19 nm. Cyclic voltammetry was also used to monitor the growth of the $\{SiO_2/Hb\}_n$ films by scanning the film after each assembly cycle (Fig. 7). A pair of chemically reversible reduction–oxidation peaks at about −0.26 V vs. SCE was found for the Hb heme Fe(III)/Fe(II) redox couple with peaks that increased with the number of SiO_2/Hb bilayer (n) up to 6. Hb in the 7th bilayer showed no further increase in CV-peak height.

Comparisons between amount of protein deposited by QCM and amount of electroactive protein by CV can be used to assess the fraction of electroactive protein in these films as a function of bilayer number (n). The total amount of Hb in each bilayer was about the same and Hb in the first bilayer closest to the electrode surface was about 100% electroactive. The fraction of electroactive Hb in the succeeding bilayers decreased significantly with n [41]. In bilayers at $n > 6$, very little Hb was electrochemically addressable. Thus, the distance between Hb and electrode is important for efficient electron exchange, which probably occurs by an electron hopping mechanism in these films. The UV-vis and RAIR spectra of $\{SiO_2/protein\}_n$ films indicated that Mb and Hb in layer-by-layer films with SiO_2 nanoparticles essentially retain the secondary structure similar to that of their native state at medium pH. On the other hand, even when the proteins and silica were both negatively charged, stable layer-by-layer $\{SiO_2/protein\}_n$ films were successfully fabricated, although amounts of protein were smaller than when nanoparticles and proteins had opposite charges. Results suggest the importance of localized Coulombic attraction between the negative nanoparticle surface and positively charged amino acid residues on the

protein surfaces for the assembly and stability of {nanoparticle/protein}$_n$ films [41].

Core-shell protein nanocluster films of proteins and nanoparticles have also been developed [44]. The film construction included two main steps. In the first step, positively charged heme protein Hb or Mb and negatively charged poly(styrenesulfonate) (PSS) were alternately adsorbed on the surface of SiO_2 nanoparticles, forming core-shell SiO_2-(protein/PSS)$_m$ nanoclusters. In the second step, the SiO_2-(protein/PSS)$_m$ nanoclusters and polycationic poly(ethylenimine) (PEI) were assembled layer by layer on various solid substrates, forming {[SiO_2-(protein/PSS)$_m$]/PEI}$_n$ films. Zeta potential or electrophoretic mobility was used to monitor the assembly of SiO_2-(Hb/PSS)$_m$ core-shell nanoclusters (Figure 8). The negatively charged SiO_2 nanoparticles showed a zeta potential at about −10 mV in pH 5.0 buffer. When positively charged Hb was adsorbed on SiO_2, the zeta potential increased to about −5 mV. In the next step, the adsorption of polyanionic PSS resulted in a decrease of zeta potential to about −13 mV. The zeta potential then switched between −4 and −13 mV when Hb and PSS were alternately adsorbed onto the nanoparticle surface as the outermost layer.

When positively charged Hb was the outermost layer, the zeta potentials were not positive as expected but always negative, which is not fully understood. Nevertheless, regular alternating zeta potentials were observed depending on whether Hb or PSS was the outermost layer, providing qualitative evidence for the stepwise alternate adsorption of Hb and PSS, and suggesting multilayer growth of charged macromolecule shells on SiO_2 nanoparticle cores. {[SiO_2-(protein/PSS)$_m$]/PEI}$_n$ films on PG electrodes exhibited well-defined, chemically reversible cyclic voltammetric reduction-oxidation peaks characteristic of the heme Fe(III)/Fe(II) redox couples. The proteins in the films retained near native conformations in the medium pH range, and the films catalyzed electrochemical reduction of oxygen and hydrogen peroxide. Advantages of the nanocluster films over the simple {SiO_2/protein}$_n$ layer-by-layer

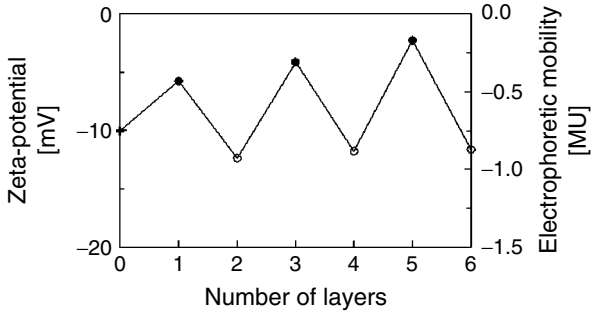


Fig. 8 Zeta potential and electrophoretic mobility of (Hb/PSS)$_m$ multilayers assembled layer by layer on surface of SiO_2 nanoparticles with the adsorption step: (+) pure SiO_2 nanoparticles; (•) the Hb adsorption step; and (o) the PSS adsorption step. (Adapted with permission from [44]. Copyright 2004 American Chemical Society).

films include a larger fraction of electroactive protein and higher specific biocatalytic activity. Using this approach, biocatalytic activity can be tailored and controlled by varying the number of bilayers deposited on the nanoparticle cores and the number of nanocluster layers on electrodes.

2.1.4 Conclusions

In this chapter, we have summarized progress made during the past decade in the area of composite inorganic electrode materials and films. Articles in recent years that concern synthesis of such materials involve the use of CVD, sol–gel, precipitation, coprecipitation, hydrothermal alteration, high temperature routes, layer-by-layer adsorption, electrodeposition, electroless plating, and thin film deposition by a variety of methods. Other methods including photochemical and laser ablation, radio frequency sputter deposition, deposition via resistive heating, metal atom vaporization, molecular beam epitaxy are also under investigation. In years to come, novel approaches involving two or more of these techniques and other methods such as microwave deposition and plasma deposition may become more common.

In areas of characterization of composite films, a multitude of methods have been used to understand their fundamental physical and chemical properties. Table 1 and studies on layered films suggest that some of the more common methods to characterize inorganic composite films are FTIR, Raman, surface methods, QCM, AFM, cyclic voltammetry, and other electrochemical methods. As other methods become more common, those like X-ray absorption and neutron scattering will be used to study the nature of the interfaces between the components of the composites. Understanding the nature of these interfaces and the surface areas of the individual components may become more important in order to improve transport properties.

Applications that we have touched upon include supercapacitors, battery materials, sensors, biosensors, catalysts, fuel cell electrodes, electrochemical ion exchange switches and others. Composite catalysts for fuel cells is an area that is rapidly expanding. Use of nanomaterials in all these applications is also an ongoing pursuit. Potential uses in ceramics and optoelectronics are also areas of interest.

Acknowledgments

Suib acknowledges the support of the US Department of Energy, Office of Basic energy and Geosciences, the National Science Foundation under the NIRT program, and Yardney Technical Products for battery studies. Hu is grateful for financial support from the National Natural Science Foundation of China (20275006 and 20475008), and the State Key Laboratory of Electroanalytical Chemistry of Changchun Institute of Applied Chemistry, Chinese Academy of Sciences. Rusling gratefully acknowledges support for Grant ES03154 from the National Institute of Environmental Health Sciences (NIEHS), NIH, and CTS-0335345 from NSF, USA.

References

1. A. J. Bard, T. Mallouk, in *Molecular Design of Electrode Surfaces; Techniques of Chemistry Series* (Ed.: R. W. Murray), Wiley-Interscience, New York, 1992, pp. 271–312, Vol. 22.
2. J. F. Rusling, S. L. Suib, *Adv. Mater.* **1994**, *6*, 922–930.
3. P. Gomez-Romero, M. Lira-Cantru, *Adv. Mater.* **1997**, *9*, 144–147.

4. P. Gomez-Romero, M. Lira-Cantru, *Proc. Electrochem. Soc.* **1997**, *96*, 158–161.
5. A. Aurian, B. Blajeni, S. C. Holleck et al., *J. Appl. Electrochem.* **1989**, *19*, 331–335.
6. V. V. Guliants, M. A. Carreon, Y. S. Lin, *J. Membr. Sci.* **2004**, *235*, 53–72.
7. P. Innocenzi, G. Brusatin, S. Licoccia et al., *Chem. Mater.* **2003**, *15*, 4790–4797.
8. I. Zhitomirsky, M. Niewczas, A. Petric, *Mater. Lett.* **2003**, *57*, 1045–1050.
9. C. S. Giannoulis, T. A. Desai, *J. Mater. Sci.* **2002**, *13*, 75–80.
10. J. Benavente, J. R. R. Barrado, A. Cabeza et al., *Curr. Top. Electrochem.* **1997**, *5*, 119–129.
11. J. Brinker, *Curr. Opin. Coll. Surf. Sci.* **1998**, *3*, 166–173.
12. a) B. Wang, B. Li, Q. Deng et al., *Anal. Chem.* **1998**, *70*, 3170–3174; b) B. Wang, B. Li, Z. Wang et al., *Anal. Chem.* **1999**, *71*, 1935–1939; c) J. Zhang, B. Li, Z. Wang et al., *Anal. Chim. Acta* **1999**, *388*, 71–78; d) X. Chen, G. Cheng, S. Dong, *Analyst* **2001**, *126*, 1728–1732; e) J. Jia, B. Wang, A. Wu et al., *Anal. Chem.* **2002**, *74*, 2217–2223; f) X. Chen, S. Dong, *Biosens. Bioelectron.* **2003**, *18*, 999–1004; g) X. Chen, J. Jia, S. Dong, *Electroanalysis* **2003**, *15*, 608–612.
13. a) J. Yu, H. Ju, *Anal. Chem.* **2002**, *14*, 3579–3583; b) J. Yu, H. Ju, *Anal. Chim. Acta* **2003**, *486*, 209–216; c) J. Yu, S. Liu, H. Ju, *Biosens. Bioelectron.* **2003**, *19*, 401–409; d) J. Yu, S. Liu, H. Ju, *Biosens. Bioelectron.* **2003**, *19*, 509–514.
14. O. Y. Nadzhafova, V. N. Zaitsev, M. V. Drozdova et al., *Electrochem. Commun.* **2004**, *6*, 205–209.
15. D. Walsh, S. Mann, *Adv. Mater.* **1997**, *9*, 658–662.
16. W. Que, X. Hu, *J. Phys. D* **2003**, *36*, 908–914.
17. K. W. Leitner, B. Gollas, M. Winter et al., *Electrochim. Acta* **2004**, *50*, 199–204.
18. P. G. Russell, S. Iaconetti, J. P. DiCarlo et al., *Proc. Power Sources Conf.* **2002**, *40*, 234–237.
19. G. M. Ehrlich, C. Durand, X. Chen et al., *J. Electrochem. Soc.* **2000**, *147*, 886–891.
20. A. Samokhvalov, R. W. Gurney, M. Lahav et al., *J. Phys. Chem. B* **2003**, *107*, 4245–4252.
21. P. Haering, R. Koetz, G. Repphun et al., *Appl. Phys. A* **1998**, *A66*, S481–S486.
22. N. Miura, S. Oonishi, R. P. Kajendra, *Electrochem. Sol. State Lett.* **2004**, *7*, A247–A249.
23. J. Reyes-Gomez, J. A. Medina, K. M. Jeerage et al., *J. Electrochem. Soc.* **2004**, *151*, D87–D92.
24. L. Espinal, S. L. Suib, J. F. Rusling, *J. Am. Chem. Soc.* **2004**, *126*, 7676–7682.
25. Y. Zhou, N. Hu, Y. Zeng et al., *Langmuir* **2002**, *18*, 211–219.
26. C. Lei, F. Lisdat, U. Wollenberger et al., *Electroanalysis* **1999**, *11*, 274.
27. Y. Sallez, P. Bianco, E. Lojou, *J. Electroanal. Chem.* **2000**, *493*, 37.
28. C. Fan, Y. Zhuang, G. Li et al., *Electroanalysis* **2000**, *12*, 1156.
29. E. Topoglidis, C. J. Campbell, A. E. G. Cass et al., *Langmuir* **2001**, *17*, 7899–7906.
30. Y. Zhang, P. He, N. Hu, *Electrochim. Acta* **2004**, *49*, 1981–1988.
31. Q. Li, G. Luo, J. Feng, *Electroanalysis* **2001**, *13*, 359–363.
32. E. Topoglidis, Y. Astuti, F. Duriaux et al., *Langmuir* **2003**, *19*, 6894–6900.
33. S. Liu, Z. Dai, H. Chen et al., *Biosens. Bioelectron.* **2004**, *19*, 963–969.
34. D. Cao, P. He, N. Hu, *Analyst* **2003**, *128*, 1268–1274.
35. Z. Li, N. Hu, *J. Electroanal. Chem.* **2003**, *558*, 155–165.
36. A.-E. F. Nassar, J. M. Bobbitt, J. O. Stuart et al., *J. Am. Chem. Soc.* **1995**, *117*, 10986.
37. Y. Lvov, in *Protein Architecture: Interfacing Molecular Assemblies and Immobilization Biotechnology* (Eds.: Y. Lvov, H. Mohwald), Marcel Dekker, New York, 2000, pp. 125–166.
38. Y. Lvov, in *Handbook of Surfaces and Interfaces of Materials* (Ed.: R. W. Nalwa), Academic Press, San Diego, 2001, pp. 170–189, Vol. 3.
39. J. F. Rusling, in *Protein Architecture: Interfacing Molecular Assemblies and Immobilization Biotechnology* (Eds.: Y. Lvov, H. Mohwald), Marcel Dekker, New York, 2000, pp. 337–354.
40. Y. Zhou, Z. Li, N. Hu et al., *Langmuir* **2002**, *18*, 8573–8579.
41. P. He, N. Hu, J. F. Rusling, *Langmuir* **2004**, *20*, 722–729.
42. P. He, N. Hu, *Electroanalysis* **2004**, *16*, 1122–1131.
43. Y. Lvov, B. Munge, O. Giraldo et al., *Langmuir* **2000**, *16*, 8850.
44. H. Liu, J. F. Rusling, N. Hu, *Langmuir* **2004**, *20*, 10700–10705.

2.2 Synthesis of Layered Polyelectrolyte Films

Merlin Bruening
Michigan State University, East Lansing, Michigan, USA

James Rusling
University of Connecticut, Storrs, Connecticut, USA

Although this section focuses on films prepared by alternating deposition of polyelectrolytes [1], there are a number of ways to prepare layered polymer films. Metal-ion coordination [2], hydrogen bonding [3], charge-transfer interactions [4], covalent bonding [5, 6], interaction of biological molecules that are attached to polymers [7, 8], and electrostatic forces [9] were all used to prepare layered polymeric films. Of these methods, alternating polyelectrolyte deposition using electrostatic attachment is especially attractive for two primary reasons. First, synthesis of layered polyelectrolyte films (LPFs) is both convenient and environmentally friendly. Deposition of these coatings can occur using only water as a solvent and is adaptable to automation. Second, a wide variety of films are possible because the only stipulation on what materials can be used is that they contain sufficient charge.

Synthesis of LPFs begins by immersing a charged substrate into a solution containing an oppositely charged polyelectrolyte and subsequently rinsing with water. This results in an electrostatically bound ''monolayer'' of polyelectrolyte on the substrate and a change in the sign of the charge on the surface as the polyelectrolyte overcompensates the initial surface charge. Immersion in a second solution containing an oppositely charged polyelectrolyte results in deposition of another layer on the surface as shown in Fig. 1 [9]. Repetitive alternating immersions in solutions containing polycations and polyanions result in a multilayer film. Synthesis of films containing hundreds of layers is possible, and the very simple ''dip and rinse'' method is easily amenable to robotic deposition.

LPFs are extremely versatile because the only restriction on film constituents is that they contain sufficient charge. Materials used to construct LPFs include poly(sulfonates) [10, 11], poly(carboxylates) [12, 13], poly(ammoniums) [10, 11], redox-active polymers [14], proteins [15, 16], viruses [17], conducting polymers [18], and inorganic sheets [19, 20]. This range of materials provides a highly versatile platform to synthesize films for possible applications including sensing [21–23], drug delivery [24], and light-emitting diodes [25].

In addition to changing the constituents of polyelectrolyte films, one can control the structure of these films by varying deposition conditions such as the concentration of supporting electrolyte and pH. The thickness of LPFs can increase dramatically with increasing ionic strength of the deposition solution [26]. One possible reason for such increases in thickness is that supporting electrolyte screens the charges on the polymer allowing it to form loops and tails. (When no salt is present in solution, the charged groups on the polymer chain repel one another resulting in an extended conformation of the polymer chains that maximizes separation of charged groups.) Schlenoff suggests that the primary effect of the salt is to increase overcompensation of surface charge [27]. In this model, the depositing layer will penetrate through several underlying layers resulting in large increases in thickness. In any case, the presence of salt in deposition solutions can

Encyclopedia of Electrochemistry. Edited by A.J. Bard and M. Stratmann
Vol. 10 *Modified Electrodes*. Edited by M.Fujihira, I.Rubinstein, and J.F.Rusling
Copyright © 2007 Wiley-VCH Verlag GmbH & Co. KGaA, Weinheim. ISBN: 978-3-527-30402-8

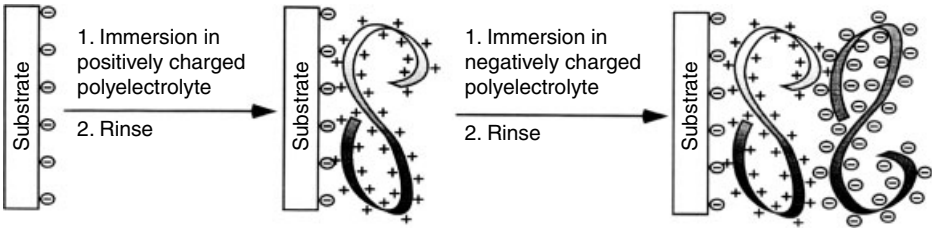


Fig. 1 Schematic diagram of the synthesis of one layer pair of a layered polyelectrolyte film. Repetition of steps 1 and 2 produces multilayer films.

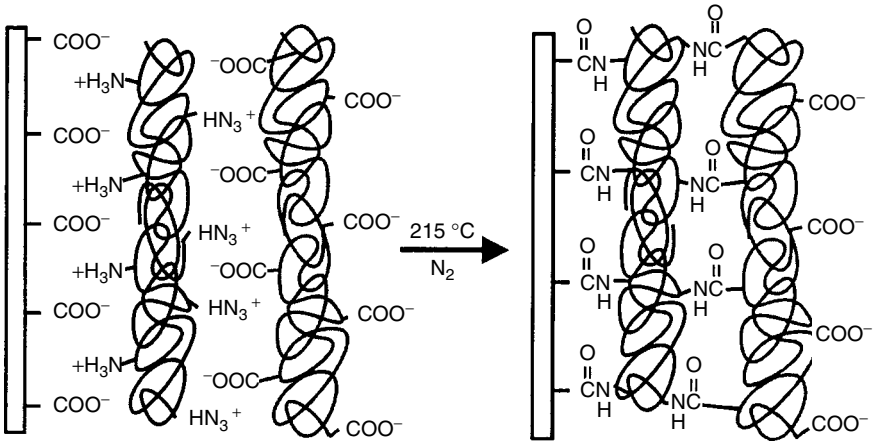


Fig. 2 Schematic diagram showing cross-linking of a PAA/PAH film through heat-induced amidation.

increase thickness by up to fivefold in the case of poly(styrene sulfonate)/protonated poly(allylamine) (PSS/PAH) multilayer films [26]. As discussed in the following, this type of change in structure dramatically alters the permeability of polyelectrolyte films on electrodes. When weak acids or bases are used as polyelectrolytes, the pH of deposition solutions also affects the thickness of polyelectrolyte films [12]. This phenomenon is similar to that resulting from screening by supporting electrolyte. As the amount of charge on a polyelectrolyte molecule decreases, the chains can form loops and tails resulting in a film with thicker layers. Rubner and coworkers showed that changes in pH can alter the thickness of poly(acrylic acid)/poly(allylamine hydrochloride) films up to 20-fold [12]. The use of weak polyelectrolytes also permits the variation of structure after film deposition. Changes in ambient pH alter the charge in the film and in some cases yield a remarkable porous structure [28]. However, extremes in pH can result in delamination of weak polyelectrolyte films [28, 29].

Postdeposition cross-linking provides yet another means of modifying the properties of some polyelectrolyte films [30]. Cross-linking of PAA/PAH films (shown schematically in Fig. 2) increases the stability of these films while decreasing

their permeability and dielectric constant [28, 31]. Cross-linking occurs through heat-induced amidation that results in nylon-like films. FTIR and XPS spectra show that >80% of the carboxylate-ammonium salts are converted into amides resulting in a stable, highly resistive film. In other cases, specific cross-linking groups can be introduced into polyelectrolytes to provide photo-induced cross-linking [32]. This method is gentler, but likely results in a lower cross-link density.

2.2.1 Film Structure

Although synthesis of LPFs occurs in a layer-by-layer fashion, these films do not contain distinct layers or polycation–polyanion layer pairs. Using electroactive polyelectrolytes (see the following), Schlenoff demonstrated that four intervening layer pairs are necessary to prevent electron hopping between redox-active polyelectrolytes [14]. From studies of neutron diffraction of partially deuterated PAH/PSS films, Decher suggests that PAH and PSS components are highly interpenetrating and that a single deposition of deuterated PSS stretches over two layer pairs [9].

A second issue of relevance to modifying electrodes with LPFs is how electrical neutrality is maintained in the film. Is there any salt inside these films that compensates charges on the polymers, or are polycations and polyanions intrinsically compensating? X-ray photoelectron spectroscopy studies of LPFs show no evidence for counterions such as Cl^- or Na^+ in the film [9]. Radioactive labeling also showed no significant amount of Ca^{2+} or CH_3COO^- ions in films of strongly acidic and basic polyelectrolytes [33]. However, a few studies suggest that under conditions of high salt or when using weakly acidic or weakly basic polyelectrolytes, compensation by counterions might occur [34, 35]. Additionally, by changing the pH of solutions in which LPFs composed of weak-acid or weak-base polyelectrolytes are immersed, one can create additional ion-exchange sites in the film. For example, immersing PAA/PAH films in solutions at a lower pH than that at which they were deposited results in more ammonium groups and less carboxylate groups. The ammonium groups should behave as ion-exchange sites.

2.2.2 Electrodes Modified with Layered Polyelectrolytes

Modification of electrodes with LPFs occurs by the process shown in Fig. 1. The only stipulation on the electrode is that it contains a permanent charge on its surface, for example, gold electrodes modified with an ionizable self-assembled monolayer. As would be expected, the presence of a layered polyelectrolyte on an electrode surface often decreases Faradaic currents when the polyelectrolyte is not electroactive. In the case of PAH/PSS films prepared in the presence of 0.5 M supporting electrolyte, cyclic voltammograms of $Fe(CN)_6^{3-}$ at gold electrodes show minimal current after the deposition of 3 bilayers (Fig. 3) [29]. Similar trends occur with positively charged redox couples such as $Ru(NH_3)_6^{3+}$ and $Os(bpy)_3^{3+}$ [29, 36]. However, not all LPFs effectively block electrodes. Gold electrodes covered with PAA/PAH films as thick as 44 nm still show quasi-reversible cyclic voltammograms [29]. The high permeability of PAA/PAH films may be due to their small, hydrophilic side chains.

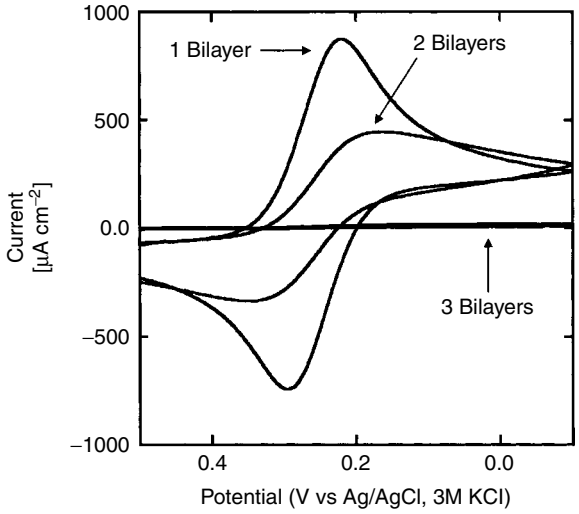


Fig. 3 Cyclic voltammograms of $Fe(CN)_6^{3-}$ (0.005 M $Fe(CN)_6^{3-}$ in 1 M Na_2SO_4) at gold electrodes coated with 1, 2 and 3 layer pairs of PAH/PSS. Scan rate of 100 mV s^{-1}.

The structure of LPFs also has a large effect on the permeability of these films. In the case of PAH/PSS systems, films prepared with no supporting electrolyte are much more permeable than films prepared in 0.5 M salts. Impedance plots show that preparation of PAH/PSS films in the presence of a supporting electrolyte increases charge-transfer resistance ($Fe(CN_6)^{3-/4-}$ couple) by a factor of 1500 compared to films of similar thicknesses prepared without supporting electrolyte [29]. Evidently the extra loops and tails make the film much more blocking.

Using cyclic voltammetry of $Fe(CN)_6^{4-}$ at a rotating disk electrode, Schlenoff provided evidence that decreases in Faradaic current due to the presence of PSS/poly(diallydimethylammonium chloride) occur because of slow movement of $Fe(CN)_6^{4-}$ through the film [37]. Peak currents are independent of potential suggesting that diffusion rather than kinetics is limiting current. This is in agreement with the fact that cyclic voltammograms measured at stationary electrodes have a plateau shape.

One possible explanation why LPFs hinder diffusion of highly charged redox species to electrode surfaces is that a Donnan potential forms due to the fixed charge on the outer layer of the membrane. (Inner layers are assumed to be intrinsically compensated.) If this were the case, then currents in cyclic voltammograms should depend on whether the outer layer of the film is a polycation or a polyanion. The effect of outer layer charge on cyclic voltammograms of blocking films is not very significant and suggests that Donnan repulsion at the surface is not a major factor in passivating electrodes [37].

Schlenoff proposes that the mechanism of transport of redox species to the electrode surface is hopping between anion-exchange sites and that this hopping is slow enough to reduce Faradaic currents. One piece of evidence for this is that the

concentration of supporting electrolyte in $Fe(CN)_6^{4-}$ solutions affects the passivation of electrodes by LPFs. Peak currents in rotating disk linear scan voltammograms increased 10-fold upon changing the supporting salt concentration from 1.2 to 2.0 M [37]. Higher concentrations of salt could create more ion-exchange sites because more supporting electrolyte enters the film and extrinsically compensates the fixed charges, thus creating more ion-exchange sites. The increase in exchange sites would result in more hopping of $Fe(CN)_6^{4-}$ through the film. Films also swell in solutions of high ionic strength [38].

Most investigations of the permeability of LPFs were done with highly charged redox couples such as $Fe(CN)_6^{3-/4-}$ and $Ru(NH_3)_6^{3+/2+}$, but a few studies show that singly charged cations and anions rapidly move through polyelectrolyte films. Iodide electrochemistry is hardly affected by the presence of layered polyelectrolytes [37]. Studies of transport through layered polyelectrolyte membranes clearly show that diffusion of singly charged cations and anions is hardly affected by LPFs [39, 40].

Although some PAH/PSS films passivate electrodes, impedance studies show that they are not sufficiently passivating to provide substantial protection from corrosion [29, 31, 36]. To prepare polyelectrolytes with a much higher blocking ability, Harris and coworkers employed postdeposition cross-linking of PAA/PAH films as shown in Fig. 2 [30]. The as-deposited PAA/PAH films hardly affect Faradaic currents at the electrode, but after cross-linking, charge-transfer resistance increases by 3 to 4 orders of magnitude. Dai and coworkers deposited PAA/PAH films on aluminum/aluminum oxide electrodes and showed that cross-linked PAA/PAH films have resistance of up to $10^7\,\Omega\,cm^2$ [31]. In spite of the fact that this magnitude of film resistance is probably not sufficient for long-term corrosion protection, considering the minimal thickness of these films (100–300 Å), the value is substantial.

Control of the permeability of LPFs will play a crucial role in their possible application as sensor materials or protective coatings. The earlier-mentioned experiments show that it is possible to prepare LPFs with a variety of permeabilities. Constituent polyelectrolytes, deposition conditions, and postdeposition treatments can all be chosen to tailor a film for specific needs.

2.2.3 Electroactive Layered Polyelectrolyte Films

Two methods, adsorption of redox-active species and synthesis of redox-active polymers, were used to prepare electroactive LPFs. In the following text, each of these methods is discussed in turn. Lowy and Finklea showed that a variety of redox species such as $Fe(CN)_6^{4-}$ and $Cu(EDTA)^{2-}$ will adsorb on the surface of polyelectrolyte films [41]. The top layer of LPFs is not intrinsically compensated and thus contains many ion-exchange sites. Redox species adsorbed on the surface of LPFs are electroactive, but the thin film-like cyclic voltammograms of these species showed substantial peak splitting (generally 60 mV or more at a scan rate of 100 mV s^{-1}, even when the redox species was separated from the electrode by just one layer of poly(4-vinylmethylpyridinium)). Adsorption of the redox couple is likely restricted to the surface of the film thus limiting the amount of electroactive material that can be included.

In a similar vein, Anson showed that an adsorbed film of poly(acrylic acid) containing $Ru(NH_3)_6^{3+}$ or $Co(NH_3)_6^{3+}$ on glassy carbon behaves as a thin-film electrode [42].

When using weakly acidic or basic polyelectrolytes, one can create anion-exchange sites and adsorb redox couples throughout LPFs. Cheng and Corn prepared poly(L-lysine)/poly(L-glutamic acid) films at pH 8.0, and then adsorbed $Fe(CN)_6^{3-/4-}$ into these films at a pH of 5.6 [43]. At the lower pH, there should be extrinsically compensated ammonium groups on poly(lysine) due to protonation of previously neutral amine groups. FTIR spectra showed that the amount of $Fe(CN)_6^{3-/4-}$ adsorbed in the films increased monotonically with the number of bilayers deposited. The $Fe(CN)_6^{3-/4-}$ remained in the film when it was immersed in 1,2-dichloroethylene containing 10 mM tetrabutylammonium tetraphenylborate, and the cyclic voltammogram of this system showed typical thin-film behavior. When prepared under appropriately acidic conditions, some PAH/PSS films will also adsorb large amounts of $Fe(CN)_6^{4-}$. Han and Lindholm–Sethson report $Fe(CN)_6^{4-}$ concentrations in PAH/PSS films as high as 0.28 M [36]. When these films are immersed in aqueous solutions of 0.1 M Na_2SO_4, however, the $Fe(CN)_6^{4-}$ is mostly desorbed within 30 min.

A second method for producing LPFs that are electrochemically active is to synthesize and deposit redox-active polymers. Cyclic voltammograms of poly(butyl viologen)/PSS films show typical thin-film voltammogram behavior with peak currents that increase proportionally to the number of layers deposited as shown in Fig. 4 [14]. Virtually all of the viologen groups in the film are electroactive. If films are prepared with four layer pairs of PAH/PSS separating the electroactive layer pairs, electron transfer decreases to undetectable levels. The presence of only three separating layers of PAH/PSS, however, is not sufficient to significantly decrease electron transfer.

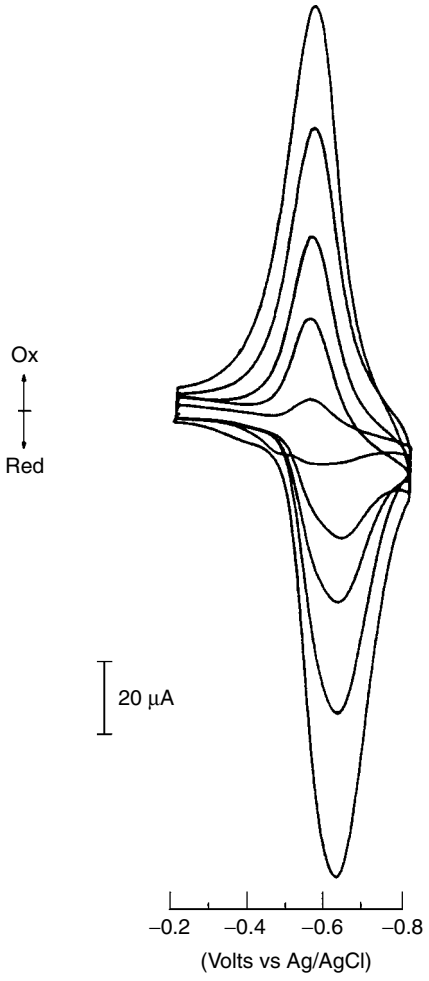


Fig. 4 Cyclic voltammetry of 2, 4, 6, 8, and 10 bilayer PBV/PSS pairs deposited onto a silver electrode. Peak currents increase monotonically with the number of bilayers. The supporting electrolyte was 0.05 M KBr and the scan rate was 50 mV/second. (Figure adapted from [14] with permission. Copyright 1997 American Chemical Society).

Bilayer thicknesses in this case were approximately 60 Å, and this suggests that layer interpenetration occurs through 3 bilayers as electron transfer over distances of 60 Å would be extremely slow.

Other redox-active polyelectrolyte films were prepared from ferrocene-derivatized polly(allylamine) and poly(vinyl pyridine) as well as an osmium complex of poly(vinyl pyridine) [44–46]. These films were synthesized to mediate electron transfer between the electrode and a charged enzyme that was a constituent of the polyelectrolyte film. In the case of ferrocene-derivatized poly(allylamine) or poly(vinyl pyridine), cyclic voltammetry of the bound ferrocene moiety showed small peak splittings ($\leq$50 mV at a scan rate of 50 and 20 mV s^{-1}, respectively) [45, 46]. The amount of electroactive material increased with the number of deposited layers, but the first layer contained significantly more electroactive ferrocene than the later layers in the poly(allylamine) system [46].

Redox-active polyelectrolyte films are capable of serving as mediators for electron transfer to enzymes. Coimmobilization of glucose-oxidase with the above-mentioned redox-active polyelectrolytes results in films that respond to glucose amperometrically. A careful study of the poly(allylamine)ferrocene system, however, suggests that <1% of the enzymes are actually active [46].

2.2.4 Direct Voltammetry Using Layered Protein-polyion Films

Lvov and coworkers made ultrathin films of a variety of proteins and oppositely charged polyions by the layer-by-layer method [15, 47, 48]. Enzymes retained high activity in these films. Intermixing between nearest neighbor protein and polyion layers is likely, as found for films of linear polycations and polyanions [9].

Direct electron exchange between electrodes and the iron heme proteins myoglobin (Mb) and cyt P450cam was achieved in layer-by-layer films [49]. Films were built on a chemisorbed layer of mercaptopropanesulfonate (MPS) on gold electrodes, which was required for direct voltammetry. Reversible cyclic voltammograms were obtained for the Fe^{III}/Fe^{II} redox couple of these proteins (Fig. 5). Reversible voltammetry was also found for films of polycations and putidaredoxin, the natural redox partner of cyt P450cam [50]. No voltammetric peaks were found for any of these proteins in solutions on bare gold electrodes.

On smooth Au, only the protein layer closest to the electrode was fully electroactive, while second layers were 20 to 40% electroactive [49]. Additional protein layers did not communicate with the electrode.

A larger active enzyme loading per unit area can be provided by increasing the number of electroactive layers. This was achieved by growing films on rough pyrolytic graphite (PG) electrodes and adsorbing coiled polyions from solutions of high salt concentrations. This approach gave many more layers of electroactive Mb than smooth gold [51], as did Mb adsorbed alternately with negative MnO_2 or SiO_2 nanoparticles [52]. Cyclic voltammograms show up to 7–10 electroactive Mb layers for these systems (Fig. 6). Electrode roughness seems to be an important factor.

Average $E^{o\prime}$-values versus NHE for Mb were −0.085 V (pH 7) for [PSS(0.5 M NaCl)/Mb]$_6$, −0.037 V (pH 5.5) for PSS/PDDA/SiO_2(Mb/SiO_2)$_9$, and −0.028 V (pH 5.5) for PSS/PDDA/MnO_2 (Mb/MnO_2)$_{10}$. These were similar to values for Mb in cast phospholipid and ionomer films, but more negative than the

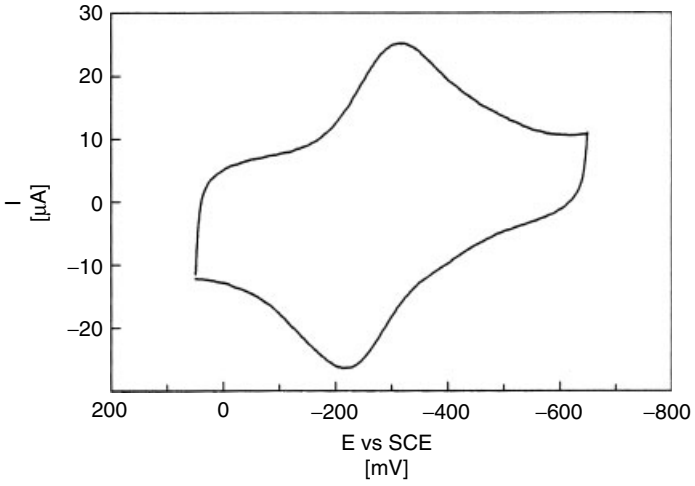


Fig. 5 Cyclic voltammogram at scan rate 0.5 V s^{-1} of Au – MPS/PEI/PSS/Cyt P450cam film in TRIS buffer, pH 7 (Adapted from [49] with permission. Copyright 1998 American Chemical Society.).

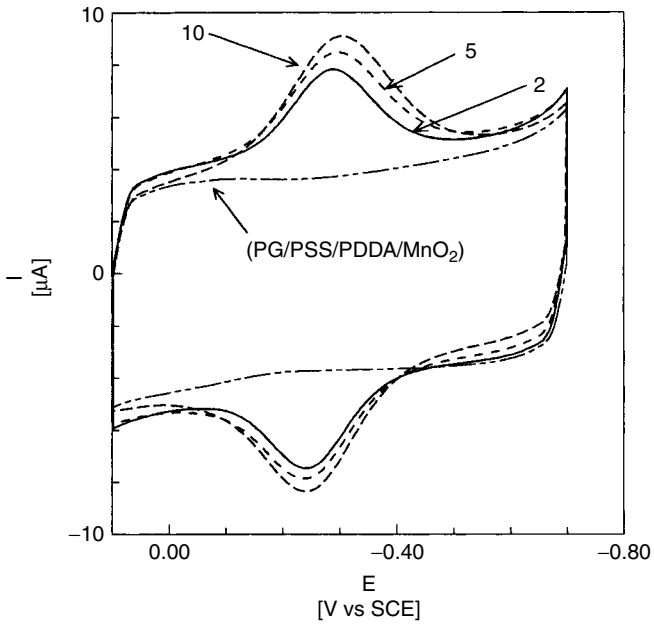


Fig. 6 Cyclic voltammograms at 0.3 V s^{-1} in pH 5.5 buffer of PSS/PDDA/MnO_2 (Mb/MnO_2)*n* films with $n = 2$, 5, and 10 on rough PG electrodes. (Adapted from [52] with permission. Copyright 2000 American Chemical Society.).

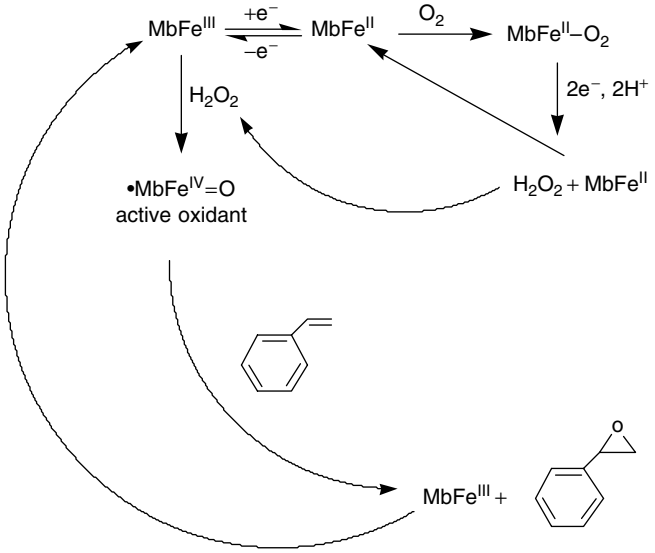
solution values, for example, 0.05 V at pH 7 [53]. $E^{o\prime}$-values in these films shift negative by 50–59 mV/pH unit, indicating participation of a proton in the electron transfer reaction. Analysis of square-wave voltammetry data on 75 nm [PSS(0.5 M NaCl)/Mb]$_6$ films on rough PG with a standard potential dispersion model gave an average standard electrochemical rate constant of 53 s^{-1} [51], in the same range as Mb-surfactant and cast Mb-polyion films [53].

Layer mass measured by QCM for SiO_2-Mb films indicated sufficient protein in the film to completely coat each nanoparticle. Complete protein coating of each particle may provide connected pathways that facilitate charge propagation by electron hopping.

Mb loading per unit area on rough PG electrodes depended on the materials used. PSS and DNA adsorbed from 0.5 M NaCl gave larger loadings of Mb per unit electrode area for up to 6 bilayers, with PSS giving slightly larger amounts than DNA. Increases in electroactivity extended to 10 bilayers for MnO_2 and SiO_2 nanoparticle films, but smaller total Mb loadings were obtained.

2.2.5 Electrode-driven Enzyme-like Catalysis

Prototype bioreactors have been based on the layer-by-layer films discussed earlier. Epoxidation of styrene and its derivatives was achieved by using Mb and cyt P450cam in layered polyion films [54]. This oxidation mimics natural cyt P450-catalyzed oxidations, and involves an unusual combined oxidation-reduction pathway. The reaction pathway (Scheme 1) is similar to that of Mb in aqueous solutions and microemulsions [55]. The electrode reduces $MbFe^{III}$ to $MbFe^{II}$, which reacts with oxygen to give $MbFe^{II}$-O_2, which is reduced electrochemically to H_2O_2. $MbFe^{III}$ is converted by H_2O_2 to the radical $\bullet MbFe^{IV}{=}O$. This ferryl radical epoxidizes styrene. Thus, a



Scheme 1 Electrode-driven Mb-catalyzed oxidation of styrene.

catalytic electrochemical *reduction* drives a catalytic enzyme-like *oxidation* in a *doubly catalytic* process.

Catalytic activities of films containing Mb or cyt P450 enzymes on electrodes were compared for styrene epoxidations. Electrolyses were done at −0.6 V versus SCE at 4 °C on gold foil cathodes coated with layer-by-layer polyion-protein films on both sides. The cathode compartment contained oxygenated pH 7.4 buffer saturated with styrene or a styrene derivative. Cyt P450cam-polyion films on Au-MPS electrodes gave better catalytic activities than Mb films. Stereochemistry for the epoxidation of *cis*-β-methylstyrene depended on oxygen availability. There appear to be two pathways. The stereoselective pathway utilizes the high valent iron-oxygen intermediate, as does the natural enzyme system. The nonstereoselective pathway may involve a peroxyl radical near the protein surface, which forms in the presence of oxygen.

Layer-by-layer protein films made with polyions or nanoparticles are relatively new to bioelectrochemistry, and may have advantages over other film types. The enzymes retain high activity, and only sub-nanomolar amounts are required. The films are mechanically stable, and Mb and cyt P450 cam films have storage stability of at least a month in cold buffer.

Acknowledgments

James Rusling is grateful for support from grant No. ES03154 from National Institute of Environmental Health Sciences (NIEHS), NIH. Contents are solely the responsibility of the authors and do not necessarily represent official views of NIEHS, NIH. We also thank Prof. John Schenkman of the University of Connecticut Health Center for expert collaboration on the work with cytochrome P450s. Merlin Bruening is grateful for support from the National Science Foundation Division of Chemistry and the Department of Energy Office of Basic Energy Sciences.

References

1. For an excellent review of layered polyelectrolyte films, see P. Bertrand, A. Jonas, A. Laschewsky et al., *Macromol. Rapid Commun.* **2000**, *21*, 319–348.
2. P. Kohli, G. J. Blanchard, *Langmuir* **1999**, *15*, 1418–1422.
3. W. B. Stockton, M. F. Rubner, *Macromolecules* **1997**, *30*, 2717–2725.
4. Y. Shimazaki, M. Mitsuishi, S. Ito et al., *Langmuir* **1998**, *14*, 2768–2773.
5. D. Beyer, T. M. Bohanon, W. Knoll et al., *Langmuir* **1996**, *12*, 2514–2518.
6. Y. Liu, M. L. Bruening, D. E. Bergbreiter et al., *Angew. Chem., Int. Ed. Engl.* **1997**, *36*, 2114–2116.
7. C. Bourdillon, C. Demaille, J. Moiroux et al., *J. Am. Chem. Soc.* **1995**, *117*, 11499–11506.
8. J.-I. Anzai, Y. Kobayashi, N. Nakamura et al., *Langmuir* **1999**, *15*, 221–226.
9. G. Decher, *Science* **1997**, *277*, 1232–1237.
10. G. Decher, J. D. Hong, *Ber. Bunsen-Ges. Phys. Chem.* **1991**, *95*, 1430–1434.
11. G. Decher, J.-D. Hong, J. Schmitt, *Thin Solid Films* **1992**, 831–835.
12. S. S. Shiratori, M. F. Rubner, *Macromolecules* **2000**, *33*, 4213–4219.
13. D. Yoo, S. S. Shiratori, M. F. Rubner, *Macromolecules* **1998**, *31*, 4309–4318.
14. D. Laurent, J. Schlenoff, *Langmuir* **1997**, *13*, 1552–1557.
15. Y. Lvov, K. Ariga, I. Ichinose et al., *J. Am. Chem. Soc.* **1995**, *117*, 6117–6123.
16. F. Caruso, D. N. Furlong, K. Ariga et al., *Langmuir* **1998**, *14*, 4559–4565.
17. Y. Lvov, H. Haas, G. Decher et al., *Langmuir* **1994**, *10*, 4232–4236.
18. J. H. Cheung, W. B. Stockton, M. F. Rubner, *Macromolecules* **1997**, *30*, 2712–2716.
19. H.-N. Kim, S. W. Keller, T. E. Mallouk, *Chem. Mater.* **1997**, *9*, 1414–1421.
20. E. R. Kleinfeld, G. S. Ferguson, *Science* **1994**, *265*, 370–373.
21. X. Yang, S. Johnson, J. Shi et al., *Sens. Actuators, B* **1997**, *45*, 87–92.

22. M. M. Montrel, G. B. Sukhorukov, A. I. Petrov et al., *Sens. Actuators, B* **1997**, *42*, 225–231.
23. F. Caruso, K. Niikura, D. N. Furlong et al., *Langmuir* **1997**, *13*, 3427–3433.
24. E. Donath, G. B. Sukhorukov, F. Caruso et al., *Angew. Chem., Int. Ed. Engl.* **1998**, *37*, 2202–2205.
25. O. Onitsuka, A. C. Fou, M. Ferreira et al., *J. Appl. Phys.* **1996**, *80*, 4067–4071.
26. G. Ladam, P. Schaad, J. C. Voegel et al., *Langmuir* **2000**, *16*, 1249–1255.
27. J. B. Schlenoff, S. T. Dubas, *Macromolecules* **2001**, *34*, 592–598.
28. J. D. Mendelsohn, C. J. Barrett, V. V. Chan et al., *Langmuir* **2000**, *16*, 5017–5023.
29. J. J. Harris, M. L. Bruening, *Langmuir* **2000**, *16*, 2006–2013.
30. J. J. Harris, P. M. DeRose, M. L. Bruening, *J. Am. Chem. Soc.* **1999**, *121*, 1978–1979.
31. J. Dai, D. M. Sullivan, M. L. Bruening, *Ind. Eng. Chem.* **2000**, *39*, 3528–3535.
32. J. Sun, T. Wu, F. Liu et al., *Langmuir* **2000**, *16*, 4620–4624.
33. J. B. Schlenoff, H. Ly, M. Li, *J. Am. Chem. Soc.* **1998**, *120*, 7626–7634.
34. E. Donath, D. Walther, V. N. Shilov et al., *Langmuir* **1997**, *13*, 5294–5305.
35. K. Lowack, C. A. Helm, *Macromolecules* **1998**, *31*, 823–833.
36. S. Han, B. Lindholm-Sethson, *Electrochim. Acta* **1999**, *45*, 845–853.
37. T. Farhat, J. B. Schlenoff, *Langmuir* **2001**, *17*, 1184–1192.
38. G. B. Sukhorukov, J. Schmitt, G. Decher, *Ber. Bunsen-Ges. Phys. Chem.* **1996**, *100*, 948–953.
39. L. Krasemann, B. Tieke, *Langmuir* **2000**, *16*, 287–290.
40. J. J. Harris, J. L. Stair, M. L. Bruening, *Chem. Mater.* **2000**, *12*, 1941–1946.
41. D. A. Lowy, H. O. Finklea, *Electrochim. Acta* **1997**, *42*, 1325–1335.
42. R. Jiang, F. C. Anson, *J. Phys. Chem.* **1992**, *96*, 10565–10571.
43. Y. Cheng, R. M. Corn, *J. Phys. Chem. B* **1999**, *103*, 8726–8731.
44. Y. Sun, J. Sun, X. Zhang et al., *Thin Solid Films* **1998**, 327–329, 730–733.
45. S.-F. Hou, H.-Q. Fang, H.-Y. Chen, *Anal. Lett.* **1997**, *30*, 1631–1641.
46. J. Hodak, R. Etchenique, E. J. Calvo et al., *Langmuir* **1997**, *13*, 2708–2716.
47. M. Onda, Y. Lvov, K. Ariga et al., *J. Ferment. Bioeng.* **1996**, *82*, 502.
48. Y. Lvov, in *Protein Architecture: Interfacing Molecular Assemblies and Immobilization Biotechnology* (Eds.: Y. Lvov, H. Möhwald), Marcel Dekker, New York, 2000, pp. 125–167.
49. Y. M. Lvov, Z. Lu, J. B. Schenkman et al., *J. Am. Chem. Soc.* **1998**, *120*, 4073.
50. Z. Lu, Y. M. Lvov, I. Jansson et al., *J. Colloid Interface Sci.* **2000**, *224*, 162.
51. H. Ma, N. Hu, J. F. Rusling, *Langmuir* **2000**, *16*, 4969.
52. Y. Lvov, B. Munge, O. Giraldo et al., *Langmuir* **2000**, *16*, 8850–8857.
53. J. F. Rusling, *Acc. Chem. Res.* **1998**, *31*, 363.
54. X. Zu, Z. Lu, Z. Zhang et al., *Langmuir* **1999**, *15*, 7372.
55. A. C. Onuoha, X. Zu, J. F. Rusling, *J. Am. Chem. Soc.* **1997**, *119*, 3979.

3
Epitaxial Electrochemical Growth

Michael D. Ward
New York University, NY, USA

3.1 **Introduction** **399**

3.2 **Design Approaches for Epitaxial Organic Films** **399**

3.3 **The Advantages of Electrochemistry and Atomic Force Microscopy** . **400**

3.4 **Atomic Force Microscopy in Electrochemical Cells** **401**

3.5 **Real-time Visualization of Electrochemical Growth** **403**
3.5.1 Growth of Molecular Overlayers 403
3.5.2 Electrochemical Annealing of Organic Overlayers 405

3.6 **Rules of Epitaxy for Organic Films** **406**
3.6.1 Epitaxial Nucleation of an Overlayer 406
3.6.2 Definitions of Epitaxy 406
3.6.3 Lattice Modeling and Prediction of Epitaxy 409

3.7 **Nucleation of Molecular Films** **411**

3.8 **Related Articles** **412**
References 412

Encyclopedia of Electrochemistry. Edited by A.J. Bard and M. Stratmann
Vol. 10 *Modified Electrodes*. Edited by M.Fujihira, I.Rubinstein, and J.F.Rusling
Copyright © 2007 Wiley-VCH Verlag GmbH & Co. KGaA, Weinheim. ISBN: 978-3-527-30402-8

3.1 Introduction

Fabrication of organic thin films requires a thorough understanding of the factors that govern their formation if they are to be used in applications such as light emitting diodes, nonlinear optical materials, field-effect transistors, rectifying junctions, and photovoltaic devices. The growing interest in organic films stems largely from the premise that collective optical and electronic properties can be systematically manipulated through molecular design. Many of these properties depend strongly upon film structure and orientation with respect to the substrate upon which they are deposited. If both the substrate and overlayer are crystalline, careful attention must be paid to the role of *epitaxy*, which refers to the registry between the overlayer and substrate lattices. As described herein, however, epitaxy between high-symmetry crystalline substrates and organic films that typically have large, low-symmetry unit cells requires a different approach than the more simplistic ones commonly used to describe epitaxy. The combination of electrochemistry and atomic force microscopy (AFM) allows one to observe directly the nucleation and growth events associated with the growth of organic films so that the epitaxial conditions at the interfaces can be deduced in a rather straightforward manner. This chapter will describe the electrochemical growth of a representative organic film, the use of real-time in situ AFM for the visualization of growth, the rules for epitaxy that govern the molecular organization of these films, and nucleation studies that illustrate how one can examine small ensembles of molecules that are physically constrained in ''corrals'' on the substrate.

3.2 Design Approaches for Epitaxial Organic Films

One approach to the design and synthesis of crystalline molecular films on ordered substrates involves relying on the ''native'' structure of the primary molecular overlayer, presumed to be at or near its minimum energy configuration, based on layer motifs existing in the corresponding bulk crystals. Organic crystals tend to assemble in the solid state as two-dimensional (2-D) layers with strong intralayer bonding (e.g. through hydrogen bonding, charge transfer, or heteroatom–heteroatom interactions). Thus, molecular layer motifs in bulk crystals

Encyclopedia of Electrochemistry. Edited by A.J. Bard and M. Stratmann
Vol. 10 *Modified Electrodes*. Edited by M.Fujihira, I.Rubinstein, and J.F.Rusling
Copyright © 2007 Wiley-VCH Verlag GmbH & Co. KGaA, Weinheim. ISBN: 978-3-527-30402-8

are ideal starting points for the design of robust films. This concept can be illustrated by the two different structural forms of the organic salts $(ET)_2X$ (ET = bis(ethylenedithiolo)tetrathiafulvalene; $X = I_3$), which actually are electrical conductors and, under certain conditions, superconductors at low temperatures. These compounds exhibit layers in the (001) planes, which are clearly evident from models derived from single-crystal X-ray diffraction analysis (Fig. 1). Interestingly, the two forms, referred to as α-$(ET)_2I_3$ and β-$(ET)_2I_3$, differ with respect to the tilt of the ET molecules in the layers and, more importantly, with respect to the symmetry of the two-dimensional unit cell of their respective (001) planes. As we shall see in the forthcoming sections, this symmetry affects the lattice registry of these planes with a growth substrate.

3.3 The Advantages of Electrochemistry and Atomic Force Microscopy

The nucleation and growth of organic thin films, and thin films in general, is challenging because it is difficult to initiate a nucleation process in a controlled manner. Furthermore, it is difficult to visualize these processes directly, particularly for growth processes occurring in a solution. The $(ET)_2X$ compounds, and other redox-active materials, can be grown by electrocrystallization, in which the ET molecule is oxidized at an electrode

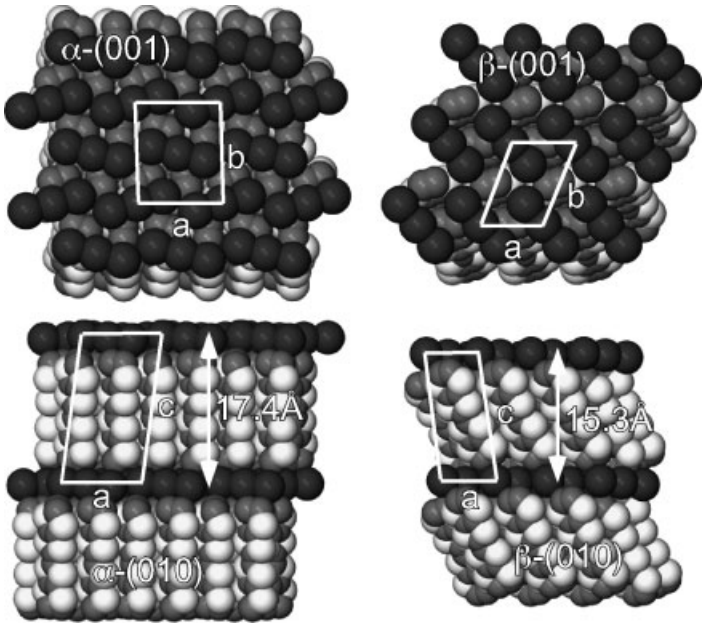


Fig. 1 Views of the (001) (upper) and (010) (lower) planes of the crystalline α (left) and β (right) phases of $(ET)_2I_3$. The thicknesses of the (001) layers differ because of the tilt angle of the ET molecules. The subtle packing differences between these two phases leads to a phase selectivity during epitaxial growth on highly oriented pyrolytic graphite.

surface that is immersed in a solution containing the X^- counterion, thereby precipitating as the $(ET)_2X$ salt. This allows nucleation to be initiated simply by applying a potential to the electrode surface, and subsequent growth to be controlled by regulation of that potential. The ability to trigger nucleation by electrochemically driven changes in redox state provides for accurate measurement of nucleation times from a common reference time (when the electrode potential is switched to the value for ET oxidation). The solute concentration at the substrate surface can be controlled potentiostatically, and monolayers can be repeatedly grown and removed electrochemically so that a statistically meaningful number of nucleation and growth events can be obtained. When combined with the real-space topographical imaging mechanism of AFM, which can be practiced in electrochemical cells with real-time visualization of near-molecular scale events, redox-active systems are ideal for examining the fundamental aspects of nucleation and growth of organic films.

3.4 Atomic Force Microscopy in Electrochemical Cells

Before illustrating actual examples of electrochemical growth of epitaxial organic films and their visualization by AFM, a brief description of the AFM method in this context is warranted. An atomic force microscope operates much like a surface profilometer. A small tip, usually of silicon or silicon nitride, at the end of a silicon cantilever is moved in small increments with piezoelectric actuators over the sample (or the sample is moved under the tip) while in contact with the sample surface. A two-dimensional image is acquired by rastering the tip over a specified area of the sample. Imaging can be accomplished at constant force, wherein the tip traces the topography of the surface with a vertical resolution approaching 0.1 Å, or in constant height mode, wherein the tip is kept at a constant height above the sample and the force between the tip and sample is measured. The force between the sample and tip is deduced from the position of a laser beam, reflected off the back of the cantilever, on a spatially sensitive photodiode detector (Fig. 2). When the tip experiences an attractive force, the cantilever bends toward the sample so that the laser position on the detector moves downward. Conversely, a repulsive interaction causes the cantilever to bend away from the sample so that the laser position moves upward. The deflection of the tip is calculated from the laser spot intensity from quadrants $(A + B) - (C + D)$.

A key issue for imaging of organic films is their susceptibility to mechanical damage as the AFM tip is rastered across the surface in the contact mode. Forces in excess of 10^{-11} N are sufficient to cause mechanical damage on soft organic crystal surfaces. This is problematic when imaging in air or vacuum where the van der Waals interaction is strongly attractive and the tip strongly engages the sample. Mechanical damage is exacerbated in air by capillary forces between the tip and sample, which result from capillary condensation of water between the closely spaced tip and sample. Under these conditions, etching of the sample surface as the tip is rastered is quite common.

Fortunately, performing AFM in solution eliminates capillary forces. Furthermore, in suitable fluids, tip–sample forces

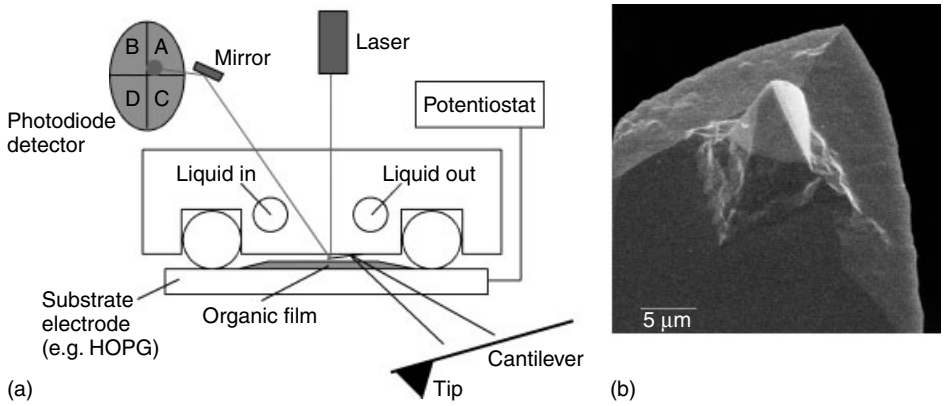


Fig. 2 (a) Schematic of atomic force microscopy detection method. A laser is reflected off the cantilever and detected with a four-segment detector. This allows visualization of both topographical and frictional information. (b) Scanning electron micrograph of a pyramidal Si_3N_4 AFM tip at the end of a silicon cantilever.

are reduced by the liquid medium. In general terms, the van der Waals energy between two objects is given by $w(r) = -Cr^{-6}$, where C is a constant (in units of J m^6) with a magnitude proportional to the attractive interaction between the two objects. Laws describing the interactions between two objects of various geometries can be devised by integrating the energies of all the atoms in one object with all the atoms in the other, to derive a ''two-body'' potential that can be described in terms of the Hamaker constant A, which is given by $A = \pi^2 C\rho_1\rho_2$, where ρ_1 and ρ_2 are number densities (in units of m^{-3}). In the case of a sphere (i.e. the AFM tip) interacting with a planar surface (i.e. a flat sample), the interaction energy between the tip and the sample can be approximated as $W = -AR/6D$, where R is the radius of curvature of the tip and D is the tip–sample separation. The Hamaker constant for materials 1 and 2 interacting across medium 3, obtained from a modified form of the Lifshitz theory, is given by Eq (1).

$$A_{132} = \frac{3kT}{4}\left(\frac{\varepsilon_1 - \varepsilon_3}{\varepsilon_1 + \varepsilon_3}\right)\left(\frac{\varepsilon_2 - \varepsilon_3}{\varepsilon_2 + \varepsilon_3}\right) + \frac{3\hbar\omega}{8\sqrt{2}} \left[\frac{(n_1^2 - n_3^2)(n_2^2 - n_3^2)}{(n_1^2 + n_3^2)^{1/2}(n_2^2 + n_3^2)^{1/2}[(n_1^2 + n_3^2)^{1/2} + (n_2^2 + n_3^2)^{1/2}]}\right] \quad (1)$$

where A_{132} is the Hamaker constant between the tip (1) and sample (2) in the liquid medium (3), ε_i and n_i are the dielectric constant and refractive index of medium I respectively, and $\hbar\omega$ is the ground state oscillation energy of the electron. For example, the Hamaker constant for the (tip)Si_3N_4|air|HOPG(sample) is 1.2×10^{-19} J, whereas for (tip)Si_3N_4|ethanol|HOPG(sample) A it is 9.0×10^{-20} J. The reduced interaction and the absence of capillary forces conspire to reduce the mechanical etching of soft samples.

Another consequence of imaging in fluids is an improvement in the lateral resolution. The resolution scale RS of AFM,

determined by the area of contact between the tip and the sample, is described by Eq. (2), where R_0 and D_0 are the AFM tip radius and the minimum tip–surface separation allowed by repulsive contact forces, respectively; K is the combined elastic modulus of the tip and sample, and A_{132} is the Hamaker constant. According to this equation, AFM resolution decreases with increasing van der Waals attraction between the tip and the sample.

$$RS = \left(\frac{A_{132} R_0^2}{8 K D_0^2} \right)^{\frac{1}{3}} \qquad (2)$$

It is important to note that the imaging mechanism does not involve contact of the sample with a single atom on the tip. The interaction force between a macroscopic tip and surface is actually rather long range, scaling as D^{-2}, where D is the tip–sample separation. This increases the effective contact area of the tip, thereby limiting the resolution to the radius of curvature of the tip, which typically has values of approximately 30 and 15 nm for conventional Si_3N_4 and Si tips, respectively.

This resolution limit seems to contradict the numerous AFM images that have been reported, in which atomic or molecular-scale periodicities are observed. The atomic or molecular-scale contrast is actually due to the periodic forces felt by the tip as it moves over the surface of the periodic lattice of the sample, generating what is tantamount to a Moire' pattern of the convolved forces between the macroscopic tip and periodic lattice of the sample. Fortunately, molecularly smooth films with sufficiently large domains, such as those described herein, allow attainment of molecular-scale contrast. But it must be emphasized that molecular-scale *contrast* is not identical to molecular-scale *resolution*.

The ability to image organic crystals and films with molecular-scale contrast enables determination of the lattice parameters of the imaged plane, while step heights can provide the lattice constant normal to the plane. Consequently, AFM can be useful for identification or confirmation of crystal structure. AFM and crystallographic dimensions will typically differ by <5%. These differences may be attributed partially to measurement error inherent in the AFM, although surface reconstruction with concomitant reduction in surface energy is also likely. Much of this data is acquired in liquids, so reconstruction can also result from surface interaction with solvent molecules.

3.5 Real-time Visualization of Electrochemical Growth

3.5.1 Growth of Molecular Overlayers

The aforementioned ET_2X layers fulfill three principal criteria for examining *electrochemical* growth of organic films: (1) the bulk crystals were intrinsically 2-D because of strong $\pi-\pi$ overlap between the molecules along one dimension and strong dispersive interactions between polarizable heteroatoms along a second dimension, which should favor overlayers that are structurally robust and amenable to study, (2) the ability to grow the films electrochemically enabled regulation of nucleation and growth that was not achievable with redox-inert systems, and (3) the growth of these films occurs under ambient conditions so that their assembly can be examined directly with AFM.

The electrocrystallization of $(ET)_2I_3$ salts on highly oriented pyrolytic graphite

(HOPG) were examined with real-time in situ AFM by using the HOPG substrate as an electrode [1]. Upon application of an anodic potential sufficient to generate ET^+ at the HOPG electrode that is immersed in an ET/acetonitrile solution confined within the AFM liquid cell, two-dimensional islands were formed on the HOPG surface. These islands exhibited an average thickness, as measured from the height difference with respect to the substrate, of 15.5 ± 0.5 Å (Fig. 3), identical to the thickness of the (001) layers of the β-$(ET)_2I_3$ crystals ($d_{001} = 15.28$ Å). The islands grew anisotropically along preferred growth directions on the HOPG surface ($10 \pm n60^\circ$ with respect to the graphite steps), eventually terminating at the edge of a graphite step or coalescing into a contiguous 15.5 Å thick overlayer.

AFM images acquired on small regions within the islands or on the contiguous overlayer revealed an ordered, periodic structure expected of a robust, crystalline organic film. The lattice parameters deduced from the real space and Fourier data revealed a 2-D unit cell with the lattice parameters $b_1 = 6.2 \pm 0.5$ Å, $b_2 = 9.4 \pm 0.8$ Å, and $\beta = 107 \pm 4^\circ$, comparing favorably to the single-crystal X-ray parameters of the (001) plane of bulk β-$(ET)_2I_3$ ($a = 6.6$ Å, $b = 9.1$ Å, and $\gamma = 110^\circ$). Notably, the overlayer lattice parameters and thickness do *not* correspond to the (001) layer in α-$(ET)_2I_3$ ($a = 9.183$ Å, $b = 10.804$ Å, $\gamma = 90.85^\circ$, and $d_{001} = 17.4$ Å) nor to any other crystallographic plane in either phase. These data clearly indicate that the overlayer formed on HOPG mimics the (001) layer in bulk β-$(ET)_2I_3$. The lattice rotation of the overlayer with respect to the underlying substrate lattice was deduced by imaging the substrate prior to overlayer deposition or imaging the substrate after overlayer deposition by using the AFM tip, at a higher applied force, to carve a hole in the overlayer. These measurements revealed an azimuthal relation between the overlayer and substrate lattices of ca 19° as measured from selected principal lattice vectors of the substrate and overlayer. Similar behavior can be observed for other $(ET)_2X$ salts, such as $(ET)_2ReO_4$.

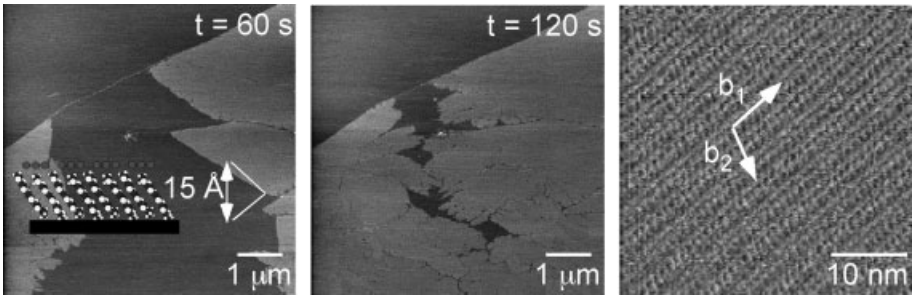


Fig. 3 AFM images acquired during growth of an β-$(ET)_2I_3$ overlayer on HOPG at 60 seconds (a) and 120 seconds (b). (c) Unfiltered molecular contrast AFM data of a monolayer film of ET_2I_3 on HOPG. The monolayer has a measured height of 15 Å, which closely resembles the layer height of the (001) plane taken from the bulk X-ray crystal structure of the β phase of ET_2I_3. The angle of azimuth between the overlayer and substrate is ca 19°.

3.5.2 Electrochemical Annealing of Organic Overlayers

Lateral force imaging, which relies on lateral twisting of the AFM cantilever caused by friction between the tip and sample, revealed that the "contiguous" β-$(ET)_2I_3$ overlayers were actually formed by the coalescence of separate domains. These domains had identical heights but three different orientations, evident in both lattice images and friction level, due to the symmetry of the HOPG substrate, leading to domain boundary defects. Frictional contrast between differently oriented compositionally identical domains is quite remarkable – the lateral twisting of the tip is apparently highly sensitive to the orientation of the molecular groups protruding at the surface. Furthermore, it corroborates the mechanical robustness and crystalline integrity of these films.

When imaging was performed such that the cantilever scan direction was perpendicular to the cantilever long axis (90° scanning mode) the domain boundaries were clearly distinguished by large friction values compared with those of the domain interiors (Fig. 4a). The enhanced friction at the domain boundaries can be attributed to disorder and decreased rigidity in these regions. Lateral force imaging at 0° produced larger differences between the domain surfaces (Fig. 4b). The observation of different friction levels in different domains when scanning at either of these fixed angles must be due to the three possible orientations of the crystalline domains, since the domains are of identical composition and structure.

The application of a potential that was cathodic compared to the overlayer stripping potential (550 mV versus Ag/AgCl) resulted in film dissolution at the domain boundaries [2], the rate of dissolution at the boundaries increasing with decreasing domain size. Cycling the film potential between 550 and 675 mV, cathodic compared with the stripping potential and anodic compared with the

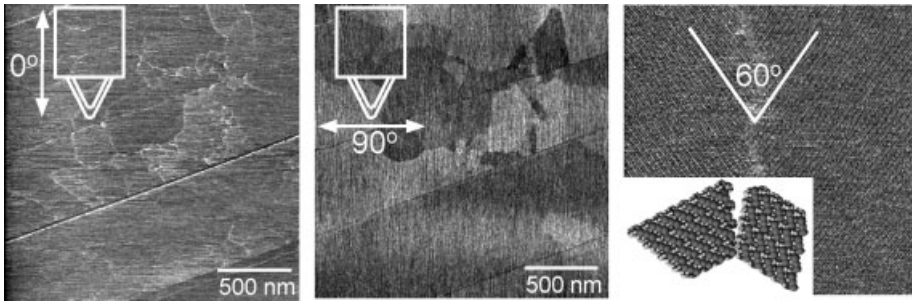


Fig. 4 Different contrast for domains of the β-$(ET)_2I_3$ films were observed depending upon the scan direction of the AFM tip. The left image (taken with the tip scanning at 0°) exhibits little contrast between domains (a), while the center image (taken with the tip scanning at 90°) exhibits marked contrast between domains (b). This phenomenon is due to the molecular orientations within different domains, in addition to the different sensitivity imparted to the tip by scanning at different angles. Different molecular orientations between domains are depicted on the right, with a model of the β-$(ET)_2I_3$ structure with a 60° domain boundary superimposed on a molecular contrast AFM image of a domain boundary (c).

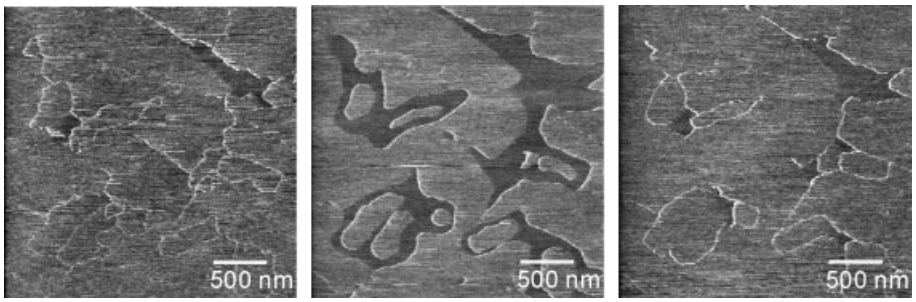


Fig. 5 AFM images illustrating the electrochemical annealing process for an overlayer of β-$(ET)_2I_3$. A nearly coherent overlayer (a) begins to dissolve (b) upon switching the electrochemical potential to a value less than the oxidizing potential for ET. During regrowth, the monolayer fills in the dissolved areas (c), mimicking the process of Ostwald ripening.

deposition potential, respectively, resulted in progressive growth of the larger domains at the expense of smaller domains (Fig. 5). Incompletely dissolved domains regrew with the same orientation as the smaller domain, but growth from the surrounding larger domains intruded onto the region previously occupied by the smaller domain. These observations illustrated that overlayers can be *electrochemically* annealed by simple potential cycling of the deposition and dissolution potentials, suggesting a facile approach to the fabrication of high-quality redox-active molecular films on substrates, including those with nonplanar geometries.

3.6 Rules of Epitaxy for Organic Films

3.6.1 Epitaxial Nucleation of an Overlayer

The observation of a preferred orientation for an organic film, such as that observed for the β-$(ET)_2I_3$ overlayers, is a signature of epitaxy, wherein the substrate and the overlayer lattices are related by a phase relationship in which some registry is achieved. Growth of an organic overlayer near thermodynamic equilibrium involves reversible adsorption of molecules on the substrate surface and the aggregate edges, with the molecules arriving at the edges through surface diffusion following arrival on the substrate (Fig. 6). Nucleation involves fluctuations in which nuclei of various sizes continually assemble and disassemble at different azimuthal orientations on the substrate. An aggregate with a good epitaxial match corresponds to a more negative E_{inter}, which affords a smaller barrier to nucleation and sustained growth.

3.6.2 Definitions of Epitaxy

Epitaxy is often described simply as an overlap between a pair of substrate lattice vectors and a pair of overlayer-substrate vectors, wherein the lengths of the coinciding lattice vectors of the opposing lattices are related by integral multiples. This generates a condition known as *commensurism*, wherein each overlayer lattice point sits on one of a set of translationally

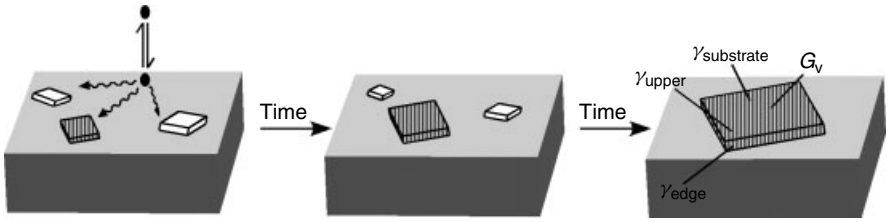


Fig. 6 Growth of a molecular overlayer near thermodynamic equilibrium involves reversible adsorption of molecules (black) on the substrate surface and the aggregate edges, the molecules arriving at the edges through surface diffusion following arrival on the substrate. Nucleation involves fluctuations in which nuclei of various sizes continually assemble and disassemble at different azimuthal orientations on the substrate. Achievement of critical nucleus dimensions at the preferred azimuthal orientation occurs when the sum of the aggregate volume-free energy (G_v, the sum of individual E_{intra} contributions) and the overlayer–substrate interface energy (E_{inter}) overcomes the contribution of the surface energies γ_{upper}, γ_{edge}, $\gamma_{substrate}$. An aggregate with a good epitaxial match (striped) corresponds to a more negative E_{inter}, which affords a smaller barrier to nucleation and sustained growth. The epitaxial aggregation at the expense of others in nonepitaxial alignments (white) tend to dissociate because of less favorable E_{inter} values.

equivalent substrate lattice point. If the lengths are not integral multiples, then a percentage mismatch based on the difference between the two coinciding vectors is used to describe the ''quality of epitaxy.'' In the case of organic films, this may not be the best approach for characterizing epitaxy. Efforts in our laboratory have demonstrated oblique, low-symmetry unit cells that are characteristic of organic layers, which cannot achieve commensurism with high-symmetry substrates, achieve epitaxy through *coincidence*, in which the ''point-on-point'' (POP) commensurism between a densely packed overlayer and the substrate is achieved only at the vertices of a supercell comprising several primitive unit cells of the overlayer. The achievement of commensurism or coincidence is governed by a delicate balance of the intralayer interactions between the molecules and local interactions between the molecules and the substrate. When the former dominates, coincidence is possible.

To understand this in more detail, it is necessary to describe an epitaxial interface using seven parameters, the lattice parameters of the substrate, a_1, a_2, and α, the lattice parameters of the overlayer, b_1, b_2, and β, and the azimuthal angle θ, between the lattice vectors $\vec{a}_1$ and $\vec{b}_1$ (Fig. 7). The substrate and overlayer lattice vectors for a given azimuthal orientation θ are related through the transformation matrix [**C**] in Eq. (3), where the matrix coefficients are defined by Eqs (4)–(7).

$$\begin{bmatrix} \vec{b}_1 \\ \vec{b}_2 \end{bmatrix} = [\mathbf{C}] \begin{bmatrix} \vec{a}_1 \\ \vec{a}_2 \end{bmatrix} = \begin{bmatrix} p & q \\ r & s \end{bmatrix} \begin{bmatrix} \vec{a}_1 \\ \vec{a}_2 \end{bmatrix} \tag{3}$$

$$p = b_1 \sin(\alpha - \theta)/a_1 \sin(\alpha) \tag{4}$$

$$q = b_1 \sin(\theta)/a_2 \sin(\alpha) \tag{5}$$

$$r = b_2 \sin(\alpha - \theta - \beta)/a_1 \sin(\alpha) \tag{6}$$

$$s = b_2 \sin(\theta + \beta)/a_2 \sin(\alpha) \tag{7}$$

Employing this matrix as a mathematical guide, epitaxy can be classified generally according to three principal categories that illustrate the complexity of epitaxy [3], particularly for low-symmetry overlayers:

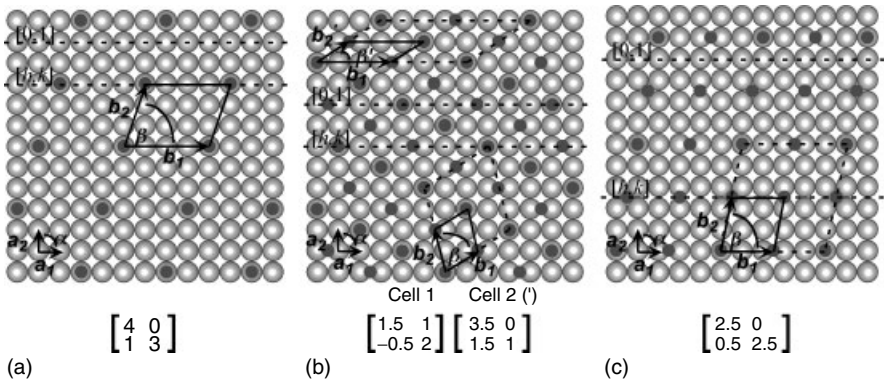


Fig. 7 Schematic representation of the possible modes of epitaxy. Overlayer lattice points are depicted as small filled circles and substrate lattice points are depicted as larger shaded circles and the overlayer primitive cells are indicated by solid lines. (a) In a commensurate overlayer, every overlayer lattice point coincides with a substrate lattice point and certain overlayer [*h*, *k*] lines; in this case [1,4] overlayer lattice lines, coincide with primitive [0,1] substrate lines. Although one matrix element is zero in this example, this is not required for commensurism. (b) Coincidence-IA point-on-line (POL) overlayers require that all four matrix elements be rational with two integers confined to one column. All overlayer lattice points, here distributed on overlayer [1,2] lattice lines, must lie on a particular primitive substrate line, here [0,1]. The 2×2 supercell for this overlayer is indicated by dashed lines connecting the supercell corners. An alternative choice of the primitive unit cell is depicted by lattice vectors $\vec{b}_1'$ and $\vec{b}_2'$. The area and transformation matrix determinants are identical for both cells. (c) A coincidence-II overlayer, with *p*, *q*, and *r*, rational and *s* equal to zero. Along both primitive substrate directions, every point-on-line overlayer lattice point is compensated by a lattice point that lies between primitive substrate lines.

- *Commensurism (POP)*: $p, q, r,$ and s are all integers. All the overlayer lattice points lie simultaneously on *two* primitive substrate lattice lines and coincide with symmetry-equivalent substrate points (Fig. 7a). This can be described alternatively as POP coincidence. Each primitive overlayer lattice vector is an integral multiple of an identically oriented (primitive or nonprimitive) substrate lattice vector. This condition is generally regarded the energetically most favorable one with respect to the overlayer–substrate interface because the surface potentials of the two opposing lattices, which have periodicities that conform to the lattice dimensions, are phase coherent. This coherence optimizes the attractive interactions that drive the formation of the overlayer. The overlayer lattice points in the illustration are placed on substrate lattice points for ease of visualization. The actual positions of the overlayer lattice points will be dictated by the surface potentials, but the phase coherence is independent of overlayer translation (note that the transform matrix describes rotation only).
- *Coincidence-I (POL)*: Among $p, q, r,$ and s are at least two integers confined to a single column of the matrix. Certain $[h, k]$ lines of the overlayer coincide with one set of *primitive* substrate lines (i.e. [0,1]). Therefore, the condition $\vec{b}_1^* = \vec{a}_1^*$ applies if the unit cell is

properly constructed. Every lattice point of the overlayer lies at least on *one* primitive lattice line of the substrate, a condition that can be described as *point-on-line* (POL) coincidence. POL coincidence can be subdivided into two classes depending on whether one of the noninteger matrix elements is rational or irrational:

Coincidence-IA (POL): $p, q, r,$ and s are all rational numbers. A supercell, which in the case of Fig. 7(b) is a 2×2 array of primitive cells, defines the phase-coherent registry with the substrate. By convention, the supercell is defined by corners that coincide with substrate lattice points. If these sites are considered energetically preferred, this condition implies that the other overlayer lattice points on or within the perimeter of the supercell are less favorable. Consequently, if only the overlayer–substrate interface is considered, coincidence is less preferred than commensurism. Two alternative primitive unit cells are depicted here, constructed from different primitive lattice vectors. Though the matrix elements differ, the determinants and, therefore, the areas are identical. Note that the description of the unit cell with $\vec{b}_1'$ coinciding with [0,1] illustrates the reciprocal space criterion $\vec{b}_1'^* = m\vec{a}_1^*$ ($m = 1$).

Coincidence-IB (POL): At least one of the noninteger elements in the matrix is an irrational number. The irrational element(s) produce(s) an incommensurate relation between the overlayer and substrate along the coinciding primitive lattice vector. In this case, the supercell is only defined at infinity along this primitive lattice vector. From a practical point of view, a coincidence-IA cell may appear to be a coincidence-IB cell if its supercell size exceeds the bounds of the experimental measurement.

- *Coincidence-II*: $p, q, r,$ and s are rational numbers, but no column consists of integers. Only *some* $[h, k]$ lines of the overlayer coincide with the [0,1] lines of the substrate. Consequently, only *some* of the overlayer lattice points lie on primitive substrate lattice lines. This condition demands that $\mathbf{b}_1* = f\mathbf{a}_1*$ (here $\mathbf{b}_1^*$ and $\mathbf{a}_1^*$ denote reciprocal space lattice vectors, not necessarily reciprocal space lattice *basis* vectors), where f must be a rational fraction (if f is irrational, the overlayer must be incommensurate). Because a supercell can still be constructed, as illustrated in Fig. 7(c), this configuration technically fulfills the criterion for coincidence. This mode of epitaxy, however, violates the aforementioned reciprocal space criterion for coincidence.

 Incommensurism: At least one of the elements $p, q, r,$ and s is irrational and neither column of the translation matrix consists of integers. Under this condition, no distinctive registry between the substrate lattice and the deposit lattice exists.

3.6.3 Lattice Modeling and Prediction of Epitaxy

A conceptually simple approach to determining the most likely epitaxial orientation for a given overlayer on a given substrate relies on the direct space analysis of the phase coherence between the two opposing lattices, that is by a superposition of plane waves. This approach, which is contained within a program we have dubbed EpiCalc, consists of a real-space *analytic* expression that evaluates the phase coherence between overlayer and substrate

lattices at a specified azimuthal angle for a specified set of lattice parameters (EpiCalc is available on the World Wide Web at http://www.wardgroup.umn.edu/software/software.html) [4]. The premise for this method is the correspondence between the lattice periodicities of the overlayer and substrate and their respective surface potentials, described as simple plane waves that are modeled as cosine functions. The algorithm is constructed so that the analytic function returns a dimensionless potential V/V_o, over a user-defined range of azimuthal angles and angle increments, requiring as input only the substrate lattice parameters and either a single set or range of overlayer lattice parameters. The function returns discrete values of $V/V_o = 1$ and $V/V_o = 0.5$ for incommensurism and POL coincidence, respectively, $V/V_o = 0$ for commensurism on nonhexagonal substrates, and $V/V_o = -0.5$ for commensurism on hexagonal substrates. The supercell size of a coincident overlayer can be determined by finding the integers (c and d) needed to generate integer values for the matrix coefficients of $\vec{a}_1$ and $\vec{a}_2$, where $cb_1 \times db_2$ is the supercell size.

If this analysis is applied to the (001) β-$(ET)_2I_3$ film on HOPG an azimuthal orientation of ca 19° between overlayer and substrate lattices is predicted, in agreement with the results. This layer is found by EpiCalc to be coincident, preserving the bulk crystal structure with a 1×3 supercell and an azimuthal rotation of 19° (Fig. 8), in agreement with the experimental measurements. Similar analyses of numerous organic films fabricated by us and others revealed that coincidence was quite common and more important was that the EpiCalc results almost always detected the epitaxial configurations observed experimentally or predicted by higher level potential energy calculations [5]. The lattice analysis provided by EpiCalc, however, can be performed in minutes, making this a valuable tool for the design of epitaxial organic films.

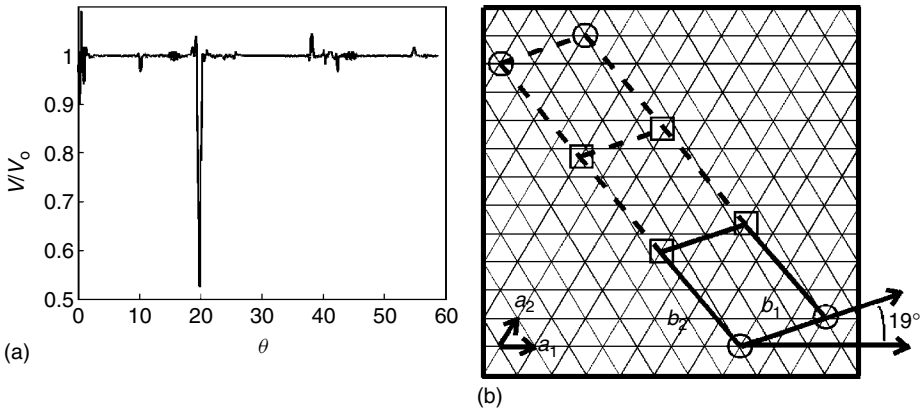


Fig. 8 (a) EpiCalc results for an (001) ET_2I_3 overlayer on an HOPG substrate. The V/V_o minimum of 0.5 at 19° indicates coincidence at this angle of azimuth. The resulting translation matrix $\vec{b}_1 = 2\vec{a}_1 + 1\vec{a}_2$, $\vec{b}_2 = -4\vec{a}_1 + 10/3\vec{a}_2$ indicates a supercell size of $1b_1 \times 3b_2$. (b) The overlayer-substrate relationship for this system. Open circles mark locations of lattice coincidence, while open squares mark locations of noncoinciding lattice points.

3.7 Nucleation of Molecular Films

Though the example above illustrates film growth, it does not reveal the actual nucleation events responsible for the initiation of film growth. Direct visualization of nucleation by scanning probe microscopy is complicated by the probabilistic and stochastic nature of the process, which frustrates observation of nucleation events on selected substrate regions at desired times and requires numerous observations for meaningful statistical analysis. Furthermore, nucleation must be examined at length scales near the critical dimensions to probe molecular ordering, precisely.

These obstacles can be overcome, at least partially, by electrochemical growth of organic overlayers, such as the β-$(ET)_2I_3$ overlayers, in ''pits'' or ''corrals'' that can be generated thermally on HOPG substrates. On such surfaces, overlayer growth occurred predominantly on the terraces surrounding the pits, with the pits usually filling only after the terrace was completely covered by the β-$(ET)_2I_3$ monolayer (Fig. 9) [6]. When nucleation did occur in a pit, the growth was sufficiently fast that the pit filled completely on the timescale of image acquisition (ca 1 minute). Consequently, the actual growth of nuclei could not be observed, but the formation of a monolayer in a pit signifies a nucleation event. Numerous trials indicated that (1) monolayer nucleation was not initiated at pit edges, in agreement with the absence of step-initiated growth on untreated HOPG terraces, (2) monolayers on the terrace did not induce nucleation in the pit, and (3) overlayer nucleation within a pit, when it did occur in the absence of terrace growth, did not induce nucleation on the surrounding terrace. Nucleation occurred at different terrace locations and in different pits in successive growth sequences, consistent with random nucleation events and the absence of persistent nucleation centers.

The broad distribution of pit sizes on a single HOPG substrate enabled simultaneous measurement of β-$(ET)_2I_3$ nucleation in different pit sizes, while the ability to repeat the growth sequence by electrochemical removal of grown overlayers enabled the acquisition of statistically meaningful number of measurements. Furthermore, overlayer formation in the pits can be deduced from AFM data without having to obtain molecular-scale contrast, enabling measurements on

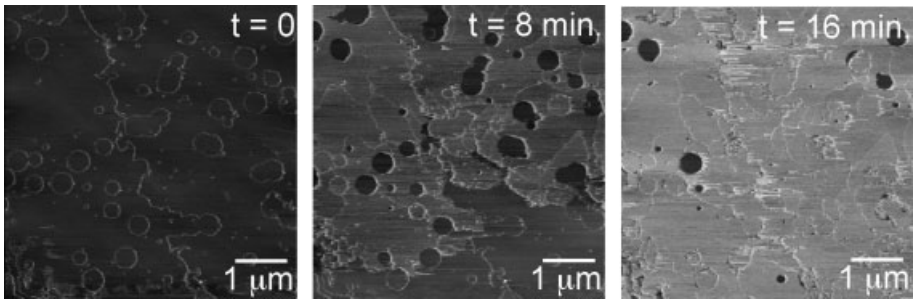


Fig. 9 Real-time in situ AFM images acquired during growth of a type I β-$(ET)_2I_3$ overlayer on a pitted HOPG electrode substrate. Lateral force images are shown here to depict better the contrast between the monolayer and the HOPG substrate. The overlayer initially covers the open terraces, with pits filling in over time, from larger to smaller pits, statistically.

large substrate areas in a single image frame so that many nucleation events can be recorded simultaneously. Nucleation statistics were compiled for both overlayer types by measuring the fraction of pits filled for differently sized pits at specific times following the application of the overlayer growth potential. Analysis of a large amount of data revealed that growth in the pits was limited by transport from the bulk solution, principally because the pit edge served as a barrier to molecules from the surrounding terraces. More important, β-$(ET)_2I_3$ overlayers never formed in pits with diameters smaller than 100 nm. This observation, as well as modeling of the experimental data, suggested that the critical nucleus size was roughly 3000 $(ET)_2I_3$ "units."

3.8 Related Articles

2-D Phase Transitions in Adsorbed Layers Thermodynamics and Electrified Interfaces, Vol 10; Atomically Controlled Deposition and Dissolution of Metals Thermodynamics and Electrified Interfaces, Vol 10; Molecular Epitaxy in Electrochemistry Thermodynamics and Electrified Interfaces, Vol 10; In Situ Imaging Interfacial Kinetics and Mass Transport, Vol 10; Electrochemical Nucleation and Growth Interfacial Kinetics and Mass Transport, Vol 10; Electrodeposition of nanoparticles Interfacial Kinetics and Mass Transport, Vol 10; Electrochemical AFM Instrumentation and Electroanalytical Chemistry, Vol 10; Layer-by-layer Assemblies of Thin Films on Electrodes Modified Electrodes, Vol 10; Organic Polymer Modified Electrodes Modified Electrodes, Vol 10; AFM, In Situ Methods Modified Electrodes, Vol 10.

References

1. J. A. Last, A. C. Hillier, D. E. Hooks et al., *Chem. Mater.* **1998**, *10*, 422.
2. J. A. Last, M. D. Ward, *Adv. Mater.* **1996**, *8*, 730.
3. D. E. Hooks, T. Fritz, M. D. Ward, *Adv. Mater.* **2001**, *13*, 227.
4. A. C. Hillier, M. D. Ward, *Phys. Rev. B* **1996**, *54*, 14037.
5. J. A. Last, D. E. Hooks, A. C. Hillier et al., *J. Phys. Chem. B* **1999**, *103*, 6723.
6. D. E. Hooks, C. M. Yip, M. D. Ward, *J. Phys. Chem. B* **1998**, *102*, 9958.

4
Organic Polymer Modified Electrodes

Susumu Kuwabata
Graduate School of Engineering, Osaka University, Osaka, Japan

Hiroshi Yoneyama
Anan National College of Technology, Tokushima, Japan

4.1 **Doping of Molecules Having Specific Functions in the Conducting Polymers** **415**

4.2 **Covalent Binding of Functional Molecules to the Conducting Polymers** **418**

4.3 **Composites of the Conducting Polymers and Inorganic Materials** . . **419**

4.4 **Conducting Polymers Having Specific Morphology** **421**
References 422

Encyclopedia of Electrochemistry. Edited by A.J. Bard and M. Stratmann
Vol. 10 *Modified Electrodes*. Edited by M.Fujihira, I.Rubinstein, and J.F.Rusling
Copyright © 2007 Wiley-VCH Verlag GmbH & Co. KGaA, Weinheim. ISBN: 978-3-527-30402-8

4.1
Doping of Molecules Having Specific Functions in the Conducting Polymers

Electrically conducting polymers of high popularity, such as polypyrrole, polythiophene, polyaniline, and their derivatives, are easily prepared by oxidative polymerization of the corresponding monomers. Both electrochemical oxidation and chemical oxidation using an appropriate oxidizing agent such as Fe(III) are useful. When the polymerization takes place, the resulting polymers obey positive charges, which allow spontaneous doping of anions present in the polymerization baths to compensate the positive charges of the polymers. The doped anions can easily come out on reduction of the polymers if the size of the anions is small in the relative sense. If the size of the anions is great, however, the doped anions are retained even when the as-prepared conducting polymers are reduced. Instead, cations in the electrolyte solutions used for reducing the as-prepared polymers are doped in such cases, as schematically illustrated in Fig. 1. Such highly stable properties of doped anions are utilized as the means of attaching special functions to the conducting polymers. The validity of the idea was first demonstrated for cobalt porphyrin–doped polypyrrole films prepared by electrochemical polymerization of pyrrole in the presence of the cobalt porphyrin sulfonate [1, 2]. The prepared polymer-coated electrodes exhibited their catalytic activities for electrochemical reduction of oxygen due to the immobilized cobalt porphyrin in the polypyrrole films. If metal-phthalocyanines having electrochromic properties were doped in polypyrrole films using the same technique, the resulting polymer films showed vivid electrochromic responses [3, 4]. Both polypyrrole and the doped phthalocyanine are involved in the redox reaction of the polymer film in such a way as to cause color change of the polymer films. Similar methods were adopted to prepare the conducting polymers doped with inorganic ions [5–8], organic compounds [9, 10], heteropolyanions [11–14], and metal complexes [15–23] to attach the special functions of the dopants to the conducting polymers, as shown in Table 1.

Anions having greater sizes, such as poly(styrenesulfonate) [24–36], poly(vinyl sulfate) [24, 36–40], and Nafion [41–45], which are known as polyelectrolytes, are also used as the dopants in the conducting polymers. Electrochemical polymerization of the monomer in the presence of the polyelectrolyte in the polymerization bath yields the conducting polymer films

Encyclopedia of Electrochemistry. Edited by A.J. Bard and M. Stratmann
Vol. 10 *Modified Electrodes*. Edited by M.Fujihira, I.Rubinstein, and J.F.Rusling
Copyright © 2007 Wiley-VCH Verlag GmbH & Co. KGaA, Weinheim. ISBN: 978-3-527-30402-8

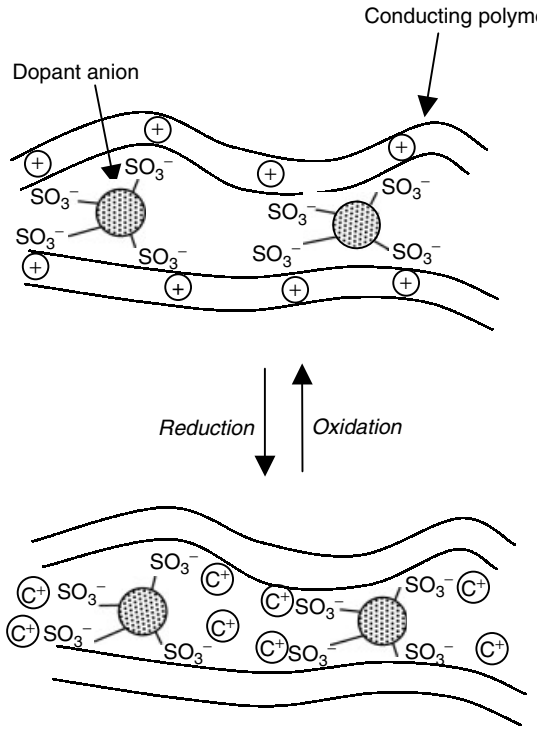


Fig. 1 Redox reaction schemes of a conducting polymer doped with large electrolyte anions. C^+ denotes electrolyte cation.

Tab. 1 Conducting polymers doped with electrolyte anions having specific functions

Conducting polymer	*Dopant*	*Function*	*Ref.*
Polypyrrole or its derivatives	Porphyrin derivative	Electrocatalytic activities	1, 2
	Phthalocyanine derivative	Electrochromic properties electrocatalytic activities	3, 4, 15–17
	Anthraquinone-1-sulfonate	Redox activities	9
	Calixarene	Ion-sensitivities	10
	$Fe(CN)_6^{4-}$	Redox activities	18–20
	Heteropolyanion	Electrocatalytic activities	11
	Prussian blue	Redox activities, pH sensitivities	21–23
	MoS_4^{2-}, MoS_3	Redox activities	5–8
Poly-3-methylthiophene	Heteropolyanion	Electrocatalytic activities	12
Polyaniline	Heteropolyanion	Electrocatalytic activities	12–14

containing the anionic polyelectrolytes. Since the polyelectrolyte anions occupy a large geometric fraction of the deposited films, the polymerized materials can be regarded as the composites. The redox reaction schemes of the composites are the same as those of conducting polymers containing anions of large sizes as mentioned

above and as illustrated in Fig. 1. Similar composites of a conducting polymer and an anionic polyelectrolyte are also prepared by using polyelectrolyte film-covered electrodes as the anode [46–51]. The polyelectrolyte film-covered electrodes are easily prepared, because the polyelectrolyte can easily be formed in a thin film form on conducting electrode substrates. The polymerization reactions in such cases are initiated at the surface of the electrode substrate, and the polymer film grows in a direction perpendicular to the electrode substrate with the use of anions of the polyelectrolyte film as the charge compensator for positive charges of the conducting polymers. The composites made of a conducting polymer and a polyelectrolyte have almost the same electrical conductivity as the corresponding polymer film containing conventional anions and they have high mechanical strength, allowing them to be free standing in both liquid and gas phases.

Though anionic species are incorporated in the conducting polymers in their preparations, the immobilization of a large cationic molecule in a composite film was also achieved by electrochemically polymerizing aniline in the presence of methylene blue and Nafion [42, 43]. Only a fraction of the negative charges of Nafion is used to bind electrostatically methylene blue cations, and the remaining negative charges of Nafion are utilized for immobilizing methylene blue–bound Nafion in polyaniline.

A lot of biomolecules like enzymes can also be immobilized in the conducting polymer film by electrochemical polymerization of a monomer in the presence of the biomolecules, because many kinds of biomolecules are negatively charged in neutral aqueous solutions where the electrochemical polymerization can be carried out. The most extensive studies that have been made in the area are to immobilize glucose oxidase in several kinds of conducting polymers to fabricate amperometric glucose sensors of small sizes [52–87], the working principle of which is as follows. The glucose oxidase immobilized in polypyrrole films catalyzes oxidation of glucose, resulting in reduction of the immobilized enzyme. The reduced enzyme is then spontaneously oxidized to its original chemical state by an appropriate electron acceptor, which is present in the glucose solution such as dissolved oxygen. The electron acceptor is then reduced and its amount is determined by measuring anodic currents at the enzyme-immobilized polypyrrole films that are polarized anodically. Several kinds of redox agents such as anionic ferrocene and quinone derivatives work well as the earlier-mentioned electron acceptors, and those redox agents are easily immobilized together with glucose oxidase, if the conducting polymers are prepared in the presence of glucose oxidase and redox agents having anionic groups such as sulfonate groups [31, 88–95]. The immobilization of other biomolecules in polypyrrole films using the oxidative polymerization of the monomer in the presence of dissolved biomolecules was successfully achieved for alcohol dehydrogenase [96, 97], cholesterol oxidase [98–100], galactose oxidase [101–103], glutamate oxidase [104–106], peroxidase [73, 105, 107–115], sacrosine oxidase [116–120], urease [121–123], uricase [124–128], and other biomolecules [106, 129–144], resulting in preparation of biocatalytic electrodes with characteristics of the doped molecules. Table 2 summarizes those results.

Tab. 2 Conducting polymers doped with biomolecules

Conducting polymer	*Biomolecule doped*	*Ref.*
Polypyrrole or its derivatives	Glucose oxidase	31, 52–75, 88–95
	Alcohol dehydrogenase	96, 97
	Cholesterol oxidase	98, 99
	Flavin reductase	129, 130
	Fructose dehydrogenase	131–133
	Galactose oxidase	101
	Glucose dehydrogenase	134
	Glutamate oxidase	104–106
	Glutamate dehydrogenase	135
	P-450	136
	Penicillinase	137
	Peroxidase	73, 105, 107–110
	Polyphenol oxidase	106, 138
	Pyruvate oxidase	139
	Sacrosine oxidase	116, 117
	Sulfite oxidase	119, 120
	Urease	121, 122
	Uricase	124–127
	Xanthine oxidase	140
Polythiophene or its derivatives	Glucose oxidase	76, 77
	Nitrate reductase	142
Polyaniline or its derivatives	Glucose oxidase	78–86
	Ascorbate oxidase	145
	Cholesterol oxidase	100
	Choline oxidase	143
	Galactose oxidase	102, 103
	Lactate dehydrogenase	144
	Peroxidase	111–115
	Sacrosine oxidase	118
	Urease	123
	Uricase	128
	Xanthine oxidase	141
Polyindole	Glucose oxidase	87

4.2 Covalent Binding of Functional Molecules to the Conducting Polymers

Besides the electrostatically driven spontaneous doping of anionic functional molecules in the conducting polymers as mentioned earlier, chemical derivatization of the conducting polymers with functional molecules are also useful as the means of attaching special functions to the conducting polymers. For example, ferrocenecarbonyl group is easily coordinated to the nitrogen atoms of the pyrrole rings of polypyrrole just by immersing the polypyrrole film in a ferrocenecarbonyl chloride solution [146]. When monomers substituted by functional molecules are used for the electrochemical polymerization reactions, conducting polymer films having chemical functions characteristic of the covalently bound groups are prepared as given in Table 3 [111, 147–179].

Tab. 3 Conducting polymers chemically derivatized with functional molecules

Base polymer	*Substituted molecule*	*Ref.*
Polypyrrole	Anthraquinone	147
	Ferrocene	146, 148, 149
	Metal–bipyridine complexes	150–153
	Polyether or crown ether	154–156
	Porphyrin	157, 158
	Metal–cyclam complexes	159
	Oligonucleotide	160
	Glucose oxidase	161–164
Polythiophene	Metal porphyrin	165
	Polyether or crownether	166–178
Polyaniline	Ferrocene	111, 179

Interestingly, the electrochemical polymerization of the pyrrole monomers derivatized with electrochemically active species such as ferrocene and Ni-cyclam in the presence of glucose oxidase yields polymer films capable of determining the amount of glucose without using any redox agents in the solution [149, 159]. As a related subject, the chemical derivatization of nonconducting polymers (polyvinylpyridine or polyimidazole) with both an osmium complex as a redox agent and glucose oxidase were successfully used to prepare high-performance amperometric glucose sensors [180–182].

4.3 Composites of the Conducting Polymers and Inorganic Materials

The immobilization of inorganic materials having special functions in the conducting polymers was also achieved, as shown in Table 4 [183–208]. Since the inorganic materials possess usually no active sites

Tab. 4 Composites of conducting polymer and inorganic material

Conducting polymer	*Inorganic material*	*Function*	*Ref.*
Polypyrrole	Pt	Electrocatalytic activity	183, 184
	RuO_2	Electrocatalytic activity (O_2 evolution)	185
	WO_3	Electrochromic activity Photoactivity	186–189
	MnO_2, $LiMn_2O_4$	Positive electrode material	190–195
	TiO_2	Photoactivity	196, 197
	SiO_2	Hole transportation	198
	Pt	Electrocatalytic activity	183, 184
Polyaniline	TiO_2	Photoactivity	199–201
	V_2O_5	Positive electrode material	202
	WO_3	Electrochromic activity Photoactivity	203, 204
	CdS	Photoactivity	205, 206
	Au	Electrocatalytic activity	207
	Pt	Electrocatalytic activity	208

that are useful for being immobilized in the conducting polymers, a little different approach from the case of the earlier-mentioned organic anion doping is needed to immobilize the inorganic materials into the conducting polymers. One approach that has been taken for the immobilization is to use anionic inorganic substances such as RuO_4^{2-} [185] and $PtCl_6^{2-}$ [183] as the starting material for immobilizing RuO_2 and Pt, respectively, in the conducting polymer films. Electrochemical polymerization of pyrrole in the presence of RuO_4^{2-} or $PtCl_6^{2-}$ yields polypyrrole films containing these anionic species. Succeeding electrochemical reduction of the prepared polypyrrole films gave polypyrrole films containing RuO_2 [185] or metallic platinum [183]. A similar technique was used to synthesize polypyrrole films containing Pt [184] with the use of $PtCl_4^{2-}$ as a dopant and polyaniline films containing Pt [208] and Au [207]. Since RuO_2 works as an efficient electrocatalyst for evolving oxygen from aqueous solution, RuO_2-immobilized polypyrrole film coated on n-type GaP electrodes worked well for photo-assisted oxidation of water to evolve oxygen [185]. The immobilized Pt or Au in the conducting polymers worked well as the electrocatalyst for O_2 reduction [183] and oxidation of methanol [184].

Immobilization of a large amount of oxide particles in the conducting polymer was successfully achieved using a different approach. Oxides having isoelectric point (*isp*) smaller than ca. 6 such as SiO_2, WO_3, and SnO_2 obey negative charges in aqueous neutral solutions, in which oxidative polymerization of pyrrole can be performed. Thus, the anodic oxidation of pyrrole in aqueous suspensions containing one of these oxides results in polypyrrole films containing the oxide particles [209]. Oxide content as large as 80 wt% was achieved for the electrochemical immobilization of WO_3, and then the prepared materials were regarded as composites, which showed electrochromism due both to WO_3 and polypyrrole and behaved as photosensitive electrodes due to the WO_3 [186]. Composite formation using metallic oxide particles whose *isp* is greater than ca. 6 was also accomplished with the assistance of electrolyte anions that specifically adsorb on the suspended oxide particles. Composites consisting of polypyrrole and TiO_2 were prepared electrochemically using iodide ions as the specifically adsorbing ions [196], and chloride ions were used in the preparation of polyaniline–TiO_2 composites [199–201], polyaniline–WO_3 composites [203], and polyaniline–CdS composites [205]. Composite films consisting of polyaniline and either TiO_2 or WO_3 were found to be useful for erasable recording of photo-images of high resolution [199, 200, 203] (see Chapter 23 in Volume 6). The same synthesis principle was also applied to electrochemical synthesis of β-MnO_2-polypyrrole and lithiated manganese oxide-polypyrrole [190, 191], and V_2O_5–polyaniline composites [202] using chloride ions as the specifically adsorbing ions.

Besides electrochemical synthesis, chemical synthesis of β-MnO_2–polypyrrole and $LiMn_2O_4$–polypyrrole composites was achieved using acidic pyrrole solutions containing the suspended manganese oxides as the oxidizing agent [192, 195]. The content of the oxide in the composites is usually varied more or less by changing the amount of oxide in the polymerization bath, as shown in Fig. 2 for the cases of chemically synthesized β-MnO_2–polypyrrole and $LiMn_2O_4$–polypyrrole composites [192]. The conducting polymers containing β-MnO_2, $LiMn_2O_4$,

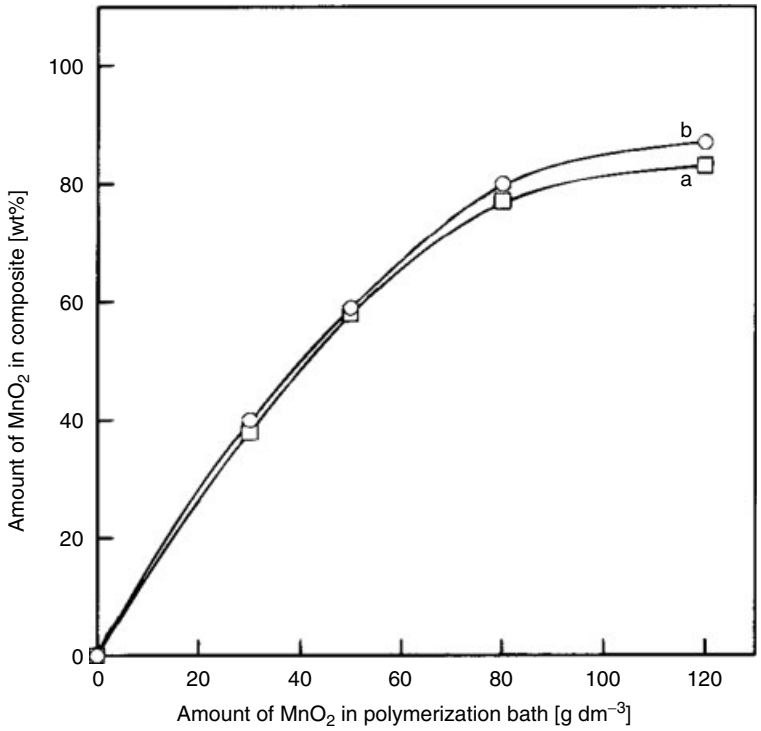


Fig. 2 Plots of the amount of MnO_2 in polypyrrole/$LiMn_2O_4$ (a) and polypyrrole/β-MnO_2 (b) composites as a function of that suspended in the polymerization bath containing 0.1 mol dm^{-3} pyrrole and 1 mol dm^{-3} $HClO_4$. The reaction time was 20 min.

or V_2O_5 described here were useful as the positive electrode materials for rechargeable lithium batteries. It is well known that these oxides serve as the cathode materials. The role of the conducting polymers of the composites is to work both as the conducting network for the immobilized oxides and as the cathode active materials. Composites of polypyrrole and SiO_2 were prepared by using a slightly different electrochemical polymerization technique of using a nonaqueous solution containing pyrrole and silanol [198]. Neucleophilic attack of silanol to pyrrole produces silanol-derivatized pyrrole, which is polymerized to give silanol-derivatized polypyrrole. Heat-treatment of the material results in dehydration of the silanol group to give composites consisting of SiO_2 and polypyrrole, which were used as a hole transport layer in a poly(*N*-vinylcarbazol) electroluminescence device.

4.4 Conducting Polymers Having Specific Morphology

The redox reaction of the conducting polymers is usually accompanied by insertion of electrolyte anions and elimination of the inserted anions. Then, the rate of the redox reaction is mostly controlled by diffusion of the anions in the polymer films,

the situation being more marked for the thicker polymer films. The enhancement of the redox reaction was made by making the conducting film porous. One strategy chosen for that purpose was to deposit polypyrrole on the electrode substrates covered with porous nitrile butadiene rubber (NBR), followed by dissolving the NBR, giving a porous polypyrrole film formed on the electrode substrate [210, 211].

Other strategies employed were to use template synthesis, which has been widely used to prepare a variety of regulated nanostructured materials [212–215]. Commercially available polycarbonate and alumina membranes have plenty of well-organized nanopores of thickness equal to that of the membranes. Synthesis of polypyrrole on polycarbonate or alumina membrane–covered electrodes, followed by dissolution of the membranes resulted in polypyrrole nanotubules of a high surface density on the electrode substrates [216–218].

References

1. K. Okabayashi, O. Ikeda, H. Tamura, *J. Chem. Soc., Chem. Commun.* **1983**, 684–685.
2. O. Ikeda, K. Okabayashi, N. Yoshida et al., *J. Electroanal. Chem. Interfacial Electrochem.* **1985**, *191*, 157–174.
3. M. Velazquez Rosenthal, T. A. Skotheim, C. A. Linkous, *Synth. Met.* **1986**, *15*, 219–227.
4. C. S. Choi, H. Tachikawa, *J. Am. Chem. Soc.* **1990**, *112*, 1757–1768.
5. D. Belanger, G. Laperriere, L. Gravel, *J. Electrochem. Soc.* **1990**, *137*, 365–366.
6. F. Girard, S. Ye, G. Laperriere et al., *J. Electroanal. Chem.* **1992**, *334*, 35–55.
7. S. Ye, F. Girard, D. Belanger, *J. Phys. Chem.* **1993**, *97*, 12373–12378.
8. B. Garcia, F. Roy, D. Belanger, *J. Electrochem. Soc.* **1999**, *146*, 226–231.
9. H. Yoneyama, Y. Li, S. Kuwabata, *J. Electrochem. Soc.* **1992**, *139*, 28–32.
10. G. Bidan, M.-A. Niel, *Synth. Met.* **1997**, *85*, 1387–1388.
11. G. Bidan, E. M. Genies, M. Lapkowski, *J. Electroanal. Chem. Interfacial Electrochem.* **1988**, *251*, 297–306.
12. M. Lapkowski, G. Bidan, M. Fournier, *Synth. Met.* **1991**, *41*, 411–414.
13. G. Bidan, E. M. Genies, M. Lapkowski, *J. Chem. Soc., Chem. Commun.* **1988**, 533–535.
14. M. Hasik, A. Pron, I. Kulszewicz-Bajer et al., *Synth. Met.* **1993**, *55*, 972–976.
15. R. A. Bull, F. R. Fan, A. J. Bard, *J. Electrochem. Soc.* **1983**, *130*, 1636–1638.
16. D. J. Walton, C. E. Hall, A. Chyla, *Synth. Met.* **1991**, *45*, 363–371.
17. V. Vijayanathan, S. Venkatachalam, V. N. Krishnamurthy, *Polymer* **1993**, *34*, 1095–1097.
18. M. Zagorska, A. Pron, S. Lefrant et al., *Synth. Met.* **1987**, *18*, 43–48.
19. M. Zagorska, H. Wycislik, J. Przyluski, *Synth. Met.* **1987**, *20*, 259–268.
20. M. Tolgyesi, A. Szucs, C. Visy et al., *Electrochim. Acta* **1995**, *40*, 1127–1133.
21. O. Ikeda, H. Yoneyama, *J. Electroanal. Chem. Interfacial Electrochem.* **1989**, *265*, 323–327.
22. A. A. Karyakin, M. F. Chaplin, *J. Electroanal. Chem.* **1994**, *370*, 301–303.
23. R. Koncki, O. S. Wolfbeis, *Anal. Chem.* **1998**, *70*, 2544–2550.
24. T. Iyoda, A. Ohtani, T. Shimidzu et al., *Chem. Lett.* **1986**, *15*, 687–690.
25. L. A. Prezyna, G. E. Wnek, Y. J. Qiu et al., *Synth. Met.* **1991**, *41*, 979–981.
26. F. Li, W. J. Albery, *J. Chem. Soc., Faraday Trans.* **1991**, *87*, 2949–2954.
27. T. Osaka, T. Momma, K. Nishimura, *Chem. Lett.* **1992**, *21*, 1787–1790.
28. Y. Kang, M. H. Lee, S. B. Rhee, *Synth. Met.* **1992**, *52*, 319–328.
29. T. Amemiya, K. Hashimoto, A. Fujishima, *J. Phys. Chem.* **1993**, *97*, 4192–4195.
30. T. Momma, K. Nishimura, T. Osaka et al., *J. Electrochem. Soc.* **1994**, *141*, 2326–2331.
31. P. Caglar, G. E. Wnek, *J. Macromol. Sci.* **1995**, *Pure Appl. Chem.* 349–359.
32. X. Ren, P. G. Pickup, *Electrochim. Acta* **1996**, *41*, 1877–1882.
33. X. Ren, P. G. Pickup, *J. Electroanal. Chem.* **1997**, *420*, 251–257.
34. D.-K. Kim, J.-M. Jin, Y. Lee et al., *Mol. Cryst. Liq. Cryst. Sci. Technol., Sect. A* **1997**, *294*, 233–236.

35. M. Morita, S. Miyazaki, H. Tanoue et al., *J. Electrochem. Soc.* **1994**, *141*, 1409–1413.
36. T. Iyoda, A. Ohtani, T. Shimidzu et al., *Synth. Met.* **1987**, *18*, 747–751.
37. T. Shimidzu, A. Ohtani, T. Iyoda et al., *J. Chem. Soc., Chem. Commun.* **1986**, 1415–1417.
38. T. Shimidzu, A. Ohtani, T. Iyoda et al., *J. Electroanal. Chem. Interfacial Electrochem.* **1987**, *224*, 123–135.
39. T. Shimidzu, A. Ohtani, K. Honda, *J. Electroanal. Chem. Interfacial Electrochem.* **1988**, *251*, 323–337.
40. C. Barbero, M. C. Miras, O. Haas et al., *J. Electrochem. Soc.* **1997**, *144*, 4170–4174.
41. G. Bidan, B. Ehui, *J. Chem. Soc., Chem. Commun.* **1989**, 1568–1570.
42. S. Kuwabata, K. Mitsui, H. Yoneyama, *J. Electroanal. Chem. Interfacial Electrochem.* **1990**, *281*, 97–107.
43. S. Kuwabata, K. Mitsui, H. Yoneyama, *J. Electrochem. Soc.* **1992**, *139*, 1824–1830.
44. E. K. W. Lai, P. D. Beattie, F. P. Orfino et al., *Electrochim. Acta* **1999**, *44*, 2559–2569.
45. T. Momma, S. Kakuda, H. Yarimizu et al., *J. Electrochem. Soc.* **1995**, *142*, 1766–1769.
46. F. R. F. Fan, A. J. Bard, *J. Electrochem. Soc.* **1986**, *133*, 301–304.
47. P. Aldebert, P. Audebert, M. Armand et al., *J. Chem. Soc., Chem. Commun.* **1986**, 1636–1638.
48. T. Hirai, S. Kuwabata, H. Yoneyama, *J. Electrochem. Soc.* **1988**, *135*, 1132–1137.
49. D. Orata, D. A. Buttry, *J. Electroanal. Chem. Interfacial Electrochem.* **1988**, *257*, 71–82.
50. F. Endres, G. Schwitzgebel, *Synth. Met.* **1997**, *88*, 73–78.
51. C. Bala, G. L. Radu, D. E. Gheorghe et al., *J. Med. Biochem.* **1997**, *1*, 47–54.
52. G. Fortier, D. Belanger, *Biotechnol. Bioeng.* **1991**, *37*, 854–858.
53. M. Umana, J. Waller, *Anal. Chem.* **1986**, *58*, 2979–2983.
54. P. N. Bartlett, R. G. Whitaker, *J. Electroanal. Chem. Interfacial Electrochem.* **1987**, *224*, 37–48.
55. D. Belanger, J. Nadreau, G. Fortier, *J. Electroanal. Chem. Interfacial Electrochem.* **1989**, *274*, 143–155.
56. S. Yabuki, H. Shinohara, M. Aizawa, *J. Chem. Soc., Chem. Commun.* **1989**, 945–946.
57. G. Fortier, E. Brassard, D. Belanger, *Biosens. Bioelectron.* **1990**, *5*, 473–490.
58. D. Belanger, E. Brassard, G. Fortier, *Anal. Chim. Acta* **1990**, *228*, 311–315.
59. D. R. Yaniv, L. McCormick, J. Wang et al., *J. Electroanal. Chem. Interfacial Electrochem.* **1991**, *314*, 353–361.
60. D. Belanger, J. Nadreau, G. Fortier, *Electroanalysis (New York)* **1992**, *4*, 933–940.
61. M. Marchesiello, E. M. Genies, *Electrochim. Acta* **1992**, *37*, 1987–1992.
62. A. Begum, H. Tsushima, T. Suzawa et al., *Sens. Actuators, B* **1993**, *14*, 576–577.
63. E. M. Genies, M. Marchesiello, *Synth. Met.* **1993**, *57*, 3677–3682.
64. J. M. Cooper, D. Bloor, *Electroanalysis (New York)* **1993**, *5*, 883–886.
65. M. Marchesiello, E. Genies, *J. Electroanal. Chem.* **1993**, *358*, 35–48.
66. N. F. Almeida, E. J. Beckman, M. M. Ataai, *Biotechnol. Bioeng.* **1993**, *42*, 1037–1045.
67. M.-C. Shin, H.-S. Kim, *Anal. Lett.* **1995**, *28*, 1017–1031.
68. K. Kojima, H. Nasu, M. Shimomura et al., *Synth. Met.* **1995**, *71*, 2245–2246.
69. P. Gros, A. Bergel, *J. Electroanal. Chem.* **1995**, *386*, 65–73.
70. M.-C. Shin, H. C. Yoon, H.-S. Kim, *Anal. Sci.* **1996**, *12*, 597–604.
71. K. Ramanathan, S. Annapoorni, A. Kumar et al., *J. Mater. Sci. Lett.* **1996**, *15*, 124–128.
72. P. J. H. J. van Os, A. Bult, C. G. J. Koopal et al., *Anal. Chim. Acta* **1996**, *335*, 209–216.
73. G. E. De Benedetto, F. Palmisano, P. G. Zambonin, *Biosens. Bioelectron.* **1996**, *11*, 1001–1008.
74. A. Griffith, A. Glidle, G. Beamson et al., *J. Phys. Chem. B* **1997**, *101*, 2092–2100.
75. S. Cosnier, A. Senillou, M. Gratzel et al., *J. Electroanal. Chem.* **1999**, *469*, 176–181.
76. M. Hiller, C. Kranz, J. Huber et al., *Adv. Mater.* **1996**, *8*, 219–222.
77. T. Oubda, P. Zhao, G. E. Nauer, *Polym. News* **1998**, *23*, 331–338.
78. H. Shinohara, T. Chiba, M. Aizawa, *Sens. Actuators* **1987**, *13*, 79–86.
79. S. Mu, H. Xue, B. Qian, *J. Electroanal. Chem. Interfacial Electrochem.* **1991**, *304*, 7–16.
80. D. T. Hoa, T. N. S. Kumar, N. S. Punekar et al., *Anal. Chem.* **1992**, *64*, 2645–2646.
81. J. C. Cooper, E. A. H. Hall, *Biosens. Bioelectron.* **1992**, *7*, 473–485.
82. J. C. Cooper, E. A. H. Hall, *Electroanalysis (New York)* **1993**, *5*, 385–397.

83. S.-Y. Lu, C.-F. Li, D.-D. Zhang et al., *J. Electroanal. Chem.* **1994**, *364*, 31–36.
84. S. Mu, J. Kan, *Electrochim. Acta* **1995**, *40*, 241–246.
85. J. Dumont, G. Fortier, *Biotechnol. Bioeng.* **1996**, *49*, 544–552.
86. N. G. Skinner, E. A. H. Hall, *J. Electroanal. Chem.* **1997**, *420*, 179–188.
87. P. C. Pandey, *J. Chem. Soc., Faraday Trans. 1* **1988**, *84*, 2259–2265.
88. C. Iwakura, Y. Kajiya, H. Yoneyama, *J. Chem. Soc., Chem. Commun.* **1988**, 1019–1020.
89. Y. Kajiya, H. Sugai, C. Iwakura et al., *Denki Kagaku oyobi Kogyo Butsuri Kagaku* **1988**, *56*, 1110–1111.
90. P. Janda, J. Weber, *J. Electroanal. Chem. Interfacial Electrochem.* **1991**, *300*, 119–127.
91. Y. Kajiya, H. Sugai, C. Iwakura et al., *Anal. Chem.* **1991**, *63*, 49–54.
92. Y. Kajiya, H. Yoneyama, *J. Electroanal. Chem.* **1992**, *341*, 85–92.
93. Z. Sun, H. Tachikawa, *Anal. Chem.* **1992**, *64*, 1112–1117.
94. W. Schuhmann, *Biosens. Bioelectron.* **1995**, *10*, 181–193.
95. M. Trojanowicz, O. Geschke, T. Krawczynski vel Krawczyk et al., *Sens. Actuators, B* **1995**, *28*, 191–199.
96. S. Yabuki, H. Shinohara, Y. Ikariyama et al., *J. Electroanal. Chem. Interfacial Electrochem.* **1990**, *277*, 179–187.
97. A. Ramanavicius, K. Habermueller, E. Csoeregi et al., *Anal. Chem.* **1999**, *71*, 3581–3586.
98. Y. Kajiya, R. Tsuda, H. Yoneyama, *Denki Kagaku oyobi Kogyo Butsuri Kagaku* **1990**, *58*, 1213–1214.
99. B. F. Y. Yon Hin, C. R. Lowe, *Sens. Actuators, B* **1992**, *48*, 339–342.
100. H. Wang, S. Mu, *Sens. Actuators, B* **1999**, *56*, 22–30.
101. Y. Yang, S. Mu, H. Chen, *Synth. Met.* **1998**, *92*, 173–178.
102. S. Mu, *J. Electroanal. Chem.* **1994**, *370*, 135–139.
103. J. Kan, H. Xue, S. Mu et al., *Synth. Met.* **1997**, *87*, 205–209.
104. J. M. Cooper, P. L. Foreman, A. Glidle et al., *J. Electroanal. Chem.* **1995**, *388*, 143–149.
105. S. Yoshida, H. Kanno, T. Watanabe, *Anal. Sci.* **1995**, *11*, 251–256.
106. S. Cosnier, C. Innocent, L. Allien et al., *Anal. Chem.* **1997**, *69*, 968–971.
107. U. Wollenberger, V. Bogdanovskaya, S. Bobrin et al., *Anal. Lett.* **1990**, *23*, 1795–1808.
108. T. Tatsuma, M. Gondaira, T. Watanabe, *Anal. Chem.* **1992**, *64*, 1183–1187.
109. T. Tatsuma, T. Watanabe, T. Watanabe, *Sens. Actuators, B* **1993**, *14*, 752–753.
110. T. Tatsuma, T. Watanabe, T. Watanabe, *J. Electroanal. Chem.* **1993**, *356*, 245–253.
111. C.-L. Wang, A. Mulchandani, *Anal. Chem.* **1995**, *67*, 1109–1114.
112. P. N. Bartlett, P. R. Birkin, F. Palmisano et al., *J. Chem. Soc., Faraday Trans.* **1996**, *92*, 3123–3130.
113. Y. Yang, S. Mu, *J. Electroanal. Chem.* **1997**, *432*, 71–78.
114. E. I. Iwuoha, D. S. De Villaverde, N. P. Garcia et al., *Biosens. Bioelectron.* **1997**, *12*, 749–761.
115. P. N. Bartlett, P. R. Birkin, J. H. Wang et al., *Anal. Chem.* **1998**, *70*, 3685–3694.
116. H. Yamato, M. Ohwa, W. Wernet, *Anal. Chem.* **1995**, *67*, 2776–2780.
117. Y. Shi, Y. Yang, J. Kan et al., *Biosens. Bioelectron.* **1997**, *12*, 655–659.
118. Y. Yang, S. Mu, *J. Electroanal. Chem.* **1996**, *415*, 71–77.
119. S. B. Adeloju, S. J. Shaw, G. G. Wallace, *Electroanalysis (New York)* **1994**, *6*, 865–870.
120. S. B. Adeloju, J. N. Barisci, G. G. Wallace, *Anal. Chim. Acta* **1996**, *332*, 145–153.
121. S. B. Adeloju, S. J. Shaw, G. G. Wallace, *Anal. Chim. Acta* **1997**, *341*, 155–160.
122. E. C. Hernandez, A. Witkowski, S. Daunert et al., *Mikrochim. Acta* **1995**, *121*, 63–72.
123. J. Laska, J. Wlodarczyk, W. Zaborska, *J. Mol. Catal. B: Enzym.* **1999**, *6*, 549–553.
124. P. C. Pandey, A. P. Mishra, *Analyst (London)* **1988**, *113*, 329–331.
125. S. Mu, S. Cheng, *J. Electroanal. Chem.* **1993**, *356*, 59–66.
126. J. Kan, S. Mu, Y. Li, *Bull. Electrochem.* **1998**, *14*, 74–77.
127. R. Dobay, G. Harsanyi, C. Visy, *Anal. Chim. Acta* **1999**, *385*, 187–194.
128. S. Mu, J. Kan, J. Zhou, *J. Electroanal. Chem.* **1992**, *334*, 121–132.
129. S. Cosnier, M. Fontecave, D. Limosin et al., *Anal. Chem.* **1997**, *69*, 3095–3099.
130. S. Cosnier, M. Fontecave, C. Innocent et al., *Electroanalysis* **1997**, *9*, 685–688.
131. G. F. Khan, E. Kobatake, H. Shinohara et al., *Anal. Chem.* **1992**, *64*, 1254–1258.

132. G. F. Khan, E. Kobatake, Y. Ikariyama et al., *Anal. Chim. Acta* **1993**, *281*, 527–533.
133. C. A. B. Garcia, G. de Oliveira Neto, L. T. Kubota, *Anal. Chim. Acta* **1998**, *374*, 201–208.
134. Y. Kajiya, H. Matsumoto, H. Yoneyama, *J. Electroanal. Chem. Interfacial Electrochem.* **1991**, *319*, 185–194.
135. S. Yabuki, F. Mizutani, T. Katsura et al., *Bioelectrochem. Bioenerg.* **1992**, *28*, 489–493.
136. N. Sugihara, Y. Ogoma, K. Abe et al., *Polym. Adv. Technol.* **1998**, *9*, 307–313.
137. M. Nishizawa, T. Matsue, I. Uchida, *Sens. Actuators, B* **1993**, *13*, 53–56.
138. S. Cosnier, C. Gondran, J.-C. Watelet et al., *Anal. Chem.* **1998**, *70*, 3952–3956.
139. T. Haruyama, H. Shinohara, Y. Ikariyama et al., *J. Electroanal. Chem.* **1993**, *347*, 293–301.
140. H. Xue, S. Mu, *J. Electroanal. Chem.* **1995**, *397*, 241–247.
141. W. Nadruz Jr., E. T. A. Marques, W. M. Azevedo et al., *Braz. J. Med. Biol. Res.* **1996**, *29*, 347–350.
142. I. Willner, E. Katz, N. Lapidot et al., *Bioelectrochem. Bioenerg.* **1992**, *29*, 29–45.
143. M. Hidaka, M. Aizawa, *Denki Kagaku oyobi Kogyo Butsuri Kagaku* **1995**, *63*, 1113–1120.
144. M. Gerard, K. Ramanathan, A. Chaubey et al., *Electroanalysis* **1999**, *11*, 450–452.
145. H. Wang, S. Mu, *J. Electroanal. Chem.* **1997**, *436*, 43–48.
146. M. Velazquez Rosenthal, T. Skotheim, J. Warren, *J. Chem. Soc., Chem. Commun.* **1985**, 342–343.
147. S. Moteki, A. G. Sykes, *J. Electroanal. Chem.* **1998**, *447*, 91–95.
148. J. G. Eaves, R. Mirrazaei, D. Parker et al., *J. Chem. Soc., Perkin Trans. 2* **1989**, 373–376.
149. N. C. Foulds, C. R. Lowe, *Anal. Chem.* **1988**, *60*, 2473–2478.
150. F. Daire, F. Bedioui, J. Devynck et al., *J. Electroanal. Chem. Interfacial Electrochem.* **1987**, *224*, 95–110.
151. C. Caix, S. Chardon-Noblat, A. Deronzier, *J. Electroanal. Chem.* **1997**, *434*, 163–170.
152. S. Hamar-Thibault, J.-C. Moutet, S. Tingry, *J. Organomet. Chem.* **1997**, *532*, 31–37.
153. S. Chardon-Noblat, A. Deronzier, R. Ziessel et al., *J. Electroanal. Chem.* **1998**, *444*, 253–260.
154. P. N. Bartlett, A. C. Benniston, L. Y. Chung et al., *Electrochim. Acta* **1991**, *36*, 1377–1379.
155. H. K. Youssoufi, M. Hmyene, F. Garnier et al., *J. Chem. Soc., Chem. Commun.* **1993**, 1550–1552.
156. H. Korri Youssoufi, M. Hmyene, A. Yassar et al., *J. Electroanal. Chem.* **1996**, *406*, 187–194.
157. C. Armengaud, P. Moisy, F. Bedioui et al., *J. Electroanal. Chem. Interfacial Electrochem.* **1990**, *277*, 197–211.
158. F. Bedioui, M. Voisin, J. Devynck et al., *J. Electroanal. Chem. Interfacial Electrochem.* **1991**, *297*, 257–269.
159. I. Taniguchi, K. Matsushita, M. Okamoto et al., *J. Electroanal. Chem. Interfacial Electrochem.* **1990**, *280*, 221–226.
160. F. Garnier, H. Korri-Youssoufi, P. Srivastava et al., *Synth. Met.* **1999**, *100*, 89–94.
161. S. E. Wolowacz, B. F. Y. Yon Hin, C. R. Lowe, *Anal. Chem.* **1992**, *64*, 1541–1545.
162. B. F. Y. Yon-Hin, M. Smolander, T. Crompton et al., *Anal. Chem.* **1993**, *65*, 2067–2071.
163. K. Kojima, T. Unuma, T. Yamauchi et al., *Synth. Met.* **1997**, *85*, 1417–1418.
164. W. Schuhmann, C. Kranz, J. Huber et al., *Synth. Met.* **1993**, *61*, 31–35.
165. B. Ballarin, S. Masiero, R. Seeber et al., *J. Electroanal. Chem.* **1998**, *449*, 173–180.
166. J. Roncali, R. Garreau, D. Delabouglise et al., *J. Chem. Soc., Chem. Commun.* **1989**, 679–681.
167. J. Roncali, R. Garreau, M. Lemaire, *J. Electroanal. Chem. Interfacial Electrochem.* **1990**, *278*, 373–378.
168. J. Roncali, L. H. Shi, F. Garnier, *J. Phys. Chem.* **1991**, *95*, 8983–8989.
169. L. H. Shi, J. Roncali, F. Garnier, *Macromolecules* **1992**, *25*, 6425–6429.
170. P. Baeuerle, S. Scheib, *Adv. Mater.* **1993**, *5*, 848–853.
171. M. J. Marsella, T. M. Swager, *J. Am. Chem. Soc.* **1993**, *115*, 12214–12215.
172. P. Baeuerle, G. Goetz, M. Hiller et al., *Synth. Met.* **1993**, *61*, 71–79.
173. R. D. McCullough, S. P. Williams, *J. Am. Chem. Soc.* **1993**, *115*, 11608–11609.
174. M. J. Marsella, P. J. Carroll, T. M. Swager, *J. Am. Chem. Soc.* **1994**, *116*, 9347–9348.
175. R. D. McCullough, S. P. Williams, *Chem. Mater.* **1995**, *7*, 2001–2003.
176. M. J. Marsella, P. J. Carroll, T. M. Swager, *J. Am. Chem. Soc.* **1995**, *117*, 9832–9841.
177. I. Levesque, M. Leclerc, *J. Chem. Soc., Chem. Commun.* **1995**, 2293–2294.

178. I. Levesque, M. Leclerc, *Chem. Mater.* **1996**, *8*, 2843–2849.
179. W. E. Rudzinski, M. Walker, C. P. Horwitz et al., *J. Electroanal. Chem.* **1992**, *335*, 265–279.
180. Y. Degani, A. Heller, *J. Am. Chem. Soc.* **1989**, *111*, 2357–2358.
181. I. Katakis, A. Heller, *Anal. Chem.* **1992**, *64*, 1008–1013.
182. E. Csoeregi, D. W. Schmidtke, A. Heller, *Anal. Chem.* **1995**, *67*, 1240–1244.
183. S. Holdcroft, B. L. Funt, *J. Electroanal. Chem. Interfacial Electrochem.* **1988**, *240*, 89–103.
184. M. Hepel, *J. Electrochem. Soc.* **1998**, *145*, 124–134.
185. R. Noufi, *J. Electrochem. Soc.* **1983**, *130*, 2126–2128.
186. H. Yoneyama, Y. Shoji, *J. Electrochem. Soc.* **1990**, *137*, 3826–3830.
187. F. Beck, M. Dahlhaus, *J. Appl. Electrochem.* **1993**, *23*, 781–789.
188. A. M. Rocco, M.-A. De Paoli, A. Zanelli et al., *Electrochim. Acta* **1996**, *41*, 2805–2816.
189. M.-A. De Paoli, A. Zanelli, M. Mastragostino et al., *J. Electroanal. Chem.* **1997**, *435*, 217–224.
190. H. Yoneyama, A. Kishimoto, S. Kuwabata, *J. Chem. Soc., Chem. Commun.* **1991**, 986–987.
191. S. Kuwabata, A. Kishimoto, T. Tanaka et al., *J. Electrochem. Soc.* **1994**, *141*, 10–15.
192. A. H. Gemeay, H. Nishiyama, S. Kuwabata et al., *J. Electrochem. Soc.* **1995**, *142*, 4190–4195.
193. M. Nishizawa, K. Mukai, S. Kuwabata et al., *J. Electrochem. Soc.* **1997**, *144*, 1923–1927.
194. S. Kuwabata, S. Masui, H. Yoneyama, *Electrochim. Acta* **1999**, *44*, 4593–4600.
195. A. D. Pasquier, F. Orsini, A. S. Gozdz et al., *J. Power Sources* **1999**, *81–82*, 607–611.
196. K. Kawai, N. Mihara, S. Kuwabata et al., *J. Electrochem. Soc.* **1990**, *137*, 1793–1796.
197. F. Beck, M. Dahlhaus, N. Zahedi, *Electrochim. Acta* **1992**, *37*, 1265–1272.
198. S. Komaba, K. Fujihana, T. Osaka et al., *J. Electrochem. Soc.* **1998**, *145*, 1126–1130.
199. H. Yoneyama, N. Takahashi, S. Kuwabata, *J. Chem. Soc., Chem. Commun.* **1992**, 716–717.
200. S. Kuwabata, N. Takahashi, S. Hirao et al., *Chem. Mater.* **1993**, *5*, 437–441.
201. S. Kuwabata, A. Kishimoto, H. Yoneyama, *J. Electroanal. Chem.* **1994**, *377*, 261–268.
202. S. Kuwabata, T. Idzu, C. R. Martin et al., *J. Electrochem. Soc.* **1998**, *145*, 2707–2710.
203. H. Yoneyama, S. Hirao, S. Kuwabata, *J. Electrochem. Soc.* **1992**, *139*, 3141–3146.
204. P. K. Shen, H. T. Huang, A. C. C. Tseung, *J. Electrochem. Soc.* **1992**, *139*, 1840–1845.
205. H. Yoneyama, M. Tokuda, S. Kuwabata, *Electrochim. Acta* **1994**, *39*, 1315–1320.
206. S. Pethkar, R. C. Patil, J. A. Kher et al., *Thin Solid Films* **1999**, *349*, 105–109.
207. D. W. Hatchett, M. Josowicz, J. Janata et al., *Chem. Mater.* **1999**, *11*, 2989–2994.
208. R. Kostecki, M. Ulmann, J. Augustynski et al., *J. Phys. Chem.* **1993**, *97*, 8113–8115.
209. H. Yoneyama, Y. Shoji, K. Kawai, *Chem. Lett.* **1989**, *18*, 1067–1070.
210. K. Naoi, T. Osaka, *J. Electrochem. Soc.* **1987**, *134*, 2479–2483.
211. T. Osaka, K. Naoi, M. Maeda et al., *J. Electrochem. Soc.* **1989**, *136*, 1385–1388.
212. P. Hoyer, N. Baba, H. Masuda, *Appl. Phys. Lett.* **1995**, *66*, 2700–2702.
213. H. Masuda, K. Fukuda, *Science* **1995**, *268*, 1466–1468.
214. H. Masuda, M. Yotsuya, M. Ishida, *Jpn. J. Appl. Phys., Part 2* **1998**, *37*, L1090–L1092.
215. M. Nakao, S. Oku, T. Tamamura et al., *Jpn. J. Appl. Phys., Part 1* **1999**, *38*, 1052–1055.
216. R. M. Penner, C. R. Martin, *J. Electrochem. Soc.* **1986**, *133*, 2206–2207.
217. L. S. Van Dyke, C. R. Martin, *Langmuir* **1990**, *6*, 1118–1123.
218. C. R. Martin, *Acc. Chem. Res.* **1995**, *28*, 61–68.

5.1
Microporous Inorganic Molecular Materials

Mary Elizabeth Williams, Joseph T. Hupp
Northwestern University, Evanston, IL 60208, USA

5.1.1
Introduction to Microporous Inorganic Molecular Materials

An enormous number of cavity-containing inorganic molecular squares [1–4], triangles [2d, 3, 4d], rectangles [5, 6], and related macrocycles featuring metal atom corners and cis-coordinated difunctional ligand edges haves been synthesized over the past 10 years. The available cavity sizes (i.e., minimum van der Waals cavity diameters) range from ca 0.5 to 3.4 nm [1, 2]. It has been suggested, and in a number of cases experimentally demonstrated [1a, 2e, 4a–c, 7], that the frameworks and cavities can be used as hosts for recognition and binding of small molecular guests, typically in solution environments. The binding chemistry, in turn, could provide a basis for chemical sensing, chemical catalysis, phase-transfer catalysis, or other potentially technologically useful processes.

One of the most striking structural features of the inorganic macrocycles in solid-state environments is their almost universal tendency to crystallize with cavities aligned to create extended one-dimensional channels or tubule structures; one example is shown in Fig. 1. These, in turn, are aligned to create semi-infinite, two-dimensional arrays of channels; see Fig. 1. Given the structures, one might envision applications that employ the materials as electrode coating or modifying layers – for example, applications entailing molecular sieving, catalyst support, or selective electrochemical sensing. Particularly useful would be the subset of compounds featuring neutral macrocycles, such that charge-compensating counterions are absent and the channels created in the solid state are accessible to other molecules. Charge neutrality also imparts other desirable features such as hydrophobicity, which we find renders films insoluble in water and enhances the binding of certain molecular guests.

Several of the thin-film molecular materials prepared from neutral inorganic macrocycles have proved to be exceptionally microporous. (Recall that in catalytic and materials chemistry, ''microporous'' connotes porosity on the nanometer rather than micrometer scale.) A molecular materials approach should yield uniform pore sizes corresponding precisely to the sizes of the isolated molecular cavities. In addition, every macrocyclic molecule

Encyclopedia of Electrochemistry. Edited by A.J. Bard and M. Stratmann
Vol. 10 *Modified Electrodes*. Edited by M.Fujihira, I.Rubinstein, and J.F.Rusling
Copyright © 2007 Wiley-VCH Verlag GmbH & Co. KGaA, Weinheim. ISBN: 978-3-527-30402-8

comprising a thin film should, in principle, contribute to the porosity. Most of the available materials also feature exceptional void volumes – in a few cases greater than 70% of the total volume can be assigned as void volume. They also typically feature moderately high internal surface areas. For the compound in Fig. 1, for example, the internal surface area is ca 40 $m^2\ g^{-1}$ [7].

In the sections that follow, we briefly describe further the materials design approach followed in our own work. We also outline the electrochemical characterization methods used. We then describe the guest transport, size, exclusion/inclusion, and shape recognition properties of first- and second-generation microporous inorganic molecular materials employed as thin films on electrode surfaces.

5.1.2 Materials Design and Synthesis

With one exception, all the microporous inorganic molecular materials used as

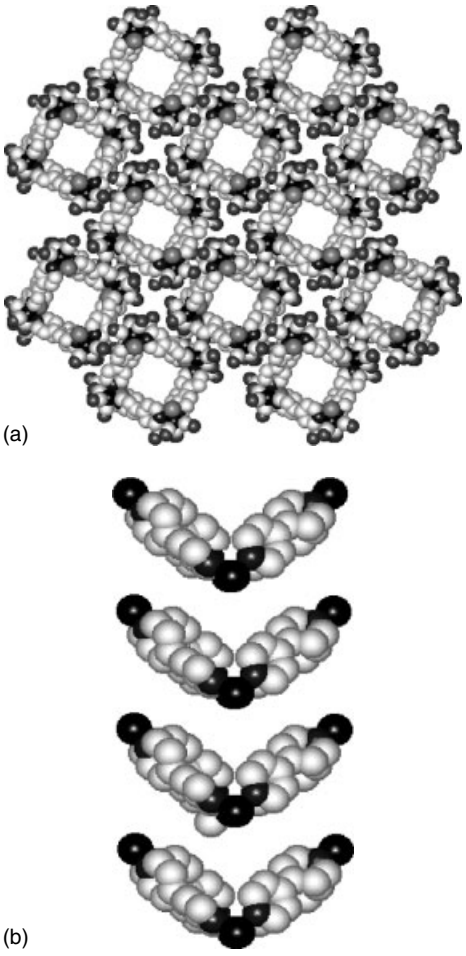
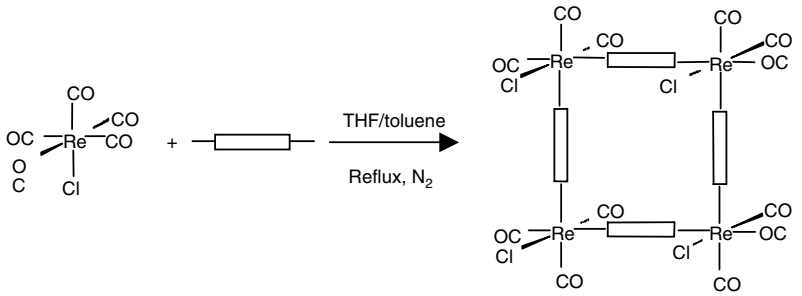


Fig. 1 Space-filled representation of the single-crystal X-ray structure of compound **2**. (a) Top view of four channels and (b) side view of a single channel. In the side view, the chloro and carbonyl ligands surrounding the corner Re atoms have been omitted for clarity; in both views the hydrogens on the bipyridine ligands have been omitted.

electrode coatings to date have employed macrocyclic coordination compounds of rhenium(I) as building blocks [1b–d, 5c, 7]. The low oxidation state ensures that coordination of just one anionic ligand per metal center or one dianionic ligand per pair of centers will yield the desired neutral compounds, and eliminate the issue of counterions. For the synthesis of tetrametallic molecular squares for thin-film studies, we have exclusively employed $Re(CO)_5Cl$ as a synthon. In the presence of coordinating ligands, L, a classic trans carbonyl-ligand labilization effect, leads exclusively to cis-coordinated compounds or fragments, $Re(CO)_3Cl(L)_2$, where the remaining carbonyls are arranged in a facial configuration. As illustrated in Sch. 1, if L is a rigid or semirigid difunctional ligand, the L to $Re(CO)_5Cl$ stoichiometry is one to one. The synthesis is carried out in an appropriate, weak coordinating solvent, and tetrametallic squares are obtained in high purity and essentially quantitative yield via a process that can legitimately be termed *covalent self-assembly*. The structures that have been prepared in our lab are shown in Fig. 2 (Interestingly, under slightly modified conditions, triangles rather than squares are obtained [2d]. To date, however, no thin-film studies of molecular triangles have been reported.)

The preparation of topologically more complex unit structures such as rectangles [5] and prisms [8] generally requires multiple synthetic steps. While not overly difficult, we omit the syntheses from the discussion here, and instead refer interested readers to the primary literature. These structures are particularly interesting because, in addition to size selection, they open up the possibility for primitive shape selection in film-based molecular guest transport and binding studies. It seems likely that many additional unit structures will eventually be designed and developed for thin-film materials studies. (Indeed, several structures of higher complexity have already been reported for molecules intended primarily for solution-phase studies [2, 4a–c]).

The available compounds are characterized by insolubility in nonpolar organic solvents and, as noted above, aqueous solutions. Significant solubility is achievable, however, in many polar organic solvents and solvent mixtures. If comparatively high volatility solvents are used, films can be prepared by spin casting, simple evaporative casting, or a hybrid protocol involving slow rotation of an inverted electrode topped with a small amount of compound-containing solution. Typically, newly cast films are subjected to several hours of additional drying, sometimes in vacuum, prior



Scheme 1 General synthetic scheme for rhenium-based molecular squares.

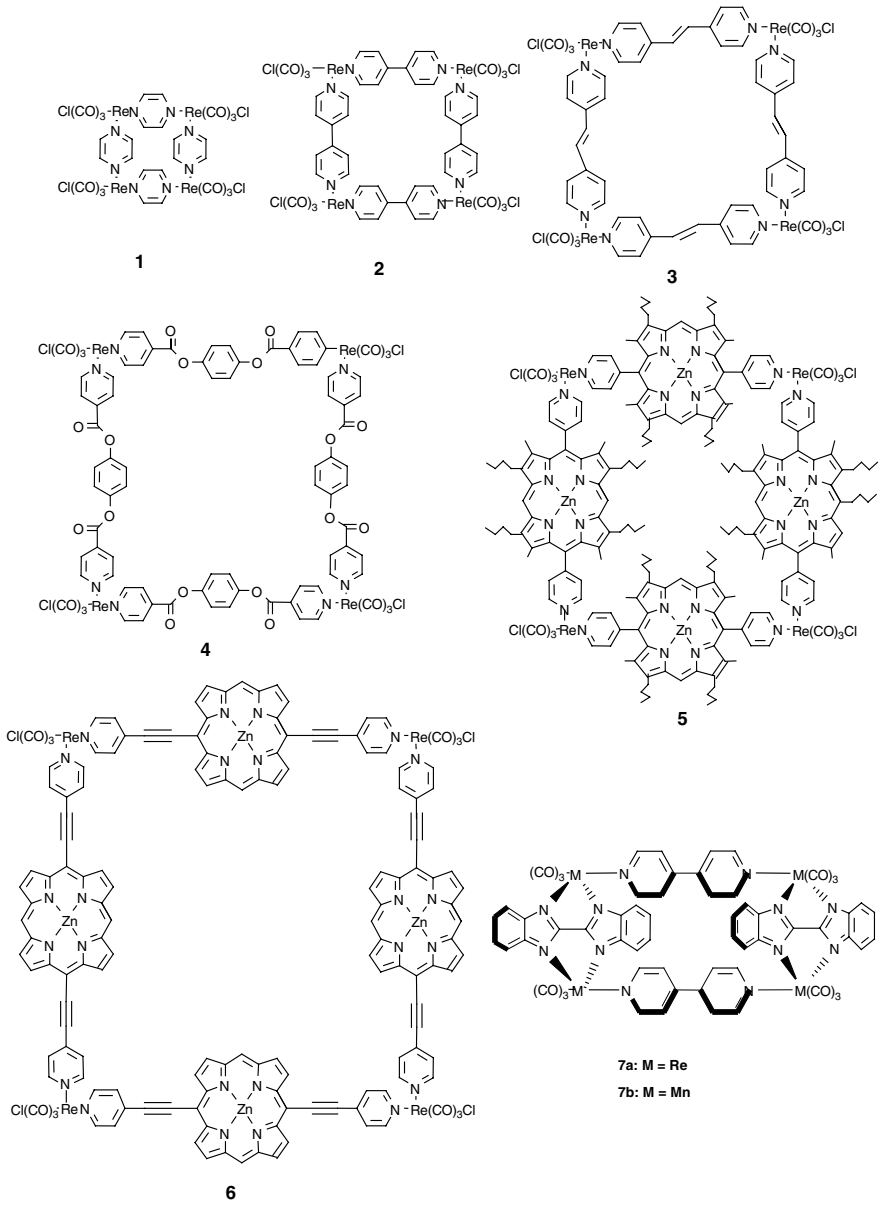


Fig. 2 Structures of molecules comprising various inorganic nanostructured materials (**1**) $[Re(CO)_3Cl(pyrazine)]_4$; (**2**) $[Re(CO)_3Cl(4,4'\text{-bipyridine})]_4$; (**3**) $[Re(CO)_3Cl(1,2\text{-bis}(4\text{-pyridyl})ethylene)]_4$; (**4**) $[Re(CO)_3Cl(1,4\text{-phenyl-bis}(picolinate))]_4$; (**5**) $[Re(CO)_3Cl(3,7,13,17\text{-tetramethyl-2,8,12,18-tetra}(n\text{-butyl})\text{-5,15 -(4-pyridyl) Zn(II) porphyrin})]_4$; (**6**) $[Re(CO)_3Cl(5,15\text{-(4-ethylnyl pyridyl) Zn (II) porphyrin})]_4$; (**7**) $[(M(CO)_3Cl)_2(4,4'\text{-bipyridine})(bisbenzimidolate)_2$.

to use. Depending on the compound, relatively pinhole-free films can be prepared with thicknesses corresponding to as few as 40 monolayer equivalents. Preliminary atomic force and light microscopy studies reveal a range of microscopic film morphologies [5, 9]. Some films appear to be composed of close-packed microcrystallites; others are evidently composed of thin, but continuous, amorphous or possibly nanocrystalline, underlayers, and sporadic microcrystalline overlayers.

5.1.3 Transport Models and Electrochemical Characterization Methods

A physical model for film transport that accommodates the available experimental observations is a conventional film permeation model [10]. Candidate permeant molecules partition into a film from solution via an equilibrium process and then diffuse through the film to the electrode surface where they undergo oxidation or reduction. The redox product molecules then diffuse to the film/solution boundary and exit the film via a reverse partitioning step that, again, is sufficiently rapid to occur at equilibrium. Faradaic electrochemical techniques are especially powerful for interrogating such processes – in part because they require permeants to traverse films essentially completely in order for signals to be observed. (Recall that interfacial electron transfer can occur with reasonable efficiency only over distances of ca 10, or perhaps 20, Å. Depending on the compound, these distances correspond to one or two film monolayers.)

According to the permeation model, the driving forces for transport are phase partitioning and reactant or product concentration gradients. Electrochemical migration is neglected. Again, Faradaic electrochemical techniques are especially useful: controlled-potential experiments permit the interfacial concentrations of reactants and products to be manipulated in accord with the Nernst equation. For film and electrode geometries employed thus far, the resulting concentration gradients have been sufficiently simple to be described adequately by one-dimensional versions of Fick's laws of diffusion.

Cyclic voltammetry has been the method of choice for screening microporous inorganic molecular materials for permeability by solution-phase molecules. When permeant passage through a film is rapid in comparison to solution-phase transport, voltammograms are unchanged by the presence of a film. When permeant passage through a film is significantly rate limiting, however, voltammetric currents are attenuated and voltammogram shapes are distorted, ultimately resembling sigmoidal microelectrode-like voltammograms.

While the voltammograms can be quantitatively analyzed to yield permeant transport parameters – for example, via numerical simulations – we have instead utilized rotating disk electrode (RDE) voltammetry for this purpose. Sequential solution and film transport problems are generally well described by a variant of the Koutecky-Levich analysis [11]. This analysis represents the series process kinetically as a reciprocal sum of pure solution-phase convection/diffusion (cd) and pure film permeation (p) rates or fluxes. Since detection is electrochemical, the fluxes can be written in terms of currents, where i_{lim} is the observed overall, mass-transport limited, current [12]:

$$i_{\mathrm{lim}}^{-1} = i_{\mathrm{cd}}^{-1} + i_{\mathrm{p}}^{-1} \qquad (1)$$

The equation can be expanded as [12]:

$$i_{\lim}^{-1} = [0.602nFAD_s^{2/3}\omega^{1/2}v^{-1/6}C_s]^{-1} + [nFAPD_fC_s/d]^{-1} \quad (2)$$

where n is the number of electrons transferred during oxidation (or reduction); F is the Faraday constant; A and ω are the area of the electrode and its angular frequency of rotation, respectively; v is the solvent kinematic viscosity; C_s, D_f, and D_s are the redox species' solution concentration, and film and solution diffusion coefficients, respectively; P is the solute partition coefficient; and d the thickness of the film.

The virtue of Eq. (2) and the RDE method is that they permit the rate of solution-phase convection/diffusion to be systematically modulated via changes in rotation rate, thereby permitting the permeation rate or flux to be determined. If the film thickness is known or can be determined, the experiment yields the permeability (PD_f) of the reactant.

A third technique employed in film transport studies is scanning electrochemical microscopy (SECM) [13]. As noted in Sect. 5.1.8, SECM is capable of yielding quantitative transport information for molecules interacting with single microcrystallites of microporous inorganic materials. We have shown elsewhere [14] that for the case of an SECM tip held above a film-covered substrate under positive feedback, the limiting SECM tip current, i_f, normalized to current obtained at identical tip height above a bare substrate (i), is given by:

$$i/i_f = 1 + (4D_sd/\pi rPD_f) \quad (3)$$

where r is the radius of the SECM tip Eq. (3) is approximate, not exact, and is applicable in the case where i_f is small in comparison to i [14].

Finally, an electrochemical methodology that is just beginning to be utilized with thin-film microporous inorganic molecular materials, but could prove especially effective for evaluating the transport of redox-silent ions, is impedance spectroscopy.

5.1.4 Size-selective Transport of Redox-active Species through Thin Films of Molecular Squares

The structure in Fig. 1 and related crystal structures for other molecular squares suggest that thin films of these materials can function as molecular sieves, where the size or sieving cutoff, c, is defined by the size of the cavity within an isolated square. Using, for example, compounds **1**–**5** one could envision a hierarchy of transport versus exclusion of guests of widely varying size, where the presence or absence of an electrochemical response from the redox-active guests at an underlying electrode would be used to gauge a film's performance. Experiments of this kind have, in fact, been reported [15]. (Compound **6** has not yet been examined as a microporous thin-film material.) The probe ions (redox-active permeants) ranged in diameter from roughly 3 Å (iodide ion) to 24 Å ($Fe[(SO_3\text{-phenyl})_2(1,10\text{-phenanthroline})]_3^{4-}$), and are shown in Fig. 3. Representative results (cyclic and RDE voltammetry measurements in aqueous solutions) using thin films of **1**, **2**, and **5**, and appropriate pairs of candidate permeants, are shown in panels A and B of Fig. 4. In each case, exclusion of the larger permeant is indicated. Table 1 summarizes size-cutoff data for thin films of **1**–**5** based on a broader set of potential permeants.

Application of the more quantitative treatment embodied in Eqs. (1) and (2) provides a means for assessing absolute permeabilities, PD_f. Note that these equations predict that the permeant flux, as measured by the quantity i_p, will decrease with increasing film thickness. Figure 5 shows the outcome of a series of film thickness experiments: i_p indeed does scale as $1/d$, suggesting that the simple permeation model outlined in Sect. 5.1.3 is an appropriate description of the transport process. For the permeant concentrations used, it is believed

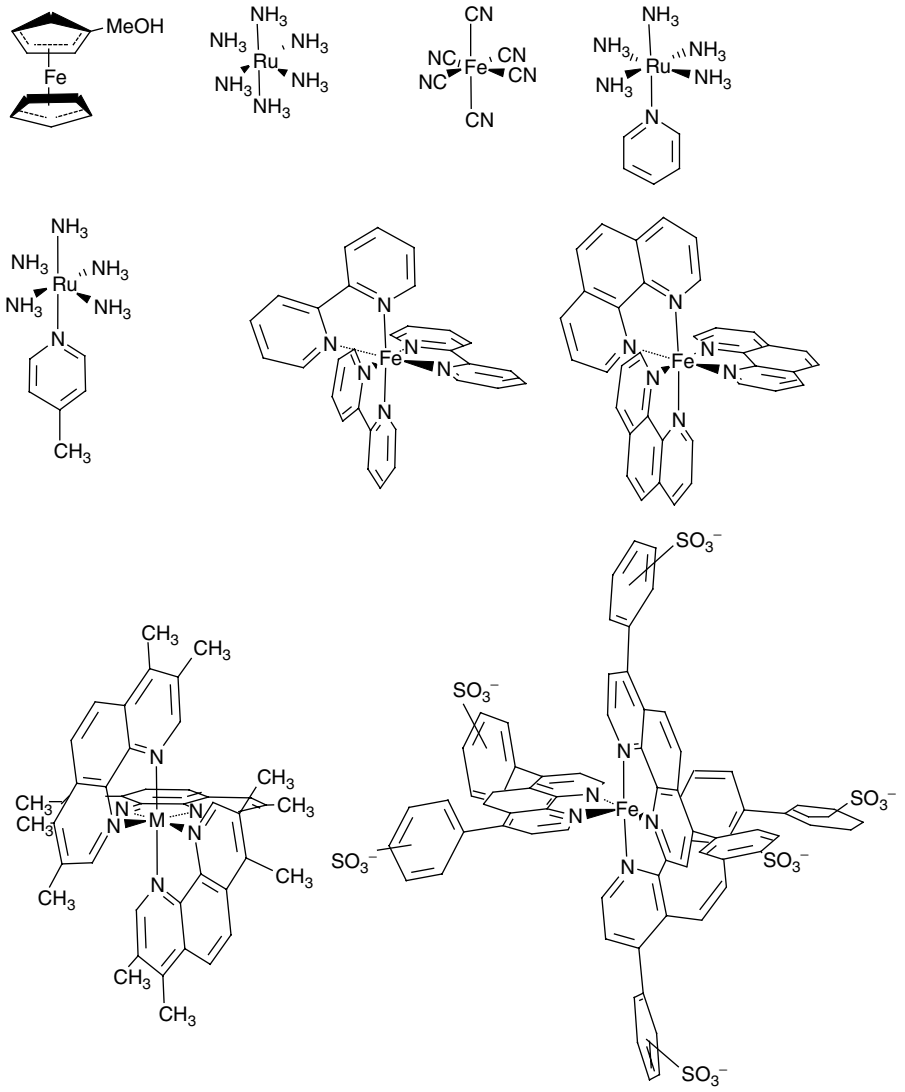


Fig. 3 Structures and average molecular diameters of redox probes used in voltammetric sieving studies.

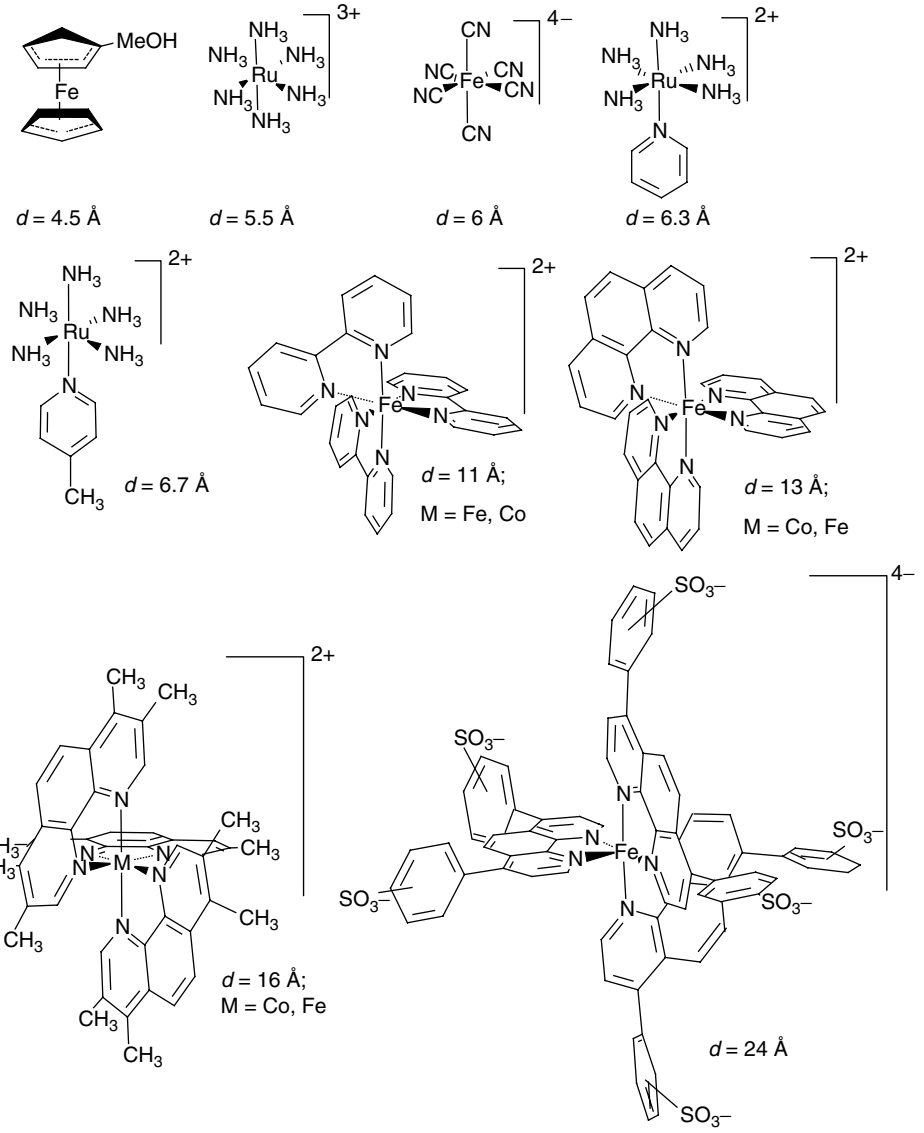


Fig. 3 (*Continued*).

that complications due to single-file diffusion or Dahms-Ruff type [16] electron-exchange enhancement of apparent electrochemical fluxes are absent. Representative PD_f values are 9×10^{-9} cm^2 sec^{-1} for permeation of thin films of **2** by $Fe(CN)_6^{4-}$, and 4×10^{-8} cm^2 sec^{-1} for permeation of thin films of **5** by $Fe(bipyridine)_3^{2+}$ [15]. Notably, these values are roughly one to one and one-half orders of magnitude larger than typically observed for permeation of amorphous

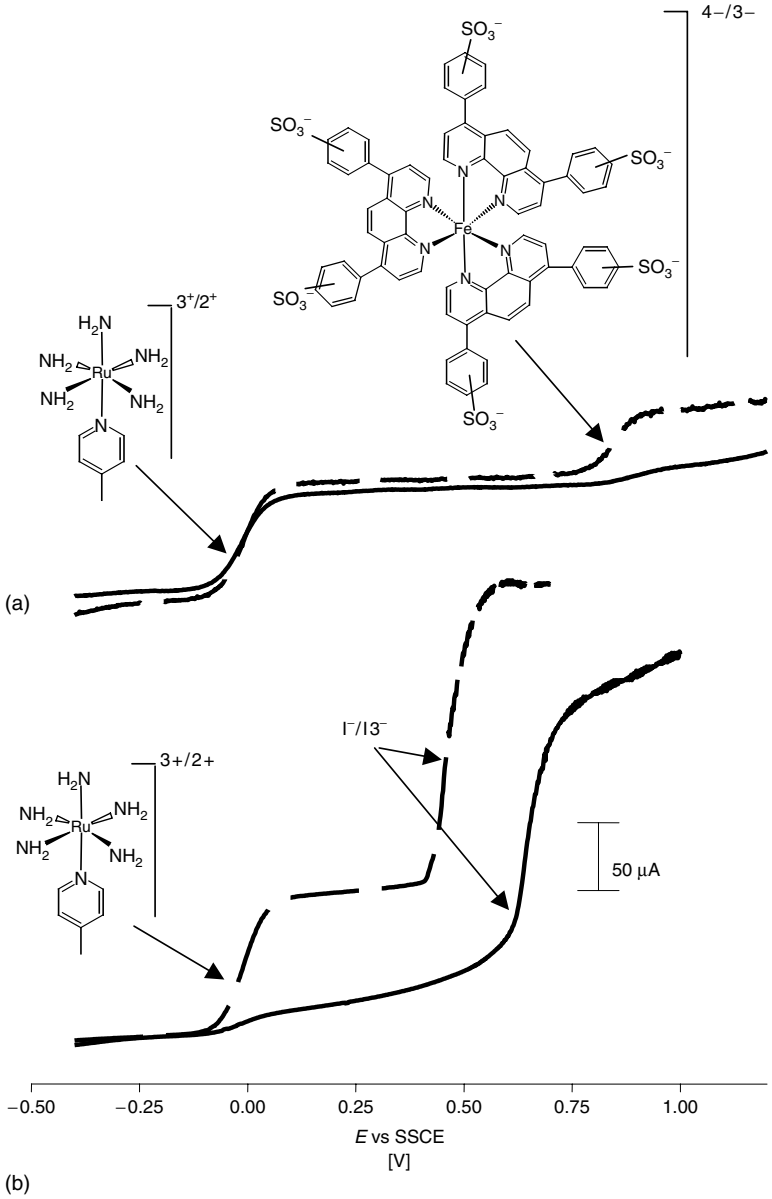


Fig. 4 Rotating disk electrochemistry of (a) a bare electrode (- - - - - -) and one modified with a thin film of **2** (———) in 1 M aqueous KNO_3 containing 5.2 mM $Ru(NH_3)_5(picoline)^{2+}$ and 5.0 mM Fe $(bphen(SO_3)_2)_3^{4-}$; (b) bare electrode (- - - - - -) and one modified with a thin film of **1** (———) in aqueous solution of 5.9 mM $Ru(NH_3)_5(picoline)^{2+}$ and 4.5 mM I^-. In both A and B, the electrode is a 3-mm-diameter glassy carbon disk electrode, the potential scan rate is 10 mV/s and the rotation rate is 500 rpm.

Tab. 1 Size-selective molecular sieving of squares

Thin-film material	*Cavity dimensions*[a] *[Å]*	*Size cutoff [Å]*
1	4 × 4	$3 < c < 7$[b]
2	8 × 8	$7 < c < 11$
3	12 × 12	$11 < c < 24$
5	18 × 18	$16 < c < 24$
8	8 × 18	$4.5 < c < 11$
9	3.5 × 3.5	$3 < c < 7$

[a] Estimated minimum van der Waals dimensions of the internal cavity.
[b] Determined from data in Sect. 5.1.6.

metallopolymers featuring similar size cutoffs [17]. The enhanced transport encountered here is ascribed to the presence of ordered one-dimensional channels.

5.1.5

Size-selective Transport of Redox-active Species through Thin Films of Porphyrinic Molecular Squares Featuring Adjustable Cavity Sizes and Tailored Channel Interiors

As an alternative to the synthesis of a new macrocyclic building block for each new molecular sieving experiment or other application, existing macrocycles and thin films can be intentionally functionalized so as to impart desired size, shape, chirality, charge, chemical affinity, catalytic reactivity, and other properties to cavities and channels. Axial ligation of metal ions found in the faces of porphyrins comprising molecular squares is one method for functionalizing cavities and channels; see Fig. 6. While any of several metal ions could, in principle, be employed, published work to date has been limited to zinc-containing porphyrins. In tetrapyrrolic environments, Zn(II) is well known to bind imine, amine, phosphine, and other ligands in a fifth – but not sixth – coordination site. Furthermore, work by Sanders and coworkers on ligand binding by Zn(II)-containing porphyrinic macrocycles [18] indicates a strong preference for interior versus exterior binding. Close-packed squares confined to thin-film environments would, of course, be expected to bind ligands only within cavities.

While only a few have been examined with respect to their effects upon molecular transport through thin films, binding of a fairly large number of ligands has been demonstrated for porphyrinic squares;

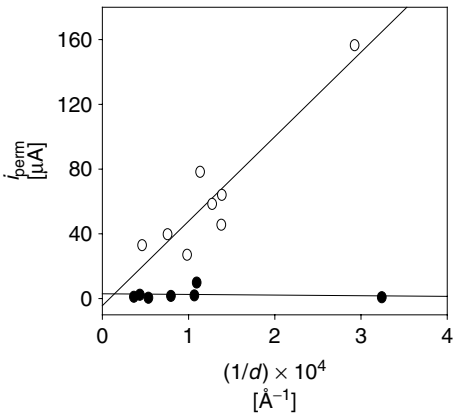


Fig. 5 Plot of the permeation current versus inverse film thickness, obtained at a glassy carbon electrode with: (○) a film of **2** in a solution of $Ru(NH)_3(pyridine)^{2+}$; (●) a film of $Re(CO)_3Cl(4\text{-phenylpyridine})_2$ "corner" in a solution of $Ru(NH)_3(pyridine)^{2+}$.

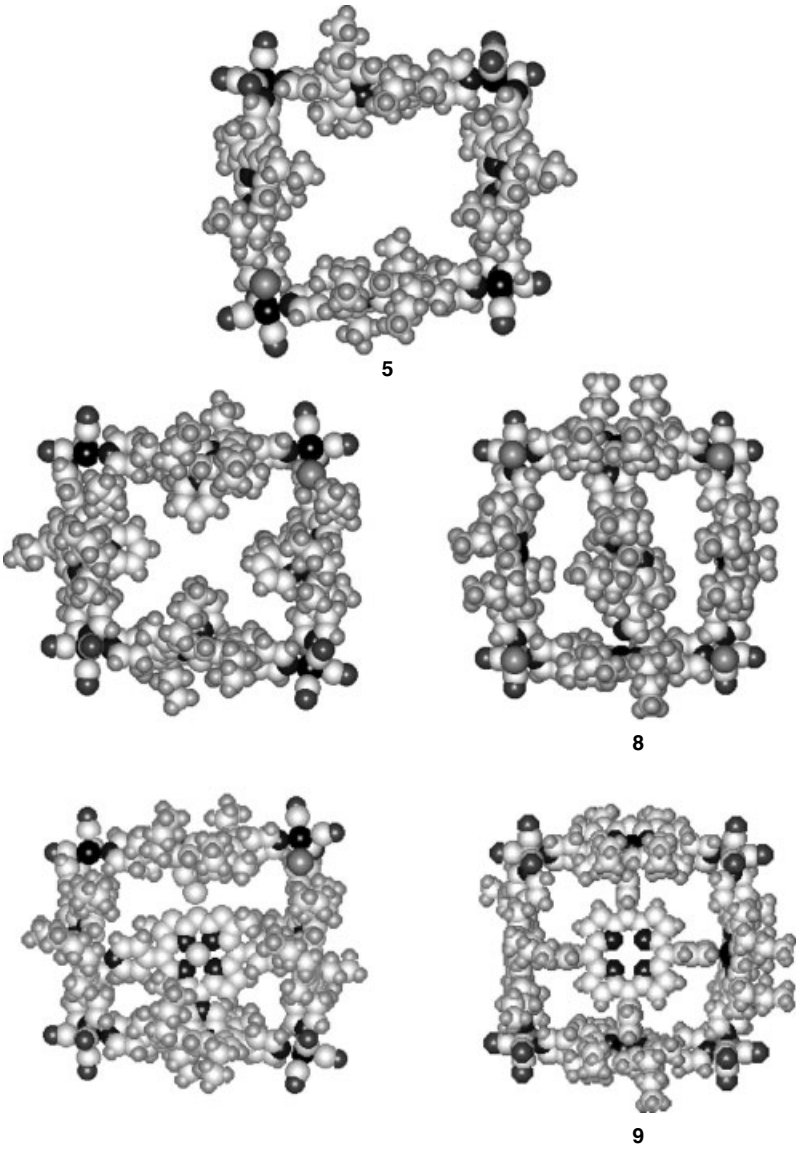


Fig. 6 Space-filled diagrams of molecular square **5**, showing one-, two-, three-, and four-point binding (middle row, clockwise from left). Structures **8** and **9** show axial ligation of (3,7,13,17-tetramethyl-2,8,12,18-tetra(*n*-butyl)-5,15-(4-pyridyl)) Zn (II) porphyrin and (5,10,15,20-(4-pyridyl)) Zn (II) porphyrin, respectively.

see Figs. 7 and 8. Notably, the collection includes chiral ligands, a catalytically active ligand, luminescent ligands, and ligands with selective metal-ion sequestering abilities. One of the more useful findings is that many ligands have higher affinities for, and display more permanent binding to, metalloporphyrins in mesoporous thin

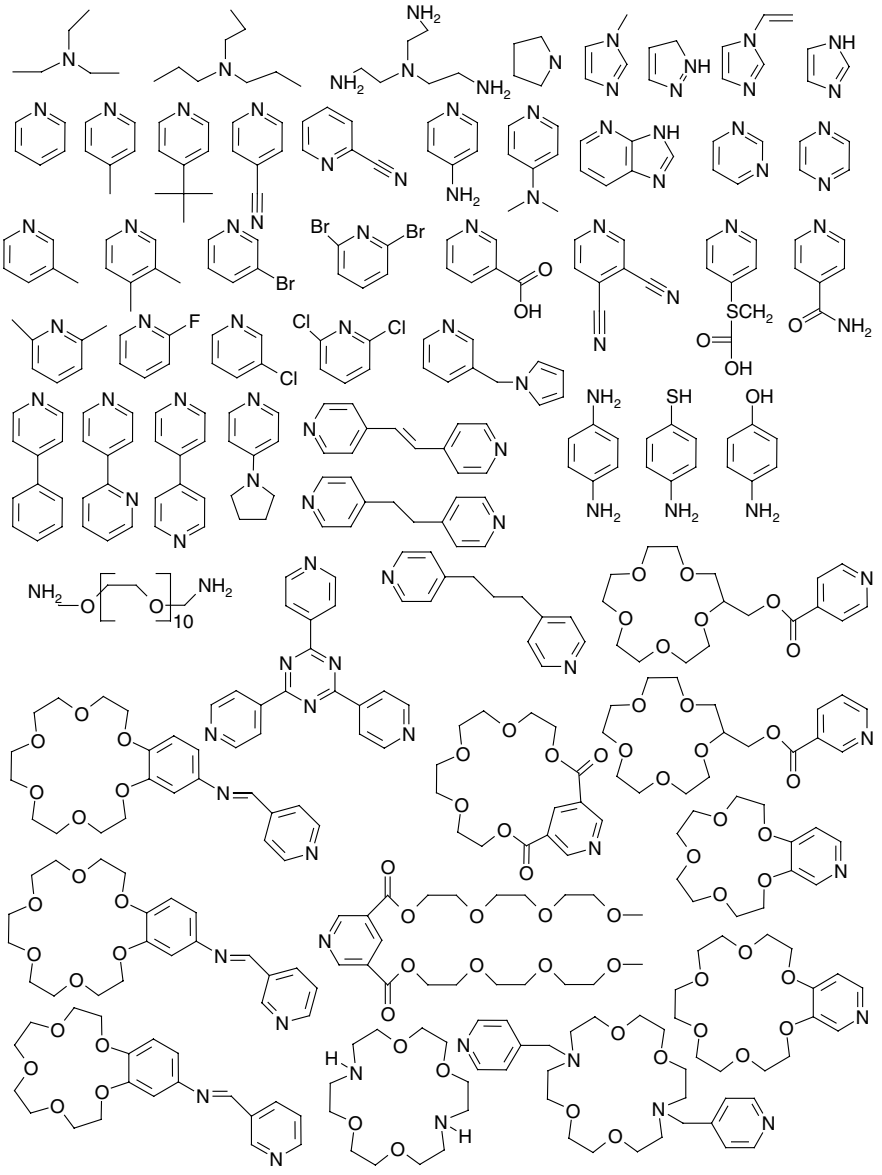


Fig. 7 Structures of ligands used to functionalize molecular square **5**.

films than metalloporphyrins in aqueous solution environments [7]. The available data suggest that the binding enhancement originates from the hydrophobicity of the film channels.

As illustrated in Fig. 6, one-point (multiple ligands), two-point, three-point, and four-point binding motifs are possible. Two- and four-point binding of pyridine-functionalized porphyrins

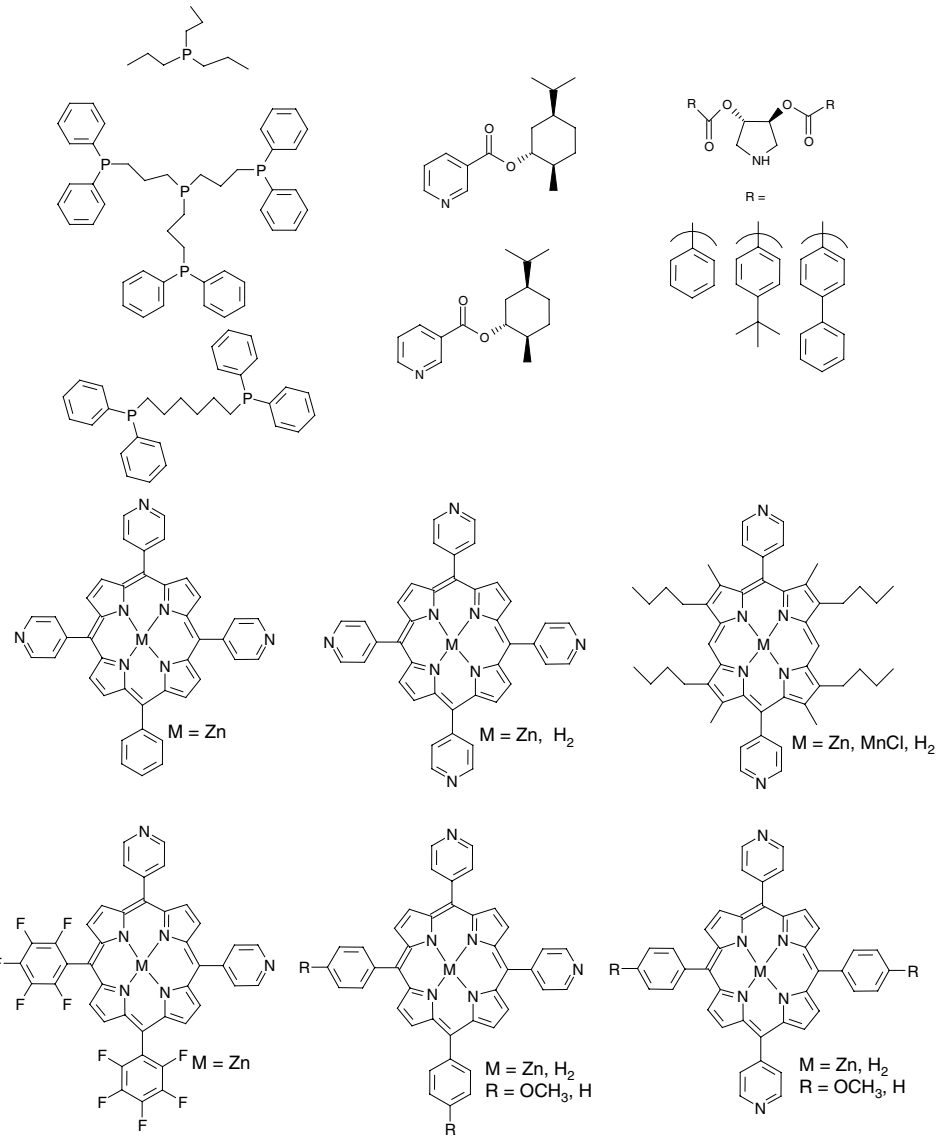


Fig. 8 More structures of ligands used to functionalize molecular square **5**.

(**8** and **9**, respectively) have been exploited in studies aimed at modifying the steric demands imposed by thin films upon candidate permeants [15]. The voltammetry measurements shown in Fig. 9 demonstrate that in thin-film transport studies, cavity functionalization can change the molecular size cutoff in a predictable fashion. In principle, other modifications could be introduced to effect shape-selective or perhaps even enantioselective molecular transport.

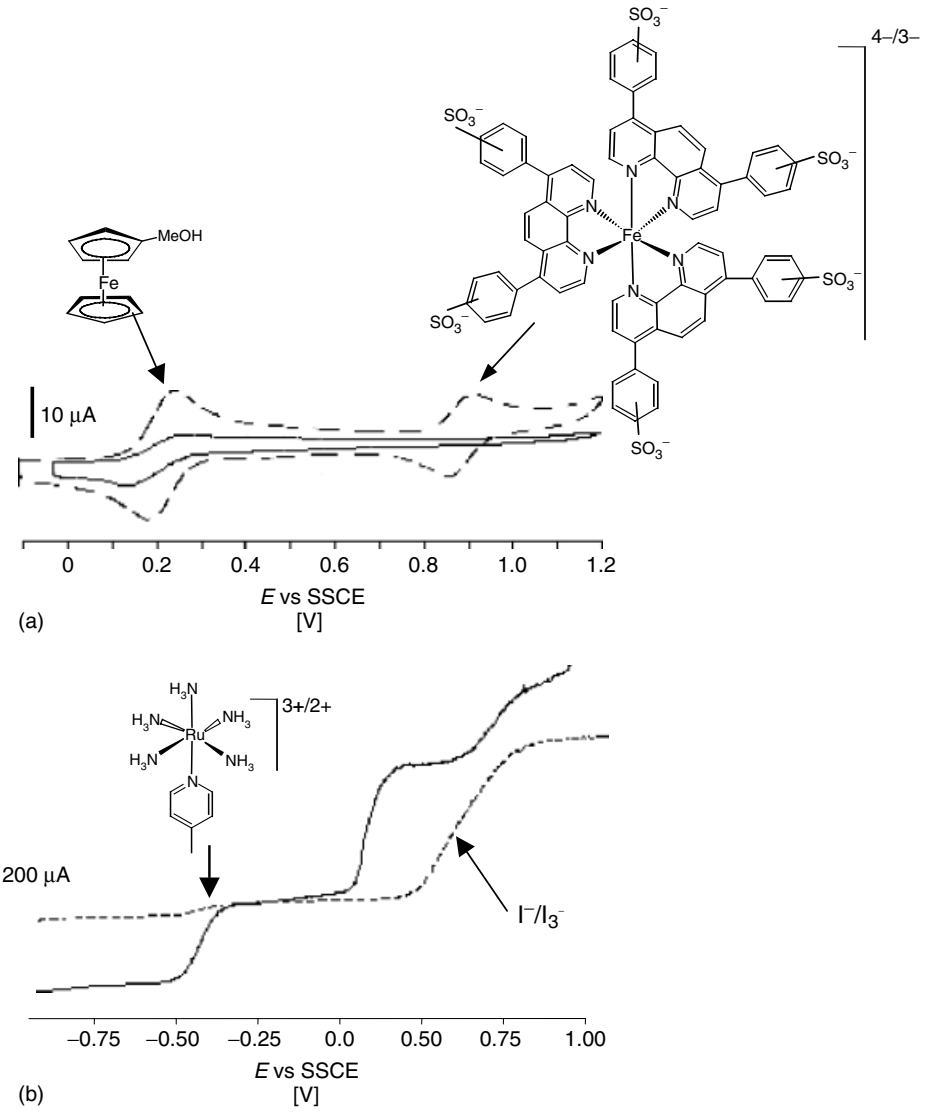


Fig. 9 Voltammetry obtained with electrodes modified with thin films of **5**. (a) Cyclic voltammetry of a bare electrode (- - - - - -) versus a **5** film-covered (190-nm thick) electrode (———), in an aqueous solution containing 1.0 mM Fe(bathophenanthroline$(SO_3)_2)_3^{4-}$ and 1.1 mM FcMeOH. (b) Rotating disk electrochemistry using a bare glassy carbon disk (- - - - - -) and an **8** film coated disk (———) in a solution containing $Ru(NH_3)_5$(picoline)$^{2+}$ and I^-. The electrode rotation rate is 500 rpm, and the potential scan rate is 10 mV sec^{-1}. (C) Cyclic voltammetry at an electrode coated with a thin film of **9** (———) and the bare electrode (- - - - - -), in a solution containing Co(bipyridine)$_3^{2+}$ and $Ru(NH_3)_6^{3+}$. Residual currents are attributed to pinhole film defects.

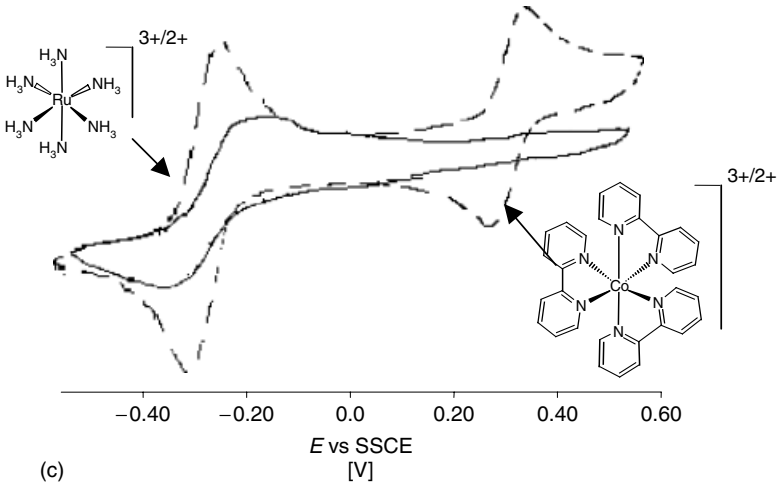
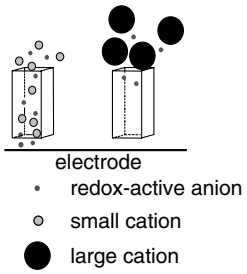


Fig. 9 (*Continued*).

Scheme 2 Depiction of size-selective permeation through a mesoporous thin film.



Other modifiers, including combinations of one- and two-point binders, have been used in selective catalysis and chemical sensing studies [19]. While these are beyond the scope of the chapter here, they do suggest that an enormous variety of films for specialized electrochemical and molecular transport applications may eventually be developed using the postsynthetic chemical functionalization approach.

5.1.6 Size-selective Transport of Redox-inactive Species through Thin Films of Molecular Squares

How can the transport of redox-silent species be investigated? Can it be done electrochemically? One approach – mentioned above, but not yet tested experimentally for thin-film microporous inorganic molecular materials – might be electrochemical impedance spectroscopy. Another would be to pair the targeted redox-inactive ion with a small redox-active counterion, that is, small enough to enter a film's cavities or channels. As shown in Scheme 2, advantage could then be taken of Coulomb's law, such that the small redox-active counterion could significantly permeate a neutral, microporous film only if the targeted ion could likewise meet the steric demands for entry created by the film's nanostructure. Successful permeation by the targeted ion would

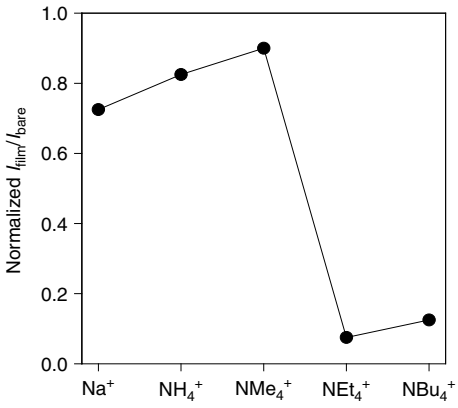


Fig. 10 Ratio of currents obtained at a glassy carbon electrode modified with a thin film of **1** (I_{film}) versus a bare electrode (I_{bare}), for aqueous solutions of I^- with various cations.

be signaled by a Faradaic electrochemical response from the counterion at the underlying electrode. Steric exclusion of the targeted ion, on the other hand, would be indicated by the absence of a Faradaic signal from the reporter ion.

Transport of small redox-*inactive* cations and blockage of larger redox-inactive cations by thin films of the pyrazine-bridged molecular square, **1**, has been demonstrated using this approach [15]. The reporter ion in each case was iodide. As illustrated in Fig. 10, the experiments, while not perfect, do reveal size-selective exclusion behavior by films of **1**. The small residual responses from iodide salts of cations too large to pass through the cavity defined by the pyrazine-bridged molecular square have been attributed to pinhole defects in the films.

Another approach, not involving electrochemical measurements, is to configure thin films as supported membranes separating solutions of candidate permeant molecules from ones lacking such molecules. If the candidate permeants are strong UV or visible-region chromophores, their passage through a membrane can be detected optically in the receiving solution [20]. This approach has been used successfully to show that thin-film membranes of **1** are permeable to phenol but blocking toward Fe(1,10-phenanthroline)$_3^{2+}$, a substantially larger molecule [21]. Similarly, thin-film membrane studies based on the porphyrinic molecular square, **5**, show that the membrane is permeable to small and intermediate sized molecules, but blocking toward the large molecular anion, Fe[(SO$_3$-phenyl)$_2$(phen)]$_3^{4-}$ ($d = 24$ Å; see Fig. 3 for molecular structure) [21]. While these species are electroactive, the approach obviously could be applied to candidate permeants that lack electroactivity.

5.1.7 Shape-selective Transport of Redox-active Species through Thin Films of Molecular Rectangles

Discrimination on the basis of permeant size represents a relatively primitive approach to engendering selective responses from thin-film coated electrodes or more generally achieving selective chemical transport. A more sophisticated mode of discrimination would be permeant shape, in combination with permeant size. One approach, not yet seriously explored, would

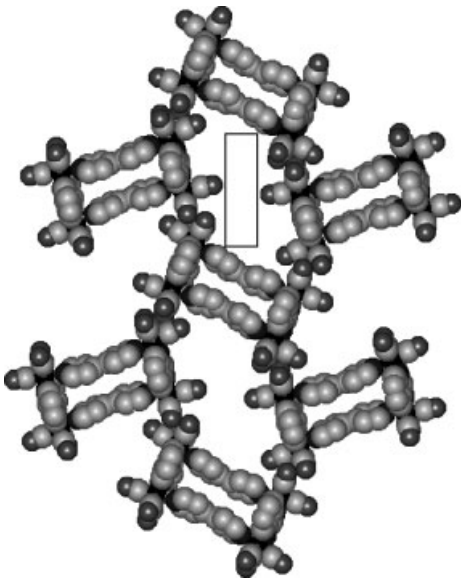


Fig. 11 Space-filled diagram of the top view of a single layer of **7b** based on its X-ray crystal structure, showing the similarly sized interstitial and intermolecular cavities.

be cavity modification, as described above. Another would be to construct appropriate macrocycles with shapes other than squares and to use these as building blocks for microporous thin-film molecular materials. Compounds **7a** and **b** are two of several members of a family of neutral, tetrametallic molecular rectangles. The average dimensions of the rectangles (length and width) as defined by the positions of the metal-ion corners are 11.2 and 5.5 Å [5]. The van der Waals cavity size, of course, is smaller. Infact it is too small for guests to pass through. Interestingly, X-ray crystallographic studies show that the rectangles are capable of packing in a fashion that yields one interstitial cavity for each intramolecular cavity. As shown in Fig. 11, the interstitial cavities are slightly larger than the intramolecular cavities, but are also roughly rectangular in shape.

Electrochemical studies using thin films of **7a** and **b** show that they function effectively as size- and shape-selective molecular transport layers. As illustrated in Table 2, the films are permeable to small molecules and to larger molecules featuring comparatively flat structures, but blocking toward those possessing incompatible sizes and shapes [11].

5.1.8
Permeation through Single Microcrystallites of Molecular Rectangles

Standard methods for assessing permeabilities, PD_f, yield ensemble average values, reflecting an average film thickness and implicitly ascribing to the film a uniform permeability. For microcrystalline films, however, significant differences in transport rates might be expected as a function of local thickness and crystallite orientation. The dependence on orientation could be spectacular for structurally anisotropic molecular materials. Differences in transport efficiency might also be expected for amorphous versus crystalline versus semicrystalline thin-film domains.

The miniaturization inherent to SECM [13] makes it an excellent technique for characterizing transport in a spatially resolved or localized fashion. Figure 12, an atomic force microscopy (AFM) image, shows an initial target material: a thin film of **7a** composed of branched, bladelike crystalline domains and a continuous amorphous layer. The blade widths are ca 20 μm, the lengths are as great as 1 mm, and the heights are typically 75–110 nm. As noted in Sect. 5.1.3, SECM can be employed in positive feedback mode to obtain quantitative measures of PD_f for redox-active permeant molecules. Furthermore, given the microcrystallite

Tab. 2 Redox probe dimensions and permeabilities in thin films of **7a**

	Redox probes	*Probe dimensions [Å]*
Permeable	FcMeOH	4.5 × 4.5 × 4.5
	$Ru(NH_3)_6^{3+}$	5.5 × 5.5 × 5.5
	$Fe(CN)_6^{4-}$	6 × 6 × 6
	Benzoquinone	3 × 5 × 8
	$Ru(NH_3)_4$(1,10-phenanthroline)$^{2+}$	5.5 × 8 × 10
	Ethylviologen^{2+}	3 × 5 × 14
	Ni_2TIED^{4+a}	4 × 8 × 16
	Anthraquinone$(SO_3Na)^{1-b}$	3 × 6 × 11
Excluded	$Ru(NH_3)_2$(1,10-phenanthroline)$_2^{2+}$	8 × 10 × 13
	Co(phenanthroline)$_3^{2+}$	13 × 13 × 13

[a] Dinickel(II) (1,1'-enebicyclo-3,6,10,13-tetraazatetradeca-2,13-dienylidene) perchlorate.
[b] Anthraquinone-2-sulfonic acid sodium salt monohydrate.

dimensions, even comparatively large SECM tips (e.g., a few microns in diameter) can be employed effectively in spatially resolved studies.

Figure 13 illustrates how both qualitative and quantitative transport information can be derived from SECM measurements. Shown in Fig. 13(a) and (b) are the SECM responses of a coated electrode (thin film of **7a**) to solutions of $Ru(NH_3)_6^{3+}$ and Fe(1,10-phenanthroline)$_3^{2+}$, respectively. The latter is too large to pass through either interstitial or intramolecular cavities. Consistent with this idea, the corresponding SECM image is structureless – implying uniform exclusion of the candidate permeant. In contrast, a fairly highly structured SECM image is obtained in solutions of the smaller permeant. The spatial variations in SECM feedback current density are interpreted in terms of film thickness variations, with the narrow, low current density features corresponding to transport through single microcrystallites. Recall that the thicker the film, the lower the flux under standard film permeation conditions (cf. Eq. 3). In any case, combining AFM estimates of microcrystallite thickness with SECM measurements of flux yields single-microcrystallite

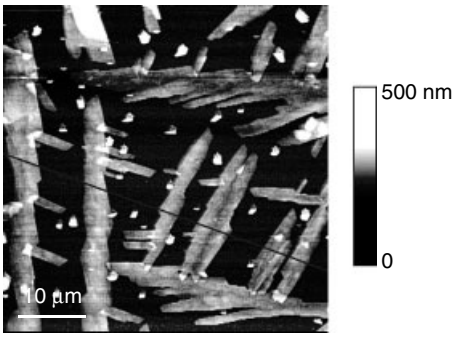


Fig. 12 Atomic force microscopy of single crystals of **7a** on indium tinoxide (ITO) covered glass.

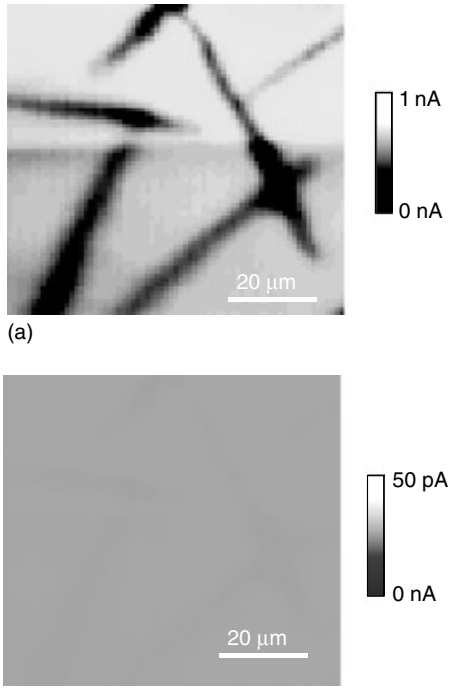


Fig. 13 Scanning electrochemical microscopy images of the sample (over a different area) from Fig. 12 using the redox mediators (a) $Ru(NH_3)_6^{3+}$ ($E_{tip} = 0$ V; $E_{ITO} = -0.35$ V); (b) $Fe(phenanthroline)_3^{3+}$ ($E_{tip} = 0$ V; $E_{ITO} = +1.0$ V). In each instance, the sample was scanned at identical tip height and a scan rate of 10 μm sec^{-1}.

PD_f values of 2.0×10^{-9} and 6.8×10^{-9} cm^2 sec^{-1} for the representative permeants, $Fe(CN)_6^{4-}$ and $Ru(NH_3)_6^{3+}$, respectively [9]. These values are significantly smaller than measured for transport of the same molecules through thin films composed of molecular squares [15]. The differences are ascribed to the absence of channels within the films composed of molecular rectangles. (In contrast, materials composed of molecular squares generally feature arrays of semi-infinite one-dimensional channels; cf. Fig. 1.) Indeed, an extended view of the packing diagram shown in part in Fig. 11 reveals that successive layers of rectangles are positioned such that molecules strategically block the areas immediately above and below each cavity, albeit not to the extent that permeation becomes impossible. It will be interesting to extend this approach to anisotropic channel-containing molecular materials.

Acknowledgments

We thank the US National Science Foundation and the Office of Naval Research for financial support of our work. We acknowledge the many contributions of our coworkers, especially Dr Suzanne Belanger, Dr Kurt D. Benkstein, Dr Robert V. Slone, Melinda H. Keefe, Dr Keith J. Stevenson, Ken F. Czaplewski, Jennifer Welch, and Brian C. Anderson.

References

1. (a) R. V. Slone, D. I. Yoon, R. M. Calhoun et al., *J. Am. Chem. Soc.* **1995**, *117*, 11813; (b) R. V. Slone, J. T. Hupp, C. L. Stern et al., *Inorg. Chem.* **1996**, *35*, 4096; (c) R. V. Slone, J. T. Hupp, *Inorg. Chem.* **1997**, *36*, 5422; (d) R. V. Slone, K. D. Benkstein, S. Belanger et al., *Coord. Chem. Rev.* **1998**, *171*, 221.
2. (a) B. Olenyuk, P. J. Fechtenkotter, P. J. Stang, *J. Chem. Soc., Dalton Trans.* **1998**, *11*, 1707; (b) P. J. Stang, B. Olenyuk, *Acc. Chem. Res.* **1997**, *30*, 502, and references therein; (c) S. Leininger, B. Olenyuk, P. J. Stang, *Chem. Rev.* **2000**, *100*, 853; (d) S. W. Lai, M. C. W. Chan, K. K. Cheung et al., *Organometallics* **1999**, *18*, 3991; (e) P. J. Stang, V. V. Zhdankin, *J. Am. Chem. Soc.* **1993**, *115*, 9809.
3. (a) S.-S. Sun, A. S. Silva, I. M. Brinn et al., *Inorg. Chem.* **2000**, *39*, 1344; (b) S.-S. Sun, E. Robson, N. Dunwoody et al., *Chem. Commun.* **2000**, *3*, 201; (c) S.-S. Sun, A. J. Lees, *Inorg. Chem.* **1999**, *38*, 4181.

4. (a) M. Fujita, J. Yakazi, K. Ogura, *J. Am. Chem. Soc.* **1990**, *112*, 5645; (b) M. Fujita, J. Yakazi, K. Ogura, *Tetrahedron Lett.* **1991**, *32*, 5589; (c) M. Fujita, S. Nagao, M. Iida et al., *J. Am. Chem. Soc.* **1993**, *115*, 1574; (d) M. Fujita, K. Ogura, *J. Chem. Soc., Chem. Commun.* **1996**, 1535; (e) W. H. Leung, J. Y. K. Cheng, T. S. M. Hun et al., *Organometallics* **1996**, *15*, 1497; (f) W. C. Kalb, Z. Demidowicz, D. M. Speckman et al., *Inorg. Chem.* **1982**, *21*, 4027; (g) P. M. Sticklen, E. J. Volcko, B. J. G. Verkade, *Inorg. Chem.* **1983**, *105*, 2494; (h) H. Rauter, E. C. Hillgeris, A. Erxleben et al., *J. Am. Chem. Soc.* **1994**, *116*, 616; (i) L.-M. Zheng, X. Fang, K.-H. Lii et al., *J. Chem. Soc., Dalton Trans.* **1999**, *14*, 2311–2316.
5. (a) K. D. Benkstein, J. T. Hupp, C. L. Stern, *J. Am. Chem. Soc.* **1998**, *120*, 12982; (b) K. D. Benkstein, J. T. Hupp, C. L. Stern, *Inorg. Chem.* **1998**, *37*, 5404; (c) K. D. Benkstein, J. T. Hupp, C. L. Stern, *Angew. Chem., Intl. Ed.* **2000**, *39*, 2891.
6. (a) T. Rajendran, B. Manimaran, F. Y. Lee et al., *Inorg. Chem.* **2000**, *39*, 2016; (b) D. J. Darensbourg, W. Z. Lee, M. J. Adams et al., *Inorg. Chem.* **1999**, *38*, 1378; (c) S. M. Woessner, J. B. Helms, Y. B. Shen et al., *Inorg. Chem.* **1998**, *37*, 540; (d) C. S. Campos-Fernandez, R. Clerac, K. R. Dunbar, *Angew. Chem., Intl. Ed.* **1999**, *38*, 3477; (e) C. Rancurel, D. B. Leznoff, J. P. Sutter et al., *Inorg. Chem.* **1999**, *38*, 4753; (f) M. Schmitz, S. Leininger, J. Fan et al., *Organometallics* **1999**, *18*, 4817; (g) D. F. Xu, H. J. Murfee, W. E. van der Veer et al., *J. Organomet. Chem.* **2000**, *596*, 53; (h) S. S. Lau, P. E. Fanwick, R. A. Walton, *J. Chem. Soc., Dalton Trans.* **1999**, *14*, 2273; (i) H. K. Fun, S. S. S. Raj, R. G. Xiong et al., *J. Chem. Soc., Dalton Trans.* **1999**, *11*, 1711.
7. M. H. Keefe, R. V. Slone, J. T. Hupp et al., *Langmuir* **2000**, *16*, 3964.
8. K. D. Benkstein, J. T. Hupp, *Mol. Cryst. Liq. Cryst.* **2000**, *342*, 151.
9. M. E. Williams, K. D. Benkstein, C. Abel, P. H. Dinolfo, J. T. Hupp, *Proc. Natl. Acad. Sci.*, **2002**, *99*, 5171.
10. D. A. Gough, J. K. Leypoldt, *Anal. Chem.* **1979**, *51*, 439.
11. (a) V. G. Levich, *Physicochemical Hydrodynamics*, Prentice-Hall, Englewood Cliffs, 1962; (b) A. J. Bard, L. R. Faulkner, *Electrochemical Methods, Fundamentals and Applications*, John Wiley & Sons, New York, 1980, pp. 280–292.
12. (a) A. G. Ewing, B. J. Feldman, R. W. Murray, *J. Phys. Chem.* **1985**, *89*, 1263; (b) J. A. Leddy, A. J. Bard, *J. Electroanal. Chem. Int. Electrochem.* **1983**, *153*, 223; (c) A. G. Ewing, B. J. Feldman, R. W. Murray, *J. Phys. Chem.* **1985**, *89*, 1263; (d) J. M. Saveant, *J. Electroanal. Chem.* **1991**, *302*, 91.
13. (a) A. J. Bard, G. Denuault, C. Lee et al., *Acc. Chem. Res.* **1990**, *23*, 357; (b) A. J. Bard, F. R. F. Fan, M. V. Mirkin, in *Electroanalytical Chemistry* (Ed.: A. J. Bard), Marcel Dekker, New York, 1994, p. 243, Vol. 18.; (c) A. L. Barker, M. Gonsalves, J. V. Macpherson et al., *Anal. Chim. Acta* **1999**, *385*, 223; (d) B. D. Bath, H. S. White, E. R. Scott, in *Scanning Electrochemical Microscopy* (Eds.: A. J. Bard, M. V. Mirkin), John Wiley & Sons, New York, 2001.
14. (a) M. E. Williams, K. J. Stevenson, A. M. Massari et al., *Anal. Chem.* **2000**, *72*, 3122; (b) T. Ikeda, R. Schmehl, M. Denisevich et al., *J. Am. Chem. Soc.* **1982**, *104*, 2683; (c) K. A. Pressprich, S. G. Maybury, R. E. Thomas et al., *J. Phys. Chem.* **1989**, *93*, 5568.
15. (a) S. Belanger, J. T. Hupp, C. L. Stern et al., *J. Am. Chem. Soc.* **1999**, *121*, 557; (b) S. Belanger, J. T. Hupp, *Angew. Chem., Intl. Ed.* **1999**, *38*, 2222; (c) S. Belanger, M. H. Keefe, J. L. Welch et al., *Coord. Chem. Rev.* **1999**, *190–192*, 29; (d) S. Belanger, B. C. Anderson, J. T. Hupp, *Proc. – Electrochem. Soc.* **1999**, *98–26*, 208.
16. (a) I. Ruff, L. Botar, *J. Chem. Phys.* **1985**, *83*, 1292; (b) I. Ruff, L. Botar, *Chem. Phys. Lett.* **1986**, *126*, 348; (c) I. Ruff, L. Botar, *Chem. Phys. Lett.* **1988**, *149*, 99; (d) H. Dahms, *J. Phys. Chem.* **1968**, *72*, 362; (e) I. Ruff, V. J. Friedrich, *J. Phys. Chem.* **1971**, *75*, 3297; (g) I. Ruff, V. J. Friedrich, K. Demeter et al., *J. Phys. Chem.* **1971**, *75*, 3303.
17. S. Belanger, K. J. Stevenson, J. T. Hupp, *Langmuir* **1999**, *15*, 837.
18. R. S. Wylie, E. G. Levy, J. K. M. Sanders, *Chem. Commun.* **1997**, *17*, 1611.
19. M. Merlau, P. Mejia, S. T. Nguyen, J. T. Hupp, *Angew. Chem.* **2001**, *40*, 4239.
20. J. C. Hulteen, K. B. Jirage, C. R. Martin, *J. Am. Chem. Soc.* **1998**, *120*, 6603.
21. K. F. Czaplewski, Northwestern University, unpublished work.

5.2
Sol–Gel Modified Electrode Films

Winny Dong
California State Polytechnic University, Pomona, CA

Bruce Dunn
University of California, Los Angeles, CA

5.2.1
Introduction

The room temperature, liquid-phase reaction of the sol–gel process lends itself very well to synthesizing modified electrodes. Sol–gel chemistry enables one to synthesize a wide range of oxides, including transition metal oxides, to incorporate organic and inorganic dopants within the oxide and to prepare the material with controllable pore size and surface area. Over the last 15 years, sol–gel has emerged as one of the most versatile electrode preparation methods because of its ability to modify both the surface and the bulk of the electrode film.

Materials made through the sol–gel process have found applications in lasers, optical fibers, solid electrolytes, and many types of coatings [1–3]. In the early 1990s, it was shown that enzymes and other proteins encapsulated in a sol–gel silica matrix retained the chemical and biological function of the biomolecule and improved thermal stability [4, 5]. This discovery spurred considerable activity and led to the commercialization of sol–gel electrodes for biosensing applications. Other sol–gel electrode applications include electrodes for fuel cells and electrochromic devices, and amperometric sensors for analytes in the gas phase [6, 7]. Another potentially important advance in the field is the development of an ink-jet printing technique for depositing the sol–gel electrodes [8]. This can be the technology needed to make sol–gel a true mass production method for electrodes and other devices.

Sol–gel processing is a room temperature synthesis method that involves the reaction of liquid chemical precursors to form inorganic ceramic and glass materials [9]. The sol–gel process is important in that it provides a low temperature alternative for the synthesis of oxides. This process offers a different approach to the conventional high-temperature preparation of transition metal oxides. It also presents several advantages over other electrode preparation methods. One significant advantage is the ability to obtain homogeneous multicomponent systems. These multicomponent systems can be metal/metal oxide or organic molecule/metal oxide. A homogeneous distribution of dopants is possible because the liquid precursors of the sol–gel process can be easily mixed at the nanometer level. In contrast, the grinding of powders achieves particle mixing at micron dimensions.

A second important advantage is that the temperatures required for material processing can be lowered noticeably, leading to unusual glasses or ceramics [10]. This has led to synthesis of metastable, or kinetically trapped, phases. Amorphous metal oxides have demonstrated unusual and often beneficial properties compared to their crystalline counterparts. The low processing temperature also enables one to synthesize oxides containing an extraordinary range of dopants; the list includes organic components, from dye molecules to monomers, and biological molecules such as enzymes, antibodies, proteins, and cells [4, 11, 12].

Encyclopedia of Electrochemistry. Edited by A.J. Bard and M. Stratmann
Vol. 10 *Modified Electrodes*. Edited by M.Fujihira, I.Rubinstein, and J.F.Rusling
Copyright © 2007 Wiley-VCH Verlag GmbH & Co. KGaA, Weinheim. ISBN: 978-3-527-30402-8

The third advantage is that the sol–gel process provides the experimentalist excellent control over the entire synthesis process. The resulting gels can be formed at room temperature into fibers or films by a variety of techniques. The sol–gel process is especially convenient for the formation of thin films. It has very definite advantages over other film deposition techniques requiring expensive vacuum equipment and is especially suitable for large-scale industrial utilization [13]. The resulting microstructural properties such as density, porosity, pore size distribution, and so on, can also be well controlled. Moreover, by careful selection of the precursors, very pure materials can be synthesized. In this way, it is possible to synthesize "tailor-made" materials by controlling the chemistry of the precursors, the rate of gelation, the addition of catalysts, and the drying method.

The purpose of this section is to introduce the reader to the chemistry of sol–gel materials and the electrochemical properties of sol–gel modified electrode films. Section 5.2.2 reviews sol–gel chemistry and the preparation of different types of sol–gel derived films. Electrodes for the many different applications that involve various synthesis and modification techniques are discussed in Sect. 5.2.3. The electrochemical properties of the various sol–gel films will also be summarized.

5.2.2 Synthesis of Sol–gel Films

5.2.2.1 Sol–gel Chemistry

The chemistry of the sol–gel process is based on the hydrolysis and condensation of molecular precursors [14]. The sol–gel process derives its name from the two fairly distinct physical stages of the precursors. The "sol" is the stage where the metal–oxygen colloids are suspended in a liquid (solvent). Once enough bridging bonds are formed between the metal–oxygen clusters, the precursors no longer flow, and the sol becomes a "gel". The gel consists of amorphous primary particles (5–10 nm or smaller) with an interstitial liquid phase that fills the pore volume (Fig. 1). The most versatile precursors for making modified electrodes are metal alkoxides, $M(OR)_n$, where the transition metal is represented by M, n is the valence of the metal, and R is an alkyl group such as methyl, ethyl, propyl, and so on. Transition metal alkoxides are versatile because they are known for almost all transition metal elements [15]. Also the M−OR bonds dissociate easily to form M−OH bonds upon hydrolysis. Other commonly used precursors are inorganic salts.

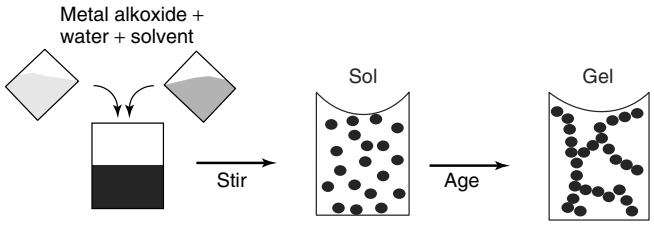


Fig. 1 Sol–gel synthesis. The sol consists of metal-oxygen colloids suspended in a solvent. The gel is an interconnected, rigid network of metal/oxygen/hydroxide polymeric chain and solvent filled pores.

Transition metal oxides are readily prepared using sol–gel chemistry. Because full coordination is usually not satisfied in the molecular precursor, there is the ability for coordination expansion to occur, leading to reactivity toward nucleophilic reagents such as water [15]. This makes the transition metal alkoxides ideal candidates for the hydrolysis and condensation reactions, which are central to the sol–gel process. However, when carried to the extreme, this reactivity can also present problems such as the formation of precipitates rather than a stable sol. Therefore, most transition metal alkoxides must be handled with great care, in a dry environment, and are often stabilized by chemical modification to prevent precipitation upon hydrolysis [16].

Hydrolysis of the alkoxide occurs when water is added and a reactive M−OH hydroxo group is generated [14].

$$H_2O + MOR \longrightarrow MOH + ROH \quad (1)$$

This follows a nucleophilic substitution mechanism [16]. The rate of reaction will depend on the coordination unsaturation and oxidation state of the metal atom. The higher the unsaturation and lower the oxidation state, the faster the substitution reaction. Condensation occurs as bridging bonds between M and O are formed and alcohol and/or water are generated.

$$MOH + MOR \longrightarrow M{-}O{-}M + ROH \quad (2)$$

$$MOH + MOH \longrightarrow M{-}O{-}M + H_2O \quad (3)$$

After a significant amount of hydrolysis and condensation has taken place, a three-dimensional network of metal and oxygen forms within the sol and the viscosity of the sol increases. As condensation continues, the sol transforms into a nonfluid gel as an interconnected and fairly rigid 3-D network extends throughout the entire sample container. The resulting wet gel is an amorphous, porous metal oxide, with an aqueous alcohol phase filling the pore volume.

When the full coordination of the metal atom is not satisfied in the alkoxide, bridging hydroxo groups can be formed in place of bridging oxygen.

$$M{-}OH + M{-}ROH \longrightarrow M{-}OH{-}M + ROH \quad (4)$$

$$M{-}OH + M{-}HOH \longrightarrow M{-}OH{-}M + H_2O \quad (5)$$

Since the coordination for most transition metals is not saturated in the alkoxide, metal hydroxides can form very quickly. As a result, terminal oxygen bonds form, instead of bridging oxygen bonds, leading to precipitation rather than a 3-D network. This reaction must be slowed to form a transition metal oxide with bridging oxygen bonds throughout the structure. The fundamental considerations for the sol–gel chemistry of transition metal oxides has been reviewed by Livage et al. [14].

Many parameters can be changed during the sol–gel process to affect the final gel structure. Some of the most important parameters are the solvents used, molar ratio of water to metal alkoxide, temperature, presence and concentration of catalysts, and the pH of the sol. These affect the hydrolysis and/or condensation rates which in turn, influence the final density, surface area, degree of polymerization, and the interconnected morphology of the final gel. Generally, linear polymers form when hydrolysis is fast and condensation is slow. The reverse gives rise to bulky, large, and highly cross-linked polymers [6].

Furthermore, the connectivity of a dried gel can be controlled by the amount of water used for hydrolysis. Films made with low water content can be sintered to dense crystalline films, whereas those made with more water may remain highly porous after firing [17].

5.2.2.2 Film Formation

Various types of oxide films with controlled thickness and microstructure can be deposited from the sol by dipping, spin coating, or spraying [9]. A sol with low viscosity is generally desirable to prevent cracking and unevenness in film thickness. Once the film has gelled, the process of aging begins. Aging is characterized by further polymerization, syneresis and evaporation of the solvents, particle coarsening, and phase transformations. In most films, aging takes place simultaneously with drying and results in film shrinkage. Because of the constraints of the substrate, aging and drying of the film can sometimes lead to cracking. This can be avoided by controlling film thickness below a critical value [18, 19]. Most sol–gel films remain crack free below 0.1–0.5 μm in thickness [20]. Thicker films can be prepared through deposition of multiple layers.

Solvent evaporation and gelation occur quickly after film formation because of the high surface-to-volume ratio. The quick gelation rate minimizes the degree of cross-linking, and it is possible to redissolve films even after complete drying [21]. One method to increase the strength of the film is to age the film in a solvent-saturated environment. This delays the drying process until the gel is fully aged and results in an overall decrease in surface area and an increase in pore size. By separating the aging and drying processes, the film will have time to fully polymerize (during aging) before most of the shrinkage (during drying) occurs.

5.2.2.3 Heat Treatment of Films

Heat treatments are often performed to further consolidate the film. Sintering is a densification process that is driven by surface energy to eliminate the pores within the gel [6]. A thorough review and a mathematical treatment of the sintering process for sol–gel films are given by Scherer [20]. In general, sol–gel films are rarely sintered to their fully dense crystalline form. This is due to a few factors. First, although the substrate provides sites for heterogeneous nucleation, it also constrains the film and inhibits shrinkage. Second, grain growth retards densification by increasing the length of the diffusion path [20]. One method used to achieve dense crystalline films is to delay crystallization (through rapid heating) until the film has achieved a desired density [22]. If amorphous films are desired, removal of the OH groups should be delayed as much as possible since there is evidence that the amorphous phase is stabilized by the OH groups [23].

5.2.2.4 Typical Heat Treatments

The high concentration of OR groups in the sol–gel film can lead to blistering or cracking during rapid heating. A low temperature treatment (~200 °C) is generally used to remove the water and/or organic solvents remaining from the hydrolysis and condensation reactions. Structurally bound water, H_2O, leaves the network in the range of 250–300 °C. Heat treatments of 200–300 °C yield amorphous films with densities below 1.0 g cm^{-3} [24]. Higher treatment temperatures (~ 400–800 °C) can produce crystallization and densification through sintering.

5.2.3 Further Modification of the Sol–gel Electrodes

The oxides prepared by sol–gel methods can be modified through manipulation of their surface reactivity to alter such fundamental physical properties as surface area and density. They can be further modified through the incorporation of a second oxide, organic molecules, or biological molecules to influence their electrochemical properties. Sol–gel chemistry can also be easily combined with the polymerization of π-conjugated polymers such as polypyrrole, polythiophene, and polyaniline. The different approaches to the incorporation of a second phase are through covalent bonding, sol–gel doping, impregnation, and intercalation. A very thorough review of these processes is given by Lev et al. [25]. A few methods used to modify sol–gel synthesized film electrodes will be discussed in this section. Modifications of silica and transition metal–oxide surfaces and structure are described in Sects 5.2.2.3.1 and 5.2.2.3.2. The following three sections then describe modification through the incorporation of a second phase.

5.2.3.1 Silica

Silica gels prepared from silicon alkoxides have been very well characterized and the chemical process is well understood. The sol–gel chemistry of silica has been reviewed by Iler [26] and Hench and West [27]. The field of silica-modified electrodes began in the late-1980s and has seen exponential growth since the mid-1990s [28]. A more recent impetus for this growth came from the discovery that silica can be used as an efficient support for enzymes without inhibiting its biological activity [29–31]. Sol–gel derived silica is especially suitable for biosensing applications because of its rigidity, porosity, and electrochemical inertness.

Adsorption or precipitation of organic compounds onto an electrochemically inert gel is the traditional method of modifying a sol–gel electrode. It stands to reason that the surface chemistry and surface reactivity of the electrode are very important. The versatility of a sol–gel derived silica lies in the various properties the gel can exhibit depending on the synthesis conditions. The silica surface consists of various types of silanols and siloxanes. The silanol groups are considered to be strong adsorption sites while the siloxanes are usually hydrophobic [32, 33]. The reactivity of the silanol groups can be modified by deprotonating with ammonia or organic amines. Ionization of silanols has been shown to enhance the fixation of metal cations on silica surfaces [34, 35]. By choosing different precursors, sol–gel silica can be either hydrophobic (alkyl- or phenyl-trialkoxysilanes) or hydrophilic (tetraalkoxysilanes). The ability to tailor and manipulate specific properties (degree of hydrophobicity, reactivity of surface groups, etc.) has made silicates the sol–gel modified electrode matrix of choice. In addition, silicates have good adhesion to electrode surfaces, favorable abrasion resistance, and high optical transparency. Other inert oxides used for biosensing are zirconia and alumina gel films.

5.2.3.2 Transition Metal Oxides

Transition metal compounds are generally redox-active and are important materials for electrochemical processes and catalysis. A list of transition metal–oxide films prepared through the sol–gel method is presented in Table 1. One subgroup of transition metal oxides (MoO_3, V_2O_5,

Tab. 1 Transition metal–oxide films prepared by the sol–gel method

Material	*Application*	*Properties*	*Cycleability*	*References*
$LiNiO_2$	Electrode for Li battery	135 mAh g^{-1} (4 V)	–	36
$LiNi_xCo_{1-x}O_2$	Electrode for Li battery	180 mAh g^{-1}	–	36
$LiMn_2O_4$	Electrode for Li battery	75 mAh g^{-1} (4 V)	>100 cycles	37
$LiMn_{2-x}Me_xO_4$	Electrode for Li battery	120–160 mAh g^{-1} (4 V)	–	38–40
$LiCoO_2$	Electrode for Li battery	(4 V)	–	41
V_2O_5	Electrode for Li battery	250 mAh g^{-1}	>450 cycles	2
V_2O_5	Electrode in supercapacitor	80–200 F g^{-1}	–	42
V_2O_5	Counterelectrode for electrochromic devices	Red/yellow–green upon oxidation	–	43
CeO_2-ZrO_2	Electrode for fuel cells	–	–	44
CeO_2-ZrO_2	Transparent counterelectrode for electrochromic or photoionic devices	–	–	44
CeO_2-ZrO_2	Electrode for Li battery	–	–	44
MnO_2	Supercapacitor	698 F g^{-1}	1500 cycles	45
RuO_2	Supercapacitor	720 F g^{-1}	–	46
WO_3	Electrode for electrochromic devices	Transparent/yellow–blue upon reduction	1600 cycles	13, 24
TiO_2	Electrode for electrochromic devices	Transparent–gray/blue upon reduction	–	47
Nb_2O_5	Electrode for electrochromic devices	Transparent–gray/blue upon reduction	–	48
Co_3O_4	Electrode for electrochromic devices	Yellow–dark brown upon oxidation	–	49
$Fe_2V_4O_{13}$	Electrochromic devices	–	–	50
$P_2O_5-SiO_2$	Humidity sensors	–	–	51
$NiCo_2O_4$	Anode for water electrolysis	–	200 h	52
$Sr_{1-x}Ba_xMeO_y$	Ferroelectric memory devices and batteries	–	–	53
α-Fe_2O_3	NO_2 and CO gas sensors	Det. Limit: 100–600 ppm	–	54
SnO_2	CO gas detectors	–	–	55
Nb_2O_5	Solar cells	Conv. Eff.: 49%	–	56

MnO_2, etc.) has gained additional attention in the field of electrochemistry because of its ability to intercalate solvated lithium and sodium ions, as well as larger molecules. These oxides can intercalate ions and molecules while the mixed-valent transition metal centers allow for electron transfer. These properties make transition metal–oxides ideal electrode materials for applications in electrochromics, secondary batteries, and capacitors. Another important subgroup is the *n*-type semiconductor oxides (ZnO, $BaTiO_3$, TiO_2, etc.) which have found extensive use in photoelectrochemical devices [25].

The electrochemical reactivity of the transition metal oxides contributes to complications during sol–gel synthesis. The higher electronegativity, combined with the transition metal's ability to exhibit several coordination states, results in a much higher reactivity toward nucleophilic reagents such as water [15]. Therefore, unless reaction rates are carefully controlled, precipitates of hydroxides and hydrous oxides will readily occur upon hydrolysis.

Reaction rates can be controlled through several methods. It has been found that the rate of hydrolysis decreases with the increasing size of the alkyl groups [57, 58]. The larger the alkyl group, the less electronegative the metal atom because of steric hindrance (shielding of the metal atom by the alkyl group). Solvate formation (dilution with a chemically inert solvent) is another way of expanding the coordination and slowing down the hydrolysis rate. This approach is used in the synthesis of vanadium pentoxide (V_2O_5) gels. To prevent precipitation (by slowing the hydrolysis and olation rates), a very small amount of water is added, which is diluted in copious amounts of acetone [59]. Another method is to chemically modify the metal alkoxides by using additives. Selected solvents [60], acid and base catalysts [61], and stabilizing agents [62, 63] can react with the alkoxide, giving rise to a less reactive molecular precursor. Since transition metal oxides exhibit several oxidation states, their structure is sensitive to the redox state and the pH [25].

5.2.3.3 Type I Composites

Modification of a one-component system was discussed in the previous two subsections. The following subsections deal with modification of the sol–gel synthesized electrode through the addition of a second component. The simplest way to form a multicomponent system is to introduce a second constituent that does not interact with the hydrolysis or condensation reactions of the sol–gel matrix. In other words, the inorganic oxide functions as a matrix while another inorganic or organic component is somehow incorporated into the structure. This is termed a *Type I composite*, where the two phases are linked together through relatively weak bonds (hydrogen, van der Waals, or ionic bonds) [64]. The second phase can be added either before or after gelation (this process is generally termed *impregnation*). Biomolecules embedded in transition metal–oxide gels, as discussed in more detail in Sect. 5.2.2.3.4, are Type I composites.

Another example of a Type I composite is the carbon–silicate electrode. Carbon–silicate electrodes are porous glass networks containing a homogeneous distribution of carbon powder and have been used in a variety of electrochemical studies [25]. Another popular approach for developing electronic conduction has involved the use of conducting polymers. The lack of crystallinity in the sol–gel prepared oxide films results in a flexible structure that allows for easy intercalation or incorporation of both inorganic and organic

constituents. Oxides with an inherently layered structure (even in the amorphous state) lend themselves particularly well to this type of processing. Aniline, pyrrole, thiophene, and other monomers have been chemically polymerized within vanadium pentoxide and molybdenum trioxide layers [65, 66]. Polypyrrole- and polyaniline-silicate films have also been prepared by electrochemical polymerization [67–69]. Dispersions of nanocrystalline materials in an amorphous gel can also lead to other desirable properties besides electronic conduction. For example, ceria grains in a ceria–titania film are the redox-active centers, while the amorphous titania enhances lithium mobility toward the ceria grains [70].

The synthesis of Type I composites is similar to that of a single-phase sol–gel material. The precursors are the same transition metal alkoxides for both pre- and postgelation doping. For postgelation doping, the synthesis of the oxide is identical to the single-phase material. The second phase is introduced by a liquid or vapor phase impregnation. For pregelation doping, the second phase is usually dispersed as particulates in the alkoxide sol and the gel are formed around the dispersed second phase. However, the second phase can also be introduced in a liquid phase. Transition metal–oxide/polymer hybrids synthesized through copolymerization, resulting in two interpenetrating networks, have been reported [71].

5.2.3.4 Impregnation with Biomolecules

The encapsulation of biological molecules such as enzymes and other proteins into an inorganic network has been a common direction for modified sol–gel electrodes [5, 72, 73]. This area has emerged because of the ability of the biomolecules to retain their chemical and biological function inside the porous matrix. The highly porous inorganic network stabilizes the biomolecule from denaturation pathways and at the same time allows reactant molecules to reach the encapsulated biomolecules. There is evidence suggesting that most of the biomolecules are trapped in isolated ''cages''. This apparently suppresses aggregation and unfolding, and leads to considerable thermal stabilization [74]. In addition, the biomolecule remains active during long-term storage [72]. Table 2 provides a list of biomolecules commonly incorporated in sol–gel electrode films, along with the sol–gel matrix and the application.

The preparation methods used for encapsulating biomolecules are similar to those described in Sect. 5.2.2.2 with the exception of including a buffer solution. This is to ensure that the pH of the sol is suitable for biomolecule survival. The biomolecules are added to the sol, and as the inorganic network forms they become trapped within the pores along with the solvent phase [30]. The presence of alcohol in the solvent can denature proteins by causing chain unfolding, aggregation, and destruction of secondary and tertiary protein structures [89]. This has prompted the development of an alcohol-free sol–gel process [72]. Biomolecules do experience some conformational changes because of interactions with the sol and in the case of heme proteins these changes are shown by changes in the wavelength maximum and intensity of optical absorption [74]. One method of reducing the conformational changes is by decreasing the sol pH [90, 91]. However, once the gel network is formed, further conformational changes are not observed [91]. This suggests that by increasing the gelation rate, conformational changes can be minimized and correspondingly, an inverse relationship

Tab. 2 Sol–gel electrode films modified with biomolecules

Matrix	*Active biomolecule*	*Function*	*References*
SiO_2	Enzyme glucose oxidase	Glucose biosensor	75
SiO_2 (with Ru dopant)	Enzyme glucose oxidase	Glucose and oxygen sensor	75
SiO_2 (modified with aminopropyltriethoxysilane)	Glucose oxidase	Glucose sensor	76
SiO_2	Horseradish peroxidase	Glucose sensor	6
V_2O_5	Glucose oxidase	Glucose sensor	77
V_2O_5	Horseradish peroxidase	Glucose sensor	78
SiO_2–graphite	Xanthine oxidase	Hypoxanthine sensors	79
SiO_2	Oxazine-170	Ammonia and acid vapors	80
SiO_2	Bromophenol blue	pH sensors	81
SiO_2	Fluorescein	pH sensors	82
SiO_2	Ru complex	Oxygen sensor	83
SiO_2	Myoglobin	Oxygen sensor	84
SiO_2	Polyclonal antifluorescein	Fluorescein sensor	85
SiO_2	Pyoverdin	Fe(III) sensor	86
SiO_2	Metalloproteins	Spectroscopy	5
SiO_2	Metalloproteins	NO and Co sensor	87
SiO_2	Cytochrome C	Redox catalyst	72
SiO_2	Myoglobin	O_2 transporter	72
SiO_2	Hemoglobin	O_2 transporter	72
SiO_2	Liver catalase	Enzymatic catalyst	72
SiO_2	Pseudomonas stutzeri (whole cell extract)	Reduction of nitrate to nitrogen	88
SiO_2	Thiobacillus thiooxidans (whole cell extract)	H_2S removal	88

between gelation time and absorbance has been observed [72]. It has also been found that biomolecules tend to prevent pores from collapsing during gel drying [92].

5.2.3.5 Type II Composites

Type II composites contain two or more phases that are linked together through strong chemical bonds (covalent or iono-covalent bonds) [64]. Some very good examples of Type II composites are ORMOCers (organically modified ceramics). By using starting monomers containing organic functional groups directly linked to the transition metal atom of the sol–gel precursor, it is possible to prepare a large variety of organic–inorganic hybrid gels or ORMOCers. The modified precursors contain both the MO−R bonds, which experience hydrolysis/condensation reactions described in Sect. 5.2.2.2.1, and the nonhydrolyzable M−C bonds. In the most common case, the sol–gel precursors contain Si−C bonds that do not participate in the hydrolysis and condensation reactions. Rather, these organofunctional groups remain exposed on the surface of the gel [25]. Typical organo-silicate precursors are 3-aminopropyltriethoxysilane (APTEOS), iso-butyltrimethoxysilane (BTMOS), phenyltrimethoxysilane (PTMOS), methyltrimethoxy-silane (MTMOS), and tetramethoxysilane (TMOS) [93]. With these precursors, formation of the sol and gel is very similar to that of the single-phase material. However, most transition metals

do not form stable bonds with carbon and therefore a complexing ligand is needed in the synthesis to form the necessary links between the organic and inorganic components. A thorough review of the synthesis of Type II hybrids is given by Judeinstein and Sanchez [64].

5.2.4 Summary

The sol–gel method of preparing electrodes is extremely versatile and can be utilized to synthesize a virtually endless list of electrochemically active composites. This section summarized the various methods that can be used to control the electrochemical properties of the sol–gel electrode films. What was not discussed at length is the myriad of ways these electrodes can be manipulated to control such physical properties as surface area, pore size distribution, and density. These features can be controlled through the use of different drying and templating methods. In such high surface area materials, the chemistry of the oxide is mainly governed by the surface properties of these solids and the resulting electrodes may be readily modified. Studies of silica surfaces are an active area of investigation [94].

One final topic that is destined to emerge as a popular means of preparing modified electrodes is the use of templating techniques [95, 96]. By using sol–gel synthesis in combination with various templating media (surfactants, block copolymers, organic and inorganic colloids), it is possible to produce oxide phases with highly ordered pore networks and very narrow and controllable pore diameter distributions, ranging from 2 nm to the micrometer range. Thin film approaches for these materials are just developing [97, 98]. The ability to design three-dimensional electrodes with highly controlled morphology represents a novel opportunity, which is certain to be of interest to the community.

References

1. G. Brusatin, M. Guglielmi, P. Innocenzi et al., *J. Electroceram.* **2000**, *4*, 151.
2. B. B. Owens, H. S. Smyrl, J. J. Xu, *J. Power Sources* **1999**, *81–82*, 150.
3. D. R. Uhlmann, G. Teowee, *J. Sol.-Gel Sci. Technol.* **1998**, *13*, 813.
4. S. Braun, S. Rappoport, R. Zusman et al., *Mater. Lett.* **1990**, *10*, 1.
5. L. M. Ellerby, C. R. Nishida, F. Nishida et al., *Science* **1992**, *255*, 1113.
6. K. S. Alber, J. A. Cox, *Mikrochim. Acta* **1997**, *127*, 131.
7. B. Dunn, G. C. Farrington, B. Katz, *Solid State Ionics* **1994**, *70–71*, 3.
8. J. Wang, P. V. A. Pamidi, D. S. Park, *Anal. Chem.* **1996**, *68*, 2705.
9. C. J. Brinker, G. W. Scherer, *Sol Gel Science, The Physics and Chemistry of Sol Gel Processing*, Academic Press, New York, 1990.
10. J. D. Mackenzie, *J. Non-Cryst. Solids* **1985**, *73*, 631.
11. D. Ganguli, *Bull. Mater. Sci.* **1995**, *18*, 47.
12. S. Y. Chia, J. Urano, F. Tamanoi et al., *J. Am. Chem. Soc.* **2000**, *122*, 6488.
13. N. Ozer, *Thin Solid Films* **1997**, *304*, 310.
14. J. Livage, M. Henry, C. Sanchez, *Prog. Solid State Chem.* **1988**, *18*, 259.
15. D. C. Bradley, R. C. Mehrotra, D. P. Gaur, *Metal Alkoxides*, Academic Press, London, 1978.
16. C. Sanchez, J. Livage, M. Henry et al., *J. Non-Cryst. Solids* **1988**, *100*, 65.
17. R. A. Lipeles, D. J. Coleman, M. S. Leung, in *Better Ceramics Through Chemistry II* (Eds.: C. J. Brinker, D. E. Clark, D. R. Ulrich), Materials Research Society, Pittsburgh, 1986, p. 665.
18. M. S. Hu, A. G. Evans, *Acta Metall. Mater.* **1989**, *37*, 917.
19. P. Innocenzi, M. O. Abdirashid, M. Guglielmi, *J. Sol.-Gel Sci. Technol.* **1994**, *3*, 47.
20. G. W. Scherer, *J. Sol.-Gel Sci. Technol.* **1997**, *8*, 353.
21. R. W. Schwartz, J. A. Voigt, C. D. Buchheit et al., *Ceram. Trans.* **1994**, *43*, 145.

22. D. R. Uhlmann, B. J. Zelinski, L. Silverman, in *Science of Ceramic Chemical Processing* (Eds.: L. L. Hench, D. R. Ulrich), Wiley, New York, 1986, p. 173.
23. Ph. Colomban, V. Vendange, *J. Non-Cryst. Solids* **1992**, *147–148*, 245.
24. C. G. Granqvist, *Sol. Energy Mater. Sol. Cells* **2000**, *60*, 201.
25. O. Lev, Z. Wu, S. Bharathi et al., *Chem. Mater.* **1997**, *9*, 2354.
26. R. K. Iler, *The Chemistry of Silica*, Wiley, New York, 1979.
27. L. L. Hench, J. K. West, *Chem. Rev.* **1990**, *90*, 33.
28. A. Walcarius, *Electroanalysis* **1998**, *10*, 1217.
29. A. L. Crumbliss, J. Stonehuerner, R. W. Henkens et al., *New J. Chem.* **1994**, *18*, 327.
30. B. C. Dave, B. Dunn, J. S. Valentine et al., *Anal. Chem.* **1994**, *66*, 1120A.
31. O. Lev, M. Tionsky, L. Rabinovich et al., *Anal. Chem.* **1995**, *67*, 22A.
32. K. K. Unger, *Porous Silica*, Elsevier, Amsterdam, 1979.
33. M. L. Hair, W. Hertl, *J. Phys. Chem.* **1969**, *73*, 4269.
34. A. P. Robertson, J. O. Leckie, *J. Colloid Interface Sci.* **1997**, *188*, 444.
35. A. Walcarius, J. Bessiere, *Anal. Chim. Acta* **1998**, *361*, 273.
36. C.-C. Chang, P. N. Kumta, *J. Power Sources* **1998**, *75*, 44.
37. Y. J. Park, J. G. Kim, M. K. Kim et al., *J. Power Sources* **2000**, *87*, 69.
38. K. Amine, H. Tukamoto, H. Yasuda et al., *J. Power Sources* **1997**, *68*, 604.
39. Y.-K. Sun, D.-W. Kim, Y.-M. Choi, *J. Power Sources* **1999**, *79*, 231.
40. L. Hernan, J. Morales, L. Sanchez et al., *J. Electrochem. Soc.* **1997**, *144*, 1704.
41. I.-H. Oh, S.-A. Hong, Y.-K. Sun, *J. Mater. Sci.* **1997**, *32*, 3177.
42. M. J. Parent, S. Passerini, B. B. Owens, in *Proceedings of the Symposium on Electrode Materials and Processes for Energy Conversion and Storage IV* (Ed.: J. McBreen, S. Mukerjee, S. Srinivasan), Electrochemical Society Inc., Montreal, 1997, p. 195.
43. J. Livage, G. Guzman, F. Beteilie, *J. Sol.-Gel Sci. Technol.* **1997**, *8*, 857.
44. Z. Bin, *Solid State Ionics* **1999**, *119*, 305.
45. S. C. Pang, M. A. Anderson, T. W. Chapman, *J. Electrochem. Soc.* **2000**, *147*, 444.
46. J. P. Zheng, P. J. Cygan, T. R. Jow, *J. Electrochem. Soc.* **1995**, *142*, 2699.
47. N. Ozer, *Thin Solid Films* **1992**, *214*, 17.
48. N. Ozer, M. D. Rubin, C. M. Lampert, *Sol. Energy Mater. Sol. Cells* **1996**, *40*, 285.
49. F. Svegl, B. Orel, M. G. Hutchins et al., *J. Electrochem. Soc.* **1996**, *143*, 1532.
50. A. Surca, B. Orel, U. O. Krasovec et al., *J. Electrochem. Soc.* **2000**, *147*, 2358.
51. M. D'Apuzzo, A. Aronne, S. Esposito et al., *J. Sol.-Gel Sci. Technol.* **2000**, *17*, 247.
52. H. B. Suffredini, J. L. Cerne, F. C. Crnkovic et al., *Int. J. Hydrogen Energy* **2000**, *25*, 425.
53. M. S. Tomar, K. A. Kuenhold, *Mater. Sci. Forum* **1996**, *223–224*, 229.
54. H. Sun, C. Cantalini, M. Faccio et al., *Thin Solid Films* **1995**, *269*, 97.
55. R. Rella, A. Serra, P. Siciliano et al., *Thin Solid Films* **1997**, *304*, 339.
56. P. Guo, M. A. Aegerter, *Thin Solid Films* **1999**, *351*, 290.
57. G. Winter, *J. Oil Colour Chem. Assoc.* **1953**, *34*, 30.
58. E. Bistan, I. Gomory, *Chem. Zvesti* **1956**, *10*, 91.
59. H. P. Wong, B. dunn, K. Salloux et al., *Electrochem. Soc. Proc.* **1995**, *95–22*, 46.
60. K. C. Chen, T. Tsuchiya, J. D. Mackenzie, *J. Non-Cryst. Solids* **1986**, *81*, 227.
61. E. J. A. Pope, J. D. Mackenzie, *J. Non-Cryst. Solids* **1986**, *87*, 185.
62. J. C. Debsikdar, *J. Mater. Sci.* **1985**, *20*, 44.
63. J. C. Debsikdar, *J. Non-Cryst. Solids* **1986**, *86*, 231.
64. P. Judeinstein, C. Sanchez, *J. Mater. Chem.* **1996**, *6*, 511.
65. M. Lira-Cantu, P. Gomez-Romero, *J. Electrochem. Soc.* **1999**, *146*, 2029.
66. W. Dong, B. Dunn, in *Organic/Inorganic Hybrid Materials II*, MRS Symposium Proceedings (Ed.: L. C. Klein, L. F. Francis, M. R. De Guire, J. E. Mark), Materials Research Society, Warrendale, PA, 1999, p. 269, Vol. 576.
67. M. Onoda, T. Moritake, T. Matsuda et al., *Synth. Met.* **1995**, *71*, 2255.
68. M. Onoda, T. Matsuda, H. Nakayama, *Jpn. J. Appl. Phys.* **1996**, *35*, 294.
69. M. M. Verghese, K. Ramanathan, S. M. Ashraf et al., *Chem. Mater.* **1996**, *8*, 822.
70. D. Keomany, J. P. Petit, D. Deroo, *Sol. Energy Mater. Sol. Cells* **1995**, *36*, 397.
71. J. H. Harreld, B. Dunn, L. F. Nazar, *Int. J. Org. Mater.* **1999**, *1*, 135.
72. D.-M. Liu, I.-W. Chen, *Acta Mater.* **1999**, *47*, 4535.

73. J. Livage, C. Roux, J. M. Costa et al., *J. Sol.-Gel Sci. Technol.* **1996**, *7*, 109.
74. E. H. Lan, B. C. Dave, J. M. Fukuto et al., *J. Mater. Chem.* **1999**, *9*, 45.
75. O. S. Wolfbeis, I. Oehme, N. Papkovskaya et al., *Biosens. Bioelectron.* **2000**, *15*, 69.
76. P. C. Pandey, S. Upadhyay, H. C. Pathak, *Sens. Actuators, B* **1999**, *B60*, 83.
77. V. Glezer, O. Lev, *J. Am. Chem. Soc.* **1993**, *115*, 2533.
78. V. Glezer, M. Tsionsky, J. Gun et al., *Abstracts of 44th Meeting of the International Society of Electrochemistry, Berlin, Germany, September* 1993, p. 580.
79. J. Niu, J. Y. Lee, *Sens. Actuators, B* **2000**, *62*, 190.
80. V. Chernyak, R. Reisfield, R. Gvishi et al., *Sens. Mater. (Japan)* **1990**, *2*, 117.
81. D.-D. Lee, S.-D. Choi, K.-W. Lee, *Sens. Actuators, B* **1995**, *24–25*, 607.
82. C. A. Browne, D. H. Tarrant, M. S. Olteanu et al., *Anal. Chem.* **1996**, *68*, 2289.
83. B. D. MacCraith, C. M. McDonagh, G. O'Keeffe et al., *Sens. Actuators, B* **1995**, *29*, 51.
84. K. E. Chung, E. H. Lan, M. S. Davidson et al., *Anal. Chem.* **1995**, *67*, 1505.
85. R. Wang, U. Narang, P. N. Prasad et al., *Anal. Chem.* **1993**, *65*, 2671.
86. J. M. Barrero, C. Camara, M. C. Perez-Conde et al., *Analyst* **1995**, *120*, 431.
87. D. J. Blyth, J. W. Aylott, D. J. Richardson et al., *Analyst* **1995**, *120*, 2725.
88. G. Carturan, R. Campostrini, S. Dire et al., *J. Mol. Catal.* **1989**, *57*, L13.
89. J. M. Miller, B. Dunn, J. S. Valentine et al., *J. Non-Cryst. Solids* **1996**, *202*, 279.
90. A. Kondo, J. Mihara, *J. Colloid Interface Sci.* **1996**, *177*, 214.
91. A. Kondo, H. Fukuda, *J. Colloid Interface Sci.* **1998**, *198*, 34.
92. B. Dunn, J. M. Miller, B. C. Dave et al., *Acta Mater.* **1998**, *46*, 737.
93. H. Wei, M. M. Collinson, *Anal. Chim. Acta* **1999**, *397*, 113.
94. E. F. Vansnat, P. Van der Voort, K. C. Vrancken, *Characterisation and Chemical Modification of the Silica Surface*, Elsevier, Amsterdam, 1995.
95. J. N. Cha, G. D. Stucky, D. E. Morse et al., *Nature* **2000**, *403*, 289.
96. Y. Xia, B. Gates, Y. Yin et al., *Adv. Mater.* **2000**, *12*, 693.
97. D. Zhao, P. Yang, N. Melosh et al., *Adv. Mater.* **1998**, *10*, 1380.
98. J. L. Hedrick, R. D. Miller, C. J. Hawker et al., *Adv. Mater.* **1998**, *10*, 1049.

5.3 Metal-ion Binding to Self-assembled Monolayers on Surfaces

Alexander Vaskevich, Israel Rubinstein
Weizmann Institute of Science, Rehorot, Israel

5.3.1 Introduction

Interaction of molecules with a solid surface is an essential factor determining the 2D organization of a molecular assembly on the surface. Self-assembled monolayers (SAMs) on solid substrates can be classified by the energy of interaction between the adsorbate and the support. In case of a weak interaction with the surface (usually termed *physisorption*), the dominant factor in the supramolecular structure is the interactions between the molecules themselves. This type of SAMs is exemplified by the organization of certain organic adsorbates on highly-oriented pyrolytic graphite (HOPG) and metal surfaces [1–3]. A different behavior is observed when the adsorbate–substrate binding is sufficiently strong (usually termed *chemisorption*), such that both the substrate–adsorbate and adsorbate–adsorbate interactions affect the resulting SAM structure.

SAMs on solid substrates discussed in this chapter fall into the latter category: most of the SAM-modified substrates are prepared by exploiting either the strong interaction between sulfur-bearing organic molecules and metal surfaces [4] or the covalent siloxane bonds [5]. The effect of metal-ion coordination in such chemisorbed layers, unlike that in the case of solution chemistry or physisorbed systems, is in influencing the local order in the SAM, while in most cases a new superstructure with an in-plane long-range order is not created. Metal-organic coordination has been extensively applied to directional organization of *multilayer* structures normal to the substrate surface [6–8], where the role of the metal ion is quite similar to that in traditional solution-based chemistry, that is, directional binding of organic ligands defined by the specific stereochemistry of the central metal ion [9].

Application of metal-organic coordination to supramolecular chemistry on solid substrates can be generally divided into two broad groups: (1) Complexation of metal ions in SAMs containing ligand-bearing functional groups. This class includes numerous analytical and sensing applications as well as various attempts to introduce or alter functional properties of SAMs upon complexation of metal ions. (2) Use of metal-organic coordination as a tool for connecting molecular layers in multilayer structures, as described earlier. Both approaches were introduced nearly simultaneously. Rubinstein, Sagiv, Shanzer, and coworkers [10, 11] prepared SAMs containing bisacetoacetate groups that selectively bind tetracoordinated divalent cations (Cu^{2+}, Pb^{2+}, Zn^{2+}) and reject Fe^{3+} and Fe^{2+} ions, while Mallouk and coworkers [6, 12] introduced the layer-by-layer (LbL) construction of multilayer films of alkanebisphosphonates bound by Zr^{4+} ions.

In this chapter, we limit the discussion to systems where metal ions interact with organic, ligand-bearing SAMs; the case of coordination-based multilayers is outside the scope of this text. Other topics related to the reviewed area, that is, electrochemistry of SAMs and the role of metal ions in biomimetic systems, are covered in other chapters of the Encyclopedia (see Volume 9) and in reviews [13–15].

Encyclopedia of Electrochemistry. Edited by A.J. Bard and M. Stratmann
Vol. 10 *Modified Electrodes*. Edited by M.Fujihira, I.Rubinstein, and J.F.Rusling
Copyright © 2007 Wiley-VCH Verlag GmbH & Co. KGaA, Weinheim. ISBN: 978-3-527-30402-8

5.3.2 Binding of Metal Ions to Functionalized SAMs: General Phenomena and Case Studies

Functionalized SAMs are formed by molecules bearing a chemically active group in addition to the anchoring group, the latter responsible for surface immobilization. In most cases, the functional and anchoring groups are spatially separated to ensure maximal exposure of the functional group to the environment, thus enabling its interaction with chemical species.

Several examples of functional molecules forming ion-binding SAMs are presented in Fig. 1. Examination of the structure of these molecules indicates that the properties of ion-binding SAMs may vary significantly. Formation of a well-ordered, compact structure is expected for the carboxyl-terminated terphenylthiolate SAM (Fig. 1a), while dithizone- and bishydroxamate-bearing layers (Fig. 1b,e) would be less compact. The fluoroionophore SAM in Fig. 1(d), tethered to oxide surfaces, is most likely disordered, but the calixarene cavity is readily accessible to cations in solution. While the carboxyl (Fig. 1a), dithizone (Fig. 1b), and nitrilotriacetic acid (NTA) (Fig. 1c) ligands provide a saturated coordination sphere to the bound ions, the bishydroxamate-Zr^{4+} complex (Fig. 1e) does not, thus requiring charge compensation by counterions or additional ligands. The latter, exemplified by the binding of additional ligand molecules to a bishydroxamate-Zr^{4+} monolayer to form a bilayer [16] (Fig. 1e), is a widely used scheme in supramolecular chemistry on surfaces and will be discussed in Sect. 5.3.4. The receptor groups in the SAM may be either densely packed on the surface (as in Fig. 1a) or diluted with inert molecules (as in Fig. 1c); the density of ion-binding sites on the surface has to be tailored to the specific application. For example, in the case of the Ni^{2+}–NTA monolayer (Fig. 1c), dilution of the binding groups provides freedom of conformational changes and biological activity of bound proteins [17].

An abundant scheme for the preparation of surface metal-organic complexes is ligand exchange, where one of the ligands of a metal complex in solution is substituted with a surface-confined ligand, leading to immobilization of the metal ion in the functional SAM. Examples of this process include Co and Os terpyridine complexes [22]; Ru tetraamine [23] and dinuclear Ru [24] complexes; salen complexes with Fe, Co, and Mn [25]; and Zr acetylacetonate [26].

Ion binding to functionalized SAMs is commonly achieved by dipping the substrate in a metal-ion-containing solution. Recently, microcontact printing (μCP) was applied to the exchange of metal ions between a salt inked on a polydimethylsiloxane (PDMS) stamp and a ligand-terminated monolayer [27]. Ni^{2+} ions were exchanged into a sodium carboxylate–terminated monolayer using a $Ni(ClO_4)_2$ inked PDMS stamp. The combination of metal-ion exchange and surface patterning makes μCP a potentially useful approach to ion binding in ligand SAMs.

5.3.2.1 Stoichiometry of Surface Metal-organic Complexes

As a complexation process, metal-ion binding to a SAM presents a ligand-exchange equilibrium for the metal ions between the solution and the surface. In contrast with solution-based systems, direct in situ quantitative measurement of the composition of a SAM is experimentally challenging. Therefore, a variety of in situ

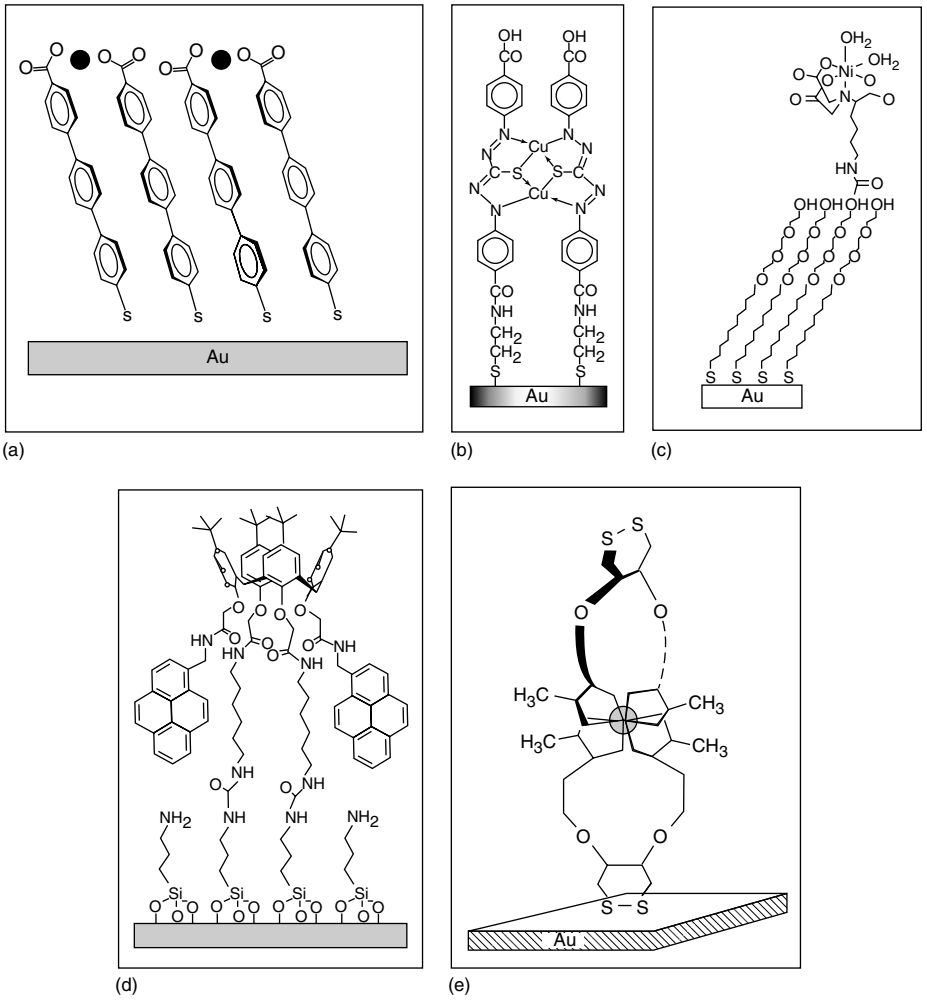
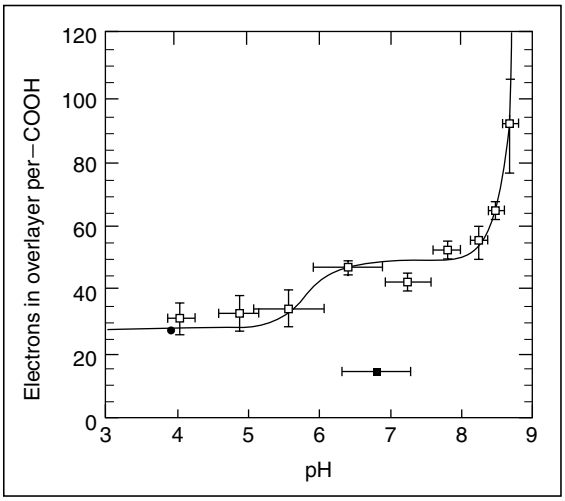
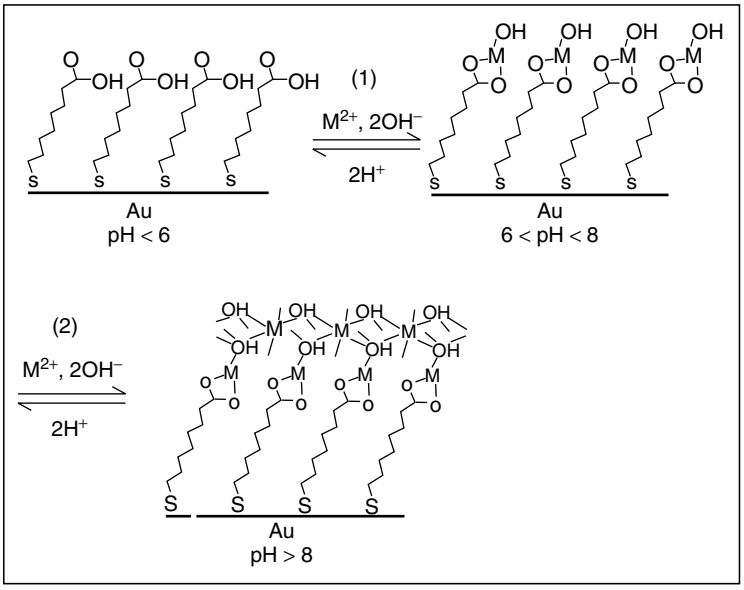


Fig. 1 Examples of ion-binding SAMs. (a) Terphenylthiolate SAM with bound Cu^{2+} ions [18]. (b) Secondary complex of Cu^{+} with dithizone-functionalized SAM [19]. (c) Ni^{2+}–nitrilotrioacetic acid complex immobilized in a mixed SAM [20]. (d) Na^{+}-sensitive fluoroionophore SAM on glass [21]. (e) A disulfide-bishydroxamic acid bilayer based on Zr^{4+}, Ce^{4+}, or Ti^{4+} binding [16].

and ex situ methods have been applied to quantify the surface composition. In the case of the widely used high-vacuum techniques (e.g. X-ray photoelectron spectroscopy (XPS)), sample preparation for analysis includes emersion from solution, rinsing with solvents and drying, and transfer to the high-vacuum chamber for analysis. It is assumed that the SAM composition remains unchanged during the operation. Support for this approach was obtained by comparing X-ray reflectivity data of in situ and ex situ measured Cd^{2+}-carboxylate SAMs [28]. The metal-ion layer was shown to withstand rinsing and drying without change of the reflectivity.



(a)



(b)

Fig. 2 Coordination binding of Cd^{2+} to carboxylate-terminated SAMs. (a) The number of electrons in the counterion overlayers per carboxylic acid group at the SAM surface held in 1 mM Cd^{2+} solutions at different pH values, obtained by fitting X-ray reflectivity curves. The filled circles represent measurements using synchrotron radiation; the open circles were obtained using a rotating anode X-ray source. The line is a fit calculated using a modified BET multilayer adsorption model. (b) Schematic presentation of the pH-dependent equilibrium for binding of Cd^{2+} ions to a MHA SAM (adapted from Ref. 28).

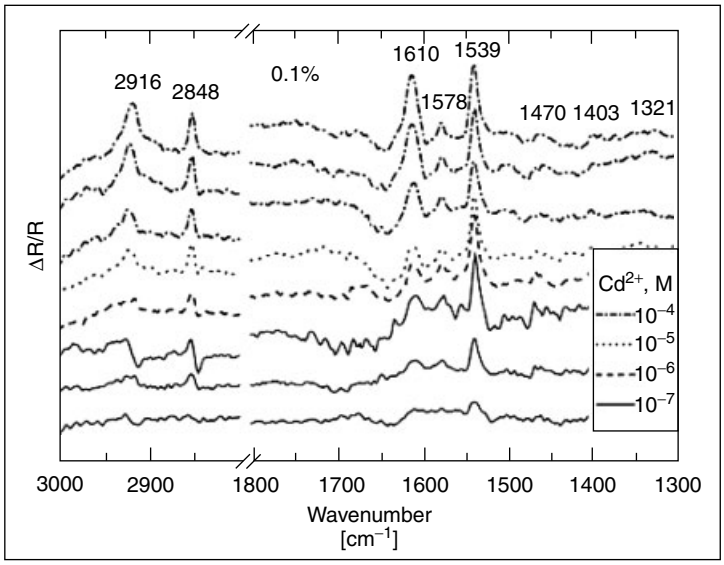
Owing to the experimental difficulties, in situ determination of SAM composition is nearly absent. The only data of this kind were obtained by in situ X-ray reflectivity measurements of the binding of Cd^{2+} to a SAM of mercaptohexadecanoic acid (MHA), $HOOC(CH_2)_{15}SH$, as a function of the solution pH [28]. Complexation of the metal ion by the carboxylate-terminated SAM depends on the protonation equilibrium of $-COOH$ groups in the SAM and hydration of ion in solution. A series of X-ray reflectivity measurements were performed with SAMs prepared on single-crystal Au(111) substrates in 1 mM $CdCl_2$ solutions of variable pH from 3.9 to 8.5.

The results in Fig. 2(a) show the electron density in the overlayer bound to the SAM versus the number of $-COOH$ groups. The electron density is constant and independent of the potential in the pH range below ~6, where the carboxylic acid groups are protonated and there is no Cd^{2+} binding. Cd^{2+} ions begin to bind to the SAM around pH ~ 6.4 and reach saturation at pH ~ 8. The sharp increase of the electron density at pH > 8 corresponds to the formation of hydroxide on the SAM. The maximum binding capacity of the SAM gives a 1 : 1 ratio of Cd^{2+} to $-COO^-$ groups in the monolayer, indicating that about half the charge is compensated by counterions or another negatively charged ligand. The suggested equilibrium scheme is shown in Fig. 2(b), where the metal ion binds as $Cd(OH)^+$ (at $6 < pH < 8$) and as a $Cd(OH)_2$-like layer (at pH > 8).

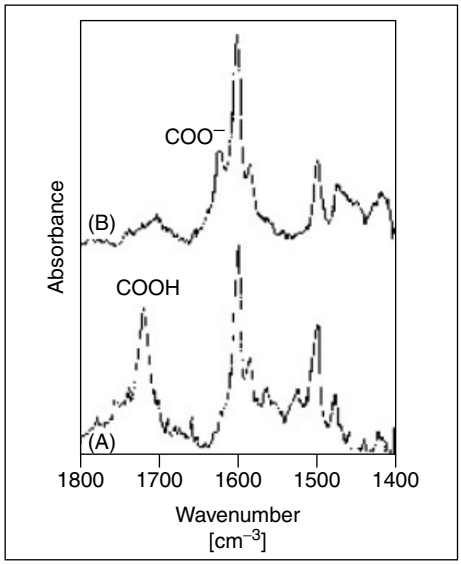
The effect of metal-ion concentration on the stoichiometry of surface complexes was studied by in situ attenuated total reflection Fourier-transform infrared spectroscopy (ATR-FTIR) spectroscopy, monitoring the binding of Cd^{2+} to a carboxylate-terminated SAM [29]. Specific interactions of Cd^{2+} with the terminal $COOH/COO^-$ groups at pH 6 were viewed by the increase of the $\nu_a(COO^-)$ and $\nu_s(COO^-)$ at ca. 1539 and 1411 cm^{-1}, respectively (see Fig. 3a). Increase of the Cd^{2+}–carboxylate interaction with time yields, after 1 hour, well-defined peaks at 1577 and 1610 cm^{-1}. A qualitative estimate of the surface concentration of bound Cd^{2+} showed that in equilibrium with μM solutions the surface complex corresponds to a 2 : 1 carboxylate-metal stoichiometry, while an increase of the concentration causes transition to a 1 : 1 binding. The latter agrees well with X-ray reflectivity [28] and quartz-crystal microbalance [30] data.

Binding of Cu^{2+} ions to carboxyl-terminated SAMs was extensively studied by FTIR [31, 32], XPS [18, 31–33], and electrochemistry [33]. Formation of the surface complex was observed in ethanolic [7, 18, 31, 32, 34–36] and aqueous [33, 37] solutions containing Cu^{2+} ions. In some cases the acid-terminated SAM was deprotonated by immersion in a basic solution prior to Cu^{2+} binding [35]. Deprotonation and salt formation was verified by FTIR spectroscopy [7, 32, 34], that is, the COOH peak at 1715 cm^{-1} was replaced by the COO^- peak at 1621 cm^{-1}, similarly to binding of Cd^{2+} ions (Fig. 3b).

This indicates that a surface Cu-carboxylate salt was formed, where each Cu^{2+} ion is bound to two COO^- groups. This scheme is consistent with XPS data on the stoichiometry of Cu^{2+} ion binding to various monocarboxylate-terminated SAMs [7, 18, 32, 37]. Although reduction of Cu^{2+} by photoelectrons during the XPS measurement affects the accuracy of the analysis, the measured Cu/COO^- ratio varied between 0.40 and 0.46, in good agreement with the expected 0.5 theoretical value. Note



(a)



(b)

Fig. 3 FTIR spectra for metal-ion binding in carboxylate-terminated SAMs. (a) Spectra of the octadecylsilane/palmitic acid bilayers on Ge, exposed to Cd^{2+} solutions of different concentrations at pH 6. The lower, center, and upper curves for $[Cd^{2+}] = 10^{-7}$ and 10^{-4} M were obtained at 20-min intervals, in that order. The spectrum recorded in a Cd^{2+}-free solution at pH 6 was used as a reference (adapted from Ref. 29). (b) Spectra of a carboxylate-terminated SAM on Au for (A) initial, metal-ion free SAM; (B) after binding of Cu^{2+} ions (adapted from Ref. 32).

that in some cases the Cu^{2+} binding scheme was extended to the formation of coordination-based multilayers [7, 33, 38, 39].

Carboxyl-terminated terphenylthiolate molecules form a bilayer on Au surface owing to hydrogen bonding between the protonated carboxylates [18]. Exposure of the bilayer to a K^+ solution resulted in the intercalation of K^+ ions between the layers without removal of the second layer. A stoichiometric ratio of $K/O = 0.53$ determined by XPS is consistent with hexacoordinated K^+ ions in the bilayer. On the other hand, dipping in a Cu^{2+} solution led to binding of the metal ions and removal of the second organic layer (Fig. 1a). The measured ratio of $Cu/O = 0.21$ is close to the expected value of 0.25 for Cu^{2+} ions coordinated with two $-COO^-$ groups. It should be noted that intercalation in self-assembled multilayers was first demonstrated with amphiphilic silane bilayers [40].

5.3.2.2 Solution-surface Equilibrium

Solution-surface equilibrium of metal ions is a central issue in ion-binding SAMs. The fraction of the SAM ligand groups occupied by metal ions may vary with solution pH [30], concentration of the metal ions in solution [41], and electrode potential, when applied [42].

Binding of Cu^{2+} ions by catechol-terminated SAMs was studied by thin-layer UV–vis spectrophotometry combined with a long-optical-pass cell [43]. Since the pK values are 9.23 and 13.0 for the first and second catechol deprotonation, respectively, experiments were carried out at pH = 7.3 to ensure that the ligand is in its neutral form. Under these conditions, assuming formation of a 1:1 ligand–metal ion complex both in solution and on the surface, formation constants for the equilibrium reactions (1) and (2) were determined from direct mass-balance calculations.

$$H_2L_{soln} + Cu^{2+} \Longleftrightarrow CuL_{soln} + 2H^+ \quad (1)$$

$$H_2L_{surface} + Cu^{2+} \Longleftrightarrow L{-}Cu_{surface} + 2H^+ \quad (2)$$

The log(K) values obtained for reactions (1) and (2) are −8.42 for solution-based species and −7.56 for surface-bound Cu^{2+}. Hence, the equilibrium constants are of the same order of magnitude, with a small increase in the stability of the surface complex compared to the one in solution.

A similar behavior was observed with NTA-terminated SAMs [41]. The proposed ion-binding scheme at pH 7.4 is presented in Fig. 4.

Indirect determination of the binding equilibrium of Cu^{2+} and Ni^{2+} to the NTA-thioalkane SAM was carried out by impedance spectroscopy in chloride-containing solutions. For comparison, the complexation equilibrium of Cu^{2+} and Ni^{2+} to a dissolved fluorescine-bearing NTA derivative was studied by fluorescence quenching upon metal binding and by isothermal calorimetry. Quantitative fitting of the data gives very similar apparent dissociation constants for metal-ion binding to NTA on the surface and in solution: 4.8 ± 2.1 nM versus 2.2 ± 0.5 nM, respectively, for Cu^{2+}; and 0.28 ± 0.04 μM versus 0.47 ± 0.1 μM, respectively, for Ni^{2+}.

Binding constants of metal ions to ligand SAMs are largely unknown, while in many cases the values in solution are available. Therefore the similarity of the surface and solution values shown in the works described earlier is important for predicting ion affinity to various ligand SAMs.

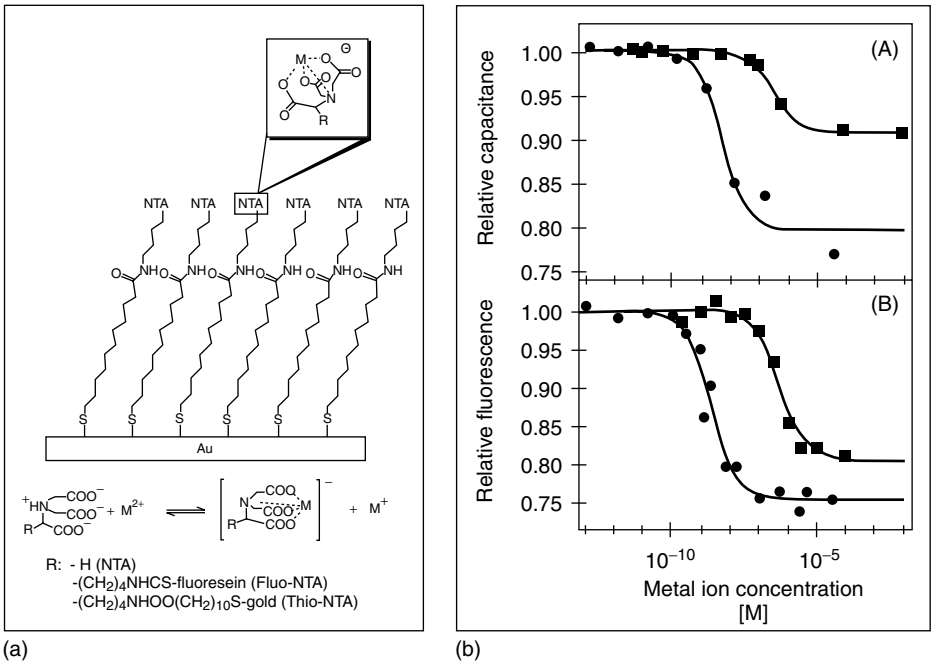


Fig. 4 Equilibrium between metal ions in solution and coordinated to an NTA-functionalized SAM. (a) Scheme of a thiol-NTA monolayer on an Au electrode, and metal-ion binding equilibrium to the NTA group. (b) Binding of Cu^{2+} (●) and Ni^{2+} (■) to a thiol-NTA layer on Au surface (A) and to fluo-NTA in bulk solution (B). The results were fitted to Langmuir isotherms (———). For comparison, the measured signals were normalized to the value of the respective fits at 10^{-13} M (adapted from Ref. 41).

5.3.3 SAMs as Metal-ion Receptors

The original work of Nuzzo and Allara [4] on the use of the strong interaction between gold surfaces and organosulfur compounds for monolayer construction opened the field of SAMs prepared by molecular self-assembly on metal substrates via formation of metal-thiolate (or disulfide or dialkyl sulfide) bonds [15]. The introduction of functional SAMs on metal substrates was a natural development that followed [10, 11]. Owing to the similarity with highly specialized biological membranes, functional SAMs are sometimes called *artificial membranes*.

Much effort has been devoted to the development of systems showing selective ion binding to SAMs. In most cases the general methodology is quite simple, namely, an organosulfur molecule bearing a metal-ion binding group forms a SAM on an Au electrode. The response (electrochemical, optical, etc.) of the monolayer-modified electrode to the presence of certain metal ions in solution, that is, ion binding to the SAM, is measured.

Detection of metal-ion binding to a ligand SAM may be achieved by electrochemical means, either direct (measurement of the electrochemical response of the complexed ion) or indirect (change of the

electrochemical response of a redox probe in solution; change in the impedance of the electrode–electrolyte interface). A variety of optical techniques (ellipsometry, surface plasmon resonance (SPR), fluorescence), as well as atomic force microscopy (AFM) and other surface analytical methods, have also been applied in the detection of metal-ion binding to ligand SAMs.

5.3.3.1 Ion Binding to SAMs: Direct Electrochemical Reporting

Selective complexation of Cu^{2+} ions by a bisacetoacetate-terminated SAM while rejecting Fe^{3+} or Fe^{2+} ions was demonstrated using cyclic voltammetry (CV), as shown in Fig. 5 [10, 11, 42, 44].

Since the detection of selective ion binding to the SAM is done by direct observation of the electrochemical reactivity of bound ions, nonspecific ion penetration must be avoided. Therefore, the quality of the ligand SAM and elimination of defects and pinholes, usually present in SAM-modified electrodes [15], is a requirement in this case [15]. The latter was achieved by adopting a two-step procedure, that is, deposition of the receptor SAM followed by pinhole blocking by an inert component. Two approaches to pinhole blocking were employed: (1) electropolymerization [10], using 1-naphthol as the monomer; (2) self-assembly of inert molecules, either *n*-octadecylmercaptan (OM) [10] or *n*-octadecyltrichlorosilane (OTS) [42, 44] (Fig. 5a). Figure 5(b) shows a typical CV of a bare Au electrode in a solution containing millimolar concentrations of Cu^{2+} and Fe^{2+}. The Fe^{2+}/Fe^{3+} redox peaks appear around 0.45 V; reduction of Cu^{2+} occurs in two steps: Cu underpotential deposition (upd) around 0.25 V and diffusion-limited bulk deposition around −0.25 V, followed by Cu dissolution (around 0.05 V) on the reverse scan. The voltammetric response of the SAM-modified electrode differs substantially from that of the bare Au (Fig. 5b,c). Access of Fe^{2+} ions to the electrode surface is effectively blocked by the monolayer, seen as complete disappearance of the Fe^{2+}/Fe^{3+} redox peaks (Fig. 5c) on a current scale 10^3 times more sensitive than the one used for the bare electrode (Fig. 5b). On the other hand, Cu^{2+} ions bind to the SAM and undergo electrochemical reduction/reoxidation (Fig. 5c). The amount of Cu dissolved from the SAM varies linearly with Cu^{2+} solution concentration, pointing to possible analytical applications [44]. The system enables detection of trace amounts of Cu^{2+} ions in the presence of $>10^3$ excess of (otherwise interfering) Fe^{2+} ions.

Another example of selective rejection of an interfering substance is determination of Fe^{3+} at an Au electrode modified with a mercaptodecanesulfonic acid SAM in the presence of catechol [45]. In acid solution where formation of a catechol–Fe^{3+} complex is suppressed, both species are reduced in the same potential range. However, at the SAM-modified Au electrode, the reduction current of 20 μM Fe^{3+} remains nearly unchanged in the presence of 2 mM catechol in solution.

Binding of metal ions to ligand SAMs followed by direct electrochemical determination of the charge consumed by their surface reaction was exploited for the determination of Cd^{2+} [46], $Cr_2O_7^{-}$ [47], Hg^{2+} [48], and Cu^{2+} [49–53], in dilute solutions of the ions. The experimental scheme follows stripping voltammetry protocols, with complexation of a metal ion by the ligand SAM at open circuit serving as the preconcentration step. It is usually assumed that metal ions reaching the electrode during preconcentration are irreversibly bound to the SAM owing to the high equilibrium constant.

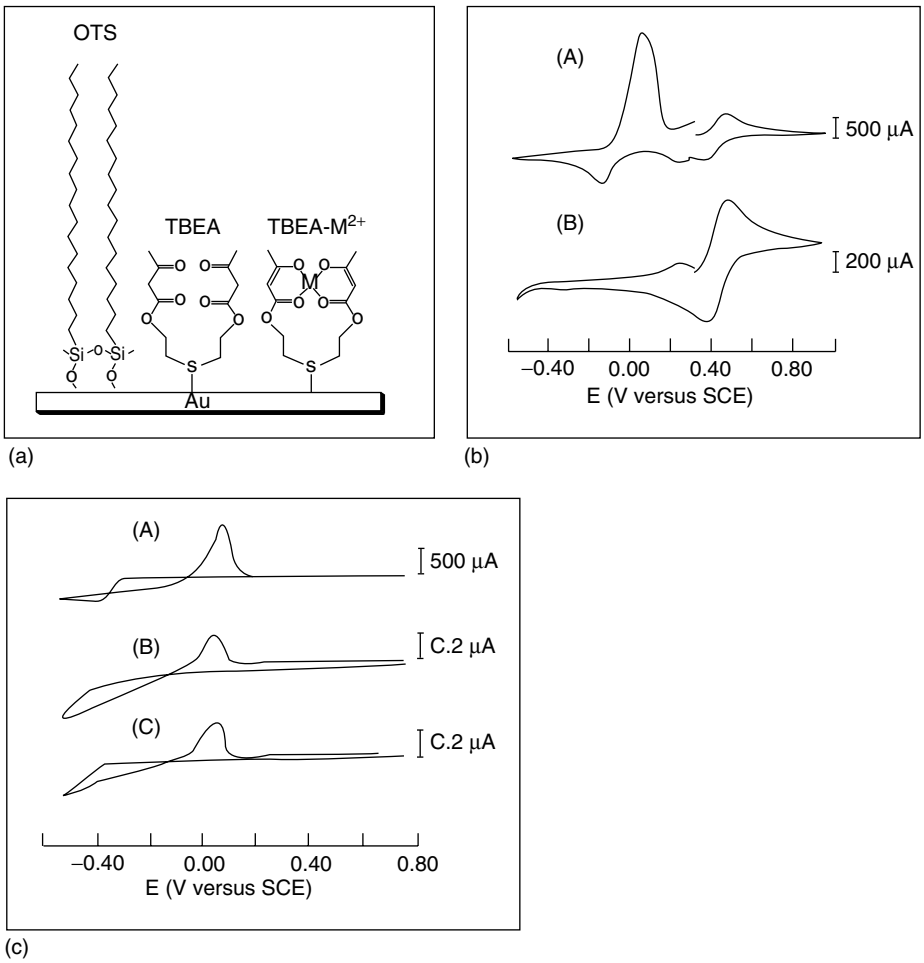


Fig. 5 Electrochemical response of a SAM-modified Au electrode in solutions containing Cu^{2+} and Fe^{2+} ions (electrode area: 0.65 cm^2; electrolyte: 0.10 M H_2S0_4; scan rate: 0.1 V/s, first scan always shown). (a) Schematic representation of a TBEA + OTS monolayer membrane on an Au electrode. M^{2+} is a bound ion (Cu^{2+}, Pb^{2+}, Zn^{2+}). The mode of attachment of OTS to the gold is not entirely clear; it is assumed that the major stabilizing factor is the lateral polymerization of the siloxane groups. (b) CV for a bare Au electrode in a solution containing (A) 10^{-3} M $Cu^{2+} + 3 \times 10^{-3}$ M Fe^{2+}, (B) 10^{-5} M $Cu^{2+} + 3 \times 10^{-3}$ M Fe^{2+}. (c) CV for an Au/(TBEA + OTS) electrode in a solution containing (A) 10^{-3} M Cu^{2+}, (B) 10^{-6} M Cu^{2+}, and (C) 10^{-6} M $Cu^{2+} + 3 \times 10^{-3}$ M Fe^{2+} (adapted from Refs 10, 44).

Such an example is illustrated in Fig. 6 for the determination of chromate ions [47]. A SAM of 4-(2-mercaptoethyl)pyridinium was found to be highly effective for chromate preconcentration. Excellent selectivity was demonstrated, that is, determination of 3×10^{-10} M chromate with nearly no interference by millimolar concentrations of Fe^{3+}, Ag^{+}, Cu^{2+}, VO_4^{-}, Cr^{3+}, Cl^{-},

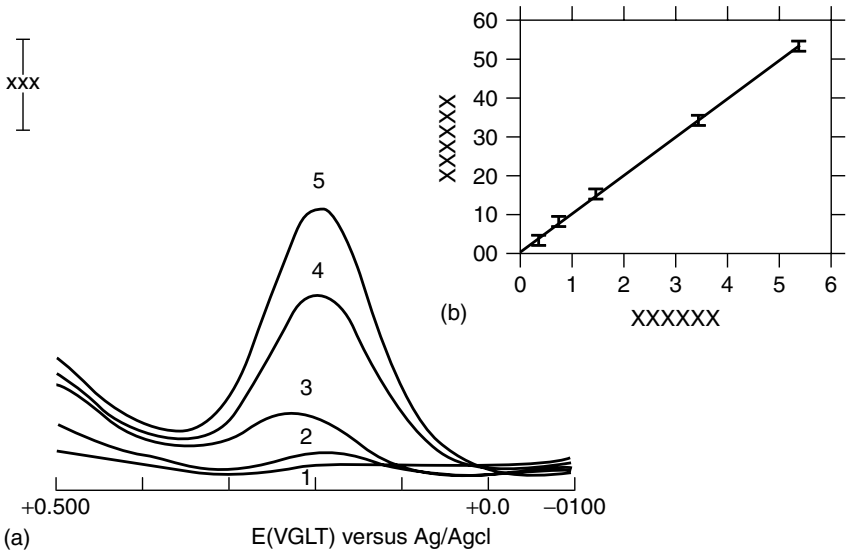


Fig. 6 (a) Square-wave voltammetry of a 4-(2-mercaptoethyl)pyridinium-modified gold electrode (scan rate: 90 mV/s) after a preconcentration step in solutions containing different concentrations of Cr(VI): (1) 0, (2) 4.20×10^{-11}, (3) 8.27×10^{-11}, (4) 3.53×10^{-10}, and (5) 5.44×10^{-10} M. (b) Calibration curve for chromium(VI), obtained from the peak currents. (Adapted from Ref. 47).

NO_3^-, CH_3COO^-, PO_4^{3-}, and SCN^-. Only molybdate ions showed substantial interference, possibly owing to their similar structure and size.

Effective complexation of Cu^{2+} ions was achieved with L-cysteine SAMs [49, 50, 54]. It was assumed that the Cu^{2+} ion interacts with both the amino and carboxylate groups to form a stable surface complex with a 2:1 cysteine-to-Cu ratio [49]. Complex formation was pH-dependent, reaching a maximum at pH 5–6 [49, 54], where the zwitterionic form of the amino acid is stable. The Cu^{2+} surface complex was exceptionally stable, with the electrochemical response remaining unchanged upon repetitive cycling between the Cu^{2+} and Cu^+ forms. The high selectivity of Cu^{2+} binding was seen as nearly no interference by the common cations and anions in solution [54]. Other effective functional groups for Cu^{2+} binding are the tripeptide Gly-Gly-His [51, 53] and poly-L-asparartic acid [52], both showing high selectivity and sensitivity. A SAM terminated with poly-L-asparartic acid was employed successfully in a metal chelating ion-exchange column [55, 56].

SAMs of dithiols are capable of binding metal ions to the terminal thiol groups, as in the case of Cu^{2+} ion binding to 1,6-hexanedithiol [33] and 1,4-benzendimethanethiol [57] SAMs on Au. The electrochemical response indicated that Cu^{2+} ions undergo reduction to Cu^+ upon binding to a thiol-terminated SAM. Multilayer films were also constructed using Cu–S coordination binding and dithiol molecules as repeat units [33, 39].

5.3.3.2 Binding of Electrochemically Inert Ions: Reporting by Redox Reactions of Solution Species

Interfacial electrochemical properties of functional SAMs are generally different from those of well-organized, densely packed long-chain alkanethiol SAMs [15]. Functional SAMs usually comprise more bulky molecules assembled in a less ordered manner. Electrolyte penetration implies that the structure and properties of the electrode/SAM/electrolyte interface may be quite sensitive to changes in the SAM composition and/or the externally applied potential. It should be noted that the actual perturbations in the structure of ion-binding SAMs are largely unknown, and the experimental results are often rationalized using a model equivalent circuit applied to the specific system. The experimental approach frequently applied to detecting ion binding to ligand SAMs is similar to that employed for monitoring the response of pH-sensitive SAMs, primarily the measurement of the electrode kinetics of solution redox couples at the SAM-modified electrode at different pH values. Examples of the latter include pH-induced changes in the CV of $Ru(NH_3)_6^{3+}$ and $Fe(CN)_6^{3-}$ at electrodes modified with various ω-substituted alkanethiol SAMs [58], pH-dependent electrode kinetics at 4-aminothiophenol [59] and thioctic acid [60] SAM-coated electrodes, as well as a thiol-containing phosphate lipid SAM [61]. Changes in the charge-transfer kinetics of solution electroactive species at the SAM-coated electrodes were compared with changes in ion permeation through biological membranes. Correspondingly, this type of electrode response to ion binding is often termed ion-gate characteristics [61–63].

Ca^{2+} binding to carboxylic groups in a glutathione SAM on Au enhances dramatically the electroreduction kinetics

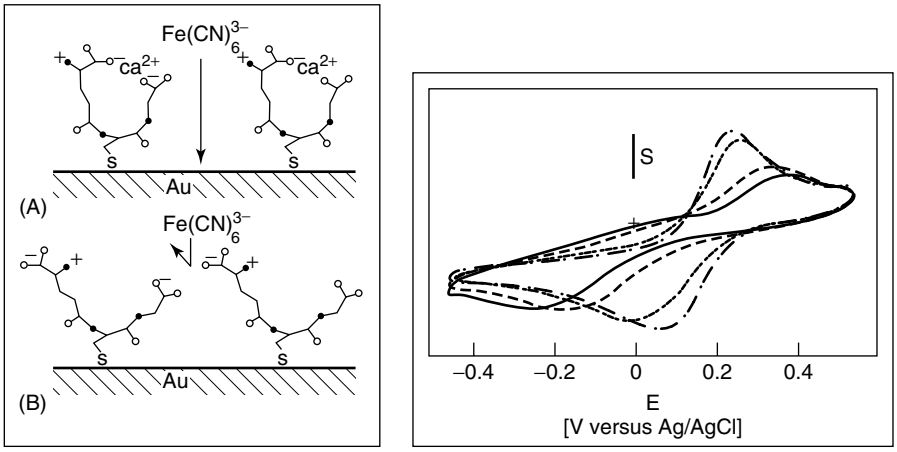


Fig. 7 (a) Schematic illustrations of glutathione (GSH) molecules confined to a Au surface, with (A) and without (B) Ca^{2+} ion at neutral and slightly acidic conditions. Nitrogen and oxygen atoms are indicated by full and empty circles, respectively. (b) CVs obtained in 0.5 mM $Fe(CN)_6 3-$ containing different concentrations of Ca^{2+} using a GSH/Au electrode at pH 5.7; increasing currents correspond to 0.5, 1.0, 5.0, 10.0 mM $CaCl_2$. Scan rate: 50 mV/s; scale bar S = 0.5 μA (adapted from Refs 62, 63).

of $Fe(CN)_6^{3-}$ (Fig. 7) [62]. This type of ion-gate behavior upon complexation of alkaline, alkaline-earth, and lanthanide metal cations was demonstrated with several kinds of functional SAMs, that is, dicarboxylate [62–66], phosphate [67, 68] and phosphate esters [69], cysteine [70], and 4-acyl-5-pyrozolone [71]. As a general rule, the higher the charge of the binding cation, the more sensitive is the ion gate. The highest sensitivity of the kinetics of redox markers to ion complexation in SAMs was achieved for binding of La^{3+} and Al^{3+} from micromolar solutions to phosphate ester-terminated SAMs [69]. Quantification of data such as those in Fig. 7 has yet to be done, owing to lack of adequate electrochemical kinetic models for ion-gate SAMs.

Binding of an electrochemically inert ion to a ligand SAM can be detected quantitatively using a competition scheme. While the complexation of Cu^{2+} to a bisacetoacetate-terminated SAM can be monitored by the voltammetric reduction–reoxidation of the Cu^{2+} ions in the SAM [10], binding of Zn^{2+} ions to the same SAM cannot be detected by direct voltammetry as the ions are not reduced in the applied potential range. However, competition between Cu^{2+} and Zn^{2+} ions for binding sites in the SAM enables quantitative determination of trace amounts of Zn^{2+} by the decrease in the Cu^{2+} voltammetric currents in the presence of Zn^{2+} ions [11, 44].

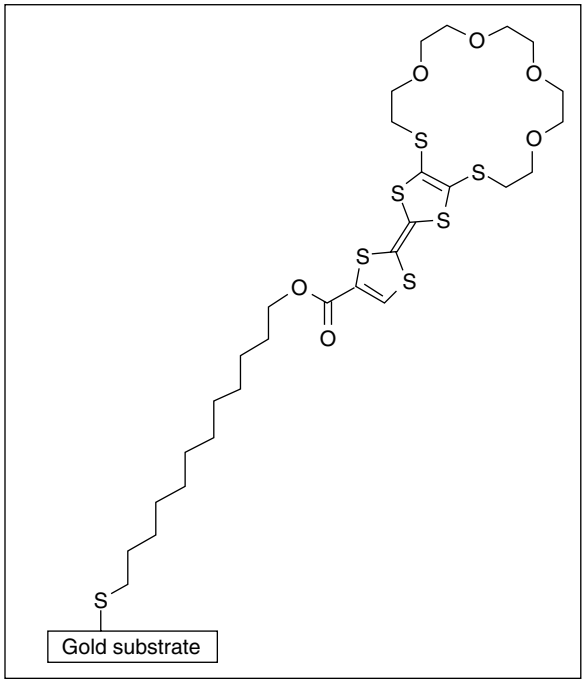
5.3.3.3 Binding of Electrochemically Inert Ions: Reporting by Redox Centers in the SAM

In a SAM (on Au) comprising a metal-binding macrocycle coupled to an electroactive tetrathiafulvalene (TTF) group [72], the redox behavior of the TTF changes upon complexation of a metal ion by the macrocycle ligand (Fig. 8). The TTF shows two sequential redox waves (solid line in Fig. 8b); addition of metal cations to the solution causes an anodic shift of the first oxidation wave, indicating metal complexation to the macrocycle. The magnitude of the shift depends on the metal ion, that is, 10–20 mV for Li^+ and K^+, 45–55 mV for Na^+ and Ba^{2+}, and 60–90 mV for Ag^+. It was argued that at potentials positive of the first oxidation wave the complex becomes unstable; hence the potential of the second oxidation wave is unchanged.

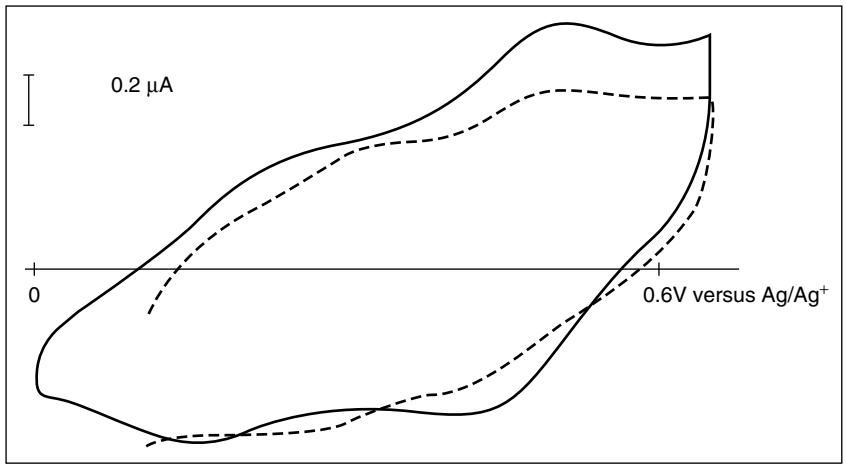
Exceptionally stable and electrochemically well-behaved SAMs bearing dithiacrown-annelated TTF derivatives were prepared using bipodal binding of the receptor molecules to Au electrodes [73, 74]. The CVs in Fig. 9 are of much better quality compared to those in Fig. 8, indicating that formation of TTF^+ crown after the first oxidation does not repel the metal ion from the complex. The interplay between macrocycle size and cation size influences the shift of the redox waves upon complexation. The redox potentials of the SAM of **1a** are not sensitive to the presence of Li^+ and K^+ in solution, while Na^+ causes a small shift of 10 mV in the first wave. The SAM of **1b** shows high sensitivity to Na^+ (55–60 mV, both waves) and a moderate sensitivity to K^+ (20–30 mV), but Li^+ does not influence the signal.

5.3.3.4 Binding of Electrochemically Inert Ions: Application of Electrochemical Impedance Spectroscopy (EIS)

Formation of a SAM on an electrode surface, limiting (or blocking) solution access to the surface, results in substantial changes in the properties of the metal/solution interface [15]. Complexation of metal ions to ligand SAMs is also accompanied by significant modification

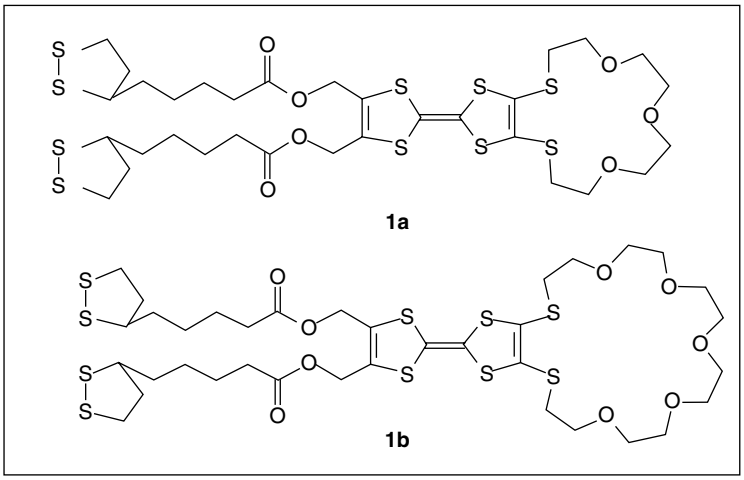


(a)

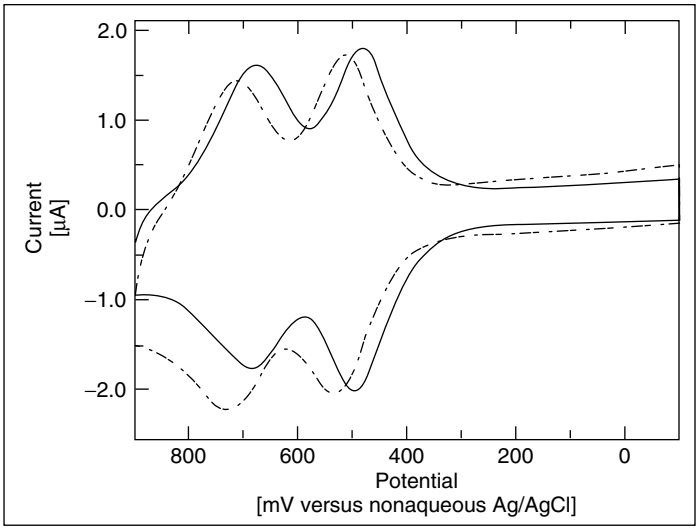


(b)

Fig. 8 Response of a TTF SAM to Ag^+ ions. (a) A receptor molecule bearing a metal-ion binding macrocycle and an electroactive tetrathiafulvalene group, attached to the electrode via a dodecanethiolate chain. (b) CVs for a SAM of TTF in supporting electrolyte (———) and in 0.085 M $AgClO_4$ solution (- - - - - -). Pt electrode, 1.6-mm diameter; solution: 0.2 M $LiClO_4$ in acetonitrile; scan rate: 0.2 V/s (adapted from Ref. 72).



(a)



(b)

Fig. 9 Sensing of Na^+ ions by a crown-ether SAM. (a) Crown-ether annelated TTF ligands. (b) CVs of SAMs of **1b** in THF solution containing 0.1 M Bu_4NPF_6 in the absence (———) and in the presence (· · · ·) of 5.0 mM $NaPF_6$. Scan rate: 0.4 V/s; reference electrode: Ag/AgCl in 0.1 M Bu_4NPF_6 in THF (adapted from Ref. 73).

of the properties of the electrical double layer and of the electrochemical response of the electrode. Such variations are conveniently treated as changes in the electrical impedance of the interface. Electrochemical impedance spectroscopy (EIS) can thus be used as a highly effective tool for monitoring metal-ion binding to functional SAMs. Two basic properties of the system are usually determined, that is,

charge-transfer resistance of a redox probe in solution and the interfacial capacitance. The impedance is commonly measured in a wide frequency range by applying a small-amplitude AC-voltage modulation, and the results are interpreted using an analog equivalent circuit. EIS was successfully applied to a variety of ligand SAMs on metal [41, 75–85] and semiconductor [86, 87] substrates.

A simple model of deprotonation of the terminal group of a SAM in contact with a solution predicted that the capacitance of the electrode was pH-dependent [88]. Study of the impedance of electrodes modified with 4-mercaptopyridine (4-MP) and 4-aminothiophenol (4-ATP) SAMs in supporting electrolyte showed that the system can be described as a series combination of a resistor and a capacitor. Capacitance values extracted from the experimental data indeed show that the double-layer capacitance is pH-dependent with a maximum at the equivalent point [89].

One of the problems in defining an equivalent circuit and interpreting impedance data is the almost unavoidable presence of microscopic defects (pinholes) in the SAM. This issue was addressed in the case of surface complexation of Fe^{3+} ions by biomimetic tris-hydroxamic acid (THB) receptor SAMs (Fig. 10), studied in detail by EIS [77]. In order to eliminate the effect of pinholes on the system response, long-chain alkanethiol (OM) molecules were adsorbed on the electrode following assembly of the ion-bearing ligand SAM. Reduction of the capacitance from ca. 14 $\mu F\,cm^{-2}$ for a Fe(III)-THB SAM to ca. 6 $\mu F\,cm^{-2}$ for the mixed Fe(III)-THB + OM SAM (Fig. 11a,b) indicates formation of an almost pinhole-free

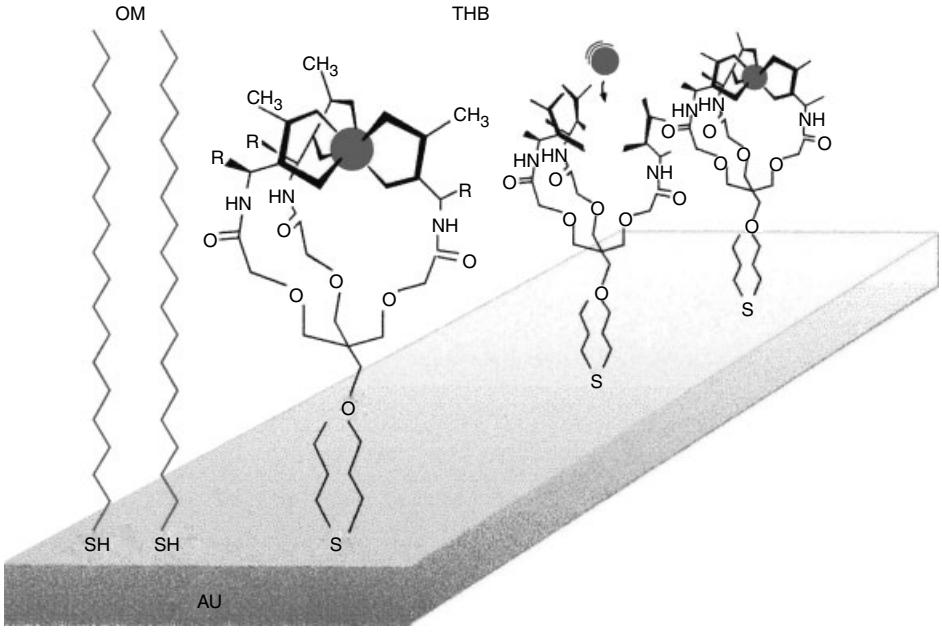


Fig. 10 Schematic representation of a SAM comprising Fe^{3+}-tris-hydroxamate binder (THB) and octadecylmercaptane (OM), the latter serving for pinhole blocking (adapted from Ref. 77).

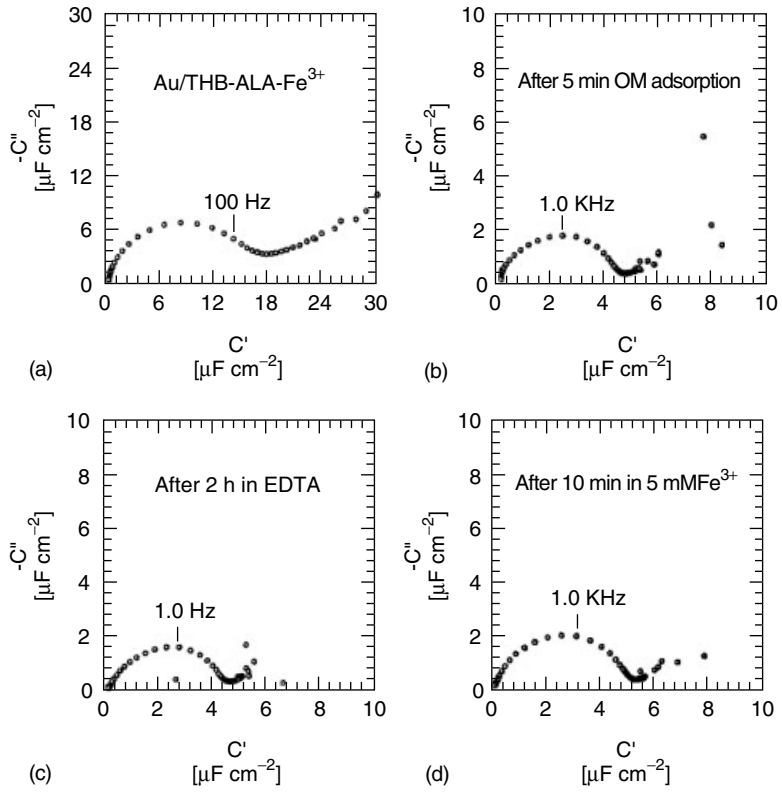
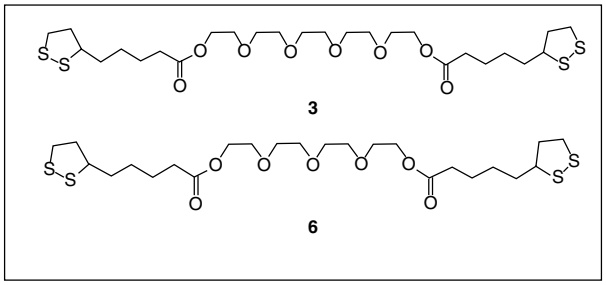


Fig. 11 Experimental complex capacitance plots measured in 0.1 Na_2SO_4 at 0.3 V (versus MSE) for Au/THB electrode at different stages of an experiment showing Fe^{3+} release/rebinding (adapted from Ref. 77).

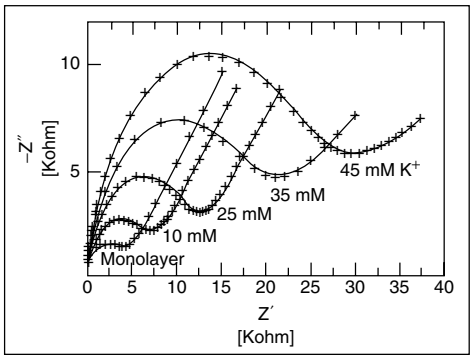
SAM, with OM molecules blocking defect sites and pinholes. Extraction of Fe^{3+} ions from the SAM by EDTA and subsequent complexation of the metal ion show a corresponding response of the impedance (Fig. 11b,d), demonstrating the reversible ion-binding capability of the ligand SAM.

Complexation of alkali metal ions by 15-crown-5 and 12-crown-4 terminated SAMs was studied by EIS [78, 80]. The impedance of SAM-covered electrodes in the presence of a redox probe (usually $Ru(NH_3)_6^{2+/3+}$) was described by the Randles equivalent circuit, and the charge-transfer resistance R_{CT} changed systematically with the metal-ion concentration. Binding of Na^+ ions to a 12-crown-4 terminated SAM resulted in an increase of R_{CT} from 0.25 kΩ in pure electrolyte solution to a limiting value of 145 kΩ in the presence of 23 mM Na^+. Saturation of the response was consistent with the expected behavior of the adsorption isotherm. A sharp decrease in the selectivity was seen in mixed crown ether–heptanethiol SAMs. This suggests that the ions are bound as 2 : 1 (ligand : metal ion) sandwich complexes. Dilution of the functional molecules with inert ones reduced the concentration of ligand pairs necessary for the formation of sandwich complexes. Such complexes show good selectivity for K^+ versus

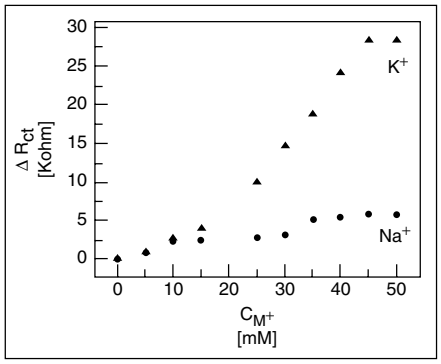
Na^+: $K_{Na+}/K_{K+} = 30$ for 12-crown-4, and $K_{K+}/K_{Na+} = 450$ for 15-crown-5 SAMs. Additional EIS studies showed that the presence of redox couples in the solution does not influence the capacitive behavior of crown-ether SAM-coated electrodes [79].



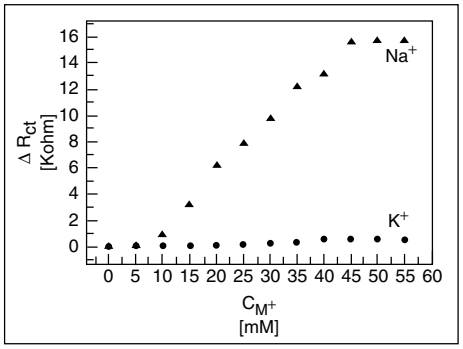
(a)



(b)



(c)



(d)

Fig. 12 (a) Bis-thiooctic ester derivatives (**3, 6**) of oligoethyleneglycol for SAM formation. (b) Impedance response of a monolayer of **3** in the absence and presence of varying amounts of K^+. Solution: 0.1 M Et_4NCl + 1 mM $Ru(NH_3)_6^{2+/3+}$ redox probe, the potential set at the formal potential of the redox couple. (c) Plot of the relative change in R_{CT} for **3**, with the solution containing K^+ and Na^+. (d) Plot of the relative change in R_{CT} for **6**, with the solution containing K^+ and Na^+ (adapted from Refs 81, 83).

Hence, association constants of metal ions in such SAMs, determined from changes in the charge-transfer resistance of solution redox couples, are similar to those calculated from capacitance data.

The receptor SAMs capable of selective ion binding of Na^+ and K^+ ions shown in Fig. 12(a) comprise oligoethyleneglycol fragments that can form pseudo crown-ether cavities upon complexation of the appropriate metal ion [81–83]. The EIS response of a SAM of ligand **3** (forming a pseudo 18-crown-6 receptor) to change in K^+ concentration in solution (Fig. 12b) showed a high sensitivity of the charge-transfer resistance to surface complexation of the metal ion. Ligand **6** (forming a pseudo 15-crown-5 receptor) showed a similar sensitivity to the presence of Na^+ ions. R_{CT} values obtained with SAMs of ligands **3** and **6** (Fig. 12c,d) showed significant selectivity for concentrations of the metal ions above 10 mM. Interestingly, compared to selectivity results of crown-ether SAMs [78, 80], pseudo crown-ethers form stable complexes with one additional ethyleneglycol unit in the ring, that is, 5 versus 4 for complexation of Na^+ and 6 versus 5 for K^+. The question whether both ends of the bipodal ligands **3** and **6** are attached to the Au substrate remains open, and further study is necessary to establish the structure of the SAMs.

The apparent availability of free thiol groups in a bis-mercaptoacetamide SAM was exploited for binding of Re ions (Fig. 13a) [90]. XPS analysis of the SAM of ligand **7** shows that nearly half the thiol groups remain protonated, indicating that only one end of the ligand is attached to the Au surface. The vertically extended molecular orientation in the SAM may be promoted by amide–amide intermolecular interactions, known to provide lateral stabilization of monolayer structures [91, 92]. Metal-ion binding in SAMs of **7** was confirmed by XPS analysis and electrochemistry, showing irreversible oxidation of Re^{5+} in the surface complex (Fig. 13b).

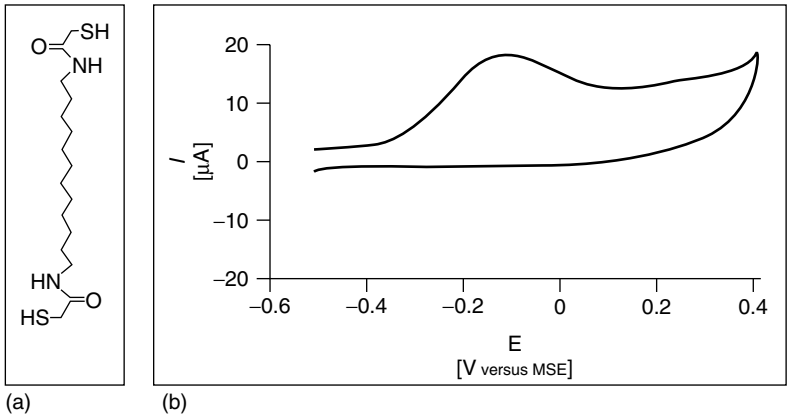


Fig. 13 (a) 1,12-Bis(2-mercaptoacetamido)dodecane ligand **7**. (b) CV of a monolayer of adsorbate **7** after immersion in Re(V) gluconate solution for 3 h. Only one oxidation peak at −0.14 V is present, but it disappears, producing a featureless trace after 20–30 scans. Scan rate: 0.1 V/s; electrolyte: 0.1 M K_2SO_4 (adapted from Ref. 90).

5.3.3.5 Optical Methods for Control and Reporting of Ion Binding to SAMs

The possibility of photoswitching of metal-ion chelating in SAMs was demonstrated using a (pyridylazo)phenol SAM, exploiting the reversible photoinduced trans–cis isomerization of azo compounds. The SAM is capable of binding Ni^{2+} and Co^{2+} ions in the trans form, while no binding occurs in the cis form (Fig. 14) [93]. Reversible photoswitching of the SAM without metal ions was tested by electrochemistry and UV–vis spectroscopy of SAMs deposited on ultrathin transparent Au electrodes (Fig. 15a). Exposure of SAM-coated Au electrodes to a Ni^{2+} solution resulted in no significant change of the UV–vis spectrum of the cis SAM, while the spectrum of the trans SAM showed substantial change of the absorption band (Fig. 15b, compare with Fig. 15a). UV–vis titration of the trans SAM with Ni^{2+} showed an isosbestic point for the transition from the 365-nm band to the 433-nm band. Saturation of the SAM with Ni^{2+} ions occurs in the millimolar concentration range.

As a reflection technique, ellipsometry is particularly suited to the study of SAMs on metal surfaces. Application of ellipsometry to monitoring of selective ion binding in ligand SAMs was carried out by exploiting the change in the ellipsometric parameters, particularly the phase parameter Δ, upon formation of light-absorbing SAM–metal ion complexes [42]. Binding of Cu^{2+} ions to a bisacetoacetate-terminated SAM was seen as a marked decrease in Δ, especially pronounced at a wavelength close to the absorbance maximum of the complex. The change in Δ was reversible, returning to its original value upon removal of the bound ion. The binding selectivity was seen as essentially

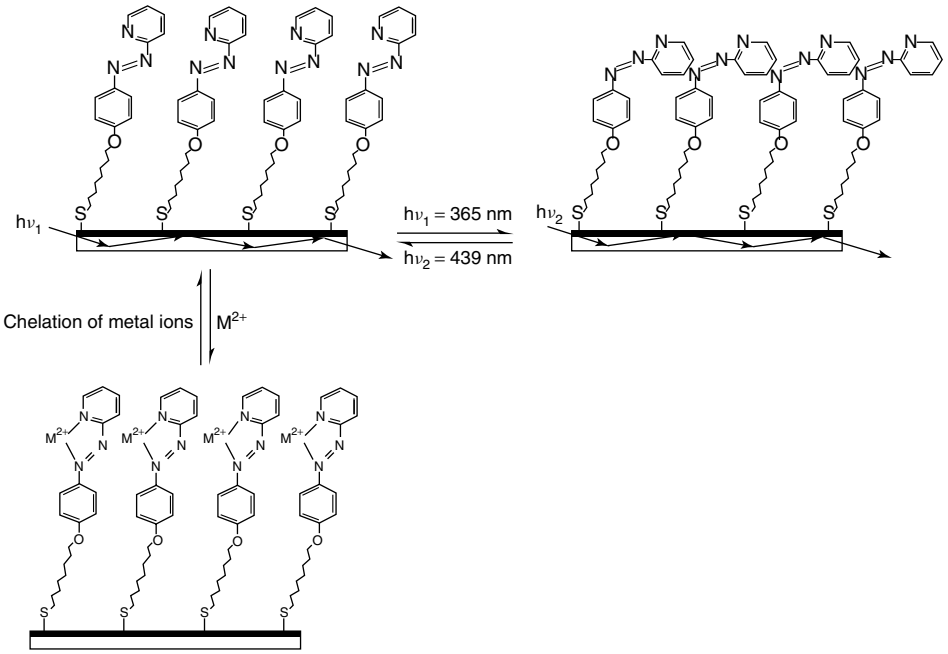


Fig. 14 Chelation of Ni^{2+} by a photoswitchable (pyridilazo)phenol SAM [93].

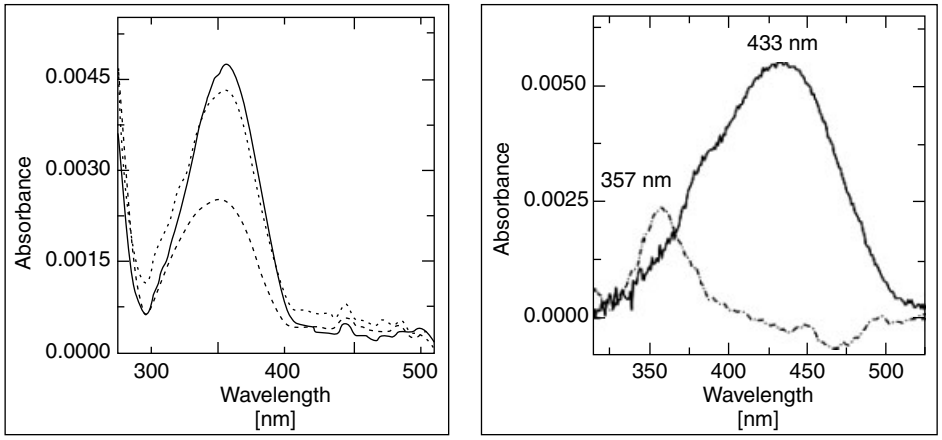


Fig. 15 UV–vis extinction spectra of a (pyridilazo)phenol SAM. (a) Spectra of the as-prepared SAM (———), the SAM following UV irradiation (- - - - -), and the SAM after subsequent visible irradiation (· · · ·). (b) Spectra for the trans (———) and cis (-.-.-.) isomers of the SAM following interaction with 2.4 mM $Ni(NO_3)_2$ solution (adapted from Ref. 93).

no change in Δ in the presence of Fe^{3+} ions, in agreement with the electrochemical results.

SPR was used to follow complexation of Pb^{2+} ions to a dithizone-terminated SAM [94, 95], allowing measurement of the kinetics of the process. Fluorescence detection of ion binding to a monolayer of calix[4]arene receptors covalently immobilized on glass through a silane bond was demonstrated by measuring the fluorescence of pyrene fluorophore groups in the receptor molecules. Upon Na^+ binding to the receptor SAM, the emission spectra showed a decrease of the pyrene monomer and increase of the excimer fluorescence [21]. Selectivity constants for Na^+ versus K^+ and Cs^+ were greater than 100.

Fluorescence reporting was also applied to selective binding of Pb^{2+} by urea in the presence of other metal ions (Zn^{2+}, Ca^{2+}). Mixed SAMs containing a ligand (urea) and a fluorescent group (dansyl, coumarine) were assembled on glass slides. Binding of Pb^{2+} resulted in quenching of the probe fluorescence, with reasonable selectivity [96]. This type of signal transduction is applicable to indium tin oxide (ITO) electrodes and therefore enables combined electrochemical and optical detection schemes.

Binding of Zn^{2+} ions through metallation of a porphyrin monolayer covalently bound to silanized silica was monitored by UV–vis spectroscopy [97]. Attachment of three bidendate ligands, 1,4-diazabicyclo[2.2.2]octane, 4,4′-bipyridine and 1,3-di(4-pyridyl)propane via axial ligation to the Zn-porphyrin was found to be much stronger than binding to the solution porphyrin. UV–vis spectroscopy was used for monitoring the insertion of dissolved metal ions (Co^{2+}, Mn^{2+}, Fe^{2+}, Ni^{2+}, Cu^{2+} and Zn^{2+}) into SAMs of thiolated porphyrins [98]. Catalytic activity of the ion-containing monolayers toward electrochemical oxygen reduction was demonstrated. Metallation of a porphyrin SAM

was also achieved electrochemically using pulsed cathodic polarization in organic solutions [99].

5.3.4 Bilayers Formed by Metal-organic Coordination

5.3.4.1 Coordinated Organic Bilayers

A layer of ligand molecules can be assembled on top of an already existing SAM of ion-binding molecules, via coordination to the bound layer of metal ions through ligand exchange. The result is a bilayer of ligand molecules connected via coordination of the central ion. Coordination-based bilayers (and multilayers) have been constructed using a step-by-step scheme of this kind. Successful application of the stepwise construction scheme depends on the steric compatibility of the formed complex with the density and arrangement of binding sites in the base monolayer. This issue was addressed in a study of bilayers on Au surface based on a sandwich arrangement of two bishydroxamate disulfide ligand molecules bound through octacoordinated Ce^{4+}, Zr^{4+}, or Ti^{4+} ions (Fig. 1e)) [16]. The authors compared the properties of bilayers prepared from the preformed bimolecular complex with those of bilayers prepared by stepwise assembly of the components (first monolayer, metal ions, second layer). The properties of the two types of bilayers are comparable with somewhat better values for the stepwise bilayers (95% coverage versus 87% for the preformed layer [100]; higher ellipsometric thickness). This difference suggests a different packing of the first monolayer compared to the preformed complex. XPS analysis indicated that binding of the second layer through metal-ion coordination was almost complete in the stepwise preparation scheme. The good tolerance of the stepwise coordination scheme to monolayer defects is similar to that observed with phosphonate-based systems [101].

Coordination bilayers constructed from cavitand-based cages were monitored directly by AFM imaging [102]. The average height of the SAM at different stages of bilayer construction was measured relative to areas on the same slide covered by an inert alkanethiol SAM. Changes in the height, measured directly by AFM, were consistent with the calculated dimensions of the coordination assembly. Preparation of layers with a large lateral separation between the binding sites allowed direct detection of individual cavitands and coordination complexes embedded in the inert SAM.

Coordination of Zr^{4+} with phosphonate anions [6] was exploited for binding of Ru-complexes to a phosphonate-terminated SAM [103]. The Ru(II) complexes, containing a terpyridyl–phosphonate ligand, were bound to Zr^{4+}-terminated 1,4-thiobutylphosphonate SAM on Au. The structures of the complex bilayers were studied by matrix-assisted laser desorption/ionization time-of-flight mass spectrometry (MALDI-TOFMS), confirming the presence of Ru-complexes in the desorption products.

A bilayer of binuclear metal complexes was prepared using a ligand-exchange process [22]. A mixed SAM of the two complexes $[Os(tpy\text{-}SH)_2]^{2+}$ and $[Os(tpy\text{-}SH)(tppz)]^{2+}$ (tpy = terpyridine, tppz = tetrapyridylpyrazine) was prepared on an Au electrode and showed electroactivity of the $[Os(tpy\text{-}SH)_2]^{2+}$ groups. After exposure of the SAM to a solution containing $[Co(tppz)(Cl)_2]$, a second redox process was observed, attributed to $[Co(tppz)_2]^{2+}$ moiety complexed onto the first layer. The overall assumed structure corresponds to

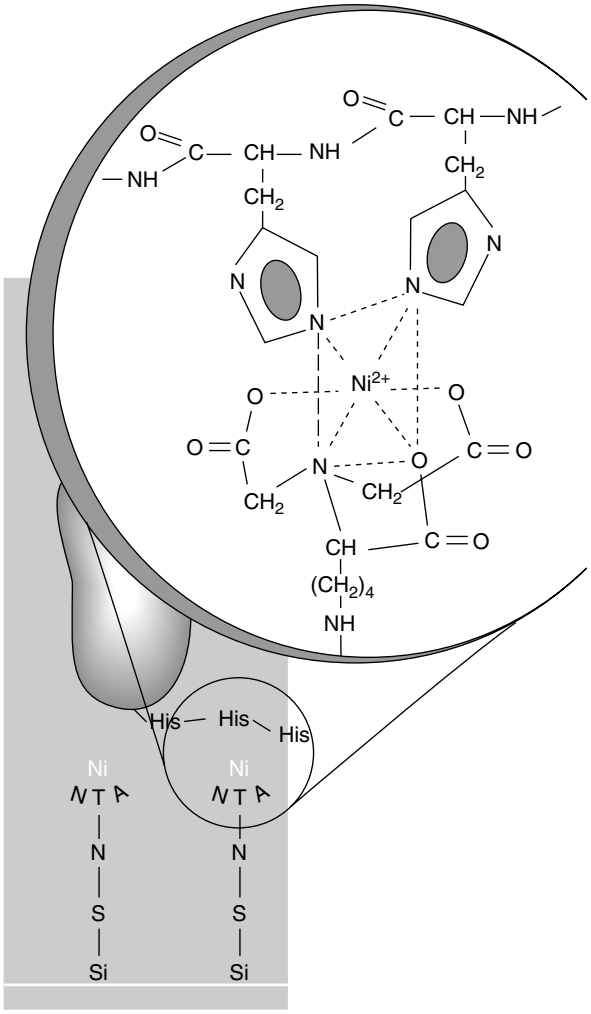


Fig. 16 NTA–Ni^{2+} chelator for His-tagged biomolecules. Schematic representation of the binding of a His-tagged protein to a quartz substrate functionalized with a SAM terminated with NTA. Binding of Ni^{2+} ions enables immobilization of His-tagged proteins via the histidine residues (adapted from Ref. 17).

the binuclear surface complex Au/-S-tpy-Os-tppz-Co-tppz.

The ability of a Cu^{2+}-carboxylate terminated SAM to bind an additional organic ligand was used for selective binding of the nerve-agent simulant diisopropyl methylphosphonate (DIMP) [34, 104]. FTIR studies showed a strong interaction of phosphoryl oxygen with surface-confined Cu^{2+} to yield a DIMP/Cu^{2+} adduct [105]. The strong affinity of DIMP to surface Cu^{2+} carboxylate is potentially

useful in the construction of chemically sensitive interfaces for detection of organophosphonates.

Carboxylate metal ion terminated SAMs are capable of binding a second layer of carboxylate-terminated molecules. This approach was used for preparing bilayers where the upper layer comprises carboxylate-terminated dendrimers [35], Au nanoparticles (NP) [106, 107] and protoporphyrin IX (PPIX) [108]. Polyphenylene dendrimers ($G2Td(COOH)_{16}$) (equivalent diameter, ca. 4 nm) were ionized and then adsorbed on a Cu^{2+}-carboxylate SAM [35]. SAMs with variable concentrations of binding groups were assembled using mixed monolayers of HOOC-C10-SH and CH3-C11-SH, prepared either by adsorption from solution containing both molecules or by sequential adsorption (HOOC-C10-SH followed by partial exchange with CH3-C11-SH). The latter procedure is particularly effective for preparing mixed SAMs with high dilution of coordination binding group [109, 110]. Using mixed SAMs with diluted binding sites, the individual G2 ions were observed by noncontact AFM [35]. The dicarboxylate porphyrin PPIX was coordinatively attached to a Cu^{2+}-terminated 11-mercaptoundecanoic acid (MUA) SAM on Au [108]. The use of Cu^{2+} ions for binding between the carboxylate groups of PPIX and MUA was shown to promote better organization of the porphyrin layer compared to binding of PPIX directly to the MUA SAM.

5.3.4.2 Immobilization of Biological Molecules through Coordination Binding

Use of coordination binding via metal ions for immobilization of proteins started with the introduction of immobilized metal (ion) affinity chromatography (IMAC) [111]. This approach is now used in various applications, including purification, protein surface topography studies, and biosensing [112]. Of the various coordination binding groups, $NTA-Ni^{2+}$ is of particular interest [113], owing to its strong and stable binding to histidine-tagged proteins. Two imidazole groups ($2 \times$ His-tag) are needed to complete the coordination of Ni^{2+} (see Figs. 1c and 16); however, a more stable complexation is achieved with six consecutive histidine tags ($6 \times$ His-tag). The strength of the coordination binding between His-tags and $NTA-Ni^{2+}$ complex was measured by AFM [114–116]. The binding force was 300 pN [114] and 150 pN [116] for a substrate with $NTA-Ni^{2+}$ centers and tip with His-tags, and much lower (ca. 40 pN [115]) for the opposite combination ($NTA-Ni^{2+}$ on tip and His-tag on substrate). The magnitude of the force increased substantially with contact time [117]. Although the higher values are low compared to covalent bonds (2.0 nN for Si—C and 1.4 nN for Au–S bonds [118]), they are larger than the 50–100 pN values characteristic of binding forces in single receptor–ligand interactions [116]. The relatively high binding energy of the $NTA-Ni^{2+}-His$ complex is the reason for its wide application in IMAC and protein binding to SAM applications.

Binding of polyhistidine-modified proteins to $NTA-Ni^{2+}$ terminated SAMs was extensively studied [20, 119–123]. The complexation was monitored by various techniques, primarily SPR [20, 124–126] and FTIR [125, 127, 128]. Exposure to imidazole solution induced protein release from the binding site by ligand competition [20], while most of the Ni^{2+} ions remained bound to the SAM [122]. It should be noted that protein immobilization through His-tags

preserves its biological activity. Hence, binding of specific antibodies to the NTA–Ni^{2+} immobilized His-tag protein [20] and docking of lipoprotein receptor to the capsid of human rhinovirus particles [129] were demonstrated.

Oligonucleotides with a terminal phosphate group were bound to Zr^{4+}-charged phosphonate-derivatized SAMs [130]. This immobilization procedure is rather straightforward and shows long-term stability (months) of the binding site, and therefore may be useful for actual applications.

Coordination binding was used for attachment of electroactive proteins to a SAM on Au [131]. SAMs of long-chain thiol derivatives of metalloporphyrins (Fe^{3+}, Zn^{2+}) served as anchors for the reconstitution of apomyoglobin, forming the respective Fe–and Zn–myoglobin proteins at the interface. Formation of an electroactive surface complex of myoglobin and Fe-porphyrin was achieved by laterally separating the binding molecules using a mixed monolayer of thiolated Fe-porphyrin and 10-hydroxydecanethiol, thus preventing intermolecular interactions between porphyrins in the SAM.

5.3.4.3 Binding of Macrocycle Molecules

Immobilization of macrocycle molecules onto SAMs on solid substrates has been widely studied because of potential applications of such systems in light harvesting and catalytic processes. An abundant scheme for macrocycle attachment is coordination binding of the metallomacrocycle molecule to a preformed SAM terminated with a suitable ligand.

Axial ligation of the metal ion in metalloporphyrin and metallophtalocyanine macrocycles to functional groups in SAMs has been widely used for macrocycle immobilization onto surfaces. Functional groups involved in metallomacrocycle binding include imidazole [132, 133], pyridine [134–136], [137–139] amine [134, 135, 140], isocyanide [141], and isonicotinate [142]. Two types of organizations have been demonstrated, that is, parallel and perpendicular orientation of the macrocycle relative to the substrate.

Planar orientation of the macrocycle has been realized in various cases of axial ligation of the metal center to a functional SAM [132–139, 141–146], as exemplified in Fig. 17(a) [133]. Characterization of the coordinated SAMs by FTIR, ellipsometry, and XPS confirmed the near-planar orientation of the macrocycle. High-resolution STM images [133] showed regions of increased tunneling probability of the size of the flat porphyrin projection. However, the detailed organization of a macrocycle layer can deviate substantially from the ideal planar configuration, owing to interaction of peripheral groups with the tethering monolayer [136]. The optimal organization of the tethering SAM remains unclear; however, a SAM with diluted anchoring molecules leads to better organization of the macrocycle layer [133]. Note that the parallel orientation of macrocycles has been exploited frequently for the construction of metallomacrocycle multilayers on surfaces, assembled in an LbL scheme [133, 138, 141, 147].

The ability of the metal center in the macrocycle to bind two axial ligands was employed for positioning metallomacrocycle molecules perpendicular to an Au substrate (Fig. 17a) [148, 149]. The SAM comprised bifunctional molecules with a cyclic disulfide group for surface immobilization and a dipodal imidazole ligand for viselike binding of the metalloporphyrin, where the supramolecular organization on the surface is dictated by the disulfide attachment to the Au. This combination

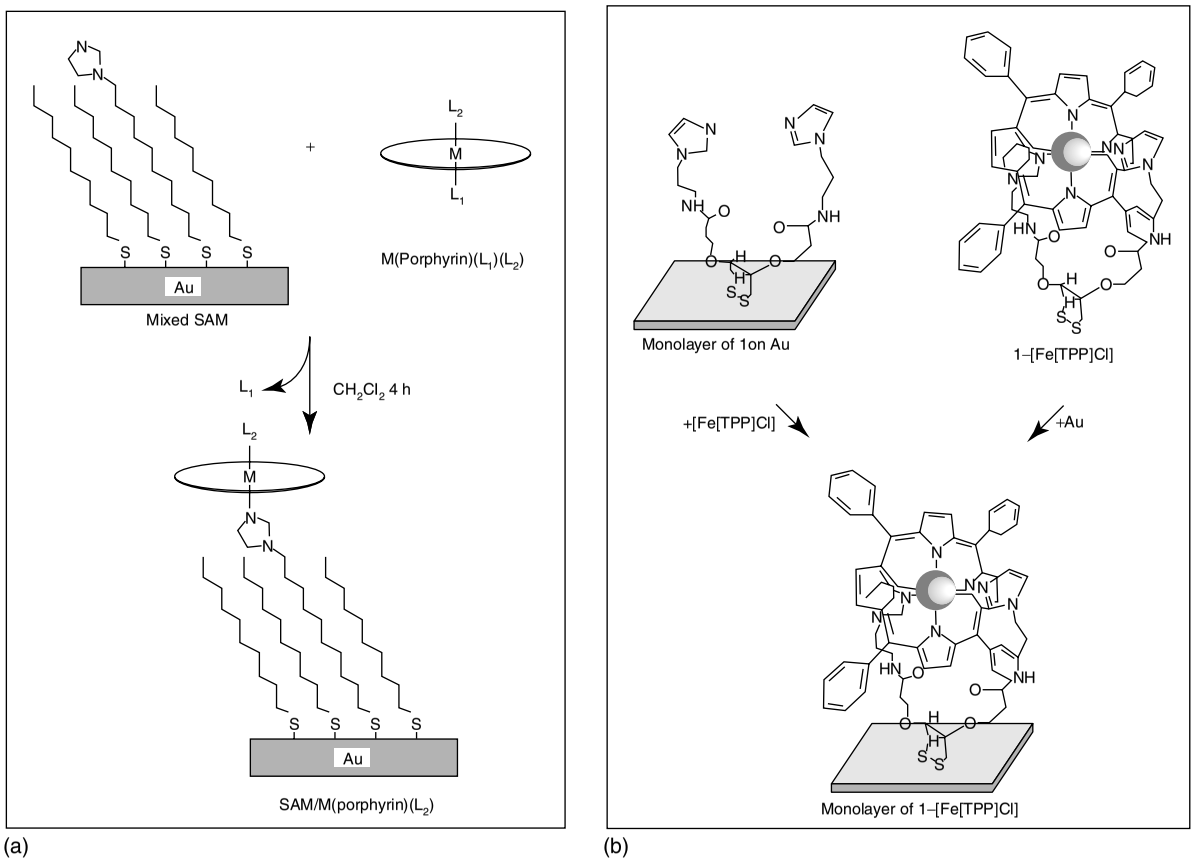


Fig. 17 (a) Deposition procedure and proposed mode of attachment of M(porphyrin)(L2) to a mixed SAM of C9-SH and imid-SH on a Au substrate. L1 is a labile ligand (adapted from Ref. 133). (b) Schematic illustration of the stepwise (left) and preformed (right) methods for the adsorption of the complex **1**-Fe^{3+} (TPP)Cl onto a Au surface (adapted from Ref. 148).

ensured a perpendicular orientation of the macrocycle ring relative to the surface. Fetetraphenylporphyrin immobilized in this manner showed electrochemical reactivity. The porphyrin monolayer was formed either in a stepwise manner or by using a preformed complex (Fig. 17b). The latter scheme provided better packing of the SAM and higher concentration of porphyrin groups in the monolayer.

References

1. S. M. Barlow, R. Raval, *Surf. Sci. Rep.* **2003**, *50*, 201–341.
2. F. Rosei, M. Schunack, Y. Naitoh et al., *Prog. Surf. Sci.* **2003**, *71*, 95–146.
3. S. De Feyter, F. C. De Schryver, *Chem. Soc. Rev.* **2003**, *32*, 139–150.
4. R. G. Nuzzo, D. L. Allara, *J. Am. Chem. Soc.* **1983**, *105*, 4481–4483.
5. J. Sagiv, *J. Am. Chem. Soc.* **1980**, *102*, 92–98.
6. H. Lee, L. J. Kepley, H. G. Hong et al., *J. Phys. Chem.* **1988**, *92*, 2597–2601.
7. S. D. Evans, A. Ulman, K. E. Goppert-Berarducci et al., *J. Am. Chem. Soc.* **1991**, *113*, 5866–5868. '
8. A. Hatzor, T. Moav, H. Cohen et al., *J. Am. Chem. Soc.* **1998**, *120*, 13469–13477.
9. J. M. Lehn, *Supramolecular Chemistry: Concepts and Perspectives*, VCH, Weinheim, 1995.
10. I. Rubinstein, S. Steinberg, Y. Tor et al., *Nature* **1988**, *332*, 426–429.
11. I. Rubinstein, S. Steinberg, Y. Tor et al., *Nature* **1989**, *337*, 217–217.
12. H. Lee, L. J. Kepley, H. G. Hong et al., *J. Am. Chem. Soc.* **1988**, *110*, 618–620.
13. A. Ulman, *Chem. Rev.* **1996**, *96*, 1533–1554.
14. H. O. Finklea, L. Liu, M. S. Ravenscroft et al., *J. Phys. Chem.* **1996**, *100*, 18852–18858.
15. H. O. Finklea in *Electroanal. Chem.* (Eds.: A. J. Bard, I. Rubinstein), Marcel Decker, New York, 1996, pp. 109–335, Vol. 19.
16. T. Moav, A. Hatzor, H. Cohen et al., *Chem. Eur. J.* **1998**, *4*, 502–507.
17. E. L. Schmid, T. A. Keller, Z. Dienes et al., *Anal. Chem.* **1997**, *69*, 1979–1985.
18. H. J. Himmel, A. Terfort, R. Arnold et al., *Mater. Sci. Eng., C* **1999**, 8 – 9, 431–435.
19. F. Mirkhalaf, D. J. Schiffrin, *J. Chem. Soc., Faraday Trans.* **1998**, *94*, 1321–1327.
20. G. B. Sigal, C. Bamdad, A. Barberis et al., *Anal. Chem.* **1996**, *68*, 490–497.
21. N. J. van der Veen, S. Flink, M. A. Deij et al., *J. Am. Chem. Soc.* **2000**, *122*, 6112–6113.
22. M. Maskus, H. D. Abruna, *Langmuir* **1996**, *12*, 4455–4462.
23. J. Luo, S. S. Isied, *Langmuir* **1998**, *14*, 3602–3606.
24. H. Takagi, A. Ichimura, T. Yano et al., *Electrochemistry* **1999**, *67*, 1192–1193.
25. M. Nielsen, N. B. Larsen, K. V. Gothelf, *Langmuir* **2002**, *18*, 2795–2799.
26. C. Dicke, M. Morstein, G. Hahner, *Langmuir* **2002**, *18*, 336–344.
27. K. L. Yang, K. Cadwell, N. L. Abbott, *Adv. Mater.* **2003**, *15*, 1819–1823.
28. J. Li, K. S. Liang, G. Scoles et al., *Langmuir* **1995**, *11*, 4418–4427.
29. I. C. Stefan, D. Mandler, D. A. Scherson, *Langmuir* **2002**, *18*, 6976–6980.
30. M. Sastry, V. Patil, K. S. Mayya, *J. Phys. Chem. B* **1997**, *101*, 1167–1170.
31. T. L. Freeman, S. D. Evans, A. Ulman, *Thin Solid Films* **1994**, *244*, 784–788.
32. T. L. Freeman, S. D. Evans, A. Ulman, *Langmuir* **1995**, *11*, 4411–4417.
33. M. Brust, P. M. Blass, A. J. Bard, *Langmuir* **1997**, *13*, 5602–5607.
34. L. J. Kepley, R. M. Crooks, A. J. Ricco, *Anal. Chem.* **1992**, *64*, 3191–3193.
35. H. Zhang, P. C. M. Grim, D. Liu et al., *Langmuir* **2002**, *18*, 1801–1810.
36. H. Ohno, L. A. Nagahara, W. Mizutani et al., *Jpn. J. Appl. Phys. Part 1* **1999**, *38*, 180–185.
37. R. C. Major, X. Y. Zhu, *J. Am. Chem. Soc.* **2003**, *125*, 8454–8455.
38. S. D. Evans, T. L. Freeman, T. M. Flynn et al., *Thin Solid Films* **1994**, *244*, 778–783.
39. T. L. Brower, J. C. Garno, A. Ulman et al., *Langmuir* **2002**, *18*, 6207–6216.
40. R. Maoz, S. Matlis, E. DiMasi et al., *Nature* **1996**, *384*, 150–153.
41. T. Stora, R. Hovius, Z. Dienes et al., *Langmuir* **1997**, *13*, 5211–5214.
42. S. Steinberg, Y. Tor, E. Sabatani et al., *J. Am. Chem. Soc.* **1991**, *113*, 5176–5182.

43. N. J. Simmons, K. O. A. Chin, J. A. Harnisch et al., *J. Electroanal. Chem.* **2000**, *482*, 178–187.
44. S. Steinberg, I. Rubinstein, *Langmuir* **1992**, *8*, 1183–1187.
45. I. Turyan, D. Mandler, *Isr. J. Chem.* **1997**, *37*, 225–233.
46. I. Turyan, D. Mandler, *Anal. Chem.* **1994**, *66*, 58–63.
47. I. Turyan, D. Mandler, *Anal. Chem.* **1997**, *69*, 894–897.
48. S. Berchmans, S. Arivukkodi, V. Yegnaraman, *Electrochem. Commun.* **2000**, *2*, 226–229.
49. D. W. M. Arrigan, L. Le Bihan, *Analyst* **1999**, *124*, 1645–1649.
50. W. R. Yang, J. J. Gooding, D. B. Hibbert, *J. Electroanal. Chem.* **2001**, *516*, 10–16.
51. W. R. Yang, D. Jaramillo, J. J. Gooding et al., *Chem. Commun.* **2001**, 1982–1983.
52. W. R. Yang, J. J. Gooding, D. B. Hibbert, *Analyst* **2001**, *126*, 1573–1577.
53. W. R. Yang, E. Chow, G. D. Willett et al., *Analyst* **2003**, *128*, 712–718.
54. A. C. Liu, D. C. Chen, C. C. Lin et al., *Anal. Chem.* **1999**, *71*, 1549–1552.
55. T. C. Miller, J. A. Holcombe, *Anal. Chem.* **1999**, *71*, 2667–2671.
56. T. C. Miller, J. A. Holcombe, *Anal. Chim. Acta* **2002**, *454*, 37–44.
57. M. Venkataramanan, K. Murty, T. Pradeep et al., *Langmuir* **2000**, *16*, 7673–7678.
58. C. E. D. Chidsey, D. N. Loiacono, *Langmuir* **1990**, *6*, 682–691.
59. L. Sun, B. Johnson, T. Wade et al., *J. Phys. Chem.* **1990**, *94*, 8869–8871.
60. Q. Cheng, A. Brajter-Toth, *Anal. Chem.* **1992**, *64*, 1998–2000.
61. N. Nakashima, T. Taguchi, Y. Takada et al., *Chem. Commun.* **1991**, 232–233.
62. K. Takehara, Y. Ide, M. Aihara et al., *Bioelectrochem. Bioenerg.* **1992**, *29*, 103–111.
63. K. Takehara, Y. Ide, M. Aihara, *Bioelectrochem. Bioenerg.* **1992**, *29*, 113–120.
64. K. Takehara, M. Aihara, N. Ueda, *Electroanalysis* **1994**, *6*, 1083–1086.
65. Z. W. Jiang, W. K. Xin, W. Y. Zhu et al., *J. Rare Earths* **1996**, *14*, 246–249.
66. M. Aihara, F. Tanaka, Y. Miyazaki et al., *Anal. Lett.* **2002**, *35*, 759–765.
67. N. Nakashima, T. Taguchi, *Colloids Surf. A* **1995**, *103*, 159–165.
68. S. W. Chen, K. Huang, *Anal. Chem.* **2000**, *72*, 2949–2956.
69. M. Takaya, P. Buhlmann, Y. Umezawa, *Mikrochim. Acta* **1999**, *132*, 55–60.
70. K. Takehara, M. Aihara, Y. Miura et al., *Bioelectrochem. Bioenerg.* **1996**, *39*, 135–138.
71. T. Ito, *J. Electroanal. Chem.* **2001**, *495*, 87–97.
72. A. J. Moore, L. M. Goldenberg, M. R. Bryce et al., *Adv. Mater.* **1998**, *10*, 395–398.
73. H. Y. Liu, S. G. Liu, L. Echegoyen, *Chem. Commun.* **1999**, 1493–1494.
74. S. G. Liu, H. Y. Liu, K. Bandyopadhyay et al., *J. Org. Chem.* **2000**, *65*, 3292–3298.
75. M. Stelzle, G. Weissmuller, E. Sackmann, *J. Phys. Chem.* **1993**, *97*, 2974–2981.
76. A. L. Plant, *Langmuir* **1993**, *9*, 2764–2767.
77. Y. Gafni, H. Weizman, J. Libman et al., *Chem. Eur. J.* **1996**, *2*, 759–766.
78. S. Flink, B. A. Boukamp, A. van den Berg et al., *J. Am. Chem. Soc.* **1998**, *120*, 4652–4657.
79. S. Flink, F. van Veggel, D. N. Reinhoudt, *J. Phys. Chem. B* **1999**, *103*, 6515–6520.
80. S. Flink, H. Schonherr, G. J. Vancso et al., *J. Chem. Soc., Perkin Trans. 1* **2000**, *2*, 2141–2146.
81. K. Bandyopadhyay, H. Y. Liu, S. G. Liu et al., *Chem. Commun.* **2000**, 141–142.
82. K. Bandyopadhyay, L. H. Shu, H. Y. Liu et al., *Langmuir* **2000**, *16*, 2706–2714.
83. M. A. Herranz, B. Colonna, L. Echegoyen, *Proc. Natl. Acad. Sci. U. S. A.* **2002**, *99*, 5040–5047.
84. J. Ekeroth, P. Konradsson, F. Hook, *Langmuir* **2002**, *18*, 7923–7929.
85. J. Ekeroth, P. Konradsson, F. Bjorefors et al., *Anal. Chem.* **2002**, *74*, 1979–1985.
86. C. Miller, P. Cuendet, M. Gratzel, *J. Electroanal. Chem.* **1990**, *278*, 175–192.
87. S. Terrettaz, H. Vogel, M. Gratzel, *J. Electroanal. Chem.* **1992**, *326*, 161–176.
88. C. P. Smith, H. S. White, *Langmuir* **1993**, *9*, 1–3.
89. M. A. Bryant, R. M. Crooks, *Langmuir* **1993**, *9*, 385–387.
90. K. J. C. van Bommel, A. Friggeri, D. Mateman et al., *Adv. Funct. Mater.* **2001**, *11*, 140–146.
91. R. S. Clegg, S. M. Reed, R. K. Smith et al., *Langmuir* **1999**, *15*, 8876–8883.
92. H. Rapaport, I. Kuzmenko, M. Berfeld et al., *J. Phys. Chem. B* **2000**, *104*, 1399–1428.
93. Z. X. Wang, M. J. Cook, A. M. Nygard et al., *Langmuir* **2003**, *19*, 3779–3784.

94. F. Mirkhalaf, D. Whittaker, D. J. Schiffrin, *J. Electroanal. Chem.* **1998**, *452*, 203–213.
95. F. Mirkhalaf, D. J. Schiffrin, *J. Electroanal. Chem.* **2000**, *484*, 182–188.
96. M. Crego-Calama, D. N. Reinhoudt, *Adv. Mater.* **2001**, *13*, 1171–1174.
97. D. W. J. McCallien, P. L. Burn, H. L. Anderson, *J. Chem. Soc., Perkin Trans. 1* **1997**, 2581–2586.
98. N. Nishimura, M. Ooi, K. Shimazu et al., *J. Electroanal. Chem.* **1999**, *473*, 75–84.
99. T. Nann, U. Kielmann, C. Dietrich, *Anal. Bioanal. Chem.* **2002**, *373*, 749–753.
100. E. Sabatani, J. Cohenboulakia, M. Bruening et al., *Langmuir* **1993**, *9*, 2974–2981.
101. M. M. Fang, D. M. Kaschak, A. C. Sutorik et al., *J. Am. Chem. Soc.* **1997**, *119*, 12184–12191.
102. S. A. Levi, P. Guatteri, F. van Veggel et al., *Angew. Chem., Int. Ed. Engl.* **2001**, *40*, 1892–1896.
103. T. Fukuo, H. Monjushiro, H. G. Hong et al., *Rapid Commun. Mass Spectrom.* **2000**, *14*, 1301–1306.
104. R. C. Thomas, A. J. Ricco, C. R. Dirubio et al., *Proc. Electrochem. Soc.* **1997**, *97-19*, 202–211.
105. R. M. Crooks, H. C. Yang, L. J. McEllistrem et al., *Faraday Discuss.* **1997**, *107*, 285–305.
106. A. C. Templeton, F. P. Zamborini, W. P. Wuelfing et al., *Langmuir* **2000**, *16*, 6682–6688.
107. F. P. Zamborini, J. F. Hicks, R. W. Murray, *J. Am. Chem. Soc.* **2000**, *122*, 4514–4515.
108. M. Wanunu, A. Vaskevich, I. Rubinstein, *J. Am. Chem. Soc.* **2004**, *126*, 5569–5576.
109. A. Friggeri, H. Schonherr, H. J. van Manen et al., *Langmuir* **2000**, *16*, 7757–7763.
110. A. Friggeri, H. J. van Manen, T. Auletta et al., *J. Am. Chem. Soc.* **2001**, *123*, 6388–6395.
111. J. Porath, J. Carlsson, I. Olsson et al., *Nature* **1975**, *258*, 598–599.
112. E. K. M. Ueda, P. W. Gout, L. Morganti, *J. Chromatogr., A* **2003**, *988*, 1–23.
113. E. Hochuli, H. Dobeli, A. Schacher, *J. Chromatogr.* **1987**, *411*, 177–184.
114. M. Conti, G. Falini, B. Samori, *Angew. Chem., Int. Ed. Engl.* **2000**, *39*, 215–218.
115. L. Schmitt, M. Ludwig, H. E. Gaub et al., *Biophys. J.* **2000**, *78*, 3275–3285.
116. F. Kienberger, G. Kada, H. J. Gruber et al., *Single Mol.* **2000**, *1*, 59–65.
117. E. L. Florin, M. Rief, H. Lehmann et al., *Biosens. Bioelectron.* **1995**, *10*, 895–901.
118. M. Grandbois, M. Beyer, M. Rief et al., *Science* **1999**, *283*, 1727–1730.
119. T. A. Keller, C. Duschi, D. Kroeger et al., *Supramol. Sci.* **1996**, *2*, 155–160.
120. M. Liley, T. A. Keller, C. Duschl et al., *Langmuir* **1997**, *13*, 4190–4192.
121. G. Kada, C. K. Riener, P. Hinterdorfer et al., *Single Mol.* **2002**, *3*, 119–125.
122. O. Du Roure, C. Debiemme-Chouvy, J. Malthete et al., *Langmuir* **2003**, *19*, 4138–4143.
123. P. Rigler, W. P. Ulrich, P. Hoffmann et al., *Chem. Phys. Chem.* **2003**, *4*, 268–275.
124. S. W. Keller, H. N. Kim, T. E. Mallouk, *J. Am. Chem. Soc.* **1994**, *116*, 8817–8818.
125. L. Schmitt, T. M. Bohanon, S. Denzinger et al., *Angew. Chem., Int. Ed. Engl.* **1996**, *35*, 317–320.
126. L. Nieba, S. E. NiebaAxmann, A. Persson et al., *Anal. Biochem.* **1997**, *252*, 217–228.
127. D. Kroger, M. Liley, W. Schiweck et al., *Biosens. Bioelectron.* **1999**, *14*, 155–161.
128. T. Stora, Z. Dienes, H. Vogel et al., *Langmuir* **2000**, *16*, 5471–5478.
129. C. K. Riener, F. Kienberger, C. D. Hahn et al., *Anal. Chim. Acta* **2003**, *497*, 101–114.
130. G. Nonglaton, I. O. Benitez, I. Guisle et al., *J. Am. Chem. Soc.* **2004**, *126*, 1497–1502.
131. L. H. Guo, G. McLendon, H. Razafitrimo et al., *J. Mater. Chem.* **1996**, *6*, 369–374.
132. J. P. Collman, M. S. Ennis, D. A. Offord et al., *Inorg. Chem.* **1996**, *35*, 1751–1752.
133. D. A. Offord, S. B. Sachs, M. S. Ennis et al., *J. Am. Chem. Soc.* **1998**, *120*, 4478–4487.
134. G. Kalyuzhny, A. Vaskevich, S. Matlis et al., *Rev. Anal. Chem.* **1999**, *18*, 237–242.
135. G. Kalyuzhny, A. Vaskevich, G. Ashkenasy et al., *J. Phys. Chem. B* **2000**, *104*, 8238–8244.
136. N. Kanayama, T. Kanbara, H. Kitano, *J. Phys. Chem. B* **2000**, *104*, 271–278.
137. F. Da Cruz, K. Driaf, C. Berthier et al., *Thin Solid Films* **1999**, *349*, 155–161.
138. V. Huc, M. Saveyroux, J. P. Bourgoin et al., *Langmuir* **2000**, *16*, 1770–1776.
139. D. M. Sarno, B. W. Jiang, D. Grosfeld et al., *Langmuir* **2000**, *16*, 6191–6199.
140. Z. J. Zhang, R. S. Hu, Z. F. Liu, *Langmuir* **2000**, *16*, 1158–1162.
141. V. Huc, J. P. Bourgoin, C. Bureau et al., *J. Phys. Chem. B* **1999**, *103*, 10489–10495.

142. T. A. Eberspacher, J. P. Collman, C. E. D. Chidsey et al., *Langmuir* **2003**, *19*, 3814–3821.
143. D. Q. Li, L. W. Moore, B. I. Swanson, *Langmuir* **1994**, *10*, 1177–1185.
144. Z. J. Zhang, S. F. Hou, Z. H. Zhu et al., *Langmuir* **2000**, *16*, 537–540.
145. S. Z. Zou, R. S. Clegg, F. C. Anson, *Langmuir* **2002**, *18*, 3241–3246.
146. Z. J. Zhang, T. Imae, H. Sato et al., *Langmuir* **2001**, *17*, 4564–4568.
147. V. Huc, F. Armand, J. P. Bourgoin et al., *Langmuir* **2001**, *17*, 1928–1935.
148. G. Ashkenasy, G. Kalyuzhny, J. Libman et al., *Angew. Chem., Int. Ed. Engl.* **1999**, *38*, 1257–1261.
149. G. Ashkenasy, A. Ivanisevic, R. Cohen et al., *J. Am. Chem. Soc.* **2000**, *122*, 1116–1122.

6.1
XPS, UPS, Penning Ionization, and Auger Electron Spectroscopy

Masamichi Fujihira
Tokyo Institute of Technology, Yokohama, Japan

Electron spectroscopies such as X-ray photoelectron spectroscopy (XPS) and ultraviolet photoelectron spectroscopy (UPS) using photons, Penning ionization spectroscopy (PIS) using metastable noble-gas atoms, and Auger electron spectroscopy (AES) using high-energy electrons as probing particles are widely used for surface characterization of chemically modified electrodes. However, these methods are well described in textbooks of surface chemistry. Therefore, in this section, we simply cite several representative textbooks in the following further reading.

Further Reading

1. D. Briggs, M. P. Seah (Eds.), *Practical Surface Analysis, Auger and X-ray Photoelectron Spectroscopy*, 2nd edition, John Wiley & Sons, Chichester, 1990, Vol. 1.
2. L. E. Davis, N. C. MacDonald, P. W. Palmberg et al., *Handbook of Auger Electron Spectroscopy*, 2nd edition, Physical Electronics Industries, Minnesota, 1976.
3. B. Feuerbacher, B. Fitton, R. F. Willis (Eds.), *Photoemission and Electronic Properties of Surfaces*, John Wiley & Sons, Chichester, 1978.
4. W. Adamson, A. P. Gast, *Physical Chemistry of Surfaces*, 6th edition, Wiley, New York, 1997.
5. A. Ulman, *An Introduction to Ultrathin Organic Films from Langmuir-Blodgett to Self-Assembly*, Academic Press, San Diego, 1991.
6. H. Ozaki, Y. Harada, K. Nishiyama et al., *J. Am. Chem. Soc.* **1987**, *109*, 950–951.

Encyclopedia of Electrochemistry. Edited by A.J. Bard and M. Stratmann
Vol. 10 *Modified Electrodes*. Edited by M.Fujihira, I.Rubinstein, and J.F.Rusling
Copyright © 2007 Wiley-VCH Verlag GmbH & Co. KGaA, Weinheim. ISBN: 978-3-527-30402-8

6.2
Scanning Probe Microscopies as Chemical Force microscopy for Self-assembled Monolayers

Masamichi Fujihira, Hiroki Okui, Fuminobu Sato
Tokyo Institute of Technology, Yokohama, Japan

6.2.1
Introduction

For more than a decade, friction at a sliding interface between organic monolayers such as Langmuir–Blodgett (LB) films and self-assembled monolayers (SAMs) has been studied experimentally by friction force microscopes (FFM) [1–3] and surface force apparatuses (SFA) [4]. The difference in friction between hydrocarbon (HC) and fluorocarbon (FC) [5–16] and among monolayers of alkyl chains having different terminal groups [17–20] against atomic force microscope (AFM) tips with or without monolayers having different terminal groups has been observed.

The chemical modification by silanization (or other chemical reactions) of carbon, oxide, or metal electrode surfaces [21, 22] or SAM formation on gold surfaces with thiol or disulfide compounds [23] has been utilized for the tip functionalization. The systematic chemical derivatization of the tips was carried out with silane [10, 24–27] or thiol [17, 18, 20, 28–37] derivatives. Today, chemical differentiation of the terminal groups by FFM [5–20, 28, 36, 37] or adhesive force measurements [17, 18, 20, 24–28, 30–37] is called *chemical force microscopy* (CFM) [17]. Adhesive and frictional forces can be mapped in $x-y$ planes as CFM images. The adhesive force mapping was performed quickly by pulsed-force-mode atomic force microscopy (PFM-AFM) [37–41].

Recently, we attempted to interpret the origin of the friction differences among the organic monolayers by comparing the MD (Molecular Dynamics) simulation of the sliding friction between these monolayers with a corresponding simplified phenomenological simulation [42–46]. The dependence of friction and adhesive forces between the sample and the AFM tip surfaces on the terminal functional groups was also studied using the simplified phenomenological simulation [44] and using PFM-AFM with chemically modified tips [36, 37].

6.2.2
Chemical Modification of AFM Tips

Chemical modification of AFM tips can be performed reproducibly by our previous method [36]. The chemical modification of AFM tips just after vapor deposition of gold in an Olympus factory and the modification of the commercially available gold-coated tips after cleaning in our laboratory gave almost the same results for chemical differentiation of surface chemical species [36]. Therefore, in our laboratory, chemically modified AFM tips were prepared from Olympus Si_3N_4 rectangular cantilevers OMCL-RC800PB-1 (0.73 or 0.38 N m^{-1}) with a sharpened pyramidal tip according to the following procedure. The commercially available tips were already coated with Cr/Au films when we received them. The tips were first cleaned using an ozone cleaner (Nippon Laser & Electronics Lab.) for 30 minutes and immediately after the oxidation step, the gold-coated tips were immersed in pure, hot ethanol at ca 65° for 30 minutes for complete

Encyclopedia of Electrochemistry. Edited by A.J. Bard and M. Stratmann
Vol. 10 *Modified Electrodes*. Edited by M.Fujihira, I.Rubinstein, and J.F.Rusling
Copyright © 2007 Wiley-VCH Verlag GmbH & Co. KGaA, Weinheim. ISBN: 978-3-527-30402-8

reduction of surface gold oxides. Further chemical modification was performed by immersing the cleaned gold tips into a 1 mM 1-decanethiol ($CH_3(CH_2)_9SH$) or 11-mercaptoundecanoic acid ($HOOC(CH_2)_{10}SH$) ethanol solution for 24 hours at room temperature immediately after the two-step cleaning procedure. Finally, the modified tips were rinsed thoroughly with pure ethanol and dried under a stream of nitrogen. The chemically modified tips with $CH_3(CH2)_nSH$ and $HOOC(CH_2)_nSH$ will be called hereafter CH_3 [9, 10, 13, 17, 18, 20, 24–37] and COOH tips [17, 18, 20, 28–37], respectively. In addition to these two types of tips, other functional groups, such as $-CF_3$ [9, 10, 13, 29], $-OH$ [27–29, 31–33, 35], $-SH$ [26], $-OCOCH_3$ [26], $-SCOCH_3$ [26], $-CH{=}CH_2$ [27], $-CH_2Br$ [28], $-CO_2CH_3$ [28, 33], $-NH_2$ [30, 31, 34, 35], $-OCH_3$ [33], $-CONH_2$ [33, 35], $-PO_3H_2$ [34], and $-SO_3$ [47], can be introduced on AFM tips.

6.2.3 Sample Surfaces with Various Patterns

The chemically modified sample surfaces with patterns were prepared according to the following procedures [36, 48–50]. First, a phase-separated mixed monolayer was formed by spreading a mixed chloroform solution of a carboxylic acid with a partially fluorinated carbon ($C_9F_{19}C_2H_4OC_2H_4COOH$, PFECA) and octadecyltrichlorosilane ($C_{18}H_{37}SiCl_3$, OTS) and by compressing a mixed monolayer at an air–water interface in a Langmuir trough. Secondly, the resulting phase-separated monolayer was deposited on an oxidized Si(111) wafer by the LB method, followed by heating at 80 °C overnight and then ultrasonication in ethanol. The bare oxidized Si surface was exposed by removing the physically adsorbed PFECA domains, but the chemically bound OTS monolayer domains remained on the Si surface even after ultrasonication. In this way, an oxidized Si wafer surface partially covered with HC monolayer domains was prepared. The sample thus prepared was used for comparison between friction force and adhesive force mapping by FFM and PFM-AFM, respectively.

A stamp for microcontact printing (μ-CP) was fabricated as described previously [37] according to the method invented by Kumar and Whitesides [51–53]. The height of the convexities of the stamp was determined to be ca 0.4 μm from a cross section of the AFM image. The gold-coated substrates were prepared by the following method. Microcover glass plates obtained from Matsunami Glass Industry were cleaned by the same ozone cleaning for 30 minutes as that used for the AFM tips described above. Gold films (ca 11 nm) were deposited on the cleaned cover glass plates with a Hitachi E-1030 ion sputter using an argon plasma at about 6 Pa, 15 mA with a deposition rate of about 11 nm min^{-1} [54, 55]. In addition to the sputtered gold films, we also used gold films (ca 100 nm) with Au(111) surfaces prepared by gold vacuum vapor deposition (at a rate of ca 0.2 nm sec^{-1}) at ca 300 °C followed by annealing at ca 400 °C for 2 hours [55].

The patterned SAM samples were prepared by the procedures illustrated in Fig. 1 [56]. As the first step, two types of μ-CP methods [53, 57] were used to make stamped patterns on the gold-coated substrates. One is called the *wet-inking* method, in which inking of the stamp was done by placing a thiol ethanol solution for 30 seconds and then removing the excess solution under a stream of nitrogen. The

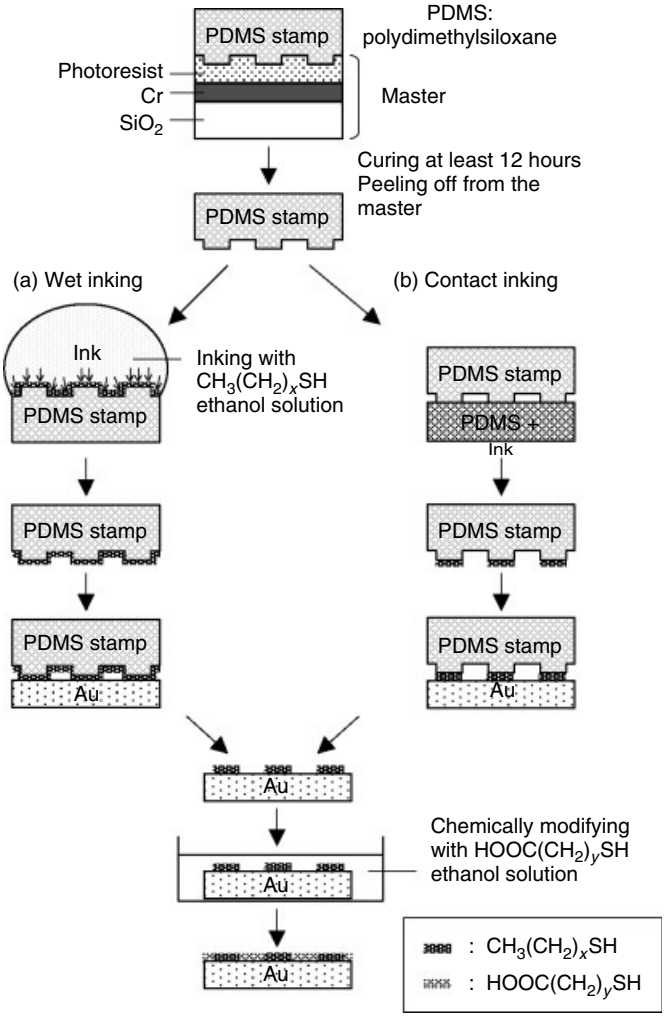


Fig. 1 Preparation procedures of patterned samples with (a) the wet-inking and (b) the contact-inking method, followed by further chemical modification of the unprinted area with a 1 mM $HOOC(CH_2)_{10}SH$ ethanol solution for ca 5 minutes.

ethanol solution with a thiol concentration of 0.1 mM was examined as the inking solution. 1-Alkanethiols $CH_3(CH2)_nSH$ with different chainlengths of $n = 11$, 15, and 19 were examined as the inking thiol compounds. The other is called the *contact-inking* method, in which an inker pad (ca $3 \times 15 \times 15\ mm^3$) made of polydimethylsiloxane (PDMS) was dipped overnight in a 0.1 mM thiol ethanol solution, then the excess solution was removed by a stream of nitrogen, and finally the stamp was placed for 30 seconds on the inker pad impregnated with the thiol solution. The second step for pattern formation was the same for the two

methods and the gold surfaces patterned with alkanethiols by μ-CP were further reacted with $HOOC(CH_2)_{10}SH$ in a 1 mM ethanol solution for ca 5 minutes. The resulting patterns with CH_3- and $COOH-$ terminated regions were analyzed by imaging the adhesive forces in an aqueous solution with the chemically modified gold-coated AFM tips with a SAM of CH_3 terminal functional groups.

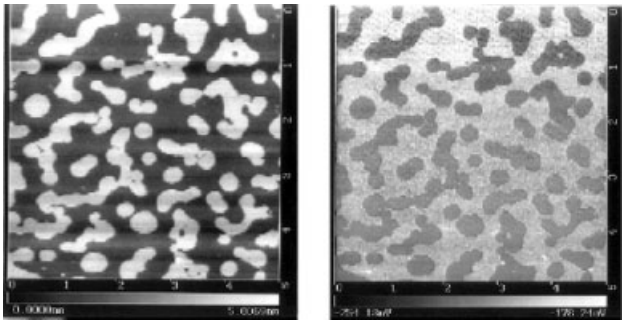
6.2.4 FFM and PFM-AFM Measurements

All measurements of AFM, FFM, and the adhesive force mapping with PFM-AFM were performed with a commercial AFM (a Seiko Instruments SPA 300 AFM unit with an SPI-3700 AFM controller) and a PFM box [40, 41]. The cantilever bending forces [49] for FFM and PFM-AFM were ca 10 and 3 nN, respectively. The frequency and the amplitude for PFM-AFM were 0.5–1 kHz and 30–70 nm, respectively. Relative humidity of measuring air atmospheres was 50–60%. The adhesive force mappings in water were performed in a 0.1 mM $NaHCO_3$ aqueous solution at room temperature. This slightly basic aqueous solution was used to confirm dissociation of the surface COOH terminal groups [31]. Brighter contrast in friction and adhesive force maps correspond to higher friction and adhesive forces.

6.2.5 Friction and Adhesive Force Imaging as CFM

6.2.5.1 CFM of Patterned Surface Prepared by the LB Method

In Fig. 2 are shown $5 \times 5\ \mu m^2$ (256×128) images of (a) a topography and (b) a friction force map of an oxidized Si wafer partially covered with polymerized OTS monolayer domains prepared by the LB method described above [36, 48–50]. These two images were taken simultaneously by contact-mode AFM, using a CH_3 tip. The height of the HC domains in Fig. 2(a) was determined to be ca 2.2 nm by AFM. The AFM result indicated that the HC layer was a polymerized OTS monolayer and the lower surface was the bare oxidized Si surface. In Fig. 2(b), the much higher friction was observed on the bare oxidized Si surface than on the HC domains. As discussed previously [49], the contrast



(a) (b)

Fig. 2 $5 \times 5\ \mu m^2$ (256×128) images of (a) a topography and (b) a friction force mapping, simultaneously obtained by contact-mode AFM using a CH_3 tip in air for a patterned sample prepared with the LB method.

in the friction map can be attributed to the change in the effective normal loads rather than the difference in the intrinsic friction forces between these two domains with different chemical species [10]. In other words, a hydrophilic surface on the oxidized Si substrate was covered with a water film in the ambient atmosphere and water capillary forces on this region would increase the effective normal load [49].

To do adhesive force mapping, we also performed PFM-AFM on the same surface using the same CH_3 AFM tip. Figure 3 shows a $5 \times 5\ \mu m^2$ (256×128) image of (a) an adhesive force map taken by PFM-AFM and (b) a histogram of the adhesive forces in the adhesive force map in Fig. 3(a). Here, the histogram shows the adhesive force versus the number of times, with which this force was observed in 32 768 times (256×128) adhesive force measurements during the adhesive force mapping. In PFM-AFM, the z-position of the sample is controlled so as to keep the peak signal constant using sample and hold circuits and a feed back loop in AFM, which is used to produce a topographic image [40, 41]. The cantilever bending forces for the peak signal of the PFM was ca 3 nN and the frequency and the amplitude for the images were 1 kHz and 70 nm, respectively. The height of the HC domains was found to be the same as that observed in the contact-mode AFM topography in Fig. 2(a) with a cantilever bending force of ca 10 nN. The adhesive force map shown in Fig. 3(a) gave also a clear contrast between the HC and the bare oxidized Si domain. As we would expect, the higher adhesive forces were observed on the hydrophilic oxidized Si surface than on the hydrophobic HC domain. From the histogram shown in Fig. 3(b), average values of the adhesive forces on the Si and the HC surface were found to be ca 3.9 and 1.6 nN, respectively.

As described above, it was found that CFM, by mapping the friction and the adhesive force with FFM and PFM-AFM, respectively, is useful for the patterned sample of the oxidized Si wafer partially covered with polymerized OTS monolayer domains. Similar measurements were also carried out using a COOH tip. In both images of FFM and PFM-AFM, the much higher contrast was observed between these two domains using this hydrophilic

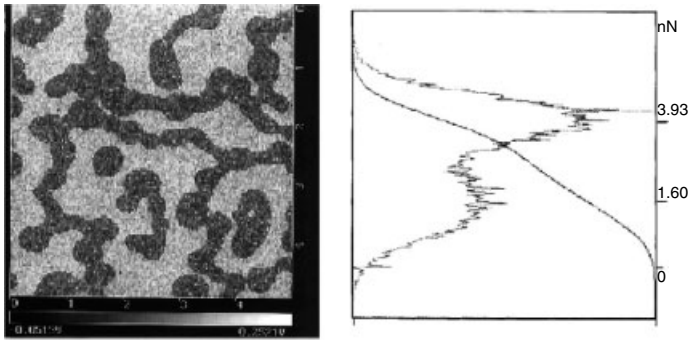


Fig. 3 A $5 \times 5\ \mu m^2$ (256×128) image of (a) an adhesive force map obtained by PFM-AFM and (b) a histogram of the adhesive forces measured in Fig. 3(a), using the same CH_3 tip on the same patterned surface that was observed in Fig. 2.

tip. The water capillary force is again considered as the main origin of the contrast obtained with this tip.

6.2.5.2 Friction Force Map in Phase-separated HC-FC Mixed LB Films with Ca^{2+} Counterions

In our first report of FFM of phase-separated HC and FC mixed monolayers, we used cationic polymers as the counterions of Langmuir mixed monolayers of carboxylates with HC and FC long chains [5, 6]. The phase-separated mixed monolayers were, however, found to be of the ''on-top'' structure rather than the conventional ''side-by-side'' structure [58]. One of the factors giving an unusual two-story structure was considered to be due to an amphiphilic property of cationic polymers. Therefore, we attempted to form phase-separated HC and FC mixed monolayers with ''side-by-side'' structure, using hydrophilic counterions such as Ca^{2+} ions. Figures 4(a) and (b) show $8 \times 8\ \mu m^2$ images of a topography and a friction force map of a phase-separated mixed monolayer with a molar ratio of behenic acid ($C_{21}H_{43}COOH$) to perfluorotetradecanoic acid ($C_{13}F_{27}COOH$) of 2 : 1 [59]. The subphase was water from a Milli-Q system containing 3 mM $CaCl_2$ and 0.1 mM NaOH (pH 9–10). The resulting mixed monolayers exhibited ''side-by-side'' structure, as we would expect. From comparison of the FFM image shown in Fig. 4(b) with previous HC and FC patterned samples using silanization reagents [9], we could conclude safely that the frictional contrast of the present FFM images of the ''side-by-side'' monolayer was surprisingly low. The possible explanation of the low contrast is that compositions of the separated two phases can be similar to each other. To confirm the idea, we also observed a surface potential map of the same area with scanning surface potential microscopy (SSPM) [58, 60–62].

The image of the surface potentials is shown in Fig. 4(c). It is known from the surface potential measurements of single component films [58] that the difference in the surface potentials between the pure FC and the pure HC domains is expected to be ca 1.3 V. The potential difference observed in Fig. 4(c) was found to be only 0.2 V [59]. The result clearly supports the idea that the low contrast in FFM image reflects similar

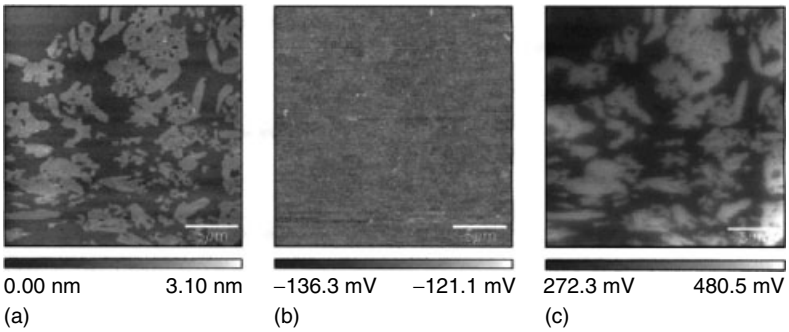


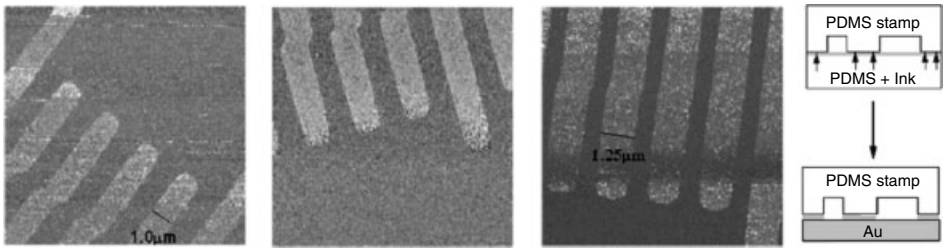
Fig. 4 $22 \times 22\ \mu m^2$ (256 × 128) images of (a) an AFM topography, (b) an FFM friction observed simultaneously by contact-mode AFM, and (c) a surface potential mapping by SSPM of the same area of a mixed monolayer of behenic acid and perfluorotetradecanoic acid with a molar ratio of 2 : 1 deposited on an oxidized *n*-type Si(111) surface using a gold-coated tip.

compositions of the separated two phases. In this way, simultaneous observation of FFM and SSPM images of the same samples is useful to chemical recognition of the phase-separated domains. As the other useful combinations of two different methods, we already demonstrated that combination of scanning near-field optical microscopy (SNOM) with FFM [63] or SSPM [64] is a powerful tool for chemical recognition with lateral resolutions of submicron scales.

6.2.5.3 CFM of Patterned Surfaces Prepared by μ-CP

To develop a new method by which we can study the mixing of two components in each domain in the patterned surfaces, we studied CFM of patterned surfaces prepared by μ-CP methods. Figure 5 shows a comparison between the patterned samples prepared by two different μ-CP methods, that is, the wet-inking and the contact-inking methods [57]. All adhesive force maps in Fig. 5 were observed in a 0.1 mM $NaHCO_3$ aqueous solution using a CH_3 tip on three samples. The z-piezo was modulated sinusoidally at a frequency of 0.5 kHz with amplitudes of ca 30–70 nm. Figures 5(a) and (b) are $10 \times 10\ \mu m^2$ adhesive force maps of the samples prepared by the contact-inking method, using ink pads impregnated with 0.1 mM ethanol solutions of 1-hexadecanethiol and 1-octanethiol, respectively [56]. For comparison, in Fig. 5(c) is shown an image of adhesive forces observed on a sample prepared by the wet-inking method with 0.1 mM 1-hexadecanethiol ethanol solution [56]. The latter sample was prepared with 30 seconds for both the inking and the stamping time. Although the conditions, such as the solution concentration for impregnation and the times for inking and stamping, have not been optimized yet, the contrast of the adhesive forces was observed on the patterned samples prepared by the contact-inking method as shown in Figs. 5(a) and (b).

It is most interesting to note that the widths observed on the samples prepared by the contact-inking method were 1.0 μm for both cases using ink pads impregnated with 1-hexadecanethiol and 1-octanethiol as shown in Figs. 5(a) and (b), respectively, while the width for the sample prepared by the wet-inking method was 1.25 μm as



(a) (b) (c)

Fig. 5 $10 \times 10\ \mu m^2$ (256 × 128) CFM images of patterned samples prepared by the contact-inking method using a 0.1 mM ethanol solution of 1-alkanethiol $CH_3(CH2)_nSH$ with different chain lengths (a) $n = 15$ and (b) $n = 7$, respectively, and by the wet-inking method with (c) $n = 15$, followed by the further reaction with $HOOC(CH_2)_{10}SH$. The inking only on faces of the convexities is possible by the contact-inking method, which prevents any noticeable spread of thiols from the points of contact.

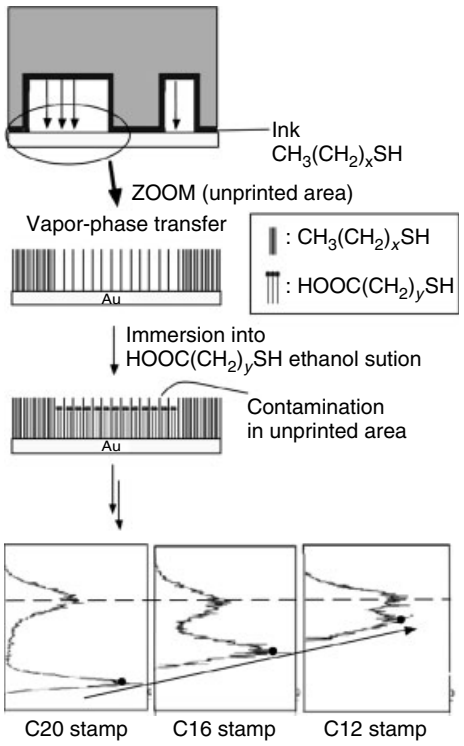


Fig. 6 The loss of contrast in adhesive force mapping by the vapor phase transfer.

shown in Fig. 5(c). In terms of the spatial resolution of the printed pattern, it was found clearly that the contact-inking method was much better than the wet-inking method. As to the defect density on the printed area, a further study will be necessary for the optimization of the contact-inking method, because the defect density seemed to be higher for the samples prepared by the contact-inking method than those by the wet-inking method when the same thiol concentration was used for impregnation and for wet inking. This was concluded from the less clear peak separation in their histograms of the adhesive force mappings on the patterned samples prepared with the contact-inking method than the wet-inking method. In other words, mixed SAMs were formed over the printed area through the further chemical modification with $HOOC(CH_2)_{10}SH$ due to the much higher defect concentration in the printed area with the contact-inking method.

In the case of the wet-inking method, the contamination via vapor phase transfer can be expected to increase with the decrease in the chain lengths of alkanethiols due to the increase in their vapor pressures [65]. Therefore, in addition to the sample used for Fig. 5(c), other samples were prepared using 1-alkanethiols, $CH_3(CH2)_nSH$ with different chain lengths of $n = 11$ and 19 as inks in the wet-inking method. It is clear from these adhesive force maps that the contrast of the adhesive force map becomes better as the chain length increases. It seems to be possible in the beginning that the improvement of the contrast may be interpreted by the lower amount of contamination of the unprinted area by vapor phase transfer. To express the degree of contamination more quantitatively, we had to make histograms from the adhesive force maps as illustrated in Fig. 6. It was found from the histograms (not shown) that average adhesive forces in the CH_3 and the COOH terminated regions could be obtained readily and that the values were always higher in the CH_3 regions than in the COOH regions with the CH_3 tip in the aqueous environment. In addition, it was also found that the two peaks corresponding to the high and low adhesive forces on the CH_3 and the COOH region, respectively, separate more clearly with the increase in the chain lengths. The results looked as if the unprinted regions were covered with a mixed SAM of $HOOC(CH_2)_{10}SH$ and $CH_3(CH_2)_nSH$ and the concentration of 1-alkanethiol in the mixed SAMs increased with the

decrease in the chain lengths as shown in Fig. 6. It was found later, however, from the more careful and quantitative adhesive force measurements that this explanation is not correct.

For a quantitative comparison among measured adhesive forces on different samples, a series of measurements were carried out using the same CH_3 tip. An example is shown in Fig. 7, in which images were taken in this order (from left to right). The same AFM tip was used to avoid the change in the observed adhesive force due to the change in the tip radii. In addition, after every PFM-AFM imaging, the tip surface was reactivated by chemical modification with the same alkanethiol to avoid the effect of surface damage or surface contamination of the CH_3 tip. Finally, the same test sample was observed to confirm reproducible quantitative adhesive force measurements. As shown in Fig. 7, adhesive forces observed on the CH_3-terminal group decreased with the decrease in the chain lengths of the first inks. The results indicate that the vapor phase transfer mechanism is not applicable to the decrease in the observed contrast in the adhesive force mapping. Rather, insufficient ink transfer even in the wet-inking method was found to be responsible for the decrease in the contrast. That is, the mixed monolayer was formed in the printed areas, where the second thiol $HOOC(CH_2)_{10}SH$ was inserted into defects during the following reaction in solution, and became more hydrophilic with the decrease in chain lengths of the first alkane thiol ink due to exposure or protrusion of the terminal −COOH group.

6.2.6 Effect of Experimental Environments and Surface Roughness

The effects of experimental environments such as humid air [10, 49] and various solvents [66] have also been studied extensively for friction and adhesive

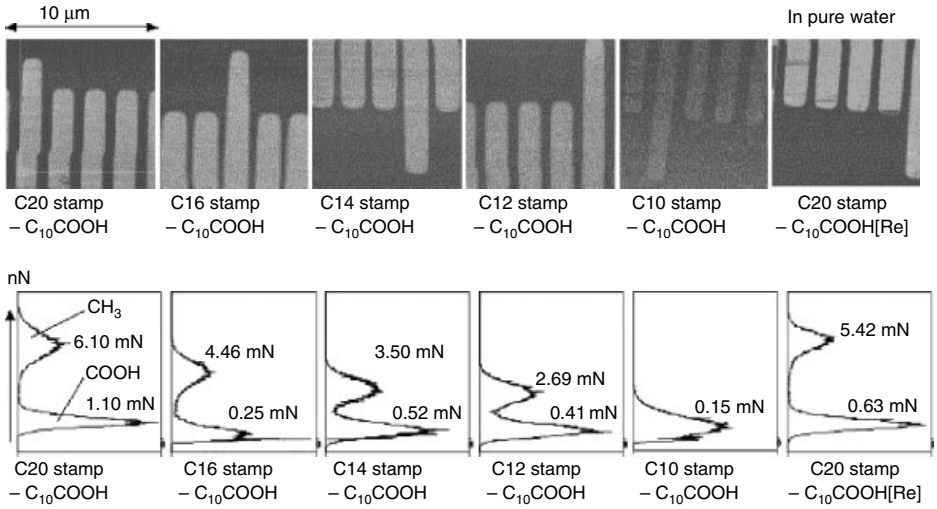


Fig. 7 The adhesive force maps on patterns prepared by the wet-inking method with $CH_3(CH2)_nSH$ inks with different chain lengths followed by the further reaction with $HOOC(CH_2)_{10}SH$ in ethanol.

force measurements. These are important because basically the measured adhesive forces are related to surface energies as well as interfacial energies before and after the contact [19, 20, 23, 27–31, 33–40]. These can be discussed in detail on the bases of intermolecular and surface forces [66]. Effects of the surface roughness of samples have been also studied in detail and discussed in terms of surface forces [55].

6.2.7 Other Approaches for CFM

Friction and adhesive forces have been used widely as measurable properties [67], which can be obtained easily by SPM (Scanning Probe Microscopy) as described above. However, other properties such as surface potentials or contact potential difference (CPD) [29, 58–62], phases in tapping mode AFM [68, 69], and fluorescence intensities under SNOM [70–76] can be used for CFM [17, 67, 77].

To increase lateral resolution in CFM, Lieber and coworkers [78–80] have utilized carbon nanotubes (CNs) as an AFM tip for CFM. The tip end of CNs can be functionalized by using a chemical modification of graphite [21].

Molecular-scale imaging in FFM [46, 81], PFM-AFM [82], noncontact atomic force microscopy (nc-AFM) [83–88] and anisotropy in friction and molecular stick-slip motion [89] have been discussed. Other important issues in CFM are chiral discrimination [90–92] and calibration of AFM cantilever spring constants [67, 93, 94] and tip radii [39, 95].

6.2.8 Concluding Remarks

Dependence of friction and adhesion on surface chemical species on samples has been studied by FFM and PFM-AFM, respectively, using chemically modified AFM tips. Here, we have concentrated on (1) how to modify gold-coated AFM tips reproducibly with thiol compounds, (2) examination of chemical recognition of Si(100) surfaces partially covered with HC monolayer domains using the modified tips, (3) dependence of friction and adhesion on composition of phase-separated domains in mixed HC and FC LB films, (4) CFM of SAMs prepared by μ-CP, and (5) effects of experimental environments and surface roughness. These films were also studied with SSPM, which provided information on permanent dipole moments of the terminal groups. Application of phase imaging by tapping mode AFM, SNOM with tip-sample separation control by AFM (SNOM-AFM), and nc-AFM to chemical or atomic recognition were also introduced.

References

1. C. M. Mate, G. M. McClelland, R. Erlandsson et al., *Phys. Rev. Lett.* **1987**, *59*, 1942–1945.
2. G. Meyer, N. M. Amer, *Appl. Phys. Lett.* **1990**, *57*, 2089–2091.
3. O. Marti, J. Colchero, J. Mlynek, *Nanotechnology* **1990**, *1*, 141–144.
4. J. N. Israelachvili, A. M. Homola, P. M. McGuiggan, *Science* **1988**, *240*, 189–191.
5. E. Meyer, R. Overney, R. Lüthi et al., *Thin Solid Films* **1992**, *220*, 132–137.
6. R. Overney, E. Meyer, J. Frommer et al., *Nature* **1992**, *359*, 133–135.
7. R. M. Overney, E. Meyer, J. Frommer et al., *Langmuir* **1994**, *10*, 1281–1286.
8. M. Fujihira, H. Takano, *Thin Solid Films* **1994**, *243*, 446–449.
9. M. Fujihira, Y. Morita, *J. Vac. Sci. Technol., B* **1994**, *12*, 1609–1613.
10. M. Fujihira, in *Forces in Scanning Probe Methods* (Eds.: H.-J. Güntherodt, D. Anselmetti, E. Meyer), *NATO ASI Series E: Applied Sciences*, Kluwer Academic Publishers, Dordrecht, 1995, pp. 567–591, Vol. 286.

11. M. Fujihira, in *Micro/Nanotribology and its Applications* (Ed.: B. Bhushan), *NATO ASI Series E: Applied Science*, Kluwer Academic Publishers, Dordrecht, 1997, pp. 239–260, Vol. 330.
12. R. W. Carpick, M. Salmeron, *Chem Rev.* **1997**, *97*, 1163–1194.
13. T. Ishida, S. Yamamoto, W. Mizutani et al., *Langmuir* **1997**, *13*, 3261–3265.
14. T. Kajiyama, S. Ge, K. Kojio et al., *Supramol. Sci.* **1996**, *3*, 123–130.
15. H. I. Kim, T. Koini, T. R. Lee et al., *Langmuir* **1997**, *13*, 7192–7196.
16. S. Yamada, J. Israelachvili, *J. Phys. Chem. B* **1998**, *102*, 234–244.
17. C. D. Frisbie, L. F. Rozsnyai, A. Noy et al., *Science* **1994**, *265*, 2071–2074.
18. J.-B. D. Green, M. T. McDermott, M. D. Porter et al., *J. Phys. Chem.* **1995**, *99*, 10960–10965.
19. J. L. Wilbur, H. A. Biebuyck, J. C. MacDonald et al., *Langmuir* **1995**, *11*, 825–831.
20. A. Noy, C. D. Frisbie, L. F. Ronzsnyai et al., *J. Am. Chem. Soc.* **1995**, *117*, 7943–7951.
21. M. Fujihira, in *Topics in Organic Electrochemistry* (Eds.: A. J. Fry, W. E. Britton), Plenum Press, New York, 1986, pp. 255–294.
22. R. Murry, in *Techniques of Chemistry* (Ed.: A. Weissberger), Wiley, New York, 1992, Vol. 22.
23. J. Tien, Y. Xia, G. M. Whitesides, in *Thin Films* (Ed.: A. Ulman), Academic Press, San Diego, 1998, pp. 227–254, Vol. 24.
24. T. Nakagawa, K. Ogawa, T. Kurumizawa et al., *Jpn. J. Appl. Phys.* **1993**, *32*, L294–L296.
25. T. Nakagawa, K. Ogawa, T. Kurumizawa, *J. Vac. Sci. Technol., B* **1994**, *12*, 2215–2218.
26. L. A. Wenzler, G. L. Moyes, G. N. Raikar et al. *Langmuir* **1997**, *13*, 3761–3768.
27. T. Ito, M. Namba, P. Bühlmann et al., *Langmuir* **1997**, *13*, 4323–4332.
28. J. E. Frommer, *Thin Solid Films* **1996**, *273*, 112–115.
29. R. C. Thomas, P. Tangyunyong, J. E. Houston et al., *J. Phys. Chem.* **1994**, *98*, 4493–4494.
30. R. C. Thomas, J. E. Houston, R. M. Crooks et al., *J. Am. Chem. Soc.* **1995**, *117*, 3830–3834.
31. D. V. Vezenov, A. Noy, L. F. Rozsnyai et al., *J. Am. Chem. Soc.* **1997**, *119*, 2006–2015.
32. T. Han, J. M. Williams, T. P. Beebe Jr., *Anal. Chim. Acta* **1995**, *307*, 365–376.
33. S. K. Sinniah, A. B. Steel, C. J. Miller et al., *J. Am. Chem. Soc.* **1996**, *118*, 8925–8931.
34. E. W. van der Vegte, G. Hadziioannou, *J. Phys. Chem. B* **1997**, *101*, 9563–9569.
35. E. W. van der Vegte, G. Hadziioannou, *Langmuir* **1997**, *13*, 4357–4368.
36. M. Fujihira, Y. Okabe, Y. Tani et al., *Ultramicroscopy* **2000**, *82*, 181–191.
37. Y. Okabe, M. Furugori, Y. Tani et al., *Ultramicroscopy* **2000**, *82*, 203–212.
38. A. Rosa, E. Weilandt, S. Hild et al., *Meas. Sci. Technol.* **1997**, *8*, 1333–1338.
39. Th. Stifter, E. Weilandt, O. Marti et al., *Appl. Phys. A* **1998**, *66*, S597–S605.
40. T. Miyatani, M. Horii, A. Rosa et al., *Appl. Phys. Lett.* **1997**, *71*, 2632–2634.
41. T. Miyatani, S. Okamoto, A. Rosa et al., *Appl. Phys. A* **1998**, *66*, S349–S352.
42. T. Ohzono, J. N. Glosli, M. Fujihira, *Jpn. J. Appl. Phys.* **1998**, *37*, 6535–6543.
43. T. Ohzono, J. N. Glosli, M. Fujihira, *Jpn. J. Appl. Phys.* **1999**, *38*, L675–L678.
44. M. Fujihira, T. Ohzono, *Jpn. J. Appl. Phys.* **1999**, *38*, 3918–3931.
45. T. Ohzono, M. Fujihira, *Jpn. J. Appl. Phys.* **2000**, *39*, 6029–6034.
46. T. Ohzono, M. Fujihira, *Phys. Rev. B* **2000**, *62*, 17055–17071.
47. J. C. Lin, W. H. Chuang, *J. Biomed. Mater. Res.* **2000**, *51*, 413–423.
48. T. Arai, D. Aoki, Y. Okabe et al., *Thin Solid Films* **1996**, *273*, 322–326.
49. M. Fujihira, D. Aoki, Y. Okabe et al., *Chem. Lett.* **1996**, *25*, 499–500.
50. M. Fujihira, Y. Tani, M. Furugori et al., *Stud. Surf. Sci. Catal.* **2001**, *132*, 469–476.
51. A. Kumar, G. M. Whitesides, *Appl. Phys. Lett.* **1993**, *63*, 2002–2004.
52. Y. Xia, G. M. Whitesides, *Angew. Chem., Int. Ed.* **1998**, *37*, 550–575.
53. B. Michel, A. Bernard, A. Bietsch et al., *IBM J. Res. Dev.* **2001**, *45*, 697–719.
54. M. Fujihira, Y. Tani, M. Furugori et al., *Ultramicroscopy* **2001**, *86*, 63–73.
55. F. Sato, H. Okui, U. Akiba et al., *Ultramicroscopy* **2003**, *97*, 303–314.
56. M. Fujihira, M. Furugori, U. Akiba et al., *Ultramicroscopy* **2001**, *86*, 75–83.
57. L. Libioulle, A. Bietsch, H. Schmid et al., *Langmuir* **1999**, *15*, 300–304.
58. M. Fujihira, *Annu. Rev. Mater. Sci.* **1999**, *29*, 353–380.
59. K. Yagi, M. Fujihira, *Appl. Surf. Sci.* **2000**, *157*, 405–411.
60. M. Fujihira, H. Kawate, M. Yasutake, *Chem. Lett.* **1992**, *21*, 2223–2226.

61. M. Fujihira, H. Kawate, *Thin Solid Films* **1994**, *242*, 163–169.
62. M. Fujihira, H. Kawate, *J. Vac. Sci. Technol., B* **1994**, *12*, 1604–1608.
63. H. Muramatsu, N. Chiba, M. Fujihira, *Appl. Phys. Lett.* **1997**, *71*, 2061–2063.
64. Y. Horiuchi, K. Yagi, T. Hosokawa et al., *J. Microsc.* **1999**, *194*, 467–471.
65. E. Delamarche, H. Schmid, A. Bietsch et al., *J. Phys. Chem. B* **1998**, *102*, 3324–3334.
66. J. Israelachivili, *Intermolecular & Surface Forces*, 2nd edition, Academic Press, San Diego, 1992.
67. A. Noy, D. V. Vezenov, C. M. Lieber, *Annu. Rev. Mater. Sci.* **1997**, *27*, 381–421.
68. K. Sasaki, Y. Koike, H. Azehara et al., *Appl. Phys. A* **1998**, *66*, S1275–S1277.
69. A. Noy, C. H. Sanders, D. V. Vezenov et al. *Langmuir* **1998**, *14*, 1508–1511.
70. R. C. Dunn, *Chem. Rev.* **1999**, *99*, 2891–2927.
71. D. W. Pohl, D. Courjon (Eds.), *Near Field Optics, NATO ASI Series E: Applied Sciences*, Kluwer Academic Publishers, Dordrecht, 1993, Vol. 242.
72. O. Marti, R. Moeller (Eds.), *Photons and Local Probes, NATO ASI Series E: Applied Sciences*, Kluwer Academic Publishers, Dordrecht, 1995, Vol. 300.
73. M. Nieto-Vesperinas, N. Garcia (Eds.), *Optics at the Nanometer Scale, Imaging and Storing with Photonic Near Fields, NATO ASI Series E: Applied Sciences*, Kluwer Academic Publishers, Dordrecht, 1996, Vol. 319.
74. M. A. Paesler, P. J. Moyer, *Near-Field Optics, Theory, Instrumentation, and Applications*, John Wiley & Sons, New York, 1996.
75. M. Ohtsu (Ed.), *Near-Field Nano/Atom Optics and Technology*, Springer-Verlag, Tokyo, 1998.
76. X. Zhu, M. Ohtsu (Eds.), *Near Field Optics: Principles and Applications*, World Scientific, Singapore, 2000.
77. H. Takano, J. R. Kenseth, S.-S. Wong et al., *Chem. Rev.* **1999**, *99*, 2845–2890.
78. S. S. Wong, E. Joselevich, A. T. Woolley et al., *Nature* **1998**, *394*, 52–55.
79. S. S. Wong, A. T. Woolley, E. Joselevich et al., *J. Am. Chem. Soc.* **1998**, *120*, 8557–8558.
80. S. S. Wong, A. T. Woolley, E. Joselevich et al., *Chem. Phys. Lett.* **1999**, *306*, 219–225.
81. H. Takano, M. Fujihira, *J. Vac. Sci. Technol., B* **1996**, *14*, 1272–1275.
82. Y. Okabe, U. Akiba, M. Fujihira, *Appl. Surf. Sci.* **2000**, *157*, 398–404.
83. S. Fujii, U. Akiba, M. Fujihira, *Appl. Surf. Sci.* **2003**, *210*, 79–83.
84. S. Fujii, U. Akiba, M. Fujihira, *Nanotechnology* **2004**, *15*, S19–S23.
85. T. Shiokawa, T. Ohzono, M. Fujihira, *Appl. Surf. Sci.* **2003**, *210*, 117–122.
86. B. Bat-Uul, S. Fujii, T. Shiokawa et al., *Nanotechnology* **2004**, *15*, 710–715.
87. S. Fujii, M. Fujihira, *Jpn. J. Appl. Phys.* **2006**, *45*, 1986–1991.
88. S. Fujii, M. Fujihira, *Nanotechnology* **2006**, *17*, S112–S120.
89. M. R. Overney, H. Takano, M. Fujihira et al., *Phys. Rev. Lett.* **1994**, *72*, 3546–3549.
90. R. McKendry, M.-E. Theoclitou, T. Rayment et al., *Nature* **1998**, *391*, 566–568.
91. R. McKendry, M.-E. Theoclitou, C. Abell et al., *Jpn. J. Appl. Phys.* **1999**, *38*, 3901–3907.
92. M. Mahapatro, C. Gibson, C. Abell et al., *Ultramicroscopy* **2003**, *97*, 297–301.
93. D. D. Koleske, G. U. Lee, B. I. Gans et al., *Rev. Sci. Instrum.* **1995**, *66*, 4566–4574.
94. C. T. Gibson, B. L. Weeks, C. Abell et al., *Ultramicroscopy* **2003**, *97*, 113–118.
95. K. Akimoto, F. Sato, T. Morikawa et al., *Jpn. J. Appl. Phys.* **2004**, *43*, 4492–4498.

7.1 Sum Frequency Generation (SFG) Evaluation of the Chemically Modified Solid Surface

Shen Ye, Kohei Uosaki
Hokkaido University, Sapporo, Japan

7.1.1 Introduction

It is well known that the surface/interface of materials usually exhibits properties and behaviors that are considerably different from the bulk phase. The functionality of the solid surface modified by an organic thin film, such as a self-assembled monolayer (SAM), Langmuir–Blodgett (LB) ultrathin film or polymer thin film, depends significantly on its surface molecular structure [1–4]. Therefore, elucidation and control of the surface molecular structure is essential to understand the novel functionality introduced by the modification. Most existing surface techniques require the sample to be placed in an ultrahigh vacuum (UHV) environment [5] and are therefore unsuitable for studies in either air or liquid. On the other hand, as comprehensively reviewed in this chapter, a number of modern instrumental analysis methods, such as infrared reflection absorption spectroscopy (IRRAS), Raman scattering, surface plasmon resonance (SPR) and ellipsometry, can provide useful information about the molecular structure, orientation, and conformation on the modified electrode surfaces under both ex situ and in situ conditions. Most of these optical techniques are, however, not intrinsically surface-specific, and hence it is hard to distinguish the contribution from the surface and bulk of the materials (e.g. LB or polymer thin films). Scanning tunneling microscope (STM) and atomic force microscope (AFM) measurements can probe the surface morphology with an atomic resolution. Difficulties are, however, often encountered to explain the real meaning of the image observed because it does not always provide direct structural information of the molecules arranged on the surface. Surface enhanced Raman scattering (SERS) [6–8] and surface enhanced infrared absorption spectroscopy (SEIRAS) [9] are used to detect the surface species but difficulties in sample preparation and quantitative spectral analysis limit their application.

As a 2nd-order nonlinear optical technique, sum frequency generation (SFG) is attracting much attention in surface science due to its high surface selectivity, sensitivity, and versatile applicability, and is now used at the gas/solid,

Encyclopedia of Electrochemistry. Edited by A.J. Bard and M. Stratmann
Vol. 10 *Modified Electrodes*. Edited by M.Fujihira, I.Rubinstein, and J.F.Rusling
Copyright © 2007 Wiley-VCH Verlag GmbH & Co. KGaA, Weinheim. ISBN: 978-3-527-30402-8

gas/liquid, liquid/liquid, solid/solid, and liquid/solid interfaces in various environments (UHV, air, liquid, etc.) [10–12]. Not only the static interfacial molecular structures [13–20] but also the ultrafast surface dynamics [21–27] can be investigated by this method. The number of papers on experimental and theoretical SFG studies is increasing rapidly in the multidisciplinary research field of physics, chemistry, polymer science, and biophysics. A great deal of valuable structure information at the interface has been acquired by the nonlinear optical technique, which is difficult to obtain by the conventional vibrational spectroscopy.

In this section, after an introduction on theory and experimental setup of SFG, we will briefly review some recent results of SFG studies on the interfacial molecular structure of the solid surface modified by organic thin films. It should be mentioned here that SFG is still in its infancy compared to infrared and Raman spectroscopy. More efforts including theoretical analysis [28–33] are required to understand its real capability and to make this method as a routine spectroscopic technique.

7.1.2 Theory

In an electric field (E), a dipole moment (μ) in a molecule can be induced as a result of charge separation and can be written as a power series of E [10, 34]:

$$\begin{aligned}\mu &= \mu^0 + \mu^{(1)} + \mu^{(2)} + \mu^{(3)} + \cdots \\ &= \mu^0 + \sum_i \sum_j \alpha_{ij} E_i + \sum_i \sum_{jk} \beta_{ijk} E_j E_k \\ &\quad + \sum_i \sum_{jkl} \gamma_{ijkl} E_j E_k E_l + \cdots \end{aligned} \tag{1}$$

where μ^0 is the static dipole moment, α is the linear polarizability while β and γ are the 1st and 2nd hyperpolarizabilities representing the nonlinear response to the field. α, β, and γ are tensors of rank 2, 3, and 4 respectively, and consist of 9 (3^2), 27 (3^3), and 81 (3^4) elements. For example, the tensor element β_{ijk} represents Cartesian component i ($i = x, y, z$) of the hyperpolarizability induced by Cartesian components j and k ($j, k = x, y, z$) of the electric field, respectively. For convenience, $\mu^{(n)}$ is usually expressed by the shorter notation $\alpha \cdot E(n = 1)$, $\beta : EE(n = 2)$, and $\gamma \vdots EEE(n = 3)$.

Generally, in bulk material, it is more convenient to express the response to the external electric field in terms of the polarization (P), which is defined as the average dipole moment per unit volume:

$$\begin{aligned}P &= N\langle\mu\rangle \\ &= P^{(0)} + P^{(1)} + P^{(2)} + P^{(3)} + \cdots \\ &= P^{(0)} + \chi^{(1)} \cdot E + \sum_i \sum_{jk} \chi^{(2)}_{ijk} E_j E_k \\ &\quad + \sum_i \sum_{jkl} \chi^{(3)}_{ijkl} E_j E_k E_l + \cdots \\ &= P^{(0)} + \chi^{(1)} \cdot E + \chi^{(2)} : EE \\ &\quad + \chi^{(3)} \vdots EEE + \cdots \end{aligned} \tag{2}$$

where N is the molecule density and the angular bracket indicates an ensemble average over all of the dipoles in the medium. $\chi^{(i)}$ is the ith-order susceptibility as an $(i + 1)$ rank tensor. It is worth noting that the field in the above equations is the total field applied, which can be a superposition of many fields at different frequencies. When the total field is expanded in terms of its Fourier components, the polarization

will consist of several components oscillating at various frequencies. For example, if the total field consists of two waves oscillating at ω_1 and ω_2 ($E_1(r)\cdot\cos\omega_1 t$, $E_2(r)\cdot\cos\omega_2 t$), then the 2nd-order nonlinear polarization $P^{(2)}$ can be written as:

$$\begin{aligned} P^{(2)} &= \chi^{(2)} : EE \\ &= \chi^{(2)} : (E_1 + E_2)(E_1 + E_2) \\ &= \frac{1}{2}\left\{\begin{array}{l} C + \chi^{(2)} : E_1(r)E_1(r)\cos 2\,\omega_1 t \\ +\chi^{(2)} : E_2(r)E_2(r)\cos 2\,\omega_2 t \\ +2\chi^{(2)} : E_1(r)E_2(r)[\cos(\omega_1+\omega_2)t \\ +\cos(\omega_1-\omega_2)t] \end{array}\right\} \end{aligned} \tag{3}$$

where C equals $\chi^{(2)} : E_1(r)E_1(r) + \chi^{(2)} : E_2(r)E_2(r)$. As shown in Eq. (3), $P^{(2)}$ radiation has components oscillating at double ($2\,\omega_1$, $2\,\omega_2$), sum ($\omega_1+\omega_2$), difference frequencies ($\omega_1-\omega_2$) of the two applied fields, and a DC term at zero frequency. The oscillating polarizations will emit light at diverse frequencies (ω) with intensities proportional to the square of each $P^{(2)}$ (ω) [10, 34]. This is the origin for the 2nd-order nonlinear optical process such as second harmonic generation (SHG), SFG and difference frequency generation (DFG). It is clear that SHG can be regarded as a special case of SFG when $\omega_1 = \omega_2$.

As shown in Eq. (3), $P^{(2)}$ depends on the magnitude of $\chi^{(2)}$. Since $\chi^{(2)}$ is invariant in a centrosymmetric material but changes its sign by the inversion operation, $\chi^{(2)}$ must be zero in the bulk medium with inversion symmetry, that is, the intrinsic symmetry properties of $\chi^{(2)}$ forbid 2nd-order nonlinear processes to occur in centrosymmetric materials such as gases, liquids, and a large number of solids [10–12]. Under the electric dipole approximation, $P^{(2)}$ radiation only occurs in noncentrosymmetric solids and at interfaces between centrosymmetric media where the bulk symmetry is broken [10]. Therefore, $P^{(2)}$ radiation (SFG, DFG, and SHG) can be used to probe the physical and chemical properties of surfaces or interfaces of centrosymmetric materials.

Let us consider an SFG process in which two laser beams oscillating at visible (ω_{vis}) and infrared (ω_{IR}) frequencies are mixed on an interface in (a) copropagating and (b) counterpropagating incident geometry as shown in Fig. 1. The interface is assumed to be in the *xy*-plane while the incident plane of the visible and IR beams are taken to be in the *xz*-plane in the Cartesian coordinate system in the laboratory.

Since the energy ($E = h\omega$) and momentum parallel to the light propagating direction are conserved [10], we have

$$\omega_{SFG} = \omega_{vis} + \omega_{IR} \tag{4a}$$

$$p_{x,SFG} = p_{x,vis} + p_{x,IR} \tag{4b}$$

As $p = h/\lambda$ and $\omega = 2\pi c/\lambda$, the above equations can be written as,

$$\frac{1}{\lambda_{SFG}} = \frac{1}{\lambda_{vis}} + \frac{1}{\lambda_{IR}} \tag{5a}$$

$$\frac{\sin\theta_{SFG}}{\lambda_{SFG}} = \frac{\sin\theta_{vis}}{\lambda_{vis}} + \frac{\sin\theta_{IR}}{\lambda_{IR}} \tag{5b}$$

Thus, SFG wavelength (λ_{SFG}) and its emitting direction (θ_{SFG}) can be exactly calculated from the incident beam conditions. In the case of DFG, similarly, we have,

$$\frac{1}{\lambda_{DFG}} = \frac{1}{\lambda_{vis}} - \frac{1}{\lambda_{IR}} \tag{6a}$$

$$\frac{\sin\theta_{DFG}}{\lambda_{DFG}} = \frac{\sin\theta_{vis}}{\lambda_{vis}} - \frac{\sin\theta_{IR}}{\lambda_{IR}} \tag{6b}$$

that is, both SFG and DFG from a surface are coherent and are propagating in a well-defined direction away from the surface.

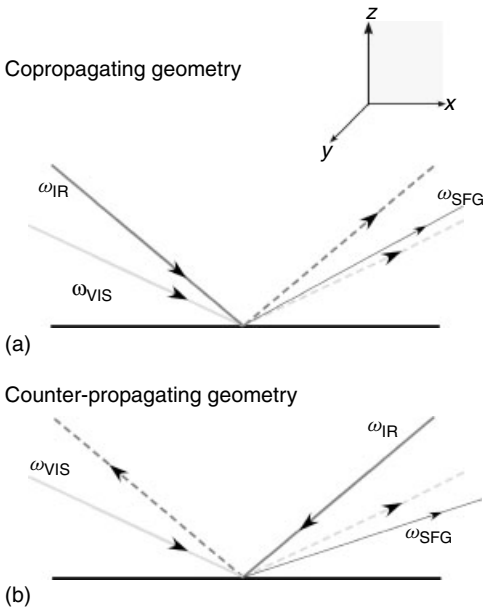


Fig. 1 Incident and emitted light for SFG using (a) copropagating and (b) counterpropagating incident geometry. The visible (ω_{vis}, 800 nm) and IR (ω_{IR}, 3300 nm) lasers are incident at 65° and 50°, respectively. A Cartesian coordination system is shown as inset. See text for details.

Under the electric dipole approximation, and assuming that both ω_{sum} and ω_{vis} are far away from electronic resonance in the molecule, $\chi^{(2)}_{ijk}$ can be expressed as [35, 36],

$$\chi^{(2)}_{ijk} \propto \frac{N M_{ij} A_k}{\hbar(\omega_{IR} - \omega_v + i\Gamma_v)} \qquad (7)$$

where ω_v and Γ_v are resonant frequency and damping width for an excited vth vibrational level, respectively. M_{ij} and A_k are the Raman polarizability tensor and IR dipole moment of the vth vibrational mode, respectively. According to Eq. (7), a vibrational mode must be both IR ($A_k \neq 0$) and Raman ($M_{ij} \neq 0$) active to give rise to SFG. When the frequency of IR (ω_{IR}) is equal to ω_v, $\chi^{(2)}$ is resonantly enhanced and a peak is observed in the SFG spectrum. By measuring an SFG spectrum as a function of IR frequency, the vibrational modes of the molecules at the surface/interface can be probed. It should be noted here that the excited states for visible and SFG light may be virtual ones in the IR-resonant SFG spectroscopy. SFG spectrum is expected to be enhanced when visible and/or SFG are doubly resonant with existing surface states as expected by theory and experiments [31, 37].

By measuring individual $\chi^{(2)}$, one can determine the structure and orientation of the molecule on the interface. As described above, $\chi^{(2)}$ is a tensor of rank 3 and has 27 elements. However, the number of the nonzero $\chi^{(2)}$ elements can be often reduced by invoking symmetry constraints. For example, there are only four independent nonzero elements for a surface with azimuthally isotropic symmetry: $\chi^{(2)}_{zzz}$, $\chi^{(2)}_{xxz} = \chi^{(2)}_{yyz}$, $\chi^{(2)}_{xzx} = \chi^{(2)}_{yzy}$, $\chi^{(2)}_{zxx} = \chi^{(2)}_{zyy}$. A surface with the C_{3v} symmetry only consists of five independent elements as $\chi^{(2)}_{zzz}$, $\chi^{(2)}_{xxz} = \chi^{(2)}_{yyz}$, $\chi^{(2)}_{xzx} = \chi^{(2)}_{yzy}$, $\chi^{(2)}_{zxx} = \chi^{(2)}_{zyy}$, $\chi^{(2)}_{xxx} = -\chi^{(2)}_{yyx} = -\chi^{(2)}_{xyy} = -\chi^{(2)}_{yxy}$. [10, 38, 39]

It should be mentioned here that these nonlinear polarizations are important only when an intense electric field is applied ($\sim 10^{10}$–10^{12} V m^{-1}), which is usually generated by a pulsed laser. Generally, the SFG intensity in terms of photon per pulse can be expressed by [12]:

$$\begin{aligned} S(\omega_s) &= \frac{I_{SFG}}{\hbar\omega_{SFG}} AT \\ &= \frac{8\pi^3 \omega_{SFG}^2 \sec^2\theta_{SFG}}{\hbar c^3 n_{SFG} n_{vis} n_{IR}} \\ &\quad \times \left| \sum_i \sum_{j,k} L_{ii}(\omega_{SFG}) \chi_{ijk}^{(2)} L_{jj}(\omega_{vis}) \right. \\ &\quad \left. \times L_{kk}(\omega_{IR}) \right|^2 I_{vis} I_{IR} AT \end{aligned} \tag{8}$$

Here I_{SFG}, $I_{vis,}$ and I_{IR} are the power densities of SFG, visible and infrared beams, respectively, while n_ω is the refractive index. A is the beam cross-section at the interface and T is the pulse duration. L_{ii}, $L_{jj,}$ and $L_{kk}(i, j, k = x, y, z)$ are the Fresnel coefficients relating the input field to the field in the interfacial layer and are given by [15]:

$$L_{xx}(\omega) = \frac{2n_1(\omega)\cos\theta_2}{n_2(\omega)\cos\theta_1 + n_1(\omega)\cos\theta_2} \tag{9a}$$

$$L_{yy}(\omega) = \frac{2n_1(\omega)\cos\theta_1}{n_2(\omega)\cos\theta_2 + n_1(\omega)\cos\theta_1} \tag{9b}$$

$$\begin{aligned} L_{zz}(\omega) &= \frac{2n_2(\omega)\cos\theta_1}{n_2(\omega)\cos\theta_1 + n_1(\omega)\cos\theta_2} \\ &\quad \times \left(\frac{n_1(\omega)}{n'(\omega)}\right)^2 \end{aligned} \tag{9b}$$

where n' is the refractive index of the interfacial layer between n_1 and n_2. Since the interfacial layer is only one or a few monolayers thick, n' can be different from the bulk value. To quantitatively deduce the molecular structure on the interface, it is necessary to determine the individual $\chi^{(2)}$ components. As shown in Eq. 8, the Fresnel coefficient, which can be also regarded as a field correction, is important to determine the absolute value of $\chi^{(2)}$ and is also useful to optimize the experimental conditions (see below). Usually, $\chi^{(2)}$ elements are determined from the SFG measurements with different polarization combination, such as *ssp*, *sps*, *pss*, and *ppp*, where the polarizations are listed in the order of decreasing frequency (SFG, visible and infrared). For example, the SFG intensities of an isotropic surface with the polarization combinations of *ssp*, *sps*, and *ppp* can be related to their $\chi^{(2)}$ as:

$$I_{ssp} \propto |L_{yyz}\sin\theta_{IR} \cdot \chi_{yyz}^{(2)}|^2 \cdot I_{vis} I_{IR} \tag{10a}$$

$$I_{sps} \propto |L_{yzy}\sin\theta_{vis} \cdot \chi_{yzy}^{(2)}|^2 \cdot I_{vis} I_{IR} \tag{10b}$$

$$\begin{aligned} I_{ppp} &\propto \left| \begin{array}{l} -L_{xxz}\cos\theta_{SFG}\cos\theta_{vis}\sin\theta_{IR} \cdot \chi_{xxz}^{(2)} \\ -L_{xzx}\cos\theta_{SFG}\sin\theta_{vis}\cos\theta_{IR} \cdot \chi_{xzx}^{(2)} \\ +L_{zxx}\sin\theta_{SFG}\cos\theta_{vis}\cos\theta_{IR} \cdot \chi_{zxx}^{(2)} \\ +L_{zzz}\sin\theta_{SFG}\sin\theta_{vis}\sin\theta_{IR} \cdot \chi_{zzz}^{(2)} \end{array} \right|^2 \\ &\quad \cdot I_{vis} I_{IR} \end{aligned} \tag{10c}$$

where L_{ijk} $(i, j, k = x, y, z)$ is defined as a product of L_{ii} (ω_{SFG}), L_{jj} (ω_{vis}), and L_{kk} (ω_{IR}). Approximately, the *ssp* polarization is known to be sensitive to the vibrational modes with transition moments that have components perpendicular to the surface, whereas, the *sps* and *pss* to those parallel to the surface. The intensity under *ppp* polarization contains contributions from four elements, that is, both perpendicular and parallel components will be present in the *ppp*-polarized spectra.

7.1.3 Quantitative Analysis of SFG Spectra

Generally, both resonant ($\chi^{(2)}_{R,\upsilon}$) and nonresonant ($\chi^{(2)}_{\mathrm{NR}}$) components contribute to $\chi^{(2)}$ observed; thus, the intensity of an SFG spectrum can be expressed as:

$$
\begin{aligned}
I_{\mathrm{SFG}} &\propto \left| \sum_{\nu} \chi^{(2)}_{\mathrm{R},\upsilon} + \chi^{(2)}_{\mathrm{NR}} \right|^2 \\
&= \left| \sum_{\nu} \chi^{(2)}_{\mathrm{R},\upsilon} e^{-i\varepsilon_\nu} + \chi^{(2)}_{\mathrm{NR}} e^{-i\delta(\omega)} \right|^2 \\
&= \left| \sum_{\nu} \frac{A_\upsilon}{\omega_{\mathrm{IR}} - \omega_\upsilon + i\Gamma_\nu} e^{-i\varepsilon_\nu} \right. \\
&\quad \left. + \chi^{(2)}_{\mathrm{NR}} e^{-i\delta(\omega)} \right|^2 \qquad (11)
\end{aligned}
$$

$\delta(\omega)$ is a frequency-dependent phase for the nonresonant background, mainly from substrate. Here, ε_ν is the relative phase angle for each vibrational mode. Normally, one assumes that these resonance modes are in phase ($\varepsilon_\nu = 0$) or out of phase ($\varepsilon_\nu = \pi$), which can give rise to constructive or destructive interference between them. Furthermore, the phase difference, $\varepsilon_\nu - \delta$, between the resonance mode and nonresonant background will significantly affect the shape of the SFG spectra when the nonresonant background cannot be ignored. The Lorentzian-type function is usually employed to analyze the SFG spectra.

Figure 2 gives an example to show how the shape of an SFG spectrum is considerably influenced by cross-section terms in Eq. (11). The dotted lines in Figs. (2a

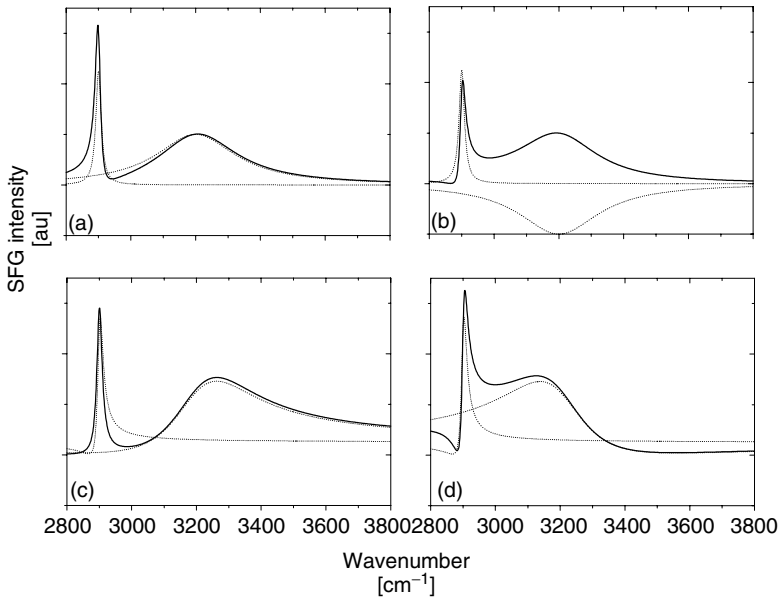


Fig. 2 Simulation of SFG spectra using Eq. (11) with two resonance modes ($\omega_1 = 2900\ \mathrm{cm}^{-1}$, $\omega_1 = 3200\ \mathrm{cm}^{-1}$) under the following conditions: (a) $A_1 = 15$, $\Gamma_1 = 10$, $A_2 = 150$, $\Gamma_2 = 150$, $\chi_{\mathrm{NR}} = 0$, $\varepsilon_1 = \varepsilon_2 = 0$; (b) same with (a) except $\varepsilon_2 = \pi$; (c) same with (a) except $\chi_{\mathrm{NR}} = 0.5$ and $\delta = 0$; (d) same with (b) except $\chi_{\mathrm{NR}} = 0.5$ and $\delta = 0$. See text for details.

and b) show the simulated SFG spectra from two independent resonance modes at $2900\,\mathrm{cm}^{-1}$ ($A_1 = 15, \Gamma_1 = 10$) and $3200\,\mathrm{cm}^{-1}$ ($A_2 = 150, \Gamma_2 = 150$), where the nonresonant background is assumed to be zero ($|\chi_{\mathrm{NR}}| = 0$) and where the upward peak components have a phase angle of 0 and the downward peak components have a phase angle of π. If the two peak components are in phase ($\varepsilon_1 = \varepsilon_2 = 0$, Fig. 2a), the SFG spectrum shows a small tail on the lower wavenumber side of Peak 1 and a deep valley between Peak 1 and 2. If the two peak components are out of phase $\varepsilon_1 = 0$, $\varepsilon_2 = \pi$, Fig. 2b), the SFG intensity on the region of Peak 1 is lower and the valley between Peaks 1 and 2 is shallower than that of $\varepsilon_1 = \varepsilon_2 = 0$. Furthermore, Figs. (2c and 2d) show the same result as that shown in Figs. (2a and 2b) except an additional nonresonant background ($|\chi_{\mathrm{NR}}| = 0.5, \delta = 0$) is included, respectively. Again, the spectral shape and relative intensity in the simulated SFG spectra are largely affected by the phase and relative intensity of each resonant component as well as those of the nonresonant signal. The effect of the nonresonant signal becomes very important when some metal substrates, such as Au and Ag, are used, which have electronic transition bands in the visible frequency region in the normal SFG measurement. Therefore, to quantitatively extract the information of the vibrational mode (such as frequencies, line widths, and mode strengths), generally, one has to fit the SFG spectrum by using an appropriate expression for $\chi^{(2)}$ such as Eq. (11). A quantitative discussion is not possible until a reliable fitting analysis for the SFG spectrum has been carried out.

SFG spectroscopy has been successfully applied to determine the orientation and conformation of a lot of groups, such as methyl (CH_3) [38–41] and phenyl [42–44] on many organic thin film surfaces. As an example, a brief description about the procedures for estimating the orientation of the CH_3 group in a long-chain hydrocarbon molecule is given below.

Hirose et al. treated the local symmetry of the terminal CH_3 group in a hydrocarbon molecule to a distorted C_{3v} and discussed the formulas for the analysis of the C–H stretching modes of CH_3 group observed by SFG measurements [38, 39]. On the basis of these discussions, $\chi^{(2)}$ expressions for the symmetric(s) and asymmetric (as) C–H stretching modes of CH_3 group can be given in Eqs. (12) and (13), respectively [41].

$$\chi^{(2)}_{\gamma\gamma z,\mathrm{s}} = \frac{N L_{\gamma\gamma z}\beta_{ccc}}{2} \times [(r+1)\langle\cos\theta\rangle + (r-1)\langle\cos^3\theta\rangle] \tag{12a}$$

$$\chi^{(2)}_{\gamma z\gamma,\mathrm{s}} = -\frac{N L_{\gamma z\gamma}\beta_{ccc}}{2} \times [(r-1)(\langle\cos\theta\rangle - \langle\cos^3\theta\rangle)] \tag{12b}$$

$$\chi^{(2)}_{\gamma\gamma z,\mathrm{as}} = -N L_{\gamma\gamma z}\beta_{caa}(\langle\cos\theta\rangle - \langle\cos^3\theta\rangle) \tag{13a}$$

$$\chi^{(2)}_{\gamma z\gamma,\mathrm{as}} = N L_{\gamma z\gamma}\beta_{caa}\langle\cos^3\theta\rangle \tag{13b}$$

where $r = \beta_{aac}/\beta_{ccc}$ is the ratio between the two independent components of the molecular hyperpolarizability in a molecular-fixed coordinate (a, b, c), and θ is defined as the tilt angle between the c axis of the methyl group and the surface normal. $\langle\rangle$ denotes ensemble average by a distribution function. From Eqs. (12) and (13), we have

$$\frac{\chi^{(2)}_{\gamma\gamma z,\mathrm{as}}}{\chi^{(2)}_{\gamma z\gamma,\mathrm{as}}} = -\frac{L_{\gamma\gamma z}}{L_{\gamma z\gamma}} \times \frac{\langle\cos\theta\rangle - \langle\cos^3\theta\rangle}{\langle\cos^3\theta\rangle} \tag{14a}$$

$$\frac{\chi^{(2)}_{yyz,as}}{\chi^{(2)}_{yyz,s}} = -\frac{\langle\cos\theta\rangle - \langle\cos^3\theta\rangle}{\langle\cos\theta\rangle(1+r) - \langle\cos^3\theta\rangle(1-r)} \times \frac{\beta_{caa}}{\beta_{ccc}} \quad (14b)$$

Since the intensities of SFG spectra with *ssp*- and *sps*-polarization on an isotropic surface can be directly related to $\chi^{(2)}_{yyz}$ and $\chi^{(2)}_{yzy}$, respectively, if one can obtain both *ssp*- and *sps*-SFG spectra for the same sample, the tilt angle (θ) of the terminal CH_3 group and therefore, the tilt angle (α) of the hydrocarbon chain ($\alpha = 35.2 - \theta$) can be estimated from Eq. (14a), after considering the effects of the Fresnel coefficients for the geometry used. Both equations should give similar results if the model is consistent. If only *ssp*-polarized SFG spectrum is available, one has to use Eq. (14b) to do the estimation. However, a number of unknown parameters are included in the Eq. (14b), that is, β_{aac}/β_{ccc} ($\equiv r$) and β_{caa}/β_{ccc}. On the basis of the molecular hyperpolarizabilities for the CH_3 group calculated by Hirose et al., we have $\beta_{caa} \approx -\beta_{aac}$ [41]. Equation (14b) can be further reduced to

$$\frac{\chi^{(2)}_{yyz,as}}{\chi^{(2)}_{yyz,s}} \approx \frac{\langle\cos\theta\rangle - \langle\cos^3\theta\rangle}{\langle\cos\theta\rangle(1+r) - \langle\cos^3\theta\rangle(1-r)} \times r \quad (14c)$$

A range of values of r has been reported between 4 and 1.5 [41, 45–47]. Fig. 3 shows a calculation of $\chi^{(2)}_{yyz,as}/\chi^{(2)}_{yyz,s}$ as a function of orientation of angle (θ) based on the Eq. (14c). Fortunately, the ratio is not very sensitive to r when the θ is less than 40° [48–50]. Generally, the calculations using both Eq. (14a or b) should give similar results otherwise the calculation results are not reliable.

7.1.4 Experimental Setup

Two pulsed laser beams are spatially and temporally overlapped on an interface

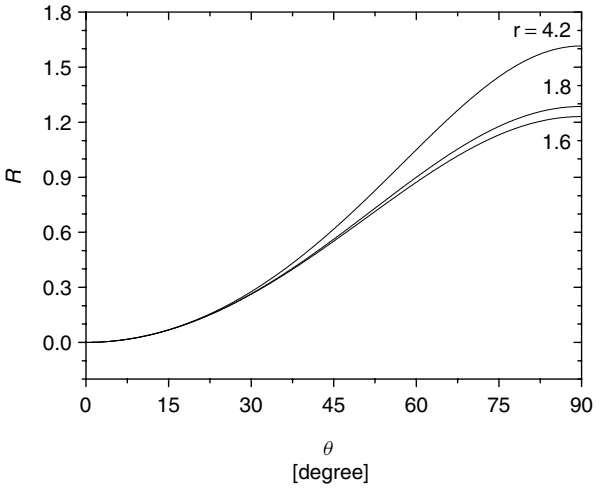


Fig. 3 Theoretical ratio ($R = A_{yyz,as}/A_{yyz,s}$) of methyl group as a function of the tile angle θ for several possible values of r (β_{aac}/β_{ccc}). The calculation assumes a δ-function angular distribution. See text for details.

to generate an SFG signal. In general, frequency of the visible beam is fixed in the visible, near-IR or UV region (ω_{vis}), while that of IR beam is tunable in the infrared region (ω_{IR}).

Generation of a tunable infrared laser is the most important aspect of the IR-visible resonant SFG spectroscopy. The surface SFG spectrum was not realized until the tunable IR source became available [51, 52]. Now, there are a number of ways to generate the infrared pulse for SFG measurements. (1) Free-electron laser (FEL): FEL is based on the generation of coherent light by the interaction of relativistic electrons with a periodic transverse magnetic field structure and provides a tunable ps–fs infrared beam in a wide region from 2.5 μm to several hundred micrometers, which covers the entire molecular vibration and rotation region [53]. Two FELs have been used for SFG: CLIO (France) and FELIX (Netherlands) [54–57]. FEL is especially useful for wavelengths longer than 10 μm [58] but is still too expensive and complicated for normal use. (2) Raman shifting: The output from a tunable dye-laser is directed into a high-pressure multipass cell containing a scattering gas such as H_2 and its wavelength is down-converted to lower wavelengths by the process of stimulated Raman scattering (SRS). A photon efficiency of >20% can be routinely achieved with this method for IR wavelength up to 5 μm [13]. (3) OPG/OPA/DFG: this method has been widely adopted with the progress in all-solid laser and amplifier techniques. By frequency mixing of two synchronous beams (signal, idler, or pump light) generated by an optical parametric generation/amplification (OPG/OPA) stage, in a nonlinear crystal (such as $AgGaS_2$, $LiNbO_3$, and GaSe), a tunable IR pulse with wavelengths as long as 10 μm (15 μm when GaSe is used) can be obtained in the DFG process. A number of homebuilt and commercial systems are available [15–17].

On the other hand, the second harmonic (532 nm) and fundamental (1064 nm) output from ns (nanosecond)–ps (picosecond) Nd:YAG laser as well as fundamental output (~800 nm) from ps (picosecond)–fs (femtosecond) Ti:Sapphire laser are widely used as visible beams [15–17]. By using the OPA/OPG techniques, one can also change the frequency of the visible beam now, which is especially useful in the doubly resonant SFG measurement.

SFG signal can be collected by a gated photomultiplier tube (PMT) or by charge coupled devices (CCD) with spectral filtering and polarization regulation. On the basis of Eq. (8), normally, a ps laser system can yield 10^3–10^5 SFG peak photons/pulse depending on the beam density ($\chi^{(2)} \sim 10^{-15}$ *esu*, a typical value for a monolayer) [12]. Since the SFG radiation is coherent and highly directional, the spatial filtering can be easily employed in addition to spectral filtering to suppress the unwanted luminescence and scattering background noise. Assuming the noise level of a detection system is 0.1 photon/pulse and the detection efficiency is 10% (which are not difficult to obtain for present optical detection systems using PMTs or CCD), the signal-to-noise (S/N) ratio is expected to be ca. 10^3–10^5.

To date, SFG has been carried out mainly with ns or ps light pulses, which typically have bandwidths narrow enough (< several wavenumbers) for the vibrational spectroscopy measurements. One has to scan the IR wavelength during the measurement and it is hard to get an SFG spectrum with high time resolution. On the other hand, the heating effect and

sample damage are other problems for using ns laser pulses.

Since SFG intensity is inversely proportional to the pulse duration, the fs ultrashort laser pulse is expected to give even better performance in SFG measurements [12]. However, as the pulse duration is as short as fs, the frequency bandwidth becomes too wide, which cannot be ignored for vibrational spectroscopy. The pulse duration (Δt, FWHM) and spectral width ($\Delta \nu$, FWHM) of an ultrashort pulse with the Gaussian shape are related to each other by the uncertainty principle in quantum mechanics as [59]:

$$\Delta t \cdot \Delta \nu \geq 0.441 \qquad (15)$$

When the equality is reached in Eq. 15, the pulse is called a Fourier transform–limited pulse. For example, a pulse with duration of 10 ps has a minimum spectral bandwidth $\Delta \nu = 4.41 \times 10^{10}$ Hz, that is, $\Delta \omega = 1.47\ \mathrm{cm}^{-1}$. This spectral width is narrow enough to probe most vibrational structures. When the pulse duration becomes 100 times shorter, $\Delta t = 100$ fs, then $\Delta \nu = 4.41 \times 10^{12}$ Hz ($\Delta \omega = 147\ \mathrm{cm}^{-1}$). This spectral width is too wide to investigate any fine band structures in vibrational spectroscopy; so fs ultrashort pulses were considered to be unsuitable for vibrational spectroscopy. Recently, this situation has changed completely and fs pulses are employed for SFG vibrational spectroscopy after several significant progresses [56, 60]. Richter et al. self-dispersed the broadband SFG signal generated by an fs IR pulse and a narrowband ps visible pulse, which are generated from a table-top fs laser source, onto a monochromator with a CCD detector [60]. SFG spectra are obtained with relatively short acquisition times and a high S/N ratio in a spectral region of ca. 400 cm^{-1} without tuning IR wavelength. The spectral resolution depends on the input pulse characteristics, particularly the bandwidth of the narrowed visible pulse. Ishibashi et al. generated the narrowband visible pulse ($\lambda = 400$ nm) using a phase-conjugated pulse mixing device with a higher (~30%) conversion efficiency [61]. This pulse can be further used to pump an OPA to obtain wavelength-tunable narrowbandwidth ps laser light in the visible and near-IR region [62]. The SFG systems using fs pulses are now adopted in several labs for the studies of static molecular structures [63–66] as well as ultrafast dynamics [67].

Shen et al. proposed a different Fourier transform (FT) approach using fs pulses that combines a virtually unlimited spectral resolution with high SFG signals [68]. By varying time delay between two fs IR pulses using a Michelson interferometer, interferograms based on the SFG generated from the IR beams and a visible beam at various delays of visible beam can be obtained. FT of the interferograms yielded the SFG spectra of the organic monolayer on the fused quartz surface which is in agreement with that obtained by conventional SFG measurement. It is expected that an FT–SFG spectrometer with a high resolution can be commercialized by combining with the Michelson interferometer widely used in FTIR spectrometers.

Table 1 briefly summarizes the recent information about the visible and IR light sources used in main groups in the world. It is expected that SFG spectroscopy will be widely employed in more labs such as physical chemistry, electrochemistry, and biophysics if the ultrashort all-solid laser systems become cheaper and reliable.

As already shown in Fig. 1, the incident geometry in the SFG measurement can be either copropagating or counterpropagating [13]. With ns or ps pulses, as estimated

Tab. 1 Several selected SFG groups and their recent studies

	SFG system		
	Visible	***IR***	
Shen group (UC Berkeley)	532 nm, 20 ps 1.064 μm, 25 ps 800 nm, 100 fs	2.5–9 μm 3.2–3.6 μm 2.7–3.6 μm	• Liquid [69–79] • Surfactant [35, 80–84] • Polymer [44, 85–92] • Si(111) [93–95]
Davies group (Cambridge)	532 nm, 8 ns	Raman Shift	• Surfactant [96–103] • LB and thin films [104, 105] • Nanoparticles [106, 107]
Bain group (Oxford)	532 nm, 3–4 ns	1700–3200 cm^{-1} Raman shift	• Surfactant [108–115] • Metal surface [116–119] • Phase transition [120–122]
Tadjeddine group (CNRS)	532 nm, 11 ps 532 nm, 70 ps	2.5–9 μm 2–17 μm, ps–200 fs (CLIO-FEL)	• Electrode interface [54, 123–135] • Dynamics [23, 136] • SAMs [137–139]
Eliel group (Leiden Univ.)	532 nm, 7 ps	10–50 μm, 0.5–2 ps (FELIX)	• SAMs [55, 56, 58]
Richter group (NIST)	795–810 nm, 50–100 fs	2.5–12 μm (BB)	• SAMs [60, 63, 140] • Polymer [43, 141–143]
Uosaki group (Hokkaido Univ.)	532/1064 nm, 20 ps 800 nm, 100 fs	2.3–8.5 μm 2.5–10 μm (BB)	• SAMs [144, 145] • Solid/solution [146–150] • Si(111) [95, 151–153]
Ishibashi group (KAST)	400 nm, 5.3 ps variable	2.5–10 μm (BB)	• SAMs [61, 62, 154] • Si(111) [155]
Wolf group (Freie Univ. Berlin)	800 nm, 110 fs	2–10 μm (BB)	• Dynamics [25, 26, 67, 156] • Water [157]
Guyot-Sionnest group (Chicago Univ.)	532 nm, 8 ps	2–11 μm	• SAM/electrode [158] • Dynamics [24, 159–161]
Daum group (TU Clausthal)	532 nm, 22 ps	2.5–10 μm	• Electrode [162–165]
Somorjai group (UC Berkeley)	532 nm, 20 ps	2000–4000 cm^{-1}	• Catalytic reaction [166–172] • Electrode surface [173–178] • Polymer [179–189]
Chen group (Michigan Univ.)	532 nm, 20 ps	1000–4300 cm^{-1}	• Polymer [18, 49, 190–200]
Baldelli group (Houston Univ.)	532 nm, 20 ps	1000–4000 cm^{-1}	• Liquid [201]
Gewirth group (Univ of Illinos)	532 nm, 12 ps	4–10 μm	• Electrode [202]
Peremans group (Univ. Notre-Dame)	532 nm, 12 ps	2.5–10 μm	• Electrode [148] • SAMs [139, 203–205]

(*continued overleaf*)

Tab. 1 (*continued*)

	SFG system		
	Visible	***IR***	
Dhinojwala group (Univ. of Akron)	800 nm, 15 ns	2700–3200 cm^{-1}	• Polymer [42, 48, 206–208]
Richmond group (Univ. of Oregon)	800 nm, 2 ps	2700–4000 cm^{-1}	• Liquid interface [19, 209–223] • Solid/liquid [224–226]
Cremer group (Texas A&M)	532 nm, 21 ps	2800–3600 cm^{-1}	• Water interface [227–234]
Yeganeh group (Exxon)	532 nm, 7 ns	2.5–10 μm	• Solid/solution [235–237] • Organic thin films [238–240]
Wolfrum group (Munchen Tech. Univ.)	532 nm, 2.7 ps	2400–4200 cm^{-1}	• Liquid [45, 241–243] • Lipid [244, 245]
Shultz group (Tufts Univ.)	532 nm, 20 ps	2500–4000 cm^{-1}	• Liquid [246–252] • TiO_2 film [253, 254]
Allen group (Ohio State Univ.)	800 nm 85 fs 532 nm 29 ps	2500–4000 cm^{-1} (BB)	• Liquid [66, 255–259]
Kakiuchi group (Kyoto Univ.)	775 nm 150 fs	3200–2800 cm^{-1} (BB)	• SAMs [65, 260]
Ouchi group (Nagoya Univ.)	532 nm, 24 ps	2.3–8 μm	• Liquid [261]
Nozoye group (Tsukuba)	532 nm, 20 ps	2.3–8 μm	• Polymer [262–266]
Knoesen group (UC Davies)	532 nm, 22 ps	2–10 μm	• SAMs [267]
Messmer group (Leihigh Univ.)	532 nm, 7 ns	3.1–3.8 μm	• SAMs [268–270] • Polymer [271, 272]
Himmelhaus group (Heidelberg Univ.)	532 nm, 40 ps	2.5–10 μm	• SAMs [273, 274]
Domen group (Tokyo Inst. Tech.)	532 nm, 35 ps	900–3700 cm^{-1}	• Catalytic reaction [275–284] • Time-resolved SFG [27, 285–288]
Florsheimer group (Munster Univ.)	532 nm, 8 ns	2.3–3.7 μm	• SFG/SHG imaging [289–292]
Saykally group (UC Berkeley)	800 nm, 30–80 fs	2.8–10 μm	• SFG imaging [293, 294]
Conboy group (Univ. Utah)	532 nm, ns	2750–3100 cm^{-1}	• Lipid bilayer [295, 296] • Ionic liquid [297]
Ye group (Hokkaido Univ.)	800 nm, 100 fs	2.5–10 μm (BB)	• SAMs and LB films [64, 107, 298, 299] • Polymer [50, 299–301] • Electrode [302]

from Eq. (5b), the counterpropagating geometry has an advantage that the angle between the SFG and reflected pump visible beam is larger than that of the copropagating geometry, which can reduce the influence of the scattering visible light and aid the collection of the SFG light with higher efficiency. With fs laser pulses, copropagating beams must be used as temporal overlap is poor with counterpropagating beams. One has to pay attention to the fact that the shape of the SFG spectra also significantly depends on the incident geometry. Now, copropagating geometry is widely adopted in many labs.

On the other hand, in situ SFG measurements at solid/solution interface will face the problem that IR light will be heavily absorbed by the liquid and thus, SFG signal from solid/solution interface can be greatly attenuated by loss of IR light intensity. This can be minimized through design of a thin-layer cell used in infrared reflection absorption spectroscopy (IRRAS) [13, 16]. In spite of this, it is still hard to investigate the frequency region where IR beam energy loss by the solvent is high.

Another possibility is to direct the laser beams onto the interface through the solid sample under the total internal reflection (TIR) geometry. Figure 4 shows the Fresnel coefficients at (a, c) fused quartz/air interface and (b, d) fused quartz/water interfaces, with polarization combination of (a, b) *ssp* and (c, d) *sps*, as a function of incident angle of visible light at 800 nm (the incident angle for IR beam at 3300 nm is fixed at 50°). It is clear that the local electric fields on these interfaces are significantly dependent on the incident geometry. For

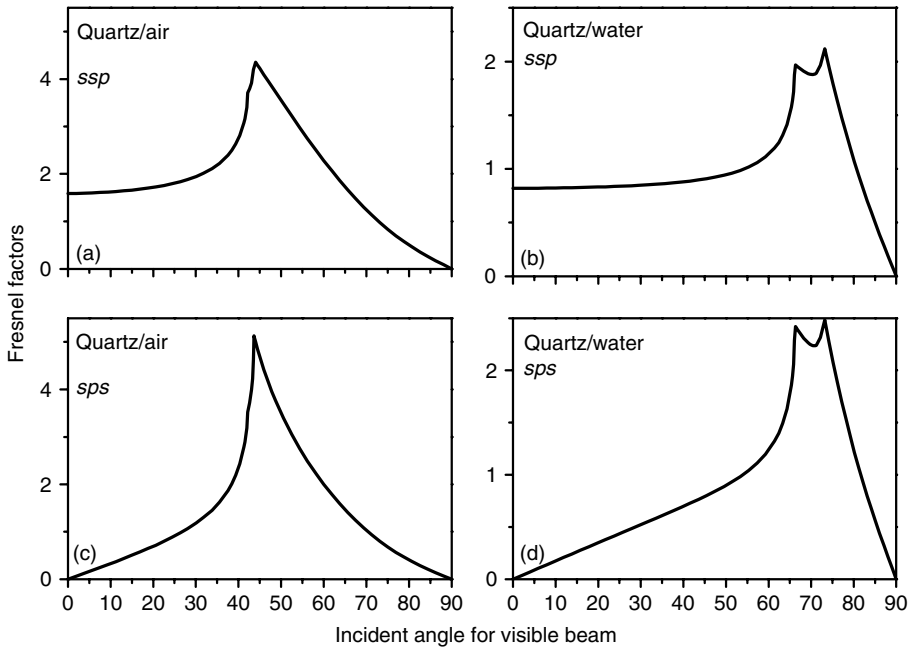


Fig. 4 Fresnel factors calculated for *ssp*- and *sps*-polarization at (a, c) fused quartz/air interface and (b, d) fused quartz/water interface, respectively, as function of incident angle for visible beam (ω_{vis}, 800 nm). The incident angle for IR beam (ω_{IR}, 3300 nm) is fixed at 50°.

example, the strength of the local field reaches a maximum at the critical angle (~45°) at fused quartz/air interfaces and therefore, large enhancement of SFG signal can be obtained if the probe beams are incident at or near the critical angle (Eq. 8). The TIR geometry can also avoid absorption problem of IR by bulk liquid and the mass-transfer limitations by the thin-layer geometry. The TIR geometry has been used so far to examine adsorption on optically transparent substrate [13, 15, 19, 146]. As shown in Fig. 4, if one selects the incident angle of the visible light at ~70° near its critical angle at quartz/water interface (~72°), an enhanced surface electric field can be quite easily obtained. The incident angle of the infrared light was set at 50°, which is far from its critical angle, in order to avoid a large change in the Fresnel coefficient when the frequency of IR beam is scanned in the absorption region of the OH stretching vibration of water [15, 147].

Recently, it has been shown that the interfacial structure at a metal can be examined in a similar fashion by depositing them as ultrathin films on such substrates [116, 144], so that the electrode/electrolyte solution interface can be monitored by SFG measurements during the electrochemical reactions [148].

7.1.5 SFG Studies in the Molecular Structure on the Organic Thin Film Interfaces

As mentioned earlier, SFG is now widely applied in different fields. Table 1 briefly summarizes the SFG studies carried out in some groups. Owing to the specialized purpose and page limitation of the review, we will concentrate our interest on the study of the interfacial molecular structure on the modified solid surfaces by SAM and LB films, both in air and in solution. SFG study on polymer interface is a very interesting subject but is not included here.

7.1.5.1 Modified Solid Surfaces in Gas Phase

Since Shen and coworkers reported the first SFG spectrum of an organic monolayer on a solid substrate [52], a great deal of SFG experiments have been carried out on the solid surfaces modified by the organic thin films such as SAM, LB, and polymer.

7.1.5.1.1 SAMs Figure 5 shows SFG spectra with polarization combination of (a) *ppp*; (b) *ssp*; and (c) *sps* for a fused quartz surface modified by an octadecyltriosilane (OTS) monolayer with a full coverage, in the C–H stretching region between 2800 and 3000 cm^{-1}. The circles in Fig. 5 represent the experimentally observed SFG signals, while the solid lines correspond to the fitting results given in Eq. 11, with various peak components given by dotted lines. The OTS monolayer, which is formed by the coupling reaction between silane group of OTS and the silanol groups on the oxide surface [303], is stable both in air and in solution and has been extensively characterized by SFG measurements [41, 72, 81, 147, 242, 270, 304]. As shown in Fig. 5, the SFG spectra highly depend on the polarization combination. In the *ppp*-SFG spectrum (Fig. 5a), three large peaks at 2879, 2940, and 2970 cm^{-1} are assigned to the C–H symmetric stretching, Fermi resonance between C–H symmetric stretching and the bending overtone, and C–H asymmetric stretching, respectively, of the terminal CH_3 group in OTS monolayer. The *ssp*-SFG spectrum mainly shows two peaks for C–H symmetric stretching and Fermi resonance (Fig. 5b) while the *sps*-SFG spectrum is dominated by

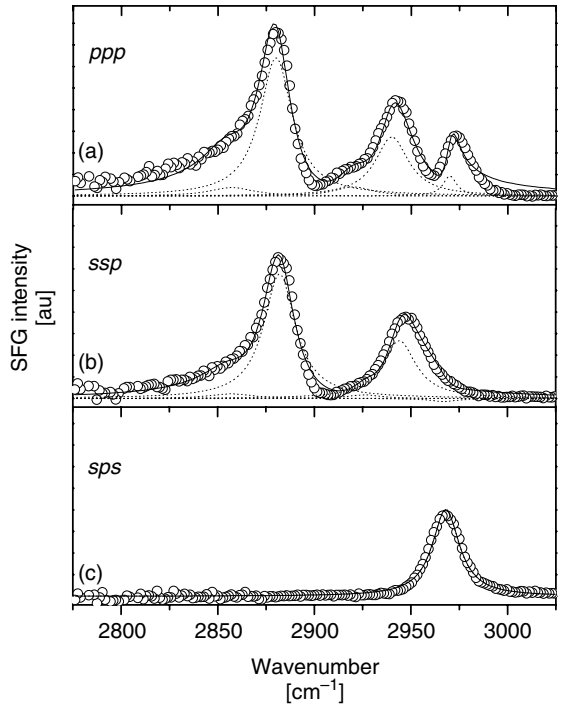


Fig. 5 SFG spectra of fused quartz surface modified by OTS monolayer with polarization combination of (a) *ppp*, (b) *ssp*, and (c) *sps* in the region between 2800 and 3000 cm^{-1}. See text for details.

one peak for C–H asymmetric stretching (Fig. 5c), of the CH_3 group.

On the other hand, the SFG peaks due to CH_2 groups are very weak in comparison with those of the CH_3 group. Since OTS molecules form a densely packed crystalline monolayer in which the hydrocarbon chains are essentially *all-trans*, the *all-trans* orientated CH_2 groups in a nearly centrosymmetric environment give rise to less contribution to the SFG spectra. Only the terminal CH_3 group lacks local centrosymmetry and mainly contributes to the SFG spectrum of the OTS monolayer.

The quantitative fitting results by Eq. (11) reveal that the C–H symmetric stretching and Fermi-resonance modes, which are in phase ($\varepsilon = 0$), have opposite phase with that of C–H asymmetric mode ($\varepsilon = \pi$) in the SFG spectra, as previously pointed out by Wolfrum et al. [45]. The orientation of the terminal CH_3 and hydrocarbon chain can be characterized by using amplitudes for the C–H symmetric ($A_{yyz,s}$) and asymmetric stretching ($A_{yyz,as}$ and $A_{yzy,as}$) determined from the fitting for *ssp* (Fig. 5b) and *sps* spectra (Fig. 5c). Similar conformation can be obtained from Eq. (14a or c). The tilt angle of CH_3 group was estimated to be ca. 20°, and hence hydrocarbon chain decline was ca. 15°.

When the coverage of the OTS is lower, peaks due to the C–H stretching of the CH_2 group are easily observed at 2850 cm^{-1} (symmetric stretching mode) and 2920 cm^{-1} (asymmetric) while those due to CH_3 are significantly decreased, demonstrating that many gauche defects exist and the OTS monolayer becomes more disordered [147, 270]. By using SFG spectroscopy, Messmer et al. found that

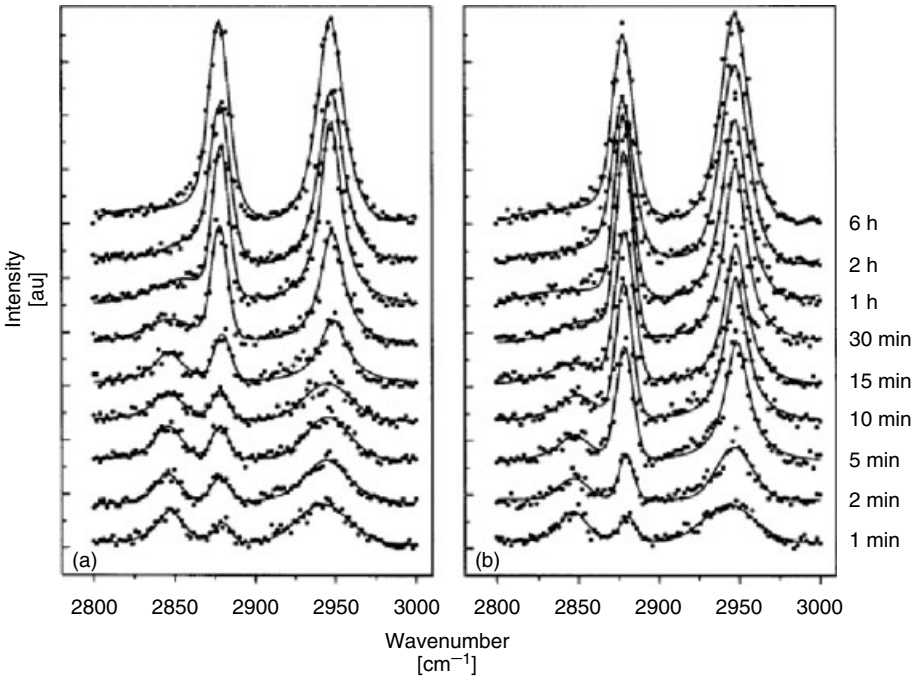


Fig. 6 SFG spectra of OTS layers on the fused quartz surface prepared varying deposition times with (a) low and (b) high water-content solvent [270]. Polarization: *ssp*.

the alkyl chain conformational changes of OTS monolayer occur in three stages [270]. Figure 6 shows their SFG spectra of OTS layers on the fused quartz surface prepared with varying deposition times with (a) low and (b) high water-content solvent. During the first stage, the alkyl chains in the film are almost completely disordered, though a significant increase in surface coverage occurs (1–15 min). This initial stage includes OTS adsorption from solution and the beginning of island formation. The second stage shows dramatic changes in alkyl chain conformation within the film from disordered gauche conformation to an ordered mainly *all-trans* conformation, while only a small increase in surface coverage occurs. The final stage is a much slower adsorption process although the surface coverage increases from 90% to a complete monolayer, only a slight increase in the SFG band intensities is observed. Messmer et al. reported that the water in the bulk solvent also plays an important role on the OTS film formation [270]. The asymmetric C–H stretch of OTS film prepared with higher water contents solvent (Fig. 6b) increases much faster than low water-content solvent (Fig. 6a), indicating that the alkyl chains are more ordered when more water is present.

Himmelhaus et al. investigated adsorption kinetics of docosanethiol, $CH_3(CH_2)_{21}SH$, onto a Au surface by ex situ SFG measurements [274]. Figure 7 shows the SFG spectra of a Au surface immersed in a 3 μM ethanol solution for different periods (1.5 min–48 h). The nonresonant signal (χ_{NR}) and relative phase angle (δ) from the Au substrate are dependent on the wavelength of the visible light [62, 204] as well as its incident

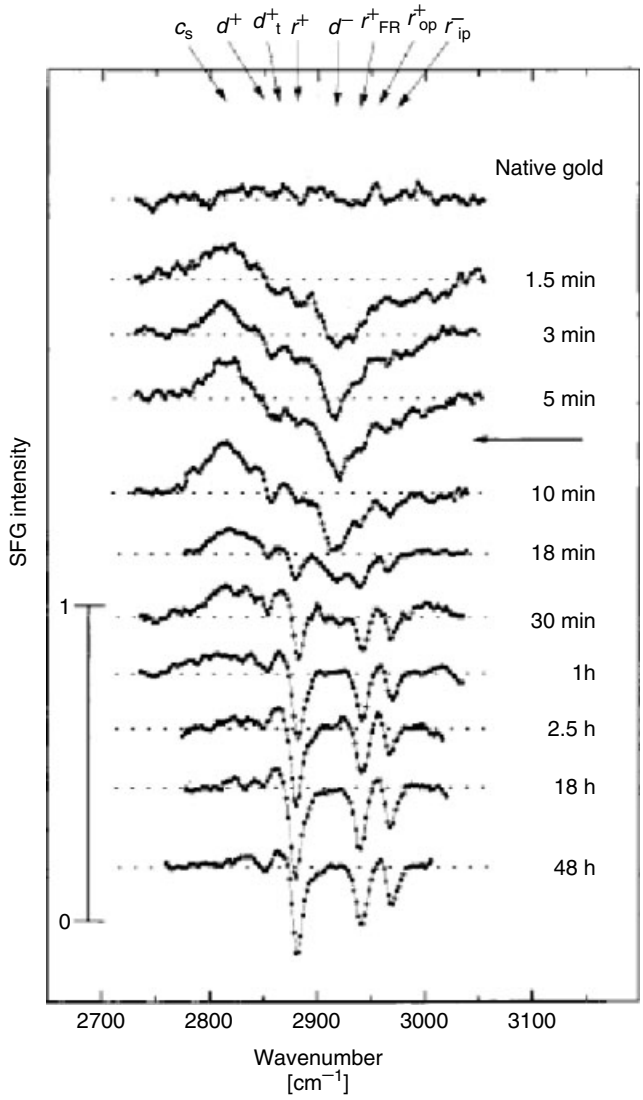


Fig. 7 *ppp*-SFG spectra of SAM of docosanethiol, $CH_3(CH_2)_{21}SH$, onto a polycrystalline Au surface immersed bars mark the different vibrational modes [274]. The arrow indicates the completion of the first fast step.

geometry [158] and the strength of χ_{NR} for Au is normally higher in comparison with resonance signals from the monolayer. As already discussed in Fig. 2, the significant interference between χ_{NR} and resonance signals should appear in the SFG spectra. As shown in these SFG spectra for SAMs on Au substrate (Fig. 7), the SFG peaks mainly appear as downward ones [13]. The assignments for these bands

were given in the same figure. They identified adsorption process with three stages in significantly different timescales. The fastest step is related to formation of the Au–S bond, which is characterized by hydrocarbon chains with a high fraction of gauche kinks (Fig. 7, ~5 min). The second step is three to four times slower and comprises the straightening of the hydrocarbon chains (Fig. 7, ~18 min). A pronounced band around 2813 cm^{-1}, which is attributed to the softening mode of the C–H vibrations due to the interaction with the Au substrate, was observed during the first two steps. The timescale of the final step is much slower than the rate of chain stretching and encompasses the reorientation of the terminal CH_3 groups (Fig. 7, 30 min–48 h). The terminal CH_2 group (i.e. the one adjacent to the terminal CH_3 group) exhibits the same behavior as that of the CH_3 group, and thus behaves oppositely to the other CH_2 groups. These SFG results demonstrate that the adsorption of the last few percent of the thiol molecules to a full monolayer induces the transition from a high number of gauche defects to an *all-trans* conformation in the monolayer [274].

SFG is also widely used to determine the conformation of surfactant monolayers on solid and liquid surfaces [20, 82–84, 98, 99, 108–112, 120, 122]. Figure 8 shows the SFG spectra of a loosely packed monolayer of a cationic surfactant, dioctadecyldimethylammonium chloride (DOAC, $(CH_3(CH_2)_{17})_2N^+(CH_3)_2Cl^-$), on the fused quartz surface (density: 2.8 chains/nm^2) in air with polarization combination of (a) *ssp*; (b) *sps*; and (c) *ppp* [82–84]. In addition to the SFG peaks at 2875, 2955, and 2940 cm^{-1}, which can be attributed to the terminal CH_3 group in a long hydrocarbon chain, the peaks at 2850 and 2920 cm^{-1}, which can be attributed respectively to the symmetric and asymmetric stretches of the CH_2 groups in the alkyl chain, can be observed clearly in comparison with

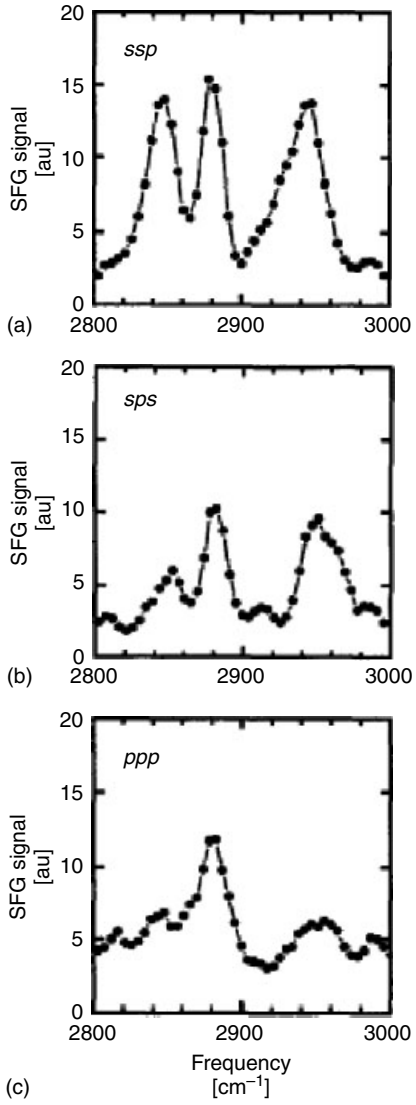


Fig. 8 SFG spectra for a DOAC monolayer at the quartz/air interface with polarization combination of (a) *ssp*, (b) *sps*, and (c) *ppp* [82].

those of OTS monolayer (Figures 5 and 6). This result indicates that the DOAC monolayer possesses considerable amount of defects. Considering that a fully packed monolayer of alkyl chains has a typical density of ca. 5.0 chains/nm^2, this result is to be expected from the low surface density of the monolayer (2.8 chains/nm^2). As we will show in the following, the conformation of the DOAC monolayer is changed completely after immersion into different kinds of liquid solvent due to the chain–chain interaction between the surfactant monolayer and solvent [82–84].

7.1.5.1.2 **LB Films** The LB technique is one of the important fabrication methods for solid surfaces using ordered ultrathin organic films and has been widely applied in the studies of molecular electronics, nonlinear materials, and biosensors [1–4]. Although the structures of LB films have been extensively investigated by different methods, a number of issues, especially for the differences in molecular structures of the LB surface compared to its bulk, are still not clear due to the limitation of the previous characterization methods. SFG measurements have been successfully applied to explore the molecular structures at the LB surface and the layer–layer interface in the multilayer system in LB films, by using its advantage of high sensitivity on the interface.

Ye et al. investigated the surface molecular structures of LB films of stearic acid with various thicknesses formed on the hydrophilic substrates (Au and fused quartz) by SFG [64, 298]. Figure 9(A) shows SFG spectra of LB films of cadmium stearate with different thicknesses (1-, 2-, 3-, 9-, and 12-layers) on the Au surface in air [64]. The main spectral features of these SFG spectra are associated with those of terminal CH_3 groups. The peak intensities of the two peaks due to the CH_2 group slightly increased with thickness of the L–B films, which can be attributed to the increase in *gauche* defects introduced during the deposition process of LB film in this experiment (normally, the peaks attributed to CH_2 groups are very weak). As shown in Fig. 9(A), the SFG peak intensity of the terminal CH_3 groups does not change much with an increase in the layers

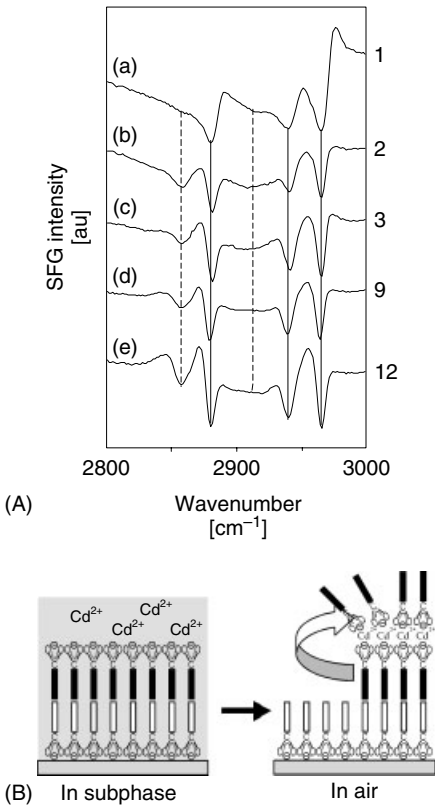


Fig. 9 (A) SFG spectra of LB films of cadmium stearate with different thicknesses (1-, 2-, 3-, 9-, and 12-layers) on the Au surface. Polarization: *ppp*. (B) A proposed model of the structural change at the outermost layer in the even-numbered LB film in air [64].

of the LB films. This behavior is totally different from that observed in the IRRAS spectra in which the intensities of the IR peaks of the CH_2 and CH_3 groups linearly increase with an increase in the layers of the LB films, confirming that SFG probes the interface. Furthermore, the SFG spectra of the even-numbered LB films were almost the same as those of the odd-numbered films, although it is expected that the molecular structures of the outermost layer for the even- and odd-numbered layers are different in the ideal model. Similar phenomena were also observed on the fused quartz surface [64, 298]. In combination with AFM measurements, these experimental results are explained in terms of a flip-over model (Fig. 9B) for the structural changes at the outermost layer of the even-numbered LB films in air. The new bilayer structure formed on the surface of the even-numbered LB film in air is expected to be stabilized by both the electrostatic chelate interaction pair ($COO^- : Cd^{2+} : COO^-$) and low surface energy of the terminal hydrophobic methyl group exposed to air. As observed by in situ SFG measurements (see below), the similar interfacial structure changes on the even-numbered fatty acid LB films also take place in aqueous solution containing Cd^{2+} cation [298].

Holman et al. investigated the LB multilayer films of the cadmium salts of five long-chain fatty acids (C_nCOOH, $n = 14$, 16, 18, 20, and 22) deposited onto Au surface modified by perdeuterated octadecanethiol (d-ODT) monolayer (denoted as ''hydrophobic'' Au surface) by SFG spectroscopy [104, 105]. By cleverly designing the LB multilayer films using perprotonated and perdeuterated fatty acids, they demonstrated the possibility of selectively probing the molecular structures both on surface and interfaces buried within the L–B films. Figure 10(a) presents SFG spectra in the C–H stretching region of two-layer cadmium arachidate LB films deposited on a d-ODT-modified Au surface [104], where the upper spectrum is that measured from a film composed of a perdeuterated (D) lowermost layer and a perprotonated (H) uppermost layer and the lower spectrum is that obtained from a film comprising an H lowermost layer and a D uppermost layer. In this way, one can explore the molecular structure of the single H layer in any position within the film in C–H stretching region by SFG measurements. Although the main spectral features in Fig. 10(a) were basically from with those of the CH_3 groups, it is noteworthy that (1) SFG peaks were observed in opposite direction in two SFG spectra shown Fig. 10(a); (2) peak positions of the bottom layer were red-shifted with respect to those of the top layer. Feature (1) is due to the reversed polar orientations of the perprotonated fatty acids in the bottom and top layers, which differ in phase angle (ε) by π. As expected from Eq. (11), they should give SFG peaks in opposite directions when a nonresonance background (i.e. one from Au substrate) exists. On the other hand, red-shift of the peak position (Feature 2) can be considered as the difference in the local environment of the CH_3 groups terminated fatty acid alkyl chains in the two films (air vs. a condensed phase). In fact, Holman et al. observed that all buried layers except the topmost layer are significantly offset to lower values from the SFG measurements [104]. It is well known that IR peak frequencies decrease when a molecule is transferred from a gaseous phase to a liquid-like (solid-like) phase [305–307]. This is the first report in which one can exactly distinguish the molecular structure on the LB surface and

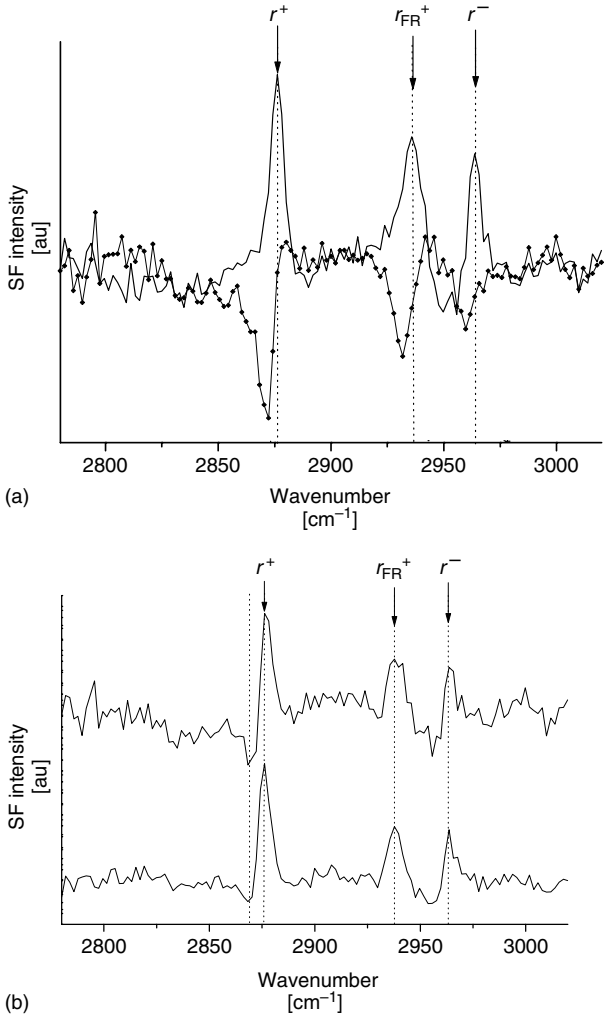


Fig. 10 (a) SFG spectra of two-layer cadmium arachidate LB films on a d-ODT-modified Au surface. Upper spectrum: a perdeuterated lowermost layer and a perprotonated uppermost layer; Lower spectrum: a perprotonated lowermost layer and a perdeuterated uppermost layer. (b) Upper spectrum: a stimulated SFG spectrum by numerical addition of the two spectra in Fig. 10(a); Lower spectrum: SFG spectrum of 2 layer perprotonated cadmium arachidate LB film [104]. Polarization: *ppp*.

in LB bulk, implying extremely high capability of the SFG spectroscopy.

Numerical summation of the two spectra of Fig. 10(a) yields a prediction of the SFG spectrum in Fig. 10(b) (upper spectrum). This simulated SFG spectrum is almost identical to the experimentally observed SFG spectrum of a two-layer film

comprising solely perprotonated cadmium arachidate within noise level (lower spectrum, Fig. 10(b)). This finding implies that the SFG spectra of the multilayer LB films deposited on the "hydrophobic" Au surface are independent of the multilayer thickness and are contributed to both by topmost and lowermost layers. There is a sizable detectable contribution from the lowermost layer, which acts to modify the observed line shapes and spectral intensity [104, 105]. These results suggest that interpretation of SFG spectra of LB multilayer films deposited on metal substrates must be performed with care and that deconvolution of spectra in terms of contributing layers is imperative. This method has been successfully employed to determine the structural change in the LB multilayer of cadmium arachidate during the formation of CdS nanoparticles [107].

Recently, more detailed experiments and discussion have also been carried out on the fused quartz surface modified by a perdeuterated fatty acid in which the nonresonant signal is quite small. Although it is not a simple numerical addition this time, the general conclusion about the SFG spectrum for a multilayer LB film on the hydrophobic quartz surface is dominated by the contribution from topmost and lowermost layers.

7.1.5.2 Modified Solid Surfaces in Solution

7.1.5.2.1 SAMs in Solution Davies and Bain investigated the molecule structure changes on the interface between alkoxy-terminated hexadecanethiols $CH_3(CH_2)_nO\text{-}(CH_2)_{16}SH$ ($n = 0-3$) monolayers on Au surfaces and various liquids in detail by in situ SFG spectroscopy [96, 97]. Figure 11 shows SFG spectra of (A) MeOHT ($n = 0$) and (B) BuOHT ($n = 3$) monolayers on Au in contact with (a) air; (b) hexane-d_{14}; (c) acetonitrile-d_3; and (d) water. They

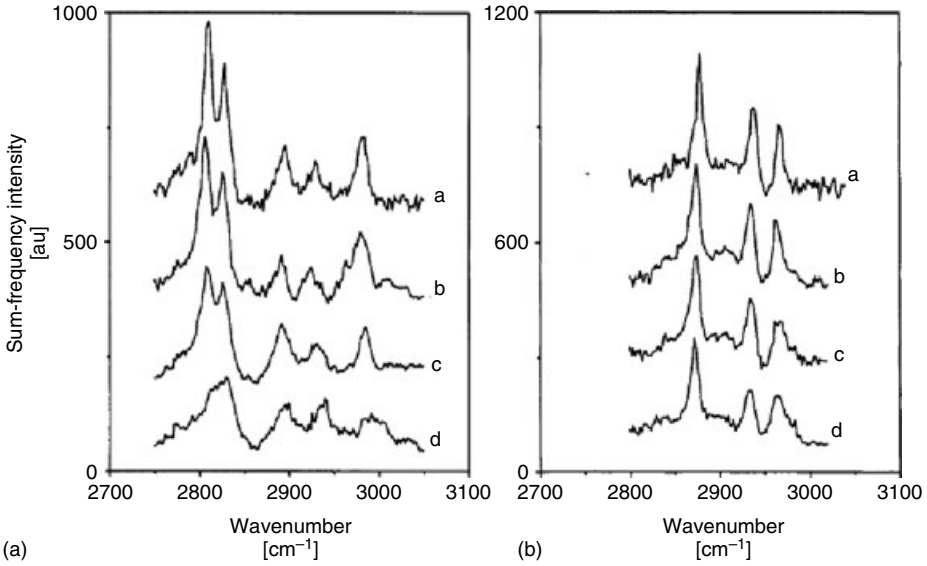


Fig. 11 SFG spectra of (A) MeOHT ($n = 0$) and (B) BuOHT ($n = 3$) monolayers on Au in contact with (a) air; (b) hexane-d_{14}; (c) acetonitrile-d_3; and (d) water [97]. Polarization: *ppp*.

found that liquids perturb the structure of organic monolayers. The changes were most pronounced in the monolayer of MeOHT in contact with water (Fig. 11A), but much less in the monolayer of BuOHT (Fig. 11B). The hydrogen bonds were formed between the polar ether group in the SAMs and water molecules. As the length of the terminal alkyl chain is increased, and hence the ether group is removed further from the monolayer-liquid interface, the effect of molecular interactions on the structure of the monolayer rapidly decreases. As the oxygen atom was progressively "buried" in the hexadecanethiol molecule, its influence became less pronounced and it no longer had an observable effect on the SFG spectra of the BuOHT (Fig. 11B). These structural changes correspond well to those of surface wettability observed by contact angle measurements. These findings imply that the surface structure of an organic material in contact with air may be significantly different from that in contact with a liquid, particularly when the formation of hydrogen bonds is possible.

Shen and coworkers studied the conformation of a loosely arranged monolayer of a cationic surfactant, DOAC, in various solvents by in situ SFG spectroscopy [82–84]. Figure 12 shows a series of *ssp*-polarized SFG spectra for a DOAC monolayer at a fused quartz surface in various perdeuterated liquid alkane solvents with long-chain length (C_{10} – C_{16}) [84]. The perdeuterated alkanes were used here to avoid the overlap between DOAC and solvent in the C–H stretching region (2800–3000 cm^{-1}). A peak at 2850 cm^{-1}, which is attributed to the CH_2 group in the DOAC monolayer, was clearly observed in air (Fig. 12, topmost curve), indicating that the alkyl chains are not in the perfect *all-trans* conformation and must contain some *gauche* defects. However, the other curves in the SFG spectra show that the peak intensity of the CH_2 group is effectively suppressed after contact with various alkanes (Fig. 12, C_{10}–C_{16}). These SFG spectra demonstrate that *gauche* defects in the DOAC monolayer significantly decreased after immersion in the long-chain alkanes and almost disappeared when the chain length was longer than 14, indicating

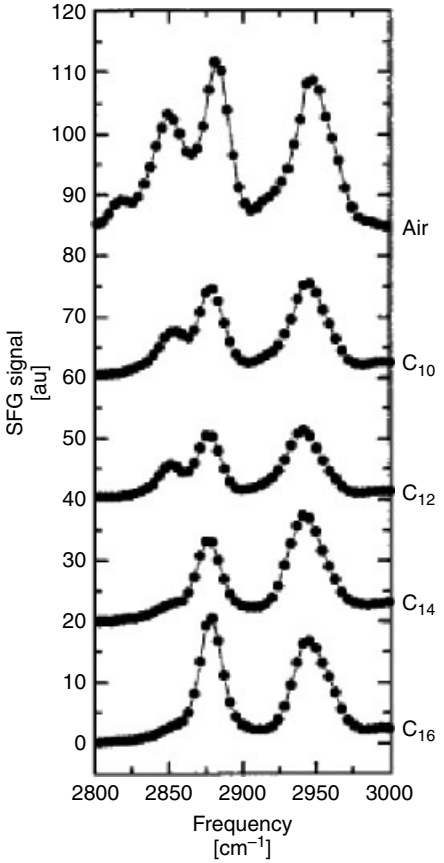


Fig. 12 A series of *ssp*-SFG spectra for a DOAC monolayer at a fused quartz surface in various deuterated liquid alkane solvent with sufficiently long-chain length (C_{10}–C_{16}) [84].

that the hydrocarbon chains in the DOAC monolayer are almost ''straightened up'' to *all-trans* conformation, that is, conformational order of the surfactant chains largely increased. The alkane solvents wedging into the surfactant monolayer possess a sufficiently long-chain length to provide enough chain–chain interaction (i.e. Van der Waals interaction) between alkane and surfactant to ''straighten up'' the C_{18} chains in DOAC monolayer. On the other hand, it is interesting to note that the similar conformation changes could not be observed in the surfactant with shorter chain length (DDAC, didecyldimethylammonium chloride, $(CH_3(CH_2)_9)_2N^+(CH_3)_2Cl^-$) and that with lower surface density (DMOAP, N-octadecyldimethyl [(3-trimethoxysilyl)propyl]ammonium chloride, $CH_3(CH_2)_{17}N^+(CH_3)_2(CH_2)_3Si(CH_3O)_3Cl^-$), suggesting that the minimum chain length and chain density of the surfactant monolayer are necessary for the chain straightening to happen [83, 84].

One may expect that the same conformation change to occur if the DOAC monolayer is in contact with the long-chain alcohols. As shown in Fig. 13(A), SFG spectra of DOAC monolayer nearly vanished in the neat alcohols of all chain lengths (C_4–C_{16}), indicating that the DOAC chains must have folded in this case [84]. It is surprising to find that when the DOAC monolayer is immersed in a dilute 0.5 M hexadecanol CCl_4 solution (Fig. 13B-(a)), the DOAC chains effectively become *all-trans* again. The SFG spectrum is greatly enhanced when perprotonated alcohol is used instead of perdeuterated alcohol (Fig. 13B-(b)), indicating that the chains of hexadecanol and DOAC are oriented in the same direction (i.e. CH_3 groups of hexadecanol and DOAC are in phase). This situation can be explained by the scheme given in Fig. 13(C) [84]. The terminal OH group and the alkyl chain of alcohol should have opposing effects on the DOAC chains; one tends to induce conformational disordering in the chains, and the other straightens the chains by chain–chain interaction. When only pure long-chain alcohol molecules are used, a hydrogen-bonded network is formed at the interface with the OH terminals facing the DOAC chains (Fig. 13C-(a)), surfactant chains must have contained a large amount of *gauche* defects (i.e. ''chain folding''), and hence the SFG intensity from CH_3 groups in DOAC monolayer largely decreased. When the hexadecanol is diluted in CCl_4 solvent, the hydrogen bonding network on the DOAC surface should be disrupted and the hydrophobic interaction between the long alkyl chains becomes more important and the individual hexadecanol molecules can now adsorb into the DOAC monolayer to straighten the DOAC chains via chain–chain interaction as shown in Fig. 13C-(b). Enhancement of the SFG signal using perprotonated hexadecanol suggests that the chain orientations of the alcohol and DOAC are in the same direction [84].

Guyot–Sionnest et al. investigated SAMs of alkanethiols ($C_nH_{2n+1}SH$, n = 9, 10, 18) on Au (poly), Ag(111), and Pt(111) surfaces in aqueous electrolyte solution under electrochemical control by in situ SFG measurement using a thin-layer cell [158]. They demonstrated that the SAMs on Au and Ag(111) were well ordered with *all-trans* conformations, but that on Pt there was significant disordering in the chains due to its lower surface density. The conformation of the SAMs on the Pt(111) electrode surface reversibly changed with electrochemical potential, which is attributed to straightening of the chains by the penetration of electrolytes into the monolayer at sufficiently negative

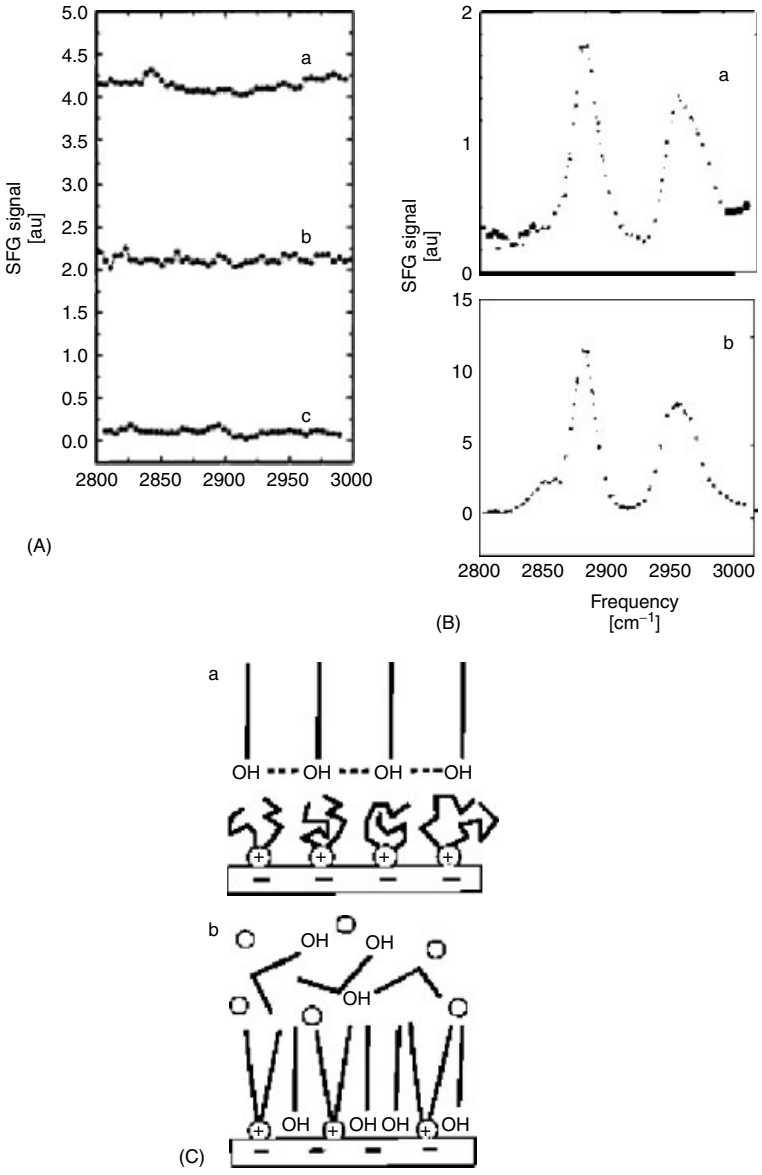


Fig. 13 (A) *ssp*-SFG spectra for a DOAC monolayer on the fused quartz surface in contact with (a) deuterated C_4, (b) deuterated C_8, and (c) deuterated C_{16} alcohols; (B) *ssp*-SFG spectra for a DOAC monolayer on the fused quartz surface in contact with (a) 0.5 M deuterated hexadecanol ClC_4 solution and (b) 0.5 M regular hexadecanol ClC_4 solution. (C) Schematics of the structures of (a) SiO_2/DOAC/neat hexadecanol and (b) SiO_2/DOAC/0.5 M hexadecanol CCl_4 solutions [84]. Chains are represented by solid lines, surfactant headgroups by plus signs within circles, and CCl_4 by open circles.

potential region. Such kinds of potential dependence was not observed at Au(poly) and Ag(111) electrode surfaces.

7.1.5.2.2 **LB Films in Solution** As already discussed in 5.1.2, the topmost layer of the even-numbered LB film of fatty acid changes its structure in air when the LB film is passing through the meniscus during the pulling-up action by the flip-over mechanism. One may expect that the even-numbered LB film on a hydrophilic substrate will keep its ideal ordered structure only in the water subphase. The interaction of the water and cation with the carboxylate headgroup, which locates on the surface of the even-numbered LB film, can stabilize the structure. It is interesting to study whether it is really stable in the water subphase, especially when other chemical or physical interactions exist. Ye et al. have demonstrated for the first time using in situ SFG measurement that the interfacial molecular structure at the LB bilayer of stearic acid on the hydrophilic substrates significantly change with immersion in the water subphase containing Cd^{2+} while such a structural change has not been observed in the water subphase without Cd^{2+} [298].

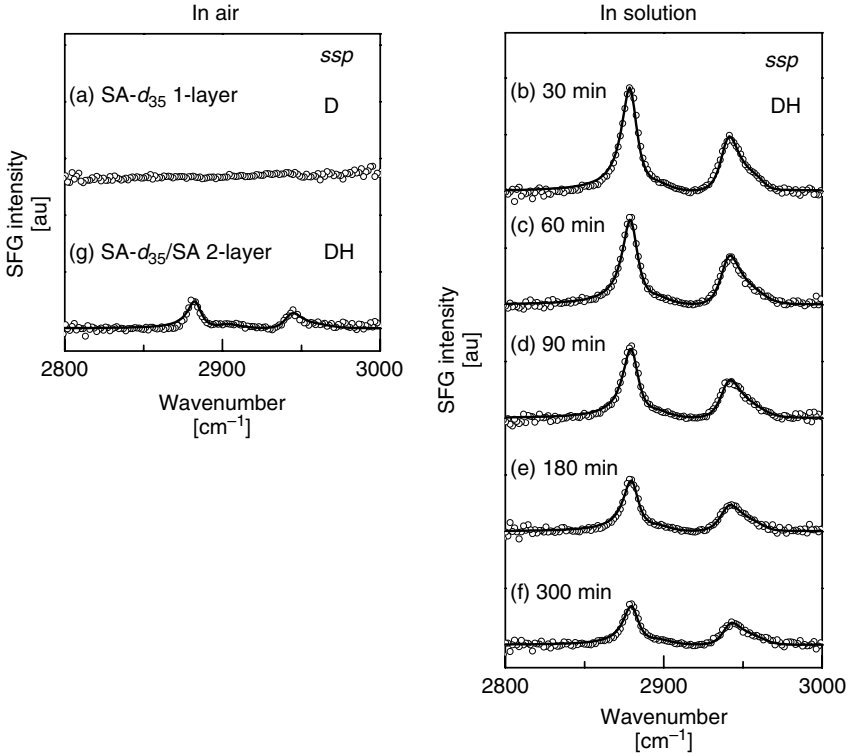


Fig. 14 In situ SFG spectra of L–B films on a fused quartz surface of (a) deuterated stearic acid-d_{35} monolayer (D) in air and (b–f) DH bilayer in 0.3 mM $NaHCO_3$ with 0.2 mM Cd^{2+} for different immersion periods. (g) is an SFG spectrum in air lifted from subphase after (f). The polarization combination is *ssp* [298]. See text for details.

Figure 14(a) shows an *ssp* spectrum of a deuterated stearic acid monolayer (D) on a fused quartz surface in air, deposited from a 0.3 mM $NaHCO_3$ containing 0.2 mM Cd^{2+} [298]. No peak was observed in the C–H stretching region since no C–H bond was included in the D-monolayer. After the first D-layer was deposited on the substrate, the second layer using regular stearic acid (H) was deposited on the top of the D-layer during the pulling-down action to form a bilayer (i.e. DH) and was then installed in an in situ SFG cell filled with the same solution. Caution was paid during this setup process to avoid any contact of the LB film with air, which may possibly damage the surface structure of the even-numbered LB film. Figure 14(b–f) show a series of in situ SFG spectra of the DH bilayer on the fused quartz surface for different immersion times in 0.3 mM $NaHCO_3$ solution with 0.2 mM Cd^{2+}. Two intense peaks around 2875 and 2940 cm^{-1} in Fig. 14b, which can be attributed to the symmetric and Fermi-resonance C–H stretching modes of the terminal CH_3 group in the top layer H, indicating that a well-ordered H-layer was formed as a second layer. This spectrum resembled that of the stearic acid monolayer on the fused quartz surface in air except a small interference effect from the OH stretching modes of the interfacial water molecules. The intensities of these two SFG peaks became weaker with an increase in the immersion time in the subphase (Figs. 14b–14f). After a 5-h immersion, the peak intensities decreased to ca. one-third of its original values (Fig. 14f), suggesting that the structure of the top layer (H) of the DH bilayer significantly changed during the immersion process in the subphase solution. When the bilayer sample was withdrawn from the subphase after Fig. 14f, the SFG spectrum in air (Fig. 14g) became much weaker in comparison with its original one (Fig. 14b), confirming again the surface structure of the bilayer changed in both the immersion and lift-up processes.

The same experiment using the DH bilayer was carried out in the same 0.3 mM $NaHCO_3$ solution but without the Cd^{2+} cation (Fig. 15) [298]. In comparison with the initial SFG spectrum of the bilayer DH in solution with 0.2 mM Cd^{2+} (Fig. 14b), the SFG spectrum (Fig. 15b) was similar except for the slightly stronger CH_2 bands, which may be related to a slightly higher density of *gauche* defects contained in the top layer (H) of the bilayer. On the other hand, relatively strong and broad backgrounds as well as a small dip around 2950 cm^{-1} were observed in the in situ SFG spectrum (Fig. 15b), which are related to the interference effect of the OH stretching modes of the interfacial water molecules. Influence from the interfacial water molecules seems to be larger (Fig. 15b) than those observed in the subphase containing the Cd^{2+} cation (Fig. 14b). This is reasonable if one considers that the structure of water at the surface of the stearic acid bilayer significantly depends on the coordination interaction between the deprotonated carboxylate headgroup and Cd^{2+} cation.

It is most interesting to note that the intensities of the SFG peaks were almost the same as the increase in the immersion time in 0.3 mM $NaHCO_3$ solution without Cd^{2+} during the 4.5-h immersion period (Figs. 15b–f). Even after removing the bilayer from the subphase, the SFG spectrum was almost the same as that dipped in the subphase, suggesting no surface change takes place when the bilayer was pulled from the 0.3 mM $NaHCO_3$ solution. These results

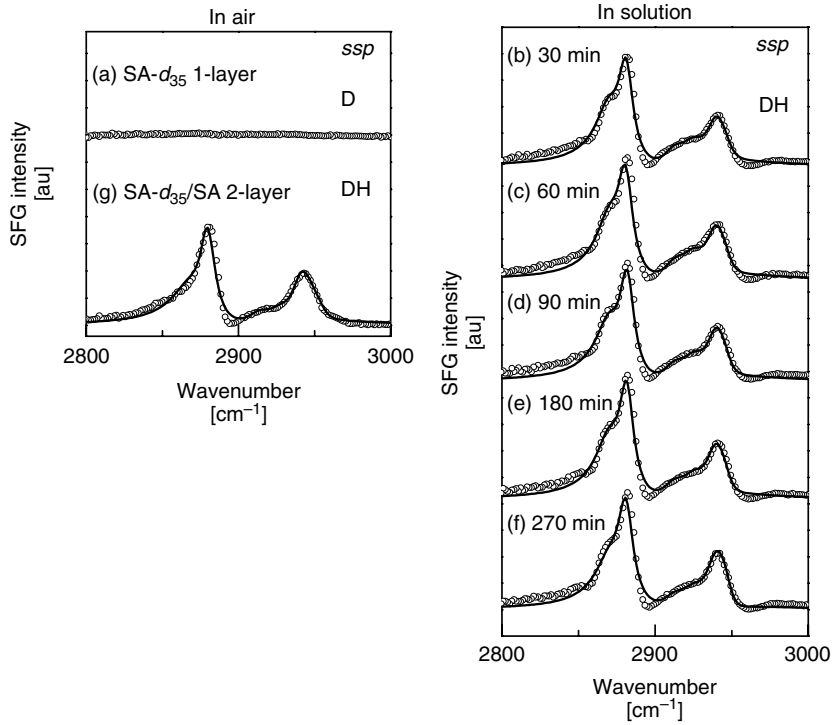


Fig. 15 In situ SFG spectra of L–B films on a fused quartz surface of (a) deuterated stearic acid-d_{35} monolayer (D) in air and (b–f) DH bilayer in 0.3 mM $NaHCO_3$ without Cd^{2+} for different immersion periods. (g) is an SFG spectrum in air lifted from subphase after (f). The polarization combination is *ssp* [298]. See text for details.

are totally distinct from those observed in the subphase with the Cd^{2+}.

These in situ SFG results convincingly demonstrate that the surface structure of the even-numbered stearic acid LB film is not stable in the water subphase containing the Cd^{2+} and its top bilayer structure changes with the increasing immersion time in the subphase. When the even-layered LB film was deposited on the hydrophilic substrate surface, an ideal bilayer structure is formed during the initial stage. This bilayer structure is stabilized by both the hydrophobic interaction between the long alkyl tails and by the hydrophilic interaction between the water molecules and carboxylate headgroup. However, the stabilization interaction will be even higher by the strong electrostatic interaction between the carboxylate headgroup via the divalent Cd^{2+}, which can form an extremely stable chelating structure ($COO^- : Cd^{2+} : COO^-$). To reach such an energetically stable state, part of the topmost-layer molecules are flipped over to the top of the L–B film gradually forming a new bilayer structure via the Cd^{2+} in solution, as that also observed in air (Fig. 9). This surface reorganization process is significantly accelerated when the even-numbered LB film is lifted from the same solution containing Cd^{2+}. In addition to the electrostatic interaction between the carboxylate headgroup and Cd^{2+}, the

reorganized surface structure is further stabilized by the hydrophobic interaction of the long alkyl chain facing the air. Part of the stearic acid molecules in the LB bilayer may also be dissolved to form micelles in the solution containing Cd^{2+} ion, which can generate the same changes in the SFG spectra. Detailed experiments using in situ AFM observation will be useful to distinguish these differences. The present results strongly suggest the extremely important role of the Cd^{2+} cation in the reorganization process of the LB films of stearic acid on the solid surface both in air and in solution [298].

Recently, Cremer et al. showed interesting experimental results, which demonstrates the water structures on the surface of an eicosanoic acid LB monolayer on air/water interface significantly affected by the existence of divalent metal ions (Zn^{2+} and Mg^{2+}) [227]. The effect of the metal divalent cations on the interfacial molecular structures of the LB films is a very attractive subject to be investigated in detail.

Conboy et al. also investigated the flip-flop and phase transition processes of lipid bilayer on soild substrate by in situ SFG measurements [295, 296]. Application of SFG in the field of biophysics will is expected to significantly increase.

7.1.5.2.3 **Interfacial Water Structures on the Modified Solid Surface** Water structures on the modified solid surface play an import role in its functionality. With conventional IR and Raman measurements, it is hard to distinguish the water molecules on surface from those in bulk, whereas, SFG spectroscopy is expected to probe only interfacial water molecules.

Shen and coworkers first reported the SFG spectra of the water molecules on the fused quartz surface [69, 148]. They observed that the water structure at quartz/solution interfaces depended on the solution pH. They found that the SFG intensity of hydrogen-bonded OH stretching was enhanced in an alkaline solution due to the surface charge of the deprotonated silanol groups on the quartz substrate surface. When the fused quartz surface was modified by OTS monolayer, a sharp peak was observed at 3680 cm^{-1}, which is similar to that observed at water/air interface [71], indicating the existence of OH groups without hydrogen bonding. The position and shape of the OH stretching bands of the interfacial water molecules at the OTS surface closely resembles that of a hexagonal ice surface in air, confirming that interfacial water molecules are aligned in a well-ordered structure as a result of the hydrophobic effect.

To date, the water structural changes have been investigated in detail at solid surfaces modified by various organic thin films, such as (1) OTS [147]; (2) positively charged polyelectrolyte, polydiallydimethylammonium chloride (PDDA) [228, 232]; (3) protein of bovine serum albumin (BSA) [230] and lysozyme [231], and lipid bilayers [229]; (4) amino-terminated SAMs of N-(2-aminoethyl)-3-aminopropylmethoxylsilane (AAS) and 3-aminopropylmethoxylsilane (APS) [146, 149]; (5) surfactant of sodium dodecyl sulfate (SDS), [225, 226] by using in situ SFG measurements.

Here, we will present an SFG study on (1) [147] as an example. Ye and Uosaki demonstrated that the water molecules at the quartz/OTS surface flip its orientation while the water molecules at the OTS surface maintain their orientation when the solution pH is changed from neutral to acidic. The results show that most of the silanol groups still exist on the fused quartz surface even after a silane

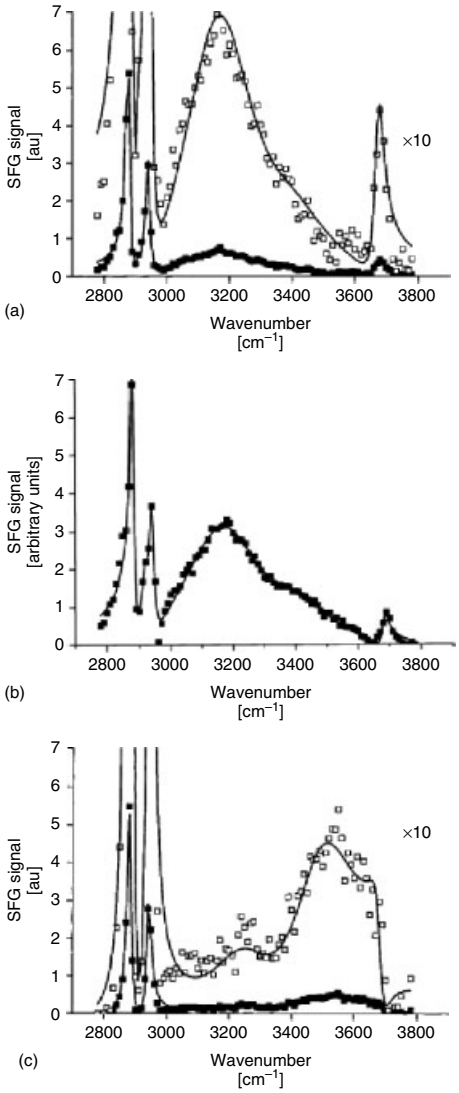


Fig. 16 SFG spectra of a fused quartz modified by the OTS monolayer with full coverage measured in the phosphate buffer solutions of (a) pH = 7; (b) pH = 11 and (c) pH = 1, in the region between 2800 and 3800 cm^{-1} [147]. Polarization: *ssp*.

coupling reaction of OTS under the reported experimental conditions [147].

Figure 16 shows SFG spectra of a fused quartz modified by the OTS monolayer with full coverage measured in phosphate buffer solutions of (a) pH = 7; (b) pH = 11 and (c) pH = 1, in the region between 2800 and 3800 cm^{-1}. In neutral solution, only two large peaks at 2879 and 2940 cm^{-1}, which are attributed to the CH_3 group, can be observed in the C–H stretching region, indicating that the OTS monolayer maintained a highly ordered structure in the electrolyte solution similar to that in air. The enlarged spectra in the OH stretching region, that is, between 3000 and 3800 cm^{-1}, were also shown in these figures. In addition to a broad peak at 3180 cm^{-1} with a shoulder around 3400 cm^{-1}, a sharp peak was observed at 3680 cm^{-1}. The broad peak at 3200 cm^{-1} is known to be that of ''ice-like water,'' representing the symmetric O–H stretching (ν_1) of tetrahedrally coordinated water molecules. The shoulder around 3400 cm^{-1} is known to be that of ''liquid-like water'', representing the asymmetric O–H stretching (ν_3) of water molecules in a more random arrangement. The peak at 3690 cm^{-1} has been assigned to the O–H stretching of water molecules without hydrogen bonding as ''free OH'' [71, 72]. The SFG peaks of OH with hydrogen bonding are very broad due to the strong coupling between the vibration of neighboring water molecules and Fermi resonance with the overtone of the HOH bending mode (ν_2) [308]. It is interesting to note that the SFG spectrum in the OH stretching region was similar to that of the ice/air interface with the significantly suppressed peak corresponding to ''liquid-like water'' at 3400 cm^{-1} compared to the SFG spectra of the quartz/water interface

in the solution of the same pH. These results show that the water molecules at the OTS/water interface are well ordered. Ordering of the interfacial water molecules has also been observed at the water/CCl_4 interface [19]. The highly hydrophobic nature of the OTS surface should be the most important origin for the ordering process.

SFG peak intensities of hydrogen-bonded OH modes observed in alkaline solution (Fig. 16b) were higher than those observed in the neutral solution (Fig. 16a), while that of the free OH seemed to be nearly the same. The bond corresponding to ''liquid-like water,'' which was just a shoulder in Fig. 16(a) became a noticeable peak in Fig. 16(b). On the other hand, the shape of the SFG spectrum observed in acidic solution (Fig. 16c) is totally different from those observed in neutral (Fig. 16a) and alkaline solutions (Fig. 16b). The peak of ''ice-like water'' was hardly observed and the SFG signal with a broad shape was observed around 3400–3700 cm^{-1}. The SFG spectrum of the interfacial water molecule is very distinctive and has never been reported.

Since the in situ SFG spectra significantly depend on solution pH, even when the fused quartz surface is modified with OTS molecules with a full monolayer coverage, it is expected that there are still a lot of unreacted silanol groups on the quartz surface after the silane coupling reaction [303]. Two kinds of interfacial water molecules, that is, ones located on the top of the OTS monolayer (denoted as H_2O_{OTS}, which is pH independent) and ones located in the space between the OTS and quartz surface (H_2O_{quartz}), can be distinguished and observed using the present in situ SFG measurement.

As schematically shown in Fig. 17, the unreacted silanol groups on the OTS-coated quartz surface are deprotonated in alkaline solution and an electric double layer is induced by the surface negative charges on the quartz surface. More water

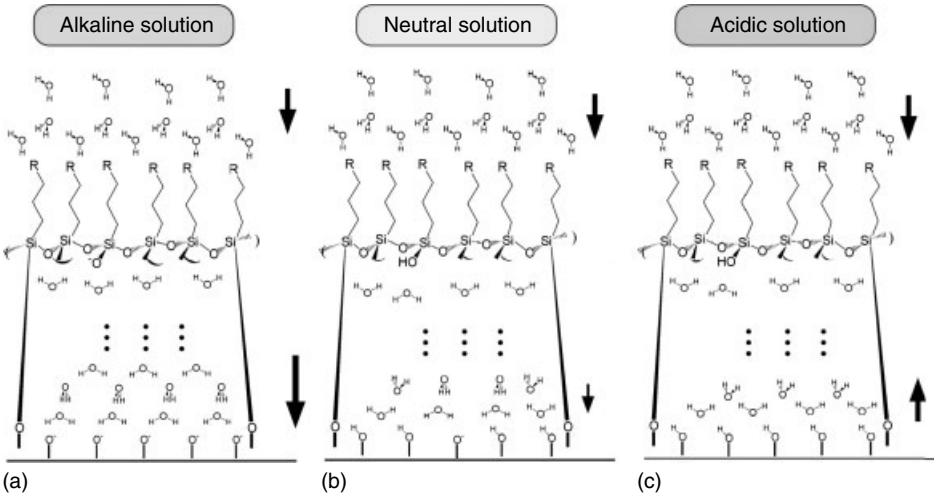


Fig. 17 Schematic structural models of interfacial water molecules on the fused quartz/OTS/solution interface in (a) alkaline, (b) neutral and (c) acidic phosphate buffered solutions. Arrows show the direction of the dipole moment of the interfacial water molecules [147].

molecules at the interface are aligned in order within the electric double layer and a higher SFG intensity for bands corresponding to interfacial water should be obtained. It should be mentioned here that the dipole moments of the hydrogen-bonded O–H for the H_2O_{OTS} and H_2O_{quartz} have the same direction in alkaline solution from the fitting process (as shown by arrows in Fig. 17a), which should also contribute to the intensity of the stronger SFG spectra of water molecules under the given condition.

In neutral solution, the silanol groups of the quartz surface are only partly deprotonated and the electric double layer on the quartz surface becomes weaker (Fig. 17b). The ordered structure of the H_2O_{quartz} is expected to significantly decrease compared to that in alkaline solution. Thus, the SFG signals observed in the neutral solution are considered to be mainly from H_2O_{OTS} and not from H_2O_{quartz}. The fitting results suggested that the interfacial water molecules maintain the same phase angle in neutral and alkaline solutions.

In acidic solution, the silanol groups left on the OTS-coated quartz surface are expected to be totally – SiOH. The fitting results show that the bonded OH changed its phase from 0 to π when the pH was changed from neutral to acidic, thus H_2O_{quartz} shows the opposite dipole moment with that of H_2O_{OTS} (Fig. 17c). The SFG signals of the ''ice-like water'' from H_2O_{quartz} and H_2O_{OTS} may cancel each other due to the their opposite dipole moments. As a result, only a broad ''liquid-like water'' peak, which was mainly from those of H_2O_{quartz}, and a free OH band appeared in the SFG spectrum in acidic solution.

In conclusion, water molecules at the quartz/OTS surface are expected to flip while the water molecules on the OTS surface maintain their orientation, when the solution pH is changed from neutral to acidic as a result of the protonation of the silanol group. Such a flipping phenomenon of the interfacial water on the bare quartz surface was demonstrated by Shen et al. for the first time by interference trace measurement [309]. The flipping takes place even on the OTS-coated quartz surface because most of the silanol groups are still on the quartz surface even after OTS formation.

7.1.6 Summary

As briefly reviewed in this section, SFG vibrational technique has significant advantages to the conventional vibrational spectroscopy. A great deal of new information on the interfacial molecular structure will be elucidated by this method, which is important and useful for understanding and controlling the surface property and functionality of materials. Appearance of the new techniques such as SFG imaging as well as FT-SFG will make this method more powerful and more easy to use. It is also expected that more theoretical studies will be carried out to quantitatively understand all the information we can get from SFG measurements and to anticipate what we can further obtain from this method.

On the other hand, although a number of studies have been carried out on the electrochemical interfaces by in situ SFG measurements, the spectroscopic information obtained on these electrochemical interfaces is still very limited. One can say that the real advantage of the SFG has not yet realized to date and more efforts are still necessary to promote the application of SFG spectroscopy in electrochemistry.

Acknowledgment

Y.S. gratefully acknowledges the support from PRESTO, Japan Science and Technology Corporation (JST). Y.S. also would like to acknowledge the support from the SHISEIDO Fund for Science and Technology, 2001 Corning Research Grants, Akiyama Foundation and Nippon Sheet Glass Foundation for Materials Science and Engineering.

References

1. A. Ulman, *An Introduction to Ultra-Thin Organic Films from Langmuir-Blodgett to Self-Assembly*, Academic Press, San Diego, CA., 1991.
2. M. C. Petty, *Langmuir-Blodgett Films: An Introduction*, Cambridge University Press, Cambridge, 1996.
3. D. K. Schwartz, *Surf. Sci. Rep.* **1997**, *27*, 245–334.
4. J. B. Peng, G. T. Barnes, I. R. Gentle, *Adv. Colloid Interface Sci.* **2001**, *91*, 163–219.
5. G. A. Somorjai, *Introduction to Surface Chemistry and Catalysis*, John Wiley & Sons, New York, 1994.
6. K. Kneipp, H. Kneipp, I. Itzkan et al., *Chem. Rev.* **1999**, *99*, 2957–2976.
7. W. E. Smith, C. Rodger, Surface-enhanced Raman scattering in *Handbook of Vibrational Spectroscopy* (Eds.: J. M. Chalmers and P. R. Griffiths), John Wiley & Sons, Chichester, 2002, pp. 775–784.
8. Z.-Q. Tian, B. Ren, D.-Y. Wu, *J. Phys. Chem. B* **2002**, *106*, 9463–9483.
9. M. Osawa, Surface-enhanced infrared absorption spectroscopy in *Handbook of Vibrational Spectroscopy* (Eds.: J. M. Chalmers and P. R. Griffiths), John Wiley & Sons, Chichester, 2002, pp. 785–799.
10. Y. R. Shen, *The Principles of Nonlinear Optics*, John Wiley & Sons, Inc., New York, 1984.
11. Y. R. Shen, *Nature* **1989**, *337*, 519–525.
12. Y. R. Shen, Surface spectroscopy by nonlinear optics in *Frontiers in Laser Spectroscopy, Proceedings of the International School of Physics "Enrico Fermi", Course CXX* (Eds.: T. W. Hansch and M. Inguscio), Elsevier, Amsterdam, 1994, pp. 139–165.
13. C. D. Bain, *J. Chem. Soc., Faraday Trans.* **1995**, *91*, 1281–1296.
14. Y. R. Shen, *Proc. Natl. Acad. Sci. U.S.A.* **1996**, *93*, 12104–12111.
15. P. B. Miranda, Y. R. Shen, *J. Phys. Chem. B* **1999**, *103*, 3292–3307.
16. A. Tadjeddine, A. Peremans, Non-linear optical spectroscopy of the electrochemical interface in *Spectroscopy for Surface Science* (Eds.: R. J. H. Clark and R. E. Hester), Wiley & Sons Ltd, Chichester, UK, 1998, pp. 159–216.
17. M. Buck, M. Himmelhaus, *J. Vac. Sci. Technol. A* **2001**, *19*, 2717–2736.
18. Z. Chen, Y. R. Shen, G. A. Somorjai, *Annu. Rev. Phys. Chem.* **2002**, *53*, 437–465.
19. G. L. Richmond, *Chem. Rev.* **2002**, *102*, 2693–2724.
20. C. D. Bain, Non-linear optical techniques in *Modern Characterization Methods of Surfactant Systems* (Eds.: B. P. Binks), Marcel Dekker, New York, 1999, pp. 335–373.
21. M. Morin, P. Jakob, N. J. Levinos et al., *J. Chem. Phys.* **1992**, *96*, 6203–6212.
22. K. Kuhnke, M. Morin, P. Jakob et al., *J. Chem. Phys.* **1993**, *99*, 6114–6125.
23. A. Peremans, A. Tadjeddine, W. Q. Zheng et al., *Surf. Sci.* **1996**, *368*, 384–388.
24. C. Matranga, P. Guyot-Sionnest, *J. Chem. Phys.* **2000**, *112*, 7615–7621.
25. C. Hess, M. Wolf, M. Bonn, *Phys. Rev. Lett.* **2000**, *85*, 4341–4344.
26. M. Bonn, C. Hess, M. Wolf, *J. Chem. Phys.* **2001**, *115*, 7725–7735.
27. H. Noguchi, T. Okada, K. Onda et al., *Surf. Sci.* **2003**, *528*, 183–188.
28. I. Benjamin, *Phys. Rev. Lett.* **1994**, *73*, 2084–2086.
29. A. Morita, J. T. Hynes, *Chem. Phys.* **2000**, *258*, 371–390.
30. A. Morita, J. Hynes, *J. Phys. Chem. B.* **2001**, *106*, 673–685.
31. M. Hayashi, S. H. Lin, M. B. Raschke et al., *J. Phys. Chem. A* **2002**, *106*, 2271–2282.
32. A. J. Moad, G. J. Simpson, *J. Phys. Chem. B.* **2004**, *108*, 3548–3562.
33. J. Wang, Z. Paszti, M. A. Even et al., *J. Phys. Chem. B.* **2004**, *108*, 3625–3632.
34. R. L. Sutherland, *Handbook of Nonlinear Optics*, Marcel Dekker, New York, 1996.
35. J. H. Hunt, P. Guyot-Sionnest, Y. R. Shen, *Chem. Phys. Lett.* **1987**, *133*, 189–192.

36. A. L. Harris, C. E. D. Chidsey, N. J. Levinos et al., *Chem. Phys. Lett.* **1987**, *141*, 350–356.
37. M. A. Belkin, Y. R. Shen, *Phys. Rev. Lett.* **2003**, *91*, 213907.
38. C. Hirose, N. Akamatsu, K. Domen, *J. Chem. Phys.* **1992**, *96*, 997–1004.
39. C. Hirose, N. Akamatsu, K. Domen, *Appl. Spectrosc.* **1992**, *46*, 1051–1072.
40. C. Hirose, H. Yamamoto, N. Akamatsu et al., *J. Phys. Chem.* **1993**, *97*, 10064–10069.
41. N. Watanabe, H. Yamamoto, A. Wada et al., *Spectrochim. Acta* **1994**, *50A*, 1529–1537.
42. G. P. Harp, H. Rangwalla, M. S. Yeganeh et al., *J. Am. Chem. Soc.* **2003**, *125*, 11283–11290.
43. K. A. Briggman, J. C. Stephenson, W. E. Wallace et al., *J. Phys. Chem. B* **2001**, *105*, 2785–2791.
44. M. Oh-e, S. C. Hong, Y. R. Shen, *Appl. Phys. Lett.* **2002**, *80*, 784–786.
45. K. Wolfrum, A. Laubereau, *Chem. Phys. Lett.* **1994**, *228*, 83–88.
46. D. Zhang, J. Gutow, K. B. Eisenthal, *J. Phys. Chem.* **1994**, *98*, 13729–13734.
47. X. Zhuang, P. B. Miranda, D. Kim et al., *Phys. Rev. B* **1999**, *59*, 12632–12640.
48. K. S. Gautam, A. Dhinojwala, *Macromolecules* **2001**, *34*, 1137–1139.
49. J. Wang, C. Chen, S. Buck et al., *J. Phys. Chem. B* **2001**, *105*, 12118–12125.
50. S. Ye, S. Morita, G. Li et al., *Macromolecules* **2003**, *36*, 5694–5703.
51. X. D. Zhu, H. Suhr, Y. R. Shen, *Phys. Rev. B* **1987**, *35*(()6), 3047–3050.
52. Y. R. Shen, *IEEE J. Sel. Top. Quantum Electron.* **2000**, *6*, 1375–1379.
53. D. Luchini, H. Motz, *Undulator and Free Electron Lasers*, Oxford University Press, Oxford, 1990.
54. A. Tadjeddine, A. Le Rille, O. Pluchery et al., *Phys. Status Solidi A* **1999**, *175*, 89–107.
55. E. W. M. van der Ham, Q. H. F. Vrehen, E. R. Eliel, *Surf. Sci.* **1996**, *368*, 96–101.
56. E. W. M. van der Ham, Q. H. F. Vrehen, E. R. Eliel, *Opt. Lett.* **1996**, *21*, 1448–1450.
57. J. M. Ortega, J. M. Berset, R. Chaput et al., *Nucl. Instrum. Methods Phys. Res. Sect. A* **1996**, *375*, 618–625.
58. R. Braun, B. D. Casson, C. D. Bain et al., *J. Chem. Phys.* **1999**, *110*, 4634–4640.
59. C. Hirlimann, Pulse Optics in *Femtosecond Laser Pulses* (Eds.: C. Rulliere), Springer, Heidelberg, 1998, pp. 25–52.
60. L. J. Richter, T. P. Petralli-Mallow, J. C. Stephenson, *Opt. Lett.* **1998**, *23*, 1594–1596.
61. T. Ishibashi, H. Onishi, *Appl. Spectrosc.* **2002**, *56*, 1298–1302.
62. T. Ishibashi, H. Onishi, *Appl. Phys. Lett.* **2002**, *81*, 1338–1340.
63. C. S.-C. Yang, L. J. Richter, J. C. Stephenson et al., *Langmuir* **2002**, *18*, 7549–7556.
64. S. Ye, H. Noda, S. Morita et al., *Langmuir* **2003**, *19*, 2238–2242.
65. N. Nishi, D. Hobara, M. Yamamoto et al., *J. Chem. Phys.* **2003**, *118*, 1904–1911.
66. G. Ma, H. C. Allen, *J. Am. Chem. Soc.* **2002**, *124*, 9374–9375.
67. S. Funk, M. Bonn, D. N. Denzler et al., *J. Chem. Phys.* **2000**, *112*, 9888–9897.
68. J. A. McGuire, W. Beck, X. Wei et al., *Opt. Lett.* **1999**, *24*, 1877–1879.
69. R. Superfine, J. Y. Huang, Y. R. Shen, *Phys. Rev. Lett.* **1991**, *66*, 1066–1069.
70. Q. Du, R. Superfine, E. Freysz et al., *Phys. Rev. Lett.* **1993**, *70*, 2313–2316.
71. Q. Du, E. Freysz, Y. R. Shen, *Phys. Rev. Lett.* **1994**, *72*, 238–241.
72. Q. Du, E. Freysz, Y. R. Shen, *Science* **1994**, *264*, 826–828.
73. C. Raduge, V. Pflumio, Y. R. Shen, *Chem. Phys. Lett.* **1997**, *274*, 140–144.
74. X. Wei, P. B. Miranda, Y. R. Shen, *Phys. Rev. Lett.* **2001**, *86*, 1554–1557.
75. M. A. Belkin, T. A. Kulakov, K.-H. Ernst et al., *Phys. Rev. Lett.* **2000**, *85*, 4474–4477.
76. M. A. Belkin, S. H. Han, X. Wei et al., *Phys. Rev. Lett.* **2001**, *87*, 113001.
77. S. H. Han, N. Ji, M. A. Belkin et al., *Phys. Rev. B* **2002**, *66*, 165415.
78. N. Ji, Y. R. Shen, *J. Chem. Phys.* **2004**, *120*, 7107–7112.
79. N. Ji, Y. R. Shen, *J. Am. Chem. Soc.* **2004**, *126*, 15008–15009.
80. P. Guyot-Sionnest, J. H. Hunt, Y. R. Shen, *Phys. Rev. Lett.* **1987**, *59*, 1597–1600.
81. P. Guyot-Sionnest, R. Superfine, J. H. Hunt et al., *Chem. Phys. Lett.* **1988**, *144*, 1–5.
82. P. B. Miranda, V. Pflumio, Y. R. Shen, *Chem. Phys. Lett.* **1997**, *264*, 387–392.
83. P. B. Miranda, V. Pflumio, H. Saijo et al., *Thin Solid Films* **1998**, *327–329*, 161–165.
84. P. B. Miranda, V. Pflumio, H. Saijo et al., *J. Am. Chem. Soc.* **1998**, *120*, 12092–12099.
85. X. Wei, X. Zhuang, S. C. Hong et al., *Phys. Rev. Lett.* **1999**, *82*, 4256–4259.
86. X. Wei, S. C. Hong, X. Zhuang et al., *Phys. Rev. E* **2000**, *62*, 5160–5172.

87. D. Kim, Y. R. Shen, *Appl. Phys. Lett.* **1999**, *74*, 3314–3316.
88. D. Kim, M. Oh-e, Y. R. Shen, *Macromolecules* **2001**, *34*, 9125–9129.
89. M. Oh-e, S.-C. Hong, Y. R. Shen, *J. Phys. Chem. B* **2000**, *104*, 7455–7461.
90. M. Oh-e, A. I. Lvovsky, X. Wei et al., *J. Chem. Phys.* **2000**, *113*, 8827–8832.
91. M. Oh-e, D. Kim, Y. R. Shen, *J. Chem. Phys.* **2002**, *115*, 5582–5588.
92. N. Ji, V. Ostroverkhov, F. Lagugne-Labarthet et al., *J. Am. Chem. Soc.* **2003**, *125*, 14218–14219.
93. M. Y. Mao, P. B. Miranda, D. S. Kim et al., *App. Phys. Lett.* **1999**, *75*, 3357–3359.
94. M. Y. Mao, P. B. Miranda, D. S. Kim et al., *Phys. Rev. B* **2001**, *64*, 35415.
95. S. Ye, T. Saito, S. Nihonyanagi et al., *Surf. Sci.* **2001**, *476*, 121–128.
96. T. H. Ong, R. N. Ward, P. B. Davies et al., *J. Am. Chem. Soc.* **1992**, *114*, 6243–6245.
97. T. H. Ong, P. B. Davies, C. D. Bain, *Langmuir* **1993**, *9*, 1836–1845.
98. D. C. Duffy, P. B. Davies, C. D. Bain, *J. Phys. Chem.* **1995**, *99*, 15241–15246.
99. M. S. Johal, E. W. Usadi, P. B. Davies, *J. Chem. Soc., Faraday Trans.* **1996**, *92*, 573–578.
100. A. M. Briggs, M. S. Johal, P. B. Davies et al., *Langmuir* **1999**, *15*, 1817–1828.
101. A. G. Lambert, D. G. Neivandt, R. A. McAloney et al., *Langmuir* **2000**, *16*, 8377–8382.
102. A. G. Lambert, D. J. Neivandt, A. M. Briggs et al., *J. Phys. Chem. B* **2002**, *106*, 10693–10700.
103. A. G. Lambert, D. J. Neivandt, A. M. Briggs et al., *J. Phys. Chem. B* **2002**, *106*, 5461–5469.
104. J. Holman, P. B. Davies, D. J. Neivandt, *J. Phys. Chem. B* **2004**, *108*, 1396–1404.
105. J. Holman, D. J. Neivandt, P. B. Davies, *Chem. Phys. Lett.* **2004**, *386*, 60–64.
106. T. Kawai, D. J. Neivandt, P. B. Davies, *J. Am. Chem. Soc.* **2000**, *122*, 12031–12032.
107. J. Holman, S. Ye, D. J. Neivandt et al., *J. Am. Chem. Soc.* **2004**, *126*, 14322–14323.
108. C. D. Bain, P. B. Davies, R. N. Ward, *Langmuir* **1994**, *10*, 2060–2063.
109. R. N. Ward, P. B. Davies, C. D. Bain, *J. Phys. Chem.* **1993**, *97*, 7141–7143.
110. R. N. Ward, D. C. Duffy, P. B. Davies et al., *J. Phys. Chem.* **1994**, *98*, 8536–8542.
111. G. R. Bell, C. D. Bain, R. N. Ward, *J. Chem. Soc., Faraday Trans.* **1996**, *92*, 515–523.
112. G. R. Bell, S. Manning-Benson, C. D. Bain, *J. Phy. Chem. B* **1998**, *102*, 218–222.
113. S. R. Goates, D. A. Schofield, C. D. Bain, *Langmuir* **1999**, *15*, 1400–1409.
114. R. Fraenkel, G. E. Butterworth, C. D. Bain, *J. Am. Chem. Soc.* **1998**, *120*, 203–204.
115. D. A. Beattie, S. Haydock, C. D. Bain, *Vib. Spectrosc.* **2000**, *24*, 109–123.
116. C. T. Williams, Y. Yang, C. D. Bain, *Langmuir* **2000**, *16*, 2343–2350.
117. C. D. Bain, E. B. Troughton, Y. T. Tao et al., *J. Am. Chem. Soc.* **1989**, *111*, 321–335.
118. C. D. Bain, P. B. Davies, T. H. Ong et al., *Langmuir* **1991**, *7*, 1563–1566.
119. E. A. Potterton, C. D. Bain, *J. Electroanal. Chem.* **1996**, *409*, 109–114.
120. B. D. Casson, R. Braun, C. D. Bain, *Faraday Discuss.* **1996**, *104*, 209–229.
121. B. D. Casson, C. D. Bain, *J. Am. Chem. Soc.* **1999**, *121*, 2615–2616.
122. B. D. Casson, C. D. Bain, *J. Phys. Chem. B.* **1999**, *103*, 4678–4686.
123. P. Guyot-Sionnest, A. Tadjeddine, *Chem. Phys. Lett.* **1990**, *172*, 341–345.
124. A. Tadjeddine, P. Guyot-Sionnest, *Electrochim. Acta* **1991**, *36*, 1839–1847.
125. A. Peremans, A. Tadjeddine, *J. Chem. Phys.* **1995**, *103*, 7197–7203.
126. A. Tadjeddine, A. Peremans, *Surf. Sci.* **1996**, *368*, 377–383.
127. A. L. Rille, A. Tadjeddine, W. Q. Zheng et al., *Chem. Phys. Lett.* **1997**, *271*, 95–100.
128. P. Hebert, A. L. Rille, W. Q. Zheng et al., *J. Electroanal. Chem.* **1998**, *447*, 5–9.
129. A. Tadjeddine, O. Pluchery, A. Le Rille et al., *J. Electroanal. Chem.* **1999**, *473*, 25–33.
130. A. Tadjeddine, A. L. Rille, *Electrochim. Acta* **1999**, *45*, 601–609.
131. O. Pluchery, A. Tadjeddine, *J. Electroanal. Chem.* **2001**, *500*, 379–387.
132. F. Vidal, B. Busson, C. Six et al., *Surf. Sci.* **2002**, *502–503*, 485–489.
133. W. Q. Zheng, O. Pluchery, A. Tadjeddine, *Surf. Sci.* **2002**, *502–503*, 490–497.
134. F. Vidal, B. Busson, C. Six et al., *J. Electroanal. Chem.* **2004**, *563*, 9–14.
135. B. Bozzini, C. Mele, A. Fanigliulo et al., *J. Electroanal. Chem.* **2004**, *574*, 85–94.
136. A. Peremans, A. Tadjeddine, P. Guyot-Sionnest, *Chem. Phys. Lett.* **1995**, *247*, 243–248.
137. Y. Caudano, A. Peremans, P. A. Thiry et al., *Surf. Sci.* **1997**, *377–379*, 1071–1075.

138. A. Peremans, Y. Caudano, P. A. Thiry et al., *Phys. Rev. Lett.* **1997**, *78*, 2999–3002.
139. C. Humbert, M. Buck, A. Calderone et al., *Phys. Status Solidi A* **1999**, *175*, 129–136.
140. L. J. Richter, C. S.-C. Yang, P. T. Wilson et al., *J. Phys. Chem. B.* **2004**, *108*, 12547–12559.
141. P. T. Wilson, K. A. Briggman, W. E. Wallace et al., *Appl. Phys. Lett.* **2002**, *80*, 3084–3086.
142. P. T. Wilson, L. J. Richter, K. A. Briggman et al., *Chem. Phys. Lett.* **2002**, *363*, 161–168.
143. C. S.-C. Yang, P. T. Wilson, L. J. Richter, *Macromolecules* **2004**, *37*, 7742–7746.
144. S. Ye, S. Nihonyanagi, K. Fujishima, Conformational order of octadecanethiol monolayer at gold/solution interface: internal reflection SFG study in *Studies in Surface Science and Catalysis 132* (Eds.: Y. Iwasawa, N. Oyama, H. Kunieda), Elsevier, Tokyo, 2000, pp. 705–710.
145. S. Ye, S. Nihonyanagi, K. Uosaki, *Nonlinear Opt.* **2000**, *24*, 93–98.
146. S. Ye, S. Nihonyanagi, K. Uosaki, *Chem. Lett.* **2000**, *29*, 734–735.
147. S. Ye, S. Nihonyanagi, K. Uosaki, *Phys. Chem. Chem. Phys.* **2001**, *3*, 3463–3469.
148. S. Nihonyanagi, S. Ye, K. Uosaki et al., *Surf. Sci.* **2004**, *573*, 11–16.
149. S. Nihonyanagi, S. Ye, K. Uosaki, *Electrochim. Acta* **2001**, *46*, 3057–3061.
150. K. Uosaki, T. Yano, S. Nihonyanagi, *J. Phys. Chem. B* **2004**, *108*, 19086–19088.
151. M. E. Quayum, T. Kondo, S. Nihonyanagi et al., *Chem. Lett.* **2002**, *31*, 208–209.
152. S. Nihonyanagi, D. Miyamoto, S. Idojiri et al., *J. Am. Chem. Soc.* **2004**, *126*, 7034–7040.
153. K. Uosaki, M. E. Quayum, S. Nihonyanagi et al., *Langmuir* **2004**, *20*, 1207–1212.
154. T. Ishibashi, H. Onishi, *Chem. Phys. Lett.* **2001**, *346*, 413–418.
155. T. Ishibashi, M. Ara, H. Tada et al., *Chem. Phys. Lett.* **2003**, *367*, 376–381.
156. C. Hess, M. Bonn, *Surf. Sci.* **2002**, *502–503*, 123–128.
157. D. N. Denzler, C. Hess, R. Dudek et al., *Chem. Phys. Lett.* **2003**, *376*, 618–624.
158. M. A. Hines, J. A. Todd, P. Guyot-Sionnest, *Langmuir* **1995**, *11*, 493–497.
159. P. Guyot-Sionnest, P. Dumas, Y. J. Chabal et al., *Phys. Rev. Lett.* **1990**, *64*, 2156–2159.
160. P. Guyot-Sionnest, A. L. Harris, Surface vibrational dynamics probed by sum frequency generation in *Laser Spectroscopy and Photochemistry on Metal Surfaces* (Eds.: H. Dai and W. Ho), World Scientific, Singapore, 1995, pp. 405–458.
161. P. Guyot-Sionnest, P. H. Lin, E. M. Hiller, *J. Chem. Phys.* **1995**, *102*, 4269–4278.
162. W. Daum, K. A. Friedrich, C. Klunker et al., *Appl. Phys. A.* **1994**, *59*, 553–562.
163. F. Dederichs, K. A. Friedrich, W. Daum, *J. Phys. Chem.* **2000**, *104*, 6626–6632.
164. F. Dederichs, A. Petukhova, W. Daum, *J. Phys. Chem. B* **2001**, *105*, 5210–5216.
165. K. A. Friedrich, W. Daum, F. Dederichs et al., *Z. Phys. Chem.* **2003**, *217*, 527–545.
166. X. Su, P. S. Cremer, Y. R. Shen et al., *Phy. Rev. Lett.* **1996**, *77*, 3858–3860.
167. X. Su, Y. R. Shen, G. A. Somorjai, *Chem. Phys. Lett.* **1998**, *280*, 302–307.
168. X. Su, L. Lianos, Y. R. Shen et al., *Phys. Rev. Lett.* **1999**, *80*, 1533–1536.
169. P. S. Cremer, X. Su, Y. R. Shen et al., *J. Phys. Chem.* **1996**, *100*, 16302–16309.
170. P. S. Cremer, X. Su, Y. R. Shen et al., *J. Phys. Chem. B.* **1997**, *101*, 6474–6478.
171. P. S. Cremer, X. Su, G. A. Somorjai et al., *J. Mol. Catal. A* **1998**, *131*, 225–241.
172. S. Baldelli, A. S. Eppler, E. Anderson et al., *J. Chem. Phys.* **2000**, *113*, 5432–5438.
173. S. Baldelli, N. Markovic, P. Ross et al., *J. Phys. Chem. B* **1999**, *103*, 8920–8925.
174. S. Baldelli, G. Mailhot, P. Ross et al., *J. Phys. Chem. B.* **2001**, *105*, 654–662.
175. S. Baldelli, G. Mailhot, P. N. Ross et al., *J. Am. Chem. Soc.* **2001**, *123*, 7697–7702.
176. S. Hoffer, S. Baldelli, K. Chou et al., *J. Phys. Chem. B* **2002**, *106*, 6473–6478.
177. K. C. Chou, N. M. Markovic, J. Kim et al., *J. Phys. Chem. B* **2003**, *107*, 1840–1844.
178. K. C. Chou, J. Kim, S. Baldelli et al., *J. Electroanal. Chem.* **2003**, *554–555*, 253–263.
179. D. Zhang, Y. R. Shen, G. A. Somorjai, *Chem. Phys. Lett.* **1997**, *281*, 394–400.
180. D. H. Gracias, Z. Chen, Y. R. Shen et al., *Acc. Chem. Res.* **1999**, *32*, 930–940.
181. Z. Chen, R. Ward, Y. Tian et al., *J. Am. Chem. Soc.* **2000**, *122*, 10615–10620.
182. Q. Chen, D. Zhang, G. Somorjai et al., *J. Am. Chem. Soc.* **1999**, *121*, 446–447.
183. J. Kim, G. A. Somorjai, *J. Am. Chem. Soc.* **2003**, *125*, 3150–3158.
184. J. Kim, A. Opdahl, K. C. Chou et al., *Langmuir* **2003**, *19*, 9551–9553.
185. A. Opdahl, S. Hoffer, B. Mailhot et al., *Chem. Rec.* **2001**, *1*, 101–122.

186. A. Opdahl, G. A. Somorjai, *Langmuir* **2002**, *18*, 9409–9412.
187. A. Opdahl, R. A. Phillips, G. A. Somorjai, *J. Phys. Chem. B* **2002**, *106*, 5212–5220.
188. J. Kim, T. S. Koffas, C. C. Lawrence et al., *Langmuir* **2004**, *20*, 4640–4646.
189. T. S. Koffas, E. Amitay-Sadovsky, J. Kim, G. A. Somorjai, *Biomater. Sci., Polymer Edn.*, **2004**, *15*, 475–509.
190. J. Wang, S. E. Woodcock, S. M. Buck et al., *J. Am. Chem. Soc.* **2001**, *123*, 9470–9471.
191. C. Chen, J. Wang, S. E. Woodcock et al., *Langmuir* **2002**, *18*, 1302–1309.
192. C. Y. Chen, J. Wang, M. A. Even et al., *Macromolecules* **2002**, *35*, 8093–8097.
193. C. Y. Chen, M. A. Even, J. Wang et al., *Macromolecules* **2002**, *35*, 9130–9135.
194. J. Wang, S. M. Buck, M. A. Even et al., *J. Am. Chem. Soc.* **2002**, *124*, 13302–13305.
195. J. Wang, S. M. Buck, Z. Chen, *J. Phys. Chem. B* **2002**, *106*, 11666–11672.
196. J. Wang, Z. Paszti, M. A. Even et al., *J. Am. Chem. Soc.* **2002**, *124*, 7016–7023.
197. J. Wang, S. M. Buck, Z. Chen, *Analyst* **2003**, *128*, 773–778.
198. J. Wang, M. L. Clarke, Y. Zhang et al., *Langmuir* **2003**, *19*, 7862–7866.
199. C. Y. Chen, C. L. Loch, J. Wang et al., *J. Phys. Chem. B.* **2003**, *107*, 10440–10445.
200. C. Y. Chen, J. Wang, C. L. Loch et al., *J. Am. Chem. Soc.* **2004**, *126*, 1174–1179.
201. S. Baldelli, *J. Phy. Chem. B* **2003**, *107*, 6148–6152.
202. Z. D. Schultz, M. E. Biggin, J. O. White et al., *Anal. Chem.* **2004**, *76*, 604–609.
203. L. Dreesen, C. Humbert, P. Hollander et al., *Chem. Phys. Lett.* **2001**, *333*, 327–331.
204. L. Dreesen, C. Humbert, M. Celebi et al., *Appl. Phys. B Lasers Opt.* **2002**, *74*, 621–625.
205. C. Humbert, L. Dreesen, A. A. Mani et al., *Surf. Sci.* **2002**, *502–503*, 203–207.
206. K. S. Gautam, A. D. Schwab, A. Dhinojwala et al., *Phys. Rev. Lett.* **2000**, *85*, 3854–3857.
207. K. S. Gautam, A. Dhinojwala, *Phy. Rev. Lett.* **2002**, *88*, 145501.
208. G. P. Harp, K. S. Gautam, A. Dhinojwala, *J. Am. Chem. Soc.* **2002**, *124*, 7908–7909.
209. H. C. Allen, D. E. Gragson, G. L. Richmond, *J. Phys. Chem. B* **1999**, *103*, 660–666.
210. H. C. Allen, E. A. Raymond, G. L. Richmond, *J. Phys. Chem. A* **2001**, *105*, 1649–1655.
211. M. G. Brown, D. S. Walker, E. A. Raymond et al., *J. Phys. Chem. B* **2003**, *107*, 237–244.
212. J. C. Conboy, M. C. Messmer, G. L. Richmond, *J. Phys. Chem. B.* **1997**, *101*, 6724–6733.
213. J. C. Conboy, M. C. Messmer, G. L. Richmond, *Langmuir* **1998**, *14*, 6722–6727.
214. D. E. Gragson, G. L. Richmond, *J. Phys. Chem. B* **1998**, *102*, 3847–3861.
215. D. E. Gragson, G. L. Richmond, *J. Am. Chem. Soc.* **1998**, *120*, 366–375.
216. L. F. Scatena, G. L. Richmond, *J. Phys. Chem.* **2001**, *106*, 11240–11250.
217. B. L. Smiley, G. L. Richmond, *J. Phys. Chem. B* **1999**, *103*, 653–659.
218. R. A. Walker, J. C. Conboy, G. L. Richmond, *Langmuir* **1997**, *13*, 3070–3073.
219. R. A. Walker, D. E. Gragson, G. L. Richmond, *Colloids Surf. Sci. A* **1999**, *154*, 175–185.
220. M. R. Watry, G. L. Richmond, *Langmuir* **2002**, *18*, 8881–8887.
221. M. R. Watry, G. L. Richmond, *J. Phys. Chem. B* **2002**, *106*, 12517–12523.
222. M. R. Watry, T. L. Tarbuck, G. L. Richmond, *J. Phys. Chem. B* **2003**, *107*, 512–518.
223. E. A. Raymond, T. L. Tarbuck, M. G. Brown et al., *J. Phys. Chem. B* **2003**, *107*, 546–556.
224. K. A. Becraft, G. L. Richmond, *Langmuir* **2001**, *17*, 7721–7724.
225. K. A. Becraft, F. G. Moore, G. L. Richmond, *J. Phys. Chem. B* **2003**, *107*, 3675–3678.
226. K. A. Becraft, F. G. Moore, G. L. Richmond, *Phys. Chem. Chem. Phys.* **2004**, *6*, 1880–1889.
227. M. C. Gurau, G. Kim, S. M. Lim et al., *ChemPhysChem* **2003**, *4*, 1231–1233.
228. J. Kim, P. S. Cremer, *J. Am. Chem. Soc.* **2000**, *122*, 12371–12372.
229. J. Kim, G. Kim, P. S. Cremer, *Langmuir* **2001**, *17*, 7255–7260.
230. J. Kim, P. S. Cremer, *ChemPhysChem* **2001**, *2*, 543–546.
231. G. Kim, M. Gurau, J. Kim et al., *Langmuir* **2002**, *18*, 2807–2811.
232. J. Kim, G. Kim, P. S. Cremer, *J. Am. Chem. Soc.* **2002**, *124*, 8751–8756.
233. S. Kataoka, M. C. Gurau, F. Albertorio et al., *Langmuir* **2004**, *20*, 1662–1666.
234. M. C. Gurau, S.-M. Lim, E. T. Castellana et al., *J. Am. Chem. Soc.* **2004**, *126*, 10522–10523.
235. S. R. Hatch, R. S. Polizzotti, S. Dougal et al., *Chem. Phys. Lett.* **1992**, *196*, 97–102.
236. S. R. Hatch, R. S. Polizzotti, S. Dougal et al., *J. Vac. Sci. Tech A.* **1993**, *11*, 2232–2238.

237. M. S. Yeganeh, S. M. Dougal, H. S. Pink, *Phys. Rev. Lett.* **1999**, *83*, 1179–1182.
238. M. S. Yeganeh, S. M. Dougal, R. S. Polizzotti et al., *Phys. Rev. Lett.* **1995**, *74*, 1811–1814.
239. D. Zhang, S. M. Dougal, M. S. Yeganeh, *Langmuir* **2000**, *16*, 4528–4532.
240. M. S. Yeganeh, *Phy. Rev. E* **2002**, *66*, 041607.
241. K. Wolfrum, H. Graener, A. Laubereau, *Chem. Phys. Lett.* **1993**, *213*, 41–46.
242. J. Lobau, K. Wolfrum, A. Romphorst et al., *Thin Solid Films* **1996**, *289*, 272–281.
243. J. Lobau, K. Wolfrum, *J. Opt. Soc. Am. B* **1997**, *14*, 2505–2512.
244. W. Pohle, M. Saß, C. Selle et al., *Vib. Spectrosc.* **1999**, *19*, 321–327.
245. J. Lobau, M. Sass, W. Pohle et al., *J. Mol. Struc.* **1999**, *480*, 407–411.
246. M. S. Shultz, S. Baldelli, C. Schnitzer et al., *J. Phys. Chem. B* **2002**, *106*, 5313–5324.
247. S. Baldelli, D. J. Campbell, C. Schnitzer et al., *J. Phys. Chem. B* **1997**, *101*, 4607–4612.
248. S. Baldelli, C. Schnitzer, M. J. Shultz et al., *Chem Phys. Lett.* **1998**, *287*, 143–147.
249. S. Baldelli, S. Cheryl, M. J. Shultz, *Chem. Phys. Lett.* **1999**, *302*, 157–163.
250. D. Simonelli, S. Baldelli, M. J. Shultz, *Chem. Phys. Lett.* **1998**, *298*, 400–404.
251. C. Schnitzer, S. Baldelli, D. J. Campbell et al., *J. Phys. Chem. A.* **1999**, *103*, 6383–6386.
252. C. Schnitzer, S. Baldelli, M. J. Shultz, *J. Phys. Chem. B* **2000**, *104*, 585–590.
253. C.-y. Wang, H. Groenzin, M. J. Shultz, *Langmuir* **2003**, *19*, 7330–7334.
254. C.-y. Wang, H. Groenzin, M. J. Shultz, *J. Phys. Chem. B* **2004**, *108*, 265–272.
255. G. Ma, H. C. Allen, *J. Phys. Chem. B* **2003**, *107*, 6343–6349.
256. E. L. Hommel, H. C. Allen, *Analyst* **2003**, *128*, 750–755.
257. E. L. Hommel, H. C. Allen, *Phys. Chem. B* **2003**, *107*, 10823–10828.
258. D. Liu, G. Ma, L. Levering et al., *J. Phys. Chem. B* **2004**, *108*, 2252–2260.
259. L. L. Van Loon, H. C. Allen, *J. Phys. Chem. B.* **2004**, *108*, 17666–17674.
260. N. Nishi, D. Hobara, M. Yamamoto et al., *Langmuir* **2003**, *19*, 6187–6192.
261. T. Iimori, T. I. wahashi, H. Ishii et al., *Chem. Phys. Lett.* **2004**, *389*, 321–326.
262. T. Miyamae, K. Tsukagoshi, O. Matsuoka et al., *Langmuir* **2001**, *17*, 8125–8130.
263. T. Miyamae, Y. Yamada, H. Uyama et al., *Surf. Sci.* **2001**, *493*, 314–318.
264. T. Miyamae, H. Nozoye, *J. Photochem. Photobiol.* **2001**, *145*, 93–99.
265. T. Miyamae, Y. Yamada, H. Uyama et al., *Vacuum* **2002**, *66*, 305–310.
266. T. Miyamae, H. Nozoye, *Surf. Sci.* **2003**, *532–535*, 1045–1050.
267. S. Follonier, W. J. W. Miller, N. L. Abbott et al., *Langmuir* **2003**, *19*, 10501–10509.
268. R. L. Pizzolatto, Y. J. Yang, K. Wolf et al., *Anal. Chim. Acta* **1999**, *397*, 81–92.
269. Y. J. Yang, R. L. Pizzolatto, M. C. Messmer, *J. Opt. Soc. Am. B* **2000**, *17*, 638–645.
270. Y. Liu, L. K. Wolf, M. C. Messmer, *Langmuir* **2001**, *17*, 4329–4335.
271. Y. Liu, M. C. Messmer, *J. Am. Chem. Soc.* **2002**, *124*, 9714–9715.
272. Y. Liu, M. C. Messmer, *J. Phys. Chem. B.* **2003**, *107*, 9774–9779.
273. M. Himmelhaus, M. Buck, M. Grunze, *Appl. Phys. B* **1999**, *68*, 595–598.
274. M. Himmelhaus, F. Eisert, M. Buck et al., *J. Phys. Chem. B* **2000**, *104*, 576–584.
275. A. Wada, N. Watanabe, K. Iwatsu et al., *Surf. Sci.* **1996**, *357–358*, 651–655.
276. T. Anzai, H. Maeoka, A. Wada et al., *J. Mol. Struc.* **1995**, *352–353*, 455–463.
277. H. Ishida, K. Iwatsu, J. Kubota et al., *Surf. Sci.* **1996**, *366*, l724–l728.
278. H. Ishida, K. Iwatsu, J. Kubota et al., *J. Chem. Phys.* **1998**, *108*(()14), 5957–5964.
279. H. Yamamoto, N. Watanabe, A. Wada et al., *J. Chem. Phys.* **1997**, *106*, 4734–4744.
280. S. Katano, A. Bandara, J. Kubota et al., *Surf. Sci.* **1999**, *427–428*, 337–342.
281. C. Hirose, A. Bandara, S. Dobashi et al., *Surf. Sci.* **1997**, *387*, 312–319.
282. C. Hirose, H. Ishida, K. Iwatsu et al., *J. Chem. Phys.* **1998**, *108*, 5948–5956.
283. A. Bandara, S. Katano, J. Kubota et al., *Chem Phy. Lett.* **1998**, *290*, 261–267.
284. A. Bandara, J. Kubota, A. Wada et al., *Appl. Phys. B* **1999**, *68*, 573–578.
285. K. Domen, A. Bandara, J. Kubota et al., *Surf. Sci.* **1999**, *427–428*, 349–357.
286. A. Bandara, J. Kubota, K. Onda et al., *Surf. Sci.* **1999**, *427–428*, 331–336.
287. K. Kusafuka, H. Noguchi, K. Onda et al., *Surf. Sci.* **2002**, *503*, 313–318.
288. J. Kubota, E. Yoda, N. Ishizawa et al., *J. Phys. Chem. B* **2003**, *107*, 10329–10332.
289. M. Florsheimer, C. Brillert, H. Fuchs, *Langmuir* **1999**, *15*, 5437–5439.

290. M. Florsheimer, *Phys. Status Solidi A* **1999**, *173*, 15–27.
291. M. Florsheimer, C. Brillert, H. Fuchs, *Mater. Sci. Eng., C* **1999**, *8–9*, 335–341.
292. M. Florsheimer, M. T. Bootsmann, H. Fuchs, *Phys. Rev. B* **2002**, *65*, 125406.
293. R. D. Schaller, R. J. Saykally, *Langmuir* **2001**, *17*, 2055–2058.
294. R. D. Schaller, J. C. Johnson, K. R. Wilson et al., *J. Phys. Chem. B* **2002**, *106*, 5143–5154.
295. J. Liu, J. C. Conboy, *J. Am. Chem. Soc.* **2004**, *126*, 8376–8377.
296. J. Liu, J. C. Conboy, *J. Am. Chem. Soc.* **2004**, *126*, 8894–8895.
297. B. D. Fitchett, J. C. Conboy, *J. Phys. Chem. B*. **2004**, *108*, 20255–20262.
298. S. Ye, H. Noda, T. Nishida et al., *Langmuir* **2004**, *20*, 357–365.
299. W. Zhou, S. Ye, M. Abe, T. Nishida, K. Uosaki, M. Osawa, Y. Sasaki, *Chem. Eur. J.*, **2004**, in press.
300. G. Li, S. Ye, S. Morita et al., *J. Am. Chem. Soc.* **2004**, *126*, 12198–12199.
301. S. Morita, S. Ye, G. Li et al., *Vib. Spectrosc.* **2004**, *35*, 15–19.
302. T. Nishida, S. Ye, M. Osawa, submitted.
303. J. Sagiv, *J. Am. Chem. Soc.* **1980**, *102*, 92–97.
304. A. S. Lagutchev, K. J. Song, J. Y. Huang et al., *Chem. Phys.* **1998**, *226*, 337–349.
305. D. G. Cameron, S. C. His, J. Umemura et al., *Can. J. Chem.* **1981**, *59*, 1357–1360.
306. M. D. Porter, T. B. Bright, D. L. Allara et al., *J. Am. Chem. Soc.* **1987**, *109*, 3559–3568.
307. T. Baum, S. Ye, K. Uosaki, *Langmuir* **1999**, *15*, 8577–8579.
308. D. Eisenberg, W. Kauzmann, *The Structure and Properties of Water*, Oxford University Press, London, 1969.
309. Y. R. Shen, *Solid State Commun.* **1998**, *108*, 399–406.

7.2 Quartz Crystal Microbalance (QCM)

Katsuaki Shimazu
Hokkaido University, Japan

7.2.1 Introduction

A quartz crystal microbalance (QCM) is an extremely attractive and powerful tool to examine mass transport processes at electrode/solution interfaces because of its capability of detecting nanogram changes in mass [1–5]. Often used are AT-cut quartz crystals with a 5 to 10-MHz fundamental frequency. Their sensitivities are simply given by Sauerbrey's equation, the usefulness of which has been experimentally confirmed by many research groups. The frequency change of 1 Hz of a 5-MHz QCM corresponds to a mass change of 17.7 ng cm^{-2}. The noise level of a carefully assembled 5-MHz QCM apparatus is below 0.1 Hz, and therefore, the detection limit on the basis of $S/N = 4$ is approximately several nanograms per centimeter square. This means that any kind of chemical species, except hydrogen, involved in interfacial reactions at monomolecular films and polymer films can be detected by the QCM (the number of molecules in the monomolecular film is in the range of 10^{-10} to 10^{-9} mol cm^{-2}). With this capability, how solvents and electrolyte ions participate in interfacial processes can be clarified. Such information is particularly important for modified electrode systems, because the solvent incorporation and ion association accompanying the redox or dissociation of functional groups often take place and because most spectroscopic and the other techniques are lacking in this capability.

7.2.2 Self-assembled Monolayer (SAM)

Because of the difficulty in assembling a highly stable QCM apparatus, the QCM was not applied to self-assembled monolayers until the late 1980s. The first application was made by Buttry and coworkers [6–8]. They examined the electrochemically induced adsorption and desorption of redox surfactants bearing the ferrocene functionality in the presence of a surfactant in solution as a function of the chain length, concentration of the surfactant and temperature. The QCM adequately monitored the desorption following oxidation. The desorption occurred more easily when a shorter chain surfactant was used and/or at a low surfactant concentration and elevated temperatures.

7.2.2.1 Construction of Well-ordered SAMs

7.2.2.1.1 Self-assembly In situ monitoring of the self-assembly process of thiol derivatives was first reported by Shimazu et al. [9]. They injected a small aliquot of ferrocenyl-undecanethiol (FcC11SH) solution into constantly stirred hexane and followed the frequency change. The time course of the frequency shows that the initial adsorption is fast, followed by the slow adsorption whose rate was 2 orders of magnitude lower (Fig. 1). These results are in agreement with the previous reports based on ex situ electrochemical and ellipsometric measurements. The total frequency change agreed well with that expected from the electrochemical charge associated with the redox of the SAM in 1 M $HClO_4$. The frequency change, which may be caused by the change in the solution composition by the addition of the thiol solution (from pure hexane to

Encyclopedia of Electrochemistry. Edited by A.J. Bard and M. Stratmann
Vol. 10 *Modified Electrodes*. Edited by M.Fujihira, I.Rubinstein, and J.F.Rusling
Copyright © 2007 Wiley-VCH Verlag GmbH & Co. KGaA, Weinheim. ISBN: 978-3-527-30402-8

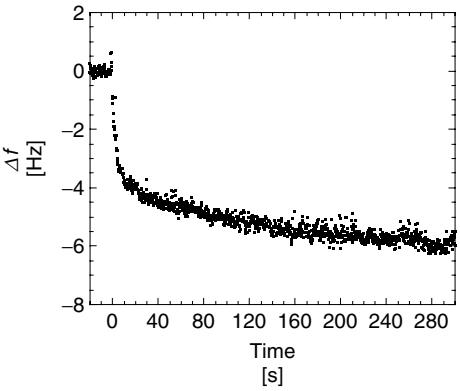


Fig. 1 Frequency change (5 MHz) during the self-assembly of FcC11SH on a Au electrode in hexane. Final concentrations of thiols are 0.5 mM. (Adapted from Shimazu et al.[9].)

0.5 mM FcC11SH/hexane) was estimated using the equation derived by Kanazawa and Gordon [10] to be less than 5% of the total frequency change. The above adsorption behavior, initially fast and then slow, is commonly observed for many other thiols such as ω-(N-pyrrolyl)alkanethiols [11], the alkanethiol derivatives of viologen [12] and phospholipids [12], and 3-thiophene [13].

The kinetics of the self-assembly process of octanethiol (C8SH) and octadecanethiol (C18SH) was examined in more detail by Karpovich and Blanchard [14]. For these cases, the kinetics is well described by the following equation based on the Langmuir adsorption isotherm,

$$\theta(\mathrm{t}) = K'[1 - \exp(-k_{\mathrm{obs}}t)] \qquad (1)$$

$$k_{\mathrm{obs}} = k_{\mathrm{a}}C + k_{\mathrm{d}} \qquad (2)$$

where k_{a} and k_{d} are the adsorption and desorption rate constants, respectively, C is the thiol concentration, and $K' = C/(C + (k_{\mathrm{d}}/k_{\mathrm{a}}))$. From the concentration dependence of k_{obs} (Eq. 2) determined from time course of the coverage (Eq. 1), both k_{a} and k_{d} were determined to be 2059–2440 $\mathrm{M}^{-1}\,\mathrm{s}^{-1}$ and 0.16–0.19 s^{-1} for C18SH, respectively. The k_{a} value for C8SH is smaller (811 $\mathrm{M}^{-1}\,\mathrm{s}^{-1}$) than that for C18SH. Using these data, they calculated the equilibrium constant, K_{eq} ($= k_{\mathrm{a}}/k_{\mathrm{d}}$), and the free energy of adsorption, ΔG_{ads} ($= -\mathrm{R}T\ln K_{\mathrm{eq}}$): $K_{\mathrm{eq}} =$ 10850–15250 M^{-1} and $\Delta G_{\mathrm{ads}} = -5.5 -$ -5.6 kcal mol^{-1} for C18SH, $K_{\mathrm{eq}} =$ 1930 M^{-1} and $\Delta G_{\mathrm{ads}} = -4.4$ kcal mol^{-1} for C8SH. These values of ΔG_{ads} are virtually the same as the aliphatic interchain interaction energies. The Langmuir type of adsorption was also reported based on the QCM data for the self-assembly of o-xylene-α,α'-dithiol (o-XDT) on Au, and anthraquinone-2-carboxylic acid (AQ-2-COOH) on Ag by Kim and coworkers [15–17]. Following Karpovich and Blanchard's analysis, they determined k_{a} and k_{d} to be $2.2 \times 10^4\ \mathrm{M}^{-1}\,\mathrm{s}^{-1}$ and 0.18 s^{-1} for o-XDT in hexane, respectively. These values correspond to a K_{eq} of 1.1×10^5 and a ΔG_{ads} of -28.9 kJ mol^{-1}. The equilibrium constant of adsorption can be obtained using the frequency values when the equilibrium is attained (Δf_{eq}) and using the following equation,

$$\frac{C}{\Delta f_{\mathrm{eq}}} = \frac{C}{\Delta f_{\mathrm{max}}} + \frac{1}{K_{\mathrm{eq}}\Delta f_{\mathrm{max}}} \qquad (3)$$

where Δf_{max} is the frequency change at the saturated coverage. For AQ-2-COOH on Ag, K_{eq} is 9.1×10^3.

The formation of multilayers and the dissolution of gold during the immersion of

an Au substrate in thiol solution were also demonstrated by the QCM measurements. Bard's group [18] using ex situ QCM determined the formation of approximately four monolayers after a six-day immersion of the gold substrate in C18SH ethanol solution (only monolayers were formed for less than a 3-h immersion). Matsumoto et al. [19] measured the QCM response of a Au electrode after the injection of 2,5-dimercapto-1,3,4-thiadiazole (DMcT) into *N*-methyl-2-pyrrolidinone. The initial frequency decrease due to the adsorption was followed by a monotonous frequency increase. This shows that the adsorption of DMcT induces the dissolution of the Au surface. The dissolution was also observed for a Cu electrode in the presence of DMcT. The dissolution of Cu was much faster than that of Au.

7.2.2.1.2 **Postassembly Derivation of SAM Surfaces** The QCM is also useful for monitoring the immobilization of functional molecules onto SAMs. On the basis of the observed frequency change, either a monolayer or multilayer formation was concluded. Fullerene C_{60} binds to cysteamine and cysteamine/ethanethiol SAMs presumably by N–H addition to the C=C bonds in the C_{60}, which fuses two six-membered rings, and forms a monolayer [20]. Cyclodextrins forms aggregates (multilayers) on MPA and mercaptooctanoic acid SAMs, but not monolayers through an electrostatic interaction although the surface negative charge was considered to improve the level of organization of the CD aggregates [21].

Rubinstein et al. [22] used the SAM of *p*-aminothiophenol to increase the polyaniline (PANI) film/substrate adhesion. It became possible to calculate the film density from the mass data using the QCM and thickness data by ellipsometry. They found that films of higher density were formed on the SAM compared to bare Au. The construction of a denser polypyrrole (PPY) film with good adhesion on ω-(*N*-pyrrolyl)alkanethiol SAMs was also reported [11].

The QCM was also used to monitor the electrochemical removal of protecting groups (hydroquinones) from the hydroquinone monoester of thioacetic acid and the 12,12′-dithiobis-(dodecanoic acid hydroquinone monoester) SAMs to form carboxylic acid-terminated SAMs for immobilizing the oligodeoxynucleotides [23].

The immobilization of silver nanoparticles (10.3 ± 4.4 nm) on 4-carboxythiophenol SAM [24], citrate-stabilized gold nanoparticles (11 nm) on aminoundecanethiol (AUT) SAM [25], and dodecanethiol (C12SH)-protected gold nanoparticles (4.8 ± 0.5 nm) on C12SH SAM [26] were examined using the QCM. The adsorption up to a 10–18% surface coverage was commonly observed. The adsorption kinetics follows Eq. (1), and K_{eq} was determined to be 238 for gold nanoparticle on the AUT SAM.

7.2.2.1.3 **Layer-by-layer Growth of Multilayers** Yang et al. [27] monitored the construction of metal alkyl- and arylbisphosphnate multilayers in a layer-by-layer fashion using a QCM. The frequency linearly decreased with an increasing layer number up to 6 for copper biphenylbis(phosphonate) layers and up to 100 for copper octanebis(phosphonate) layers. The mass increase per layer calculated from the slope was reasonably explained on the basis of the molecular area, roughness factor and some smoothing of the rough surface of the thick films.

The layer-by-layer growth of gold nanoparticle multilayers was performed by alternating exposures of

pyridine-terminated thiol SAM-coated Au electrodes to solutions of 0.1 M $Cu(NO_3)_2$ and gold nanoparticles covered with mixed pyridine-terminated thiol/octanethiol monolayers (Fig. 2a) [28]. The frequency change linearly increased with the number of dipping cycles (Fig. 2b). The Cu^{2+} ions clearly functioned as binding centers for chelating interactions. Exposure to an EDTA solution caused almost complete removal of the nanoparticles as demonstrated by QCM. The alternative dipping to solutions of poly(allylamine) and mercaptoundecanoic acid (MUA) functionalized nanoparticles caused the incorporation of about 3.5 monolayers of nanoparticles into the film per dipping cycle [29]. This value was in agreement with that determined by spectroscopy.

7.2.2.2 **Reductive Desorption**

Porter and coworkers [30, 31] found that the Au–S bond was cleaved when the negative electrode potential was applied. This reaction is described as follows.

$$Au-S-R + e^- \longrightarrow Au + R-S^- \quad (4)$$

The reductive desorption has received particular attention for the following reasons. First, we can calculate the number of thiols adsorbed on the electrode surface from the desorption charge, even if the SAM does not have an electroactive functional group. Second, the adsorption states of the thiol can also be characterized from the desorption potential, which has been found to be strongly dependent on the identity of the thiol, packing state, surface crystallinity of the substrate, and several other factors. The first application

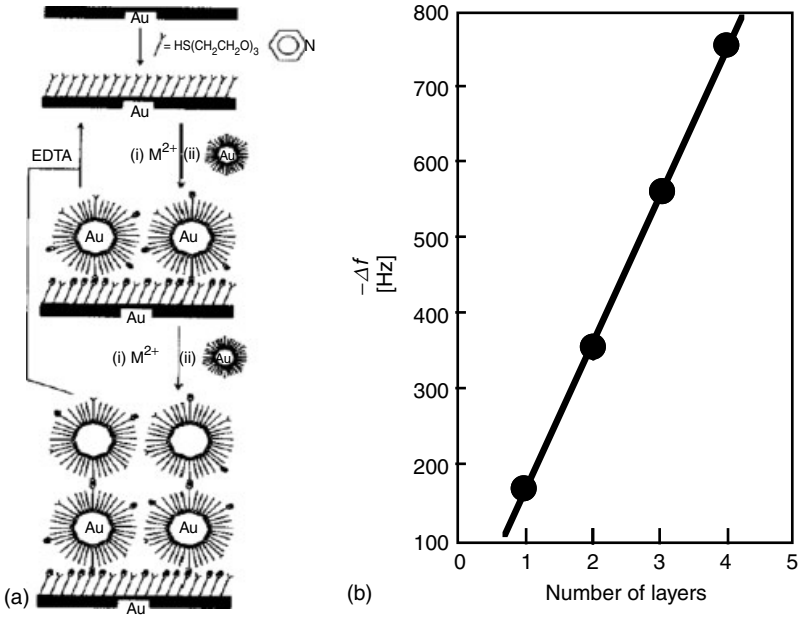


Fig. 2 Layer-by-layer growth of gold nanoparticle multilayers by alternative dipping in 0.1 M $Cu(NO_3)_2$/ethanol and gold nanoparticle/CH_2Cl_2-ethanol solutions. (a) Procedure for nanoparticle assembly, (b) frequency change (8 MHz) as a function of dipping cycle. (Adapted from Chen et al. [28].)

of EQCM to the analysis of the desorption process was made by Schneider and Buttry for alkanethiol SAMs on Au [29]. The frequency increase at the reduction peak was observed for the C12SH and C10SH SAMs in a DMF and acetonitrile solution containing electrolyte and a low concentration of thiol, showing the desorption of the adsorbed thiol molecules. The desorption charge in DMF was approximately twice as much as that expected from the frequency change and Eq. (4). They attributed this discrepancy to the significant contribution of the charge due to the double-layer charging to the total charge because the drastic change in double-layer structure takes place upon a desorption.

Recently, a detailed QCM examination of the reductive desorption of alkanethiols and mercaptoalkanoic acids from Au electrodes in various ethanolic alkaline solutions and supporting electrolytes was conducted by Shimazu and coworkers [32]. They accurately determined the desorption charge by subtracting the contribution from the double-layer charging, which can be determined by the following equation,

$$Q_{\mathrm{dl}} = [(E_{\mathrm{p}} - \mathrm{pzc}_{\mathrm{Au}})C_{\mathrm{Au}}] - [(E_{\mathrm{n}} - \mathrm{pzc}_{\mathrm{SAM}})C_{\mathrm{SAM}}] \quad (5)$$

where pzc_x and C_x are the potential of zero charge and the capacitance of x (x = uncoated gold or SAM), respectively, and E_{p} and E_{n} ($E_{\mathrm{p}} > E_{\mathrm{n}}$) are the potential limits between which the reduction current in a linear sweep voltammogram was integrated. Using the determined desorption charge and the total frequency change obtained during desorption, the mass change when one mole of electrons (one Faraday) passed was obtained according to Eq. (5). This mass change was denoted as the mass per electron (*mpe*).

$$mpe = \frac{-\Delta f \cdot \mathrm{S}}{(Q_{\mathrm{des}}/\mathrm{F})} \quad (6)$$

The symbol S is a proportionality constant in Sauerbrey's equation (e.g. 17.7×10^{-9} g cm^{-2} Hz^{-1} for 5-MHz AT-cut quartz crystals). It should be mentioned that different names such as the apparent molar mass, $\mathrm{MW}_{\mathrm{app}}$, are also denoted to the quantity given by Eq. (6) instead of *mpe*.

The *mpe* was determined for the reductive desorption of alkanethiol SAMs of various chain lengths from hexanethiol (C6SH) to C18SH in a 0.1 M KOH/ethanol solution. It linearly increases with the chain length with a slope close to the mass of CH_2, as expected for a one-electron process. However, the *mpe* is much smaller (by 148 g mol^{-1}) than the molar mass of the desorbed alkanethiol. This difference is attributed to the simultaneous adsorption of cation species from solution, which is supported by the observed cation dependence of *mpe* and by the fact that the pzc of a bare gold electrode is more positive than the desorption potential.

Various pieces of information on the SAM and/or SAM/solution interfaces can be obtained from the *mpe* values. On the basis of the *mpe* for the reductive desorption of mercaptoalkanoic acid SAMs of various chain lengths (mercaptopropionic acid (MPA) to mercaptoundecanoic acid (MUA)), for example, Shimazu and coworkers concluded in the same paper [32] that the terminal carboxylate of a SAM is associated with the solvated cation (the solvation numbers are 1.6, 2.4–3.0 and 0.2 for Li^+, K^+ and Cs^+, respectively).

The mass decrease upon the reductive desorption was sometimes extremely greater than that expected for the monolayer. Although we should take into

account the contribution from the solvent incorporation into the SAM and/or the interfacial association such as the case described above, the large mass decrease is often evidence for the multilayer formation. Such a large mass decrease was observed upon the desorption of the C10SH SAM, which was conducted in acetonitrile a short time after the self-assembly initiation [33].

Surface plasmon resonance (SPR) provides thickness information at the electrode/solution interfaces on a nanometer level. Therefore, SPR has recently been recognized as an alternative method to obtain information concerning the material transport. Bailey et al. [34] examined the reductive desorption of C18SH SAMs in 0.1 M TEAP/acetonitrile using an SPR/QCM combined system for the simultaneous acquisition of both data. The two techniques gave nearly identical results for the desorption kinetics of the film prepared by a 465-min immersion of the electrode in a thiol solution. For the film prepared by a 160-min immersion, however, the results were significantly different from each other (Fig. 3). This was considered to be due to the difference in their physicochemical properties, on which both techniques are based. When the film is desorbed, namely, the C18S-rich layer in solution quickly lose rigidity, resulting in the fact that the QCM is sensitive only to the actual desorption event. Because the change in the refractive index before and after desorption is relatively small, SPR follows the diffusion of the desorbed C18S-rich layer to the bulk solution. It should be noted that the lengths at which we can see the thiol molecules are comparable for both techniques.

7.2.2.3 Evaluation of End-group Functions

7.2.2.3.1 **Redox Properties** The mass transport accompanying the redox of the ferrocene-terminated alkanethiol SAMs was examined by Buttry and coworkers [8] and by Uosaki, Shimazu, and their coworkers [9, 35–38]. The frequency decreased upon oxidation to the ferricenium cation, and increased upon reduction to the uncharged ferrocene (Fig. 4). These behaviors are interpreted by the interfacial association between the ferricenium cation in the SAM and anion in solution. Although these behaviors were observed in all examined cases, the *mpe* for the redox of the ferrocene functionality was dependent on the SAM, the packing density of the ferrocene-terminated alkanethiol and the identity of the anion. It is approximately half of the molar mass of

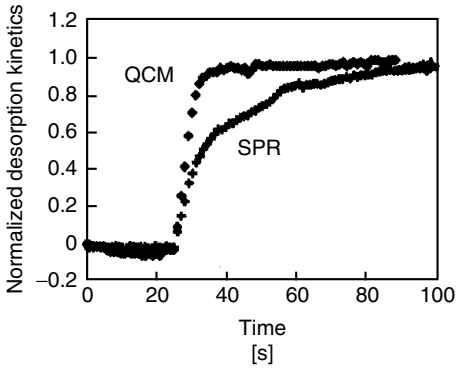


Fig. 3 Comparison of C18S desorption kinetics as measured by QCM (5 MHz) and SPR for the SAM prepared by 160-min immersion. Both QCM and SPR kinetics are nearly identical for the SAM prepared by 465 min immersion. (Adapted from Bailey et al. [34].)

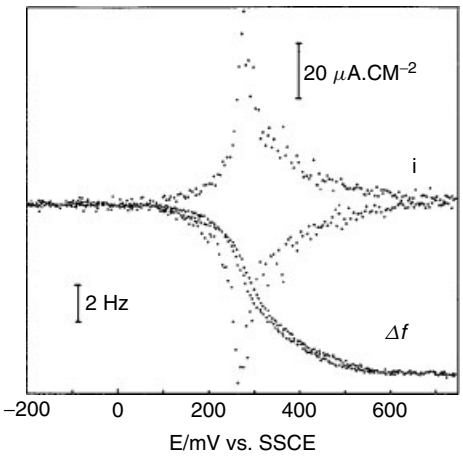


Fig. 4 Cyclic voltammogram (50 mV s^{-1}) of a FcC11SH SAM (3.1×10^{14} molecules cm^{-2}) on Au in 1 M $HClO_4$ together with frequency response (5 MHz). (From Shimazu et al. [36].)

the anion (ClO_4^-) (ca. 50 g mol^{-1}) for the *p*-(ferrocene-carbamyl) phenyl disulfide (FcADS) SAM in 1 M $HClO_4$ [8]. At the saturated coverage of FcC11SH SAM ($\Gamma_{Fc} = 3.0 \times 10^{-10}$ mol cm^{-2}), however, the *mpe* (103 g mol^{-1}) is the same as the molar mass of ClO_4^- [36]. The latter indicates the strong binding between the ferrocenium cation and ClO_4^-, and is taken as evidence for ion-pair formation. In the case of the FcADS SAM, on the other hand, some fraction of the ferrocenium cations seem to be weakly associated with anions in solution adjacent to the SAM so that these anions cannot be detected by the QCM because they do not oscillate together with the quartz.

The *mpe* is much larger at low FcC11SH coverages. For example, it is 370 g mol^{-1} at $\Gamma_{Fc} = 0.6 \times 10^{-10}$ mol cm^{-2} in 1 M $HClO_4$ [36]. Similar behaviors, a smaller *mpe* at a high coverage and larger *mpe* at a low coverage, were also observed for FcADS in 0.1 M NaCl; 25 g mol^{-1} at $\Gamma_{Fc} = 3.0 \times 10^{-10}$ mol cm^{-2}, 410 g mol^{-1} at $\Gamma_{Fc} = 1.6 \times 10^{-10}$ mol cm^{-2} [8]. It is considered that this is due to the orientational change in the adsorbed ferrocene derivatives induced by the redox of the ferrocene moiety in the SAMs. The molecular orientation of the adsorbed species changes from more parallel to more perpendicular upon oxidation probably due to the electrostatic interaction between the charged neighboring species. As a result, the solvent molecule can be incorporated into the space created by this orientational change so that the *mpe* becomes much larger than the molar mass of the anion. This model was experimentally confirmed using an FT–IR reflection absorption spectroscopy/QCM-combined system developed by them [35, 37].

For the mixed ferrocenyloctanethiol (FcC8SH)/C18SH monolayers, the *mpe* was independent of the surface FcC8SH fraction at higher fractions, and increased with the decreasing fraction. Because alkanethiol molecules occupied the space between the FcC8SH molecules, the change in the orientation of the alkyl chain of FcC8SH was strongly prohibited. Kawaguchi et al. [39] explained the large *mpe* values for the lower FcC8SH fractions by a ''pocket'' model; the perchlorate and water molecules are incorporated into the pocket surrounded by the C18SH molecules and a FcC8SH

molecule at the bottom upon the oxidative formation of a positive charge, which makes the pocket hydrophilic. The constant and low *mpe* values at higher surface fractions, on the other hand, show that no such pocket exists, suggesting the mixed monolayers consisting of single-component domains. Thus, the *mpe* is considered to be a diagnostic parameter showing the microenvironment around a surface-confined FcC8SH molecule.

The ion-pairing between the electroactive center of the SAM and ion in solution was also demonstrated by the QCM for SAMs of the alkanethiol derivatives of viologen ($CH_3(CH_2)_{n-1}V^{2+}$ $(CH_2)_mSH$ = *n*VmSH, V is viologen group) [40]. The frequency decrease due to anion loss was observed upon the reduction for all the examined viologen SAMs (1V12SH, 10V3SH, and 10V10SH). The number of water molecules expelled from the SAM together with the anion was calculated from the *mpe* values. It depends on the identity of the anion and on the proximity of the viologen moiety to the monolayer/solution interface.

7.2.2.3.2 **Acid/Base Properties and Reactions** Wong et al. [41] first applied the QCM to the evaluation of the acid/base properties of SAMs. When the pH of the phosphate buffer solution in contact with the mercaptohexadecanoic acid (MHDA) SAM–coated QCM was incrementally increased by adding 0.1 M NaOH, the resonance frequency sigmoidally increased to 1200 Hz. On the basis of the impedance analysis and the frequency measurements using the BT-cut QCM, it was concluded that the observed large frequency increase is mainly attributed to changes in the viscoelastic properties of the hydrodynamic layer in contact with the QCM, with a minor contribution from the increase in the tensile stress with increasing pH. The apparent pK_a determined from the inflection point of the frequency-pH curve exceeded eight, depending on the electrolyte concentration.

Totally different results were obtained by Shimazu and coworkers for the titrations of the SAMs of mercaptoalkanoic acids of different chain lengths (MPA, MHA=mercaptohexanoic acid, MUA, and MHDA) [42–44]. The resonance frequency of the QCM was continuously monitored when the pH of an unbuffered 0.1 M NaCl solution was increased by adding 0.1 M NaOH at a constant flow rate (Fig. 5). The frequency decreased by ca. 2 Hz independent of the chain length in the NaCl/NaOH solution, but was dependent on the cation (K^+, Cs^+) used for the electrolyte and titarant solutions. The impedance analysis also showed that the

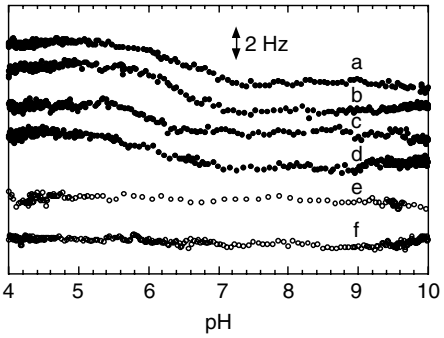


Fig. 5 Surface mass titration curves for (a–e) SAMs of thiols and (f) bare Au. (a) MHDA, (b) MUA, (c) MHA, (d) MPA, (e) mercaptodecanethiol. QCM: 5 MHz. (From Shimazu et al. [42].)

change in the viscoelastic properties at the interface had no effect on the resonance frequency. Therefore, it is concluded that the frequency decrease is attributed to the change in mass due to the cation association with the carboxylate anion formed by the surface acid/base reaction. This technique was called *surface mass titration*.

The surface pK_a determined from the pH at half the total frequency change is 6.4–5.8 and slightly dependent on the chain length of the thiol; the longer chain mercaptoalkanoic acid produces a larger surface pK_a (Fig. 5). The surface pK_a of MUA in its self-assembled single-component adlayers of various coverages and in the mixed monolayers with alkanethiol has been also examined. The pK_a value shifted in a positive direction with an increase in the surface coverage of MUA in both monolayers, showing the repulsive interaction between neighboring carboxylates. The pK_a at zero coverage is 4.8 for the single-component adlayers and 5.6 for the mixed monolayer. Therefore, the surface pK_a is structure-dependent or sensitive to the environment around the surface carboxylic acid group. There exists a linear relation between the total frequency change and the coverage of the single-component adlayers with the slope of 48 $g \cdot mol^{-1}$ from which it is concluded that the cation is associated in the hydrated form of $Na^+ \cdot 1.4H_2O$.

The apparent surface pK_a of the MHDA monolayers was also determined under potential control [44]. It shifted in a negative direction from 6.4 at −200 mV to 4.3 at −700 mV versus Ag/AgCl. When applying potentials more positive than 600 mV, the pK_a has a tendency to shift in the positive direction. These results demonstrate that the surface acid/base properties of the SAMs can be controlled by the electrode potential.

The surface reactions between the acid/base functionalities of the SAMs and a weak base or acid were also examined in the vapor phase in relation to the sensing of these materials. Sun et al. [45] has measured the frequency response of an ST-cut SAW device while passing a $CH_3(CH_2)_9NH_2/N_2$ vapor stream through the MUA SAM. Although a rapid condensation of multilayers was formed, most of them desorbed upon N_2 purging except for the 0.9 monolayer adsorbed on the acid surface. Okahata et al. [46] examined the adsorption of acetic acid from vapor phase onto various functional groups of SAMs such as $-NH_2$, $-CONH_2$, and $-COOH$ using a 9-MHz QCM at seven times overtone mode. The adsorption isotherms were analyzed using the BET equation. The ratio of the binding constants of the monolayer and multilayer adsorption was calculated to be 62, 4.6, 5.6 and 1.9 for the $-CONH_2$, $-COOH$, $-NH_2$, and $-CH_3$ monolayers. In other words, acetic acid tends to be adsorbed as a monolayer on $-CONH_2$, and as multilayers on the other SAMs. Data for the low vapor pressures were also analyzed using the Langmuir adsorption isotherm. The association constant on $-COOH$ monolayer ($4.9 \times 10^4\ M^{-1}$) is smaller than those on a $-CONH_2$, and $-NH_2$ monolayers ($6.3–6.9 \times 10^4\ M^{-1}$). The modes of binding interactions are thought to be acid/base for the $-NH_2$ monolayer and a hydrogen bond for the $-CONH_2$ and $-COOH$ monolayers. The three times increase in the association constant on $-COOH$ was also demonstrated by the mixed monolayers of $-COOH$ and alkanethiols. It was thought that the cleavage of the lateral hydrogen bonds between the neighboring carboxylic acids was important for strengthening the hydrogen bonding with acetic acid.

7.2.2.3.3 **Molecular Recognition on SAM** The inclusion of guest molecules into the cavity of macrocyclic compounds confined to the electrode surface was also examined using a QCM. The *p-Tert*-butylcalix[4]arenetetrathiolate (BCAT) monolayers exhibited higher QCM responses for alkylbenzene molecules compared with nonalkylbenzene molecules [47]. The percentage of filled cavities reached more than 80% for the alkylbenzene molecules, but was below 15% for the nonalkylbenzene molecules.

Recently, the enantioselective detection of a chiral amino acid, D- and L-phenylalanine (Phe), was demonstrated using (*R*)- and (*S*)-1,1′-binaphthalene-2,2′-dithiol (BNSH) SAMs and a QCM by Nakanishi et al. [48]. An increase in the steady state mass of ca. 8 ng cm^{-2} was observed for the D-Phe/(*S*)BNSH SAM and L-Phe/(*R*)BNSH SAM systems, whereas, no net mass change was observed for the D-Phe/(*R*)BNSH SAM and L-Phe/(*S*)BNSH SAM systems (Fig. 6).

The QCM measurements of the DNA hybridization were conducted by several groups [49–55]. Okahata et al. [49, 50] detected the hybridization between the adlayer of the thiol-derivatized 10-mer deoxynucleotide (coverage: 8%) and a target M13 phage single-strand DNA and various 10-mer oligonucleotides in aqueous solutions. The kinetic measurements of the DNA hybridization was performed using a 27 MHz QCM and biotinylated oligonucleotides immobilized to avidin monolayers. The association and dissociation constants were obtained from the time course of the hybridization and Eqs. (1–2). The k_a and k_d values and hence the association constant K_a ($= k_a/k_d$) are dependent on the ionic strength of the solution, temperature, chain length of the nucleotide, and the number of mismatching bases. K_a increased with the increasing ionic strength ($0.24–24 \times 10^6$ M^{-1} for 0.1–0.5 M NaCl) and chain length of the nucleotide ($1.2–39000 \times 10^6$ M^{-1} for 10–30-mer), and with decreasing temperature ($1.7–26 \times 10^6$ M^{-1} for 30–0 °C) and the number of mismatching bases ($4.8–570 \times 10^6$ M^{-1} for 3–0 in 20-mer target nucleotide). For the hybridization between a 20-mer probe nucleotide on the QCM and a 20-mer target nucleotide, the percent hybridization is 100% for the fully complementary nucleotide (MM0), and 50% for the nucleotide having one mismatching base (MM1). For 30-mer probe and target having one mismatching base, on the other hand, nearly 100% hybridization efficiency was reported [53]. From the

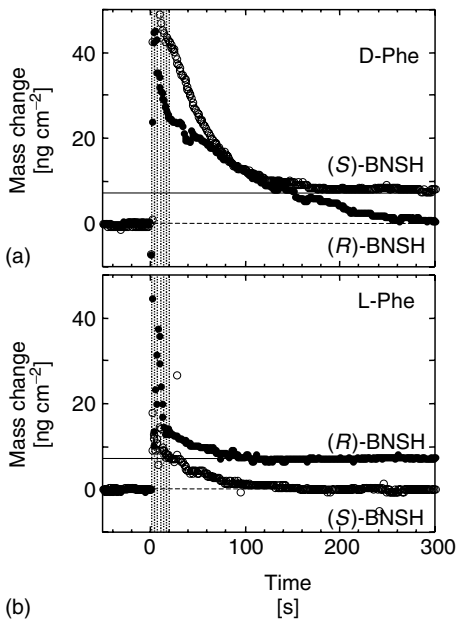


Fig. 6 QCM (9 MHz) responses of BNSH SAMs upon the injection of D- (a) and L-Phe (b). Filled and open symbols indicate responses on (*R*)- and (*S*)-BNSH, respectively. (From Nakanishi et al. [48].)

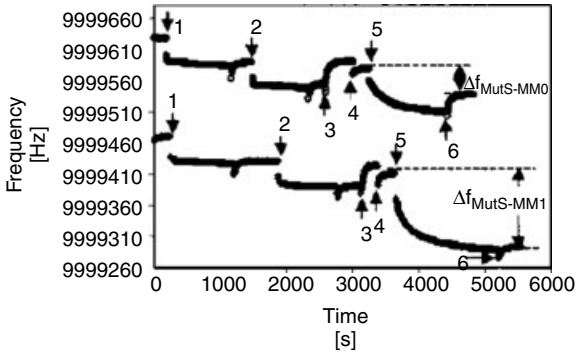


Fig. 7 Frequency responses of streptavidin-treated QCMs (10 MHz) to (1) probe (biotin-terminated 30-mer nucleotide) immobilization, (2) MM0 target (upper curve) and MM1 target (lower curve) DNA hybridization, and (5) MutS protein binding. Arrows (3), (4), and (6) show the change in buffer system. (From Su et al. [53].)

maximum binding amount obtained from the isotherm and Eq. (3), an approximate 1 : 1 binding between the target and probe nucleotides was demonstrated. MutS protein, a component of the *Escherichia Coli* mismatch repair system, binds the DNA containing mispaired and unpaired bases. Although the hybridization signals of the 30-mer probe DNA were very similar for MM0 to MM1, the MutS binding signals after the formation of DNA duplex were remarkably different for these nucleotides (Fig. 7), and showed a discrimination between these nucleotides by a factor of 2.9, which is smaller than that obtained by SPR (>10). This is due to the viscoelasticity effect on the QCM frequency.

The association constants between streptavidin and the biotin group were determined from the study of the construction of protein-DNA double and triple layers (1st layer: biotinylated lipid monolayer, 2nd: streptavidin, 3rd: biotinylated lipid double-strand oligonucleotide, 4th: streptavidin) using a 9-MHz QCM, and found to be 4.8×10^7, 3.2×10^8 and 3.6×10^5 M^{-1} for the binding between 1st-to-2nd, 2nd-to-3rd, and 3rd-to-4th layers, respectively [52].

7.2.2.4 Application for Sensors

In order to use the QCM as a sensor, it is important to increase the sensing sites. Collected in this section are studies using well-ordered multilayers and the self-assembled adlayers immobilized on porous silica particles as sensing matrices. The copper biphenylbis(phosphonate) thin films (5 and 20 layers) grown in a layer-by-layer fashion were used for the gas phase sensing of NH_3 [56]. The QCM responses due to the NH_3 intercalation were demonstrated over a wide range of NH_3 concentrations (0.01–25%), although linearity between the frequency response and concentration was not observed. The response time is about 90 s. The L–B films of poly{3-[ω-hydroxyhexyl(thiophene)]} and poly[3-(octylthio)-2,2′bithiophene] exhibited an adsorption of the first-row transition ions in the order of $Cu^{2+} > Ni^{2+} > Co^{2+} > Zn^{2+} > Fe^{2+}$ due to the complexation of metal ion with sulfur atoms in the polymers [57]. The LB films also showed higher

responses for Ag^+ and Hg^{2+} ions. The signal linearly increased over a wide range from 0.1 to 100 ppm in aqueous solutions. The bound mercury can be removed by EDTA solutions. The QCM sensing device for trace uranium was prepared by immobilizing an *N*-[3-(triethoxysilyl)propyl] phthalamic acid ligand on silica gel embedded in the adhesion layer on the Au electrode of the QCM [58, 59]. The detection of $UO_2{}^{2+}$ was conducted in a flow cell. Data were corrected for the solution density effects, which was estimated using the reference crystal bearing no immobilized ligands. The corrected frequency change linearly increased up to several μM concentrations. The subsequent flushing with acetate and water reestablished the original oscillation.

7.2.3 Polymeric Film Electrodes

7.2.3.1 Conducting Polymers

7.2.3.1.1 Electrosynthesis It is well known that the electropolymerization of pyrrole is followed by the doping and simultaneous incorporation of the anion as shown by

$$\mathrm{nPy} - (2+\delta)\mathrm{n\ e^-} + \delta\mathrm{nX^-} = (\mathrm{Py}^{+\delta}X_\delta{}^-)_\mathrm{n} + 2\mathrm{n\ H^+} \quad (7)$$

where δ is the charge per pyrrole unit created by the oxidative doping and is known to typically be in the range of 0.20–0.40 depending on the polymerization conditions. Baker and Reynold [60] examined the efficiency of the polymerization of pyrrole in nonaqueous solvents by determining the δ values using an EQCM. The nearly constant δ values were obtained at relatively high concentrations of pyrrole (0.05–0.1 M). These values are 0.3 for tosylate as the dopant anion and 0.2 for perchlorate in acetonitrile. During the initial stage of the polymerization, δ is higher than the expected range, showing the formation of soluble oligomers. The low efficiency was also demonstrated for the polymerization at a low pyrrole concentration.

The so-called self-doped polypyrrole is a copolymer of pyrrole having a covalent bonded anionic functionality and unsubstituted pyrrole. The charge for the doping of the polymer was determined to be 0.21 from the slope of the frequency change versus charge plot [61], which is in good agreement with 0.25 from the elemental analysis. These results show that the polymerization proceeds with 100% efficiency. Higher charges for the doping, which show a lower efficiency, were obtained when ''aged'' pyrrole solutions were used.

The EQCM was used to determine the doping charge during the electrosynthesis of poly(3-methylthiophene) by potential cycling in a $LiClO_4$ solution in acetonitrile [62]. The value of 0.33 was obtained.

For the electrosynthesis of polyaniline, much lower efficiencies were reported (40% for the potential cycling and 15% for the potentiostatic method) [63], although there exists a linear relationship between the frequency change and charge. These results were derived on the basis of the ''dry'' frequency change, which is the difference in the frequency between the dry polyaniline film and the bare crystal. The as-grown or wet film incorporates solvent molecules. To determine the number of water molecules incorporated in the film, Orata and Buttry [63] first determined the mass of the polyaniline film from the ''dry'' frequency change and the mass of the incorporated anion from the analysis of the EQCM data during the redox of the polyaniline films as

described in the following. By subtracting contributions of the polyaniline film and anion from the total frequency change obtained during the electropolymerization in aqueous solutions, they estimated the number of water molecules per polyaniline unit to be in the range of five to seven. The effect of the electrolyte anion on the grow rate was examined for $HClO_4$, 4-toluenesulfonic acid (HTSA), and 5-sulfosalicylic acid (HSSA); the order is HTSA > HSSA > $HClO_4$.

The electrosynthesis of a polyaniline film in nonaqueous solutions was investigated using an EQCM by Naoi et al. [64]. The growth rate of the film was quite slow during the initial stage of the polymerization in acetonitrile containing 0.5 M $LiClO_4$. The authors considered that the charges during the initial stage were consumed for the production of dimers to produce enough protons to allow a further polymerization. This was supported by the fact that the growth rate during the initial stage increased with the addition of CF_3COOH to the acetonitrile.

7.2.3.1.2 **Redox (Doping/Undoping)** The EQCM is a powerful technique for evaluating the mass transport accompanying the redox switching of the conducting polymer between the conducting and insulating states. The first study was made by Kaufman et al. [65]. From their study and the subsequent studies conducted by other groups, the following general trends are obtained as to the ion transport during the redox of polypyrrole [66]. For the polypyrroles prepared in the presence of small anions such as ClO_4^-, Cl^- and tosylate, charge compensation is achieved by cation and anion transport at less and more positive potentials of the redox wave, respectively (Fig. 8a). The cation transport becomes predominant through the wave for polypyrroles prepared with large anions

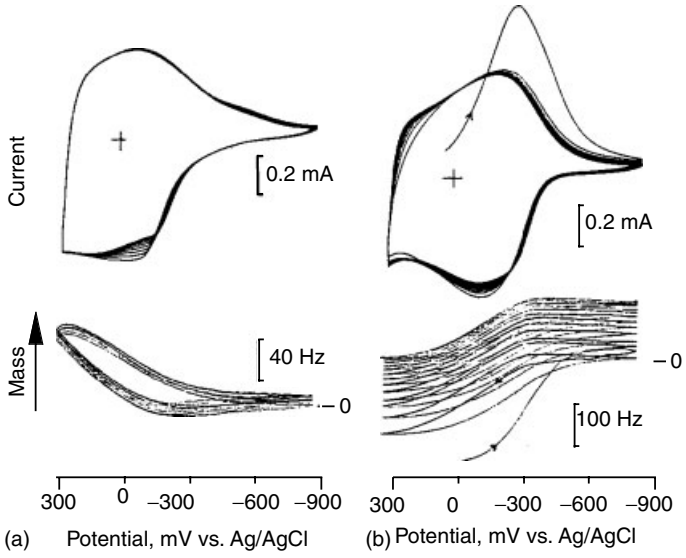


Fig. 8 Cyclic voltammograms (50 mV s^{-1}) and QCM responses of (a) freshly prepared PPY and (b) PP–PS films in 0.2 M KCl. (Adapted from Basak et al. [61].)

such as poly(4-styrenesulfonate). For the self-doped copolymer of polypyrrole, poly{pyrrole-co-[3-(pyrrole-1-yl)propanesulfonate]}, ion transport accompanying the redox is restricted to the cationic species (Fig. 8b) [61, 67].

Cohen et al. [68] recently found using AFM that freshly prepared (in polyethylene carbonate) and long-term cycled PPY films showed quite different micromorphologies and mass transport behaviors; the freshly prepared PPY films of unusual strictly oriented bunches of short fibrils showed a combined anion–cation transport as a function of the potential, whereas the cycled PPY of a typically granular film only revealed an anion exchange. It is also reported [69] that the repetitive redox cycling of PPY films caused the accumulation of a neutral salt and solvent in the film.

Hillman et al. examined the mass transport accompanying the redox of polybithiophene in acetonitrile containing tetraalkylammonium salts [70]. The mass change is similar, but not identical to the value anticipated when a permselective anion transport is assumed. Detailed consideration as well as several pieces of experimental evidence show the involvement of the salt and solvent transport in opposite directions. The anion transport accompanying the solvent was reported for poly(3,4-ethylenedioxthiophene) films in 0.1 M $TEAPF_6$/acetonitrile [71].

In the case of the redox of polyaniline films, charge compensation is basically achieved by anion transport. However, the actual ion transport is influenced by the solution pH. Orata and Buttry [63] first examined this process using EQCM. Two redox waves appeared in the cyclic voltammograms in aqueous solutions. The first redox wave is attributed to the redox between the fully reduced polyaniline form and emeraldine salt. In the case that the reduced polyaniline is not protonated, simple anion transport should take place. On the other hand, when the reduced polyaniline is fully protonated, only proton transport takes place because the anion is already incorporated even in the reduced film to compensate the positive charge of the protonated polyaniline. At the acid concentrations often used (0.1–1.0 M), the reduced polyaniline is partially protonated. Orata and Buttry estimated the fraction of protonated aniline units in the reduced form, f_r, using the following equations:

$$Q_{ox} = F f_o \Gamma_{PAn} \tag{8}$$

$$\Delta f_{ox} = (f_o - f_r)\Gamma_{PAn}\frac{MW_a}{S} \tag{9}$$

where Q_{ox} is the charge passed during oxidation, F is the Faraday constant, Γ_{PAn} is the number of aniline units in the film, f_o is the fraction of aniline units with an accompanying anion in the oxidized form, MW_a is the molar mass of the incorporated anion, and S is a proportionality constant which converts from frequency to mass per unit area. The equation shows that the positive charge formed during the oxidation is simply compensated by the anion. The fraction of protonated aniline units (f_r) is also equal to that of aniline units with the accompanying anion in the reduced form. Since this fraction is smaller than that in the oxidized form, more anions corresponding to $(f_o - f_r)\Gamma_{PAn}MW_a$ in mass should be incorporated upon the oxidation. Both f_o and f_r can be determined using the equations. The pK_a of the reduced polyaniline is given by the pH at which half of the aniline units are protonated and is between −0.3 and −0.4.

Inzelt et al. [72, 73] examined the mass transport during the redox of polyaniline films in various supporting electrolyte solutions containing the same anion used

in the electrosynthesis. The anions they used were Cl^-, SO_4^{2-} or HSO_4^-, ClO_4^-, HTSA, and HSSA. The main features are independent of the identity of the anion. Upon oxidation during the first CV wave, the small mass decrease at lower potentials of the wave is followed by a large mass increase during the latter stage of the wave. The former mass decrease is attributed to proton expulsion and the latter to the incorporation of an anion. As described earlier, proton release results from the protonation of the reduced polyaniline. Therefore, the contribution of this process is strongly dependent on the degree of the protonation. With the increasing pH, as a result, proton expulsion becomes less substantial. It is also concluded from the *mpe* values that a counterflux of solvent molecules prevails when large anions such as HTSA and HSSA are used.

A pronounced mass loss was observed during the second oxidation wave in the CV taken in various aqueous solutions. This results from the deprotonation of the polyaniline, which accompanies oxidation to the imine form.

The redox behavior of the polyaniline films in nonaqueous solutions was examined by Daifuku et al. [74]. The mass response during the first wave in 0.5 M $LiClO_4$ + acetonitrile was similar to that in aqueous solutions. However, the mass continuously increased upon oxidation during the second wave instead of the mass decrease observed in aqueous solutions. To account for the anion incorporation, the oxidation of emeraldine to the protonated imine was proposed.

7.2.3.2 Redox Polymers

7.2.3.2.1 **Break-in Process** As-prepared virgin films, which are uncharged and unhydrated, often require several (at least one) potential scans to become fully electroactive and for the voltammogram to reach the steady state. This phenomenon is known as ''break-in'', which was first found and defined by Kaufman [75]. The break-in process of poly(vinylferrocene) (PVF) films in a 0.1 M $NaClO_4$ solution was examined by Hillman et al. [76]. They estimated the neutral species flux during the potential cycling from the current and mass response assuming that electroneutrality of the film is simply maintained by the ingress of the anion (permselective conditions, see following text). The entry of water into the unhydrated and reduced film did not occur until 40% of the film was oxidized. It should be mentioned that anion transport took place along with a small amount of water even during this initial oxidation stage. Of the water taken up during the first scan, about 50% was retained upon reduction, and consequently the film became swollen. This partially irreversible uptake of water was also reported by Inzelt and Bacskai [77]. The break-in process is rather complicated in the presence of NO_3^-, and hence the EQCM response during the first cycle was dependent on the conditions of the film preparation.

7.2.3.2.2 **Redox** The most widely examined are the poly-(vinylferrocene) (PVF) films, since Varineau and Buttry first reported them [78]. For the SAMs of ferrocenylalkanethiols and their analogs, ion association took place only at the SAM/solution interface. For the polymeric films, however, it took place not only at the interface but also through the bulk of the polymeric film layer. The *mpe* is a strong function of the electrolyte concentration, identity of the electrolyte anion and even the conditions of the film preparation. The observed *mpe* for ClO_4^- ranges from 105 to 250 g mol^{-1} at the low electrolyte

concentrations below 0.1 M. The cation (Na^+, NH_4^+, $N(Me)_4^+$, $N(Et)_4^+$) has no effect on the *mpe* [79]. Therefore, ion transport is considered to be a permselective (only anion incorporated into the polymer film to compensate for the cationic charge of the ferrocenium ion formed during the oxidation of PVF), and the excess mass is attributed to solvent incorporation. After the break-in or under the steady state redox conditions, the mass transport is reversible. Hillman et al. [79] found a linear relationship between the *mpe* and molar mass of the anion used (NO_3^-, ClO_4^-, PF_6^- and tosylate) with a nonzero intercept and the slope of 1.9. These results indicate that different anions carry different amounts of solvent (water). Different results are also reported for the anion dependence of the *mpe* by Inzelt and Backskai [77]; the *mpe*s for NO_3^- and SO_4^{2-} are slightly and much (more than twice) greater than that for ClO_4^-, respectively. They considered that the hydration of the anion played an important role. The PF_6^- insertion with no accompanying solvent was reported by Varineau and Buttry [78], and interpreted by the weak hydration nature of this anion. In a NaCl solution, a large frequency increase was observed after a slight decrease during the oxidation of PVF. This is due to the electrochemically induced dissolution or delamination of the film, although there remains the possibility that it is due to the high degree of film swelling. The anion transport with accompanying solvent is generally observed not only in an aqueous solution but also in a nonaqueous solution [80].

At high electrolyte (ClO_4^-) concentrations above 1 M, the *mpe* became greater with the increasing concentration up to 430 g mol^{-1} at 5 M [79]. This is due to the failure of the permselectivity or the ingress of the salt. On the basis of transient chronoamperometric/EQCM measurements, it was concluded that transport rates decrease in the order $ClO_4^- > NaClO_4^- > H_2O$ [81].

Ion exchange of multiply charge anions into oxidized PVF films occurs during repetitive potential cycling in a KNO_3 solution containing either $Fe(CN)_6^{3-}$ or $Fe(CN)_6^{4-}$ [82, 83]. The increase in the mass of the reduced PVF and small mass change during each cycle show that an irreversible exchange gradually proceeds due to the electrostatic cross-linking by these anions, resulting in the deactivation of the PVF films. Inactivation of the PVF films demonstrated by the current and frequency responses was also observed for ferrocene-modified siloxane polymers in NO_3^- and HPO_4^{2-} solutions [84]. This was ascribed to the irreversible formation of ionlike complexes between the inserted anionic species and oxidized ferrocene moieties.

Oyama et al. [85] reported that the QCM response of *N*-isopropylacrylamide/vinylferrocene copolymer film is reversed between above and below the swelling/shrinking transition temperature shown by the admittance measurements. In the shrunken state (higher temperature), ion transport is rather selective toward the anion, while not in the swollen state (lower temperature).

Ion transport at redox polymers other than PVF and its derivatives, such as $[Os(bpy)_2(PVP)Cl]^+$ (bpy = 2,2′-bipyridine), PVP = poly(4-vinylpyridine) [86, 87] and poly(*N*, *N*′-dimethylanilinium) film containing $Fe(bphen)_3^{4-}$ (bphen = bathophenanthroline) [88, 89] was also examined using a QCM. Only when the film rigidity, which depends on the film nature, electrolyte anion and the concentration, was confirmed, ionic transport was evaluated on the basis of the QCM data.

The highly selective recognition of halide ions by a cross-linked polyviologen film prepared by ''anion-imprinted electropolymerization'' was demonstrated by Kamata et al. [90] using a QCM/UV-vis(reflection mode) combined system. All quantities (charge, frequency, and absorbance changes) determined during the redox are strongly depressed for anions larger than the template anion used during the polymerization, but are independent for the same or smaller anions.

7.2.4 Inorganic Films

7.2.4.1 Clay-modified Electrodes

The self-assembly of the 2 : 1 smectite-type clay containing thiol groups on Au was performed in a chloroform suspension of clay [91]. The formation of a monolayer or a partial double layer was demonstrated from the frequency change. In other studies on the clay-modified electrodes, the clay-precoated QCM was used to examine the swelling of the clay films, and the adsorption and redox of the metal complexes.

Oyama et al. [92, 93] conducted admittance measurements of a montmorillonite clay film and a montmorillonite clay/poly(vinyl alcohol) composite film in various concentrations of Na_2SO_4. A drastic change in the equivalent circuit resistance was observed at the concentration of ca. 0.2–0.3 M, and was attributed to a structural change in the clay film from a face-to-face structure in a higher concentration to an edge-to-face structure in a lower concentration. The latter structure is considered to be relatively flexible, swollen and viscoelastic, and therefore, acts as a resistance to the oscillation. In the case of the clay/PVP composite film, the motion freedom of the individual clay platelets is limited due to the plausible hydrogen bonds between the PVP and clay. As a result, no drastic change in the equivalent resistance was observed. The resistance was also dependent on the valence of the cation.

The adsorption and redox of metal complexes on clay-modified electrodes were examined by Yao et al. [94]. The species adsorbed on a saponite clay film by the exchange with a hydrated sodium ion in the clay film were identified from the mass change and absorbance change of the metal complexes in solution as follows: $[Ru(bpy)_3]^{2+}\cdot 1/2SO_4^{2-}$ for racemic body, $[Ru(bpy)_3]^{2+}$ and $[Ru(bpy)_3]^{2+}\cdot 1/2SO_4^{2-}$ for enantiomers, and $[Ru(NH_3)_6]^{3+}\cdot SO_4^{2-}$. The EQCM results revealed that one $[Ru(bpy)_3]^{3+}$ molecule was eliminated from the clay film when three $[Ru(bpy)_3]^{2+}$ ions were oxidized [95]. The charge balance during the redox reactions was accomplished by the transport of SO_4^{2-} and Na^+ in the cases of $[Ru(NH_3)_6]^{3+}$ and $[Fe(CN)_6]^{4-}$. The adsorption and redox of $[Fe(CN)_6]^{4-}$ on an anionic clay-modified electrode (hydrotalcite) were also examined [96].

7.2.4.2 Oxide Films

The intercalation and deintercalation of unsolvated Li^+ ions into and out of electrochromic oxide films (WO_3, V_6O_{13}) were clarified by the *mpe* (ca. 7 g mol^{-1}) during the redox of the oxide films in $LiClO_4$/propylene carbonate [97, 98].

$$WO_3 + xLi^+ + xe^- = Li_xWO_3 \quad (10)$$

$$V_6O_{13} + xLi^+ + xe^- = Li_xV_6O_{13} \quad (11)$$

The addition of trifluoroacetic acid into the electrolyte solution decreased the *mpe* to ca. 4 g mol^{-1}, suggesting the contribution of proton transport [97].

7.2.4.3 Prussian Blue and its Analogs

More extensive studies were conducted for the formation and redox of Prussian Blue (PB) films and its analogs, which are also considered as potential electrochromic materials.

The EQCM studies of the formation and redox of PB films were first and extensively conducted by Feldman and Melroy [99]. The electroreductive deposition is usually performed in an equimolar mixture of $K_3Fe(CN)_6$ and $FeCl_3$ (pH = 2). They reported the *mpe* value of 643.5 g mol^{-1} for the deposition process in 2 mM solutions. The *mpe* obtained using the dry mass was 327.9 g mol^{-1}, showing the incorporation of water molecules in the as-grown films. Shimazu et al. [100] obtained somewhat smaller *mpe* values of 478 on Au and 378.7 g mol^{-1} on indium tin oxide(ITO) in 10 mM solutions. Clearly, the extent of water incorporation is dependent on the experimental conditions.

The frequency decreased upon the reduction of the PB films, and increased upon their reoxidation (Fig. 9) [101]. The oxidation of PB films was also accompanied by a frequency increase [102]. The *mpe* depends on the cation used [103]. These results indicate that the cation transport is predominant in both redox processes. The *mpe* values in neutral aqueous solutions were smaller than the molar mass of the cation (23.3 g mol^{-1} for the reduction of PB on Au in KNO_3), thus showing the simultaneous transport of water molecules; the cation inclusion is accompanied by water exclusion. Shimazu et al. [100] examined the redox of PB films on ITO using an EQCM/UV-vis spectroscopy combined system they had developed [104]. The absorbance at 700 nm (absorption maximum of PB films) was simultaneously recorded together with the current and frequency. The absorbance decreased upon the reduction and oxidation of PB films. The *mpe* values were determined using the absorbance change (the molar absorption coefficient was determined from the slope in absorbance-charge plot for the film deposition) instead of the charge to avoid uncertainty in the charge caused from the difficult estimation of an accurate double-layer charging current. They were 28 and 33 g mol^{-1} for the reduction and oxidation of the PB films, respectively. On the basis of these results, the following reaction schemes were derived for the reduction of PB

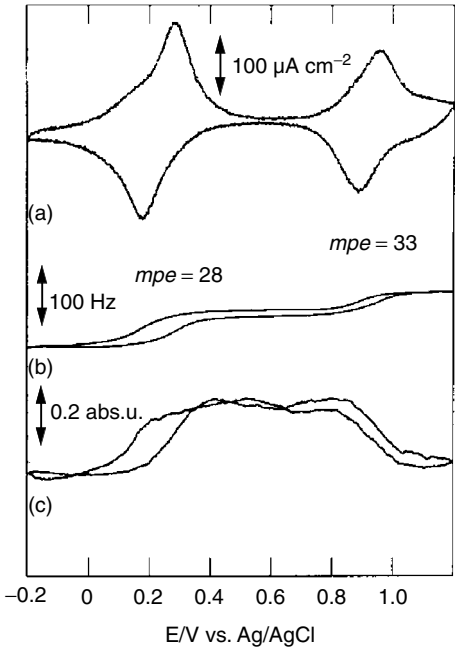


Fig. 9 (a) Cyclic voltammogram (10 mV s^{-1}) of a PB film on an ITO electrode in 1 M KCl with simultaneously obtained (b) frequency change (5 MHz), and (c) absorbance change (700 nm). (From Shimazu et al. [100].)

$$Fe_4^{III}[Fe^{II}(CN)_6]_3 \cdot 3KCl \cdot 3H_2O + 4e^- + 4K^+ \longrightarrow K_4Fe_4^{II}[Fe^{II}(CN)_6]_3 \cdot 3KCl \cdot 1/3H_2O - 8/3H_2O \quad (12)$$

and for the oxidation of PB

$$Fe_4^{III}[Fe^{II}(CN)_6]_3 \cdot 3KCl \cdot 3H_2O - 3e^- + H_2O \longrightarrow Fe_4^{III}[Fe^{III}(CN)_6]_3 \cdot 3Cl^- \cdot 4H_2O + 3K^+ \quad (13)$$

The transport of water during the redox of the nickel analog of PB (nickel ferrocyanide) in the opposite direction against the cation transport was adequately demonstrated by a comparison of the frequency changes in H_2O and D_2O. For the redox of PB films in acidic solutions, the proton transport contributed to a greater extent as shown by the smaller *mpe* values.

References

1. M. R. Deakin, D. A. Buttry, *Anal. Chem.* **1989**, *61*, 1147A–1154A.
2. M. Thompson, A. L. Kipling, W. C. Duncan-Hewitt et al., *Analyst* **1991**, *116*, 881.
3. D. A. Buttry, M. D. Ward, *Chem. Rev.* **1992**, *92*, 1355–1379.
4. D. A. Buttry in *Electrochemical Interfaces: Modern Techniques for In-Situ Interface Characterization* (Eds.: H. D. Abruna), VCH Publishers, New York, 1991, Chap. 10.
5. G. Z. Sauerbrey, *Z. Phys.* **1959**, *155*, 206.
6. J. J. Donohue, D. A. Buttry, *Langmuir* **1989**, *5*, 671.
7. L. L. Nordyke, D. A. Buttry, *Langmuir* **1991**, *7*, 380.
8. H. C. De Long, J. J. Donohue, D. A. Buttry, *Langmuir* **1991**, *7*, 2196.
9. K. Shimazu, I. Yagi, Y. Sato et al., *Langmuir* **1992**, *8*, 1385.
10. K. K. Kanazawa, J. G. Gordon II, *Anal. Chem.* **1985**, *57*, 1771.
11. C.-G. Wu, S.-C. Chiang, C.-H. Wu, *Langmuir* **2002**, *18*, 7473.
12. N. Nakamura, H.-X. Huang, D.-J. Qian et al., *Langmuir* **2002**, *18*, 5804.
13. H. Ahn, M. Kim, D. J. Sandman et al., *Langmuir* **2003**, *19*, 5303.
14. D. S. Karpovich, G. J. Blanchard, *Langmuir* **1994**, *10*, 3315.
15. C. H. Kim, S. W. Han, T. H. Ha et al., *Langmuir* **1999**, *15*, 8399.
16. S. W. Han, T. H. Ha, C. H. Kim et al., *Langmuir* **1998**, *14*, 6113.
17. Y. J. Lee, I. C. Jeon, W. Paik et al., *Langmuir* **1996**, *12*, 5830.
18. Y.-T. Kim, R. L. McCarley, J. Bard, *Langmuir* **1993**, *9*, 1942.
19. F. Matsumoto, M. Ozaki, Y. Inatomi et al., *Langmuir* **1999**, *15*, 857.
20. W. B. Caldwell, K. Chen, C. A. Mirkin et al., *Langmuir* **1993**, *9*, 1945.
21. L. A. Godinez, J. Lin, M. Munoz et al., *Langmuir* **1998**, *14*, 137.
22. I. Rubinstein, J. Rishpon, E. Sabatani et al., *J. Am. Chem. Soc.* **1990**, *112*, 6135.
23. K. Kim, H. Yang, E. Kim et al., *Langmuir* **2002**, *18*, 1460.
24. V. Patil, K. S. Mayya, M. Sastry, *Langmuir* **1999**, *15*, 6587.
25. T. Sagara, N. Kato, N. Nakashima, *J. Phys. Chem. B* **2002**, *106*, 1205.
26. M. Aslam, I. S. Mulla, K. Vijayamohanan, *Langmuir* **2001**, *17*, 7487.
27. H. C. Yang, K. Aoki, H.-G. Hong et al., *J. Am. Chem. Soc.* **1993**, *115*, 11855.
28. S. Chen, R. Pei, T. Zhao et al., *J. Phys. Chem. B* **2002**, *106*, 1903.
29. J. F. Hicks, Y. Seok-Shon, R. W. Murray, *Langmuir* **2002**, *18*, 2288.
30. C. A. Widrig, C. Chung, M. D. Porter, *J. Electroanal. Chem.* **1991**, *310*, 335.
31. M. M. Walczak, D. D. Popenoe, R. S. Deinhammer et al., *Langmuir* **1991**, *7*, 2687.
32. T. Kawaguchi, H. Yasuda, K. Shimazu et al., *Langmuir* **2000**, *16*, 9830–9840.
33. T. W. Schneider, D. A. Buttry, *J. Am. Chem. Soc.* **1993**, *115*, 1239.
34. L. E. Bailey, D. Kambhampati, K. K. Kanazawa et al., *Langmuir* **2002**, *18*, 479.
35. K. Shimazu, S. Ye, Y. Sato et al., *J. Electroanal. Chem.* **1994**, *375*, 409.
36. K. Shimazu, I. Yagi, Y. Sato et al., *J. Electroanal. Chem.* **1994**, *372*, 117.
37. S. Ye, T. Haba, K. Shimazu et al., *Phys. Chem. Chem. Phys.* **1999**, *1*, 3653.
38. K. Shimazu, Y. Sato, I. Yagi et al., *Bull. Chem. Soc. Jpn.* **1994**, *67*, 863.
39. T. Kawaguchi, K. Tada, K. Shimazu, *J. Electroanal. Chem.* **2003**, *543*, 41.

40. H. C. De Long, D. A. Buttry, *Langmuir* **1992**, *8*, 2491.
41. J. Wang, L. M. Frostman, M. D. Ward, *J. Phys. Chem.* **1992**, *96*, 5224.
42. K. Shimazu, T. Teranishi, K. Sugihara et al., *Chem. Lett.* **1998**, *27*, 669.
43. K. Sugihara, T. Teranishi, K. Shimazu et al., *Electrochemistry* **1999**, *7*, 1172.
44. K. Sugihara, K. Shimazu, K. Uosaki, *Langmuir* **2000**, *16*, 7101.
45. L. Sun, R. M. Crooks, *Langmuir* **1993**, *9*, 1775.
46. Y. Okahata, K. Matsuura, K. Ito et al., *Langmuir* **1996**, *12*, 1023.
47. M. T. Cygan, G. E. Collins, T. D. Dunbar et al., *Anal. Chem.* **1999**, *71*, 142.
48. T. Nakanishi, N. Yamakawa, T. Asahi et al., *J. Am. Chem. Soc.* **2002**, *124*, 740.
49. Y. Okahata, K. Matsunobu, M. Ijiro et al., *J. Am. Chem. Soc.* **1992**, *114*, 8299.
50. Y. Okahata, M. Kawase, K. Niikura et al., *Anal. Chem.* **1998**, *70*, 1288.
51. S. Yamaguchi, T. Shimomura, T. Tatsuma et al., *Anal. Chem.* **1993**, *65*, 1925.
52. K. Ijiro, H. Ringsdorf, E. Birch-Hirschfeld et al., *Langmuir* **1998**, *14*, 2796.
53. X. Su, R. Robelek, Y. Wu et al., *Anal. Chem.* **2004**, *76*, 489.
54. C. Larsson, M. Rodahl, F. Hook, *Anal. Chem.* **2003**, *75*, 5080.
55. L. H. Pope, S. Allen, M. C. Davies et al., *Langmuir* **2001**, *17*, 8300.
56. L. C. Brousseau, T. E. Mallouk, *Anal. Chem.* **1997**, *69*, 679.
57. S. C. Ng, X. C. Zhou, Z. K. Chen et al., *Langmuir* **1998**, *14*, 1748.
58. R. Cox, D. A. Buttry, P. Bonnesen et al., *CHEMTECH* **1994**, *24*, 18.
59. R. Cox, D. Gomez, D. A. Buttry et al., in *ACS Symposium Series No.561, Interfacial Design and Chemical Sensing* (Eds.: T. E. Mallouk, Eds.: D. J. Harrison), American Chemical Society, 1994.
60. C. K. Baker, J. R. Reynolds, *J. Electroanal. Chem.* **1988**, *251*, 307.
61. S. Basak, C. S. C. Bose, K. Rajeshwar, *Anal. Chem.* **1992**, *64*, 1813.
62. S. Servagent, E. Vieil, *J. Electroanal. Chem.* **1990**, *280*, 227.
63. D. Orata, D. A. Buttry, *J. Am. Chem. Soc.* **1987**, *109*, 3574.
64. K. Naoi, Y. Nagatomi, N. Oyama, *Denki Kagaku* **1992**, *60*, 1091.
65. J. H. Kaufman, K. K. Kanazawa, G. B. Street, *Phys. Rev. Lett.* **1984**, *53*, 2461.
66. K. Naoi, M. M. Lien, W. H. Smyrl, *J. Electroanal. Chem.* **1989**, *272*, 273.
67. J. R. Reynolds, N. S. Sundraresan, M. Pomerantz et al., *J. Electroanal. Chem.* **1988**, *250*, 355.
68. Y. S. Cohen, M. D. Levi, A. Aurbach, *Langmuir* **2003**, *19*, 9804.
69. A. Bund, A. Baba, S. Berg et al., *J. Phys. Chem. B* **2003**, *107*, 6743.
70. A. R. Hillman, M. Swann, S. Bruckenstein, *J. Electroanal. Chem.* **1990**, *291*, 147.
71. A. Baba, J. Lubben, K. Tamada et al., *Langmuir* **2003**, *19*, 9058.
72. S. Pruneanu, E. Csahok, V. Kertesz et al., *Electrochem. Acta* **1998**, *43*, 2305.
73. J. Bacskai, V. Kertesz, G. Inzelt, *Electrochem. Acta* **1993**, *38*, 3935.
74. H. Daifuku, T. Kawagoe, N. Yamamoto et al., *J. Electroanal. Chem.* **1989**, *274*, 313.
75. A. H. Schroeder, F. B. kaufman, V. Patel et al., *J. Electroanal. Chem.* **1980**, *113*, 193.
76. A. R. Hillman, N. A. Huhes, S. Bruckenstein, *J. Electrochem. Soc.* **1992**, *139*, 74.
77. G. Inzelt, J. Bacskai, *Electrochim. Acta* **1992**, *37*, 647.
78. P. T. Varineau, D. A. Buttry, *J. Phys. Chem.* **1987**, *91*, 1292.
79. A. R. Hillman, D. C. Loveday, S. Bruckenstein, *J. Electroanal. Chem.* **1989**, *274*, 157.
80. M. Mizunuma, T. Ohsaka, H. Miyamoto et al., *Bull. Chem. Soc. Jpn.* **1991**, *64*, 2887.
81. A. R. Hillman, D. C. Loveday, S. Bruckenstein, *J. Electroanal. Chem.* **1991**, *300*, 67.
82. M. D. Ward, *J. Electrochem. Soc.* **1988**, *135*, 2747.
83. M. D. Ward, *J. Phys. Chem.* **1988**, *92*, 2049.
84. S. Ikeda, N. Oyama, *Anal. Chem.* **1993**, *65*, 1910.
85. N. Oyama, T. Tatsuma, K. Takahashi, *J. Phys. Chem.* **1993**, *97*, 10504.
86. A. J. Kelly, T. Ohsaka, N. Oyama et al., *J. Electroanal. Chem.* **1990**, *287*, 185.
87. A. J. Kelly, N. Oyama, *J. Phys. Chem.* **1991**, *95*, 9579.
88. N. Oyama, T. Ohsaka, M. Nakanishi, *J. Macromol. Sci., Chem.* **1987**, *A24*, 375.
89. N. Oyama, M. Kitagawa, M. Iwaku et al., *J. Makromol. Symp. Chem.* **1994**, *81*, 337.
90. K. Kamata, T. Kawai, T. Iyoda, *Langmuir* **2001**, *17*, 155.

91. Y. Hotta, K. Inukai, M. Taniguchi et al., *Langmuir* **1997**, *13*, 6697.
92. T. Okajima, H. Sakurai, N. Oyama et al., *Bull. Chem. Soc. Jpn.* **1992**, *65*, 1884.
93. N. Oyama, K. Takada, T. Tatsuma et al., *Sens. Actuators, B* **1993**, *13–14*, 372.
94. K. Yao, K. Shimazu, M. Nakata et al., *J. Electroanal. Chem.* **1998**, *442*, 235.
95. K. Yao, K. Shimazu, M. Nakata et al., *J. Electroanal. Chem.* **1998**, *443*, 253.
96. K. Yao, M. Taniguchi, M. Nakata et al., *J. Electroanal. Chem.* **1998**, *457*, 119.
97. H. Inaba, M. Iwaku, T. Tatsuma et al., *Denki Kagaku* **1993**, *61*, 783.
98. H.-K. Park, K. Podolske, Z. Munshi et al., *J. Electrochem. Soc.* **1991**, *138*, 627.
99. B. J. Feldman, O. R. Melroy, *J. Electroanal. Chem.* **1987**, *234*, 213.
100. K. Shimazu in *Science of Electrocatalysis* (Eds.: H. Kita), Hokkaido University Press, Sapporo, 1995, p. 63.
101. K. Aoki, T. Miyamoto, Y. Ohsawa, *Bull. Chem. Soc. Jpn.* **1989**, *62*, 1658.
102. M. R. Deakin, H. Byrd, *Anal. Chem.* **1989**, *61*, 290.
103. S. J. Lasky, D. A. Buttry, *J. Am. Chem. Soc.* **1988**, *110*, 6258.
104. K. Shimazu, M. Takechi, Y. Ohtomo et al., *Denki Kagaku* **1994**, *62*, 516.

7.3 Electrochemical Scanning Tunneling Microscopy

Kingo Itaya
Tohoku University, Sendai, Japan

7.3.1 Introduction

Until recently, there were few in situ methods available for the structural determination of an electrode surface, in solution, at the atomic level. Atomic-level information had previously been acquired only via surface spectroscopic techniques in ultrahigh vacuum (UHV) [1, 2]. However, since its invention by Binnig and Rohrer [3], scanning tunneling microscopy (STM) has been immediately established as an invaluable and powerful surface analysis technique with atomic resolution in UHV. On the other hand, developments in STM operated at solid–liquid interfaces led to its valuation as the premier technique for atomic-level surface structural investigations of chemical processes taking place at solid–liquid interfaces. It has been demonstrated that in situ STM makes it possible to monitor, under reaction conditions, a wide variety of electrode processes such as the adsorption of inorganic and organic species, the reconstruction of electrode surfaces, and the dissolution and deposition of metals and semiconductors. Several review articles on in situ STM and related techniques such as in situ atomic force microscopy (AFM) have been published [4–7]. The reviews by Gewirth and Niece [6] and the present author [7] are the most comprehensive in terms of results obtained on various substrates of metals and semiconductors.

Because of publication limitations, the present chapter describes only a few topics for adlayer structures of iodine, sulfate/bisulfate, and simple aromatic molecules on well-defined single-crystal electrodes. Experimental procedures are only briefly described, because detailed reviews on this aspect have already been written [5].

7.3.2 Experimental Aspects

7.3.2.1 Principle of Scanning Tunneling Microscopy

In conventional STM operated in vacuum or air, a voltage (V) is applied between the substrate and tip electrodes as shown schematically in Fig. 1. The tunneling current density (i_T) can be expressed by Eq. (1) when a low-bias voltage is applied [8].

$$i_T = \frac{e^2}{h^2}\frac{(2m\bar{\phi})^{1/2}}{\Delta s} V \exp(-A\bar{\phi}^{1/2}\Delta s) \quad (1)$$

Where e and h are the charge of electron and the Planck's constant, respectively. $\bar{\phi}$ is the mean barrier height. Δs is the distance between the two electrodes. A is defined by Eq. (2).

$$A = 4\pi(2m)^{1/2}/h \quad (2)$$

where m is the mass of electron. As can be seen in Eq. (1), the tunneling current is exponentially dependent on the width of the potential barrier (Δs) (and the square root of the mean barrier height. This characteristic exponential dependence allows STM to achieve the high resolution in the z axis. For typical metals ($\bar{\phi} = 4–5$ eV) the predicted change in the tunneling current (i_T) by 1 order of magnitude for the change $\Delta s = 0.1$ nm has been verified. If the tunneling current

Encyclopedia of Electrochemistry. Edited by A.J. Bard and M. Stratmann
Vol. 10 *Modified Electrodes*. Edited by M.Fujihira, I.Rubinstein, and J.F.Rusling
Copyright © 2007 Wiley-VCH Verlag GmbH & Co. KGaA, Weinheim. ISBN: 978-3-527-30402-8

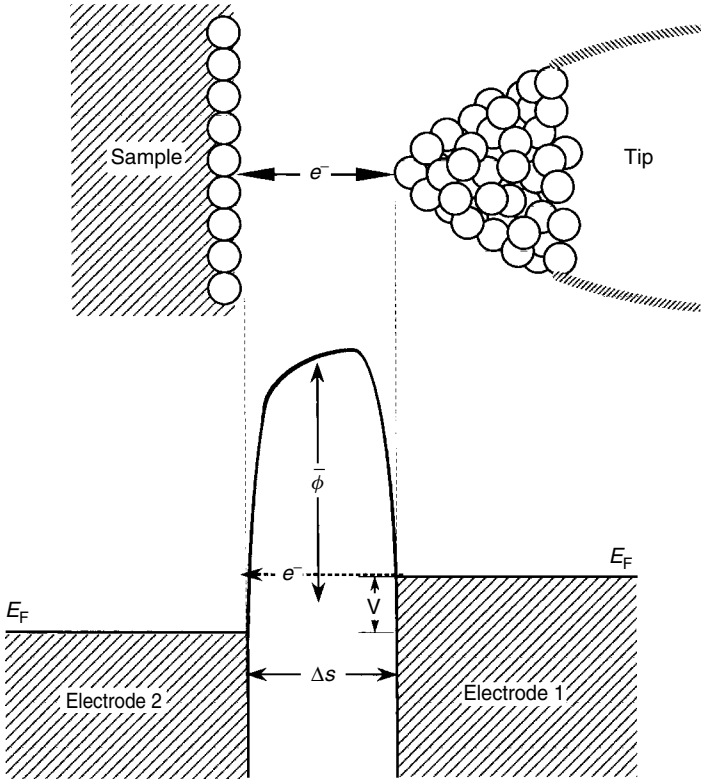


Fig. 1 Tunneling barrier between two metal electrodes (substrate and tip).

is kept constant to within 2%, then the tunneling gap (Δs) remains constant to within 0.001 nm.

7.3.2.2 Principle of Electrochemical Scanning Tunneling Microscopy

The review by Siegenthaler describes a detailed comparison between various types of electric circuits to control the electrode potentials of the tunneling tip and the substrate independently using the so-called bipotentiostat [5]. Figure 2(a) illustrates the apparatus of in situ STM with the four-electrode configuration. Figure 2(b) depicts the electrochemical cell for the four-electrode configuration. Using a bipotentiostat, the electrode potentials of the substrate (WE_1) and the tunneling tip (WE_2) can be controlled independently with respect to a reference electrode (RE). The electrochemical current (i_F) flowing through the substrate and the counter-electrode (CE) can be monitored from the output of a current follower. The tunneling current (i_T) can be measured by the other amplifier. The potential difference

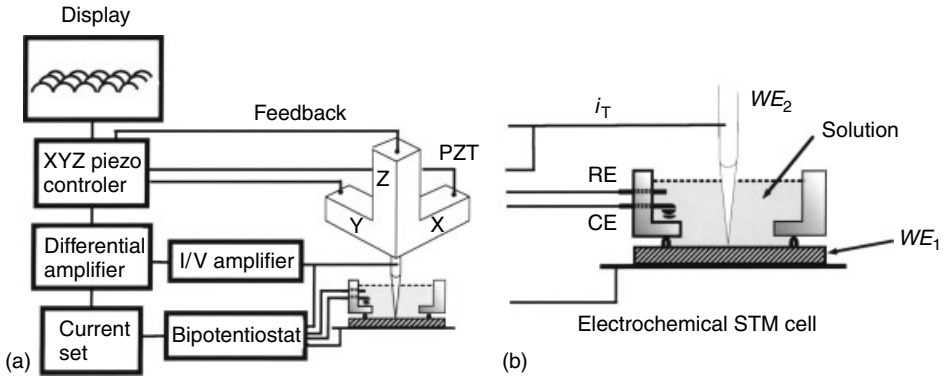


Fig. 2 Apparatus of in situ STM with the four-electrode configuration.

between WE_1 and WE_2 is equivalent to the bias voltage (V) in Fig. 1.

The sidewall of the tip must be isolated to reduce a background electrochemical current flowing through the tip. Soft glass, organic polymers, and Apiezon wax have been used. Details of tip coating methods have been described by Siegenthaler [5].

7.3.2.3 Preparation of Well-defined Electrode Surfaces

As a fundamental basis for all STM studies, electrode–electrolyte interfaces must be prepared reproducibly, and methods must be established to observe these interfaces accurately. Well-defined single crystalline surfaces must be exposed to solution to understand surface structure-reactivity relationships on the atomic scale. Efforts have succeeded to produce extremely well-defined, atomically flat surfaces of various electrodes made of noble metals, base metals, and semiconductors without either oxidation or contamination in solution.

7.3.2.3.1 Flame-annealing and Quenching Method A unique and very convenient way to expose well-defined clean Pt into aqueous solution was proposed by Clavilier in 1980, in which mechanically exposed single-crystal Pt was annealed in an oxygen flame and quenched in pure water [9]. He also established a method of preparing a single-crystal Pt electrode by melting a Pt wire in the flame. This technique was extended by Hamelin for Au [10], by Furuya for Ir [11] and by us for Rh and Pd [12].

Figure 3 shows typical examples of cyclic voltammograms (CVs) of the three low-indexed Pt surfaces in a sulfuric acid solution obtained in our laboratory. The result shown in Fig. 3 shows that the hydrogen adsorption–desorption reaction is a very structure-sensitive reaction on the Pt surfaces, as indicated by the different shapes and peak positions for the CVs of the different crystalline faces. Although Clavilier and coworkers quantitatively analyzed the binding sites of hydrogen using systematically prepared stepped surfaces [13], more recent investigations using a CO replacement technique clearly indicate that the charges shown in Fig. 3 include a significant contribution of the adsorption and desorption of sulfate/bisulfate [14].

Nevertheless, a direct evidence to support the existence of well-defined surface in solution was demonstrated by us in 1990 using electrochemical STM [15].

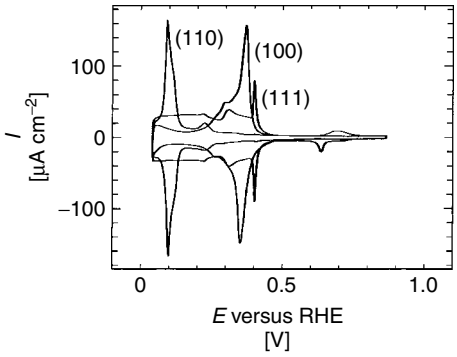


Fig. 3 Cyclic voltammograms of Pt(111), Pt(110), and Pt(100) in 0.5 M H_2SO_4. Scan rate: 50 mV s^{-1}.

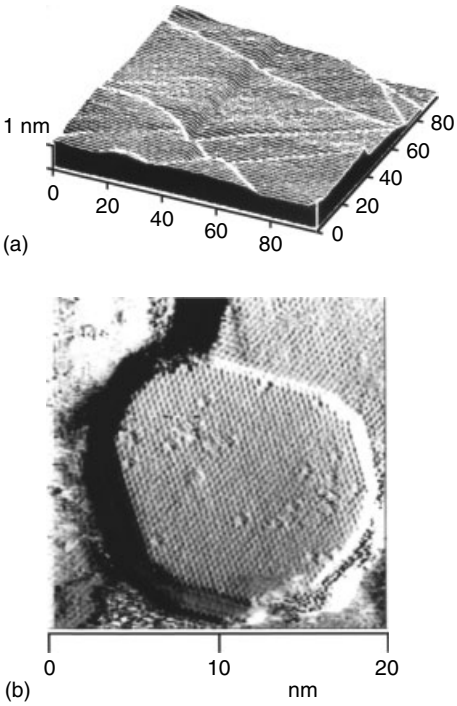


Fig. 4 *In situ* STM images of the flame-annealed Pt(111) in solution.

Figure 4(a) shows our first STM image of a flame-annealed Pt(111) in sulfuric acid solution. The height of each step is ca 0.23 nm in accord with the monatomic step height of 0.238 nm on the Pt(111) surface. The monatomic steps observed on the surface are usually located on nearly parallel straight lines or form an angle of 60° as expected for the surface with threefold symmetry. The terraces seem to be atomically flat. Later, it was shown that the terrace was composed of Pt atoms forming a (1×1) structure as shown in Fig. 4(b) [16]. On the upper and lower terraces, the Pt(111)-(1×1) structure was clearly discerned at potentials near the hydrogen evolution reaction. The nearest-neighbor spacing and corrugation height were 0.28 and 0.03 nm, respectively.

Flame-annealed Au single crystals were more frequently used for various studies including the potential induced reconstruction investigated by several groups [6, 7, 17]. However, it must be emphasized that the flame-annealing method can be applied only to Au, Pt, Rh, Pd, Ir, and possibly Ag.

7.3.2.3.2 **UHV-electrochemical (EC) Methods** It is well established that clean surfaces are exposed in UHV by cycles of Ar-ion bombardment and high-temperature annealing. The surface structure and composition are usually determined by low-energy electron diffraction (LEED) and Auger electron spectroscopy (AES). By using an ultrahigh vacuum-electrochemical (UHV-EC) system, in which a chamber for electrochemical measurements was interfaced to a UHV apparatus, well-defined substrates can be transferred into an electrochemical cell in purified Ar atmosphere. This experimental procedure was successfully applied to various metals such as Pt, Au, Pd, Rh, and so on [1, 2]. However, for some

metals such as Ni, the oxidation of the surface took place in the electrochemical chamber before immersion of the electrode into electrolyte solutions due to the presence of trace amounts of oxygen and water vapor [18]. The same difficulty was encountered for Cu electrodes [19]. It is clear that the problem of substrate oxidation of reactive metals occurring during the immersion and emersion processes is still unsolved in the UHV-EC method.

7.3.2.3.3 **Iodine-CO Replacement Technique** It is important to note that iodine adlayers are known to protect highly sensitive surfaces of metal single crystals from oxidation and contamination in the ambient atmosphere, providing easy preparation and handling of well-defined surfaces in many aspects during electrochemical measurements [1, 2]. The iodine/CO replacement is known to be a method for exposing well-defined and clean surfaces of such electrodes as Pt and Rh in solution [20, 21]. The adsorbed iodine on these surfaces can be replaced by a CO adlayer. Clean surfaces are then exposed in solution by the electrochemical oxidation of CO from the surface.

7.3.2.3.4 **Electrochemical Etching Method** As described above, the flame-annealing and quenching method can only be applied to limited metals such as Pt, Au, Rh, Pd, and Ir and cannot be used for more industrially important, less noble metals such as Ni, Co, Fe, and Cu, because they are heavily oxidized in the flame as well as in air. These metals are also difficult to transfer into electrolyte solutions without oxidation even by using UHV-EC.

However, it was recently found that the anodic dissolution of various metals and semiconductors occurs only at the step edge under carefully adjusted electrochemical conditions, resulting in atomically flat terrace-step structures [22]. Although the etching method has not yet been well recognized as a promising method for exposing well-defined surfaces of various metals, we demonstrated that the layer-by-layer dissolution occurs on various semiconductors, such as Si, GaAs, and InP, resulting in the formation of atomically flat terrace-step structures [7]. It was also found that the layer-by-layer dissolution occurs on various metals such as Ni, Ag, Co, Pd, and Cu [7, 22].

7.3.3 Structure of Specifically Adsorbed Anions

7.3.3.1 **Iodine Adlayers**

The adsorption of anions such as iodide, bromide, cyanide, and sulfate/bisulfate on electrode surfaces is currently one of the most important subjects in electrochemistry. It is well known that various electrochemical surface processes, such as the underpotential deposition of hydrogen and metal ions, are strongly affected by coadsorbed anions [1, 2]. Particularly, structures of the iodine adlayers on Pt, Rh, Pd, Au, and Ag surfaces have been extensively investigated using UHV-EC techniques such as LEED [1]. For example, the commensurate $(\sqrt{3} \times \sqrt{3})R30^\circ$, (3×3), and $(\sqrt{7} \times \sqrt{7})R19.1^\circ$ adlattices were found to form on the well-defined Pt(111)-(1×1) surface, depending on the electrode potential and pH of the solution [23]. More recently, these structures were confirmed by STM in both air [24] and solution [25]. In contrast with Pt(111), only one phase of the commensurate $(\sqrt{3} \times \sqrt{3})R30^\circ$ structure was observed on Pd(111) and Rh(111) surfaces with in situ STM [26, 27].

On the other hand, it has recently been recognized that the iodine adlayer structures are more complicated on Au and Ag surfaces. Although several discrepancies about the iodine adlayer structure on Au(111) (I–Au(111)) are found in the literature [28], surface X-ray scattering (SXS) studies recently carried out by Ocko et al. revealed structural changes of I–Au(111) in KI solution [29]. They found an increasing degree of compression, the so-called electrocompression, of the iodine adlattice with increasing iodine coverage and electrode potential. Instead of commensurate structures found on Pt(111), Rh(111), and Pd(111) as described above, they proposed that the iodine adlayer on Au(111) should be characterized as two distinct series of incommensurate adlattices, a centered rectangular phase and a rotated hexagonal phase [29]. We have reported the structures of I–Au(111) in KI solution determined by both ex situ LEED and in situ STM [28], which agree with Ocko et al.'s SXS results. Similar electrocompression was also found on Ag(111) using the LEED and in situ STM techniques [30]. Our results clearly demonstrate that the complementary use of LEED and in situ STM is a powerful technique for determining atomic structures of the iodine adlayers on single-crystal electrodes.

7.3.3.2 Sulfate/bisulfate on Au(111), Pt(111), Rh(111), Ir(111), Pd(111), and Cu(111)

It has been demonstrated by several groups that in situ STM can be used to visualize adsorbed sulfate/bisulfate (designated below simply as sulfate) species on Au(111), Pt(111), and Rh(111). An ordered structure with a $(\sqrt{3} \times \sqrt{7})$ symmetry was first observed for the adsorbed sulfate/bisulfate on Au(111) in sulfuric acid by Magnussen et al. [31], who proposed a model structure on the basis of the assumption that the adsorbed species is bisulfate, not sulfate, with a surface coverage of 0.4. More recently, Weaver and coworkers reported STM images with the same symmetry of $(\sqrt{3} \times \sqrt{7})$ on Au(111) [32], as that observed by Magnussen et al. However, they proposed a possibility of incorporation of hydronium cations in the ordered sulfate adlayer by taking into account that the surface coverage of sulfate on Au(111) determined by chronocoulometry and radiochemical assay is 0.2 [33]. Note that this surface coverage is one-half of that for the structure proposed by Magnussen et al. as described above.

Stimming and his coworkers found by in situ STM that adsorbed sulfate ions on Pt(111) form the same adlayer structure as that found on Au(111) [34]. Ordered domains with $(\sqrt{3} \times \sqrt{7})$ symmetry appeared in the potential range between 0.5 and 0.7 V versus a reversible hydrogen electrode (RHE) in 0.05 M H_2SO_4. As shown in Fig. 3, only the (111) surface shows the characteristic butterfly peaks at potentials slightly negative than 0.5 V. Their STM observations confirmed that the butterfly peaks are formed because of the adsorption and desorption of sulfate ions as indicated by the CO replacement technique used by Clavilier as described above [14]. STM images obtained on Pt(111) were interpreted in terms of the coadsorption of sulfate anions and water.

High-resolution STM imaging conducted on atomically flat terraces of Rh(111) in H_2SO_4 readily discerned atomic features as shown in Fig. 5(a) obtained near the step edges [35]. The image areas include three terraces with monatomic steps. It is clearly seen that parallel atomic rows in each domain are located in the directions forming angles of

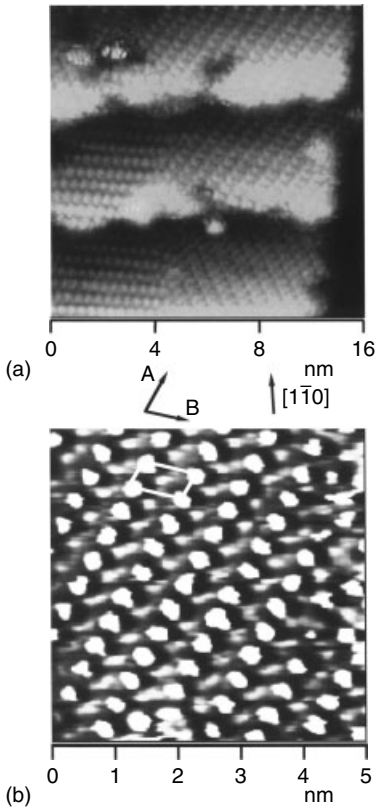


Fig. 5 High-resolution STM images of sulfate adlayer on Rh(111) obtained in H_2SO_4.

nearly 60 or 120°. It is also recognized that individual bright spots exist very near the monatomic step. This observation strongly indicates that the entire surface of Rh(111) is almost completely covered by adsorbed sulfate ions even very near the end of the terraces.

Figure 5(b) presents an STM image showing a more detailed internal structure acquired in an area where a single domain appeared on a wide terrace. It can be seen that there are two different parallel rows with a 30° rotation relative to the underlying Rh lattice. One row appears as bright spots. The observed atomic distance in these bright rows along the *A* direction is equal to 0.46 nm. The average distance between neighboring bright rows is ca 0.7–0.73 nm. The interatomic distance of 0.74–0.75 nm observed along the *B* direction in this particular STM image in Fig. 5(b) is slightly larger than that of the $\sqrt{7}a$Rh (0.707 nm), probably because of a small thermal drift during the acquisition of the image. However, it was ascertained that the distance along the *B* direction is very close to the $\sqrt{7}a$Rh based on the averaging of all atomic images. The angle between the directions marked by arrows A and B in Fig. 5(b) is ca 72°. The above results strongly indicate that the unit cell can be defined by the so-called $(\sqrt{3} \times \sqrt{7})$ structure.

The structure described above is almost the same as those reported on Au(111) by Magnussen et al. [31] and other investigators [32] and those observed on Pt(111) [34]. Magnussen et al. proposed a model structure with a unit cell, the so-called $(\sqrt{3} \times \sqrt{7})$, for the adlayer of bisulfate (HSO_4^-) on Au(111). Both bright and dark spots were interpreted as bisulfate ions adsorbed on Au(111). Therefore, the surface coverage of this proposed structure is 0.40. According to the coverage value of ca 0.2 obtained on Rh(111) by Wieckowski et al. [36], it is reasonable to expect that only the bright spots in the STM images observed on Rh(111) correspond to the adsorbed sulfate or bisulfate. If sulfate or bisulfate is assumed to be also trigonally coordinated on Rh(111), a ball model can be presented as shown in Fig. 6(a), where the SO_4^{2-} (or HSO_4^-) is positioned at the threefold hollow sites. It can be seen in Fig. 6(a) that the sulfate ions along the $\sqrt{3}$ direction form an almost close-packed row. On the other hand, an open space can be found between neighboring rows of the sulfates. As described above, Weaver and

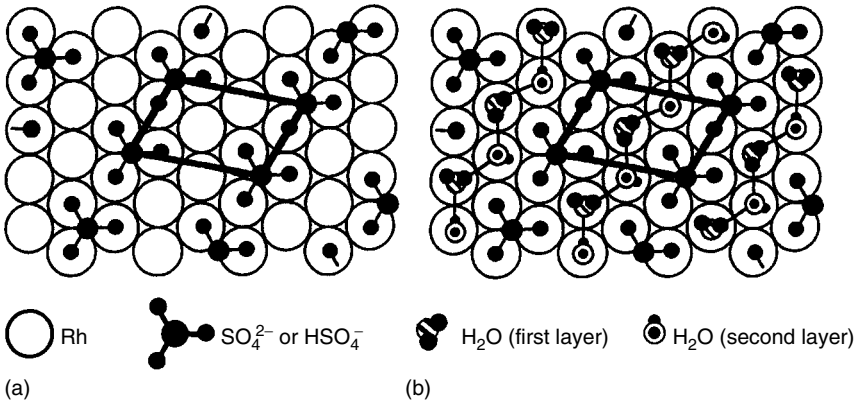


Fig. 6 Model structures of the sulfate adlayer on Rh(111) surface: (a) sulfate on the threefold site; (b) coadsorption of sulfate and hydrogen-bonded water chains.

coworkers proposed a model where coadsorbed hydronium cations exist along the $\sqrt{3}$ direction between neighboring rows of sulfates [32]. The dark spots that appeared in the STM images were assigned to be the coadsorbed hydronium cations. Such cation coadsorption was expected to minimize the coulombic repulsion between adjacent SO_4^{2-} on Au(111). Although the coadsorption of hydronium cations is thought to be a factor which explains the nonuniform interatomic distances of the $(\sqrt{3} \times \sqrt{7})$ structure, it is not clear why the adsorbed sulfates have different spacings along the $\sqrt{3}$ and $\sqrt{7}$ directions. In our previous paper, we proposed a new model to explain the nonuniform spacing in the unit cell of $(\sqrt{3} \times \sqrt{7})$ [35]. The reader can see in Fig. 6(a) that uncoordinated Rh atoms are arranged in a zigzag form in the $\sqrt{3}$ direction between neighboring rows of the adsorbed sulfates. In a new model shown in Fig. 6(b), hydrogen-bonded water chains are simply inserted along the $\sqrt{3}$ direction between neighboring rows of the sulfates. The model shown in Fig. 6(b) includes the adsorbed sulfate/bisulfate and hydrogen-bonded water chains formed along the $\sqrt{3}$ direction. The model shows only the first water bilayer. Water molecules in the first layer are bonded directly to Rh atoms at the ontop site via the oxygen lone pair. According to the model, it is possible that the dark spots that appeared in the STM image shown in Fig. 5(b) arise from the water molecules in the second layer. Although the model presented here would seem to be equivalent or similar to the model proposed by Weaver et al. [32], our model more confidently explains the feature of the nonuniform interatomic distances in the $(\sqrt{3} \times \sqrt{7})$ structure. It is also noteworthy that the hydrogen-bonded water chains are expected to form hydronium cations in acidic solutions. If the water molecule in the second layer is protonated to form hydronium cations, the model presented here is equivalent to the model proposed by Weaver et al. [32]. According to the model structure shown in Fig. 6(b), each chain of water molecules should appear in a zigzag configuration with different heights. Only a single dark spot in the unit cell has been distinguished in previous studies using Au(111), Pt(111), and Rh(111). However, it was reported in our recent papers that sulfate anions formed highly ordered adlayers on Ir(111) and Pd(111) in sulfuric acid

with the same ($\sqrt{3} \times \sqrt{7}$) symmetry as observed on Au(111), Pt(111), and Rh(111) as described above. Surprisingly, zigzag rows of hydrogen-bonded water molecules between neighboring sulfate rows along the $\sqrt{3}$ direction were clearly revealed on Ir(111) and Pd(111) [37, 38]. These results further supported the proposed model of sulfate coadsorption with hydrogen-bonded water molecules as shown in Fig. 6(b). The adsorption of sulfate was investigated on Cu(111) surface in sulfuric acid by Wandelt's and Nichols's groups [39–41]. They have observed an ordered sulfate structure with the same ($\sqrt{3} \times \sqrt{7}$) symmetry. The adlayer was proposed to be located on a reconstructed first Cu(111) layer, resulting in a distinct Moiré pattern. Nevertheless, it is now clear that sulfate anions form adlayers with the same structure and symmetry on at least six different substrates, Au(111), Pt(111), Rh(111), Ir(111), Pd(111), and Cu(111). In general, structures of many adlayers depend strongly on the substrates. The appearance of the same ($\sqrt{3} \times \sqrt{7}$) structure on the substrates with different lattice parameters might suggest that the coadsorption of sulfate and water illustrated in Fig. 6(b) is flexible with respect to the change in lattice parameter of the substrate. Such a flexibility may be due to the existence of water molecules between the sulfate chains with a relatively weak hydrogen bonding.

7.3.4 Adsorption of Simple Aromatic Molecules

The adsorption of organic molecules onto bare electrode surfaces in electrolyte solutions under potential control has long been investigated for elucidating the role of the structure and property of adsorbed molecules in electrochemical reactions [1, 2, 42]. Although conventional electrochemical and optical techniques, such as IR, Raman, and SHG spectroscopies have been extensively applied to the investigation of molecular adsorption at electrode surfaces in solution [42], they can usually provide only averaged information on the molecular orientation and packing within an adlayer. Ex situ techniques such as LEED and AES, using the UHV-EC technique, have also been extensively employed for an understanding of the relationship between the adsorbed molecules and the atomic structure of the electrode surfaces [1, 2]. More recently, in situ STM has been well recognized as an important in situ method for structural investigation of adsorbed organic molecules on well-defined electrode surfaces in electrolyte solution with atomic resolution. The high resolution achieved in solution strongly encouraged us to investigate the adsorption of relatively small and simple aromatic molecules, such as benzene, directly attached to the electrode surface to understand the electrocatalytic activities of noble metals such as Pt and Rh. On the other hand, voluminous reports describe investigation of the adsorption in UHV of aromatics, such as benzene and its derivatives on Pt, Rh, Ni, Ir, Ru, and Pd, which were performed by using various surface-sensitive techniques such as LEED, AES, and electron energy-loss spectroscopy (EELS). The purpose of those investigations was to evaluate gas-phase catalytic reactions such as hydrogenation, dehydrogenation, and dehydrocyclization [43]. In UHV the (3×3) superlattice of benzene and CO coadsorbed on Rh(111) revealed a well-ordered array of ringlike features associated with adsorbed benzene molecules, while CO did not appear in STM images [44, 45].

Nevertheless, we described, for the first time, the adlayer structures of benzene adsorbed on Rh(111) and Pt(111) in HF solutions [46]. High-resolution STM images allowed us to determine the packing arrangement and even the internal structure of each benzene molecule in solution.

7.3.4.1 Benzene on Rh(111) in HF

Figure 7 shows CVs of Rh(111) electrode in the absence and presence of benzene in 0.01 M HF. In the absence of benzene, the CV obtained on the well-defined Rh(111) exhibited several highly reversible characteristic peaks as shown in Fig. 7(a). It was noted that the heights and widths of these characteristic peaks depended on the quality of the surface of Rh(111) prepared by the flame-annealing and quenching method. After the Rh(111) electrode was subjected to CV measurement in the pure HF solution, it was transferred into a 0.01 M HF solution containing ca 1 mM benzene. The CV indicated a featureless double-layer region between 0.3 and 0.7 V as shown in Fig. 7(b). The cathodic current commencing at about 0.3 V was considered to be the result of simultaneously occurring processes such as the desorption of adsorbed benzene, the adsorption of

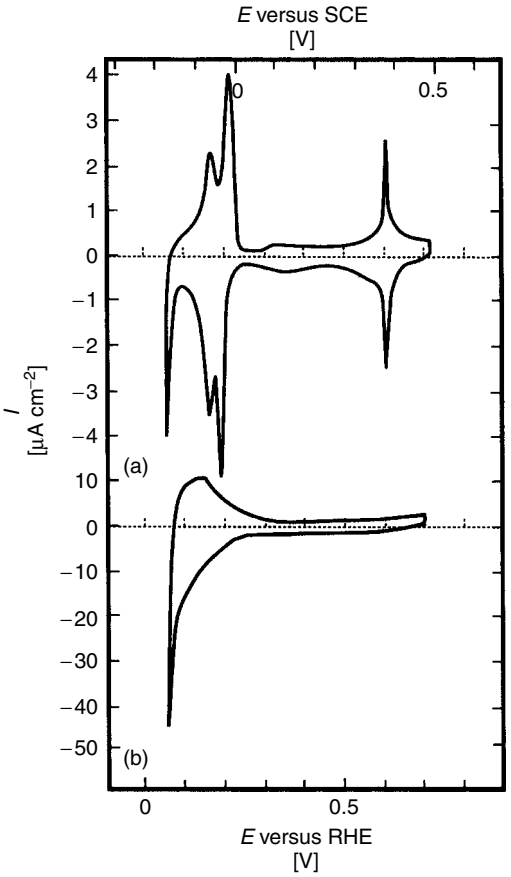


Fig. 7 Cyclic voltammograms of Rh(111) without (a) and with (b) 1 mM benzene.

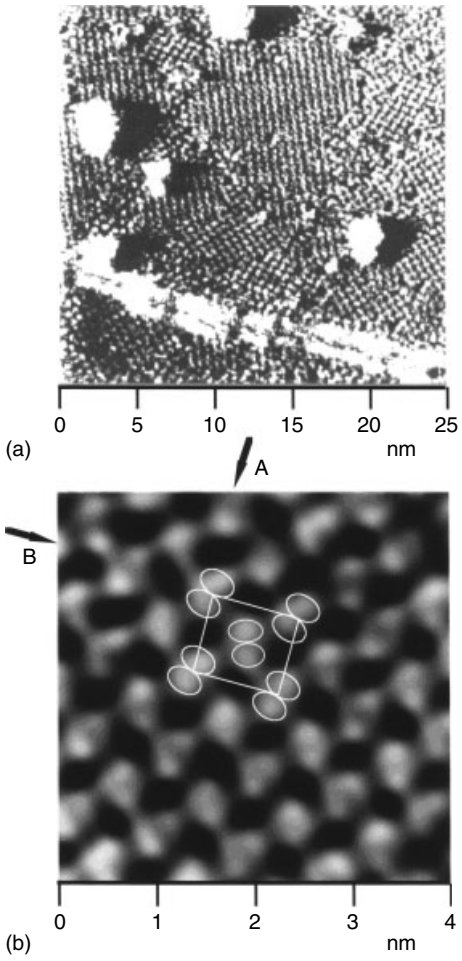


Fig. 8 High-resolution STM images of the $c(2\sqrt{3} \times 3)$*rect* benzene adlayer on Rh(111) in HF.

hydrogen, and the irreversible hydrogenation of benzene to cyclohexane, according to the previous studies using differential electrochemical mass spectrometry (DEMS) [47]. A similar featureless CV was obtained with a benzene-dosed Rh(111) electrode in pure 0.01 M HF. The Rh(111) electrode was immersed in 0.01 M HF containing 1 mM benzene for 1 minute at the open-circuit potential and then transferred to the pure HF solution. These results strongly suggest that benzene was chemisorbed and remained on the surface of Rh(111), at least in the potential range between 0.3 and 0.7 V. After achieving the atomic resolution of the Rh(111)-(1×1) structure in HF, a small amount of 1 mM benzene solution was directly added to the STM cell at 0.45 V. The average concentration of benzene in 0.01 M HF was 10 μM. Immediately after the injection of benzene, completely different patterns appeared in STM images. Figure 8(a) shows an example of the STM images acquired at 0.45 V [46]. It is evident that the atomically flat terraces are now covered by ordered benzene adlayers. An averaged domain size was about 10 nm × 10 nm. The adsorbed benzene molecules appear to form a square adlattice in each domain. Furthermore, the molecular rows in a given domain cross each other forming boundaries at an angle of either 60 or 120°. More details of the orientation of benzene in the adlayer are revealed by the higher resolution STM image shown in Fig. 8(b). It is seen in Fig. 8(b) that the molecular rows along the direction of arrows A and B cross each other at 90°, and they are always parallel with the close-packed and $\sqrt{3}$ directions of the Rh(111) substrate, respectively. The intermolecular distances along these directions are not equal to each other and were found to be on the average, 0.8 and 0.9 nm respectively. On the basis of the orientation of molecular rows and the intermolecular distances, we concluded that the benzene adlayer was composed of rectangular unit cells, namely, $c(2\sqrt{3} \times 3)$*rect* ($\theta = 0.17$), as shown in Fig. 8(b). The known lattice spaces of $2\sqrt{3}$ and 3 on Rh(111) (0.268 nm) correspond to 0.93 and 0.80 nm respectively, which are consistent with our experimental values.

Surprisingly, the STM image allowed us to determine the internal structure and microorientation of each benzene molecule adsorbed on Rh(111). It is clear that each spot is split into two bright spots, forming a characteristic dumbbell shape for each benzene molecule. The STM discerned a 0.01 nm corrugation between the valley and the ridge of each benzene molecule. It can also be seen from Fig. 8(b) that the orientation of dumbbell-shaped benzene is not the same for all molecules, but depends on their positions. The dumbbell shape of the central benzene molecule in the unit cell shown in Fig. 8(b) is clearly rotated by 60° with respect to the molecules located on the four corners of the unit cell. The molecules on the corners of the unit cell appeared with an identical feature, suggesting that they are situated on an identical binding site. It is also seen that the orientation of these dumbbells is always rotated by 30° with respect to the direction of close-packed rows (arrow A in Fig. 8(b)) of the Rh(111) substrate. The STM image shown in Fig. 8(b) provides more detailed information on the orientation of molecules in the unit cell as discussed below. The $c(2\sqrt{3} \times 3)rect$ structure described above was consistently observed in the potential range between 0.4 and 0.7 V without additional structural transitions. On the other hand, it was found that the adlayer structure changed at negative potentials. A negative potential step from 0.45 to 0.35 V induced a reconstruction in the benzene adlayer from $c(2\sqrt{3} \times 3)rect$ symmetry to an ordered hexagonal pattern. The electrode potential of 0.35 V is near the onset potential of the cathodic current as shown in Fig. 7.

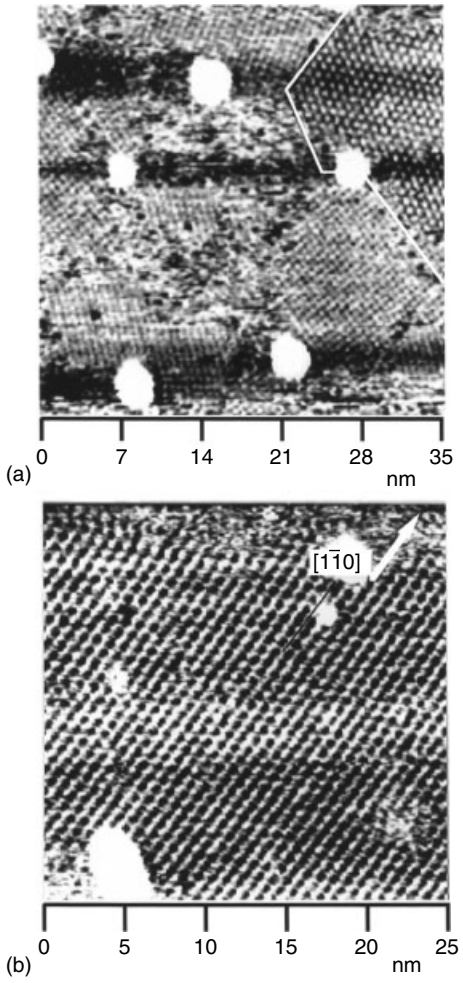


Fig. 9 STM images of (a) domain boundaries of $c(2\sqrt{3} \times 3)rect$ and (3×3) benzene adlayers; (b) the pure (3×3) structure on Rh(111).

Figure 9 shows a set of STM images acquired in almost the same area to reveal the dynamic process of phase transition [46]. It is clearly seen from Fig. 9(a) that a new domain appeared with the hexagonal array of benzene on the upper right corner marked by solid lines, while the $c(2\sqrt{3} \times 3)rect$ structure remained as the main phase. A further cathodic step to 0.25 V resulted in a predominantly hexagonal phase, while eliminating the $c(2\sqrt{3} \times 3)rect$ domains as shown in Fig. 9(b). Such a long-range ordered hexagonal pattern could be seen

over almost the entire area of the terrace at 0.25 V. All benzene molecules exhibited the same corrugation height of 0.07 nm, similar to that in the $c(2\sqrt{3} \times 3)$ *rect* structure.

To reveal the internal molecular structure in the hexagonal phase, STM images were acquired under particularly carefully adjusted experimental conditions with minimal thermal drift. Figure 10(a) shows one of the highest resolution images acquired on the terrace shown in Fig. 9(b). Compared with the crystal orientation, $[1\bar{1}0]$, determined by the Rh(111)-(1×1) atomic image, it can be seen that all benzene molecules are almost perfectly aligned along three close-packed directions of Rh(111). The molecular rows cross each other at an angle of either 60 or 120° within an experimental error (±2°). The intermolecular distance along these rows was found to be 0.8 nm, which corresponds to three times the lattice parameter of Rh(111). Therefore, we conclude that the hexagonal structure is (3×3)-C_6H_6 ($\theta = 0.11$) as shown by the unit cell superimposed in Fig. 10(a). Moreover, a careful examination of the image reveals that each benzene molecule appears as a set of three spots with similar intensities. It can also be seen that a clear dip exists in the center of each triangle with three lobes. These features can be more clearly seen in the height-shaded surface plot obtained by applying a mild 2D Fourier transform filter method as shown in Fig. 10(b). The spacing between the two lobes in each molecule was found to be about 0.3 nm. In addition, a weaker additional spot with a small corrugation of about 0.02 nm can be seen in the unit cell. It is important to note that all these features of the STM image for the (3×3) adlayer observed at 0.25 V are essentially identical to those found for the coadsorbed benzene and CO adlayer on Rh(111) in UHV reported by Ohtani et al. [44]. They also found the weaker spot, which was attributed to the coadsorbed CO or artifacts caused by asymmetric tips [44].

When the electrode potential was stepped further in the negative direction, the ordered (3×3) domain became islands with the same internal structure, suggesting that the desorption of

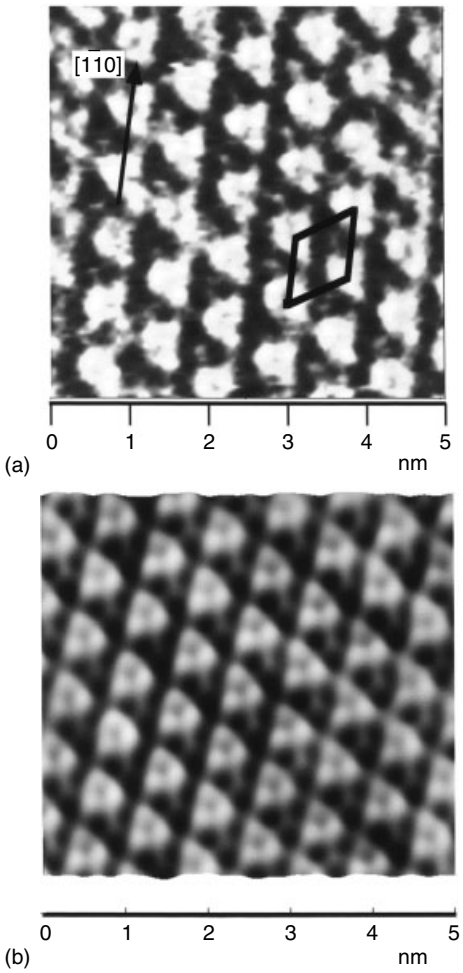


Fig. 10 High-resolution STM images of the (3×3) structure on Rh(111). (a) Top view; (b) height-shaded plot.

benzene occurred preferentially at the edges of the islands of ordered (3×3) domains [46]. Eventually, all adsorbed benzene molecules were desorbed from the surface at 0.1 V, partially because of hydrogen adsorption and partially hydrogenation, as expected from the result obtained by DEMS [47], and the Rh(111)-(1×1) structure was consistently discerned at 0.1 V. The structural changes described above were reversible. When the electrode potential was stepped back to the positive region, the (3×3) and $c(2\sqrt{3} \times 3)rect$ phases returned at the potentials described above.

The structures and registries of chemisorbed benzene on Rh(111) have been thoroughly scrutinized by surface-sensitive techniques such as LEED, EELS, and angle-resolved UV photoemission spectroscopy (ARUPS) in UHV [43]. These previous studies revealed various structures for benzene, including well-known structures such as $c(2\sqrt{3} \times 4)rect$ and (3×3), depending on whether CO was present unintentionally or intentionally in the UHV chambers. Although it has been repeatedly demonstrated that the adlayer structures of benzene on Rh and Pt were greatly affected by the presence of CO in the adlayer, the structure of the pure benzene adlayer has not yet been fully understood. Neuber et al. reported that a completely new structure with a $(\sqrt{19} \times \sqrt{19})R23.4^\circ$ symmetry appeared for the pure benzene adsorption on Rh(111) under cleaner UHV conditions in the absence of CO, and the previously known structures of $c(2\sqrt{3} \times 4)rect$ and (3×3) were found to appear upon admission of CO [48].

However, it was found in our study [46] that the anodic peak due to the oxidation of CO was hardly detectable in CV even after a prolonged STM experiment for several hours in an air-saturated HF solution. We strongly believe that the adlayer structures found in HF solution described above did not result from contamination with CO.

It is extremely important to recognize that in the previous study of the adsorbed benzene on Rh(111) in UHV [48], one of the structures of the pure benzene adlayer was attributed to the $c(2\sqrt{3} \times 3)rect$ structure, which was found in solution. This result strongly suggests that the existence of water molecule on top of the benzene adlayer plays a minor role in determining the structure of benzene.

Figure 11(a) shows a proposed model for the $c(2\sqrt{3} \times 3)rect$ structure [46]. All of the adsorbed benzene molecules are assumed to be located on the twofold bridging sites. The benzene molecule at the center of the unit cell also occupies a twofold site, but it is rotated by 60° from the orientation of the molecules at the corners. Weiss and Eigler reported three distinct types of STM images for isolated benzene molecules located at threefold, hollow and atop bridge sites on Pt(111) at 4 K [49]. They assigned the single bump, elongated perpendicularly to the bridge, to the bridge-bonded benzene. In Fig. 8(b) each benzene molecule is seen with the dumbbell shape on Rh(111) and elongated perpendicularly to the bridge. It is clear that the direction of each elongated dumbbell is always rotated by approximately 30° with respect to that of the corresponding atomic row of Rh(111).

These detailed features can be explained by the model structure shown in Fig. 11(a), where two lobes marked by the circles are assumed to be localized near carbon atoms (1, 2, 6 and 3, 4, 5) bonded across the Rh atoms.

The STM image obtained at 0.25 V shown in Fig. 10 can be explained by the structural model with the (3×3) symmetry illustrated in Fig. 11(b). Although the

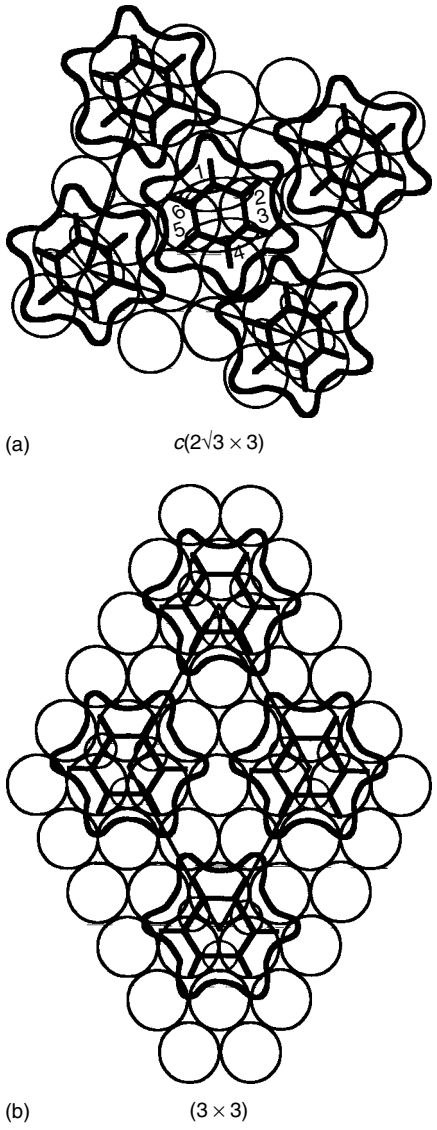


Fig. 11 Space models of (a) the $c(2\sqrt{3} \times 3)$*rect* and (b) the (3×3) structures.

structure proposed here is basically the same as that proposed previously, based on the LEED, EELS [43], and STM [44] studies in UHV, for the adlayer of coadsorbed benzene and CO on Rh(111), two CO molecules thought to be located at the threefold hollow sites in the unit cell are omitted in Fig. 11(b). Each benzene molecule is assumed to bond at the threefold hollow site. The coadsorption of CO was unlikely to take place in the solution under the present condition, because no oxidation peak was observed as described above. Instead of CO, water molecules or hydronium cations might be coadsorbed near the uncoordinated threefold hollow sites to stabilize the (3×3) structure, their function being similar to that of the coadsorbed CO. The weak small spots seen in Fig. 10 might be due to such coadsorbed water molecules or hydronium cations.

7.3.4.2 Other Molecules

It was also found that naphthalene molecules formed an ordered structure on Rh(111) [50]. A high-resolution image acquired in an ordered domain is shown in Fig. 12. It is clearly seen that the molecular rows parallel the <110> direction of the substrate indicated by the arrows in Fig. 12(a). More importantly, the STM image allowed us to determine the internal structure and orientation of each naphthalene molecule. The elongated features along the longer molecular axis (C_2) were discerned for each molecule. In addition, the images of some molecules clearly show a two-ring structure expected from the molecular model. It can also be seen that naphthalene molecules are perfectly aligned with a regular microorientation along the molecular rows. Periodical rotation of the molecules of naphthalene by 60° is seen within each molecular row with every third molecule being in the same orientation. A further magnified view in height-shaded mode is shown in Fig. 12(b), in which the two-ring structure can be more clearly seen. The nearest-

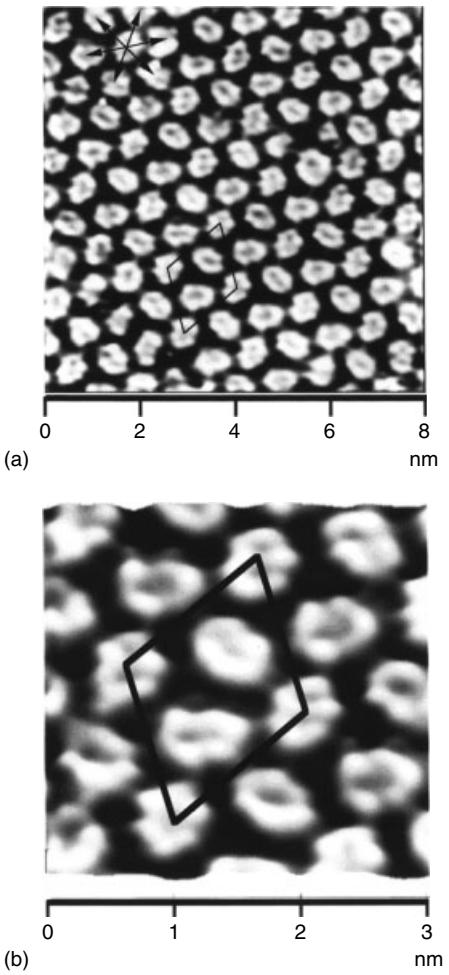


Fig. 12 High-resolution STM images of naphthalene on Rh(111). (a) Top view; (b) perspective view.

neighbor distance of an average of 0.82 nm is equivalent to three times the Rh lattice parameter of 0.268 nm.

According to the results described above, the unit cell can be defined as a $(3\sqrt{3} \times 3\sqrt{3})R30^\circ$ symmetry as shown in Fig. 12(b) [50]. It is now clear that all naphthalene molecules align their C_2 axes along the close-packed directions of Rh substrate. The molecules aligned along the <112> direction, which is the so-called $\sqrt{3}$ direction, have the same orientation. The spacing between two adjacent molecules along the $\sqrt{3}$ direction is measured to be 1.4 nm, which is three times the $\sqrt{3}$ spacing. In our model structure [50], two carbon atoms at the 9- and 10-positions are assumed to be attached directly to an Rh atom. It is noteworthy that this structure is identical to that previously proposed from LEED results by UHV workers [51]. If one recalls the identical results for benzene adsorbed on Rh(111) in UHV and in HF solution as described above, the results obtained with naphthalene further support the predominant adsorbate–substrate interaction for hydrophobic molecules and the minor role of water molecules.

Although anthracene molecules formed a disordered adlayer on Rh(111), high-resolution STM images unambiguously disclosed the internal molecular structure of anthracene [50]. The use of the other metals instead of Rh and Pt is extremely important to understand the role of the interaction between substrate and adsorbates in ordering processes of adsorbed organic molecules. The adsorption of benzene, naphthalene, and anthracene was investigated using a well-defined Cu(111) in solution [52]. It was surprising to find an extraordinarily ordered adlayer of anthracene on Cu(111) in view of the fact that anthracene formed completely disordered adlayers on Rh(111) and Pt(111). Cu electrodes are interesting substrates with which to investigate the adsorption of organic molecules in solution, because of the weak interaction between aromatic hydrocarbons and Cu [52].

In situ STM was also employed to study adlayer structures of benzoic acid (BA) and terephthalic acid at a well-defined Pt(111) electrode in solution [53].

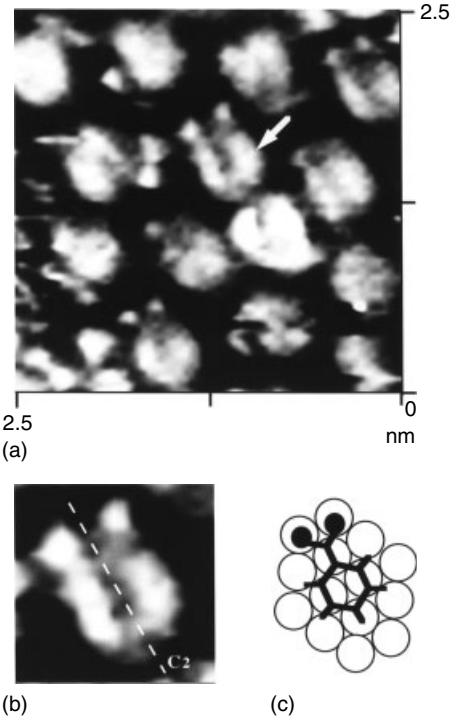


Fig. 13 High-resolution STM images of benzoic acid on Pt(111). (a) Image acquired in an area of 2.5 nm ×2.5 nm; (b) the expanded image of the single benzoic acid molecule marked by an arrow in (a); (c) a real-space model.

The high-resolution STM image acquired in an area of 2.5 nm × 2.5 nm shown in Fig. 13(a) discloses the packing arrangement and even the internal structure of a single BA molecule. Figure 13(b) shows an enlarged image of the single BA molecule marked by the arrow in Fig. 13(a). The pair of elongated features and two bright spots on the sides are thought to correspond to the aromatic ring and the carboxylate group of the BA molecule. These STM images strongly suggest that BA molecules are adsorbed with their molecular plane parallel to the Pt(111) surface. It can also be seen that the in-plane rotational relationship of BA molecules with respect to the Pt(111) substrate is indicated by their C_2 axes, aligned along the $\sqrt{3}$ directions. The C_2 axis of a BA molecule runs along two apical carbons and bisects the two oxygen atoms of the −COOH group as indicated by the dashed line in Fig. 13(b). In addition, the elongated appearance of the aromatic ring with a dumbbell shape indicates that the BA molecules are adsorbed at twofold bridge sites on Pt(111). The tentative molecular model in Fig. 13(c) assigns the aromatic ring to a twofold bridge site with the carboxylic acid group aligned along the $\sqrt{3}$ direction. Two oxygen atoms of the −COOH group play an important role in determining the packing arrangement.

Surprisingly, it was found in our previous study [53] that terephthalic acid formed highly ordered adlayers on Pt(111). The typical arrangement of a monolayer of terephthalic acid at Pt(111) is revealed by the STM image in Fig. 14(a). Well-ordered arrays consisting of oriented terephthalic acid molecules can immediately be identified, which contrasts markedly with the disordered arrangement of BA. The patchy appearance of these ordered structures is actually attributed to rotational domains of an ordered structure. The presence of a long-range ordered pattern allowed STM imaging with molecular resolution. Figure 14(b) displays a high-resolution STM image that discerns the internal structure of terephthalic acid molecules. It is clear that two orthogonally intersected molecular rows of I and II are to parallel the close-packed and $\sqrt{3}$ directions of the Pt(111) substrate, respectively. The intermolecular distances of ca 1.1 and 0.96 nm along these two directions can be interpreted as the unit vectors of 4 and $2\sqrt{3}$, respectively. This structure is thus characterized as $c(2\sqrt{3} \times 4)rect$, $\theta = 0.125$, and

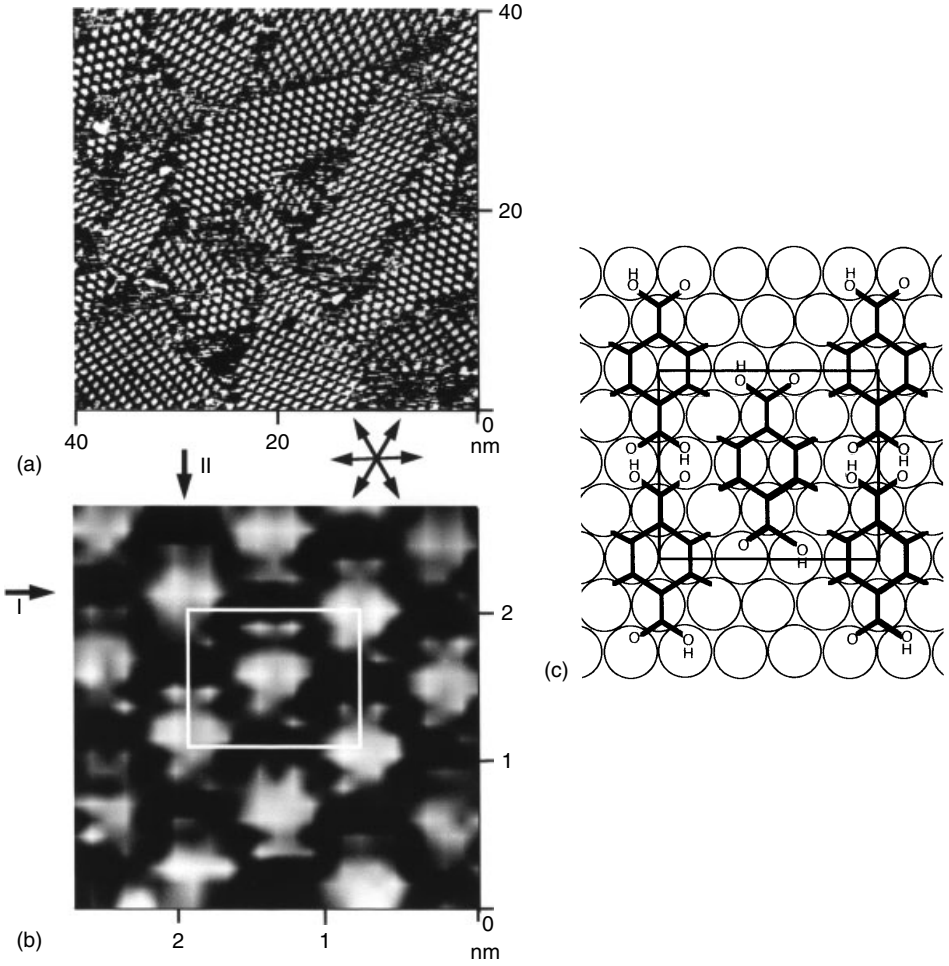


Fig. 14 (a and b) High-resolution STM images of terephthalic acid on Pt(111). (c) A real-space model. Arrows show the close-packed directions of the Pt(111) substrate.

the rectangular unit cell is outlined in Fig. 14(b).

With these high-resolution STM images, the determination of the packing arrangement of adsorbed molecules is straightforward. It can be concluded that the terephthalic acid molecules are adsorbed horizontally like BA. The elongated dumbbell-shaped image and two adjacent pairs of spots are attributed to the aromatic ring and two −COOH functional groups at the para positions of each benzene ring. The space of ca 0.22 nm observed between the two oxygen spots for a −COOH functional group agrees with the value derived from the molecular structure. It is worthwhile noting that all the molecules are arranged with the same orientation with their longer C_2 axes being aligned along the $\sqrt{3}$ direction and two acidic groups of two neighboring molecules facing each other. Two

nearest oxygen spots belonging to two neighboring terephthalic acid molecules are separated by 0.25 nm. The STM image of Fig. 14(b) leads to a structural model of terephthalic acid on Pt(111) as shown in Fig. 14(c). As in the model for BA shown in Fig. 13(c), terephthalic acid molecules are assigned to twofold bridge sites, with all oxygen atoms in the −COOH groups residing near the bridge sites. The two −COOH groups at the para positions of a terephthalic acid molecule have exactly the same coordination environment with the Pt substrate. The result described above strongly suggests that intermolecular interactions play an important role in the formation of ordered adlayers of organic molecules.

Spontaneously chemisorbed monolayers of organosulfur molecules such as thiols and disulfides on Au electrodes have also been extensively investigated using STM [54]. High-resolution STM images of simple thiols such as 4-mercaptopyridine adsorbed on Au(111) revealed the internal structures and microorientation of each molecule [55, 56]. Because of publication limitations, this chapter has only focused on in situ STM of simple aromatic molecules.

7.3.5 Conclusion

The methods for exposing well-defined electrode surfaces in solution were reviewed. The flame-annealing and quenching method can be applied to Au, Pt, Rh, Pd, and Ir single-crystal electrodes. The UHV-EC method can be applied to Pt, Au, Pd, and Rh. For some metals such as Ni and Cu, surface oxidation takes place in the electrochemical chamber before immersion of the electrode into electrolyte solutions.

The structures of specifically adsorbed iodine on the (111) surfaces of various metals were briefly discussed, indicating that complementary use of in situ STM and ex situ LEED is a powerful combination to characterize the atomic structure of adsorbed iodine. The adsorption of sulfate/bisulfate on Au(111), Pt(111), Rh(111), Ir(111), Pd(111), and Cu(111) was described, with emphasis on the fact that the same $(\sqrt{3} \times \sqrt{7})$ structure is formed on these substrates. Our model indicates that hydrogen-bonded water chains are inserted along the $\sqrt{3}$ direction between neighboring rows of the adsorbed sulfates.

The adlayer structure of benzene on Rh(111) was also described in detail; it was found to be dependent on the electrode potential. The (3×3) structure found on Rh(111) in the cathodic potential range is almost identical to that found in UHV for the coadsorbed benzene and CO. The molecular shapes of naphthalene and anthracene could be clearly discerned by in situ STM. It was pointed out that the use of another substrate such as Cu(111) is important to understand the role of the interaction between substrates and adsorbates in the ordering processes of adsorbed molecules.

Terephthalic acid formed a highly ordered adlayer with $c(2\sqrt{3} \times 4)$*rect* symmetry. Two carboxylate functional groups at the para position were clearly discerned. The adlayer of terephthalic acid thought to be stabilized by hydrogen bonding between adjacent −COOH groups, formed molecular chains along the $\sqrt{3}$ direction. This result suggests that intermolecular interactions also played an important role in the formation of the ordered adlayer.

This chapter clearly demonstrates that in situ STM allows us not only to determine interfacial structures but also to follow electrochemical reactions. It is

certain that in situ STM will continue to be the premier technique for atomic-level structural investigations of modified electrodes.

Acknowledgment

This work was supported partly by a Grand-in-Aid for Science Research (A) (No. 12305055) from the Ministry of Education, Science, Sport, and Culture, Japan and partly by the ERATO-Itaya Electrochemiscopy Project organized by the Japan Science and Technology Corporation (JST).

References

1. A. T. Hubbard, *Chem. Rev.* **1988**, *88*, 633–656.
2. M. P. Soriaga, *Prog. Surf. Sci.* **1992**, *39*, 325–443.
3. H.-J. Guntherodt, R. Wiesendanger, (Eds.), *Scanning Tunneling Microscopy I*, Springer-Verlag, Berlin, 1991.
4. P. A. Christensen, *Chem. Soc. Rev.* **1992**, *21*, 197–208.
5. H. Siegenthaler, in *Scanning Tunneling Microscopy II* (Eds.: R. Wiesendanger, H.-J. Guntherodt), Springer-Verlag, Berlin, 1992, pp. 7–49.
6. A. A. Gewirth, B. K. Niece, *Chem. Rev.* **1997**, *97*, 1129–1162.
7. K. Itaya, *Prog. Surf. Sci.* **1998**, *58*, 121–247.
8. J. G. Simmons, *J. Appl. Phys.* **1963**, *34*, 2581–2590.
9. J. Clavilier, R. Faure, G. Guinet et al., *J. Electroanal. Chem.* **1980**, *107*, 205–209.
10. A. Hamelin, in *Modern Aspects of Electrochemistry* (Eds.: B. E. Conway, R. E. White, J. O. M. Bockris), Plenum Press, New York, 1985, pp. 1–101, Vol. 16.
11. S. Motoo, N. Furuya, *J. Electroanal. Chem.* **1984**, *167*, 309–315.
12. K. Sashikata, N. Furuya, K. Itaya, *J. Vac. Sci. Technol.* **1991**, *B9*, 457–464.
13. J. Clavilier, A. Rodes, K. El. Achi et al., *J. Chim. Phys.* **1991**, *88*, 1291–1337.
14. J. M.Feliu, J. M. Orts, R. Gomez et al., *J. Electroanal. Chem.* **1994**, *372*, 265–268.
15. K. Itaya, S. Sugawara, K. Sashikata et al., *J. Vac. Sci. Technol.* **1990**, *A8*, 515–519.
16. S. Tanaka, S.-L. Yau, K. Itaya, *J. Electroanal. Chem.* **1995**, *396*, 125–130.
17. D. M. Kolb, *Prog. Surf. Sci.* **1996**, *51*, 109–173.
18. K. Wang, G. S. Chottiner, D. A. Scherson, *J. Phys. Chem.* **1993**, *97*, 10108–10111.
19. J. L. Stickney, C. B. Ehlers, B. W. Gregory, *Langmuir* **1988**, *4*, 1368–1373.
20. M. Hourani, A. Wieckowski, *J. Electroanal. Chem.* **1987**, *227*, 259–264.
21. C. M. Vitus, S.-C. Chang, B. C. Schardt et al., *J. Phys. Chem.* **1991**, *95*, 7559–7563.
22. K. Itaya, in *Interfacial Electrochemistry-Theory, Experiment, and Applications* (Ed.: A. Wieckowski), Marcel Dekker, New York, 1999, pp. 187–210.
23. F. Lu, G. N. Salaita, H. Baltruschat et al., *J. Electroanal. Chem.* **1987**, *222*, 305–320.
24. B. C. Schardt, S.-L. Yau, F. Rinaldi, *Science* **1989**, *243*, 1050–1053.
25. J. Imukai, Y. Osawa, M. Wakisaka et al., *J. Phys. Chem.* **1998**, *102*, 3498–3505.
26. K. Sashikata, Y. Matsui, K. Itaya et al., *J. Phys. Chem.* **1996**, *100*, 20027–20034.
27. L.-J. Wan, S.-L. Yau, G. M. Swain et al., *J. Electroanal. Chem.* **1995**, *381*, 105–111.
28. T. Yamada, N. Batina, K. Itaya, *J. Phys. Chem.* **1995**, *99*, 8817–8823.
29. B. M. Ocko, G. M. Watson, J. Wang, *J. Phys. Chem.* **1994**, *98*, 897–906.
30. T. Yamada, K. Ogaki, S. Okubo et al., *Surf. Sci.* **1996**, *369*, 321–335.
31. O. M. Magnussen, J. Hagebock, J. Hotlos et al., *Faraday Discuss.* **1992**, *94*, 329–338.
32. G. J. Edens, X. Gao, M. J. Weaver, *J. Electroanal. Chem.* **1994**, *375*, 357–366.
33. Z. Shi, J. Lipkowski, M. Gamboa et al., *J. Electroanal. Chem.* **1994**, *366*, 317–326.
34. A. M. Funtikov, U. Stimming, R. Vogel, *J. Electroanal. Chem.* **1997**, *428*, 147–153.
35. L.-J. Wan, S.-L. Yau, K. Itaya, *J. Phys. Chem.* **1995**, *99*, 9507–9513.
36. P. Zelenay, A. Wieckowski, *J. Electrochem. Soc.* **1992**, *139*, 2552–2558.
37. L.-J. Wan, M. Hara, J. Inukai et al., *J. Phys. Chem. B* **1999**, *103*, 6978–6983.
38. L.-J. Wan, T. Suzuki, K. Sashikata et al., *J. Electroanal. Chem.* **2000**, *484*, 189–193.
39. M. Wilms, P. Broekmann, C. Stulmann et al., *Surf. Sci.* **1998**, *416*, 121–140.
40. M. Lennartz, P. Broekmann, M. Arenz et al., *Surf. Sci.* **1999**, *442*, 215–222.

41. W.-H. Li, R. J. Nichols, *J. Electroanal. Chem.* **1998**, *456*, 153–160.
42. J. Lipkowski, P. N. Ross, (Eds.), *Adsorption of Molecules at Metal Electrodes*, VCH, New York, 1992.
43. G. A. Somorjai, *Introduction to Surface Chemistry and Catalysis*, John Wiley & Sons, New York, 1994.
44. H. Ohtani, R. J. Wilson, S. Chiang et al., *Phys. Rev. Lett.* **1988**, *60*, 2398–2401.
45. H. A. Yoon, M. Salmeron, G. A. Somorjai, *Surf. Sci.* **1997**, *373*, 300–306.
46. S.-L. Yau, Y.-G. Kim, K. Itaya, *J. Am. Chem. Soc.* **1996**, *118*, 7795–7803.
47. H. Baltruschat, U. Schmiemann, *Ber. Bunsen-Ges. Phys. Chem.* **1993**, *97*, 452–460.
48. M. Neuber, F. Schneider, C. Zubragel et al., *J. Phys. Chem.* **1995**, *99*, 9160–9168.
49. P. S. Weiss, D. M. Eigler, *Phys. Rev. Lett.* **1993**, *71*, 3139–3142.
50. S.-L. Yau, Y.-G. Kim, K. Itaya, *J. Phys. Chem. B* **1997**, *101*, 3547–3553.
51. R. F. Lin, R. J. Koestner, M. A. Van Hove et al., *Surf. Sci.* **1983**, *134*, 161–183.
52. L.-J. Wan, K. Itaya, *Langmuir* **1997**, *13*, 7173–7179.
53. Y.-G. Kim, S.-L. Yau, K. Itaya, *Langmuir* **1999**, *15*, 7810–7815.
54. G. E. Poirier, *Chem. Rev.* **1997**, *97*, 1117–1127.
55. T. Sawaguchi, F. Mizutani, I. Taniguchi, *Langmuir* **1998**, *14*, 3565–3569.
56. L.-J. Wan, Y. Hara, H. Noda et al., *J. Phys. Chem. B* **1998**, *102*, 5943–5946.

7.4
Atomic Force Microscopy

Masamichi Fujihira
Tokyo Institute of Technology, Yokohama, Japan

Atomic force microscopy (AFM) in situ is also useful for studies of electrochemical interfaces of chemically modified electrodes. Application of AFM in situ to the study of electrode surfaces is described in detail in Vol. 3 in this series. Therefore, in this section, we simply cite several representative references [1–5] and our related works [6–12]. In addition, a conducting cantilever for AFM, one side of which was coated with a thin metal (e.g., gold) film, can be used to study the surface stress change [13] as a function of electrode potentials [14]. The cyclic voltammogram and the electrocapillary curve were measured in the double-layer region of a thin gold film on the rectangular cantilever. The change in surface stress due to electrochemical oxygen and hydrogen adsorption was also studied on gold and platinum deposited on rectangular cantilevers [14]. Hybridization of DNA was detected as a change in surface stress on a gold coated cantilever modified with ss-DNA [15–17].

References

1. J. J. Macpherson, in *Encyclopedia of Electrochemistry* (Eds.: A. J. Bard, M. Stratmann), Wiley-VCH, Weinheim, 2003, pp. 415–443, Vol. 3.
2. A. A. Gewirth, B. K. Niece, *Chem. Rev.* **1997**, *97*, 1129–1162.
3. H. Siegenthaler, R. Christoph, in *Scanning Tunneling Microscopy and Related Methods* (Eds.: R. J. Behm, N. Garcia, H. Rohrer), NATO ASI Series E, Kluwer Academic Publishers, Dordrecht, 1990, pp. 315–333, Vol. 184.
4. H. Siegenthaler, in *Scanning Tunneling Microscopy II* (Eds.: R. Wiesendanger, H.-J. Guentherodt), *Springer Series of Surface Sciences*, Springer-Verlag, Berlin, 1992, pp. 7–49, Vol. 28.
5. R. J. Colton, A. Engel, J. E. Frommer et al. (Eds.), *Procedures in Scanning Probe Microscopies*, John Wiley & Sons, Chichester, 1998.
6. T. Arai, M. Fujihira, *J. Electroanal. Chem.* **1994**, *374*, 269–273.
7. T. Arai, D. Aoki, Y. Okabe et al., *Thin Solid Films* **1996**, *273*, 322–326.
8. T. Arai, M. Fujihira, *J. Vac. Sci. Technol., B* **1996**, *14*, 1378–1382.
9. W. A. Ducker, T. J. Senden, R. M. Pashley, *Nature* **1991**, *353*, 239–241.
10. T. Miyatani, M. Horii, A. Rosa et al., *Appl. Phys. Lett.* **1997**, *71*, 2632–2634.
11. T. Miyatani, S. Okamoto, A. Rosa et al., *Appl. Phys. A* **1998**, *66*, S349–S352.
12. M. Fujihira, *Annu. Rev. Mater. Sci.* **1999**, *29*, 353–380.
13. T. Miyatani, M. Fujihira, *Jpn. J. Appl. Phys.* **1997**, *36*, 5280–5281.
14. T. Miyatani, M. Fujihira, *J. Appl. Phys.* **1997**, *81*, 7099–7115.
15. J. Fritz, M. K. Baller, H. P. Lang et al., *Science* **2000**, *288*, 316–318.
16. R. McKendry, J. Y. Zhang, Y. Arntz et al., *Proc. Natl. Acad. Sci. U.S.A.* **2002**, *99*, 9783–9788.
17. A. Bietsch, J. Y. Zhang, M. Hegner et al., *Nanotechnology* **2004**, *15*, 873–880..

Encyclopedia of Electrochemistry. Edited by A.J. Bard and M. Stratmann
Vol. 10 *Modified Electrodes*. Edited by M.Fujihira, I.Rubinstein, and J.F.Rusling
Copyright © 2007 Wiley-VCH Verlag GmbH & Co. KGaA, Weinheim. ISBN: 978-3-527-30402-8

7.5 Voltammetry of the Reductive Desorption of Thiol Self-assembled Monolayers from Electrode Surface

Takashi Kakiuchi
Department of Energy and Hydrocarbon Chemistry, Kyoto University, Kyoto, Japan

The voltammetry of the reduction desorption of organothiolate molecules in a self-assembled monolayer on a metal surface, first reported by Porter and his coworkers [1, 2], has been widely used for diagnosing the adsorbed state of the self-assembled monolayer (SAM) [3–54] and for nanometer-scale engineering of SAMs [55–65]. When the electrode covered with a single-component SAM of a thiol derivative is cathodically polarized, typically in an aqueous alkaline solution, a single peak or more complicated multiple peaks appear on the voltammogram. The shape and the location of the peak can be utilized for studying the surface properties of the SAMs. The reductive desorption in an alkaline medium is formally written as

$$\mathrm{RS-M} + \mathrm{e}^- = \mathrm{RS}^- + \mathrm{M} \qquad (1)$$

where RS–M and RS^- represent the organothiolate adsorbed on the metal surface and the organothiolate in the solution after the desorption. The actual mechanism of the desorption is, however, more complicated than what is expressed in Eq. (1), as the desorption is a cooperative process where the adsorbed thiolate molecules are tightly packed in a regular array, for example, the $(\sqrt{3} \times \sqrt{3})\mathrm{R}30^\circ$ structure on Au(111). The shape of the voltammogram is strongly affected by the state of the monolayer, such as the packing density and the magnitude of the lateral interaction between the adsorbed molecules. This means that the electrochemical signal reflects the state of the monolayer; the shape of the voltammogram contains rich information regarding not only the molecular properties of adsorbed thiolates but also those related to the state of the monolayer. Another electrochemical technique employed is chronoamperometry, which usually shows the nucleation and growth-type transients in the timescale of less than a few tenths of a second, depending on the type of desorbing thiolates [7, 31, 66–69], and is therefore suitable for studying the kinetics of desorption. In this chapter, the first part summarizes the fundamental properties of the voltammetry of the reductive desorption of SAMs. The second part introduces a model of the reductive desorption that can account for the salient features of the voltammetry of the reductive desorption. The third part deals with the voltammetry of binary SAMs and its use for studying and engineering the SAMs.

7.5.1 Voltammetry of the Reductive Desorption of SAMs: Experimental Features

7.5.1.1 Reductive Desorption of Alkanethiolate SAMs

The shape of the voltammograms for the desorption of alkanethiolate SAMs depends on the state of the monolayer. Figure 1 shows cyclic voltammograms recorded in 0.5 mol dm^{-3} aqueous KOH for the Au(111) electrodes after being immersed in a 1 μmol dm^{-3} ethanol solution of undecanethiol (UT) for different periods of time. Two humps at −0.6 V and −1 V seen at short immersion times metamorphoses into a single peak at −1.05 V. This change in the shape of the voltammograms reflects the change of the adsorbed state of the UT molecules, which though initially lying flat on the surface, gradually stand

Encyclopedia of Electrochemistry. Edited by A.J. Bard and M. Stratmann
Vol. 10 *Modified Electrodes*. Edited by M.Fujihira, I.Rubinstein, and J.F.Rusling
Copyright © 2007 Wiley-VCH Verlag GmbH & Co. KGaA, Weinheim. ISBN: 978-3-527-30402-8

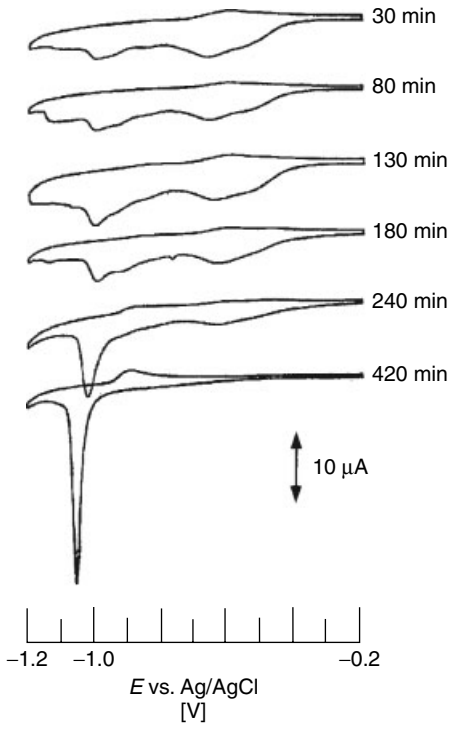


Fig. 1 Change in the shape of voltammograms recorded in 0.5 mol dm^{-3} KOH for a series of SAM substrates prepared at varying times (indicated by line) of immersion of the Au substrates in 1 μmol dm^{-3} undecanethiol in ethanol. Scan rate: 20 mV s^{-1}. (Reproduced from ref. 111 by permission. Copyright: The Japan Society for Analytical Chemistry.)

up to form a densely packed monolayer of UT. A single peak of asymmetric shape that emerged 420 min after the immersion of the gold substrate in the ethanol solution of UT is characteristic of the reductive desorption of a tightly packed SAM.

The annealing of SAM-covered gold substrates for facilitating the ripening of the SAM domains and reducing the number of vacancy islands is effective for obtaining reproducible voltammograms having the shape of a gradual rise in the peak followed by a sharp fall in the base current level [70]. The peak potential and the full width at half maximum vary with the scan rate as shown in Fig. 2. This fact suggests that, on one hand, the kinetics of the desorption processes is slow as shown in chronoamperometry [31, 67], but on the other, the reductive desorption may be treated as a quasi-reversible process at slow scan rates of 10–20 mV s^{-1}. The effect of the chain length of the alkanethiols on the linear-scan voltammograms is illustrated in Fig. 3. The peak shifts to negative potentials with increasing number of

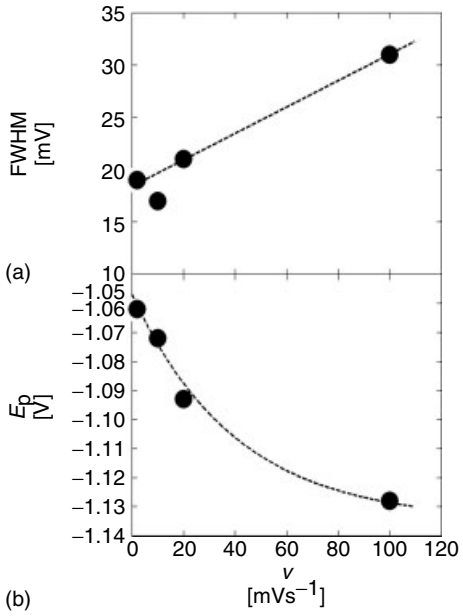


Fig. 2 Dependence of FWHM (**a**) and E_p (**b**) on the linear-scan voltammograms on the scan rate for reductive desorption of decanethiolate self-assembled monolayer on Au(111). Broken lines in **a** and **b** are to guide the eye. (Reproduced from Ref. 70 by permission. Copyright: The American Chemical Society.)

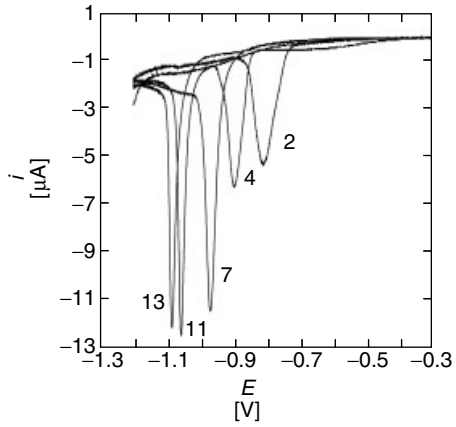


Fig. 3 Cyclic voltammograms for reductive desorption of self-assembled monolayers composed of alkanethiolates recorded under the same conditions as those in Fig. 1. The number of methylene units is indicated by each curve. Curves are for annealed SAMs except for curve 4. (Reproduced from Ref. 70 by permission. Copyright: The American Chemical Society.)

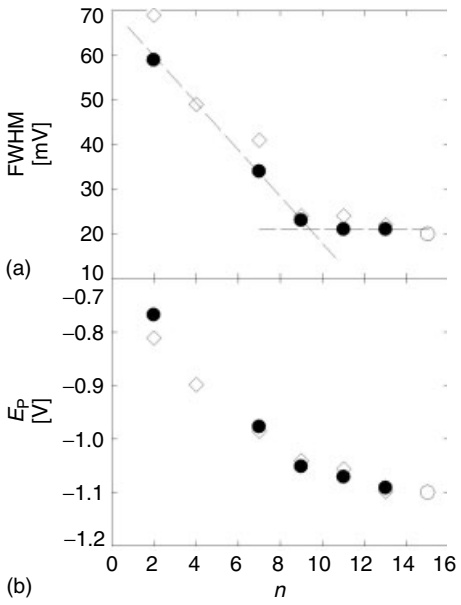


Fig. 4 Dependencies of FWHM (**a**) and E_p (**b**) on n. Filled circles and open diamonds are from annealed SAMs and from nonannealed SAMs, respectively. Open circles are from the literature data. (Reproduced from Ref. 70 by permission. Copyright: The American Chemical Society.)

methylene units, n, that is, the alkyl-chain length. Simultaneously, the full width at half maximum (FWHM) becomes narrower with n. When n is greater than 9, this narrowing reaches a limiting value, 20 mV at the scan rate of 20 mV s^{-1} (Fig. 4a). This saturation tendency seen in the FWHM at higher values of n is less clear in the shift of E_p with n (Fig. 4b). The area under the peak remains constant irrespective of the value of n and is 110 ($\pm$15) μC cm^{-2}. This value is considerably greater than what is predicted from the $(\sqrt{3} \times \sqrt{3})R30^\circ$ structure on Au(111), 7.6×10^{-10} mol cm^{-2} or 73 μC cm^{-2}.

Other interesting features, which are out of the scope of this chapter, about the reductive desorption of organothiolate SAMs from a metal surface include the micelle-like aggregates that are formed after the desorption [11, 12, 25, 71], the appearance of multiple peaks on the voltammogram [9, 31, 33, 72], the effects of pH [44], the reoxidative adsorption after the desorption [11, 73–75], the effect of the nature of the metal and the facets on SAMs [10, 19, 76–79], the role of solvents used for the formation of SAMs [27, 80], the effect of the type of ω-terminal on the desorption behavior [3, 14, 34, 38, 81], the rate of the ion penetration [1], the

effect of the temperature on the shape of voltammograms [82], and the desorption of SAMs other than alkanethiols [23, 24, 32, 49, 50, 53, 83–86].

7.5.2 Modeling of the Reductive Desorption Processes

Chronoamperometric studies show that the reductive desorption of adsorbed alkanethiolates from a metal surface is an event that takes place in less than a second and, typically, in much shorter time [67]. Within this timescale, a nucleation-and-growth type treatment [67, 68, 69], and possibly, the ion penetration into the desorbed SAM [1] are needed to be considered. However, in conventional voltammetry of the scan rate that is less than 100 mV s^{-1}, an equilibrium approach assuming an adsorption isotherm to correlate the amount of adsorbed species and its concentration in the adjacent solution phase is useful for interpreting the voltammograms [87, 70].

The reductive desorption is initiated by a one-electron reduction of adsorbed thiolates followed by the desorption of reduced species, alkanethiolates, from the surface [1, 88].

$$\mathrm{Ox(ads)} + \mathrm{e}^- \rightleftarrows \mathrm{Rd(ads)} \qquad (2)$$

$$\mathrm{Rd(ads)} \rightleftarrows \mathrm{Rd(sol)} \qquad (3)$$

$$\mathrm{Rd(sol)} \rightleftarrows \mathrm{Rd(micl)} \qquad (4)$$

where (ads), (sol), and (micl) indicate adsorbed, solution, and micelle, respectively.

When the desorption process is fast enough and the contribution of the aggregates formation of desorbed species to the mass transfer of desorbed species in the solution phase is negligible, these three steps may be seen as a one-step one-electron reductive desorption [1, 89]:

$$\mathrm{Ox(ads)} + \mathrm{e}^- \rightleftarrows \mathrm{Rd\ (sol)} \qquad (5)$$

There are several ways to incorporate the effect of intermolecular interactions to the rate equation [90]. In the present treatment, we use the expression

$$-\frac{i_\mathrm{F}}{FA} = \overrightarrow{k}\, f(\theta) - \overleftarrow{k}\, c_\mathrm{Rd} \qquad (6)$$

where i_F is the faradaic current for the redox reaction, Eq. (5), F is the Faraday constant, A is the area of the electrode surface, $\overrightarrow{k}$ and $\overleftarrow{k}$ are the rate constants of the reduction and oxidation respectively, $f(\theta)$ is the activity of the oxidized species in the monolayer, and θ is the surface coverage defined as the ratio of the adsorbed amount of alkanethiolates per unit area, Γ, to its saturated value, Γ_m. In Eq. (6), c_Rd is the concentration of the reduced species in the solution adjacent to the electrode surface.

On the other hand, as the faradaic current is directly related to the desorption reaction (5), we have:

$$-\frac{i_\mathrm{F}}{FA} = -\frac{\mathrm{d}\Gamma}{\mathrm{d}t} \qquad (7)$$

where t is time. Combining Eqs. (6) and (7), we obtain a differential equation with respect to θ:

$$-\frac{\mathrm{d}\theta}{\mathrm{d}t} = \overrightarrow{k'}\, f(\theta) - \overleftarrow{k'}\, m_\mathrm{Rd} \qquad (8)$$

where $\overrightarrow{k'} = \overrightarrow{k}/\Gamma_\mathrm{m}$ and $\overleftarrow{k'} = \overleftarrow{k}\,{}^\mathrm{b}c_\mathrm{Rd}/\Gamma_\mathrm{m}$ and $m_\mathrm{Rd} = c_\mathrm{Rd}/{}^\mathrm{b}c_\mathrm{Rd}$ is the dimensionless concentration of Rd. Here, ${}^\mathrm{b}c_\mathrm{Rd}$, the hypothetical reference concentration of the reduced species in the solution, has been introduced for the normalization. $\overrightarrow{k'}$ and $\overleftarrow{k'}$ have the dimension of the inverse of time. Once we know the form of $f(\theta)$, that

is, the form of the adsorption isotherm, Γ can be calculated as a function of time for given values of $\overrightarrow{k'}$ and $\overleftarrow{k'}$.

Among adsorption isotherms of various types, those that can take into account the intermolecular interaction between adsorbed molecules are required to describe reaction (5). The Frumkin isotherm [91], which is based on the mean-field approximation, is the most frequently used in electrochemistry where electrochemical reactions involve adsorption and desorption processes. The Frumkin isotherm predicts the FWHM for the desorption peak to be ~60 mV near the critical point, much broader than experimentally observed values of about 20 mV. To describe the phase transition of adsorbed molecules, Retter examined several isotherms and found that those based on the Ising model can reproduce the sharper phase transitions experimentally observed in the adsorption of heterocyclic compounds on mercury [92].

We use the isotherm based on the sticky site model in combination with the two-dimensional Ising model [93], which was proposed by Blum and Huckaby and has been used successfully to describe the voltammetry of the underpotential deposition of Cu^{2+} on Au(111) [94]. We hereafter call it the BH isotherm.

For the adsorption of a single species on a regular lattice, the BH isotherm has the form:

$$\theta = \eta\theta_{\mathrm{L}} + (1-\eta)\theta_{\mathrm{H}}. \tag{9}$$

Here, θ_{L} and θ_{H} are expressed in the form of the Padé approximant:

$$\theta_{\mathrm{L}} = \frac{z + z(g_2-1)P(g_2,z)}{1 + z + z(g_2-1)P(g_2,z)} \tag{10}$$

and

$$\theta_{\mathrm{H}} = \frac{1}{1 + 1/\xi + (1/\xi)(g_2-1)P(g_2,\xi)}$$
$$\text{where } \xi = 1/[z g_2^6] \tag{11}$$

In Eqs. (10) and (11), P is a function of the interaction parameter, g_2, and the fugacity of the reduced species, z. The functional form of P is given in the Appendix. In Eq. (9), η is a smooth empirical switching function of the form:

$$\eta = \frac{1}{\pi}\left[\frac{\pi}{2} + \arctan\left(\frac{y-1}{s}\right)\right] \tag{12}$$

where $y = (z \cdot g_2^3)^{-1}$. In the case of a triangular lattice, the critical value of g_2 is 3 and the isotherm exhibits the phase transition when $g_2 > 3$ [94]. The value of s is 0.001 when $g_2 > 3$ and $(3.001 - g_2)/5$ when $g_2 < 3$. The pairwise interaction energy between the adsorbed alkanethiolate molecules, w, is related to g_2 through

$$g_2 = \exp\left(\frac{-w}{k_{\mathrm{B}}T}\right) \tag{13}$$

where k_{B} is the Boltzmann constant. One attractive point of the BH isotherm is that θ is a continuous and single-valued function of the fugacity, which readily enables the calculation of voltammograms beyond the critical value of g_2. The form of the BH isotherms is displayed in Fig. 5 for several values of g_2.

We assume that the dependence of $\overrightarrow{k'}$ and $\overleftarrow{k'}$ on the applied potential is expressed by the Butler–Volmer-type equations:

$$\overrightarrow{k'} = k_0' \exp\left[-(1-\alpha)\left(\frac{F}{RT}\right)(E - E_0')\right] \tag{14}$$

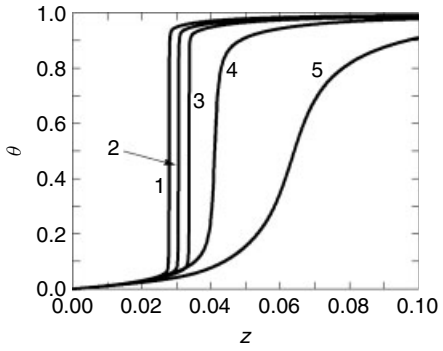


Fig. 5 The BH adsorption isotherms at the values g_2 being 3.3 (curve 1), 3.2 (curve 2), 3.1 (curve 3), 2.9 (curve 4), and 2.5 (curve 5) calculated from Eq. (9).

and

$$\overleftarrow{k'} = k_0' \exp\left[\alpha\left(\frac{F}{RT}\right)(E - E_0')\right] \quad (15)$$

where k_0' is the standard rate constant, α is the transfer coefficient, E is the electrode potential, and E_0' is the formal potential for the reduction of the adsorbed alkanethiolates at the limit of $\theta \to 0$.

After the desorption, long-chain alkanethiolates tend to form micelles or aggregates and stay on the electrode surface, while shorter-chain alkanethiolates seem to diffuse into the aqueous phase [12, 25, 71]. With the combination of Eq. (6) with the semi-infinite linear diffusion model for the mass transport of desorbed thiolates in the solution, cyclic voltammograms can be numerically calculated, for example, using a finite difference method. The dimensionless current, Φ, is defined as

$$\Phi = -\frac{i_F}{FA}\frac{1}{(DvF/RT)^{1/2}\ {}^{b}c_{Rd}} \quad (16)$$

where D is the diffusion coefficient of the alkanethiolate in solution and v is the scan rate. On the other hand, i_F is related to $d\Gamma/dt$ (Eq. 7). From Eqs. (7) and (16),

$$-\frac{i_F}{FA} = \Gamma_m \frac{L}{t_k}\Phi \times K \quad (17)$$

where L defines the number of digitization of simulated time t_k and K is a constant, which is usually set to unity in the present numerical calculation.

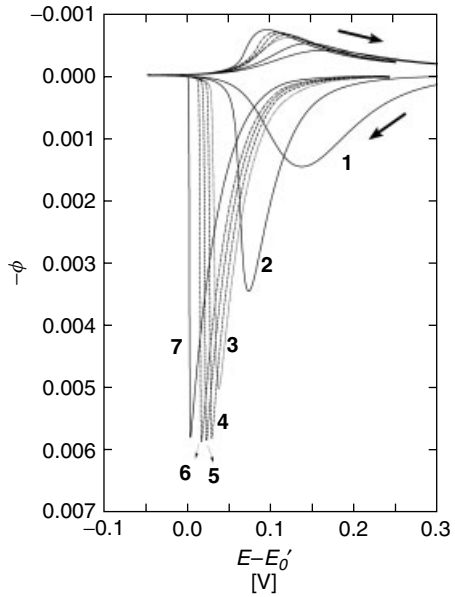


Fig. 6 Calculated voltammograms for $k_0' = 100\ s^{-1}$ at $g_2 = 1$ (curve 1), 2 (curve 2), 2.9 (curve 3), 3.1 (curve 4), 3.3 (curve 5), 3.5 (curve 6), 4.0 (curve 7). Other parameters: $k_0' = 100\ s^{-1}$, $K = 1$, and $\delta E = 0.2$ mV. (Reproduced from Ref. 70 by permission. Copyright: The American Chemical Society.)

7.5.2.1 Characteristics of Theoretical Voltammograms Based on the BH Isotherm

Figure 6 illustrates calculated voltammograms at several different values of g_2 when $E^{0\prime} = 0$, $v = RT/F\ \mathrm{s}^{-1}$, $k_0' = 100\ \mathrm{s}^{-1}$, and the increment of E, δE being 0.2 mV. With increasing g_2, the peak becomes sharper and shifts to the negative direction. The shape of the peak is asymmetric and the FWHM narrows down to 20 mV when $g_2 > 3$. A further increase in g_2 beyond the critical value does not change the FWHM, while E_p continues to shift to the negative direction of the potential. On the reverse scan, an oxidation peak appears. The peak height is much smaller than that in the forward scan. These characteristic features well agree with experimentally observed features shown in Figs. (3 and 4).

A theoretical dependence of FWHM on w obtained from the voltammograms calculated for $k = 10^5\ \mathrm{s}^{-1}$ and the increment of the potential being 0.2 mV is well fitted to the experimental plot of FWHM on n (Fig. 7a). In the fitting, it was assumed that the point of the inflection at $-w/k_\mathrm{b}T = 1.10$ ($g_2 = 3$) in the theoretical FWHM versus w plot agreed with the point of the inflection experimentally observed at $n = 9$ (Fig. 4a) and that the theoretical variation of FMHM with w when $-w/k_\mathrm{b}T < 1.10$ was fitted to the experimental points. Figure 7(a) indicates that the interaction energy between adsorbed alkanethiolates is roughly proportional to n.

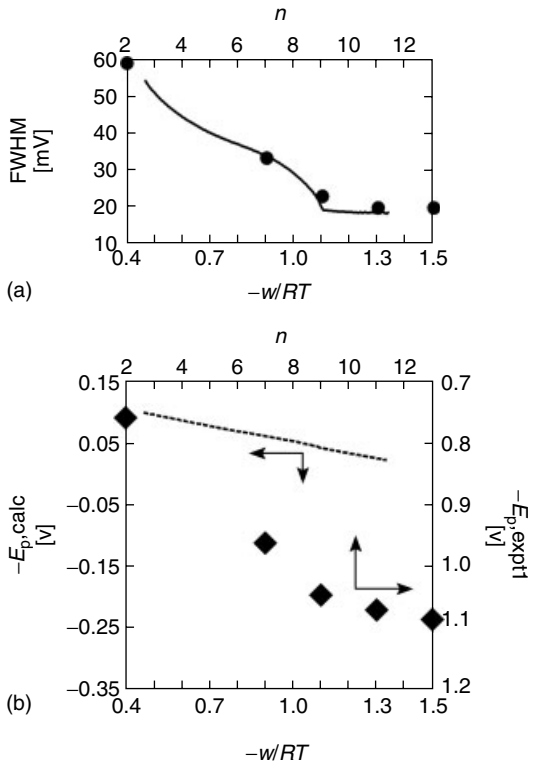


Fig. 7 Fitting of calculated FWHM (dashed line) to experimental points (a) and the comparison of theoretical prediction of the shift of E_p (- - - -) with experimental data (b). Parameters for calculation: $k_0' = 10^4\ \mathrm{s}^{-1}$, $K = 1$, and $\delta E = 0.2$ mV. (Reproduced from Ref. 70 by permission. Copyright: The American Chemical Society.)

Another important point in Fig. 6(a) is that the present model explains why the FWHM levels off beyond $n = 9$. When the attractive interaction is strong enough to cause the phase transition in the adsorbed monolayer, the shape of the adsorption isotherm, or more precisely, the sharpness of the phase transition becomes insensitive to the value of g_2 when $g_2 > 3$ (curves 1–3, Fig. 5) [95]. In other words, the appearance of the point of inflection suggests the occurrence of the phase transition in the course of the desorption. The critical value of w at the point of inflection corresponds to 2.7 kJ mol^{-1} at 25 °C. This value reflects not only the magnitude of the lateral interaction between two adsorbed thiolate molecules but also other contributions including those from solvent molecules [95].

By using the phenomenological correspondence between w and n in Fig. 7(a), the theoretical dependence of E_p on w is compared in Fig. 6(b) with experimental E_p versus n plot (Fig. 4b). The comparison of experimental data for well-annealed SAMs with the theoretical curve in Fig. 7(b) indicates that the experimental shift in E_p is much greater than the theoretical prediction. For example, the theoretical prediction of the difference in E_p between $n = 2$ and 9 is 0.05 V, while the experimental difference is about 0.28 V. This discrepancy indicates the importance of the work to dissolve alkanethiolates in the solution in determining the position of the reduction peak [72]. If the contribution of the methylene units to the adsorption Gibbs energy of the thiolates is taken to be the difference between experimental and theoretical values of E_p at $n = 9$, 0.243 V or 23.4 kJ mol^{-1}, the contribution of one methylene unit is 2.6 kJ mol^{-1}. This is comparable to the values of the transfer Gibbs energy of one methylene unit from water to a pure alkane (3.7 kJ mol^{-1}) or to a nonionic micelle (2.9 kJ mol^{-1}) [96].

A lesser degree of the variation of E_p with n when $n > 9$ (Fig. 4b), where the desorption accompanies the phase transition of the monolayer, is likely to be attributable to the formation of micelles or aggregates of alkanethiolates formed in the vicinity of the electrode surface after the desorption [12, 25, 71]. When the desorbed species is in the form of such aggregates on the electrode surface, the value of the transfer Gibbs energy of the thiolates from the electrode surface to the aggregates would be much smaller than that into the bulk aqueous phase, giving rise to the smaller shift of the E_p with n.

The effect of the magnitude of $k_0{}'$ on E_p is illustrated in Fig. 8. Curves 5 and 6 calculated for $k_0' = 10^3$ and 10^4 s^{-1}, respectively, agree with each other, showing the reversible behavior. A comparison of experimental values of FWHM with the results in Fig. 8 suggests that the reductive desorption is dc reversible at $v = 20$ mV s^{-1}. This figure can also be interpreted as the one showing the effect of the magnitude of v on the voltammograms, as the rate constant used in the calculation is relativized with respect to $\sqrt{v}$. The E_p shifts to the negative direction with increasing v, as experimentally seen (Fig. 2b). Figure 8 also shows that the oxidation peak shifts to the negative direction with the increase in k_0', that is, the peak separation narrows with $k_0{}'$.

7.5.2.2 Contribution of Charging Current

The peak area of the reductive desorption has conveniently been used to estimate the adsorbed amount of alkanethiolates [2, 4, 5, 8, 16, 32]. However, the charge under the peak usually exceeds the value estimated

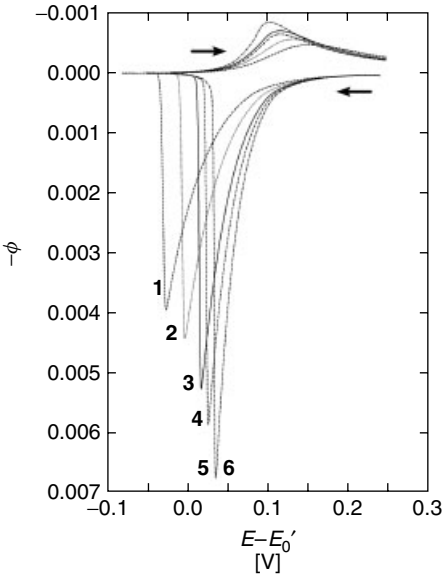


Fig. 8 Variation of voltammograms with the value of k_0': $k_0'(s^{-1}) = 10$ (curve 1), 20 (curve 2), 50 (curve 3), 10^2 (curve 4), 10^3 (curve 5), 10^4 (curve 6). Other parameters: $g_2 = 3.1$, $K = 1$, and $\delta E = 0.2$ mV. (Reproduced from Ref. 70 by permission. Copyright: The American Chemical Society.)

from the $(\sqrt{3} \times \sqrt{3})R30^\circ$ structure of adsorbed thiolates. The degree of the excess varies from 10 to 50%, the latter of which found in the present study is far greater than that predicted by the surface roughness, 1.1 ~ 1.2 [3, 97, 98].

To estimate the magnitude of the charging current in the course of the desorption, a certain functional form that relates θ with the surface charge density, q, is required. The charging current, i_c, is then calculated by differentiating q with respect to t,

$$-i_c = \frac{dq}{dt} = \frac{v\,dq}{dE} \tag{18}$$

The negative sign on the left-hand side is for the conformity with the convention of the faradaic current described earlier. One of the simplest models for q is the Frumkin's two-parallel-plate capacitor model [99], which has been successfully employed to describe the adsorption of organic molecules on electrodes [100],

$$q = q_0(1-\theta) + q'\theta \tag{19}$$

where q_0 is the surface charge density of the uncovered part of the electrode and q' is that covered with the SAM. By differentiating q with respect to E, we obtain

$$\frac{dq}{dE} = C_0(1-\theta) + C'\theta + \left[(C'-C_0)\phi - C'\phi_N\right]\frac{d\theta}{dE} \tag{20}$$

where C_0 and C' are the double-layer capacitances at $\theta = 0$ and $\theta = 1$, respectively, and are assumed to be independent of the applied potential. The potential in Eq. (21), ϕ, is referred to as the potential of zero charge, pzc, at $\theta = 0$, that is,

$$\phi = E - E_{pzc,\theta=0} \tag{21}$$

and

$$\phi_N = E_{pzc,\theta=1} - E_{pzc,\theta=0} \tag{22}$$

where $E_{pzc,\theta=1}$ is the pzc at $\theta = 1$ referred to as the same reference electrode as $E_{pzc,\theta=0}$ refers to.

The first two terms on the right-hand side of Eq. (21) represent the static part of the charging current, reflecting the change in the double-layer capacitance before and after the desorption, whereas the third term represents the dynamic part or pseudocapacitance part involving $d\theta/dE$. In the Frumkin's two-parallel-plate capacitor model, i_c is then given simply by

the sum of the two terms:

$$i_c = i_{c,static} + i_{c,dynamic} \qquad (23)$$

The presence of the dynamic term implies that the magnitude of this contribution depends on the sharpness of the desorption. To evaluate the latter contribution to i_c, a functional form of $d\theta/dE$ is required as a function of E. In fact, $i_{c,dynamic}$ is proportional to i_F, as can be seen from Eqs. (8) and (21). We used the calculated $d\theta/dE$ predicted by the model described earlier when $k_0 = 10^4$ cm s^{-1}, $g = 3.1$ and $\Gamma_m = 7.67 \times 10^{-10}$ mol dm^{-2}, and $v = 25.6926$ mV s^{-1}. Experimentally, it is not possible to separately estimate i_F and i_c by changing v in linear-scan voltammetry, as $d\theta/dE$ does not depend on v, when $k_0{}'$ is sufficiently large (curves 5 and 6 in Fig. 8), and, from a practical viewpoint, a faster scan of the potential would invalidate the present approach resorting to the adsorption isotherm.

The pzc of Au(111) in 0.1 mol dm^{-3} $HClO_4$ is 0.42 V (vs. Ag|AgCl|satd. KCl) [101]. Although OH^- ions specifically adsorb on Au(111) [102] in an alkaline solution commonly used for the reductive desorption studies, it is presumably negligible in the potential range where the reductive desorption takes place. It is then reasonable to assume that $E_{pzc,\theta=1} = 0.42$ V (vs. Ag|AgCl|satd. KCl). For a value of $E_{pzc,\theta=1}$, a good estimate is -0.49 V (vs. Ag|AgCl|satd. KCl), which was obtained from the potential-dependent contact angle measurements of a UT SAM on Au(111) [103], and agrees with an earlier estimate reported using a Wilhelmy method, -0.5 V (vs. SCE) for a dodecanethiol SAM [104].

It is difficult to have a reliable value of E_0' for the reductive desorption of an alkanethiolate. A plausible assumption would be to use a value of $E_0{}'$ for S atoms adsorbed on Au(111) estimated from the extrapolation of E_p at $v = 0$ to $n = -1$, -0.64 V (vs. satd. KCl|AgCl|Ag) [105], although, strictly speaking, E_0' to be used in the calculation is the value for the formal potential of the reduction of an isolated alkanethiol molecule adsorbed on Au(111), which is probably more negative than the value for the reduction of adsorbed S atoms. Assuming that $E_0' = -0.64$ V, $C_0 = 40$ [56], and $C' = 2$ μF cm^{-2} [1], the charging current was calculated (Fig. 9).

The contribution of i_c to the area under the peak is substantial. In this example, one can see from Fig. 9 that the charge due to the charging current amounts to 42 μC cm^{-2}, that is, one-third of the total charge of 116 μC cm^{-2} that was experimentally obtained. This charging current can well explain experimental values, $1.1 \sim 1.2 \times 10^{-9}$ mol cm^{-2}, for the adsorbed amount of thiolates formally obtained from the peak area for well-annealed SAMs of alkanethiols on Au(111)-rich surfaces [8, 29, 43]. The contribution of the dynamic part is much larger than the static one, as shown in the inset of Fig. 9. The dynamic part of the charging current explains why the area under the peak often gives the charge that is significantly greater than that expected from a close-packed monolayer and the roughness factor.

The BH isotherm can explain, at least semiquantitatively, the salient features of voltammograms of the reductive desorption, that is, the asymmetric shape, a narrow value of the FWHM, the dependence of the FWHM on n, the leveling off of the FWHM at larger n, and the dependence of the FWHM and E_p on the scan rate of linear-scan voltammetry. It also provides a reasonable dependence of θ on E, which is decisive in evaluating the contribution of the charging current to

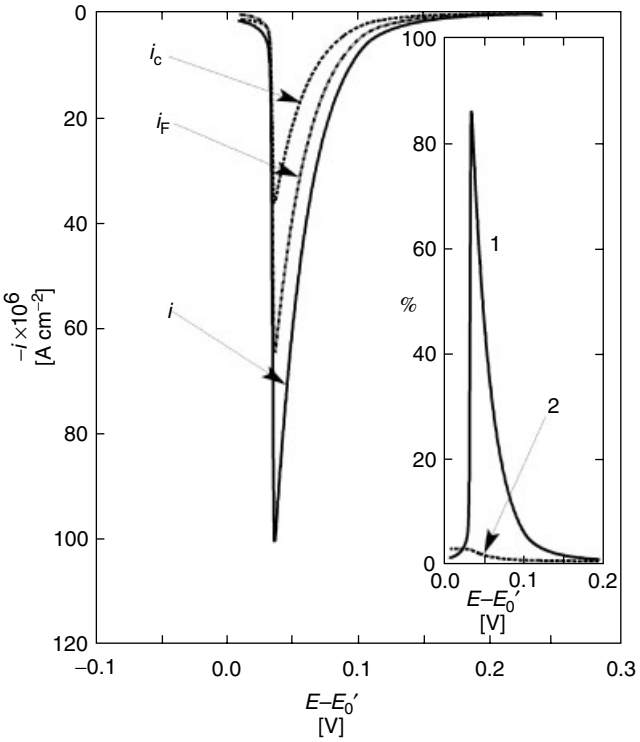


Fig. 9 Illustration of the contribution of charging current, i_c, to the voltammetric peak current of reductive desorption, i. Parameters for calculating i_F are the same as in Fig. 8. See text for other parameters. Inset illustrates the relative contribution of $i_{c,dynamic}$ (curve 1) and $i_{c,static}$ (curve 2). (Reproduced from Ref. 70 by permission. Copyright: The American Chemical Society.)

the peak area of the reductive desorption. More elaborate models are to be developed to have a better insight for the cases that are beyond the framework of the BH model, as in certain cases of the reductive desorption, voltammograms show even narrower FWHM, for example, those for SAMs of ω-carboxyl alkanethiolates [14].

7.5.3 Reductive Desorption of Binary SAMs

7.5.3.1 Miscibility

Voltammetry can sensitively detect the mixing state of binary SAMs. When two different thiol species are coadsorbed, they are either phase-separated to form discrete domains or mix with each other on the metal surface depending on the degree of the lateral interactions between the adsorbed thiolates. The two species A and B form a homogeneously mixed monolayer when the lateral interaction energy between the like pair, A–A and B–B, is similar in magnitude to that of the A–B pair. A typical example of this type is shown in Fig. 10(a) for the reductive desorption of SAMs composed of UT and 11-mercaptoundecanoic acid (MUA). The single cathodic peak on

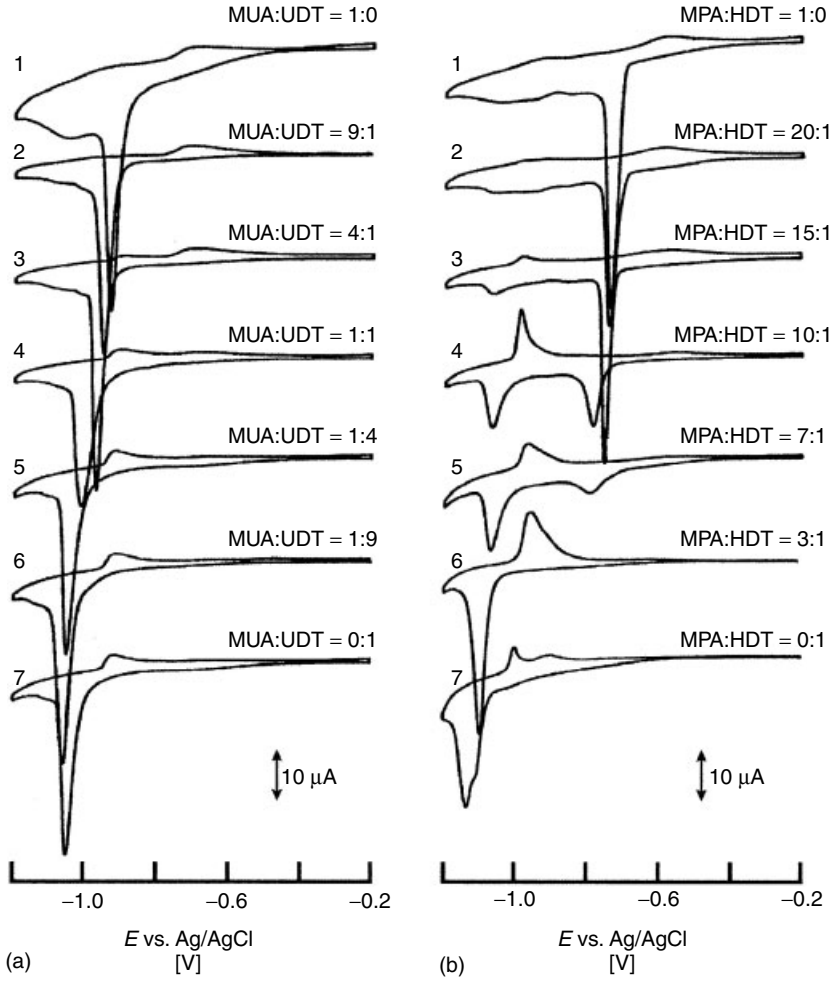


Fig. 10 (a) Cyclic voltammograms for the reductive desorption of UDT–MUA mixed monolayers prepared at different ratios of MUA : UDT in ethanol; 1 : 0 (curve 1), 9 : 1 (curve 2), 4 : 1 (curve 3), 1 : 1 (curve 4), 1 : 4 (curve 5), 1 : 9 (curve 6), and 0 : 1 (curve 7). (b) Cyclic voltammograms for the reductive desorption of HDT–MPA mixed monolayers prepared at different ratios of MUA : UDT in ethanol; 1 : 0 (curve 1), 20 : 1 (curve 2), 15 : 1 (curve 3), 10 : 1 (curve 4), 7 : 1 (curve 5), 3 : 1 (curve 6), and 0 : 1 (curve 7). Scan rate: 20 mV s^{-1} (Reproduced from Ref. 43 by permission. Copyright: The American Chemical Society.)

the voltammogram shifts from −0.91 to −1.06 V by increasing ratio of the UT on the surface, which was estimated from the XPS signal from O 1s (Fig. 11). The parallelism between E_p and the XPS signal in Fig. 11 indicates that the shift in E_p reflects the change in the surface composition. The homogeneous mixing of MUA and UT has been confirmed by STM imaging of the SAMs, which show

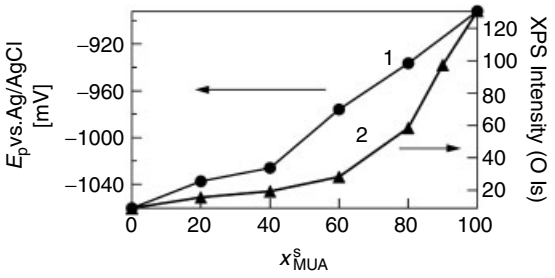


Fig. 11 Peak potential of CVs and the peak area of oxygen 1s XPS spectra for the mixed monolayer of MUA and UDT as a function of the ratio of MUA in ethanol when preparing the mixed monolayers. (Reproduced from Ref. 43 by permission. Copyright: The American Chemical Society.)

no sizable domains of MUA nor those of UT. The shift of E_p has been used as a convenient measure for estimating the degree of the surface composition of the two thiolate species [13, 21, 22, 24].

In contrast, in the case of the binary SAM of MPA and HDT, two peaks appear in the voltammograms at the positions near the E_ps for single-component SAMs of MPA and HDT, respectively (Fig. 10b). The appearance of the two distinct peaks manifests the presence of the phase-separated two domains in the SAM. This phase separation forming nanometer-scale domains can be directly seen in the STM images of the SAM [17, 42]. This binary SAM is a typical example of the case when the interaction between A–A or B–B pairs is stronger than that of A–B pairs.

A useful criterion for the phase behavior of binary SAMs of alkanethiolate derivatives is the difference between the peak potentials, ΔE_p, for the reduction of corresponding single-component SAMs. Table 1 summarizes the values of ΔE_p and the miscibility of several pairs of an ω-carboxyl alkanethiolate and an alkanethiolate on Au(111). For the phase separation of the SAMs at room temperature, a value of ΔE_p greater than 20 mV is required.

Another interesting type of binary SAMs is the one formed when the intermolecular interaction between A–B pairs is much stronger than those of the like pairs. In this case, A and B preferentially mix with each other, resulting in the SAMs of 1 : 1 ratio of the adsorbed A and B on the surface over the wide range of the mixing ratio of A and B in the solution phase. A typical example of this case is the SAM composed of 2-aminoethanethiol (AET) and 2-mercaptoethanesulfonic acid (MESA). The SAMs show a single reduction peak with a narrow FWHM of about 20 mV and the E_p little depends on

Tab. 1 Phase behavior of the binary SAMs of alkanethiolates and ω-carboxyl alkanethiolates on Au(111)

Thiols	*ΔE_p[V*]*	*Phase***
MPA/HDT	0.44	D
MPA/UT	0.41	D
MPA/HT	0.25	D
MPA/PT	0.12	S
MUA/HDT	0.25	D
MUA/DDT	0.21	D
MUA/UT	0.19	S
MUA/DT	0.16	S
MDA/DT	0.18	S
MDDA/HDT	0.21	D

*Scan rate: 20 mV s^{-1}. **D and S indicate the appearance of double peaks and a single peak, respectively, in voltammograms of the reductive desorption. MPA: mercaptopropionic acid; HDT: hexadecanethiol; UT: undecanethiol; HT: hexanethiol; PT: propanethiol; MUA: mercaptoundecanoic acid; MDA; mercaptodecanoic acid; MDDA: mercaptododecanoic acid.

the solution composition, suggesting the equimolar mixing of AET and MESA on the surface [106].

7.5.3.2 Minimum Size of the Domains that can be Recognized as an Independent Domain

Even when only a single peak appears on a voltammogram, STM images often show clusters of molecules that appear to consist of several like molecules [43, 107]. On the other hand, in many of the voltammograms for the reductive desorption of phase-separated SAMs, a small hump is discerned [17, 40]. Figure 12 shows cyclic voltammograms for the binary SAM of 1-tetradecanethiol (TDT) and 3-mercapto-1-propanol (MPOH) prepared at three different total concentrations of TDT and MPOH, 1×10^{-6} (curve a), 1×10^{-4} (curve b), and 1×10^{-2} (curve c) mol dm^{-3} in ethanol. A hump appears between the two major reduction peaks that are ascribed to the desorption of MPOH-rich and TDT-rich domains [40]. The presence of this hump and the small clustering of like molecules in STM images taken for the SAMs that give only a single reduction peak suggest that a certain minimum domain size is required for a distinct peak to emerge on the voltammogram, that is, to be an independent two-dimensional bulk phase.

From a detailed comparison of the peak areas and the STM images, the minimum size of the domain that behaves as a two-dimensional bulk phase is about 15 nm^2 or 50 thiolate molecules in the case of binary SAM of HDT and MPA [17]. A domain that consists of less than 50 molecules has a desorption potential in the middle of the two peaks corresponding to the desorption of phase-separated two types of domains.

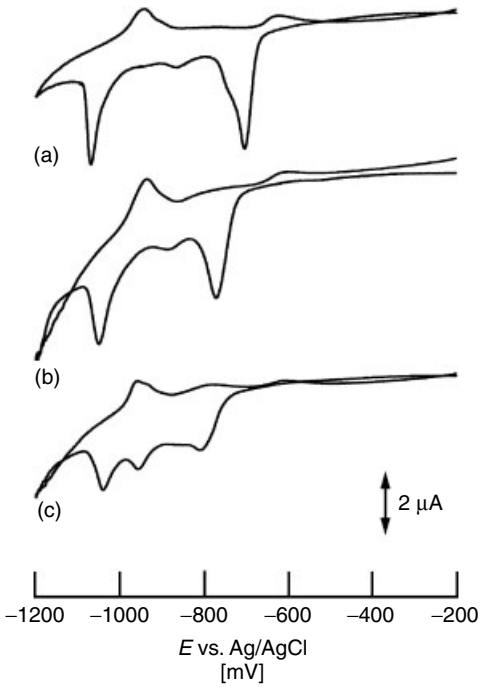


Fig. 12 Cyclic voltammograms for the reductive desorption of binary SAMs composed of MPOH and TDT. The SAMs were formed from solutions whose total thiol concentrations were (a) 10^{-6} mol dm^{-3}, (b) 10^{-4} mol dm^{-3}, and (c) 10^{-2} mol dm^{-3}. The ratios of MPOH and TDT in the solutions were (a) 1 : 1, (b) 3 : 1, and (c) 7 : 1, respectively. (Reproduced from Ref. 40 by permission. Copyright: Elsevier B.V.)

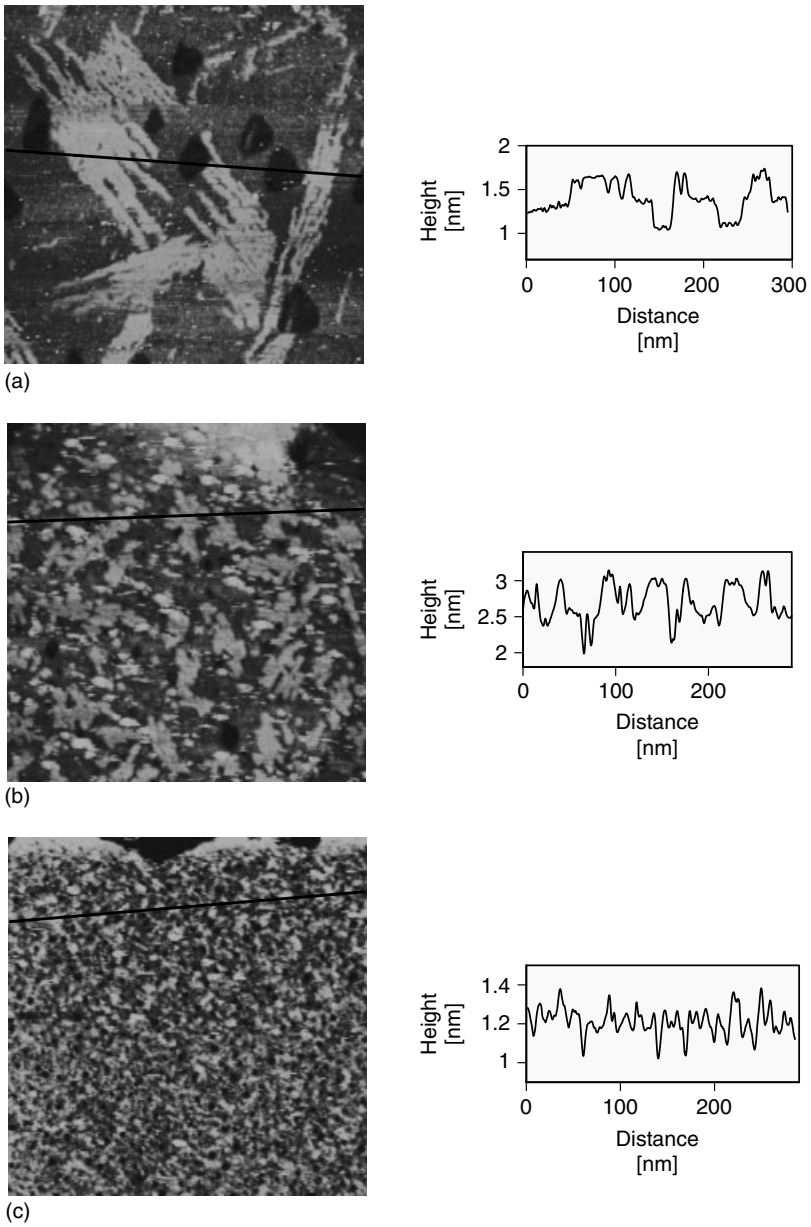


Fig. 13 STM images of binary SAMs of TDT and MPOH formed from (1) 1×10^{-6} mol dm^{-3}, (b) 1×10^{-4} mol dm^{-3}, and (c) 1×10^{-2} mol dm^{-3} total concentrations of TDT and MPOH. The ratio of TDT and MPOH at the surface was about 1 to 1 for all SAMs. The brighter parts in the images correspond to higher points. Scan area: 300 nm × 300 nm. (Reproduced from Ref. 40 by permission. Copyright: Elsevier B.V.)

The size of the domains depend on the thiol concentration in the bathing ethanol solution in preparing the SAMs (Fig. 13) [40]. The lower the concentration, the greater is the domain size. The hump becomes smaller at the lower concentrations (Fig. 12). This concentration dependence is similar to the effect of the rate of cooling of the solution on the crystal size in the crystallization of a solute from the solution phase.

7.5.3.3 Mutual Solubility of the Thiolates

The phase separation of thiol SAMs observed experimentally is in quasi-equilibrium in nature. Unlike the phase separation of binary solutions, the mutual solubility of the adsorbed thiolates depends on the composition, $\chi_A^{surf} = \Gamma_A/(\Gamma_A + \Gamma_B)$, where Γ_i is the adsorbed amount $i (i = A \text{ or } B)$. The fact that the peak potential for the desorption of the phase-separated domains varies with χ_{MPOH}^{surf} (Fig. 14) can only be understood by the substantial mutual solubility. This is shown in Fig. 14 for the case of SAMs of TDT and MPOH at three total concentrations of TDT and MPOH in ethanol. The variation of the mutual solubility with χ_{MPOH}^{surf} is probably due to the slow surface diffusion of adsorbed thiolates. The slope of χ_{MPOH}^{surf} for the desorption of MPOH-rich domains increases with the increase in the total concentration of the thiols in the bathing solution; the smaller the domain, the larger the slope is. The slope and its concentration dependence are much smaller for the reduction of TDT-rich domains.

In analogy with the desorption of homogeneously mixed SAMs, the magnitude of the shift in E_p can be taken as a measure of the solubility of the minor component in the domain mainly composed of the other component. By extrapolating the straight lines to $\chi_{MPOH}^{surf} = 0$ for the reduction of MPOH-rich domains and $\chi_{MPOH}^{surf} = 1$ for the reduction of TDT-rich domains, the maximum solubility of TDT in MPOH-rich domains is 8 mol% and that of MOPH in TDT-rich domains is 8.5 mol% when the total thiol concentration used for preparing the substrate was

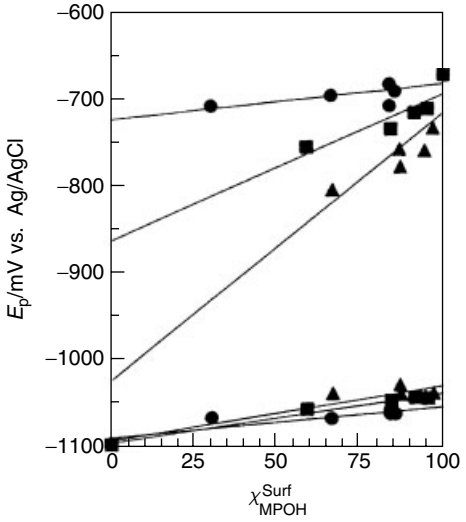


Fig. 14 Dependence of peak potentials of the reductive desorption on the surface composition of binary SAMs of TDT and MPOH. The SAMs were formed from solutions whose total thiol concentrations were 10^{-6} mol dm^{-3} (●), 10^{-4} mol dm^{-3} (■), and 10^{-2} mol dm^{-3} (▲). (Reproduced from Ref. 40 by permission. Copyright: Elsevier B.V.)

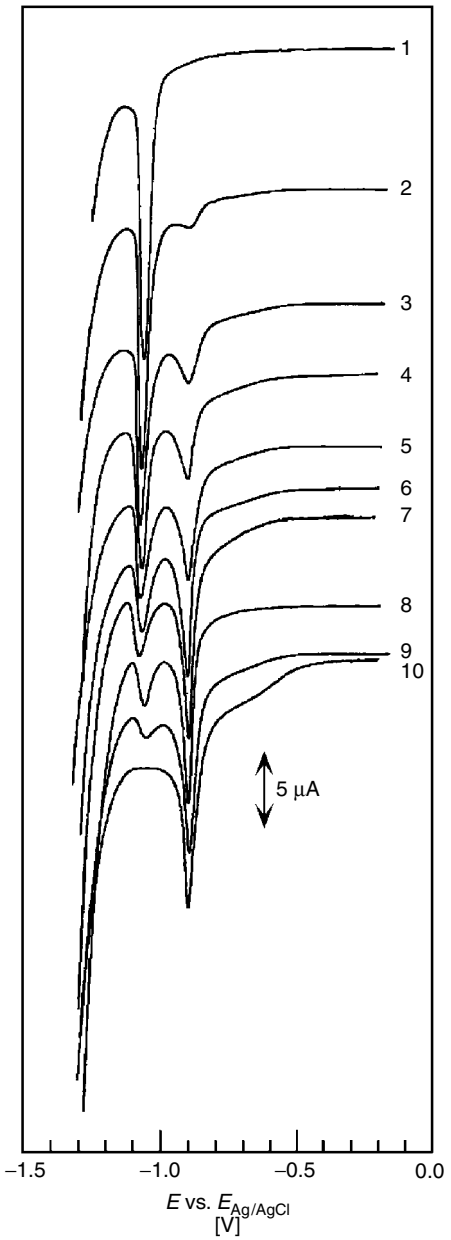


Fig. 15 Cyclic voltammograms for reductive desorption of HDT self-assembled monolayers after immersion in 1 mmol dm^{-3} MDDA ethanol solution at 31 °C. Time of immersion: 0 (curve 1), 24 (curve 2), 48 (curve 3), 72 (curve 4), 96 (curve 5), 124 (curve 6), 144 (curve 7), 168 (curve 8), 219 (curve 9), and 336 (curve 10) h. (Reproduced from Ref. 29 by permission. Copyright: The American Chemical Society.)

1 μmol dm^{-3}. The mutual solubility also depends on the concentration of thiols in the bathing solution. The solubility is smaller in the SAMs formed from 1×10^{-6} mol dm^{-3} than those formed from 1×10^{-2} mol dm^{-3} (Fig. 14).

7.5.3.4 Rate of the Replacement of Adsorbed Thiolates with Thiols in the Solution Phase

When a metal substrate covered with a thiol SAM is soaked in a thiol solution, the adsorbed thiolates are replaced with the thiol in the solution phase [108–110]. CV of the reductive desorption is a useful means to detect the replacement reaction. Figure 15 shows a series of voltammograms for the HDT SAM-covered substrates after immersion in an ethanol solution containing 1 mmol dm^{-3} 12-mercaptododecanoic acid (MDDA) in a different period of time at 31 °C [29]. The peak corresponding to the desorption of the HDT domain gradually decreases with the concomitant increase of the peak height corresponding to the desorption of MDDA. After 336 h, the HDT peak was not detected at all, showing the completion of the replacement. From the variation of the two peak heights, the rate constant for a pseudo-first-order desorption reaction is evaluated to be 9.1×10^{-3} h^{-1}. This small rate constant is probably because of the tightness of the HDT SAMs [29].

Interestingly, the replacement takes place not in a random manner but with the formation of new MDDA domains, which grow with time. The positions of the two

peaks changed little in the course of the replacement. This suggests that the adsorbed thiolates at the domain boundaries are more readily replaced owing probably to the less ordered structure of UT molecules at the domain edge. The formation of sizable domains in the replacement process has been confirmed by STM imaging of the substrates [29].

The CV of the reductive desorption also revealed that the reverse process, the replacement of MDDA on Au(111) with HDT, is much slower. The stronger resistance of MDDA SAMs against the replacement has been attributed to the hydrophilic environment of the MDDA surface, possibly including the hydrogen bonding between carboxyl groups [29].

7.5.3.5 Rate of the Surface Chemical Reactions

Any processes that can lead to the formation or disappearance of phase-separated or homogeneously mixed binary SAMs can be monitored through the change in the desorption peak in voltammograms. Figure 16 shows an example of detecting the rate of a surface chemical reaction using the shift in E_p. When isocyanic acid *n*-butyl ester in toluene reacted with MPOH SAMs on the surface in the presence of trimethylamine, the product, [*N*-butylcarbamoyl]ethylthiolate, is gradually formed, as seen in the negative shift in E_p with time. The deviation from the theoretical curve for the first-order surface reaction (solid line in Fig. 16) suggests the autoinhibition, that is, the hindrance of the reactant to approach unreacted sites by the products on the surface [111].

7.5.4 Electrochemical Engineering of Binary SAMs

7.5.4.1 Partial Desorption and Insertion

Of the two types of domains in a phase-separated binary SAM, the domains having less negative desorption potential can be selectively removed from the surface by holding the electrode potential at a value between the two reduction potentials.

Figure 17 shows voltammograms of phase-separated HDT–MPA binary SAM before the selective desorption (a), after the selective desorption of the MPA-rich domains (b), and after the immersion of selectively removed substrate into an ethanol solution of MPA (c) [56]. It is possible to introduce different thiol molecules

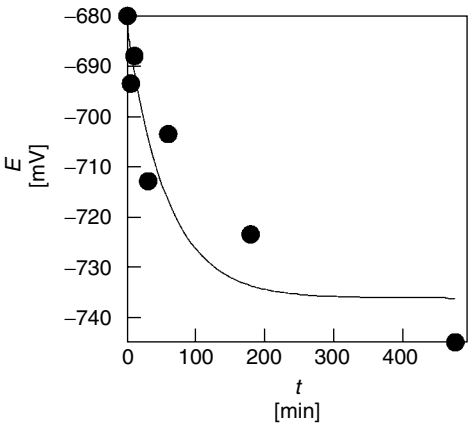


Fig. 16 Reaction-time dependence of the peak potential for the reductive desorption of SAMs. Toluene solutions containing 1 mol dm^{-3} isocyanic acid *n*-butyl ester and 0.2 mol dm^{-3} triethylamine were reacted with MPOH SAMs on Au(111) at room temperature. (Reproduced from Ref. 111 by permission. Copyright: The Japan Society for Analytical Chemistry.)

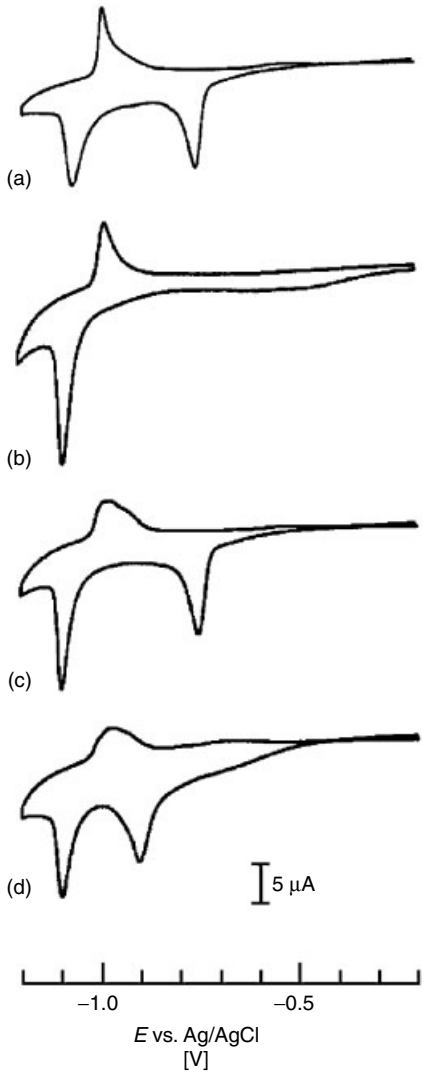


Fig. 17 Cyclic voltammograms for the reductive desorption of various SAMs in 0.5 M KOH solution: (a) original phase-separated binary SAM of MPA and HDT where the surface mole fraction of MPA is 0.49; (b) SAM after the selective desorption of MPA; (c) regenerated binary SAM of MPA and HDT; (d) binary SAM of MUA and HDT after the selective replacement of MPA with MUA. Initial potential, −0.2 V; scan rate, 20 mV s^{-1}; electrode area, 0.5 cm^2. (Reproduced from Ref. 56 by permission. Copyright: The American Chemical Society.)

into the domains originally occupied with MPA. Mercaptoheptanoic acid (a), MUA (b), heptanethiol (c), and mercaptohexanol (d) (Figs. 17 and 18) can be introduced into the vacant domains. Trace (e) is the voltammogram on the second scan of the voltage for the substrate with the SAM of HDT and mercaptoheptanoic acid.

STM imaging confirmed the completion of the replacement [59]. After the desorption, however, the gold surface was not exposed to the solution, but thiol molecules adjacent to the desorbed region entirely covered the surface, lying flat on the surface previously occupied by MPA molecules. From the peak areas in the voltammograms before and after the replacement, it seems that these weakly adsorbed molecules are replaced or pushed aside by the third component newly adsorbed from the solution side.

Several variants of the selective desorption technique has been reported for preparing nanopores in an SAM [60], oligonucleotide attachment and DNA hybridization [62], selective immobilization of enzymes [63, 112], controlled release of biological cells [65], and trace analysis [64, 113, 114].

7.5.4.2 Preparation and Use of Artificially Phase-separated Binary SAMs

By using this selective replacement technique, artificially phase-separated SAMs can be prepared. For example, MUA and UT form a homogeneously mixed SAM when they are made to be coadsorbed from a bathing solution. MPA domains of phase-separated UT–MPA SAM can

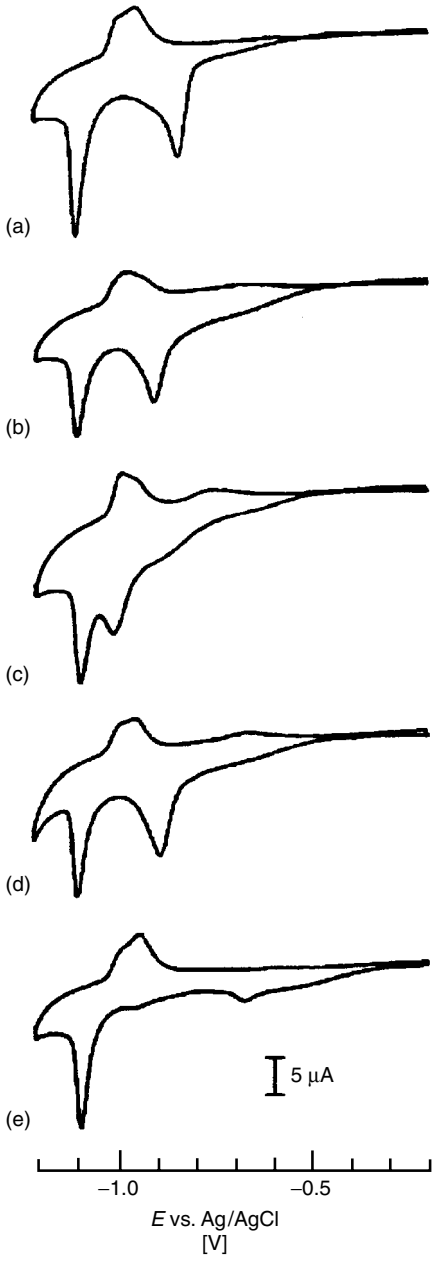


Fig. 18 Cyclic voltammograms for the reductive desorption of various SAMs composed of HDT and (a) 7-mercaptoheptanoic acid (first scan); (b) 11-mercaptoundecanoic acid (first scan); (c) 1-heptanethiol (first scan); (d) 6-mercapto-1-hexanol; (e) 7-mercaptoheptanoic acid (second scan). Other conditions are the same as those in Fig. 17. (Reproduced from Ref. 56 by permission. Copyright: The American Chemical Society.)

be first electrochemically removed and are succeedingly filled with MUA to form a phase-separated UT–MUA SAM. These artificially phase-separated monolayers are useful for studying certain surface properties of SAMs, which are difficult to prepare by the coadsorption method. Following are two examples of the use of such artificially phase-separated SAMs.

7.5.4.2.1 **Wetting** The mixing state of two adsorbed species on the surface can affect the wetting properties of the surface. A well-known relationship between the contact angle of a surface composed of two different components and those of two neat constituents, the Cassie's equation, predicts the linear relationship between the cosine of the contact angle of the two-component surface and the cosines of the contact angles of the neat surfaces. The wetting of the homogeneously mixed SAM of UT and MUA follows Cassie's equation (Fig. 19) [57]. However, the phase-separated SAM of MPA and HDT shows a significant deviation from the linear relationship as shown in Fig. 19. The surface is hydrophobic even when the surface ratio of MUA is higher than 0.5.

To examine the effect of the domain size, the contact angle was measured for the artificially phase-separated SAMs of MUA and UT that were prepared by the electrochemical partial desorption and

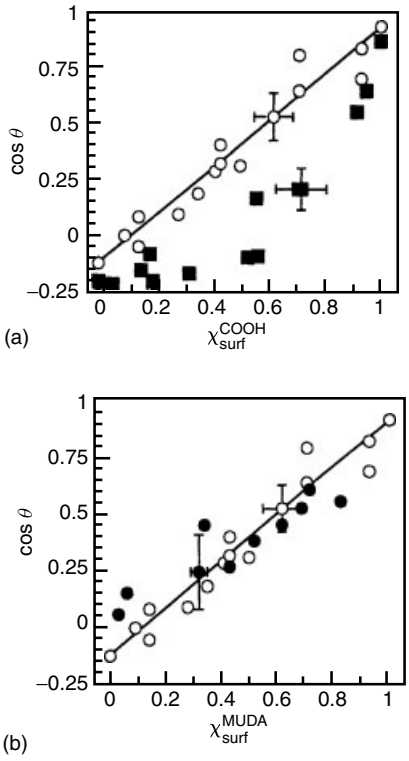


Fig. 19 Advancing contact angle of water, $\cos\theta$, plotted against the mole fraction of MUA, χ_{surf}^{MUA}, for (a) phase-separated binary SAMs of HDT and MPA (■) and homogeneously mixed binary SAMs of UDT and MUA (○); (b) homogeneously mixed (○) and phase-separated (●) binary SAMs of UDT and MUA. The solid line represents the prediction from the Cassie equation. (Reproduced from Ref. 57 by permission. Copyright: The American Chemical Society.)

the refilling technique. The results in Fig. 19(b) indicate that the contact angle of the artificially phase-separated SAM follows Cassie's equation, suggesting that the deviation is not ascribed to the domain size but to other factors such as the difference in the height between the HDT domains and the MPA domains.

7.5.4.2.2 **Surface Diffusion** Figure 20 shows cyclic voltammograms for the reductive desorption of the phase-separated binary SAMs of UT and MUA as a function of the annealing time at 60 °C in water. Before annealing, two peaks appear at −0.91 V (peak I) and −1.03 V (peak II). These two peaks correspond to the desorption of UT-rich domains and MUA-rich domains, respectively (curve a in Fig. 20) [61]. After 186 h, peak II remained at −1.03 V but its area decreased (curve b), whereas peak I at −0.91 V shifted to −0.96 V. After 212 h in water, peak I grew further and concomitantly peak II became smaller (curve c). Finally, the two peaks merged into a single peak at −1.01 V after 355 h (curve d). This time dependence of the shape of the voltammogram apparently reflects the surface mixing of initially phase-separated UT and MUA into a thermodynamically stable, homogeneously mixed SAM. The average diffusion coefficient is on the order of 10^{-18} cm^2 s^{-1} at 60 °C. This is one order of magnitude smaller than the value, 10^{-17} cm^2 s^{-1}, for a mixed SAM of HDT 16-metoxy-1-hexadecanethiol on gold deduced from the coalescence of the domains [115] and the $1 \sim 4 \times 10^{-17}$ cm^2 s^{-1} determined from the coalescence of holes of 1-dodecanethiol at 90 °C [116].

7.5.5 Conclusions

Voltammetry of the reductive desorption of thiol SAMs from a metal surface is a simple and versatile method of detecting the state of the monolayer at the molecular level. It is an invasive technique, that is, it destroys a SAM after the measurement. However, a

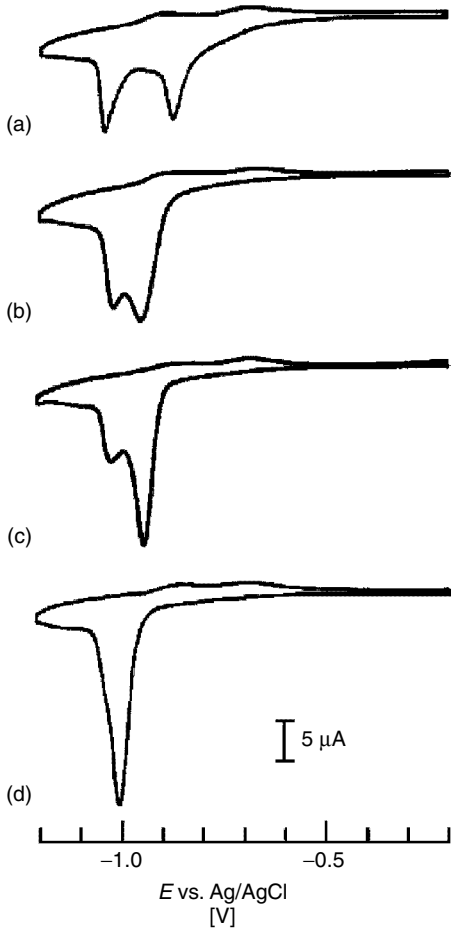


Fig. 20 Cyclic voltammograms for the reductive desorption of artificially prepared phase-separated binary SAMs of UDT and MUDA measured at 20 mV s^{-1} in 0.5 M KOH solution. SAM-adsorbed gold substrate was annealed at 60 °C in pure water for 0 h (a), 186 h (b), 212 h (c), and 355 h (d). Surface mole fraction of UDT is ca. 0.5. Initial potential, −0.2 V; electrode area, 0.5 cm^2. (Reproduced from Ref. 61 by permission. Copyright: The American Chemical Society.)

few applications of the technique described earlier exemplify the usefulness of this technique as a handy tool for diagnosing the state of SAMs. The model of the electrochemical reductive desorption based on the BH isotherm concludes, however, that care must be exercised in the use of this convenient technique for obtaining quantitative information about the SAMs, such as the adsorbed amount of thiolates. Further theoretical developments of the reductive desorption process of SAMs, including multicomponent SAMs, will widen the applicability of this method. While microscopic pictures of the SAMs can be obtained at a molecular or atomic level using a variety of surface-specific techniques, the voltammetry of the reductive desorption grasps the macroscopic properties of the SAM. This fact situates the SAMs in a unique position among systems that prompt us to study the correspondence between macroscopic behavior and the molecular details. The control of the state of SAM-covered metal substrates through the external control of the electrode potential provides us a means of manipulating and engineering the nanoscale domains.

References

1. C. A. Widrig, C. Chung, M. D. Porter, *J. Electroanal. Chem.* **1991**, *310*, 335–359.
2. M. M. Walczak, D. D. Popenoe, R. S. Deinhammer et al., *Langmuir* **1991**, *7*, 2687–2693.
3. D. Weisshaar, M. M. Walczak, M. D. Porter, *Langmuir* **1993**, *9*, 323–329.
4. M. T. Rojas, R. Königer, J. F. Stoddart et al., *J. Am. Chem. Soc.* **1995**, *117*, 336–343.
5. W. R. Everett, T. L. Welch, L. Reed et al., *Anal. Chem.* **1995**, *67*, 292–298.
6. M. M. Walczak, C. A. Alves, B. D. Lamp et al., *J. Electroanal. Chem.* **1995**, *396*, 103–114.
7. J. J. Calvente, Z. Kováčová, M. D. Sanchez et al., *Langmuir* **1996**, *12*, 5696–5703.
8. D.-F. Yang, C. P. Wilde, M. Morin, *Langmuir* **1996**, *12*, 6570–6577.

9. C.-J. Zhong, M. D. Porter, *J. Electroanal. Chem.* **1997**, *425*, 147–153.
10. C.-J. Zhong, J. Zak, M. D. Porter, *J. Electroanal. Chem.* **1997**, *421*, 9–13.
11. D.-F. Yang, C. P. Wilde, M. Morin, *Langmuir* **1997**, *13*, 243–249.
12. D.-F. Yang, H. Al-Maznai, M. Morin, *J. Phys. Chem. B* **1997**, *101*, 1158–1166.
13. S. Arnold, Z. Q. Feng, T. Kakiuchi et al., *J. Electroanal. Chem.* **1997**, *438*, 91–97.
14. S. Imabayashi, M. Iida, D. Hobara et al., *J. Electroanal. Chem.* **1997**, *428*, 33–38.
15. M. Nishizawa, T. Sunagawa, H. Yoneyama, *J. Electroanal. Chem.* **1997**, *436*, 213–218.
16. H. Zhang, H. Xia, H. Li et al., *Chem. Lett.* **1997**, *26*, 721–722.
17. D. Hobara, M. Ota, S. Imabayashi et al., *J. Electroanal. Chem.* **1998**, *444*, 113–119.
18. J. S. Peanasky, R. L. McCarley, *Langmuir* **1998**, *14*, 113–123.
19. D. Oyamatsu, M. Nishizawa, S. Kuwabata et al., *Langmuir* **1998**, *14*, 3298–3302.
20. D. Oyamatsu, S. Kuwabata, H. Yoneyama, *J. Electroanal. Chem.* **1999**, *473*, 59–67.
21. H. Azehara, S. Yoshimoto, H. Hokari et al., *Electrochemistry* **1999**, *67*, 1227–1230.
22. H. Azehara, S. Yoshimoto, H. Hokari et al., *J. Electroanal. Chem.* **1999**, *473*, 68–74.
23. S. Yoshimoto, M. Yoshida, S. Kobayashi et al., *J. Electroanal. Chem.* **1999**, *473*, 85–92.
24. K. Nishiyama, T. T. Kie, I. Taniguchi, *Chem. Lett.* **1999**, 753–754.
25. M. Byloos, H. Al-Maznai, M. Morin, *J. Phys. Chem. B* **1999**, *103*, 6554–6561.
26. C.-J. Zhong, R. C. Brush, J. Anderegg et al., *Langmuir* **1999**, *15*, 518–525.
27. D. Hobara, K. Ueda, S. Imabayashi et al., *Electrochemistry* **1999**, *67*, 1218–1220.
28. N. Kanayama, H. Kitano, *Langmuir* **2000**, *16*, 577–583.
29. T. Kakiuchi, K. Sato, M. Iida et al., *Langmuir* **2000**, *16*, 7238–7244.
30. Q. Chi, J. Zhang, J. U. Nielsen et al., *J. Am. Chem. Soc.* **2000**, *122*, 4047–4055.
31. N. Mohtat, M. Byloos, M. Soucy et al., *J. Electroanal. Chem.* **2000**, *484*, 120–130.
32. J. Zhang, Q. Chi, J. U. Nielsen et al., *Langmuir* **2000**, *16*, 7229–7237.
33. S.-S. Wong, M. D. Porter, *J. Electroanal. Chem.* **2000**, *485*, 135–143.
34. T. Kawaguchi, H. Yasuda, K. Shimazu et al., *Langmuir* **2000**, *16*, 9830–9840.
35. K. V. Gobi, F. Mizutani, *J. Electroanal. Chem.* **2000**, *484*, 172–181.
36. K. V. Gothelf, *J. Electroanal. Chem.* **2000**, *494*, 147–150.
37. C. Vericat, G. Andreasen, M. E. Vela et al., *J. Chem. Phys.* **2001**, *115*, 6672–6678.
38. M. J. Esplandiú, H. Hagenström, D. M. Kolb, *Langmuir* **2001**, *17*, 828–838.
39. T. Sawaguchi, Y. Sato, F. Mizutani, *Phys. Chem. Chem. Phys.* **2001**, *3*, 3399–3404.
40. D. Hobara, T. Kakiuchi, *Electrochem. Commun.* **2001**, *3*, 154–157.
41. H. Munakata, S. Kuwabata, Y. Ohko et al., *J. Electroanal. Chem.* **2001**, *496*, 29–36.
42. T. Sawaguchi, Y. Sato, F. Mizutani, *J. Electroanal. Chem.* **2001**, *496*, 50–60.
43. T. Kakiuchi, M. Iida, N. Gon et al., *Langmuir* **2001**, *17*, 1599–1603.
44. H. Munakata, S. Kuwabata, *Chem. Commun.* **2001**, 1338–1339.
45. K. Gobi, Y. Sato, F. Mizutani, *Electroanalysis* **2001**, *13*, 397–403.
46. O. Azzaroni, M. E. Vela, H. Martin et al., *Langmuir* **2001**, *17*, 6647–6654.
47. I. C. N. Diógenes, F. C. Nart, M. L. A. Temperini et al., *Inorg. Chem.* **2001**, *40*, 4884–4889.
48. B. Vaidya, J. Chen, M. C. Porter et al., *Langmuir* **2001**, *17*, 6569–6576.
49. R. Madueño, T. Pineda, J. M. Sevilla et al., *Langmuir* **2002**, *18*, 3903–3909.
50. Y.-Y. Long, H.-T. Rong, M. Buck et al., *J. Electroanal. Chem.* **2002**, *524–525*, 62–67.
51. H. Martin, C. Vericat, G. Andreasen et al., *J. Chem. Phys.* **2002**, *117*, 2293–2298.
52. R. Naumann, S. M. Schiller, F. Giess et al., *Langmuir* **2003**, *19*, 5435–5443.
53. V. Brunetti, B. Blum, R. C. Salvarezza et al., *Langmuir* **2003**, *19*, 5336–5343.
54. N. Nishi, D. Hobara, M. Yamamoto et al., *Anal. Sci.* **2003**, *19*, 887–890.
55. D. Weisshaar, B. D. Lamp, M. D. Porter, *J. Am. Chem. Soc.* **1992**, *114*, 5860–5862.
56. S. Imabayashi, D. Hobara, T. Kakiuchi et al., *Langmuir* **1997**, *13*, 4502–4504.
57. S. Imabayashi, N. Gon, T. Sasaki et al., *Langmuir* **1998**, *14*, 2348–2351.
58. S. Kuwabata, H. Kanemoto, D. Oyamatsu et al., *Electrochemistry* **1999**, *67*, 1254–1257.
59. D. Hobara, T. Sasaki, S. Imabayashi et al., *Langmuir* **1999**, *15*, 5073–5078.
60. D. Oyamatsu, H. Kanemoto, S. Kuwabata et al., *J. Electroanal. Chem.* **2001**, *497*, 97–105.
61. S. Imabayashi, D. Hobara, T. Kakiuchi, *Langmuir* **2001**, *17*, 2560–2563.

62. M. Satjapipat, R. Sanedrin, F. Zhou, *Langmuir* **2001**, *17*, 7637–7644.
63. D. Hobara, Y. Uno, T. Kakiuchi, *Phys. Chem. Chem. Phys.* **2001**, *3*, 3437–3441.
64. L. Cheng, J. Seneviratne, G. E. Pacey et al., *Electroanalysis* **2002**, *14*, 1339–1343.
65. X. Jiang, R. Ferrigno, M. Mrksich et al., *J. Am. Chem. Chem.* **2003**, *125*, 2366–2367.
66. D. F. Yang, M. Morin *J. Electroanal. Chem.* **1997**, *429*, 1–5.
67. D.-F. Yang, M. Morin, *J. Electroanal. Chem.* **1998**, *441*, 173–181.
68. I. A. Vinokurov, M. Morin, J. Kankare, *J. Phys. Chem. B* **2000**, *104*, 5970–5796.
69. W. H. Mulder, J. J. Calvente, R. Andreu, *Langmuir* **2001**, *17*, 3273–3280.
70. T. Kakiuchi, H. Usui, D. Hobara et al., *Langmuir* **2002**, *18*, 5231–5238.
71. D. Hobara, K. Miyake, S. Imabayashi et al., *Langmuir* **1998**, *13*, 3590–3596.
72. D. W. Hatchett, R. H. Uibel, K. J. Stevenson et al., *J. Am. Chem. Soc.* **1998**, *120*, 1062–1069.
73. D. W. Hatchett, K. J. Stevenson, W. B. Lacy et al., *J. Am. Chem. Soc.* **1997**, *119*, 6596–6606.
74. T. Kondo, T. Sumi, K. Uosaki, *J. Electroanal. Chem.* **2002**, *538–539*, 59–63.
75. T. Sumi, H. Wano, K. Uosaki, *J. Electroanal. Chem.* **2003**, *550–551*, 321–325.
76. J. J. Calvente, R. Andreu, L. González et al., *J. Phys. Chem. B* **2001**, *105*, 5477–5488.
77. O. Azzaroni, M. E. Vela, G. Andreasen et al., *J. Phys. Chem. B* **2002**, *106*, 12267–12273.
78. O. Azzaroni, M. E. Vela, M. Fonticelli et al., *J. Phys. Chem. B* **2003**, *107*, 13446–13454.
79. T. Ariga, N. Takashima, K. Arihara et al., *Phys. Chem. Chem. Phys.* **2003**, *5*, 3758–3761.
80. R. Yamada, K. Uosaki, *Chem. Lett.* **1999**, 667–668.
81. M. Petri, D. M. Kolb, U. Memmert et al., *Electrochim. Acta* **2003**, *49*, 175–182.
82. M. Byloos, H. Al-Maznai, M. Morin, *J. Phys. Chem. B* **2001**, *105*, 5900–5905.
83. Y.-T. Tao, C.-C. Wu, J.-Y. Eu et al., *Langmuir* **1997**, *13*, 4018–4023.
84. T. Baunach, D. M. Kolb, *Anal. Bioanal. Chem.* **2002**, *373*, 743–748.
85. M. S. El-Deab, T. Ohsaka, *J. Electroanal. Chem.* **2003**, *5*, 214–219.
86. N. Nishi, D. Hobara, M. Yamamoto et al., *Langmuir* **2003**, *19*, 6187–6192.
87. J. J. Calvente, Z. Kováčová, R. Andreu et al., *J. Chem. Soc., Faraday Trans.* **1996**, *92*, 3701–3708.
88. C.-J. Zhong, M. D. Porter, *J. Am. Chem. Soc.* **1994**, *116*, 11616–11617.
89. H. Angerstein-Kozlowska, J. Klinger, B. E. Conway, *J. Electroanal. Chem.* **1977**, *75*, 45–60.
90. F. C. Anson, *J. Electroanal. Chem.* **1973**, *47*, 279–285.
91. A. N. Frumkin, *Z. phys. Chem.* **1925**, *116*, 466–484.
92. U. Retter, *J. Electroanal. Chem.* **1987**, *236*, 21–30.
93. D. A. Huckaby, L. Blum, *J. Chem. Phys.* **1990**, *94*, 2646–2649.
94. L. Blum, D. A. Huckaby, *J. Chem. Phys.* **1991**, *94*, 6887–6894.
95. L. Blum, D. A. Huckaby, M. Legault, *Electrochim. Acta* **1996**, *41*, 2207–2227.
96. J. N. Israelachvili, *Intermolecular and Surface Forces*, Academic Press, London, 1992, Chapter 16.
97. J. F. Rodriguez, T. Mebrahtu, M. P. Soriaga, *J. Electroanal. Chem.* **1987**, *233*, 283–289.
98. J. B. Schlenoff, M. Li, H. Ly, *J. Am. Chem. Soc.* **1995**, *117*, 12528–12536.
99. A. N. Frumkin, *Z. Phys.* **1926**, *35*, 792–802.
100. B. B. Damaskin, O. A. Petrii, V. V. Batrakov, *Adsorption of Organic Compounds on Electrodes*, Plenum Press, New York, 1971.
101. U. W. Hamm, D. Kramer, R. S. Zhai et al., *J. Electroanal. Chem.* **1996**, *414*, 85–89.
102. A. Chen, Z. Shi, D. Bizzotto et al., *J. Electroanal. Chem.* **1999**, *467*, 342–353.
103. Y. Iwami, D. Hobara, M. Yamamoto et al., *J. Electroanal. Chem.* **2004**, *564*, 77–83.
104. J. A. M. Sondag-Huethorst, L. G. Fokkink, *Langmuir* **1992**, *8*, 2560–2566.
105. M. E. Vela, H. Martin, C. Vericat et al., *J. Phys. Chem. B* **2000**, *104*, 11878–11882.
106. Y. Ooi, D. Hobara, M. Yamamoto et al., Submitted for publication to Langmuir.
107. L. Li, S. Chen, S. Jiang, *Langmuir* **2003**, *19*, 3266–3271.
108. C. D. Bain, G. M. Whitesides, *J. Am. Chem. Soc.* **1988**, *110*, 3665–3666.
109. C. D. Bain, J. Evall, G. M. Whitesides, *J. Am. Chem. Soc.* **1989**, *111*, 7155–7164.
110. P. E. Laibinis, M. A. Fox, J. P. Folkers et al., *Langmuir* **1991**, *7*, 3167–3173.
111. T. Kakiuchi, D. Hobara, *Bunseki Kagaku* **2002**, *51*, 1089–1101.

112. D. Hobara, Y. Uno, T. Kakiuchi, *Bunseki Kagaku* **2002**, *51*, 455–460.
113. H. Matsuura, Y. Sato, T. Sawaguchi et al., *Chem. Lett.* **2002**, 618–619.
114. H. Matsuura, Y. Sato, T. Sawaguchi et al., *Sens. Actuator, B-Chem.* **2003**, *91*, 148–151.
115. S. J. Stranick, A. N. Parikh, Y. Y. Tao et al., *J. Phys. Chem.* **1994**, *98*, 7636–7646.
116. C. Schönenberger, J. Jorritsma, J. A. M. Sondag-Huethorst et al., *J. Phys. Chem.* **1995**, *99*, 3259–3271.

Appendix

$P(g_2, z)$ is defined by [94]:

$$P(g_2, z) = \sum_{i=1}^{N} p_i z^i \tag{A1}$$

and the first seven terms are [94]:

$$p_1 = 6 \tag{A2}$$

$$p_2 = 3(-15 + 11g_2 + 2[g_2]^2) \tag{A3}$$

$$p_3 = 2(187 - 266g_2 + 46[g_2]^2 + 30[g_2]^3 + 6[g_2]^4) \tag{A4}$$

$$p_4 = 3(-1100 + 2306g_2 - 1190[g_2]^2 - 156[g_2]^3 + 83[g_2]^4 + 45[g_2]^5 + 10[g_2]^6) \tag{A5}$$

$$p_5 = 6(5047 - 13944g_2 + 11897[g_2]^2 - 1778[g_2]^3 - 1276[g_2]^4 - 114[g_2]^5 + 99[g_2]^6 + 56[g_2]^7 + 14[g_2]^8) \tag{A6}$$

$$p_6 = -285682 + 978458g_2 - 1161412[g_2]^2 + 459060[g_2]^3 + 67758[g_2]^4 - 41124[g_2]^5 - 17876[g_2]^6 - 1652[g_2]^7 + 1288[g_2]^8 + 952[g_2]^9 + 217[g_2]^{10} + 7[g_2]^{11} \tag{A7}$$

$$p_7 = 2751258 - 11237190g_2 + 17065398[g_2]^2 - 10735704[g_2]^3 + 1150716[g_2]^4 + 1126218[g_2]^5 + 41376[g_2]^6 - 117342[g_2]^7 - 43824[g_2]^8 - 7788[g_2]^9 + 3810[g_2]^{10} + 2430[g_2]^{11} + 600[g_2]^{12} + 48[g_2]^{13} \tag{A8}$$

8
Electron Transfer

Harry O. Finklea
Bennett Department of Chemistry, West Virginia University, Morgantown, WV, USA

8.1 **Self-assembled Monolayers (SAMs)** **625**

8.2 **Blocking SAMs, Pinholes, and Defects** **627**

8.3 **Electroactive SAMs** **629**

8.4 **Theoretical Model for Electron Transfer** **631**

8.5 **Measurements of Kinetic Parameters** **634**

8.6 **Electronic Coupling versus Distance** **639**

8.7 **Electronic Coupling versus Other Factors** **642**

8.8 **Reorganization Energies** **643**

8.9 **Future Directions** **644**
References 645

Encyclopedia of Electrochemistry. Edited by A.J. Bard and M. Stratmann
Vol. 10 *Modified Electrodes*. Edited by M.Fujihira, I.Rubinstein, and J.F.Rusling
Copyright © 2007 Wiley-VCH Verlag GmbH & Co. KGaA, Weinheim. ISBN: 978-3-527-30402-8

8.1
Self-assembled Monolayers (SAMs)

Self-assembled monolayers (henceforth abbreviated as SAMs) are single layers of molecules on a substrate, sharing a common orientation (Fig. 1). Self-assembly implies that the monolayers form spontaneously when the substrate is exposed to a solution or a vapor containing the adsorbing molecules. The molecules contain head groups that have an affinity for the substrate and tail groups that pack together in a dense structure. For metals typically used as electrodes (gold, platinum, mercury, silver), the most commonly used molecules are alkane thiols and related molecules (disulfides, sulfides), since the sulfur head group has a strong affinity for the metals and the alkane chains readily adopt a close-packed all-trans structure.

Within the broad area of chemically modified electrodes (see Sect. 8.1), SAMs have proven to be especially popular. The reasons for this popularity are easy to understand. Formation of a SAM is one of the simplest and easiest methods for chemically modifying an electrode surface. SAM is generally stable over a wide range of electrode potentials and electrolyte compositions. Because of the high affinity of sulfur for the metal electrode, the exposed surface of the SAM can include a diverse variety of functional groups, with properties ranging from nonpolar to polar, hydrophobic to hydrophilic, and inert to highly reactive. Patterned SAMs of two or more molecules are readily fabricated (although relatively little electrochemical work has been done with patterned SAMs). Postdeposition modification of SAMs permits the creation of quite elaborate structures targeted toward goals such as biosensors.

The focus of this chapter is the use of SAMs to study electron-transfer kinetics. Densely packed SAMs inhibit the approach of a redox molecule to the electrode. If the redox molecules freely diffuse in the contacting electrolyte, the SAM is described as blocking (Fig. 1a). Electroactive SAMs have the redox molecule covalently or ionically attached to them, generally with no redox molecules in the electrolyte (Fig. 1b). The specific advantages of each configuration will be discussed below. For kinetic measurements, the general advantages are derived from the replacement of the electrolyte Helmholtz layer with the body of the SAM and the control of the spacing between the electrode and the redox molecule. Alkanethiol SAMs with chain lengths of 10 or more methylenes create a layer with a low dielectric constant (close to that of pure hydrocarbon) between the metal and the electrolyte. The capacitance of the electrode/SAM/electrolyte interface

Encyclopedia of Electrochemistry. Edited by A.J. Bard and M. Stratmann
Vol. 10 *Modified Electrodes*. Edited by M.Fujihira, I.Rubinstein, and J.F.Rusling
Copyright © 2007 Wiley-VCH Verlag GmbH & Co. KGaA, Weinheim. ISBN: 978-3-527-30402-8

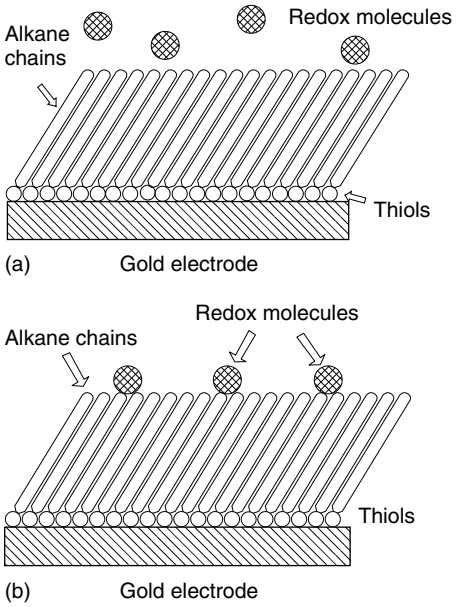


Fig. 1 (a) A well-ordered self-assembled monolayer of alkane thiols on gold that is perfectly blocking to freely diffusing redox molecules. (b) A well-ordered SAM with attached redox molecules.

is reduced by more than an order of magnitude relative to the capacitance of the bare electrode/electrolyte interface and is nearly independent of the applied potential and the composition of the electrolyte. Consequently, the time constants and double-layer effects of the cell are greatly diminished. Because the redox molecules are typically separated from the electrode surface by distances greater than a nanometer, the rate of electron transfer is decreased by many orders of magnitude compared to that observed for a bare electrode. Rate constants can be obtained at large driving forces (overpotentials) for simple one-electron redox molecules. Because the rate constants of electron transfer for such redox molecules are usually very fast, measurements at large overpotentials are difficult to impossible to obtain at bare metal electrodes. Electroactive SAMs with attached redox molecules have no diffusion component in the current, which simplifies both the kinetic measurement methods and the equations describing the current–voltage relationships.

Several reviews are available for those seeking more detail on the formation and characterization of SAMs on metals [1–6]. The electrochemistry of SAMs based on thiols and related molecules has been extensively discussed by the author [7].

This section discusses the preparation of monolayer-modified electrodes. SAMs on electrodes are usually prepared by cleaning the electrode surface and immersing the electrode in a solution containing the self-assembling molecules. ''Virgin'' metal surfaces are customarily prepared by a vacuum deposition of the metal onto a smooth substrate such as silicon or mica; these surfaces often exhibit the single-crystal character. Bulk metal electrodes may be pretreated with etchants and/or powerful oxidants (e.g. ''piranha'' solution, a hot mixture of sulfuric acid and hydrogen peroxide) to remove all contaminants. Any residual oxide is usually removed by chemical or electrochemical treatment. The exact conditions of the deposition are dependent on variables such as the quality of the SAM desired and the nature of the metal and the assembling molecules. Typically, the metal is immersed in a dilute (millimolar or lower concentration) solution of the molecules for periods of hours to days and then rinsed with solvent to remove loosely adsorbed molecules. SAMs can be formed on the pure metals or on metals coated with a second metal monolayer formed by underpotential deposition [8, 9].

The non-electrochemical methods used to characterize SAMs on metals include virtually every known surface analytical tool. The most popular are ellipsometry, wetting contact angle, surface IR and Raman spectroscopy, X-ray photoelectron spectroscopy, and the scanning probe microscopies (scanning tunneling and atomic force microscopy). From these studies, some general statements can be made about the alkanethiol SAMs; these statements are likely to be relevant to other types of SAMs (e.g. those based on other head groups and chain compositions). The SAMs are closely packed and highly oriented. The thickness of the SAM scales linearly with the chain length. The alkane chains form domains that are often commensurate with the metal lattice. The chain tilt is dependent on the head group spacing and the tail group diameter. In some cases (e.g. alkane thiol on Au(111)), the chain tilt is about 30° away from the surface normal. Consequently, tilt grain boundaries exist between domains of alkane thiols in the SAM. Pits are often observed for alkanethiol SAMs on gold; the pits are one gold atom deep and contain alkane thiols. The majority of the evidence points toward the formation of a metal–thiolate bond upon adsorption of either a thiol or a disulfide. In situ probes show that the alkanethiol SAMs are intact in an aqueous electrolyte with or without potential control. Nonaqueous electrolytes promote more disorder in the form of gauche defects in the alkane chain. The degree of molecular mixing or phase separation when two different alkane thiols are coadsorbed is of interest. Phase separation is promoted by the somewhat different solubilities of the two components in the deposition solution, high temperatures, and long deposition times.

8.2 Blocking SAMs, Pinholes, and Defects

A densely packed SAM prevents both the solvent and ions from reaching the metal surface. Thus, faradaic reactions involving the solvent or ion flux to the electrode are strongly inhibited. Gold, platinum, and mercury oxidation can be suppressed to potentials up to 0.5 V more than the normal potential limits exhibited by these metals in a given electrolyte. Faradaic reactions of solution redox molecules are similarly inhibited. An advantage of a blocking SAM for kinetic studies is that any redox molecule whose formal potential lies in the accessible potential range can be studied. In a perfectly packed monolayer, electron transfer between the electrode and the redox molecule requires tunneling of the electron across the full width of the SAM. When the current is controlled by the kinetics of tunneling and the rate of tunneling is uniform across the entire area of the electrode, then it rises exponentially with the overpotential (see Sect. 8.4).

In practice, currents at an electrode with a blocking SAM often show peaks or plateaus at potentials close to the formal potential of the redox molecule (Fig. 2). Current peaks or plateaus are indicative of electron transfer limited by mass transfer of the redox couple to the electrode. These currents are interpreted as electron transfer at defects and pinholes in the SAM. A defect is a region in the SAM by which, by virtue of loose packing, a redox molecule can penetrate partway to the electrode surface. A pinhole is a site of exposed electrode surface. Voltammetry of SAM-coated electrodes is an extraordinarily sensitive tool for evaluating the presence of defects and pinholes in a SAM because nonlinear mass transfer of redox molecules to the defects or pinholes greatly

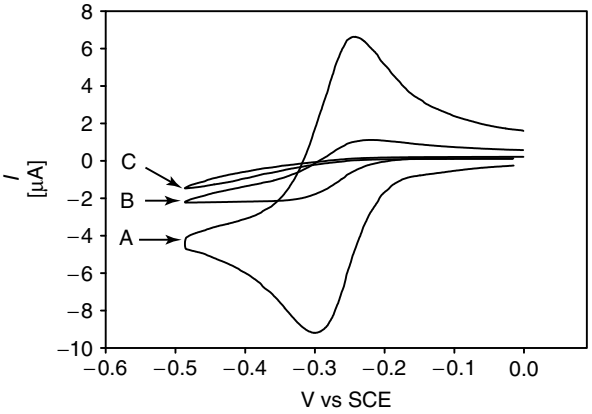


Fig. 2 A: CV of 0.7 mM $Ru(NH_3)_6(Cl)_3$ in 0.5 M NaF, pH 5, at 0.1 V s^{-1} on a bare gold bead electrode (area ca 0.1 cm^2). B: CV of the same electrode after immersion in octadecanethiol ethanolic deposition solution for 30 min. Plateau currents are visible at low overpotentials indicating the presence of pinholes. C: CV of the same electrode after multiple immersions in the deposition solution followed by CVs. The plateau currents are smaller and shifted to larger overpotentials. Note that the charging currents near 0 V versus saturated calomel electrode in B and C are reduced to invisibility on this scale.

increases the flux of current at those sites. Qualitative modeling of the pinholes and defects can be performed by treating the SAM-coated electrode as a microarray electrode, but quantitative determination of the density and size of the pinholes is much more difficult [10–14]. The magnitude of the pinhole and defect currents can be reduced via multiple immersions of the electrode in the deposition solution (compare Fig. 2b with c). SAM-coated electrodes with a very low level of defects can appear to exhibit tunneling currents with a quasi-exponential dependence. However, Tafel plots (plots of log of the current versus the overpotential) have anomalously low slopes, which are inconsistent with the theory of electron tunneling across the full width of the SAM (Sect. 8.4) [15–17] and are therefore attributed to the electron transfer at defects in the SAM.

Miller and coworkers have defined criteria for ensuring that pinhole and defect currents are an insignificant component of the total current [18–22].

(a) Current–overpotential plots are reproducible from one SAM to another.
(b) Currents at a constant overpotential decrease by a factor of 2 to 3 upon insertion of an extra methylene (CH_2) in the alkane chain.
(c) Currents are insensitive to factors that affect diffusion coefficients (viscosity).
(d) Currents are insensitive to procedures for filling pinholes and defects (e.g. adding a surfactant such as 1-octanol to the solution).

By these criteria, there are only a few reported systems that exhibit tunneling currents with negligible defect currents

across the full width of the SAM: the ω-hydroxyalkanethiol SAMs on gold of Miller and coworkers [18–22], one study of simple alkane thiols on gold [23], and alkanethiol SAMs on mercury [24–27].

Manipulation of the permeability of the SAM to selected redox molecules can be achieved through the inclusion of "molecular gates" [28–38] or changes in the charge density of the SAM via an ionizable moiety [39–43]. These manipulations are directed toward the fabrication of selective chemical sensors.

8.3 Electroactive SAMs

When the redox molecule is attached to the SAM, the tunneling experiments are much less sensitive to the presence of pinholes and defects in the SAM. This advantage was first recognized by Chidsey [44, 45]. The second advantage noted is that diffusion no longer contributes to the current, so equations for the current can be derived considering only thermodynamics and kinetics. The third advantage is that the surface concentration of the redox centers is readily obtained from a cyclic voltammogram (CV) (Fig. 3). For either the anodic or the cathodic peak, the faradaic current i_f is isolated by extrapolating the charging current baseline before and after the peak. The area under the peak $Q_{tot}(= \int i_f dt)$ is related to the surface coverage via Faraday's law (Eq. 1):

$$\Gamma = Q_{tot}/nFA \qquad (1)$$

where Γ is the surface coverage in moles per square centimeter, n is the number of electrons transferred per redox molecule,

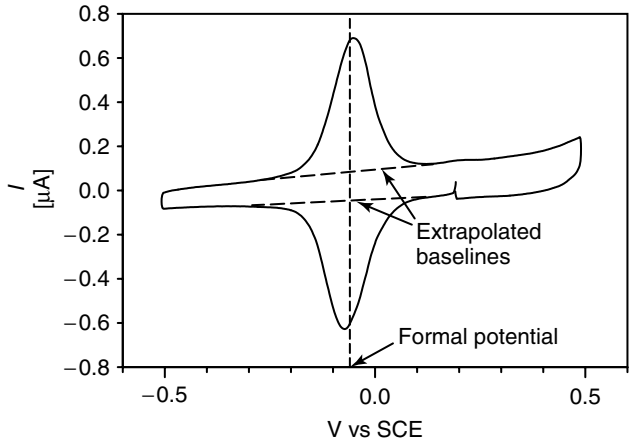


Fig. 3 CV of a mixed SAM of $HS(CH_2)_{15}COOH + HS(CH_2)_{15}CON(H)CH_2pyRu(NH_3)_5$ on gold in 0.5 M NaF, pH 5, at 0.02 V s^{-1}. The formal potential $E^{0\prime}$ is the average of the two peak potentials. Charging current baselines are extrapolated across the faradaic current peaks. The area of either the anodic or cathodic faradaic peak after correction for charging current is Q_{tot}. The average Q_{tot} is 3.5 μC. Given a geometric area of 0.9 cm^2, the coverage Γ is 4.0×10^{-11} mol cm^{-2}. The peak splitting is 18 mV and the average peak half-width is 102 mV.

F is Faraday's constant, and A is the electrode area.

When the scan rate is sufficiently low such that the CV can be considered to be reversible (under thermodynamic control), then additional information is obtained from the CV (Fig. 3). The average of the anodic and cathodic peak positions is the formal potential $E^{0\prime}$ of the redox molecules. In theory, the peak splitting ΔE_p should be zero and the peak half-width ΔE_{fwhm} of each peak should be 3.53 RT/nF or 91 mV/n at room temperature. A number of electroactive SAMs exhibit CVs whose peak splitting and half-width are very close to these criteria [44–50]. Frequently, a finite peak splitting independent of the scan rate and a peak half-width somewhat larger than the theoretical value are observed (as in Fig. 3). The cause of the nonzero peak splitting is not understood, but is attributed to changes in the monolayer structure (e.g. formation or dissolution of ion pairs) as a function of the oxidation state of the redox molecules [51]. Larger peak half-widths can be manifestations of a number of causes, such as a spread of formal potentials about an average value or double-layer effects. Double-layer effects become particularly important when the coverage of the redox molecules is high and one of the oxidation states has zero charge [52].

In many reports, the proof of attachment of the redox center is given in the form of a plot of the peak current i_p versus scan rate ν. For reversible conditions, i_p is linear with respect to ν for attached redox molecules, whereas it is linear with respect to the square root of the scan rate for freely diffusing redox molecules. A better criterion for the proof of attachment is a peak area Q_{tot} that is independent of the scan rate. This criterion does not require reversible behavior of the attached redox molecules.

For kinetic studies, the desired SAM structure is a densely packed and well-oriented SAM with the redox molecules located on the surface in full contact with the electrolyte. The redox centers should be sufficiently separated along the SAM such that electron hopping between the redox molecules can be neglected. All faradaic current represent electron transfer between each redox center and the electrode. This configuration minimizes the double-layer effects and permits rapid transfer of ions to and from the electrolyte during changes in the oxidation state. Under these conditions, kinetic measurements should reflect the true rate of electron transfer between the electrode and the redox molecule, and not another process such as ion transfer [53].

Preparation of an electroactive SAM follows one of the following two strategies. In the first strategy, the redox molecules are synthesized with a pendant head group, and SAM is formed by adsorbing these molecules with or without diluent molecules (e.g. alkane thiols with no redox centers). The coverage of the redox molecules can be controlled by adjusting the ratio of the electroactive molecules to the diluent molecules in the deposition solution and by annealing the SAM in a solution of the diluent after the initial deposition. The coverage of redox molecules is usually less than 30% of the maximum coverage possible to ensure that the redox centers are well separated. The formation of well-ordered SAMs by this approach is sometimes a problem because of the disparate solubility of the electroactive and diluent molecules in the deposition solvent and the possible formation of phase-separated domains. In the second strategy, a well-ordered SAM is

formed by adsorbing an alkanethiol with a pendant functional group, and the redox molecule is subsequently attached via bond formation to that functional group. The coverage is achieved via control of the reaction time and temperature. Facile attachment of a number of redox centers can be achieved via the formation of an amide bond between a SAM with a terminal carboxylate and a redox molecule with a pendant amine. Peptide catalysts such as carbodiimides work well in this coupling.

Examples of attached redox molecules on alkanethiol, disulfide, and sulfide SAMs include ferrocenes [9, 44, 47–49, 53–113], pentaaminepyridine ruthenium complexes [46, 50, 105, 114–119], polypyridyl complexes of ruthenium [120, 121] and osmium [122], viologens [123–135], quinones [127, 136–150], and porphyrins [127, 142, 151–163]. Cytochrome *c* and azurins can be adsorbed on SAMs terminating in ionizable or coordinating groups [164–190]; see the chapter by Niki in Volume 9. SAMs containing osmium polypyridyl complexes are formed when one of the ligands contains a pendant aromatic nitrogen (e.g. pyridine) [191–196]. Formal potentials are generally close to values of fully solvated analogs, indicating that the solvation of the attached redox molecules is similar to that of freely diffusing molecules.

8.4 Theoretical Model for Electron Transfer

The model that has been successfully applied to electron-transfer kinetics on SAM-coated metal electrodes is the Marcus DOS model (DOS = density of states) (see also Chapter 1 of Volume 2). A particularly clear discussion of this model has been given by Miller [197]. Similar models have been developed for semiconductor and semimetal electrodes [198–201]. The basis of the model is shown in Fig. 4. Both the metal and the redox molecule are represented by a DOS as a function of energy, with zero energy corresponding to the Fermi energy of the metal. Consider the reduction of an oxidized (OX) molecule located at the surface of a SAM on an electrode. Marcus theory introduces the reorganization energy λ. It is related to the energy associated with the change in the internal structure of the OX molecule and the change in solvation as the molecule is converted to the reduced (RED) molecule. When the reorganization energies of the OX and RED forms are identical, the OX molecules are represented by a Gaussian distribution of electron acceptor levels given by the function (Eq. 2):

$$D_{\mathrm{OX}}(\varepsilon, \lambda, \eta) = (4\pi\lambda k_{\mathrm{B}}T)^{-1/2} \times \exp(-(\varepsilon - \lambda - e\eta)^2/(4\lambda k_{\mathrm{B}}T)) \quad (2)$$

where ε is the energy at which the electron is transferred (with respect to the Fermi energy in the electrode), η is the overpotential ($=E - E^{0\prime}$), e is the charge of an electron, k_{B} is the Boltzmann's constant, and T is the temperature. The width and the peak position of the Gaussian distribution of D_{OX} are proportional to λ. The corresponding distribution of electron donor levels in the electrode are given by the Fermi function $f(\varepsilon)$ (Eq. 3):

$$f(\varepsilon) = (1 + \exp(\varepsilon/k_{\mathrm{B}}T)^{-1} \quad (3)$$

At a given energy, the electronic coupling between the metal and redox acceptor states is (Eq. 4)

$$|V|^2 = \rho(\varepsilon)|H_{\mathrm{kA}}|^2 \quad (4)$$

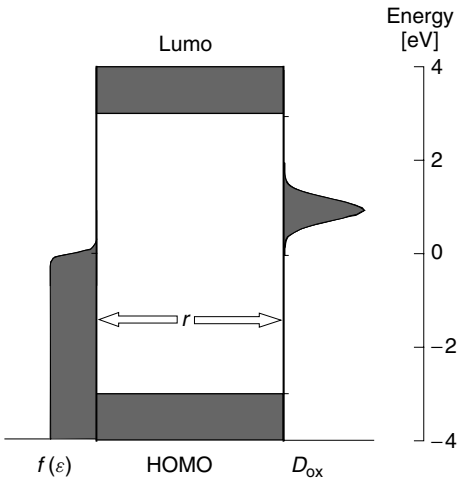


Fig. 4 Principal components of the Marcus DOS model. The vertical axis is energy referenced with respect to the Fermi energy of the metal electrode. The occupied metal states are represented by the Fermi function $f(\varepsilon)$; the DOS $\rho(\varepsilon)$ is assumed to be independent of energy near the Fermi energy. The redox molecule acceptor states D_{OX} is a Gaussian function with respect to energy ε, the reorganization energy λ, and the overpotential η (Eq. 2). In this diagram, the electrode is set at the formal potential of the redox molecule ($\eta = 0$) and λ is 1 eV. The rate of electron transfer from the metal to the acceptor states is proportional to the overlap between the functions $f(\varepsilon)$ and D_{OX}. More negative potentials cause the Gaussian D_{OX} to shift down relative to $f(\varepsilon)$, increasing the overlap and the rate constant. The rate is also controlled by the electronic coupling between the donor and acceptor states. The electronic coupling is a function of the distance r between the donor and acceptor states and the energies of the highest occupied (HOMO) and lowest unoccupied molecular orbitals (LUMO) of the SAM.

where $\rho(\varepsilon)$ is the DOS in the metal near the Fermi energy, and the electronic coupling between the redox acceptor state and an electronic state of wave vector $\boldsymbol{k}$, averaged over all wave vectors, is given by $|H_{kA}|^2$ [202]. Theoretical calculations indicate that "d" states in the metal couple much more weakly than "sp" states when electron tunneling occurs over a significant distance; so $\rho(\varepsilon)$ is defined by the "sp" states in the electrode [202]. The rate constant for reduction k_{cat} is given by integration over all energies (Eq. 5):

$$k_{cat} = (2\pi/\hbar) \int D_{OX}(\varepsilon, \lambda, \eta) f(\varepsilon) |V|^2 d\varepsilon \quad (5)$$

Typically, $|V|^2$ is assumed to be independent of energy over the range of energies needed for integration and is moved out of the integral. Numerical integration of $D_{OX}(\varepsilon, \lambda, \eta)$ and $f(\varepsilon)$ can be done easily. There is no true analog solution, but approximation expressions for k_{cat} have been derived [203–205]. Analogous expressions are readily obtained for the anodic rate constant k_{an} by replacing the Fermi function with its complement $1 - f(\varepsilon)$ and replacing $-\lambda$ with $+\lambda$ in the exponential term in Eq. (2). The standard rate constant k^0 can be calculated by setting η to zero. The standard rate constant k^0 is approximately proportional to $\exp(-\lambda/4k_BT)$, and is thus quite sensitive to λ.

The consequences of Eq. (5) are shown in the theoretical Tafel plots of Figs. 5 and 6. In Fig. 5, $\ln(k_{cat})$ is plotted versus absolute η at 298 K for λ equal to 0.5, 1.0, and 1.5 eV. The rate constants are normalized with respect to the standard rate constant k^0 for $\lambda = 1$ eV. At low overpotentials ($\eta \ll e\lambda$), the Tafel plots are linear with a slope consistent with the Butler–Volmer expression for the cathodic rate constant (Eq. 6) (see Chapter 1 of Volume 2):

$$k_{cat}(\mathrm{BV}) = k^0 \exp(-\alpha n F \eta / RT) \qquad (6)$$

where α, the transfer coefficient, has a value of 0.5 at $\eta = 0$ V. The Tafel plots

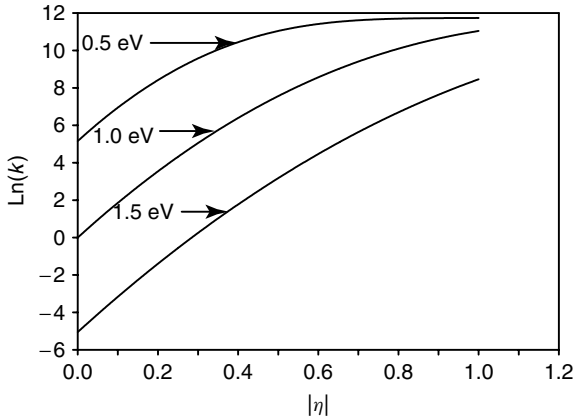


Fig. 5 Theoretical Tafel plots as a function of the reorganization energy. The plots are normalized with respect to the standard rate constant at $\eta = 0$ V and $\lambda = 1.0$ eV. The relative values of k^0 are 175 for $\lambda = 0.5$ eV and 0.0064 for $\lambda = 1.5$ eV.

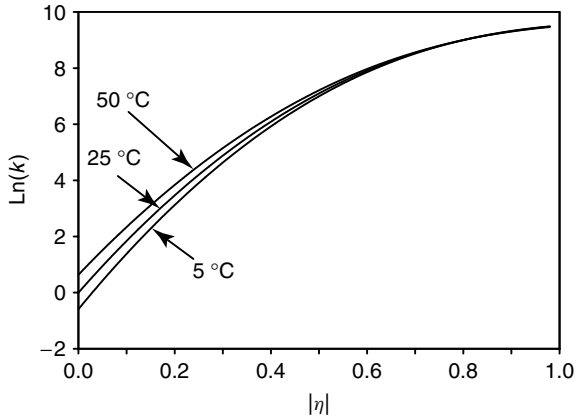


Fig. 6 Theoretical Tafel plots as a function of temperature for $\lambda = 0.8$ eV. The plots are normalized at 25 °C. The relative values of k^0 are 0.55 for 5 °C and 1.9 for 50 °C.

show the curvature (α is dependent on the overpotential) with a greater value evident at lower η for smaller λ.

The theoretical Tafel curves approach the same limiting value at large overpotentials ($\eta \gg e\lambda$), independent of λ. The maximum rate constant $k_{cat,max}$ corresponds to the complete overlap of the electrode donor states and the redox molecule acceptor states (Fig. 4). The integral of $D_{OX}(\varepsilon, \lambda, \eta)$ and $f(\varepsilon)$ in Eq. (5) is equal to 1, and, consequently (Eq. 7):

$$k_{cat,max} = (2\pi/\hbar)|V|^2 \qquad (7)$$

In Fig. 6, the effects of temperature on Tafel behavior are shown with the assumption that λ and $|V|^2$ are independent of temperature. Again, at large overpotentials, the Tafel plots converge to a temperature-independent value, while $\ln(k^0)$ at $\eta = 0$ V is sensitive to temperature. If the entropy of activation is zero, an Arrhenius plot of the standard rate constant is related to the reorganization energy via Eq. (8):

$$\lambda = x(R/F)(\mathrm{d}\ln(k^0/T^{1/2})/\mathrm{d}(1/T)) \quad (8)$$

where x is close to 4 ($x = 4.03$ works well for $\lambda = 0.7$–1.0 eV and temperatures near room temperature) [95]. If the entropy of activation is not zero, then a correction can be made on the basis of the shift of the formal potential with temperature [95, 192, 194, 195, 206].

Experimental kinetic measurements at SAM-coated electrodes yield two parameters, the standard rate constant k^0 and the reorganization energy λ. The latter can be obtained either by measuring the rate constant versus the overpotential and fitting a Tafel plot to the theoretical curves or by measuring the standard rate constant versus temperature and using Eq. (8). Once k^0 and λ have been determined, k_{max} and the electronic coupling $|V|^2$ can be calculated.

The effect of SAM on the electronic coupling is expected to follow the tunneling law (Eq. 9):

$$|V|^2 \approx \exp(-\beta_r r) \qquad (9)$$

where r is the distance between the redox center and the electrode surface and β_r is the distance tunneling parameter. The quantum tunneling model treats the SAM as a dielectric barrier with the barrier height based on the lowest unoccupied molecular orbital of the SAM chain (Fig. 4). Theoretical estimates of β_r based on this model for an alkanethiol SAM and including image dipole effects are in the range of 1.3–1.8 Å^{-1} [115]. Experimental evidence suggests that the electron tunneling is coupled specifically via the tether connecting the metal electrode to the redox center (described as ''through-bond'' tunneling). When the chain contains a repeating unit, such as a methylene group in an alkane chain, calculations can be made to estimate the dependence of the electronic coupling with respect to the number of repeat units m (Eq. 10) [207, 208]:

$$|V|^2 \approx \exp(-\beta_m r) \qquad (10)$$

For an alkane chain of 10 or more methylene units on a gold electrode, the theoretical value of β_m is 1.0 per methylene unit [207].

8.5 Measurements of Kinetic Parameters

The objectives are to measure the standard rate constant k^0 and, if possible, the rate constant k as a function of the overpotential η. In all voltammetric methods, it is necessary to correct the effects of

mass transfer, charging current, and uncompensated resistance in order to extract these kinetic parameters. The majority of the methods described here assume that the redox molecule is attached to the SAM, and hence mass-transfer effects are nonexistent. Further assumptions include a homogeneous rate constant for all redox molecules on or near the SAM and the absence of double-layer effects. Double-layer effects (see Chapter 3 of Volume 1) can be defined as changes in the surface concentration (for freely diffusing redox molecules) or the driving force for electron transfer because of changes of the electrostatic potential at the plane of the redox molecules (the plane of electron transfer) [52]. For SAMs of sufficient thickness and low dielectric constant, simple electrostatic arguments show that any changes in the electrode potential result in changes in the electrostatic potential within the body of the SAM, with minimal changes at the plane of the redox molecules. Changing the oxidation states of the attached redox molecules can also cause the electrostatic potential at the plane of electron transfer to change. This effect can be minimized by making the ionic strength of the electrolyte high (1 M or greater) and by reducing the surface coverage of the redox centers to 10% or less than that of a complete monolayer [52, 209, 210].

For perfectly blocking SAMs and free diffusion redox molecules, linear scan voltammetry (LSV) in an unstirred electrolyte provides a facile method for obtaining k versus η [18–22, 211–213]. The rate constant (units of centimeters per second) can be extracted directly from the current via Eq. (11):

$$k = i/(nFAC_s) \tag{11}$$

where C_s is the solution concentration of the oxidized or the reduced form of the redox molecule at the monolayer surface. At sufficiently small currents, the surface concentration can be equated to the bulk concentration. As currents increase, mass-transfer (diffusion) effects become important. The effects of diffusion can be removed by calculating the surface concentration via semi-integration of the current [20]. This calculation assumes that diffusion is linear and that the rate of electron transfer is uniform across the surface of the blocking SAM. The kinetically limited current is obtained by multiplying the measured current by the ratio of the bulk concentration to the surface concentration.

Having a nearly continuous plot of kinetically controlled current over a wide range of overpotentials (in excess of 1 V) permits a unique method of extracting λ. If the Fermi distribution $f(\varepsilon)$ is assumed to be a step function, the derivative of the kinetically controlled current with respect to the overpotential is the Gaussian distribution of the redox donor or acceptor levels (Eq. 2) multiplied by a constant [20]. Fitting either the peak position or the peak width of the Gaussian distribution yields λ.

For SAMs with attached redox molecules, k^0 (units of s^{-1}) can be measured by cyclic voltammetry, chronoamperometry (CA), alternating current impedance spectroscopy (ACIS), alternating current voltammetry (ACV), AC electroreflectance spectroscopy, and an indirect laser-induced temperature (ILIT) jump method.

As the scan rate of a CV increases, kinetic control causes the anodic current peak to move positive and the cathodic current peak to move negative of $E^{0\prime}$ (Fig. 7). Laviron has published working curves for the peak splitting ΔE_p as a function of scan rate and k^0 [214]. The working curves assume that the transfer coefficient α is

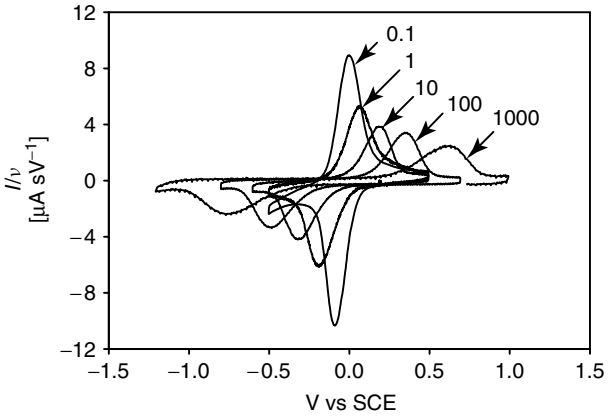


Fig. 7 Overlay CVs for a mixed SAM of $HS(CH_2)_{15}COOH + HS(CH_2)_{15}CON(H)CH_2pyRu(NH_3)_5$ on gold in 0.5 M NaF, pH 5, as a function of the scan rate. The currents are normalized with respect to the scan rate. Scan rates are shown in volts per second.

independent of the overpotential. Several researchers have performed simulations of CVs using the rate constants obtained from Eq. (5) to generate working curves of $E_p - E^{0\prime}$ for different values of λ [204, 215, 216]. When ΔE_p is less than 200 mV, the working curves are relatively insensitive to λ, and Laviron's working curve can be used to obtain k^0. These methods assume that the iR drop is negligible (the product of the peak current i_p times the uncompensated resistance R_u is less than 10 mV).

In ACIS, a DC potential is combined with a small AC potential (10 mV or less) of amplitude E_{AC} and frequency f. The in-phase and out-of-phase AC current components are measured as a function of the frequency. The data are analyzed in terms of an equivalent circuit (Fig. 8) containing the uncompensated resistance, the interfacial capacitance, and a series RC circuit for the faradaic current component. Laviron has derived expressions for the adsorption resistance R_A and adsorption capacitance C_A, assuming that α is 0.5 [217]. At $\eta = 0$ V, the expressions are particularly simple (Eqs 12 and 13):

$$R_A = 2RT/(nFQ_{tot}k^0) \qquad (12)$$

$$C_A = Q_{tot}/(4RT/nF) \qquad (13)$$

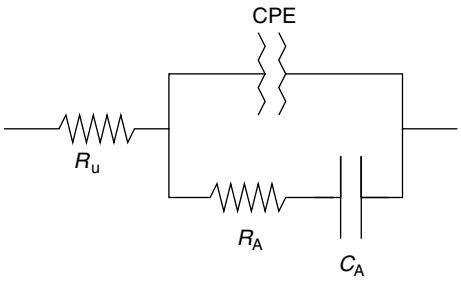


Fig. 8 Equivalent circuit for an electroactive SAM. R_u is the uncompensated resistance, CPE is the constant phase element, R_A is the adsorption resistance and C_A is the adsorption capacitance.

Hence, k^0 equals $1/(2R_AC_A)$. Problems arise from this method because accurate fitting of the four-element equivalent circuit requires measurements versus frequency over many orders of magnitude. Over this wide frequency range, the interfacial capacitance element behaves not as a pure capacitance but as a constant phase element (CPE) [218]. ACV offers a solution to this problem. The DC potential is scanned or stepped over a sufficiently wide range ($E^{0\prime} \pm 0.3$ V) while a small AC potential of fixed frequency is applied. The in-phase and out-of-phase AC current components are measured as a function of the DC potential. The total impedance (ratio of the applied potential to the complex current) is corrected for R_u (obtained by high-frequency ACIS) and converted to the interfacial admittance. The nonfaradaic (CPE) admittance is extrapolated from the potential wings, where faradaic admittance is negligible, and subtracted to obtain the faradaic admittance versus DC potential. The faradaic admittance is fitted to Laviron's equations to obtain k^0 [217]. Alternately, the cotangent of the phase of the faradaic admittance at $\eta = 0$ V versus the radial frequency $\omega(=2\pi f)$ is plotted. The plot should be linear with a slope of $1/(2k^0)$. Creager has proposed a variation of ACV in which the ratio of the total AC at $\eta = 0$ V to the nonfaradaic total current is plotted against $\log(f)$ and the data fitted to Laviron's equations [219]. This method is especially useful when the coverage of the redox centers on SAM is low and signal to noise is a problem. AC electroreflectance spectroscopy is similar to ACIS and ACV (DC + AC applied potential) but with a twist. A monochromatic beam of light is reflected from the electrode and the in-phase and out-of-phase AC components of the reflected light intensity are measured. If there is a large difference in absorptivity for the two oxidation states of the attached redox molecules, and if electrochromic effects (changes in interfacial optical constants versus potential) are negligible, then the analyses analogous to those in the preceding discussion yield k^0 [132, 133, 164, 169, 170, 174, 175, 220–225].

For electrodes with areas on the order of square millimeters to square centimeters, the upper limit for k^0 values measured by purely electrochemical methods is in the order of 10^4 to 10^5 s^{-1}, principally because of errors introduced by the uncertainty in the uncompensated resistance. Measurements of standard rate constants up to 10^7 s^{-1} are possible on ultramicroelectrodes [104].

The ILIT method [95, 102, 105, 106, 226] requires a short laser pulse to heat the electrode/SAM/electrolyte interface extremely rapidly. The open-circuit potential change versus time can be modeled to extract k^0. This method is best for extremely large standard rate constants (10^4–10^7 s^{-1}).

For SAMs with attached redox molecules, only CA and CV methods have been used to obtain k at large η. In the CA method, the electrode potential is customarily stepped from an initial potential either well positive (all redox molecules initially oxidized) or well negative (all redox molecules initially reduced) to a final potential and the current is recorded until the current transient has decayed to zero. Because large currents arise during the transient, it is often necessary to correct the applied potential for the iR drop to obtain the true overpotential via Eq. (14).

$$\eta(t) = E_{appl}(t) - E^{0\prime} - i(t)R_u \qquad (14)$$

The faradaic current at any time is related to the instantaneous rate constant

via Eq. (15):

$$i_f(t) = k(t)(Q(t) - Q_{\text{Nernst}}(t)) \qquad (15)$$

where $k(t)$ is the sum of the cathodic and anodic rate constants for overpotential $\eta(t)$, $Q(t)$ is the charge corresponding to the amount of reactant redox molecules (oxidized or reduced form) remaining (Eq. 16) and $Q_{\text{Nernst}}(t)$ is the charge which should remain if the redox molecules were in equilibrium with the instantaneous overpotential (Eq. 17):

$$Q(t) = Q_{\text{tot}} - \int_0^t i_f(t)\mathrm{d}t \qquad (16)$$

$$Q_{\text{Nernst}}(t) = Q_{\text{tot}}(1/(1 + \exp(nF\eta(t)/RT))) \text{ (reduced form) or}$$

$$Q_{\text{tot}}(\exp(nF\eta(t)/RT)/(1 + \exp(nF\eta(t)/RT))) \text{ (oxidized form)} \qquad (17)$$

These equations are valid for any overpotential. Consequently, k^0 can be determined by stepping to $E^{0\prime}$. If $\eta(t)$ is more than 120/n mV beyond $E^{0\prime}$, then $Q_{\text{Nernst}}(t)$ is essentially zero. $k(t)$ is calculated from Eq. (15) and is paired with the corresponding $\eta(t)$ from Eq. (14). The principal difficulty is the isolation of the faradaic current transient from the total current transient, which includes the charging current transient. To the extent that the SAM-coated electrode behaves like the equivalent circuit in Fig. 8, the current transient will consist of approximately two exponential decays with time constants of $\tau_c(=R_uC_i)$ for the charging current and $\tau_f(=k(t)^{-1})$ for the faradaic current. If τ_c is substantially smaller than τ_f, it is convenient to wait for the charging current transient to decay to negligible values before analyzing the remaining faradaic current. If the iR drop is negligible and $Q_{\text{Nernst}}(t)$ is zero, then the true overpotential and rate constant are independent of time and the current transient is a simple exponential decay:

$$i_{\text{far}}(t) = kQ_{\text{tot}}\exp(-kt) \qquad (18)$$

The analysis of the faradaic and charging current components requires the simulation of differential equations when the two time constants become similar and when the interfacial ''capacitance'' exhibits CPE character [104].

CV offers a more convenient approach for isolating the faradaic current from the charging current. With the usual assumptions (negligible double-layer effects, densely packed SAM), the interfacial capacitance (or CPE) is essentially independent of the potential at any given scan rate (see Fig. 7). Linear extrapolation of the charging current underneath the current peak and its subtraction yields the faradaic current transient. Equations (14–17) can be used to obtain $k(t)$ as a function of $\eta(t)$. Since the faradaic current transient covers a range of potentials in the order of 0.2 to 0.5 V (Fig. 7), depending on the sweep rate and kinetics, it is possible, in principal, to obtain Tafel plot data over a considerable overpotential range with one single CV.

As noted earlier, working curves have been calculated for the peak potential as a function of the scan rate, standard rate constant, and reorganization energy [204, 215, 216]. Fitting experimental peak potentials versus $\log(\nu)$ to the working curves yields both k^0 and λ. This approach requires that the iR drop be negligible at all scan rates. Several factors (iR drop, double-layer effects) that can complicate the measurement of rate constants have already been discussed. An additional complicating factor, kinetic heterogeneity, is apparent in many kinetic measurements on electroactive SAMs [78, 81, 83, 115, 216, 227].

Kinetic heterogeneity is defined as a spread of rate constants for the redox molecules on a SAM at a given overpotential. It appears as deviations in the measurements or in the Tafel plots from the expected behavior. In CA experiments, plots of $\ln(i)$ versus t are curved instead of being linear (Eq. 18 predicts a linear plot). In AC experiments, plots of the cotangent of the faradaic phase angle versus radial frequency at $\eta = 0$ V are curved and those of peak-to-background AC current ratios versus log frequency are broadened [228]. In CV experiments, rate constants at a given overpotential vary with the scan rate that is used to acquire the CV. The observed trend is that, for a given overpotential, rate constants obtained at shorter times or higher frequencies are higher than rate constants obtained at longer times or lower frequencies. Electron transfer with the kinetically faster redox molecules dominates the current at shorter times or higher frequencies, whereas that with the kinetically slower redox molecules control the current at longer times or lower frequencies.

There are several possible sources for kinetic heterogeneity [227]. First, thermodynamic heterogeneity, a spread of formal potentials, would result in nonuniform overpotentials for the redox molecules at a given applied potential. Thermodynamic heterogeneity can arise from redox molecules confined to somewhat different chemical environments on the electrode with the timescale for interconversion being long compared to the experimental timescale. This situation can sometimes be detected by a CV under reversible conditions; the peak halfwidth is broader than the theoretical 3.53 RT/nF or 91 mV/n at room temperature. However, even thermodynamically homogeneous electroactive SAMs can exhibit kinetic heterogeneity. Because kinetic measurements occur at much shorter timescales than reversible measurements, configurations in the SAM or the redox molecule that rapidly interconvert during the reversible measurement may be ''frozen'' during the kinetic measurement. This condition would result in a variation of the electronic coupling $|V|^2$ and/or differences in the reorganization energy for different redox molecules.

Methods for assessing the degree of kinetic heterogeneity are based on measuring the kinetics of a subset of the entire ensemble of redox centers. In CA and CV experiments, $k(t)$ and $\eta(t)$ data pairs are obtained for a fixed fraction of the remaining reactant redox centers ($Q(t)/Q_{\text{tot}}$; see Eq. 16). Tafel plots are generated and fitted to the theory for each fixed fraction (or percentage) [83, 116, 117, 229]. In ACIS or ACV experiments, the standard rate constant is measured at a fixed phase angle for the faradaic peak admittance. Simulations of kinetic heterogeneity suggest that the working curves of peak potential versus $\log(\nu)$ yield an average rate constant regardless of the degree of heterogeneity [215].

8.6 Electronic Coupling versus Distance

There is considerable interest in understanding the factors that control long-range (>10 Å) electron transfer, especially in proteins [230] and DNA [231]. The alkanethiol SAMs offer an excellent means of controlling the spacing between a redox molecule and the metal electrode with a spatial resolution of approximately 1 Å (corresponding to the insertion of one methylene in the alkyl chain). Standard rate constants versus number of methylenes m have been measured for alkanethiol SAMs on gold

with a number of attached redox centers in aqueous electrolytes: ferrocene [45, 69, 95, 98, 104, 105], pyRu$(NH_3)_5$ [105, 115, 229], cytochrome *c* [170, 183, 184, 186, 232], and azurin [190]. A semilog plot of some of the results is shown in Fig. 9. For the longer chain lengths, k^0 values were obtained by CA and CV experiments, while values for the shorter chain lengths were obtained mainly by AC methods and the ILIT method. The slopes of the plots yield β_m, the tunneling parameter. Experimental values of β_m fall in the range of 1.0–1.2 per methylene, independent of the attached redox molecule. Values of β_m for blocking alkanethiol SAMs and freely diffusing redox centers are also 1.1 per methylene, independent of the redox molecule and nearly independent of the electrode potential [20, 23]. These values of the tunneling parameter are in good agreement with the theoretical prediction for through-bond tunneling [233] and are substantially less than the predictions for through-space tunneling [115]; hence, through-bond tunneling (also called the *superexchange mechanism*) is considered to be the correct mechanism for electron transfer. One might expect a different β_m in nonaqueous electrolytes, since the SAM alkane chains tend to become less densely packed and more solvated. However, a β_m of 1.1 per methylene was obtained in a cryogenic mixture of chloroethane and butyronitrile [55]. The conversion of β_m to β_r requires assumptions about the orientation of the SAM. On Au(111), the alkanethiol chains are in an all-trans conformation with the axis of the chain tilted 30° from the normal. From known C–C bond lengths and geometry, β_r is calculated to be 1.0–1.2 $Å^{-1}$.

The preceding analysis assumed a constant reorganization energy with distance for the chain lengths in question. As the redox center gets closer to the metal electrode, image charge interactions should result in a decrease

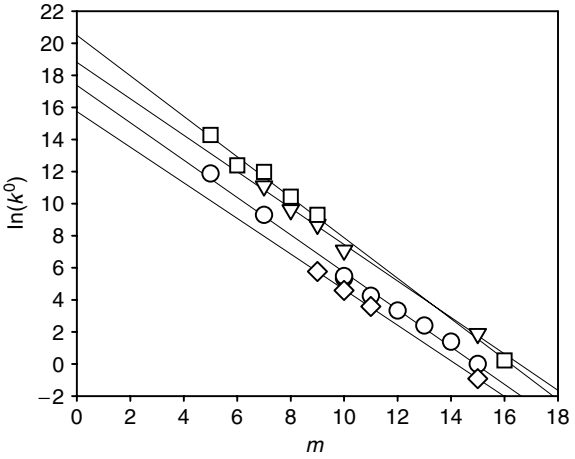


Fig. 9 Semilog plot of k^0 versus alkane chain length *m* for different redox molecules. Data are shown for ferrocene (squares and inverted triangles), pyRu$(NH_3)_5$ (circles), and cytochrome *c* (diamonds). Linear regression lines for each redox molecule are shown.

in the reorganization energy. For chain lengths greater than 1 nm, the measured reorganization energies are nearly constant, in agreement with theory, so the values of β_m from standard rate constants are valid. Reorganization energies for ferrocenes and pyRu$(NH_3)_5$ are significantly lower than those predicted at shorter chain lengths, for reasons that are not clear yet [105]. Also, at chain lengths shorter than 1 nm, the electronic coupling term (Eq. 14) appears to reach a limiting value of 10^{-10} s^{-1}, at least an order of magnitude lower than that predicted by contemporary theories of electron transfer [105].

Kinetic measurements of cytochrome *c* electrostatically adsorbed onto ω-carboxylalkanethiol SAMs are affected by the ionic strength, pH, and viscosity of the electrolyte, and, at shorter chain lengths, exhibit a limiting k^0 on the order of 10^3 s^{-1} in 10 mM phosphate buffer [170, 186]. A similar limiting standard rate constant is observed for azurin adsorbed on mixed methyl- and hydroxyl-terminated SAMs [190]. This phenomenon is attributed to kinetic limitation by a chemical step, a ''configurational rearrangement'' involving the reorientation of the adsorbed protein on the SAM, before the electron-transfer step. However, a limiting standard rate constant is also observed for cytochrome *c* linked by the coordination of a terminal pyridine on the SAM to the heme site [183, 184]. The limiting kinetics are more likely to be due to changes in the internal structure of the protein (polarization relaxation) combined with changes in the local solvent structure prior to electron transfer.

Several other repeating units in a SAM have been investigated to date, with ferrocene as the pendant redox center. The phenyl–ethynyl group possesses both rigidity and extended π conjugation and might be expected to electronically couple the electrode and the redox molecule more effectively than an alkane chain. This is indeed the case; β_r for HS-(*p*-phenyl−C≡C-)$_m$ is approximately 0.3 $Å^{-1}$, substantially less that the 0.9–1.0 $Å^{-1}$ observed for linear alkanes [88, 106, 107]. However, the plot of $\ln(k^0)$ or $\ln(|V|)$ versus distance is nonmonotonic and sensitive to side chains on the phenyls, suggesting that conformation variations (e.g. angle of rotation of the phenyls with respect to each other) between different numbers of repeat units may be controlling the observed rate to a large degree. The phenyl–vinyl group avoids rotational freedom of the phenyls and forces the extended π system to be aligned over the length of the linker. SAMs with up to five repeat – (*p*-phenyl−C=C-) units exhibit larger standard rate constants than any other linker, but the plot of $\ln(|V|)$ versus distance appears to approach a saturation value of 10^{11} s^{-1} at the shorter lengths [102, 103, 106]. The source of the rate constant saturation and the different saturation values for linear alkanes and conjugated π systems is a subject of investigation now. Finally, there is one study of electron-transfer kinetics through SAMs containing two to six oligoglycine units [49]. For linkers containing two to four glycines, the standard rate constants and the β value of 1.0 per atom were very similar to the corresponding values for linear alkanes. A smaller β value was observed for linkers with five and six glycines.

A related system worthy of mention is a SAM based on DNA double-helical oligomers [231, 234, 235]. The standard rate constant for an anthraquinone derivative (daunomycin) intercalated at known positions along the double helix is found to be independent of the intercalation site

and of breaks in the sugar-phosphate backbone. These observations indicate that β_r is quite small ($\approx$0.1 Å^{-1}) and support the hypothesis that long-range electron transfer along stacked base pairs in a DNA helix can be remarkably efficient.

8.7 Electronic Coupling versus Other Factors

Besides distance (number of repeat units), a number of other factors affecting the electronic coupling between the metal and redox couple have been investigated.

Tafel plots for a single type of SAM with pendant pyRu(NH_3)$_5$ redox molecules have been acquired using gold, platinum, and silver electrodes [236]. The reorganization energies are independent of the metal. The standard rate constant for the Pt and Ag electrodes are 1.7 and 0.6, respectively, relative to the standard rate constant for gold. The DOS $\rho(\varepsilon)$ for Pt is about 7.5 times higher than that of Au because of the ''d'' band states near the Fermi energy in Pt. The small increase in the standard rate constant for Pt is consistent with the theoretical prediction that ''d'' band states couple very weakly across a SAM and that the electronic coupling is dominated by the ''sp'' states [202].

In some systems, electronic coupling is affected by the nature and length of the diluent thiol in the SAM. The tunneling parameter $\beta_m = 0.8/CH_2$ has been measured using mixed SAMs containing an electroactive thiol (pyRu(NH_3)$_5$ redox molecule) of fixed length ($m = 15$) and diluent thiols of progressively shorter lengths ($m = 10–15$) [229]. This value is nearly the same as that determined as a function of the number of methylenes in the tether connecting the redox center to the metal. This observation suggests that electronic coupling can occur efficiently via alkane chains that are not covalently attached to the redox molecule.

Similarly, the total electronic coupling can proceed via electronic coupling between adjacent alkane chains [237]. Tunneling currents across perfectly blocking alkanethiol SAMs on mercury increase when the mercury drop is expanded [25, 26]. Expanding the drop causes the SAM to become thinner via increasing tilt of the alkane chains. If the electronic coupling proceeds along a single chain, then the increasing tilt and introduction of gauche conformations in the chain should result in a decrease in the through-bond electronic coupling. Consequently, a SAM with highly tilted alkane chains allows the optimum ''path'' of electronic coupling to jump from one chain to an adjacent one.

Introduction of an oxygen, double or triple bond in the alkane chain of the SAM causes a decrease in the total electronic coupling [112, 211]. Replacing two methylenes with an amide link in the tether causes no significant change in the electronic coupling of a ferrocene with a gold electrode if the substitution is near the ferrocene [69]. However, SAMs containing buried amide bonds exhibit an increase in electronic coupling relative to alkanethiol SAMs with the same length [48, 109]. Intermolecular hydrogen bonding among the adjacent amide bonds is identified to be the source of the increased electronic coupling. The rate of electron transfer to ferrocenes with a 1,4-phenyl ring in the bridge is an order of magnitude greater than that of ferrocenes with a 1,3-phenyl ring, indicating the importance of topology in electronic coupling [70].

8.8 Reorganization Energies

In the Marcus DOS model, the total reorganization energy is the sum of the inner-sphere (internal vibrations) and outer-sphere (solvent molecules) components (Eq. 19):

$$\lambda = \lambda_{is} + \lambda_{os} \tag{19}$$

The inner-sphere λ can be calculated from the measured force constants of the redox molecule in each oxidation state. It is possible to have distinctly different λ_{is} values for each oxidation state. The outer sphere λ for heterogeneous electron transfer can be estimated from the dielectric continuum theory (Eq. 20) [238]:

$$\lambda_{os} = (\Delta e)^2(1/D_{op} - 1/D_s)(1/(2a) - 1/(2r)) \tag{20}$$

where Δe is change in the charge of the redox molecule, D_{op} and D_s are the optical and static dielectric constants of the electrolyte, and a is the (mean) radius of the redox molecule. Consequently, λ_{os} is the same for the oxidation and reduction steps in simple electron-transfer reactions. Several predictions can be made from Eq. (20). An increase in the size of the redox molecule or a decrease in the distance between the redox molecule and the electrode causes a decrease in λ_{os}. As the solvent of the electrolyte is changed from highly polar to weakly polar, the static dielectric constant approaches the optical dielectric constant and λ_{os} decreases again.

Table 1 contains predictions of reorganization energies of selected redox molecules in water at a distance of 2 nm. All the redox couples have small changes in bond lengths with oxidation state, and are therefore expected to have a small λ_{is}($\approx$0.05 eV); the values in Table 1 are based on Eq. (20). These values can be considered to be nearly independent of temperature in the 0–50 °C range [99]. A more sophisticated calculation of λ (which includes the effect of the SAM and of image charges in the metal) predicts a smaller value of 0.93 eV for ferrocene at infinite distance, dropping to 0.87 eV at 20 Å from the electrode and rapidly decreasing at shorter distances [239].

Tab. 1 Reorganization energies (λ) of selected redox centers

Redox centers	*Theoretical λ[eV]*[a]	*Measured λ[eV]*[b]
Ferrocene$^{+/0}$	0.95	0.9
pyRu$(NH_3)_5^{3+/2+}$	0.95	0.9
$Fe(CN)_6^{3-/4-}$	0.95	1.0
Fe(bpy)$(CN)_4^{-/2-}$	0.80	1.0
Fe$(bpy)_2(CN)_2^{+/0}$	0.65	0.8
Fe$(bpy)_3^{3+/2+}$	0.55	0.55

[a] Estimates of the theoretical reorganization energies of redox centers in water at 2-nm separation from a metal electrode, based on Eq. (20).
[b] Measured by fitting Tafel or Arrhenius data to the Marcus model for alkanethiol SAMs with 14–18 methylenes. Uncertainty is typically $\pm$0.1 eV.
py: pyridine, bpy: 2,2'-bipyridine.

Table 1 also includes the typical measured reorganization energies for selected redox molecules blocked by SAMs or attached to SAMs in aqueous electrolytes. The outer-sphere reorganization energy dominates the total reorganization energy for most of the examined redox molecules. The agreement between the measured and the theoretical values from Eq. (20) is quite good. Measured reorganization energies are independent of the composition of the connecting chain or the SAM as long as the redox center is well exposed to the electrolyte and is at a distance greater

than 1 nm. As noted in the earlier discussion, the reorganization energy appears to decrease more rapidly than expected at distances of less than 1 nm [105]. For ferrocenes and pyRu$(NH_3)_5$, symmetrical Tafel plots are expected, and are, in fact, generally observed. Similarly, anodic and cathodic peak potentials in CVs are found to shift equally with respect to the formal potential. Reports of asymmetry in the anodic and cathodic rate constants at a given magnitude of overpotential have been attributed to ion pairing for a relatively thick alkanethiol SAM [22] or to a large dipole moment in a oligoalanine linker [111].

8.9 Future Directions

The preceding discussion illustrates the versatility of electroactive SAMs for addressing fundamental issues in electron-transfer kinetics. So far, an extended kinetic analysis with comparison to theory has been applied only to simple one-electron-transfer redox molecules. Clearly, there is an opportunity to study more complex redox systems. For example, a triruthenium cluster bound to a SAM exhibits multiple oxidation states and the reversible binding and release of CO [240]. Another area deserving more quantitative work is electrocatalysis in which the attached redox molecule mediates the electron transfer between a solution redox molecule and the electrode.

The kinetics of proton-coupled electron transfer is an area that is ready for exploitation using redox couples attached to SAMs. There are sporadic reports of kinetic measurements on attached redox molecules with relatively complex two-electron, two-proton (2e2H) mechanisms: quinones [127, 136, 149, 241, 242] and azobenzenes [243–246]. The standard rate constant for attached quinones decreases substantially as the electrolyte pH is made more acidic [148] while that for attached azobenzenes exhibits a minimum at pH 6–7 [244]. The tunneling parameter β_m has been measured for attached quinones ($\beta_m = 1.04$ per CH_2 at pH 4.0, $m = 1$, 4, 6, 8, 10, 12) [242] and azobenzenes ($\beta_m = 1.3 \pm 0.2$ per CH_2 at pH 5.2, $m = 2$, 4, 6) [245]. Electron-transfer kinetics for the azobenzene redox molecule are remarkably sluggish. An azobenzene redox molecule with a spacer of only two methylene units exhibits a standard rate constant in the order of 10^{-5} s^{-1}, while a spacer of six methylene units drops k^0 below 10^{-7} s^{-1} [245]. These slow kinetics arise in part from a large λ_{is} and in part from steric hindrance to a significant change in molecular structure [247].

Two 1e1H redox systems have been attached to SAMs, and full studies of the kinetics as a function of electrolyte pH have been performed [248–250]. The data were compared to the predictions of the stepwise mechanism. In this mechanism, electron and proton transfers are separate steps and proton transfer is treated as an equilibrium [251, 252]. With the inclusion of a potential-dependent transfer coefficient [253], two testable predictions can be made. A plot of $\log(k^0)$ versus pH has a V shape, and a plot of $\alpha(0)$ (the transfer coefficient at the formal potential) versus pH oscillates about 0.5. These predictions are consistent with kinetic data collected for a SAM with an attached galvinol (a phenol-like redox molecule) at pHs greater than 8 [248, 249]. However, the data obtained for an osmium complex ([$Os^{III/II}$(bpy)2(py)(L)], L = OH or H_2O) deviate substantially from the predictions. The plot of $\ln(k^0)$ versus pH is much less dependent on pH than expected, and the

plot of $\alpha(0)$ versus pH hovers around a value of 0.46. Currently, these results are being interpreted in terms of a concerted mechanism in which the proton and electron are transferred in the same step.

There are numerous reports of the existence of electrocatalysis via an attached redox center on a SAM (see Sect. 4.3), but few reports in which the rates of electron transfer between the electrode and the attached redox molecule and between the attached redox molecule and the solution redox molecule are measured. It would be interesting to study the electron-transfer kinetics in SAMs with multiple redox molecules linked along a single tether (such as porphyrins [157] or metal–terpyridine complexes) [122]. From such a system, one could derive the rate of electron transfer between two redox molecules connected by a molecular bridge and check the considerable data available on intramolecular transfer obtained by other methods [254]. For a variety of applications, measurements of the rates of electron transfer between an electrode and metal nanoparticles tethered to the SAM are also of interest [255].

References

1. A. R. Bishop, R. G. Nuzzo, *Colloid Interface Sci.* **1996**, *1*, 127–136.
2. L. H. Dubois, R. G. Nuzzo, *Annu. Rev. Phys. Chem.* **1992**, *43*, 437–463.
3. Th. Wink, S. J. van Suilen, A. Bult et al., *Analyst* **1997**, *122*, 43R–50R.
4. C.-J. Zhong, M. D. Porter, *Anal. Chem.* **1995**, *67*, 709A–715A.
5. A. Ulman, *An Introduction to Ultrathin Organic Films*, Academic Press, New York, 1991.
6. G. M. Whitesides, P. E. Laibinis, *Langmuir* **1990**, *6*, 87–96.
7. H. O. Finklea, *Electroanal. Chem.* **1996**, *19*, 109–335.
8. G. K. Jennings, P. E. Laibinis, *Langmuir* **1996**, *12*, 6173–6175.
9. G. K. Jennings, P. E. Laibinis, *J. Am. Chem. Soc.* **1997**, *119*, 5208–5214.
10. E. Sabatani, I. Rubinstein, *J. Phys. Chem.* **1987**, *91*, 6663–6669.
11. H. O. Finklea, D. A. Snider, J. Fedyk et al., *Langmuir* **1993**, *9*, 3660–3667.
12. L. Sun, R. M. Crooks, *J. Electrochem. Soc.* **1991**, *138*, L23–L25.
13. L. Sun, R. M. Crooks, *Langmuir* **1993**, *9*, 1951–1954.
14. F. P. Zamborini, R. M. Crooks, *Langmuir* **1997**, *13*, 122–126.
15. X. Cui, D. Jiang, P. Diao et al., *J. Electroanal. Chem.* **1999**, *470*, 9–13.
16. H. O. Finklea, D. A. Snider, J. Fedyk, *Langmuir* **1990**, *6*, 371–376.
17. J. Xu, H.-L. Li, Y. Zhang, *J. Phys. Chem.* **1993**, *97*, 11497–11500.
18. C. Miller, M. Gratzel, *J. Phys. Chem.* **1991**, *95*, 5225–5233.
19. C. Miller, P. Cuendet, M. Gratzel, *J. Phys. Chem.* **1991**, *95*, 877–886.
20. A. M. Becka, C. J. Miller, *J. Phys. Chem.* **1992**, *96*, 2657–2668.
21. A. M. Becka, C. J. Miller, *J. Phys. Chem.* **1993**, *97*, 6233–6239.
22. S. Terrettaz, A. M. Becka, M. J. Traub et al., *J. Phys. Chem.* **1995**, *99*, 11216–11224.
23. D. E. Khoshtariya, T. D. Dolidze, L. D. Zusman et al., *J. Phys. Chem. A* **2001**, *105*, 1818–1829.
24. A. Demoz, D. J. Harrison, *Langmuir* **1993**, *9*, 1046–1050.
25. K. Slowinski, R. V. Chamberlain, R. Bilewicz et al., *J. Am. Chem. Soc.* **1996**, *118*, 4709–4710.
26. K. Slowinski, R. V. Chamberlain, C. J. Miller et al., *J. Am. Chem. Soc.* **1997**, *119*, 11910–11919.
27. K. Slowinski, K. U. Slowinska, M. Majda, *J. Phys. Chem. B* **1999**, *103*, 8544–8551.
28. O. Chailapakul, R. M. Crooks, *Langmuir* **1993**, *9*, 884–888.
29. O. Chailapakul, R. M. Crooks, *Langmuir* **1995**, *11*, 1329–1340.
30. R. Bilewicz, T. Sawaguchi, R. V. Chamberlain II et al., *Langmuir* **1995**, *11*, 2256–2266.
31. K. Slowinski, R. Bilewicz, M. Majda, *Chem. Anal. (Warsaw)* **1995**, *40*, 329–339.
32. A. E. Kaifer, *Isr. J. Chem.* **1996**, *36*, 389–397.
33. M. T. Rojas, R. Königer, J. F. Stoddart et al., *J. Am. Chem. Soc.* **1995**, *117*, 336–343.
34. M. T. Rojas, A. E. Kaifer, *J. Am. Chem. Soc.* **1995**, *117*, 5883–5884.

35. I. Rubinstein, S. Steinberg, Y. Tor et al., *Nature* **1988**, *332*, 426–429.
36. S. Steinberg, Y. Tor, E. Sabatani et al., *J. Am. Chem. Soc.* **1991**, *113*, 5176–5182.
37. S. Steinberg, I. Rubinstein, *Langmuir* **1992**, *8*, 1183–1187.
38. S. Steinberg, Y. Tor, A. Shanzer, in *Organic Thin Films and Surfaces* (Ed.: A. Ulman), Academic Press, New York, 1995, pp. 183–205.
39. K. Takehara, H. Takemura, Y. Ide, *Electrochim. Acta* **1994**, *39*, 817–822.
40. F. Malem, D. Mandler, *Anal. Chem.* **1993**, *65*, 37–41.
41. I. Turyan, D. Mandler, *Anal. Chem.* **1994**, *66*, 58–63.
42. I. Turyan, D. Mandler, *Anal. Chem.* **1997**, *69*, 894–897.
43. N. Nakashima, T. Taguchi, Y. Takada et al., *J. Chem. Soc., Chem. Commun.* **1991**, 232–233.
44. C. E. D. Chidsey, C. R. Bertozzi, T. M. Putvinski et al., *J. Am. Chem. Soc.* **1990**, *112*, 4301–4306.
45. C. E. D. Chidsey, *Science* **1991**, *251*, 919–922.
46. H. O. Finklea, D. D. Hanshew, *J. Electroanal. Chem.* **1993**, *347*, 327–340.
47. J. P. Collman, N. K. Devaraj, C. E. D. Chidsey, *Langmuir* **2004**, *20*, 1051–1053.
48. S. Sek, A. Misicka, R. Bilewicz, *J. Phys. Chem. B* **2000**, *104*, 5399–5402.
49. S. Sek, A. Sepiol, A. Tolak et al., *J. Phys. Chem. B* **2004**, *108*, 8102–8105.
50. E. Tran, M. A. Rampi, G. M. Whitesides, *Angew. Chem., Int. Ed. Engl.* **2004**, *43*, 3835–3839.
51. S. W. Feldberg, I. Rubinstein, *J. Electroanal. Chem.* **1988**, *240*, 1–15.
52. C. P. Smith, H. S. White, *Anal. Chem.* **1992**, *64*, 2398–2405.
53. J. J. Sumner, S. E. Creager, *J. Phys. Chem. B* **2001**, *105*, 8739–8745.
54. W. B. Caldwell, K. Chen, B. R. Herr et al., *Langmuir* **1994**, *10*, 4109–4115.
55. M. T. Carter, G. K. Rowe, J. N. Richardson et al., *J. Am. Chem. Soc.* **1995**, *117*, 2896–2899.
56. O. Clot, M. O. Wolf, *Langmuir* **1999**, *15*, 8549–8551.
57. S. E. Creager, G. K. Rowe, *Langmuir* **1993**, *9*, 2330–2336.
58. S. E. Creager, G. K. Rowe, *J. Electroanal. Chem.* **1994**, *370*, 203–211.
59. H. C. De Long, J. J. Donohue, D. A. Buttry, *Langmuir* **1991**, *7*, 2196–2202.
60. T. J. Gardner, C. D. Frisbie, M. S. Wrighton, *J. Am. Chem. Soc.* **1995**, *117*, 6927–6933.
61. J.-B. D. Green, M. T. McDermott, M. D. Porter, *J. Phys. Chem.* **1996**, *100*, 13342–13345.
62. L.-H. Guo, J. S. Facci, G. McLendon, *J. Phys. Chem.* **1995**, *99*, 8458–8861.
63. Z. He, S. Bhattacharyya, W. E. Cleland et al., *J. Electroanal. Chem.* **1995**, *397*, 305–310.
64. B. R. Herr, C. A. Mirkin, *J. Am. Chem. Soc.* **1994**, *116*, 1157–1158.
65. J. J. Hickman, D. Ofer, C. Zou et al., *J. Am. Chem. Soc.* **1991**, *113*, 1128–1132.
66. K. S. Alleman, K. Weber, S. E. Creager, *J. Phys. Chem.* **1996**, *100*, 17050–17058.
67. L. A. Hockett, S. E. Creager, *Langmuir* **1995**, *11*, 2318–2321.
68. K. Hu, Z. Chai, J. K. Whitesell et al., *Langmuir* **1999**, *15*, 3343–3347.
69. J. J. Sumner, K. S. Weber, L. A. Hockett et al., *J. Phys. Chem. B* **2000**, *104*, 7449–7454.
70. J. J. Sumner, S. E. Creager, *J. Am. Chem. Soc.* **2000**, *122*, 11914–11920.
71. R. S. Ingram, R. W. Murray, *J. Chem. Soc., Faraday Trans.* **1996**, *92*, 3941–3946.
72. H. Ju, D. Leech, *Langmuir* **1998**, *14*, 300–306.
73. T. Kondo, M. Takechi, Y. Sato et al., *J. Electroanal. Chem.* **1995**, *381*, 203–209.
74. M. C. Leavy, S. Bhattacharyya, W. E. Cleland et al., *Langmuir* **1999**, *15*, 6582–6586.
75. A. Niemz, E. Jeoung, A. K. Boal et al., *Langmuir* **2000**, *16*, 1460–1462.
76. S. D. O'Connor, G. T. Olsen, S. E. Creager, *J. Electroanal. Chem.* **1999**, *466*, 197–202.
77. T. Ohtsuka, Y. Sato, K. Uosaki, *Langmuir* **1994**, *10*, 3658–3662.
78. S. R. Peck, L. S. Curtin, L. M. Tender et al., *J. Am. Chem. Soc.* **1995**, *117*, 1121–1126.
79. D. D. Popenoe, R. S. Deinhammer, M. D. Porter, *Langmuir* **1992**, *8*, 2521–2530.
80. J. Redepenning, J. M. Flood, *Langmuir* **1996**, *12*, 508–512.
81. L. S. Curtin, S. R. Peck, L. M. Tender et al., *Anal. Chem.* **1993**, *65*, 386–392.
82. J. N. Richardson, G. K. Rowe, M. T. Carter et al., *Electrochim. Acta* **1995**, *40*, 1331–1338.
83. J. N. Richardson, S. R. Peck, L. S. Curtin et al., *J. Phys. Chem.* **1995**, *99*, 766–772.

84. G. K. Rowe, S. E. Creager, *J. Phys. Chem.* **1994**, *98*, 5500–5507.
85. S. Rubin, J. T. Chow, J. P. Ferraris et al., *Langmuir* **1996**, *12*, 363–370.
86. R. C. Sabapathy, S. Bhattacharyya, W. E. Cleland et al., *Langmuir* **1998**, *14*, 3797–3807.
87. R. C. Sabapathy, S. Bhattacharyya, M. C. Leavy et al., *Langmuir* **1998**, *14*, 124–136.
88. S. B. Sachs, S. P. Dudek, R. P. Hsung et al., *J. Am. Chem. Soc.* **1997**, *119*, 10563–10564.
89. Y. Sato, H. Itoigawa, K. Uosaki, *Bull. Chem. Soc. Jpn.* **1993**, *66*, 1032–1037.
90. Y. Sato, K. Uosaki, in *Redox Mechanisms and Interfacial Properties of Molecules of Biological Importance* (Eds.: F. A. Schultz, I. Taniguchi), The Electrochemical Society, Pennington, 1993, pp. 299–311.
91. Y. Sato, B. L. Frey, R. M. Corn et al., *Bull. Chem. Soc. Jpn.* **1994**, *67*, 21–25.
92. Y. Sato, F. Mizutani, K. Shimazu et al., *J. Electroanal. Chem.* **1999**, *474*, 94–99.
93. K. Shimazu, I. Yagi, Y. Sato et al., *J. Electroanal. Chem.* **1994**, *372*, 117–124.
94. K. Shimazu, Y. Sato, I. Yagi et al., *Bull. Chem. Soc. Jpn.* **1994**, *67*, 863–865.
95. J. F. Smalley, S. W. Feldberg, C. E. D. Chidsey et al., *J. Phys. Chem.* **1995**, *99*, 13141–13149.
96. J. A. M. Sondag-Huethorst, L. G. J. Fokkink, *Langmuir* **1994**, *10*, 4380–4387.
97. R. Voicu, T. H. Ellis, H. Ju et al., *Langmuir* **1999**, *15*, 8170–8177.
98. K. Weber, L. Hockett, S. Creager, *J. Phys. Chem. B* **1997**, *101*, 8286–8291.
99. K. S. Weber, S. E. Creager, *J. Electroanal. Chem.* **1998**, *458*, 17–22.
100. S. Ye, Y. Sato, K. Uosaki, *Langmuir* **1997**, *13*, 3157–3161.
101. L. Zhang, L. A. Godinez, T. Lu et al., *Angew. Chem., Int. Ed. Engl.* **1995**, *34*, 235–237.
102. H. D. Sikes, J. F. Smalley, S. P. Dudek et al., *Science* **2001**, *291*, 1519–1523.
103. S. P. Dudek, H. D. Sikes, C. E. D. Chidsey, *J. Am. Chem. Soc.* **2001**, *123*, 8033–8038.
104. D. B. Robinson, C. E. D. Chidsey, *J. Phys. Chem. B* **2002**, *106*, 10706–10713.
105. J. F. Smalley, H. O. Finklea, C. E. D. Chidsey et al., *J. Am. Chem. Soc.* **2003**, *125*, 2004–2013.
106. J. F. Smalley, S. B. Sachs, C. E. D. Chidsey et al., *J. Am. Chem. Soc.* **2004**, *126*, 14620–14630.
107. S. Creager, C. J. Yu, C. Bamdad et al., *J. Am. Chem. Soc.* **1999**, *121*, 1059–1064.
108. B. Liu, A. J. Bard, M. V. Mirkin et al., *J. Am. Chem. Soc.* **2004**, *126*, 1485–1492.
109. S. Sek, B. Palys, R. Bilewicz, *J. Phys. Chem. B* **2002**, *106*, 5907–5914.
110. S. Sek, E. Maicka, R. Bilewicz, *Electrochim. Acta* **2005**, *50*, 4857–4860.
111. S. Sek, A. Tolak, A. Misicka et al., *J. Phys. Chem. B* **2005**, *109*, 18433–18438.
112. A. M. Napper, H. Liu, D. H. Waldeck, *J. Phys. Chem. B* **2001**, *105*, 7699–7707.
113. K. Seo, I. C. Jeon, D. J. Yoo, *Langmuir* **2004**, *20*, 4147–4154.
114. H. O. Finklea, M. S. Ravenscroft, D. A. Snider, *Langmuir* **1993**, *9*, 223–227.
115. H. O. Finklea, D. D. Hanshew, *J. Am. Chem. Soc.* **1993**, *114*, 3173–3181.
116. H. O. Finklea, M. S. Ravenscroft, *Isr. J. Chem.* **1997**, *37*, 179–184.
117. M. S. Ravenscroft, H. O. Finklea, *J. Phys. Chem.* **1994**, *98*, 3843–3850.
118. J. Redepenning, H. M. Tunison, H. O. Finklea, *Langmuir* **1993**, *9*, 1404–1407.
119. E. Tran, C. Grave, G. M. Whitesides et al., *Electrochim. Acta* **2005**, *50*, 4850–4856.
120. Y. Sato, K. Uosaki, *J. Electroanal. Chem.* **1995**, *384*, 57–66.
121. C. Hortholary, F. Minc, C. Coudret et al., *Chem. Commun.* **2002**, 1932–1933.
122. M. Maskus, H. D. Abruna, *Langmuir* **1996**, *12*, 4455–4462.
123. H. C. De Long, D. A. Buttry, *Langmuir* **1990**, *6*, 1319–1322.
124. H. C. De Long, D. A. Buttry, *Langmuir* **1992**, *8*, 2491–2496.
125. S. Dong, J. Li, *Bioelectrochem. Bioenerg.* **1997**, *42*, 7–13.
126. E. Katz, N. Itzhak, I. Willner, *Langmuir* **1993**, *9*, 1392–1396.
127. E. Katz, I. Willner, *Langmuir* **1997**, *13*, 3364–3373.
128. J.-H. Kim, K. A. B. Lee, R. A. Uphaus et al., *Thin Solid Films* **1992**, *210*(211), 825–827.
129. K. A. B. Lee, *Langmuir* **1990**, *6*, 709–712.
130. J. Li, G. Cheng, S. Dong, *Thin Solid Films* **1997**, *293*, 200–205.
131. T. Sagara, H. Kawamura, K. Ezoe et al., *J. Electroanal. Chem.* **1998**, *445*, 171–177.
132. T. Sagara, N. Kaba, M. Komatsu et al., *Electrochim. Acta* **1998**, *43*, 2183–2193.
133. T. Sagara, H. Maeda, Y. Yuan et al., *Langmuir* **1999**, *15*, 3823–3830.

134. X. Tang, T. Schneider, D. A. Buttry, *Langmuir* **1994**, *10*, 2235–2240.
135. X. Tang, T. W. Schneider, J. W. Walker et al., *Langmuir* **1996**, *12*, 5921–5933.
136. A. Doron, M. Portnoy, M. Lion-Dagan et al., *J. Am. Chem. Soc.* **1996**, *118*, 8937–8944.
137. Z. He, S. Bhattacharyya, M. C. Leavy et al., *J. Electroanal. Chem.* **1998**, *458*, 7–16.
138. C. D. Hodneland, M. Mrksich, *Langmuir* **1997**, *13*, 6001–6003.
139. E. Katz, H.-L. Schmidt, *J. Electroanal. Chem.* **1993**, *360*, 337–342.
140. E. Katz, H.-L. Schmidt, *J. Electroanal. Chem.* **1994**, *368*, 87–94.
141. E. Y. Katz, V. V. Borovkov, R. P. Evstigneeva, *J. Electroanal. Chem.* **1992**, *326*, 197–212.
142. T. Kondo, M. Yanagida, S. Nomura et al., *J. Electroanal. Chem.* **1997**, *438*, 121–126.
143. E. Lorenzo, L. Sanchez, F. Pariente et al., *Anal. Chim. Acta* **1995**, *309*, 79–88.
144. J. Lukkari, M. Meretoja, I. Kartio et al., *Langmuir* **1999**, *15*, 3529–3537.
145. Y. Mo, M. Sandifer, C. Sukenik et al., *Langmuir* **1995**, *11*, 4626–4628.
146. Y. Sato, M. Fujita, F. Mizutani et al., *J. Electroanal. Chem.* **1996**, *409*, 145–154.
147. D. A. Shultz, G. N. Tew, *J. Org. Chem.* **1994**, *59*, 6159–6160.
148. A. G. Larsen, K. V. Gothelf, *Langmuir* **2005**, *21*, 1015–1021.
149. S. Ye, A. Yashiro, Y. Sato et al., *J. Chem. Soc., Faraday Trans.* **1996**, *92*, 3813–3821.
150. M. Kazemekaite, A. Bulovas, Z. Talaikyte et al., *Tetrahedron Lett.* **2004**, *45*, 3551–3555.
151. T. Akiyama, H. Imahori, Y. Sakata, *Chem. Lett.* **1994**, 1447–1450.
152. J. E. Hutchison, T. A. Postlethwaite, R. W. Murray, *Langmuir* **1993**, *9*, 3277–3283.
153. J. E. Hutchison, T. A. Postlethwaite, C. Chen et al., *Langmuir* **1997**, *13*, 2143–2148.
154. H. Imahori, H. Norieda, S. Ozawa et al., *Langmuir* **1998**, *14*, 5335–5338.
155. T. Lötzbeyer, W. Schuhmann, E. Katz et al., *J. Electroanal. Chem.* **1994**, *377*, 291–294.
156. N. Nishimura, M. Ooi, K. Shimazu et al., *J. Electroanal. Chem.* **1999**, *473*, 75–84.
157. D. A. Offord, S. B. Sachs, M. S. Ennis et al., *J. Am. Chem. Soc.* **1998**, *120*, 4478–4487.
158. T. A. Postlethwaite, J. E. Hutchison, K. W. Hathcock et al., *Langmuir* **1995**, *11*, 4109–4116.
159. K. Uosaki, T. Kondo, X.-Q. Zhang et al., *J. Am. Chem. Soc.* **1997**, *119*, 8367–8368.
160. J. Zak, H. Yuan, M. Ho et al., *Langmuir* **1993**, *9*, 2772–2774.
161. Z. Zhang, S. Hou, Z. Zhu et al., *Langmuir* **2000**, *16*, 537–540.
162. T. A. Eberspacher, J. P. Collman, C. E. D. Chidsey et al., *Langmuir* **2003**, *19*, 3814–3821.
163. A. A. Yasseri, D. Syomin, V. L. Malinovskii et al., *J. Am. Chem. Soc.* **2004**, *126*, 11944–11953.
164. S. Arnold, Z. Q. Feng, T. Kakiuchi et al., *J. Electroanal. Chem.* **1997**, *438*, 91–97.
165. R. A. Clark, E. F. Bowden, *Langmuir* **1997**, *13*, 559–565.
166. M. Collinson, E. F. Bowden, M. J. Tarlov, *Langmuir* **1992**, *8*, 1247–1250.
167. J. M. Cooper, K. R. Greenough, C. J. McNeil, *J. Electroanal. Chem.* **1993**, *347*, 267–275.
168. A. El Kasmi, J. M. Wallace, E. F. Bowden et al., *J. Am. Chem. Soc.* **1998**, *120*, 225–226.
169. Z. Q. Feng, S. Imabayashi, T. Kakiuchi et al., *J. Electroanal. Chem.* **1995**, *394*, 149–154.
170. Z. Q. Feng, S. Imabayashi, T. Kakiuchi et al., *J. Chem. Soc., Faraday Trans.* **1997**, *93*, 1367–1370.
171. L. Jiang, A. Glidle, A. Griffith et al., *Bioelectrochem. Bioenerg.* **1997**, *42*, 15–23.
172. W. Knoll, G. Pirwitz, K. Tamada et al., *J. Electroanal. Chem.* **1997**, *438*, 199–205.
173. T. M. Nahir, E. F. Bowden, *J. Electroanal. Chem.* **1996**, *410*, 9–13.
174. T. Ruzgas, L. Wong, A. K. Gaigalas et al., *Langmuir* **1998**, *14*, 7298–7305.
175. T. Sagara, K. Niwa, A. Sone et al., *Langmuir* **1990**, *6*, 254–262.
176. Y. Sato, F. Mizutani, *J. Electroanal. Chem.* **1997**, *438*, 99–104.
177. S. Song, R. A. Clark, E. F. Bowden et al., *J. Phys. Chem.* **1993**, *97*, 6564–6572.
178. M. J. Tarlov, E. F. Bowden, *J. Am. Chem. Soc.* **1991**, *113*, 1847–1849.
179. M. C. Leopold, E. F. Bowden, *Langmuir* **2002**, *18*, 2239–2245.
180. T. M. Nahir, E. F. Bowden, *Langmuir* **2002**, *18*, 5283–5286.
181. J. Petrovic, R. A. Clark, H. Yue et al., *Langmuir* **2005**, *21*, 6308–6316.
182. J. Wei, H. Liu, A. R. Dick et al., *J. Am. Chem. Soc.* **2002**, *124*, 9591–9599.
183. J. Wei, H. Liu, D. E. Khoshtariya et al., *Angew. Chem., Int. Ed. Engl.* **2002**, *41*, 4700–4703.

184. D. E. Khoshtariya, J. Wei, H. Liu et al., *J. Am. Chem. Soc.* **2003**, *125*, 7704–7714.
185. D. H. Murgida, P. Hildebrandt, J. Wei et al., *J. Phys. Chem. B* **2004**, *108*, 2261–2269.
186. A. Avila, B. W. Gregory, K. Niki et al., *J. Phys. Chem. B* **2000**, *104*, 2759–2766.
187. K. Niki, J. R. Sprinkle, E. Margoliash, *Bioelectrochemistry* **2002**, *55*, 37–40.
188. K. Niki, W. R. Hardy, M. G. Hill et al., *J. Phys. Chem. B* **2003**, *107*, 9947–9949.
189. J. J. Wei, H. Liu, K. Niki et al., *J. Phys. Chem. B* **2004**, *108*, 16912–16917.
190. K. Fujita, N. Nakamura, H. Ohno et al., *J. Am. Chem. Soc.* **2004**, *126*, 13954–13961.
191. R. J. Forster, L. R. Faulkner, *J. Am. Chem. Soc.* **1994**, *116*, 5444–5452.
192. R. J. Forster, L. R. Faulkner, *J. Am. Chem. Soc.* **1994**, *116*, 5453–5461.
193. R. J. Forster, L. R. Faulkner, *Langmuir* **1995**, *11*, 1014–1023.
194. R. J. Forster, *Inorg. Chem.* **1996**, *35*, 3394–3403.
195. R. J. Forster, J. P. O'Kelly, *J. Phys. Chem.* **1996**, *100*, 3695–3704.
196. R. J. Forster, J. G. Vos, T. E. Keyes, *Analyst* **1998**, *123*, 1905–1911.
197. C. J. Miller, in *Physical Electrochemistry: Principles, Methods, and Applications* (Ed.: I. Rubinstein), Marcel Dekker, New York, 1995, pp. 27–79, Vol. 2.
198. Y. Q. Gao, Y. Georgievskii, R. A. Marcus, *J. Chem. Phys.* **2000**, *112*, 3358–3369.
199. N. S. Lewis, *Annu. Rev. Phys. Chem.* **1991**, *42*, 543–580.
200. K. E. Pomykal, A. M. Fajardo, N. S. Lewis, *J. Phys. Chem.* **1996**, *100*, 3652–3664.
201. W. J. Royea, A. M. Fajardo, N. S. Lewis, *J. Phys. Chem. B* **1997**, *101*, 11152–11159.
202. S. Gosavi, R. A. Marcus, *J. Phys. Chem. B* **2000**, *104*, 2067–2072.
203. T. M. Nahir, R. A. Clark, E. F. Bowden, *Anal. Chem.* **1994**, *66*, 2595–2598.
204. M. J. Honeychurch, *Langmuir* **1999**, *15*, 5158–5163.
205. D. B. Robinson, C. E. D. Chidsey, *J. Phys. Chem.* **2002**, *106*, 10706–10713.
206. R. J. Forster, T. E. Keyes, *J. Phys. Chem. B* **1998**, *102*, 10004–10012.
207. C.-P. Hsu, R. A. Marcus, *J. Chem. Phys.* **1997**, *106*, 584–598.
208. C. Liang, M. D. Newton, *J. Phys. Chem.* **1993**, *97*, 3199–3211.
209. R. Andreu, J. J. Calvente, W. R. Fawcett et al., *Langmuir* **1997**, *13*, 5189–5196.
210. R. Andreu, J. J. Calvente, W. R. Fawcett et al., *J. Phys. Chem. B* **1997**, *101*, 2884–2894.
211. J. Cheng, G. Saghi-Szabo, J. A. Tossell et al., *J. Am. Chem. Soc.* **1996**, *118*, 680–684.
212. J. Cheng, S. Terrettaz, J. I. Blankman et al., *Isr. J. Chem.* **1997**, *37*, 259–266.
213. S. Terrettaz, J. Cheng, C. J. Miller, *J. Am. Chem. Soc.* **1996**, *118*, 7857–7858.
214. E. Laviron, *J. Electroanal. Chem.* **1979**, *101*, 19–28.
215. K. Weber, S. E. Creager, *Anal. Chem.* **1994**, *66*, 3164–3172.
216. L. Tender, M. T. Carter, R. W. Murray, *Anal. Chem.* **1994**, *66*, 3173–3181.
217. E. Laviron, *J. Electroanal. Chem.* **1979**, *97*, 135–149.
218. G. J. Brug, A. L. G. Van Den Eeden, M. Sluyters-Rehbach et al., *J. Electroanal. Chem.* **1984**, *176*, 275–295.
219. S. E. Creager, T. T. Wooster, *Anal. Chem.* **1998**, *70*, 4257–4263.
220. Z. Q. Feng, T. Sagara, K. Niki, *Anal. Chem.* **1995**, *67*, 3564–3570.
221. Z. Q. Feng, S. Imabayashi, T. Kakiuchi et al., *J. Electroanal. Chem.* **1996**, *408*, 15–20.
222. A. K. Gaigalas, G. Niaura, *J. Electroanal. Chem.* **1999**, *465*, 96–101.
223. T. Sagara, S. Igarashi, H. Sato et al., *Langmuir* **1991**, *7*, 1005–1012.
224. T. Sagara, J. Iizuka, K. Niki, *Langmuir* **1992**, *8*, 1018–1025.
225. T. Sagara, T. Midorikawa, D. A. Shultz et al., *Langmuir* **1998**, *14*, 3682–3690.
226. J. F. Smalley, C. V. Krishnan, M. Goldman et al., *J. Electroanal. Chem.* **1988**, *248*, 255–282.
227. G. K. Rowe, M. T. Carter, J. N. Richardson et al., *Langmuir* **1995**, *11*, 1797–1806.
228. J. Li, K. Schuler, S. E. Creager, *J. Electrochem. Soc.* **2000**, *147*, 4584–4588.
229. H. O. Finklea, L. Liu, M. S. Ravenscroft et al., *J. Phys. Chem.* **1996**, *100*, 18852–18858.
230. J. R. Winkler, H. B. Gray, *Chem. Rev.* **1992**, *92*, 369–379.
231. S. O. Kelley, N. M. Jackson, M. G. Hill et al., *Angew. Chem., Int. Ed. Engl.* **1999**, *38*, 941–945.
232. E. F. Bowden, *Interface* **1997**, *6*, 40–44.
233. C.-P. Hsu, *J. Electroanal. Chem.* **1997**, *438*, 27–35.
234. T. G. Drummond, M. G. Hill, J. K. Barton, *J. Am. Chem. Soc.* **2004**, *126*, 15010–15011.

235. T. Liu, J. K. Barton, *J. Am. Chem. Soc.* **2005**, *127*, 10160–10161.
236. H. O. Finklea, K. Yoon, E. Chamberlain et al., *J. Phys. Chem. B* **2001**, *105*, 3088–3092.
237. H. Yamamoto, D. H. Waldeck, *J. Phys. Chem. B* **2002**, *106*, 7469–7473.
238. R. A. Marcus, N. Sutin, *Biochim. Biophys. Acta* **1985**, *811*, 265–322.
239. Y.-P. Liu, M. D. Newton, *J. Phys. Chem.* **1994**, *98*, 7162–7169.
240. W. Zhou, S. Ye, M. Abe et al., *Chem. – Eur. J.* **2005**, *11*, 5040–5054.
241. F. Mukae, H. Takemura, K. Takehara, *Bull. Chem. Soc. Jpn.* **1996**, *69*, 2461–2464.
242. H.-G. Hong, W. Park, *Langmuir* **2001**, *17*, 2485–2492.
243. H.-Z. Yu, Y.-Q. Wang, J.-Z. Cheng et al., *Langmuir* **1996**, *12*, 2843–2848.
244. H.-Z. Yu, H.-L. Zhang, Z.-F. Liu et al., *Langmuir* **1998**, *14*, 619–624.
245. H.-Z. Yu, H. B. Shao, Y. Luo et al., *Langmuir* **1997**, *13*, 5774–5778.
246. D. J. Campbell, B. R. Herr, J. C. Hulteen et al., *J. Am. Chem. Soc.* **1996**, *118*, 10211–10219.
247. W. B. Caldwell, D. J. Campbell, K. Chen et al., *J. Am. Chem. Soc.* **1995**, *117*, 6071–6082.
248. H. O. Finklea, R. Haddox, *Phys. Chem. Chem. Phys.* **2001**, *3*, 3431–3436.
249. R. M. Haddox, H. O. Finklea, *J. Electroanal. Chem.* **2003**, *550-551*, 351–358.
250. R. M. Haddox, H. O. Finklea, *J. Phys. Chem. B* **2004**, *108*, 1694–1700.
251. E. Laviron, *J. Electroanal. Chem.* **1980**, *109*, 57–67.
252. E. Laviron, *J. Electroanal. Chem.* **1981**, *124*, 1–7.
253. H. O. Finklea, *J. Phys. Chem. B* **2001**, *105*, 8685–8693.
254. S. S. Isied, M. Y. Ogawa, J. F. Wishart, *Chem. Rev.* **1992**, *92*, 381–394.
255. J. F. Hicks, F. P. Zamborini, R. W. Murray, *J. Phys. Chem. B* **2002**, *106*, 7751–7757.

9
Charge Transport in Polymer-modified Electrodes

György Inzelt
Eötvös Loránd University, Budapest, Hungary

9.1	**General Considerations**	**653**
9.2	**Electron Transport**	**655**
9.2.1	Electron-exchange Reaction	655
9.2.2	Problems with the Verification of the Model	658
9.2.3	Advanced Theories Predicting Nonlinear $D(c)$ Function	658
9.2.4	Transition between Percolation and Diffusion Behaviors	659
9.2.5	Potential Dependence of Diffusion Coefficient	660
9.2.6	Electronic Conductivity	660
9.3	**Ion Transport**	**665**
9.4	**Coupling of Electron and Ionic Charge Transport**	**667**
9.5	**Other Transport Processes**	**669**
9.5.1	Solvent Transport	669
9.5.2	Dynamics of Polymeric Motion	670
9.6	**Film Structure and Morphology**	**670**
9.6.1	Thickness	672
9.6.2	Synthesis Conditions, Nature of Electrolyte	672
9.6.3	Effect of Electrolyte Concentration and Temperature	673
9.7	**Relaxation and Hysteresis Phenomena**	**674**
9.8	**Measurements of the Rate of Charge Transport**	**677**
	References	678

Encyclopedia of Electrochemistry. Edited by A.J. Bard and M. Stratmann
Vol. 10 *Modified Electrodes*. Edited by M.Fujihira, I.Rubinstein, and J.F.Rusling
Copyright © 2007 Wiley-VCH Verlag GmbH & Co. KGaA, Weinheim. ISBN: 978-3-527-30402-8

9.1
General Considerations

The elucidation of the nature of charge-transfer and charge transport processes in electrochemically active polymer films may be the most interesting theoretical problem of the field. It is also a question of great practical importance, because in the majority of their applications, fast charge propagation through the film is needed. It has become clear that the elucidation of their electrochemical behavior proves to be a very difficult task due to the complex nature of these systems [1–14].

In the case of traditional electrodes, the electrode reaction involves mass transport of the electroactive species from the bulk solution to the electrode surface and electron-transfer step at the electrode surface. A polymer film electrode can be defined as an electrochemical system in which at least three phases are contacted successively in such a way that between a first-order conductor (usually a metal) and a second-order conductor (usually an electrolyte solution) is an electrochemically active polymer layer. The polymer layer is more or less stably attached to the metal, mainly by adsorption (adhesion).

The fundamental observation that should be explained is that even rather thick polymer films in which most of the redox sites are as far from the metal surface as 100–10 000 nm (i.e., the surface concentration, $\Gamma = 10^{-8}$–10^{-6} mol cm^{-2}) may be electrochemically oxidized or reduced.

According to the classical theory of simple electron-transfer reactions, the reactants get very close to the electrode surface, and then electrons can tunnel over the short distance (some tenths of nanometer) between the metal and the activated species in the solution phase.

In the case of polymer-modified electrodes, the active parts of the polymer cannot approach the metal surface, because polymer chains are trapped in a tangled network, and chain diffusion is usually much slower than the timescale of the transient electrochemical experiment (e.g., cyclic voltammetry). Although we should not exclude the possibility that polymer diffusion may play a role in carrying charges, even the redox sites may get close enough to the metal surface when the film is held together by physical forces. It may also be assumed that in ion-exchange polymeric systems, where the redox-active ions are held by electrostatic binding (e.g., $Ru(bpy)_3^{3+/2+}$ in Nafion), some of these ions can reach the metal surface. However, when the redox sites are covalently bound to the polymer chain (i.e., no free diffusion of the sites occurs) and especially when the polymer chains are connected by

Encyclopedia of Electrochemistry. Edited by A.J. Bard and M. Stratmann
Vol. 10 *Modified Electrodes*. Edited by M.Fujihira, I.Rubinstein, and J.F.Rusling
Copyright © 2007 Wiley-VCH Verlag GmbH & Co. KGaA, Weinheim. ISBN: 978-3-527-30402-8

chemical cross-linkages (i.e., only segmental motions are possible) an explanation should be provided as to how the electrons traverse the film.

Therefore, the transport of electrons can be assumed to occur either via an electron-exchange reaction (electron hopping) between neighboring redox sites if the segmental motions make it possible or delocalized electrons can move through the conjugated systems (electronic conduction). The former mechanism is characteristic of redox polymers that contain covalently attached redox sites, either built in the chain or as pendant groups, or redox-active ions held by electrostatic binding.

Polymers that possess electronic conduction are called *conducting polymers*. Electrochemical transformation – usually oxidation – of the nonconducting form of these polymers usually leads to a reorganization of the bonds of the macromolecule and the development of an extensively conjugated system. The electron-hopping mechanism is likely to be operative between the chains (interchain conduction) and defects even in the case of conducting polymers.

However, attention has to be paid not only to the electronic charging of the polymer film (i.e., to the electron exchange at the metal/polymer interface and the electron transport through the surface layer) since, in order to preserve electroneutrality within the film, ions will cross the film/solution interface. The motion of counterions (or less frequently that of the coions) may also be the rate-determining step. The thermodynamic equilibrium between the polymer phase and the contacting solutions requires $\tilde{\mu}_i$ (film) = $\tilde{\mu}_i$ (solution) for all mobile species. In fact, we may regard our film as a membrane or a swollen polyelectrolyte gel (i.e., the

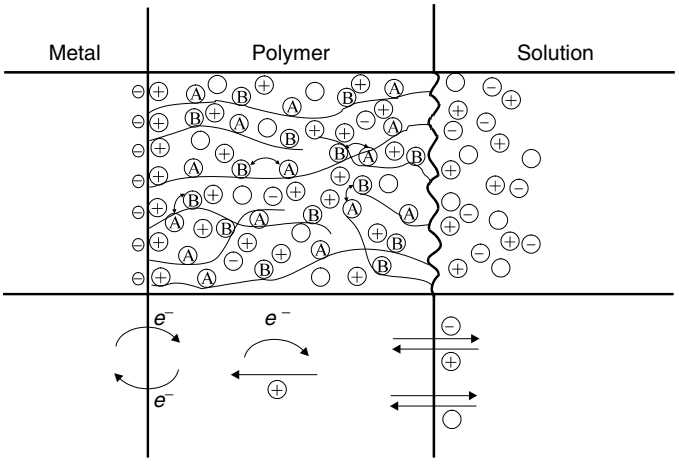


Fig. 1 A schematic picture of a polymer film electrode. Electron transfer occurs at the metal/polymer interface that initiates the electron propagation through the film via electron-exchange reaction between redox couples A and B. Ion-exchange processes take place at the polymer/solution interface, in the simplest case counterions enter the film and compensate the excess charges of the polymer. Neutral (solvent) molecules (O) may also be incorporated into the film (swelling) or leave the polymer layer.

charged film contains solvent molecules and, depending on the conditions, coions, in addition to the counterions).

A simple model of the charge-transfer and transport processes in a polymer film electrode is shown in Fig. 1.

As a consequence of the incorporation of ions and solvent molecules into the film, swelling or shrinkage of the polymer matrix takes place. Depending on the nature and the extent of cross-links, reversible elastic deformation or irreversible changes (e.g., dissolution) may occur. Other effects, such as dimerization, ion-pair formation, cross-linking, and so forth, should also be considered.

We have already mentioned several effects that are connected with the polymeric nature of the layer. It is evident that all the charge transport processes listed are affected by the physicochemical properties of the polymer. Therefore, we must also deal with the properties of the polymer layer if we wish to understand the electrochemical behavior of these systems. The elucidation of the structure and properties of polymer (polyelectrolyte) layers as well as the changes in their morphology caused by the potential and potential-induced processes and by other parameters (e.g., temperature, electrolyte composition) set an entirely new task for electrochemists. Owing to the long relaxation time characteristic of polymeric systems the equilibrium or steady-state situation often has not been reached within the scale of the experiment.

However, the application of combined electrochemical and nonelectrochemical techniques has allowed a very detailed insight into the nature of ionic and electronic charge-transfer and charge transport processes.

It is intended here to outline some relevant experiences, to discuss the existing models and theories, as well as to summarize and systematize the knowledge accumulated with respect to the charge transport processes occurring in redox and conducting polymer films.

9.2 Electron Transport

As it has already been mentioned in redox polymers – which are localized state conductors – electron transport occurs via a process of sequential electron self-exchange between neighboring redox groups. In the case of electronically conducting polymers – where polymer backbone is extensively conjugated, which makes a considerable charge delocalization possible – the transport of the charge carriers along a conjugated strand can be described by the band model characteristic to metals and semiconductors. Besides this intrachain conduction that provides a very high intrinsic conductivity, various hopping and tunneling processes are considered for the nonintrinsic (interstrand and interfiber) conduction processes.

9.2.1 Electron-exchange Reaction

The elementary process is the transfer of an electron from an electron donor orbital on the reductant (e.g., Fe^{2+}) to the acceptor orbital of the oxidant (e.g., Fe^{3+}). The rate of the electron transfer is very high; it takes place within 10^{-16} seconds; however, the reorganization of the bonds may range from 10^{-13} to 10^{-14} seconds, the reorientation of the solvent dipoles (e.g., water molecules in the hydration sphere) needs 10^{-11}–10^{-12} seconds and the duration

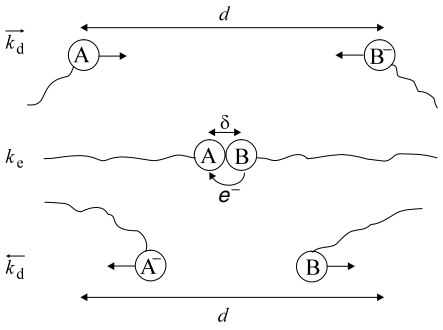


Fig. 2 A schematic microscopic picture of the electron-exchange process coupled to isothermal diffusion. The upper part shows that species A and B^- start to diffuse toward each other from their average equilibrium distance (d) with the diffusion rate coefficient, k_d. The next stage is the "forward" electron-transfer step after the formation of precursor complex characterized with rate coefficient, k_e and the mean distance of the redox centers, $\delta \cong 2r_A$. The lower part depicts the separation of products, A^- and B.

of the rearrangement of the ionic atmosphere is ca 10^{-8} seconds. The rate coefficients are much higher for electron-exchange reactions occurring practically without structural changes (outer-sphere reactions) than those for reactions requiring high energy of activation due to the reorganization of the bonds (inner sphere mechanism).

However, the probability of electron transfer (tunneling) depends critically on the distance between species participating in the electron-exchange reaction. A reaction can take place between two molecules if they encounter. It follows that the rate-determining step can be either the mass transport (generally, diffusion is considered, but the effect of migration cannot be excluded) or the reaction (the actual rate of electron transfer in our case). For an electron-exchange process coupled to isothermal diffusion the following kinetic scheme may be considered:

$$A + B^- \underset{\overleftarrow{k}_d}{\overset{\vec{k}_d}{\rightleftharpoons}} \{AB^-\} \overset{k_e}{\rightleftharpoons} A^- + B \quad (1)$$

where $\vec{k}_d$, $\overleftarrow{k}_d$, and k_e are the rate coefficients for diffusive approach, for separation, and for the forward reaction, respectively. Note that $\vec{k}_d$ is a second-order rate coefficient, while $\overleftarrow{k}_d$ and k_e are first order. The overall second-order rate coefficient can be given by

$$k = \vec{k}_d k_e / \overleftarrow{k}_d + k_e \quad (2)$$

Figure 2 illustrates schematically the microscopic events occurring in the course of an electron-exchange reaction.

If the reaction has small energy of activation, consequently k_e is high ($k_e \gg \overleftarrow{k}_d$), the rate-determining step is the approach of the reactants. Under these conditions $k = \vec{k}_d$. The kinetics are activation controlled for reactions with large activation energies ($\Delta G^{\neq} > 20\ \mathrm{kJ\ mol^{-1}}$ for reactions in aqueous solutions), and then

$$k = k_e \vec{k}_d / \overleftarrow{k}_d \quad (3)$$

Since $\vec{k}_d / \overleftarrow{k}_d$ is the equilibrium constant K for formation of the precursor complex k can be expressed as

$$k = k_e\, K \quad (4)$$

The rate of the collision, k_d, can be estimated by using Smoluchowski's equation:

$$k_d = 1000 \times 4\pi N_A r_{AB} D_{AB} \quad (5)$$

where N_A is the Avogadro constant, r_{AB} is the mean distance between the centers of the species involved in the electron exchange ($r_{AB} \approx 2r_A$ for identical species where r_A is the radius of the reactant molecule) and D_{AB} is the relative diffusion coefficient of the reacting molecules. The diffusion coefficients of ions in aqueous solutions at 298 K are typically $1-2 \times 10^{-9}$ m^2 s^{-1}, except $D_{H^+} = 9.1 \times 10^{-9}$ m^2 s^{-1} and $D_{OH^-} = 5.2 \times 10^{-9}$ m^2 s^{-1}. For a small ion $r_{AB} = 0.5$ nm. By inserting these values into Eq. (5) we obtain $k_d = 8 \times 10^9$ dm^3 mol^{-1} s^{-1}. Consequently, if $k_e > 10^9$ dm^3 mol^{-1} s^{-1} the reaction is diffusion controlled. In aqueous solutions fast electron-transfer and acid–base reactions fall within this category. On the other hand, if the viscosity (η) of the solvent is high, due to the inverse relationship between D and η, k_d may be smaller by orders of magnitude. Similarly, the diffusion of macromolecules is also slow, $D = 10^{-10}-10^{-16}$ m^2 s^{-1}. In the case of polymer film electrodes, where the polymer chains are trapped in a tangled network, rather small values for the diffusion coefficient of the chain and segmental motions can be expected. If the latter motions are frozen-in (e.g., at low temperatures or without the solvent swelling which has a plasticizing effect on the polymer film) the electron transport may be entirely restricted.

It follows that a diffusion control is more frequently operative in polymeric systems than in the case of ordinary solution reactions, because due to the low D values, k_d and k_e are more likely comparable [15–22]. If the electron-exchange reaction occurs between ionic species (charged polymer sites) the coulombic forces may reduce or enhance both the probability of the encounter of the ions and the rate of the electron transfer. For the activation-controlled case k_e can be given as follows [23]:

$$\ln k_e = \ln k_e^o - \frac{z_A z_B e^2}{2 r_A \varepsilon k_B T} \qquad (6)$$

where z_A and z_B are the charges of the ions and ε is the dielectric permittivity of the medium. If z_A and z_B have the same sign, k_e decreases; in the opposite case k_e increases. The effect can be modified by using a solvent with high or low ε values or by adding a large amount of inert electrolyte into the solution. In the latter case, the effect of ionic strength can approximately be given by

$$\ln k = \ln k^o + z_A z_B A \sqrt{I} \qquad (7)$$

where A is the constant of the Debye-Hückel equation.

The electron-exchange reaction (electron hopping) occurs continuously between the molecules of a redox couple in a random way. A macroscopic charge transport takes place, however, only when a concentration or potential gradient exists in the phase at least for one of the components of the redox couple. In this case the hydrodynamic displacement is shortened for the diffusive species by $\delta \sim 2r_A$, because the electron exchange (electron diffusion) contributes to the flux. The contribution of the electron diffusion to the overall diffusion flux depends on the relative magnitude of k_e and k_d or D_e and D_{AB} (i.e., the diffusion coefficients of the electron and ions, respectively).

According to the Dahms-Ruff theory of electron diffusion [15–18]

$$D = D_{AB} + D_e = D_{AB} + k_e \delta^2 c/6 \qquad (8)$$

for three-dimensional diffusion where D is the measured diffusion coefficient, c is the concentration of redox centers and

k_e is the bimolecular electron-transfer rate coefficient. Factors 1/4 and 1/2 can be used instead of 1/6 for two- and one-dimensional diffusion, respectively.

This approach has been used in order to describe the electron propagation through surface polymer films [19–23]. In these models it was assumed that transport occurs as a sequence of successive steps between adjacent redox centers of different oxidation states. The electron hopping has been described as a bimolecular process in the direction of the concentration gradient. The kinetics of the electron transfer at the electrode–polymer film interface, which initiates electron transport in the surface layer, is generally considered as a fast process, which is not rate limiting. It was also presumed that the direct electron transfer between the metal substrate and the polymer involves only those redox sites situated in the layer immediately adjacent to the metal surface. As follows from the theory (Eq. 8) the measured charge transport diffusion coefficient should increase linearly with c, whenever the contribution from the electron-exchange reaction is important; therefore the concentration dependence of D may be the test of theories based on the electron-exchange reaction mechanism. Despite the fact that considerable efforts have been made to find the predicted linear concentration dependence of D, it has been observed only in a few cases and for a limited concentration range.

There may be several reasons why this model has not fulfilled expectations although the mechanism of electron transport as described might be correct.

9.2.2 Problems with the Verification of the Model

The uncertainty in the determination of D by potential step, impedance, or other techniques is substantial due to problems such as the extraction of D from a $D^{1/2}c$ product (this combination appears in all the methods), the difficulty arising from the *in situ* thickness estimation, nonuniform thickness, film inhomogeneity, incomplete electroactivity, and ohmic drop effect. It may be forecast, for example, that the film thickness increases, thus c decreases, due to the solvent swelling of the film, however, D_{AB} increases, making the physical diffusion of ions and segmental motions less hindered simultaneously. In addition, the solvent swelling changes with the potential, and it is sensitive to the composition of the supporting electrolyte. Because of the interactions between the redox centers or between the redox species and the film functional groups, the morphology of the film will also change with concentration of the redox groups. We will deal with these problems in Sects. 9.5–9.7. It is reasonable to assume that in many cases $D_{AB} \gg D_e$ (i.e., the electron hopping makes no contribution to the diffusion) or the most hindered process is the counterion diffusion, coupled to electron transport.

9.2.3 Advanced Theories Predicting Nonlinear $D(c)$ Function

According to the theory of the *extended electron transfer* δ may be higher than $2r_A$, and it predicts an exponential dependence on the average site–site distance (d) (i.e., on the site concentration) [24]:

$$k_e = k_0 \exp \frac{-(d-\delta)}{s} \qquad (9)$$

where s is a characteristic distance (ca 10^{-10} m).

An alternative approach for the description of the relationship between the

diffusion coefficient and redox site concentration is based on the assumption that at high enough concentration of redox centers, several electron hops may become possible because more than two sites are immediately adjacent, that is, the charge donated to a given redox ion through diffusional encounter may propagate over more than one site in the direction of the concentration gradient. It is the case in systems where the electron-exchange rate is high; therefore the rate of the electron transport is determined by the physical diffusion of redox species incorporated in an ion-exchange membrane or that of the chain- and segmental motions. This enhances the total electron flux. Formally, this is equivalent to an increase of the electron-hopping distance by a certain factor, f; thus D can be expressed as follows [25]:

$$D = D_0 + \frac{k_e c(\delta f)^2}{6} \qquad (10)$$

Assuming a Poisson distribution of the electroactive species, the enhancement factor can be expressed as a power series of a probability function, which is related to the concentration. At low concentrations the probability of finding more than one molecule in the hemisphere with the radius of molecular collision distance is nearly zero and $f = 1$. The factor, and therefore D_e, increase noticeably at higher concentrations.

The model suggests that k_e or D_e should first have an exponential-like rise with increasing c, then flatten at high concentrations. The exponential rise occurs because, as the concentration increases, d becomes smaller, which promotes intersite electron transfer. As the minimum center-to-center separation is approached, when each redox center has a nearest neighbor practically in contact, k_e or D_e asymptotically nears its theoretical maximum value. Similar results have been obtained by a microscopic model, which describe electron (or hole) diffusion in a rigid three-dimensional network. This conception is based on simple probability distribution arguments and on a random walk [26].

9.2.4 Transition between Percolation and Diffusion Behaviors

When physical motion is either nonexistent or much slower than electron hopping, charge propagation is fundamentally a percolation process, because the microscopic distribution of redox centers plays a critical role in dictating the rate of charge transport [27–29]. Any self-similarity of the molecular clusters between successive electron hops imparts a memory effect, making the exact adjacent-site connectivity between the molecules important. The redox species can move about their equilibrium position of the irreversible attachment with the polymer (in the three-dimensional network the redox species are either covalently or electrostatically bound), which is referred to as *bounded diffusion*. In the opposite extreme (free diffusion), rapid molecular motion thoroughly rearranges the molecular distribution between successive electron hops, thus leading a mean-field behavior. The mean-field approximation presupposes that $k_d > k_e$, and leads to Dahms-Ruff-type behavior for freely diffusing redox centers, but the following corrected equation should be applied [28]:

$$D = D_{AB}(1 - x) f_c + D_e x \qquad (11)$$

where x is the fractional loading, which is the ratio of the total number of molecules to the total number of lattice sites. The factor $(1 - x)$ in the first term accounts

for the blocking of physical diffusion and f_c is a correlation factor, which depends on x. When D_{AB} becomes less than D_e, percolation effects appear. If $D_e \gg D_{AB}$ a characteristic static percolation behavior ($D = 0$ below the percolation threshold and an abrupt onset of conduction at the critical fractional loading) should be observed. The mechanistic aspects of the charge transport can be understood from D versus x plots. When D_{AB} is low, that is in the case of bounded diffusion, [27–29]

$$D = D_e x = k_e \delta^2 x^2 c/6 \qquad (12)$$

Thus D varies with x^2, when the rate of physical diffusion is slow.

In the case of free diffusion, the apparent diffusion coefficient becomes

$$D = D_{AB} f(1 - x) \qquad (13)$$

Accordingly D will decrease with x. This situation originates in the decreased availability of vacant sites (free volume) within the polymer film. When both electron-hopping and physical diffusion processes occur at the same rate ($D_{AB} = D_e$), D becomes invariant with x.

9.2.5
Potential Dependence of Diffusion Coefficient

In the simple models D_e is independent of the potential because the effects of both the counterion activity and interactions of charged sites (electron–electron interactions) are neglected. However, in real systems, the electrochemical potential of counterions is changed as the redox state of the film is varied, the counterion population is limited and interaction between electrons arises. The potential dependence of the electron diffusion coefficient can be expressed as follows [30]:

$$D_e = k_e \delta^2 \left\{ 1 + \lfloor z_i^{-1} (x_e - z_s)^{-1} + g/k_B T \rfloor x_e (1 - x_e) \right\} \qquad (14)$$

where x_e is the fraction of sites occupied by electrons, z_s and z_i are the charge of the sites and counterions, respectively, and g is the occupied site interaction energy. (The g parameter is similar to that of the Frumkin isotherm.) In the case of noninteracting sites ($g = 0$) and in the presence of large excess of supporting electrolyte ($z_s = \infty$), $D_e = k_e \delta^2$ and is a diffusion coefficient. In general, D_e is not constant as the potential, that is the film redox composition is changed. D_e does not vary substantially with potential within the reasonable range of g and z_s (e.g., if $g = 4$, D_e will only be doubled compared with its value at $g = 0$), and a maximum (if $g > 0$) or a minimum (if $g < 0$) will appear at the standard redox potential of the system.

9.2.6
Electronic Conductivity

Electronically conducting polymers consist of polyconjugated, polyaromatic, or polyheterocyclic macromolecules, and these differ from redox polymers in that the polymer backbone is itself electronically conducting in ''doped'' state. The term *doping* as it is often applied to the charging process of the polymer, is somewhat misleading. In semiconductor physics, doping describes a process when dopant species of small quantities occupy positions within the lattice of the host material, resulting in a large-scale change in the conductivity of the doped material, as compared to the undoped one. The ''doping'' process in

conjugated polymers is, however, essentially a charge-transfer reaction, resulting in the partial oxidation (or less frequently reduction) of the polymer. Although conjugated polymers may be charged positively or negatively, the study of the charging mechanism has mostly been devoted to the case of *p*-doping. The electronic conductivity shows a drastic change (up to 10–12 orders of magnitude) from its low value for the initial (noncharged) state of the polymer corresponding to a semiconductor or even an insulator, to the values within 1–1000 S cm^{-1} (even up to 10^5 S cm^{-1} comparable to metals) [11, 14].

In general, the mobility of initial portions of the incorporated electronic charge is rather low. At higher charging levels the conductivity increases much more rapidly than the charge and then levels out, or even decreases. This onset of conductivity has been interpreted as an insulator-metal transition due to various electron–electron interactions [31, 32]. The temperature dependence of the conductivity in the highly charged state does not correspond in most cases to metallic type [33]. In conformity with quantum-chemical expectations the electron spin resonance (ESR) measurements demonstrated the presence of unpaired spins inside the polymer film. However, the spin concentration passes through a maximum at a relatively low charging level, usually before the high conductivity increase, and then vanishes [34–38]. Various models have been developed to explain the mechanism of charge transport in conducting polymer film electrodes. Two extreme approaches exist. According to the delocalized band model, the charges and unpaired electrons are delocalized over a large number of monomer units [37–45], while in the chemical model, the charge is localized in the polymer chain [46], or at most only some monomer units are involved. Because the approach assuming localized charges does not differ essentially from that applied for redox polymers, and the semiconductor or one-dimensional metal models [32] have been generally accepted, we will deal with the latter theories. Although the precise nature of charge carriers in conjugated systems varies from material to material, in general the following delocalized defects are considered: solitons (neutral defect state), polarons (a neutral and a charged soliton in the same chain, which are essentially single charged cation radicals at the polymer chain coupled with local deformations), and bipolarons (two charged defects form a pair, these doubly oxidized, spinless dications usually exist at higher charging levels) [32, 42–46].

The macroscopic charge transport in a conducting polymer matrix represents a superposition of local transport mechanism. The intrinsic conductivity, which refers to the conduction process along a conjugated chain, can be described in terms of the band theory, which is well established for solid materials. Metallic conductors are characterized by either a partially filled valence band or an overlap between valence and conduction bands. Semiconductors and insulators possess a band gap between the top of the valence band and the bottom of the conduction band. The band gap energy is relatively small for a semiconductor but rather large for an insulator. The neutral (reduced, undoped) polymer has a full valence and empty conduction band, separated by a band gap (insulator).

Chemical or electrochemical doping (oxidation and incorporation of counterions) results in the generation of a polaron level at midgap. Further oxidation leads to the formation of bipolaron energy bands in

the band gap. Electronic conductivity is rationalized in terms of bipolaron hopping. Because the overall size of the polymer is limited, interchain electron transfer must also be considered. The intrachain conductivity of the polymer is usually very high if the polymer chain is long, and contains no defects; therefore, in a good quality polymer, the interchain conductivity is rate determining [47]. (If the polymer morphology is fibrillar, the fiber-to-fiber electron transport may also be the most hindered process.) The essential aim is to synthesize conducting polymers so that the mean free path is limited by intrinsic scattering events from the thermal vibrations of the lattice (phonons). One of the problems is that quasi-one-dimensional electronic systems are prone to localization of electronic states due to disorder. In the case of electronic localization, the carrier transport is limited by phonon-assisted hopping, according to the Mott model [48]. The Mott model of variable range hopping gives the following equation for the conductivity (σ)

$$\sigma = \sigma_0 \exp\left[-\left(\frac{T_0}{T}\right)^{\gamma}\right] \qquad (15)$$

where σ_0 and T_0 are constants and γ is a number related to the dimensionality (d) of the hopping process ($\gamma = (d+1)^{-1}$).

The σ_0 value depends on the electron-phonon-coupling constant, while T_0 is in connection with the localized density of states near the Fermi level and the decay length of the wave function, respectively. It can be seen that conductivity increases with temperature in contrast to that of the metals. This type of conductivity behavior has been verified for many conjugated polymer systems. The problem of localization is less important if the molar mass of the polymer is high and only a few defects are present, as well as a relatively intense interchain coupling prevails. In this case the mean free path becomes quite large and it is determined by photon scattering as in true metals. Under such conditions the conductivity is high, and its value increases with the molar mass of the polymer and decreases with the temperature.

The mechanism of fluctuation-induced tunneling is expected for the electrical conductivity if large regions of a highly conductive (''metallic'') phase in an inhomogeneous material are separated from each other by an insulating phase. The latter acts as a potential barrier. Due to the exponential dependence of the tunneling probability, tunneling will effectively occur only in the regions of closest approach of the metallic segments.

The parabolic barrier approximation for the fluctuation-induced tunneling gives the following relationship in respect of the temperature dependence of conductivity [49, 50]:

$$\sigma = \sigma_0 \left[-\frac{T_1}{T - T_0}\right] \qquad (16)$$

where T_1 and T_0 parameters are in connection with the characteristics of the tunnel junction (its effective area, width, the height of the potential barrier, effective mass, and dielectric permittivity). For instance, the temperature dependence of the conductivity of polypyrrole has been analyzed by using this theory. On the basis of this analysis, an interesting conclusion has been drawn regarding the structure of the polymer, namely, the polymer consists of islands with a two-dimensional (macrocyclic) structure, which are connected (cross-linked) by one-dimensional polypyrrole chains [51].

The conductivity may depend on other factors, for instance, on the pH of the contacting solution (proton doping in the case

of polyaniline) or on the presence of electron donor molecules in the gas phase. The decrease of the pH of the solution increases the conductivity of polyaniline [39, 52, 53], while the resistance of dry polyaniline or polypyrrole increases in ammonia atmosphere [54, 55]. The electron conducting polymers can easily be switched between conducting and insulating states, just by changing the potential, by electrochemical (or chemical) oxidation and reduction, respectively, or by varying the composition of the contacting fluid media (H^+ - ion activity of the solution or the NH_3, NO concentration in the gas phase). The variation of the resistance of polyaniline as a function of potential nicely demonstrates the conversion from the insulating to conduction state and vice versa (Fig. 3). This is a unique property in comparison with the majority of electron conducting material (e.g., metals). When the oxidation state of the polymers is varied, not only is their conductivity altered, but other properties (e.g., color) also change. It is this very feature that can be exploited in many practical applications [14]. The charging/discharging (or redox switching) processes are usually fast, but their nature is rather complex. The steady-state cyclic voltammograms represent in most cases a combination of broad anodic and cathodic peaks with a plateau of the current at higher potentials. It is illustrated in Fig. 4. The current is proportional to the scan rate, that is, from the electrical point of view, the film behaves like a capacitor [56–62]. However, this simple result is the consequence of a complicated phenomenon, which includes the faradaic process (generation of charged electronic entities at the polymer chains near the electrode surface by electron transfer to the metal), the transport of those species throughout the film, and the ion exchange at the film/solution interface (see mass changes during charging/discharging cycles in Fig. 4). Despite the above mentioned quasiequilibrium character of the cyclic voltammetric curves, a pronounced hysteresis, that is, a considerable difference between the anodic and cathodic peak potentials, can be observed. Slow heterogeneous electron transfer, effects of local rearrangements of polymer chains, slow mutual transformations of

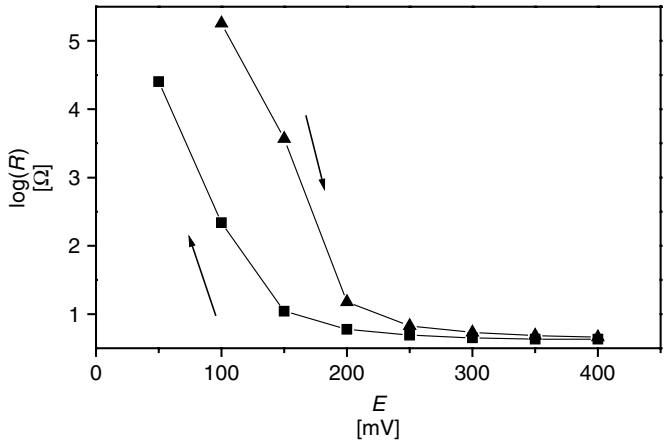


Fig. 3 The changes of the resistance of a polyaniline film in contact with 1 M H_2SO_4 as a function of the potential [53].

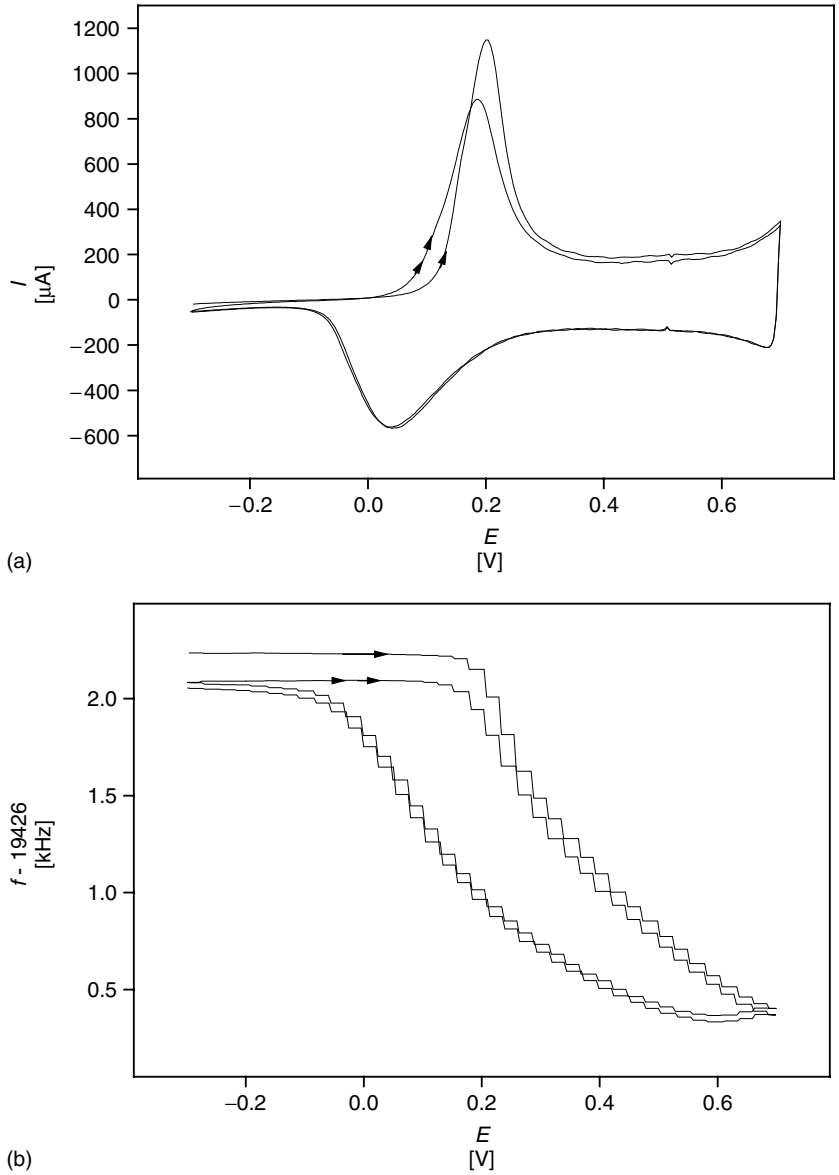


Fig. 4 (a) Cyclic voltammograms (two cycles) and (b) the simultaneously detected EQCM frequency changes for a polyaniline film ($L = 2.9$ µm) in contact with 1 M H_2SO_4. Sweep rate: 100 mV s^{-1}.

various electronic species, phase transition of first order due to an S-shaped energy diagram (e.g., due to attractive interactions between the electronic and ionic charges), dimerization, and insufficient conductivity of the film at the beginning of the anodic process, have been proposed as possible origins of the hysteresis [44, 53, 63–71].

9.3 Ion Transport

In the course of electrochemical oxidation or reduction of the surface polymer films or membranes, the overall electroneutrality of the polymer phase is retained by ion-exchange processes between the polymer film and the bulk electrolyte solution [3, 72]. Not only has ion transport to be considered, but solvent and other neutral molecules may also enter or leave the film during the charging/discharging processes [73–78]. In order to maintain electroneutrality in the simplest case either counterions enter the film or coions leave it. The relative contributions of the ions carrying different charges to the overall charge transport may depend on their physical properties (e.g., size) and/or on their chemical nature (e.g., specific interactions with the polymer), as well as on other parameters (e.g., potential) [1–4, 73–92].

There is a wide variation of the reaction schemes; however, most redox transformations, including the participation of mobile ions of the contacting electrolyte, might be represented as follows:

Reduction

$$P + e^- + M^+ \rightleftharpoons P^{\bullet -}M^+ \qquad (17)$$

$$P^{\bullet -}M^+ + e^- + M^+ \rightleftharpoons P^{2-}M_2^+ \qquad (18)$$

Dimerization and protonation may also occur:

$$P + P^{\bullet -}M^+ \rightleftharpoons P_2^{\bullet -}M^+ \qquad (19)$$

$$2P^{\bullet -}M^+ \rightleftharpoons P_2^{2-}M_2^+ \qquad (20)$$

$$P^{\bullet -}M^+ + e^- + H^+ \rightleftharpoons PH^-M^+ \qquad (21)$$

$$P + 2e^- + 2H^+ \rightleftharpoons PH_2 \qquad (22)$$

where P is a polymer with reducible groups and M^+ is the counterion (cation). A typical example is poly(tetracyanoquinodimethane) [3, 75, 80, 82]. For organic redox or conducting polymers, partly or wholly, the nine-member square scheme elaborated for the electrochemical transformation of quinones can be applied, because electron transfer is always coupled with protonation, depending on the pH of the contacting solutions.

Oxidation

$$P + X^- \rightleftharpoons P^+X^- + e^- \qquad (23)$$

where X^- is a counterion (anion).

(e.g., polyvinylferrocene [73, 74, 79])

$$P + X^- \rightleftharpoons P^{\bullet +}X^- + e^- \qquad (24)$$

$$P^{\bullet +}X^- + X^- \rightleftharpoons P^{2+}X_2^- + e^- \qquad (25)$$

(e.g., poly(tetrathiafulvalene), dimeric species are also formed [81]).

In the reactions (17–25) cations (M^+ or H^+) and anions (X^-) enter the film during reduction and oxidation, respectively. In some cases cations leave the polymer film during oxidation:

$$M_2^+[A(II)B(II)L_6]^{2-} \rightleftharpoons M^+[A(II)B(III)L_6]^- + M^+ \qquad (26)$$

(e.g., $K_2^+[Ni(II)Fe(II)(CN)_6]$ [85])

Oxidation of organic polymers is often coupled with deprotonation instead of or beside anion incorporation [3, 63]. It can be illustrated by the scheme of the redox transformations and protonation equilibria of polyaniline (Fig. 5).

The results obtained by different techniques (radiotracer [80, 84], quartz crystal microbalance [73–76, 78, 83, 85–87, 90, 92–110], probe beam deflection (PBD) [88–90], etc.) have revealed that the situation may further be complicated. It has

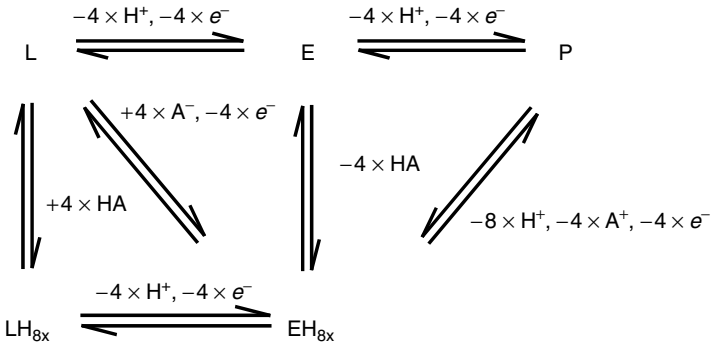


Fig. 5 Scheme of redox transformations and protonation equilibria of polyaniline where L, E, P, LH_{8x}, EH_{8x} represent different oxidation and protonation states. L – leucoemeraldine, E – emeraldine, P – pernigraniline, LH_{8x} – protonated leucoemeraldine, EH_{8x} – protonated emeraldine forms.

been found that the relative contribution of anions and cations to the overall ionic charge transport process depends upon several factors, such as the oxidation state of the polymer (potential) and the composition of the supporting electrolyte as well as on the film thickness [3, 73–92]. The latter effect is shown in Fig. 6. These phenomena can be elucidated in terms of morphological changes, mobility of ions, interactions between the polymer and mobile species (ions and solvent molecules), size exclusion and so forth [73–117]. For instance, if large size counterions are used during the film deposition (electropolymerization), mostly coion exchange can be found. In this case, the large, sometimes polymeric counterions, are trapped in the polymeric layer owing to strong van der Waals and electrostatic forces.

The charge transport diffusion coefficient that can be determined by transient techniques is characteristic of the rate-limiting step (which is either the electron or the ionic charge transport). However, by appropriate experimental techniques, the decoupling of the electron and ion transport is possible; therefore the rate of the fundamental charge transport processes can be determined separately (see Sect. 9.8).

The transport of ionic species can be described with the help of the Nernst-Planck equation. In the absence of mediated reaction, the convection term can be omitted, because any stirring of solution has no effect inside the film. At high concentrations, the fluxes have a more complicated form, owing to the upper limits on concentrations and/or short-range interactions between the species. Because of the nonlinear character of the resulting equations, the solutions are usually obtained using various approximations. The Poisson equation is usually replaced by the local electroneutrality condition, which is justified at a sufficiently large ratio of the film thickness to its Debye screening length and with a slow variation in potential. In the presence of excess supporting electrolyte, the migration contribution to the flux may also be neglected. Diffusion-migration transport equations have been solved mostly for one-dimensional transport [3–5, 118, 119].

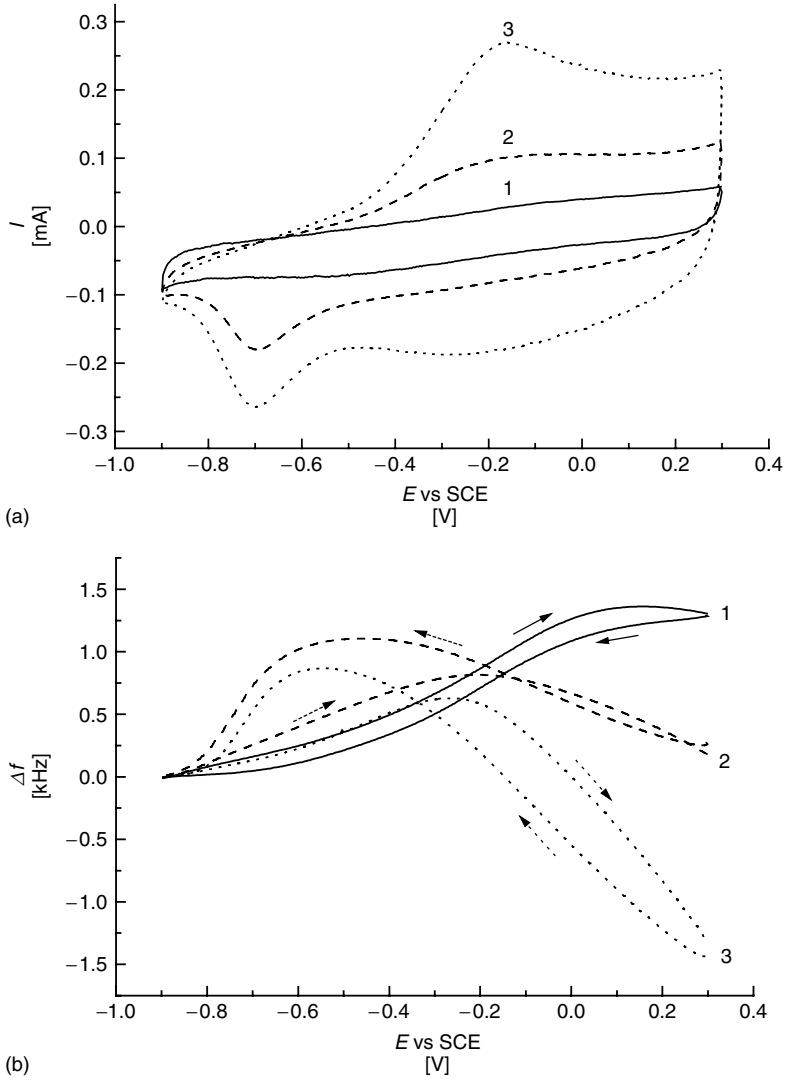


Fig. 6 Effect of the thickness on cyclic voltammetric (a) and EQCM (b) responses of polypyrrole films. The thicknesses are (1) 0.14, (2) 0.48, and (3) 0.96 μm, respectively. Solution: 1 M NaCl; $\nu = 10$ mV s^{-1} [83].

9.4 Coupling of Electron and Ionic Charge Transport

Electronic and ionic charge transport processes are coupled by electroneutrality condition. This statement is valid for systems of different structures (e.g., uniform and porous films) as well as for different mechanisms of electronic charge transport (e.g., electron hopping between redox centers, migration-diffusion transport of incorporated electroactive component across the film or long-distance movement of

charged sites of the matrix); however, each case needs slightly different theoretical treatments and the experimental manifestation (e.g., in the steady-state or transient current) of this effect depends on other factors (e.g., on the concentration of background electrolyte and charging level of the polymer) [120–135]. Typically, two mobile species are considered, assuming that a Donnan exclusion exists (i.e., coions do not participate in the charge transport). However, a theoretical model involving diffusion and migration charge transport mechanisms with three charge carriers has also to be developed [135]. A fundamental feature of all these analyses is that electron transport is not only driven by a concentration gradient, but that migration also plays a role. It was recognized that the electron-hopping process cannot be described by the usual combination of the classical Fick and Nernst-Planck laws, when the effect of electric field is considered, but rather a second-order law should be derived from the bimolecular character of electron hopping, as opposed to the unimolecular character of ion displacement [136–145]. For systems in which the ratio of the oxidized and reduced forms is fixed and kept constant, that is the total charge of the redox species and hence the concentration of counterions are fixed, the theory predicts a maximum of the steady-state current (redox conductivity) near the formal potential of the redox couple. The current due to the electron hopping is higher than that in the absence of migration. The detailed analysis of the modified Nernst-Planck equation derived from the diffusion-migration model for coupled transport of the electronic and ionic charge carriers indicates that under both steady-state and transient conditions, migration always leads to an enhancement of the intersite electron hopping, and somewhat surprisingly the enhancement is getting higher as the mobility of the counterions decreases. Migration diminishes in all cases as the relative concentration of electroactive fixed counterions is increased (i.e., the fixed counterions play a role similar to that of the supporting electrolyte in solution studies). This is especially so when the diffusion coefficient of the mobile counterions is small compared to the diffusion coefficient for electron hopping. Another important result of this theory is that the charge transport diffusion coefficient, which can be determined by chronoamperometry, increases with the concentration of the redox species more intensively than predicted by the Dahms-Ruff equation [28]. (D varies proportionately to c^2 or even c^3.)

Besides the electric-field effects, the ion association within the polymer films plays an important role in the dynamics of electron hopping within the films. (Extensive ion association might be expected due to the high ion content and the low dielectric permittivity that prevail in the interior of many redox polymers.) According to the model including ion association, the sharp rise in the apparent diffusion coefficient as the concentration of the redox couple in the film nears saturation is an expected consequence of the shifting of the ionic association equilibrium to produce larger concentrations of the oxidized half of the redox couple, which is well matched for rapid electron acceptance from the reduced half of the couple [146].

Ion association effect has been considered also in the case of conducting polymers. It is assumed that ions inside the polymer films exist in two different forms. The bound or immobile ions are associated either with the neutral sites or with the charged sites of the polymer matrix. With the help of the assumption of

the formation of bonds between the neutral sites and ions the splitting of the cyclic voltammetric curves and the minimum of the mass versus charge relationship can be explained [147].

The advanced models elaborated for the low-amplitude potential perturbation of metal/conducting polymer film/solution systems also take into account the different mobilities of electronic (polarons) and ionic species within the uniform film. An important feature of this approach is that the difference in the electric and ionic mobilities ($D_e \neq D_i$) leads to a nonuniformity of the electric field inside the bulk film which increases as D_e/D_i ratio increases and vanishes when $D_e = D_i$ [120, 121, 124].

9.5 Other Transport Processes

In addition to the counterions' sorption/desorption, the exchange of solvent, and in some cases that of the salt (acid) molecules between the polymer film and background electrolyte, is theoretically expected and has indeed been found experimentally.

9.5.1 Solvent Transport

The equilibrium distribution of neutral molecules depends on the difference of their standard chemical potentials in the polymer and solution phases, respectively. The free energy of transfer is higher, that is the sorption of neutral molecules in the polymer phase is larger, if the character of the neutral species and the polymer is similar [72]. For instance, more water will be incorporated in hydrophilic polymers containing polar groups. Because in many cases a neutral polymer is converted into a polyelectrolyte as a function of potential, the partitioning of water into the polymer film will change during the charging/discharging processes. It may cause a swelling or deswelling of the layer. The extent of swelling is strongly affected by the electrolyte composition (both the nature and concentration of the electrolyte) and temperature [3, 72, 76, 77, 83, 148].

The expansion and contraction of the polymer network, which is in conjunction with the sorption/desorption of solvent molecules and ions, can be described in terms of mechanical work. This mechanical contribution should be considered in the calculation of the equilibrium electrode potential. The deformation which is coupled to the redox reaction, is elastic in nature. A plastic deformation occurs when a neutral, dry film is immersed in electrolyte solution and electrolyzed. It has been observed for a range of neutral polymer films freshly deposited on metal substrates by solvent evaporation technique that several potential sweeps are required for the films to become fully electroactive [3, 77, 80, 148, 149]. This phenomenon has been referred to as the *break-in effect* (Fig. 7). A secondary break-in effect may be observed when the film is in its neutral form for a longer period of time before a repeated charging process. Both break-in effects are attributed to the incorporation of solvent molecules and ions into the film phase during electrolysis, as well as to potential-dependent morphological changes. The rate of the diffusive transport of solvent molecules depends on the structure of the polymer and the motion of polymer segments. In crystalline and cross-linked polymers or below the glass-transition temperature, the movement of the incorporating species may be rather slow. On the other hand, solvent molecules

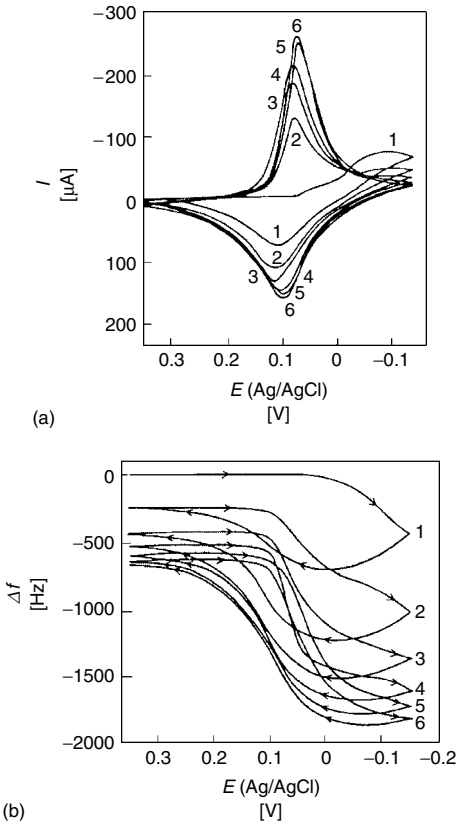


Fig. 7 Cyclic voltammetric break-in of a poly(tetracyanoquinodimethane) electrode. Electrolyte: 2.5 M LiCl. Sweep rate: 6 mV s^{-1}. (a) Consecutive cyclic voltammograms, (b) simultaneously obtained EQCM frequency curves [148].

act as plasticizers, and therefore increase the rate of diffusion for both neutral and ionic species inside the film.

9.5.2 Dynamics of Polymeric Motion

The rate of chain and segmental motions is of utmost importance since these processes may determine the rate of the diffusional encounter and consequently the rate of the electron transport process within the polymer film. Below the glass-transition temperature (T_m) the polymeric motion is practically frozen-in. Above T_m the frequency of the chain and segmental motions strongly increase with temperature [3, 150]. The plasticizing effect of the solvent enhances the rate of all kinds of motions in the polymer phase. At high electrolyte concentrations the ionic shielding of the charged sites of the polymer increases, and the polymer film will adopt a more compact structure. In this case the activity of the solvent is also low; consequently the film swelling is less [3, 79, 148]. In the more compact structure, the molecular motions become more hindered. Covalent or electrostatic cross-linking diminishes the rate of all of the physical diffusion processes.

9.6 Film Structure and Morphology

In a general sense, the swollen polymer films can be considered as a polymer, polyelectrolyte gel [3]. Various microscopic techniques have revealed a pronounced heterogeneity of the surface layer [151–159]. In this respect, one has to distinguish between macropores (whose diameter exceeds 10 nm considerably) and nanopores (which represent solvent molecules and ions between the polymer chains). Inside the macropores, the thermodynamic and transport properties of ions and solvent molecules practically do not differ from that of the contacting bulk solution. The space-charge regions (electric double layers) are formed at the interface between the polymer and solution phases whose thickness is much lower than the characteristic sizes of macroelements (fibrils, grains, and pores). The

polymer phase itself consists of a polymer matrix with incorporated ions and solvent molecules which do not form a separate continuous phase. Strong coulombic attractions between electronic and ionic charges prevent their separations at the distance significantly exceeding the Debye screening length of the medium (ca 0.1–0.3 nm in charged state). There are three principal approaches to modeling the structure of the polymer phase [14, 125]. One may consider a uniform, homogeneous film [72, 120–122, 125, 139], or a porous medium [43, 59, 160–164] or an inhomogeneous homogeneous phase where the properties of the first layer differ from those of the bulk film [165, 166]. In the case of uniform films, the polymer phase contains macromolecules, ions, and solvent molecules. In equilibrium, its state is determined by the equality of the electrochemical potentials for all mobile species in each adjoining phase. Both electronic and ionic species participate in the formation of the space charges at the interfaces with the surrounding media, metal and solution, respectively. The electroneutrality condition prevails inside the film and a small disbalance of the charge related to the electric double-layer species inside the metal or the solution parts of the interfaces is only assumed. The overall electrode potential represents a sum of two interfacial contributions corresponding to the metal/polymer and polymer/solution interfaces. The potential distributions across the metal/film/solution depend on the electrolyte concentration and the partitioning equilibrium. At sufficiently high concentrations of coions inside the film, the potential drop at the polymer/solution interface is almost constant. In the opposite limiting case, the potential profile shows a gradual transformation as a function of charging level and the potential drops vary at both interfaces [72]. This model considers diffusion-migration transport of electronic and ionic charge carriers in a uniform medium, coupled with a possibly nonequilibrium charge transfer across the corresponding interfaces at the boundaries of the film.

An extension of the uniform model is the inhomogeneous homogeneous model [165, 166] where, due to the strong interaction between the adsorbed polymer molecules and the metal substrate (the nature of the metal and its surface geometry may play an important role) the properties of this layer are different from the rest of the film. It can be described formally by the introduction of an adsorption pseudocapacitance and a resistance connected with the charging/discharging process within the first layer of the film at the metal interface.

The alternative approach, the porous medium model [43, 59, 160–164] separates polymer chains and ions + solvent molecules, respectively, into two different phases. Physically, it represents a porous membrane, which includes a matrix formed by the polymer and pores filled with electrolyte. Therefore, this macroscopically homogeneous two-phase system consists of an electronically conducting solid phase and an ionically conducting electrolyte phase. The transport properties of ions and solvent molecules in this phase may significantly differ from those in bulk electrolyte solutions. Each of these phases has specific electric resistivities (they may be inhomogeneous), and the two phases (i.e., these resistivities) are interconnected continuously by the double-layer capacitance at the surface between the solid phase and the pores. A further interconnection results from the charge transfer at the surface of the pores. There is also an electron exchange between the regions in

the polymer having different degrees of oxidation. Despite seemingly opposite ways of describing the polymer phase in these approaches, the results concerning the responses to dc and ac perturbations turned out to be often similar or even identical.

Porosity effects in the charging process have been implicated for a long time in the discussion of the faradaic and capacitive contributions to the current, especially in the case of electronically conducting polymers. For instance, peaks of the cyclic voltammograms are attributed to the faradaic process, while the plateaus of the current are considered as the indication of the capacitive term [58, 61, 66, 167–171]. However, this straightforward analogy to the metal/solution interface does not work in reality; the obviously faradaic process of redox transformation of the redox species in the surface layer does not lead to a direct current, unlike similar reaction for solute species.

9.6.1 Thickness

According to the theory of the metastable adsorption of de Gennes [172], when an adsorbed polymer layer is in contact with a pure solvent, the layer density diminishes from the substrate (e.g., metal) surface. The behavior of several polymer film electrodes (e.g., poly(tetracyanoquinodimethane) [173], poly(vinylferrocene) [21, 92], polypyrrole [174], and polyaniline [37, 175]) has been explained by the assumption that the film density decreases with the film thickness, that is from the metal surface to the polymer/solution interface. During electropolymerization (e.g., in the case of polyaniline) first, a compact layer (thickness $L \sim 200$ nm) is formed on the electrode surface via a potential-independent nucleation and a two-dimensional (2-D, lateral) growth of polyaniline islands. In the advanced stage 1-D growth of polymer chain with continuous branching leading to an open structure takes place [176, 177].

9.6.2 Synthesis Conditions, Nature of Electrolyte

In the synthesis of polypyrrole, the current density is a crucial parameter. At low current densities, the structure of polypyrrole is dominated by one-dimensional chains, while at high current densities two-dimensional microscopic structures of the polymer are formed. The higher conductive 2-D islands are interconnected by short 1-D chain segments acting as tunneling barriers [51]. Although the region close to the electrode surface shows a more or less well-defined structure, in general, the polymer layer can be considered an amorphous material. However, there are reports on crystalline structure, too. For instance, poly(*p*-phenylene) films obtained by electrooxidation of benzene in concentrated H_2SO_4 emulsion show a highly crystalline structure [178]. Higher electronic conductivity has been achieved by template synthesis, using polycarbonate membranes and this method can be exploited to obtain nanostructures [179, 180].

The film morphology (compactness, swelling) is strongly dependent on the composition of the solution, notably on the type of counterions present in the solution used in the course of electrodeposition, and the plasticizing ability of the solvent molecules. For instance, in the case of polyaniline BF_4^-, ClO_4^- and F_3CCOO^- promote the formation of a more compact structure, while the use of HSO_4^-, NO_3^- or Cl^- results in a more open structure [63, 76, 152, 181]. Similarly, poly(vinylferrocene) is more swollen

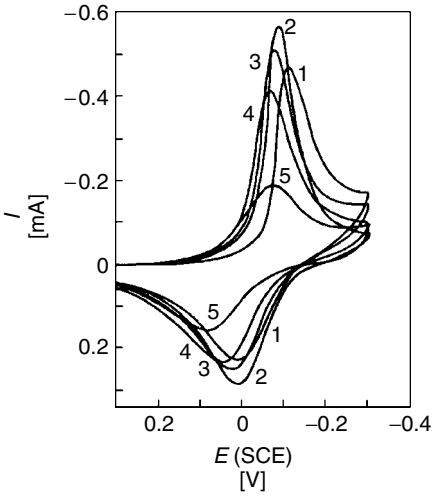


Fig. 8 Cyclic voltammograms of a poly(tetracyanoquinodimethane) electrode ($\Gamma = 13$ nmol cm^{-2}) in contact with lithium-chloride solution at different concentrations: (1) 0.625, (2) 1.25, (3) 2.5, (4) 5.0, and (5) 10.0 mol dm^{-3}. Sweep rate: 60 mV s^{-1} [77].

in the presence of NO_3^- ions than in ClO_4^- -containing electrolytes. It can be explained by the higher formation constant of ion pairs between the oxidized sites and the ClO_4^- ions compared with NO_3^- ions. This conclusion is in accordance with the higher positive formal potential of ferrocene/ferricenium redox couple in $NaNO_3$ solutions compared with $NaClO_4$ electrolyte. The higher swelling reflects the more extensive interaction between water and the charged ferricenium sites in the presence of NO_3^- containing, than in ClO_4^- -containing, electrolytes [74, 92].

9.6.3 Effect of Electrolyte Concentration and Temperature

The swelling and shrinking of a polyelectrolyte gel are strongly affected by the concentration of the contacting electrolyte solution and temperature [3, 73, 74, 77, 83]. Thermodynamical theory that considers three contributions to the free energy of the gel (i.e., mixing of constituents, network deformation, and electrostatic interactions) predicts a gel shrinkage as the salt concentration is increased or temperature is decreased [182]. Usually, the shrinking process occurs smoothly, but under certain conditions, the process becomes discontinuous, and a tiny addition of salt leads to the collapse of the gel that is a drastic decrease of the volume to a fraction of its original value. The onset of shrinking and swelling substantially depends on temperature. This phenomenon is akin to thermodynamic phase transitions in other branches of physical chemistry. The abrupt deterioration of the charge transport rate in poly(tetracyanoquinodimethane) or poly(vinylferrocene) films at high electrolyte concentrations (10 mol dm^{-3} LiCl or 5 mol dm^{-3} $CaCl_2$) and its temperature dependence can be interpreted on the basis of the thermodynamical theory [77, 79]. In a more compact structure, the rate of electron hopping may increase since the concentration of redox sites is high; however, simultaneously, a deterioration of the film permeability concerning the counterions due to the decrease of the free volume is expected. The maximum observed in the peak current versus salt concentration curves is the result of the balanced effects of the enhanced electron-exchange process and the hindered counterion motion (Fig. 8). The abrupt change in the free volume of solvent-filled cavities causes a sharp decrease in the charge transport diffusion coefficient [3].

9.7 Relaxation and Hysteresis Phenomena

Owing to the long relaxation times characteristic of polymeric systems, the equilibrium or steady-state situation often has not been reached within the timescale of the experiment. Figure 9 shows the changes of the resistance of polyaniline after potential steps. It can be seen that the achievement of a constant resistance value takes a rather long time, especially during conducting-to-insulating transition. Consequently, even slow sweep rate cyclic voltammetry does not supply reliable thermodynamic quantities, which can otherwise be derived by analyzing the changes in the peak potentials. The

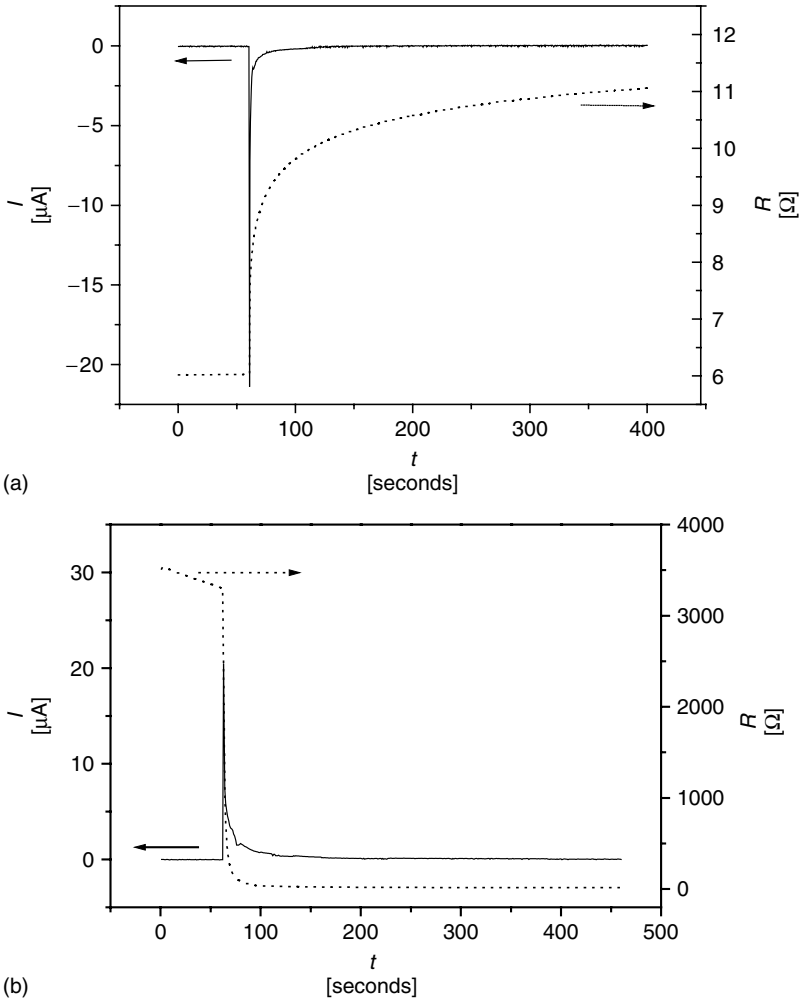


Fig. 9 The current transients and the respective resistance-time curves obtained for a polyaniline film following potential steps (a) from 0.2 to 0.15 V and (b) from 0.15 to 0.2 V. Solution: 2 M H_2SO_4 [53].

manifestation of the polymeric nature of these systems is most striking in the relaxation phenomena, which are in connection with the changes of the conditions (potential, temperature, etc.) and appear in different effects, such as hysteresis, ''first cycle'' and memory effects [45, 53, 63, 69, 77, 183–189].

The first cycle or waiting time effects (the shape of the cyclic voltammograms and the peak potentials depend on the delay time at potentials where the polymer is in its neutral (discharged) state – see also secondary break-in) have been interpreted in terms of slow morphological changes and/or with the difficulty of the removal of the remaining charges from an insulating surrounding [183, 188]. It should be mentioned that this problem also arises in the case of redox polymers [77, 79–82]. The results of fast scan rate voltammetry, chronoamperometry, and chronopotentiometry have been explained also by a model assuming an instantaneous two-dimensional nucleation and the growth of conducting zones and it has been concluded that the oxidation and reduction must proceed by different pathways and involve different degrees of disorder [63]. The slow change of the local pH has also been accounted for [188]. For the conducting-to-insulating conversion, the slow relaxation effect has been interpreted within the framework of percolation theory [184, 185] and by the electrochemically stimulated conformational relaxation (ESCR) model [69, 187], respectively. Both theories predict a logarithmic time dependence. The percolation theory assumes that the slow relaxation after rapid conducting–insulating conversion is composed of three interrelated processes: statistical structure formation, random fluctuation, and electron transfer. Accordingly, the rate-determining step is either the electrochemical reaction that occurs in electrode-percolated conducting clusters or the random rearrangement of conducting clusters by electron-exchange reaction between conducting and insulating species and/or diffusion of polymer chain. The rate of the conducting–insulating conversion suddenly slows down at the percolation threshold. The ESCR model assumes that two main processes are operative, concerning the kinetics of the redox switching of conducting polymers. The first is the charging–discharging process that includes the electronic and ionic charge transport. The second is the induced conformational change of the polymer that affects the rate of the electrochemical transformation and due to the slowness of the relaxation of the polymer this process may last much longer than the actual oxidation or reduction process. The latter model was used to describe the redox switching of polypyrrole, where an extensive volume increase occurs during oxidation. An extra mechanical energy has been taken into account that is needed to open the originally compact structure. The hysteresis effect has been explained by the difference in the oxidation and reduction sequences (see Figs. 3 and 9). The hysteresis effect and the non-Nernstian behavior for polyaniline have also been elucidated with the help of the polaron models, considering that the formation energies of both polarons and bipolarons increase with an increasing degree of oxidation [43, 44]. A first-order phase transition due to an S-shaped energy diagram that is in connection with attractive interactions between electronic and ionic charges has also been proposed [186]. The hysteresis phenomenon has also been explained by the stabilization of the oxidized polymer molecules, considering that the originally twisted, benzoid conformation is transformed into a more planar, quinoid-like structure with better

π-conjugation which, therefore, can be reduced at lower potentials (with lower energy). The planarization of the twisted segments within a chain takes place in the first stage of the charging process and due to the interactions between the π-electron clouds of the neighboring charged segments an intermolecular stabilization can also occur. Intermolecular interactions are favorable in the crystalline domains of the polymer. It is assumed that the stabilization process is fast [66]. Recently, even an intermolecular coupling of two π-radical centers forming a σ-bond and the dimerization and disproportion of the polaronic segments have been proposed [67, 68]. It is worth mentioning that the considerable difference between the anodic and cathodic peak potentials of cyclic voltammograms in the case of polytetracyanoquinodimethane redox electrode has been explained by the formation of dimeric species, that is, a slow formation of mixed valence dimer during reduction (charging) and fast reoxidation of dimer dianion resulting in the mixed valence dimer during the discharging process [77, 82]. The shielding effects of the counterions may also contribute to the overall stabilization energy.

While the effect of the potential-induced relaxation phenomena has been extensively studied, fewer efforts have been made concerning the temperature effect. A notable exception is a temperature shock experiment on poly(tetracyanoquinodimethane) electrode. It was found that when the electrode returned from an elevated temperature to room temperature, a relatively long time (>30 minutes) was needed to restore the original voltammetric response characteristic for room temperature as seen in Fig. 10. Apparently, the polymer adopts an extended, perhaps solvent, swollen

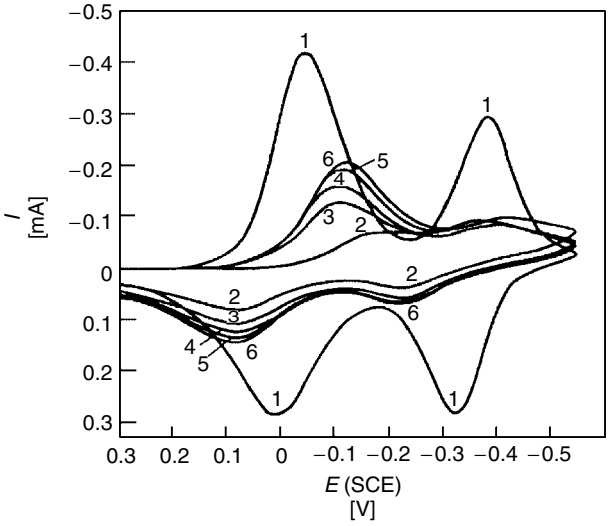


Fig. 10 Cyclic voltammograms obtained for poly(tetracyanoquinodimethane) electrode in contact with 10 M LiCl at (1) 69 °C and (2–6) after rapid cooling at 22 °C recorded after delays of (2) 4, (3) 9, (4) 13.5, (5) 22.5, and (6) 38.5 minutes [77].

conformation at the elevated temperatures that requires a long time for the restoration of the room temperature structure [77]. Such behavior is observed in the studies of polymer gels, when the variation of temperature results in the hysteresis of macroscopic polymer properties such as swelling, elasticity, turbidity, and so forth.

9.8 Measurements of the Rate of Charge Transport

The rate of charge transport within an electrochemically active polymer film has been successfully studied by transient electrochemical techniques. One may distinguish methods using large and small potential or current perturbations, respectively. For the basic characterization cyclic voltammetry, potential (less often current) step and pulse techniques have been applied [1–10]. With the help of these techniques, average values for the charge transport diffusion coefficient can be obtained, since the properties of the polymer continuously change and large amounts of ions and/or solvent molecules are exchanged between the polymer phase and the bulk solution during the experiments. Owing to the marginal perturbation from equilibrium (steady state) by low-amplitude (<5 mV) sinusoidal voltage, the advantage of electrochemical impedance spectroscopy (EIS) over other techniques involving large perturbations is evident [3, 4, 35–37, 43, 59, 100, 118–135, 139, 152–156, 160–167, 190, 191]. For instance, even the potential dependence of the charge transport diffusion coefficient can be determined, which may reveal the nature of charge carriers and interactions within the film. In addition, it gives a wealth of information on the kinetic processes occurring in these systems, as well as on ohmic resistance, double-layer and redox capacitances.

Most of the studies have been carried out on asymmetrical systems (cells) which is the classical polymer film electrode arrangement:

reference electrode|electrolyte solution|polymer film|inert metal.

This type of electrode involves the transport of electrons through the inert metal|polymer interface and ions through polymer|electrolyte interface, respectively. With the help of symmetric arrangements

reference electrode|electrolyte| polymer membrane|electrolyte| reference electrode

or

inert metal|polymer film|inert metal

either ion transport (electron transport across both interfaces is blocked) or electron transport (ion transfer at both interfaces is blocked) can be studied separately, provided there are no redox ions present in the electrolyte solutions. The study of a given system by using the combination of these three arrangements is extremely effective, because the frequency analysis provides information on both types of transport [120, 123–125, 191].

Radiotracer technique [62, 77, 80, 84] is well suited to the investigation of the motion of counterions and coions coupled to the electron-transfer and transport processes, and offers the opportunity of studying the attainment of equilibrium and steady states in regard to the sorbed ions at any potential that is at any ratio of oxidized and reduced sites in the film, without disturbing the original experimental conditions. Piezoelectric microgravimetry at

electrochemical quartz crystal microbalance (EQCM) with nanogram sensitivity has also emerged as an important technique for monitoring the surface mass change [73–77, 83, 85–87, 90–110, 148, 149, 189, 192, 193]. A comparison of the change of the surface mass with the charge consumed in the course of the redox transformations may shed light on the mechanism of the electrochemical reactions. It may supply information also on the sorption of neutral species and protonation equilibria. Conclusions can be drawn concerning the relative contribution of different anions and cations to the overall ion-exchange process, as well as the rate of the mass transport processes.

PBD involves the measurement of the deflection of a light beam, aligned parallel to the electrode surface [88–90, 194]. This *in situ* method is also a very convenient tool for the study of ion transport and reaction mechanism. The deflection is not significantly perturbed by solvent transfer between the polymer film and the solution. The combination of radiotracer and EQCM or EQCM and PBD techniques is especially useful because it allows access to individual ion and solvent flux contributions to mass transport dynamics [90].

In situ conductivity measurements [52, 53, 164, 189, 195–202], luminescence techniques [203], different spectroscopies in combination with electrochemical methods [35–39, 82, 114, 115, 153–156, 204–208], and surface plasmon resonance [209] have also supplied valuable information about the ionic and electronic charge-transfer and charge transport processes. Microscopies have given new insights into the structure and morphology of surface polymer films, as well as their changes with the experimental conditions [151–159, 210–218]. The successful application of scanning electrochemical microscope for *in situ* determination of film thickness is also a very important achievement, because it allows the extraction of correct D values from the $D^{1/2}c$ products [207, 208]. This method is more straightforward than ellipsometry [113, 175, 219, 220], where the refractive index must be available, or profilometry, which is not applicable to easily deformed films.

In summary, the application of new and powerful techniques has allowed a detailed insight into the nature of the charge transport and charge transfer as well as of the chemical and physical processes occurring in these systems. Therefore, the production of electrochemically active polymers, polymeric films, and composites with desired properties, has become a well-established area of electrochemical and material sciences. Considering the pace of the ever-growing applications of polymers in electrochemical cells, it may be declared that electrochemistry is in transition from the bronze age (i.e., typically using metals) to the era of polymers.

References

1. R. W. Murray, in *Electroanalytical Chemistry* (Ed.: A. J. Bard), Marcel Dekker, New York, 1984, pp. 191–368, Vol. 13.
2. R. W. Murray (Ed.), *Molecular Design of Electrode Surfaces, Techniques of Chemistry*, Wiley, New York, 1992, Vol. 22.
3. G. Inzelt, in *Electroanalytical Chemistry* (Ed.: A. J. Bard), Marcel Dekker, New York, 1994, pp. 89–241, Vol. 18.
4. M. E. G. Lyons (Ed.), *Electroactive Polymer Electrochemistry*, Part I, Plenum Press, New York, 1994.
5. M. E. G. Lyons (Ed.), *Electroactive Polymer Electrochemistry*, Part II, Plenum Press, New York, 1996.
6. H. S. Nalwa (Ed.), *Handbook of Organic Conducting Molecules and Polymers*, Wiley, New York, 1997, Vols 1–4.

7. M. Fujihira, in *Topics in Organic Electrochemistry* (Eds.: A. J. Fry, W. E. Britton), Plenum Press, New York, 1986, pp. 225–294.
8. R. G. Linford (Ed.), *Electrochemical Science and Technology of Polymers*, Elsevier, UK, 1987, Vol. 1.
9. R. G. Linford (Ed.), *Electrochemical Science and Technology of Polymers*, Elsevier, UK, 1990, Vol. 2.
10. G. P. Evans, in *Electrochemical Science Engineering* (Eds.: H. Gerischer, C. W. Tobias), VCH Press, Weinheim, 1990, pp. 1–74, Vol. 1.
11. T. A. Skotheim (Ed.), *Handbook of Conducting Polymers*, Marcel Dekker, New York, 1986, Vols 1–2.
12. R. J. Forster, J. G. Vos, in *Comprehensive Analytical Chemistry* (Ed.: G. Svehla), Elsevier, Amsterdam, 1992, pp. 465–530, Vol. 27.
13. W. J. Albery, A. R. Hillman, *Annu. Rev. C. R. Soc. Chem. London* **1981**, *78*, 377–437.
14. G. Inzelt, M. Pineri, J. W. Schultze et al., *Electrochim. Acta* **2000**, *45*, 2403–2421.
15. H. Dahms, *J. Phys. Chem.* **1968**, *72*, 362.
16. I. Ruff, V. J. Friedrich, *J. Phys. Chem.* **1971**, *75*, 3297.
17. I. Ruff, V. J. Friedrich, K. Demeter et al., *J. Phys. Chem.* **1971**, *75*, 3303.
18. L. Botár, I. Ruff, *Chem. Phys. Lett.* **1986**, *126*, 348.
19. C. P. Andrieux, J. M. Saveant, *J. Electroanal. Chem.* **1980**, *111*, 377.
20. E. Laviron, *J. Electroanal. Chem.* **1980**, *112*, 1.
21. P. J. Peerce, A. J. Bard, *J. Electroanal. Chem.* **1980**, *114*, 89.
22. D. A. Buttry, F. C. Anson, *J. Electroanal. Chem.* **1981**, *130*, 333.
23. I. Rubinstein, *J. Electroanal. Chem.* **1985**, *188*, 227..
24. S. Feldberg, *J. Electroanal. Chem.* **1986**, *198*, 1.
25. P. He, X. Chen, *J. Electroanal. Chem.* **1988**, *256*, 353.
26. I. Fritsch-Faules, L. R. Faulkner, *J. Electroanal. Chem.* **1989**, *263*, 237.
27. E. Leiva, P. Meyer, W. Schmickler, *J. Electrochem. Soc.* **1988**, *135*, 1993.
28. D. N. Blauch, J. M. Saveant, *J. Am. Chem. Soc.* **1992**, *114*, 3323.
29. L. Srinivasa Mohan, M. V. Sangaranarayanan, *J. Electroanal. Chem.* **1992**, *323*, 375.
30. C. E. D. Chidsey, R. W. Murray, *J. Phys. Chem.* **1986**, *90*, 1479.
31. B. Wessling, in *Handbook of Organic Conducting Molecules and Polymers* (Ed.: H. S. Nalwa), Wiley, New York, 1997, p. 497, Vol. 3.
32. S. Roth, *One-Dimensional Metals*, VCH, Weinheim, 1995.
33. E. M. Conwell, in *Handbook of Organic Conducting Molecules and Polymers* (Ed.: H. S. Nalwa), Wiley, New York, 1997, p. 1, Vol. 3.
34. E. M. Genies, A. Boyle, M. Lapkowski et al., *Synth. Met.* **1990**, *36*, 139.
35. A. M. Waller, R. G. Compton, *J. Chem. Soc., Faraday Trans.* **1989**, *85*, 977.
36. F. Li, W. J. Albery, *J. Chem. Soc., Faraday Trans.* **1991**, *87*, 2949.
37. S. H. Glarum, J. H. Marshall, *J. Electrochem. Soc.* **1987**, *134*, 2160.
38. J. Scott, P. Pfluger, M. T. Krounbi et al., *Phys. Rev. B* **1983**, *28*, 2140.
39. A. G. MacDiarmid, A. J. Epstein, *Faraday Discuss. Chem. Soc.* **1989**, *88*, 317.
40. M. Fujihira, in *Topics in Organic Electrochemistry* (Eds.: A. J. Fry, W. E. Britton), Plenum Press, New York, 1986, p. 255.
41. J.-L. Bredas, G. B. Street, *Acc. Chem. Res.* **1985**, *18*, 309.
42. R. P. Chance, D. S. Boudreaux, J. L. Bredas et al., in *Handbook of Conducting Polymers* (Ed.: T. A. Skotheim), Marcel Dekker, New York, 1986, p. 825, vol. 2.
43. K. Rossberg, G. Paasch, L. Dunsch et al., *J. Electroanal. Chem.* **1998**, *443*, 49.
44. G. Paasch, P. H. Nguyen, A. J. Fischer, *Chem. Phys.* **1998**, *227*, 219.
45. L. I. Daikhin, M. D. Levi, *J. Chem. Soc., Faraday Trans.* **1992**, *88*, 1023.
46. W. J. Albery, Z. Chen, B. R. Horrocks et al., *Faraday Discuss. Chem. Soc.* **1989**, *88*, 247.
47. A. J. Heeger, *Faraday Discuss. Chem. Soc.* **1989**, *88*, 203.
48. N. F. Mott, E. A. Davis, *Electronic Processes in Non-Crystalline Materials*, Clarendon Press, Oxford, 1979.
49. P. Sheng, *Phys. Rev. B* **1980**, *21*, 2180.
50. G. Paasch, *Synth. Met.* **1992**, *51*, 7.
51. G. Paasch, D. Smeisser, A. Bartl et al., *Synth. Met.* **1994**, *66*, 135..
52. E. W. Paul, A. J. Ricco, M. S. Wrighton, *J. Phys. Chem.* **1985**, *89*, 1441.
53. E. Csahók, E. Vieil, G. Inzelt, *J. Electroanal. Chem.* **2000**, *482*, 168.

54. Q. Pei, O. Inganas, *Synth. Met.* **1993**, *55/57* 3730.
55. G. Harsányi, *Polymer Films in Sensor Applications*, Technomic, Switzerland, 1995.
56. A. F. Diaz, K. K. Kanazawa, G. P. Gardini, *J. Chem. Soc., Chem. Commun.* **1979**, 635.
57. A. F. Diaz, J. A. Logan, *J. Electroanal. Chem.* **1980**, *111*, 111.
58. S. W. Feldberg, *J. Am. Chem. Soc.* **1984**, *106*, 4671.
59. I. Rubinstein, E. Sabatini, J. Risphon, *J. Electrochem. Soc.* **1987**, *134*, 3078.
60. M. Kalaji, L. M. Peter, *J. Chem. Soc., Faraday Trans.* **1991**, *87*, 853.
61. E. M. Genies, J. F. Penneau, E. Vieil, *J. Electroanal. Chem.* **1990**, *283*, 205.
62. G. Horányi, G. Inzelt, *Electrochim. Acta* **1988**, *33*, 947.
63. M. Kalaji, L. Nyholm, L. M. Peter, *J. Electroanal. Chem.* **1991**, *313*, 271.
64. S. W. Feldberg, I. Rubinstein, *J. Electroanal. Chem.* **1988**, *240*, 1.
65. S. Gottesfeld, A. Redondo, I. Rubinstein et al., *J. Electroanal. Chem.* **1989**, *265*, 15.
66. K. Meerholz, J. Heinze, *Electrochim. Acta* **1996**, *41*, 1839.
67. J. Heinze, P. Tschuncky, A. Smie, *J. Solid State Electrochem.* **1998**, *2*, 102.
68. A. Neudeck, A. Petr, L. Dunsch et al., *J. Phys. Chem. B* **1999**, *103*, 912.
69. T. Otero, H.-J. Grande, J. Rodriguez, *J. Phys. Chem. B* **1997**, *101*, 3688.
70. M. A. Vorotyntsev, J. Heinze, *Electrochim. Acta* **2001**, *46*, 3309.
71. D. Posadas, M. I. Florit, *J. Phys. Chem. B* **2004**, *108*, 15470.
72. K. Doblhofer, in *Electroactive Polymer Electrochemistry* (Ed.: M. E. G. Lyons), Part I, Plenum Press, New York, 1994, pp. 375–437.
73. A. R. Hillman, D. C. Loveday, S. Brucken stein, *J. Electroanal. Chem.* **1989**, *274*, 157.
74. G. Inzelt, J. Bácskai, *Electrochim. Acta* **1992**, *37*, 647.
75. G. Inzelt, *J. Electroanal. Chem.* **1990**, *287*, 171.
76. S. Pruneanu, E. Csahók, V. Kertész et al., *Electrochim. Acta* **1998**, *43*, 2305.
77. G. Inzelt, *Electrochim. Acta* **1989**, *34*, 83.
78. D. A. Buttry, in *Electroanalytical Chemistry* (Ed.: A. J. Bard), Marcel Dekker, New York, 1991, pp. 1–85, Vol. 17.
79. G. Inzelt, L. Szabó, *Electrochim. Acta* **1986**, *31*, 1381.
80. G. Inzelt, G. Horányi, J. Q. Chambers, *Electrochim. Acta* **1987**, *32*, 757.
81. G. Inzelt, J. Q. Chambers, F. B. Kaufman, *J. Electroanal. Chem.* **1983**, *159*, 443.
82. G. Inzelt, R. W. Day, J. F. Kinstle et al., *J. Phys. Chem.* **1983**, *87*, 4592.
83. G. Inzelt, V. Kertész, A.-S. Nybäck, *J. Solid State Electrochem.* **1999**, *3*, 251.
84. G. Inzelt, G. Horányi, *J. Electroanal. Chem.* **1987**, *230*, 257.
85. J. Bácskai, K. Martinusz, E. Czirók et al., *J. Electroanal. Chem.* **1995**, *385*, 241.
86. A. R. Hillman, D. C. Loveday, M. J. Swann et al., *Faraday Discuss. Chem. Soc.* **1989**, *88*, 151.
87. M. Skompska, A. R. Hillman, *J. Chem. Soc., Faraday Trans.* **1996**, *92*, 4101.
88. C. Barbero, M. C. Miras, O. Haas et al., *J. Electrochem. Soc.* **1991**, *138*, 669.
89. E. Vieil, K. Meerholz, T. Matencio et al., *J. Electroanal. Chem.* **1994**, *368*, 183.
90. M. J. Henderson, A. R. Hillman, E. Vieil, *J. Phys. Chem. B* **1999**, *103*, 8899.
91. H. Daifuku, T. Kawagoe, N. Yamamoto et al., *J. Electroanal. Chem.* **1989**, *274*, 313.
92. H. L. Bandey, M. Gonsalves, A. R. Hillman et al., *J. Electroanal. Chem.* **1996**, *410*, 219.
93. E. P. Cintra, R. M. Torresi, G. Louarn et al., *Electrochim. Acta* **2004**, *49*, 1409.
94. K. Fehér, G. Inzelt, *Electrochim. Acta* **2002**, *47*, 3551.
95. C. Barbero, E. J. Calvo, R. Etchenique et al., *Electrochim. Acta* **2000**, *45*, 3895.
96. S.-M. Chen, Y.-H. Fa, *J. Electroanal. Chem.* **2004**, *567*, 9.
97. A. Lisowska-Oleksiak, K. Kazubowska, A. Kupniewska, *J. Electroanal. Chem.* **2001**, *501*, 54.
98. L. Adamczyk, P. J. Kulesza, K. Miecznikowski et al., *J. Electrochem. Soc.* **2005**, *152*, E98.
99. C. Gabrielli, M. Keddam, N. Nadi et al., *J. Electroanal. Chem.* **2000**, *485*, 101.
100. H. Varela, R. M. Torresi, *J. Electrochem. Soc.* **2000**, *147*, 665.
101. S.-J. Choi, S.-M. Park, *J. Electrochem. Soc.* **2002**, *149*, E26.
102. L. P. Bauerman, P. N. Bartlett, *Electrochim. Acta* **2005**, *50*, 1537.
103. V. Syritski, A. Öpik, O. Forsén, *Electrochim. Acta* **2003**, *48*, 1409.
104. S. Bruckenstein, K. Brzezinska, A. R. Hillman, *Phys. Chem. Chem. Phys.* **2000**, *2*, 1221.

105. C. Gabrielli, J. J. Garcia-Jareno, H. Perrot, *Electrochim. Acta* **2001**, *46*, 4095.
106. L. M. Abrantes, C. M. Cordas, E. Vieil, *Electrochim. Acta* **2002**, *47*, 1481.
107. C. W. Weidlich, K.-M. Mangold, K. Jüttner, *Electrochim. Acta* **2005**, *50*, 1547.
108. D. Benito, C. Gabrielli, J. J. Garcia-Jareno et al., *Electrochim. Acta* **2003**, *48*, 4039.
109. R. Ansari Khalkhali, W. E. Prize, G. G. Wallace, *React. Funct. Polym.* **2003**, *56*, 141.
110. Z. Puskás, G. Inzelt, *Electrochim. Acta* **2005**, *50*, 1481.
111. R. Patil, Y. Harima, K. Yamashita et al., *J. Electroanal. Chem.* **2002**, *518*, 13.
112. L. Lizarraga, E. M. Andrade, F. V. Molina, *J. Electroanal. Chem.* **2004**, *561*, 127.
113. L. M. Abrantes, J. P. Correia, M. Savic et al., *Electrochim. Acta* **2001**, *46*, 3181.
114. A. A. Nekrasov, V. F. Ivanov, A. V. Vannikov, *Electrochim. Acta* **2001**, *46*, 3301.
115. A. A. Nekrasov, V. F. Ivanov, O. L. Gribkova et al., *Electrochim. Acta* **2005**, *50*, 1605.
116. T. F. Otero, J. Padilla, *J. Electroanal. Chem.* **2004**, *561*, 167.
117. E. M. Andrande, F. V. Molina, D. Posadas et al., *J. Electrochem. Soc.* **2005**, *152*, E75.
118. R. Armstrong, *J. Electroanal. Chem.* **1986**, *198*, 177.
119. C. Gabrielli, O. Haas, H. Takenouti, *J. Appl. Electrochem.* **1987**, *17*, 82.
120. M. A. Vorotyntsev, L. I. Daikhin, M. D. Levi, *J. Electroanal. Chem.* **1994**, *364*, 37.
121. M. F. Mathias, O. Haas, *J. Phys. Chem.* **1993**, *97*, 9217.
122. R. P. Buck, M. B. Madaras, R. Mäckel, *J. Electroanal. Chem.* **1993**, *362*, 33.
123. R. P. Buck, C. Mundt, *Electrochim. Acta* **1999**, *44*, 1999.
124. M. A. Vorotyntsev, C. Deslouis, M. M. Musiani et al., *Electrochim. Acta* **1999**, *44*, 2105.
125. M. A. Vorotyntsev, J.-P. Badiali, G. Inzelt, *J. Electroanal. Chem.* **1999**, *472*, 7.
126. G. Garcia-Belmonte, J. Bisquet, *Electrochim. Acta* **2002**, *47*, 4263.
127. G. Garcia-Belmonte, *Electrochem. Commun.* **2003**, *5*, 236.
128. M. D. Levi, D. Aurbach, *J Electrochem. Soc.* **2002**, *149*, E215.
129. T. Komura, M. Ishihara, T. Yamaguchi et al., *J. Electroanal. Chem.* **2000**, *493*, 84.
130. O. Levin, V. Kontratiev, V. Malev, *Electrochim. Acta* **2005**, *50*, 1573.
131. Y. N. Ivanova, A. A. Karyakin, *Electrochem. Commun.* **2004**, *6*, 120.
132. X. Tu, Q. Xe, C. Xiang et al., *J. Phys. Chem. B* **2005**, *109*, 4053.
133. M. Ujvári, G. Láng, G. Inzelt, *Electrochem. Commun.* **2000**, *2*, 497.
134. G. G. Láng, M. Ujvári, G. Inzelt, *J. Electroanal. Chem.* **2004**, *572*, 283.
135. G. Láng, G. Inzelt, *Electrochim. Acta* **1999**, *44*, 2037.
136. C. P. Andrieux, J. M. Saveant, *J. Phys. Chem.* **1988**, *92*, 6761.
137. J. M. Saveant, *J. Electroanal. Chem.* **1988**, *242*, 1.
138. J. M. Saveant, *J. Phys. Chem.* **1988**, *92*, 4526.
139. R. P. Buck, *J. Electroanal. Chem.* **1986**, *210*, 1.
140. R. P. Buck, *J. Electroanal. Chem.* **1987**, *219*, 23.
141. R. P. Buck, *J. Phys. Chem.* **1988**, *92*, 4196.
142. R. P. Buck, *J. Phys. Chem.* **1988**, *92*, 6445.
143. R. P. Buck, *J. Electroanal. Chem.* **1989**, *258*, 1.
144. M. Sharp, B. Lindholm, E.-L. Lind, *J. Electroanal. Chem.* **1989**, *274*, 35.
145. C. J. Baldy, C. M. Elliot, S. W. Feldberg, *J. Electroanal. Chem.* **1990**, *283*, 53.
146. F. C. Anson, D. N. Blauch, J. M. Saveant et al., *J. Am. Chem. Soc.* **1991**, *113*, 1922.
147. M. A. Vorotyntsev, E. Vieil, J. Heinze, *J. Electroanal. Chem.* **1998**, *450*, 121.
148. J. Bácskai, G. Inzelt, *J. Electroanal. Chem.* **1991**, *310*, 379.
149. A. R. Hillman, S. Bruckenstein, *J. Chem. Soc., Faraday Trans.* **1993**, *89*, 339.
150. M. J. Pinkerton, Y. LeMest, H. Zhang et al., *J. Am. Chem. Soc.* **1990**, *112*, 8217.
151. C. M. A. Brett, A.-M. C. F. Oliveira Brett, J. L. C. Pereira et al., *J. Appl. Electrochem.* **1993**, *23*, 332.
152. G. T. Andrade, M. J. Aquirre, S. R. Baggio, *Electrochim. Acta* **1998**, *44*, 633.
153. S. R. Biaggio, C. L. F. Oliveira, M. J. Aguirre et al., *J. Appl. Electrochem.* **1994**, *24*, 1059.
154. K. Rossberg, L. Dunsch, *Electrochim. Acta* **1999**, *44*, 2061.
155. Y.-T. Kim, H. Yang, A. J. Bard, *J. Electrochem. Soc.* **1991**, *138*, L71.
156. M. J. Rodriguez Presa, H. L. Bandey, R. I. Tucceri et al., *Electrochim. Acta* **1999**, *44*, 2073.
157. M. Lieder, C. W. Schläpfer, *J. Electroanal. Chem.* **1996**, *41*, 87.

158. S. Yonezawa, K. Kanamura, Z. Takehara, *J. Chem. Soc., Faraday Trans.* **1995**, *91*, 3469.
159. F. Rourke, J. A. Crayston, *J. Chem. Soc., Faraday Trans.* **1993**, *89*, 295.
160. C. D. Paulse, P. G. Pickup, *J. Phys. Chem.* **1988**, *92*, 7002.
161. R. Penner, C. R. Martin, *J. Phys. Chem.* **1989**, *93*, 984.
162. W. J. Albery, C. M. Elliot, A. R. Mount, *J. Electroanal. Chem.* **1990**, *288*, 15.
163. S. Fletcher, *J. Chem. Soc., Faraday Trans.* **1993**, *89*, 311.
164. C. Ehrenbeck, K. Jüttner, S. Ludwig et al., *J. Electroanal. Chem.* **1998**, *43*, 2781.
165. G. Láng, J. Bácskai, G. Inzelt, *Electrochim. Acta* **1993**, *38*, 773.
166. C. Bonazzola, E. J. Calvo, *J. Electroanal. Chem.* **1998**, *449*, 111.
167. G. Tourillon, in *Handbook of Conducting Polymers* (Ed.: T. A. Skotheim), Marcel Dekker, New York, 1986, pp. 293–350.
168. E. M. Genies, J. M. Pernaut, *Synth. Met.* **1984**, *10*, 117.
169. Y. Tezuka, K. Aoki, K. Shinozaki, *J. Electroanal. Chem.* **1989**, *30*, 369.
170. T. Matencio, E. Vieil, *Synth. Met.* **1991**, *41/43* 3001.
171. A. F. Diaz, J. Bargon, in *Handbook of Conducting Polymers* (Ed.: T. A. Skotheim), Marcel Dekker, New York, 1986, pp. 81–115.
172. P. G. de Gennes, *Macromolecules* **1981**, *14*, 1637.
173. M. Karimi, J. Q. Chambers, *J. Electroanal. Chem.* **1987**, *217*, 313.
174. R. A. Bull, J. R. F. Fan, A. J. Bard, *J. Electrochem. Soc.* **1982**, *129*, 1009.
175. C. M. Carlin, L. J. Kepley, A. J. Bard, *J. Electrochem. Soc.* **1986**, *132*, 353.
176. K. Bade, V. Tsakova, J. W. Schultze, *Electrochim. Acta* **1992**, *37*, 2255.
177. C. M. G. S. Cruz, E. A. Ticianelli, *J. Electroanal. Chem.* **1997**, *428*, 185.
178. M. D. Levi, E. Yu. Pisarevskaya, E. B. Molodkina et al., *Synth. Met.* **1993**, *54*, 195.
179. C. R. Martin, R. Parthasarathy, V. Menon, *Synth. Met.* **1993**, *55/57*, 1156.
180. J. D. Noll, M. A. Nicholson, P. G. Van Patten et al., *J. Electrochem. Soc.* **1998**, *145*, 3320.
181. G. Zotti, S. Cattarin, N. Comissio, *J. Electroanal. Chem.* **1988**, *239*, 387.
182. R. Rydzewski, *Continuum Mech. Thermodyn.* **1990**, *2*, 77.
183. C. Odin, M. Nechtschein, *Phys. Rev. Lett.* **1992**, *67*, 1114.
184. K. Aoki, T. Edo, J. Cao, *Electrochim. Acta* **1998**, *43*, 285.
185. J. Cao, K. Aoki, *Electrochim. Acta* **1996**, *41*, 1787.
186. M. A. Vorotyntsev, J.-P. Badiali, *Electrochim. Acta* **1998**, *39*, 289.
187. H. Grande, T. F. Otero, *Electrochim. Acta* **1999**, *44*, 1893.
188. K. Fraouna, M. Delamar, C. P. Andrieux, *J. Electroanal. Chem.* **1996**, *418*, 109.
189. G. Inzelt, *Electrochim. Acta* **2000**, *45*, 3865.
190. T. Komura, T. Yamaguchi, E. Kunitani et al., *J. Electroanal. Chem.* **2003**, *557*, 49.
191. I. Betova, M. Bojinov, E. Lankinen et al., *J. Electroanal. Chem.* **1999**, *472*, 20.
192. C. Gabrielli, M. Keddam, N. Nadi et al., *Electrochim. Acta* **1999**, *44*, 2095.
193. R. A. Etchenique, E. J. Calvo, *Electrochem. Commun.* **1999**, *1*, 167.
194. H. Salavagione, J. Arias-Pardilla, J. M. Pérez et al., *J. Electroanal. Chem.* **2005**, *576*, 139.
195. J. Kankare, E.-L. Kupila, *J. Electroanal. Chem.* **1992**, *322*, 167.
196. B. W. Johnson, D. C. Read, P. Christensen et al., *J. Electroanal. Chem.* **1994**, *364*, 103.
197. P. N. Bartlett, J. H. Wang, *J. Chem. Soc., Faraday Trans.* **1996**, *92*, 4137.
198. E. Lankinen, M. Pohjakallio, G. Sundholm et al., *J. Electroanal. Chem.* **1997**, *437*, 167.
199. M. Probst, R. Holze, *Electrochim. Acta* **1995**, *40*, 213.
200. C. Zhang, B. Yao, J. Huang et al., *J. Electroanal. Chem.* **1997**, *440*, 35.
201. T. M. Swager, *Acc. Chem. Res.* **1998**, *31*, 201.
202. N. A. Surridge, J. C. Jernigan, E. F. Dalton et al., *Faraday Discuss. Chem. Soc.* **1989**, *88*, 1.
203. M. Majda, L. R. Faulkner, *J. Electroanal. Chem.* **1984**, *169*, 97.
204. Z. Ping, G. E. Nauer, H. Neugebauer et al., *J. Chem. Soc., Faraday Trans.* **1997**, *93*, 121.
205. D. D. Schlereth, A. A. Karyakin, *J. Electroanal. Chem.* **1995**, *395*, 221.
206. W. Zhang, P. Schmidt-Zhang, G. Kossmehl et al., *J. Solid State Electrochem.* **1999**, *3*, 135.
207. Cs. Visy, J. Kankare, *J. Electroanal. Chem.* **1998**, *442*, 175.
208. E. M. Genies, M. Lapkowski, *Synth. Met.* **1988**, *24*, 61.
209. F. S. Damos, R. C. S. Luz, L. T. Kubota, *J. Electroanal. Chem.* **2005**, *581*, 231.

210. M. V. Mirkin, F.-R. Fan, A. J. Bard, *Science* **1992**, *257*, 364.
211. F.-R. F. Fan, M. V. Mirkin, A. J. Bard, *J. Phys. Chem.* **1994**, *98*, 1475.
212. C. Froeck, A. Bartl, L. Dunsch, *Electrochim. Acta* **1995**, *40*, 1421.
213. F. Chao, M. Costa, C. Tian, *Synth. Met.* **1993**, *53*, 127.
214. R. Nyffenegger, E. Amman, H. Siegenthaler et al., *Electrochim. Acta* **1995**, *40*, 1411.
215. O. A. Semenikhin, L. Jiang, T. Iyoda et al., *J. Phys. Chem.* **1996**, *100*, 18603.
216. T. Silk, Q. Hong, J. Tamm et al., *Synth. Met.* **1998**, *93*, 59.
217. M. F. Suarez, R. G. Compton, *J. Electroanal. Chem.* **1999**, *462*, 211.
218. M. H. Troise Frank, G. Denuault, *J. Electroanal. Chem.* **1993**, *354*, 331.
219. J. Rishpon, A. Redondo, C. Derouin et al., *J. Electroanal. Chem.* **1990**, *294*, 73.
220. R. Greef, M. Kalaji, L. M. Peter, *Faraday Discuss. Chem. Soc.* **1989**, *88*, 277.

10.1
Oxygen Electrocatalysis

Nagao Kobayashi
Tohoku University, Sendai, Japan

To date reported oxygen electrocatalysis has been carried out mostly in the presence of metallomacrocycles such as metalloporphyrins and phthalocyanines, and is important in several aspects. In particular, oxygen reduction using these complexes has two important applications. First, as a model reaction of cytochrome oxidase, which reduces oxygen to water at the end of the respiratory chain, and second, as an attractive candidate for the cathode reaction of a fuel cell. On the other hand, electrocatalytically activated oxygen has often been used for the oxidation, and in particular, epoxidation of organic molecules. In this section, oxygen electroreduction itself in the presence of iron, cobalt, manganese, and a few other metalloporphyrins and phthalocyanines is mainly described, and then some examples of oxidation reactions of organic molecules are briefly stated.

First, we have to understand the O_2 molecule and why its interaction with transition metals is important in O_2 electrocatalysis. In the ground state, the 16 electrons of the O_2 molecule are distributed over its molecular orbitals according to

$$(\sigma_g 1s)^2(\sigma_u^* 1s)^2(\sigma_g 2s)^2(\sigma_u^* 2s)^2 \times (\sigma_g 2p_x)^2(\pi_u 2p_{y,z})^4(\pi_g^* 2p_{y,z})^2,$$

which is a $^3\Sigma_g^-$ state with bond order 2. The O−O bond strength corresponds to $\Delta H_{f^\circ}(298\ K) = 498.7\ kJ\ mol^{-1}$, and this rather high bond strength (compared to $-334\ kJ\ mol^{-1}$ for the C−C and $-431\ kJ\ mol^{-1}$ for the C−H bonds) implies that one of the impediments in oxygen reduction is the breaking of the O−O bond. The other possible first step is the transfer of the first electron, that is, $O_2 + e^- \rightarrow O_2^-$, which is energetically unfavorable ($\Delta G^\circ = 31.8\ kJ\ mol^{-1}$, $E^\circ = -0.33\ V$ [1]) and is accordingly slow as well. The task of the electrocatalytic system is therefore to promote these two reactions. Since the ground state is triplet, there is a fundamental restriction on its reactivity with general molecules that are singlet in the ground state. However, this spin restriction can be removed by coordination with a transition metal center that has unpaired electrons, which is why transition metal compounds have been extensively used in electrocatalytic reactions of oxygen. Possible interactions between oxygen and substrates, that is, metals in this case, can be expressed by the following

Encyclopedia of Electrochemistry. Edited by A.J. Bard and M. Stratmann
Vol. 10 *Modified Electrodes*. Edited by M.Fujihira, I.Rubinstein, and J.F.Rusling
Copyright © 2007 Wiley-VCH Verlag GmbH & Co. KGaA, Weinheim. ISBN: 978-3-527-30402-8

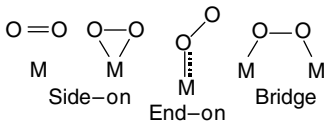


Fig. 1 Interactions of oxygen with a metal.

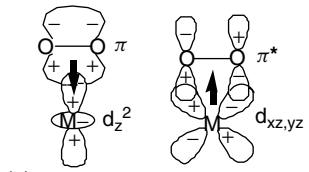
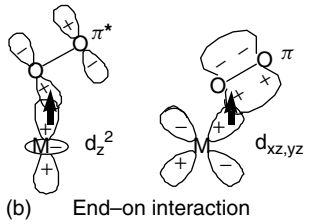


Fig. 2 Orbital overlap in (a) side – on and (b) end – on interaction.



molecular orbital description. (1) A bonding interaction, caused by overlaps of the occupied $\pi_u 2p$ orbital of O_2 and empty orbitals of the substrate, which weaken the O−O bond and alter the electron density in O_2. (2) A back-bonding interaction, caused by overlap of occupied orbitals of the substrate and the partially occupied antibonding $\pi_g * 2p$ orbital of oxygen, which will function mainly to reduce the bond order of O_2.

These interactions can be visualized using three models (Fig. 1). In the side-on model, both the bonding and back-bonding interaction occur (Fig. 2a) and weaken the O−O bond and an increment in length of this bond.

This type of binding, however, has no activity for the electroreduction of oxygen. The end-on binding (Fig. 2b), first proposed by Pauling [2], is likely to occur on transition metal electrocatalysts. As seen in this figure, transition metals with occupied d_{xz} and d_{yz} orbitals and an empty d_z^2 orbital are able to have the most effective interaction; that is, a bonding overlap of π_g^* and d_z^2: $\sigma(\pi_u \rightarrow d_z^2)$ and a back bonding overlap of π_g^* with the degenerate $d_{xz,yz}$ orbitals: $\pi(d_{xz,yz} \rightarrow \pi_g^*)$. This interaction is frequently thought to give a superoxo (O_2^-) ligand by partial charge-transfer from the metal to the O_2 molecule [3]. The bridge model [4], which may occur on bimetal complexes with a macrocyclic ring, provided the spacing of the metal atoms is correct [5, 6], involves similar electronic interactions, where the O_2 molecule interacts with two metal centers simultaneously and equally. When the electrocatalyst functions first to form the superoxide ion, O_2^-, the main reaction product may be either H_2O_2 or H_2O; while when the rupture of the O−O bond is catalyzed first, the product is H_2O only. The latter is known as a direct four-electron process: reaction (1) in Fig. 3. When H_2O_2 is produced as an intermediate, the reaction is termed a

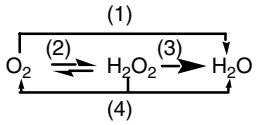


Fig. 3 Reduction of oxygen in protic media.

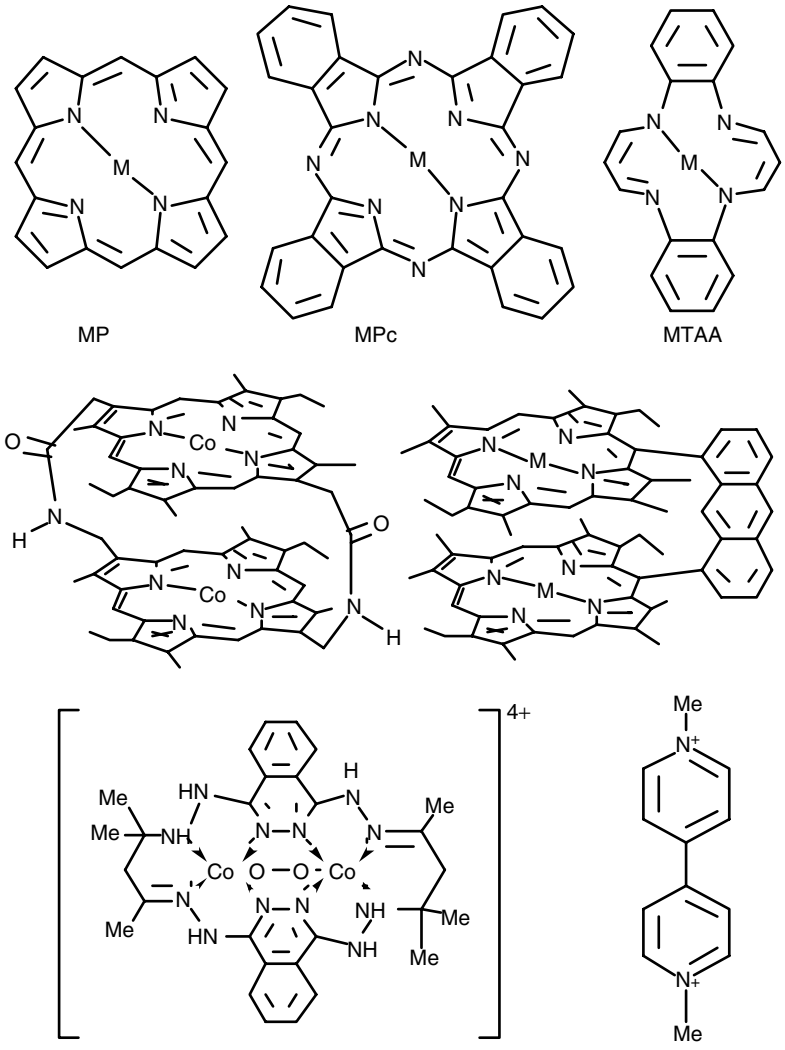


Fig. 4 Representative skeletal structures of the catalysts used for O_2 – electroreduction.

consecutive or peroxide pathway, or simply $2 + 2$ process: reaction (2) followed by either reaction (3) or (4) in Fig. 3.

Figure 4 shows the representative skeletal structures of catalysts used for the electroreduction of oxygen. Compounds with

four nitrogenous ligands (N_4^-) have exhibited activity and stability greater than those with N_2O_2, $N_2S_2^-$, O_4^-, and S_4^- chelates [7]. Of these, by far the most important are the porphyrins (Ps), phthalocyanines (Pcs), and dihydrodibenzotetraazaannulenes (TAAs) with the most common central metal ion (M) being iron, cobalt, or manganese for the reasons mentioned earlier (when incorporated in macrocycles, these metals are present either as a divalent or trivalent ion). Several reviews have been published on the electroreduction of oxygen using these macrocycles from the 1980s [7–16]. According to these, there are various factors affecting the catalytic activity of monomeric catalysts, as follows in order of importance.

(1) The nature of the central metals. In this respect, what we call, a volcano-shaped relationship (Fig. 5) between oxygen reduction activity and redox potential of the central metal ion (Mt(II/III)) is known [17]. Although iridium tetraphenylporphyrin, IrTPP, was thought to be the best catalyst, it was proven later that iridium octaethylporphyrin, IrOEP, has exceptionally high catalytic activity [18], being the best catalyst reported to date. This achieved a four-electron reduction without producing H_2O_2 at 0.72 V versus NHE at pH 1. Apart from this, however, it is generally accepted that Co and Fe have the highest activity [7–16, 19–61], although for some compounds Fe is better, while for others Co is superior. Manganese [17, 25, 62, 63], ruthenium [17, 64], rhodium [17, 25, 65], platinum [66] are also highly active, and, in particular, the latter two compounds can produce water as a result of four-electron or two two-electron reduction via H_2O_2. Other metals such as Cu, Ni, Al, Cr, Sn, Ga, Sb, Na, Zn, Ag, Pd, Zn, and the vanadyl ion have little catalytic activity [7, 17, 25].

(2) The structure of the macrocyclic compounds. The N_4chelates have the highest activity. Compared with phthalocyanines, porphyrins have higher activity in terms of the reduction potential, that is, O_2 is reduced at higher potential when porphyrinic

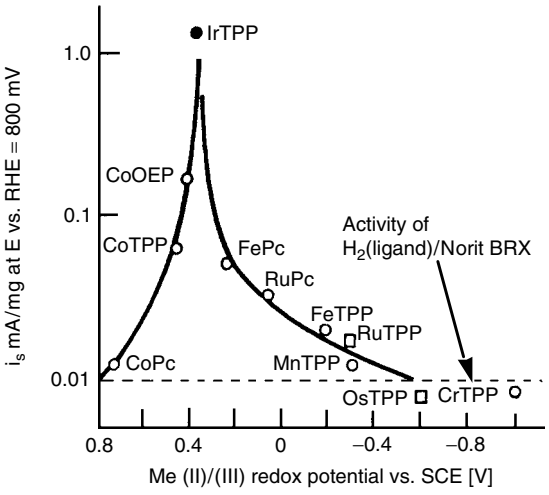


Fig. 5 Qualitative representation of the volcano-shaped relationship between oxygen reduction activity and redox potential of the central metal ion (redrawn from ref. 17).

macrocycles are used [7–16]. Electron-donating substituents increase the catalytic activity significantly, and in this respect, data on cobalt complexes are particularly interesting. Cobalt complexes generally catalyze only from O_2 to H_2O_2. However, a four-electron reduction to water is achieved when methyl groups are attached at the *para* positions of the phenyl groups of tetraphenylporphyrin [61], or when four $Ru(NH_3)_5^{2+}$ cations are coordinated to the *para* positions of *meso*-tetrakis(4-pyridyl)porphyrin [67] or cyano groups of tetrakis(*p*-cyano)phenylporphyrin [68]. In these cases, the electron density at the central cobalt is increased, either by intramolecular electron transfer or π-back-bonding interactions, thereby facilitating the electron transfer from Co to O_2. In the case of CoPcs, a four-electron reduction was attained using a plurality CoPcs linked by CN groups [69] and by CoPc containing eight carboxyimide groups on the periphery [54]. In the case of iron porphyrins, it is known that the amount of adsorbed porphyrin required to attain a four-electron reduction decreases significantly with increasing number of amino groups at the *para* positions of tetraphenylporphyrin [70].

(3) Polymerization of the catalyst itself or incorporation of the catalyst in polymers such as polypyrrole or polystylene often improves the activity [47, 71].

(4) Thermal treatment of the modified electrode. Catalyst performance can be improved by thermal treatment of the catalyst-modified electrode in an inert atmosphere [12, 21, 46, 72]. The treatment temperature differ from species to species, but in many cases, degradation of macrocycles starts to occur at 800–900 °C. The heat-treated catalysts are believed to be particularly effective as peroxide elimination catalysts in alkaline solutions.

The factors described earlier are for monomeric catalysts; however, dinuclear acatalysts have often been found to be better catalysts [5, 6, 73]. For cofacial diporphyrins, the following combination of metal centers were examined: Co−Co, Co−Cu, Co−Fe, Fe−Fe, Fe−H_2. For a Co−Co combination, O_2 was reduced to H_2O without the release of H_2O_2 at an acidic pH of less than 4 when the bridge connecting the two porphyrin rings consisted of only four atoms, or when the bridge was 1,8-anthracene or diphenylene. In the absence of O_2, the Co(III/II) redox couple was split into two potentials. In the presence of O_2, O_2 reduction was observed at slightly positive potentials where the second Co is reduced from Co(III) to Co(II). The Co−Cu diporphyrin catalyzed the reduction to only H_2O_2 but no further. The other Co−Fe, Fe−Fe, Fe−H_2 catalysts all exhibited reduction pathways leading to both H_2O_2 and H_2O. In the case of Co−Co complexes, two cobalt centers were proposed to be positioned so that a μ-peroxo complex could be formed.

Reaction mechanisms differ from system to system, but in most of the cases when the catalysts were dissolved in solution they were not adsorbed onto electrodes, and in some cases in catalyst-adsorbed systems, many monomeric iron and cobalt systems were explained by an electrochemical catalyst regeneration mechanism, where the catalyst was first reduced, and this reduced form of the catalyst reacted with oxygen [16, 22, 24, 27, 30, 31, 38, 39, 44, 49, 57, 62, 64]. When the iron catalyst-adsorbed electrodes

were used, the reduction of O_2 is sometimes shifted to potentials much more positive than the formal potential of the Fe(III/II) couple of the dissolved iron catalysts [33]. This positive shift has been reasonably explained by a positive shift in formal Fe(III/II) potential, conjectured to be caused by back bonding from Fe(II) to the unsaturated surface ligand of electrodes such as carbonyl-like groups [52]. A redox mechanism is also reported in many adsorbed systems [4, 7–10, 34]. In this mechanism, the central metal atom of the electrocatalysts releases an electron to the adsorbed reactant (O_2 and at higher overpotentials HO_2), which is subsequently further reduced to products (HO_2^- and OH^- respectively). When O_2 is reduced to H_2O, both a direct four-electron reduction and two subsequent two-electron reductions via H_2O_2 were observed. This also depends on the system, the catalyst preparation, the amount of catalyst adsorbed on the electrode surface, heat treatment, and the electrode materials.

Oxygen can be reduced to H_2O_2 by benzo-, naphtho-, and anthraquinone-modified electrodes [74] and by poly(viologen)-modified electrodes [75]. A Prussian blue-modified electrode catalyses electroreduction of O_2 to H_2O by the four-electron transfer reaction [76].

Electrocatalytic oxidations (mainly epoxidation) of alkenes by manganese porphyrins [77, 78] and a Schiff-base [79] and iron and cobalt porphyrins [78] have been achieved. Hydrogen peroxide or the superoxide ion (O_2^-) was generated electrochemically by reduction of dioxygen in solvents containing an acid or acid anhydride, the metal compounds as catalysts, and olefins as substrates, in the presence or absence of an axial base. The reaction was believed to take place through the formation of a high valent metal oxo porphyrin, produced by electroreducing O_2. However, unfortunately, these reactions have not been carried out at modified electrodes with the exception of one case [77c].

References

1. J. P. Hoare, GMR 2948 Research Publication **1979**.
2. L. Pauling, *Nature* **1964**, *203*, 182–183.
3. F. Basolo, B. M. Hoffman, J. A. Ibers, *Acc. Chem. Res.* **1975**, *8*, 384–392.
4. E. Yeager, *Nati. Bureau Stand. Spec. Publ.* **1976**, *455*, 203–219.
5. J. P. Collman, P. Denisevich, Y. Konai et al., *J. Am. Chem. Soc.* **1980**, *103*, 6027–6036.
6. A. van der Putten, A. Elzing, W. Wissher et al., *J. Chem. Soc., Chem. Commun.* **1986**, 477–479.
7. F. van den Brink, E. Barendrecht, W. Vissher, *Recl. Trav. Chim. Pays-Bas* **1980**, *99*, 253–262.
8. H. Jahnke, M. Schonborn, G. Zimmermann, *Top. Curr. Chem.* **1976**, *61*, 133–181.
9. M. R. Terasevich, K. A. Radyushkina, *Russ. Chem. Rev. (Engl. Transl.)* **1980**, *49*, 718–730.
10. J. A. R. van Veen, J. F. van Baar, *Rev. Inorg. Chem.* **1982**, *4*, 293–305.
11. D. J. Shiffrin, *Electrochemistry* **1983**, *8*, 126–157.
12. E. Yeager, *Electrochim. Acta* **1984**, *29*, 1527–1537.
13. E. Yeager, *J. Mol. Catal.* **1986**, *38*, 5–25.
14. P. Vasudevan, T. Santosh, N. Mann et al., *Transition Met. Chem.* **1990**, *15*, 81–90.
15. J. H. Zagal, *Coord. Chem. Rev.* **1992**, *119*, 89–136.
16. N. Kobayashi, W. A. Nevin, *Appl. Organomet. Chem.* **1996**, *10*, 579–590.
17. J. A. R. van Veen, J. F. van Baar, C. J. Kroese et al., *Ber. Bunsen-Ges. Phys. Chem.* **1981**, *85*, 693–700.
18. J. P. Collman, K. Kim, *J. Am. Chem. Soc.* **1986**, *108*, 7847–7849.
19. H. Jahnke, M. Schonborn, G. Zimmermann, *Top. Curr. Chem.* **1976**, *61*, 133–181.
20. J. Zagal, R. Sen, E. Yeager, *J. Electroanal. Chem. Interfacial Electrochem.* **1977**, *83*, 207–283.
21. H. Behret, W. Clauberg, G. Sandstede, *Ber. Bunsen-Ges. Phys. Chem.* **1977**, *81*, 54–60.
22. T. Kuwana, M. Hujihira, K. Sunakawa et al., *J. Electroanal. Chem. Interfacial Electrochem.* **1978**, *88*, 299–303.

23. N. Kobayashi, M. Fujihira, K. Sunakawa et al., *J. Electroanal. Chem. Interfacial Electrochem.* **1979**, *101*, 269–273.
24. N. Kobayashi, T. Matsue, M. Fujihira et al., *J. Electroanal. Chem. Interfacial Electrochem.* **1979**, *103*, 427–431.
25. J. A. R. van Veen, C. Visser, *Electrochim. Acta* **1979**, *24*, 921–928.
26. H. Behret, W. Clauberg, G. Sandstede, *Ber. Bunsen-Ges. Phys. Chem.* **1979**, *83*, 139–147.
27. A. Battelheim, R. J. Chan, T. Kuwana, *J. Electroanal. Chem. Interfacial Electrochem.* **1980**, *110*, 93–102.
28. J. Zagal, P. Bindra, E. Yeager, *J. Electrochem. Soc.* **1980**, *127*, 1506–1517.
29. H. Behret, W. Clauberg, G. Sandstede et al., *J. Electroanal. Chem. Interfacial Electrochem.* **1981**, *117*, 29–42 and many ref. cited therein.
30. P. A. Forshey, T. Kuwana, *Inorg. Chem.* **1981**, *20*, 693–700; **1983**, *22*, 699–707.
31. P. A. Forshey, T. Kuwana, N. Kobayashi, in *Electrochemical and Spectrochemical Studies of Biological Redox Components, ACS Advances in Chemistry Series, Vol. 192* (Ed.: S. J. Miller), American Chemical Society, Washington, 1982, pp. 601–624.
32. R. R. Durand, F. C. Anson, *J. Electroanal. Chem. Interfacial Electrochem.* **1982**, *134*, 273–289.
33. K. Shigehara, F. C. Anson, *J. Phys. Chem.* **1982**, *86*, 2776–2783.
34. F. van den Brink, W. Visser, E. Barendrecht, *J. Electroanal. Chem. Interfacial Electrochem.* **1983**, *157*, 283–304, 305–318; **1983**, *181*, 295–300; **1984**, *172*, 301–325; **1984**, *175*, 279–289.
35. J. H. Zagal, M. Paez, J. Sturm et al., *J. Electroanal. Chem. Interfacial Electrochem.* **1984**, *157*, 283–304.
36. D. Ozer, R. Parash, F. Broitman et al., *J. Chem. Soc., Faraday Trans. 1,* **1984**, *80*, 1139–1149.
37. S. Zecevic, B. Simic-Glavaski, E. Yeager et al., *J. Electroanal. Chem. Interfacial Electrochem.* **1985**, *196*, 339–358.
38. N. Kobayashi, Y. Nishiyama, *J. Phys. Chem.* **1985**, *89*, 1167–1170.
39. O. Ikeda, K. Okabayashi, N. Yoshida et al., *J. Electroanal. Chem. Interfacial Electrochem.* **1985**, *191*, 157–174.
40. R. J. Chan, Y. O. Su, T. Kuwana, *Inorg. Chem.* **1985**, *24*, 3777–3784.
41. C.-L. Ni, F. C. Anson, *Inorg. Chem.* **1985**, *24*, 4754–4756.
42. M. R. Hempstead, A. B. P. Lever, C. C. Leznoff, *Can. J. Chem.* **1987**, *65*, 2677–2684.
43. D. van den Ham, C. Hinnen, G. Magner et al., *J. Phys. Chem.* **1987**, *91*, 4743–4748.
44. F. Arifuku, K. Iwatani, K. Ujimoto et al., *Bull. Chem. Soc. Jpn.* **1987**, *60*, 1661–1665.
45. A. A. Tanaka, C. Fierro, D. Scherson et al., *J. Phys. Chem.* **1987**, *91*, 3799–3807 and many refs. cited therein.
46. S. Dong, R. Jiang, *Ber. Bunsen-Ges. Phys. Chem.* **1987**, *91*, 479–484.
47. P. Janda, N. Kobayashi, P. A. Auburn et al., *Can. J. Chem.* **1989**, *67*, 1109–1119.
48. S. Antoniando, A. D. Jannakoudakis, E. Theodoridou, *Synth. Met.* **1989**, *30*, 283–294.
49. Y. O. Su, T. Kuwana, S.-M. Chen, *J. Electroanal. Chem. Interfacial Electrochem.* **1990**, *288*, 177–195 and refs. therein.
50. R. Jiang, S. Dong, *J. Phys. Chem.* **1990**, *94*, 7471–7476.
51. R. Jiang, S. Dong, *Electrochim. Acta* **1990**, *35*, 1227–1232.
52. C. Shi, F. C. Anson, *Inorg. Chem.* **1990**, *29*, 4298–4305.
53. D. Sazou, C. Araullo-McAdams, B. C. Han et al., *J. Am. Chem. Soc.* **1990**, *112*, 7879–7886.
54. N. Kobayashi, K. Sudo, T. Osa, *Bull. Chem. Soc. Jpn.* **1990**, *63*, 571–575.
55. N. Kobayashi, K. Adachi, T. Osa, *Anal. Sci.* **1990**, *6*, 449–453.
56. J. Ouyang, K. Shigehara, A. Yamada et al., *J. Electroanal. Chem. Interfacial Electrochem.* **1991**, *297*, 489–498.
57. F. Arifuku, K. Mori, T. Muratani et al., *Bull. Chem. Soc. Jpn.* **1992**, *65*, 1491–1495.
58. J. Zagal, M. Paez, A. A. Tanaka et al., *J. Electroanal. Chem. Interfacial Electrochem.* **1992**, *339*, 13–30.
59. D.-W. Pang, Z.-L. Wang, *J. Electroanal. Chem. Interfacial Electrochem.* **1992**, *340*, 35–40.
60. N. Kobayashi, P. Janda, A. B. P. Lever, *Inorg. Chem.* **1992**, *31*, 5172–5177.
61. C. Shi, B. Steiger, M. Yuasa et al., *Inorg. Chem.* **1998**, *37*, 1037–1043.
62. N. Kobayashi, H. Saiki, T. Osa, *Chem. Lett.* **1985**, 1917–1920.
63. O. Ikeda, T. Kojima, H. Tamura, *J. Electroanal. Chem. Interfacial Electrochem.* **1986**, *200*, 323–332.
64. A. Battelheim, D. Ozer, R. Harth et al., *J. Electroanal. Chem. Interfacial Electrochem.* **1988**, *246*, 139–154.

65. (a) N. Kobayashi, *Science Report*, Tohoku University, Sendai, Japan, **1996**, pp. 15–19; (b) Y.-H. Tse, P. Seymour, N. Kobayashi et al., *Inorg. Chem.* **1991**, *30*, 4453–4459.
66. C. Paritrio, A. Hamnett, J. B. Goodenough, *J. Electroanal. Chem. Interfacial Electrochem.* **1984**, *160*, 359–367.
67. C. Si, F. C. Anson, *J. Am. Chem. Soc.* **1991**, *113*, 9564–9570; *Inorg. Chem.* **1992**, *31*, 5078–5083.
68. B. Steiger, F. C. Anson, *Inorg. Chem.* **1997**, *36*, 4138–4140.
69. O. Ikeda, S. Itoh, H. Yoneyama, *Bull. Chem. Soc. Jpn.* **1988**, *61*, 1428–1430.
70. N. Kobayashi, Y. Nishiyama, *J. Electroanal. Chem. Interfacial Electrochem.* **1984**, *181*, 107–117.
71. (a) L. Kreja, R. Dobrowski, *J. Power Sources* **1981**, *6*, 35–46 and refs. 9, 10, 11 cited therein; (b) J. Blomquist, U. Helgeson, L. C. Moberg et al., *Electrochim. Acta* **1982**, *27*, 1445–1451; (c) G.-X. Wan, K. Shigehara, E. Tsuchida et al., *J. Electroanal. Chem. Interfacial Electrochem.* **1984**, *179*, 239–250; (d) O. Ikeda, K. Okabayashi, Y. Yoshida et al., *J. Electroanal. Chem. Interfacial Electrochem.* **1985**, *191*, 157–174; (e) T. Osaka, K. Naoi, T. Hirabayashi et al., *Bull. Chem. Soc. Jpn.* **1986**, *59*, 2717–2722; (f) R. Jiang, S. Dong, *J. Electroanal. Chem. Interfacial Electrochem.* **1988**, *246*, 101–117; (g) S. Dong, T. Kuwana, *Electrochim. Acta* **1988**, *33*, 667–674; (h) D. Ozer, R. Harth, U. Mor et al., *J. Electroanal. Chem. Interfacial Electrochem.* **1989**, *266*, 109–123; (i) A. E. Hourch, S. Belcadi, P. Moisy et al., *J. Electroanal. Chem. Interfacial Electrochem.* **1992**, *339*, 1–12; (j) D.-W. Pang, Z.-L. Wang, *J. Electroanal. Chem. Interfacial Electrochem.* **1992**, *340*, 35–40.
72. (a) A. J. Appleby, M. Savy, *Electrochim. Acta* **1977**, *22*, 1315–1323; (b) O. Ikeda, H. Fukuda, H. Tamura, *J. Chem. Soc., Faraday Trans. 1* **1986**, *82*, 1561–1573; (c) O. Ikeda, T. Kojima, H. Tamura, *Bull. Chem. Soc. Jpn.* **1986**, *59*, 3335–3340; (d) T. Sawaguchi, T. Itabashi, T. Matsue et al., *J. Electroanal. Chem. Interfacial Electrochem.* **1990**, *279*, 219–230; (e) A. Biloul, O. Contamin, G. Scarbeck et al., *J. Electroanal. Chem. Interfacial Electrochem.* **1992**, *335*, 163–186; (f) M. Laudoucer, G. Lalande, D. Guay et al., *J. Electrochem. Soc.* **1993**, *140*, 1974–1981 and many refs. therein.
73. (a) R. R. Durand, C. S. Bencosme, J. P. Collman et al., *J. Am. Chem. Soc.* **1983**, *105*, 2710–2718; (b) R. R. Durand, J. P. Collman, F. C. Anson, *J. Electroanal. Chem. Interfacial Electrochem.* **1983**, *151*, 289–294; (c) H.-Y. Liu, I. Abdalmuhdi, C. K. Chang et al., *J. Phys. Chem.* **1985**, *89*, 665–670; **1987**, *91*, 1158–1166; (d) J. P. Collman, N. H. Hendricks, C. R. Leidner et al., *Inorg. Chem.* **1988**, *27*, 387–393; (e) C. K. Chang, H. Y. Liu, I. Abdalmuhdi, *J. Am. Chem. Soc.* **1984**, *106*, 2725–2726.
74. (a) C. Degrand, *J. Electroanal. Chem. Interfacial Electrochem.* **1984**, *169*, 259–268 and refs. 1–4 therein; (b) S. Holdcroft, B. L. Funt, *J. Electroanal. Chem. Interfacial Electrochem.* **1987**, *225*, 177–186.
75. N. Oyama, N. Oki, H. Ohno et al., *J. Phys. Chem* **1983**, *87*, 3642–3647.
76. K. Itaya, N. Shoji, I. Uchida, *J. Am. Chem. Soc.* **1984**, *106*, 3423–3429.
77. (a) S. E. Creager, S. A. Raybuck, R. W. Murray, *J. Am. Chem. Soc.* **1986**, *108*, 4225–4227; (b) S. E. Creager, R. W. Murray, *Inorg. Chem.* **1987**, *26*, 2612–2618; (c) H. Nishihara, K. Pressprich, R. W. Murray et al., *Inorg. Chem.* **1990**, *29*, 1000–1006; (d) C.-Y. Lin, Y. O. Su, *J. Electroanal. Chem. Interfacial Electrochem.* **1989**, *265*, 305–310.
78. F. Ojima, N. Kobayashi, T. Osa, *Bull. Chem. Soc. Jpn.* **1990**, *63*, 1374–1380.
79. C. P. Holwitz, S. E. Creager, R. W. Murray, *Inorg. Chem.* **1990**, *29*, 1006–1011.

10.2 Organic Electrocatalysis

Theodore Kuwana
University of Kansas, USA

Tetsuo Osa
Emeritus, Tohoku University, Japan

Yoshitomo Kashiwagi
Graduate School of Pharmaceutical Sciences, Tohoku University, Japan

The concept of organic electrocatalysis with chemically modified electrodes (CMEs) was born in the mid-1970s when Miller and coworkers achieved functionalization of a graphite electrode surface with an optically active amino acid [1]. This innovation was the starting point to initiate a wide area of research, which is still growing [2–8]. CMEs have provided the possibility of intelligently designing and altering the surface of conventional electrodes in order to improve their functionality by utilizing the intrinsic properties of modifiers for selective electrochemical reactions.

Organic electrocatalysis with CMEs can be defined as the use of electron mediators to reduce the activation overpotential and accelerate the charge transfer rate with organic compounds. The first catalytic CME was reported by Evans and coworkers [9] who demonstrated catalytic enhancement of the oxidation of ascorbic acid with a benzidine coated graphite electrode (Scheme 1).

Since the appearance of this work, many different kinds of electrocatalytic reactions of organic compounds with CMEs have been carried out with various mediators and surface modification methods. Additional applications of mediator functionalized CMEs have been their use as amperometric detectors in liquid chromatography and as biosensors.

The kind of mediators and modification methods can be classified as follows:

1. Mediator
 a. organic redox compounds,
 b. organometallic redox complexes,
 c. conducting polymers, and
 d. fine metallic particles.

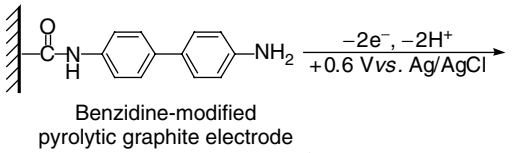
 Effective mediators embody the properties of electrochemical reversibility, fast electron transfer between mediator, electrode and substrate, and chemical stability in the reaction environment.
2. Modification methods
 a. monolayers or partial coverage of mediators on electrode surfaces via chemisorption, Langmir–Blodget films, or affixed via chemical bond,
 b. conductive multilayer polymer films on electrode surfaces, and
 c. heterogeneous multilayer films on electrode surfaces with different functions.

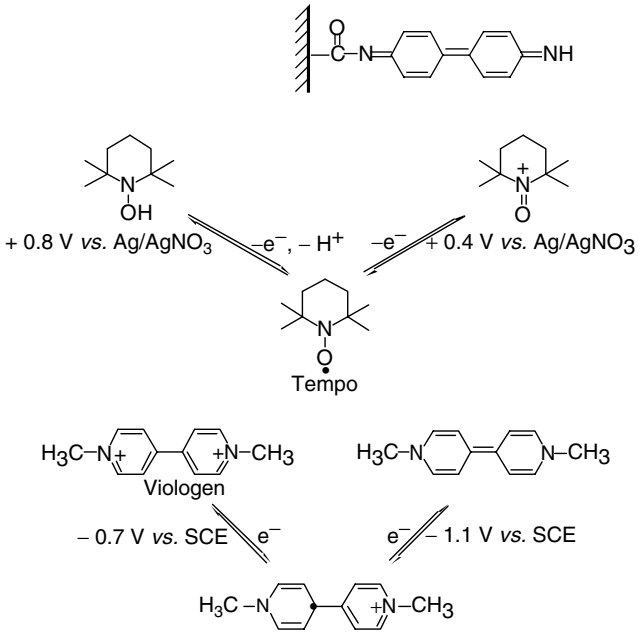
Typical mediation reactions with 2,2,6,6-tetramethylpiperidin-1-oxyl (TEMPO) for oxidation [10] and viologen for reduction [11], respectively, are examples (Scheme 2).

A theoretical understanding of the mechanism of mediation is important in the design of catalytic CMEs [12]. For example, it is known that the mechanisms of monolayer immobilized mediator, as shown in Fig. 1(a), proceeds in two steps. The first step is electron transfer between the electrode and mediator followed by the second step of charge transfer between the activated mediator and substrate in an electrolyte solution. The rate of electron transfer is often high (10^4 s^{-1}). On the other hand, the steps to consider as being important with polymer film immobilized mediator, as schematically shown

Encyclopedia of Electrochemistry. Edited by A.J. Bard and M. Stratmann
Vol. 10 *Modified Electrodes*. Edited by M.Fujihira, I.Rubinstein, and J.F.Rusling
Copyright © 2007 Wiley-VCH Verlag GmbH & Co. KGaA, Weinheim. ISBN: 978-3-527-30402-8

Scheme 1





Scheme 2

in Fig. 1(b) [8], is the rate of permeation of the substrate into the polymer and the rate of mediator regeneration by the electrode. The overall process is greatly influenced by the number of catalyst sites in the polymer film that can undergo reaction with the substrate [13]. If the substrate permeates the film very slowly, then only the outermost catalyst sites at the polymer-solution interface [14] may participate in the electrocatalytic reaction. Electron transfer in the film can proceed by electron hopping and/or charge transfer; the former needs to have neighboring mediators in close proximity while the latter is usually characterized by a very slow rate.

In this section, examples of organic electrocatalysis by CMEs are shown according to the method of modification. Monolayer attachment by chemisorption often uses irreversible adsorption of mediators onto surfaces of platinum, carbon, mercury, silver, or gold electrodes. Graphite electrodes are especially effective in chemisorbing mediators that have extended π-bond system. Examples of chemisorption are tetracyano-*p*-quinodimethane (TCNQ), tetrathiafulvalene (TTF), and 1,1′-dimethylferrocene (DMFc) for the electrocatalytic oxidation of ascorbic acid (Scheme 3) [15]. Gold electrodes strongly adsorb mediators containing mercaptide groups, which have been exploited for self-assembly of thiols with active redox functionalities such as nitroxyl radicals

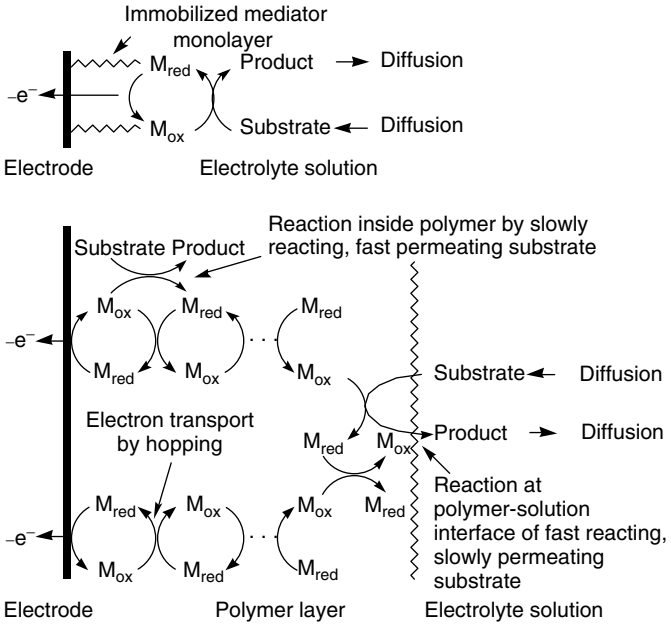
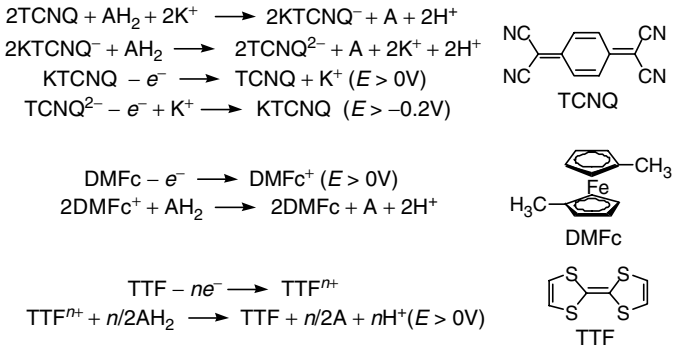


Fig. 1 Electron transfer mechanism between electrode and substrate of mediator-modified electrodes used for electrocatalysis; (a) an immobilized mediator monolayer and (b) an immobilized mediator polymer layer.



Scheme 3 Electrocatalytic oxidation of ascorbic acid by TCNQ, DMFc, or TTF.

for electrocatalytic oxidation of alcohols [16, 17].

The chemical attachment of various kinds of functional groups to the surface of carbonaceous materials, such as graphite, glassy carbon, and pyrolytic graphite; metals such as Pt or Ti; and metal oxides such as SnO_2, TiO_2, and dimensionally stable anode (DSA), has been reported [18, 19]. This mode of attachment has been used by many investigators. An example of a suitably reactive metal oxide surface is platinum oxide terminated by Pt–OH groups [20], which served as sites

to bond ferrocene carboxaldehyde [21]. The alkylamine-silanized Pt oxide was applied to the electrocatalytic oxidation of ascorbic acid [22]. Carbon surfaces are also readily oxidized to produce a high density of carbonyl groups [23] through which amide bonds can be formed [9]. Ascorbic acid oxidation has been reported via the carboxyl-amide immobilization of 3,4-dihydroxybenzylamine [24] and α-aminoethylferrocene [25].

In polymeric films, electroactivity is often unnecessary because the electrode is designed to preconcentrate selectively or transport substrates through the film to the electrode, based on membrane partitioning or permeability effect. Electron transfer then proceeds directly with the electroactive species at the surface of the base electrode.

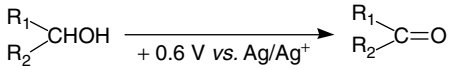
On the other hand, the electrodes attaching electroactive polymer films and polymer CMEs having ionic, electronically conductive, or redox property have been widely studied. Electronically conducting polymers, which are usually more conductive than redox polymers, can be doped to increase their intrinsic conductivity. Such films are now popular because they are technically easier to modify by applying polymer onto an electrode compared to covalent monolayer formation. Polymer films generally adhere satisfactorily to electrodes simply by forces of chemisorption or by being insoluble in the contacting solvent.

The characteristics of polymer electrodes can be summarized as follows:

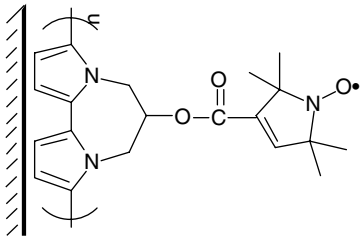
1. In general, polymer films are more stable than monolayer films. This stability imparts longer life, which is an important consideration in their use.
2. A high density of mediators can be placed in polymer layers.
3. In many circumstances, the electrocatalytic efficiency in polymers may be enhanced.
4. Mediators can be readily entrapped by physical forces or chemical bonding.
5. The thickness of the polymer layer can be easily controlled, for example, by dip coating of electrode into polymer solution.
6. Mediators can be easily immobilized by using functional groups of the polymer.
7. Hyrophilicity and lipophilicity of polymer layers can be controlled by the presence or absence of functional groups – example is the existence of carboxylic acids in polymer structure.
8. Functional groups on polymers can serve as a preconcentrating medium or as a transport carrier.
9. A selective size domain can be obtained by cross-linking of functional groups in polymers, thereby constructing a supramolecular structure.

Conductive polymer films on electrodes have been prepared by electrochemical polymerization of electroactive monomers such as a pyrrole-substituted mediator, or by evaporating solutions containing preformed polymer. Examples of electrocatalyses reported include the oxidation of alcohols by pyrrole-substituted 2,2,5,5-tetramethyl-3-pyrroline-1-oxyl [26] and organohalide dehalogenation by pyrrole-substituted 4,4′-bipyridinium salt [27]. The preparation of mediator-modified electrode by evaporating solutions of preformed polymers was carried out by dip-coating polymers including mediators on electrode surface or by covalent attachment of mediators to dip-coated polymers on electrode surfaces. Examples of the former electrocatalyses are selected from the several reports on the oxidation of NADH by dopamine

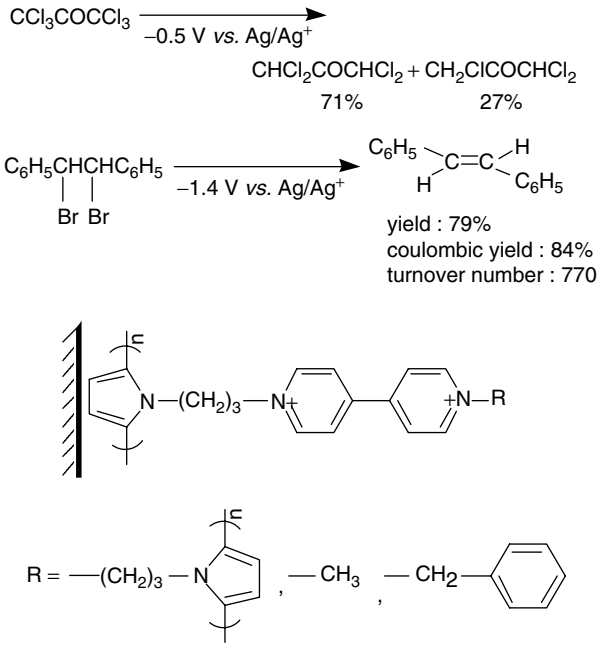
polymer [28], and oxidation of alcohols [29] or amines [30] by TEMPO polymer. The latter electrocatalyses are demonstrated by the reductive cross-coupling reaction of ethyl iodide and acrylonitrile [29], by the dehalogenation of organohalides [31] and alkylation of activated olefins [32] with vitamin B_{12} polymer (Schemes 4 and 5).



R_1	R_2	Yield/[%]	Coulombic yield/[%]
p-Cresol	H	87	68
1-Nap	H	27	54
p-Tol	H	36	80
Ph	H	23	68
Ph	Ph	2	25

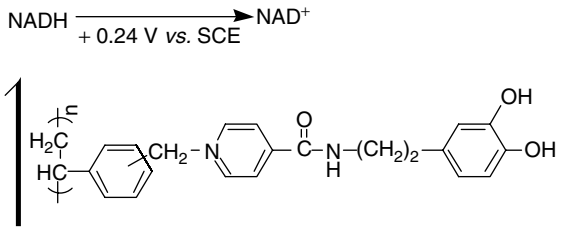


Scheme 4
Poly(pyrrole-PROXYL)-modified carbon felt electrode.

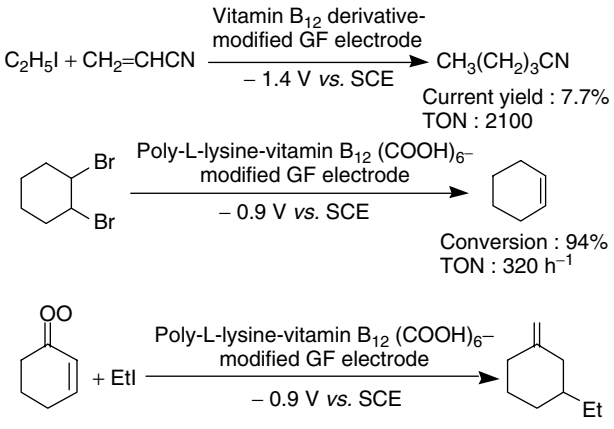


Scheme 5 Pyrrole-substituted 4,4′-bipyridinium salt-modified carbon felt electrode.

Further examples of covalent attachment of mediators by dip-coating polymers on electrode surfaces are described below in connection with preparative electrocatalytic synthesis (Schemes 6 and 7). The requirement for high-density current for preparative organic electrosynthesis on CMEs is different than what is needed for conventional electroanalytical uses of such electrodes. However, most CMEs for electrosynthetic purposes have not achieved the required level of high current density. Graphite felt (GF) is an excellent candidate as an electrode substrate material, due to high surface area. Moutet and coworkers have demonstrated its utility for such purposes [26, 27]. Another example is the work of Osa and Kashiwagi, as shown below [33, 34]. A poly(acrylic acid) (PAA) layer ca. 40-nm thick coated on GF having a surface of ca. 0.7 $m^2\ g^{-1}$ was reacted with 4-amino-TEMPO (64%), followed by cross-linking with hexamethylenediamine (16%) and by butylation with butyl sulfate to block the remaining carboxylate groups (20%). The density of TEMPO on the electrode thus prepared was 24 $\mu mol\ cm^{-3}$. The results of using the TEMPO CME for preparative electrosynthesis are listed in Tables 1–3. Table 1 contains the results for the oxidation of alcohols [35], thiols [36], naphthols [37], methylquinolines [34], and amines [38] by the CME of 4-amino-TEMPO-modified PAA on GF. Table 2 lists the enantioselective oxidation of racemic alcohols [39], stereoselective lactonization of methyl-substituted diols [40], and enantioselective coupling of naphthol [41] in the presence of chiral base of (−)-sparteine as a deprotonating agent

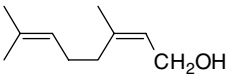
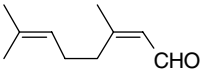
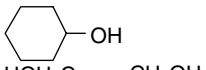
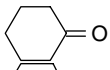
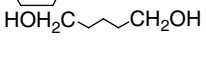
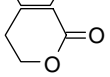
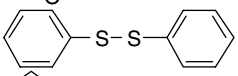
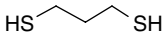
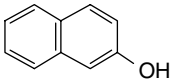
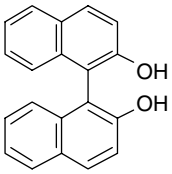
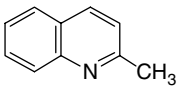
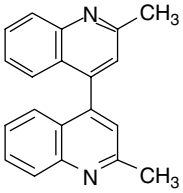
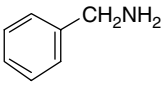
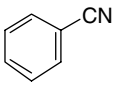


Scheme 6 Dopamine polymer-modified GC electrode.



Scheme 7

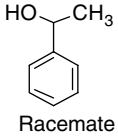
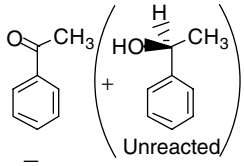
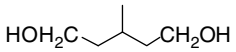
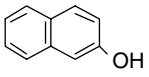
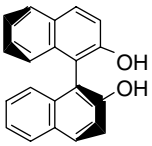
Tab. 1 Electrocatalytic oxidation of organic compounds on TEMPO-modified GF electrode

Substrate	*Product*	*η [%]*	*Con. [%]*	*Yield [%]*	*TON*	*Ref.*
		94.2	52.2	52.2	196	[33]
		95.6	33.1	33.1	124	[33]
		42.4	11.8	5.5	96	[8]
		98.6	100	100	410	[34]
		68.0	49.5	34.7	290	[34]
		95.2	98.6	98.6	410	[35]
		93.6	96.6	96.6	410	[32]
		93.5	70.9	68.9	284	[36]

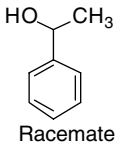
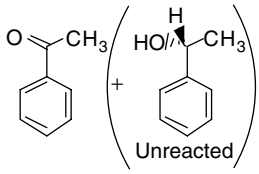
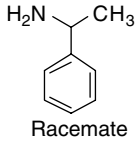
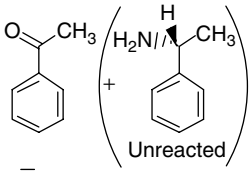
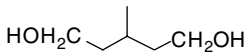
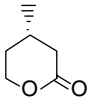
in an oxygen free and anhydrous acetonitrile solution. A chiral TEMPO-modified PAA on GF electrode, where a chiral mediator is 1-aza-4-amino-2,2,7-trimethyl-10-isopropylspiro[5.5]undecane-1-oxyl, was used successfully in the enantioselective [42] or stereoselective [43] electrosynthesis as shown in Table 3. Such a high enantioselective or stereoselective electrocatalytic oxidation may proceed in a suitable size of domain in a PAA layer. GF electrodes coated with Fc-modified PAA layer [44, 45], and viologen-modified Nafion or PAA layers [46] were also successfully prepared for the purpose of preparative electroenzymatic synthesis. 1,2-Dibromocyclohexane was electrocatalytically reduced to cyclohexene on nickel(II) pentaazamacrocyclic complex-modified GF electrode in high current efficiency (91%) and yield (85%) with a turnover number of ca. 1400 [47].

Examples of electrocatalysis with other conductive polymeric electrodes are (1) reaction of hydroquinone/benzoquinone redox couple by polyaniline (PANI) [48], PANI derivatives [49], or poly(*o*-phenylenediamine) (POPD) [50];

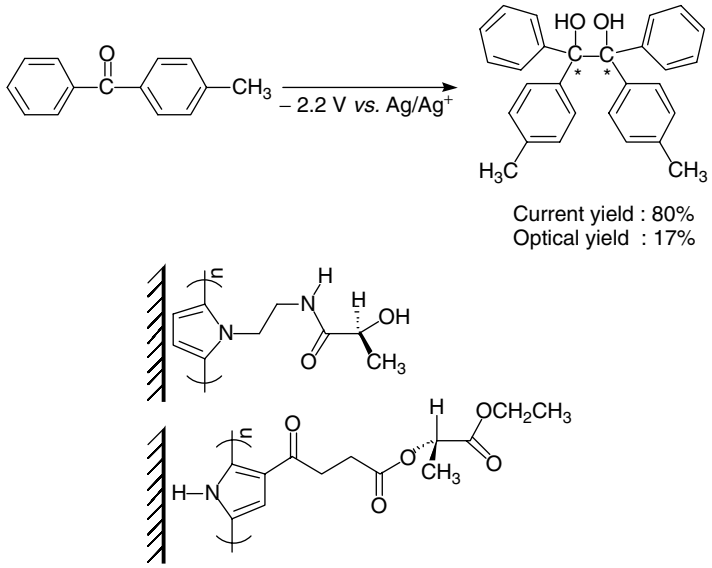
Tab. 2 Enantioselective and stereoselective, electrocatalytic oxidations on TEMPO-modified GF electrode in the presence of (−)-sparteine

Substrate	*Product*	*η [%]*	*Con [%]*	*Yield [%]*	*ee [%]*	*TON*	*Ref.*
 Racemate	 Unreacted	95.1	53.8	52.4(46.2)	99	87	[38]
		92.6	98.5	93.6	98	307	[40]
		88.8	93.6	93.6	99	384	[39]

Tab. 3 Enantioselective and stereoselective, electrocatalytic oxidations on chiral TEMPO-modified GF electrode

Substrate	*Product*	*η [%]*	*Con. [%]*	*Yield [%]*	*ee [%]*	*TON*	*Ref.*
 Racemate	 Unreacted	99.1	50.7	50.4(49.3)	99	74	[40]
 Racemate	 Unreacted	92.7	52.8	50.8(47.2)	99	78	[41]
		97.0	99.2	96.5	99	71	[40]

(2) reduction of 1,2-naphthoquinone sulfate and viologens by PANI [51]; (3) oxidation of catechol by POPD [52]; (4) oxidation of ascorbic acid by PANI [53]; (5) electropolymerized diphenylamine [54] or copolymerized aniline with 3,4-dihydrobenzoic acid [55]; and (6) asymmetric reduction of benzophenone



Scheme 8 Chiral poly(pyrrole)-modified Pt electrodes.

derivatives by some chiral Ppys (Scheme 8) [56].

Ion exchange polymeric films, for instance, Nafion are electroactive by exchange of some of their charge-compensating counterions for electroactive ones [57, 58]. In such films, electrons are transported in part by physical diffusion of electroactive ions, which may also undergo self-exchange as part of the transport process.

Integrated systems refer to heterogeneous films on electrodes designed to contain a mixture of constituents with different functions. For instance, electrocatalysis of organics were successfully achieved with the incorporation of catalytic monomers in carbon paste matrix. Examples are oxidations of alcohol by ruthenium oxo complex [59] and ascorbic acid by catechol or aminophenol [60], *p*-phenylenediamine, or tetramethyl-*p*-phenylenediamine [61], and Prussian blue [62]. A CME prepared by dip coating a mixed cobalt phthalocyanine/cellulose acetate solution onto an electrode surface was used to oxidize ascorbic acid [63].

References

1. a) B. F. Watkins, J. B. Behling, E. Kariv et al., *J. Am. Chem. Soc.* **1975**, *97*, 3549–3550; b) B. E. Firth, L. L. Miller, M. Matani et al., *J. Am. Chem. Soc.* **1976**, *98*, 8271–8272.
2. R. W. Murray, *Acc. Chem. Res.* **1980**, *13*, 135–141.
3. R. W. Murray in *Electroanalytical Chemistry* (Ed.: A. J. Bard), Marcel Dekker, New York, 1980, Vol. 13.
4. R. W. Murray, A. G. Ewing, R. A. Durst, *Anal. Chem.* **1987**, *59*, 379A–390A.
5. G. J. Patriarche, J.-M. Kauffmann, J.-C. Viré, in *Redox Chemistry & Interfacial Behavior of Biological Molecules* (Eds.: G. Dryhurst, K. Niki), Plenum Publishing Corporation, New York, 1988, pp. 479–498.
6. R. W. Murray, (Eds.), Molecular design of electrode surface *Techniques of Chemistry*, Wiley, New York, 1992, Vol. 22.

7. A. M. Titse, A. M. Timinov, G. A. Shagisultanova, *Coord. Chem. Rev.* **1993**, *125*, 43–52.
8. T. Osa, in *New Challenges in Organic Chemistry* (Ed.: T. Osa), Gordon and Breach Scientific Publishers, Amsterdam, 1998, pp. 183–219.
9. J. F. Evans, T. Kuwana, T. M. Henne et al., *J. Electroanal. Chem.* **1977**, *80*, 409–416.
10. M. F. Semmelhack, C. R. Schmid, D. A. Cortes et al., *J. Am. Chem. Soc.* **1983**, *105*, 4492–4493.
11. T. Osa, T. Kuwana, *J. Electroanal. Chem.* **1969**, *22*, 389–406.
12. C. P. Andrieux, J. M. Dumas-Bouchiat, J. M. Saveant, *J. Electroanal. Chem.* **1982**, *131*, 1–35.
13. F. C. Anson, T. Ohsaka, J. M. Saveant, *J. Am. Chem. Soc.* **1983**, *105*, 4883–4890.
14. C. R. Leidner, R. W. Murray, *J. Am. Chem. Soc.* **1984**, *106*, 1606–1614.
15. J. Kulys, A. Drungiline, *Electroanalysis* **1991**, *3*, 209–219.
16. T. Fuchigami, T. Shintani, A. Konno et al., *Denki Kagaku (presently Electrochemistry)* **1997**, *65*, 506–507.
17. Y. Kashiwagi, K. Uchiyama, F. Kurashima et al., *Electrochemistry* **1999**, *67*, 900–902.
18. T. Osa, M. Fujihira, in *Electroorganic Chemistry*, Kagaku Zokan No. 86, (Eds.: T. Osa, T. Shono, K. Honda), Kagaku Doujin, 1980, pp. 7–21.
19. a) M. Fujihira, T. Matsue, T. Osa, *Chem. Lett.* **1976**, 875–878; b) T. Osa, M. Fujihira, *Nature* **1976**, *264*, 349; c) M. Fujihira, A. Tamura, T. Osa, *Chem. Lett.* **1977**, 361–366; d) M. Fujihira, T. Matsue, T. Osa, *Electrokhimiya* **1977**, *13*, 1679–1684.
20. H. Abruña, T. J. Meyer, R. W. Murray, *Inorg. Chem.* **1979**, *11*, 3233–3240.
21. M. Sharp, M. Petersson, K. Edström, *J. Electroanal. Chem.* **1980**, *109*, 271–288.
22. M. Petersson, *Anal. Chim. Acta* **1986**, *187*, 333–338.
23. G. Nagy, G. A. Gerhardt, A. F. Oke et al., *J. Electroanal. Chem.* **1985**, *188*, 85–94.
24. C. Ueda, D. C.-S. Tse, T. Kuwana, *Anal. Chem.* **1982**, *54*, 850–856.
25. P. Jego, C. Moinet, in *Novel Trends in Electroorganic Synthesis* (Ed.: S. Torii), Springer-Verlag, Tokyo, 1997, pp. 161–164.
26. A. Deronzier, D. Limosin, J.-C. Moutet, *Electrochim. Acta* **1987**, *32*, 1643–1647.
27. a) L. Coche, J.-C. Moutet, *J. Electroanal. Chem.* **1987**, *224*, 112–122; b) L. Coche, J.-C. Moutet, *J. Electroanal. Chem.* **1986**, *198*, 187–193; c) L. Coche, J.-C. Moutet, *J. Electroanal. Chem.* **1988**, *245*, 313–319.
28. A. N. K. Lau, L. L. Miller, *J. Am. Chem. Soc.* **1983**, *105*, 5271–5277.
29. T. Osa, U. Akiba, I. Segawa et al., *Chem. Lett.* **1988**, 1423–1426.
30. F. MacCorquodale, J. A. Crayston, J. C. Walton et al., *Tetrahedorn Lett.* **1990**, *31*, 771–774.
31. A. Ruhe, L. Walder, R. Scheffold, *Helv. Chim. Acta* **1985**, *68*, 1301–1311.
32. D.-L. Zhou, C. K. Njue, J. F. Rusling, *J. Am. Chem. Soc.* **1999**, *121*, 2909–2914.
33. T. Osa, Y. Kashiwagi, Z. Ma, in *Electroorganic Synthesis* (Eds.: D. Little, N. L. Weinberg), Marcel Dekker, New York, 1991, pp. 343–353.
34. Y. Kashiwagi, H. Ono, T. Osa, *Chem. Lett.* **l993**, 257–260.
35. T. Osa, Y. Kashiwagi, K. Mukai et al., *Chem. Lett.* **1990**, 75–78.
36. Y. Kashiwagi, A. Ohsawa, T. Osa et al., *Chem. Lett.* **1991**, 581–584.
37. Y. Kashiwagi, H. Ono, T. Osa, *Chem. Lett.* **1993**, 81–84.
38. Y. Kashiwagi, F. Kurashima, C. Kikuchi et al., *J. Chin. Chem. Soc.* **1998**, *45*, 135–138.
39. Y. Kashiwagi, Y. Yanagisawa, F. Kurashima et al., *J. Chem. Soc., Chem. Commun.* **1996**, 2745–2746.
40. Y. Yanagisawa, Y. Kashiwagi, F. Kurashima et al., *Chem. Lett.* **1996**, 1043–1044.
41. T. Osa, Y. Kashiwagi, Y. Ynagisawa et al., *J. Chem. Soc., Chem. Commun.* **1994**, 2535–2537.
42. Y. Kashiwagi, F. Kurashima, C. Kikuchi, in *Novel Trends in Electroorganic Synthesis* (Ed.: S. Torii), Springer-Verlag, Tokyo, 1997, pp. 169–172.
43. Y. Kashiwagi, F. Kurashima, C. Kikuchi, in *Novel Trends in Electroorganic Synthesis* (Ed.: S. Torii), Springer-Verlag, Tokyo, 1997, pp. 173–174.
44. Y. Kashiwagi, T. Osa, *Chem. Lett.* **1993**, 185–188.
45. T. Osa, Y. Kashiwagi, Y. Yanagisawa, *Chem. Lett.* **1994**, 367–370.
46. Y. Kashiwagi, Y. Yanagisawa, N. Shibayama et al., *Electrochim. Acta.* **1997**, *42*, 2267–2270.
47. Y. Kashiwagi, C. Kikuchi, J. Anzai et al., *J. Electroanal. Chem.*, in press.
48. a) J. Yano, K. Ogura, A. Kitani et al., *Synth. Met.* **1992**, *52*, 21–31; b) J. Yano, K. Ogura, A. Kitani et al., *Can. J. Chem.* **1992**, *70*,

1009–1010; c) J. C. Cooper, E. A. H. Hall, *Electroanalysis* **1993**, *5*, 385–397; d) Z. Mandic, L. Duic, *J. Electroanal. Chem.* **1996**, *403*, 133–141; e) N. Pekmez, A. Yildiz, *Ber. Bunsen-Ges. Phys. Chem.* **1998**, *102*, 843–847; f) A. Malinauskas, R. Holze, *Electrochim. Acta* **1998**, *43*, 2563–2575.
49. a) J. Yano, M. Kokura, K. Ogura, *J. Appl. Electrochem.* **1994**, *24*, 1164–1169; b) A. Malinauskas, R. Holze, *Ber. Bunsen-Ges. Phys. Chem.* **1996**, *100*, 1740–1745; c) W. Wang, T. Yamaguchi, K. Takahashi et al., *Denki Kagaku (presently Electrochemistry)* **1998**, *66*, 1032–1033.
50. M. D. Levi, E. Y. Pisarevskaya, *Synth. Met.* **1993**, *55*, 1377–1378.
51. A. Malinauskas, R. Holze, *J. Electroanal. Chem.* **1999**, *461*, 184–193.
52. J. Yano, A. Shimoyama, K. Ogura, *J. Chem. Soc., Faraday Trans.* **1992**, *88*, 2523–2527.
53. I. Casella, M. R. Guascito, *Electroanalysis* **1997**, *9*, 1381–1386.
54. A. Bagheri, F. Emami, M. R. Nateghi, *Anal. Lett.* **1997**, *30*, 2023–2028.
55. J. J. Sun, D. M. Zhou, H. Q. Fang et al., *Talanta* **1998**, *45*, 851–856.
56. a) S. Pleus, M. Schwientek, *Synth. Commun.* **1997**, *27*, 2917–2930; b) S. Pleus, M. Schwientek, *Synth. Met.* **1998**, *95*, 233–238; c) S. Pleus, C. H. Hamann, M. Schwientek et al., in *Elektrochemische Reaktion-Stechnik und Synthese, GDCh Monographie* (Eds.: J. Russow, G. Sandstede, R. Staab), Gesellschaft Deutscher Chemiker, Frankfurt am Main, 1999, p. 173, Vol. 14.
57. T. Osa, T. Matsue, A. Yokozawa et al., *Denki Kagaku* **1985**, *53*, 104–108.
58. T. Matsue, A. Aoki, I. Uchida et al., *Bull. Chem. Soc. Jpn.* **1987**, *60*, 3591–3595.
59. W. Kutner, T. J. Meyer, R. W. Murray, *J. Electroanal. Chem.* **1985**, *195*, 375–394.
60. K. J. Stutts, R. M. Wightman, *Anal. Chem.* **1983**, *55*, 1576–1579.
61. K. Ravichandran, R. P. Baldwin, *Anal. Chem.* **1983**, *55*, 1586–1591.
62. F. Li, S. Dong, *Electrochim. Acta* **1987**, *32*, 1511–1513.
63. J. Wang, T. Golden, R. Li, *Anal. Chem.* **1988**, *60*, 1642–1645.

10.3 Electrocatalysis of Inorganic Chemicals by Chemically Modified Electrodes

Bineta Keita, Louis Nadjo
Université Paris-Sud, 91405 Orsay Cedex, France

10.3.1 Inorganic

In the fabrication of chemically modified electrodes (CMEs), ''one deliberately seeks, in some hopefully rational fashion, to immobilize a chemical on an electrode surface, so that the electrode thereafter displays the chemical, electrochemical, optical, and other properties of the immobilized molecule (s)'' (Ref. 1 and references therein). Ordinarily, electrocatalysis at a CME features a mediation of electron-transfer reactions, by the immobilized redox couple, between the electrode and some substrate that would otherwise undergo a slow electrochemical reaction at a naked electrode [1]. However, in the following, electrocatalysis will be taken in the broad sense usually attached to this term in most applications of chemically modified electrodes [2] and which can be defined as the ''dependence of the electrode reaction rate on the nature of the electrode material''. In this section, we are not concerned about cases in which the electrode material is catalytic per se. In other words, intentional modification of the electrode composition or surface is necessary. In line with this choice, examples of electrocatalyses triggered by deposited adatoms will be included. Selection was made of and emphasis put on examples, old and recent, that illustrate the above definitions, but the recent literature will be mostly retained, from which older material can easily be traced. Therefore, no effort will be made for exhaustiveness. Rather, wherever possible, mechanistic proposals and unresolved problems will be presented and discussed, in an attempt to stimulate future work on the subject. Finally, references with essentially analytical purposes are collected, as well as those in which the products of the electrocatalysis are identified and, sometimes, quantified. The main substrates retained herein for examination concern the small inorganic ions and molecules, which have been receiving attention for several decades recently. Our selection includes the reduction of protons or oxidation of hydrogen, the reduction of oxygen, and the electrochemical processes of nitrogen oxides (NO_x) and carbon oxides (CO_x), complemented by the electrocatalysis of chlorate, bromate, and so on. All of them have important implications in environmental problems and/or are potentially considered as abundant and inexpensive sources for the production of useful chemicals [3].

10.3.2 The Three Main Strategies as Applied to the NO_x

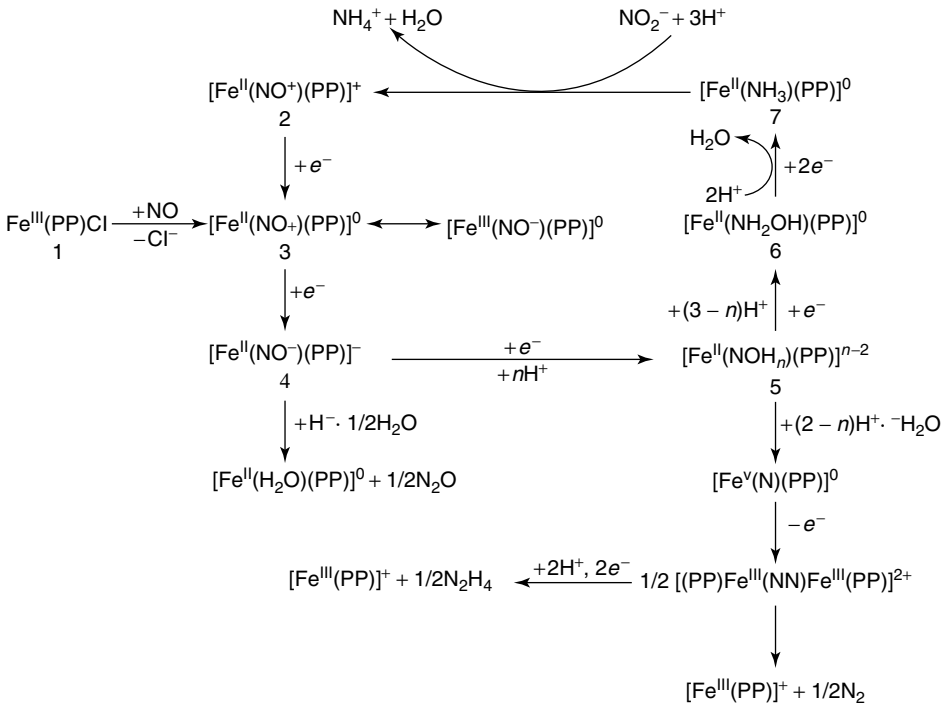
Three main strategies can be distinguished. *The first strategy* is illustrated by the attempts to transfer to electrode surfaces, the real or putative catalytic properties of inorganic complexes in homogeneous solutions toward these nitrogen oxides. Essentially, nitrate (NO_3^-), nitrite (NO_2^-), and nitric oxide (NO) were studied and reported in the literature. Similarly, Tanaka et al. [4, 5] realized the catalytic reduction of NO_3^- to NH_3 on a glassy carbon electrode modified with $(n\mathrm{Bu_4N})_3[Mo_2Fe_6S_8(SPh)_9]$. The controlled potential electrolysis was performed at -1.25 V versus the standard

Encyclopedia of Electrochemistry. Edited by A.J. Bard and M. Stratmann
Vol. 10 *Modified Electrodes*. Edited by M.Fujihira, I.Rubinstein, and J.F.Rusling
Copyright © 2007 Wiley-VCH Verlag GmbH & Co. KGaA, Weinheim. ISBN: 978-3-527-30402-8

calomel electrode (SCE) in a phosphate buffer. The current efficiency was as high as 80.3% at pH 10. Nitrite and hydroxylamine were found as intermediates but were very easily reduced to ammonia. A small amount of hydrogen was also obtained. The same electrode reduced NO_2^- to N_2O at -1.10 V versus the SCE, without any appearance of NH_3. One of the most interesting results concerns the molybdenum–iron–sulfur cluster, which is prepared in drastic anaerobic conditions: the authors claim that, this complex, modified on a glassy carbon plate, ''does not undergo a degradation during the reduction of NO_3^-'' [5]. The same strategy with simpler complexes is illustrated by the use of various assemblies: Nafion and *trans*-Co(III) cyclams coated on gold or amalgamated gold electrodes reduce NO_3^- into hydroxylamine, NH_2OH, in a concentrated sodium hydroxide solution [6]. Electrocatalytic reduction of nitric oxide is readily observed at glassy carbon electrodes modified with electropolymerized films of $[Cr(v\text{-}tpy)_2]^{3+}$ where (v-tpy) stands for 4′-vinyl-2,2′,6′,2′′-terpyridyl [7]. Upon further modification with a thin film of Nafion, such electrodes proved suitable as NO sensors in solution, with submicromolar detection limits and fast response. Similarly, iron alizarin complexone {iron(III) [(3,4-dihydroxy-2-anthraquinolyl)methyl)imino]diacetic acid} strongly adsorbed on graphite electrode surfaces catalyzes the reduction of both nitrite and nitric oxide, mainly into NH_2OH and NH_3 [8]. Coordination of the NO_2^- to the surface complex appeared likely on the basis of a small potential shift of the complex wave observed upon addition of nitrite. The formation of an adduct with NO is straightforwardly indicated by the appearance of a new wave [8]. Such a nitrosyl formation is also clearly demonstrated as a key step in the electrocatalytic reduction of nitrite by iron(III) protoporphyrin IX dimethyl ester immobilized in an electropolymerized film [9]. The major products of the catalytic reductions were ammonia, nitrous oxide, nitrogen, and hydroxylamine. A striking observation is worth emphasizing: N_2 appears as a major product in the immobilized metalloporphyrin-mediated nitrite reduction, in contrast with the previously studied solution-phase monomeric porphyrin catalysts [10–12]. The proximity of the redox sites within the polymeric matrix was invoked as a possible explanation for this modification of selectivity. A plausible mechanism for the whole reduction process, suggested by Meyer et al. [9] is shown in Sch. 1.

The bicatalyst electrocatalytic reduction and oxidation of nitrite by Fe(II) and Cu(II) complexes constitutes another interesting achievement [13]. A two-layer film of iron(II) complex and Cu(II) complex adsorbed on a glassy carbon electrode was used to oxidize NO_2^- to NO_3^- through the iron(II/III) complex redox couple and to reduce nitrite to nitrous oxide through the copper(II/I) redox couple [13].

The preceding examples and many others, for instance those from Malinski's group [14–18], might suggest the metal–NO_x interaction to build up a complex center where subsequent redox events are to take place directly [19]. Several papers show, however, that such a generalization is inappropriate. For instance, after studying the coordination of nitric oxide (NO) to Co(II) phthalocyanine (CoPc) in dimethyl sulfoxide, it was established that ring-centered processes may be involved in the subsequent catalytic reduction of NO [20]. As a consequence, the following mechanism was proposed, taking this



Scheme 1 Possible mechanism for the electrolytic reduction of NO_2^- or NO.

finding into account [20]:

$$Co^{II}Pc(-2) + NO \rightleftharpoons (NO)Co^{III}Pc(-2) \quad (1)$$

$$(NO)Co^{III}Pc(-2) + e^- \rightleftharpoons (NO)Co^{II}Pc(-2) \quad (2)$$

$$(NO)Co^{II}Pc(-2) + e^- \rightleftharpoons (NO)Co^{I}Pc(-2) \quad (3)$$

$$(NO)Co^{I}Pc(-2) + e^- \rightleftharpoons (NO)Co^{I}Pc(-3) \quad (4)$$

$$(NO)Co^{I}Pc(-3) + ne^- \rightleftharpoons NH_3 \text{ and other products} \quad (5)$$

In the detection and quantification of NO, it was even demonstrated that the central metal in these complexes might not be essential [21–23]. The same electrocatalytic activity toward NO was found for glassy carbon electrodes coated with the conductive polymeric film of nickel(II) tetrakis(3-methoxy-4-hydroxyphenyl) porphyrin before and after demetalation [21]. A simple Nafion coating on a gold microelectrode reliably detects NO in the nanomolar concentration range while minimizing the interference of nitrite [22]. Also, Abruna and coworkers described a sensor for the direct determination of NO based on its oxidation at a platinum electrode modified with Nafion and cellulose acetate [23]. Whereas the purpose of Nafion was to exclude interfering anions, the cellulose acetate serves to discriminate on the basis of size. A sharp selectivity for nitrate over perchlorate, iodide, and bromide was demonstrated with

a film obtained by electropolymerization of pyrrole onto glassy carbon electrodes in the presence of $NaNO_3$ [24]. At least two significant drawbacks in the strategy of electrode modification with elaborate inorganic complexes might be pointed out: first, some cumbersome modification procedures must be used; second, and particularly, the long term stability of the complex is not guaranteed upon repeated use or cycling.

The second strategy is roughly based on the catalytic behaviors of metals in the dispersed state. Basically, the concept of active sites on metal surfaces [25] remains the ultimate, widely used rationale for catalytic processes at surfaces and interfaces. For example, nitrous oxide (N_2O) is easily reduced to N_2, using a gas-diffusion electrode loaded with a platinum catalyst [26]. There is abundant literature concerning the deposition of metal atoms or aggregates on noncatalytic electrode surfaces for catalysis purposes. However, a critical evaluation of the performance must be made to ensure that metal deposition does not result merely in an increase of the active surface and to demonstrate true catalysis. Thus, the electrocatalytic reduction of nitrate is mediated by underpotential-deposited cadmium on gold and silver electrodes in acid media [27]. The efficiency of material doping was demonstrated in the reduction of nitrite and nitrate using thin-film, B-doped diamond electrodes [28]. The use of bimetallic electrodes can be considered as an amplification of the same concept, with some possibility to control and direct the selectivity. Such an example is illustrated by the electrocatalytic reduction of NO_3^- on palladium/copper electrodes [29]. One monolayer of Cu gives a selectivity different from bulk Cu. As a whole, copper is claimed to activate the first electron transfer; the role of palladium is to steer the selectivity toward N_2 [29].

The last strategy utilizes the properties of a single family of chemicals, namely oxides, and is therefore separated from the two preceding ones even though the techniques might seem close. This strategy might ultimately be traced to the discovery that some precious-metal oxides display far superior performances than the corresponding precious metals themselves [30]. Attention was then sharply focused on metal oxides as electrode materials [31, 32]. Furthermore, synergistic effects have appeared in many instances as a result of admixing single oxides, producing a material with properties superior to a linear combination of the constituents. The chemistry and geometric factors that lead to better catalytic properties are, at best, only partially understood. To keep closely with the classical idea of electrode modification, the astonishing activation of glassy carbon surfaces with alumina is worth mentioning [33, 34]. This example is cited here even though the activated surface was applied to the catalytic oxidation of organic chemicals, including ascorbic acid. As a molecular illustration of the basic electrocatalytic properties of oxides, extensive work is being carried out for years by Keita and Nadjo on oxometalates, including heteropoly and isopoly oxometalates. Examples of Keggin- and Dawson-type heteropolyanion structures [35] are shown in Fig. 1. The incentive for such investigations originated from several facts: (1) oxometalates appear as molecular metal oxides; in particular, heteropolyanions may closely mimic mixed metal oxides, with the geometric factors imposed by crystallographic structures; (2) the redox properties of

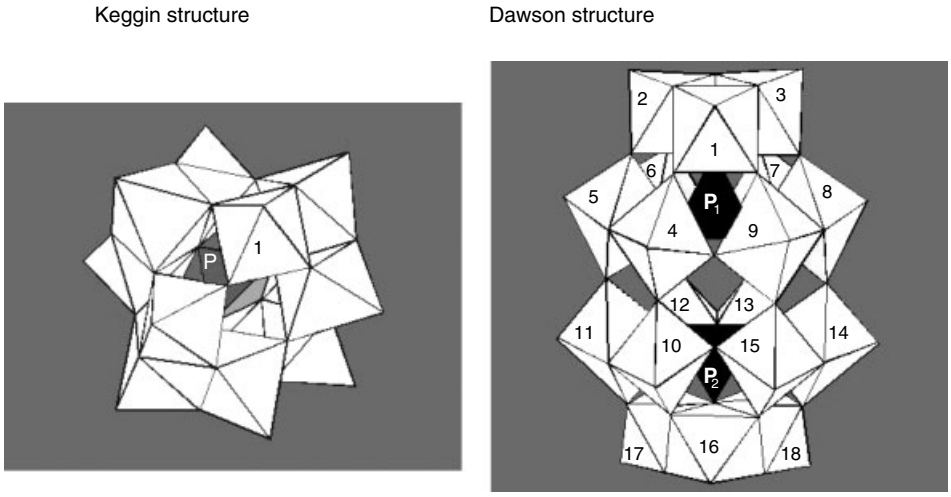


Fig. 1 Keggin and Dawson structures.

these compounds may be very flexible and chosen on purpose by changing their composition; and (3) their reduced forms can act as donors or acceptors of several electrons while maintaining their structure. It is expected that this behavior might serve as a valuable aid when an attempt at studying catalysis and electrocatalysis at a molecular level is tackled. Solution electrochemistry of a large variety of such oxometalates and their derivatives shows electrocatalytic behaviors toward the reduction of nitrite and nitric oxide [36, 37]. The main product detected after electrolysis at potentials more negative than the first redox couple of the heteropolyanions was N_2O [38]. It was even possible to demonstrate that a series of one- and two-electron reduced unsubstituted, lacunary as well as substituted heteropolyanions convert quantitatively NO into N_2O in acidic aqueous media [39]. Entrapment of selected heteropolyanions in polyaniline (PANI) films or in slightly quaternized polyvinyl pyridinium (QPVP) films on a glassy carbon electrode, demonstrates that stable conductive as well as redox polymer assemblies can be fabricated [40, 41]. The catalytic behaviors observed in solution remain [38]. In comparison with the polished glassy carbon electrode, the improvement in operational potential observed for a current density of $53\,\mu A\ cm^{-2}$ varies from 0.800 to 1.200 V, depending on the specific heteropolyanion used. Figure 2 illustrates the electrocatalytic reduction of nitrite by a PANI/$[SiMo_{12}O_{40}]^{4-}$ assembly, in a pH 2 solution, with a potential improvement of at least 600 mV compared to the bare glassy carbon electrode [38]. This example illustrates a case in which cross-check experiments are useful to demonstrate true electrocatalytic behavior. As a matter of fact, pure PANI apparently catalyzes the reduction of nitrite, but in contrast with the PANI/$[SiMo_{12}O_{40}]^{4-}$ assembly, does not stand repetitive cycling in the presence of NO_2^-, and therefore is not useful for a long term electrocatalysis. Combining this oxide strategy with the properties of inorganic complexes, Anson et al. have proposed a bicatalyst coating

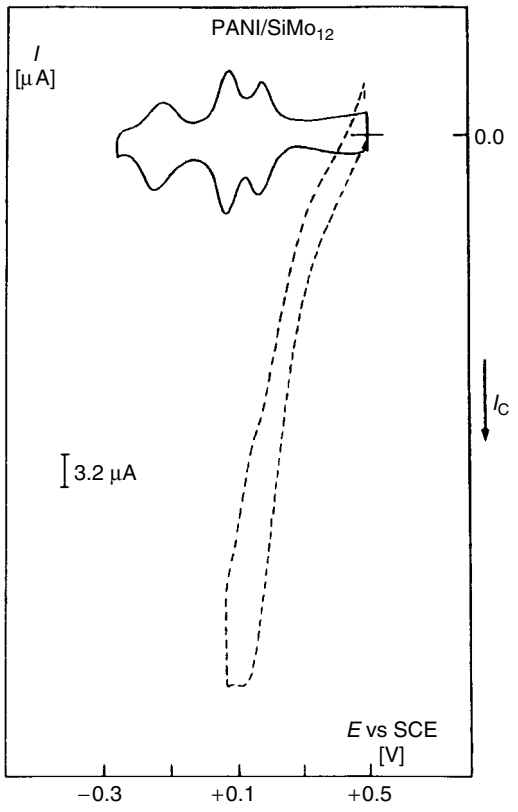


Fig. 2 Cyclic voltammograms showing the electrocatalytic reduction of nitrite at PANI/polyoxometalate coated electrodes. Electrolyte: 0.2 M $Na_2SO_4 + H_2SO_4$ (pH = 2). Scan rate $\nu = 5$ mV s^{-1}. Solid line: cyclic voltammetry, restricted to the stability domain of PANI, of the PANI/$SiMo_{12}$ assembly, in the supporting electrolyte; Dotted line: effect of the addition of 10^{-2} M $NaNO_2$ to the electrolyte.

on roughly polished edge plane pyrolytic graphite electrodes: the coating consists of alternating layers of $[P_2Mo_{18}O_{62}]^{6-}$ anions and Os(II) or Ru(II)-polypyridine cations [42]. The assembly was used for the reduction of HNO_2 and the oxidation of benzyl alcohol. Electrocatalytic behavior was demonstrated for both anionic $[P_2Mo_{18}O_{62}]^{6-}$ and cationic $[cis\text{-}Ru(dcbpy)_2(OH_2)_2]^{2+}$ (dcbpy = 6, 6′-dichloro-2,2′-bipyridine). However, it turns out that the stacking of multilayers on top of the first layer of $[P_2Mo_{18}O_{62}]^{6-}$ adsorbed on the electrode produced almost no increase in catalytic currents for the reduction of HNO_2 to N_2O and the activity of $[cis\text{-}Ru(dcbpy)_2(OH_2)_2]^{2+}$ in coatings for the catalytic oxidation of benzyl alcohol was short-lived.

Developments of all the three strategies as applied to the redox processes of the NO_x continue unabated [43–47] every time a new chemical shows promise for electrocatalytic reduction of the NO_x. There are several recent examples, which cannot be cited exhaustively. In particular, the electrocatalytic reduction of nitrite has become a popular test of the electrocatalytic behaviors of polyoxometalates [48–52].

Falling in this group of achievements, the electrocatalytic reduction of nitrate was realized by using Cu^{2+}- and Ni^{2+}-containing Dawson-type

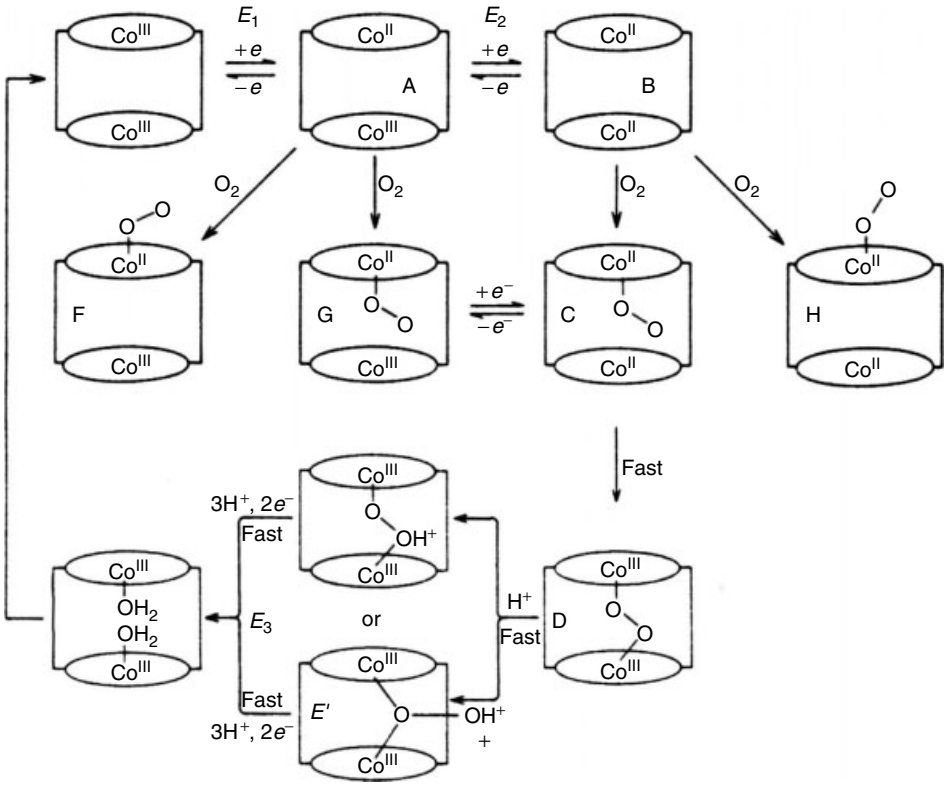
polyoxometalates [53]. The presence of these substituents seems necessary, in contrast with the observed catalytic reduction of nitrite and nitric oxide, for which even nonsubstituted polyoxometalates were active. With the first series of derivatives, the electrocatalysis is triggered by the electrodeposited copper; Ni^{2+}-containing heteropolyanions mimic more closely the catalytic reduction of nitrate by metal ion cyclams and related complexes. Several such examples have been described recently and await their possible transfer to electrode surfaces [54–57]. Among them must be stressed the Keggin dimer, $[Fe_6(OH)_3(A\text{-}\alpha\text{-}GeW_9O_{34}(OH)_3)_2]^{11-}$, which shows an important catalytic activity toward the reduction of nitrate [56]. As a final relevant example, the behaviors of the supramolecular complex $[Cu_{20}Cl(OH)_{24}(H_2O)_{12}(P_8W_{48}O_{184})]^{25-}$ were studied recently [58]. This molecule shows a strong catalytic activity toward nitrate and nitrite. Comparison with the activity per copper atom of previously studied copper-substituted heteropolyanions indicates the supramolecular complex to be significantly more efficient, a feature that reinforces the notion that accumulation of transition metals within polyoxometalates should be beneficial for the relevant catalytic processes. This superior efficiency of $[Cu_{20}Cl(OH)_{24}(H_2O)_{12}(P_8W_{48}O_{184})]^{25-}$ is due both to the accumulation of Cu centers and to the more positive potential locations of catalytically active Cu and W waves compared to the corresponding waves of other Cu-substituted polyoxometalates. As another example, it was found recently [59] that the dimeric pentacopper(II)-substituted tungstosilicate $[Cu_5(OH)_4(H_2O)_2(A\text{-}\alpha\text{-}SiW_9O_{33})_2]^{10-}$ catalyzes the reduction of nitrous oxide (N_2O).

10.3.3 Other Illustrative Examples: O_2, H_2, ClO_3^-, CO_x

The three basic strategies developed by taking as examples the catalytic redox processes of the NO_x are used, sometimes with slight variations, for the electrocatalysis of dioxygen reduction (sometimes associated with hydrogen peroxide reduction) or dioxygen evolution reaction [30–32, 47–85], chlorine evolution, bromine or iodine production [30–32, 76, 77, 86–88], hydrogen evolution reaction (HER), or the oxidation of hydrogen [64, 88–93], the CO_x processes [94–109]. Preference is given to the pioneering work on these chemicals unless recent breakthrough justifies specific development, as will appear in the following. It frequently happens, in the case of metal dispersion or metal alloys, that the same catalysts are operative for the reduction of dioxygen and the oxidation of hydrogen. Efficient dioxygen reduction, in particular, its four-electron reduction to water, remains a subject of continuing efforts. Work from Collman's group [70, 71, 110–113] and from Anson's group [69, 72, 111–117], in cooperation or separately, are particularly illustrative in this domain. The basic ideas behind their strategy and the evolution of this strategy for designing and synthesizing suitable metal complexes to achieve the four-electron reduction of dioxygen can be summarized as follows: As a central point of note, it is recognized that the stepwise reduction of dioxygen first to hydrogen peroxide ($E^\circ = 0.68$ V versus standard hydrogen electrode) and subsequently to water is not a viable pathway if the cathode is to operate near the thermodynamic O_2/H_2O potential ($E^\circ = 1.23$ V). Then, it is desirable to supply four electrons more or less simultaneously to the dioxygen substrate

at as positive a potential as possible. Furthermore, a mononuclear complex seems highly unlikely to effect such a reduction in a rapid fashion. The idea then emerged to try and mimic the mechanism of enzyme action of cytochrome *c* oxidase, which carries out the four-electron reduction of dioxygen to water without forming free H_2O_2. It is desirable that hydrogen peroxide, if any, be not an intermediate but merely a minor side product. Hence the first approach to this problem involved the "face-to-face" (FTF*X*, in which *X* stands for the number of atoms of the linking group) porphyrin dimer, a structure that holds two metal centers in close proximity so that they can act jointly in coordination and reduction of the substrate. The strategy proved successful, first with Co_2FTF4 adsorbed on pyrolytic graphite electrodes. The synthetic subtleties used to achieve a parallel orientation of the two cofacial metalloporphyrin rings and the different interporphyrin separations can be found in the original papers. A detailed study of Co_2FTF4, in particular, as a function of pH has revealed a gradual conversion of the dioxygen reduction product to hydrogen peroxide as the supporting electrolyte was changed from acidic to neutral or alkaline. An example of accommodation [113] of the main observations in acidic media results in the proposal of the mechanistic pathways presented in Sch. 2.

In this scheme, the proposed intermediates constitute reasonable guesses. A



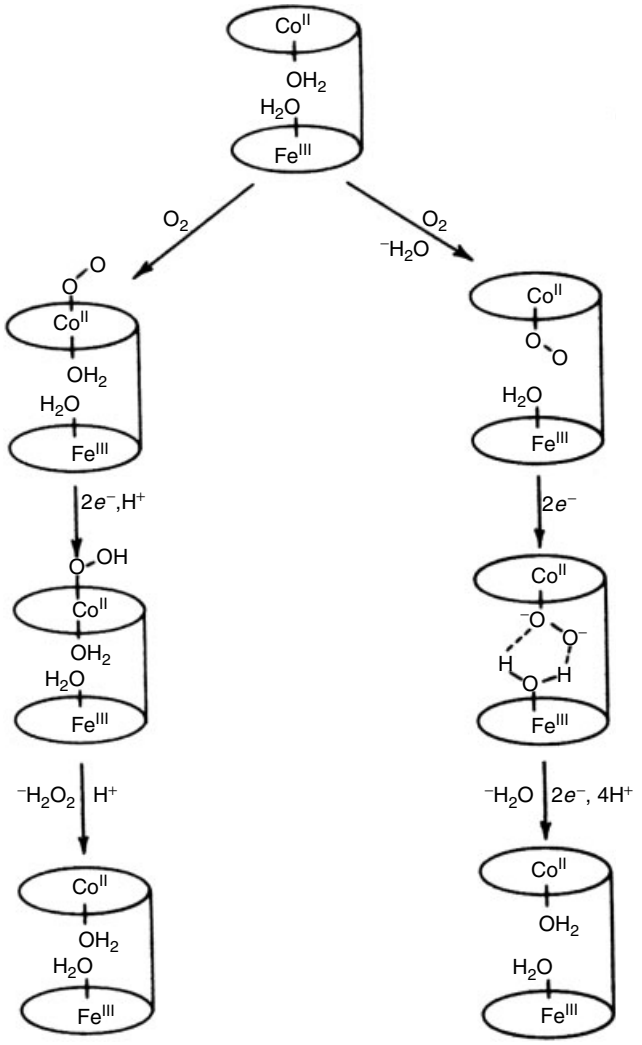
Scheme 2

catalytic mechanism is also given in the absence of proton.

Numerous other assemblies have been designed and proved successful in the four-electron reduction of dioxygen. The wish to mimic as closely as possible multielectron redox enzymes functioning at physiological pH with heterometallic active centers suggested the synthesis of mixed metal porphyrins. An interesting example in this domain [114] is provided by the study of anthracene-linked dimeric metalloporphyrins with the following combination of metal centers: Co−Cu, Co−Fe, Fe−Fe, Fe−H_2. Except for the Co−Cu diporphyrin, which failed to catalyze the reduction of dioxygen beyond H_2O_2, all the other assemblies exhibited mixed reduction pathways to both H_2O and H_2O_2, with the pathways that lead to H_2O not involving H_2O_2 as an intermediate, as sketched in Sch. 3 [114].

Continuation of these efforts have recently led Collman et al. to the successful synthesis of close analogs of the cytochrome *c* oxidase Fe_{a3}/Cu_B center that show clean four-electron electrocatalytic reduction of O_2 to H_2O at physiological pH [71, 110]. With the same basic ideas but in a somewhat different direction, Anson et al. [116] attached four $Ru(NH_3)_5$ groups to cobalt meso-tetrakis(4-pyridyl)porphyrin within Nafion coatings on graphite electrodes. The resulting complex, $[CoP(pyRu(NH_3)_5)_4]^{8+}$, acts as a catalyst for the four-electron reduction of O_2 under conditions in which mixtures of the same porphyrin with uncoordinated $[Ru(NH_3)_6]^{2+}$ or $[Ru(NH_3)_5py]^{2+}$ do not. In contrast with experiments showing that the presence of multiple electron-donating groups is not sufficient to ensure multiple electron catalysis, these results provide evidence for the intramolecular delivery of four electrons from the four coordinated $[Ru(NH_3)_5]^{2+}$ groups to O_2 molecules associated with the Co(II) center of the porphyrin. One of the key requirements for this success stems from the fact that the four coordinated groups do not interact strongly and have essentially the same formal potential. Also, it has been possible, using the complex of Co(III) with the macrocyclic ligand C-meso-5,7,7,12,14,14-hexamethyl-1,4,8,11-tetraazacyclotetradecane, to obtain clear evidence for the intermediacy of the hydroperoxo complex presumed to be formed during the catalyzed reduction of O_2 to H_2O_2 by cobalt porphyrins [117].

Completely mineral catalysts are also being applied to the reduction of dioxygen. In a recent example, a Pd-containing polyoxometalate, $[Cs_2Na(H_2O)_8Pd_3(\alpha\text{-}AsW_9O_{33})_2]^{9-}$, has shown a remarkable catalytic effect for this process [118]. The active surface was the deposited Pd^0 films. The case might be considered to parallel somewhat the observations made with the wheel-shaped copper complex $[Cu_{20}Cl(OH)_{24}(H_2O)_{12}(P_8W_{48}O_{184})]^{25-}$ in the electrocatalytic reduction of nitrate, for which the active surface was the deposited Cu^0 electrode (vide supra) [58]. The voltammetric pattern of $[Cs_2Na(H_2O)_8Pd_3(\alpha\text{-}AsW_9O_{33})_2]^{9-}$ features the characteristics of the deposition behavior of Pd^0 on the glassy carbon electrode surface. These surfaces turn out to display the electrocatalytic behavior usually expected for Pd^0 films in the electrocatalytic reduction of dioxygen. Figure 3 shows the superposition of the voltammograms obtained with the deposited Pd^0 film in a pure, pH 5 electrolyte, after bubbling air and pure dioxygen, respectively, through the solution. It must be noted that no reduction of dioxygen occurred on the bare glassy carbon surface in the



Scheme 3

potential domain explored. In contrast, a very efficient reduction of dioxygen was observed on the Pd^0-modified surface as can be judged from the relatively positive potential location of the process. The catalytic process was efficient enough for the voltammograms to be polarogram-shaped. Furthermore, the plateau currents scale up roughly with the concentration of dioxygen in solution. Typically, a thin Pd^0 film comprising roughly six monolayers was used for the experiments shown in Fig. 3. Actually, several film thicknesses were used and very efficient dioxygen reduction was observed whatever the film thickness. Finally, prolonged cycling of these electrodes in the presence of dioxygen did not induce any deactivation of the surfaces.

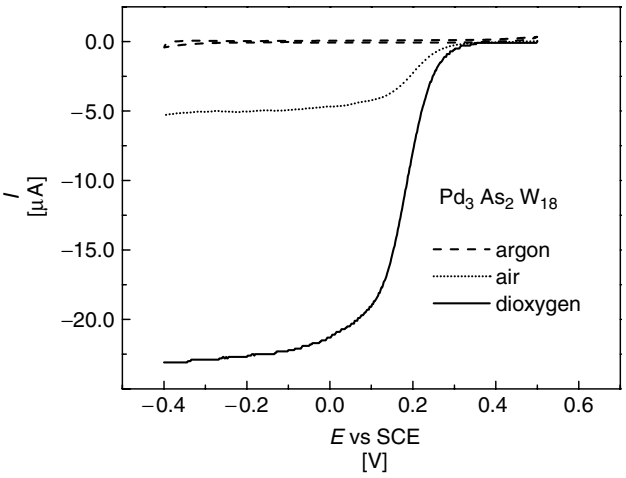


Fig. 3 Cyclic voltammetry characterization in (0.4 M $CH_3COO^- + CH_3COOH$), pH = 5 buffer, of the electrocatalytic reduction of dioxygen on a thin film of Pd^0 (six monolayers) deposited from 2 on a glassy carbon electrode. Reference electrode: SCE; scan rate: 2 mV s^{-1}. The polarogram-shaped voltammograms were obtained respectively with the Pd^0 film in pure supporting electrolyte deaerated with argon; after bubbling air through the solution; after bubbling pure dioxygen through the solution.

The facilitation of the reduction of chlorate on a suitably modified electrode is another example that highlights the properties of polymer/catalyst assemblies [119]. In Fig. 4(a) are superimposed the cyclic voltammograms run with a freshly polished glassy carbon electrode in a solution containing 10^{-3} M $[PMo_{12}O_{40}]^{3-}$ in 50% (v/v) dioxane/water mixture with 0.5 M H_2SO_4 before and after addition of 10^{-1} M $KClO_3$; practically, catalysis begins on the third wave of the heteropolyanion and intensifies just past this wave. A stronger catalysis was observed upon slowing down the scan rate from 5 to 2 mV s^{-1}, as appears from the inset in Fig. 4(a). In contrast, Fig. 4(b) shows the cyclic voltammograms observed in the same electrolyte, except that the heteropolyanion is entrapped in a QPVP matrix. Strikingly, catalysis of the ClO_3^- reduction now starts on the second wave of the heteropolyanion, even when a potential scan rate as unfavorable as 5 mV s^{-1} is chosen. As expected, the inset in Fig. 4b demonstrates that the conditions are still more favorable at 2 mV s^{-1}. In fact, the catalysis is maintained on this second wave even at 20 mV s^{-1} and moves to the third wave only at 100 mV s^{-1}. A striking enhancement of the redox catalytic activity of $[PMo_{12}O_{40}]^{3-}$ entrapped in the present polymer is demonstrated. Clear experimental evidence of this kind, although expected on theoretical grounds [120], is scarce in the literature.

Electrocatalysis of the reduction of the CO_x has generated an abundant literature [94–109]. The distribution of the various products obtained upon reduction of CO_2 depends crucially on the reaction conditions, including electrode materials, solvent systems, the nature of the metal in

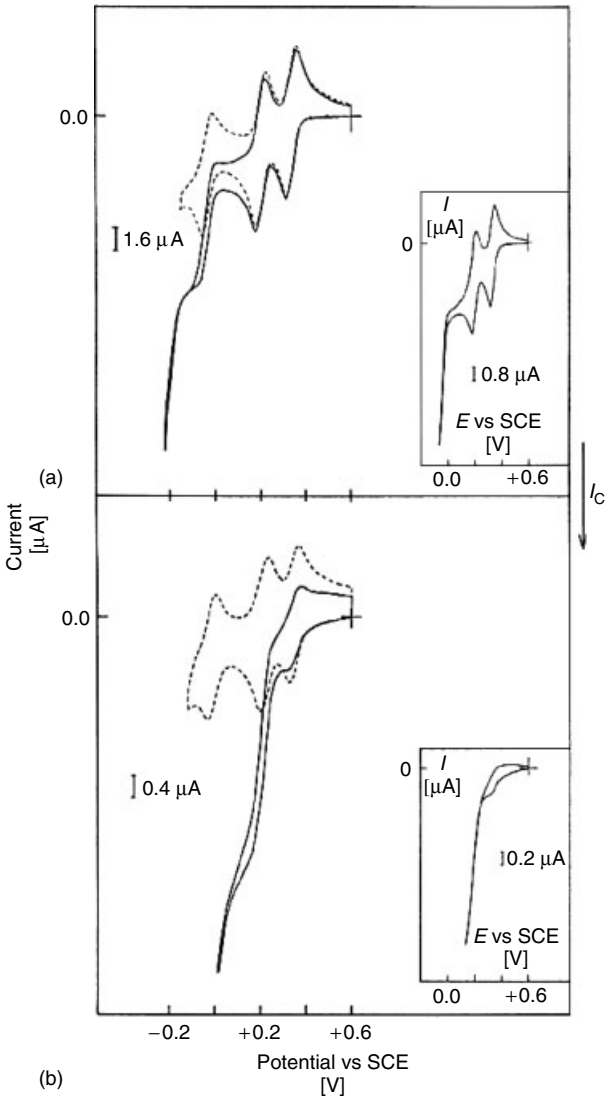


Fig. 4 (a) Cyclic voltammetry patterns obtained with a freshly polished glassy carbon electrode at a scan rate of 5 mV s^{-1} in 10^{-3} M $[PMo_{12}O_{40}]^{3-}$ solution in 50% (v/v) dioxane/water mixture containing 0.5 M H_2SO_4 (dotted line); effect of the addition of 10^{-1} M $KClO_3$ to the preceding solution (solid line). The inset was obtained at 2 mV s^{-1}. (b) Cyclic voltammetric patterns obtained with a glassy carbon electrode covered with QPVP and with $[PMo_{12}O_{40}]^{3-}$ entrapped in the polymer. The supporting electrolyte is the same as in Fig. 3(a). Dotted line: in pure supporting electrolyte; solid line: effect of the addition of 10^{-1} M $KClO_3$. The inset was run at 2 mV s^{-1}.

complexes, and so on. As a consequence, all the aforementioned techniques are routinely met in the literature: metal-particle-modified electrodes, alloys, metal oxides and their mixtures, metal complexes. Numerous metal complexes have been developed to this end, among which tetraazamacrocyclic metal complexes, metal phthalocyanines, and tetraphenylporphyrins have retained much attention. Also, methods have been devised to support some of those complexes which still prove active after deposition on electrode materials. Whatever the strategy, sharp selectivity toward a single chemical with good current efficiency was claimed only in a few examples.

10.3.4 A Brief Overview of the Dimensionally Stable Anodes (DSA) Story

Coming now to an industrial aspect, electrocatalysis in the anodic evolution of dioxygen and chlorine was the incentive for what can be termed "the greatest technological breakthrough of the past 50 years of electrochemistry" [77]. Oxide electrodes, known as *dimensionally stable anodes* (DSA) worldwide, are essentially constituted of a mixture of oxides usually prepared by thermal decomposition of the appropriate precursors. With high conductivity, good chemical stability, excellent electrocatalytic properties, low cost, the possibility for the electrodes to be constructed in the form of nets, meshes, and expanded metals, as well as other beneficial properties, DSAs brought about extraordinary success in the chlorine industry [30–32, 78, 86, 121–124]. Specifically, most active electrocatalysts for Cl_2 evolution are based mainly on RuO_2 and IrO_2, with substantial efforts to use spinels also. Additives useful to stabilize the electrodes or to improve selectivity are, for instance, TiO_2 or SnO_2. While the situation appears satisfactory for chlorine evolution, much effort continues to be devoted for improving dioxygen anodes [77–124]. In parallel, the remarkable behavior of DSAs prompted their use in more and more varied applications, among which their possibilities as activated cathodes for hydrogen evolution must be emphasized. Such electrodes were also used for water electrolysis, and chlorate or bromate synthesis. Particularly, their use for the redox processes of the CO_x is worth emphasizing. Very good reviews on DSAs exist [30–32, 77, 122, 123] and they may be referred to for thorough developments.

10.3.5 Electrocatalysis by Oxide Materials Electrodeposited from Oxometalates

10.3.5.1 Hydrogen Evolution Reaction (HER)

Keita and Nadjo discovered that, whatever the oxometalate in acidic solution, setting a potential of -1.2 V versus SCE at the working electrode brings about a persistent modification of the surface [125–142]. Typically, the evolution of the electrochemical behavior of a glassy carbon electrode used for such an electrolysis in the presence of $[PW_{12}O_{40}]^{3-}$ in 0.5 M H_2SO_4 are sketched in Fig. 5. As a remarkable observation, Fig. 5(b), recorded on a much less sensitive scale than that used for Fig. 4(a), shows that the voltammetric pattern is now dominated by the HER. During the modification process and after its completion, the heteropolyanion waves that are not obscured by the HER retain their initial peak current intensities. The conclusion is that the enhanced kinetics for the HER is not due primarily to the surface increase.

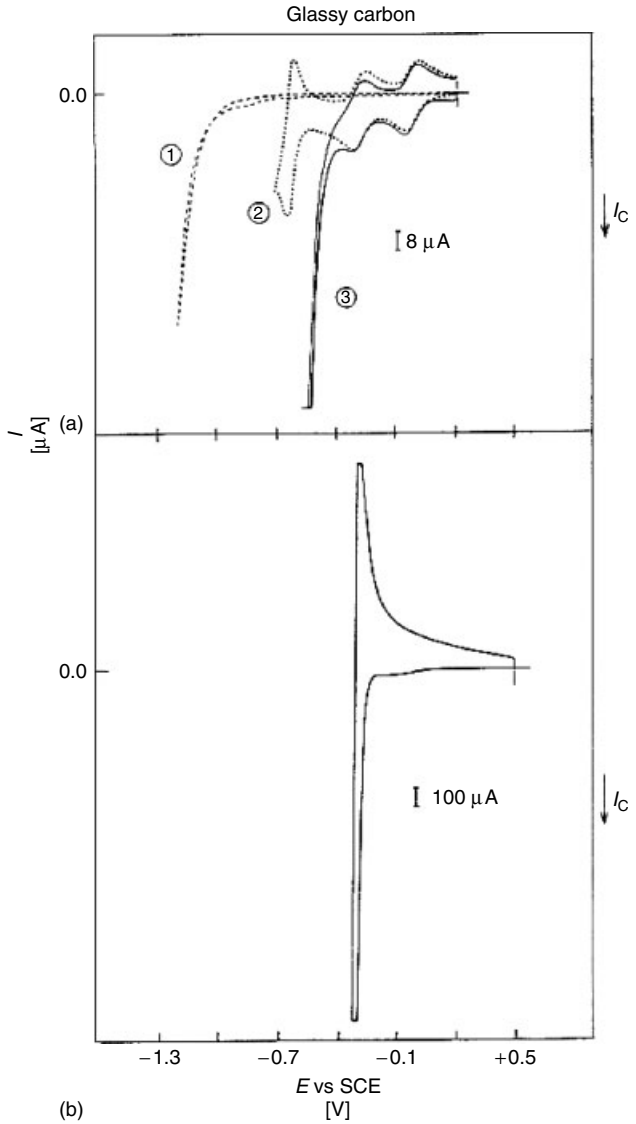


Fig. 5 Cyclic voltammograms obtained under various conditions up to the complete modification of a freshly polished glassy carbon electrode. Scan rate: 100 mV s^{-1}. Electrode surface area: 0.07 cm^2. (a) Curve 1: background current in 0.5 M H_2SO_4 with a freshly polished glassy carbon electrode. Curve 2: cyclic voltammogram, with the same electrode, of $[PW_{12}O_{40}]^{3-}$ in 0.5 M H_2SO_4, restricted to the third wave. Curve 3: cyclic voltammogram obtained in the preceding medium after the electrode has been set at −1.2 V versus SCE for several minutes. (b) Final cyclic voltammetric pattern obtained after the completion of the electrode modification and showing essentially the HER wave.

Electrode materials as diverse as glassy carbon, graphite, tungsten, gold, mercury, and even platinum, have been derivatized successfully, even though the interest on some of these electrode materials might remain an academic curiosity. After modification, all these materials, most of which show usually poor kinetics as regards the HER, become remarkably good cathodes for this process. Several semiconductors have also been activated along the same lines. The modified electrodes can be taken out of the modification bath, rinsed thoroughly, and transferred to pure electrolyte solutions, in which they work as excellent and stable hydrogen cathodes. The catalytic properties of these modified metallic or semiconductor surfaces are remarkably stable in solution over a wide pH range and also in air. Some electrodes have been kept for several years and still show the same activity toward the HER at each use. The gas evolved was checked by gas chromatography to be pure hydrogen. Its quantity shows, to a good approximation, that the whole current was used for this reaction. Several duration tests for more than 3000 hours without interruption under galvanostatic conditions (1 A cm^{-2}) show no drift of the electrode potential toward negative values. Detailed characterization of the surfaces of these new materials is given in the original papers. Tables 1–4 gather the main kinetic parameters obtained for these efficient hydrogen cathodes. Particularly remarkable are their aforementioned stability in time and also their resistance to impurities and additives that are known to be poison for hydrogen-evolving cathodes [138]. It was shown that the modification could be successfully accomplished starting with a particularly simple chemical like Na_2SO_4 [143]. Also, after entrapment

Tab. 2 Decimal logarithm of exchange current densities for the hydrogen evolution reaction, measured in 0.5 M H_2SO_4, before and after derivatization of a glassy carbon surface (G.C., Tokai, Japan). The modification has been performed with various oxometalates. For other conditions, see text

Modification medium 0.5 M H_2SO_4 + 10^{-3} M oxometalate	$-\log(i_o[A\ cm^{-2}])$
No modification (freshly polished glassy carbon)	7.2–8.5
α_1-$K_6P_2W_{17}MoO_{62}$	2.2–2.3
α_2-$K_6P_2W_{17}MoO_{62}$	2.2–2.3
α - $K_6P_2W_{18}O_{62}$	2.4–2.5
α - $H_3PW_{12}O_{40}$	2.3–2.4
α - $H_4SiW_{12}O_{40}$	2.0–2.3
α - $H_3PMo_{12}O_{40}$	3.0–3.4
α - $(NH_4)_6H_2W_{12}O_{40}$	2.4–2.6
H_2WO_4 in 12.4 M HCl [a]	2.4–2.5[a]

[a] The modification medium is 12.4 M HCl. The characterization has been performed in 1 M HCl (see Ref. 43).

Tab. 1 Tafel parameters of the HER on variously modified glassy carbon electrodes. For modification procedures, see text. The test solution is 0.5 M H_2SO_4

Treatment medium	$-\log(i_o[A\ cm^{-2}])$	α
None (freshly polished glassy carbon)	7.2 to 8.5	0.15 to 0.28
0.5 M H_2SO_4	3.97	0.38
0.5 M H_2SO_4 + 10^{-3} M $H_3PW_{12}O_{40}$	1.8	0.54

Tab. 3 Exchange current densities measured in 0.5 M H_2SO_4 for the hydrogen evolution reaction on various electrode materials, before and after derivatization with $[SiW_{12}O_{40}]^{4-}$

Material	$-\log(i_o/A\ cm^{-2})$ *Untreated*	*Modified*
Pt	3 to 3.3 (2.9 to 3.3)	2.5 to 2.8
Au	5.7 (5.9 to 6.7)	2.5
W	6.8 (6 to 7.1)	2.6
GC[a]	7.2 to 8.5(−)	2 to 2.3
Hg	11 to 12.7 (11.6 to 12.5)	3 to 3.9

Literature results (in parentheses, *J. Electroanal. Chem.* **1972**, *39*, 163) for untreated materials are quoted for comparison
[a]GC: glassy carbon (Tokai, Japan).

of oxometalates in polymer matrices, the reductive modification of the whole assembly remains possible and generates good hydrogen cathodes [41]. In the same line, Kulesza and Faulkner [144] deposited nonstoichiometric tungsten (VI,V) oxide aggregates and used them for the electrocatalytic reduction of bromate to bromide, eventually followed in strongly acidic media, by a homogeneous chemical reaction giving bromine. Codeposition of Pt with these oxides gives materials that were tested for the HER [145].

10.3.5.2 Oxygen Reduction

The preceding reductively modified electrodes [125–142] have been used for the reduction of dioxygen. Figure 6 shows the waves obtained in 0.5 M H_2SO_4 for this process on polished glassy carbon and on glassy carbon modified in the presence of $[PW_{12}O_{40}]^{3-}$. A considerable and spectacular decrease in overpotential for the reduction of dioxygen is observed on passing from one electrode to the other. This improvement is routine in the range of 800 to 900 mV and is also observed upon modification of the glassy carbon electrode with another oxometalate. The positive move of the reduction peak potential of dioxygen is accompanied by a concomitant growth and sharpening of this peak. Remarkably enhanced kinetic parameters are obtained

Tab. 4 Stability tests in various media and Tafel parameters[a] of the HER on various electrode materials modified with $[PW_{12}O_{40}]^{3-}$. The stability test was performed at 1 A cm^{-2}

Material	*Ion*	*Test duration [hours]*	$-\log(i_o[A\ cm^{-2}]$	*Slope [mV]*	*Comments*
Pt	None	100	2.58	97	Values obtained in different experiments lie in the range: $-\log i_o \simeq 3 - 2.45$, Slope $\simeq$ 79–100 mV
	Fe^{3+}	105	2.65	90	
	Cu^{2+}	110	3	76	
Glassy carbon	None	110	2.18	102	$-\log i_o \simeq 2.4 - 1.8$, Slope $\simeq$ 90–110 mV
	Fe^{3+}	118	2.46	86	
	Ni^{2+}	95	2.6	78	
	Cu^{2+}	121	2.8	76	

[a]Tafel parameters were measured at the end of the stability test in $\sim$ 0.5 M H_2SO_4.

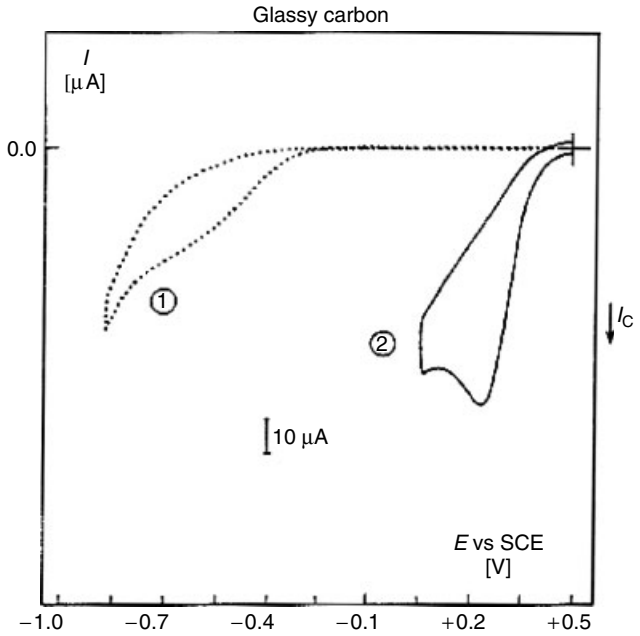


Fig. 6 Cyclic voltammogram obtained in a pH = 0.51 solution saturated with dioxygen. Scan rate: 100 mV s^{-1}. Electrode surface area: 0.07 cm^2. Dotted line: freshly polished glassy carbon electrode; solid line: glassy carbon electrode modified in the presence of $[PW_{12}O_{40}]^{3-}$ as described in the text.

as $\log(i_o/A\ cm^{-2})$ increases from −8.3 for unmodified glassy carbon to −5.6 for the same material modified in the presence of $[PW_{12}O_{40}]^{3-}$. The results of Kuwana et al. [146] obtained in 1 M H_2SO_4 using a platinum-loaded poly(vinylacetic acid)-modified glassy carbon electrode, with a platinum loading of 25 μg cm^{-2}, compare well with the present experiment. In their case, with a medium more acidic than that used for the oxometalate-modified electrode, the overpotential for dioxygen reduction was decreased by ca 800 mV, albeit with the use of Pt microparticles. Related work using platinized bronzes has been published [64].

Finally, it is interesting to point out the activation of the gassy carbon surface even toward the simple outer-sphere electrode reaction of hexammine ruthenium(III) cation, for which the apparent electron-transfer rate constant becomes as high as on the gold surface [134].

10.3.6 Electrocatalysis and Analysis

Chemically modified electrodes are widely used for analytical purposes. For instance, Nafion-coated glassy carbon electrodes modified with diethyldithiocarbamic acid or 1,4,7,10,13,16-hexaoxacyclooctadecane (18-crown-6) were used to promote the sensitivity in the stripping voltammetry determination of Pb(II), Cu(II), and Hg(II). The lifetime of each electrode exceeds three weeks [147]. The subject [148] is covered in recent reviews, which also

highlight the importance and specificity of self-assembled monolayers [149], zeolites [150–152], and clays [153] and will not be further developed here. Even though the purpose and the practice are somewhat different, clay- and zeolite-covered surfaces must be retained in the broad family of oxide electrodes. The interest aroused by the introduction of clay-modified electrode by Bard et al. [154] is worth mentioning. As examples of mostly or fully mineral assemblies, Keita and Nadjo have immobilized a Keggin heteropolyanion, α-$[(H_2)W_{12}O_{40}]^{6-}$, in clays on electrode surfaces [155–157]. Two main types of clays that were coated on glassy carbon surface were montmorillonite and layered double hydroxides. In the case of montmorillonite, the acidic protons or sodium cations were exchanged by octadecyltrimethylammonium cations which bind α-$[(H_2)W_{12}O_{40}]^{6-}$. The system was very stable and was used successfully for the electrocatalytic reduction of dioxygen.

10.3.7 Some Recent Trends in Electrode Surface Modification Techniques

In addition to classical surface modification techniques (chemisorption, covalent bonding, and film deposition) a few other methods have become progressively popular or have found a renewed interest: here, emphasis is put on the sol–gel process and the layer-by-layer (LBL) technique. Only a few illustrative recent references will be cited, from which most of the older extensive literature can be traced out.

Typically, the sol–gel approach involves mixing an alkoxysilane with water, alcohol, and a catalyst such as HCl or NH_3. The silane hydrolyzes and condenses as depicted schematically by the following simplified reaction mechanism:

$$Si(OCH_3)_4 + H_2O \longrightarrow \equiv Si{-}OH + CH_3OH \quad (6)$$

$$\equiv Si{-}OH + HO{-}Si\equiv \longrightarrow \equiv Si{-}O{-}Si\equiv + H_2O \quad (7)$$

Even though the procedure has been known for more than a century and a half, the recent interest was aroused by the demonstration that various inorganic species and organic molecules, including proteins, could be incorporated and remain active within the porous ceramic matrix. Specifically, deposition of a small volume of the silica sol, dip coating, or spin coating are the techniques of interest to obtain thin films on electrode surfaces [158–161]. Various nuances of deposition process have been devised, depending on the desired properties [162–166]. The remarkable properties that make the sol–gel process attractive are summarized in several reviews [167, 168]. Appropriately doped materials obtained by sol–gel processing have found applications in several areas. They have been used as pH sensors [169], for the chemical oxidation of formaldehyde and isobutyraldehyde [170], in the electrochemistry and electrochemiluminescence of ruthenium complexes [171–173], in the amperometric detection of hydrogen peroxide or nitrogen oxides like nitrite [174], in the reduction of dioxygen [175] in the amperometric detection of insulin [176–178] or nicotinamide adenine dinucleotide (NADH) [179], and so on. Finally, a recent trend is to combine sol–gel processing with carbon paste electrodes [180–182].

The LBL technique of immobilization of substances on a surface has appeared rather recently. Decher and coworkers are

considered as the pioneers in the development of the procedure [183–186]. In short, the procedure consists of electrostatic deposition of oppositely charged polyelectrolytes in the alternate LBL. The procedure could be applied successfully to a wide range of charged molecules, including globular proteins, enzymes, nanoparticles, organic and polymeric microcrystals, ceramics and clay, and so on. The remarkable properties of these films have been described in most of the references. Among the wealth of techniques used to characterize such films, attention is drawn here, for illustration, to the electrochemical methods, as applied in particular to LBL films containing polyoxometalates [187–190]. In using this fabrication procedure, the known sensitivity of polyoxometalates must be kept in mind. Detailed discussions of some of the encountered difficulties are presented in electrochemistry papers: they concern the integrity or not of the incorporated polyoxometalate, its interactions with the matrix, its electrochemical behavior within the matrix, the stability of the film, and so on. In contrast, several appreciable applications have already been described. Thermochromic properties of LBL films doped with $[NaP_5W_{30}O_{110}]^{14-}$ make them suitable as thermic sensors [191, 192]; photochromism was detected with $[H_4SiW_{12}O_{40}]$ alternating with 1,10-diaminodecane used to build a film; a pH sensor was constructed by immobilizing a sandwich-type polyoxometalate, $[Co_4(H_2O)_2P_4W_{30}O_{112}]^{16-}$, in a polyallylamine hydrochloride film [193]; proton catalytic reduction was observed with an LBL film containing $[NaP_5W_{30}O_{110}]^{14-}$, a feature that designates this assembly as a potential hydrogen cathode [194]; finally, several examples were described that concern the electrocatalytic reduction in solution of nitrogen oxides, dioxygen, and hydrogen peroxide [194–199]. Also, the presence of NADH could be detected by Ru(bpy)33 + (bpy = 2,2'-bipyridine) immobilized in a LBL film [200, 201].

10.3.8 Concluding Remarks

One of the ultimate goals of electrochemistry is the optimization of electrode processes for energy saving and/or for carrying out selective or environmentally friendly processes. In this context, manipulation of electrode surfaces to realize a chosen purpose has become a necessity. The results obtained thus far are promising; especially, surfaces modified by oxides might show the appropriate durability in electrocatalytic processes.

References

1. R. W. Murray, in *Electroanalytical Chemistry* (Ed.: A. J. Bard), Marcel Dekker, New York, 1984, pp. 191–368, Vol. 13.
2. W. Kutner, J. Wang, M. L'Her et al., *Pure Appl. Chem.* **1998**, *70*, 1301–1318.
3. W. R. Epperly, *Chemtech* **1991**, *21*, 429–431.
4. S. Kuwabata, S. Uezumi, K. Tanaka et al., *J. Chem. Soc. Chem. Commun.* **1986**, 135–136.
5. S. Kuwabata, S. Uezumi, K. Tanaka et al., *Inorg. Chem.* **1986**, *25*, 3018–3022.
6. H. L. Li, J. Q. Chambers, D. T. Hobbs, *J. Electroanal. Chem.* **1988**, *256*, 447–453.
7. M. Maskus, F. Pariente, Q. Wu et al., *Anal. Chem.* **1996**, *68*, 3128–3134.
8. J. Zhang, A. B. P. Lever, W. J. Pietro, *Inorg. Chem.* **1994**, *33*, 1392–1398.
9. J. N. Younathan, K. S. Wood, T. J. Meyer, *Inorg. Chem.* **1992**, *31*, 3280–3285.
10. M. H. Barley, K. Takeuchi, W. R. Murphy Jr. et al., *J. Chem. Soc. Chem. Commun.* **1985**, 507–508.
11. M. H. Barley, K. J. Takeuchi, T. J. Meyer, *J. Am. Chem. Soc.* **1986**, *108*, 5876–5885.
12. M. H. Barley, M. R. Rhodes, T. J. Meyer, *Inorg. Chem.* **1987**, *26*, 1746–1750.

13. S. M. Chen, *J. Electroanal. Chem.* **1998**, *457*, 23–30.
14. T. Malinski, Z. Taha, *Nature* **1992**, *358*, 676–678.
15. T. Malinski, Z. Taha, S. Grunfeld et al., *Anal. Chim. Acta* **1993**, *279*, 135–140.
16. T. Malinski, M. Kapturczak, J. Dayharsh et al., *Biochem. Biophys. Res. Commun.* **1993**, *194*, 654–658.
17. T. Malinski, M. W. Radomski, Z. Taha et al., *Biochem. Biophys. Res. Commun.* **1993**, *194*, 960–965.
18. T. Malinski, Z. Taha, S. Grunfeld et al., *Biochem. Biophys. Res. Commun.* **1993**, *193*, 1076–1082.
19. J. H. Zagal, *Coord. Chem. Rev.* **1992**, *119*, 89–136.
20. S. L. Vilakazi, T. Nyokong, *Polyhedron* **1998**, *17*, 4415–4423.
21. A. Ciszewski, E. Kubaszewski, M. Lozynski, *Electroanalysis* **1996**, *8*, 293–295.
22. F. Lantoine, S. Trévin, F. Bedioui et al., *J. Electroanal. Chem.* **1995**, *392*, 85–89.
23. F. Pariente, J. L. Alonzo, H. D. Abruna, *J. Electroanal. Chem.* **1994**, *379*, 191–197.
24. R. S. Hutchins, L. G. Bachas, *Anal. Chem.* **1995**, *67*, 1654–1660.
25. H. S. Taylor, *Proc. R. Soc. Lond.A* **1925**, *108*, 105–111.
26. N. Furuya, H. Yoshiba, *J. Electroanal. Chem.* **1991**, *303*, 271–275.
27. X. Xing, D. A. Scherson, C. Mak, *J. Electrochem. Soc.* **1990**, *137*, 2166–2175.
28. C. Reuben, E. Galun, H. Cohen et al., *J. Electroanal. Chem.* **1995**, *396*, 233–239.
29. A. C. A. de Vooys, R. A. van Santen, J. A. R. van Veen, *J. Mol. Catal. A: Chem.* **2000**, *154*, 203–215.
30. H. B. Beer, *J. Electrochem. Soc.* **1980**, *127*, 303C.
31. S. Trasatti, (Ed.), *Electrodes of Conductive Metallic Oxides, Part A and Part B*, Elsevier, Amsterdam, 1980–1981.
32. S. Trasatti, in *Electrochemistry at Novel Materials* (Eds.: J. Lipkowski, P. N. Ross), VCH, Weinheim, 1994, pp. 207–295.
33. J. Zak, T. Kuwana, *J. Am. Chem. Soc.* **1982**, *104*, 5514–5515.
34. S. Dong, T. Kuwana, *J. Electrochem. Soc.* **1984**, *131*, 813–819.
35. M. T. Pope, *Hetropoly and Isopoly Oxometalates*, Springer, Berlin, Heidelberg, 1983.
36. B. Keita, L. Nadjo, R. Contant et al., Réduction Catalytique de Composés d'azote, (CNRS), French Patent, 89/1, 728, 1989.
37. B. Keita, L. Nadjo, R. Contant et al., Process for the selective catalytic reduction of nitrogen compounds, and catalysts used, (CNRS), Eur. Patent Appl. EP382, 644, 1990; *Chem. Abst.* **1991**, *114*, 191882u.
38. B. Keita, A. Belhouari, L. Nadjo et al., *J. Electroanal. Chem.* **1995**, *381*, 243–250.
39. A. Belhouari, B. Keita, L. Nadjo et al., *New J. Chem.* **1998**, 83–86.
40. B. Keita, K. Essaadi, L. Nadjo, *J. Electroanal. Chem.* **1989**, *259*, 127.
41. B. Keita, D. Bouaziz, L. Nadjo, *J. Electroanal. Chem.* **1988**, *255*, 303.
42. G. M. Kloster, F. C. Anson, *Electrochim. Acta* **1999**, *44*, 2271–2279.
43. S. Vilakaszi, T. Nyokong, *Polyhedron* **2000**, *19*, 229–234.
44. J. H. Pei, X. Y. Li, *Talanta* **2000**, *51*, 1107–1115.
45. X. C. He, J. Y. Mo, *Analyst* **2000**, *125*, 793–795.
46. K. K. Hansen, E. M. Skou, H. Christensen, *J. Electrochem. Soc.* **2000**, *147*, 2007–2012.
47. T. Hibino, T. Inoue, M. Sano, *Solid State Ionics* **2000**, *130*, 19–29.
48. S. Shanmugam, B. Viswanathan, T. K. Varadarajan, *Indian J. Chem. Sect. A* **2005**, *44A*, 994–1000.
49. S. Liu, D. Volkmer, D. G. Kurth, *Anal. Chem.* **2004**, *76*, 4579–4582.
50. M. Huang, L. H. Bi, Y. Shen et al., *J. Phys. Chem. B* **2004**, *108*, 9780–9786.
51. W. Li, L. Li, Z. Wang et al., *J. Zhao Mater. Lett.* **2001**, *49*, 228–234.
52. B. Keita, I. M. Mbomekalle, L. Nadjo et al., *C. R. Chim.* **2005**, *8*(6–7), 1057–1066.
53. B. Keita, E. Abdeljalil, L. Nadjo et al., *Electrochem. Commun.* **2001**, *3*, 56–62.
54. B. Keita, I. M. Mbomekalle, L. Nadjo, *Electrochem. Commun.* **2003**, *5*, 830.
55. B. Keita, I. M. Mbomekalle, Y. W. Lu et al., *Eur. J. Inorg. Chem.* **2004**, 3462.
56. L.-H. Bi, U. Kortz, S. Nellutla et al., *Inorg. Chem.* **2005**, *44*, 896.
57. D. Jabbour, B. Keita, I. M. Mbomekalle et al., *Eur. J. Inorg. Chem.* **2004**, 2036.
58. D. Jabbour, B. Keita, L. Nadjo et al., *Electrochem. Commun.* **2005**, *7*, 841–847.
59. S. Nellutla, J. van Tol, N. S. Dalal et al., *Inorg. Chem.* **2005**, *44*, 9795–9806.
60. A. A. Tanaka, C. Fierro, D. Scherson et al., *J. Phys. Chem.* **1987**, *91*, 3799–3807.

61. K. V. Ramesh, A. K. Shukla, *J. Power Sources* **1987**, *19*, 279–285.
62. M. C. Pham, J. E. Dubois, *J. Electroanal. Chem.* **1986**, *199*, 153–164.
63. G. Kokkinidis, D. Sazou, *J. Electroanal. Chem.* **1986**, *199*, 165–176.
64. J. O. M. Bockris, J. McHardy, *J. Electrochem. Soc.* **1973**, *120*, 61–66.
65. G. Couturier, D. W. Kirk, P. J. Hyde et al., *Electrochim. Acta* **1987**, *32*, 995–1005.
66. C. Degrand, *J. Electroanal. Chem.* **1984**, *169*, 259–268.
67. J. A. Cox, R. K. Jaworski, *J. Electroanal. Chem.* **1990**, *281*, 163–170.
68. S. M. Sayed, K. Juttner, *Electrochim. Acta* **1983**, *28*, 1635–1641.
69. H. Y. Liu, I. Abdalmuhdi, C. K. Chang et al., *J. Phys. Chem.* **1985**, *89*, 665–670.
70. J. P. Collman, K. Kim, C. R. Leidner, *Inorg. Chem.* **1987**, *26*, 1152–1157.
71. J. P. Collman, R. Schwenninger, M. Rapta et al., *J. Chem. Soc. Chem. Commun.* **1999**, 137–138.
72. J. Ouyang, K. Shigehara, A. Yamada et al., *J. Electroanal. Chem.* **1991**, *297*, 489–498.
73. K. Juttner, *Electrochim. Acta* **1984**, *29*, 1597–1604.
74. S. Holdcroft, L. Funt, *J. Electroanal. Chem.* **1987**, *225*, 177–186.
75. A. Bettelheim, B. A. White, R. W. Murray, *J. Electroanal. Chem.* **1987**, *217*, 271–286.
76. M. D. Spasojevic, N. V. Krstajic, M. M. Jaksic, *J. Mol. Catal.* **1987**, *40*, 311–326.
77. S. Trasatti, *Electrochim. Acta* **2000**, *45*, 2377–2385.
78. J. Prakash, H. Joachin, *Electrochim. Acta* **2000**, *45*, 2289–2296.
79. N. Alonso Vante, P. Bogdanoff, H. Tributsh, *J. Catal.* **2000**, *190*, 240–246.
80. S. Cattarin, I. Frateur, P. Guerriero et al., *Electrochim. Acta* **2000**, *45*, 2279–2288.
81. H. N. Cong, K. El Abbassi, P. Chartier, *Electrochem. Solid State lett.* **2000**, *3*, 192–195.
82. D. G. Shchukin, D. V. Sviridov, *Electrochem. Commun.* **2002**, *4*, 402–405.
83. D. Martel, A. Kuhn, *Electrochim. Acta* **2000**, *45*, 1829–1836.
84. S. Gaspar, L. Muresan, A. Patrut et al., *Anal. Chim. Acta* **1999**, *385*, 111–117.
85. L. Gurban, A. Tézé, G. Hervé, *C. R. Acad. Sci. Paris, Serie IIc.* **1998**, *1*, 397–403.
86. S. G. Roscoe, B. E. Conway, *J. Electroanal. Chem.* **1987**, *224*, 163–188.
87. S. Dong, L. Cheng, X. Zhang, *Electrochim. Acta* **1998**, *43*, 563–568.
88. L. Cheng, J. A. Cox, *Chem. Mater.* **2002**, *14*, 6–8.
89. K. Shimazu, D. Weisshaar, T. Kuwana, *J. Electroanal. Chem.* **1987**, *223*, 223–234.
90. D. E. Bartak, B. Kazee, K. Shimazu et al., *Anal. Chem.* **1986**, *58*, 2756–2761.
91. D. E. Brown, M. N. Mahmood, M. C. M. Man et al., *Electrochim. Acta* **1984**, *29*, 1551–1556.
92. C. C. Hu, C. Y. Weng, *J. Appl. Electrochem.* **2000**, *30*, 499–506.
93. Y. Matsuzaki, I. Yasuda, *J. Electrochem. Soc.* **2000**, *147*, 1630–1635.
94. S. Meshitsuka, M. Ichikawa, K. Tamaru, *J. Chem. Soc. Chem. Commun.* **1974**, 158–159.
95. S. Kapusta, N. Hackerman, *J. Electrochem. Soc.* **1984**, *131*, 1511–1514.
96. M. Koudelka, A. Monnier, J. Augustynski, *J. Electrochem. Soc.* **1984**, *131*, 745–750.
97. Y. Hori, A. Murata, S. Y. Ito et al., *Chem. Lett.* **1989**, 1567–1570.
98. G. Arai, T. Harashina, I. Yasumori, *Chem. Lett.* **1989**, 1215–1218.
99. A. Bandi, *J. Electrochem. Soc.* **1990**, *137*, 2157–2160.
100. N. Furuya, K. Matsui, *J. Electroanal. Chem.* **1989**, *271*, 181–191.
101. M. Watanabe, M. Shibata, A. Katoh et al., *J. Electroanal. Chem.* **1991**, *305*, 319–328.
102. M. Watanabe, M. Shibata, A. Katoh et al., *Denki Kagaku (English)* **1991**, *59*, 508–516.
103. T. Atoguchi, A. Aramata, A. Kazusaka et al., *Denki Kagaku (English)* **1991**, *59*, 526–527.
104. S. Daniele, P. Ugo, G. Bontempelli et al., *J. Electroanal. Chem.* **1987**, *219*, 259–271.
105. M. L. Marcos, J. M. Vara, J. Gonzalez-Velasco et al., *J. Electroanal. Chem.* **1987**, *224*, 189–198.
106. C. deAlwis, J. A. Crayston, T. Cromie et al., *Electrochim. Acta* **2000**, *45*, 2061–2074.
107. S. Ikeda, A. Hattori, M. Maeda et al., *Electrochemistry* **2000**, *68*, 257–261.
108. A. S. Arico, E. Modica, I. Ferrara et al., *J. Applied Electrochemistry* **1998**, *28*, 881–887.
109. W. B. Kim, T. Voitl, G. J. Rodriguez-Rivera et al., *Angewandte Chemie Int. Ed.* **2005**, *44*, 778–782.
110. J. P. Collman, M. Rapta, M. Bröring et al., *J. Am. Chem. Soc.* **1999**, *121*, 1387–1388.

111. J. P. Collman, P. Denisevich, Y. Konai et al., *J. Am. Chem. Soc.* **1980**, *102*, 6027–6036.
112. J. P. Collman, C. S. Bencosme, R. R. Durand Jr. et al., *J. Am. Chem. Soc.* **1983**, *105*, 2699–2703.
113. R. R. Durand Jr., C. S. Bencosme, J. P. Collman et al., *J. Am. Chem. Soc.* **1983**, *105*, 2710–2718.
114. C. L. Ni, I. Abdalmuhdi, C. K. Chang et al., *J. Phys. Chem.* **1987**, *91*, 1158–1166.
115. C. Shi, F. C. Anson, *Inorg. Chem.* **1990**, *29*, 4298–4305.
116. C. Shi, F. C. Anson, *J. Am. Chem. Soc.* **1991**, *113*, 9564–9570.
117. C. Kang, Y. Xie, F. C. Anson, *J. Electroanal. Chem.* **1996**, *413*, 165–174.
118. L.-H. Bi, U. Kortz, B. Keita et al., *Eur. J. Inorg. Chem.* **2005**, *15*, 3034–3041.
119. B. Keita, J. P. Hauessler, L. Nadjo, *J. Electroanal. Chem.* **1988**, *243*, 481–491.
120. W. I. Albery, A. R. Hillman, *Annu. Rep. C, 1981*, The Royal Society of Chemistry, London, 1983, pp. 377–437.
121. S. Trasatti, *Electrochim. Acta* **1984**, *29*, 1503–1512.
122. S. Trasatti, *Electrochim. Acta* **1991**, *36*, 225–241.
123. S. Trasatti, in *Advances in Electrochemical Science and Engineering*, (Eds.: H. Gerisher, C. W. Tobias), VCH, Weinheim, 1992, pp. 1–85.
124. C. P. De Pauli, S. Trasatti, *J. Electroanal. Chem.* **1995**, *396*, 161–168.
125. B. Keita, L. Nadjo, *J. Electroanal. Chem.* **1985**, *191*, 441–448.
126. L. Nadjo, B. Keita, Nouvelles électrodes activées à l'aide d'hétéropolyacides, leur préparation et leur application, French Patent n 84 180 94 (CNRS) 1984.
127. L. Nadjo, B. Keita, Electrodes activated with heteropoly acids, notably as cahtodes for water electrolysis in acidic media, Eur. Pat. Appl. N° 85 402 340.5; *Chem. Abstr.* **1986**, *106*, 75016.
128. L. Nadjo, B. Keita, Procédé d'électrolyse de l'eau en milieu alcalin utilisant des électrodes activées à l'aide des acides tungstique, molybdique ou vanadique, ou des isopolyacides ou hétéropolyacides correspondants et obtention de telles électrodes, French Patent n° 87 10820 (CNRS).
129. B. Keita, L. Nadjo, *J. Electroanal. Chem.* **1986**, *199*, 229–237.
130. B. Keita, J. P. Haeussler, L. Nadjo, *J. Electroanal. Chem.* **1987**, *230*, 85–97.
131. B. Keita, L. Nadjo, *J. Electroanal. Chem.* **1987**, *227*, 265–270.
132. B. Keita, L. Nadjo, G. Krier et al., *J. Electroanal. Chem.* **1987**, *223*, 287–294.
133. B. Keita, L. Nadjo, *J. Electroanal. Chem.* **1988**, *243*, 87–103.
134. B. Keita, L. Nadjo, J. M. Saveant, *J. Electroanal. Chem.* **1988**, *243*, 105–116.
135. B. Keita, L. Nadjo, *J. Electroanal. Chem.* **1988**, *247*, 157–172.
136. B. Keita, L. Nadjo, R. Parsons, *J. Electroanal. Chem.* **1989**, *258*, 207–218.
137. B. Keita, L. Nadjo, *Mater. Chem. Phys.* **1989**, *22*, 77–103.
138. B. Keita, L. Nadjo, *J. Electroanal. Chem.* **1989**, *269*, 447–453.
139. B. Keita, L. Nadjo, *J. Electroanal. Chem.* **1990**, *287*, 149–157.
140. B. Keita, D. Bouaziz, L. Nadjo, *J. Electroanal. Chem.* **1990**, *296*, 275–282.
141. B. Keita, D. Bouaziz, L. Nadjo, *Electroanalysis* **1991**, *3*, 637–646.
142. A. Mahmoud, B. Keita, L. Nadjo et al., *J. Electroanal. Chem.* **1999**, *463*, 129–145.
143. B. Keita, D. Bouaziz, L. Nadjo, *J. Electroanal. Chem.* **1990**, *284*, 431–444.
144. P. J. Kulesza, L. R. Faulkner, *J. Am. Chem. Soc.* **1988**, *110*, 4905–4913.
145. P. J. Kulesza, L. R. Faulkner, *J. Electrochem. Soc.* **1989**, *136*, 707–713.
146. W. H. Kao, T. Kuwana, *J. Am. Chem. Soc.* **1984**, *106*, 473–476.
147. Z. Chen, Z. Pourabedi, D. B. Hibbert, *Electroanalysis* **1999**, *11*, 964–968.
148. J. A. Cox, M. E. Tess, T. E. Cummings, *Rev. Anal. Chem.* **1996**, *15*, 173–223.
149. D. Mandler, I. Turyan, *Electroanalysis* **1996**, *8*, 207–213.
150. A. Walcarius, *Electroanalysis* **1996**, *8*, 971–986.
151. A. Walcarius, *Electroanalysis* **1998**, *10*, 1217–1235.
152. A. Walcarius, *Anal. Chim. Acta* **1999**, *384*, 1–16.
153. S. M. Macha, A. Fitch, *Mikrochim. Acta* **1998**, *128*, 1–18.
154. P. K. Ghosh, A. J. Bard, *J. Am. Chem. Soc.* **1983**, *105*, 5691–5693.
155. B. Keita, N. Dellero, L. Nadjo, *J. Electroanal. Chem.* **1991**, *302*, 47–57.
156. B. Keita, A. Belhouari, L. Nadjo, *J. Electroanal. Chem.* **1991**, *314*, 345–352.

157. B. Keita, A. Belhouari, L. Nadjo, *J. Electroanal. Chem.* **1993**, *355*, 235–251.
158. P. N. Deepa, M. Kanugo, G. Claycomb et al., *Anal. Chem.* **2003**, *75–20*, 5399–5405.
159. J. Brinker, G. Scherer, *Sol-Gel Science*, Academic Press, New York, 1989.
160. K. Flora, J. D. Brennan, *Anal. Chem.* **1998**, *70*, 4505.
161. L. L. Hench, J. K. West, *Chem. Rev.* **1990**, *90*, 33.
162. J. D. Jordan, R. A. Dunbar, D. J. Hook et al., *Chem. Mater.* **1998**, *10*, 1041–1051.
163. R. Shacham, D. Avnir, D. Mandler, *Adv. Mater.* **1999**, *11*, 384–388.
164. J. A. Cox, K. S. Alber, *J. Electrochem. Soc.* **1996**, *143*, 126.
165. M. E. Tess, J. A. Cox, *Anal. Chem.* **1998**, *70*, 187.
166. M. Tatsumisago, T. Minami, *J. Am. Ceram. Soc.* **1989**, *72*, 484.
167. O. Lev, M. Tsionsky, L. Rabinovich et al., *Anal. Chem.* **1995**, *67*, 22–30.
168. D. Avnir, *Acc. Chem. Res.* **1995**, *28*, 328.
169. E. Wang, K.-F. Chow, V. Kwan et al., *Anal. Chim. Acta* **2003**, *495*, 45–50.
170. O. A. Kholdeeva, M. P. Vanina, M. N. Timofeeva et al., *J. Catal.* **2004**, *226*, 363–371.
171. M. M. Collinson, B. Narok, S. A. Martin et al., *Anal. Chem.* **2000**, *72*, 2914.
172. M. Sykora, K. A. Maxwell, T. J. Meyer, *Inorg. Chem.* **1999**, *38*, 3596.
173. M. M. Collinson, J. S. Taussing, S. A. Martin, *Chem. Mater.* **1999**, *11*, 2594.
174. X. Wang, Z. Kang, E. Wang et al., *J. Electroanal. Chem.* **2002**, *523*, 142–149.
175. J. Liu, A. C. Co, S. Paulson et al., *Solid State Ionics* **2006**, *177*, 377–387.
176. W. Gorski, C. A. Aspinwall, J. R. T. Lakey et al., *J. Electroanal. Chem.* **1997**, *425*, 191.
177. J. Wang, X. Zhang, *Anal. Chem.* **2001**, *73*, 844.
178. M. Pikulski, W. Gorski, *Anal. Chem.* **2000**, *72*, 2696.
179. A. Salimi, R. Hallaj, M. Ghadermazi, *Talanta* **2005**, *65*, 888–894.
180. W. S. Cardoso, Y. Gushikem, *J. Electroanal. Chem.* **2005**, *583*, 300–306.
181. M. S. P. Francisco, W. S. Cardoso, Y. Gushikem, *J. Electroanal. Chem.* **2005**, *574*, 291–297.
182. Q. Wang, G. Lu, B. Yang, *Sens. Actuators, B: Chem.* **2004**, *B99*(1), 50–57.
183. G. Decher, *Science* **1997**, *277*, 1232.
184. G. Decher, Y. Lvov, *J. Schmitt. Thin Solid Films* **1994**, *244*, 985.
185. Y. Lvov, G. Decher, H. Möhwald, *Langmuir* **1993**, *9*, 481.
186. G. Decher, J. D. Hong, *Macromol. Chem. Macromol. Symp.* **1991**, *46*, 321.
187. L.-H. Bi, Y. Shen, J. Jiang et al., *Anal. Chim. Acta* **2005**, *534*, 343–351.
188. J. Liu, L. Cheng, B. Liu et al., *Langmuir* **2000**, *16*, 7471–7476.
189. M. Jiang, E. B. Wang, X. Wang et al., *Appl. Surf. Sci.* **2005**, *242*, 199–206.
190. H. Ma, J. Peng, Z. Han et al., *Thin Solid Films* **2004**, *446*, 161–166.
191. M. Jiang, E. B. Wang, L. Xu et al., *J. Solid State Chem.* **2004**, *177*, 1776–1779.
192. M. Jiang, E. B. Wang, G. Wei et al., *J. Colloid Interface Sci.* **2004**, *275*, 596–600.
193. S. Liu, D. G. Kurth, D. Volkmer, *Chem. Commun.* **2002**, 976–977.
194. M. Huang, L. H. Bi, Y. Shen et al., *J. Phys. Chem. B* **2004**, *108*, 9780–9786.
195. L. Bi, H. Wang, Y. Shen et al., *Electrochem. Commun.* **2003**, *5*, 913–918.
196. S. Zhai, J. Liu, J. Jiang et al., *Electroanalysis* **2003**, *15*, 1165–1170.
197. K. Karnicha, M. Chojak, K. Miecznikowski et al., *Bioelectrochem* **2005**, *66*, 79–87.
198. S. Zhai, S. Gong, J. Jiang et al., *Anal. Chim. Acta* **2003**, *486*, 85–92.
199. M. Huang, Y. Shen, W. Cheng et al., *Anal. Chim. Acta* **2005**, *535*, 15–22.
200. G. E. Pacey, S. D. Puckett, L. Cheng et al., *Anal. Chim. Acta* **2005**, *533*, 135–139.
201. M. E. Napier, H. H. Thorp, *J. Fluoresc.* **1999**, *9*, 181.

11
Redox-active Dendrimers in Solution and as Films on Surfaces

Kazutake Takada
Nagoya Institute of Technology, Graduate School of Engineering, Gokiso, Showor, Nagoya, Japan

Jonas I. Goldsmith
Department of Chemistry, Bryn Mawr College, Bryn Mawr, PA, USA

Stefan Bernhard
Department of Chemistry, Frick Laboratory, Princeton University, Princeton, NY, USA

Héctor D. Abruña
Department of Chemistry and Chemical Biology, Baker Laboratory, Cornell University, Ithaca, NY, USA

11.1 Introduction **731**
11.1.1 Dendrimer Properties and Applications 733
11.1.2 Redox-active Dendrimers 733

11.2 Dendrimers with Electroactive Moieties in the Core **734**
11.2.1 Dendrimers with Cores Containing Transition Metal or Organometallic Complexes 734
11.2.2 Dendrimers with Cores Containing Electroactive Organic Species . . 737

11.3 Dendrimers with Electroactive Moieties in the Branches and Throughout the Molecule **737**
11.3.1 Dendrimers with Transition Metal Complexes in the Branches 738
11.3.2 Dendrimers with Organic Redox-active Moieties in the Branches . . . 740

11.4 Dendrimers with Redox-active Moieties at Periphery **741**
11.4.1 Ferrocenyl-modified Dendrimers 741
11.4.1.1 Silicon-based Dendrimers 741
11.4.1.2 Poly(propylenimine) Dendrimers 742
11.4.1.3 Poly(aryl ether)-based Dendrimers 743

Encyclopedia of Electrochemistry. Edited by A.J. Bard and M. Stratmann
Vol. 10 *Modified Electrodes*. Edited by M.Fujihira, I.Rubinstein, and J.F.Rusling
Copyright © 2007 Wiley-VCH Verlag GmbH & Co. KGaA, Weinheim. ISBN: 978-3-527-30402-8

11.4.1.4 Other Ferrocenyl-modified Dendrimers 744
11.4.2 Cobaltocenyl Dendrimers 744
11.4.3 Ferrocenyl- and Cobaltocenyl-containing Dendrimers 744
11.4.4 Ruthenium Terpyridyl and Bipyridyl Dendrimers 745
11.4.5 Cobalt Terpyridyl Dendrimers 746
11.4.6 Iron Terpyridyl Dendrimers 746
11.4.7 Tetrathiafulvalenyl Dendrimers 747
11.4.8 Viologenyl Dendrimers 748

11.5 Applications 748
11.5.1 Light Harvesting 748
11.5.2 Catalysis 748
11.5.3 Organic LEDs 749
11.5.4 Oxygen Carriers 749
11.5.5 Molecule-sized Gates 749
11.5.6 Molecular Recognition 750
11.5.7 Mediators 751
11.5.8 Biosensors 751
References 751

11.1 Introduction

There has been, and continues to be, a widespread interest in the preparation and characterization of a novel class of molecules called *dendrimers*, in part, as a result of their potential materials and pharmaceutical applications [1, 2]. These molecules are a specific form of highly branched globular molecules, consisting of a core, self-replicating branching units and peripheral surface groups (Fig. 1). There are currently two synthetic strategies for the preparation of dendrimers: the divergent and convergent approaches. A divergent dendrimer synthesis [3–8] starts with a branched core molecule with multiple reaction sites. The initial synthetic steps proceed through branching reactions to prepare a molecule with more reactive sites than the initial core molecule (first-generation dendrimer). The repetition of this synthetic pattern results in an (often geometric) increase in the number of reactive sites with each step (higher generations). A final step in the divergent synthetic approach often involves the modification of the outermost reactive sites with chemically active or inert groups, for the purpose of deliberately designing the dendrimer with specific physical and chemical properties and functionalities (Fig. 2).

The convergent synthesis [9–12], on the other hand, starts from these latter surface groups, with the dendrimer being built from the periphery toward a central core. After the initial reaction of multiple surface groups with a branching unit, the resulting moiety is then transformed into a molecule that is capable of reacting with another branching unit. After successive repetitions of this reaction scheme, several of the resulting molecules (i.e. wedges), having reached the desired size, are connected to a suitable core to yield the targeted dendrimer (Fig. 3). During a convergent synthetic procedure, it is easier to purify the reaction products, since there are, compared to a divergent synthetic approach, only a small number of reacting sites involved in each step.

Since the development of modern ionization techniques (i.e. matrix assisted laser desorption ionization, MALDI [13–15] and electrospray [16–18]), mass spectrometry (MS) has proven to be one of the foremost tools for the characterization of numerous dendrimers. Gel permeation chromatography (GPC) has been successfully and widely applied to the characterization of the molecular weight and polydispersity of these dendrimer molecules [19]. Furthermore, a great deal of information about the structural impurities and defects in dendrimers has

Encyclopedia of Electrochemistry. Edited by A.J. Bard and M. Stratmann
Vol. 10 *Modified Electrodes*. Edited by M.Fujihira, I.Rubinstein, and J.F.Rusling
Copyright © 2007 Wiley-VCH Verlag GmbH & Co. KGaA, Weinheim. ISBN: 978-3-527-30402-8

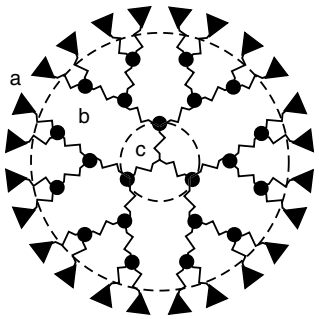


Fig. 1 The topology of a dendrimer with the three structural units (a) surface groups, (b) self-replicating branching units, and (c) core.

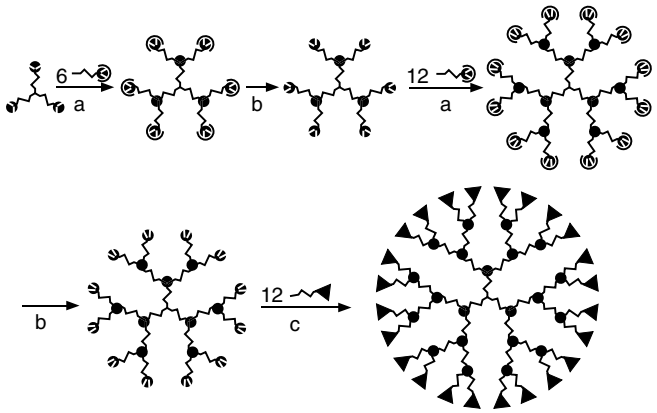


Fig. 2 Strategy for a divergent second-generation dendrimer synthesis with two repetitive steps ((a) branching reaction, (b) activation reaction) and (c) a surface modification reaction.

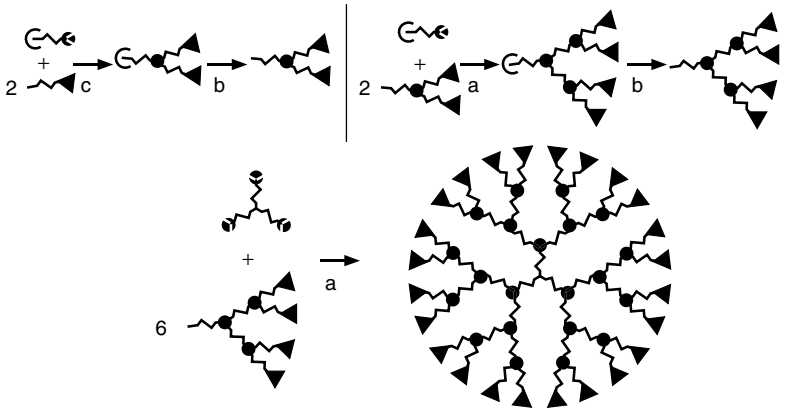


Fig. 3 The convergent synthetic approach for second-generation dendrimers: the initial modification of a branched oligomer with (c) prospective surface groups, and (b) after a series of activation and (a) branching steps, a last branching reaction with a suitable core yields the final product (bottom).

been garnered through the application of nuclear magnetic resonance (NMR) spectroscopy studies employing various nuclei with emphasis on ^{1}H, ^{13}C, ^{14}N, ^{19}F, ^{31}P, ^{29}Si [7, 20–23].

11.1.1 Dendrimer Properties and Applications

The physical and chemical properties of dendrimers are controlled by the three structural moieties (core, branching units, and surface groups) of which they are composed. A multitude of surface groups have been used to modify the periphery of dendrimers for the purpose of giving them tailored characteristics for applications as catalysts, light-harvesting devices [24–26], and magnetic resonance imaging (MRI) [27–29] contrast agents among others. Another major area of current interest in dendrimers involves the study of the encapsulation properties of the higher-generation dendrimers toward smaller molecules. The driving force behind these studies is the possibility of dissolving hydrophobic drug molecules in an aqueous environment for prospective pharmaceutical drug delivery applications [30–32]. Host–guest interactions and exchange kinetics of these clathrates have been studied with NMR, UV–visible, emission, and electron paramagnetic resonance (EPR) spectroscopies. Alternatively, encapsulated guest molecules can also become permanently confined inside a ''dendritic box'' by modifying the surface of the dendrimer with sterically demanding groups.

11.1.2 Redox-active Dendrimers

To the authors' knowledge, the earliest example of a dendrimer containing redox-active groups was published by Balzani and coworkers [33], in which they used the complexation reaction of Ru(II) and Os(II) with bridging ligands to build dendrimers with up to 22 metal centers, for the purpose of preparing light-harvesting supramolecular structures. Later on, dendrimers with surface ferrocenyl groups were synthesized and characterized electrochemically, with the intent of preparing multielectron reservoirs [34]. In recent years, a multitude of dendrimers containing a variety of redox centers (organic, organometallic, coordination complexes) have been prepared, electrochemically characterized, and employed for various applications. For the deliberate design of dendrimers with specific, desired attributes, redox centers have been localized in the dendrimer core, the branching units, or on the dendrimer surface (Fig. 4).

The main objective behind the electrochemical studies on dendrimers with redox-active cores is to understand the electron-transfer mechanisms through the surrounding dendrimer branches. Dendrimers with either transition metal complexes or purely organic cores as well as dendrimers with purely organic center units have been prepared and characterized. As mentioned above, dendrimers have also been prepared through the formation of coordination bonds with redox centers distributed throughout the dendrimer (core, branching units, surface groups). Other studies involved the preparation of molecules by functionalizing an organic core with electroactive moieties and then subsequently capping the electroactive branches with inert surface groups.

Dendrimers prepared with redox-active groups at the surface, on the other hand, enabled the investigation of intramolecular charge-transfer mechanisms between these groups. This family of dendrimers is unique with regard to its ability to

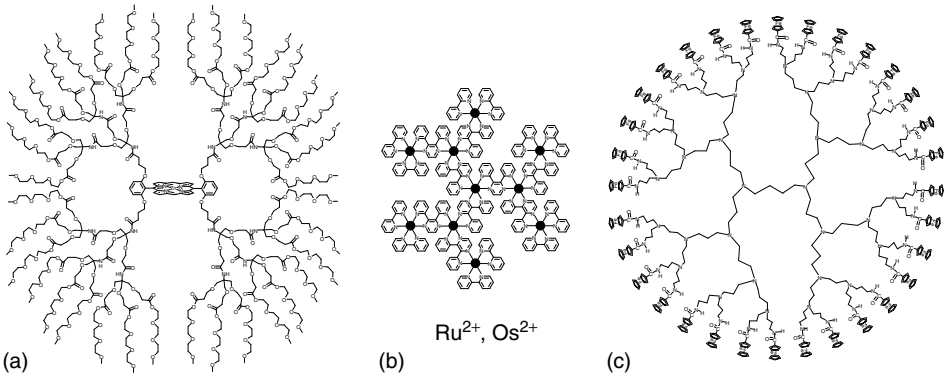


Fig. 4 Examples of three different of redox-active dendrimers: (a) redox-active core, (b) electrochemically active branching units, and (c) redox-active peripheral groups.

undergo electrochemical reactions with up to 128 electrons per molecule. Their preparation builds upon purely organic dendrimers, some of which are the commercially available starburst™ dendrimers (poly(amidoamine), PAMAM), by attaching redox-active groups to the periphery.

11.2 Dendrimers with Electroactive Moieties in the Core

There has been considerable investigation of dendritic species with redox-active moieties placed at the center of the molecule. Various metal-polypyridyl complexes, as well as porphyrins and phthalocyanines, have been used as cores around which dendrimers have been built. Dendritic molecules with metallocenes at or near the core and dendrimers with central metal clusters have also been synthesized. In addition to metal complexes, electroactive organic moieties have been placed at the cores of various types of dendrimers. The rate of electron transfer between redox-active species and a working electrode, and its relative kinetic facility, are necessarily affected by the distance between them. A molecule in close contact with an electrode surface will generally transfer electrons more readily than the same species at a longer distance. One might then anticipate that placing a dendritic shell around the redox site of interest will result in a diminution of the rate of electron transfer, and that is indeed borne out in numerous experimental examples. While many of the examples that follow do not specifically involve species immobilized on electrode surfaces, it is, nevertheless, instructive to understand the behavior of these complex molecules in solution.

11.2.1 Dendrimers with Cores Containing Transition Metal or Organometallic Complexes

Kaifer and coworkers have synthesized hyperbranched molecules of various sizes that contain a single ferrocene asymmetrically located near the dendrimer core [35–37]. The redox properties of these materials were investigated and, as would be expected, both the diffusion coefficients of the dendrimers as well as

their electron-transfer rate constants were found to decrease with increasing molecular size. Also, the value of the formal potential, $E^{\circ\prime}$, for ferrocene oxidation was observed to shift in the negative direction with increasing dendrimer size; $E^{\circ\prime} = +0.63$ V versus Ag/AgCl for the molecule with MW = 628 and $E^{\circ\prime} = +0.54$ V versus Ag/AgCl for the compound with MW = 4725. This indicates that the interior of the dendrimer stabilizes and is favorable for the development of positive charges [35]. Dendrimers with oligo-ether chains branching off a central ferrocene were synthesized by Smith and used as redox probes to investigate the characteristics of the dendritic interior. No significant shifts in $E^{\circ\prime}$ were seen as a function of dendrimer generation, indicating that, in this case, the ferrocene redox couple is not sensitive to changes in environment caused by the oligo-ether branches [38].

Three generations of dendritic molecules constructed around an Fe(II) bis-terpyridine core were synthesized by Chow et al., and it was found that the Fe(II/III) redox process became more (electrochemically) irreversible as the generation of the dendrimer increased [39]. Ruthenium bis-terpyridine ($[Ru(tpy)_2]^{+2}$) [40] and ruthenium tris-bipyridine ($[Ru(bpy)_3]^{+2}$) moieties [41, 42] have also been used as central anchor points around which hyperbranched macromolecules may be created. In studies of the $[Ru(bpy)_3]^{+2}$-containing compounds, the metal-localized oxidation process (Ru(II/III)) became more electrochemically irreversible as the size of the dendritic sheath increased [42].

Using a copper phenanthroline complex as a core, Armaroli et al. synthesized a dendritic compound with fullerene-functionalized branches. Electrochemical studies showed that there was no electronic communication between the copper core and the fullerenes, that the dendritic branches hindered electron transfer, and that the larger generations of dendrimers showed irreversible redox behavior [43].

Gorman and coworkers have prepared five generations of dendrimers with cores composed of iron–sulfur clusters and with dendritic branches of varying flexibility [44, 45]. Electrochemical measurements were carried out to determine diffusion coefficients as well as heterogeneous electron-transfer rates. The rate of electron transfer decreased monotonically with increasing dendrimer size, and the rigid dendrimers exhibited a much larger attenuation of the rate of electron transfer than the flexible ones [45].

In an attempt to create biomimetic systems, there has been much research on designing dendritic molecules with porphyrins and similar molecules at their cores. Diederich et al. have synthesized dendrimers with iron and zinc-porphyrin cores in an effort to model heme and cytochrome *c* systems [46–49]. In these cases, the redox reactions occurring at the center of the molecule were found to be affected by the nature of the dendritic foliage. The porphyrin-centered (the Zn(II) is not electroactive) first oxidation in the zinc-containing dendrimers shifts from +1.08 V versus SCE for zinc-tetraphenylporphyrin to +0.65 V for the largest zinc-porphyrin dendrimer (compare to the results of Kaifer [35] above). However, for the iron porphyrin dendrimers, the Fe(II/III) redox couple shifts from −0.23 V versus SCE for the smaller dendrimer to +0.19 V for the larger one [48]. In a different set of experiments, Diederich and coworkers demonstrated that increasing the amount

of dendritic material around the zinc-porphyrin core led to an irreversible electrochemical response from the dendrimers [46].

Dendrimers with zinc-porphyrin cores were also investigated by Fréchet and coworkers. Their results were similar to those of Diederich in that electron transfer became more difficult as the size of the dendrimer increased. However, they observed that the redox processes became more irreversible at somewhat smaller dendrimer sizes than in the experiments by Diederich et al. (Fig. 5). This variation has been attributed to differences in the nature of the specific dendritic branches utilized [50].

In addition to porphyrins, phthalocyanines have been placed in the middle of hyperbranched molecules. Cobalt phthalocyanines with dendritic branches have been synthesized, and the analysis of their electrochemical behavior suggests that electron transfer between the phthalocyanine core and an electrode is considerably hindered by the dendritic structure [51]. Dendrimers with phthalocyanine cores and electroactive tetrathiafulvalene (TTF) branches have also been synthesized and examined [52].

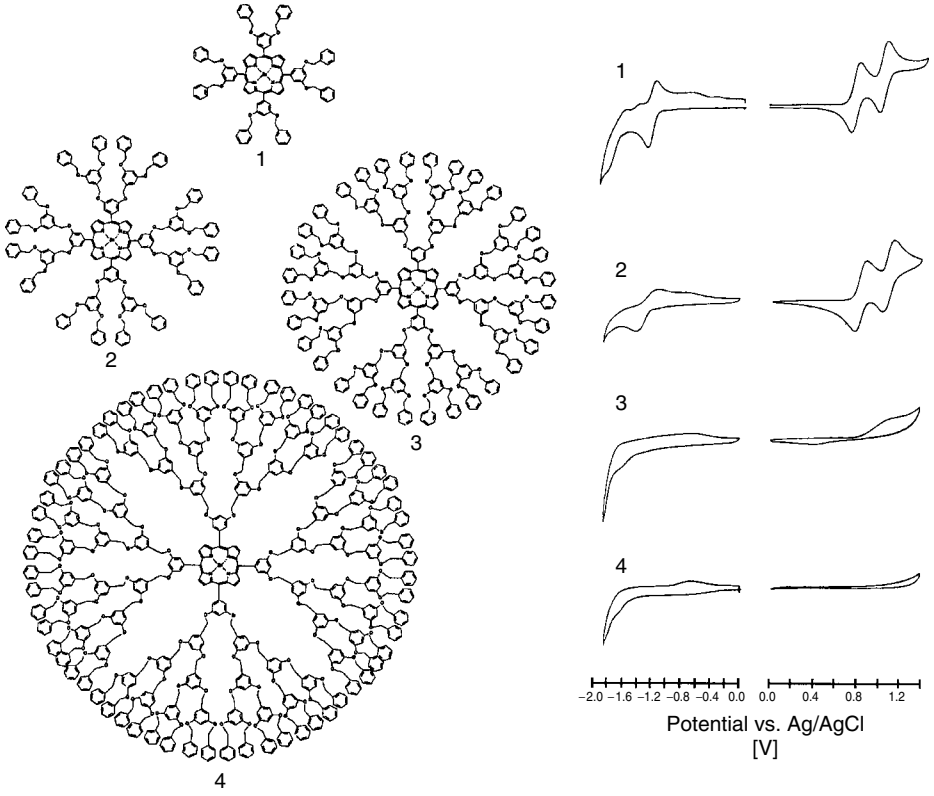


Fig. 5 Cyclic voltammograms of dendrimers with zinc porphyrin in (1–4) core in TBAP-supporting electrolyte solution at 100 mV s^{-1}. Positive scans were performed in a CH_2Cl_2 solution and negative scans were performed in DMF solution. From Ref. 50 with permission.

11.2.2
Dendrimers with Cores Containing Electroactive Organic Species

There has also been considerable effort invested in the study of dendrimers with cores composed of electrochemically active organic moieties. Conjugated oligothiophene chains of various sizes have been modified at their ends with poly(benzylether) dendrimers. The dendritic end groups appeared to stabilize the cation radical and the dication species formed from electrochemical oxidation, and irreversibility of the oxidation of the oligothiophene core was noted under circumstances where the dendritic end groups were large compared to the electroactive core [53]. A somewhat similar system of conjugated oligothienylenevinylenes with dendritic endcaps of various generations has been studied by Roncali and coworkers. In contrast to the previously mentioned result, they observed no kinetic limitation to the electron-transfer process between an electrode and the core of the dendrimer, even for the largest dendrimer endcaps. However, none of the compounds used in that study had enough dendritic structure to entirely surround the redox-active core [54]. This result suggests that the dendrimer can rotate rapidly in proximity to the electrode, allowing the redox-active core access to the electrode, which would lead to the observation of reversible electrochemistry.

Miller et al. used various oligoimides in conjunction with several generations of poly(benzylether) dendrons to synthesize ''molecular dumbells'', the largest of which extended 9.6 nm in length. The electrochemistry of the imide reduction was studied using cyclic voltammetry at scan rates up to $100\ V\ s^{-1}$, and it was found that the dendrimer did not affect the ease of electron transfer. This result, very different from the behavior of redox-cored dendrimers containing metal centers, might be attributable to the rigid nature of the oligoimide, which holds the dendrons fixed and far apart, allowing better access to the redox core [55].

Newkome et al. have synthesized several dendrimers which contain a core of four diaminoanthraquinone molecules tethered together. Dendritic branches grow from these redox centers, and various isomers of the anthraquinones (AQs) have been examined. There were differences noted in the electrochemical behavior for the various isomers of diaminoanthraquinone, and, as might be expected, the electrochemical response of the redox centers became more irreversible as the dendrimer became larger [56].

Fullerenes have been used as cores for redox dendrimers, and a system of fullerenes functionalized with poly(arylacetylene) dendritic branches has been studied. However, electrochemical experiments indicated no significant interaction between the dendrimers and the fullerene core [57].

11.3
Dendrimers with Electroactive Moieties in the Branches and Throughout the Molecule

Previously, dendrimers with electroactive sites at the core have been discussed, but it is also possible to locate the redox-active portions of a dendrimer in the ''branches'' of the molecule so that the redox sites are dispersed throughout the entire assembly. Metal-polypyridyl compounds have usually been placed throughout the framework of dendrimers, and a variety of

organic electroactive moieties have also been utilized.

11.3.1 Dendrimers with Transition Metal Complexes in the Branches

In 1992, Balzani and coworkers first synthesized a series of dendritic molecules based on ruthenium polypyridyl complexes. The use of bridging ligands allowed the synthesis of molecules with up to 22 redox-active species distributed throughout [33]. Dendrimers with more than one type of metal complex (e.g. 1 osmium at the core and 21 rutheniums surrounding it) have also been synthesized [58]. The electrochemical behavior of such systems is necessarily very complex, and it has been studied in some detail with a variety of techniques. For heterometallic compounds, it is possible to observe the oxidation of each type of metal center separately by differential pulse voltammetry [25]. For structures that contain a single transition metal type, the oxidation of the metal occurs at a potential that varies with its connectivity and location within the dendrimer framework [59]. The ligand-based reductions in these types of molecules exhibit very complex electrochemical responses with up to 26 reductions observed in one case. It was noted that the bridging ligands tended to be reduced at less negative potentials than the terminal ligands [60]. Further studies on a similar, six-ruthenium-containing, molecule utilizing electrochemical experiments in liquid SO_2 (which allows very positive potentials to be reached) allowed the observation of the sequential oxidation of the peripheral metal centers at +1.46 V versus SCE, the inner metal centers at +2.11 V, and the ligands at potentials higher than +3.0 V [61].

Using ruthenium bis-terpyridyl complexes, Constable and Harverson have synthesized an 18-ruthenium-containing dendrimer with six branches extending from a central benzene molecule. The electrochemical response observed was that of a single reversible wave for the Ru(II/III) oxidation, indicating that there was no electronic communication between metal centers [62]. Ruthenium bis-terpyridyl units were also used by Newkome and coworkers to form strong linkages within the branches of a dendritic molecule. The size of the dendrimer was noted to affect the reversibility of the Ru(II/III) couple; the more sterically hindered dendrimer exhibited a more irreversible behavior [63]. In a different set of experiments, varying the placement of the dendritic groups within each molecule was shown to have a significant effect on the electrochemical behavior of the metal centers. If the dendrons were placed at the periphery of the molecule, all Ru(II/III) oxidations occurred at the same potential. When the dendrons were placed toward the interior of the molecule, giving it some internal rigidity, two waves were observed by cyclic voltammetry for the Ru(II/III) process (Fig. 6), indicating the possibility of some communication between the redox centers [64].

Newkome and coworkers also examined a dendritic system in which bipyridine molecules, incorporated into the branches, were subsequently complexed to yield dendrimers containing ruthenium tris-bipyridyl moieties dangling from the dendritic arms. In the electrochemistry of these compounds, the metal centers, surrounded by a dendritic network, exhibited irreversible kinetic behavior, as is commonly found in such systems. On the other hand, there are three separately identifiable ligand-based reductions, each of the

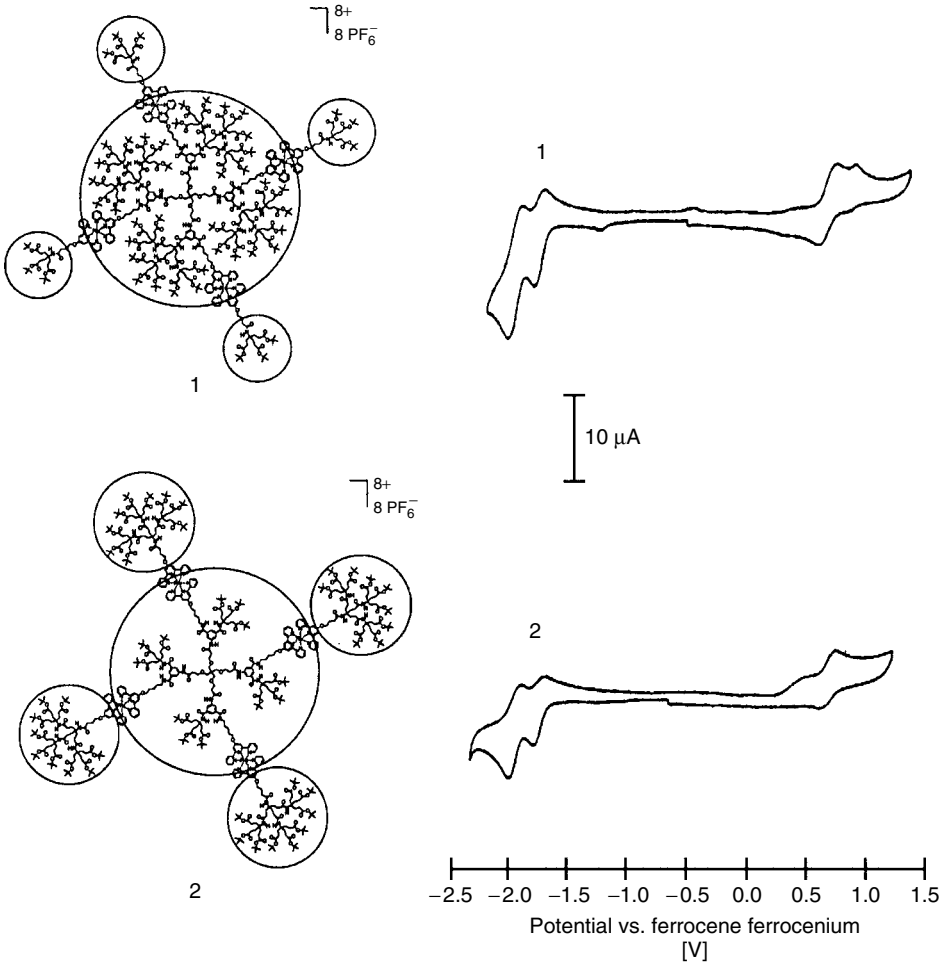


Fig. 6 Cyclic voltammograms of 1.0 mM solutions of dendrimers modified with ruthenium bis-terpyridyl in branches in a 0.1 M $TBABF_4$/AN solution at 200 mV s^{-1}. From Ref. 64 with permission.

three bipyridines being electrochemically unique [65].

Haga and coworkers examined the electrochemical response from a tetranuclear ruthenium polypyridine compound with a dendritic morphology, and using cyclic voltammetry, they were able to observe the central metal of the complex being oxidized at a potential about 150 mV less positive than that for the oxidation of the three surrounding metal complexes [66]. This result, the results from the electrochemical studies carried out in liquid SO_2 [61], and the two waves observed for Ru(II/III) in the dendrimers with more rigid internal structure [64] are especially interesting because examples of metallodendrimers where all the metal centers do not behave as one unit are rare.

11.3.2 Dendrimers with Organic Redox-active Moieties in the Branches

It is possible to place electrochemically active transition metal centers in the branches of the dendrimers, and many researchers have investigated dendritic macromolecules with organic redox-active moieties in the dendritic branches. Some of the redox-active organic species that have been incorporated include quinone and quinone-type compounds, TTF, fullerenes, and others. The wide variety of organic groups that can be used in such dendrimers makes this a growing area of investigation.

Bryce and coworkers have synthesized dendrimers that contain TTF units at the core, at each of the dendritic bifurcations, and at the end of each branch. The redox properties of these materials were studied using thin-layer cyclic voltammetry, and it was observed that all TTF units were oxidized simultaneously and completely giving, for the largest dendrimer, the +21 cation radical $(TTF^{\bullet+})_{21}$ and the +42 dication $(TTF^{+2})_{21}$ [67, 68]. An intradendrimer aggregation of the cation radical redox centers was observed during spectroelectrochemical studies of these compounds [68].

The redox properties of a macromolecule comprised of a fullerene core functionalized with a porphyrin and 10 dendritic branches of various lengths have been reported. The dendritic branches were found to affect not only the redox properties of the fullerene core but also the electrochemical behavior of the porphyrin; both the fullerene- and the porphyrin-based reductions shifted to more negative potentials as the size of the dendritic branches increased [69].

Armaroli et al. have designed a series of dendrimers, mentioned briefly in the preceding text, built around a phenanthroline core and functionalized with fullerene-containing branches. The largest macromolecule synthesized was a dendrimer with 16 fullerenes around the central core. Electrochemical studies of the fullerene reductions indicated that the first was electrochemically reversible, whereas the second was followed by a chemical reaction. It was also noted that, when a copper ion was complexed with the phenanthroline, the larger dendrimers entirely shielded it and completely prevented its oxidation [43].

Heinen and Walder have synthesized dendrimers in which the dendritic skeletons are composed of viologen units; the largest molecule contains 45 redox-active viologens. The dendrimers exhibit reversible electrochemical behavior, and, when neutral (i.e. doubly reduced), they adsorb onto the electrode surface. Intramolecular interactions, the degree of which increased with increasing dendrimer size, are evident between cation radicals on a single molecule [70].

An interesting dendrimer containing diarylamino groups at the periphery and phenylenediamine groups in the interior has been studied by Selby and Blackstock. The exterior arylamino moieties are more difficult to oxidize than the phenylenediamines, forming a redox gradient within the molecule. Electrochemical oxidation of the interior groups occurs in two steps: a one-electron step at +0.48 V versus SCE and a two-electron step at +0.63 V. Oxidation of all the diarylamino groups, which are not connected to each other, occurs at +0.88 V. The authors propose that this system could be used for charge storage; the oxidation of the interior would be promoted by the surrounding arylamino

functionalities, and the reduction of the oxidized interior would be hindered by them [71].

Newkome and coworkers have modified their diaminoanthraquinone-containing dendrimers [56] by incorporating a redox-active aromatic nitro-containing group into the internal structure of the dendrimer. These compounds were studied by cyclic voltammetry, and it was determined that the presence of the nitro group had a significant effect on the redox process of the AQ moiety, causing the peak potential of the AQ reduction to shift 100 mV in the positive direction [72].

11.4 Dendrimers with Redox-active Moieties at Periphery

The peripheral modification of dendrimers with redox-active moieties and their characterization have attracted much attention since such dendrimers could have potential applications as sensors, catalysts, and electron-transfer mediators. As mentioned in the introduction, if the redox-active moieties are incorporated at the core or within the backbone structure of the dendrimer, the electrochemical activity becomes lower for higher-generation dendrimers because of the longer distance between the redox-active site and an electrode. On the other hand, the modification of the dendrimer at its periphery with redox centers has advantages for practical applications, since one would anticipate a higher electron-transfer rate because of the shorter distance between the active sites and an electrode. In addition, higher charge transport rates can also be expected because of faster segmental motion and faster counterion transport, since the redox-active moieties are exposed to the solution.

In this section, the electrochemical properties of dendrimers peripherally modified with redox-active moieties and their applications will be reviewed.

11.4.1 Ferrocenyl-modified Dendrimers

11.4.1.1 Silicon-based Dendrimers

Ferrocenyl (-Fc) modified dendrimers have been the most intensively investigated redox-active dendrimers owing to their well-defined redox properties. Cuadrado and coworkers first reported the syntheses of four silicon-based dendrimers (G (generations) 0 and 1) functionalized with ferrocenyl residues at the periphery (two of them have −NH− in the backbone structure and the other two do not) [73]. Although detailed electrochemical studies were not carried out in this report, all the ferrocenyl sites underwent redox reaction at the same potential ($E^{\circ\prime} = +0.56$ (G0) and +0.55 V (G1) for dendrimers with −NH− and +0.40 (G0) and +0.44 V versus SCE (G1) for the dendrimers without −NH− group) in tetra-n-butylammonium hexafluorophosphate (TBAH)/CH_2Cl_2 solution. The detailed electrochemical properties of the two dendrimers without −NH− in the backbone structure were studied by cyclic voltammetry, differential pulse voltammetry, and bulk coulometry in CH_2Cl_2 solution containing the dendrimers [74]. The zero and first generations of the dendrimers, with four and eight ferrocenyl sites, respectively, also showed a simultaneous multielectron transfer at the same potential. Upon oxidation, the dendrimers deposited onto the electrode, resulting in their modification with a film of the dendrimer. The resulting films were found to be stable in acetonitrile as well as in aqueous electrolyte solution. The cyclic voltammogram exhibited small

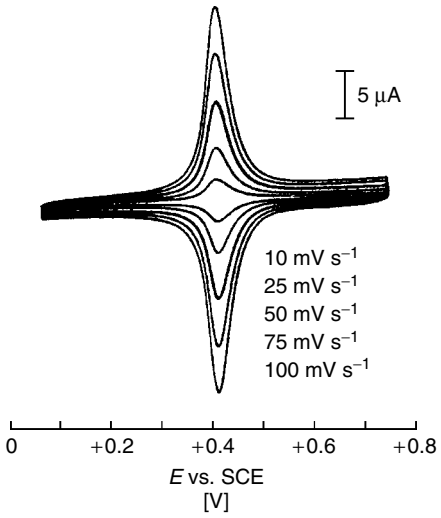


Fig. 7 Cyclic voltammograms at different sweep rates for a Pt disk electrode modified with a film of a silicon-based dendrimer functionalized with eight ferrocenes at the periphery (G1) in a 0.1 M $TBAH/CH_2Cl_2$ solution. Adapted from Ref. 74.

peak separations (ΔE_p) between anodic and cathodic peaks (10 mV at 100 mV s^{-1}), which is typical for surface-confined redox-active species and indicates a large value of the electron-transfer rate (Fig. 7).

Cuadrado and coworkers have also synthesized silicon-based dendrimers (G0 and 1) possessing two ferrocenyl moieties linked to a silicon atom at each branch [75]. These dendrimers exhibited two well-separated and reversible redox waves in $TBAH/CH_2Cl_2$ solution ($E_1^{\circ\prime} = +0.42$ and $E_2^{\circ\prime} = +0.59$ V versus SCE for the G0 dendrimer with eight ferrocenyl moieties), indicating the existence of significant interactions between the two ferrocenyl sites linked together by the bridging silicon atom. Additionally, the cathodic counterpart of the most positive peak appeared to be stripping in shape. This fact indicated that the dendrimers precipitated onto the electrode surface upon complete oxidation of the ferrocenyl moieties and quickly redissolved into the solution upon reduction. They also demonstrated that when the dendrimer-modified electrode was transferred to pure $TBAH/CH_2Cl_2$ solution, the dendrimers remained on the electrode surface and exhibited two successive well-defined reversible redox waves each with a small ΔE_p ($E_1^{\circ\prime} = +0.40$ and $E_2^{\circ\prime} = +0.55$ V versus SCE for the zero generation dendrimer, Fig. 8).

11.4.1.2 Poly(propylenimine) Dendrimers

Cuadrado and coworkers have synthesized and characterized poly(propylenimine) dendrimers modified with neutral ferrocenyl (Fc) groups (diammino butane-*dend*-$(NHCOFc)_n$, $n = 4$, 8, 16, 32, and 64, for G0, 1, 2, 3, and 4, respectively, Fig. 4b) [76]. These dendrimers also showed a ferrocene-based single redox wave at the same potential ($E^{\circ\prime} = +0.59$, $+0.57$, $+0.59$, $+0.58$, and $+0.59$ V versus SCE for G0, 1, 2, 3, and 4, respectively) in $TBAH/CH_2Cl_2$ solution, pointing to the absence of electronic interactions. In addition, the anodic peak appeared to be diffusional, whereas the cathodic peak appeared to be stripping in shape. These results suggested the deposition of dendrimers during oxidation and their abrupt redissolution upon reduction.

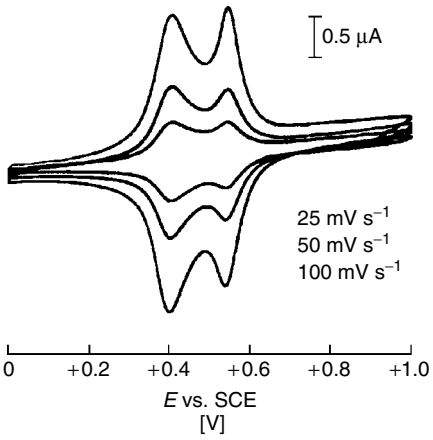


Fig. 8 Cyclic voltammograms at different sweep rates for a Pt disk electrode modified with a film of a silicon-based dendrimer (G0) possessing two ferrocenyl moieties linked to a silicon atom at each branch (eight ferrocenes in total) in a 0.1 M TBAH/CH_2Cl_2 solution. Adapted from Ref. 75.

The details of the deposition and dissolution processes of the DAB-*dend*-$(NHCOFc)_n$ in tetra n-butyl ammonium perchorate (TBAP)/CH_2Cl_2 solution were investigated using the electrochemical quartz crystal microbalance (EQCM) technique as well as admittance measurement of the quartz crystal resonator by Takada et al. [77]. It was found that the oxidized form of the dendrimers deposited onto the Pt electrode likely due to the low solubility of the salt composed of the oxidized dendrimer (ferricenium form) and ClO_4^- anions. On the other hand, the reduced form of the dendrimers easily redissolved except for the first monolayer, which appeared to be strongly adsorbed. Further, the mass-transfer process, during the redox reaction of the adsorbed dendrimers in an AN solution, was found to be of the anion exchange type. The resistance measurements of the quartz crystal resonator based on the admittance also supported the results obtained by EQCM.

The adsorption thermodynamics and kinetics of DAB-*dend*-$(NHCOFc)_n$ onto a Pt electrode were also studied. The adsorption thermodynamics of the reduced form of the dendrimers in a CH_2Cl_2 solution were well represented by the Langmuir adsorption isotherm with a free energy of adsorption, whose value was generation dependent. The surface coverage of these DAB-*dend*-$(NHCOFc)_n$ increased in the order DAB-*dend*-$(NHCOFc)_{64}$ < DAB-*dend*-$(NHCOFc)_{32}$ < DAB-*dend*-$(NHCOFc)_8$, which suggests that it is likely controlled by size. The kinetics of adsorption were found to be activation rather than diffusion controlled and were dependent upon the identity of the dendrimer, but independent of concentration. In general, the adsorption rate constant was found to increase with generation.

11.4.1.3 Poly(aryl ether)-based Dendrimers

Shu et al. synthesized and characterized poly(aryl ether)-based dendrimers modified with 3, 6, 12, and 24 ferrocenyl moieties (G0, 1, 2, and 3, respectively) [78]. Cyclic and normal pulse voltammetry studies suggested that all ferrocenyl sites underwent electron transfer at the same potential in TBAH/CH_2Cl_2 solution. The generations 0 and 1 dendrimers showed typical diffusional cyclic voltammograms, whereas generations 2 and 3 dendrimers showed that the oxidized form of the

dendrimers deposited onto the electrode surface in CH_2Cl_2 solution. From normal pulse voltammetry, the half-wave potential ($E^{\circ\prime}$) was found to be independent of the dendrimer generation in the TBAH/AN-CH_2Cl_2 (3 : 5) solution ($E^{\circ\prime} \approx +0.21$ V versus Ag/Ag^+).

11.4.1.4 Other Ferrocenyl-modified Dendrimers

Catalano and coworkers reported the synthesis and brief electrochemical characterization of $[PtMe_2Br(bpy\text{-}Fc_2)CH_2\text{-}]_nR$ (R = substituted phenyl groups) [79]. In TBAH/AN solution, these dendrimers exhibited a single redox wave centered at +0.50 V versus Ag/AgCl corresponding to the Fc/Fc^+ redox reaction. Diffusion coefficients were also determined by a combination of chronocoulometry and cyclic voltammetry using a microelectrode and were found to be 1.1 to 1.7×10^{-6} cm^2 s^{-1} in DMF/TBAP solution.

Astruc et al. have convergently synthesized and electrochemically characterized a phenoltriallyl-based dendrimer with 54 ferrocenyl residues at the periphery [80]. The dendrimer showed a single diffusional redox wave in DMF solution, whereas it showed a mixture of diffusional and surface wave characteristics in CH_2Cl_2 solution, suggesting deposition of the dendrimer onto the electrode. In fact, when such a dendrimer-modified electrode was transferred to pure TBAH/CH_2Cl_2 solution, it exhibited surface waves with $\Delta E_p = 0$ at ca. 0 V versus Fc/Fc^+.

11.4.2 Cobaltocenyl Dendrimers

The cobaltocenium-functionalized poly(propylenimine) dendrimers (DAB-*dend*-$(NHCOCb)_n$, $n = 4$, 8, 16, and 32 for G0, 1, 2, and 3, respectively), which have the same backbone structures as the above-mentioned ferrocenyl-modified poly(propylenimine) dendrimers, have been synthesized and characterized by Cuadrado and coworkers [81]. The interesting point is that although they have structures similar to those of the ferrocenyl dendrimers mentioned above, these dendrimers possess a positive charge at each cobaltocenium site, meaning that they could be reduced to a zero net charge state. As anticipated from these properties, the dendrimers exhibited a singe diffusional wave during reduction and a sharp stripping peak upon oxidation in aqueous NaCl solution ($E^{\circ\prime} \approx -0.8$ V versus Ag/AgCl), indicating the deposition of the dendrimers upon reduction likely due to the low solubility of the neutral-state dendrimers.

The details of the deposition and dissolution processes of the dendrimers in TBAH/AN solution were investigated using an EQCM technique as well as an admittance measurement of the quartz crystal resonator by Takada et al. [82]. EQCM measurements showed that upon reduction of the cobaltocene sites, electrodeposition of multilayer equivalents of the dendrimers took place. The additional material gradually desorbed upon reoxidation so that only a monolayer equivalent remained on the electrode surface. Admittance measurements of the quartz crystal resonator revealed that films of the lower dendrimer generations behave rigidly, whereas the higher generations exhibit viscoelastic behavior.

11.4.3 Ferrocenyl- and Cobaltocenyl-containing Dendrimers

Dendrimers in this category, which have different functional redox-active residues

in the same molecule, are interesting since they could exhibit special properties and be utilitized in a variety of applications. Poly(propylenimine)-based dendrimers functionalized with both ferrocene and cobaltocenium (G0, 1, 2, and 3 with cobaltocenium/ferrocene ratios of 3 : 1, 6.5 : 1.5, 13 : 3, and 19 : 13, respectively) have been synthesized and characterized by Cuadrado and coworkers [83]. In TBAH/AN solution, the dendrimers showed two single and independent redox waves corresponding to ferrocene- (centered at ca. +0.58 V versus SCE for G2) and cobaltocenium-based (centered at ca. −0.75 V for G2) redox reactions, respectively. In addition, it was found that reduction (i.e. at the cobaltocenium centers) resulted in the deposition of the neutral dendrimers onto the electrode and that oxidation resulted in redissolution. When dendrimer-modified electrodes were transferred to aqueous solution, they exhibited two well-defined redox peaks corresponding to ferrocene ($E^{\circ\prime} = +0.47$ V versus SCE for G2) and cobaltocenium ($E^{\circ\prime} = -0.83$ V for G2) residues.

11.4.4 Ruthenium Terpyridyl and Bipyridyl Dendrimers

Polypyridyl transition metal complexes, especially those of ruthenium(II), have been extensively applied in light harvesting and information storage, because they exhibit a wide range of photophysical and electrochemical properties. Storrier et al. have reported the synthesis and characterization of PAMAM dendrimers functionalized with tris(bipyridyl) ruthenium(II) (dend-*n*-$[Ru(bpy)_3]^{2+}$) or bis(terpyridyl) ruthenium(II) (*dend*-*n*-$[Ru(tpy)_2]^{2+}$) complexes (G0, 1, 2, 3, and 4 with 4, 8, 16, 32, and 64 ruthenium complexes, respectively) [84]. Electrochemical studies of the dendrimer complexes in TBAP/AN solution showed metal-centered (+1.31 V versus Ag/AgCl for *dend*-64-$[Ru(tpy)_2]^{2+}$) and ligand-centered (−1.18 and −1.40 V for *dend*-64-$[Ru(tpy)_2]^{2+}$) redox couples, in a manner analogous to the behavior of the discrete transition metal complexes in solution. Using the EQCM technique, they found that the higher-generation dendrimers deposit onto the electrode upon ruthenium-centered oxidation, likely due to salt formation with supporting electrolyte counteranions, and dissolve upon reduction. For the lower generations, it was suggested that although they do not deposit upon metal-centered oxidation, a monolayer-equivalent dendrimer film is present on the electrode surface. Upon ligand-centered reductions, all the dendrimers were found to deposit onto the electrode, likely due to the lower solubility of the electrically neutral dendrimers.

The thermodynamics and kinetics of adsorption of these dendrimers in AN solution have also been studied using electrochemical methods [85]. All the dendrimers adsorbed onto Pt electrodes when the Ru sites of the dendrimers have +2 charges (i.e. as prepared) and the adsorption thermodynamics are well characterized by the Langmuir adsorption isotherm. It was also reported that the electrochemically determined coverages were significantly larger than calculated values determined from the dimensions of the metallodendrimers obtained from molecular modeling. These comparisons suggested that upon adsorption the dendrimers appear to compress to dimensions significantly smaller than those calculated. The kinetics of adsorption were found to be activation controlled with the rate constant increasing with increasing dendrimer generation.

11.4.5
Cobalt Terpyridyl Dendrimers

PAMAM dendrimers functionalized with bis(terpyridyl) cobalt(II) (*dend-n*-$[Co(tpy)_2]^{2+}$, G1 and 3 with $n = 8$ and 32, respectively), similar to those functionalized with *dend-n*-$[Ru(tpy)_2]^{2+}$, have been synthesized and characterized by the same group [86]. In TBAH/AN solution, when the potential was scanned between +0.60 and −1.20 V versus Ag/AgCl, the dendrimers showed two redox couples with formal potential values of +0.30 and −0.75 V versus Ag/AgCl, which correspond to the Co(II/III) and Co(I/II) processes, respectively (Fig. 9b). Interestingly, when cyclic voltammetry was performed immediately after the immersion of a Pt electrode into a solution containing *dend-n*-$[Co(tpy)_2]^{2+}$, the peak current of the Co(I/II) redox process initially appeared to be the same as that of Co(II/III) (Fig. 9a). However, the Co(I/II) peaks grew (relative to the Co(II/III process) with successive potential scanning. This phenomena was attributed to a manifestation of faster electron self-exchange of the Co(I/II) redox couple relative to Co(II/III). The electron self-exchange was discussed in terms of the Dahms–Ruff equation [87, 88]. In addition, the growing of the Co(I/II) peak clearly indicated adsorption and/or deposition of *dend-n*-$[Co(tpy)_2]^{2+}$ onto the electrode surface.

EQCM studies of the dendrimer complexes showed that they deposit onto the electrode following the Co(II/I) reduction process and that the resulting films prevent further deposition upon successive potential scanning. Further, the thermodynamics and kinetics of adsorption of the dendrimers have been studied. These *dend-n*-$[Co(tpy)_2]^{2+}$ adsorbed (up to a monolayer equivalent) when the Co sites have +2 charges, and the adsorption thermodynamics are well characterized by the Langmuir adsorption isotherm. The kinetics of adsorption are activation controlled and the rate constant is larger for the higher-generation (larger) metallodendrimer.

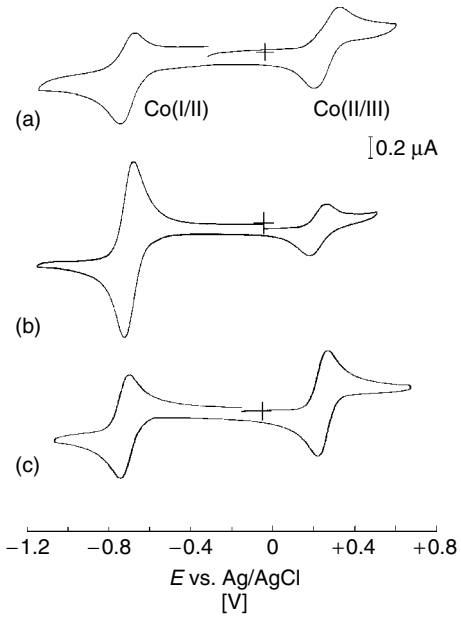


Fig. 9 Cyclic voltammograms of a Pt disk electrode at 100 mV s^{-1} in a 0.1 M TBAH/AN solution containing *dend*-32-$[Co(tpy)_2]^{2+}$ (a) immediately after immersion and (b) 15 after immersion. (c) Cyclic voltammogram of $[Co(tpy)_2]^{2+}$ in solution (other experimental conditions are the same).

11.4.6
Iron Terpyridyl Dendrimers

Kimura et al. synthesized and characterized the third-generation PAMAM dendrimer modified, peripherally, with 32 terpyridyl iron(II) complexes [89].

In TBAH/AN solution, the dendrimer showed a single reversible redox wave at +0.82 V versus Fc/Fc^+ corresponding to the Fe(II/III) process, indicating simultaneous electron transfer at the same potential. Unlike the other dendrimers in the same generation as mentioned above, deposition onto the electrode was not evident in this case.

Diáz et al. have demonstrated a unique method of forming highly ordered layers of terpyridyl-modified PAMAM dendrimers (*dend-n*-tpy, $n = 4$, 8, and 32) with Fe^{2+} or Co^{2+} [90]. The films were prepared onto a highly oriented pyrolytic graphite (HOPG) surface by the interfacial reaction of the *dend-n*-tpy dissolved in CH_2Cl_2 with aqueous Fe^{2+} or Co^{2+}. Molecularly resolved STM images of the films revealed that they form highly ordered 2-D hexagonal arrays, which appear to be composed of one-dimensional polymeric strands with a repeat unit of $(tpy\text{-}dend\text{-}tpy\text{-}M)_x$ (Fig. 10).

11.4.7 Tetrathiafulvalenyl Dendrimers

Bryce and coworkers have synthesized and characterized a series of aryl-ester-based dendrimers surface functionalized with TTF with different cores such as 1,3,5-substituted benzene [91], 1,4-substituted benzene, biphenyl, and phenyl ether [92, 93]. These TTF-modified dendrimers exhibited two quasi-reversible redox waves ($E_1^{\circ\prime} \approx +0.45$ and $E_2^{\circ\prime} \approx +0.85$ V versus Ag/AgCl) in TBAH/AN, DMF, or AN-CH_2Cl_2 (1 : 1) solution. They have also reported the synthesis and characterization of aryl-ester dendrimers modified with both TTF and AQ at the periphery (generations 1 and 2 with ratios of TTF and AQ of 4 : 2 and 8 : 4, respectively) [94]. The TTF served as a π-donor, whereas the AQ served as a π-acceptor. In TBAH/AN solution, the TTF-AQ-modified dendrimer showed two reversible four-electron TTF-centered waves and two reversible two-electron AQ-centered redox waves, respectively.

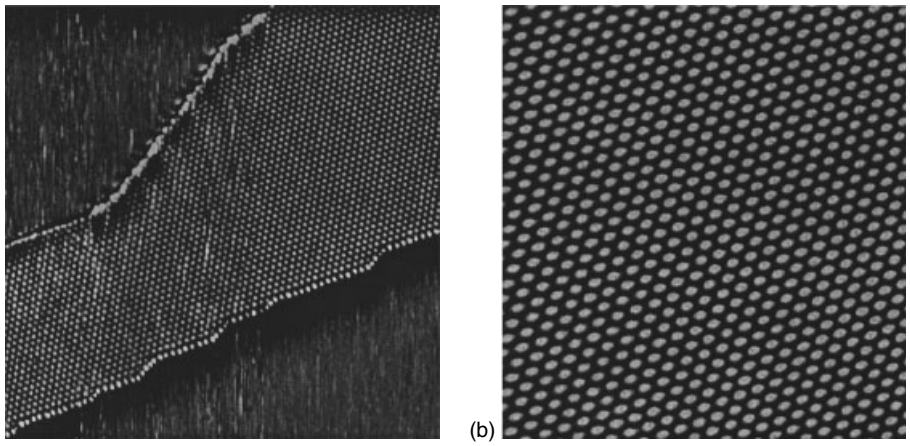


Fig. 10 Unfiltered STM images of *dend*-8-tpy/Fe^{2+} on HOPG. (a) 304 nm × 304 nm image of a well-ordered domain being delimited by the substrate's step edges. (b) 200 nm × 200 nm image featuring a highly ordered 2-D hexagonal domain. Imaging conditions (scanning mode, bias, set-point current): (a) constant height, 146 mV, 1.5 nA, (b) constant current, 150 mV, 1.70 nA. Adapted from Ref. 90.

11.4.8
Viologenyl Dendrimers

Baker reported on the synthesis and electrochemical characterization of a series of viologen-functionalized PAMAM dendrimers [95]. Tapping-mode AFM measurements suggested that the oxidized form of the dendrimers adsorbed onto Au(111), whereas cyclic voltammetry suggested that the reduced dendrimers electrodeposited onto a Pt electrode in KNO_3 aqueous solution ($E^{\circ\prime}$ is ca. −0.54 V versus Ag/AgCl for the G4). Using the chronoamperometry technique with a Pt microelectrode, the diffusion coefficient and number of electrons transferred (n) of the dendrimer (G4) upon reduction were determined to be 1.2×10^{-6} cm^2 s^{-1} and 13, respectively, although NMR and UV–vis measurements showed that the fourth-generation dendrimer has 19 viologen moieties.

11.5
Applications

Because of their electroactive multifunctionality, redox-containing dendrimers have been considered for a number of applications. In many cases, the dendrimers can be viewed as large switchable reservoirs that can either deliver or accept large numbers of charges to or from a desired location. It has been suggested that this ability could be harnessed for many purposes including catalysis, light harvesting, and applications as molecular devices and information storage systems. Since the behavior of the redox couples in many types of dendrimers is sensitive to their environment, their application as sensors for a variety of species has been considered. Other applications, particular to a single type of redox-active dendrimer, have also been investigated.

11.5.1
Light Harvesting

Balzani and coworkers have proposed the use of dendrimers containing ruthenium polypyridyl moieties as key elements of light-harvesting devices. These dendrimers have up to 22 redox centers that absorb visible light via a metal-to-ligand charge transfer (MLCT) band, and it has been determined that energy transfer between neighboring units is very fast. The goal is to be able to absorb light energy in a large number of sites at the periphery and have that energy transfer vectorially along the framework of the molecule toward the center. If the energy collected by many metal centers can be transferred all the way to a single metal center at the core of the molecule, it is possible that a charge-separated state could be achieved, the redox energy of which could then be harnessed [25, 58].

11.5.2
Catalysis

Miedaner et al. have made molecules with a palladium core and four palladium phosphine groups within a dendritic structure of organophosphine moieties, as well as dendrimers with a silicon core and four palladium phosphine branches. The utility of these compounds, when complexed with acetonitrile, as catalysts for CO_2 reduction, has been studied, and significant current enhancements were found when the solvent contained CO_2. Up to 40% of the charge passed was utilized to reduce CO_2 to CO [96]. In a very different

type of system, Newkome and coworkers have synthesized and studied a dendrimer, which, at its periphery, contains four polyoxometalate clusters, each with the formula $[H_4P_2V_3W_{15}O_{62}]^{5-}$. The catalytic activity of these materials for the oxidation of tetrahydrothiophene was examined and found to be significant [97].

While they are not strictly redox-containing dendrimers, Crooks and Zhao have encapsulated platinum and other metallic nanoparticles inside PAMAM dendrimers. The catalytic properties of these materials have been examined using cyclic voltammetry, and it was found that a gold electrode, modified with large hydroxyl-terminated PAMAM dendrimers containing clusters of 60 platinum atoms, was readily able to catalyze O_2 reduction [98]. Similar results have been reported for palladium clusters encapsulated in the same hydroxyl-terminated PAMAM dendrimers [99].

A pentaerythritol-based dendrimer modified with bis-terpyridyl Ru(II) was shown to be effective as a catalyst for the electrochemical oxidation of methionine (L-Met) and cystine (L-Cys) in aqueous solution or the mixed solvent AN–water (12% AN) [100]. In this case, the dendrimer was mixed with carbon powder and, using a sol–gel binder, the carbon electrode doped with the $[Ru(tpy)_2]^{2+}$-functionalized dendrimer was prepared. The oxidation peak of $[Ru(tpy)_2]^{2+}$ was enhanced by the addition of L-Met, indicating the electrocatalytic effect of the dendrimer. Using the composite electrode doped with the dendrimer as an amperometric detector for flow-injection analysis, a linear calibration curve was obtained over the range 1–10 μM of L-Met in phosphate buffer (pH 7.0). A similar calibration curve was obtained for L-Cys over the range 1–10 μM in phosphate buffer (pH 2.3).

11.5.3 Organic LEDs

Katsuma and Shirota have synthesized several dendrimers that contain multiple phenylamine moieties and investigated their potential use as components of organic light-emitting diode (LEDs). They found that these materials were well suited for use in the hole-transport layer of multilayer LEDs, exhibiting comparable performance to previously utilized materials [101].

11.5.4 Oxygen Carriers

Dendrimers with porphyrin moieties at their centers have been investigated in some detail by Diederich and coworkers because of the similarity they have with biological molecules such as *heme* and *cytochrome c* [47–49]. Applications such as synthetic oxygen carriers for blood replacement can be envisioned for these materials. Also, a synthetic analog to *cytochrome c* could be utilized to transfer electrons in light-harvesting systems, albeit slightly different from the ones discussed previously.

11.5.5 Molecule-sized Gates

Composite monolayers of PAMAM dendrimers and *n*-alkanethiols immobilized on a Au surface were used as ion gates for $[Ru(NH_3)_6]^{3+}$ and $[Fe(CN)_6]^{3-}$ based on electrostatic interactions [102, 103]. It should be emphasized that in this case the PAMAM dendrimers were not functionalized with redox-active moieties. In aqueous solution, containing $[Ru(NH_3)_6]^{3+}$ and $[Fe(CN)_6]^{3-}$ and at pH 6.3 where the terminal amino groups of the dendrimers are

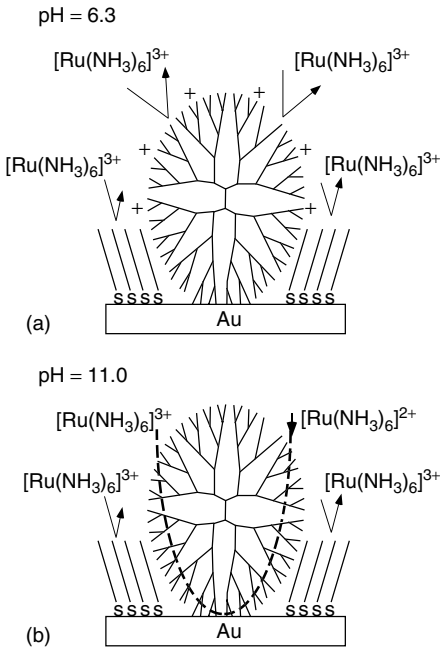


Fig. 11 Schematic illustration of a molecular gate consisting of PAMAM dendrimers and *n*-alkanethiols immobilized on a Au surface. Adapted from Ref. 102.

protonated, only the negatively charged $[Fe(CN)_6]^{3-}$ can penetrate to the electrode surface through the composite monolayer because of electrostatic interactions (Fig. 11a). On the other hand, at pH 11, where the dendrimers are fully deprotonated (in neutral form), both $[Ru(NH_3)_6]^{3+}$ and $[Fe(CN)_6]^{3-}$ can penetrate the film (Fig. 11b).

11.5.6 Molecular Recognition

DAB-*dend*-$(NHCOFc)_n$ ($n = 4$, 8, and 16) were found to be able to carry out molecular recognition. The DAB-*dend*-$(NHCOFc)_n$ were used as guests for inclusion complexation by β-cyclodextrin (β-CD) and dimethyl-β-cyclodextrin (DM-β-CD) hosts [104]. Electrochemical and spectroscopic data indicated that the increased solubility of the hydrophobic dendrimers in aqueous solution results from the inclusion complexation of the DAB-*dend*-$(NHCOFc)_n$ by the CD hosts. For the higher-generation dendrimers, where more ferrocene residues are packed on the surface of the guest, the individual complexation events become increasingly hampered.

Similar to DAB-*dend*-$(NHCOFc)_n$, DAB-*dend*-$(NHCOCb)_n$ were also used as guests for β-CD. The positively charged DAB-*dend*-$(NHCOCb^+)_n$ are not complexed by β-CD in aqueous solution. However, electrochemical reduction to the neutral form triggers the formation of inclusion complexes between the peripheral cobaltocene residues and the diffusing β-CD hosts.

Ferrocenyl-modified dendrimers were found to be able to recognize small inorganic anions [105, 106]. From shifts of the ferrocene-based peak potentials in cyclic voltammetry in CH_2Cl_2 solution and shifts of δ_{NH} in ^1H NMR, resulting from the titration of the dendrimers with the tetrabutylammonium salts of anions such as $H_2PO_4^-$, HSO_4^-, Cl^-, and NO_3^-, changes in the apparent association constant of the anion with the ferrocenyl dendrimer were monitored.

A similar method was used in silicon-based ferrocenyl dendrimers for the recognition of inorganic anions in CH_2Cl_2 solution [107]. In addition, this technique was also applied to the dendrimer immobilized on a glassy carbon electrode in AN solution, where the dendrimers are insoluble and where $H_2PO_4^-$, HSO_4^-, Cl^-, and Br^- were successfully recognized.

11.5.7 Mediators

Silicon-based ferrocenyl dendrimers have been used as mediators in amperometric biosensors for glucose [108]. The dendrimers were incorporated into carbon paste electrodes with glucose oxidase (GOx) and paraffin oil as binder. The ferrocene-centered oxidation peak was enhanced by the addition of glucose, whereas the reduction peak decreased. Such behavior clearly indicated that the ferrocenyl-modified dendrimers worked as mediators for glucose oxidation with GOx. The larger dendrimers, which possess longer branches, were found to have higher efficiency for electron-transfer mediation likely due to higher flexibility. Using amperometry, the highest sensitivity was found to be 57 mA mM^{-1} up to ca. 1.5 mM of glucose.

PAMAM-based dendrimers partially functionalized with various degrees of ferrocenyl moieties have also been used as mediators for glucose [109]. The dendrimers were alternatively deposited with periodate-oxidized GOx on a Au electrode, forming an electrochemically and enzymatically active multilayered assembly of enzyme toward glucose oxidation. The electrocatalytic signals from the electrodes were shown to be directly correlated to the number of deposited bilayers.

11.5.8 Biosensors

A PAMAM dendrimer (G4) monolayer partially functionalized with both ferrocenyl and biotinamidocaproate residues was constructed on a Au electrode and utilized as a biosensor for avidin on the basis of its binding to biotin [110]. The electrochemical response was generated by the oxidation of free glucose catalyzed by GOx present in the electrolyte. The magnitude of the response was dependent on the degree of coverage of the sensing surface with avidin. The sensor signal decreased concomitantly with increasing avidin concentration (coverage) at the dendrimer periphery, since the captured avidins block the charge transfer between the electrode and GOx. The ferrocenyl residues of the dendrimer served as electron-transfer mediator for the oxidation reaction of glucose catalyzed by GOx. The detection limit of avidin was about 4.5 pM, and the response was linear from 1.5 pM to 10 nM.

References

1. F. Zeng, S. C. Zimmerman, *Chem. Rev.* **1997**, *97*, 1681–1712.
2. O. A. Matthews, A. N. Shipway, J. F. Stoddart, *Prog. Polym. Sci.* **1998**, *23*, 1–56.
3. H. B. Mekelburger, K. Rissanen, F. Voegtle, *Chem. Ber.* **1993**, *126*, 1161–1169.
4. D. A. Tomalia, D. R. Swanson, J. W. Klimash et al., *Polym. Prepr.* **1993**, *34*, 52–53.
5. Z. Xu, M. Kahr, K. L. Walker et al., *J. Am. Chem. Soc.* **1994**, *116*, 4537–4550.
6. S. Mattei, P. Seiler, F. Diederich et al., *Helv. Chim. Acta* **1995**, *78*, 1904–1912.
7. P. R. Ashton, D. W. Anderson, C. L. Brown et al., *Chem. Eur. J.* **1998**, *4*, 781–795.
8. V. Sartor, L. Djakovitch, J.-L. Fillaut et al., *J. Am. Chem. Soc.* **1999**, *121*, 2929–2930.
9. C. J. Hawker, J. M. J. Frechet, *J. Am. Chem. Soc.* **1990**, *112*, 7638–7647.
10. T. M. Miller, T. X. Neenan, *Chem. Mater.* **1990**, *2*, 346–349.
11. E. W. Kwock, T. X. Neenan, T. M. Miller, *Chem. Mater.* **1991**, *3*, 775–777.
12. H. Meier, M. Lehmann, U. Kolb, *Chem. Eur. J.* **2000**, *6*, 2462–2469.
13. H. Sahota, P. M. Lloyd, S. G. Yeates et al., *J. Chem. Soc., Chem. Commun.* **1994**, 2445–2446.
14. J. W. Leon, J. M. J. Frechet, *Polym. Bull.* **1995**, *35*, 449–455.
15. D. Seebach, G. F. Herrmann, U. D. Lengweiler et al., *Helv. Chim. Acta* **1997**, *80*, 989–1026.
16. B. L. Schwartz, A. L. Rockwood, R. D. Smith et al., *Rapid Commun. Mass Spectrom.* **1995**, *9*, 1552–1555.

17. C. Moucheron, M. A. Kirsch-De, A. Dupont-Gervais et al., *J. Am. Chem. Soc.* **1996**, *118*, 12834–12835.
18. J.-W. Weener, J. L. J. van Dongen, E. W. Meijer, *J. Am. Chem. Soc.* **1999**, *121*, 10346–10355.
19. P. L. Dubin, S. L. Edwards, J. I. Kaplan et al., *Anal. Chem.* **1992**, *64*, 2344–2347.
20. A. D. Meltzer, D. A. Tirrell, A. A. Jones et al., *Macromolecules* **1992**, *25*, 4549–4552.
21. A. D. Meltzer, D. A. Tirrell, A. A. Jones et al., *Macromolecules* **1992**, *25*, 4541–4548.
22. G. Greiveldinger, D. Seebach, *Polym. Mater. Sci. Eng.* **1997**, *77*, 134–135.
23. U. Herzog, C. Notheis, E. Brendler et al., *Fresenius' J. Anal. Chem.* **1997**, *357*, 503–504.
24. G. M. Stewart, M. A. Fox, *J. Am. Chem. Soc.* **1996**, *118*, 4354–4360.
25. V. Balzani, S. Campagna, G. Denti et al., *Acc. Chem. Res.* **1998**, *31*, 26–34.
26. S. L. Gilat, A. Adronov, J. M. J. Frechet, *Angew. Chem., Int. Ed. Engl.* **1999**, *38*, 1422–1427.
27. E. C. Wiener, M. W. Brechbiel, H. Brothers et al., *Magn. Reson. Med.* **1994**, *31*, 1–8.
28. E. Toth, D. Pubanz, S. Vauthey et al., *Chem. Eur. J.* **1996**, *2*, 1607–1615.
29. W. Krause, N. Hackmann-Schlichter, F. K. Maier et al., *Top. Curr. Chem.* **2000**, *210*, 261–308.
30. S. W. Poxon, P. M. Mitchell, E. Liang et al., *Drug Deliv.* **1996**, *3*, 255–261.
31. R. DeLong, K. Stephenson, T. Loftus et al., *J. Pharm. Sci.* **1997**, *86*, 762–764.
32. M. Liu, J. M. J. Frechet, *Pharm. Sci. Technol. Today* **1999**, *2*, 393–401.
33. S. Serroni, G. Denti, S. Campagna et al., *Angew. Chem., Int. Ed. Engl.* **1992**, *31*, 1493–1495.
34. F. Moulines, L. Djakovitch, R. Boese et al., *Angew. Chem., Int. Ed. Engl.* **1993**, *32*, 1075–11077.
35. C. M. Cardona, A. E. Kaifer, *J. Am. Chem. Soc.* **1998**, *120*, 4023–4024.
36. Y. Wang, C. M. Cardona, A. E. Kaifer, *J. Am. Chem. Soc.* **1999**, *121*, 9756–9757.
37. C. M. Cardona, T. D. McCarley, A. E. Kaifer, *J. Org. Chem.* **2000**, *65*, 1857–1864.
38. D. K. Smith, *J. Chem. Soc., Perkin Trans. 2* **1999**, 1563–1565.
39. H.-F. Chow, I. Y. K. Chan, D. T. W. Chan et al., *Chem. Eur. J.* **1996**, *2*, 1085–1091.
40. M. Kimura, T. Shiba, T. Muto et al., *Chem. Commun.* **2000**, 11–12.
41. J. Issberner, F. Vögtle, L. D. Cola et al., *Chem. Eur. J.* **1997**, *3*, 706–712.
42. F. Vögtle, M. Plevoets, M. Nieger et al., *J. Am. Chem. Soc.* **1999**, *121*, 6290–6298.
43. N. Armaroli, C. Boudon, D. Felder et al., *Angew. Chem., Int. Ed. Engl.* **1999**, *38*, 3730–3733.
44. C. B. Gorman, *Adv. Mater.* **1997**, *9*, 1117–1119.
45. C. B. Gorman, J. C. Smith, M. W. Hager et al., *J. Am. Chem. Soc.* **1999**, *121*, 9958–9966.
46. P. J. Dandliker, F. Diederich, M. Gross et al., *Angew. Chem. Int. Ed. Engl.* **1994**, *33*, 1739–1742.
47. P. J. Dandliker, F. Diederich, J.-P. Gisselbrecht et al., *Angew. Chem., Int. Ed. Engl.* **1995**, *34*, 2725–2728.
48. P. J. Dandliker, F. Diederich, A. Zingg et al., *Helv. Chim. Acta* **1997**, *80*, 1773–1801.
49. P. Weyermann, J.-P. Gisselbrecht, C. Boudon et al., *Angew. Chem., Int. Ed. Engl.* **1999**, *38*, 3215–3219.
50. K. W. Pollak, J. W. Leon, J. M. J. Frechet et al., *Chem. Mater.* **1998**, *10*, 30–38.
51. M. Kimura, Y. Sugihara, T. Muto et al., *Chem. Eur. J.* **1999**, *5*, 3495–3500.
52. M. R. Bryce, W. Devonport, L. M. Goldenberg et al., *Chem. Commun.* **1998**, 945–952.
53. J. J. Apperloo, R. A. J. Janssen, P. R. L. Malenfant et al., *J. Am. Chem. Soc.* **2000**, *122*, 7042–7051.
54. I. Jestin, E. Levillain, J. Roncali, *Chem. Commun.* **1998**, 2655–2656.
55. L. L. Miller, B. Zinger, J. S. Schlechte, *Chem. Mater.* **1999**, *11*, 2313–2315.
56. G. R. Newkome, V. V. Narayanan, L. A. Godinez et al., *Macromolecules* **1999**, *32*, 6782–6791.
57. A. G. Avent, P. R. Birkett, F. Paolucci et al., *J. Chem Soc., Perkin Trans. 2* **2000**, 1409–1414.
58. V. Balzani, S. Campagna, G. Denti et al., *Coord. Chem. Rev.* **1994**, *132*, 1–13.
59. S. Campagna, G. Denti, S. Serroni et al., *Chem. Eur. J.* **1995**, *1*, 211–221.
60. M. Marcaccio, F. Paolucci, C. Paradisi et al., *J. Am. Chem. Soc.* **1999**, *121*, 10081–10091.
61. P. Ceroni, F. Paolucci, C. Paradisi et al., *J. Am. Chem. Soc.* **1998**, *120*, 5480–5487.
62. E. C. Constable, P. Harverson, *Inorg. Chim. Acta* **1996**, *252*, 9–11.

63. G. R. Newkome, R. Güther, C. N. Moorefield et al., *Angew. Chem., Int. Ed. Engl.* **1995**, *34*, 2023–2026.
64. G. R. Newkome, E. He, L. A. Godinez, *Macromolecules* **1998**, *31*, 4382–4386.
65. G. R. Newkome, A. K. Patri, L. A. Godinez, *Chem. Eur. J.* **1999**, *5*, 1445–1451.
66. M. Haga, M. M. Ali, H. Sato et al., *Inorg. Chem.* **1998**, *37*, 2320–2324.
67. C. Wang, M. R. Bryce, A. S. Batsanov et al., *J. Mater. Chem.* **1997**, *7*, 1189–1197.
68. C. A. Christensen, L. M. Goldenberg, M. R. Bryce et al., *Chem. Commun.* **1998**, 509–510.
69. X. Camps, E. Dietel, A. Hirsch et al., *Chem. Eur. J.* **1999**, *5*, 2362–2373.
70. S. Heinen, L. Walder, *Angew. Chem., Int. Ed. Engl.* **2000**, *39*, 806–809.
71. T. D. Selby, S. C. Blackstock, *J. Am. Chem. Soc.* **1998**, *120*, 12155–12156.
72. G. R. Newkome, V. V. Narayanan, L. A. Godinez, *J. Org. Chem.* **2000**, *65*, 1643–1649.
73. B. Alonso, I. Cuadrado, M. Morán et al., *J. Chem. Soc., Chem. Commun.* **1994**, 2575–2576.
74. B. Alonso, M. Morán, C. M. Casado et al., *Chem. Mater.* **1995**, *7*, 1440–1442.
75. I. Cuadrado, C. M. Casado, B. Alonso et al., *J. Am. Chem. Soc.* **1997**, *119*, 7613–7614.
76. I. Cuadrado, M. Moran, C. M. Casado et al., *Organometallics* **1996**, *15*, 5278–5280.
77. K. Takada, D. J. Díaz, H. D. Abruña et al., *J. Am. Chem. Soc.* **1997**, *119*, 10763–10773.
78. C.-F. Shu, H.-M. Shen, *J. Mater. Chem.* **1997**, *7*, 47–52.
79. S. Achar, C. E. Immoos, M. G. Hill et al., *Inorg. Chem.* **1997**, *36*, 2314–2320.
80. S. Nlate, J. Ruiz, D. Astruc et al., *Chem. Commun.* **2000**, 417–418.
81. B. González, C. M. Casado, B. Alonso et al., *Chem. Commun.* **1998**, 2569–2570.
82. K. Takada, D. J. Díaz, H. D. Abruña et al., *Chem. Eur. J.* **2001**, *7*, 1109–1117.
83. C. M. Casado, B. González, I. Cuadrado et al., *Angew. Chem., Int. Ed. Engl.* **2000**, *39*, 2135–2138.
84. G. D. Storrier, K. Takada, H. D. Abruña, *Langmuir* **1999**, *15*, 872–884.
85. K. Takada, G. D. Storrier, M. Morán et al., *Langmuir* **1999**, *15*, 7333–7339.
86. K. Takada, G. D. Storrier, J. I. Goldsmith et al., *J. Phys. Chem. B* **2001**, *105*, 2404–2411.
87. I. Ruff, I. Korösi-ódor, F. C. Anson, *Inorg. Chem.* **1970**, *9*, 186–188.
88. I. Ruff, V. J. Friedrich, *J. Phys. Chem.* **1971**, *75*, 3297–3303.
89. M. Kimura, K. Mizuno, T. Muto et al., *Macromol. Rapid Commun.* **1999**, *20*, 98–102.
90. D. J. Díaz, G. D. Storrier, S. Bernhard et al., *Langmuir* **1999**, *15*, 7351–7354.
91. M. R. Bryce, W. Devonport, A. J. Moore, *Angew. Chem., Int. Ed. Engl.* **1994**, *33*, 1761–1763.
92. M. R. Bryce, W. Devonport, *Synth. Met.* **1996**, *76*, 305–307.
93. W. Devonport, M. R. Bryce, G. J. Marshallsay et al., *J. Mater. Chem.* **1998**, *8*, 1361–1372.
94. M. R. Bryce, P. de Miguel, W. Devonport, *Chem. Commun.* **1998**, 2565–2566.
95. W. S. Baker, *Electrochem. Soc. Interface* **1999**, *8*, 56–57.
96. A. Miedaner, C. J. Curtis, R. M. Barkley et al., *Inorg. Chem.* **1994**, *33*, 5482–5490.
97. H. Zeng, G. R. Newkome, C. L. Hill, *Angew. Chem., Int. Ed. Engl.* **2000**, *39*, 1772–1774.
98. M. Zhao, R. M. Crooks, *Adv. Mater.* **1999**, *11*, 217–220.
99. M. Zhao, R. M. Crooks, *Chem. Mater.* **1999**, *11*, 3379–3385.
100. S. D. Holmstrom, J. A. Cox, *Anal. Chem.* **2000**, *72*, 3191–3195.
101. K. Katsuma, Y. Shirota, *Adv. Mater.* **1998**, *10*, 223–226.
102. M. Zhao, H. Tokuhisa, R. M. Crooks, *Angew. Chem., Int. Ed. Engl.* **1997**, *36*, 2596–2598.
103. H. Tokuhisa, M. Zhao, L. A. Baker et al., *J. Am. Chem. Soc.* **1998**, *120*, 4492–4501.
104. R. Castro, I. Cuadrado, B. Alonso et al., *J. Am. Chem. Soc.* **1997**, *119*, 5760–5761.
105. C. Valério, J.-L. Fillaut, J. Ruiz et al., *J. Am. Chem. Soc.* **1997**, *119*, 2588–2589.
106. J. Guittard, J.-C. Blais, D. Astruc et al., *Pure Appl. Chem.* **1998**, *70*, 809–818.
107. C. M. Casado, I. Cuadrado, B. Alonso et al., *J. Electroanal. Chem.* **1999**, *463*, 87–92.
108. J. Losada, I. Cuadrado, M. Morán et al., *Anal. Chim. Acta* **1997**, *338*, 191–198.
109. H. C. Yoon, M.-Y. Hong, H.-S. Kim, *Anal. Chem.* **2000**, *72*, 4420–4427.
110. H. C. Yoon, M.-Y. Hong, H.-S. Kim, *Anal. Biochem.* **2000**, *282*, 121–128.

12
Electrochemical Formation of Organic Thin Films

Tetsuo Saji
Tokyo Institute of Technology, Tokyo, Japan

12.1 **Introduction** **757**

12.2 **Formation of Organic Thin Films Using Surfactants with a Ferrocene Group** **758**

12.3 **Formation of Organic Thin Films Using Surfactants with an Azobenzene Group** **759**

12.4 **Scope of Film-forming Compounds** **760**

12.5 **Rate of Film Growth** **761**

12.6 **Properties of Film** **761**

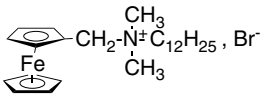
12.7 **Applications** **761**
References 762

Encyclopedia of Electrochemistry. Edited by A.J. Bard and M. Stratmann
Vol. 10 *Modified Electrodes*. Edited by M.Fujihira, I.Rubinstein, and J.F.Rusling
Copyright © 2007 Wiley-VCH Verlag GmbH & Co. KGaA, Weinheim. ISBN: 978-3-527-30402-8

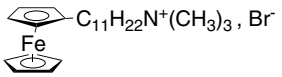
12.1 Introduction

The electrochemical formations of thin films by direct electrolysis of electroactive film-forming species have been reviewed by many authors. The purpose of this section is to review the electrochemical formation of organic thin films using electroactive surfactants, which have some advantages over the direct electrolysis method, since the molecular structure of the film-forming compounds does not change during the electrolysis. Details of the electrochemical behavior [1, 2], the electrochemically controlled release of drugs [3], solubilizate [4], and Marangoni phenomenon [5, 6] using electroactive surfactants are not included in this section. The origin of this method is based on the fact that the micelles formed by cationic surfactants with a ferrocene group (FTMA and FDDA, Fig. 1) can be broken up into monomers when the surfactants are chemically or electrochemically oxidized [1, 2]. Hoshino and Saji extended this phenomenon to the formation of organic thin films using these surfactants [7]. The micelles formed by the surfactants are broken up into monomers when the surfactants are electrochemically oxidized; a solubilizate is released from the micelles and then deposited onto the electrode (Fig. 2, mechanism A). Later, the preparation of organic pigment thin films using nonionic surfactants with a ferrocene group (FPEG, Fig. 1) was reported [8, 9]. These studies showed that organic pigment particles are not actually incorporated into the micelles formed by the surfactants, but are dispersed by having the surfactant adsorbed onto the particle surface (Fig. 2, mechanism B). Formation of the film on a base metal using this surfactant was not possible due to its oxidation at the electrolysis potential of the film formation (+0.5 V versus saturated calomel electrode (SCE). In 1994, Saji et al. reported the formation of a thin film using a surfactant with an azobenzene group (AZPEG, Fig. 1). This surfactant loses its amphiphilic function by reduction and forms on a base metal, for example, copper, nickel, or aluminum. Films were formed by immersion in the solution without electrolysis [10]. Suzuki et al. reported application of a surfactant with an anthraquinone group (AQPEG, Fig. 1) for the formation of an organic thin film, which was prepared by electrochemical reduction under alkaline condition with stirring [11]. Details of the formation of organic films using the surfactants with a ferrocene or an azobenzene group are described in the following sections.

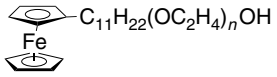
Encyclopedia of Electrochemistry. Edited by A.J. Bard and M. Stratmann
Vol. 10 *Modified Electrodes*. Edited by M.Fujihira, I.Rubinstein, and J.F.Rusling
Copyright © 2007 Wiley-VCH Verlag GmbH & Co. KGaA, Weinheim. ISBN: 978-3-527-30402-8



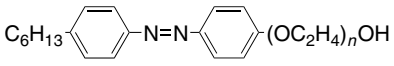
FTMA



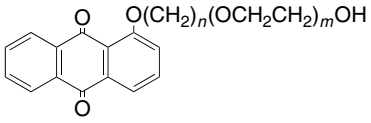
FDMA



FPEG (n = 12.3)



AZPEG (n = 21.4)



AQPEG (n = 8, m = 13.5)

Fig. 1 Molecular structures of electroactive surfactants.

Tab. 1 Half-wave potential ($E_{1/2}$) and critical micelle concentration (*cmc*) of electroactive surfactants

Surfactant	$E_{1/2}$ *versus SCE [V]*	*cmc [mM]*	*References*
FDDA	+0.43	5×10^{-1}	2
FTMA	+0.15	7×10^{-2}	1
FPEG	+0.28	8×10^{-3}	8
AZPEG	−0.2[a]	7×10^{-6}	10
AQPEG	−0.67 (pH 12)	0.9	11

[a] Irreversible reduction peak.

12.2 Formation of Organic Thin Films Using Surfactants with a Ferrocene Group

Table 1 shows the physicochemical properties of the surfactants with a ferrocene group. The critical micelle concentration values of these surfactants depend on the type of hydrophilic group and are in the order FPEG < FTMA < FDDA [9]. Cyclic voltammograms of these surfactants in aqueous solution show a one-electron reversible oxidation step at approximately +0.2 ~ +0.4 V versus SCE, which is close to that of ferrocene (Table 1).

Hoshino and Saji [7] first reported the preparation of azo-dye thin films using FTMA. These films were prepared by controlled-potential electrolysis of the FTMA micelle aqueous solution solubilizing the azo dye at +0.3 V versus SCE. The azo-dye molecules exist as solubilizate in the micelles, and are then released from the micelles and deposited

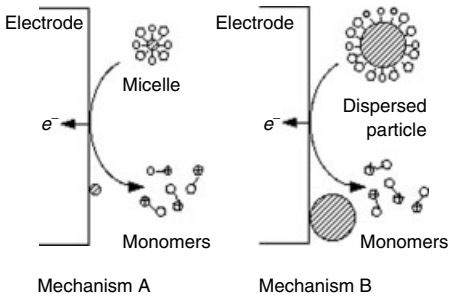
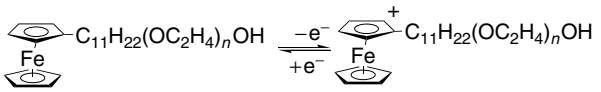


Fig. 2 Mechanisms of film formation using electroactive surfactants.



FPEG (n = 12.3) FPEG$^+$(n = 12.3)

Fig. 3 Redox reaction of FPEG [9].

onto the electrode (Fig. 2, mechanism A). Results of the film formation under various conditions were explained on the basis of a solubilization and adsorption equilibrium for the azo dye released from the micelle [12]. The film was formed in two steps: a layer of globular nuclei was formed on the electrode, followed by the growth of needlelike crystals on the layer. Formation of the thin films of metal phthalocyanines (MPc) using FPEG was reported by Saji and coworkers [8, 9, 13, 14]. These studies showed that MPc particles are dispersed by the surfactant adsorbed onto the particle surface (mechanism B). The agreement of the absorption spectra and X-ray diffraction patterns among the CuPc powders, their micellar solutions, and their films indicated that the crystalline form of CuPc is maintained throughout the film preparation process [13]. Thin films of MgPc and AlPcCl prepared using FPEG exhibit an intense near-infrared absorption [14]. Thin films of a wide variety of organic compounds were prepared using FTMA and FPEG [9] (Tables 2, 3). The crystal size of the film increased with the electrolysis time in the case of the film prepared, using FTMA, and is the same for the added particles in the case of the film prepared using FPEG [9]. The adsorption isotherm of FPEG on the pigment particle surface shows that they form monolayers at saturation, which supports the fact that the film formation proceeds through mechanism B [9].

12.3 Formation of Organic Thin Films Using Surfactants with an Azobenzene Group

A cyclic voltammogram of AZPEG in a 0.1 M HCl aqueous solution shows

Tab. 2 Results of film-formation studies of organic compounds incorporated in the micelles in 2 mM FTMA −0.2 M Li_2SO_4 aqueous solution

Compound	C_{sol} [μM]	*Appearance*[a]	*References*
Sudan I	39	Orange	9
Para Red	5	Red	9
Naphthyl Red	410	Yellow	9
Naphthol AS	36	White	9
Spyropyrane	27	White	9
N-Vinylcarbozol	420	White	9
Cetylalcohol	180	White	9
Dioctadecyl-dimethyl-ammonium	63	White	9
1,1'-Didodecyl-4,4'-bipyridinium dibromide	800	White	17

[a] All of the films in this table are opaque.

an irreversible reduction step at approximately $-0.1 \sim -0.3$ V versus SCE [9]. In an acidic solution, the reduction of azobenzene is a four-electron reduction process with cleavages of the nitrogen–nitrogen bond, which leads to the formation of aniline derivatives [15].

The films prepared using AZPEG were formed under an acidic condition ($pH \leqq 3$), which was explained by the loss of its ability to disperse particles due to the acid-catalyzed formation of the aniline derivatives from hydrazobenzene [15]. Thin films of pigment particles were prepared on base metal plates by immersing them in the dispersion without electrolysis. Such electroless plating was explained by the chemical reduction of AZPEG with the base metals, since the standard potentials of the base metals are more negative than that of AZPEG [9]. Thin films of pigment particles were prepared on noble metals and indium tin oxide (ITO) plates by immersing both the noble metal (or ITO) and aluminum plates in the above dispersion, where these two plates were short circuited with a metal clip [16]. Such a technique has been used in the field of metal plating.

12.4 Scope of Film-forming Compounds

This method enables the preparation of thin films from a wide variety of organic

Tab. 3 Results of film formation of pigments using electroactive surfactants

Pigment	*Particle size [μm]*	*Surfactant*	*Appearance*	*References*
Disazo Yellow AAMX	–	AZPEG	Yellow	18
Disazo Yellow HR	–	AZPEG	Reddish yellow	18
Cromophtal Yellow GR	–	AZPEG	Reddish yellow	18
Perylene Vermillion	0.2–0.4	FPEG, AZPEG	Red	9, 18
	0.03–0.04	FPEG, AZPEG	Red	9, 18
Dianthraquinoyl Red	0.02–0.04	FPEG, AZPEG	Red	9, 18
Perylene Red	0.1–0.4	FPEG, AZPEG	Red	9, 18
Perylen Maroon	0.05–0.1	FPEG, AZPEG	Dark red	9, 18
Perylene Scarlet	0.2–0.4	FPEG, AZPEG	Red	9, 18
Pyranthrone Red	0.2–0.3	FPEG, AZPEG	Red	9, 18
Rhodamin B Lake	–	FPEG	Reddish purple	18
Dioxazine Violet	–	FPEG, AZPEG	Bluish purple	18
Indanthron Blue	–	FPEG, AZPEG	Reddish blue	9, 18
Carbon Black	–	AZPEG	Black	19
Copper phthalocyanine (α-form, α-CuPc)	0.1–0.2	FPEG, AZPEG	Reddish blue	13, 18
β-CuPc	0.1–0.2	FPEG, AZPEG	Greenish blue	13, 18
ε-CuPc	0.05–0.1	FPEG, AZPEG	Reddish blue	9, 18
H_2Pc	0.1–0.2	FPEG, AZPEG	Yellowish green	9, 18
$CuPcCl_{16}$	0.05–0.1	FPEG, AZPEG	Bluish green	9, 18
$CuPcCl_6Br_{10}$	0.1–0.2	FPEG, AZPEG	Yellowish green	9, 18
MgPc	–	FPEG	Blue	14
AlPcCl	–	FPEG	Blue	14
CoPc	–	FPEG	Blue	20
NiPc	–	FPEG	Blue	20
FePc	–	AZPEG	Green	19, 20

compounds (Tables 2 and 3). Table 4.6.2 lists the organic compounds that formed films via mechanism A. Generally these compounds are soluble in organic solvents and are solubilized in a micellar aqueous solution. In the case of some compounds which have a relatively high solubility, their films grow thicker than 1 μm.

Table 3 lists the organic compounds for which film formation occurs through mechanism B. All of these organic compounds are particles and satisfy the following conditions:

1. Hydrophobic and not soluble in water.
2. Size of the particles is submicron; precipitation of the particles more than 1 μm predominates over Brownian motion.

12.5 Rate of Film Growth

The amount of the film prepared through mechanism A was proportional to that of the electricity through the electrode, which was explained by the dependence of the growth on the amount of compound released from the micelles [9]. On the other hand, the amount of film prepared through mechanism B was not proportional to the electricity that passed through the electrode. The deposition of particles occurs by the desorption of the surfactant from the surface coverage of the pigment, and free surfactant does not contribute to the film formation [9, 21]. The film thickness of the film increases with immersion time. The thickness of the film increased to more than 10 μm during an overnight immersion of the substrate, which was explained by the penetration of the surfactant into the film due to the existence of a small space in the film [9].

12.6 Properties of Film

The films prepared through mechanism B have a uniform thickness and are composed of particles [9, 13]. Size and shape of these particles are the same as those used for the preparation of the dispersion. Most of these films are transparent. The absorption spectrum of the film from the dispersion of the β-type CuPc was very similar to that of the β-type CuPc film prepared by vacuum sublimation [13], which means that control of the crystalline structure of the film is possible.

12.7 Applications

The preparation of color filters for liquid crystalline displays (LCDs) using FPEG has been tried [22]. These color filters were prepared using the dispersion containing two or three pigments that touch the LCD. A phthalocyanine photoelectrochemical cell prepared using FPEG was found to be more photoactive compared with that prepared by a vacuum sublimation technique [23]. Coloration of the metal plating was studied by electrochemical deposition of Ni on the substrate covered with a pigment film [19, 24]. The deposited Ni occupies the space between the pigment particles and the substrate. Electroless plating of organic pigments onto a metal fine particle was also reported [25].

A few methods for the photochemical deposition of pigments have been reported. Harima et al. reported the photochemical deposition of pigments onto a TiO_2 substrate [26]. Photogenerated holes from the valence band edge oxidize the FPEG. Mizuno et al. reported

the photoinduced patterned film formation of organic pigments using tris(2,2'-bipyridine)ruthenium (II) and FPEG [27]. The photoinduced oxidation of FPEG leads to deposition of the pigments. Yamanouchi et al. reported the photochemical formation of pigment thin films and photoimages on a nonconductive substrate by the photochemical reduction of AZPEG [28].

References

1. T. Saji, K. Hoshino, S. Aoyagui, *J. Am. Chem. Soc.* **1985**, *107*(24), 6865–6868.
2. T. Saji, K. Hoshino, S. Aoyagui, *J. Chem. Soc., Chem. Commun.* **1985**, *13*, 865.
3. Y. Takeoka, T. Aoki, K. S Sanui et al., *J. Controlled Release* **1995**, *33*, 79–87.
4. Y. Kakizawa, H. Sakai, T. Saji et al., *J. Jpn. Soc. Colour Mater.* **1999**, *72*(2), 78–87.
5. D. E. Bennett, B. S. Gallardo, N. L. Abbott, *J. Am. Chem. Soc* **1996**, *118*(27), 6499–6499.
6. B. S. Gallardo, V. K. Gupta, F. D. Eagerton et al., *Science* **1999**, *283*, 57–60.
7. K. Hoshino, T. Saji, *J. Am. Chem. Soc.* **1987**, *109*, 5881–5883.
8. T. Saji, *Chem. Lett.* **1988**, *4*, 693–696.
9. T. Saji, K. Hoshino, Y. Ishii et al., *J. Am. Chem. Soc.* **1991**, *113*, 450–456.
10. T. Saji, K. Ebata, K. Sugawara et al., *J. Am. Chem. Soc.* **1994**, *116*(2), 6053–6054.
11. M. Suzuki, T. Saji, *Denki Kagaku* **1997**, *64*(10), 462–466.
12. K. Hoshino, T. Saji, *J. Chem. Soc. Jpn.* **1990**, *10*, 1014–1019.
13. T. Saji, Y. Ishii, *J. Electrochem. Soc.* **1989**, *136*(10), 2953–2956.
14. T. Saji, *Bull. Chem. Soc. Jpn.* **1989**, *62*, 2992–2994.
15. (a) T. Saji, K. Ebata, K. Sugawara et al., *J. Am. Chem. Soc.* **1994**, *116*, 6053–6054; (b) Y. Ito, T. Saji, *Langmuir* **2002**, *18*, 6633–6636; (c) Y. Kowase, Y. Ito, Y. Okamoto et al., *J. Jpn. Soc. Colour Mater.* **2004**, *77*, 154–157.
16. T. Saji, Y. Igusa, K. Kobayashi et al., *Chem. Lett.* **1995**, *5*, 401–402.
17. K. Hoshino, T. Saji, *Chem. Lett.* **1987**, 1439–1442.
18. T. Saji, unpublished data.
19. N. K. Shrestha, T. Saji, *J. Jpn. Soc. Colour Mater.* **2000**, *73*, 227–233.
20. T. Saji in *Phthalocyanines Properties and Applications* (Eds.: C. C. Leznoff, A. B. P. Lecer), VCH Publishers, New York, 1993, 163–195, Vol. 2.
21. T. Saji, M. Goto, F. Takeo, in *Electrochemistry in Colloids and Dispersions* (Eds.: R. Mackey, J. Texter), VCH Publishers, New York, 1992, pp. 87–94.
22. *Nikkei New Mater.* **1989**, 7, 25.
23. Y. Harima, K. Yamashita, T. Saji, *Appl. Phys. Lett.* **1988**, *52*(18), 1542–1543.
24. N. K. Shrestha, T. Saji, *J. Sur. Fin. Soc. Jpn.* **1995**, *46*(11), 1066–1067.
25. T. Saji, A. Nakane, S. Liu, *J. Sur. Fin. Soc. Jpn.* **1996**, *47*(6), 552–553.
26. Y. Harima, K. Matsumoto, S. Yokoyama et al., *Thin Solid Films* **1993**, *224*, 101.
27. H. Mizuno, K. Hoshino, J. Hanna et al., *Chem. Lett.* **1992**, *5*, 751–754.
28. H. Yamanouchi, T. Saji, *Chem. Lett.* **1996**, *7*, 531–532.

13
Electron Transfer and Transport in Ordered Enzyme Layers

Agnès Anne, Christophe Demaille, Jacques Moiroux, and Jean-Michel Savéant
Laboratoire d'Electrochimie Moléculaire, Université de Paris 7, Paris Cedex 05, France

Christian Bourdillon
Laboratoire de Technologie Enzymatique, Université de Technologie de Compiègne, Compiègne Cedex, France

13.1 Introduction 765

13.2 Catalytic Currents from a Redox Enzyme and a One-electron Mediator in Solution 766
13.2.1 Derivation of the Enzyme Kinetics from Cyclic Voltammetric Experiments 766
13.2.2 Molecular Recognition of an Enzyme by Artificial One-electron Cosubstrates? 772

13.3 Monomolecular Layers of Enzyme 775
13.3.1 Antigen–Antibody Construction of an Immobilized Enzyme Monolayer and Kinetic Analysis of the Enzymatic Catalytic Reaction with the Cosubstrate in Solution 775
13.3.2 Application to the Kinetic Characterization of Biomolecular Recognition 778
13.3.3 Immobilization of Both the Enzyme and the Cosubstrate 784
13.3.4 Electron Transfer and Electron Transport in Integrated Systems . . . 785

13.4 Spatially Ordered Multimonomolecular Layer Enzyme Coatings . . . 789
13.4.1 Step-by-step Antigen–Antibody Construction of Multimonomolecular Layer Enzyme Coatings 789
13.4.2 Reaction Dynamics with the Cosubstrate in Solution: Evidence for Spatial Order 791
13.4.3 Inhibition by products: Proton Gradients 801

Encyclopedia of Electrochemistry. Edited by A.J. Bard and M. Stratmann
Vol. 10 *Modified Electrodes*. Edited by M.Fujihira, I.Rubinstein, and J.F.Rusling
Copyright © 2007 Wiley-VCH Verlag GmbH & Co. KGaA, Weinheim. ISBN: 978-3-527-30402-8

13.5 Perspectives **809**
References 811

13.1 Introduction

Connecting an electrode with a redox enzyme and controlling the dynamics of the resulting system is an important and an actively pursued objective. It indeed allows the transduction of specific chemical events taking place at the prosthetic group of the enzyme into easy-to-use electric signals or, conversely, to trigger and control enzymatic reactions by easy-to-manipulate potential and current variables. Applications may concern biosensors and preparative-scale transformations [1–6].

Although the construction of artificial protein architectures well defined at a molecular level has only been reported recently, enzyme immobilization at electrodes has been extensively investigated during the last 30 years for electrocatalytic purposes. The main steps involved in the evolution of concepts and techniques in the field were as follows.

In first approaches, the electrodes were covered with a polymeric membrane of macroscopic size, the enzymes being embedded within the porous matrix [1, 7, 8]. Such thick films are often unduly referred to as *multilayered films*. In fact, there are no distinct layers in these films, whose thickness is usually larger than 10 μm. The main immobilization procedures were entrapment in organic gels or sol gels and cross-linking by means of bifunctional reagents like glutaraldehyde, adsorption, ionic exchange, or covalent binding onto the inert matrix. Several drawbacks have been met with the resulting structures: deactivation and/or leak of the enzyme and large diffusion barriers both for the electron carriers and the substrates. Also, the thickness of the membrane is generally too large to allow an adequate optimization of the coupling between the enzyme activity and the electrochemical reaction even if the mediator shuttling the electrons between the electrode and the enzyme sites is free to move through the structure.

A second contemporary approach used the chemical modified electrode technology [9, 10] with covalent linking of the enzyme onto the electrode surface. One such approach consisted in strong oxidation of carbon surfaces so as to generate the maximal amount of carboxylic groups to be used for the formation of peptide bonds with accessible amino groups of the enzyme [11–13]. High catalytic current densities may thus be obtained with soluble mediators. The main disadvantage of such procedures is the existence of large background currents resulting from the strong oxidative treatment of the surface and the difficulty in controlling the amount

Encyclopedia of Electrochemistry. Edited by A.J. Bard and M. Stratmann
Vol. 10 *Modified Electrodes*. Edited by M.Fujihira, I.Rubinstein, and J.F.Rusling
Copyright © 2007 Wiley-VCH Verlag GmbH & Co. KGaA, Weinheim. ISBN: 978-3-527-30402-8

of enzyme grafted onto the electrode surface. Grafting of appropriately substituted phenyl radicals onto carbon surface by electrochemical reduction of the parent diazonium cations, followed by coupling of the substituent with the enzyme, is an alternative surface derivatization strategy [14]. Unfortunately, only a small percentage of the enzyme survives the attachment procedure.

If the presence of a soluble mediator shuttling the electrons between the electrode and the enzyme is to be avoided, other modes of "wiring" [15] the enzyme to the electrode ought to be sought after. One may think of direct electron transfer between the electrode and the enzyme at the adsorbed state. It has indeed been shown that small redox proteins, such as cytochrome *c* or ferredoxins may show an unmediated reversible electrochemical response when the electrode surface is adequately prepared [16–19]. There have been few reports of direct electron transfer with redox enzymes [20, 21]. With flavoenzymes, the observed signals are likely to be those of the free flavin deriving from the denaturation of the enzyme [21]. The high probability of denaturation of the adsorbed enzyme prevents the viability of this mode of electron transport in most cases.

"Wiring" [15] was thus rather performed by means of immobilized redox centers [22, 23], the connection between them and the electrode and between them and the enzyme involving electron hopping [24, 25] between adjacent electron donor/electron acceptor moieties. Other wiring systems have been used such as redox hydrogels [15, 26, 27], conducting salts [28, 29], and functionalized polypyrroles [30–34]. It is noteworthy that the polypyrrole films thus built are, in most cases, not used within their range of electronic conductivity and that the presence of an additional redox electron shuttle is required.

Molecular recognition between biomolecules is another strategy that has been used to deposit assemblies of redox enzyme on electrodes. It has led to the construction of true monomolecular layers and of spatially defined multimonomolecular structures. The dynamics of these systems has been fully characterized and the activity of the deposited enzyme tested quantitatively, which has been very seldom the case with the systems depicted in the preceding text. For this reason, the following sections focus on these structures. Besides describing the construction procedures, emphasis is laid on the detailed analysis of the catalysis responses and on the mechanisms it allows one to uncover. As a prelude to such kinetic analyses, the catalytic responses of a redox enzyme with a one-electron mediator in solution are first examined.

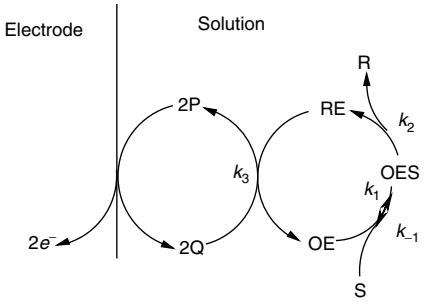
13.2 Catalytic Currents from a Redox Enzyme and a One-electron Mediator in Solution

13.2.1 Derivation of the Enzyme Kinetics from Cyclic Voltammetric Experiments

For the sake of simplicity, we consider an enzymatic reaction where the Michaelis–Menten kinetics involves only the oxidized form of the enzyme as sketched in Sch. 1. As is often the case with redox enzymes, two electrons are exchanged in the reaction of the enzyme with one-electron cosubstrates. The subsequent analysis may be adapted with no difficulty to other reaction schemes.

Taking as example glucose oxidase with a ferricenium/ferrocene couple serving as

Scheme 1



S: substrate, R: product,
OE: oxidized form of the enzyme,
OES: its complex with the substrate,
RE: reduced form of the enzyme,
P: reduced form of the mediator (cosubstrate),
Q: oxidized form of the mediator (cosubstrate).

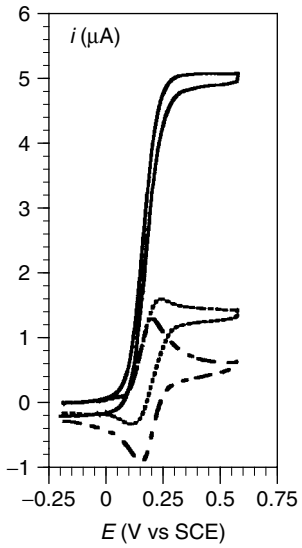


Fig. 1 Cyclic voltammetry of the catalysis of the electrochemical oxidation of β-D-glucose by glucose oxidase with ferrocene methanol as the cosubstrate. Dashed line: ferrocene methanol (0.1 M) alone; the same trace is obtained in the presence of glucose oxidase (27 μM) with no glucose present or in the presence of glucose (0.5 M) with no glucose oxidase present. Dotted and full lines: ferrocene methanol (0.1 mM) + glucose oxidase(27 μM) + glucose (0.5 M) at pH 4.5 (acetate buffer) and 6.5 (phosphate buffer), respectively. Ionic strength: 0.1 M. Scan rate: 0.08 V sec^{-1}. 0.07 cm^2 glassy carbon disk electrode. Temperature: 25 °C.

cosubstrate, Fig. 1 shows a typical cyclic voltammetric response obtained in the presence of glucose and of ferrocene methanol [35, 36]. Starting from the reversible wave of the cosubstrate, the addition of glucose oxidase and glucose to the solution results in an increase of the anodic current, a loss of reversibility of the wave, which takes a plateau shape typical of a catalytic process [37] in which the mediator is regenerated as a result of the enzymatic reaction.

The catalytic responses may be analyzed in more details by extension of previous treatments of cyclic voltammetric catalytic currents [37, 38] so as to dispose of a tool to be used for extracting the pertinent rate constants from the experimental data. The two members of the cosubstrate couple, P and Q, diffuse to and from

the electrode, while participating in the enzymatic reaction. It follows that, in the framework of the linear diffusion approximation, the concentrations of P and Q obey the following partial derivative equations.

$$\frac{\partial[\mathrm{P}]}{\partial t} = D\frac{\partial^2[\mathrm{P}]}{\partial x^2} + 2k_3[\mathrm{RE}][\mathrm{Q}] \quad (1)$$

$$\frac{\partial[\mathrm{Q}]}{\partial t} = D\frac{\partial^2[\mathrm{Q}]}{\partial x^2} - 2k_3[\mathrm{RE}][\mathrm{Q}] \quad (2)$$

with the following relations:
for $t = 0, x \geq 0$ (initial conditions) and for $x = \infty, t \geq 0$ (bulk of the solution):

$[\mathrm{P}] = C_\mathrm{P}^0$, $[\mathrm{Q}] = 0$ (C_P^0: total concentration of cosubstrate introduced into the solution) and, for $x = 0, t \geq 0$ (electrode surface):

$$[\mathrm{P}] = [\mathrm{Q}]\exp\left[-\frac{F}{RT}\left(E - E_{\mathrm{P/Q}}^0\right)\right] \quad (3)$$

(Nernst law, expressing the equilibrium at the electrode surface, $E_{\mathrm{P/Q}}^0$: standard potential of the cosubstrate)

$$\frac{i}{FSD} = \left(\frac{\partial[\mathrm{P}]}{\partial x}\right)_{x=0} = -\left(\frac{\partial[\mathrm{Q}]}{\partial x}\right)_{x=0} \quad (4)$$

(conservation of the mass fluxes at the electrode, i: current flowing through the electrode, S: electrode surface area, D: diffusion coefficient, assumed to be the same for P and Q).

It should also be taken into account that the electrode potential is scanned linearly with a scan rate v, starting from a potential, E_i:

$$E = E_\mathrm{i} + vt \quad (5)$$

and then back, at the same rate, after inversion at a potential E_f:

$$E = 2E_\mathrm{f} - E_\mathrm{i} - vt \quad (6)$$

It follows that the sum of the P and Q concentrations is constant throughout the diffusion layer at any time:

$$[\mathrm{P}] + [\mathrm{Q}] = C_\mathrm{P}^0 \quad (7)$$

Applying the steady-state approximation to the various forms of the enzyme leads to

$$[\mathrm{RE}] = \frac{C_\mathrm{E}^0}{k_3[\mathrm{Q}]\left(\dfrac{1}{k_3[\mathrm{Q}]} + \dfrac{1}{k_2} + \dfrac{1}{k_\mathrm{red}C_\mathrm{S}^0}\right)}$$

$$\text{with } k_\mathrm{red} = \frac{k_1k_2}{k_{-1} + k_2} \quad (8)$$

(C_E^0: total concentration of enzyme, C_S^0: bulk concentration of glucose, glucose is assumed to be present in excess).

We may thus formulate the diffusion-reaction problem by a set of dimensionless equations in which only the species Q is involved, namely:

$$\frac{\partial q}{\partial \tau} = \frac{\partial^2 q}{\partial y^2} - \frac{\lambda q}{1 + \sigma q} \quad (9)$$

with $q_{y\geq 0,\tau=0} = q_{y=\infty,\tau\geq 0} = 0$, $q_{y=0,\tau\geq 0} = 1/[1 + \exp(-\xi)]$

$\tau = Fv/RT$ is a dimensionless time variable, the timescale of the experiment being controlled by the scan rate v.

$\xi = (F/RT)(E - E_{\mathrm{P/Q}}^0)$ is a dimensionless potential variable, taking as origin the standard potential of the cosubstrate couple. $u = -(F/RT)(E_\mathrm{i} - E_{\mathrm{P/Q}}^0)$ defines the location of the starting potential on the ξ scale. In practice, the scan starts before the foot of the wave so as to render the current–potential response independent of the exact value of E_i ($u \to \infty$).

$y = x\sqrt{(Fv/DRT)}$ is a dimensionless space variable, normalized against the thickness of the diffusion layer which is a function, not only of the diffusion coefficient but also of the scan rate (the larger the scan rate, the larger the diffusion rate, the thinner the diffusion layer).

$q = [Q]/C_P^0$ is a dimensionless expression of the concentration of the oxidized form of the cosubstrate, normalized against the cosubstrate bulk concentration. It varies between 0 and 1 throughout the diffusion layer, its value at the electrode surface reaching 1 when the potential is made more positive than the cosubstrate standard potential.

The current flowing through the electrode may be derived from the gradient of q at the electrode surface:

$$i = FSC_P^0\sqrt{\frac{DFv}{RT}}\left(\frac{\partial q}{\partial y}\right)_{y=0} \qquad (10)$$

The kinetics of the enzymatic reaction is reflected in the current–potential response through two dimensionless parameters.

$$\lambda = \frac{2k_3C_E^0}{v}\frac{RT}{F} \quad \text{and}$$
$$\sigma = k_3C_P^0\left(\frac{1}{k_2} + \frac{1}{k_{red}C_S^0}\right) \qquad (11)$$

In all the cases, the current–potential curves tend toward a plateau as the potential becomes more and more positive. For small values of λ, the plateau is preceded by a peak, which eventually disappears as λ increases (Fig. 1). The anodic trace is then S-shaped and the reverse trace is superimposed on the forward trace (the curve obtained at pH 6.5 in Fig. 1 is close to this situation). Conversely, the plateau height becomes less and less as compared to the peak height as λ decreases.

The very fact that a plateau is reached implies that a steady state has been reached by mutual compensation of the catalytic reaction and diffusion. Under these conditions, $\partial q/\partial\tau = 0$ in Eq. (9), which may then be integrated, leading to the following closed-form expression of the plateau current.

$$\frac{i_{plateau}}{i_p^0} = \frac{\sqrt{\lambda}}{0.446}\sqrt{\frac{2}{\sigma}\left[1 - \frac{1}{\sigma}\ln(1+\sigma)\right]} \qquad (12)$$

$$i_p^0 = 0.446FSC_P^0\sqrt{\frac{DFv}{RT}} \qquad (13)$$

being the peak current of the cosubstrate alone and thus

$$i_{plateau} = FS\sqrt{D}C_P^0\sqrt{2k_3C_E^0} \times \sqrt{\frac{2}{\sigma}\left[1 - \frac{1}{\sigma}\ln(1+\sigma)\right]} \qquad (14)$$

showing that the plateau current is independent of the scan rate. It is proportional to the cosubstrate concentration and to the square root of the enzyme concentration. The concentration profile of Q is confined, at the level of the plateau current, within a reaction layer, the thickness of which, μ, may be derived from the above expression of the plateau current:

$$\mu = \sqrt{\frac{D}{2k_3C_E^0}}\frac{1}{\sqrt{\frac{2}{\sigma}\left[1 - \frac{1}{\sigma}\ln(1+\sigma)\right]}} \qquad (15)$$

In the experiments summarized in Fig. 1, the thinnest reaction layer, which corresponds to the largest plateau current, is of the order of 20 μm, that is, ca 2000 times the size of the enzyme, indicating that such experiments sense enzymes dispersed in the solution rather than a layer of enzyme confined onto the electrode surface. The peak current increases with the scan rate up to a situation where the plateau current becomes negligible (under these conditions, the current response is governed solely by diffusion, the enzymatic reaction being too slow to compete).

One could analyze the experimental data through the plateau current but this strategy would restrict artificially the range of applicability of the method, especially for slow catalytic reactions for which the peak current is a more revealing quantity. The variations of the ratio i_p/i_p^0 (where i_p is the peak current if there is a peak and the plateau current if the peak has vanished into a plateau) with the two parameters λ and σ may be obtained by finite difference resolution of Eq. (9) with the attending initial and boundary conditions. They are summarized in Fig. 2.

When $\lambda \to \infty$, that is, when reaction (3) is fast when compared to diffusion, the peak vanishes and the plateau current is proportional to $\sqrt{\lambda}$ (Eq. 12) and is independent of the scan rate (Eq. 14). If, in addition, $\sigma \to 0$, then

$$\frac{i_p}{i_p^0} = \frac{i_{plateau}}{i_p^0} = \frac{\sqrt{\lambda}}{0.446}, \qquad \text{that is,}$$

$$i_p = i_{plateau} = FS\sqrt{D}C_P^0\sqrt{2k_3C_E^0} \quad (16)$$

This situation ($\lambda \to \infty$, $\sigma \to 0$) is usually designated as "first-order conditions", in the sense that the plateau current is proportional to the cosubstrate bulk concentration.

If $\sigma \to 0$, but λ has no extreme value, Eq. (9) simplifies into

$$\frac{\partial q}{\partial \tau} = \frac{\partial^2 q}{\partial y^2} - \lambda q \quad (17)$$

a linear equation, which can be integrated, leading together with the attending initial and boundary conditions to a closed-form expression of the current–potential curve [38], from which the limiting curve $\sigma = 0$ in Fig. 2 may be derived.

Figure 3 illustrates, with the example of glucose oxidase, glucose, and ferrocene methanol, as enzyme, substrate, and cosubstrate respectively, the procedure for extracting the kinetic parameters of the catalytic enzymatic reaction from the peak, or plateau, current data. The normalized peak (or plateau) current, i_p/i_p^0, varies with the scan rate and the cosubstrate concentration. The experimental variation, at a high glucose concentration (0.5 M), displayed in Fig. 3(a) follows the predicted behavior sketched in Fig. 2. In particular, we see that a first-order behavior is followed for the smallest two values of the cosubstrate concentration indicating that σ (Eq. 11) is vanishing for these two concentrations. A significant deviation from the first-order behavior is observed for the largest value of C_P^0, 100 µM. Application of Eq. (14) to the first-order

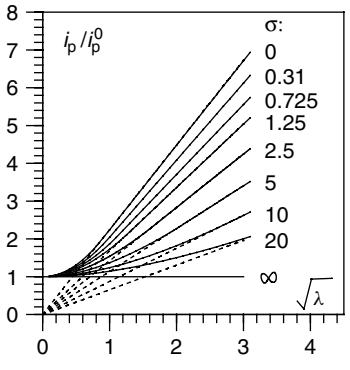


Fig. 2 Cyclic voltammetric analysis of enzymatic catalytic currents obtained with a reaction scheme of the type shown in Sch. 1. Variation of the normalized peak or plateau current (peak current when there is a peak, plateau current, when the peak has vanished into a plateau) with the two kinetic parameters λ and σ (full lines). Dotted lines: asymptotic behavior for $\lambda \to \infty$ (the wave is then plateau-shaped).

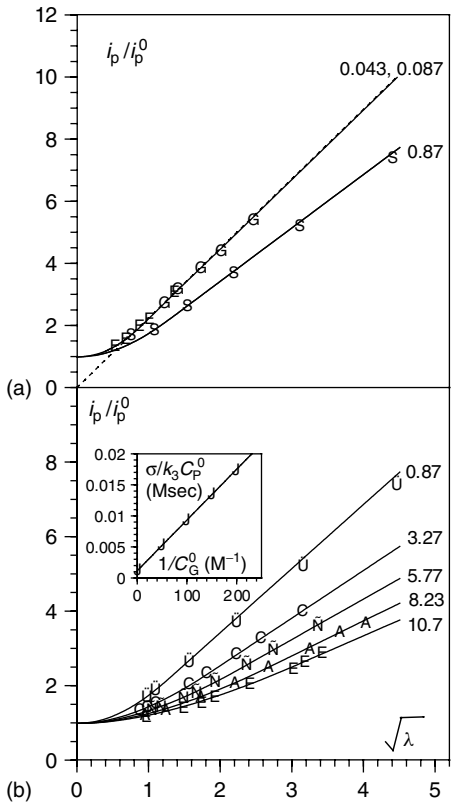


Fig. 3 Cyclic voltammetric analysis of the kinetics of an homogeneous redox enzyme reaction using a reversible one-electron mediator as the cosubstrate, taking as example the catalysis of the electrochemical oxidation of β-D-glucose by glucose oxidase (6.5 μM) with ferrocene methanol as the cosubstrate at pH = 7 (ionic strength 0.1 M, temperature: 25 °C). (a) Variation of the normalized plateau or peak current with the scan rate and the cosubstrate concentration (E: 5, G: 10, S: 100 μM), for $C_G^0 = 0.5$ M, leading to the determination of k_3. (b) Variation of the normalized plateau with the scan rate and the glucose concentration for a cosubstrate concentration of 0.1 mM, leading to the determination of $\sigma/k_3C_P^0$ as a function of glucose concentration. The resulting $\sigma/k_3C_P^0$ versus $1/C_G^0$ plot (inset) is linear. Its intercept gives $1/k_2$ and its slope, k_{red}. The number on each curve is the value of σ.

behavior in Fig. 3 leads to the value of k_3, 6×10^6 M^{-1} sec^{-1}. Knowing k_3, the experiments, shown in Fig. 3(b), where the normalized peak (or plateau) current is measured as a function of the glucose concentration, allow the determination of the factor $\sigma/k_3C_P^0$ as a function of $1/C_G^0$. From the intercept and slope of the straight line thus obtained, one derives $k_2 = 780$ sec^{-1} and $k_{red} = 1.2 \times 10^4$ M^{-1} sec^{-1}. The values of σ reported in Fig. 3(a) and (b) illustrate how an increase in the cosubstrate concentration and a decrease in glucose concentration enhance the deviation from first-order conditions. Application of Eq. (9) when the first-order conditions are not fulfilled may lead to serious errors, to the point of missing the variation of the rate constant k_3 with pH [39, 40], as discussed in the next section.

Another source of inaccuracy, or even error, originates in the assumption sometimes made [41] that the plateau current is proportional to the homogeneous rate of the enzymatic reaction, thus obeying the Lineweaver–Burk law [42]:

$$\frac{1}{\text{rate}} = \frac{1}{2k_2C_E^0} + \frac{1}{2k_{red}C_E^0C_P^0} \qquad (18)$$

The real $1/i_p$ versus $1/C_P^0$ plots are not straight lines but curves going through the origin (Fig. 4). The slope and intercept of the approximate straight line drawn through the experimental points do not therefore have the meaning suggested by Eq. (18).

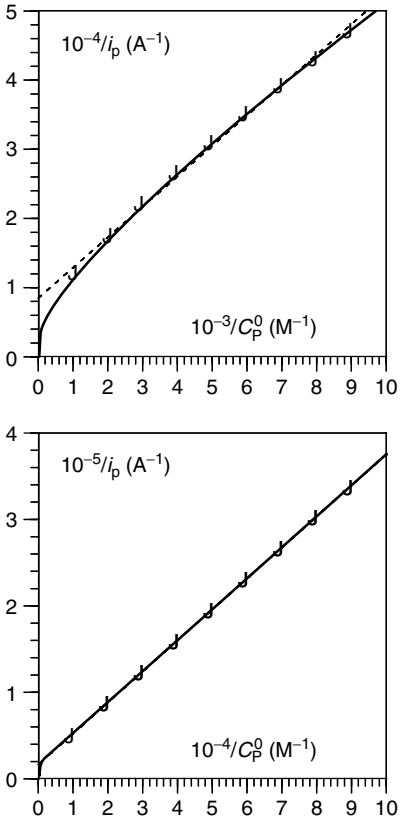


Fig. 4 An example showing the erroneous application of Lineweaver–Burk law (Eq. 8) (dotted line) to plateau current data corresponding to $k_2 = 780\ sec^{-1}$, $k_{red} = 1.2 \times 10^4\ M^{-1}\ sec^{-1}$, $k_3 = 6 \times 10^6\ M^{-1}\ sec^{-1}$, $C_E^0 = 2.7\ \mu M$, $C_G^0 = 0.05$ M, electrode surface area: 0.2 cm^2, diffusion coefficient of the cosubstrate: $6.7 \times 10^{-6}\ cm^2\ sec^{-1}$. The full line represents the rigorously predicted variation of $1/i_p$ with $1/C_P^0$.

13.2.2
Molecular Recognition of an Enzyme by Artificial One-electron Cosubstrates?

Repeat of the same kind of experiments at other pHs shows that the rate constant k_3 varies with pH in a sigmoid manner, as shown in Fig. 5 (whereas k_2 and k_{red} are practically insensitive to this factor). Figure 5 also displays the pH-dependent values of k_3 obtained with other cosubstrates than ferrocene methanol [35, 36]. The dependency of k_3 upon pH is due to the fact that, as with many redox enzymes, the prosthetic group of glucose oxidase does not merely exchange electrons with the cosubstrate but both electrons and protons. Analysis of the variation of k_3 with pH by means (Fig. 3) of Eq. (1) is thus an example of the general procedures that may be followed to uncover the role of protons. The redox and proton transfer reactions undergone by the flavin prosthetic group are summarized in Sch. 2 [35, 36]. The vertical reactions are oxidations by Q regenerating P. From the values (V versus SCE (saturated calomel electrode)) of the standard potentials of the four flavin redox couples [43–47], which are involved in Sch. 2 and those of the mediators (Table 1), all four oxidation steps may be regarded as irreversible. The horizontal reactions are deprotonations by the bases present in the buffer. From the pK_a values of the various flavin acid–base couples indicated in Sch. 2 (over or below the horizontal arrows) [43–47], reactions H2 and H4 may be regarded as irreversible and reactions H1 and H3 as reversible in the pH range of interest (4–8.5). Experiments where the concentration of the buffer was varied showed that reactions H1 and H3 remain at equilibrium. The rate constant k_3 is thus related to the various steps of Sch. 2 according to Eq. (19).

$$\frac{1}{k_3} = \frac{1 + \dfrac{K_{a,H1}}{[H^+]}}{k_{E1} + \dfrac{K_{a,H1}}{[H^+]}k_{E2}} + \frac{1 + \dfrac{K_{a,H3}}{[H^+]}}{k_{E3} + \dfrac{K_{a,H3}}{[H^+]}k_{E4}} \tag{19}$$

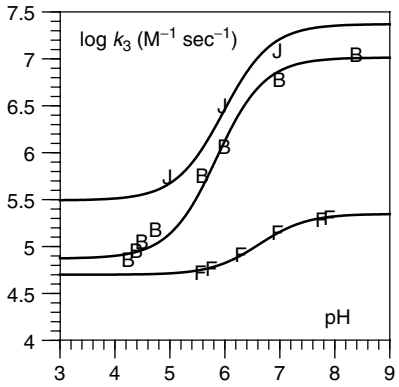
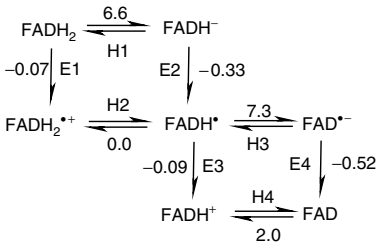


Fig. 5 Effect of changing the cosubstrate and the pH on the kinetics of an homogeneous redox enzyme reaction as exemplified by the electrochemical oxidation of glucose by glucose oxidase mediated by one-electron redox cosubstrates, ferricinium methanol (B), + ferricinium carboxylate (J),(dimethylammonio) ferricinium (F). Variation of the rate constant, k_3, with pH. Ionic strength: 0.1 M. Temperature: 25 °C.



Scheme 2 Various oxidized and reduced forms of the flavin prosthetic group.

E, s: electron transfer steps, H, s: proton transfer steps
The numbers on the vertical arrows are the standard potentials,
The numbers on the horizontal arrows are the *pKa*, s.

Fitting of the data points with Eq. (19) leads to the sigmoid lines in Fig. 4. The two limiting values of k_3, in acid and basic media, k_{ac} and k_{bas}, respectively, depend on the individual rate constants according to

$$\frac{1}{k_{ac}} = \frac{1}{k_{E1}} + \frac{1}{k_{E3}} \qquad \frac{1}{k_{bas}} = \frac{1}{k_{E2}} + \frac{1}{k_{E4}} \tag{20}$$

This detailed kinetic analysis is the typical procedure to be followed for dissecting a $-2e^- - 2H^+$ process into its electron and proton transfer elementary steps. In the present case, the electron-transfer steps are rate determining. A striking observation, which may be of general relevance to the reactions of oxidases, is that, owing to the use of artificial cosubstrates, the maximal activity of the flavin enzyme is reached above pH 8, whereas it appears around pH 5.5 with dioxygen [48].

Further insights into the reactivity of the artificial cosubstrates toward the various forms of the prosthetic group are provided by a comparison of the rate constants with the driving forces (Table 1). There is no parallelism between the kinetics and the driving forces such as the one predicted by a Marcus-type relationship (the larger the driving force, the faster the reaction) [49, 50]. In an acidic medium, where $FADH_2$ reacts under its neutral form, the rate constant is almost independent of the driving force. In a basic medium, where the reacting species is the $FADH^-$ ion, the same lack of correlation is observed. The neutral ferricinium carboxylate reacts with

Tab. 1 Thermodynamics and kinetics of the rate-determining steps

	Single-electron cosubstrates					
	Ferrocene methanol		***Ferrocene carboxylate***		***(Dimethylamino)-methylferrocene***[b]	
Standard potential[a]	0.19		0.29		0.37	
Acid medium	E1	E3	E1	E3	E1	E3
Standard free energy [eV]	−0.26	−0.28	−0.36	−0.38	−0.44	−0.46
$K_A K_E / K_B$	2.2×10^4	4.6×10^4	1.0×10^6	2.2×10^6	2.2×10^7	4.6×10^7
log k_{ac} [M^{-1} sec^{-1}]	5.1		5.0		5.7	
Basic medium	E2	E4	E2	E4	E2	E4
Standard free energy [eV]	−0.52	−0.71	−0.62	−0.81	−0.70	−0.289
$K_A K_E / K_B$	4.6×10^8	6.8×10^{11}	2.2×10^{10}	3.2×10^{13}	4.6×10^{11}	6.8×10^{14}
log k_{bas} [M^{-1} sec^{-1}]	7.4		5.6		7.7	

[a] V versus SCE.
[b] Protonated form.

approximately the same rate constant as in an acidic medium. In contrast, the positively charged ferricinium methanol and [(dimethylamino)methyl]ferricinium react about 100 times faster than in an acidic medium. In all the cases, the rate constant is much below the diffusion limit (5×10^8 M^{-1} sec^{-1}).

The X-ray crystal structure of glucose oxidase [51, 52] shows that the flavin sits at the bottom of a funnel-shaped pocket with an opening of ca 10 Å diameter at the surface of the proteinic core and a depth of ca 10 Å. The ferricinium cosubstrates may thus experience some difficulty reaching a position geometrically suitable for efficient electron transfer. Combination of the kinetic and structural observations suggests a mechanism in which any of the four electron transfers may be decomposed into three successive steps, diffusion of Q toward the opening of the pocket at the surface of the protein core of the enzyme, displacement toward the flavin in a position geometrically suited for electron transfer, and electron transfer [53]. Each of the electron-transfer steps is neither controlled by the rate of electron transfer nor by the diffusive approach of the one-electron cosubstrate toward the opening of the pocket at the surface of the protein core of the enzyme. The rate-determining factor appears to be the sterically hindered, positioning appropriately for electron transfer to occur. The kinetics thus reveals some molecular recognition between the artificial one-electron cosubstrates by the enzyme. Recent experiments, using the two enantiomers of protonated *N*,*N*-dimethyl-1-ferrocenylethylamine, reported a significant chiroselectivity of the reaction [41], implying a very precise molecular recognition. However, further attempts to reproduce these results were unsuccessful, the two enantiomers giving rise to the same catalytic response within experimental uncertainty [53]. Thus, molecular recognition is not precise enough to allow chiroselective electron transfer. Molecular recognition rather works in a rejection

mode: steric hindrance in the pocket connecting the prosthetic group to the enzyme surface slows electron transfer, offering some resistance against a largely favorable driving force. One important parameter of the recognition mechanism is the charge borne by the oxidized form of the cosubstrate. The resulting rate constants, nevertheless, remain large, allowing ferricinium ions to act as quite efficient cosubstrates. It would be interesting to test the generality of such behavior of redox enzymes toward artificial cosubstrates.

It is worth emphasizing that electrochemical techniques, such as cyclic voltammetry, allow the use of a large variety of artificial cosubstrates, since, unlike stopflow techniques, the active form of the cosubstrate need not be chemically stable. It suffices that the cosubstrate reacts with enzyme faster than any other species present in the solution.

13.3 Monomolecular Layers of Enzyme

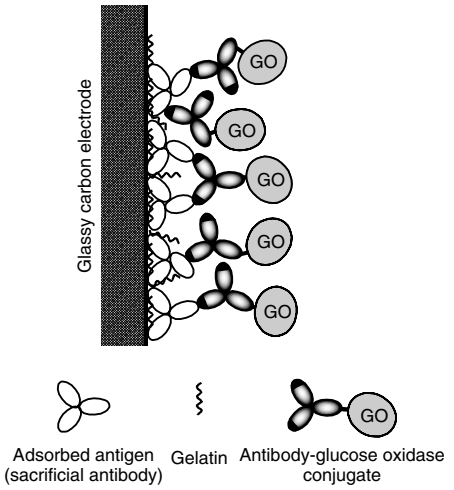
Direct adsorption of the enzyme on an electrode very often results either in no catalytic current at all or to unstable currents. For example, adsorption of glucose oxidase on a glassy carbon electrode does not produce any catalytic current. Either adsorption is too weak or it denaturates the enzyme, as it does, for example, on gold [54]. Chemical immobilization techniques [11, 14, 55, 56] also suffer the danger of enzyme denaturation. Strategies based on biomolecular recognition, involving antigen–antibody or avidin–biotin interactions, have been successful in the construction of fully active monomolecular enzyme layers on electrode surfaces. The description of these strategies is the object of the present section. The systems thus built may then be characterized kinetically using a cosubstrate dispersed in the solution. This characterization is particularly important for determining how much of the enzyme has survived the attachment procedure, an essential criteria for appreciating its suitability. The same experimental configuration may also be used for measuring the kinetics of the molecular recognition between an immobilized antigen and an antibody dispersed in the solution. Previous attempts to derive this precious kinetic information have faced the difficulty of freeing the overall response from the contribution of diffusion. Enzymatic labeling of the solute allows the use of the attending kinetic amplification to work out the problem.

There is a quest for more integrated systems in which not only the enzyme but also the mediator is immobilized on the electrode surface. Two approaches have been followed for this purpose. One uses antigen–antibody immobilization of the enzyme, while the second relies on the avidin–biotin interaction. In both cases, the cosubstrate is linked to one end of a long polyethyleneglycol chain attached to the structure by its other end.

13.3.1 Antigen–Antibody Construction of an Immobilized Enzyme Monolayer and Kinetic Analysis of the Enzymatic Catalytic Reaction with the Cosubstrate in Solution

An example of a monomolecular layer electrode coating obtained by this technique is sketched in Sch. 3. Adsorption of rabbit IgG is followed by adsorption of gelatin and specific binding of a glucose oxidase conjugated antibody [57].

Cyclic voltammetry allows a precise kinetic characterization of such systems starting from the observation of catalytic



Scheme 3 Antigen–antibody construction of a monolayer enzyme electrode: the adsorbed rabbit IgG (antigen) is coupled with a glucose oxidase conjugated antibody, the antirabbit IgG (whole molecule) produced in goats.

responses (Fig. 6a) [57]. The catalytic reaction is still as represented in Sch. 1 but we now have to take into account that the enzyme is confined in a monolayer onto the electrode surface rather then homogeneously dispersed as it was in the earlier sections. It follows that Eqs (1) and (2) do not describe the variations of the P and Q concentrations with time and space any longer. They should be replaced by the simpler Eqs (21) and (22) expressing that both P and Q merely diffuse in the solution without being engaged in any chemical reaction.

$$\frac{\partial[\mathrm{P}]}{\partial t} = D\frac{\partial^2[\mathrm{P}]}{\partial x^2} \qquad (21)$$

$$\frac{\partial[\mathrm{Q}]}{\partial t} = D\frac{\partial^2[\mathrm{Q}]}{\partial x^2} \qquad (22)$$

Instead, the catalytic reaction takes place at the surface of the electrode leading to the expression of the current given in Eq. (23)

$$\frac{i}{FS} = D\left(\frac{\partial[\mathrm{P}]}{\partial x}\right)_{x=0} + 2Fk_3\Gamma_{\mathrm{RE}}[\mathrm{Q}]_{x=0}$$
$$= -D\left(\frac{\partial[\mathrm{Q}]}{\partial x}\right)_{x=0} + 2Fk_3\Gamma_{\mathrm{RE}}[\mathrm{Q}]_{x=0} \qquad (23)$$

(Γ_{RE}: surface concentration of RE), the initial and boundary conditions being the same as in the homogeneous case, in particular, the Nernst law, Eq. (3) still applies), we find again that the surface concentration of Q is given by

$$[\mathrm{Q}]_{x=0} = \frac{C_{\mathrm{P}}^0}{1 + \exp\left[-\dfrac{F}{RT}(E - E^0)\right]} \qquad (24)$$

and that the diffusion contribution to the current (first term in Eq. 23) has the same expression as a diffusion-controlled Nernstian response, i_{dif}, as represented by the dotted line in Fig. 6(a). The second term in Eq. (23),

$$i_{\mathrm{cat}} = 2Fk_3\Gamma_{\mathrm{RE}}[\mathrm{Q}]_{x=0} \qquad (25)$$

represents the contribution of the enzymatic catalysis. It can be obtained straightforwardly by subtraction of i_{dif} from the total current. Assuming that the three forms, OE (oxidised form of the enzyme), OES (its complex with substrate), and RE (reduced form of the enzyme) obey the steady-state approximation in the surface layer, i_{cat} may be expressed as follows,

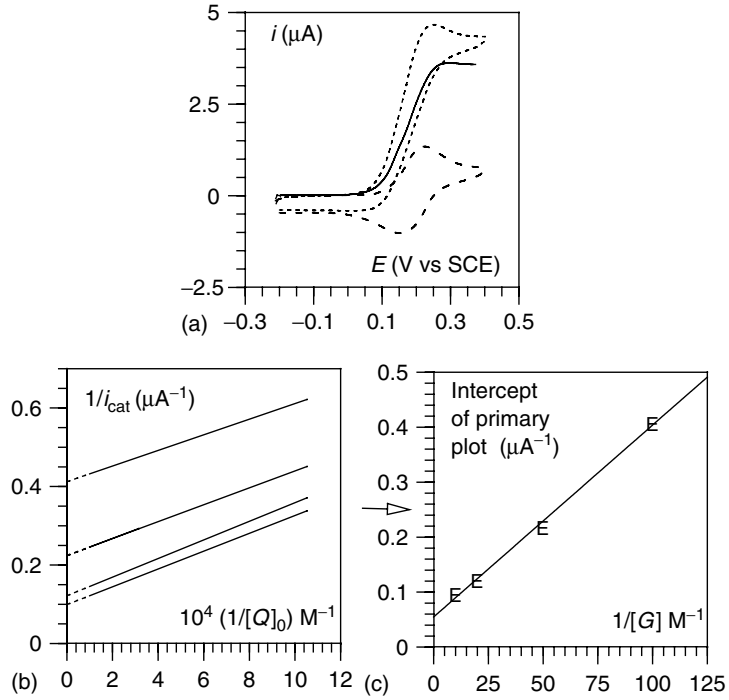


Fig. 6 Cyclic voltammetric analysis of the kinetics of an electrode coated with antigen–antibody immobilized monomolecular layer of redox enzyme with a one-electron reversible cosubstrate in the solution. (a) Cyclic voltammetry at saturation coverage (2.6×10^{-12} mol cm^{-2}) of glucose oxidase with 0.1 M glucose and 0.1 mM ferrocenemethanol in a pH 8 phosphate buffer (0.1 M ionic strength). The dotted and dashed lines represent the cyclic voltammogram (0.04 V sec^{-1}) in the absence and presence of glucose (0.1 M), respectively. The full line represents the catalytic contribution to the current, i_{cat} (see text). (b) Primary plots obtained under the same conditions with, from top to bottom, 0.01, 0.02, 0.05, and 0.1 M glucose. (c) Secondary plot derived from the intercepts of the primary plots in (b).

when the substrate, S, is in large excess.

$$i_{cat} = \frac{2Fk_3\Gamma_E^0[Q]_{x=0}}{1 + k_3[Q]_{x=0}\left(\frac{1}{k_2} + \frac{1}{k_{red}[S]}\right)} = \frac{2Fk_3\Gamma_E^0 C_P^0}{1+\exp\left[-\frac{F}{RT}(E-E^0)\right] + k_3 C_P^0\left(\frac{1}{k_2}+\frac{1}{k_{red}[S]}\right)} \quad (26)$$

(Γ_E^0 is the total surface concentration of enzyme). We may note that i_{cat} is predicted to be independent of the scan rate, a criterion worth checking when extracting i_{cat} from the raw data.

Another useful feature of i_{cat} is its proportionality to the total surface concentration of enzyme Γ_E^0. The progressive increase in the enzyme content of the coating upon increasing the time of exposure of the electrode to

the solution containing the enzyme conjugated antibody may thus be simply monitored by following the increase in i_{cat} until saturation is reached.

Equation (26), or its inverse form, (27), may also be exploited to derive

$$\frac{1}{i_{cat}} = \frac{1}{2Fk_3\Gamma_E^0}\frac{1}{[Q]_{x=0}} + \frac{1}{2F\Gamma_E^0}\left(\frac{1}{k_2} + \frac{1}{k_{red}[S]}\right) \quad (27)$$

the pertinent rate constants from the data according to the procedure summarized in Fig. 6. As far as the effect of the cosubstrate concentration is concerned, one may use the plateau current, where $[Q]_{x=0} = C_P^0$, and perform a series of experiments with several different values of the bulk concentration of mediator C_P^0. A simpler procedure consists in taking advantage of the concentration of Q at the electrode surface, Q being a known function of the electrode potential (when the P/Q couple obeys the Nernst law), as depicted in Fig. 6(b). Repeating the procedure for several values of the substrate concentration leads to a series of primary plots having the same slope from which the parameter $k_3\Gamma_E^0$ may be derived (3.4×10^{-2} cm sec^{-1}, in the present case). Plotting the intercepts of these primary plots against the inverse of the substrate concentration leads to secondary plots, which obey the following equation:

$$\frac{1}{i_{cat}} = \frac{1}{2F\Gamma_E^0}\left(\frac{1}{k_2} + \frac{1}{k_{red}[S]}\right) \quad (28)$$

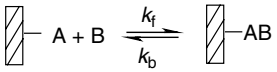
from the intercept and slope of which k_2 and k_{red} (600 sec^{-1}, 0.9×10^4 M^{-1} sec^{-1}, respectively) may be obtained. It is remarkable that these values are the same, within experimental error, as in homogeneous experiments [35, 48].

A way of estimating to what extent the immobilization procedure may affect the catalytic activity of the enzyme may be derived from the foregoing analysis in combination with an independent determination of the total amount of enzyme, active and inactive, contained in the coating. Radioactive labeling may be used for this purpose as was done with glucose oxidase leading to a value of 2.6×10^{-12} mol cm^2 [57]. The fact that using this estimate and the previously determined value of $k_3\Gamma_E^0$, one obtains a value of k_3, 1.3×10^7 M^{-1} sec^{-1}, which is the same as the homogeneous value leads to the conclusion that all the enzyme deposited is active, confirming the expectation that antigen–antibody approaches should be much milder than chemical procedures.

13.3.2 Application to the Kinetic Characterization of Biomolecular Recognition

Determining the thermodynamics and kinetics of recognition between biomolecules, particularly when one of the two is immobilized on a substrate, arouses considerable current interest as, for example, antibody–antigen recognition, recognition of single-stranded DNA oligonucleotides by partially or totally complementary DNA strands. The determination of the thermodynamic and kinetic parameters of interest requires the monitoring of the surface concentration of the binding molecule. Quartz crystal microbalance [58, 59], ellipsometry [60], acoustic wave detection [61], and surface plasmon resonance (SPR) [62–64] are employed for this purpose. The latter technique is sensitive enough to detect submonolayer coverage with a good precision as required for a reliable determination of the sought thermodynamic

Scheme 4



and kinetic parameters. It, however, necessitates the immobilization of one member of the interacting pair in a thick dextran film. The interpretation of the data may thus be complicated by the necessity of taking account of the partition of the other member of the pair between the solution and the film as well as by the interference of diffusion in the two phases [64–67].

Another technique has recently been proposed [68], based on labeling by a redox enzyme of the solute molecule and monitoring the binding by means of the electrochemical response of the electrode onto which the receptor is immobilized. The method was illustrated by its application to the kinetics of the recognition of an immobilized monolayer of goat IgG (antigen) by antigoat. Because the surface concentrations are small, owing to the large size of the molecules, this is a typical case where simple redox labeling of the target molecule would not provide sufficient sensitivity to the attachment of the antibody onto the antigen monolayer. Labeling of the antibody with a redox enzyme obviates this difficulty owing to the catalytic properties of the enzyme. The antibody was thus labeled with glucose oxidase. The anodic catalytic current observed in the presence of glucose and of ferrocene as the cosubstrate is directly proportional (with a known proportionality coefficient) to the amount of enzyme, and therefore to the amount of antibody, bound to the immobilized antigen [57]. The catalytic current was recorded under steady-state conditions using a glassy carbon disk electrode. Under these conditions, the diffusion rate may be precisely controlled by means of the rotation speed, allowing an unambiguous extraction of the kinetic parameters of the recognition reaction from the raw data after the interference of diffusion has been accounted for. Whatever the detection technique, diffusion of the target molecule toward the immobilization surface may seriously interfere in the overall response. It may even be, under certain circumstances, the rate-determining step, thus preventing the determination of any rate parameter characterizing the recognition reaction itself. Although the interference of diffusion has been emphasized in several instances [64–70], it is still often unduly neglected in recent works [59, 61].

The competition between diffusion and binding for the following recognition reaction, between the target molecule B and the receptor A, obeying a Langmuirian kinetic law may be described as follows:

$$\frac{\partial \Gamma_{AB}}{\partial t} = k_f C_0 \Gamma_A - k_b \Gamma_{AB} = \frac{D}{\delta}(C^b - C_0) \tag{29}$$

where the Γ's are the surface concentrations of the subscript species. C^b and C_0 are the concentrations of B in the bulk of the solution and at the immobilizing surface respectively. The last member of the equation expresses the diffusion flux of B toward the surface under steady-state conditions. D is the diffusion coefficient of B and δ is the thickness of the steady-state diffusion–convection layer established by the rotation of the disk electrode. The latter parameter is inversely proportional to the square root of the rotation rate of the disk electrode, ϖ, the variation of which thus

provides a convenient access to the contribution of diffusion to the overall kinetics ($\delta = 1.61\ D^{1/2}\nu^{1/6}(2\pi\varpi)^{-1/2}$, δ in cm, D in $cm^2\ sec^{-1}$, ν (kinematic viscosity of the solvent) in $cm^2\ sec^{-1}$, ϖ in rotations per second [71]. $\Gamma_A + \Gamma_{AB} = \Gamma^S$ is the total surface concentration of immobilized receptor molecules. It is convenient to introduce the fractional coverage, $\theta = \Gamma_{AB}/\Gamma^S$, of AB on the electrode. The fractional coverage, $\theta = \Gamma_{AB}/\Gamma^S$, of AB on the electrode thus obeys the following differential equation [68, 72]:

$$\frac{\partial\theta}{\partial t} = \frac{k_f C^b(1-\theta) - k_b\theta}{1 + k_f C^b t_d(1-\theta)} \qquad (30)$$

where $t_d = \delta\Gamma^S/DC^b$ is a time that characterizes the diffusion rate. Introduction of a dimensionless variable $\tau = t/t_d$, which normalizes the time variable against the diffusion time, t_d, thus seems natural. So does the introduction of two other dimensionless parameters, one characterizing the adsorption equilibrium, $\kappa = k_f C^b/k_b = KC^b$ ($K = k_f/k_b$ is the binding equilibrium constant) and the other, $\lambda = k_f C^b t_d = k_f\delta\Gamma^S/D$, which compares the rate of adsorption to the rate of diffusion. It is also convenient to normalize the fractional coverage toward the equilibrium value it reaches at long time, $\theta_{eq} = \kappa/(1+\kappa)$, $\theta^* = \theta/\theta_{eq} = (1+\kappa)\theta/\kappa$. Thus

$$\frac{\partial\theta^*}{\partial\tau} = \lambda\frac{1+\kappa}{\kappa}\frac{1-\theta^*}{1+\lambda\left(1-\frac{\kappa}{1+\kappa}\theta^*\right)} \qquad (31)$$

For the adsorption process ($\theta = 0$ for $\tau = 0$), explicit integration leads to

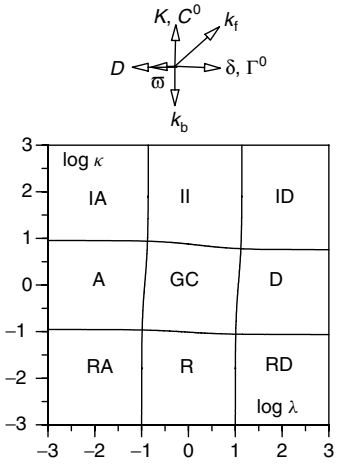
$$\theta^* - \frac{1+\kappa+\lambda}{\kappa\lambda}\ln(1-\theta^*) = \left(\frac{1+\kappa}{\kappa}\right)^2\tau \qquad (32)$$

This closed-form equation allows the prediction of all possible coverage-time curves for systems obeying Langmuirian kinetics. In order to identify the respective role of diffusion and binding kinetics, it is useful to examine various limiting situations that appear as the two parameters κ and λ take limiting large or small values. They are represented as portions of space in the ''kinetic zone diagram'' [73–75] shown in Fig. 7 together with the equations characterizing each case.

I and R corresponds to an irreversible and a reversible binding respectively. A and D represent the kinetic controls by the binding reaction and by diffusion respectively. Besides the general case (GC), the two-letter labels represent the combination of the above cases.

The way in which the boundaries between each zone were determined is illustrated in Fig. 7(a) and (b) with the example of irreversible binding (zone I). Figure 7(a) shows the variation of the fractional coverage θ^* with the dimensionless time variable, τ, in the vicinity of diffusion control (passage from zone I to zone ID), whereas Fig. 7(b) shows the variation of the fractional coverage θ^* with the dimensionless time variable, $\lambda\tau$, in the vicinity of binding control (passage from zone I to zone IA). The value of λ corresponding to the passage is defined as the value for which the time for reaching half of the equilibrium coverage ($\theta^* = 0.5$) differs by 10% in the I case and in either the ID or the IA cases, as represented by the dotted lines in Fig. 7.

The arrows on top of the diagram in Fig. 7, indicating the effect of the various experimental parameters in direction and (logarithmic) magnitude, help in navigating from one zone to the other. Among these parameters, the concentration of the target molecule in solution, C^b, and the rotation rate, ϖ, may be easily varied. Varying C^b has practically no effect on the



Zone	Characteristic equation
GC	$\theta^* - \frac{1+\kappa+\lambda}{\kappa\lambda}\ln(1-\theta^*) = \left(\frac{1+\kappa}{\kappa}\right)^2\tau$
A	$-\ln(1-\theta^*) = \frac{1+\kappa}{\kappa}\lambda\tau = \frac{1+\kappa}{\kappa}\kappa_f C^b t$
D	$\theta^* - \frac{1}{\kappa}\ln(1-\theta^*) = \left(\frac{1+\kappa}{\kappa}\right)^2\tau$
I	$\theta^* - \frac{1}{\lambda}\ln(1-\theta^*) = \tau$
R	$-\ln(1-\theta^*) = \frac{\lambda}{\kappa(1+\lambda)}\tau$
IA	$-\ln(1-\theta^*) = \lambda\tau = \kappa_f C^b t$
ID	$\theta^* = \tau$
RA	$-\ln(1-\theta^*) = \frac{\lambda}{\kappa}\tau = \kappa_b t$
RD	$-\ln(1-\theta^*) = \frac{\tau}{\kappa}$

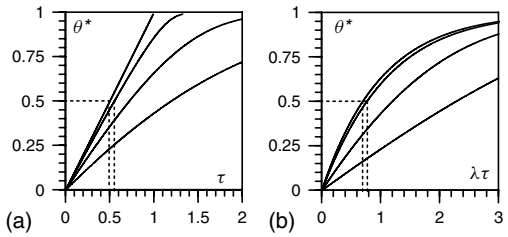


Fig. 7 Dynamics of molecular recognition. Binding of the target molecule to the receptor. Kinetic zone diagram (left), characteristic equations (center), and passage (left) from zone I to zone ID (a) and from zone I to zone IA (b). From left to right $\log\lambda = \infty$, 1.141, 0.5, 0 (a); $-\infty$, −0.858, 0, 0.5.

kinetic competition between binding and diffusion. Increasing C^b makes the system pass from a reversible to an irreversible behavior. The rotation rate, ϖ, is the key parameter for identification and control of the interference of diffusion. Increasing ϖ makes the system pass from kinetic control by diffusion to kinetic control by the binding reaction. A simple test that diffusion does not interfere is the observation that, upon increasing the disk rotation rate, the Γ_{AB} versus time curve ceases to depend on this parameter. The system is then in the A zone and the binding kinetics may easily be derived using the corresponding equation (Fig. 7). Information on the binding kinetics may, nevertheless, be extracted from the experimental data even when kinetics is under mixed diffusion/binding control (zones I, GC, and R) with, however, less and less precision as the system is closer and closer to the boundary with zones ID, D, and RD respectively. In other words, the ability of reaching fast binding kinetics

is dependent of the ability of achieving fast rotation rates. The adsorption rate constant may be determined as long as the parameter λ can be made smaller than ca 1 (Fig. 7). The upper accessible values of k_f are thus given by

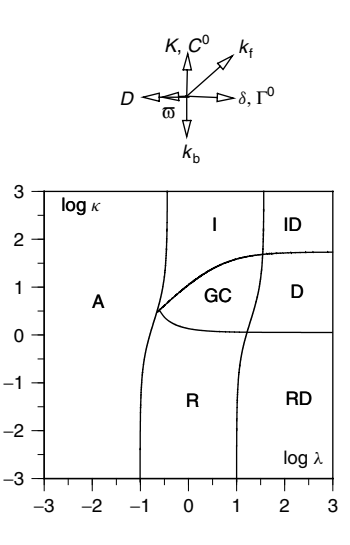
$$k_{\mathrm{f}} \leq \frac{D}{\delta\Gamma_{\mathrm{S}}} \approx 0.039 T^{2/3} r^{4/3} \rho^{-2/3} \nu^{-5/6} \sqrt{\varpi} \tag{33}$$

where k_{f} is in $\mathrm{mol}^{-1}\,\mathrm{l}\,\mathrm{sec}^{-1}$, the volumic mass, ρ, in $\mathrm{g\,cm}^{-3}$, the solvent kinematic viscosity, ν, in $\mathrm{cm}^2\,\mathrm{sec}^{-1}$, ϖ in rotations per minute, Γ_{S} in $\mathrm{mol\,cm}^2$, r, the radius of the equivalent hard sphere, in Å. In order to obtain a rough estimate of the maximal k_f, the diffusion coefficient is assumed to obey the Stokes–Einstein relationship in the last member of Eq. (11). Ten thousand rotations per minute is about the maximal rotation speed that can be reached with a rotating disk. Thus, in water at 25 °C,

$$k_{\mathrm{f}}(\mathrm{mol}^{-1}\mathrm{l}\,\mathrm{sec}^{-1}) \leq 81[\varpi\,(\mathrm{rpm})]^{1/2} r^{4/3}(\text{Å}) \tag{34}$$

The maximal binding rate constant is thus of the order of 10^6, 2×10^5, and $5 \times 10^4\ \mathrm{mol}^{-1}\,\mathrm{l}\,\mathrm{sec}^{-1}$ for typical antibodies, for DNA strands, and for conventional organic molecules respectively. It is seen that it is easier to observe the activation-controlled adsorption kinetics with large biomolecules than with conventional organic molecules, explaining why, in the latter case, the results are so scarce or so uncertain and also why the adsorption kinetics are considered to be under diffusion control in most circumstances.

The dissociation of the complex, after it has reached its equilibrium value, upon exposure to a pure solution may be examined similarly. At time $t = 0$, $\theta = \theta^* = \kappa/(1+\kappa)KC^{\mathrm{b}}/(1+KC^{\mathrm{b}})$, where C^{b} is the bulk concentration that was used during the adsorption step preceding the desorption process. Assuming that the volume-to-surface ratio is large enough for the bulk concentration of B to remain negligible throughout the experiment, the



Zone	Characteristic equation
GC	$\frac{\kappa}{1+\kappa}(1-\theta^*) + \frac{1+\lambda}{\lambda}\ln(\theta^*) = -\frac{\tau}{\kappa} = \frac{tD}{K\delta\Gamma_{\mathrm{S}}}$
A	$\ln(\theta^*) = -\frac{\lambda}{\kappa}\tau = -k_{\mathrm{b}}t$
D	$\frac{\kappa}{1+\kappa}(1-\theta^*) + \ln(\theta^*) = -\frac{\tau}{\kappa} = \frac{tD}{K\delta\Gamma_{\mathrm{S}}}$
I	$(1-\theta^*) + \frac{1+\lambda}{\lambda}\ln(\theta^*) = -\frac{\tau}{\kappa} = \frac{tD}{K\delta\Gamma_{\mathrm{S}}}$
R	$\frac{1+\lambda}{\lambda}\ln(\theta^*) = -\frac{\tau}{\kappa} = \frac{tD}{K\delta\Gamma_{\mathrm{S}}}$
ID	$(1-\theta^*) + \ln(\theta^*) = -\frac{\tau}{\kappa} = \frac{tD}{K\delta\Gamma_{\mathrm{S}}}$
RD	$\ln(\theta^*) = -\frac{\tau}{\kappa} = \frac{tD}{K\delta\Gamma_{\mathrm{S}}}$

Fig. 8 Dynamics of molecular recognition. Dissociation of the complex. Kinetic zone diagram (left), characteristic equations (right).

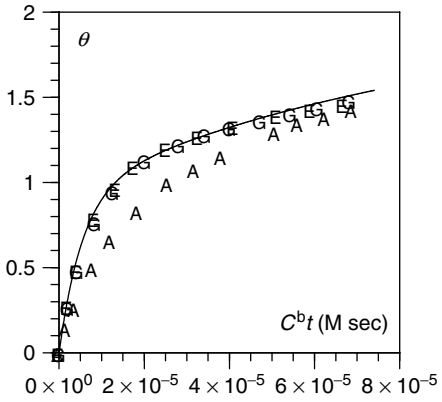


Fig. 9 Binding of polyclonal antibody glucose oxidase conjugates (in the presence of 0.1 M glucose and 0.1 mM ferrocene methanol) to a saturated monolayer of whole antigen deposited on the surface of a GC rotating disk electrode. Variation of the coverage with time at three rotation rates (G: 1600, E: 400, A: 100 rpm) for an antibody concentration of 7 nM, showing the elimination of the diffusion contribution upon increasing the rotation rate.

variation of the surface concentration with time obeys the following equation.

$$\frac{\partial \Gamma_{AB}}{\partial t} = k_f C_0 \Gamma_A - k_b \Gamma_{AB} = -\frac{D}{\delta} C_0 \tag{35}$$

The decay of the fractional coverage with time is depicted by the equation corresponding to the GC in Fig. 8. The competition between diffusion and desorption kinetics is again conveniently represented by a kinetic zone diagram. This is shown in Fig. 8 together with the equations pertaining to each zone.

An important parameter for observing the role of diffusion is the electrode rotation rate. Figure 9 gives an experimental example concerning molecular recognition between two immunoglobulins, where it is clearly seen how an increase in the rotation rate allows the elimination of the contribution of diffusion and thus the determination of the activation parameters of the molecular recognition reaction.

The Langmuirian analysis depicted so far assumes that the interactions between the bound molecules are negligible. This condition is not fulfilled in many systems, especially when the coverage comes close to saturation. In such circumstances, a Frumkin isotherm for describing equilibrium and the corresponding kinetic law may replace profitably the Langmuirian description:

$$\frac{\theta}{1-\theta} = K \exp(a\theta) C_0 \tag{36}$$

where K is the binding constant when $\theta \to 0$, that is, when the interactions vanish. $a = \Delta G_i / RT$, where ΔG_i is the free energy of interaction at unity coverage. $\Delta G_i > 0$ for attractive interactions and <0 for repulsive interactions. From a kinetic point of view, in the latter case, the interactions slow down adsorption and accelerate desorption and vice versa in the former case. ΔG_i may thus be split in two fractions: $\alpha \Delta G_i$ and $(1-\alpha)\Delta G_i$. The resulting free energies may thus be assigned to the modification of the adsorption and desorption rates respectively as a result of the interactions. The following kinetic law for binding ensues.

$$\frac{d\theta}{dt} = k_f \exp[\alpha a \theta](1-\theta) C_0 - k_b \exp[(1-\alpha) a \theta] \theta \tag{37}$$

(k_f and k_b are the adsorption and desorption constants when $\theta \to 0$). The

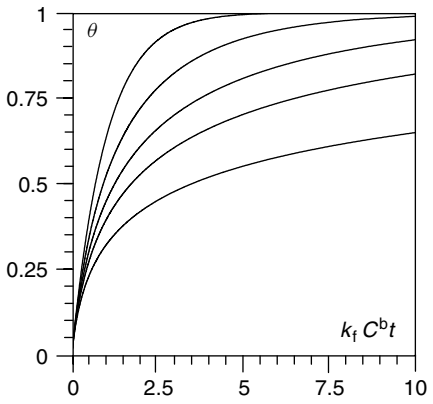


Fig. 10 Kinetics of irreversible adsorption for Frumkin-isotherm interactions between adsorbates. From left to right $\alpha a = 0, -1, -2, -3, -5$.

derivation of Eq. (19) is similar to the establishment of the Butler–Volmer kinetic law for electrochemical electron-transfer reactions, where the symmetry factor, α, is regarded as being independent from the electrode potential [76]. Likewise, in the present case, the symmetry factor, α, is assumed to be independent of the coverage, θ.

In the case of, for example, an irreversible binding reaction where the rotation rate is large enough for activation control to prevail, integration of the preceding equation leads to the following equation depicting how the coverage builds up with time [68].

$$k_f C^b t = \exp(-\alpha a)\left\{-\ln(1-\theta) + \sum_{j=1}^{\infty} \frac{(\alpha a)^j [1-(1-\theta)^j]}{j j!}\right\} \quad (38)$$

Some representative curves are shown in Fig. 10. Comparison of the curves in Figs 7 and 9 on the one hand and Fig. 10 on the other shows that the shape of the curves is not a reliable criterion for estimating the contribution of diffusion, which may well be mistaken with the effect of lateral interactions. This is the reason that the effect of rotation rate should imperatively be used for judging of the interference of diffusion.

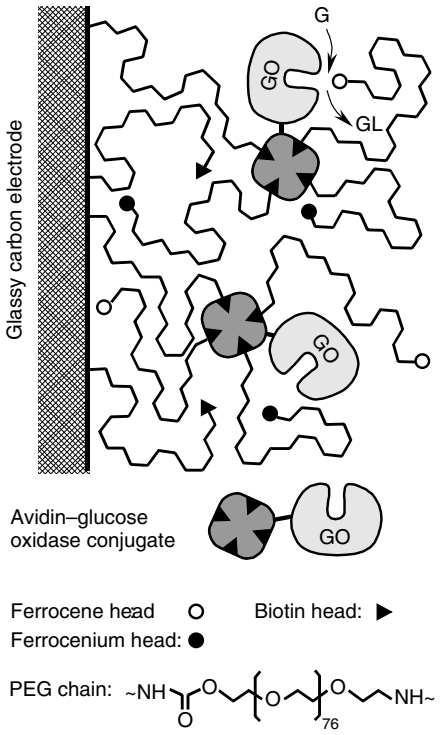
The mechanism of molecular recognition may be more complicated than depicted above, and may possibly involve multiple recognition. Examples of such situations and of how the preceding treatments may be adapted accordingly may be found in reference [68].

13.3.3 Immobilization of Both the Enzyme and the Cosubstrate

The studies depicted in the preceding text have been performed in cases where the mediator is homogeneously dispersed in the solution. There is a need for more integrated systems in which the electron carrier would be attached to the structured in a spatially defined manner and which would lend themselves to full kinetic characterization.

One strategy to reach this goal [77] has been to use the avidin–biotin technology [78–83]. The integrated system shown in Sch. 5 was built as follows [77]. The long chain biotin was first grafted,

Scheme 5



applying the *N*-hydroxysuccinimide technology [84], by reacting directly the GC surface with a chloroform solution of the commercially available *O*-2-[(*N*-hydroxysuccinimidyl) ethyloxycarbonyl] and *O′*-2-(*N*-biotinamidoethyl) polyethylene glycol ($NHS-CO_2$-PEG-biotin, average molecular weight: 3500, average number of $O-CH_2CH_2$ units: 69). The glucose oxidase conjugated avidin was then attached because of its strong affinity for the biotin moieties. Finally, the long chain biotinylated ferrocene derivative, *O*-[2 − *N*-(*β*-ferrocenyl-ethylamino)ethyloxycarbonyl], *O′*-2-(*N*-biotinamido ethyl) polyethylene glycol ($FcCH_2CH_2NHCO_2$-PEG-biotin, average number of $O-CH_2CH_2$ units: 69), to be used as cosubstrate, was bound to the remaining vacant sites of the monolayer of glucose oxidase conjugated avidin. From the surface wave obtained in cyclic voltammetry, the surface concentration of cosubstrate was estimated as 10^{-11} mol cm^{-2}.

The second strategy that has been employed rests on the same antigen–antibody interactions, as described in the preceding text, except that the cosubstrate is now attached to the structure by a long polyethylene glycol arm. An example of this type of construction is sketched in Sch. 6 [85]. The construction starts with the adsorption onto the glassy carbon electrode of an antibody produced in goat. In a second step, it serves as an antigen that is recognized by an antigoat antibody produced in mouse, previously labeled with polyethylene glycol chains terminated by a ferrocene head (PEGFc), each antibody bearing an average of 17 PEGFc chains [86]. A third layer containing the enzyme is finally grated onto the second layer exploiting the recognition of the mouse IgG immobilized in the second monolayer by the antimouse glucose oxidase conjugate. The surface concentration of cosubstrate is of the order 10^{-11} mol cm^{-2} as in the preceding case.

13.3.4 Electron Transfer and Electron Transport in Integrated Systems

Cyclic voltammetry allows the analysis of the kinetics of the two integrated systems described earlier. Figure 11 shows the case of the avidin–biotin system (Sch. 5) where the voltammogram passes from a reversible surface wave shape to a plateau shape upon addition of glucose and where the inverse of the plateau current varies linearly with the inverse of glucose concentration. Similar data are obtained with the antigen–antibody

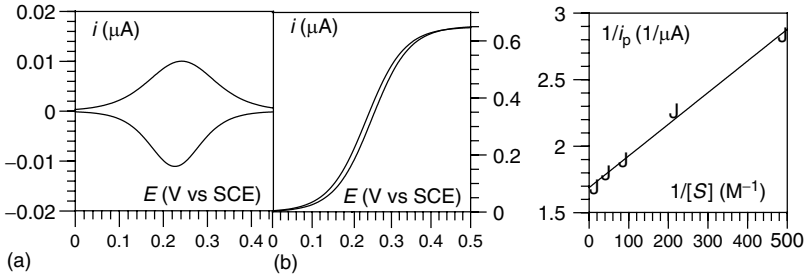
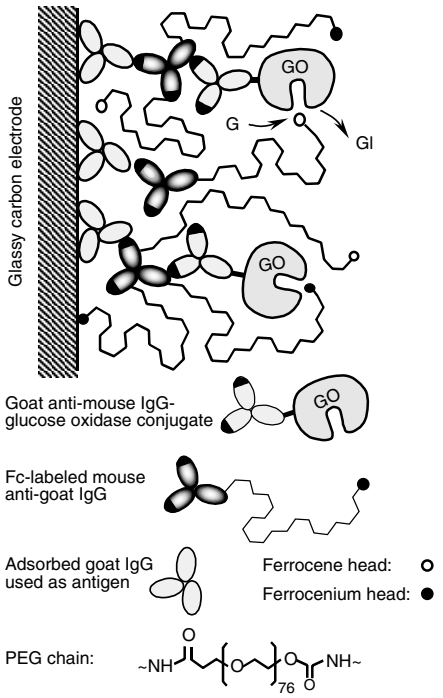


Fig. 11 Cyclic voltammetry of the avidin–biotin monolayer enzyme-cosubstrate integrated system (Sch. 5) in the absence (a) and presence of 0.5 M substrate in a phosphate buffer (pH = 8) at 25 °C and a scan rate of 0.04 V sec^{-1}. (c) Variation of the inverse of the plateau current with the inverse of substrate concentration.



Scheme 6

integrated system depicted in Sch. 6, as can be seen in Fig. 12.

In a first approximation, we may consider that the concentrations of the two forms, P and Q, of the cosubstrate are uniform within the film containing the enzyme molecules, the PEG chains, and the ferrocene and ferricenium moieties. Under such conditions, Eq. (72) is replaced by the following equations:

$$\frac{i}{FS} = -\frac{d\Gamma_P}{dt} + 2k_3\Gamma_{RE}[Q] = \frac{d\Gamma_Q}{dt} + 2k_3\Gamma_{RE}[Q] \qquad (39)$$

where Γ_P and Γ_Q are the numbers of moles of P and Q present in the coating per unit surface area. [Q], the uniform concentration of Q in the film, is equal to Γ_Q/l, where l is the thickness of the film. In the absence of substrate, the current corresponds to the $-d\Gamma_P/dt = -d\Gamma_P/dt$ term. It is thus possible, as in the preceding sections, to define a catalytic contribution to the current:

$$i_{cat} = i - i_{k_{3=0}} = 2k_3\Gamma_{RE}[Q] \qquad (40)$$

As before, when the substrate is in excess,

$$\frac{1}{i_{cat}} = \frac{1}{2Fk_3\Gamma_E^0}\frac{1}{[Q]} + \frac{1}{2F\Gamma_E^0}\left(\frac{1}{k_2} + \frac{1}{k_{red}[S]}\right) \qquad (41)$$

where Γ_E^0 is the total number of moles of enzyme per unit surface area.

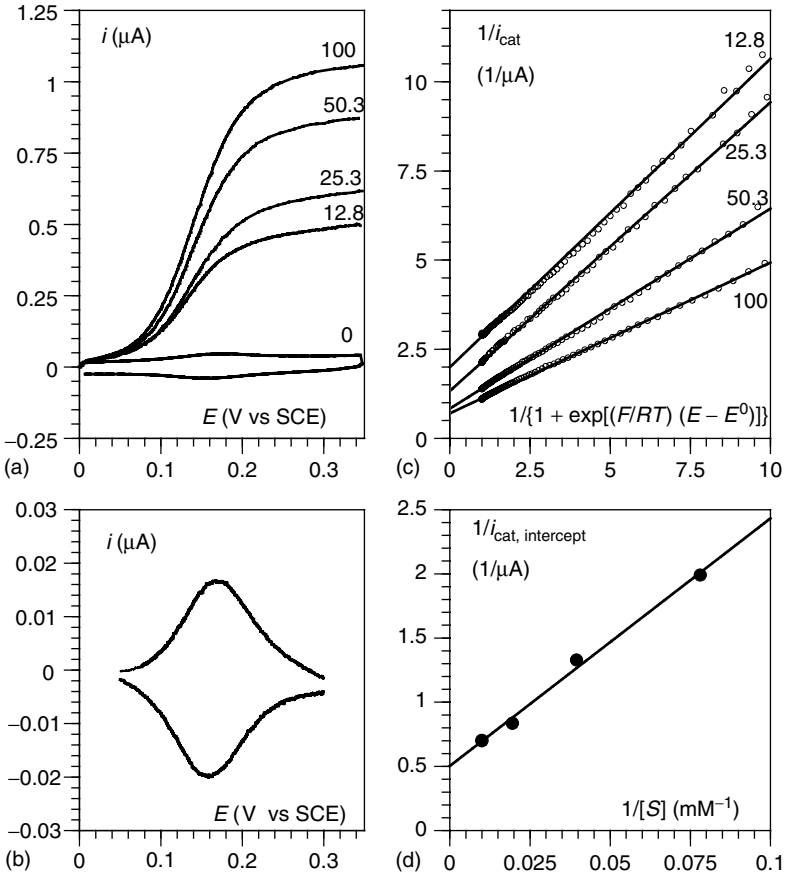


Fig. 12 Cyclic voltammetry of the antigen–antibody integrated system depicted in Sch. 6 as a function of substrate concentration. (a) Cyclic voltammograms upon addition of the substrate. (b) Cyclic voltammogram in the absence of glucose corrected from the background. (c) Primary plots obtained along the wave. (d) Secondary plot. The numbers on the curves in (a) and (c) are the values of the substrate concentration in millimolar.

From the intercept of the secondary plot shown in Fig. 11(c), it follows that $k_3\Gamma_E^0 C_P^0 = 5 \times 10^{-11}$ mol cm^{-2} sec^{-1}. Γ_E^0 may be derived from an experiment where the ferrocene methanol cosubstrate is added in the solution so as to render negligible the contribution of the attached cosubstrate to the catalytic current. Applying the analysis developed in Sect. 13.3.1 leads to $\Gamma_E^0 = 3.5 \times 10^{-12}$ mol cm^{-2} and thus to $k_3 C_P^0 = 13$ sec^{-1}. A crude estimate of C_P^0 (10^{-3} M) leads to $k_3 = 10^4$ M^{-1} sec^{-1}.

The above treatment is in fact likely to be too crude as results from a more detailed study of electron transport in the absence of the enzyme in the antigen–antibody system depicted in Sch. 6. In fact, the average plane where the PEG chains are anchored is significantly different from

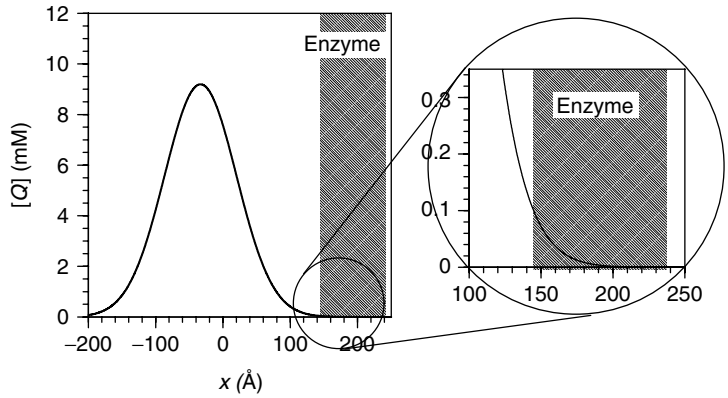


Fig. 13 Equilibrium profile of the cosubstrate heads (reduced + oxidized forms) in the integrated system depicted in Sch. 6 also showing the location of the enzyme sites.

the average plane where the enzyme prosthetic groups are located (Sch. 6, Fig. 13). The active heads of the attached cosubstrate diffuse back and forth in between the electrode surface and a plane corresponding to the maximal extension of the PEG chains [87]. These movements are governed by their diffusion coefficient, the force constant tending to restore the resting position and the maximal extension length. The current flowing through the electrode under cyclic voltammetric conditions, when the enzyme is inactivated (as, e.g., in the absence of substrate), is a function of these three parameters and of the scan rate. A low scan rate, an equilibrium distribution of the cosubstrate heads, is established and a Nernstian symmetrical wave is then predicted as follows:

$$\frac{i}{FS} = -\frac{d\Gamma_P}{dt} = \frac{d\Gamma_Q}{dt} = S\Gamma^0 \frac{Fv}{RT} \frac{\exp\left[-\frac{F}{RT}(E-E^0_{PQ})\right]}{\left\{1+\exp\left[-\frac{F}{RT}(E-E^0_{PQ})\right]\right\}^2} \quad (42)$$

where Γ_P and Γ_Q are the numbers of moles of P and Q present in the whole film respectively; Γ^0 is their sum. As seen in Fig. 12(a), this behavior is indeed observed with the integrated system under discussion. It is also observed upon raising the scan rate up to values where the enzymatic catalysis vanishes. Equilibrium is thus maintained in the experiments (Fig. 12b–d) where the enzyme is in action. Under these conditions, the fluxes of P and Q flowing through any plane in the film parallel to the electrode surface are the same. In particular, they are the same at the electrode surface and through the average plane where the enzyme prosthetic groups are located. Thus, the equations

$$i_{cat} = i - i_{k_3=0} = 2k_3\Gamma_{RE}[Q] \quad (43)$$

$$\frac{1}{i_{cat}} = \frac{1}{2Fk_3\Gamma^0_E}\frac{1}{[Q]} + \frac{1}{2F\Gamma^0_E}\left(\frac{1}{k_2} + \frac{1}{k_{red}[S]}\right) \quad (44)$$

are still valid taking into account, however, that [Q] now stands for the concentration of Q in the average enzyme plane (see Fig. 12). The ensuing primary and

secondary plots (Fig. 12c,d) are linear, thus confirming the applicability of the preceding analysis to the experiments depicted in Fig. 12. The rate constants k_2 and k_{red} thus derived are again close to the values they have in experiments where the enzyme is dispersed in the solution.

The determination of the rate constant k_3 requires the estimation of the concentration of Q in the average enzyme plane. It may be estimated using the following expression of the concentration profile derived from a model in which the PEG chain is approximated by a spring (force constant: χ_{spr}).

$$[Q](x) = \frac{\Gamma^0}{1 + \exp\left[-\frac{F}{RT}(E - E^0_{PQ})\right]} \times \frac{1}{\sqrt{\pi}}\sqrt{\frac{\chi_{spr}}{2RT}} \exp\left(-\frac{\chi_{spr}}{2RT}x^2\right) \quad (45)$$

Averaging then the Q concentration over the thickness of the enzyme ($2l$) leads to the following expression of the average Q concentration at the enzyme site.

$$[\tilde{Q}]^{es} = \frac{\Gamma^0}{1 + \exp\left[-\frac{F}{RT}(E - E^0_{PQ})\right]} \times \frac{1}{2l}\left[\mathrm{erf}\left(2.5l\sqrt{\frac{\chi_{spr}}{2RT}}\right) - \mathrm{erf}\left(1.5l\sqrt{\frac{\chi_{spr}}{2RT}}\right)\right] \quad (46)$$

Once $[\tilde{Q}]^{es}$ has been estimated, k_3 can be derived from the intercept of the primary plot (Fig. 12c). The value thus found, 1.5×10^6 M^{-1} sec^{-1}, is smaller than the value for ferrocene methanol in solution, 1.2×10^7 M^{-1} sec^{-1} (regardless of the presence of PEG chains in solution) and larger than in the case where the ferrocenes are attached to PEG chains, dispersed in the solution, 2.2×10^5 M^{-1} sec^{-1}, the rate-determining step still being the formation of a properly oriented precursor complex with the flavin. These observations are consistent with the following picture. The PEG chains sterically hinder, albeit to a modest extend, the formation of the precursor complex, steric hindrance being more serious when the PEG chains have a random coil shape as when they float in the solution than when they are largely extended as those that reach the enzyme sites in the integrated system.

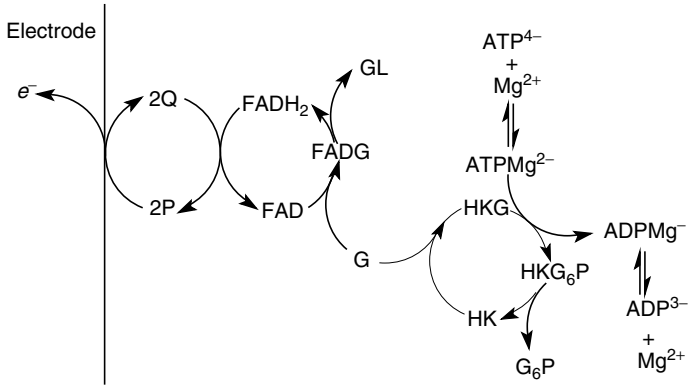
The above analysis provides a typical example of how a the application of a full analysis of cyclic voltammetric data may provide fine details in the description of the dynamics of electron transport and electron transfer in such complex systems.

13.4 Spatially Ordered Multimonomolecular Layer Enzyme Coatings

13.4.1 Step-by-step Antigen–Antibody Construction of Multimonomolecular Layer Enzyme Coatings

Both the avidin–biotin [88, 89] and antigen–antibody [90, 91] strategies have been taken up for depositing successive monomolecular layers onto electrode surfaces. The former was even used to build a bienzymatic coating associating a redox enzyme, glucose oxidase, to a nonredox enzyme, hexokinase, so as to make the electrode sensitive to the substrate of the nonredox enzyme, ATP (Sch. 7) [87].

However, the unexpected and nonnegligible reversibility of the avidin-to-biotin binding proved itself a serious obstacle

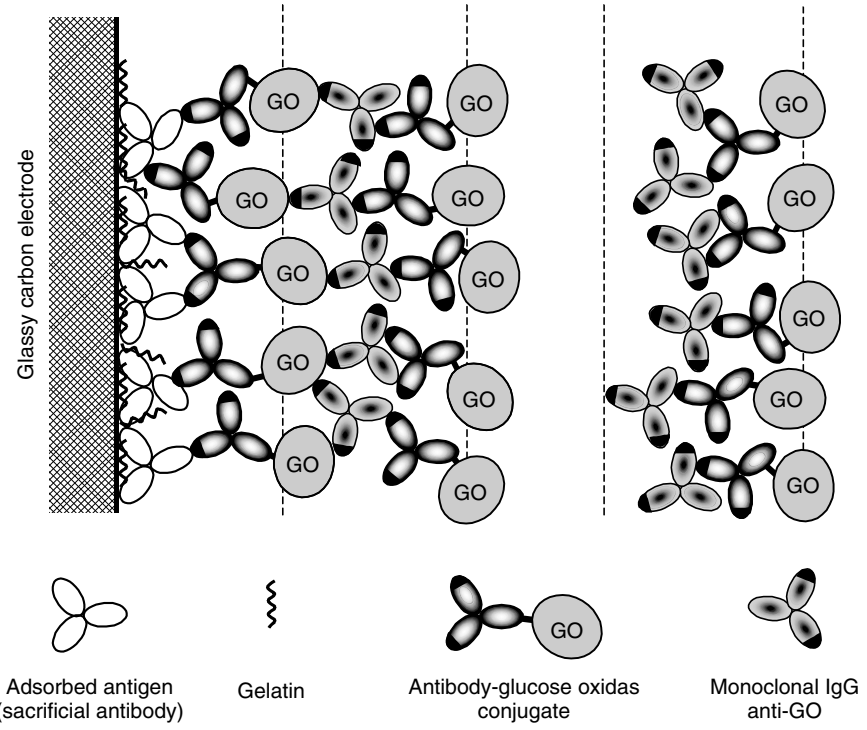


G: glucose, GL: glucono-δ-lactone, FAD: oxidized form of the flavin, FADG: its glucose complex, $FADH_2$: its rediced form, P: cosubstrate reduced form (ferrocene), P: cosubstrate oxidized form (ferriocenium), G_6P: glucose-6-phosphate, HKG, HKG_6P: hexokinase-substrate e and t hexokinase-product complexes respectively.

Scheme 7

for the routine use of this strategy to construct multilayer coatings. The antigen–antibody strategy appears easier and more reliable for the step-by-step construction of multimonomolecular layer enzyme coatings. A typical example, where glucose oxidase is the enzyme, is sketched in Sch. 8.

The enzyme monomolecular layer prepared, as depicted in Sect. 13.3.1, may serve as a template for the step-by-step building of the multimonomolecular layer system. As seen in Sch. 8, the key intermediate building block, C, linking one monomolecular layer to the other is an antiglucose oxidase monoclonal antibody. At one extremity, C recognizes the immobilized glucose oxidase. At the other, it serves as an antigen for the glucose oxidase conjugate, B. C thus plays the same role as the sacrificial antigen A, directly adsorbed on the electrode surface in the initial step. Since the monoclonal antibodies to glucose oxidase C are produced in mouse, the adsorbed antigen A has to be a mouse antibody too and the conjugate B is a glucose oxidase antimouse conjugate. It is thus possible to attach a second glucose oxidase monolayer to the first, a third to the second, and so on, the immobilized enzyme activity being monitored at each step by the determination of the electrocatalytic activity (see below). It was checked that the fixation of the monoclonal antibody C on top of glucose oxidase, producing the El-A-B-C sequence (El = electrode), does not inhibit the first layer of enzyme and has the same activity as the El-A-B sequence. Testing the enzyme activity of the second monolayer after the El-A-B-C-B sequence was achieved, it was found that the additional coverage is about 85% of the first layer when only one kind of monoclonal antibody was used. Incubating the electrode in a cocktail of two clones of monoclonal antibody leads to a 100% coverage as the first layer. This is explained by the fact that one clone of monoclonal antibody recognizes only one epitope on the glucose oxidase shell and this epitope can be masked for some immobilized enzyme molecule. This



Scheme 8

steric constraint is circumvented by the use of a mixture of two different antibodies recognizing two different epitopes. Testing the enzyme activity of each additional monomolecular layer reveals that the surface concentration of catalytically active glucose oxidase present in the layer is the same. This regularity shows that the coating does not grow in an anarchic manner and is a first indication of spatial order.

Already immobilized enzyme monolayers can be inactivated with iodoacetate and active monolayers can be attached *de novo* on top of the inactivated layers. The application of these procedures allows the construction of a large variety of structures whose spatial order can be investigated as detailed in the next section.

13.4.2 Reaction Dynamics with the Cosubstrate in Solution: Evidence for Spatial Order

In the monomolecular layer systems described so far, diffusion of the cosubstrate through the film is not a rate-limiting factor. This is true in the case of a free-moving cosubstrate, but also, at least at low scan rates, with cosubstrates attached to the structure by means of a PEG arm.

When several layers are coated on the electrode, diffusion of the cosubsrate may become rate limiting even if it is not attached to the structure [90, 91]. The rate of diffusion of the two forms of the cosubstrate increases with it concentration. One may thus expect that the enzymatic reaction, rather than diffusion, tends to be the rate-determining step upon raising the

cosubstrate concentration and that this situation is reached all the more easily if the number of layers is small. Under such conditions, the separation of the cyclic voltammetric current in two independent contributions, $i = i_{k_3=0} + i_{cat}$ is still valid. i_{cat} is thus proportional to the total amount of enzyme contained in the film per unit surface area and therefore to the number, N, of monomolecular layers deposited on the electrode:

$$i_{cat} = \frac{2FSk_3\Gamma_E^0\kappa_Q C_P^0}{1 + k_3\Gamma\kappa_Q C_P^0\left(\frac{1}{k_2} + \frac{1}{k_{red}[S]}\right)}N \tag{47}$$

where Γ_E^0 is still the number of moles of enzyme per unit surface area in each monomolecular layer and κ_Q is the partition coefficient of Q between the film and the solution. These expectations are confirmed by the experimental results displayed in Fig. 14, where it is seen that diffusion across the film interferes more and more as the mediator concentration decreases and the number of monomolecular layers decreases. The interference of diffusion is the tool owing to which the spatial structure of the film may be investigated. Experiments were carried out with several configurations of active and inactivated layers. One of these was the system dealt with in Fig. 14 in which all the enzyme layers are active. Another one consisted in 10 inactivated layers plus 1 active layers, and, still another 1 of 5 inactivated plus 1–5 active layers.

Table 2 lists the equations that govern the fluxes of the two forms of the cosubstrate in a system containing $n-1$ inactivated enzyme layers adjacent to the electrodes surface on top of which $N-n$ active layers have been deposited, thus representing any of the above experimental systems. Several assumptions underlie this set of equations. One is that diffusion is linear (corresponding to a plane electrode). Another is that the scan rate is slow enough for the diffusion layer (thickness: $\approx \sqrt{DRT/Fv} \approx 1\text{–}2 \times 10^5$ Å) to be significantly thicker than the enzyme film. An experimental test for knowing whether this condition is fulfilled is that the plateau of S-shaped catalytic current then observed is much larger than the reversible cosubstrate peak observed in the absence of substrate. It follows that the concentration profiles within the film do not depend on time. Dependency on time, if any, thus only concerns the diffusion process in the solution outside the film, leading to the two integral equations relating the fluxes and the concentrations at the film/solution interface [37].

Proper combination of the equations in Table 2 results in the following flux relationships.

$$\begin{aligned} &D\left(\frac{\partial[P]}{\partial x}\right)_{fs} + D\left(\frac{\partial[Q]}{\partial x}\right)_{fs} \\ &\quad = D_P\left(\frac{\partial[P]}{\partial x}\right)_{\pm m} + D_Q\left(\frac{\partial[Q]}{\partial x}\right)_{\pm m} \\ &\quad = D_P\left(\frac{\partial[P]}{\partial x}\right)_0 + D_Q\left(\frac{\partial[Q]}{\partial x}\right)_0 = 0 \end{aligned} \tag{48}$$

from which one infers, using the two integral equations that

$$[P]_{fs} + [Q]_{fs} = C_P^0 \quad \text{and therefore}$$
$$\frac{[P]_N}{\kappa_P} + \frac{[Q]_N}{\kappa_Q} = C_P^0 \tag{49}$$

The second space derivative of the concentration at each enzyme layer may be approximated by the difference between the two gradients on each side of the layer

$$\frac{\partial^2[P]}{\partial x^2} = \frac{\left(\frac{\partial[P]}{\partial x}\right)_+ - \left(\frac{\partial[P]}{\partial x}\right)_-}{l},$$

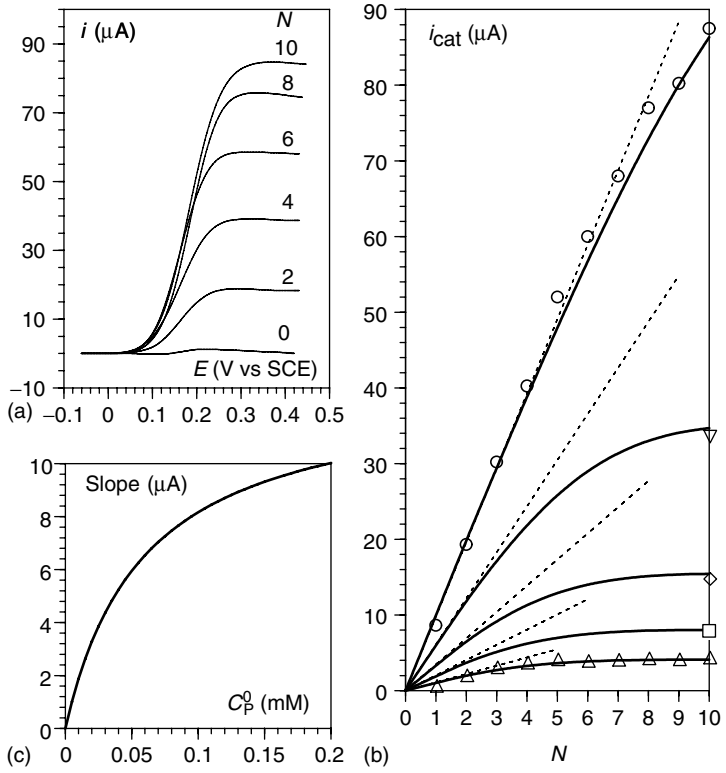


Fig. 14 Cyclic voltammetry of glucose oxidase coated glassy carbon electrodes with an increasing number (N) of monolayers in a pH 8 phosphate buffer (ionic strength: 0.1 M) solution containing 0.5 Mglucose. Scan rate: 0.04 V sec^{-1}. Temperature: 25 °C. (a) Voltammograms for 0.2 mM ferrocene methanol mediator; from bottom to top: $N = 0$, 2, 4, 6, 8, and 10 (for clarity, the odd numbers of monolayers are not represented). (b) Catalytic plateau currents as a function of N for several concentrations of the ferrocene methanol mediator, 0.2 (E), 0.05 (S), 0.02 (A), 0.01 (G), 0.005 (C). Straight lines: linear responses corresponding to $\Gamma_E^0 = 10^{-12}$ mol cm^{-2}, $k_3 = 1.2 \times 10^7$ M^{-1} sec^{-1}, $k_2 = 700$ sec^{-1}, $k_{red} = 10^4$ M^{-1} sec^{-1}. Curved lines: simulation of the interference of mediator mass transport. (c) Slope of the straight lines in (b) as a function of the cosubstrate bulk concentration.

$$\frac{\partial^2[\mathrm{Q}]}{\partial x^2} = \frac{\left(\frac{\partial[\mathrm{Q}]}{\partial x}\right)_+ - \left(\frac{\partial[\mathrm{Q}]}{\partial x}\right)_-}{l} \tag{50}$$

It thus follows from what precedes that

$$\frac{\partial^2 D_\mathrm{P}[\mathrm{P}] + D_\mathrm{Q}[\mathrm{Q}]}{\partial x^2} = 0 \tag{51}$$

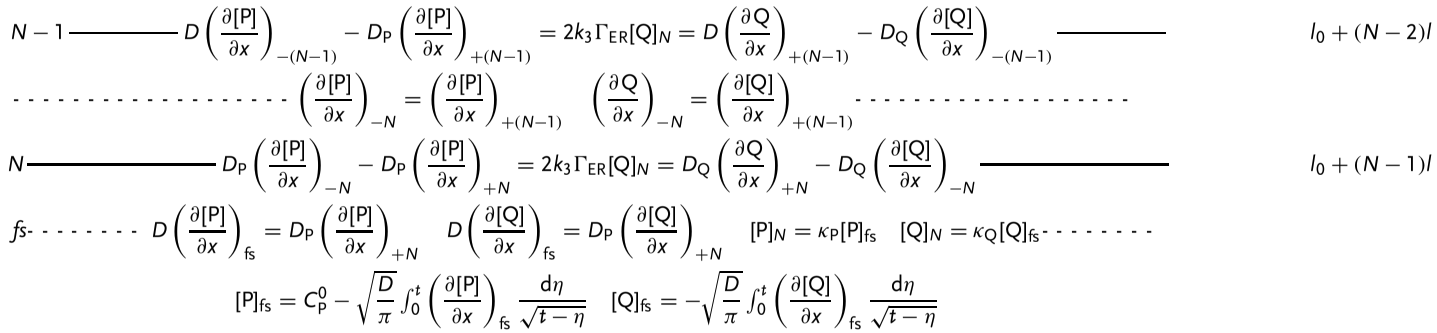
and therefore

$$D_\mathrm{P}\left(\frac{\partial[\mathrm{P}]}{\partial x}\right) + D_\mathrm{Q}\left(\frac{\partial[\mathrm{Q}]}{\partial x}\right) = D_\mathrm{P}\left(\frac{\partial[\mathrm{P}]}{\partial x}\right)_0 + D_\mathrm{Q}\left(\frac{\partial[\mathrm{Q}]}{\partial x}\right)_0 = 0 \tag{52}$$

$$D_\mathrm{P}[\mathrm{P}]_0 + D_\mathrm{Q}[\mathrm{Q}]_0 = D_\mathrm{P}[\mathrm{P}] + D_\mathrm{Q}[\mathrm{Q}] = D_\mathrm{P}[\mathrm{P}]_N + D_\mathrm{Q}[\mathrm{Q}]_N \tag{53}$$

Tab. 2 Fluxes equations in an enzyme film containing $n-1$ inactive and $N-n$ active layers

	x
el $\quad \dfrac{i}{FS} = D_P\left(\dfrac{\partial[P]}{\partial x}\right)_{el} = -D_Q\left(\dfrac{\partial[Q]}{\partial x}\right)_{el} \qquad [Q]_{el} = [P]_{el}\exp\left[\dfrac{F}{RT}(E - E^0_{P/Q})\right]$	0
$\left(\dfrac{\partial[P]}{\partial x}\right)_{-1} = \left(\dfrac{\partial[P]}{\partial x}\right)_{el} \quad \left(\dfrac{\partial[Q]}{\partial x}\right)_{-1} = \left(\dfrac{\partial[Q]}{\partial x}\right)_{el}$	l_0
1 $\quad \left(\dfrac{\partial[P]}{\partial x}\right)_{+1} = \left(\dfrac{\partial[P]}{\partial x}\right)_{-1} \quad \left(\dfrac{\partial[Q]}{\partial x}\right)_{+1} = \left(\dfrac{\partial[Q]}{\partial x}\right)_{-1}$	$l_0 + l$
$\left(\dfrac{\partial[P]}{\partial x}\right)_{+1} = \left(\dfrac{\partial[P]}{\partial x}\right)_{-n} \quad \left(\dfrac{\partial[Q]}{\partial x}\right)_{+1} = \left(\dfrac{\partial[Q]}{\partial x}\right)_{-n}$	
$n \quad D_P\left(\dfrac{\partial[P]}{\partial x}\right)_{-n} - D_P\left(\dfrac{\partial[P]}{\partial x}\right)_{+n} = 2k_3\Gamma_{ER}[Q]_n = D_Q\left(\dfrac{\partial Q}{\partial x}\right)_{+n} - D_Q\left(\dfrac{\partial[Q]}{\partial x}\right)_{-n}$	$l_0 + (n-1)l$
$\left(\dfrac{\partial[P]}{\partial x}\right)_{-(n+1)} = \left(\dfrac{\partial[P]}{\partial x}\right)_{+n} \quad \left(\dfrac{\partial[Q]}{\partial x}\right)_{-(n+1)} = \left(\dfrac{\partial[Q]}{\partial x}\right)_{+n}$	
⋮	
$m-1 \quad D_P\left(\dfrac{\partial[P]}{\partial x}\right)_{-(m-1)} - D_P\left(\dfrac{\partial[P]}{\partial x}\right)_{+(m-1)} = 2k_3\Gamma_{ER}[Q]_{(m-1)} = D_Q\left(\dfrac{\partial Q}{\partial x}\right)_{+(m-1)} - D_Q\left(\dfrac{\partial[Q]}{\partial x}\right)_{-(m-1)}$	$l_0 + (m-2)l$
$\left(\dfrac{\partial[P]}{\partial x}\right)_{-m} = \left(\dfrac{\partial[P]}{\partial x}\right)_{+(m-1)} \quad \left(\dfrac{\partial Q}{\partial x}\right)_{-m} = \left(\dfrac{\partial[Q]}{\partial x}\right)_{+(m-1)}$	
$m \quad D_P\left(\dfrac{\partial[P]}{\partial x}\right)_{-m} - D_P\left(\dfrac{\partial[P]}{\partial x}\right)_{+m} = 2k_3\Gamma_{ER}[Q]_m = D_Q\left(\dfrac{\partial Q}{\partial x}\right)_{+m} - D_Q\left(\dfrac{\partial[Q]}{\partial x}\right)_{-m}$	$l_0 + (m-1)l$
$\left(\dfrac{\partial[P]}{\partial x}\right)_{-(m+1)} = \left(\dfrac{\partial[P]}{\partial x}\right)_{+m} \quad \left(\dfrac{\partial[Q]}{\partial x}\right)_{-(m+1)} = \left(\dfrac{\partial[P]}{\partial x}\right)_{+m}$	
$m+1 \quad D_P\left(\dfrac{\partial[P]}{\partial x}\right)_{-(m+1)} - D_P\left(\dfrac{\partial[P]}{\partial x}\right)_{+(m+1)} = 2k_3\Gamma_{ER}[Q]_{(m+1)} = D_Q\left(\dfrac{\partial Q}{\partial x}\right)_{+(m+1)} - D_Q\left(\dfrac{\partial[Q]}{\partial x}\right)_{-(m+1)}$	$l_0 + ml$



el: electrode, 1 to $n-1$ inactive enzyme layers, n to N active enzyme layers, fs: film/solution interface. The minus sign in the subscripts designates the flux exiting from the enzyme layer toward the electrode; the plus sign designates the flux entering the enzyme layer from the solution side. x: distance from the electrode surface. l: average distance between two successive enzyme monomolecular layers; $l_0(<)$ is the average distance between the electrode surface and the first enzyme layer. D_P, D_Q: diffusion coefficients of P and Q in the film. D: common value of diffusion coefficients of P and Q in the solution. κ_P and κ_Q: partition coefficient of P and Q between the solution and the enzyme film. Γ_{ER}: surface concentration of the reduced form of the enzyme in each of the active enzyme layers.

Within this finite difference framework, the following approximations are also valid:

$$\left(\frac{\partial^2[\mathrm{P}]}{\partial x^2}\right)_m = \frac{\left(\frac{\partial[\mathrm{P}]}{\partial x}\right)_{+m} - \left(\frac{\partial[\mathrm{P}]}{\partial x}\right)_{-m}}{l} = \frac{[\mathrm{P}]_{m+1} - 2[\mathrm{P}]_m + [\mathrm{P}]_{m-1}}{l^2} \tag{54}$$

If, in addition, attention is focused on plateau currents rather than on whole current–potential curves, as in the experiments of Fig. 14, the concentrations of P at the electrode surface is zero.

A second consequence of the fact that the diffusion layer is much thicker than the enzyme film is that the fluxes in the solution are negligible as compared to the fluxes in the film. The two time-dependent integral equations relating the fluxes and the concentrations at the film/solution interface may be thus be replaced by

$$0 = D\left(\frac{\partial[\mathrm{P}]}{\partial x}\right)_{\mathrm{fs}} = D_{\mathrm{P}}\left(\frac{\partial[\mathrm{P}]}{\partial x}\right)_{+N} \text{ and}$$
$$0 = D\left(\frac{\partial[\mathrm{Q}]}{\partial x}\right)_{\mathrm{fs}} = D_{\mathrm{P}}\left(\frac{\partial[\mathrm{Q}]}{\partial x}\right)_{+N} \tag{55}$$

which allows the equations pertaining to the enzyme layer N to be simplified as

$$D_{\mathrm{P}}\left(\frac{\partial[\mathrm{P}]}{\partial x}\right)_{-N} = 2k_3\Gamma_{\mathrm{RE}}[\mathrm{Q}]_N = -D_{\mathrm{Q}}\left(\frac{\partial[\mathrm{Q}]}{\partial x}\right)_{-N} \tag{56}$$

Γ_{RE} is the surface concentration of the reduced form of the enzyme in each of the active enzyme layers. As seen earlier,

$$\Gamma_{\mathrm{RE}} = \frac{\Gamma_{\mathrm{E}}^0}{1 + k_3[\mathrm{Q}]\left(\frac{1}{k_2} + \frac{1}{k_{\mathrm{red}}[\mathrm{S}]}\right)} \tag{57}$$

where Γ_{E}^0: total surface concentration of the enzyme in each of the active enzyme layers.

The exact number and nature of independent factors the system is depending on may be obtained after introduction of the following dimensionless variables and parameters,

$$q = \frac{[\mathrm{Q}]}{\kappa_{\mathrm{Q}}C_{\mathrm{P}}^0},\ p = \frac{[\mathrm{P}]}{\kappa_{\mathrm{P}}C_{\mathrm{P}}^0},\ \lambda = \frac{lk_3\Gamma_{\mathrm{E}}^0}{\delta_{\mathrm{Q}}C_{\mathrm{P}}^0 D},$$
$$\sigma = k_3\kappa_{\mathrm{Q}}C_{\mathrm{P}}^0\left(\frac{1}{k_2} + \frac{1}{k_{\mathrm{red}}\kappa_{\mathrm{S}}[\mathrm{S}]}\right),\ f_0 = l/l_0,$$
$$\psi = \frac{i}{FS}\frac{l}{C_{\mathrm{P}}^0 D} \text{ with } \delta_{\mathrm{Q}} = \frac{D_{\mathrm{Q}}}{D},\ \delta_{\mathrm{P}} = \frac{D_{\mathrm{P}}}{D} \tag{58}$$

The concentrations of Q and P are normalized to the values they would have if the film were exposed to a concentration of Q or P equal to the bulk concentration of cosubstrate, C_{P}^0, taking into account the two partition coefficients, κ_{P} and κ_{Q}. Likewise, in the expression of [S], the (excess) concentration of substrate is multiplied by its partition coefficient, κ_{S}. The kinetic parameter λ, measures the competition within the enzyme film, between diffusion represented by the term $\delta_{\mathrm{Q}}D/l$ ($\delta_{\mathrm{Q}}D = D_{\mathrm{Q}}$) and the rate term $k_3\Gamma_{\mathrm{E}}^0$. The current is normalized toward the parameters of the diffusional transport of the cosubstrate in the solution. The set of equations listed in Table 3 ensues.

The system thus obtained involves $N - n + 1$ variables, including ψ, related by the same number of equations. Since $N - n$ of these are nonlinear equations because of the σq term, an iteration procedure is needed. One starts from a set of q values obtained for $\sigma = 0$. The equations then become linear and the Gauss elimination method may thus be used to obtain these starting q values. In a second round, these

Tab. 3 Dimensionless equations for an enzyme film containing $n-1$ inactive and $N-n$ active layers

$$q_n - q_{n-1} + f_0\psi = 0$$
$$q_{n+1} - q_n + f_0\psi = \frac{2\lambda q_n}{1+\sigma q_n}$$
$$q_{n+2} - 2q_{n+1} + q_n = \frac{2\lambda q_{n+1}}{1+\sigma q_{n+1}}$$

$$q_m - 2q_{m-1} + q_{m-2} = \frac{2\lambda q_{m-1}}{1+\sigma q_{m-1}}$$
$$q_{m+1} - 2q_m + q_{m-1} = \frac{2\lambda q_m}{1+\sigma q_m}$$
$$q_{m+2} - 2q_{m+1} + q_m = \frac{2\lambda q_{m+1}}{1+\sigma q_{m+1}}$$

$$q_N - 2q_{N-1} + q_{N-2} = \frac{2\lambda q_{N-1}}{1+\sigma q_{N-1}}$$
$$-q_N + q_{N-1} = \frac{2\lambda q_N}{1+\sigma q_N}$$

$$\frac{\kappa_P\delta_P}{\kappa_Q\delta_Q}q_N + (n-1+f_0)\psi = \frac{\kappa_P\delta_P}{\kappa_Q\delta_Q}$$

values are used in the σq term and a new set of q values are obtained by means of the Gauss elimination method. The procedure is repeated until the desired accuracy has been reached. The current and the concentration profiles may thus be obtained in this manner. The procedure also applies to the case where the amount of enzyme is not the same in each layer. It suffices to enter each value in the parameter λ and proceed with the calculation in the same way.

Each of these calculations requires inputting four independent parameters, namely, λ, σ, f_0, and $\kappa_P\delta_P/\kappa_Q\delta_Q$. Thus, if an estimate of l is to be derived from experimental values of the plateau current obtained with known values of the cosubstrate and substrate bulk concentrations, one ought to know from independent sources, the three rate constants, k_2, k_{red}, and k_3, the surface concentration of enzyme in each layer, Γ_E^0, the ratio of the distance between the electrode and the first enzyme layer to the distance between two successive layers, f_0, in case it differs from 1, the diffusion coefficient of the cosubstrate in the solution, D, the ratio of the diffusion coefficients of the active form of the cosubstrate in the film and in the solution, δ_Q, the partition coefficient of the cosubstrate and substrate depicting their passage from the solution to the film, κ_Q, and κ_S, respectively, and, for P, the product $\kappa_P\delta_P$.

Close form expressions of the current and of the concentration profiles may be obtained in the particular case where the film contains $n-1$ inactivated layers on top of which one active layer has been deposited. Indeed, making $n = N$ reduces the set of equations in Table 3 to the following three.

$$q_n - q_{n-1} + f_0\psi = 0 \tag{59}$$
$$-q_N + q_{N-1} = \frac{2\lambda q_N}{1+\sigma q_N} \tag{60}$$
$$\frac{\kappa_P\delta_P}{\kappa_Q\delta_Q}q_N + (n-1+f_0)\psi = \frac{\kappa_P\delta_P}{\kappa_Q\delta_Q} \tag{61}$$

Eliminating q_n and q_{n-1} and turning back to the dimensioned variables leads to

$$\frac{FS}{i} = \frac{1}{2\Gamma_E^0}\left(\frac{1}{k_2} + \frac{1}{k_{red}[S]}\right) + \frac{1}{2k_3\Gamma_E^0\kappa_Q C_P^0\left(1 - \frac{i}{FS}\frac{L}{\kappa_P\delta_P D C_P^0}\right)} \tag{62}$$

where $L = (n-1+f_0)l$ is the total thickness of the film. The concentration profiles are given by

$$\frac{C_Q}{C_P^0} = \kappa_Q\left(1 - \frac{i}{FSDC_P^0}\frac{L}{\kappa_Q\delta_Q}\right) - \frac{i}{FS\delta_Q DC_P^0}x, \quad \frac{C_P}{C_P^0} = \frac{i}{FS\delta_P DC_P^0}x \tag{63}$$

Unlike the general case, the diffusion coefficient of Q inside the film does not appear in the above expressions. The reason is that there is no competition between diffusion of Q and enzymatic reaction since the entire enzyme is confined within a single monolayer. If, in the particular case, an estimate of l were to be derived from experimental values of the plateau current, one would have to know from independent sources, the three rate constants, k_2, k_{red}, and k_3, the surface concentration of enzyme in each layer, Γ_E^0, the ratio of the distance between the electrode and the first enzyme layer to the distance between two successive layers, f_0, in case it differs from 1, the diffusion coefficient of the cosubstrate in the solution, D, the partition coefficient of the cosubstrate and substrate depicting their passage from the solution to the film, κ_Q, and κ_S, respectively, and, for P, the product $\kappa_P\delta_P$, that is, one parameter less than in the general case.

How the above treatment may be applied to the full analysis of experimental data is illustrated in Fig. 15 with the example of glucose oxidase with ferrocene methanol as the cosubstrate. The results obtained with three different electrode coatings are displayed in the figure, successively, 10 inactivated layers plus one active layer (Fig. 15a), 10 active layers (Fig. 15b) and a series with 5 inactivated plus 1–5 active layers (Fig. 15c). Several parameters are know independently, namely, the three rate constants, $k_3 = 1.2 \times 10^7$ M^{-1} sec^{-1}, $k_2 = 700$ sec^{-1}, and $k_{red} = 10^4$ M^{-1} sec^{-1}. Γ_E^0 is also known (see the pertinent values in the caption of Fig. 15). From the size of the various proteins involved, it can be estimated that $f_0 = 5/6$. The diffusion coefficient in the solution, $D = 6.7\ 10^{-6}$ cm^2 sec^{-1}.

The experiments depicted in Fig. 14, with the 10 active layers coating, enclose information about κ_Q. At high mediator concentrations (0.2–0.4 mM), in the linear region where the current response is controlled by the enzymatic reaction, the value of κ_Q does not influence the enzyme kinetics because the first term in the denominator of Eq. (79) is negligible as compared to the second term. Upon decreasing the mediator concentration, the downward deviation from proportionality takes place at smaller and smaller values of N. However, in the linear section of the $i_p - N$ plot, where the current response is still solely controlled by the enzymatic reaction, Eq. (47) applies. The first term in the denominator of Eq. (47) is no longer negligible as compared to the second term and therefore the value of κ_Q should influence the enzyme kinetics. The comparison of the slopes observed over the whole range of mediator concentrations then shows that $\kappa_Q = 1$. Additional information on the partition coefficients may be derived from the cyclic voltammetry of the enzyme electrode in the absence of glucose. At a low scan rate, the oxidation of ferrocene methanol shows a Nernstian reversible behavior and the voltammograms are practically identical at a bare glassy electrode and at the enzyme electrode. In slow scans, the diffusion layer of P and Q largely exceeds the film thickness and therefore the current response is insensitive to the diffusion of the two species within the film. The only manifestation of the presence of the film on the electrode thus derives from the partition coefficients in the relation between the bulk and the electrode concentrations, namely, the standard potential in the Nernst law, $E_{P/Q}^0$ at a bare electrode becomes $E_{P/Q}^0 + (RT/F)\ln(\kappa_P/\kappa_Q)$. Since the peak potentials are the same in the presence and absence of the film, it follows that $\kappa_P = \kappa_Q = 1$.

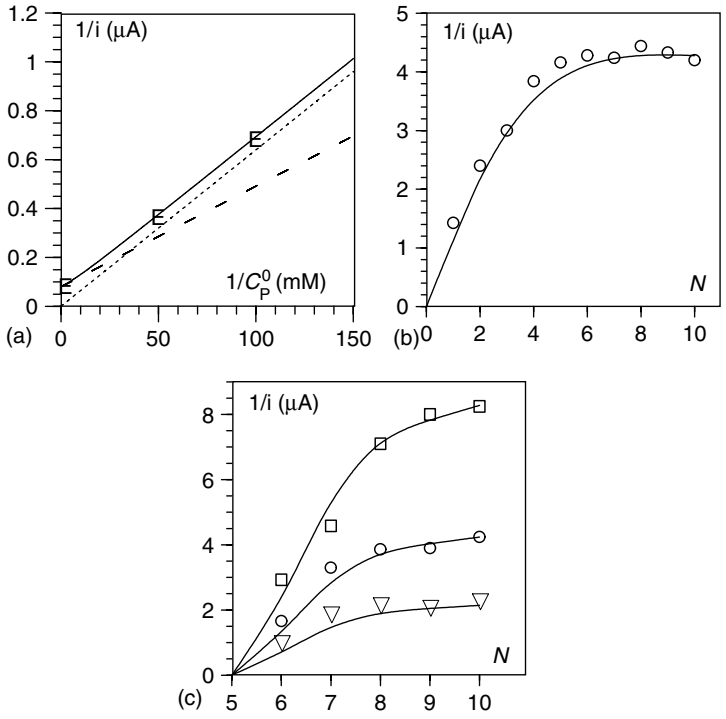


Fig. 15 Variations of the catalytic plateau current in the cyclic voltammetry of ferrocene methanol in the presence of 0.5 M glucose in a phosphate buffer (pH = 8, ionic strength = 0.1 M), at 25 °C and a scan rate of 0.04 V sec^{-1} at three different electrodes. (a) Electrode coated with 10 inactivated ($\Gamma_E^0 = 2.0 \times 10^{-12}$ mol cm^{-2}) and 1 active ($\Gamma_E^0 = 1.5 \times 10^{-12}$ mol cm^{-2}) glucose oxidase monomolecular layers. (b) Electrode coated with 1–10 active glucose oxidase monomolecular layers ($\Gamma_E^0 = 1.6 \times 10^{-12}$ mol cm^{-2}). (c) Electrode coated with 5 inactivated ($\Gamma_E^0 = 1.9 \times 10^{-12}$ mol cm^{-2}) and 1–5 active glucose oxidase monomolecular layers ($\Gamma_E^0 = 1.15 \times 10^{-12}$ mol cm^{-2} for the first and 2×10^{-12} mol cm^{-2} for the others). The full, doted, and dashed lines represent various theoretical curves as depicted in the text.

Information regarding the diffusion coefficients of the cosubstrate in the enzyme film may be derived from cyclic voltammetric experiments in the absence of substrate such as those depicted in Fig. 16. As the scan rate increases, a larger and larger portion of the diffusion layer stands inside the film (at e.g., 20 V sec^{-1}, the widths of the reaction layer and of the film are respectively 1.2 and 0.6×10^{-4} cm respectively). The cyclic voltammetric responses should thus be able to sense the characteristics of the diffusion of P and Q inside the film. In other words, the anodic and cathodic peak currents should reflect the magnitude of δ_Q and δ_P. Simulations (Fig. 16b) indicate that $\delta_Q \approx 1$ and $\delta_P < 1$. The simulation of the anodic peak current thus provides the value of δ_P if l is known and vice versa.

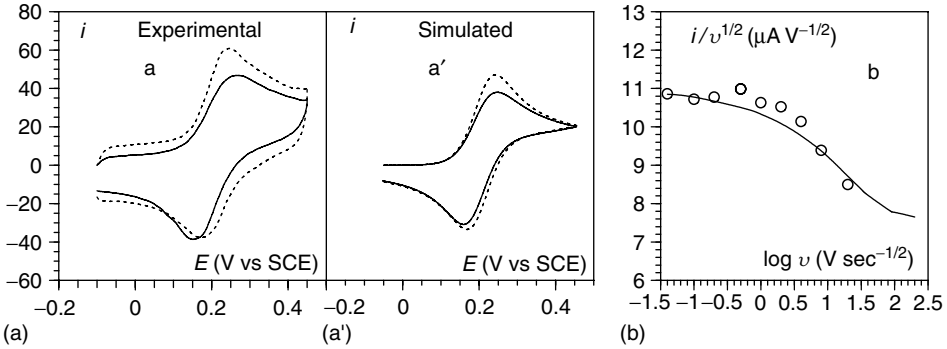


Fig. 16 Cyclic voltammetry of ferrocene methanol 0.2 mM in the absence of glucose and in pH 8 phosphate buffer (ionic strength: 0.1 M) at a bare electrode (· · · ·) and at a glucose oxidase electrode coated with 12 monolayers (———). Experimental (a) and simulated (a') voltammograms at 20 V sec^{-1}. Parameters for the simulation: $\kappa_P = \kappa_Q = 1$, $\delta_Q = 1$, $\delta_P = 0.6$, $(l/\delta_P)\ (F\nu/RTD)^{1/2} = 8.5 \times 10^{-2}$, $\alpha = 0.5$, $k_S = 0.19$ cm sec^{-1} for the bare electrode and 0.13 cm sec^{-1} for the enzyme coated electrode. (b) Experimental (E) and simulated (———) anodic peak current as a function of scan rate with the same parameters as in a, a'.

The value of l/δ_P (785 Å) is derived from the application of Eq. (57) to the results obtained with the 10 inactivated layers plus 1 active layer coating (Fig. 15a). It follows that $\delta_P = 0.6$ and $l = 470\ (\pm 15)$ Å. Although the dependency upon l and δ_P does not take the simple form with the two other coatings, iterative combination of the results obtained with these two coatings with those in Fig. 16 allows the determination of δ_P and l (Fig. 15b and c). The same two values are obtained in both cases.

The very fact that the same value of the thickness of the enzyme monomolecular layers is found with all the coatings investigated is strong evidence in favor

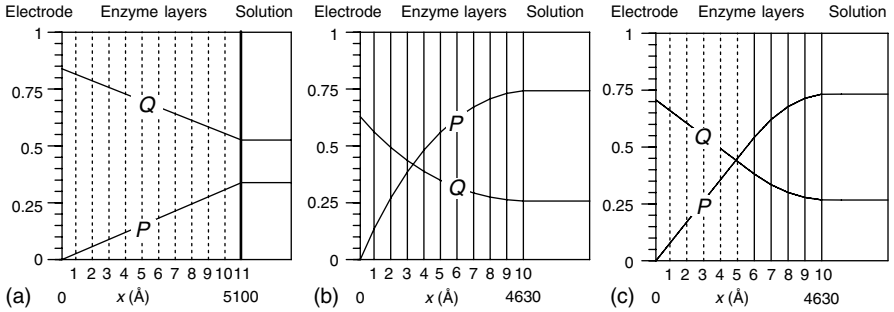


Fig. 17 Concentration profiles of the oxidized and reduced forms of the cosubstrate (normalized to the bulk concentration). (a) Electrode coated with 10 inactivated ($\Gamma_E^0 = 2.0 \times 10^{-12}$ mol cm^{-2}) and 1 active ($\Gamma_E^0 = 1.5 \times 10^{-12}$ mol cm^{-2}) glucose oxidase monomolecular layers, $C_P^0 = 0.01$ mM. (b) Electrode coated with 1 to 10 active glucose oxidase monomolecular layers ($\Gamma_E^0 = 1.6 \times 10^{-12}$ mol cm^{-2}), $C_P^0 = 0.05$ mM. (c) Electrode coated with 5 inactivated ($\Gamma_E^0 = 1.9 \times 10^{-12}$ mol cm^{-2}) and 1–5 active glucose oxidase monomolecular layers ($\Gamma_E^0 = 1.15 \times 10^{-12}$ mol cm^{-2} for the first and 2×10^{-12} mol cm^{-2} for the 4 others), $C_P^0 = 0.005$ mM.

of the spatial order of the system as represented in Sch. 8 and in Fig. 17 showing the concentrations profiles in three of the investigated films.

13.4.3 Inhibition by products: Proton Gradients

The products of the reaction they catalyze may inhibit many enzymes through Michaelis–Menten kinetic retroaction. Protons, which are involved as products or reactants in a number of cases, may also influence the enzymatic kinetics. The course of the reaction may therefore be altered by the attending production or depletion of protons. It is thus interesting to examine whether these phenomena may be revealed by the effect they might have on the electrochemical responses of immobilized enzyme films under appropriate conditions [92]. A first clue of the existence of such inhibition effects is the observation of hysteresis behaviors of the type shown in Fig. 18(a) where data obtained with 10 glucose oxidase monolayers with ferrocene methanol as cosubstrate have been taken as example. In the absence of inhibition, the forward and reverse traces should be exactly superimposed. Hysteresis increases to the point of making a peak appear on the forward trace as the scan rate decreases and as the concentration of the buffer decreases, as illustrated in Fig. 18c, c', c'', c''' by comparison with Fig. 18(a).

Inhibition by the product implies considering the reaction sequence depicted in Sch. 9 in place of Sch. 1. k_2 no longer stands for the one-step formation of the product, R, and the reduced form of the enzyme, RE, but rather the formation of the complex, RER, associating the reduced form of the enzyme with the product. To complete the Michaelis–Menten scheme pertaining to the product, the complex may dissociate reversibly with a rate constant k'_{-1} for its dissociation and a rate constant k'_1 for its formation from R and RE.

The governing flux equations are summarized in Table 4, the surface concentration of the reduced enzyme Γ_{RE} being given by Eq. (64), which replaces Eq. (57).

$$\Gamma_{RE} = \frac{\Gamma_E^0}{1 + \frac{[R]}{K'_1} + k_3[Q]\left(\frac{1}{k_2} + \frac{1}{k_{red}[S]}\right)} \quad (64)$$

with $K'_1 = k'_1/k'_{-1}$

If the enzymatic reaction produces protons, as is often the case with oxidases, the local variations of pH due to insufficient buffering may locally modify the rate of the various reactions involved and therefore influence the electrochemical response of the system. For example, in the case of glucose oxidase with ferrocene methanol as cosubstrate, the main effect of pH is on k_3 [35]:

$$k_3 = \frac{k_{3,min} + 10^{(pH - pK_a^E)} k_{3,max}}{1 + +10^{(pH - pK_a^E)}}$$

$$(\text{with: } pH = pK_a^{BH/B^-} + \log([B^-]/[BH])) \quad (65)$$

where $k_{3,min} = 6.3 \times 10^4\ M^{-1}\ sec^{-1}$, $k_{3,max} = 1.2 \times 10^7\ M^{-1}\ sec^{-1}$, and pK_a^E, the average pK_a of the $FADH_2/FADH^-$ and $FADH^{\cdot}/FAD^{\cdot -}$ couples is equal to 7 [35]. k_2 also depends on pH ($k_2 = 1900 - 150$ pH), whereas $k_{red}(= 1.1 \times 10^4\ M^{-1}\ sec^{-1})$ and K'_1 ($= 1.4 \times 10^{-2}$ M [92]) may be considered as being pH independent.

In Table 4, the boundary conditions at the electrode surface involve the Butler–Volmer law describing the kinetics of electron transfer between the electrode and the cosubstrate rather than the Nernst law describing its thermodynamics (as in Table 2), because it is interesting

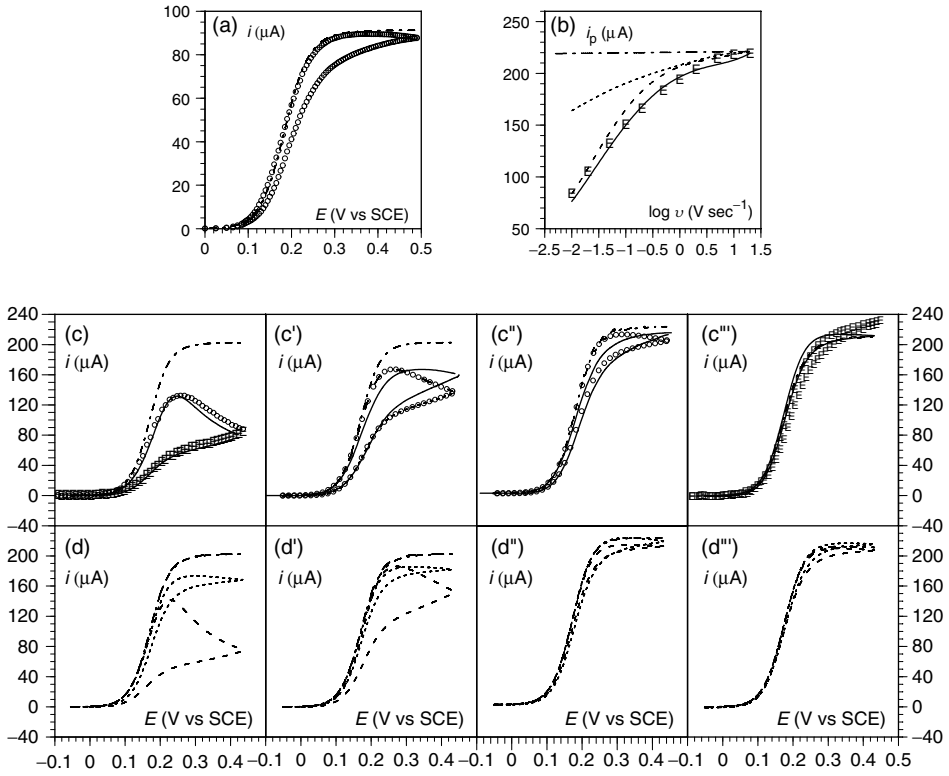
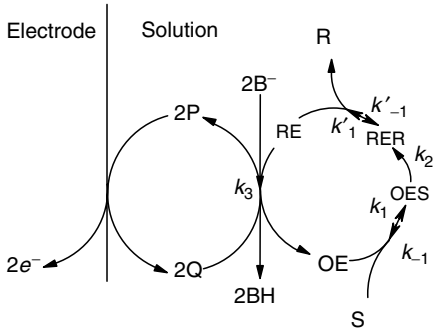


Fig. 18 Cyclic voltammetry of the catalysis of glucose oxidation at a glassy carbon disk electrode coated with 10 glucose oxidase monolayers in the presence of glucose and ferrocene methanol in pH 8.0 phosphate buffer (ionic strength, 0.1 M). Temperature: 25 °C. (a) $\Gamma_E^0 = 1.5 \times 10^{-12}$ mol cm^{-2}, cosubstrate concentration: 0.2 mM, glucose concentration: 0.5 M [$H_2PO_4^-$] = 2.65 mM, [HPO_4^{2-}] = 32.7 mM, scan rate: 0.04 V sec^{-1}. Solid line: experimental data, dashed line: simulation without product inhibition. (b, c, c', c'', c''', d, d', d'', d''') $\Gamma_E^0 = 2.65 \times 10^{-12}$ mol cm^{-2}, cosubstrate concentration: 0.4 mM, glucose concentration: 0.4 M, [$H_2PO_4^-$] = 1.48 mM, [HPO_4^{2-}] = 16.5 mM, [SO_4^{2-}] = 16.4 mM with Na^+ as counterion. Open circles: experimental data, full line: simulation of the combined effect of proton and glucono-δ-lactone production, dotted line: simulation of proton production alone, dashed line: simulation of inhibition by glucono-δ-lactone production alone, dashed-dotted line: no inhibition. (b) Variation of the peak current with the scan rate. (c, c', c'', c''') Experimental and simulated voltammograms. (d, d', d'', d''') Dissection of the combined effect of proton and glucono-δ-lactone production into its two components. Scan rate: 0.05 (c, d), 0.2 (c', d'), 1 (c'', d''), 10 (c''', d''') V sec^{-1}. Common parameters for the simulations: $k_2 = 700$ sec^{-1}, $k_3 = 1.1 \times 10^7$ M^{-1} sec^{-1}, $k_{red} = 1.1 \times 10^4$ M^{-1} sec^{-1}, $k_S = 0.19$ cm sec^{-1}, $\alpha = 0.5$, $D = 5.5 \times 10^{-6}$ cm^2 sec^{-1}, $\delta_P = 0.6$ and $l = 470$ Å.

to increase the scan rate to check the expectation that the effect of product inhibition should decrease and ultimately vanish. The kinetics of electron transfer may well interfere under such conditions. Exploring the time dependence of product inhibition leads to a different adimensionalization strategy from the one used in

Scheme 9



S: substrate, R: product,
OE: oxidized form of the enzyme,
OES: its complex with the substrate,
RE: reduced form of the enzyme,
RER: its complex with the product,
P: reduced form of the mediator (cosubstrate),
Q: oxidized form of the mediator (cosubstrate),
B^-, BH: base and acid components of the buffer.

the preceding section where only time-independent plateau currents were dealt with. The following dimensionless variables and parameters are thus introduced.

$\tau = (Fv/RT)t, \qquad \xi = (F/RT)(E - E^0_{P/Q}) = -u + \tau$ with $u = -(F/RT)(E_i - E^0_{P/Q})$ during the anodic scan starting at E_i and $\xi = -u' - \tau$ with $u' = -(F/RT)(2E_f - E_i - E^0_{P/Q})$ during the reverse cathodic scan starting at E_f.

$$
\begin{aligned}
&y=(Fv/DRT)^{1/2}x,\ \varepsilon=(Fv/DRT)^{1/2}l,\\
&\varepsilon_0=(Fv/DRT)^{1/2}l_0\\
&p=[P]/C^0_P,\ q=[Q]/C^0_P,\ r=[R]/C^0_P\\
&bh=[BH]/C^0_P,\ b^-=[B^-]/C^0_P,\ \text{with:}\\
&bh^0=C^0_{BH}/C^0_P,\ b^{-0}=C^0_{BH}/C^0_P\\
&\lambda=(k_3\Gamma^0_E/\delta_P)(RT/FVD)^{1/2},\\
&\sigma=k_3C^0_P(1/k_2+1/k_G[S])\\
&\chi=C^0_P,/K_1,\ \Lambda=k_S(RT/FVD)^{1/2}\\
&\psi=(i/FSC^0_P)(RT/FVD)^{1/2}
\end{aligned}
\tag{66}
$$

Considering as example the case of glucose oxidase and ferrocene methanol, the problem is simplified by the fact that the diffusion coefficients inside and outside the film are the same except for P where $\delta_P = D_P/D = 0.6$.

$$
\begin{aligned}
&\left[\left(\frac{\partial q}{\partial y}\right)_{1\le m\le N-1}-\left(\frac{\partial q}{\partial y}\right)_{0\le m-1\le N-2}\right]\\
&=-\delta_P\left[\left(\frac{\partial p}{\partial y}\right)_{1\le m\le N-1}-\left(\frac{\partial p}{\partial y}\right)_{0\le m-1\le N-2}\right]\\
&=\left[\left(\frac{\partial b^-}{\partial y}\right)_{1\le m\le N-1}-\left(\frac{\partial b^-}{\partial y}\right)_{0\le m-1\le N-2}\right]\\
&=-\left[\left(\frac{\partial bh}{\partial y}\right)_{1\le m\le N-1}-\left(\frac{\partial bh}{\partial y}\right)_{0\le m-1\le N-2}\right]\\
&=-2\left[\left(\frac{\partial r}{\partial y}\right)_{1\le m\le N-1}-\left(\frac{\partial r}{\partial y}\right)_{0\le m-1\le N-2}\right]\\
&=\frac{2\lambda_{1\le m\le N-1}q_{1\le m\le N-1}}{1+\chi r_{1\le m\le N-1}+\sigma_{1\le m\le N-1}q_{1\le m\le N-1}}
\end{aligned}
\tag{67}
$$

Tab. 4 Fluxes equations for inhibition by-product and acid formation in an enzyme film containing N active layers

		x
el	$\frac{i}{FS} = D_P\left(\frac{\partial[P]}{\partial x}\right)_{el} = -D_Q\left(\frac{\partial[Q]}{\partial x}\right)_{el}\left(\frac{\partial[R]}{\partial x}\right)_{el} = \left(\frac{\partial[BH]}{\partial x}\right)_{el} = \left(\frac{\partial[B^-]}{\partial x}\right)_{el} = 0$ $\frac{i}{FS} = k_S \exp\left[\frac{\alpha F}{RT}(E - E^0_{P/Q})\right]\left\{[P]_{el} - [Q]_{el}\exp\left[-\frac{F}{RT}(E - E^0_{P/Q})\right]\right\}$ $\left(\frac{\partial[P]}{\partial x}\right)_{-1} = \left(\frac{\partial[P]}{\partial x}\right)_{el}\left(\frac{\partial[Q]}{\partial x}\right)_{-1} = \left(\frac{\partial[Q]}{\partial x}\right)_{el}$	0
	$\left(\frac{\partial[R]}{\partial x}\right)_{-1} = \left(\frac{\partial[R]}{\partial x}\right)_{el}\left(\frac{\partial[BH]}{\partial x}\right)_{-1} = \left(\frac{\partial[BH]}{\partial x}\right)_{el}\left(\frac{\partial[B^-]}{\partial x}\right)_{-1} = \left(\frac{\partial[B^-]}{\partial x}\right)_{el}$	l_0
1	$2k_3\Gamma_{ER}[Q]_1 = D_P\left\{\left(\frac{\partial[P]}{\partial x}\right)_{-1} - \left(\frac{\partial[P]}{\partial x}\right)_{+1}\right\} = D_Q\left\{\left(\frac{\partial Q}{\partial x}\right)_{+1} - \left(\frac{\partial[Q]}{\partial x}\right)_{-1}\right\}$ $2D_R\left\{\left(\frac{\partial[R]}{\partial x}\right)_{-1} - \left(\frac{\partial[R]}{\partial x}\right)_{+1}\right\} =$ $D_{BH}\left\{\left(\frac{\partial[BH]}{\partial x}\right)_{-1} - \left(\frac{\partial[BH]}{\partial x}\right)_{+1}\right\} = D_B\left\{\left(\frac{\partial[B^-]}{\partial x}\right)_{-1} - \left(\frac{\partial[B^-]}{\partial x}\right)_{+1}\right\}$	$l_0 + l$
	⋮	
$m-1$	$2k_3\Gamma_{ER}[Q]_{(m-1)} = D_P\left\{\left(\frac{\partial[P]}{\partial x}\right)_{-(m-1)} - \left(\frac{\partial[P]}{\partial x}\right)_{+(m-1)}\right\} = D_Q\left\{\left(\frac{\partial Q}{\partial x}\right)_{+(m-1)} - \left(\frac{\partial[Q]}{\partial x}\right)_{-(m-1)}\right\}$ $2D_R\left\{\left(\frac{\partial[R]}{\partial x}\right)_{-(m-1)} - \left(\frac{\partial[R]}{\partial x}\right)_{+(m-1)}\right\} =$ $D_{BH}\left\{\left(\frac{\partial[BH]}{\partial x}\right)_{-(m-1)} - \left(\frac{\partial[BH]}{\partial x}\right)_{+(m-1)}\right\} = D_B\left\{\left(\frac{\partial[B^-]}{\partial x}\right)_{-(m-1)} - \left(\frac{\partial[B^-]}{\partial x}\right)_{+(m-1)}\right\}$	$l_0 + (m-2)l$

$$\left(\frac{\partial[\mathrm{P}]}{\partial x}\right)_{-m} = \left(\frac{\partial[\mathrm{P}]}{\partial x}\right)_{+(m-1)} \quad \left(\frac{\partial[\mathrm{Q}]}{\partial x}\right)_{-m} = \left(\frac{\partial[\mathrm{Q}]}{\partial x}\right)_{+(m-1)}$$

$$\left(\frac{\partial[\mathrm{R}]}{\partial x}\right)_{-m} = \left(\frac{\partial[\mathrm{R}]}{\partial x}\right)_{+(m-1)} \quad \left(\frac{\partial[\mathrm{BH}]}{\partial x}\right)_{-m} = \left(\frac{\partial[\mathrm{BH}]}{\partial x}\right)_{+(m-1)} \quad \left(\frac{\partial[\mathrm{B}^-]}{\partial x}\right)_{-m} = \left(\frac{\partial[\mathrm{B}^-]}{\partial x}\right)_{+(m-1)}$$

$$2k_3\Gamma_{\mathrm{ER}}[\mathrm{Q}]_m = D_{\mathrm{P}}\left\{\left(\frac{\partial[\mathrm{P}]}{\partial x}\right)_{-m} - \left(\frac{\partial[\mathrm{P}]}{\partial x}\right)_{+m}\right\} = D_{\mathrm{Q}}\left\{\left(\frac{\partial \mathrm{Q}}{\partial x}\right)_{+m} - \left(\frac{\partial[\mathrm{Q}]}{\partial x}\right)_{-m}\right\}$$

m —— $2D_{\mathrm{R}}\left\{\left(\frac{\partial[\mathrm{R}]}{\partial x}\right)_{-m} - \left(\frac{\partial[\mathrm{R}]}{\partial x}\right)_{+m}\right\} =$ —— $l_0 + (m-1)l$

$$D_{\mathrm{BH}}\left\{\left(\frac{\partial[\mathrm{BH}]}{\partial x}\right)_{-m} - \left(\frac{\partial[\mathrm{BH}]}{\partial x}\right)_{+m}\right\} = D_{\mathrm{B}}\left\{\left(\frac{\partial[\mathrm{B}^-]}{\partial x}\right)_{-m} - \left(\frac{\partial[\mathrm{B}^-]}{\partial x}\right)_{+m}\right\}$$

$$\left(\frac{\partial[\mathrm{P}]}{\partial x}\right)_{-(m+1)} = \left(\frac{\partial[\mathrm{P}]}{\partial x}\right)_{+m} \quad \left(\frac{\partial[\mathrm{Q}]}{\partial x}\right)_{-(m+1)} = \left(\frac{\partial[\mathrm{Q}]}{\partial x}\right)_{+m}$$

$$\left(\frac{\partial[\mathrm{R}]}{\partial x}\right)_{-(m+1)} = \left(\frac{\partial[\mathrm{R}]}{\partial x}\right)_{+m} \quad \left(\frac{\partial[\mathrm{BH}]}{\partial x}\right)_{-(m+1)} = \left(\frac{\partial[\mathrm{BH}]}{\partial x}\right)_{+m} \quad \left(\frac{\partial[\mathrm{B}^-]}{\partial x}\right)_{-(m+1)} = \left(\frac{\partial[\mathrm{B}^-]}{\partial x}\right)_{+m}$$

$$2k_3\Gamma_{\mathrm{ER}}[\mathrm{Q}]_{(m+1)} = D_{\mathrm{P}}\left\{\left(\frac{\partial[\mathrm{P}]}{\partial x}\right)_{-(m+1)} - \left(\frac{\partial[\mathrm{P}]}{\partial x}\right)_{+(m+1)}\right\} = D_{\mathrm{Q}}\left\{\left(\frac{\partial \mathrm{Q}}{\partial x}\right)_{+(m+1)} - \left(\frac{\partial[\mathrm{Q}]}{\partial x}\right)_{-(m+1)}\right\}$$

$m+1$ —— $2D_{\mathrm{R}}\left\{\left(\frac{\partial[\mathrm{R}]}{\partial x}\right)_{-(m+1)} - \left(\frac{\partial[\mathrm{R}]}{\partial x}\right)_{+(m+1)}\right\} =$ —— $l_0 + ml$

$$D_{\mathrm{BH}}\left\{\left(\frac{\partial[\mathrm{BH}]}{\partial x}\right)_{-(m+1)} - \left(\frac{\partial[\mathrm{BH}]}{\partial x}\right)_{+(m+1)}\right\} = D_{\mathrm{B}}\left\{\left(\frac{\partial[\mathrm{B}^-]}{\partial x}\right)_{-(m+1)} - \left(\frac{\partial[\mathrm{B}^-]}{\partial x}\right)_{+(m+1)}\right\}$$

.

$$2k_3\Gamma_{\mathrm{ER}}[\mathrm{Q}]_{(N-1)} = D_{\mathrm{P}}\left\{\left(\frac{\partial[\mathrm{P}]}{\partial x}\right)_{-(N-1)} - \left(\frac{\partial[\mathrm{P}]}{\partial x}\right)_{+(N-1)}\right\} = D_{\mathrm{Q}}\left\{\left(\frac{\partial \mathrm{Q}}{\partial x}\right)_{+(N-1)} - \left(\frac{\partial[\mathrm{Q}]}{\partial x}\right)_{-(N-1)}\right\}$$

$N-1$ —— $2D_{\mathrm{R}}\left\{\left(\frac{\partial[\mathrm{R}]}{\partial x}\right)_{-(N-1)} - \left(\frac{\partial[\mathrm{R}]}{\partial x}\right)_{+(N-1)}\right\} =$ —— $l_0 + (N-2)l$

$$D_{\mathrm{BH}}\left\{\left(\frac{\partial[\mathrm{BH}]}{\partial x}\right)_{-(N-1)} - \left(\frac{\partial[\mathrm{BH}]}{\partial x}\right)_{+(N-1)}\right\} = D_{\mathrm{B}}\left\{\left(\frac{\partial[\mathrm{B}^-]}{\partial x}\right)_{-(N-1)} - \left(\frac{\partial[\mathrm{B}^-]}{\partial x}\right)_{+(N-1)}\right\}$$

(*continued overleaf*)

Tab. 4 (*continued*)

		x
	$\left(\frac{\partial[\mathrm{P}]}{\partial x}\right)_{-N} = \left(\frac{\partial[\mathrm{P}]}{\partial x}\right)_{+(N-1)} \left(\frac{\partial[\mathrm{Q}]}{\partial x}\right)_{-N} = \left(\frac{\partial[\mathrm{Q}]}{\partial x}\right)_{+(N-1)}$	
	$\left(\frac{\partial[\mathrm{R}]}{\partial x}\right)_{-N} = \left(\frac{\partial[\mathrm{R}]}{\partial x}\right)_{+(N-1)} \left(\frac{\partial[\mathrm{BH}]}{\partial x}\right)_{-N} = \left(\frac{\partial[\mathrm{BH}]}{\partial x}\right)_{+(N-1)} \left(\frac{\partial[\mathrm{B}^-]}{\partial x}\right)_{-N} = \left(\frac{\partial[\mathrm{B}^-]}{\partial x}\right)_{+(N-1)}$	
	$2k_3\Gamma_{\mathrm{ER}}[\mathrm{Q}]_N = D_{\mathrm{P}}\left\{\left(\frac{\partial[\mathrm{P}]}{\partial x}\right)_{-N} - \left(\frac{\partial[\mathrm{P}]}{\partial x}\right)_{+N}\right\} = D_{\mathrm{Q}}\left\{\left(\frac{\partial \mathrm{Q}}{\partial x}\right)_{+N} - \left(\frac{\partial[\mathrm{Q}]}{\partial x}\right)_{-N}\right\}$	
N	$2D_{\mathrm{R}}\left\{\left(\frac{\partial[\mathrm{R}]}{\partial x}\right)_{-N} - \left(\frac{\partial[\mathrm{R}]}{\partial x}\right)_{+N}\right\} =$	$l_0 + (N-1)$
	$D_{\mathrm{BH}}\left\{\left(\frac{\partial[\mathrm{BH}]}{\partial x}\right)_{-N} - \left(\frac{\partial[\mathrm{BH}]}{\partial x}\right)_{+N}\right\} = D_{\mathrm{B}}\left\{\left(\frac{\partial[\mathrm{B}^-]}{\partial x}\right)_{-N} - \left(\frac{\partial[\mathrm{B}^-]}{\partial x}\right)_{+N}\right\}$	
	$D\left(\frac{\partial[\mathrm{P}]}{\partial x}\right)_{\mathrm{fs}} = D_{\mathrm{P}}\left(\frac{\partial[\mathrm{P}]}{\partial x}\right)_{+N} D\left(\frac{\partial[\mathrm{Q}]}{\partial x}\right)_{\mathrm{fs}} = D_{\mathrm{Q}}\left(\frac{\partial[\mathrm{Q}]}{\partial x}\right)_{+N}$	
fs	$D\left(\frac{\partial[\mathrm{R}]}{\partial x}\right)_{\mathrm{fs}} = D_{\mathrm{R}}\left(\frac{\partial[\mathrm{R}]}{\partial x}\right)_{+N} D\left(\frac{\partial[\mathrm{BH}]}{\partial x}\right)_{\mathrm{fs}} = D_{\mathrm{BH}}\left(\frac{\partial[\mathrm{BH}]}{\partial x}\right)_{+N} D\left(\frac{\partial[\mathrm{B}^-]}{\partial x}\right)_{\mathrm{fs}} = D_{\mathrm{B}}\left(\frac{\partial[\mathrm{B}^-]}{\partial x}\right)_{+N}$	
	$[\mathrm{P}]_N = \kappa_{\mathrm{P}}[\mathrm{P}]_{\mathrm{fs}}[\mathrm{Q}]_N = \kappa_{\mathrm{Q}}[\mathrm{Q}]_{\mathrm{fs}}\mathrm{R}_N = \kappa_{\mathrm{R}}[\mathrm{R}]_{\mathrm{fs}}[\mathrm{BH}]_N = \kappa_{\mathrm{BH}}[\mathrm{P}]_{\mathrm{fs}}[\mathrm{B}^-]_N = \kappa_{\mathrm{B}}[\mathrm{B}^-]_{\mathrm{fs}}$	
	$[\mathrm{P}]_{\mathrm{fs}} = C^0_{\mathrm{P}} - \sqrt{\frac{D}{\pi}}\int_0^t \left(\frac{\partial[\mathrm{P}]}{\partial x}\right)_{\mathrm{fs}} \frac{\mathrm{d}\eta}{\sqrt{t-\eta}}, [\mathrm{Q}]_{\mathrm{fs}} = -\sqrt{\frac{D}{\pi}}\int_0^t \left(\frac{\partial[\mathrm{Q}]}{\partial x}\right)_{\mathrm{fs}} \frac{\mathrm{d}\eta}{\sqrt{t-\eta}}$	
	$[\mathrm{R}]_{\mathrm{fs}} = -\sqrt{\frac{D}{\pi}}\int_0^t \left(\frac{\partial[\mathrm{R}]}{\partial x}\right)_{\mathrm{fs}} \frac{\mathrm{d}\eta}{\sqrt{t-\eta}},$	
	$[\mathrm{BH}]_{\mathrm{fs}} = C^0_{\mathrm{BH}} - \sqrt{\frac{D}{\pi}}\int_0^t \left(\frac{\partial[\mathrm{BH}]}{\partial x}\right)_{\mathrm{fs}} \frac{\mathrm{d}\eta}{\sqrt{t-\eta}}, [\mathrm{B}^-]_{\mathrm{fs}} = -\sqrt{\frac{D}{\pi}}\int_0^t \left(\frac{\partial[\mathrm{B}^-]}{\partial x}\right)_{\mathrm{fs}} \frac{\mathrm{d}\eta}{\sqrt{t-\eta}}$	

el: electrode, fs: film/solution interface. The minus sign in the subscripts designates the flux exiting from the enzyme layer toward the electrode; the plus sign designates the flux entering the enzyme layer from the solution side. x: distance from the electrode surface. l: average distance between two successive enzyme monomolecular layers; $l_0(<)$ is the average distance between the electrode surface and the first enzyme layer. D_{species}: diffusion coefficients of the subscript species in the film. D: common value of diffusion coefficients of all species in the solution. $\kappa_{\mathrm{species}}$: partition coefficient of the subscript species between the solution and the enzyme film. Γ_{RE}: surface concentration of the reduced form of the enzyme in each of the active enzyme layers (see text). $E^0_{\mathrm{P/Q}}$, k_S and α are the standard potential, standard rate constant and transfer coefficient of the cosubstrate couple respectively.

At the electrode surface,

$$\psi = \delta_P \left(\frac{\partial p}{\partial y}\right)_{el} = -\left(\frac{\partial q}{\partial y}\right)_{el} = \Lambda \exp(\alpha\xi)[p_{el} - q_{el}\exp(-\xi)] \quad (68)$$

$$\left(\frac{\partial b^-}{\partial y}\right)_{el} = \left(\frac{\partial bh}{\partial y}\right)_{el} = \left(\frac{\partial r}{\partial y}\right)_{el} = 0 \quad (69)$$

At the film solution interface,

$$\left[\left(\frac{\partial q}{\partial y}\right)_N - \left(\frac{\partial q}{\partial y}\right)_{N-1}\right] = -\delta_P\left[\left(\frac{\partial p}{\partial y}\right)_N - \left(\frac{\partial p}{\partial y}\right)_{N-1}\right] = \left[\left(\frac{\partial b^-}{\partial y}\right)_N - \left(\frac{\partial b^-}{\partial y}\right)_{N-1}\right] = -\left[\left(\frac{\partial bh}{\partial y}\right)_N - \left(\frac{\partial bh}{\partial y}\right)_{N-1}\right] = -2\left[\left(\frac{\partial r}{\partial y}\right)_N - \left(\frac{\partial r}{\partial y}\right)_{N-1}\right] = \frac{2\lambda_N q_N}{1 + \chi r_N + \sigma_N q_N} \quad (70)$$

and

$$p_N = 1 - \frac{1}{\sqrt{\pi}}\int_0^\tau \left(\frac{\partial p}{\partial y}\right)_N \frac{d\eta}{\sqrt{\tau - \eta}},$$

$$q_N = -\frac{1}{\sqrt{\pi}}\int_0^\tau \left(\frac{\partial q}{\partial y}\right)_N \frac{d\eta}{\sqrt{\tau - \eta}}$$

$$r_N = -\frac{1}{\sqrt{\pi}}\int_0^\tau \left(\frac{\partial r}{\partial y}\right)_N \frac{d\eta}{\sqrt{\tau - \eta}},$$

$$bh_N = bh^0 - \frac{1}{\sqrt{\pi}}\int_0^\tau \left(\frac{\partial bh}{\partial y}\right)_N \frac{d\eta}{\sqrt{\tau - \eta}},$$

$$b_N{}^- = b^{-0} - \frac{1}{\sqrt{\pi}}\int_0^\tau \left(\frac{\partial b^-}{\partial y}\right)_N \frac{d\eta}{\sqrt{\tau - \eta}} \quad (71)$$

The initial conditions ($\tau = 0$) are, whatever the space index,

$$p = 1,\ q = 0,\ r_N = 0,\ bh_N = bh^0,\ b_N^- = b^{-0}$$

Appropriate linear combinations thus lead to a series of equations involving the qs:

$$\psi = -\left(\frac{\partial q}{\partial y}\right)_{el} = \Lambda \exp(\alpha\xi)\left[1 - q_N\frac{q_{el} - q_N}{\delta_P} - q_{el}\exp(-\xi)\right] \quad (72)$$

$$\left[\left(\frac{\partial q}{\partial y}\right)_{1\le m\le N} - \left(\frac{\partial q}{\partial y}\right)_{0\le m-1\le N-1}\right] = \frac{2\lambda_{1\le m\le N}\, q_{1\le m\le N}}{1 + \chi r_{1\le m\le N} + \sigma_{1\le m\le N}\, q_{1\le m\le N}} \quad (73)$$

$$q_N = -\frac{1}{\sqrt{\pi}}\int_0^\tau \left(\frac{\partial q}{\partial y}\right)_N \frac{d\eta}{\sqrt{\tau - \eta}} \quad (74)$$

where the effect of inhibition by R appears in the term $\chi r_{1\le m\le N}$ while inhibition by acid production derives from the pH dependence of λ and σ (through the pH dependence of k_3 and k_2 respectively), the pH being related to bh and b^- through

$$pH_{el\text{ and }1\le m\le N} = pK_a^{BH/B^-} + \log(b^-_{el\text{ and }1\le m\le N}/bh_{el\text{ and }1\le m\le N}) \quad (75)$$

The r, bh, and b^- s are related to the qs by means of

$$r_{el\text{ and }1\le m\le N} = \frac{1}{2\sqrt{\pi}}\int_0^\tau \frac{\psi\, d\eta}{\sqrt{\tau - \eta}} - \frac{q_{el\text{ and }1\le m\le N}}{2} \quad (76)$$

$$bh_{el\text{ and }1\le m\le N} = bh^0 + 2r_{el\text{ and }1\le m\le N},$$

$$b^-_{el\text{ and }1\le m\le N} = b^{-0} - 2r_{el\text{ and }1\le m\le N}$$

The various dimensionless concentrations are not only functions of the space variable through the index m but also of time ($\tau = j\Delta\tau$). This double indexation can be handled as follows. After linearization of

the q gradient in each layer, Eq. (73) can be written as

$$\text{for } 1 \le m \le N-1: \quad q_{m+1,j} - 2q_{m,j} + q_{m-1,j} = \frac{2\lambda_{m,j} q_{m,j}}{1 + \chi r_{m,j} + \sigma_{m,j} q_{m,j}} \tag{77}$$

The boundary condition at the electrode surface (72) becomes

$$\frac{q_{\mathrm{el},j} - q_{1,j}}{\varepsilon_0} = \Lambda \exp(\alpha\xi)\left[1 - q_{N,j}\frac{q_{\mathrm{el},j} - q_{N,j}}{\delta_{\mathrm{P}}} - q_{\mathrm{el},j}\exp(-\xi)\right] \tag{78}$$

The boundary condition at the film/solution interface is obtained as follows:

$$\text{For } m = N,\ \frac{q_{N-1,j} - q_{N,j}}{\varepsilon} = -\left(\frac{\partial q}{\partial y}\right)_{N,j} + \frac{2\lambda_{N,j} q_{N,j}}{1 + \chi r_{N,j} + \sigma_{N,j} q_{N,j}} \tag{79}$$

while from (74),

$$q_{N,j} = -\frac{1}{\sqrt{\pi}}\left\{\begin{aligned}&\int_0^{\Delta\tau} \frac{1}{2}\left[\left(\frac{\partial q}{\partial y}\right)_{N,1} + \left(\frac{\partial q}{\partial y}\right)_{N,0}\right] \times \frac{\mathrm{d}\eta}{\sqrt{\tau - \eta}} + \dots \\ &+ \int_{(k-1)\Delta\tau}^{k\Delta\tau} \frac{1}{2}\left[\left(\frac{\partial q}{\partial y}\right)_{N,k} + \left(\frac{\partial q}{\partial y}\right)_{N,k-1}\right] \frac{\mathrm{d}\eta}{\sqrt{\tau - \eta}} + \dots \\ &+ \int_{(j-1)\Delta\tau}^{j\Delta\tau} \frac{1}{2}\left[\left(\frac{\partial q}{\partial y}\right)_{N,j} + \left(\frac{\partial q}{\partial y}\right)_{N,j-1}\right] \frac{\mathrm{d}\eta}{\sqrt{\tau - \eta}}\end{aligned}\right\} \tag{80}$$

After integration,

$$q_{N,j} = \frac{\sqrt{\Delta\tau}}{\sqrt{\pi}}\left[-\left(\frac{\partial q}{\partial y}\right)_{N,j} + \Sigma_q\right] \tag{81}$$

$$\text{with } \Sigma_q = \sum_{k=1}^{k=j-1} -\left(\frac{\partial q}{\partial y}\right)_{N,k} \times \left(\sqrt{j-k+1} - \sqrt{j-k-1}\right)$$

from (79) and (81),

$$q_{N-1,j} - \left(1 + \frac{\varepsilon\sqrt{\pi}}{\sqrt{\Delta\tau}} \times \frac{2\lambda_{N,j}}{1 + \chi r_{N,j} + \sigma_{N,j} q_{N,j}}\right) q_{N,j} = -\varepsilon\Sigma_q \tag{82}$$

For R, a similar treatment leads to

$$r_{(\text{el and } 1\le m\le N),j} = \frac{\sqrt{\Delta\tau}}{2\sqrt{\pi}}[\psi_j + \Sigma_\psi] - \frac{q_{(\text{el and } 1\le m\le N),j}}{2} \tag{83}$$

$$\text{with } \Sigma_\psi = \sum_{k=1}^{k=j-1} \psi_k \times \left(\sqrt{j-k+1} - \sqrt{j-k-1}\right)$$

The q profile may thus be obtained by an iteration procedure in which the starting q values are obtained by replacing $q_{m,j}$ by $q_{m,j-1}$ in the denominator of Eq. (30), $q_{N,j}$ by $q_{N,j-1}$ in the denominator of Eq. (81) and in Eq. (77) as well as $r_{m,j}$ by $r_{m,j-1}$, $\lambda_{m,j}$ by $\lambda_{m,j-1}$, $\sigma_{m,j}$ by $\sigma_{m,j-1}$ in Eq. (30), $r_{N,j}$ by $r_{N,j-1}$, $\lambda_{N,j}$ by $\lambda_{N,j-1}$, $\sigma_{N,j}$ by $\sigma_{N,j-1}$ in Eq. (35). The qs thus obey a system of linear equations consisting of an equation relating $q_{\mathrm{el},j}$ and $q_{1,j}$, $N-1$ equations relating $q_{m+1,j}$, $q_{m,j}$, and $q_{m-1,j}$ (from $m = 1$ to $N-1$), and one equation

relating $q_{N-1,j}$ and $q_{N,j}$. Application of the Gauss method thus allows the determination of all the $q_{(\text{el and } 1\leq m\leq N),j}$ and, from them, of $\psi_j = (q_{\text{el},j} - q_{1,j})/\varepsilon_0$ and $(\partial q/\partial y)_{N,j}$ and therefore of Σ_ψ and Σ_q. These values are then used to obtain $r_{(\text{el and } 1\leq m\leq N),j}$ from Eq. (83).

$b_{(\text{el and } 1\leq m\leq N),j}$ and $bh_{(\text{el and } 1\leq m\leq N),j}$ are then derived from $r_{(\text{el and } 1\leq m\leq N),j}$, thus allowing the calculation of the pH and, from it, of $\lambda_{(\text{el and } 1\leq m\leq N),j}$ and $\sigma_{(\text{el and } 1\leq m\leq N),j}$. All the required ingredients are thus ready for a second round of iteration. The procedure is repeated until the desired precision is reached.

An example of the application of this procedure has been described for a film made of 10 monomolecular layers of active glucose oxidase (prepared as depicted in Sect. 13.4.1) with ferrocene methanol as cosubstrate. The cyclic voltammetric data summarized in Fig. 18 show, as expected, that the effect of product inhibition increases upon decreasing the scan rate (Fig. 18 c, c', c'', c''') and the buffer concentration (compare Fig. 18a and c, c', c'', c'''). It is seen that inhibition may become so severe that it does not translate only by a hysteresis behavior but by the occurrence of a peak. Quantitatively, Fig. 18(b) shows that there is a good agreement between the experimental and simulated variations of the peak potential with the scan rate. It also shows that inhibition by acid formation is more significant than inhibition by the substrate (gluconolactone). This is also what appears in the simulation of the whole voltammograms (Fig. 18d, d', d'', d'''). The agreement between experiment and simulation is less satisfactory for the whole voltammograms. This is likely to be due to the neglect of the possible variations of the enzymatic rate constants with the ionic strength, which may vary substantially with the distance to the electrode and the electrode potential. It is indeed seen in Fig. 19 that the value of the ionic strength at the electrode surface may be quite different from its bulk value according to the potential scanned over the voltammogram. This is also true for the pH and the substrate, glucono-δ-lactone, (Fig. 19), but these variations have been taken into account in the above analysis.

13.5 Perspectives

The examples reported above show that procedures based on biomolecular recognition allow the immobilization of well-defined monomolecular layers of enzymes onto electrode surfaces. These procedures extend to the step-by-step construction of systems made of successive monomolecular layers in which each layer serves as a template for the deposition of the next layer. The same strategy allows the building of structures containing inactivated enzymes layers serving as spacers between active layers. Its versatility also permits the association of two enzymes in successive layers that can be coupled through their substrate and cosubstrate.

It is remarkable that this technology is mild enough to result in very little degradation of the enzyme activity unlike many purely chemical approaches. The stability over time of the systems thus synthesized is also worth emphasizing.

Among the biorecognition strategies that have been explored so far, namely, those based on avidin–biotin and antigen–antibody interactions, the latter is easier to handle and is more reliably applicable. This difference relates to the higher irreversibility of

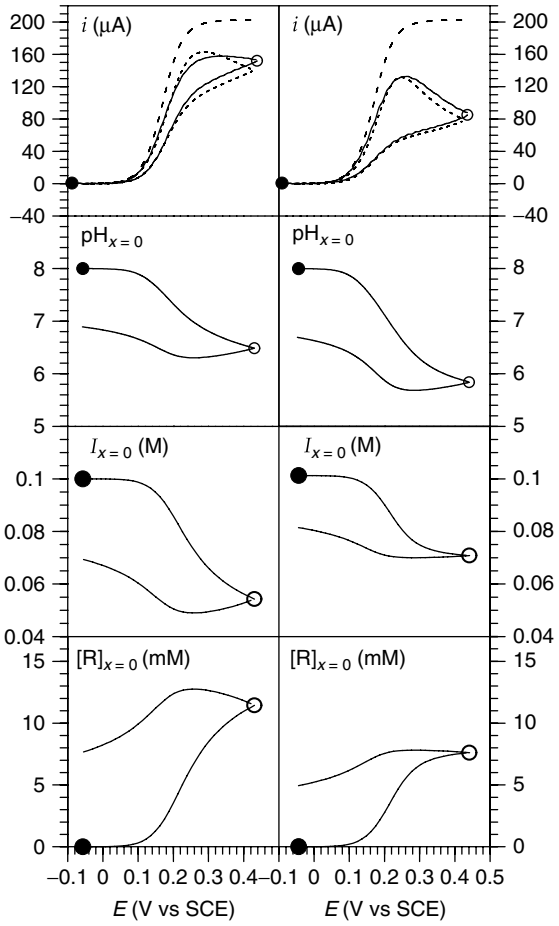


Fig. 19 Cyclic voltammetric oxidation of 0.4 M glucose by glucose oxidase at a 10-layer electrode (2.65×10^{-12} mol cm^{-2} enzyme per monolayer) in the presence of 0.4 mM ferrocene methanol. Scan rate: 0.05 V sec^{-1}. Temperature: 25 °C. pH = 8.0. Ionic strength: 0.1 M. Right: 1.48 mM NaH_2PO_4, 16.5 mM Na_2HPO_4 and 16.4 mM Na_2SO_4. Left: 32.4 mM NaH_2PO_4, 26.4 mM Na_2HPO_4. From top to bottom: cyclic voltammograms (solid lines: experimental data, dashed lines: no inhibition, dotted lines: simulation of inhibition by proton and glucono-δ-lactone production), pH, ionic strength, and glucono-δ-lactone concentration at the electrode surface. J: start of the potential scan, E: inversion of the potential scan.

the antigen–antibody interactions as compared to the avidin–biotin interaction.

Integrated systems in which not only the enzyme but also the cosubstrate is immobilized have been successfully achieved with the two technologies, so far with monomolecular layers only. In both cases, the cosubstrate is attached to the structure by means of a polyethylene glycol chain. The diffusion of the redox heads proved fast enough for not limiting the catalytic activity of the system, but the stretching ability of the chains is too limited to allow a facile access to the enzymatic site. Construction of multilayered integrated systems is a reachable objective at present, but should probably be delayed until more elastic arms and/or less extended building blocs be available in order to circumvent the current length limitations of the catalytic efficiency.

Quantitative examination of the dynamics of these systems by analysis of their time-resolved electrochemical responses is also an important objective. This is true even in the case of catalysis by a homogeneously dispersed enzyme for which a rigorous treatment has allowed the

unraveling of interesting reactivity characteristics. The analysis of the kinetics is rather straightforward for such situations, based on moderately complicated extensions of the available theory of ''catalytic currents'' in, for example, cyclic voltammetry. The same is true for monomolecular coatings with the cosubstrate in the solution. With monomolecular integrated systems, the treatment is complicated by the fact that the concentration of the cosubstrate heads is not a constant over the region of space where they shuttle electrons in between the enzyme sites and the electrode. The problem may, nevertheless, be solved with no major difficulties by injecting the flexibility and length characteristics of the attaching arm into the diffusion problem. The formulation and resolution of the diffusion-reaction problem in the case of multilayered films with a free cosubstrate is somewhat more involved but remains perfectly tractable. The most complicated case treated so far concerns such systems in the case where inhibition by-products are taken into account. However, in spite of a rather heavy formalism, the problem is solved by recourse to rather classical finite difference and integral equation procedures. When going to more and more complex systems, the real difficulty resides more in the multiplication of parameters that have to be independently known than in the formulation and calculation techniques.

The construction and analysis strategies that have been developed so far have been illustrated with a limited number of systems, mostly with application of enzymatic catalysis to sensor and synthesis as a general background. They may have obviously been applied to many other enzymatic setups within the same framework, and they may also have been useful for different purposes. A first example, which we have discussed in Sect. 13.3.2, is an application to the determination of the activation parameters of the recognition between an immobilized biomolecule and another biomolecule dispersed in the solution. Many other applications to biomolecular recognition may be thought of.

References

1. A. P. F. Turner, I. Karube, G. S. Wilson, (Eds.), *Biosensors*, Oxford University Press, Oxford, 1987
2. L. J. Blum, P. R. Coulet, (Eds.), *Biosensors, Principles and Applications*, Marcel Dekker, New York, 1991
3. H. Simon, J. Bader, H. Gunther et al., *Angew. Chem., Int. Ed. Engl.* **1985**, *24*, 539.
4. S. C. Laane, W. Pronk, M. Franssen et al., *Enzyme Microb. Technol.* **1984**, *6*, 165.
5. C. Bourdillon, R. Lortie, J. M. Laval, *Biotechnol. Bioeng.* **1988**, *31*, 553.
6. M. Frede, H. Steckhan, *Tetrahedron Lett.* **1991**, *32*, 5063.
7. J. W. Updike, P. Hicks, *Nature* **1967**, *214*, 986.
8. K. Mosbach, (Ed.), *Methods in Enzymology*, Academic Press Inc., San Diego, 1988, Vol. 137, Part D.
9. R. W. Murray, *Acc. Chem. Res.* **1980**, *13*, 135.
10. K. D. Snell, A. G. Keenan, *Chem. Soc. Rev.* **1979**, *8*, 259.
11. C. Bourdillon, J. P. Bourgeois, D. Thomas, *J. Am. Chem. Soc.* **1980**, *102*, 4231.
12. R. M. Ianniello, A. M. Yacynych, *Anal. Chem.* **1981**, *53*, 2090.
13. J. M. Laval, C. Bourdillon, J. Moiroux, *J. Am. Chem. Soc.* **1984**, *106*, 4701.
14. C. Bourdillon, M. Delamar, C. Demaille et al., *J. Electroanal. Chem.* **1992**, *336*, 113.
15. A. Heller, *Acc. Chem. Res.* **1990**, *23*, 128.
16. M. J. Eddowes, H. A. O. Hill, *J. Am. Chem. Soc.* **1979**, *101*, 7113.
17. I. Taniguchi, K. Toyosawa, H. Yamaguchi et al., *Chem. Soc., Chem. Commun.* **1982**, 1032.
18. J. Haladjian, P. Bianco, R. Pilard, *Electrochim. Acta* **1983**, *28*, 1823.
19. F. A. Armstrong, H. A. O. Hill, N. J. Walton, *Acc. Chem. Res.* **1988**, *21*, 407.

20. J. Hirst, A. Sucheta, B. A. C. Ackrell et al., *J. Am. Chem. Soc.* **1996**, *118*, 5031.
21. H. R. Pershad, J. L. C. Duff, H. A. Heering et al., *Biochemistry* **1999**, *38*, 8992.
22. Y. Degani, A. Heller, *J. Phys. Chem.* **1987**, *91*, 1285.
23. Y. Degani, A. Heller, *J. Am. Chem. Soc.* **1988**, *110*, 2615.
24. C. P. Andrieux, J.-M. Savéant, in *Molecular Design of Electrode Surfaces, Techniques of Chemistry Series* (Ed.: R. W. Murray), John Wiley and Sons, New York, 1992, pp. 207–270, Vol. 22.
25. M. Majda, in *Molecular Design of Electrode Surfaces, Techniques of Chemistry Series* (Ed.: R. W. Murray), John Wiley and Sons, New York, 1992, pp. 159–206, Vol. 22.
26. P. D. Hale, T. Inagaki, H. I. Karan et al., *J. Am. Chem. Soc.* **1989**, *111*, 3482.
27. R. Rajagopalan, A. Aoki, A. Heller, *J. Phys. Chem.* **1996**, *100*, 3719.
28. W. J. Albery, P. Bartlett, D. Craston, *J. Electroanal. Chem.* **1985**, *194*, 223.
29. J. L. Kawagoe, D. E. Niehau, R. M. Wightman, *Anal. Chem.* **1991**, *63*, 2961.
30. N. C. Foulds, C. R. Lowe, *J. Chem. Soc., Faraday Trans.* **1986**, 1259.
31. G. Fortier, D. Belanger, *Biotechnol. Bioeng.* **1991**, *37*, 854.
32. N. C. Foulds, C. R. Lowe, *Anal. Chem.* **1988**, *60*, 2473.
33. S. Cosnier, *Electroanalysis* **1997**, *9*, 894.
34. S. E. Wolowacz, B. F. Y. Yon Hin, C. R. Lowe, *Anal. Chem.* **1992**, *64*, 1541.
35. C. Bourdillon, C. Demaille, J. Moiroux et al., *J. Am. Chem. Soc.* **1993**, *115*, 2.
36. C. Bourdillon, C. Demaille, J. Moiroux et al., *Acc. Chem. Res.* **1996**, *29*, 529.
37. C. P. Andrieux, J.-M. Savéant, *Electrochemical Reactions in Investigations of Rates and Mechanisms, Techniques of Chemistry Series* (Ed.: C. F. Bernasconi), John Wiley and Sons, New York, 1992, 305–390, Vol. VI/4E, Part 2.
38. J.-M. Savéant, E. Vianello, in *Advances in Polarography* (Ed.: I. S. Longmuir), Pergamon Press, London, 1960, pp. 367–374, Vol. 2.
39. A. E. G. Cass, G. Davis, I. G. D. Francis et al., *Anal. Chem.* **1984**, *56*, 667.
40. M. J. Green, H. A. O. Hill, *J. Chem. Soc., Faraday Trans. I* **1986**, *82*, 667.
41. S. Marx-Tibbon, E. Katz, I. Willner, *J. Am. Chem. Soc.* **1995**, *117*, 9925.
42. P. W. Atkins, *Physical Chemistry*, Oxford University Press, Oxford, 1998, p. 784.
43. R. F. Williams, T. C. Bruice, *J. Am. Chem. Soc.* **1976**, *98*, 7752.
44. R. F. Williams, S. S. Shinkai, T. C. Bruice, *J. Am. Chem. Soc.* **1977**, *99*, 921.
45. G. Eberlein, T. C. Bruice, *J. Am. Chem. Soc.* **1982**, *104*, 1449.
46. M. T. Stankovich, L. M. Shopfer, V. Massey, *J. Biol. Chem.* **1978**, *253*, 4971.
47. S. Ghisla, V. Massey, *Eur. J. Biochem.* **1989**, *181*, 1.
48. M. K. Weibel, H. J. Bright, *J. Biol. Chem.* **1971**, *246*, 2734.
49. R. A. Marcus, N. Sutin, *Biophys. Biochim. Acta* **1985**, *811*, 265.
50. J.-M. Savéant, Single electron transfer and nucleophilic substitution, in *Advances in Physical Organic Chemistry* (Ed.: D. Bethel), Academic Press, New York, 1990, pp. 1–130, Vol. 26.
51. A. De Baetselier, A. Vasavada, P. Dohet et al., *Biotechnology* **1991**, *9*, 559.
52. H. J. Hecht, H. M. Kalisz, J. Hendle et al., *J. Mol. Biol.* **1993**, *229*, 153.
53. P. Alzari, N. Anicet, C. Bourdillon et al., *J. Am. Chem. Soc.* **1996**, *118*, 6788.
54. A. Szucs, G. D. Hitchens, J. O. Bockris, *J. Electrochem. Soc.* **1989**, *136*, 3748.
55. R. M. Ianiello, A. M. Yacynych, *Anal. Chem.* **1981**, *53*, 2090.
56. S. V. Sasso, R. J. Pierce, R. Walla et al., *Anal. Chem.* **1990**, *62*, 1111.
57. C. Bourdillon, C. Demaille, J. Guéris et al., *J. Am. Chem. Soc.* **1993**, *115*, 12264.
58. Y. Kyusik, E. Kobatake, M.-L. Laukkanen et al., *Anal. Chem.* **1998**, *70*, 260.
59. Y. Okahata, M. Kawase, K. Niikura et al., *Anal. Chem.* **1998**, *70*, 1288.
60. H. Nygren, *Biophys. Chem.* **1994**, *52*, 45.
61. E. Gizeli, M. Liley, R. L. Lowe et al., *Anal. Chem.* **1997**, *69*, 4808.
62. R. Karlson, A. Michaelsson, L. Mattsson, *J. Immunol. Methods* **1991**, *145*, 229.
63. C. E. H. Berger, T. A. M. Benmer, R. P. H. Kooyman et al., *Anal. Chem.* **1998**, *70*, 703.
64. P. Schuck, A. P. Minton, *Anal. Biochem.* **1996**, *240*, 262.
65. P. Schuck, *Biophys. J.* **1996**, *70*, 1230.
66. P. Schuck, A. P. Minton, *TIBS* **1996**, 458.
67. P. Schuck, *Curr. Opin. Biotechnol.* **1997**, *8*, 498.
68. C. Bourdillon, C. Demaille, J. Moiroux et al., *J. Am. Chem. Soc.* **1999**, *121*, 2401.
69. H. Nygren, M. Stenberg, *Immunology* **1989**, *66*, 321.

70. R. W. Glaser, *Anal. Biochem.* **1993**, *213*, 152.
71. V. G. Levich, *Acta Phys. Chim. USSR* **1942**, *17*, 257.
72. I. Bhugun, I. F. C. Anson, *J. Electroanal. Chem.* **1997**, *439*, 1.
73. J.-M. Savéant, E. Vianello, *Electrochim. Acta* **1963**, *8*, 905.
74. C. P. Andrieux, J.-M. Savéant, in *Electrochemical Reactions in Investigations of Rates and Mechanisms of Reactions, Techniques in Chemistry* (Ed.: C. Bernasconi), Wiley, New York, 1986, pp. 305–390, Vol. 6, 4/E, Part 2.
75. C. P. Andrieux, J.-M. Savéant, in *Catalysis at Redox Polymer Coated Electrodes in Molecular Design of Electrode Surfaces, Techniques in Chemistry* (Ed.: R. W. Murray), Wiley, New York, 1992, pp. 207–270, Vol. 22.
76. P. Delahay, *Double Layer and Electrode Kinetics*, Interscience, New York, 1965
77. N. Anicet, A. Anne, J. Moiroux et al., *J. Am. Chem. Soc.* **1998**, *120*, 7116.
78. N. M. Green, *Biochem. J.* **1966**, *101*, 774.
79. N. M. Green, Avidin in *Advances in Protein Chemistry* (Ed.: C. B. Anfisen, J. T. Edsall, F. M. Richards), Academic Press, New York, 1975, pp. 85–133, Vol. 29.
80. M. L. Jones, G. Kurzban, *Biochemistry* **1995**, *34*, 11750.
81. P. Pantano, T. H. Morton, W. G. Kuhr, *J. Am. Chem. Soc.* **1991**, *113*, 1832.
82. P. Pantano, W. G. Kuhr, *Anal. Chem.* **1993**, *65*, 623.
83. N. Dontha, W. B. Nowall, W. G. Kuhr, *Anal. Chem.* **1997**, *69*, 2619.
84. A. Anne, B. Blanc, J. Moiroux et al., *Langmuir* **1998**, *14*, 2368.
85. N. Anicet, A. Anne, C. Bourdillon, C. Demaille, J. Moiroux, J.-M. Savéant, *Faraday Discuss. Chem. Soc.* in press.
86. A. Anne, J. Moiroux, *Macromolecules* **1999**, *32*, 5829.
87. A. Anne, C. Demaille, J. Moiroux, *J. Am. Chem. Soc.* **1999**, *121*, 10379.
88. N. Anicet, C. Bourdillon, J. Moiroux et al., *J. Phys. Chem. B* **1998**, *102*, 9844.
89. N. Anicet, C. Bourdillon, J. Moiroux et al., *Langmuir* **1999**, *15*, 6527.
90. C. Bourdillon, C. Demaille, J. Moiroux et al., *J. Am. Chem. Soc.* **1994**, *116*, 10328.
91. C. Bourdillon, C. Demaille, J. Moiroux et al., *J. Am. Chem. Soc.* **1995**, *117*, 11499.
92. C. Bourdillon, C. Demaille, J. Moiroux et al., *J. Chem. Phys. B* **1999**, *103*, 8532.